Metamaterials Handbook

Theory and Phenomena of Metamaterials

Edited by

Filippo Capolino

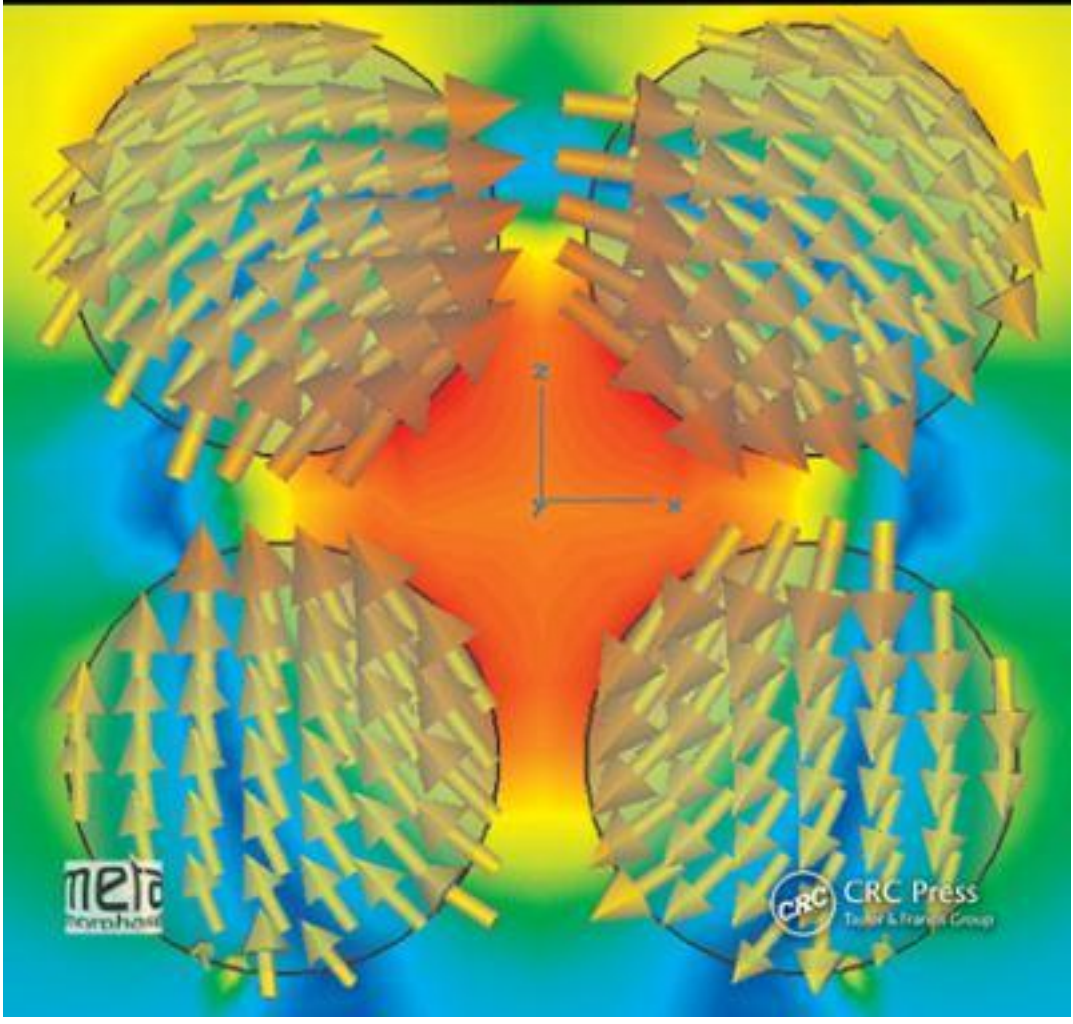

CRC Press

Metamaterials Handbook

Theory and Phenomena of Metamaterials

Edited by
Filippo Capolino

CRC Press
Taylor & Francis Group
Boca Raton London New York

CRC Press is an imprint of the
Taylor & Francis Group, an **informa** business

CRC Press
Taylor & Francis Group
6000 Broken Sound Parkway NW, Suite 300
Boca Raton, FL 33487-2742

Printed in the United States of America on acid-free paper
10 9 8 7 6 5 4 3 2 1

International Standard Book Number: 978-1-4200-5425-5 (Hardback)

Library of Congress Cataloging-in-Publication Data

Theory and phenomena of metamaterials / editor, Filippo Capolino.
p. cm.
"A CRC title."
Includes bibliographical references and index.
ISBN 978-1-4200-5425-5 (alk. paper)
1. Electronic apparatus and appliances--Materials. 2. Metamaterials. I. Capolino, Filippo.

TK7870.T47 2009
621.381--dc22 2008054553

Visit the Taylor & Francis Web site at
http://www.taylorandfrancis.com

and the CRC Press Web site at
http://www.crcpress.com

Dedication

. . .to my little jewel Mira

Contents

Part IV Artificial Chiral, Bianisotropic Media, and Quasicrystals

Part V Transmission-Line-Based Metamaterials

Part VI Artificial Surfaces

Part VII Tunable and Nonlinear Metamaterials

Foreword

This handbook is intended to be a guide for researchers in universities and industries and for designers who wish to use artificial materials for electronic devices in the whole frequency spectrum, from megahertz to optical frequencies.

Artificial materials, often called metamaterials, are artificial electromagnetic media whose physical properties are engineered by assembling microscopic and nanoscopic structures in unusual combinations. The study of these materials breaks the traditional frontiers and brings together many disciplines such as physics and microfabrication; electromagnetic theory and computational methods; optics and microwaves; and nanotechnology and nanochemistry. Their possible applications range from electronics and telecommunications to sensing, medical instrumentation, and data storage. Therefore, research in the field of artificial materials requires a multifaceted understanding of the fundamentals of science as well as the scientific and technological needs of potential applications.

The topics contained in this handbook cover the major strands: theory, modeling and design, application in practical devices, fabrication, characterization, and measurement. The strategic objectives of developing new artificial materials require close cooperation and cross-fertilization of the research in each subarea.

We, thus, felt the need to organize in two volumes all possible aspects of the results of various years of research in this exciting field. A few books on metamaterials have been published in these years but we believe that this handbook has a different aim. Topics are presented here in a concise manner, with many references to details published elsewhere, covering most of the areas where artificial materials have been developed to provide a reference guide in this difficult and broad multidisciplinary field. Most of the authors included in this handbook were associated with the European Network of Excellence "Metamorphose" (METAMaterials Organised for Radio, millimeter wave, and PHOtonic Superlattice Engineering), and this work is a result of a coordinated integration of the various experts in this network. Metamorphose gave us a rare opportunity to collect a large variety of disciplines in two volumes. We would like to thank the European Project Officer Anne de Baas, who, with professionalism and dedication, stimulated our work while also providing valid suggestions. Other selected, internationally renowned experts in the field of metamaterials have also contributed as authors.

The Editor

Filippo Capolino, University of California Irvine (previously with the University of Siena)

Preface

I am very thankful to all the authors who have contributed these informative chapters and to my Metamorphose* friends and colleagues for the fun and stimulating time we spent together as professionals. I am particularly grateful to the advisory board whose work, encouragement, and advice have been fundamental. When I proposed the idea of writing this handbook, a book that summarizes the various topics divided into many related chapters, also indicating more detailed sources to the interested reader to my Metamorphose friends and colleagues, they were all enthusiastic to contribute one or more chapters each. Then I invited some of the best experts in the field of metamaterials outside Metamorphose. I have invested a large amount of time and energy in pooling together the people and information collected in this project.

Since the aim of the two-volume handbook is to provide a reference guide that summarizes the state-of-the-art in the field of electromagnetic artificial materials, often called metamaterials, I have waited for the field to become mature, to a certain degree, before finalizing the project. In this handbook, the term "metamaterials" is used in a broad sense. With this term, we denote general composite materials made of specific micro- or nanoscatterers, whose ensemble exhibits the peculiar electromagnetic properties shown here. Some topics related to photonic or electromagnetic crystals are also summarized here because of their use in modern electrical engineering, and because their electromagnetic performance is due to the collective interaction of the micro- or nanoconstituents via the hosting element. According to many researchers, it is required that periodic metamaterials have a periodicity length much smaller than the operating wavelength. However, the boundary between metamaterials and other artificial materials based on the ratio of the size of the constitutive cells and the operating wavelength is not clearly defined, especially for the state-of-the-art metamaterials at optical frequencies where fabrication technology and power losses still represent the major challenge. Researchers have suggested different definitions for the term "metamaterials"; an example of a broad vision can be found in Refs. [1,2]. However, the aim of this handbook is not to propagate a specific definition but to provide a reference guide for researchers who are interested in the particular properties of composite artificial materials.

I hope that the efforts that have gone into writing this handbook will be useful for many others.

Filippo Capolino
University of California, Irvine, California

* Metamorphose is the FP6 Network of Excellence of metamaterials, "METAMaterials Organised for Radio, millimeter wave and PHOtonic Superlattice Engineering", funded by the European Union, FP6, contract number FP6/NMP3CT-2004-500252.

References

1. A. Lakhtakia and T.G. Mackay, Meet the metamaterials, *OSA Optics and Photonics News*, 18(1): 32–39, January 2007.
2. A. Sihvola, Metamaterials in electromagnetic, *Metamaterials*, 1(1): 2–11, March 2007.

Editor

Filippo Capolino was born in Florence, Italy, in 1967. He received his Laurea degree (*cum laude*) and his PhD in electrical engineering from the University of Florence, Florence, Italy, in 1993 and 1997, respectively.

He is currently with the Department of Electrical Engineering and Computer Science of the University of California, Irvine, California. He has been with the Department of Information Engineering of the University of Siena, Siena, Italy, since 2002.

From 1997 to 1998, he was a Fulbright research visitor with the Department of Aerospace and Mechanical Engineering, Boston University, Boston, Massachusetts; from 1998 to 1999 he continued his research there with a grant from the Italian National Research Council. From 2000 to 2001 and again in 2006, he was a research assistant visiting professor with the Department of Electrical and Computer Engineering, University of Houston, Houston, Texas, where he had also been an adjunct assistant professor for many years. In November to December 2003, he was an invited assistant professor at the Institut Fresnel, Marseille, France. He has been a member of the European Network of Excellence "Metamorphose" on metamaterials; and he has also been the coordinator of the European Union Doctoral Programmes on Metamaterials since 2004.

His research interests include metamaterials and their applications in sensors, antennas, and waveguides; micro- and nanotechnology; sensors in both microwave and optical ranges; wireless and telecommunications systems; and theoretical and applied electromagnetics in general.

Dr. Capolino was awarded with the Raj Mittra Travel Grant for senior scientists in 2006, and the "Barzilai" prize for the best paper at the National Italian Congress of Electromagnetism (XI RiNEm) in 1996. He received the R.W. P. King Prize Paper Award from the IEEE Antennas and Propagation Society for the Best Paper of the Year 2000 by an author under 36. He is also a coauthor of the "Fast Breaking Papers, October 2007" in electrical engineering and computer science, about metamaterials (a paper that had the highest percentage increase in citations in essential science indicators). One of his PhD students, A. Della Villa, was awarded with the IEEE Antennas and Propagation Society Graduate Research Award for 2007–2008. In 2002–2008, he has served as an associate editor for the *IEEE Transactions on Antennas and Propagation*. He is a founder and an editor of the new journal *Metamaterials*, by Elsevier, since 2007.

Advisory Board

Stefan Maier holds a chair in nanophotonics in the physics department of Imperial College, London. Originally from southern Germany, he spent his first years at Technische Universitaet Muenchen, Munich, Germany, before moving to Pasadena where he obtained his PhD in applied physics at the California Institute of Technology (Caltech, Pasadena, California) in 2003, working on demonstrations of metal nanoparticle plasmon waveguides in the group with Harry Atwater. Subsequently, he worked as a postdoctoral scholar with Oskar Painter (also Caltech) on fiber-coupled near-infrared plasmon waveguides. In 2004, he took up a lectureship in physics at the University of Bath in the United Kingdom, and advanced to reader in 2006. During this time, he focused on, among other topics, spoof surface plasmon polariton propagation on plasmonic metamaterials in the terahertz regime. He joined the physics department of Imperial College in November 2007, where he is heading a wide range of new efforts in plasmonics and metamaterials. Apart from organizing many conference symposia in plasmonics and nanophotonics over the last years, he currently serves on the editorial board of *Metamaterials*.

Ekmel Ozbay received his BS in electrical engineering from the Middle East Technical University, Ankara, Turkey in 1983. He received his MS and PhD from Stanford University, Stanford, California, in electrical engineering, in 1989 and 1992, respectively. From 1992 to 1994, he worked as a scientist in DOE Ames National Laboratory in Iowa State University (Ames, Iowa) in the area of photonic band gap materials. He joined Bilkent University (Ankara, Turkey) in 1995, where he is currently a full professor in electrical and electronics engineering department and physics department. He is the director of Bilkent University nanotechnology research center. His research in Bilkent involves nanophotonics, metamaterials, MOCVD growth and fabrication of GaN-based electronic and photonic devices, photonic crystals, and high-speed optoelectronics. He is the recipient of the 1997 Adolph Lomb Medal of Optical Society of America and 2005 European Union Descartes Science Award. He was a topical editor for *Optics Letters* during 2002–2008. He serves as an editor for *Photonics and Nanostructures: Fundamental Applications* since 2006. He has published 205 SCI journal papers, and these papers have received more than 4350 SCI citations.

Ari Sihvola received his degree of Doctor of Technology in 1987 from the Helsinki University of Technology (TKK), Espoo, Finland. Besides working for TKK and the Academy of Finland, he was visiting engineer in the Research Laboratory of Electronics of the Massachusetts Institute of Technology, Cambridge, Massachusetts, in 1985–1986. In 1990–1991, he worked as a visiting scientist at the Pennsylvania State University, State College, Pennsylvania. In 1996, he was visiting scientist at the Lund University, Lund, Sweden. He was visiting professor at the Electromagnetics and Acoustics Laboratory of the Swiss Federal Institute of Technology, Lausanne, Switzerland (academic year 2000–2001), and in the University of Paris 11, Orsay, France (June 2008). His research interests include waves and fields in electromagnetics, modeling of complex materials, and remote sensing and radar applications. Presently, he is academy professor at TKK.

Sergei A. Tretyakov received the candidate of sciences (PhD) diploma of engineer-physicist and the doctor of sciences degree (all in radiophysics) from the St. Petersburg State Technical University, St. Petersburg, Russia, in 1980, 1987, and 1995, respectively. From 1980 to 2000, he was with the radiophysics department of the St. Petersburg State Technical University. Presently, he is professor of radio engineering at the Department of Radio Science and Engineering, Helsinki University of Technology (TKK), Espoo, Finland, and the president of the Virtual Institute for Artificial Electromagnetic Materials and Metamaterials (Metamorphose VI, Belgium). He has been the coordinator of the European Union Network of Excellence Metamorphose, 2004–2008. His main scientific interests are electromagnetic field theory, complex media electromagnetics, and microwave engineering. Professor Tretyakov served as chairman of the St. Petersburg IEEE ED/MTT/AP chapter from 1995 to 1998.

J. (Yiannis) C. Vardaxoglou is professor of wireless communications and head of the electronic and electrical engineering department. He received his BSc in mathematical physics in 1981 from the University of Kent at Canterbury, United Kingdom, and he researched toward his PhD in electronics, which he received in 1985, at the same institution. He joined Loughborough University of Technology (Loughborough, United Kingdom) in 1988 as a lecturer, was promoted to senior lecturer in January 1992, and in 1998 he was awarded a personal chair. He established the Wireless Communications Research Group and heads the Centre for Mobile Communications Research, both at Loughborough. He has pioneered research and development into frequency-selective surfaces (FSS), metamaterials, and low-SAR antennas for mobile telephony and has commercially exploited his innovations in wireless communications applications. He has served as a consultant to various industries, holds three patents, and is the technical director of Antrum Ltd., U.K. He has published over 160 refereed journal and conference proceeding papers, and has written several book chapters and a book on FSS. He has served as chairman on several international conferences and committees for the IET and IEEE.

Contributors

Nicólaos G. Alexopóulos
The Henry Samueli School of Engineering
University of California Irvine
Irvine, California

and

Broadcom Corporation
Irvine, California

Andrea Alù
Department of Electrical and Computer Engineering
University of Texas, Austin
Austin, Texas

Koray Aydin
Nanotechnology Research Center
Department of Physics and Department of Electrical and Electronics Engineering
Bilkent University
Bilkent, Turkey

Paolo Baccarelli
Department of Electronic Engineering
Sapienza University of Rome
Rome, Italy

Paolo Burghignoli
Department of Electronic Engineering
Sapienza University of Rome
Rome, Italy

Filippo Capolino
Department of Electrical Engineering and Computer Science
University of California Irvine
Irvine, California

Alford Chauraya
Department of Electronic and Electrical Engineering
Loughborough University
Loughborough, United Kingdom

Ji Chen
Department of Electrical and Computer Engineering
University of Houston
Houston, Texas

Harry F. Contopanagos
Institute of Microelectronics
National Center for Scientific Research "Demokritos"
Athens, Greece

Christophe Craeye
Communications and Remote Sensing Laboratory
Université Catholique de Louvain
Louvain-la-Neuve, Belgium

Alessandro Della Villa
Department of Information Engineering
University of Siena
Siena, Italy

Victor Dmitriev
Department of Electrical Engineering
Federal University of Pará
Belém, Brazil

E. N. Economou
Institute of Electronic Structure and Laser
Foundation for Research and Technology Hellas
Crete, Greece

and

Department of Physics
University of Crete
Crete, Greece

George V. Eleftheriades
The Edward S. Rogers, Sr. Department of Electrical and Computer Engineering
University of Toronto
Toronto, Ontario, Canada

Nader Engheta
Department of Electrical and Systems Engineering
University of Pennsylvania
Philadelphia, Pennsylvania

Stefan Enoch
CNRS
Fresnel Institute
Marseille, France

Islam A. Eshrah
Department of Electronics and Communication Engineering
Cairo University
Giza, Egypt

Alexandros P. Feresidis
Department of Electronic and Electrical Engineering
Loughborough University
Loughborough, United Kingdom

Vincenzo Galdi
Department of Engineering
University of Sannio
Benevento, Italy

Alessandro Galli
Department of Electronic Engineering
Sapienza University of Rome
Rome, Italy

Allen W. Glisson
Department of Electrical Engineering
The University of Mississippi
University, Mississippi

Maxim Gorkunov
Institute of Crystallography
Russian Academy of Sciences
Moscow, Russia

George Goussetis
School of Engineering and Physical Sciences
Heriot-Watt University
Edinburgh, Scotland, United Kingdom

Natalia Grigorieva
Department of Physical Electronics and Technology
St. Petersburg Electrotechnical University
St. Petersburg, Russia

Ashwin K. Iyer
The Edward S. Rogers, Sr. Department of Electrical and Computer Engineering
University of Toronto
Toronto, Ontario, Canada

David R. Jackson
University of Houston
Houston, Texas

Maria Kafesaki
Institute of Electronic Structure and Laser
Foundation for Research and Technology Hellas
Crete, Greece

Boris Kalinikos
Department of Physical Electronics and Technology
St. Petersburg Electrotechnical University
St. Petersburg, Russia

Ahmed A. Kishk
Department of Electrical Engineering
The University of Mississippi
University, Mississippi

Th. Koschny
Ames Laboratory and Department of Physics and Astronomy
Iowa State University
Ames, Iowa

and

Institute of Electronic Structure and Laser
Foundation for Research and Technology Hellas
Crete, Greece

Mikhail Kostylev
School of Physics
University of Western Australia
Perth, Western Australia, Australia

Chryssoula A. Kyriazidou
The Henry Samueli School of Engineering
University of California Irvine
Irvine, California

and

Broadcom Corporation
Irvine, California

Paolo Lampariello
Department of Electronic Engineering
Sapienza University of Rome
Rome, Italy

Mikhail Lapine
Department of Physics
University of Osnabrueck
Osnabrueck, Germany

Richard Lee
Department of Electronic and Electrical Engineering
Loughborough University
Loughborough, United Kingdom

Ismo V. Lindell
Department of Radio Science and Engineering
Helsinki University of Technology
Espoo, Finland

Giampiero Lovat
Department of Electrical Engineering
Sapienza University of Rome
Rome, Italy

Ricardo Marqués
Department of Electronics and Electromagnetism
University of Sevilla
Seville, Spain

Ferran Martín
Department d' Enginyeria Electrònica
Universidad Autónoma de Barcelona
Barcelona, Spain

I. S. Nefedov
Department of Radio Science and Engineering/SMARAD Center of Excellence
Helsinki University of Technology
Espoo, Finland

Mikhail Odit
Department of Microelectronics and Radio Engineering
St. Petersburg Electrotechnical University
St. Petersburg, Russia

Ekmel Ozbay
Nanotechnology Research Center
Department of Physics and Department of Electrical and Electronics Engineering
Bilkent University
Bilkent, Turkey

Chinthana Panagamuwa
Department of Electronic and Electrical Engineering
Loughborough University
Loughborough, United Kingdom

Simone Paulotto
Department of Electronic Engineering
Sapienza University of Rome
Rome, Italy

Rui Qiang
Department of Electrical and Computer Engineering
University of Houston
Houston, Texas

Cheng-Wei Qiu
Department of Electrical and Computer Engineering
National University of Singapore
Singapore

A. Radkovskaya
Faculty of Physics
Lomonosov Moscow State University
Moscow, Russia

Xavier Radu
Communications and Remote Sensing Laboratory
Université Catholique de Louvain
Louvain-la-Neuve, Belgium

P. Russer
Department of Electrical Engineering
Munich University of Technology
Munich, Germany

Alex G. Schuchinsky
The Institute of Electronics, Communications and Information Technology
Queens University of Belfast
Belfast, United Kingdom

E. Shamonina
Erlangen Graduate School in Advanced Optical Technologies
University of Erlangen-Nuremberg
Erlangen, Germany

Ari Sihvola
Department of Radio Science and Engineering
Helsinki University of Technology
Espoo, Finland

Mário G. Silveirinha
Department of Electrical Engineering
University of Coimbra
Coimbra, Portugal

Constantin R. Simovski
Department of Radio Science and Engineering
Helsinki University of Technology
Espoo, Finland

L. Solymar
Department of Electrical and Electronic Engineering
Imperial College
London, United Kingdom

C. M. Soukoulis
Ames Laboratory and Department of Physics and Astronomy
Iowa State University
Ames, Iowa

and

Institute of Electronic Structure and Laser
Foundation for Research and Technology Hellas
Crete, Greece

and

Department of Materials Science and Technology
University of Crete
Crete, Greece

Andrei Stashkevich
Laboratory of Mechanic and Thermodynamic Properties of Materials
Galileo Institute
University of Paris
Paris, France

Sergiy Steshenko
Department of Information Engineering
University of Siena
Siena, Italy

O. Sydoruk
Erlangen Graduate School in Advanced Optical Technologies
University of Erlangen-Nuremberg
Erlangen, Germany

Gérard Tayeb
CNRS
Fresnel Institute
Marseille, France

Sergei A. Tretyakov
Department of Radio Science and Engineering
Helsinki University of Technology
Espoo, Finland

Guido Valerio
Department of Electronic Engineering
Sapienza University of Rome
Rome, Italy

Andrea Vallecchi
Department of Information Engineering
University of Siena
Siena, Italy

J. (Yiannis) C. Vardaxoglou
Department of Electronic and Electrical Engineering
Loughborough University
Loughborough, United Kingdom

Irina Vendik
Department of Microelectronics and Radio Engineering
St. Petersburg Electrotechnical University
St. Petersburg, Russia

Orest G. Vendik
Department of Physical Electronics and Technology
St. Petersburg Electrotechnical University
St. Petersburg, Russia

A. J. Viitanen
Department of Radio Science and Engineering
Helsinki University of Technology
Espoo, Finland

Donald R. Wilton
University of Houston
Houston, Texas

M. C. K. Wiltshire
Imaging Sciences Department
Imperial College London
London, United Kingdom

Alexander B. Yakovlev
Department of Electrical Engineering
The University of Mississippi
University, Mississippi

Fan Yang
Department of Electrical Engineering
The University of Mississippi
Oxford, Mississippi

M. Zedler
The Edward S. Rogers, Sr. Department of Electrical and Computer Engineering
University of Toronto
Toronto, Ontorio, Canada

O. Zhuromskyy
Institute of Optics
Information and Photonics
University of Erlangen-Nuremberg
Erlangen, Germany

Saïd Zouhdi
Laboratoire de Génie Electrique de Paris
Université Paris
France

Svetlana P. Zubko
Department of Physical Electronics and Technology
St. Petersburg Electrotechnical University
St. Petersburg, Russia

I

General Concepts

1

Historical Notes on Metamaterials

Constantin R. Simovski
Helsinki University of Technology

Sergei A. Tretyakov
Helsinki University of Technology

1.1 Introduction

The modern history of "electromagnetic metamaterials," often called simply as "metamaterials" (MTM) can probably be counted from the seminal paper [1] where an ambitious goal to create a so-called perfect lens was put forward by J. B. Pendry. For such a "lens" one needs to design an artificial medium which would possess specific properties, not observed in natural materials. Namely, the perfect lens material should be a medium with both negative permittivity and permeability in the same frequency range. In fact, the light focusing in the planar lens studied in [1] was previously considered by V. G. Veselago [2]. This review paper was devoted to phenomena that would occur in strange "left-handed" media (media with $\varepsilon < 0$ and $\mu < 0$). Such media did not exist at that time but could be imagined as possible "composites of the future." Notice, that V. G. Veselago in the period before the paper [2] had believed that such media could be found among homogenous magnetic semiconductors fabricated chemically. However, no magnetic semiconductors with doubly negative material parameters had been obtained and this failure was reported in [2]. In [3,4] it was emphasized that such media should be strongly dispersive (resonant) composites. In [2] the inverse effect in the Cerenkov radiation of a charge moving through a left-handed medium, the inversion of the Doppler shift in it and the "negative refraction" of optical rays at its interface were reviewed. It was pointed out that a slab under the condition $\varepsilon = \mu = -1$ will focus a diverging light beam. Under the condition $d = 2D$ where d is the thickness of the left-handed slab and D is the distance from the slab interface to the source, the light will be focused at the point distanced by D from the back interface without aberrations and reflections. However, V. G. Veselago missed in this work the great opportunity indicated by J. B. Pendry: the perfectness of this pseudo-lens,* i.e., the infinitesimal size of the focal spot corresponding to a point source.

* It is not a lens in its optical meaning since it does not focus a parallel light beam. It focuses only diverging beams. V. G. Veselago suggested the term pseudo-lens in [5].

The perfect lens described in [1] is not attainable as any other perfectness [5]. But it is an exciting task to approach to this perfect image, i.e., to obtain a subwavelength image in the far zone of a source. It has been known since works of Lord Rayleigh that the diffraction imposes a limit to the focal spot size. This limit is the main restriction in what concerns the spatial resolution of two closely positioned point sources or the imaging of small-scale details in complex sources [6]. The best possible resolution and the smallest size of the focal spot offered by lenses* is approximately equal to 0.4λ. This result for the focal spot diameter is still considered as not subwavelength imaging and is allowed by the diffraction limit. It practically corresponds to the focusing in a so-called solid immersion lens [7] or in dielectric spheres of certain optical size† [8].

The diffraction limit, however, implies that the image is created only by propagating waves, and the subwavelength information contained in "evanescent waves," exponentially decaying with the distance from the field source, is lost in the image domain. In the so-called near-field optical microscopy the spatial resolution is not restricted by the diffraction limit since the probe in this technique detects not the wave field components but also the near field close to the surface of the source (object). The image is created, usually, after scanning the probe (tip) over the surface. From the theoretical point of view the subwavelength details of the object are retained since the evanescent waves produced by these details are detected by the probe. The near-field scanning optical microscopes (NSOM) were invented by G. Binnig and H. Rohrer [9].‡ The evanescent waves used in this high-resolution microscopy exist only in the near zone of sources. Practically, they are detectable by NSOM at the distances of the order of 10 nm and less [10,11].

Studying the pseudo-lens design suggested by V. G. Veselago, J. B. Pendry revealed the mechanism that allows one to redistribute the evanescent (near-zone) fields in the space so that the evanescent waves are transported far from the source and take part in the formation of the far-field image. In this way one can theoretically beat the diffraction limit. This sounded exciting for specialists in the photolithography, recording and reading optical information and for experts in all domains where the near-field scanning technique cannot be practically used.

The ideas of [1] gave a strong impulse to the development of artificial materials with doubly negative constitutive parameters. In fact, theoretical papers seldom evoke such consequences. The situation with this publication was so special because the publication of [1] resonated with the simultaneous issuing of paper [4]. In this paper the first design of a structure with $\varepsilon < 0$ and $\mu < 0$ was suggested and numerically studied.§ These two seminal publications were germs of the new tree in the garden of the electromagnetic science: the electromagnetics of metamaterials. The term "metamaterials" was introduced and established in 2002–2004 in interdisciplinary scientific conferences for radio and optical engineers (such as *Progress in Electromagnetics Research, Bianisotropics*, and others). The modern concept of metamaterials is discussed below.

The electromagnetics of MTM is now a whole branch of modern science. It rose not only from pioneering works [1–4]. A long period of accumulation of knowledge resulted recently in a large number of publications on MTM. A chapter on metamaterials appeared in a monograph published in 2003 [12]. Three monographs totally devoted to metamaterials [13–15] appeared in a very short time (2 years) after establishing the appropriate terminology, and more are coming to the market.

Fortunately, the needed knowledge was accumulated by rather few specialists having enough broad vision over the electromagnetic science, while many of the modern engineers are specialists perhaps

* Following to the Rayleigh criteria.

† The result of the focusing in the second case is narrow but long focal spots called photonic nanojets.

‡ This invention together with the tunnel microscope developed in the same scientific group was awarded the Nobel Prize in 1986. More knowledge on the near-field microscopy can be obtained from [10,11].

§ Earlier results for doubly negative composites than reported in [4] are possible, but for the instance are unknown.

experienced and skillful but in a rather narrow domain. As a result, the specialists that developed concepts of negative refraction, artificial dielectrics, artificial magnetics, and artificial plasma are often considered as founders of these directions in applied electromagnetics. This is not a fruitful point of view. When we attribute artificial magnetism only to [16] and artificial plasma only to [17]* we behave as if there were nothing known about these subjects before. It is not only odd to ignore previous works, it is not instructive. The theoretical and practical potential of the concept of metamaterials is definitely not exhausted by the recent implementations. Therefore, textbooks and handbooks should pay attention to most important old works.

1.2 Prehistory of Metamaterials

1.2.1 Artificial Dielectrics

In 1948, W. E. Kock suggested to make a dielectric lens lighter by replacing heavy high-permittivity refractive materials with a mixture of small metal spheres in a light-weight matrix [18]. The artificial dielectric material was defined in this pioneering work as a composite reproducing, on a much larger scale, processes occurring in the molecules of a usual dielectric. This involved arranging metallic elements in a three-dimensional (3D) array or lattice structure to simulate the crystalline lattices of dielectric materials. Such an array responds to radio waves just as a molecular lattice responds to light waves: Free electrons in the metal elements flow back and forth under the action of the alternating electric field. Metal elements called also as lattice inclusions or lattice particles become oscillating dipoles similar to the oscillating molecular dipoles of a natural dielectric.

This concept, however, probably was first suggested by Lord Rayleigh in his pioneering work [19]. Rayleigh considered a lattice of small scatterers (molecules modeled by spheres) whose period was much smaller compared to the wavelength, as in a sample of an equivalent continuous medium. Kock reproduced this concept for arrays of metal spheres and used that for practical applications. Then this concept was developed in an important work by M. M. Kharadly and W. Jackson [20]. They calculated the effective permittivity of artificial dielectrics comprising metal ellipsoids, disks, or rods assuming that the frequency of operation is low enough and the Rayleigh quasi-static restriction holds. This restriction is usually satisfied with practical accuracy for artificial dielectrics utilized in microwave lens antennas. In a popular book [21] as well as in the famous overview [22] one can find a well explained quasi-static theory of artificial dielectrics. This theory is valid when the lattice of metal particles is sparse enough, i.e., the ratio of the lattice period to the maximal particle size is rather large (e.g., 1.5 and more). The theory of densely packed artificial dielectrics is more difficult. It was developed by mathematicians [23–25]. Artificial dielectrics with dense packaging of metal inclusions possess rather high losses and are not used in lens antennas. They are applied in absorbing sheets. Artificial dielectrics are not necessarily regular lattices. They can be random mixtures reviewed in [26]. Even the nonuniform concentration of particles is sometimes allowed, which offers unusual properties of such composite media [27,28]. When the concentration of particles exceeds the so-called percolation threshold (particles touch one another and/or the capacitive coupling between adjacent particles is very strong) artificial dielectrics in the same low frequency range become artificial conductors with complex conductivity [29]. Their conductivity can be engineered (i.e., controlled by the design parameters) and is in principle tunable magnetically or electrically. Artificial conductors have found applications in electromechanical devices, fuel cells, and other techniques where controlled heating by electric current is needed.

* We do not object to the importance of the cited works, of course.

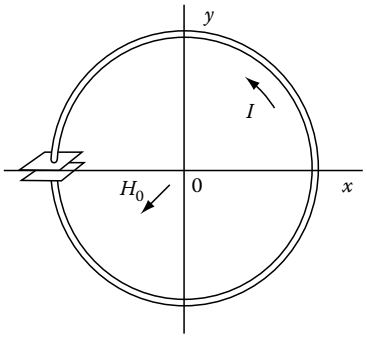

FIGURE 1.1 SRRs in the 1950s. (From Schelkunoff, S.A. and Friis, H.T., *Antennas: Theory and Practice*, John Wiley & Sons, New York, 1952. With permission.)

1.2.2 Artificial Magnetics

Magnetism without magnetic constituents has been known since 1940s due to works of S. A. Schelkunoff and H. T. Friis that suggested so-called split-ring resonators (SRRs). Figure 1.1a represents a scanned copy of a page of the classical textbook [30] which is rather popular among specialists in radio frequency antennas. A formula for the magnetic polarizability of an individual SRR element derived in this old book is visible and indicates the Lorentz frequency behavior of the element.

Notice, that the "artificial magnetism" also happens in ordinary structures, like wet snow. Here, loop-forming parts of liquid water cause diamagnetic behavior. But in lattices of SRRs the artificial magnetism is significantly enhanced in the resonant frequency range (and it is paramagnetic at lower frequencies).

Particles with metal loops of various shapes were studied in the 1980s [31,32]. In combination with other shapes, also in the 1990s [33], especially in connection with artificial bianisotropic materials for microwave applications. Polarizabilities of these bianisotropic particles in magnetic and electric fields were studied analytically, numerically, and experimentally. In Figure 1.1b another scanned copy shows possible designs of so-called double SRRs suggested in [34] in 1994 (at the bottom the simulated material parameters of corresponding composite media are shown). In these designs the bianisotropy was essentially (though not completely) compensated. Such double SRRs could be used to create artificial magnetics without chirality (see also in [35]). In [35] one finds probably the first experimental demonstration of negative permeability in artificial microwave materials (1997).

The design with strong capacitive coupling between loops suggested in [16] turned out, however, more appropriate for the artificial magnetism. The strong coupling of two loops allowed one to obtain the magnetic resonance at lower frequencies. This means that the resonant frequency is low enough to consider the lattice of SRRs as a continuous medium. Because of its planar structure SRRs suggested in [16] and shown in Figure 1.2a as well as SRRs suggested in [36] are perhaps very practical ways of creating artificial magnetism at microwaves. So-called Swiss roll metal scatterers reported in [37] and depicted in Figure 1.2b (right) turned out to be more efficient as magnetic resonators but work at considerably lower frequencies. The amplitude and frequency bandwidth of magnetic response can be enhanced by using very densely packed stacks of split rings, called metasolenoids [38].

1.2.3 Artificial Plasma

Artificial plasma, i.e., a medium with negative permittivity, has been known since 1960s due to works of J. Rotman [39] and J. Brown [22]. This medium is presently called wire medium (Figure 1.3). Usually

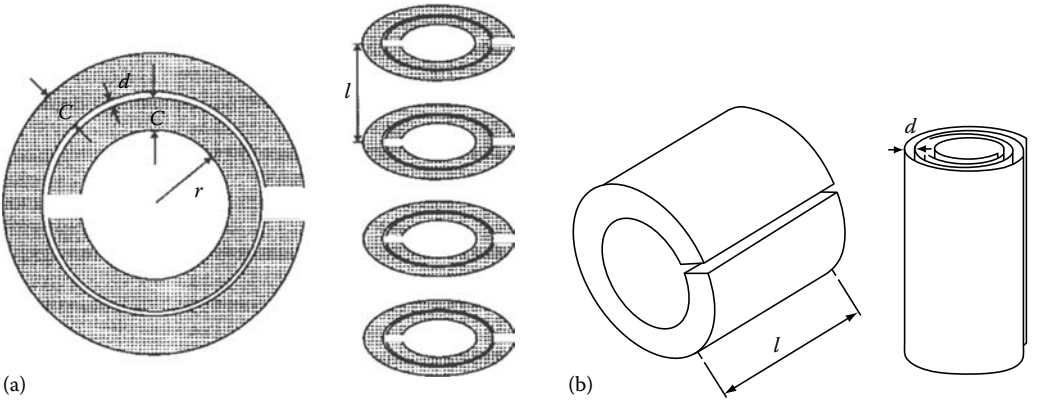

FIGURE 1.2 (a) SRRs in the 1990s. (From Pendry, J.B., Holden, A.J., Robins, D.J., and Stewart, W.J., *IEEE Trans. Microw. Theory*, 47, 2075, 1999. With permission.) (b) Swiss rolls. (From Hardy, W.N. and Whitehead, L.A., *Rev. Sci. Instrum*., 52, 213, 1981; Wiltshire, M.C., Pendry, J.B., Young, I.R., et al., *Science*, 291, 849, 2001. With permission.)

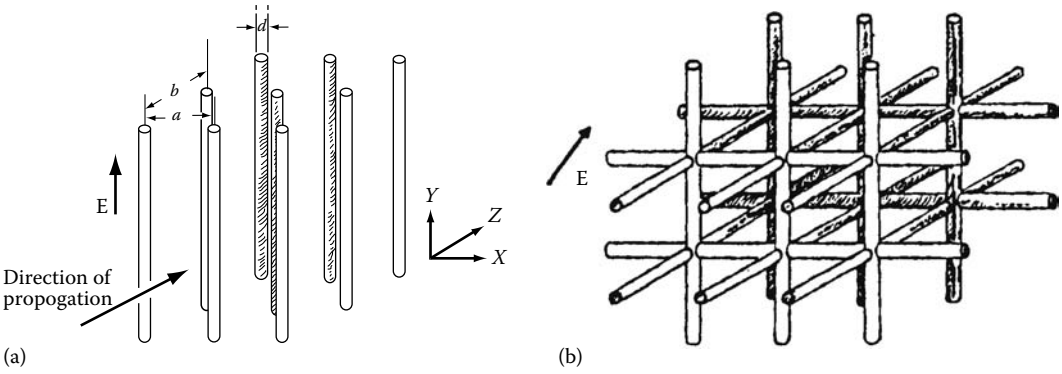

FIGURE 1.3 (a) Simple wire media in the 1960s; and (b) Triple wire media in the 1960s. (From Rotman, W., *IRE Trans. Antennas Propagat*., 10, 82, 1962. With permission.)

this is a square lattice of thin parallel wires which can be considered at microwaves as perfectly conducting ones.* Recent studies discovered for these lattices many new interesting features unknown before. These newly revealed phenomena arise due to spatial dispersion. When the wave propagates normally with respect to the wires, the spatial dispersion does not arise. Then, the effective permittivity of the wire medium obeys the so-called Drude model of electric (nonmagnetized) plasma. This formula for the simple wire medium reads as

$$\varepsilon_p = \varepsilon_0 \left(1 - \frac{\omega_p^2}{\omega^2 + \nu^2} + j\frac{\omega_p^2 \nu/\omega}{\omega^2 + \nu^2}\right) \tag{1.1}$$

In this form and with these notations it was derived in [39].

* This is the so-called simple wire medium. Double and triple wire media were also studied in [39] for the case of the axial propagation.

The lattice of parallel wires was considered up to 1990s as a kind of artificial dielectric because it was invented and practically used for applications in microwave lenses. In the 1970s tunable lattices of wires in which PiN-diodes were inserted in order to switch the negative effective permittivity of the lattice to the positive one were created and even produced by the industry [40].

The term wire media appeared after theoretically revealing the effects of spatial dispersion in recent works [41–46]. Experimental confirmation of some of these effects was also obtained [47]. Notice that the array of parallel Swiss rolls reviewed above behaves like a wire medium (of thick wires) with respect to the magnetic field of propagating wave.

1.2.4 Backward Waves in Bulk Media

The earliest fundamental publication on backward electromagnetic waves and on negative refraction was, probably, that of lecture notes of Professor L. I. Mandelshtam [48] (1879–1944) (see Figure 1.4), although waves in media with negative group velocity were discussed as early as 1904 by Lamb and 1905 by H. Pocklington [49]. The logic of Mandelshtam was simple. In isotropic media, the absolute value of the wave vector is fully determined by the frequency. Therefore, the group velocity

$$\mathbf{v}_g = \frac{d\omega(k)}{d\mathbf{k}} = \frac{\mathbf{k}}{k}\frac{d\omega}{dk} \tag{1.2}$$

is directed along vector $\mathbf{k}$ or opposite to it, depending on the sign of the derivative $d\omega/dk$. The case of the negative sign corresponds to the negative dispersion.* Mandelshtam mentioned that in the case of negative dispersion the wave in the medium is backward and the negative refraction should occur at an interface with such a medium. The possibility of the negative refraction was also mentioned by A. Schuster in [50]; however, Schuster meant the anomalous dispersion and not negative one as a possible reason of the negative refraction. Mandelshtam (with a reference to Lamb (1904) who "gave examples of fictitious 1D media with negative group velocity" of the acoustic wave) presented at the end of his life a physical example of a 3D structure supporting backward electromagnetic waves [51]. It was an inhomogeneous material with permittivity periodically varying in space. Basically, this work predicted the negative refraction in photonic crystals later rediscovered by M. Notomi [52].

In 1946–1950 L. Brillouin [53] and J. R. Pierce [54] developed the theory of backward-wave microwave tubes utilizing the series-capacitance/shunt-inductance equivalent circuit model similar to that shown in Figure 1.5, and pointed out the antiparallel phase/group velocities propagation. In 1951 G. D. Malyuzhinets (who was apparently not aware of works [53] and [54]) generalized this concept to the 3D case in a paper on the Sommerfeld radiation condition in hypothetic backward-wave media [55]. Malyuzhinets noted that in such media the phase velocity of waves at infinity should point from infinity to the source. An equivalent 1D analogue of these media was artificial transmission lines depicted by Malyuzhinets and shown in Figure 1.5 (compare with [56,57]).

Materials with negative parameters as backward-wave materials were mentioned by D. V. Sivukhin in 1957 [58]. He was probably the first who noticed that media with double negative parameters are continuous and homogeneous backward-wave media. Simultaneously he stated that "... media with $\varepsilon < 0$ and $\mu < 0$ are not known. The question on the possibility of their existence has not been clarified" [58].

During the 1960s, 1D backward-wave structures were very much studied in connection with the design of microwave tubes and slow-wave periodic systems [59–61]. Let us also refer to an interesting

* Negative dispersion is a more strong effect than the well-known anomalous dispersion described by the inequality $d\omega/dn < 0$ in which n is the refraction index $n \equiv k/\omega\sqrt{\varepsilon_0\mu_0}$. When the dispersion is anomalous in natural isotropic media the group velocity is directed positively with respect to the phase one (except the frequencies where the losses are too high and the whole concept of the group velocity becomes invalid).

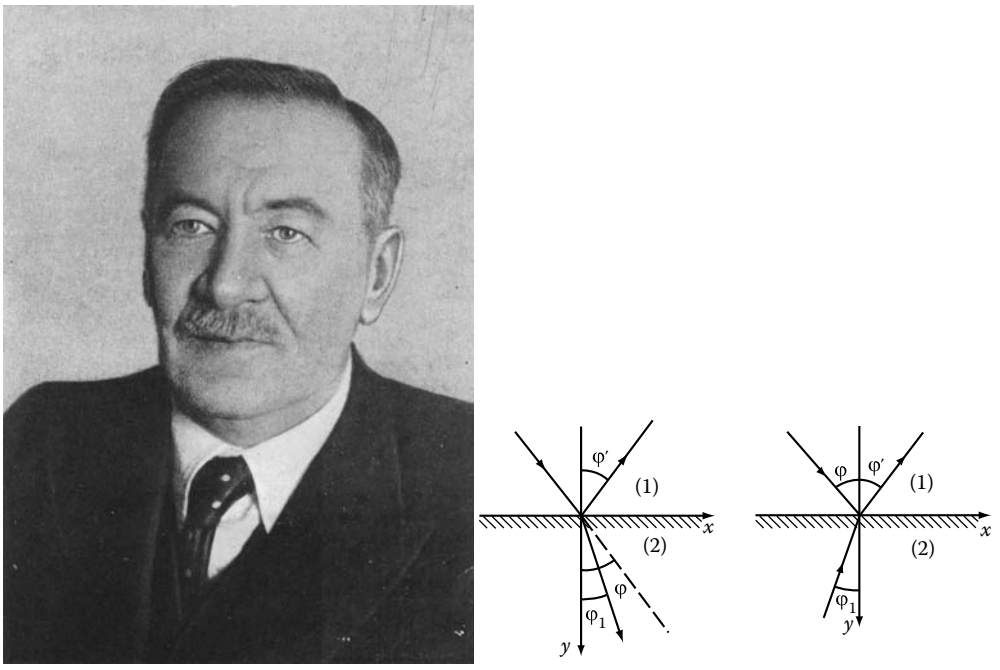

FIGURE 1.4 Professor L. I. Mandelshtam, photo 1940; An extract from his book [52]. The text reads "... However, the last equation is satisfied not only at φ_1, but also at $\pi - \varphi_1$. Demanding as before that the energy in the second medium propagates from the boundary, we arrive to the conclusion that the phase must propagate towards the boundary and, consequently, the propagation direction of the refracted wave will make with the normal the angle $\pi - \varphi_1$. Although this derivation appears to be unusual, but of course there is no wonder, because the phase velocity still tells us nothing about the direction of the energy transfer." (From Mandelshtam, L.I., Lectures on some problems of the theory of oscillations (1944), in *Complete Collection of Works*, Vol. 5, Academy of Sciences, Moscow, 1950, 428–467.)

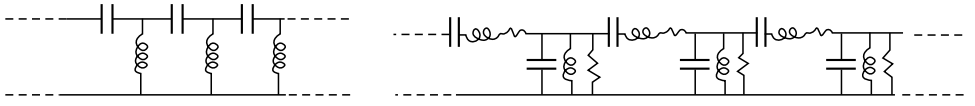

FIGURE 1.5 Backward-wave transmission lines from a paper by Malyuzhinets (1951). (From Malyuzhinets, G.D., *Zhurnal Technicheskoi Fiziki*, 21, 940, 1951.)

paper by R. A. Silin (1959) [62], where the negative refraction phenomenon in periodical 2D media was discussed. We can see it in Figure 1.6a.

An important step forward was made by V. G. Veselago (Moscow Institute of Technical Physics) in 1967, see Figure 1.6b. Professor Veselago made a systematic study of electromagnetic properties of materials with negative parameters and reported on his unsuccessful search for such media in the domain of magnetic semiconductors [2]. This study was, however, optimistic, stating that such 3D continuous media can be possibly discovered in the future. Now such media are often called left-handed media (LHM) or Veselago media. The first term is related with the fact that the triad of vectors **E**, **H**, and **k** is left handed (the vector product $\mathbf{E} \times \mathbf{H}$ determines the Poynting vector and it is opposite to the wave vector, since the Poynting vector direction in low-loss linear media coincides with that of the group velocity and the wave vector direction coincides with that of the phase velocity).

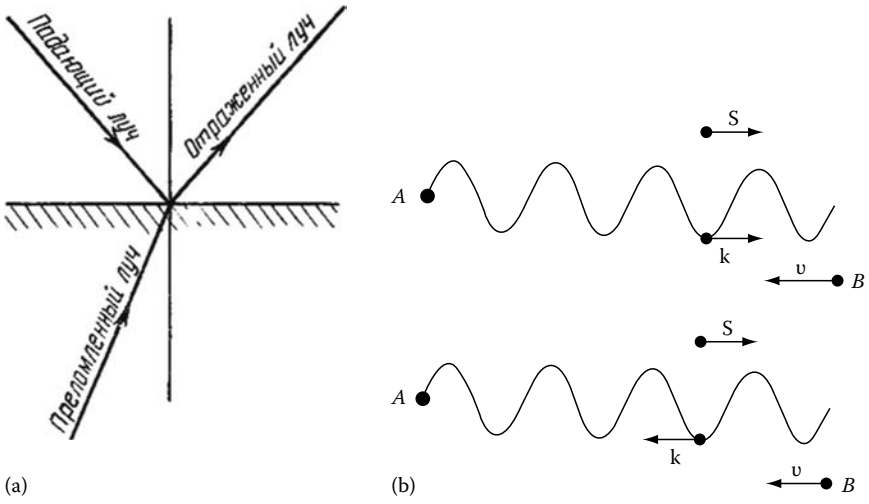

FIGURE 1.6 (a) Negative refraction in periodical media, from a paper by R. A. Silin (1959) [62]. The text reads "An illustration to the refraction law in a medium with negative dispersion." (b) Cerenkov radiation in doubly negative medium. (From Veselago, V.G., *Sov. Phys. Uspekhi*, 10, 509, 1968.)

1.3 Modern History of Metamaterials

In this historical overview we intentionally do not touch such issues as very recent and exciting works on invisibility cloaks based on MTM. In this new domain of knowledge there are still important points to be clarified. The state of the art can hardly be described reliably at the time of writing. It would be especially difficult in view of the sensational background in mass media, where the presentation of facts is sometimes distorted. It is especially so for the optical frequency range. Therefore, we cannot mention these works in the historical part of the handbook.

Also, we do not present in this part any overview of various microwave and optical applications of MTM. All these applications have been found recently and are under studies and discussions. Sometimes, the word metamaterials is mentioned in the design of antenna arrays, antenna elements, feeding lines, and other microwave components without a solid background for this term. This word is often used in order to designate the unusual design of a component. It is not a purpose of the historical introduction to clarify these points, and we avoid in it all practical questions related to applications of MTM. These applications (already established as well as possible ones) are reviewed, for example, in [13–15], and are considered with more detail in this handbook.

We concentrate on the history of the Pendry–Veselago perfect lens, because the Pendry–Veselago perfect lens is probably the best example illustrating the modern history of MTM.

1.3.1 Negative Refraction and Subwavelength Resolution

The attempts to create practically applicable isotropic 3D Veselago media in many frequency ranges from meter waves to the visible band still refer to the modern scientific reality. In spite of successful demonstration of subwavelength resolution in some works, no practically applicable super-lens has been created at this stage, and this allows one to conclude that there the encountered difficulties are really dramatic. In this section we discuss the emergence and development of the concepts of negative refraction and subwavelength imaging in the Pendry–Veselago flat lens. This is already history.

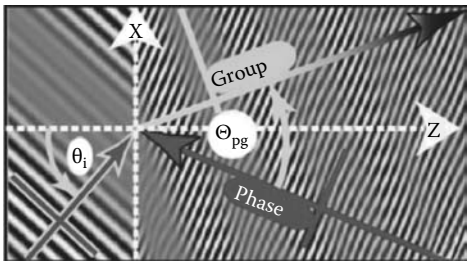

FIGURE 1.7 Vision of the negative refraction of a wave pulse in the paper [63]. (From Valanju, P.M., Walser, R.M., and Valanju, A.P., *Phys. Rev. Lett*., 88, 187401, 2002. With permission.)

The most strong objection to the negative refraction was presented by P. Valanju et al. [63]. Using the causality and the Huygens principles it was proven that the normal to the pulse front should refract positively. This consideration was taken seriously. Really, in analytical calculations and in simulations of the wave beam refraction (one example of such a simulation is shown in Figure 1.7a) the field is usually monochromatic. Monochromatic waves are physical idealizations. In [63] a frequency package was considered that corresponds to a wave pulse. Not only the forward front of the pulse has the normal that refracts positively. It also concerns the pulse as a whole: the plane at which the field of the pulse is maximal (in free space it is parallel to the phase front) refracts positively. In Figure 1.7b the normal to this plane is identified with the group velocity [63]. In the reply by J. Pendry and D. Smith [64] it was explained that this is not the group velocity. The effect of pulse reshaping after the negative refraction can be understood from Figure 1.8, presented in [64]. This is forming of the so-called interference pattern in the two-frequency wave (frequencies are close to one another and the refraction indices are slightly different for them due to the dispersion in the doubly negative medium). For the pulse comprising a continuum of frequencies and a continuum of incidence angles (i.e., for the wave beam pulse) the refraction can be illustrated by Figure 1.8b. One can see that the pulse reshapes, however, as a whole it refracts negatively.* And of course the Poynting vector of every frequency component of the pulse (i.e., the energy flux of every monochromatic wave forming the pulse) is directed strictly oppositely to the phase velocity of the wave. In the isotropic media the angle between the phase velocity and the energy flux of a harmonic wave can be either 0 or π [65], and this fact follows from the basic symmetry principles and from the physical meaning of the energy flux.

The reply by J. Pendry and D. Smith to P. Valanju et al., did not stop the discussion. However, it took a more philosophical and even terminological form. In papers [66,67] one asserted that the velocity of the plane wave pulse maximum is the best definition for the group velocity as the speed of the information transport, and that the nonzero angle between the group velocity and the Poynting vector is allowed in dispersive media.† This discussion has little practical importance today. The purpose is to obtain a low-loss doubly negative MTM where the group velocity can be defined in the usual way, i.e., by formula 1.2. Notice, that the arguments of P. Valanju et al., can be referred to anisotropic media as well. However, the negative refraction in anisotropic media is a well-known phenomenon, at least for the cases when the optical axis forms a sharp angle with the interface. What is impossible in

* If the pulse frequency range is very narrow, the pulse is very prolate along the ray direction. Then far from the forward and backward fronts of the pulse beam one still observes the refraction illustrated by Figure 1.7a.

† Because it is allowed in lossy media [66], and the dispersive media are lossy.

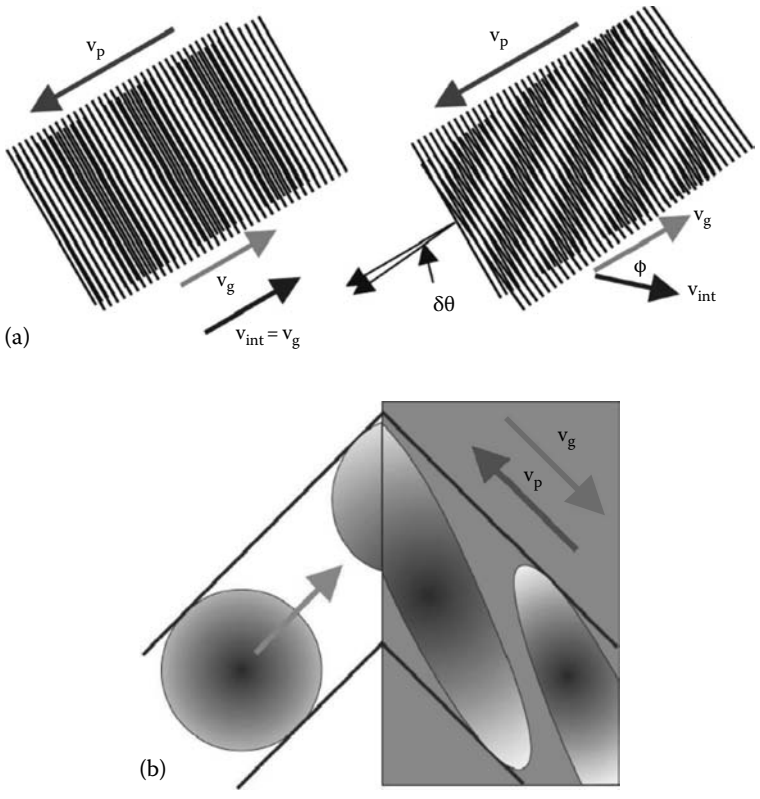

FIGURE 1.8 (a) Frequency interference pattern explained in [64]. (b) Short pulse reshaping due to the negative refraction simulated in [64]. (From Pendry, J.B. and Smith, D.R., *Phys. Rev. Lett*., 90, 029703, 2003. With permission.)

anisotropic continuous media is the all-angle negative refraction (for all possible angles of the plane wave incidence) which has been observed in composites modeling the Veselago media.

Strong attempts to overthrow the experimental observations of negative refraction in the double negative medium (started by [68] and then developed in [69,70] and other works) were made by N. Garcia and M. Nieto-Vesperinas in [67]. The structure representing the uniaxial variant of the Veselago medium in a certain frequency range is shown in Figure 1.9. It is formed by two orthogonal arrays of SRRs printed on thin dielectric sheets and long strip wires printed on the opposite side of these sheets. The anisotropy of the structure (its optical axis is vertical) does not affect the waves propagating in the horizontal plane. For waves whose electric field vector is polarized vertically there is a narrow frequency range where both permittivity and permeability have negative real parts (it is located slightly above the resonance of SRRs). The result for the negative deviation angle of wave beams was proven in experiments with prisms formed by such composites.* In [67] this result was explained not by the negative index of refraction of the composite medium but by tunneling of energy. Following to simulations made in [67], the array should possess huge losses and no propagating wave exists inside it. The transmission of the negatively diverted beam through the prism is then possible only due to the tunneling effect which is stronger in the thinner part of the prism than

* A usual prism (with a positive refraction index of the medium filling the prism) diverts a beam positively from its initial direction.

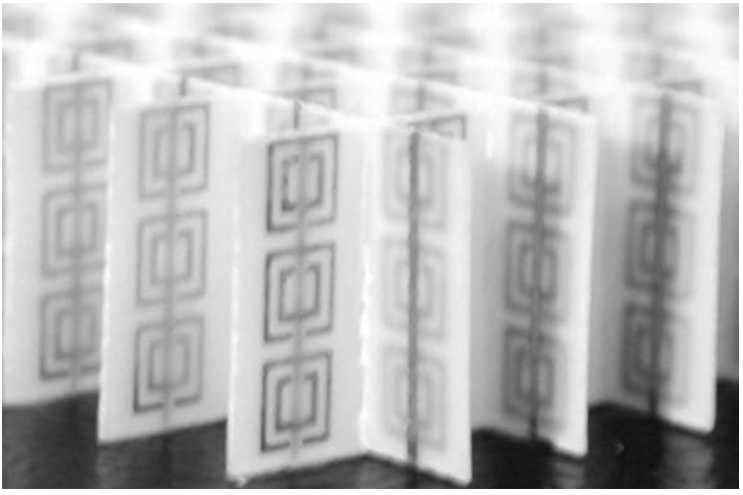

FIGURE 1.9 Uniaxial variant of the microwave Veselago medium developed in [68]. (From Shelby, R.A., Smith, D.R., and Schultz, S., *Science*, 292, 77, 2001. With permission.)

in the thicker part of it. However, calculations of losses in [67] were apparently not quite correct. Not only simulations using commercial software packages but the analytical theory [71] predicts moderate values of $\mathrm{Im}(\varepsilon)$ and $\mathrm{Im}(\mu)$ for such structures at the frequencies where $\mathrm{Re}(\varepsilon)$ and $\mathrm{Re}(\mu)$ are close to −1.

In the next discussion those who tried to decline the negative refraction in lattices of wires and SRRs suggested as an argument the following observations. It was observed that wave beams in a prism prepared from parallel wires only also experience negative deviation. This phenomenon was observed at a frequency higher than the plasma frequency ω_p of the wire lattice. At these frequencies the real part of the refraction index is positive and the negative refraction at the interface of wire lattice is apparently impossible. It was interpreted as a sign of huge losses leading to the tunneling through the wire medium. However, in fact at such high frequencies the description of the wire medium as an artificial plasma is not adequate. The wave phenomena are determined by spatial dispersion. And the negative refraction in lattices of cylinders at high frequencies is not surprising [51].

One of the first papers casting doubts on the possibility of subwavelenegth imaging in the Veselago lens suggested by J. Pendry in [1] was published in 2001 [72]. In that paper it was stated that the derivations of [1] were mathematically not strict and that the final result cannot be applied to real sources, so that the theory should be updated for practically achievable subwavelength imaging in the far zone of the source. Next, a strong objection to the whole idea of the subwavelength imaging was published in [73]. The logic of this work was as follows. The operation of the super-lens imaging a point source to a point (in the ideal case) is thought to be based on the amplification of evanescent waves across the slab of Veselago medium (evanescent waves grow from the source to the image point). It becomes theoretically possible (i.e., does not violate the energy balance) because evanescent waves do not transport energy. However, when one tries to detect the image (e.g., with a probe in which the field at the image point induces currents) this field distribution becomes perturbed. When power is consumed in the image domain, the amplification of evanescent waves across the slab of LHM will violate the energy conservation. It was also claimed in [73] that any losses, even very small, being taken into account for the Veselago medium will transform the amplification of the evanescent waves from the source to their attenuation. The following theoretical studies showed that this last assertion was not well founded: The waves which are evanescent in the lossless media become

weakly propagating in the lossy one, however, they still grow across the slab. The mechanism of this growth is related with interaction of surface waves excited by the evanescent part of the source radiation spectrum on the two sides of the LHM slab. And this phenomenon does not vanish due to small losses. The amplification of evanescent waves in the absence of the sensor at the image point is the spatial redistribution of the energy density. It is analogous, in general, to the effect of a resonance. In the absence of the sensor the presence of the LHM layer makes the field amplitude at the image point Q times larger than that without the LHM layer. Here Q is an analogue of the unloaded quality factor of a resonant circuit. When the structure is totally lossless, Q is infinite. Introducing the sensor is analogous to replacement of Q by the loaded quality factor Q_L. Of course, $Q_L < Q$, but it does not mean that $Q_L < 1$ and the presence of the Veselago medium layer is not helpful. The detailed consideration of the detection of the subwavelength focal spot by an electrically small antenna (a magnetic probe) is presented in [74]. The subwavelength imaging related to the amplification of evanescent waves across the flat layer was demonstrated in 2005 in both microwave [75]* and visible [76]† ranges in spite of the existence of losses [77–82], especially high in the last case. Though losses in the doubly negative MTM do not kill the resolution completely, they significantly deteriorate it. If the needed resolution is fixed, the losses restrict the possible distance between the source and the image. In the microwave experiments [75,77–79] and in the optical experiments [83–86] the distance from the source to the subwavelength image was larger than the wavelength λ in free space, but the mechanisms of the subwavelength imaging were different from the operation of the Veselago–Pendry super-lens.

In the optical experiment [76] the mechanism of the interaction of two surface waves on the sides of a highly polished silver layer (silver is an epsilon-negative material in the visible and ultraviolet ranges) was explored. This poor-man's super-lens was also suggested in [1] and in the practical implementation the distance D to the image was close to $\lambda/5$. The scale of the spatial resolution was approximately equal to D. The subwavelength imaging at the distance $\lambda/5$ is a certain progress with respect to the near-field microscopy; however, the distance to the image is still too small to have practical importance for the purposes of optical lithography, super-dense data storage, etc.

The influence of ohmic losses to the quality of the far-field image in super-lenses was studied, for example, in [81]. Ohmic and dielectric losses strongly restrict the possible thickness of the super-lens destroying the mechanism of the interaction of two surface wave packages which is responsible for the growing evanescent waves across the "lens" [82]. All known super-lenses are sensitive to losses, but the Veselago–Pendry super-lens is especially sensitive to them. The analysis of the current literature data allows us to conclude that this shortcoming probably makes Veselago–Pendry super-lens not the optimal passive linear device for far-field subwavelength imaging.

However, the historical importance of the studies of subwavelenghth imaging in the Veselago-Pendry super-lens is huge. These studies revealed many other possibilities to overcome the diffraction limit in the linear electrodynamics. Accurate and reliable experimental works proving the subwavelength image resolution (including far-field devices) of microwave and optical sources appeared in 2005–2007 [74,75,83–86]. In these works the design of super-lenses was very different from a slab of the Veselago medium. These works cannot be referred to the history and represent some topics of the present book.

---

* The interaction of surface waves excited by evanescent spatial harmonics of the source on two sides of the slab results in growing of these evanescent waves across the slab. This refers not only to Veselago–Pendry lens but also to photonic crystals whose interfaces support surface waves. The last case was theoretically studied in [77], and [75] provided an experimental validation of the theory.

† In that work the idea suggested in [1] has been experimentally fulfilled. It was the idea of the so-called poor-man's super-lens, which restores the part of the image created by evanescent waves, whereas the propagating harmonics do not take part in the imaging. This imaging allows reproduction of fine details of a complex source but the information of its overall shape may be lost. The poor-man's super-lens cannot form images at distances larger than the wavelength from the source.

1.3.2 Transmission-Line Networks

Many authors have noticed that bulk double negative composites based on electrically small separate scatterers seem of limited practical interest for engineering applications because these structures are strongly resonant. Consequently, they exhibit high loss and narrow bandwidth. Therefore, such structures do not constitute a good transmission medium for a modulated signal. For given dielectric losses and metal (ohmic) losses there is an unavoidable trade-off between the bandwidth and the transmission level. Due to the weaknesses of resonant-type backward-wave structures, there was a need for alternative architectures. Almost simultaneously, in June 2002, the so-called transmission-line networks (TLN) were developed as an alternative of bulk MTM in the groups of G. Eleftheriades [87], N. Oliner [88], and C. Caloz [89]. A TLN supporting backward waves can be realized as a square mesh of transmission lines as it is shown in Figure 1.10. The mesh of host lines forms a forward-wave TLN. The shunt inductances and the series capacitances in the backward-wave TLN are designed artificially. The shunt inductance can be that of a thin metal pin (or even of a lumped coil) connecting the capacitively loaded conducting mesh with the ground plane. The effective mesh with series capacitances can be designed in different ways. The two most known designs are simply meshes of microstrips with inserted bulk capacitors [14] and so-called closed multilevel mushroom structures [13] whose geometry is presented in Figure 1.11.

We can see that the TLN are 2D generalizations of a 1D backward-wave line depicted in Figure 1.5. Since backward-wave TLN are much more apt for designing the needed effective-medium parameters than the lattices of resonant scatterers [56] and their response is not resonant (TLN are especially wide-band in the so-called balanced case when a special relation between shunt and series L and C parameters holds [13,14]) it was easier to realize the super-lens namely in this 2D variant. Historically, [90] presented the first known realization of the Pendry's idea. The super-lens was based on the three-layer structure of TLN (two forward-wave TLN at two sides of the backward-wave TLN). Its picture is shown in Figure 1.12. The focal spot with the effective diameter of $\lambda/5$ was obtained in the far zone of the point source coupled to the forward-wave TLN, which excited a divergent wave of voltages and currents. A possibility for super-resolution in an isotropic 3D network of loaded transmission lines was analytically studied in [91] and probably for the first time demonstrated experimentally in [92]. The demonstration of super-lensing attracted huge attention to the transmission-line MTM; however, it was not the final goal of its inventors. In books [13,14] numerous microwave applications of such MTM are reviewed.

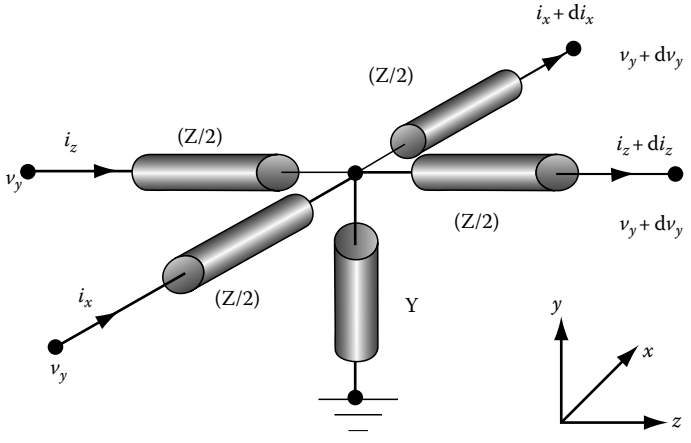

FIGURE 1.10 A transmission-line network behaving as a 2D analogue of a metamaterial. (From Eleftheriades, G.V., Iyer, A.K., and Kremer, P.C., *IEEE Trans. Microw. Theory Technique*, 50, 2702, 2002. With permission.)

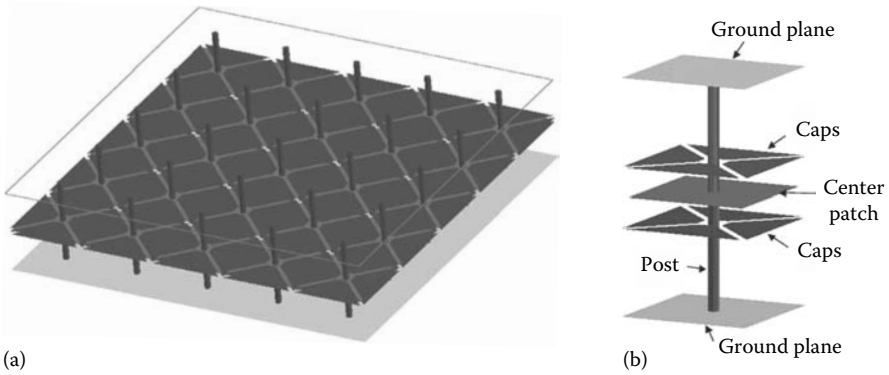

FIGURE 1.11 Closed mushroom structure: (a) overall structure and (b) unit cell. (From Caloz, C. and Itoh, T. *Electromagnetic Metamaterials: Transmission Line Theory and Microwave Applications*, John Wiley & Sons, New York, 2006. With permission.)

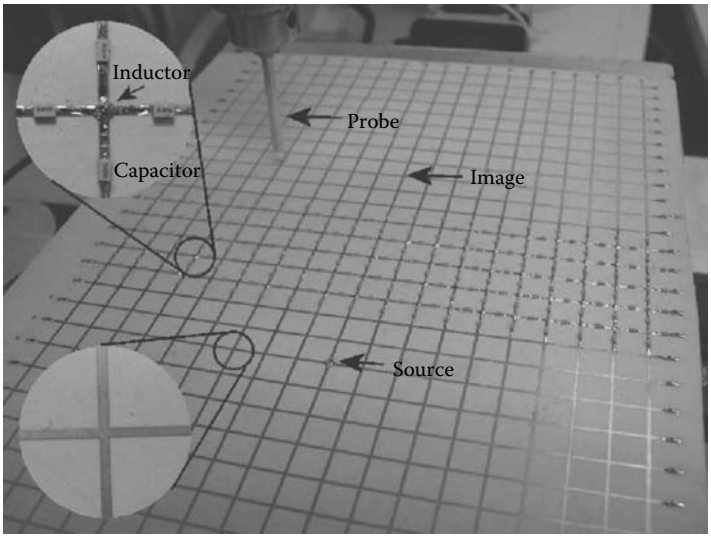

FIGURE 1.12 First known super-lens realized with transmission-line networks. (From Grbic, A. and Eleftheriades, G.V., *Phys. Rev. Lett.*, 92, 117403, 2004. With permission.)

The concept of metamaterials adopted in this book allows us to consider also so-called high-impedance surfaces, also called artificial magnetic conductors or meta-surfaces, as a class of 2D metamaterials. The theory and applications of high-impedance surfaces are well reviewed in the book [15], which also contains a rather detailed and useful overview of bulk MTM.

1.4 Conclusions

The prehistory of metamaterials together with pioneering works by V. G. Veselago, J. B. Pendry, and D. R. Smith with coauthors formed in the beginning of the twenty-first century presuppositions for quick development of a new branch of electromagnetic science—the electromagnetics of

metamaterials. In a few years of its modern history the objections to two exciting and novel opportunities offered by MTM—all-angle negative refraction and far-field subwavelength focusing—were overthrown theoretically and experimentally. No principal obstacles for the future development of MTM are visible now. However, the practical importance of already developed MTM for numerous applications (improvements offered by metamaterials in various devices as compared to conventional solutions) as well as prospectives of MTM in both technological and economical aspects are still subjects of broad and keen discussions.

References

1. J. B. Pendry, *Phys. Rev. Lett*., **85** (2000) 3966.
2. V. G. Veselago, *Sov. Phys. Uspekhi*, **10** (1968) 509 (Originally in Russian in *Uspekhi Fizicheskikh Nauk*, **92** (1967) 517).
3. D. R. Smith and N. Kroll, *Phys. Rev. Lett*., **85** (2000) 2933.
4. D. R. Smith, W. J. Padilla, D. C. Vier et al., *Phys. Rev. Lett*., **84** (2000) 4184.
5. V. G. Veselago, *Phys. Usp.*, **45** (2002) 1097.
6. L. D. Landau and E. M. Lifshitz, *The Classical Theory of Fields*, Oxford: Pergamon Press, 1989.
7. Q. Wu, G. D. Feke, R. D. Grober, and L. P. Ghislain, *Appl. Phys. Lett*., **75** (1999) 4064.
8. A. V. Itagi and W. A. Challener, *J. Opt. Soc. Am. A*, **22** (2005) 2847.
9. G. Binnig, H. Rohrer, Ch. Gerber, and E. Weibel, *Phys. Rev. Lett*., **49** (1982) 57.
10. X. Zhu and M. Obtsu (Eds.), *Near-Field Optics: Principles and Applications*, Singapore: World Scientific Publishing, 1999.
11. M. Ohtsu and H. Hori, *Near-Field Nano-Optics: From Basic Principles to Nano-Fabrication and Nano-Photonics*, New York: Plenum Publishers, 1999.
12. S. Tretyakov, *Analytical Modeling in Applied Electromagnetics*, Norwood, MA: Artech House, 2003.
13. C. Caloz and T. Itoh, *Electromagnetic Metamaterials: Transmission Line Theory and Microwave Applications*, New York: John Wiley & Sons, 2006.
14. G. Eleftheriades and K. G. Balmain, *Negative-Refraction Metamaterials: Fundamental Principles and Applications*, New York: Wiley, 2006.
15. N. Engheta and R. Ziolkowski, (Eds.), *Metamaterials Physics and Engineering Explorations*, New York: John Wiley & Sons, 2006.
16. J. B. Pendry, A. J. Holden, D. J. Robins, and W. J. Stewart, *IEEE Trans. Microw. Theory*, **47** (1999) 2075.
17. J. B. Pendry, A. J. Holden, D. J. Robins, and W. J. Stewart, *J. Phys. Condens. Matter*, **10** (1998) 4785.
18. W. E. Kock, *Bell System Technical J*., **27** (1948) 58.
19. Lord Rayleigh, *Phil. Mag*., Ser. 5, **34** (1892) 481.
20. M. M. Z. Kharadly and W. Jackson, *Proc. IEE*, **100** (1962) 199.
21. R. E. Collin, *Field Theory of Guided Waves*, 2nd edn., New York: IEEE Press, 1991, Chapter 6.
22. J. Brown, Artificial dielectrics, in *Progress in Dielectrics*, Birks, J.B. (Ed.), New York: Wiley, 1960, pp. 193–225.
23. V. Jikov, S. Kozlov, and O. Oleinik, *Homogenization of Differential Operators and Integral Functionals*, Berlin-Heidelberg-New York: Springer-Verlag, 1994.
24. N. S. Bakhvalov and G. P. Panasenko, *Averaging of Processes in Periodic Media*, Moscow: Nauka, 1984 (in Russian).
25. A. Bensoussan, J.-L. Lions, and G. Papanicolaou, *Asymptotic Analysis of Periodic Structures*, Amsterdam, the Netherlands: North-Holland, 1978.
26. A. H. Sihvola, *Electromagnetic Mixing Formulas and Applications*, London: IET Publishers, 1999.

27. S. Torquato, T. M. Truskett, and P. G. Debenedetti, *Phys. Rev. Lett*., **84** (2000) 2064.
28. S. Chapman and T. G. Cowling, *The Mathematical Theory of Non-Uniform Gases*, Cambridge: Cambridge University Press, 1953.
29. A. P. Vinogradov, *Electrodynamics of Composite Materials*, Moscow: URSS Publishers, 2001 (in Russian).
30. S. A. Schelkunoff and H. T. Friis, *Antennas: Theory and practice*, New York: John Wiley & Sons, 1952.
31. H. J. Schneider and P. Dullenkopf, *Rev. Sci. Instrum*., **48** (1977) 68.
32. W. N. Hardy and L. A. Whitehead, *Rev. Sci. Instrum*., **52** (1981) 213–216.
33. S. A. Tretyakov, F. Mariotte, C. R. Simovski et al., *IEEE Trans. Antennas Propagat*., **44** (1996) 1006.
34. M. V. Kostin and V. V. Shevchenko, *Proceedings of Chiral '94*, Périgueux, France, pp. 49–56, 1994.
35. A. N. Lagarkov, V. N. Semenenko, V. A. Chistyaev et al., *Electromagnetics*, **17** (1997) 213.
36. R. Marques, F. Medina, and R. Rafii-el-Idrissi, *Phys. Rev. B*, **65** (2002) 144440.
37. M. C. Wiltshire, J. B. Pendry, I. R. Young et al., *Science*, **291** (2001) 849.
38. S. Maslovski, P. Ikonen, I. Kolmakov et al., Artificial magnetic materials based on the new magnetic particle: Metasolenoid, in *Progress in Electromagnetics Research*, vol. 54, Cambridge: EMW Publishing, 2005, pp. 61–81.
39. W. Rotman, *IRE Trans. Antennas Propagat*., **10** (1962) 82.
40. C. Chekroun, D. Herrick, Y. M. Michel et al., *L'Onde Electrique*, **59** (1979) 89.
41. G. Shvets, Photonic approach to making a surface wave accelerator, in *CP647, Advanced Accelerator Concept: Tenth Workshop*, C.E. Clayton and P. Muggli (Eds.), American Institute of Physics, Mandaly Beach, CA, 2002, pp. 371–382.
42. P. Belov, R. Marques, M. Silveirinha et al., *Phys. Rev. B*, **67** (2003) 113103.
43. C. R. Simovski and P. A. Belov, *Phys. Rev. E*, **70** (2004) 046616.
44. M. Silveirinha, *IEEE Trans. Antennas Propagat*., **54** (2006) 1766.
45. M. Silveirinha and C. A. Fernandes, *IEEE Trans. Antennas Propagat*., **53** (2005) 59.
46. I. S. Nefedov, A. J. Viitanen, and S. A. Tretyakov, *Phys. Rev. E*, **71** (2005) 046612.
47. P. A. Belov, Y. Hao, and S. Sudhakaran, *Phys. Rev. B*, **73** (2006) 033108.
48. L. Mandelshtam, *Zhurnal Eksperimentalnoi i Teoreticheskoi Fiziki*, **15** (1945) 476 (in Russian).
49. H. C. Pocklington, *Nature*, **71** (1905) 607–608.
50. A. Schuster (Sir), *An Introduction to the Theory of Optics*, 2nd edn., London: E. Arnold, 1909.
51. L. I. Mandelshtam, Lectures on some problems of the theory of oscillations (1944), in *Complete Collection of Works*, vol. 5, Moscow: Academy of Sciences, 1950, pp. 428–467 (in Russian).
52. M. Notomi, *Phys. Rev. B*, **62** (2000) 10696.
53. L. Brillouin, *Wave Propagation in Periodic Structures*, New York: McGraw-Hill, 1946.
54. J. R. Pierce, *Traveling-Wave Tubes*, New York: Van Nostrand, 1950.
55. G. D. Malyuzhinets, *Zhurnal Technicheskoi Fiziki*, **21** (1951) 940 (English translation in *Sov. Phys. Tech. Phys.*).
56. A. Grbic and G. Eleftheriades, *IEEE Trans. Antennas Propagat*, **51** (2003) 2604.
57. C. Caloz and T. Itoh, *IEEE Trans. Antennas Propagat*, **52** (2004) 1159.
58. D. V. Sivukhin, *Opt. Spektroscopy*, **3** (1957) 308.
59. R. G. E. Hutter, *Beam and Wave Electronics in Microwave Tubes*, Princeton, NJ: Van Nostrand, 1960.
60. J. L. Altman, *Microwave Circuits*, Princeton, NJ: Van Nostrand, 1964.
61. R. A. Silin and V. P. Sazonov, *Slow-Wave Structures*, Moscow: Soviet Radio, 1966 (in Russian).
62. R. A. Silin, *Voprosy Radioelektroniki, Elektronika*, **4** (1959) 11 (in Russian).
63. P. M. Valanju, R. M. Walser, and A. P. Valanju, *Phys. Rev. Lett*., **88** (2002) 187401.
64. J. B. Pendry and D. R. Smith, *Phys. Rev. Lett*., **90** (2003) 029703.
65. V. G. Veselago and E. E. Narimanov, *Nat. Mater.*, **5** (2006) 759.
66. R. Loudon, *J. Phys. A: Gen. Phys*., **3** (1970) 233.

67. N. Garcia and M. Nieto-Vesperinas, *Opt. Lett.*, **27** (2002) 885.
68. R. A. Shelby, D. R. Smith, and S. Schultz, *Science*, **292** (2001) 77.
69. C. G. Parazzoli, R. B. Greegor, K. Li, B. E. C. Koltenbah, and M. Tanielian, *Phys. Rev. Lett.*, **90** (2003) 107401.
70. A. A. Houck, J. B. Brock, and I. L. Chuang, *Phys. Rev. Lett.* **90** (2003) 137401.
71. C. Simovski and B. Sauviac, *Phys. Rev. E*, **70** (2004) 046607.
72. G. W. t'Hooft, *Phys. Rev. Lett.*, **87** (2001) 249701.
73. N. Garcia and M. Nieto-Vesperinas, *Phys. Rev. Lett.*, **88** (2002) 207403.
74. F. Mesa, M. J. Freire, R. Marqués, and J. D. Baena, *Phys. Rev. B*, **72** (2005) 235117.
75. Z. Lu, J. A. Murakowski, C. A. Schuetz, S. Shi, G. J. Schneider, and D. W. Prather, *Phys. Rev. Lett.*, **95** (2005) 153901.
76. N. Fang, H. Lee, C. Sun, and X. Zhang, *Science*, **308** (2005) 534.
77. C. Luo, S. G. Johnson, J. D. Joannopoulos, and J. B. Pendry, *Phys. Rev. B*, **68** (2003) 045115.
78. G. V. Eleftheriades, A. K. Iyer, and P. C. Kremer, *IEEE T. Microw. Theory Technique*, **50**(12) (2002) 2702–2712.
79. A. K. Iyer, P. C. Kremer, and G. V. Eleftheriades, *Opt. Express*, **11** (2003) 696–708.
80. D. R. Smith, D. Schurig, M. Rosenbluth, S. Schultz, S. A. Ramakrishna, and J. B. Pendry, *Appl. Phys. Lett.*, **82** (2003) 1506.
81. R. Marqués and J. Baena, *Microwave Opt. Technol. Lett.*, **41** (2004) 290.
82. A. M. Bratkovski, A. Cano, and A. P. Levanyuk, *Appl. Phys. Lett.*, **87** (2005) 103507.
83. P. Ikonen, P. A. Belov, C. R. Simovski, and S. I. Maslovski, *Phys. Rev. B*, **71** (2006) 073102.
84. Z. Liu, S. Durant, H. Lee, et al. *Optics Lett.*, **32** (2007) 621.
85. S. Maslovski, S. Tretyakov, P. Alitalo, *J. Appl. Phys.*, **96**(3) (2004) 1293–1300.
86. P. Alitalo, S. Maslovski, S. Tretyakov, *Phys. Lett. A*, **357**(4–5) (2006) 397–400.
87. A. K. Iyer and G. V. Eleftheriades, in *IEEE-MTT International Symposium* vol. 2, Seattle, WA, pp. 1067–1070, June 2002.
88. A. A. Oliner, in *URSI Digest, IEEE-AP-S USNC/URSI National Radio Science Meeting*, San Antonio, TX, p. 41, June 2002.
89. C. Caloz and T. Itoh, in *Proceedings of the IEEE-AP-S USNC/URSI National Radio Science Meeting*, vol. 2, San Antonio, TX, p. 412, June 2002.
90. A. Grbic and G. V. Eleftheriades, *Phys. Rev. Lett.*, **92** (2004) 117403.
91. P. Alitalo and S. Tretyakov, *Metamaterials*, **1**(2) (2007) 81–88.
92. P. Alitalo, S. Maslovski, and S. Tretyakov, *J. Appl. Phys.*, **99** (2006) 124910.

2

Material Parameters and Field Energy in Reciprocal Composite Media

Constantin R. Simovski
Helsinki University of Technology

Sergei A. Tretyakov
Helsinki University of Technology

2.1 Introduction

Electromagnetic properties of metamaterials (MTM) are defined by the properties of inclusions (artificial molecules) and by their positioning in the matrix (in this chapter we consider only three-dimensional bulk MTM). The inclusions forming many MTM are resonant and their resonances are in the frequency range where the distance between them can be a rather small fraction of the wavelength in the host medium. In this case it is reasonable to represent such composite media as spatially uniform continuous effective media introducing for them material parameters. This modeling called homogenization allows dramatic simplification of the scattering problem and other electrodynamic problems for MTM samples. However, homogenization of MTM is not an easy task. Frequency dispersion in MTM formed by electrically (optically) small inclusions is very strong, since such particles can be effectively excited only in the vicinity of their resonant frequencies. Also, spatial dispersion effects can be strong in MTM, because inclusions or distances between them are often comparable in

size with the effective wavelength in the composite. Even if these sizes are optically small in terms of the wavelength in the host medium, the effective wavelength shortens due to the presence of resonant inclusions. In some MTM, inclusions are even much larger than the wavelength (an example is the so-called wire media discussed below).

This chapter is devoted to the homogenization of MTM formed by small scatterers. Even in this case the homogenization of MTM is a complex and difficult task that obviously implies the answers to the following questions:

- How to introduce (define) material parameters of composite media, what is the physical meaning of them, and in which electrodynamic problems such material parameters are applicable?
- What are frequency bounds in which these material parameters keep their physical meaning and applicability?
- What are physical limitations that should be imposed on these material parameters and must be taken into account in calculations, measurements, and in practical applications?

Without these answers the use of material parameters in the description of any composite media, especially MTM, is senseless. The answers can be found in the overview presented below and are based on the known theory of weak spatial dispersion (WSD) in molecular or composite media. In the beginning the second question is answered, because the bounds of homogenization models can be discussed before we introduce material parameters. The last question is answered in the end of the chapter after inspecting the energy density in composite media.

2.2 Local and Nonlocal Composite Media

2.2.1 Preliminary Remarks

From the microscopic point of view, all media, natural and artificial, are spatially discontinuous since they are formed by particles. However, a vast class of natural materials is considered as effectively continuous media, and it is not surprising since the optical size of atoms and molecules is very small at radio, microwave, and even optical frequencies. Quantum objects such as atoms can resonate at millimeter waves, at infrared or visible frequencies where their optical sizes are negligible. Therefore, the resonance phenomena in many natural media are also successfully described as if they happened in an ideally continuous medium. The most known exceptions are gases and water vapor (like in clouds) where the discontinuity is related with large molecular clusters or with considerably large particles (e.g., water drops) and leads to the Rayleigh and Mie scattering. Structures with Mie scattering usually are not considered as continuous media [1]. Structures with Rayleigh scattering where the scattering objects are optically small are described in the literature as continuous but nonuniform media: media with small-scale spatial fluctuations of permittivity [2]. This means that the homogenization of molecular arrays is possible, and the nonuniformity of the molecular concentration is taken into account as the position-dependent permittivity.

Both these situations are typical for natural media and not for composites and MTM. Specially prepared particles forming MTM usually resonate at frequencies where their size and the distance between adjacent particles are small but not negligible compared to the wavelength in the medium. We can exclude from the theory the Mie scattering by separate particles of MTM.* We also can exclude the fluctuations of the particles' density leading to the Rayleigh scattering since MTM with strongly inhomogeneous concentration of inclusions are unknown and probably hardly useful.

* MTM with such inclusions are possible but are not considered here.

The main difficulty for the homogenization of MTM is specific for all composite media. This difficulty appears in cases when the ratio a/λ, where a is the average distance between centers of adjacent particles, is not very small, such as $a/\lambda > 0.01$. In this situation we should take into account the nonuniformity of the field over the particle and over the unit cell of the composite medium. We emphasize that the effective material parameters (EMP) discussed in this chapter describe the electric and magnetic responses of the medium unit cell, i.e., they have a clear physical meaning. Below we name these EMP as "local material parameters" and explain this terminology.

In a number of recent works devoted to MTM (which are not reviewed in this book), the formal homogenization procedure is applied to spatially dispersive media, and negative permeability and permittivity are reported for them without discussion of the physical meaning of these material parameters. In Section 2.2.2 we discuss this formal homogenization, its usefulness, and the limit case of very low frequencies.

2.2.2 On Material Parameters of Media with Strong Spatial Dispersion

The formal homogenization of discontinuous media to which certain tensors of permittivity $\overline{\overline{\varepsilon}}$ and permeability $\overline{\overline{\mu}}$ are attributed is generally possible. At least it is possible under the assumption of the medium transparency, when the wave propagates without strong attenuation. Let us give an example of such formal homogenization for an infinite lattice of artificial inclusions (photonic crystal). The eigenwave in a photonic crystal can be described by its wave vector $\mathbf{q}$, and the difference of the wave field from that of the uniform plane wave can be described by higher-order terms in the well-known Bloch expansion of the eigenwave electromagnetic field [3]:

$$\begin{Bmatrix}\mathbf{E}(\mathbf{r})\\ \mathbf{H}(\mathbf{r})\end{Bmatrix} = \begin{Bmatrix}\mathbf{E}_0\\ \mathbf{H}_0\end{Bmatrix} e^{-j\mathbf{q}\cdot\mathbf{r}} + \sum_{n\neq 0}\begin{Bmatrix}\mathbf{E}_\mathbf{n}\\ \mathbf{H}_\mathbf{n}\end{Bmatrix} e^{-j(\mathbf{q}\mathbf{r}+\mathbf{G}_\mathbf{n}.\mathbf{r})}, \tag{2.1}$$

where $\mathbf{G}_\mathbf{n} \equiv (G_x, G_y, G_z) = \left(2\pi n_x/a_x, 2\pi n_y/a_y, 2\pi n_z/a_z\right)$ are multiples of the generic lattice vector, ($a_{x,y,z}$ are lattice periods, and $\mathbf{n} = (n_x, n_y, n_z)$, $n_{x,y,z} = 1, 2, \ldots, \infty$).

At the frequencies where the lattice periods are optically large, the contribution of higher-order harmonics with the amplitudes $\mathbf{E}_\mathbf{n}$, $\mathbf{H}_\mathbf{n}$ is of the same order as that of the zero-order Bloch harmonic $\mathbf{E}_0$, $\mathbf{H}_0$. At low frequencies where the periods are optically small, the zero harmonic dominates and the field is close to that of a uniform plane wave. However, at any frequency one can formally treat the plane-wave part of the field in the lattice (i.e., the zeroth Bloch harmonic) as if it were a separate plane wave traveling in an anisotropic continuous medium. Then the product of the permittivity and permeability tensors can be defined through the normal refraction vector $\mathbf{n} \equiv \mathbf{q}/k$ of the lattice (here k is the wave number in the matrix). The known plane-wave equation for an anisotropic magneto-dielectric medium [8] can be written in the form, where instead of the mean field we substitute $\mathbf{E}_0$:

$$(n^2\overline{\overline{I}} - \mathbf{nn} - \overline{\overline{\varepsilon}}\cdot\overline{\overline{\mu}})\cdot\mathbf{E}_0 = 0. \tag{2.2}$$

Here $\overline{\overline{I}}$ is the unit dyadic. The second equation for obtaining $\overline{\overline{\varepsilon}}$ and $\overline{\overline{\mu}}$ through the known $\mathbf{q}$, $\mathbf{E}_0$, and $\mathbf{H}_0$ can be found in [4]. The wave impedance $\overline{\overline{\gamma}}$ of the plane wave with vector $\mathbf{q}$ propagating in an anisotropic medium is defined by the standard relation

$$\mathbf{n}\times\mathbf{E}_0 = \overline{\overline{\gamma}}(\overline{\overline{\varepsilon}}, \overline{\overline{\mu}})\cdot\mathbf{H}_0. \tag{2.3}$$

The expression of $\overline{\overline{\gamma}}$ through $\overline{\overline{\varepsilon}}$ and $\overline{\overline{\mu}}$ of an anisotropic medium (given by relations (7) and (12) from [4]) is involved and omitted here. The aim of this example was to show that one really introduces formal material parameters $\overline{\overline{\varepsilon}}$ and $\overline{\overline{\mu}}$ at an arbitrary frequency. Really, Equations 2.2 and 2.3 allow us to find all the components of unknown $\overline{\overline{\varepsilon}}$ and $\overline{\overline{\mu}}$ through the known parameters of the lattice eigenwave.

Such material parameters for photonic crystals (and other spatially dispersive media) are dependent on **q**. If the eigenwave is not transverse electromagnetic (TEM), they also dependent on the wave polarization. Let the direction of propagation be described by the angles θ and ϕ that it makes with the lattice axes. Calculating the eigenwaves of the lattice we can express **q** and the polarization ellipse through ω, θ and ϕ. Then $\overline{\overline{\varepsilon}}$ and $\overline{\overline{\mu}}$ obtained from Equations 2.2 and 2.3 will be functions not only of the frequency ω, but also of the angles θ and ϕ. This is a typical feature of spatial dispersion [22]. The more essential is the angular dependence of material parameters, the more significant is the difference between the medium with spatial dispersion and the homogeneous anisotropic medium.

In homogeneous anisotropic dielectrics the permittivity is a tensor whose components depend only on ω. In the lossless case it is diagonal in the lattice coordinate axes and can be written in the dyadic form as

$$\overline{\overline{\varepsilon}}(\omega) = \varepsilon_{xx}(\omega)\mathbf{x}_0\mathbf{x}_0 + \varepsilon_{yy}(\omega)\mathbf{y}_0\mathbf{y}_0 + \varepsilon_{zz}(\omega)\mathbf{z}_0\mathbf{z}_0. \tag{2.4}$$

If we calculate the wavevector **q** as a solution of the dispersion equation of an anisotropic dielectric:

$$\det\left(k^2\overline{\overline{\varepsilon}} - \mathbf{q}\times\mathbf{q}\times\overline{\overline{I}}\right) = 0, \tag{2.5}$$

q will of course depend on the angles ϕ and θ. But this dependence at any frequency will be fully determined by two numbers $\varepsilon_{xx}/\varepsilon_{zz}$ and $\varepsilon_{yy}/\varepsilon_{zz}$ that do not depend on θ and ϕ. From this one can derive that iso-frequencies surfaces, i.e., surfaces $F(q_x, q_y, q_z) = 0$ for fixed ω* can be only of two types: ellipsoids and hyperboloids [5]. Ellipsoids correspond to the so-called definite media, when the signs of all components of $\overline{\overline{\varepsilon}}$ are the same, and hyperboloids correspond to the so-called indefinite media, when the signs of these components are different.

In spatially dispersive media the components of the permittivity tensor depend also on ϕ and θ. This gives freedom for iso-frequency shapes that can serve for the detection of spatial dispersion [26].

In many recent papers devoted to anisotropic MTM the following simplification of the formal homogenization is adopted. Instead of tensors of permittivity and permeability one introduces two scalar values ε and μ defining them by relations

$$\sqrt{\varepsilon(\omega,\theta,\phi)\mu(\omega,\theta,\phi)} = n, \quad \sqrt{\frac{\varepsilon(\omega,\theta,\phi)}{\mu(\omega,\theta,\phi)}} = \frac{E_0}{H_0}. \tag{2.6}$$

Indeed, why not? The physical meaning of these "material parameters" in anisotropic media with strong spatial dispersion is very limited, but it is also the case for anisotropic $\overline{\overline{\varepsilon}}$ and $\overline{\overline{\mu}}$ defined by vector equations (Equations 2.2 and 2.3). In both isotropic and anisotropic variants formally introduced material parameters do not describe the electric and magnetic polarization of the medium unit cell. It is also not clear how to use them for solving boundary problems for finite-size samples of spatially dispersive media.

However, the introduction of material parameters for a spatially dispersive lattice, i.e., its formal homogenization can be sometimes useful for the following reasons:

1. At very low frequencies the spatial dispersion vanishes, and formal material parameters of lattices defined through Equations 2.2 and 2.3 (as if it were an anisotropic continuous medium) transit to quasistatic EMP of the anisotropic composite. Respectively, for isotropic composites formal material parameters defined through Equation 2.6 transit at very low frequencies to physically sound EMP. Below we will see that in the static limit

* Called also wave surfaces in [2].

the permeability tends to its trivial value μ_0, if lattices do not comprise natural magnetic media.*

2. In spatially dispersive media one can introduce material parameters depending on ω and $\mathbf{q}$ in a different way than it was done above [10]. Together with so-called additional boundary conditions (ABC) nonlocal material parameters $\overline{\overline{\varepsilon}}(\omega, \mathbf{q})$ and $\overline{\overline{\mu}}(\omega, \mathbf{q})$ introduced in [10,11] can be used for solving the problem of plane-wave reflection and transmission in some MTM layers (at least at the frequencies up to the first Bragg resonance $a = \lambda_{\text{eff}}/2$) [11].
3. If we introduce material parameters in a formal way through Equations 2.2 and 2.3 in one special case they can be useful for the analysis of eigenwaves in photonic crystals and even give some new physical insight. This special case is the case when the analytical solution of the dispersion problem $\mathbf{n}(\omega)$ and the eigenpolarization $\mathbf{E}_0$ of the lattice are known. Then from comparison with Equation 2.2

$$(n^2\overline{\overline{I}} - \mathbf{nn} - \overline{\overline{\varepsilon}}) \cdot \mathbf{E}_0 = 0$$

we can find $\overline{\overline{\varepsilon}}$ as a function of $\mathbf{q}$ analytically.† This is, for example, the case of the wire medium, e.g., doubly periodic array of thin infinitely long parallel wires (spatial dispersion in that medium was studied in [56]) or triply periodic arrays of crossing wires (spatial dispersion in that case was studied in [57]).
4. In some special cases (e.g., so-called waveguide medium [18]) the nonlocal permittivity $\overline{\overline{\varepsilon}}(\omega, \mathbf{q})$ introduced by Equation 2.2 also can be used for solving boundary problems together with specially derived ABC.

However, below we concentrate on local EMP of composite media since only for them the physical limitations following from the causality and passivity are known.‡ The terminology of the present chapter does not allow us to consider the introduction of nonlocal EMP as homogenization.

2.2.3 Locality and Nonlocality

The physical reason of the spatial dispersion phenomenon is the nonlocality of the polarization response [20]. The nonlocality in an array of separate scatterers (particles) appears due to two reasons: an optically non-negligible size of particles d and optically non-negligible distances a between the particles (which leads to spatial dispersion even if the particles are optically negligibly small).

The first case is evident. The polarization currents in a particle are excited by the field distributed over its optically finite volume. But the overall current distribution in the particle depends on the particle geometry and size. So, the polarization at any particular point of the particle "feels" the field at other points of the same particle. Of course, in this case the electric and magnetic responses of a large particle except an isotropic and homogeneous one (a sphere) will be strongly dependent on the direction of the propagating wave and often also on its polarization. In the case of spherical inclusions spatial dispersion appears due to the second reason: if d is large, then a (which is larger than d) is obviously also large.§

---

* Of course, material parameters defined by Equation 2.6 introduced for "geometrically anisotropic" spatially dispersive composites do not follow this limit since their static analogue is anisotropic.

† Probably this is also possible for lattices with electric and magnetic inclusions, but we know only the example of the nonmagnetic lattice.

‡ Physical limitations imposed on the relations between components of the nonlocal permittivity tensor following from the spatial symmetry can be found in [22].

§ Strictly speaking it also appears due to excitation of higher-order multipoles in the spherical particle (see following text).

Existence of spatial dispersion in the case when only the particle size d is optically large can be explained as a result of the averaging of microscopic fields over an optically large volume. Really, electric and magnetic susceptibilities of the medium by definition describe the relations between the averaged electric and magnetic fields and electric and magnetic polarizations [2]. Assume that the particles are optically small. Then their electric polarization is a response to the local electric field distributed in a small volume. In other words the polarizability of the particle is local. But even in this case the electric susceptibility of the medium is nonlocal. The susceptibility relates the polarization of the unit cell (which is equal to the dipole moment of the particle and is local) to the averaged field $\mathbf{E}^{\text{av}}$. And this field is nonlocal since $d \sim \lambda$ and the interval of the averaging covers an optically large volume. The averaged field taken at the particle center contains information on the true (microscopic) field at large distances from it. That is why in the case $d \sim \lambda$ the susceptibility and therefore the permittivity are nonlocal values and can be written in the form of integral operators acting on the field distributed over a significant volume $V = d^3$ [20].

The frequency boundary between regions of the local and nonlocal (spatially dispersive) composite media can be better understood from the high-frequency analogue of the static equation of Lorentz–Lorenz–Clausius–Mossotti. This equation for lattices of electric dipoles and for lattices of magnetic dipoles has been derived in many works, unfortunately sometimes in contradictory ways.

For a simple cubic lattice of electric dipoles two totally different approaches used in papers [6,7] under the assumption $a \ll \lambda$ (practically $a < 0.1\lambda$) give the result with the correction term $C\mathbf{P}$ to the well-known static equation of Lorentz–Lorenz–Clausius–Mossotti. This term is proportional to the polarization of the unit cell $\mathbf{P}$:

$$\mathbf{E}^{\text{loc}} - \mathbf{E}^{\text{av}} = \frac{(1+C)}{3\varepsilon_0}\mathbf{P}. \tag{2.7}$$

The bulk electric polarization $\mathbf{P}$ is related to the dipole moment $\mathbf{p}$ of the reference particle to which the local field $\mathbf{E}^{\text{loc}}$ is applied as: $\mathbf{P} = \mathbf{p}/V$ (here V is the unit cell volume). The correction factor C arises due to the wave interaction of the reference dipole with the other dipoles of the lattice and for $a < 0.1\lambda$ contains only terms of the orders of $(ka)^2$ and $(ka)^3$. Let us show that this frequency-dependent correction to the static equation does not prohibit homogenization.

The dipole moment $\mathbf{p}$ is determined by the local field $\mathbf{p} = \bar{\bar{\alpha}}\mathbf{E}^{\text{loc}}$, where $\bar{\bar{\alpha}}$ is the particle polarizability tensor. Substituting $\mathbf{E}^{\text{loc}}$ from Equation 2.7, we obtain

$$\mathbf{P} = \left(V\bar{\bar{\alpha}}^{-1} - \frac{1+C}{3\varepsilon_0}\bar{\bar{I}}\right)^{-1} \cdot \mathbf{E}^{\text{av}} \equiv \kappa\mathbf{E}^{\text{av}}. \tag{2.8}$$

In Equation 2.8 the polarization at the center of the unit cell and the averaged field at the same point are uniquely related: their relation is determined only by the polarizability $\bar{\bar{\alpha}}$, the unit cell size, and the frequency, and it is independent from the wave propagation direction. In other words, this composite can be described by the local electric susceptibility κ and therefore by the local permittivity $\varepsilon = \varepsilon_0 + \kappa$.

The situation changes dramatically if the cell size is not small enough to neglect the wave-vector correction terms to the static equation of Lorentz–Lorenz–Clausius–Mossotti. Correction terms of higher orders omitted in Equation 2.7 correspond to the Taylor expansion of the known dynamic interaction constant of the dipole lattice [13]. These correction terms are significant for $a/\lambda > 0.1$ and depend not only on the normalized optical size ka in terms of the wavelength in the matrix, but also on the optical size qa in terms of the effective wavelength $\lambda = 2\pi/q$. If C is dependent on $\mathbf{q}$ in Equation 2.8 (in this case factor C is a tensor), the relationship of the polarization and the averaged field is no more local, and the medium exhibits spatial dispersion. This example shows the order of the cell optical size when the composite or molecular medium becomes nonlocal.

If the medium is still local but the particles have a complex shape, even a very small phase shift of the wave over the particle size d, such as $(qd) \sim 0.1$ can lead to a very large phase shift of the polarization current induced in it. An example of this is artificial magnetism in arrays of small metal rings.

The current induced in any ring has the opposite directions at two diametrally opposite points of the ring (the phase shift is π) but this corresponds to a very small phase shift of the wave propagating across the ring. It is well known that this effect can be described in terms of permeability [52,53]. This is the effect of WSD: If the phase shift of the wave across a ring tends to zero, the induced current in it vanishes. The permeability of artificial magnetic media can, of course, describe the local magnetization of the medium. This example shows that the homogenization of a composite (and even molecular [14]) media with vortex-type polarization currents is possible. However, if we consider not only closed metal rings, we have to take into account the possibility of multipolar polarization of particles. Then the homogenization model can lead to more material parameters in addition to the permittivity and permeability [21,23]. The general theory leading to these models is briefly presented in Section 2.3. Within this model the dynamic definition of local permeability automatically appears as a result of WSD.

2.3 Media with Weak Spatial Dispersion

2.3.1 Definition of Weak Spatial Dispersion

We saw above that the inequality $d \ll \lambda$ where d is the particle size is an obvious condition for homogenization. However, if we completely neglect all values containing the product (kd), some important phenomena drop out of the homogenization model. Even if terms containing (ka) can be neglected in Equation 2.7, similar terms should not be neglected when we analyze the electric [20] and magnetic [2] polarization currents excited in composite or even molecular media [2,20]. These phenomena are known as bianisotropy and artificial magnetism. Below we concentrate on the artificial magnetism and do not consider particles prepared from natural magnetic media. Unlike the natural one, the artificial magnetism is a reciprocal phenomenon.

The reason of WSD is possible strong variation of the phase of the polarization current in particles in the presence of a small variation of the applied electric field over it. As we already have noticed, resonant response of particles under the condition $(ka) < 1$ is possible due to complex shapes of the particles (helicoidal molecules, split-ring resonators (SRRs), Ω-shaped metal particles, etc.) It is also possible due to very high contrast of permittivity (piezoelectric particles at microwaves or so-called polaritonic semiconductors [12] at infrared).

The consequence of small phase shift of the averaged field over the domain occupied by a resonant particle is much more significant than the consequences of the phase shift of the averaged field over empty intervals between particles. We can consider the last effect as being small and have in mind the relation equation (Equation 2.7) between the local and averaged fields. The consequence of the same small phase shift of the field over the particle is its multipolar polarization and consequently the multipolar polarization of the effective medium.

Polarization at point **r** feels the field not only at the same point **r** but also around it. This is the reason why media of such particles are called media with WSD in books [23,24]. This term is, unfortunately, not commonly adopted. For example, in [15,21] WSD is referred to as the effect of the bianisotropy (gyrotropy). We follow the terminology adopted in the book [23] that treats the bianisotropy as spatial dispersion of the first order (also in books [14,17,21,24]) and the artificial magnetism as spatial dispersion of the second order (also in [24]). Both these phenomena are in our terms special cases of WSD.

The molecular theory* of media with WSD is extremely important for understanding MTM. Books [14,17,23] are mainly devoted to spatial dispersion of the first order, and only isotropic media

* That is, the theory that leads to the material equations and not the theory that studies wave processes in media described by these equations.

with second-order spatial dispersion were analyzed in [23]. Reference [24] has not been translated into English. For this reason, we present the most important steps of this molecular theory though this presentation implies rather involved expressions. This theory is based on the general multipole approach developed by R. Raab and L. Barron with members of their scientific groups in many publications, which are summarized in the monograph [25].

2.3.2 Polarization Current in Media with Weak Spatial Dispersion

When we calculate the polarization current **J** induced in the medium with WSD, the variation of the field over the scale d is not more negligible. Therefore, $\mathbf{J}(\mathbf{R})$ will be determined by not only the electric field at point **R** belonging to the particle but by field $\mathbf{E}(\mathbf{R}')$ around the observation point **R** ($|\mathbf{R} - \mathbf{R}'| \sim d$). We represent the general relation for the vector **J** in the index form:

$$J_i(\mathbf{R}) = \int_{\Omega} K_{ij}(\mathbf{R} - \mathbf{R}')\, E_j(\mathbf{R}')\, \mathrm{d}V'. \tag{2.9}$$

Here K_{ij} are components of the polarization response dyadic (which can be found for example from numerical simulations) and Ω is the effective volume of integration with characteristic size d. The electric field inside it can be expanded into Taylor series:

$$\mathbf{E}(\mathbf{R}') = \mathbf{E}(\mathbf{R}) + (\nabla_\alpha \mathbf{E})\Big|_{\mathbf{R}} (R'_\alpha - R_\alpha) + \frac{1}{2}(\nabla_\beta \nabla_\alpha \mathbf{E})\Big|_{\mathbf{R}} (R'_\alpha - R_\alpha)(R'_\beta - R_\beta) + \cdots \tag{2.10}$$

The substitution of Equation 2.10 into Equation 2.9 leads to the Taylor expansion of the polarization current:

$$J_i = j\omega(b_{ij}E_j + b_{ijk}\nabla_k E_j + b_{ijkl}\nabla_l \nabla_k E_j) + \cdots \tag{2.11}$$

Equation 2.11 with neglected higher-order terms describes the phenomenon of WSD in terms of the averaged polarization current $\mathbf{J}(\mathbf{R})$. Here we omit the discussion of the averaging procedure. There are different ways to define the averaging for fields and polarizations. Some of them [24] allow one to satisfy the usual boundary conditions for homogenized composite media, i.e., keep tangential components of averaged fields **E** and **H** continuous across the boundary.

This continuity can be preserved (see also in [7]) introducing Drude transition layers [16] across which the permittivity (and permeability) of the homogenized medium varies from its bulk value to its value in the surrounding space. The effect of the finite-thickness "boundary" of a composite medium should be obviously taken into account at high enough frequencies $(qa) > 0.1$ or even at $(qa) > 0.01$ if the composite layer is geometrically thin, i.e., comprises only a few unit cells across it [14].*

Another definition of averaged fields and polarizations [17] allowed one to avoid the use of Drude layers introducing a sharp boundary between the homogenized lattice and the surrounding medium. However, it was obtained at the price of discontinuity of all the components of electromagnetic field at this effective boundary. No practically applicable expressions for these jumps allowing to solve boundary problems were obtained in [17] (and to the best of our knowledge in any further work).

* Notice that the thickness of the Drude layers remained unknown since [16], only the case of a simple cubic lattice of dielectric or ferrite spheres was studied.

The objective of this chapter is not to discuss the averaging algorithms for composite media. We finalize this discussion by three important comments:

- In Equation 2.11 it is assumed that the polarization current **J** in Equation 2.9 is purely electric (i.e., it can be interpreted in terms of averaged charge density and charge velocity $\mathbf{J} = \rho\mathbf{V}$). We exclude from our consideration the case of natural magnetic inclusions that would require magnetic currents from the start.
- The action of the time-dependent magnetic field to samples of nonmagnetic (dielectric or conducting) media as well as to complex-shape molecules is fully described in Equation 2.9 as a response to the spatially variable local electric field [20,21]. There is no need to introduce the response of particles to the magnetic field explicitly.
- In Equations 2.9 through 2.11 we can imply the averaged field (i.e., in these formulas and below $\mathbf{E} \equiv \mathbf{E}_{av}$) instead of the local field. Though the local field is the true reason of the polarization current $\mathbf{E}_{loc}$, in media with WSD it is assumed to be uniquely related to $\mathbf{E}_{av}$ and to the polarization taken at the same point (Equation 2.7 and its anisotropic analogues).

2.3.3 Electric and Magnetic Polarization Currents

In media with multipole polarization the polarization current can be presented through the spatial derivatives of the multipole moments densities. In the index form [26] this expansion is as follows:

$$J_\alpha = j\omega P_\alpha - \frac{j\omega}{2}\nabla_\beta Q_{\alpha\beta} + e_{\alpha\beta\gamma}\nabla_\beta M_\gamma + \frac{j\omega}{6}\nabla_\gamma\nabla_\beta O_{\alpha\beta\gamma} - \frac{1}{2}e_{\alpha\beta\delta}\nabla_\gamma\nabla_\beta S_{\delta\gamma} + \cdots \tag{2.12}$$

Here P_α are Cartesian components of the electric dipole polarization vector (Greek or Latin indices below denote the coordinate axes $x,\ y,\ z$), $Q_{\alpha\beta}$ are the components of the electric quadrupole polarization tensor (dyadic), M_γ are the components of the magnetic dipole polarization vector, $S_{\delta\gamma}$ are the components of the magnetic quadrupole polarization tensor (dyadic), and $O_{\alpha\beta\gamma}$ are the components of the electric octopole polarization tensor (triadic). The Levy-Civita tensor $\overline{\overline{e}}$ with the only nonzero components $e_{xyz,zxy,yzx} = 1$ and $e_{xzy,zyx,yxz} = -1$ (totally antisymmetric unit triadic [26]) is used in Equation 2.12, which defines the root operation as

$$(\nabla \times M)_\alpha = e_{\alpha\beta\gamma}\nabla_\alpha M_\gamma. \tag{2.13}$$

Equation 2.12 can be found in the fundamental books [20,26]; however, the notations used for multipole moments in these books are more complicated, and we use the most simple and clear notations suggested in [18].

Taking into account these multipoles, we take into account effects of both first-order spatial dispersion (e.g., bianisotropy) and second-order spatial dispersion [14,15,19,23,24]. Higher-order multipoles neglected in Equation 2.12 would correspond to the spatial dispersion of the third order and higher orders, to which no known physical effects correspond.* Equation 2.12 can be rewritten in the tensor form

$$\mathbf{J} = j\omega\mathbf{P} - \frac{j\omega}{2}\nabla\overline{\overline{Q}} + \nabla \times \mathbf{M} + \frac{j\omega}{6}\nabla\nabla\overline{\overline{Q}} - \frac{1}{2}\nabla \times \nabla\overline{\overline{S}}. \tag{2.14}$$

We can see that the polarization current is the sum of two components; one of them is the vortex-free (noncirculating) polarization current that is often called the electrical one, the other one is the

* Of course, these terms cannot be neglected for media with strong spatial dispersion, but in the last case Equation 2.12 is divergent [26] and, consequently, useless.

vortex-type (circulating) polarization current that is often called the magnetic one:

$$\mathbf{J} = \mathbf{J}^{\mathrm{el}} + \nabla \times \mathbf{T}^{\mathrm{mag}}, \tag{2.15}$$

where

$$\mathbf{J}^{\mathrm{el}} = j\omega\mathbf{P} - \frac{j\omega}{2}\nabla\overline{\overline{Q}} + \cdots, \tag{2.16}$$

$$\mathbf{T}^{\mathrm{mag}} = \mathbf{M} - \frac{1}{2}\nabla\overline{\overline{S}} + \cdots \tag{2.17}$$

Equations 2.15 through 2.17 together with the expansion (Equation 2.11) are of key importance for the procedure of the introduction of material parameters in composite and molecular media [14,15,18].

2.3.4 Noncovariant Form of Material Equations of Media with WSD

Material equations for time-harmonic fields are introduced in order to get rid of averaged polarization current (the polarization charges are expressed below using the continuity equation) in Maxwell's equations for time-harmonic averaged fields in the medium

$$\nabla \times \mathbf{E} = -j\omega\mathbf{B}, \tag{2.18}$$

$$\nabla \cdot \mathbf{B} = 0, \tag{2.19}$$

$$\nabla \times \mathbf{B} = j\omega\varepsilon_0\mu_0\mathbf{E} + \mu_0\mathbf{J}, \tag{2.20}$$

$$\nabla \cdot \mathbf{E} = \frac{\rho}{\varepsilon_0} = -\frac{\nabla \cdot \mathbf{J}}{\mathrm{J}\omega\varepsilon_0}. \tag{2.21}$$

Here we follow the formalism [2] in which the main (uniquely defined and measurable) field vectors are **E** and **B** (since they define the Lorentz force), and vectors **D** and **H** are auxiliary and introduced in order to replace Equations 2.18 and 2.19 by equations that do not contain the polarization current. The formalism in which vectors **E** and **H** are considered as the main vectors and **D** and **B** are auxiliary is also possible and often convenient. However, in this case the first Maxwell's equation should be of the form: $\nabla \times \mathbf{E} = -j\omega\mu_0\mathbf{H} + \mathbf{J}^{\mathrm{mag}}$, i.e., we have to introduce magnetic currents on the start. This would correspond to the medium with natural magnetic particles. Description of both effects of natural and artificial magnetism is very difficult. If in our initial Maxwell's equations there are no magnetic currents, and the formalism Equations 2.18 through 2.21 based on the main vectors **E** and **B** is more appropriate (see, e.g., in [2]).

Substituting Equation 2.15 into Equation 2.21 we can see that in fact

$$\nabla \cdot \mathbf{E} = -\nabla \cdot \left(\frac{1}{\mathrm{J}\omega\varepsilon_0}\mathbf{J}^{\mathrm{el}}\right). \tag{2.22}$$

Substituting Equation 2.15 into Equation 2.20 we obtain

$$\nabla \times \left(\mathbf{B} - \mathbf{T}^{\mathrm{mag}}\right) = j\omega\mu_0\left(\varepsilon_0\mathbf{E} + \mathbf{J}^{\mathrm{el}}\right). \tag{2.23}$$

Therefore, defining

$$\mathbf{D} = \varepsilon_0\mathbf{E} + \mathbf{J}^{\mathrm{el}}, \quad \mathbf{H} = \mu_0^{-1}\mathbf{B} - \mathbf{T}^{\mathrm{mag}}, \tag{2.24}$$

we obtain equations

$$\nabla \times \mathbf{H} = j\omega\mathbf{D}, \tag{2.25}$$

$$\nabla \cdot \mathbf{D} = 0, \tag{2.26}$$

that complement Equations 2.18 and 2.19 and do not contain polarization currents. Taking into account Equations 2.16 and 2.17 one can see that vectors **D** and **H** are in fact defined through the multipole densities:

$$\mathbf{D} = \varepsilon_0 \mathbf{E} + \mathbf{P} - \frac{1}{2}\nabla \cdot \overline{\overline{Q}} + \frac{1}{6}\nabla \cdot (\nabla \cdot \overline{\overline{\overline{O}}}), \tag{2.27}$$

$$\mathbf{H} = (\mu_0)^{-1}\mathbf{B} + \mathbf{M} - \frac{1}{2}\nabla \cdot \overline{\overline{S}}. \tag{2.28}$$

If there are no other multipoles induced in particles in addition to electric and magnetic dipoles, these equations are reduced to the usual form:

$$\mathbf{D} = \varepsilon_0 \mathbf{E} + \mathbf{P}, \quad \mathbf{H} = (\mu_0)^{-1}\mathbf{B} - \mathbf{M}. \tag{2.29}$$

These equations are usually treated as general definitions of **D** and **B**, and for this special case the definitions of the effective permittivity and permeability are well known. However, the media from particles containing only electro-dipole and magneto-dipole moments form only a special case of media with WSD. For the correct interpretation of experimental results recently obtained for MTM it is very important to know the general theory of media with WSD.

The next step after Equations 2.27 and 2.28 is to express the multipole densities entering Equations 2.27 and 2.28 through the averaged electric field **E** and its spatial derivatives using Equation 2.12 and Equation 2.11 and relate in this way vectors **D** and **B** with **E** and its derivatives. These relations will be further derived to the form of material equations.

By analogy of Equation 2.12 with Equation 2.11 we can write a similar expansion for multipole moments densities through **E** and its derivatives

$$P_\alpha(R) = a_{\alpha\beta}E_\beta(R) + \frac{1}{2}a'_{\alpha\beta\gamma}\nabla_\gamma E_\beta(R) + \frac{1}{6}a''_{\alpha\beta\gamma\delta}\nabla_\gamma\nabla_\delta E_\beta(R) + \cdots \tag{2.30}$$

for the electro-dipole polarization,

$$Q_{\alpha\beta} = Q'_{\alpha\beta\gamma}E_\gamma + \frac{1}{2}Q''_{\alpha\beta\gamma\delta}\nabla_\delta E_\gamma + \cdots \tag{2.31}$$

for the quadrupole one,

$$M_\alpha = M'_{\alpha\beta}E_\beta + \frac{1}{2}M''_{\alpha\beta\gamma}\nabla_\gamma E_\beta + \cdots \tag{2.32}$$

for the magneto-dipole one,

$$S_{\alpha\beta} = S'_{\alpha\beta}E_\beta + \cdots \tag{2.33}$$

for the magneto-quadrupole one, and finally

$$O_{\alpha\beta\gamma} = O'_{\alpha\beta\gamma\delta}E_\delta + \cdots \tag{2.34}$$

for the electric octopole polarization $\overline{\overline{\overline{O}}}$. The second-order spatial dispersion corresponds to the omission of higher-order terms in these expansions [14,15,18,19,23,24].

Before substituting Equations 2.30 through 2.34 into Equations 2.27 and 2.28 we have to separate the symmetric (with respect to the last two indices) part and the antisymmetric part of $\overline{\overline{\overline{a}}}'$ (the electro-dipole susceptibility to the first-order derivatives of **E**). Any antisymmetric triad can be presented as a scalar product of the Levy–Civita tensor and a certain dyadic (denoted below as $2\overline{\overline{g}}/j\omega$). Therefore, we can write

$$a'_{\alpha\beta\gamma} = (a'_{\alpha\beta\gamma})^{\text{symm.}} + (a'_{\alpha\beta\gamma})^{\text{nonsym.}}_{\alpha\beta\gamma} \equiv d_{\alpha\beta\gamma} + e_{\delta\beta\gamma}\frac{2g_{\alpha\delta}}{j\omega}. \tag{2.35}$$

In paper [18] it was proven for an individual particle and in [24] it was done for bulk arrays of particles that the quadrupole susceptibility to the electric field and the symmetric part of the electro-dipole susceptibility to the derivatives of the electric field are related:

$$Q'_{\alpha\beta\gamma} = Q'_{\beta\alpha\gamma} = d_{\gamma\alpha\beta} = d_{\gamma\beta\alpha}. \tag{2.36}$$

Substituting Equations 2.30 through 2.34 into Equations 2.27 and 2.28, we can also use Maxwell's equation (Equation 2.18) rewritten in the index form:

$$B_\beta = \frac{1}{j\omega} e_{\beta\alpha\gamma} \nabla_\alpha E_\gamma. \tag{2.37}$$

After these substitutions one derives from Equations 2.27 and 2.28 the following relations [18]:

$$D_i = \varepsilon_{ij} E_j - g_{ij} B_j + \frac{1}{2}(Q'_{jki} - Q'_{ikj}) \nabla_j E_k + \beta_{ijkl} \nabla_j \nabla_k E_l \tag{2.38}$$

and

$$H_i = \mu_0{}^{-1} B_i - M'_{ij} E_j + \gamma_{ijk} \nabla_j E_k. \tag{2.39}$$

In these equations, Equations 2.35 and 2.36 were taken into account and the following notations

$$\varepsilon_{ij} = \varepsilon_0 I_{ij} + a_{ij}, \quad \beta_{ijkl} = \frac{1}{6}(a''_{iljk} - Q''_{ijkl} - O'_{iklj}), \quad \gamma_{ijk} = \frac{1}{2}(M''_{ijk} - S'_{ijk}) \tag{2.40}$$

were used. Here I_{ij} are the components of the unit dyadic $I_{ij} = 1,\ i = j,\ I_{ij} = 0,\ i \neq j$. The first formula in Equation 2.40 is the usual (static) definition of the permittivity. In media with WSD the tensor $\overline{\overline{\varepsilon}}$ is also defined through the electro-dipole susceptibility to the averaged field. Since this susceptibility corresponds to the zero-order term in the initial expansion (Equation 2.11), the permittivity represents the zero-order response of the medium to the electric field. Of course, the a_{ij} in the wave field can be frequency dispersive, and the words "zero order" refer to the spatial dispersion.

Equations 2.38 and 2.39 still cannot be named as material equations, because the dyadic M'_{ij} and the triad $(Q'_{jki} - Q'_{ikj})$ are not covariant. In [19] it was shown that for an individual particle these dyadics depend on the location of the point to which the particle multipoles are referred. This is because all the multipoles of any particle except the electric dipole moment contain by definition [20,26] the radius vector centered at an arbitrary chosen particle center. This means that all higher multipoles (electric quadrupole, magnetic quadrupole, electric octopole, etc.) are not measurable physical values [14,15,18,19]. The same concerns, in the general case, also the magnetic dipole. Only in two special cases the magnetic dipole susceptibility to the electric field and to its spatial derivatives can be covariant. The first case [15] corresponds to the frequencies at which the polarization current induced in the particle flows along a closed path (loop) and its density is uniform along this effective loop. The second case [25] corresponds to the frequencies at which the electro-dipole susceptibility to **E** and ∇**E** vanishes. The medium corresponding to the first case can be fabricated from particles performed as loops. The medium corresponding to the second case will be discussed below.

Thus, if the open part of a conductive scatterer containing a loop portion (metal split rings, Ω-shaped particles, etc.) is large, i.e., comparable with the circumference of this loop, the magnetic dipole of the particle is not covariant and therefore is not physically measurable. What is covariant (and measurable at least indirectly) is a certain combination of the magnetic dipole with higher multipoles (at least the electric quadrupole). This means that higher multipoles are significant in this case. Notice, that higher multipoles are seldom negligible for media from complex-shape molecules [14,15,18,19]. This is so because complex molecules are rarely shaped like closed loops. The only

known exception are some dies in which atoms form effective knots. Therefore, this theory is of key importance also for media of complex molecules.

In [24] it was derived (using the Equation 2.7) that from the dependence of multipoles moments of a molecule on the choice of the molecule center the dependence of the averaged multipole moments on the Cartesian coordinate origin follows. Therefore, parameters M'_{ij} and $(Q'_{jki} - Q'_{ikj})$ entering Equations 2.38 and 2.39 depend on the location of the coordinate origin for the composite medium with WSD. Of course, the medium material parameters cannot physically depend on the choice of the coordinate origin. Therefore, tensors M'_{ij} and $(Q'_{kij} - Q'_{kji})$ are still not material parameters. Respectively, vectors **D** and **B** defined by Equation 2.24 that are in the second order of spatial dispersion equivalent to noncovariant equation (Equations 2.38 and 2.39) are "not physically sound electric displacement and magnetic induction vectors" in presence of higher multipoles. Such **D** and **B** not only violate usual boundary conditions, they cannot be applied in any boundary problem (since being applied violates the causality of the solution, as it was explicitly shown in [24]). Equations 2.38 and 2.39 were named in [24] as "quasi-material equations" of media with WSD.

2.3.5 Material Equations Covariant in the First Order of WSD

In order to make **D** and **H** covariant at least within the first-order approximation of WSD we should add to **D** and **H** defined by Equation 2.24 certain vectors, denoted below as **K** and **T**, respectively. These vectors should be chosen so that the coordinate dependence of M'_{ij} and $(Q'_{kij} - Q'_{kji})$ in Equations 2.38 and 2.39 is compensated.

Maxwell's equations (Equations 2.25 and 2.26) will be not violated with this redefinition of **D** and **H** if these two additional vectors are related as

$$\mathbf{K} = \frac{1}{j\omega}\nabla \times \mathbf{T}. \tag{2.41}$$

The needed vectors **K** and **T** were found in [19]:

$$K_i = \frac{1}{2}(Q'_{jik} - Q'_{ijk})\nabla_j E_k, \quad T_i = -\frac{j\omega}{2} e_{ijk} Q'_{jkm} E_m. \tag{2.42}$$

The operation

$$\mathbf{D}^{\text{new}} = \mathbf{D}^{\text{old}} + \mathbf{K}, \quad \mathbf{H}^{\text{new}} = \mathbf{H}^{\text{old}} + \mathbf{T} \tag{2.43}$$

applied to Equations 2.38 and 2.39 leads to the following equations (terms of the second order are not shown):

$$D_i = \epsilon_{ij} E_j + \frac{1}{2} e_{ijk} e_{klm} Q'_{mls} \nabla_j E_s - g_{ij} B_j + \cdots \tag{2.44}$$

and

$$H_i = \mu_0^{-1} B_i - \left(M'_{ij} + \frac{j\omega}{2} e_{jkm} Q'_{mik} \right) E_j + \cdots \tag{2.45}$$

Using Equation 2.37, Equations 2.44 and 2.45 can be rewritten in the form

$$D_i = \epsilon_{ij} E_j - \left[g_{ij} + \frac{j\omega}{2} e_{ikm} Q'_{mjk} \right] B_j + \cdots \equiv \epsilon_{ij} E_j + j\xi_{ij} B_j, \tag{2.46}$$

$$B_i = \mu_0 H_i + \mu_0 \left(M'_{ij} + \frac{j\omega}{2} e_{jkm} Q'_{mik} \right) E_j \equiv \mu_0 H_j - j\mu_0 \xi_{ji} E_j. \tag{2.47}$$

In the final form of material equations of media with WSD of the first order derived in [19]

$$\mathbf{D} = \bar{\bar{\epsilon}} \cdot \mathbf{E} + j\bar{\bar{\xi}} \cdot \mathbf{B} + \cdots, \tag{2.48}$$

$$\mathbf{B} = \mu_0 \mathbf{H} - j\mu_0 \bar{\bar{\xi}}^{\mathrm{T}} \cdot \mathbf{E} + \cdots, \tag{2.49}$$

the molecular reciprocity theorem [27] $M'_{ij} = g_{ji}$ was used. In Equations 2.48 and 2.49, $\bar{\bar{\xi}}^{\mathrm{T}}$ denotes the transposed dyadic with respect to $\bar{\bar{\xi}} \equiv j\bar{\bar{g}} - \omega\bar{\bar{e}} : \bar{\bar{Q}}/2 = j(\bar{\bar{M}}')^{\mathrm{T}} - \omega\bar{\bar{e}} : \bar{\bar{\bar{Q}}}'/2$. Here ":" means the double scalar product of tensors.

One can see that the first-order spatial dispersion still does not give magnetic susceptibility of composite or molecular media. The material parameter $\bar{\bar{\xi}}$ is called the magnetoelectric coupling parameter (MCP) [23]. Since we consider reciprocal media, the same MCP $\bar{\bar{\xi}}$ enters both material equations (Equations 2.48 and 2.49). It contains the magneto-dipole susceptibility to the uniform (across the unit cell) part of the averaged electric field, which is equal to the electro-dipole susceptibility to the vortex part of the averaged electric field.* It also contains the quadrupole susceptibility to the uniform part of the electric field.

In lossless media tensor $\bar{\bar{\xi}}$ is purely real [21,24,28], and this is why we introduced the factor j in the definition of this tensor by Equations 2.46 and 2.47. In isotropic media $\bar{\bar{\xi}} = \bar{\bar{\xi}} I$, i.e., MCP is the scalar parameter. In this case it is called the "chirality" parameter [28].

Equations 2.48 and 2.49 are anisotropic generalizations of the so-called Post material equations

$$\mathbf{D} = \varepsilon\mathbf{E} + j\xi\mathbf{B}, \tag{2.50}$$

$$\mathbf{B} = \mu_0 \mathbf{H} - j\mu_0 \xi \mathbf{E}, \tag{2.51}$$

obtained for media formed by helicoidal molecules in [29]. It is one of the standard forms of material equations adopted in the theory of bianisotropic media [21,23,28] such as Fedorov (sometimes Drude–Born–Fedorov) equations [42] or Lindell–Sihvola equations [28]. Equations 2.48 and 2.49 can be expressed in these standard forms, for example, as Lindell–Sihvola equations

$$\mathbf{D} = \bar{\bar{\varepsilon}}' \cdot \mathbf{E} + j\bar{\bar{\kappa}} \cdot \mathbf{H}, \quad \mathbf{B} = \bar{\bar{\mu}} \cdot \mathbf{H} - j\bar{\bar{\kappa}} \cdot \mathbf{E}, \tag{2.52}$$

after some tensor algebra using Maxwell's Equations (2.18 and 2.19). These derivations were done in [48]. However, these two popular forms of bianisotropic material equations are not physically self-consistent with the molecular theory of WSD presented in this section. In Equation 2.52 the MCP $\bar{\bar{\kappa}}$ includes not only first-order parameters $\bar{\bar{\bar{M}}}'$ and $\bar{\bar{\bar{Q}}}'$ as our MCP $\bar{\bar{\xi}}$, but also the electro-dipole susceptibility $\bar{\bar{a}}$ which is the zero-order parameter [48]. Moreover, the nontrivial permeability $\bar{\bar{\mu}}$ in Equation 2.52 includes the electro-dipole susceptibility $\bar{\bar{a}}$ (zero-order parameter) and the quadrupole susceptibility $\bar{\bar{\bar{Q}}}'$ (first-order parameter) and not the parameters of the second order [24].

Physically, the nontrivial magnetic permeability in reciprocal media is the effect of the second order [23,24]. If there are higher multipoles in the medium, the formalism of F.I. Fedorov and that of I. Lindell and A. Sihvola leads to material parameters in which the effects of WSD of different orders are mixed. Therefore, the generalized Post equations (Equations 2.48 and 2.49) are more suitable for the description of WSD, while the Lindell–Sihvola formalism is sometimes more convenient for solving engineering problems.

* That is, to the uniform across the unit cell part of the magnetic field.

2.3.6 Material Equations Covariant in the Second Order of WSD

Now let us rewrite Equations 2.48 and 2.49 including in them the second-order terms from Equations 2.38 and 2.39 that the operation equation (Equation 2.43) keeps intact:

$$D_i = \varepsilon_{ij}E_j + j\xi_{ij}B_j + \beta_{ijkl}\nabla_j\nabla_k E_l \tag{2.53}$$

and

$$H_i = \mu_0{}^{-1}B_i + j\xi_{ji}E_j + \gamma_{ijk}\nabla_j E_k, \tag{2.54}$$

where tetradic tensor with components β_{ijkl} and triadic with components γ_{ijk} are defined through multipole susceptibilities by Equation 2.40. First, in the same way as we did above let us separate the antisymmetric part of the tensor $\overline{\overline{M}}''$:

$$M''_{ijk} = (M''_{ijk})^{\text{symm.}}_{ijk} + (M''_{ijk})^{\text{asym.}}_{ijk} \equiv f_{ijk} + \frac{2}{j\omega}e_{ikm}G_{jm}, \tag{2.55}$$

where again the antisymmetric tensor has been presented through the Levy–Civita triadic and a certain dyadic $\overline{\overline{G}}$. A similar relation as Equation 2.36 for electro-dipole and electro-quadrupole susceptibilities can be written for magneto-dipole and magneto-quadrupole ones [24]:

$$f_{ijk} = f_{jik} = S'_{jik} = S'_{jki}. \tag{2.56}$$

Equation 2.54 can be rewritten after substitutions of Equations 2.55 and 2.56 in the form

$$H_i = (\mu_0{}^{-1}I_{ij} + G_{ij})B_j + j\xi_{ji}E_j + (S'_{jik} - S'_{ijk})\nabla_j E_k. \tag{2.57}$$

Of course in Equation 2.57 we again took into account the relation given in Equation 2.37.

Equations 2.53 and 2.57 are still not material equations since tensors with components G_{ij} and $(S'_{jik} - S'_{ijk})$ are origin dependent. We have to find a vector $\mathbf{T}'$ so that the operation

$$D^{\text{new}} = \mathbf{D}^{\text{old}} + \nabla \times \mathbf{T}', \quad \mathbf{H}^{\text{new}} = \mathbf{H}^{\text{old}} + j\omega\mathbf{T}' \tag{2.58}$$

would give new **D** and **B** which are covariant in the second order of spatial dispersion. At this point we can notice that the coefficients in the expansion (Equation 2.11) are origin independent. This is because the current **J** is a measurable quantity, unlike all the higher multipoles. The comparison of Equations 2.11 and 2.12 gives a set of equations relating covariant coefficients b_{ij}, b_{ijk}, b_{ijkl} with origin-dependent multipole polarizabilities (see also in [24]):

$$b_{ij} = a_{ij}, \quad b_{ijk} = \frac{1}{2}(a'_{ijk} - Q'_{ikj}) + \frac{1}{j\omega}e_{ikn}M'_{nj}, \tag{2.59}$$

$$b_{ijkl} = \frac{1}{6}(a''_{ijkl} - Q''_{ikjl} + O'_{iklj}) + \frac{1}{2j\omega}e_{ikn}(M''_{njl} - S'_{nlj}). \tag{2.60}$$

The last equation rewritten in the form

$$b_{ijkl} = \frac{1}{6}(a''_{ijkl} - Q''_{ikjl} + O'_{iklj}) + \frac{1}{2j\omega}e_{ikn}(S'_{jln} - S'_{nlj}) \tag{2.61}$$

is what we need. We can notice that adding the term

$$K'_i = (\nabla \times \mathbf{T}')_i = \frac{1}{2j\omega}e_{ikn}(S'_{jln} - S'_{nlj})\nabla_k E_j \tag{2.62}$$

to $\mathbf{D}^{\text{old}}$ defined by Equation 2.53 we obtain D^{new} in the form

$$D_i = \varepsilon_{ij}E_j + j\xi_{ij}B_j + b_{ijkl}\nabla_l\nabla_k E_j, \tag{2.63}$$

i.e., an equation that contains the terms of the second order with covariant coefficients.

It is possible to show that the operation given in Equation 2.58 with vector $\mathbf{T}'$ that can be found from Equation 2.62 removes from the Equation 2.57 the term $(S'_{jik} - S'_{ijk})\nabla_j E_k$ and simultaneously adds to G_{ij} a dyadic that makes the corresponding coefficient origin independent [24]. The result of the operation (Equation 2.58) with substitution of Equation 2.62 is as follows:

$$D_i = \varepsilon_{ij}E_j + j\xi_{ij}B_j + b_{ijkl}\nabla_l\nabla_k E_j, \tag{2.64}$$

$$H_i = (\mu_{ij})^{-1}B_j + j\xi_{ji}E_j. \tag{2.65}$$

In these material equations the following notations have been introduced:

$$(\mu^{-1})_{ij} = \frac{1}{\mu_0}I_{ij} + G_{ij} - \frac{j\omega}{2}e_{jkm}S'_{imk}. \tag{2.66}$$

It is clear that the inverse tensor to $(\overline{\overline{\mu}}^{-1})$ is the medium permeability in which the magnetic susceptibility arises as an effect of the second-order spatial dispersion. The dyadic $\overline{\overline{G}}$ is the susceptibility of the magnetic dipole to the vortex part of the electric field and the triadic $\overline{\overline{\overline{S}}}$ is the susceptibility of the magnetic quadrupole to the uniform part of the electric field. This is the physical meaning of the permeability in media with WSD. Since media with WSD are local media, and material parameters in Equations 2.64 and 2.65 are covariant, these equations can be applied in boundary problems. The term $b_{ijkl}\nabla_l\nabla_k E_j$ does not comprise first spatial derivatives of $\nabla \times \mathbf{E}$ since b_{ijkl} is symmetric with respect to the pairs of indices $(j,\ k)$ and $(j,\ l)$. It follows from Equation 2.61 and the known properties of multipolar susceptibilities.* Equations 2.64 and 2.65 do not contain the bianisotropy in the second order of spatial dispersion. However, the second order of spatial dispersion for media from complex-shape molecules comprises the susceptibilities of higher multipoles.

2.3.7 Special Cases of Material Equations in Media with WSD

When higher-order multipoles are negligible, the electro-dipole and magneto-dipole polarizations give the following special results for the material parameters entering Equations 2.64 and 2.65:

$$b_{ijkl} = 0, \quad \overline{\overline{\overline{\xi}}} = j(\overline{\overline{M}}')^{\mathrm{T}}, \quad \overline{\overline{\mu}} = \mu_0(\overline{\overline{I}} + \mu_0\overline{\overline{G}})^{-1}.$$

In this case, Equations 2.64 and 2.65 take the form

$$\mathbf{D} = \overline{\overline{\varepsilon}} \cdot \mathbf{E} + j\overline{\overline{\overline{\xi}}} \cdot \mathbf{B}, \quad \mathbf{B} = \overline{\overline{\mu}} \cdot (\mathbf{H} - j\overline{\overline{\overline{\xi}}} \cdot \mathbf{E}), \tag{2.67}$$

i.e., they take the form of anisotropic Post equations. The difference between Equation 2.67 and the anisotropic Post equations for media with first-order spatial dispersion is the nontrivial permeability.

* The quadrupole susceptibility to the derivatives of **E** entering Equation 2.61 contains the nonsymmetric part with respect to indices $(j,\ k)$. However, this nonsymmetric part cancels out with the nonsymmetric part of the second term in the righthand side of Equation 2.61 containing the susceptibility of the magnetic quadrupole to **E**. As a result, the electric quadrupole polarization of particles by the magnetic field does not enter the material equation (Equation 2.64).

If the scatterers possess no bianisotropic response (the corresponding restrictions to the scatterer geometry are discussed in [23]), the MCP is also equal to zero and we have simply

$$\mathbf{D} = \overline{\overline{\varepsilon}} \cdot \mathbf{E}, \quad \mathbf{B} = \overline{\overline{\mu}} \cdot \mathbf{H}. \tag{2.68}$$

The obvious condition of these material equations is the absence of higher-order multipoles. They are evidently negligible when the medium polarization is purely an electro-dipole one. If it is not so, and there are vortex-type polarization currents, then higher multipoles can be present. When the vortex-type currents form effective loops and currents are uniform along these loops, higher multipoles are absent and we can use Equation 2.68.

In the isotropic case media with spatial dispersion of the second order can also contain higher multipoles. From the symmetry the only possible isotropic representation of the term $b_{ijkl}\nabla_l\nabla_k E_j$ in Equation 2.64 is b grad div **E**, which gives [23]

$$\mathbf{D} = \varepsilon\mathbf{E} + j\xi\mathbf{B} + b\nabla\nabla\cdot\mathbf{E}, \tag{2.69}$$

$$\mathbf{H} = \mu^{-1}\mathbf{B} + j\xi\mathbf{E}. \tag{2.70}$$

Substituting the second material equation into the first one we can rewrite these equations in the form generalizing the Lindell–Sihvola equations for reciprocal isotropic media with spatial dispersion of the first order (also called "chiral" media):

$$\mathbf{D} = \varepsilon'\mathbf{E} + j\xi'\mathbf{H} + b\nabla\nabla\cdot\mathbf{E}, \tag{2.71}$$

$$\mathbf{B} = \mu\mathbf{H} - j\xi'\mathbf{E}, \tag{2.72}$$

where new material parameters are expressed through EMP of our molecular theory as follows:

$$\varepsilon' = \varepsilon + \xi^2\mu, \quad \xi' = \xi\mu. \tag{2.73}$$

The term $b\nabla\nabla\cdot\mathbf{E}$ cannot be removed from Equation 2.71 by further redefinition of **D** and **H** since such redefinition would violate the covariance of material equations. The same concerns anisotropic equations (Equations 2.64 and 2.65). These equations can be also expressed in the generalized Lindell–Sihvola form:

$$D_i = \varepsilon'_{ij}E_j + j\xi'_{ij}H_j + b_{ijkl}\nabla_k\nabla_l\mathbf{E}_j, \tag{2.74}$$

$$B_i = \mu'_{ij}H_j - j\xi'_{ji}\mathbf{E}. \tag{2.75}$$

However, in the presence of higher multipoles effects of the zero, first and second orders will be mixed in new EMP $\overline{\overline{\varepsilon}}'$, $\overline{\overline{\mu}}'$ and $\overline{\overline{\xi}}'$.

2.4 What the Theory of WSD Reveals for MTM

The theory of WSD reveals the following features of reciprocal composite or molecular media:

- The magnetoelectric coupling is the effect of the spatial dispersion of the first order, and the artificial permeability is the effect of the spatial dispersion of the second order.
- In presence of higher multipoles induced in the particles both MCP and permeability contain contributions from multipolar susceptibilities (additionally to the electric and magnetic dipole moment susceptibilities per unit volume).
- In media with spatial dispersion of the second order (except the special case when higher-order multipoles are absent) the first material equation contains second-order derivatives of **E**, i.e., the medium cannot be described in terms of only three EMP (permittivity, permeability, and MCP).

These conclusions force us to revise many scientific publications devoted to MTM. In the literature there are numerous attempts to describe MTM with magnetic response in terms of only permittivity and permeability, i.e., using Equation 2.68. These equations are applicable if there is no bianisotropy and if, simultaneously, the higher-order multipoles are negligible. The last condition means that current circulating in a magnetic scatterer should be uniform around its closed effective path.

If this scatterer is the so-called SRR formed by two very strongly coupled concentric broken loops as in [30,31], the polarization current induced in it is practically uniform. It is the conductivity current, and the displacement currents are concentrated between the two rings [40]. This means that the magnetic dipole induced in this SRR turns out to be covariant. Simultaneously, the quadrupole moment of the SRR is negligible. Probably (though this was never studied) the other higher multipoles are also negligible close to the resonant frequency of the magnetic dipole induced in this particle and below it. Then the medium of SRRs can be really described (in the region where the spatial dispersion is weak) by Equation 2.68.

If the magnetic scatterer is an S-shaped metal particle as in [32] (in this work the negative magnetic response is attributed to composites of these as well as similar particles) or a single split ring (C-shaped particle), the conductivity current is strongly nonuniform and does not form a closed loop (the displacement currents are widely spread around the effective loop, and the significant alternating charges are accumulated at the ends of the S-shaped conductor). In other words, the S-particle is a multipolar particle. What is considered as negative magnetic response of the medium of such particles should be shared between $\overline{\overline{\mu}}$ and the material parameter located in front of the second derivatives of **E** in Equation 2.64 (the S-particles were specially paired in [32] in order to avoid the medium bianisotropy, so the MCP is zero).

If magnetic scatterers of effective media are formed by pairs of resonant electric scatterers like pairs of plasmonic nanopyramids [33], pairs of nanowires or nanoplates [34,35], higher multipoles obviously dominate over the magnetic dipole, and the use of Equation 2.68 instead of Equations 2.64 and 2.65 may lead to serious misinterpretations. What can one achieve expressing the dispersion characteristics of such media in terms of $\overline{\overline{\varepsilon}}$ and $\overline{\overline{\mu}}$ without taking into account the last term in Equation 2.64 as well as heuristically defining EMP, fitting only two tensor values $\overline{\overline{\varepsilon}}$ and $\overline{\overline{\mu}}$ to transmission and reflection characteristics? It is the same as to attribute the electric multipolar response of the material to the permeability. Physical interpretation of the results [33–35] described as artificial magnetism needs further theoretical clarification.

Let us consider an example of a complex "magnetic" particle for the visible range of frequencies realized as a closely positioned pair of small plasmonic nanoparticles. Such nanopairs forming a metamaterial were described, in [33]. As it was shown in [33] and in precedent works, within the band of the so-called plasmonic resonance of the individual nanoparticle, there is a frequency at which the magnetic mode is excited in the pair. This mode corresponds to the antiparallel excitation of resonant electric dipoles in two nanoparticles. As a result, the total electro-dipole moment of the nanopair at this mode is zero, and the particle can be presented as a superposition of a magnetic dipole and an electric quadrupole, both with susceptibilities to **E** and its spatial derivatives, and a magnetic quadrupole and electric octopole, both with susceptibilities to **E**.

Let the nanopair be excited by a wave propagating along X, as it is shown in Figure 2.1, left panel. Then at a certain frequency $\omega = \omega_{mag}$ the phase shift of the wave between two nanospheres will be such that $p_2 = -p_1 \equiv -p$, and the total electric dipole moment vanishes. In this case the magnetic moment* of the nanopair is origin independent. This was discussed above: The zero electro-dipole polarizability leads to the independence of **m** on the location of the particle center. The octopole moment can be neglected. The electric quadrupole polarization by the magnetic

* As well as the quadrupole moment.

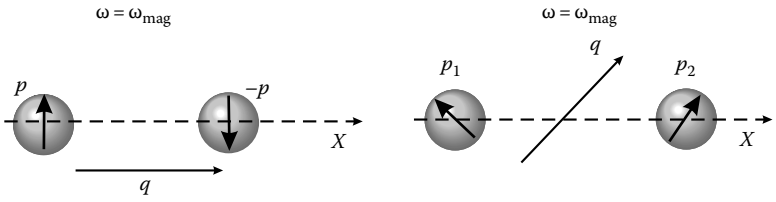

FIGURE 2.1 A nanopair of two plasmonic spheres at $\omega = \omega_{mag}$. Left: a purely magnetic mode is excited when the wave propagates along X. Right: a superposition of modes is excited when the wave propagates obliquely.

field and the magnetic quadrupole polarization by **E** does not enter into our material equations (Equations 2.64 and 2.65), as it was noticed above. This means that the local electric field (the field of the exciting wave at the pair center) does not excite the nanopair. The excitation is due to the nonzero local magnetic field (nonzero spatial derivative of **E** at the pair center).

In this special case the response of the lattice formed by parallel nanopairs is truly magnetic. This can explain why in the literature one characterizes such structures by permittivity and permeability without involving terms with $\nabla\nabla \cdot \mathbf{E}$.

However, this characterization is not fully consistent. First, beyond this special frequency the total dipole moment will be nonzero even for this special direction of propagation. And both magnetic and quadrupole moments become noncovariant. We should take into account the susceptibility of the quadrupole polarization to the spatial derivatives of **E** and use material equations (Equations 2.64 and 2.65) (with vanishing MCP $\overline{\overline{\xi}} = 0$ since a pair of equivalent dipoles is not bianisotropic). Second, material parameters of a homogeneous magnetic medium even at the special frequency $\omega = \omega_{mag}$ should not depend on the direction of propagation. If the propagation is oblique, as it is shown in Figure 2.1, right panel, the phase shift of the wave over the nanopair at the same frequency will be different. Therefore, $p_2 \neq -p_1$, i.e., not only the magnetic dipole mode but also the electro-dipole mode will be excited in every nanopair of the medium. Even at this special frequency we come to material equations (Equations 2.64 and 2.65) in which the term $\nabla\nabla \cdot \mathbf{E}$ vanishes only for a special direction of propagation.

Notice, however, that in the case of a plasmonic nanopair in which the resonance bands of the magneto-dipole and electro-dipole modes are separated on the frequency axis, the magnetic mode can be excited without parasitic excitation of the electric mode for any direction of propagation. In this case the medium of such nanopairs would behave as a resonant magnetic within the "magnetic" band and as a resonant dielectric within the "electric" band. This is not the case of nanopyramids reported in [33]. Is it the case of paired nanowires or nanoplates [34,35]? In this chapter we avoid the discussion of these works since our goal is to show the general frames of the description of homogenized MTM in terms of material parameters. We also try to motivate additional theoretical investigations of MTM with artificial magnetism taking into account resonant multipolar polarizations existing, probably, in all of them. The same remark concerns, of course, the magnetism of optical SRRs reported in works [36–40] and some other works.

In some papers (e.g., in [41,42]) isotropic [41] or anisotropic [42]* permeability is attributed to photonic crystals in order to describe their strong spatial dispersion in the vicinity of the Bragg mode. This kind of "artificial magnetism" description is not very useful because the nonlocal permittivity and permeability defined by Equations 2.2 and 2.3 can have an arbitrary sign, and only few physical

* As it was shown above, the obvious angular dependence of ε and μ is implied in both these cases.

effects can be related with their signs: the stop-band if their signs are opposite and the backward-wave regime if their signs are negative, since the product of nonlocal permittivity and permeability is by definition the square of the refraction index. However, these effects are fully described in terms of the refraction index, and there is no need to extract material parameters from it, if they anyway do not measure averaged polarization in the medium.

2.5 An Alternative Approach to the Description of WSD

An alternative approach to the description of WSD was suggested in [2] and developed in [22]. This approach is based on the definition of auxiliary field vectors **H** and **D**, instead of Equations 2.24, by equations

$$\mathbf{D} = \varepsilon_0 \mathbf{E} + \mathbf{J}, \quad \mathbf{H} = \mu_0^{-1} \mathbf{B}. \tag{2.76}$$

No splitting of the polarization current to the electric part and the vortex-type part is implied and, of course, this approach also allows us to satisfy Maxwell's equations (Equations 2.25 and 2.26). This method allows one to avoid the consideration of multipoles, and this is a serious simplification of the theory (recall that the definitions (Equation 2.24) were also not suitable for multipolar media and we have twice redefined **H** and **D** adding to them vectors **T**, **K** and **T′**, **K′** in order to introduce origin-independent material parameters). Then it is assumed that the plane wave with wave vector **q** propagates in the medium, which allows us to rewrite Equation 2.11 in the form

$$J_i = j\omega(b_{ij}E_j + jb_{ijk}q_k E_j - b_{ijkl}q_l q_k E_j + \cdots) \tag{2.77}$$

and substituting this relation into Equation 2.76, we immediately obtain

$$D_i = \varepsilon_{ij}(\omega, \mathbf{q})E_j, \quad \varepsilon_{ij}(\omega, \mathbf{q}) = \varepsilon_{ij}^{(0)}(\omega) + j\gamma_{ijk}(\omega)q_k + j\gamma_{ijkm}(\omega)q_k q_m + \cdots \tag{2.78}$$

and $\overline{\overline{\mu}} = \mu_0 \overline{\overline{I}}$. Here the expressions for coefficients $\varepsilon_{ij}^{(0)}(\omega)$, $\gamma_{ijk}(\omega)$, and γ_{ijkm} through b_{ij}, b_{ijk}, and b_{ijkl} are evident.

This simple approach is mostly fruitful if $\gamma_{ijk} \equiv 0$ (for nongyrotropic crystals in terms of [22]). The spatial dispersion studied in this book is related with the nonzero phase shift of the wave per unit cell. In fact, the term of the second order in Equation 2.78 cannot be neglected even for electro-dipole lattices (in this theory they were neglected for this case), if we inspect the fine effects accompanying the refraction of visible light into crystals. These effects are the generation of so-called exciton and polariton waves by the incident light at the crystal boundary.*

Usual boundary conditions for light are obviously complemented in this situation by additional boundary conditions, which can express different quantum states of the surface (e.g., well-known Tamm's or Shockley's states) and take into account the finite distances between surface atoms [22].

This spatial dispersion has little to do with that considered above. Though the general formula (Equation 2.11) is valid in both theories, this theory ignores the **q**-dependent corrections in the formula equation (Equation 2.7) and implies uniquely related local and averaged fields, and the theory

* Polaritons are exponentially decaying eigenwaves of the lattice of electromagnetic nature (in lossless dielectric crystals they are transversally electric (TE)-polarized with respect to the energy propagation). Excitons are waves of **E** which are not TE (nor transversally magnetic (TM)). If they are not purely longitudinal (in semiconductors) they are called real excitons (and are related to electron-hole pairs), if they are longitudinal they are mechanical ($\mathbf{E} = 0$ but $\mathbf{P} \neq 0$) and Coulomb ($\nabla \times \mathbf{E} = 0$) excitons. Excitons are not important for MTM. Polaritons in MTM lattices can be important, but this effect cannot be taken into account within the framework of the homogenized model of the lattice.

developed in [43] avoids the use of this formula. For scientists working in the optics of natural crystal media the most important effects of WSD are related with the terms that we neglected in our molecular theory. As a result, for the theory developed in [22] the concept of the local field becomes useless. All the effects of WSD are described in terms of **q**-dependent vectors and tensors (averaged polarization current **J**, averaged field **E**, and permittivity $\overline{\overline{\varepsilon}}$).

The theory of WSD neglects excitons and polaritons but takes into account the possibility of resonant frequency response of coefficients entering the expansion equation (Equation 2.78). In our case these coefficients correspond to not purely electro-dipole polarization of medium particles. Unlike [44] and similar works, we assume that the volume of integration around the particle center in Equation 2.9 is the volume of the particle. And the second-order terms can be significant due to the resonant response of the particle. As a result, the **q** dependence disappears in this theory, but we have to introduce the magnetic moment and higher multipoles.

The authors of [22] assume that the volume Ω is that of the unit cell and the second-order terms are taken into account not because they can be resonant and large, but because they are **q** dependent and their presence in the medium response makes possible polaritons and excitons. It is not a theory of local medium. In other words, the theory [22] does not offer a model of lattice homogenization.

Recently, the approach based on Equations 2.78 was applied in [43] in order to explain the negative refraction in terms of the second-order spatial dispersion. It was successfully done for isotropic media. However, on this way the authors of [43] came to our model. Additionally, to the assumption of the isotropic non-chiral medium $\varepsilon_{ij}^{(0)} = \varepsilon^{(0)} I_{ij}$ and $\gamma_{ijk} \equiv 0$ the authors of [43] introduced the assumption (formula (21) of [43]) that in their isotropic media tensor γ_{ijkm} takes the special form

$$\gamma_{ijkm}(\omega) = a_1(\omega) I_{ij} I_{km} + \frac{a_2(\omega)}{2}\left(e_{rik} e_{rjm} + e_{rim} e_{rjk}\right). \tag{2.79}$$

This substitution transforms the equation $D_i = \varepsilon_{ij}(\omega, \mathbf{q}) E_j$ in the absence of bianisotropy ($\gamma_{ijk} = 0$) into

$$\mathbf{D} = \varepsilon^{(1)}(\omega)\mathbf{E} + a_2(\omega)\nabla \times \nabla \times \mathbf{E}. \tag{2.80}$$

Let us now redefine **D** and **H** following the Equation 2.58 where $\mathbf{T}' = -a_2 \nabla \times \mathbf{E}$ and obtain

$$\mathbf{D} = \varepsilon^{(1)}(\omega)\mathbf{E}, \quad \mathbf{B} = \mu(\omega)\mathbf{H}, \tag{2.81}$$

where

$$\mu(\omega) = \frac{\mu_0}{1 - \omega^2 \mu_0 a_2^2}. \tag{2.82}$$

This redefinition does not violate the covariance of material parameters since all the parameters in the initial equation (Equation 2.78) are covariant, and it transforms the material equations of the medium with second-order spatial dispersion to material equations of a usual isotropic magneto-dielectric.

Equation 2.82 was first derived in [23] and in our theory the material equations (Equation 2.81) correspond to media without higher multipoles (compare with Equation 2.68). It is clear that formula equation (Equation 2.79) is a restrictive assumption which is equivalent to the assumption of local isotropic μ (no dependence on **q** in material equations) and to vanishing of the term grad $\nabla \cdot \mathbf{E}$ in this special case of Equation 2.71. Excitons and polaritons are then neglected in this special case, as in the theory of WSD. In other words, paper [43] gives the same results for negative refraction as compared to its previous description in terms of negative permittivity and permeability in [44]. Results of [43] confirm the theory of WSD [24].

An anisotropic analogue of formula (Equation 2.82) was derived in [10]:

$$\mu_{ii} = \frac{\mu_0}{1 - \frac{\omega^2 \mu_0}{2} \frac{\partial^2 \varepsilon_{jj}(\omega, \mathbf{q})}{\partial q_k^2}\Big|_{q_i = q_j = q_k = 0}}. \tag{2.83}$$

In Equation 2.83 the permittivity with components ε_{jj} is defined by Equation 2.78. Notice that we presented above the material parameters in arbitrary Cartesian system where they could comprise off-diagonal terms. Equation 2.83 was derived for lossless (practically for low-loss) lattices when in the lattice coordinate system the tensor $\overline{\overline{\varepsilon}}$ is diagonal. Equation 2.83 gives the same result for $\overline{\overline{\mu}}$. The model of the homogenization of lattices discussed in [20] also does not imply the existence of higher multipoles.*

Section 2.6 is devoted to the physical limitations imposed to local EMP of composite or molecular media that follow from the obvious causality and passivity conditions. These limitations are strongly related to the energetic relations in frequency-dispersive media. Therefore, we will first inspect the energy density in such media.

2.6 Energy Density in Passive Artificial Materials and Physical Limitations to Their Material Parameters

It is well known that in causal media (and all passive materials are causal), dispersion is accompanied by losses. Thus, even the definition of stored field energy is far from being trivial (the usual definition applies only to materials with negligible losses [2]). Also, causality imposes restrictions on physically possible values of material parameters. This chapter presents an overview of these aspects of metamaterial modeling. This subsection is based on previously published papers [45–47]. We restrict our analysis to the case of isotropic media without bianisotropy and higher multipoles, i.e., assume that material equations take the form as in Equation 2.81. Similar analysis for anisotropic media is possible; however, we do not need it. This chapter is concentrated on local reciprocal bulk artificial materials. In [2,§38] it was briefly noticed that the same physical limitations concern the components of the permittivity tensor of reciprocal crystal media as those imposed to the isotropic ε. The physical reason of it becomes clear if we consider the permittivity tensor in the diagonal form (i.e., in the Cartesian coordinates comprising the optical axes). Three components of $\overline{\overline{\varepsilon}}$ enter separately in the refraction coefficient of the wave propagating along Cartesian axes and having three orthogonal polarizations. The same assertion can be applied to the components of the permeability tensor $\overline{\overline{\mu}}$. In composites with both nontrivial $\overline{\overline{\varepsilon}}$ and $\overline{\overline{\mu}}$ all components of these tensors are responsible for refraction *index* and wave impedances of waves propagating along the Cartesian axes. The limitations we impose below to ε and μ of isotropic media can be referred to as components of $\overline{\overline{\varepsilon}}$ and $\overline{\overline{\mu}}$, if the composite medium is described by Equation 2.68. For the case of bianisotropic media the physical restrictions for MCP are also known [21,23]. However, in this section we do not consider biansiotropic composites and also avoid the case when 2d-order derivatives of **E** must be taken into account in material equations. The physical limitations to the corresponding material parameter are still unknown and the energy density in such multipolar media has not been studied.

2.6.1 Energy Density

It is well known that the field energy density in materials can be uniquely defined in terms of the effective material parameters only in case of small (negligible) losses [2]. This is because in the general case when absorption cannot be neglected, the terms

$$\mathbf{E} \cdot \frac{\partial \mathbf{D}}{\partial t} + \mathbf{H} \cdot \frac{\partial \mathbf{B}}{\partial t} \tag{2.84}$$

* This work allows one to understand better the bounds between weak and strong spatial dispersion and also explains the usefulness of nonlocal material parameters which was already discussed above.

describe both the rate of changing the stored energy and the absorption rate. Only if the absorption is negligible, we can write

$$\mathbf{E}\cdot\frac{\partial\mathbf{D}}{\partial t}+\mathbf{H}\cdot\frac{\partial\mathbf{B}}{\partial t}=\frac{\partial w_{\mathrm{e}}}{\partial t}+\frac{\partial w_{\mathrm{m}}}{\partial t}, \tag{2.85}$$

where w_{e} and w_{m} are the energy densities of the electric and magnetic fields, respectively.

For artificial materials based on metal or dielectric inclusions of various shapes absorption can be neglected when the operational frequency is far from the resonant frequencies of the inclusions and from the lower Bragg resonant frequency where the phase shift per period approaches 180°, if the material is periodical. For electromagnetic fields whose spectrum is concentrated near a certain frequency ω_0, the time-averaged energy density in a material with scalar frequency-dispersive parameters $\epsilon(\omega)$ and $\mu(\omega)$ reads [2,20]

$$w=w_{\mathrm{e}}+w_{\mathrm{m}}=\frac{1}{2}\left.\frac{\mathrm{d}(\omega\epsilon(\omega))}{\mathrm{d}\omega}\right|_{\omega=\omega_0}|E|^2+\frac{1}{2}\left.\frac{\mathrm{d}(\omega\mu(\omega))}{\mathrm{d}\omega}\right|_{\omega=\omega_0}|H|^2. \tag{2.86}$$

If in the vicinity of the operating frequency ω_0 the frequency dispersion can be neglected and ϵ and μ can be assumed to be independent from the frequency (e.g., when the operating frequency is far from resonant frequencies of inclusions and well below the Bragg resonance), Equation 2.86 simplifies to

$$w=\frac{1}{2}\epsilon|E|^2+\frac{1}{2}\mu|H|^2. \tag{2.87}$$

The validity of this formula is restricted to positive values of ϵ and μ because no passive media in thermodynamic equilibrium can store negative reactive energy, as this is forbidden by the thermodynamics (the second principle)* [2,49]. This means that frequency dispersion cannot be neglected when estimating the stored energy in the frequency regions where the material parameters are negative.

If the material has considerable losses near the frequency of interest, it is not possible to define the stored energy density in a general way (more precisely, it is not possible to express that in terms of the material permittivity and permeability functions) [2]. Knowledge about the material microstructure is necessary to find the energy density, and this problem is far from trivial. A general method to find the reactive energy density in lossy dispersive magnetodielectrics is presented in [45,47].

2.6.2 Material Parameter Limitations for Low-Loss Passive Linear Media

2.6.2.1 Causal Dispersion

In this section we consider passive linear materials in thermodynamic equilibrium in the frequency regions where absorption can be neglected and the field energy density can be found in terms of the effective permittivity and permeability functions. For simplicity of writing, we restrict the analysis to isotropic media.

L.D. Landau and L.M. Lifshitz in [2,§42] give a proof that for all linear "passive" materials in the frequency regions with weak absorption (here this assumption means that the frequency-domain effective parameters can be assumed to be real functions of the frequency) the value of w in Equation 2.86 is not only always positive,† but it is always larger than the energy density of the same fields

* In thermodynamically nonequilibrium states, e.g., in nonuniform magnetized plasmas, the field energy may take negative values [48] leading to power amplification and instabilities, see also [46].

† Positiveness of the derivatives in Equation 2.86 is equivalent to the Foster theorem in the circuit theory.

E and **H** in vacuum. Indeed, the following inequalities can be derived from the causality requirement assuming negligible losses [2]:

$$\frac{d\epsilon(\omega)}{d\omega} > 0 \tag{2.88}$$

(Equation 84.1 in [2]) and

$$\frac{d\epsilon(\omega)}{d\omega} > \frac{2(\epsilon_0 - \epsilon)}{\omega} \tag{2.89}$$

(Equation 84.2 in [2]). Summing these two inequalities one finds that [4, §42]

$$\frac{d(\omega\epsilon(\omega))}{d\omega} > \epsilon_0. \tag{2.90}$$

The same is true for the permeability as well, because in the frequency range where permeability can be defined as a physical linear response function, it satisfies the same physical conditions as permittivity [2]:

$$\frac{d(\omega\mu(\omega))}{d\omega} > \mu_0. \tag{2.91}$$

This has a clear physical meaning: To create fields in a material, work must be done to polarize the medium, which means that in the absence of losses more energy will be stored in the material than in vacuum. This result is very general and applies also to passive low-loss MTM with negative parameters, because this result follows only from the causality principle applied to linear systems.

Inequality (Equation 2.89) can be cast in equivalent form

$$\frac{d(\omega\epsilon(\omega))}{d\omega} > 2\epsilon_0 - \epsilon(\omega). \tag{2.92}$$

Depending on the value of ϵ, either Equation 2.90 or Equation 2.92 is the stronger inequality. As is seen from Equation 2.92, when the permittivity is negative and large in the absolute value, it must be very dispersive.

Considering plane electromagnetic waves in transparent isotropic dispersive materials, Sivukhin [50] gave one more limitation on the relative material parameters:

$$\frac{d(\omega\epsilon_r(\omega))}{d\omega} + \frac{\mu_r}{\epsilon_r}\frac{d(\omega\mu_r(\omega))}{d\omega} > 0. \tag{2.93}$$

This relation holds if "both" ϵ_r and μ_r are either positive or negative [50].

If in a certain model the material parameters are assumed to be completely lossless, the above inequalities can become equalities. For example, the lossless plasma permittivity function

$$\epsilon(\omega) = \epsilon_0\left(1 - \frac{\omega_p^2}{\omega^2}\right) \tag{2.94}$$

is just on the allowed limit, because in this case

$$\frac{d(\omega\epsilon(\omega))}{d\omega} = \epsilon_0\left(1 + \frac{\omega_p^2}{\omega^2}\right) = 2\epsilon_0 - \epsilon(\omega). \tag{2.95}$$

It is easy to check that the lossless Lorentz permittivity model [1,§2.3.4]

$$\epsilon(\omega) = \epsilon_0\left(1 + \frac{\omega_p^2}{\omega_0^2 - \omega^2}\right) \tag{2.96}$$

satisfies all the above inequalities at all frequencies. Losses in this model are taken into account by the small parameter γ ($|\gamma| \ll \omega_0$) that describes in media from natural atoms the relaxation of the electron oscillations [2], in media from complex resonant molecules the relaxation of molecular oscillations [14], and in composite media the relaxation of the polarization currents. In all these cases the dispersion relation (Equation 2.96) generalizes to the form

$$\epsilon(\omega) = \epsilon_0 \left(1 + \frac{\omega_p^2}{\omega_0^2 - \omega^2 + j\gamma\omega}\right). \tag{2.97}$$

The sign of the parameter γ will be discussed below.

Modeling of artificial magnetic materials requires more care because the very notion of permeability loses its physical meaning at high frequencies before the permittivity loses its meaning. This is so because the permeability arising due to the spatial dispersion of the 2d order is more sensitive to the spatial dispersion than the permittivity. Thus, the model permeability expressions obtained from quasi-static considerations do not necessarily satisfy the basic physical requirements at high frequencies. An important example is the effective permeability of a mixture of chiral or omega particles [51], or SRRs [52,53], or of arrays of "Swiss rolls" [53]:

$$\mu = \mu_0 \left(1 + \frac{A\omega^2}{\omega_0^2 - \omega^2 + j\gamma\omega}\right). \tag{2.98}$$

This function has a physically sound behavior (the loss coefficient γ is assumed to be small compared to ω_0) at low frequencies ($\mu(\omega) = O(\omega^2)$) and near the resonance. But in the limit $\omega \to \infty$ it essentially does not tend to μ_0. Really, Equation 2.98 gives $\mu(\omega \to \infty) \to 1 - A$; however, the amplitude of the Lorentz resonance A can be much larger than unity. However, in the limit of extremely high frequencies materials cannot be polarized at all because of inertia of electrons, so the parameters must tend to ϵ_0 and μ_0. As a result, this expression becomes nonphysical (due to instantaneous response of the material, condition given by Equation 2.91 is not satisfied) at frequencies larger than $\sqrt{3}\omega_0$. For this reason, some authors use the simple Lorentz dispersion law (Equation 2.96) to model the effective permeability of dense arrays of SRRs [54]. This model is physically sound at high frequencies, but fails in the low-frequency limit, because in that case the effective permeability does not tend to μ_0 at $\omega \to 0$. However, in the static limit artificial magnetic response cannot exist because static magnetic field cannot induce any current in nonmagnetic inclusions. In the vicinity of the resonant frequency both models give similar results.

As explained in [2,§41], the integrals in the Kramers–Krönig relations should be truncated at a high enough frequency where the permeability becomes nearly real and constant (formula (82.17) in [2]). At higher frequencies the permeability loses its physical meaning.

In [2] readers can find a discussion on effective permeability of matter at optical frequencies. In [2,§30] it is concluded that permeability in the visible is trivial (equals to μ_0). It is often thought that the permeability of any composite medium (including MTM) must be obviously equal to unity and the resonant magnetism is forbidden in the optical range as such. However, the content of [2,§30] refers only to "natural" media and is based on the observation that the magnetic susceptibility of atoms is proportional to v^2/c^2 where v is the effective velocity of electrons oscillating in an atom in the optical electric field applied to the atom. This has nothing to do with the artificial magnetism studied in this chapter, for which no restriction to the maximal positive or minimal negative values of the real part of μ is known at optical frequencies. Equation 2.98 can be referred to media from optical SRRs as well, though it is practically valid for the resonant frequency region.

In [47] it was shown that for conducting particles comprising effective loops for the induced current (like SRRs) the dispersion law (Equation 2.98) is an approximation that neglects the dielectric losses in the capacitive portions of the scatterer as compared to conductivity losses in its metal parts. In other words, the imaginary part of μ determined by Equation 2.98 properly describes the case when

the conductivity losses in the particle dominate. More accurate consideration based on the circuit model of the conducting scatterer leads to the following form of the dispersion of permeability:

$$\mu = \mu_0 \left(1 + \frac{A\omega^2 - j\omega B}{\omega_0^2 - \omega^2 + j\omega\gamma}\right). \tag{2.99}$$

Here the parameters B and γ are dependent on the effective resistor R_d "shunting" the effective capacitance C of the scatterer (the larger the dielectric losses the smaller is R_d): $B = B'/R_d$ and $\gamma = \gamma_1 + \gamma_2/R_d$. The frequency dependence of R_d was studied in [47] based on the Lorentz dispersion of the permittivity of the medium that determines the effective capacitance of the scatterer. It can be a homogeneous host medium or a special dielectric insertion into the capacitive portion of the magnetic scatterer. The losses of this medium determine R_d and practically $R_d \sim 1/\omega^2$. Then we have $\mu(\omega \to \infty) \to 1 - B'/\gamma_2$, where $B' \ll \gamma_2$ and $\mu(\omega \to \infty) \approx 1$. Formula 2.99 is not exact, but it describes the dispersion of the permeability at high frequencies much better than Equation 2.98.

Formula 2.99 can be generalized to optical frequencies if the particle can be modeled as a system of optically small effective loops with comparatively small splits. For example, it is applicable to optical SRRs since the generalization of the microwave model (Equation 2.98) to the optical range was properly done in [55].

2.6.2.2 The Sign of the Imaginary Part of Effective Parameters

Though the energy density in media composed by dispersive particles comprises the frequency derivatives of material parameters, the dissipation of energy by unit volume of the medium in unit time can be written for every frequency harmonic as [2,§61]:

$$Q = \pm\omega \left(\frac{\varepsilon_0 \mathrm{Im}(\varepsilon)\hat{E}^2}{2} + \frac{\mu_0 \mathrm{Im}(\mu)\hat{H}^2}{2}\right). \tag{2.100}$$

Here $\hat{A}$ denotes the time averaging of a real scalar function $A = A_0 \cos(\omega t + \phi)$, which is equal to $\hat{A} = A_0/2$. The plus sign in Equation 2.100 corresponds to the temporal dependence $\exp(-i\omega t)$, the minus sign corresponds to $\exp(j\omega t)$. This dissipation factor Q is obviously always positive since the second law of thermodynamics establishes the equivalence of dissipation and heating [2]. Because by varying distribution of sources one can realize arbitrary spatial distributions of fields (e.g., it is possible to distribute sources so that in some volume magnetic field is zero or very small while electric field is strong, or the other way around), it is obvious that both terms in Equation 2.100 must be positive [4]. This implies that both imaginary parts of ε and μ must be positive for $\exp(-i\omega t)$ and negative for $\exp(j\omega t)$. This also defines the sign of the loss coefficient γ in the Lorentz dispersion models and Equations 2.97 and 2.98: positive for $\exp(j\omega t)$ and negative for $\exp(-i\omega t)$. In passive low-loss media ($|\mathrm{Im}|(\varepsilon) \ll |\mathrm{Re}(\varepsilon)|$ and $|\mathrm{Im}(\mu)| \ll |\mathrm{Re}(\mu)|$) the electric and magnetic energies can be separated [2], and two terms in Equation 2.100 describe the electric and magnetic energy dissipation, respectively.

If losses are so significant that $|\mathrm{Im}|(\varepsilon) \geq |\mathrm{Re}(\varepsilon)|$ and $|\mathrm{Im}(\mu)| \geq |\mathrm{Re}(\mu)|$ holds within the resonant band of inclusions, the wave decays so fast that the local material parameters have no physical meaning. Therefore, we consider Equation 2.100 as applicable in frequency regions where the concept of local EMP makes sense.

In the modern literature devoted to MTM there are different points of view on the sign of $\mathrm{Im}(\varepsilon)$ and $\mathrm{Im}(\mu)$. In some works [58] it is assumed that one of two EMP can have the "wrong" sign of the imaginary part if the imaginary part of the refraction index n has the correct sign. In other works [59] it is stated that the requirement of the correct sign of $\mathrm{Im}(\varepsilon)$ and $\mathrm{Im}(\mu)$ is obvious, and even the known algorithm of the extraction of EMP of MTM lattices through the reflection and transmission of MTM slabs is modified so as to satisfy this condition. In other works [60] it is assumed that the

correct sign of $\mathrm{Im}(\varepsilon)$ is obvious, whereas the sign of $\mathrm{Im}(\mu)$ can be arbitrary, since μ is related to spatial dispersion. This difference between the origin of ε and μ is not a valid argument for homogenized arrays of small scatterers. The result of the theory of WSD is μ representing the local magnetic response of the medium.

The requirement of the correct sign of $\mathrm{Im}(\varepsilon)$ and $\mathrm{Im}(\mu)$ cannot be avoided for local (successfully homogenized) media. Speculations that to respect the correct sign of $\mathrm{Im}(n)$ is enough stand no critics, because the correct sign of n ensures passivity only in case of individual plane waves traveling in the medium, but not for arbitrary field distributions. It is obvious [61] that if the sign of $\mathrm{Im}(\varepsilon)$ or if the sign of $\mathrm{Im}(\mu)$ is incorrect separately, it implies "negative heating" of medium samples located in a resonator. If the medium sample with the wrong sign of $\mathrm{Im}(\varepsilon)$ is centered at the maximum of the electric field (the node of the magnetic field), energy is generated in it, since the electric field dominates over the magnetic field in the sample, and negative electric losses are more important than the positive magnetic losses. If the medium sample with the wrong sign of $\mathrm{Im}(\mu)$ is centered at the maximum of the magnetic field (the node of the electric field), energy is also generated in it.

We do not comment here on the method of extraction of EMP [59] introducing the condition of the correct sign of both electric and magnetic losses into the algorithm, since a special chapter is devoted to the correct extraction of local EMP for composite layers. However, we should notice that the correct extraction of local EMP from experimental data or data of numerical simulations should obviously satisfy this condition.

2.6.3 Concluding Remarks

MTM designed to exhibit such properties as negative permittivity and permeability have complicated microstructures. As it was noticed above, most of the interesting phenomena take place when the inclusion resonates, and within the resonant band the effective wavelength in the medium strongly shortens. Within these bands MTM exhibit spatial dispersion effects. If the spatial dispersion is strong in the meaning discussed above, i.e., if the medium is nonlocal, the usual effective material parameters lose their physical meaning. The theory of WSD briefly reported in this chapter reveals related limitations to the effective medium description. WSD is of prime importance for MTM formed by complex particles. The physical limitations to material parameters are reported above only for MTM without higher multipoles. The contribution of multipolar polarizations in MTM has not been investigated up to the present time. This study is very important. It will give a new insight of existing and prospective MTM and will help to separate MTM with strong spatial dispersion from MTM which can be homogenized.

The situation with spatial dispersion in MTM with inclusions optically long in one direction and small in other direction (directions) is totally different. This concerns for example wire media (arrays of thin conducting wires used to realize negative permittivity). Since the wires are usually quite long (large inclusions), spatial dispersion is very strong even at very low frequencies [56]. However, in simple wire media [56] this spatial dispersion holds only if the wave propagates obliquely with respect to the axes of wires. If it propagates transversally to them, the local permittivity tensor can be introduced. The component of this local permittivity tensor parallel to wires is negative at low frequencies and obeys the Drude dispersion law (more details in the corresponding chapter). For waves propagating in this transversal plane in arrays of parallel Swiss rolls [53] the theory of WSD can be applied and the local tensor of permeability can be introduced.*

* In [106] very specific "material parameters" were introduced for lattices of SRRs and Swiss rolls. They look like nonlocal (strongly angularly dependent tensor parameters) even in local media. The physical meaning of these material parameters and their applicability in boundary problems is still unclear in spite of discussions in the literature, for example in [124]. In this chapter we do not discuss these and similar exotic material parameters.

References

1. M. Born and E. Wolf, *Principles of Optics: Electromagnetic Theory of Propagation, Interference and Diffraction of Light*, New York: Cambridge University Press, 1999.
2. L.D. Landau and E.M. Lifshits, *Electrodynamics of Continuous Media,* 2nd ed., Oxford, England: Pergamon Press, 1984.
3. K. Sakoda, *Optical Properties of Photonic Crystals*, Berlin–Heidelberg–New York: Springer, 2005.
4. L.M. Barkovskii and G.N. Borzdov, The impedance tensor for electromagnetic waves in anisotropic media, *J. Appl. Spectrosc.,* 20 (1974) 836.
5. D.R. Smith and D. Shurig, Electromagnetic wave propagation in media with indefinite permittivity and permeability tensors, *Phys. Rev. Lett.*, 90 (2003) 077405.
6. B.A. Sotskii and F.I. Fedorov, Molecular theory of refraction and reflection of light at the interface of two dielectrics, *Optika i Spektroskopia (Opt. Spectrosc.)*, 4 (1958) 365 (in Russian).
7. C.R. Simovski, Application of the Fresnel formulas for reflection and transmission of electromagnetic waves beyond the quasi-static approximation, *J. Commun. Technol. Electronics*, 52 (2007) 953.
8. A.F. Konstantinova , B.V. Grechushnikov, B.V. Bokut, and E.E. Valjashko, *Optical Properties of Crystals*, Minsk: Nauka i Tekhnika, 1995 (in Russian).
9. S.P. Efimov and L.A. Yudin, Theory of excitation of media with spatial dispersion of the waveguide type, *Radiophys. Quantum Electron.*, 24 (1981) 1018.
10. M.G. Silveirinha, Metamaterial homogenization approach with application to the characterization of microstructured composites with negative parameters, *Phys. Rev.* B, 75 (2007) 115104.
11. M. Silveirinha, Transverse-average field approach for the characterization of thin metamaterial slabs, *Phys. Rev. E*, 75 (2007) 036613.
12. V. Yannopapas and A. Moroz, Negative refractive index metamaterials from inherently non-magnetic materials for deep infrared to terahertz frequency ranges, *J. Phys.: Condens. Matter*, 17 (2005) 3717.
13. P.A. Belov and C.R. Simovski, On homogenization of electromagnetic crystals formed by uniaxial scatterers, *Phys. Rev. E,* 72 (2005) 026615.
14. L.D. Barron, *Molecular Light Scattering and Optical Activity*, Cambridge: University Press, 1982.
15. E.B. Graham and J. Pierrus, Multipole moments and Maxwell equations. *J. Phys. B*, 25 (1992) 4673.
16. P. Drude, *The Theory of Optics*, 3rd ed., London: Dover, 1959.
17. A.P. Vinogradov, *Electrodynamics of Composite Materials*, Moscow: URSS, 2001 (in Russian).
18. R.E. Raab and J.H. Cloete, Circular birefringence and dichroism in non-magnetic chiral media, *J. Electromagn. Waves Applic.*, 8 (1994) 1073.
19. E.B. Graham and R.E. Raab, Covariant multipole D and H fields for reflection from a magnetic anisotropic chiral medium, in *Advances in Complex Electromagnetic Materials*, A. Priou, A. Sihvola, S. Tretyakov, and A. Vinogradov, Eds., Dordrecht, the Netherlands: Kluwer Academy Publishers, 1997, p. 55.
20. J.D. Jackson, *Classical Electrodynamics,* 3rd ed. New York: John Wiley & Sons, 1999.
21. F.I. Fedorov, *Theory of Girotropy*, Minsk: Nauka, 1976 (in Russian).
22. V.M. Agranovich and V.L. Ginzburg, *Crystal Optics with Spatial Dispersion and Excitons,* Berlin, Germany: Springer-Verlag, 1984.
23. A.N. Serdyukov, I.V. Semchenko, S.A. Tretyakov, and A. Sihvola, *Electromagnetics of Bi-Anisotropic Materials: Theory and Applications,* Amsterdam, the Netherlands: Gordon and Breach Science Publishers, 2001.
24. C.R. Simovski, *Weak Spatial Dispersion in Composite Media*, St. Petersburg: Politekhnika, 2003 (in Russian).
25. R.E. Raab and O.L. de Lange, *Multipole Theory in Electromagnetism,* Oxford: Clarendon Press, 2005.
26. S.R. de Groot and L.G. Suttorp, *Foundations of Electrodynamics*, Amsterdam, the Netherlands: North Holland Publishing Company, 1972.

27. E.B. Graham and R.E. Raab, Molecular scattering in spatially dispersive medium, *Proc. R. Soc. Lond., Ser. A*, 430 (1990) 593–614.
28. I.V. Lindell, A.H. Sihvola, S.A. Tretyakov, and A.J. Viitanen, *Electromagnetic Waves in Chiral and Bi-isotropic Media*, Boston, MA and London: Artech House, 1994.
29. E.J. Post, *Formal Structure of Electromagnetics*, Amsterdam, the Netherlands: North-Holland, 1962.
30. J.B. Pendry, A.J. Holden, D.J. Robbins, and W.J. Stewart, Magnetism from conductors and enhanced nonlinear phenomena, *IEEE Trans. Microw. Theory Tech.*, 47 (1999) 2075.
31. K. Aydin, I. Bulu, K. Guven, M. Kafesaki, C.M. Soukoulis, and E. Ozbay, Investigation of magnetic resonances for different split-ring resonator parameters and designs, *New J. Phys*. 7 (2005) 168.
32. H. Chen, L. Ran, J. Huangfu, X.M. Zhang, K. Chen, T.M. Grzegorczyk, and J.A. Kong, Left-handed materials composed of only S-shaped resonators, *Phys. Rev.* E, 70 (2004) 057605.
33. A.N. Grigorenko, A.K. Geim, H.F. Gleeson, Y. Zhang, A.A. Firsov, I.Y. Khrushchev, and J. Petrovic, Nanofabricated media with negative permeability at visible frequencies, *Nature* 438 (2005) 335.
34. G. Dolling, C. Enkrich, M. Wegener, S. Linden, J. Zhou, and C.M. Soukoulis, Cut-wire and plate capacitors as magnetic atoms for optical metamaterials, *Opt. Lett.* 30 (2005) 3198.
35. J. Zhou, L. Zhang, G. Tuttle, T. Koschny, and C.M. Soukoulis, Negative index materials using simple short wire pairs, *Phys. Rev. B*, 73 (2006) 041101.
36. S. Linden, C. Enkrich, M. Wegener, J.F. Zhou, T. Koschny, and C.M. Soukoulis, Magnetic response of metamaterials at 100 terahertz, *Science*, 306 (2004) 1351.
37. N. Katsarakis, G. Konstantinidis, A. Kostopoulos, R.S. Penciu, T.F. Gundogdu, T. Koschny, M. Kafesaki, E.N. Economou, and C.M. Soukoulis, Magnetic response of split-ring resonators in the far infrared frequency regime, *Opt. Lett*., 30 (2005) 1348.
38. C. Enkrich, S. Linden, M. Wegener, S. Burger, L. Zswchiedrich, F. Schmidt, J. Zhou, T. Koschny, and C. M. Soukoulis, Magnetic metamaterials at telecommunication and visible frequencies, *Phys. Rev. Lett.*, 95 (2005) 203901.
39. S. Zhang, W. Fan, N.C. Panoiu, K.M. Malloy, R.M. Osgood, and S.R.J. Brueck, Experimental demonstration of near-infrared negative-index metamaterials, *Phys. Rev. Lett.*, 95 (2005) 137404.
40. J. Zhou, T. Koschny, M. Kafesaki, E.N. Economou, J.B. Pendry, and C.M. Soukoulis, Limit of the negative magnetic response of split-ring resonators at optical frequencies, *Phys. Rev. Lett.*, 95 (2005) 223902.
41. K.C. Huang, M.L. Povinelli, and J.D. Joannopoulos, Negative effective permeability in polaritonic photonic crystals, *Appl. Phys. Lett.*, 85 (2004) 543.
42. S. Linden, M. Decker, and M. Wegener, Model system for a one-dimensional magnetic photonic crystal, *Phys. Rev. Lett.*, 97 (2006) 083902.
43. V.M. Agranovich and Yu.N. Gartstein, Spatial dispersion and negative refraction of light, *Phys. Usp.*, 49 (2006) 10.
44. V.G. Veselago, The electrodynamics of substances with simultaneously negative values of ε and μ, *Sov. Phys. Uspekhi.*, 10 (1968) 509.
45. S.A. Tretyakov, Electromagnetic field energy density in artificial microwave materials with strong dispersion and loss, *Phys. Lett. A*, 343 (2005) 231–237.
46. S.A. Tretyakov and S.I. Maslovski, Veselago materials: What is possible and impossible about the dispersion of the constitutive parameters, *IEEE Antennas Propagat. Mag.,* 49(1) (2007), 37–43.
47. P.M.T. Ikonen and S.A. Tretyakov, Determination of generalized permeability function and field energy density in artificial magnetics using the equivalent-circuit method, *IEEE Trans. Microw. Theory Tech.,* 55(1) (2007) 92–99.
48. B.B. Kadomtsev, A.B. Mikhailovski, and A.V. Timofeyev, Negative energy waves in dispersive media, *Zhurnal Teoretich. and Experim. Fiziki*, 47 (1964) 2266 (in Russian. English translation in *Sov. Phys. ZETF*).
49. L.A. Vainstein, *Electromagnetic Waves,* 2nd ed., Moscow: Radio i Sviaz, 1988 (in Russian).

50. D.V. Sivukhin, On the energy of electromagnetic field in dispersive media, *Optika i Spektroskopiya,* 3 (1957) 308 (in Russian).
51. S.A. Tretyakov, F. Mariotte, C.R. Simovski, T.G. Kharina, and J.-P. Heliot, Analytical antenna model for chiral scatterers: Comparison with numerical and experimental data, *IEEE Trans. Antennas Propagat*., 44 (1996) 1006.
52. M.V. Kostin and V.V. Shevchenko, Theory of artificial magnetic substances based on ring currents, *Sov. J. Commun. Technol. Electronics*, 38 (1993) 78.
53. J.B. Pendry, A.J. Holden, D.J. Robbins, and W.J. Stewart, Magnetism from conductors and enhanced nonlinear phenomena, *IEEE Trans. Microw. Theory Tech.*, 47 (1999) 2075.
54. D.R. Smith and N. Kroll, Negative refractive index in left-handed materials, *Phys. Rev. Lett.*, 85(14) (October 2000) 2933–2936.
55. M.W. Klein, C. Enkrich, M. Wegener, C.M. Soukoulis, and S. Linden, Single-slit split-ring resonators at optical frequencies: Limits of size scaling, *Opt. Lett.*, 31 (2006) 1259.
56. P.A. Belov, R. Marqués, S.I. Maslovski, I.S. Nefedov, M. Silveirinha, C.R. Simovski, and S.A. Tretyakov, Strong spatial dispersion in wire media in the very large wavelength limit, *Phys. Rev. B*, 67 (2003) 113103(1–4).
57. C.R. Simovski and P.A. Belov, Low frequency spatial dispersion in wire media, *Phys. Rev. E*, 70 (2004) 046616.
58. S.A. Cummer and B.-I. Popa, Wave fields measured inside a negative refractive index metamaterial, *Appl. Phys. Lett.*, 85 (2004) 4564.
59. X. Chen, T.M. Grzegorczyk, B.-I. Wu, J. Pacheco, and J.A. Kong, Robust method to retrieve the constitutive effective parameters of metamaterials, *Phys. Rev. E*, 70 (2004) 016608.
60. U.K. Chettiar, A.V. Kildishev, T.A. Klar, and V.M. Shalaev, Negative index metamaterial combining magnetic resonators with metal films, *Opt. Express*, 14 (2006) 7872.
61. C.R. Simovski and S.A. Tretyakov, Local constitutive parameters of metamaterials from an effective-medium perspective, *Phys. Rev. B*, 75 (2007) 195111.
62. D. Smith and J.B. Pendry, Homogenization of metamaterials by field averaging, *J. Opt. Soc. Am. B*, 23 (2006) 391.

3

Symmetry Principles and Group-Theoretical Methods in Electromagnetics of Complex Media

Victor Dmitriev
Federal University of Pará

3.1 Introduction

The notion of symmetry in its simple form is known to any engineer: a rectangle has two planes of symmetry, a sphere is indistinguishable after rotation by any angle, an infinite crystal is characterized by periodicity. Space reflections, rotations, and translations are examples of geometrical symmetries. After the publication of Einstein's theory of relativity, physicists began to consider Time as a

geometrical coordinate and to discuss the corresponding symmetries as well. But the ideas of symmetry are not restricted only by geometry. Nongeometrical symmetries, for example, gauge invariance, dynamical symmetries, etc., are effectively used in modern physics.

The group theory is a mathematical tool for description of symmetries. Many applications of group theory in crystallography, quantum mechanics, and in classical and quantum electrodynamics are described in physics and mathematics literature. In particular, the group theory had and has a deep influence on the development of molecular and solid-state physics. Group theory is used to select those mathematical models which are adequate for description of a new phenomenon. When the physical theory is developed, the group theory allows one to define some general properties of the physical object under consideration without solution of the corresponding differential equations.

The aim of this chapter is to consider some of the group-theoretical methods which are used for the study of complex media. Our discussion will be based on the magnetic group theory which includes nonmagnetic groups as a particular case.

3.2 Symmetry of Maxwell's Equations

Symmetry of mathematical objects (such as differential and algebraic equations, tensors, matrices) and the concepts of equivalence and invariants can be defined shortly as follows [1]:

> Equivalence deals with the determination of when two mathematical objects are the same under a change of variables. The symmetries of a given object can be interpreted as the group of self-equivalences. Conditions guaranteeing equivalence are most effectively expressed in terms of invariants, whose values are unaffected by the changes of variables.

Geometrical symmetry of a physical object is defined by a set of the transformations which bring the object into self-coincidence. These transformations are rotations, mirror reflections in a plane, translations and combinations of them. Often, Time reversal is also considered as an element of geometrical symmetry. In this chapter, we shall consider some symmetries which exist in classical electromagnetic theory based on Maxwell's equations. The variables of our physical problems are Space and Time coordinates.

The simplicity and elegance of Maxwell's equations are defined by their high symmetry [2]. The symmetry of Maxwell's equations in vacuum with respect to continuous translations in Space (due to homogeneity of Space), Time (due to homogeneity of Time), and rotations (due to isotropy of Space) gives rise to conservation of linear momentum, energy, and angular momentum, respectively. The combined continuous Space–Time symmetry leads to the invariance of Maxwell's equations with respect to Lorentz transformations. The special theory of relativity is closely related to this symmetry.

In addition to the continuous Space- and Time-translation symmetry, Maxwell's equations possess some discrete symmetries. They are Space inversion, Time reversal, and charge conjugation (P, T, and C, respectively), and combinations of these symmetries.

Maxwell's equations also have other types of symmetry which are not defined by change of the Space–Time variables. They are often called "hidden" symmetries [2]. For example, Heaviside's transformation for electric and magnetic fields $\mathbf{E} \rightarrow \mathbf{H}$ and $\mathbf{H} \rightarrow -\mathbf{E}$ is known in electromagnetics as the duality principle. A generalization of this transformation is $\mathbf{E} \rightarrow \mathbf{E}\cos\theta + \mathbf{H}\sin\theta$ and $\mathbf{H} \rightarrow -\mathbf{H}\cos\theta - \mathbf{E}\sin\theta$, where θ is a parameter. The hidden symmetries allow one to obtain new solutions from the known ones.

Maxwell's equations become complete with constitutive relations or with equations of medium motion. These relations and equations usually also possess some symmetry. Besides, in practical problems one should take into consideration symmetry of the electromagnetic sources and of the

boundary conditions. The resulting symmetry of the problem will depend on all these constituents. This symmetry is defined by Curie's principle of symmetry superposition and it always leaves its footprints in the solutions of the problem.

Symmetry operations form groups. Discussion of the symmetry problems is simplified greatly by using group theory (Appendix A). This theory is a natural mathematical tool for analysis of the consequences of the symmetry in solutions of the corresponding equations.

3.3 Symmetry of Complex Media and Sources

3.3.1 Symmetry of Complex Media

The simplest homogeneous stationary unbounded linear medium has continuous translational symmetry. It is also invariant under Time reversal. Any point of this medium is described by the point group of symmetry K_h (the Schoenflies system of group notations is given in Appendix B) which defines the highest possible spherical symmetry. We can consider such a medium as a special waveguide of electromagnetic waves with linear polarized plane waves as eigenmodes. A "cross section" of this waveguide, i.e., a plane normal to the wave vector, has the symmetry $C_{\infty v}$. Electromagnetic properties of this medium do not depend on direction.

An unbounded homogeneous chiral medium possesses a lower symmetry which is described by the continuous point group K. A random distribution of electrically small helixes gives this symmetry. If any point of space has the symmetry K, it is a homogeneous chiral medium with right-handed or left-handed properties. Any cross section of this medium has the symmetry C_∞. The eigenmodes of the medium are right-handed or left-handed circularly polarized plane waves. All the directions in such a medium are equivalent.

The media of the above two examples have simple properties due to their spherical symmetries. These symmetries correspond to the symmetry of scalars (the group K_h) or pseudoscalars (the group K), and the constitutive parameters of the media are scalars or a combination of scalars and pseudoscalars, respectively.

Uniaxial media with one principal axis of infinite order C_∞ can be of different types. A medium which is formed, for example, by electrically small cylindrical particles oriented in one direction has the symmetry $D_{\infty h}$. A medium formed by cones oriented along one axis possesses the symmetry $C_{\infty v}$. The uniaxial media are described by the second-rank constitutive tensors and electromagnetic properties of them depend on direction.

Anisotropic and bianisotropic media described by lower discrete groups of symmetry have usually a more number of independent parameters and more complex electromagnetic properties.

Symmetry of a complex medium is defined by the symmetry of atoms and molecules and their space conformations in natural media and by symmetry of artificial particles and their arrangements in artificial media. If both the particles and the distances between them are electrically small, some methods of electromagnetic averaging can be used to calculate the effective medium parameters. Several examples of artificial particles with different geometries are shown in Figure 3.1.

3.3.2 Symmetry of Electromagnetic Sources

Electromagnetic sources can also be described in terms of magnetic groups. The electric dipole, for example, has the symmetry $C_{\infty v}$; the magnetic dipole is described by the group $D_{\infty h}(C_{\infty h})$ (the magnetic groups and their notations are discussed in Appendix B). Symmetry of more complex sources such as continuous and discrete charge and current distributions, double electric layers, antennas and arrays of antennas can be found using Curie's principle.

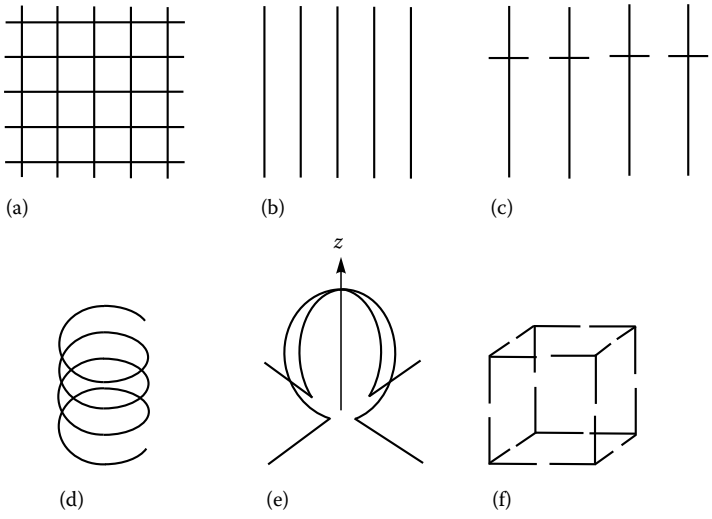

FIGURE 3.1 Examples of symmetrical artificial elements: 3D grid spaced a distance $d_z \neq d_x = d_y$ with the symmetry D_{4h} (a). 3D array of dipoles described by the symmetry D_{2h} (b). 3D array of crosses with the symmetry C_{2v} (c). Helix: the medium formed by electrically small helixes has the symmetry D_∞ (d). Omega-element in the form of a hat with the symmetry C_{4v} (e). 3D magnetic particle with the symmetry O_h (f). (From Barybin, A.A. and Dmitriev, V.A., *Modern Electrodynamics and Coupled-Mode Theory: Application to Guided-Wave Optics*, Rinton Press, Princeton, NJ, 2002. With permission.)

3.3.3 Curie's Principle of Symmetry Superposition

Artificial composite media can consist of a host material and some inclusions (particles), and may be under external fields and forces (perturbations). The host material may have a certain symmetry, the inclusions and their spatial arrangements may also be described by certain groups of symmetry. External perturbation may be of different natures (for example, electric and magnetic fields, mechanical forces, temperature fields and their combinations) and of different symmetries. In this case, the problem of determination of the symmetry group of the medium can be solved on the basis of Curie's principle, known in crystallography. In mathematical language, Curie's principle can be written as intersection of the symmetry groups of all the constitutive elements of the medium: the host material with the symmetry G_1, the shape of the particles and their arrangements with the symmetry G_2, an external perturbation with the symmetry G_3, etc.:

$$G_{\text{res}} = G_1 \cap G_2 \cap G_3 \cap \ldots . \tag{3.1}$$

This expresses the principle of symmetry superposition, that is, the symmetry of a complex object is defined by the highest common subgroup of the groups $G_1,\ G_2,\ G_3 \ldots$ which describe the object.

As examples of the use of Curie's principle to find the resultant symmetry G_{res}, let us consider the following combinations:

1. Isotropic ferrite chiral medium with applied dc magnetic field $\mathbf{H}_0$
2. Static electric field $\mathbf{E}_0$ and a uniform dc magnetic field $\mathbf{H}_0$ intersecting at a right angle

In case 1, the chiral medium under dc magnetic field acquires the symmetry $D_\infty(C_\infty)$ because the group K describing chiral medium and the group $D_{\infty h}(C_{\infty h})$ describing dc magnetic field have one common element (except the unit element), namely the axis C_∞; besides, an infinite number of axes of the second order C_2 perpendicular to the axis C_∞ are converted under dc magnetic field into the antiaxes TC_2.

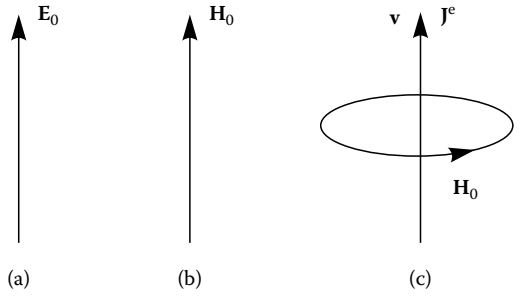

FIGURE 3.2 Examples of external perturbations: uniform static electric field $\mathbf{E}_0$ (a), uniform dc magnetic field $\mathbf{H}_0$ (b), velocity of a moving medium $\mathbf{v}$ (c). (From Barybin, A.A. and Dmitriev, V.A., *Modern Electrodynamics and Coupled-Mode Theory: Application to Guided-Wave Optics*, Rinton Press, Princeton, NJ, 2002. With permission.)

In case 2, the resultant magnetic symmetry of the two vectors $\mathbf{E}_0$ and $\mathbf{H}_0$ is $C_{2v}(C_s)$. This group has one plane with $\mathbf{H}_0$ perpendicular to it, one antiplane of symmetry (both $\mathbf{E}_0$ and $\mathbf{H}_0$ lie in this antiplane), and the antiaxis coinciding with the direction of vector $\mathbf{E}_0$.

According to Curie's principle, an isotropic medium with the symmetry K_h under an external perturbation acquires symmetry of this perturbation. For example, an isotropic dielectric medium with applied static uniform electric field $\mathbf{E}_0$ (Figure 3.2a) has the symmetry of the electric field $C_{\infty v}$. An isotropic ferrite medium under uniform dc magnetic field $\mathbf{H}_0$ depicted in Figure 3.2b acquires the symmetry of the magnetic field $D_{\infty h}(C_{\infty h})$. In still another example, the velocity $\mathbf{v}$ of a moving isotropic dielectric medium leads to electric current $\mathbf{J}^e$, which in its turn produces a dc ring magnetic field $\mathbf{H}_0$ shown in Figure 3.2c. Therefore, a moving dielectric medium acquires the magnetic symmetry $D_{\infty h}(C_{\infty v})$. These symmetries define the structure of the constitutive tensors for the corresponding media. Thus, external perturbations may change electromagnetic properties of media. In particular, an isotropic medium under perturbation may become anisotropic or even bianisotropic.

3.4 Time-Reversal Symmetry, Reciprocity, and Bidirectionality

3.4.1 Time-Reversal Symmetry

An important physical symmetry, which is widely used in physics and, particularly, in classical electrodynamics, is defined by the Time reversal. Literally, the Time-reversal operator **T** denotes the change of the sign of Time t, i.e., $t \to -t$. Maxwell's equations are invariant with respect to this operator.

In mathematical description of physical problems, the operator **T** reverses the direction of motion. In the time domain, as a result, it changes the signs of the quantities which are odd in Time: the velocity, the wave vector, the magnetic field, the Poynting vector, etc. In the frequency domain, the operator **T** also complex transposes all quantities.

One of the important consequences of the Time-reversal symmetry is the Onsager's theorem [4], which has a general nature. Symmetry of the permittivity and permeability tensors with respect to their main diagonals for nonmagnetic media, for example, follows from this theorem. In the theory of microwave circuits with nonmagnetic materials, symmetry of the scattering matrix with respect to its main diagonal is also a consequence of this symmetry.

There are certain difficulties in physical interpretation of the operator **T**. For example, in the wave equations obtained from Maxwell's equations combined with constitutive relations, the Time-reversal operator transforms a passive medium in an active one and as a consequence, a damping electromagnetic wave into a growing one. Thus, the dissipative processes are not Time reversible (notice

that in order to overcome this difficulty at least mathematically, it was suggested in [5] to use the so-called restricted Time-reversal operator $\mathcal{T}$, which preserves the passive or active nature of the medium). Another example of difficulties in the operator **T** interpretation is as follows: a plane wave diffracted on an object is transformed into a spherical one, but nobody has seen the Time-reversed process when an incoming spherical wave is transformed into the plane wave. Still another example is transformation of the sources under Time reversal into sinks.

These examples show that the approach based on the Time-reversal invariance, where the present and the past are reversible, strictly speaking is not correct. There exists "the arrow of Time" [6]. In the mathematical description of thermodynamical processes, in particular, one of the consequences of this irreversibility is splitting of the dynamical group of evolution of a physical system with an operator $U(t)$ into two semigroups, one for $U(+t)$, and the other one for $U(-t)$. In nonlinear problems, the Time reversal also should be excluded from consideration.

In spite of these difficulties in interpretation of the Time reversal, the idea of using this operator in classical electrodynamics is very fruitful. In particular, the Lorentz reciprocity theorem can be considered as a consequence of the invariance with respect to the restricted Time-reversal operator. The operator $\mathcal{T}$ is especially useful in the problems involving magnetic media.

3.4.2 Reciprocity

In general, reciprocity principles in electromagnetics are related with the interchange of cause and effect. A simple example is interchange of the positions of a source and a detector which leads to the same results in measurements. The nonreciprocity of a medium can manifest itself in difference of the wave vectors (phase, velocity difference), of the structure of electromagnetic waves (particularly, in polarization), or in amplitudes of the waves propagating in opposite directions in the medium.

For scattering and guided wave problems, the reciprocity theorems are useful tools in solving these problems. In many particular applications, reciprocity theorems are formulated often in simplified forms, for example, for linear regime and local media, for monochromatic radiation, for scalar waves, for finite regions of scatterers, for prescribed directions of the incident and reflected waves, etc. [7].

Reciprocity can be considered as a special type of symmetry. Reciprocity is closely related to the Time-reversal symmetry, though these two types of symmetry are, in general, different. The principal difference is that the Time-reversal symmetry does not exist in the presence of absorption, but the reciprocity can exist in this case. Reciprocity of the problem manifests itself in the symmetry of the constitutive tensors, scattering matrices, and Green's tensors.

3.4.3 Bidirectionality

We call a given medium bidirectional for a given direction of the wave vector **k** if there is a geometrical operator $\mathcal{R}_1$ or a combined Time-reversal geometrical operator $T\mathcal{R}_2$ such that

$$\mathcal{R}_1\mathbf{k} = -\mathbf{k}, \tag{3.2}$$

or

$$T\mathcal{R}_2\mathbf{k} = -\mathbf{k}. \tag{3.3}$$

With this condition, for any branch of the dispersion characteristic $\omega_n(\mathbf{k})$ with the vector **k** there exists another branch $\omega_m(-\mathbf{k})$ with the vector $-\mathbf{k}$ such that

$$\omega_n(\mathbf{k}) = \omega_m(-\mathbf{k}). \tag{3.4}$$

In Equation 3.4, different subindexes n and m are used because, in general, the structure of the electromagnetic field of the eigenwaves corresponding to $\mathbf{k}$ and $-\mathbf{k}$ is different.

The following symmetry elements change the sign of the vector $\mathbf{k}$ defining bidirectionality in media:

- Reflection in a plane for the direction of propagation normal to the plane
- Improper rotation about an axis for the direction of propagation along this axis
- Center of symmetry (inversion) for any direction of propagation
- Rotation about an axis through π for the directions of propagation perpendicular to this axis
- Reflection in an antiplane for the directions of propagation parallel to the antiplane
- Rotation about an antiaxis for the direction of propagation along this antiaxis

In a nonmagnetic medium, the notion of bidirectionality is related to the notion of equivalent directions. All the physical properties of a medium along the equivalent directions (not necessarily opposite) are the same. This is stipulated by the presence of some elements of symmetry: axes, planes and the center (inversion symmetry). However, existence of these symmetry elements in magnetic media does not always lead to equivalence of the directions. For example, a plane of symmetry in a nonmagnetic medium defines equivalent directions normal to the plane. But the plane of symmetry which is perpendicular to a dc magnetic field does not define equivalent directions. For the opposite directions normal to this plane, the circularly polarized eigenwaves of the same handedness have different propagation constants, and this property defines the well-known nonreciprocal Faraday effect.

Notice that the condition $\omega_n(\mathbf{k}) = \omega_m(-\mathbf{k})$ is not a sufficient condition for nonreciprocity, i.e., the bidirectional medium can be reciprocal or nonreciprocal.

3.5 Material Tensors

3.5.1 Different Forms of the Constitutive Relations

In practice, those media are usually used which have a certain symmetry. This is because the symmetrical media make it possible to choose and control physical effects used in electromagnetic components and devices. Due to very high symmetry of microscopic Maxwell's equations without sources, the resulting symmetry of the system "Maxwell's equations + a medium" is defined by the symmetry of the constitutive relations of this medium.

Using group-theoretical approach, one deals only with geometry and is not concerned with the physical properties of medium particles and their dimensions, and consequently, the numerical values of the tensor parameters.

For bianisotropic media, the vectors $\mathbf{D}$ and $\mathbf{H}$ are related to both vectors $\mathbf{E}$ and $\mathbf{B}$. The functional dependence

$$\mathbf{D} = \mathbf{D}(\mathbf{E}, \mathbf{B}), \tag{3.5}$$

$$\mathbf{H} = \mathbf{H}(\mathbf{E}, \mathbf{B}), \tag{3.6}$$

i.e., the constitutive equations may be involved and, in general, contain integral–differential operators. In the above equations, $\mathbf{E}$ and $\mathbf{H}$ are the electric and magnetic field-intensity vectors, $\mathbf{D}$ and $\mathbf{B}$ are the electric and magnetic flux-density vectors.

We shall consider unbounded linear, stationary and, in general, dissipative bianisotropic media in the frequency domain. The media under consideration are assumed to be homogeneous,

i.e., the constitutive tensors are not functions of space variables (long-wave approximation), but electromagnetic properties of the media depend, in general, on direction in space. The elements of the constitutive tensors are complex due to complex electromagnetic field consideration and due to possible losses in media. The numerical values of the tensor elements depend on frequency. It means that the media are time dispersive and obey the Kramers–Kronig relations [8] which are a consequence of causality.

In what follows, we shall be interested in the structure of macroscopic constitutive tensors. It means equality of some of their elements to each other, or equality of the element moduli but with opposite sign, or equality of the elements to zero. Such a structure is dictated by Space–Time reversal symmetry of the medium. Symmetry may reduce significantly the number of independent parameters of the tensors and simplify the following analysis of electromagnetic properties of the medium.

The linear relations between the four vectors **D**, **B**, **E**, and **H** can be written in different forms. One of them is the presentation **DB**(**EH**) which is often used in the theory of bianisotropic media:

$$\begin{pmatrix} \mathbf{D} \\ \mathbf{B} \end{pmatrix} = \underline{\mathbf{K}} \cdot \begin{pmatrix} \mathbf{E} \\ \mathbf{H} \end{pmatrix} \quad \text{where} \quad \underline{\mathbf{K}} = \begin{pmatrix} \underline{\epsilon} & \underline{\xi} \\ \underline{\zeta} & \underline{\mu} \end{pmatrix}. \tag{3.7}$$

The tensors of the second rank $\underline{\boldsymbol{\epsilon}}$ and $\underline{\boldsymbol{\mu}}$ are the tensors of the permittivity and permeability, respectively. The magnetoelectric tensors $\underline{\boldsymbol{\xi}}$ and $\underline{\boldsymbol{\zeta}}$ describe the cross-coupling between the electric and magnetic fields.

From general properties of the tensors we know that any relation between the tensors expressed as a sum or a product of them is invariant with respect to the group of permissible coordinate transformations [9]. It allows one to show that the tensor structure obtained by symmetry principles is invariant with respect to the presentations **DB**(**EH**), **EH**(**DB**), **DH**(**EB**), and **EB**(**DH**). The traditional presentation **DB**(**EH**) is convenient in some applications, particularly, in solutions of boundary value problems where the boundary conditions are written in terms of tangential components of **E** and **H** in calculations of Poynting's vector and impedances.

3.5.2 Calculation of the Constitutive Tensors and Some of Their Properties

It is well-known that the structure of the constitutive tensors can be simplified by making use of symmetry operations corresponding to the point group of the crystal [10]. The magnetic group of symmetry of a medium is defined by the symmetry of its particles, their mutual arrangement, the symmetry of the host medium, the symmetry of the external perturbations, as it follows from Curie's principle of symmetry superposition (Section 3.3.3). In this section, we discuss a method of calculation of the second-rank tensor structure for complex and bianisotropic media with a known symmetry.

The tensors $\underline{\boldsymbol{\epsilon}}$, $\underline{\boldsymbol{\mu}}$, $\underline{\boldsymbol{\xi}}$ and $\underline{\boldsymbol{\zeta}}$ of Equation 3.7 form the constitutive relations

$$\mathbf{D} = \underline{\epsilon} \cdot \mathbf{E} + \underline{\xi} \cdot \mathbf{H}, \tag{3.8}$$

$$\mathbf{B} = \underline{\zeta} \cdot \mathbf{E} + \underline{\mu} \cdot \mathbf{H}. \tag{3.9}$$

The four 3 × 3 tensors of Equations 3.8 and 3.9 in the most general form contain 36 independent parameters. The structure of the tensors describing a symmetrical medium depends on the mutual orientation of the chosen Cartesian coordinate system *x, y, z* and the symmetry axes and planes of the medium. Usually, the orientation of one of the coordinate axes is chosen to be along the symmetry axis of the highest order.

Using matrix representations of 3D point symmetry operators (see Appendix D) and transformation properties of the tensors of the second rank [23], from invariance of the medium under Space–Time reversal transformations, one can obtain the following identities:

1. For the case of unitary transformations (they correspond to Space symmetry):

$$\mathbf{R} \cdot \underline{\epsilon} = \underline{\epsilon} \cdot \mathbf{R}, \quad \mathbf{R} \cdot \underline{\mu} = \underline{\mu} \cdot \mathbf{R}, \tag{3.10}$$

$$\mathbf{R} \cdot \underline{\xi} = \det(\mathbf{R}) \underline{\xi} \cdot \mathbf{R}, \quad \mathbf{R} \cdot \underline{\zeta} = \det(\mathbf{R}) \underline{\zeta} \cdot \mathbf{R}, \tag{3.11}$$

2. For the case of antiunitary transformations (they correspond to combined Space–Time reversal symmetry):

$$\mathbf{R} \cdot \underline{\epsilon} = \underline{\epsilon}^{\mathrm{t}} \cdot \mathbf{R}, \quad \mathbf{R} \cdot \underline{\mu} = \underline{\mu}^{\mathrm{t}} \cdot \mathbf{R}, \tag{3.12}$$

$$\mathbf{R} \cdot \underline{\xi} = -\det(\mathbf{R}) \underline{\zeta}^{\mathrm{t}} \cdot \mathbf{R}, \quad \mathbf{R} \cdot \underline{\zeta} = -\det(\mathbf{R}) \underline{\xi}^{\mathrm{t}} \cdot \mathbf{R}, \tag{3.13}$$

where $\mathbf{R}$ is the 3D matrix representation of the corresponding group element and the superscript t means matrix transposition.

The number of independent parameters of the constitutive tensors can be reduced using Equations 3.10 through 3.13. It is not necessary to use all the group elements to calculate the tensors. It is sufficient to use only generators of the group (Appendix A) for this purpose. For the magnetic groups of the third category (Appendix C), the generators can be chosen as generators of the corresponding unitary subgroup and any antiunitary element.

In accordance with Hermann's theorem [11], some of the groups lead to identical tensor structure. German-Hermann's theorem for our case reads as follows: "If C_n is an axis of symmetry for a constitutive tensor (of rank 2) and $n > 2$, then the axes $C_3, C_4, \ldots, C_\infty$ are also the axes of symmetry for this tensor." In other words, all the axes of geometrical symmetry higher than 2 are converted into the axes of infinite order for the tensors. If the group also has a plane of symmetry which is perpendicular to this axis, the corresponding tensor acquires the center of symmetry.

Thus, the symmetry of medium and the symmetry of the second-rank tensor which describes this medium may not coincide. The tensor symmetry may be higher than the symmetry of the medium. This is reflected, for example, in the fact that though the cubic crystals do not have isotropic symmetry of their unit cells, nevertheless, their tensors are degenerate to scalars. Anisotropy of these crystals appears when we describe them in terms of the tensors with ranks higher than 2. The full tables of the second-rank tensors comprising 122 crystallographic and 21 continuous magnetic point groups can be found in [12].

An example of the calculated tensors for the continuous groups of the first category is given in Table 3.1 for the orientation of the axis $C_\infty \parallel z$. Notice that the calculated structures of the tensors $\underline{\epsilon}$ and $\underline{\mu}$ coincide because they have the same transformation properties and they are calculated by the analogous expressions (Equations 3.10 and 3.12).

Nonreciprocity of a medium is defined by any of the conditions [13]:

$$\underline{\epsilon} \neq \underline{\epsilon}^{t}, \quad \underline{\mu} \neq \underline{\mu}^{t}, \quad \underline{\xi} \neq -\underline{\zeta}^{t}. \tag{3.14}$$

Thus, the structure of the constitutive tensors of complex and bianisotropic media is defined in many respects by symmetry of the media and of external perturbation. The dynamical peculiarities of the media are reflected in the numerical values of the constitutive parameters and sometimes in a simplification of the tensor structure in comparison with those calculated by symmetry methods [23].

The structure of the tensors is frequency- and model-independent. In particular, it does not depend on possible effects of the mutual interaction between particles of the medium. It is a consequence of the symmetry approach used for calculations.

TABLE 3.1 Constitutive Tensors for Media Described by Continuous Groups of the First Category

N	Group	$\underline{\boldsymbol{\mu}}$	$\underline{\boldsymbol{\epsilon}}$	$\underline{\boldsymbol{\xi}}$	$\underline{\boldsymbol{\zeta}}$
1	K_h	μ	ϵ	0	0
2	K	μ	ϵ	ξ	$-\xi$
3	$D_{\infty h}$	$\begin{pmatrix}\mu_{11}&0&0\\0&\mu_{11}&0\\0&0&\mu_{33}\end{pmatrix}$	$\begin{pmatrix}\epsilon_{11}&0&0\\0&\epsilon_{11}&0\\0&0&\epsilon_{33}\end{pmatrix}$	$\begin{pmatrix}&0&\\&&\end{pmatrix}$	$\begin{pmatrix}&0&\\&&\end{pmatrix}$
4	D_{∞}	$\begin{pmatrix}\mu_{11}&0&0\\0&\mu_{11}&0\\0&0&\mu_{33}\end{pmatrix}$	$\begin{pmatrix}\epsilon_{11}&0&0\\0&\epsilon_{11}&0\\0&0&\epsilon_{33}\end{pmatrix}$	$\begin{pmatrix}\xi_{11}&0&0\\0&\xi_{11}&0\\0&0&\xi_{33}\end{pmatrix}$	$\begin{pmatrix}-\xi_{11}&0&0\\0&-\xi_{11}&0\\0&0&-\xi_{33}\end{pmatrix}$
5	$C_{\infty v}$	$\begin{pmatrix}\mu_{11}&0&0\\0&\mu_{11}&0\\0&0&\mu_{33}\end{pmatrix}$	$\begin{pmatrix}\epsilon_{11}&0&0\\0&\epsilon_{11}&0\\0&0&\epsilon_{33}\end{pmatrix}$	$\begin{pmatrix}0&\xi_{12}&0\\-\xi_{12}&0&0\\0&0&0\end{pmatrix}$	$\begin{pmatrix}0&\xi_{12}&0\\-\xi_{12}&0&0\\0&0&0\end{pmatrix}$
6	$C_{\infty h}$	$\begin{pmatrix}\mu_{11}&0&0\\0&\mu_{11}&0\\0&0&\mu_{33}\end{pmatrix}$	$\begin{pmatrix}\epsilon_{11}&0&0\\0&\epsilon_{11}&0\\0&0&\epsilon_{33}\end{pmatrix}$	$\begin{pmatrix}&0&\\&&\end{pmatrix}$	$\begin{pmatrix}&0&\\&&\end{pmatrix}$
7	C_{∞}	$\begin{pmatrix}\mu_{11}&0&0\\0&\mu_{11}&0\\0&0&\mu_{33}\end{pmatrix}$	$\begin{pmatrix}\epsilon_{11}&0&0\\0&\epsilon_{11}&0\\0&0&\epsilon_{33}\end{pmatrix}$	$\begin{pmatrix}\xi_{11}&\xi_{12}&0\\-\xi_{12}&\xi_{11}&0\\0&0&\xi_{33}\end{pmatrix}$	$\begin{pmatrix}-\xi_{11}&\xi_{12}&0\\-\xi_{12}&-\xi_{11}&0\\0&0&-\xi_{33}\end{pmatrix}$

Source: Barybin, A.A. and Dmitriev, V.A., *Modern Electrodynamics and Coupled-Mode Theory: Application to Guided-Wave Optics*, Rinton Press, Princeton, NJ, 2002. With permission.

Reciprocity of a medium is stipulated by the symmetry of the constitutive relations with respect to the restricted Time-reversal operator $\mathcal{T}$.

Besides Space–Time reversal symmetry constraints considered above, some other restrictions, when imposed on the constitutive tensors can simplify them. For example, the idealization of losslessness [13]:

$$\underline{\boldsymbol{\epsilon}} = \underline{\boldsymbol{\epsilon}}^{\dagger}, \quad \underline{\boldsymbol{\mu}} = \underline{\boldsymbol{\mu}}^{\dagger}, \quad \underline{\boldsymbol{\xi}} = \underline{\boldsymbol{\zeta}}^{\dagger} \tag{3.15}$$

leads to further reduction of the number of independent parameters. In the above equations, the symbol "†" stands for the complex conjugation and transposition. Another example of the restrictions is the so-called Post constraint [14].

A remark should be made with respect to the decomposition analysis of the constitutive tensors. One can decompose a tensor into the sum of its symmetric and antisymmetric parts, then the symmetric part can be decomposed into a sum of a spherical (scalar) one and a deviator, etc. The antisymmetric part of the tensor $\underline{\boldsymbol{\mu}}$, for example, describes an axial vector (a dc magnetic field or magnetization), the deviator of the tensor $\underline{\boldsymbol{\epsilon}}$ presents the quadrupole electrical moment. Thus we can take into account the multipole contributions in the constitutive tensors and obtain additional information about the electromagnetic properties of the medium.

Finally, we can notice that some general electromagnetic properties of linear homogeneous media can be defined by inspection of the constitutive tensors. In accordance with Neumann's principle, known in crystallography [15], symmetry of a medium defines some possible physical effects in the medium and those which are "forbidden" completely. Therefore, using the group decompositions (group trees) and the existing tables of the tensors [12], one can select those symmetrical media which can possess certain electromagnetic properties.

The group-theoretical approach is based on very general grounds, namely on symmetry principles. One can consider the tensors calculated for different groups of symmetry as a systematic classification of bianisotropic media.

3.6 Symmetry of Photonic Crystals

3.6.1 Symmetry Description of 2D Magnetic Crystal with Square Lattice

From the point of view of symmetry, any photonic crystal is a periodic structure, i.e., it possesses a discrete translational symmetry [20]. Besides, one can consider also geometrical symmetry of dielectric elements, symmetry of their material (for example, anisotropy), geometrical symmetry of the crystal

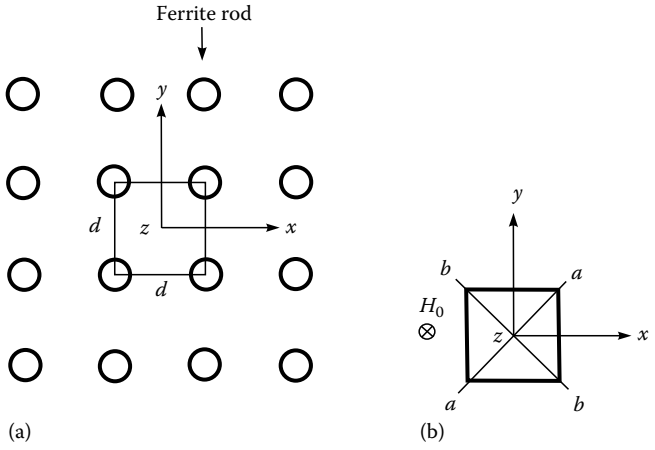

FIGURE 3.3 2D square lattice of circular cross-section ferrite rods (a), the unit cell magnetized by $\mathbf{H}_0 \parallel z$ (b).

unit cells and Time-reversal symmetry. The symmetry of possible external perturbations (such as static electric or dc magnetic fields) should also be taken into account.

We shall not discuss the consequences of the periodicity of the crystals which are mathematically expressed in Bloch's theorem and geometrically presented by the Brillouin zone (BZ). Instead we shall concentrate ourselves on the point group symmetry of the crystals.

In order to illustrate the group-theoretical approach to photonic crystals, let us apply to a relatively simple example of a 2D magnetic crystal with square lattice (Figure 3.3). The uniform in z-direction circular ferrite rods are oriented along the z-axis. They form a square lattice in the plane x–y. The permeability of the magnetized ferrite rods is a tensor of the second rank $\underline{\boldsymbol{\mu}}(\mathbf{r})$ and the permittivity is a scalar $\epsilon(\mathbf{r})$. The space between the rods is filled with a dielectric with a scalar permeability μ and a scalar permittivity ϵ. Both the ferrite and the dielectric are for simplicity considered to be lossless. Without a dc magnetic field, one can consider the ferrite rods as dielectric ones described by a scalar permeability $\mu(\mathbf{r})$.

The square unit cell of the lattice has the period d in both the x- and the y-direction (Figure 3.3a). The uniform dc magnetic field is an axial odd in Time vector with the symmetry $D_{\infty h}(C_{\infty h})$. The group $D_{\infty h}(C_{\infty h})$ contains all the rotations about the vector $\mathbf{H}_0$, the twofold rotations about the axis normal to $\mathbf{H}_0$ combined with the Time reversal T, and it also has the product of Space inversion with all the above operations. In accordance with Curie's principle of symmetry superposition, the magnetic group of the crystal is defined by the elements of symmetry which are common for the point group $C_{4v} + TC_{4v}$ of the nonmagnetic square lattice and the magnetic group $D_{\infty h}(C_{\infty h})$ of the dc magnetic field $\mathbf{H}_0$.

The resulting group of symmetry of the magnetic crystal will depend on the orientation of $\mathbf{H}_0$ with respect to the z-axis in Figure 3.3a. All the possible magnetic groups of symmetry can be obtained from the group tree of Figure 3.4. All these groups are subgroups of the group of symmetry $C_{4v}+TC_{4v}$ of our crystal in nonmagnetic state.

We shall consider the crystal magnetized by magnetic field $\mathbf{H}_0 \parallel z$ (Figure 3.3b). The resulting group of symmetry of the system "2D square lattice + dc magnetic field" is $C_{4v}(C_4)$ which contains the following eight elements:

- e is the identity element
- C_2 is a rotation by π around the z-axis
- C_4 and C_4^{-1} are rotations around the z-axis by $\pi/2$ and by $-\pi/2$, respectively

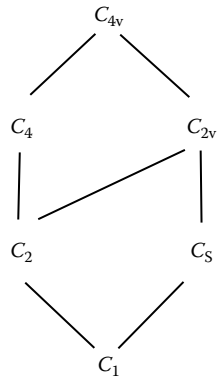

FIGURE 3.4 Subgroup decomposition of the point group C_{4v}.

- $T\sigma_x$ and $T\sigma_y$ are the antireflections in the plane $x = 0$ and in the plane $y = 0$, respectively
- $T\sigma_{(a-a)}$ and $T\sigma_{(b-b)}$ are the antireflections in the planes which pass through the z-axis and the line $(a–a)$ and $(b–b)$, respectively

Notice that application of a dc magnetic field leads in general to a reduction of symmetry of the nonmagnetic lattice.

Before discussing the symmetry of the wave vector **k**, one should define the BZ of the crystal. First of all, the shape of the BZ zone does not coincide, in general, with the shape of the unit cell of a lattice. However, in the case of the nonmagnetic square unit cell, the BZ also has the square shape.

Besides, a dc magnetic field can change the size and even the shape of the BZ. But in our case of the uniform dc magnetic field, the unit cell, and, consequently, the BZ are not changed because the translational symmetry of the crystal is unchanged after being biased by such a dc magnetic field. Thus, in spite of different magnetic symmetries, the BZ of the photonic crystal with and without magnetization is exactly the same. Therefore, for the symmetry $C_{4v}(C_4)$, we shall investigate the square BZ which is identical to the BZ of the nonmagnetic lattice.

In band calculations, we can usually restrict ourselves to a single basic domain of the BZ. This allows one to reduce the burden of numerical calculations. The basic domain for nonmagnetic crystals is defined by the smallest part of the BZ from which the whole BZ can be obtained by applying all the operators of the point group [21]. The basic domain for the nonmagnetic square lattice is the triangle ΓMX shown in Figure 3.5. It is one-eighth of the area of the whole BZ. It is not difficult to show that the basic domain for the group $C_{4v}(C_4)$ coincides with that for the group $C_{4v} + TC_{4v}$.

3.6.2 Group of Symmetry of the Wave Vector

Now, let us apply to the symmetry of the wave vector **k**. In the theory of electronic waves in crystals, the symmetry group of **k** is called the little group. In the theory of magnetic crystals, it is called the magnetic little group. We shall denote the magnetic little group for a given **k** as $\boldsymbol{M}^{\mathbf{k}}$.

There is a general symmetry property of the wave vector **k** in crystals. The groups of the wave vector **k** for different points and lines of symmetry of a given crystal are subgroups of the symmetry group of the crystal as a whole. In order to clarify this property, let us denote a magnetic group of symmetry of a crystal as $G_1(H_1)$. At any symmetric point or line of the BZ with a lower symmetry, the group of the vector **k** denoted as $G_2(H_2)$ will be a subgroup of $G_1(H_1)$. Moreover, the group H_2 is a subgroup of H_1. These subgroup relations are shown pictorially in Table 3.2 for the groups $C_{4v} + TC_{4v}$ and $C_{4v}(C_4)$.

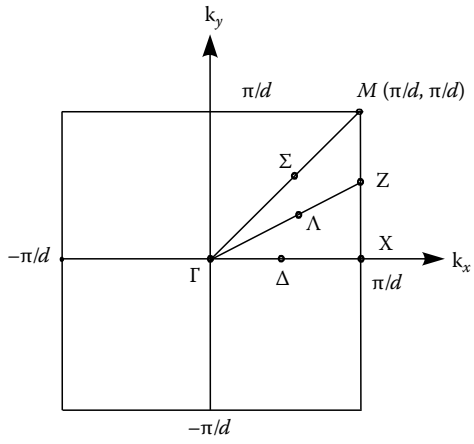

FIGURE 3.5 Reduced BZ for the 2D square lattice of circular cross-section ferrite rods. (From Dmitriev, V.A., *Eur. J. App. Phys.*, 159, 2005. With permission.)

TABLE 3.2 Subgroup Relations for the Group $C_{4v} + TC_{4v}$ and Its Subgroup $C_{4v}(C_4)$

Nonunitary Group		Unitary Subgroup
$C_{4v} + TC_{4v}$	$\longrightarrow$	C_{4v}
$\downarrow$		$\downarrow$
$C_{4v}(C_4)$	$\longrightarrow$	C_4

In order to define the group $\mathbf{M^k}$ for electromagnetic waves in magnetic photonic crystals, one should consider all the constituents of the physical problem from the point of view of magnetic symmetry. The wave vector $\mathbf{k}$ in free space is a polar odd in Time vector with the symmetry $D_{\infty h}(C_{\infty v})$. The group $D_{\infty h}(C_{\infty v})$ contains the axis of an infinite order C_∞ coinciding with $\mathbf{k}$, an infinite number of planes of symmetry σ_v passing through this axis, an antiplane $T\sigma_h$ which is perpendicular to the principal axis, an infinite number of the twofold antiaxis TC_2 lying in the antiplane $T\sigma_h$, and also the anticenter Ti.

The symmetry of $\mathbf{k}$ in free space does not depend on its orientation in Space. In a magnetic lattice, the group of symmetry of $\mathbf{k}$ (i.e., the little group $\mathbf{M^k}$) is defined by the "environment," i.e., by the symmetry of the lattice and by the symmetry of the magnetic field $\mathbf{H}_0$. $\mathbf{M^k}$ depends also on the orientation of the vector $\mathbf{k}$ and its size. The point Γ $(\mathbf{k} = 0)$ of the center of the BZ has the symmetry of the crystal as a whole.

The Time-reversal operator T as an element of the group of symmetry of a nonmagnetic crystal sends $\mathbf{k}$ into $-\mathbf{k}$, i.e.,

$$T\mathbf{k} = -\mathbf{k}. \tag{3.16}$$

In the cases of magnetic crystals, the Time reversal T does not exist in "pure" form, but it can enter in the group in the combined operations (a geometrical operation + Time reversal). Let us denote any operator of geometrical symmetry as $\mathcal{R}_1$ and an operator of combined symmetry as $T\mathcal{R}_2$. The magnetic little group $\mathbf{M^k}$ consists of those geometrical operators $\mathcal{R}_1$ which transform the wave vector $\mathbf{k}$ into itself or into $\mathbf{k} + \mathbf{G}_1$ [21]:

$$\mathcal{R}_1\mathbf{k} = \mathbf{k} \quad \text{or} \quad \mathcal{R}_1\mathbf{k} = \mathbf{k} + \mathbf{G_1}, \tag{3.17}$$

TABLE 3.3 Little Groups and Their Elements for Points and Lines of Symmetry for Square Nonmagnetic Lattice

Symmetry Symbol	Representative Wave Vector $\mathbf{k}$	Little Group	Order of the Group	Elements of the Group
Γ, M	$\pi/d(0,0)$, $\pi/d(1,1)$	C_{4v}	8	e, C_4, C_4^{-1}, C_2, σ_x, σ_y, $\sigma_{(a-a)}$, $\sigma_{(b-b)}$
X	$\pi/d(1,0)$	C_{2v}	4	e, C_2, σ_x, σ_y
Z	$\pi/d(1,\beta)$	C_s	2	e, σ_y
Σ	$\pi/d(\alpha,\alpha)$	C_s	2	e, $\sigma_{(a-a)}$
Δ	$\pi/d(\alpha,0)$	C_s	2	e, σ_x
Λ	$\pi/d(\alpha,\beta)$	C_1	1	e

and also of the combined operators $T\mathcal{R}_2$ with $\mathcal{R}_2$ which transform $\mathbf{k}$ into $-\mathbf{k}$ or into $-\mathbf{k}+\mathbf{G}_2$:

$$\mathcal{R}_2\mathbf{k} = -\mathbf{k} \quad \text{or} \quad \mathcal{R}_2\mathbf{k} = -\mathbf{k} + \mathbf{G}_2 \tag{3.18}$$

where $\mathbf{G}_1$ and $\mathbf{G}_2$ are primitive translations of the reciprocal lattice.

We shall denote a general point Λ of the BZ by $\pi/d(\alpha,\ \beta)$ which means that $\mathbf{k} = \pi/d(\alpha\boldsymbol{e}_x + \beta\boldsymbol{e}_y)$, where $\boldsymbol{e}_x$ and $\boldsymbol{e}_y$ are the unit vectors in the x and y directions, respectively.

Nonmagnetic crystal. In Table 3.3, we give a description of the little groups for the nonmagnetic crystal described by the group C_{4v}. This table can serve as a reference for the magnetic symmetry discussed below.

The points Γ and M of the BZ (Figure 3.5) have the symmetry C_{4v}. When we depart from the point Γ in the direction of M, we are on the line denoted Σ with the coordinates of the wave vector $(\alpha,\ \alpha)$, $0 < \alpha < \sqrt{2}\pi/d$. The group of symmetry of the wave vector on the line Σ is C_s which is a subgroup of C_{4v}. The group C_s contains the elements e and $\sigma_{(a-a)}$. Analogous examination can be made for other points and lines of the BZ.

Magnetic crystal. Now we apply to the magnetic crystal. The magnetization $\mathbf{H}_0 \parallel z$ reduces the symmetry of the crystal from $C_{4v} + TC_{4v}$ to $C_{4v}(C_4)$. For the points Γ and M of the BZ (Figure 3.5), the wave vectors have the symmetry $C_{4v}(C_4)$ (Table 3.4). The symmetry of the point X is $C_{2v}(C_2)$. The symmetry of the vectors Z, Σ, and Δ is $C_s(C_1)$. The wave vector Λ in a general point of the BZ has no symmetry.

One important consequence of the crystal symmetry is as follows. The dispersion characteristics $\omega_n(\mathbf{k})$ of the magnetic crystal have the full symmetry of the point magnetic group of the crystal. Thus, we can use the irreducible representations (IRREPs, Appendix A) of the magnetic little groups to classify the eigenmodes. In fact, in most cases for the correct classification of the eigenmodes, it is sufficient to use only the unitary subgroups of the corresponding magnetic little groups. The peculiarities of the IRREPs of the point magnetic groups are discussed in [21].

3.6.3 Lifting of Degeneracy by dc Magnetic Field

The points Γ and M of the BZ (Figure 3.5) in nonmagnetic state have doubly degenerate representations i.e., these representations are two-dimensional. With dc magnetic field applied to the crystal, we

TABLE 3.4 Little Groups and Their Elements for Points and Lines of Symmetry for Square Magnetic Lattice with dc Magnetic Field $\mathbf{H}_0 \parallel z$, the Crystal Group Is $C_{4v}(C_4)$

Symmetry Symbol	Representative Wave Vector $\mathbf{k}$	Little Group	Order of the Group	Elements of the Group
Γ, M	$\pi/d(0,0)$, $\pi/d(1,1)$	$C_{4v}(C_4)$	8	e, C_4, C_4^{-1}, C_2, $T\sigma_x$, $T\sigma_y$, $T\sigma_{(a-a)}$, $T\sigma_{(b-b)}$
X	$\pi/d(1,0)$	$C_{2v}(C_2)$	4	e, C_2, $T\sigma_x$, $T\sigma_y$
Z	$\pi/d(1,\beta)$	$C_s(C_1)$	2	e, $T\sigma_y$
Σ	$\pi/d(\alpha,\alpha)$	$C_s(C_1)$	2	e, $T\sigma_{(a-a)}$
Δ	$\pi/d(\alpha,0)$	$C_s(C_1)$	2	e, $T\sigma_x$
Λ	$\pi/d(\alpha,\beta)$	C_1	1	e

Source: Dmitriev, V.A., *Eur. J. App. Phys.*, 159, 2005. With permission.

can expect the corresponding eigenwaves with symmetry-induced degeneracies to be split by symmetry reduction into two different nondegenerate eigenwaves. This splitting can be predicted without numerical calculations by inspection of the irreducible representation Tables.

3.7 Conclusions

In this chapter, we have used symmetry principles and group theory as basic tools for the investigation of complex media. Advantages of the group-theoretical methods are their universality, independence of the results on frequency and on details of the structure, and simplicity of calculations. The higher the symmetry the more the information one can obtain from the theory. However, the frameworks of these methods which are purely geometrical ones are restricted and naturally, they cannot substitute the electrodynamic methods. One should consider group theory as an auxiliary analytical tool which can be used before the electrodynamic calculations.

The group-theoretical methods allow one:

1. To calculate the structure of material tensors. The calculated tensors can be used, in particular, to predict physical effects which can exist in a given medium and, according to Neumann's principle, those effects which are forbidden in the medium completely.
2. To calculate the structure of a matrix (impedance, scattering) in the circuit theory of artificial particles.
3. To resolve the problem of reciprocity and bidirectionality of a medium.
4. To define
   a. Degeneracy of eigenmodes in a given medium
   b. Lifting of degeneracy of eigenmodes in a medium by an external perturbation
   c. The structure of Green's tensors in a given medium [19]
   d. Electromagnetic modes of artificial particles
   e. Magneto-optical response of a symmetrical metamaterial [3]

Some other examples of application of group theory to electromagnetics can be found in [22,23].

Appendix A: Elements of Group Theory and Theory of Representations

In the modern literature, there are many publications devoted to the group theory (see, e.g., books [11,16–18,21] and their lists of references). We present here only a minimum relevant information from the group theory and the theory of representations which is used in this chapter.

Group. A group G is a set of distinct elements $u_i \in G$ for which a combining operation called the product is defined. By definition, the set of elements constituting a group:

1. Satisfies the following condition: if u_i and u_j are elements of G, their product $u_i u_j$ is also an element of the same group
2. Possesses an associative law of combination, i.e., $u_i(u_j u_k) = (u_i u_j)u_k$
3. Contains a unit element e such that $eu_i = u_i e = u_i$
4. For every u_i contains an inverse element u_i^{-1} such that $u_i^{-1}u_i = u_i u_i^{-1} = e$

The number of elements of a group is its order M. The order of the group may be finite or infinite. If it is possible for an infinitesimal change in a group element to come to another element, the group is called continuous. Using a small number of elements called generators one can get all the other

elements of the group, i.e., every element of a group can be written as a product of generators and their inverses.

In general, any element of a group commutes only with the unit element and with the inverse one. If all the elements of a group commute, the group is called Abelian.

Subgroup. Any subset H of G which by itself forms a group is called a subgroup. All the four above properties are inherent in a subgroup H as well. A subgroup H of a finite group G has an index. The index which is always an integer is defined by the quotient of the orders of the group and the subgroup.

Point groups. The groups of our interest are those whose elements describe geometrical or physical transformations. The geometrical transformations are Space rotations and reflections. All the symmetry operations of an object form a point group. All the axes and planes of a point group have at least one common point of intersection.

Representations. The theory of representations deals with mapping of groups on groups of linear operators (for example, matrices, see Appendix D). If a set of $N \times N$ square matrices $\underline{\mathbf{R}}_u$ has, with respect to ordinary matrix multiplication, the properties (Equations 3.2 through 3.4) of a group G written above, then this set forms a representation of G. Hence, the matrices $\underline{\mathbf{R}}_u$ satisfy the equation

$$\underline{\mathbf{R}}_{u_i} \cdot \underline{\mathbf{R}}_{u_j} = \underline{\mathbf{R}}_{u_i u_j}, \tag{3.A.1}$$

where u_i and u_j are any two elements of the group G. The square matrices $\underline{\mathbf{R}}_u$ are unitary and nonsingular and their order of them N is called the dimension of the representation. The matrices $\underline{\mathbf{R}}_u$ form a group of linear transformations.

Matrix representations of a group G can be brought into a block-diagonal form by a similarity transformation. The blocks of the transformed representations in the simplest forms which cannot be reduced further are called irreducible representations of the Group G.

Appendix B: Notations of Elements of Symmetry, Symmetry Operations, and Point Groups

Different systems of group notations are used in practice [21]. The most popular systems are the International (devised by Hermann and Mauguin), the Schoenflies and the Shubnikov ones.

Below, we shall describe briefly the Schoenflies system which is used in this chapter. Notice that the notations of group elements, of symmetry operations, and the notations of the groups themselves may coincide. For example, the symbol C_2 denotes the operation of rotation about an axis by π, and also it may denote the group C_2 consisting of the two elements: the identity e and the rotation C_2.

Notations of group elements. The n-fold proper rotations are considered as elementary operators. In order to obtain the remaining operators, one can form products of the rotations with the space inversion, or alternatively with the reflection in a plane perpendicular to the n-fold axis. We shall consider first the notations of the symmetry elements.

A proper rotation through $2\pi/n$ (where n is an integer) about a certain axis is denoted by the symbol C_n (where C means Cyklus). The symbol σ (and also C_s) defines reflection in a plane. The reflection in a plane perpendicular to the principal axis is denoted by σ_h (the subscript h for horizontal), while σ_v (the subscript v for vertical) is used for reflection in a plane passing through the axis, and σ_d (d for diagonal) designates a mirror plane containing the axis but diagonal to an already existing plane σ_v. A combined operation C_n and σ_h is denoted by S_n (where S means Spiegelaxe) which is improper rotation. Therefore, the inversion i which presents a rotation C_2 (rotation by π) followed by the reflection σ_h may also be denoted as S_2.

Group notations. Let us apply now to the group notations in the Schoenflies system. The groups with one axis of symmetry are denoted by C_n. Joining σ_h to C_n gives the groups C_{nh}. The groups

having an n-fold axis and a system of twofold axes at right angles to it are denoted by D_n (dihedral groups). D_{nd} and D_{nh} contain in addition the planes σ_d and σ_h, respectively. The higher groups T and O contain only pure rotations, but T_d also has planes of symmetry, and T_h and O_h contain the center of symmetry. The Schoenflies system is particularly suitable for notation of the magnetic groups of the third category. In this case, the notation shows explicitly the structure of the group, i.e., the unitary subgroup and the antiunitary elements.

Continuous group notations. In the continuous point groups, the index n which defines the order of the axis is replaced by the symbol ∞ for the axes of an infinite order. Thus, the axis of an infinite order is denoted by C_∞. With $n \to \infty$, the group D_n is transformed in the group D_∞, the group C_{nv} in $C_{\infty v}$, and so on. Two highest point groups describing spherical symmetry have special notations, namely, the groups consisting of an infinite number of axes of an infinite order are denoted by K. Adding an infinite number of planes of symmetry to the group K, one obtains the group K_h.

Appendix C: Brief Description of Magnetic Groups

Time-reversal operator. For magnetic structures, it is necessary to include into consideration the Time reversal T as an element of magnetic groups and combinations of space symmetry operations with T. T changes the sign of time, i.e., $(t) \to -(t)$. The Time reversal T commutes with all the space elements. It has the property $TT = T^2 = e$ (e is the unit element). Thus the elements T and e form a group. The Time-reversal operator **T** corresponding to the group element T belongs to the so-called antiunitary operators [21]. This operator has no unitary matrix representation.

When we deal with electromagnetic processes in the frequency domain, the usual description of electromagnetic quantities is in terms of complex functions. The effect of the operator **T** on time-harmonic quantities is expressed as follows. First of all, the operator reverses the velocities and changes the current directions, the signs of electron spins, magnetic fluxes, magnetic fields and Poynting's vector. All these quantities are odd in Time. Secondly, it complex conjugates all the electromagnetic quantities. This property is verified easily by considering Fourier transformation of the Time-reversed quantities [5].

Strictly speaking, there exists no Time-reversal symmetry in physical processes. The main reason of this is causality, i.e., initial conditions impose asymmetry with respect to the past and the future. In the presence of losses in a medium, the physical processes are not the same in a given and in the Time-reversed medium. For example, the operator **T** converts a damping electromagnetic wave into a growing one and vice versa because the dissipative processes are not Time reversible.

It was suggested in [5] to use along with **T** another operator which was called the restricted Time-reversal operator. This operator $\mathcal{T}$ fulfills the same functions as **T** with one exception: it is not applied to the imaginary dissipative terms of the electromagnetic quantities. This preserves the damping or growing character of the wave under the Time reversal.

Categories of magnetic groups. There exist three categories of discrete and continuous point magnetic groups. The group of the first category G consists of a unitary subgroup H (in our case, it contains the usual rotation–reflection elements) and products of T with all the elements of H. The full group is then $H + TH$ including $T = Te$, i.e., the group of the first category G is a direct product of the group H and the group formed by T and e.

In the case of magnetic groups of the second category ***G***, there are no Space elements combined with the Time reversal T, and T itself is not an element of the groups. The nomenclature and the notations of the groups of the first (nonmagnetic) category and that of the second (magnetic) category coincide. In order to distinguish them, we use bold-face type for the groups of the second category.

The magnetic groups of the third category $G(H)$ contain, in addition to the rotation–reflection elements of the unitary subgroup H, an equal number of antiunitary elements which are the product of T and the usual geometrical symmetry elements. These combined elements we call antiaxes,

TABLE 3.C.1 Content of Magnetic Groups of Symmetry

First Category	Second Category	Third Category
$G = H + TH$ including T	$\boldsymbol{G}$ without T	$G(H) = H + TH'$, $H' \neq H$ T only in combination with rotation–reflections

antiplanes, and anticenter of symmetry. The full group is $H + TH'$. Notice that the elements of H' are distinguished from those of H.

The unitary elements of a magnetic group of the third category form a unitary subgroup of index 2. It means that in every group of the third category there are equal number of elements with and without T. In contrast to the groups of the first category, the operator T itself is not an element of the magnetic groups of the third category. The content of the three categories of magnetic groups is presented in Table 3.C.1.

Appendix D: Matrix Representations of 3D Point Symmetry Operators

In order to describe symmetry operations in 3D space, such as rotations and reflections, we use 3D matrix representations of the point groups. Each element of a group corresponding to a point symmetry can be presented by a 3 × 3 square orthonormal real matrix $\underline{\mathbf{R}}$, i.e., $\underline{\mathbf{R}}^{-1} = \underline{\mathbf{R}}^{t}$, $\det\underline{\mathbf{R}} = \pm 1$; the superscript t means matrix transposition, the superscript -1 denotes the inverse matrix. Thus, these representations are unitary. The unit element of the group has the unit 3×3 matrix as a representation. The matrices $\underline{\mathbf{R}}$ fulfilling rotations through an angle α about the axes x, y, and z are

$$\underline{\mathbf{R}}_{C_x} = \begin{pmatrix} 1 & 0 & 0 \\ 0 & \cos\alpha & -\sin\alpha \\ 0 & \sin\alpha & \cos\alpha \end{pmatrix}, \quad \underline{\mathbf{R}}_{C_y} = \begin{pmatrix} \cos\alpha & 0 & \sin\alpha \\ 0 & 1 & 0 \\ -\sin\alpha & 0 & \cos\alpha \end{pmatrix}, \quad \underline{\mathbf{R}}_{C_z} = \begin{pmatrix} \cos\alpha & -\sin\alpha & 0 \\ \sin\alpha & \cos\alpha & 0 \\ 0 & 0 & 1 \end{pmatrix}, \tag{3.D.1}$$

respectively.

The 3D matrix representations for reflections in the planes $x = 0$, $y = 0$, and $z = 0$ are written respectively as

$$\underline{\mathbf{R}}_{\sigma_x} = \begin{pmatrix} -1 & 0 & 0 \\ 0 & 1 & 0 \\ 0 & 0 & 1 \end{pmatrix}, \quad \underline{\mathbf{R}}_{\sigma_y} = \begin{pmatrix} 1 & 0 & 0 \\ 0 & -1 & 0 \\ 0 & 0 & 1 \end{pmatrix}, \quad \underline{\mathbf{R}}_{\sigma_z} = \begin{pmatrix} 1 & 0 & 0 \\ 0 & 1 & 0 \\ 0 & 0 & -1 \end{pmatrix}, \tag{3.D.2}$$

and the matrix representing inversion i (the center of symmetry) is

$$\underline{\mathbf{R}}_{i} = \begin{pmatrix} -1 & 0 & 0 \\ 0 & -1 & 0 \\ 0 & 0 & -1 \end{pmatrix}. \tag{3.D.3}$$

The determinant of $\underline{\mathbf{R}}$ for rotations (3.D.1) is +1 but it is equal to −1 for reflections (3.D.2) and inversion (3.D.3).

References

1. Olver, P. J., *Equivalence, Invariants, and Symmetry*, Cambridge University Press, Cambridge, 1995.
2. Fushchich, W. I. and Nikitin, A. G., *Symmetries of Maxwell's Equations*, D. Reidel, Dordrecht, 1987.

3. Padilla, W. J., Group theoretical description of artificial electromagnetic metamaterials, *Opt. Express*, 15(4), 1639–1646, 2007.
4. Onsager, L., Reciprocal relations in irreversible processes, *Phys. Rev*., 37, 405–426, 1931.
5. Altman, C. and Suchy, K., *Reciprocity, Spatial Mapping and Time Reversal in Electromagnetics*, Kluwer, Dordrecht, 1991.
6. Prigogine, I., *From Being to Becoming: Time and Complexity in the Physical Sciences*, W. H. Freeman and Company, San Francisco, CA, 1980.
7. Potton, R. J., Reciprocity in optics, *Rep. Prog. Phys*., 67, 717–754, 2004.
8. Landau, L. D. and Lifshits, E. M., *Electrodynamics of Continuous Media*, Pergamon Press, Oxford, 1984.
9. Korn, G. A. and Korn, T. M., *Mathematical Handbook for Scientists and Engineers*, McGraw-Hill, New York, 1968.
10. Nye, J. F., *Physical Properties of Crystals*, Oxford University Press, New York, 1993.
11. Koptsik, V. A., *Shubnikov Groups, Handbook on the Symmetry and Physical Properties of Crystal Structures*, Moscow State University, Moscow, 1966 (in Russian).
12. Dmitriev, V., Tables of the second rank constitutive tensors for linear homogeneous media described by the point magnetic group of symmetry, in *Progress in Electromagnetics Research*, J. A. Kong (Ed.), PIER, EMW Publishing, Cambridge, MA, Vol. 28, pp. 47–99, 2000.
13. Kong, J. A., *Electromagnetic Wave Theory*, EMW Publishing, Cambridge, MA, 1998.
14. Post, E. J., *Formal Structure of Electromagnetics: General Covariance and Electromagnetics*, Courier Dover Publications, Mineola, NY, 1997.
15. Birss, R. R., *Symmetry and Magnetism*, North Holland, Amsterdam, 1964.
16. Dresselhaus, M. S., Dresselhaus, G., and Jorio, A., *Group Theory: Application to the Physics of Condensed Matter*, Springer-Verlag, Berlin, Heidelberg, 2008.
17. Wu-Ki Tung, *Group Theory in Physics*, World Scientific, Philadelphia, 1985.
18. Lax, M., *Symmetry Principles in Solid State and Molecular Physics*, Wiley, New York, 1974.
19. Dmitriev, V., Space–Time reversal symmetry properties of electromagnetic Green's tensors for complex and bianisotropic media, *Progress in Electromagnetic Research*, J. A. Kong (Ed.), PIER, EMW Publishing, Cambridge, MA, Vol. 48, pp. 145–184, 2004.
20. Johnson, S. G. and Joannopoulos, J. D., *Photonic Crystals: The Road from Theory to Practice*, Kluwer, Boston, MA, 2002.
21. Bradley, C. J. and Cracknell A. P., *The Mathematical Theory of Symmetry in Solids*, Clarendon, Oxford, 1972.
22. Baum C. E. and Kritikos N. H. (Eds.), *Electromagnetic Symmetry*, Taylor & Francis, Washington, DC, 1995.
23. Barybin, A. A. and Dmitriev V. A., *Modern Electrodynamics and Coupled-Mode Theory: Application to Guided-Wave Optics*, Rinton Press, Princeton, NJ, 2002.
24. Tretyakov, S. A. and Sochava, A. A., Proposed composite material for nonreflecting shields and antenna radoms, *Electron. Lett*., 29, 1048–1049, 1993.

4

Differential Forms and Electromagnetic Materials

Ismo V. Lindell
Helsinki University of Technology

4.1 Introduction

Differential-form calculus is a branch of mathematics based on the algebra of multivectors (elements of spaces $\mathbb{E}_1, \ldots, \mathbb{E}_n$) and multiforms (dual multivectors, elements of spaces $\mathbb{F}_1, \ldots, \mathbb{F}_n$) [1]. The notation applied here follows closely that of Ref. [2] and a short summary is given in the Appendix. Corresponding representation using tensors instead of dyadics can be found, e.g., in Ref. [3]. Application of differential forms to electromagnetic theory instead of the classical Gibbsian vector formalism [4,5] is suggested by the simplicity and elegance obtained in writing the basic Maxwell equations as [2]

$$\mathbf{d} \wedge \mathbf{\Phi} = \gamma_m, \quad \mathbf{d} \wedge \mathbf{\Psi} = \gamma_e. \tag{4.1}$$

Here

$$\mathbf{d} = \sum_{i=1}^{4} \mathbf{e}_i \partial_{x_i} = \mathbf{d}_s + \mathbf{e}_4 \partial_{x_4} \tag{4.2}$$

is the four-dimensional (4D) differential operator and $\wedge$ the exterior product, while

$$\mathbf{\Phi} = \mathbf{B} + \mathbf{E} \wedge \varepsilon_4, \quad \mathbf{\Psi} = \mathbf{D} - \mathbf{H} \wedge \varepsilon_4 \tag{4.3}$$

represent the 4D electromagnetic two-forms (fields depending on the spatial coordinates x_1, x_2, x_3 and the temporal coordinate $x_4 = \tau = ct$) in terms of spatial (3D) two-forms **B**, **D** and one-forms **E**, **H**. The electric and magnetic source three-forms γ_e, γ_m can be expressed as

$$\gamma_e = \rho_e - \mathbf{J}_e \wedge \varepsilon_4, \quad \gamma_m = \rho_m - \mathbf{J}_m \wedge \varepsilon_4 \tag{4.4}$$

in terms of combinations of spatial (3D) charge three-forms ρ_e, ρ_m and current two-forms $\mathbf{J}_e, \mathbf{J}_m$.

Inserting the 3D expansions (Equations 4.3 and 4.4), the 4D Maxwell equations (Equation 4.1) can be split in more familiar-looking 3D equations as

$$\mathbf{d}_s \wedge \mathbf{E} + \partial_\tau \mathbf{B} = -\mathbf{J}_m, \quad \mathbf{d}_s \wedge \mathbf{B} = \rho_m, \tag{4.5}$$

$$\mathbf{d}_s \wedge \mathbf{H} - \partial_\tau \mathbf{D} = \mathbf{J}_e, \quad \mathbf{d}_s \wedge \mathbf{D} = \rho_e. \tag{4.6}$$

Here $\mathbf{d}_s$ denotes the spatial part of the differential operator $\mathbf{d}$ and $\partial_\tau = \partial_{x_4} = \partial/\partial\tau$.

Linear medium relations between the field two-forms $\mathbf{\Phi} \in \mathbb{F}_2$ and $\mathbf{\Psi} \in \mathbb{F}_2$ can be compactly handled in terms of the medium dyadic $\underline{\mathsf{M}} \in \mathbb{F}_2\mathbb{E}_2$ as

$$\mathbf{\Psi} = \underline{\mathsf{M}} \rfloor \mathbf{\Phi}. \tag{4.7}$$

Another, equivalent, way to represent the medium relation is by mapping the one-form $\mathbf{\Psi}$ with the quadrivector $\mathbf{e}_N = \mathbf{e}_{1234}$ to the bivector $\mathbf{e}_N \lfloor \mathbf{\Psi} \in \mathbb{E}_2$, in which case the medium relation is represented as

$$\mathbf{e}_N \lfloor \mathbf{\Psi} = \underline{\mathsf{M}}_g \rfloor \mathbf{\Phi}, \tag{4.8}$$

through the modified medium dyadic

$$\underline{\mathsf{M}}_g = \mathbf{e}_N \lfloor \underline{\mathsf{M}} \in \mathbb{E}_2\mathbb{E}_2. \tag{4.9}$$

Both $\underline{\mathsf{M}}$ and $\underline{\mathsf{M}}_g$ possess 6×6 matrix components when expanded in certain bases, which means that they correspond to 36 parameters in the general case. In this presentation we consider some obvious ways to define classes of media by reducing the generality of the medium dyadic $\underline{\mathsf{M}}$ or $\underline{\mathsf{M}}_g$.

4.2 Field and Medium Equations

For simplicity, let us assume that there exist no magnetic sources $\gamma_m = 0$. Because of $\mathbf{d} \wedge \mathbf{\Phi} = 0$, the field two-form can be expressed in terms of an electric potential one-form $\boldsymbol{\alpha}_e \in \mathbb{F}_1$ in the form [2]

$$\mathbf{\Phi} = \mathbf{d} \wedge \boldsymbol{\alpha}_e, \tag{4.10}$$

whence inserting the medium Equation 4.7 in Equation 4.1 the following second-order equation can be formed for the potential:

$$\mathbf{d} \wedge \mathbf{\Psi} = \mathbf{d} \wedge \underline{\mathsf{M}} \rfloor (\mathbf{d} \wedge \boldsymbol{\alpha}_e) = \boldsymbol{\gamma}_e. \tag{4.11}$$

The differential operator in Equation 4.11 can be made more compact by transforming the equation by $\mathbf{e}_N \lfloor$ to the form

$$(\underline{\mathsf{M}}_g \lfloor\lfloor \mathbf{dd}) \rfloor \boldsymbol{\alpha}_e = \mathbf{g}_e, \tag{4.12}$$

where $\mathbf{g}_e = \mathbf{e}_N \lfloor \boldsymbol{\gamma}_e \in \mathbb{E}_1$ is the vector counterpart of the electric source three-form γ_e. Equation 4.12 represents the potential equation in terms of the dyadic operator $\underline{\mathsf{M}}_g \lfloor\lfloor \mathbf{dd} \in \mathbb{E}_1\mathbb{E}_1$. Solving Equation 4.12 analytically for a bianisotropic medium with the general dyadic $\underline{\mathsf{M}}_g$ appears to be out of reach, but solutions can be found in some special classes of media. Also, it is of interest to find possible plane-wave solutions of the form

$$\boldsymbol{\alpha}_e(\mathbf{x}) = \boldsymbol{\alpha}_o \exp(\boldsymbol{\nu} \rfloor \mathbf{x}), \tag{4.13}$$

where $\boldsymbol{\nu} \in \mathbb{F}_1$ is the 4D wave one-form corresponding to the Gibbsian 3D wave vector $\mathbf{k}$. $\boldsymbol{\alpha}_o$ is the potential amplitude one-form. Because the plane wave does not have sources in the finite region, Equation 4.12 reduces to the algebraic equation

$$(\underline{\mathsf{M}}_g \lfloor\lfloor \boldsymbol{\nu}\boldsymbol{\nu}) \rfloor \boldsymbol{\alpha}_o = 0. \tag{4.14}$$

It is of interest to compare 4D formulation of media with the classical 3D formulation using Gibbsian medium dyadics $\underline{\epsilon}_g, \underline{\xi}_g, \underline{\zeta}_g$, and $\underline{\mu}_g \in \mathbb{E}_1\mathbb{E}_1$. Medium relations (Equations 4.7 and 4.8) correspond to the conditions

$$\begin{pmatrix} \mathbf{D} \\ \mathbf{B} \end{pmatrix} = \begin{pmatrix} \underline{\epsilon}_g & \underline{\xi}_g \\ \underline{\zeta}_g & \underline{\mu}_g \end{pmatrix} \cdot \begin{pmatrix} \mathbf{E} \\ \mathbf{H} \end{pmatrix}, \tag{4.15}$$

where the fields are understood as Gibbsian vectors and "$\cdot$" is the Gibbsian dot product. A direct relation between the modified medium dyadic $\underline{\mathsf{M}}_g$ and the 3D Gibbsian medium dyadics can be expressed as [2]

$$\underline{\mathsf{M}}_g = \underline{\epsilon}_g \hat{\wedge} \mathbf{e}_4\mathbf{e}_4 - (\mathbf{e}_{123} \rfloor \underline{\mathsf{I}}^{\mathrm{T}} + \mathbf{e}_4 \wedge \underline{\xi}_g) | \underline{\mu}_g^{-1} | (\underline{\mathsf{I}} \rfloor \mathbf{e}_{123} - \underline{\zeta}_g \wedge \mathbf{e}_4), \tag{4.16}$$

which allows one to interpret results in terms of the Gibbsian medium dyadics.

4.3 Classes of Electromagnetic Media

Let us now consider some classes of media defined in terms of the medium dyadic $\underline{\mathsf{M}}$ or the corresponding modified medium dyadic $\underline{\mathsf{M}}_g$ taking a simple analytic appearance or satisfying some basic condition.

4.3.1 Perfect Electromagnetic Conductor

In Gibbsian formalism the simplest electromagnetic medium is the isotropic medium represented by two scalars ϵ and μ. Such a medium is not isotropic in the sense of differential forms. For example, in the 3D relation $\mathbf{D} = \epsilon\mathbf{E}$ the permittivity ϵ cannot be a scalar but, rather, a dyadic $\underline{\epsilon} \in \mathbb{F}_2\mathbb{E}_1$ mapping one-forms to two-forms. Moreover, a Gibbsian unit dyadic $\sum \mathbf{e}_i\mathbf{e}_i$ depends on the choice of the vector basis $\{\mathbf{e}_i\}$ while the unit dyadic $\underline{\mathsf{I}} = \sum \mathbf{e}_i\boldsymbol{\varepsilon}_i$, where $\{\boldsymbol{\varepsilon}_i\}$ is the reciprocal basis, is independent of that choice.

The only truly isotropic medium satisfies the condition

$$\boldsymbol{\Psi} = M\boldsymbol{\Phi}, \tag{4.17}$$

for some scalar M (physicists call this pseudoscalar). The medium dyadic for such a medium is, thus, of the form

$$\underline{\mathsf{M}} = M\underline{\mathsf{I}}^{(2)\mathrm{T}} = M\frac{1}{2}\underline{\mathsf{I}}^{\mathrm{T}} \hat{\wedge} \underline{\mathsf{I}}^{\mathrm{T}} = M\sum_{i<j} \boldsymbol{\varepsilon}_{ij}\mathbf{e}_{ij}. \tag{4.18}$$

Equation 4.17 describes a medium which turns out to be invariant in all affine transformations, including motion of the observer with constant velocity [4]. Inserting Equation 4.3 in Equation 4.17 yields the 3D conditions

$$\mathbf{D} = M\mathbf{B}, \quad \mathbf{H} = -M\mathbf{E}. \tag{4.19}$$

It does not appear easy to express these in terms of Gibbsian medium parameters. However, a possible representation as a bi-isotropic medium with four scalar parameters is defined through the limit [6]

$$\begin{pmatrix} \epsilon_g & \xi_g \\ \zeta_g & \mu_g \end{pmatrix} = q\begin{pmatrix} M & 1 \\ 1 & 1/M \end{pmatrix}, \quad q \to \infty. \tag{4.20}$$

Although the four Gibbsian parameters have infinite values, the following combinations remain finite:

$$\epsilon_g \mu_g - \xi_g \zeta_g = 0, \quad \epsilon_g / \mu_g = M^2. \tag{4.21}$$

This is an example of a medium which is quite simple to describe in terms of differential forms while the classical Gibbsian representation appears somewhat artificial. Anyway, Equation 4.17 is of great interest since it defines the simplest medium condition between the field two-forms.

One can show that in a medium defined by Equation 4.17 the Maxwell stress dyadic vanishes which means vanishing Poynting vector and energy density, for example, in Ref. [2]. Thus, electromagnetic fields cannot propagate in such a medium. Because the PMC and PEC media can be conceived as special cases of the present medium,

$$M = 0 \Rightarrow \mathbf{H} = 0, \ \mathbf{D} = 0, \ (\text{PMC}), \tag{4.22}$$

$$1/M = 0 \Rightarrow \mathbf{E} = 0, \ \mathbf{B} = 0, \ (\text{PEC}). \tag{4.23}$$

The medium defined by Equation 4.17 has been coined the perfect electromagnetic conductor (PEMC) and M is the PEMC admittance parameter [6,7]. In physics, the parameter M is known as the axion [3]. One can show that PEMC makes a boundary with nonreciprocal properties if the parameter satisfies $0 < |M| < \infty$. For example, a plane wave reflecting from a PEMC plane experiences rotation of polarization [6]. Besides representing a boundary, the PEMC concept is also useful as an effective medium for fields restricted by some conditions.

4.3.2 Q-Media

The general modified medium dyadic $\underline{\mathsf{M}}_g \in \mathbb{E}_2\mathbb{E}_2$ is characterized by 36 parameters. The number of parameters is reduced to 16 if it is represented in terms of a dyadic $\underline{\mathsf{Q}} \in \mathbb{E}_1\mathbb{E}_1$ in the form

$$\underline{\mathsf{M}}_g = \underline{\mathsf{Q}}^{(2)} = \frac{1}{2}\underline{\mathsf{Q}} \hat{\wedge} \underline{\mathsf{Q}}. \tag{4.24}$$

One can show that in the 3D space a dyadic mapping two-forms to bivectors can always be expressed in this form in terms of some dyadic $\underline{\mathsf{Q}}$. The reason is, of course, that the dyadic spaces $\mathbb{E}_2\mathbb{E}_2$ and $\mathbb{E}_1\mathbb{E}_1$ have the same dimension 9. This is not so in 4D, where Equation 4.24 defines a class of media labeled as that of Q-media in Refs. [2,8].

The wave equation (Equation 4.12) is radically simplified for a Q-medium. Applying the dyadic identity (Equation 4.A.25) in the form

$$\underline{\mathsf{Q}}^{(2)} \lfloor \lfloor \mathbf{dd} = (\underline{\mathsf{Q}} \| \mathbf{dd}) \underline{\mathsf{Q}} - (\underline{\mathsf{Q}} | \mathbf{d})(\mathbf{d} | \underline{\mathsf{Q}}), \tag{4.25}$$

Equation 4.12 becomes

$$(\underline{\mathsf{Q}} \| \mathbf{dd}) \underline{\mathsf{Q}} | \boldsymbol{\alpha}_e - (\underline{\mathsf{Q}} | \mathbf{d})(\mathbf{d} | \underline{\mathsf{Q}} | \boldsymbol{\alpha}_e) = \mathbf{g}_e. \tag{4.26}$$

Because the potential is not unique, one can assume an additional scalar condition (gauge condition) for the four-potential $\boldsymbol{\alpha}_e$. Assuming the condition

$$\mathbf{d} | \underline{\mathsf{Q}} | \boldsymbol{\alpha}_e = 0, \tag{4.27}$$

which can be regarded as the generalized Lorenz condition, the wave equation (Equation 4.26) is simplified to

$$(\underline{\mathsf{Q}} \| \mathbf{dd}) \boldsymbol{\alpha}_e = \underline{\mathsf{Q}}^{-1} | \mathbf{g}_e. \tag{4.28}$$

Equation 4.28 is essentially simpler than Equation 4.12, because the dyadic operator $\underline{\mathsf{M}}_g \rfloor\rfloor \mathbf{dd}$ is replaced by a scalar operator of the second order, $\mathbf{d}|\underline{\mathsf{Q}}|\mathbf{d}$. Depending on the nature of the dyadic $\underline{\mathsf{Q}}$, Equation 4.28 represents a wave equation (hyperbolic) or 4D Laplace equation (elliptic) for which standard solution processes can be applied.

Conditions for the Gibbsian medium dyadics $\underline{\epsilon}_g, \underline{\xi}_g, \underline{\zeta}_g, \underline{\mu}_g$ corresponding to the Q-medium can be found after some algebraic steps in the form [2,9]

$$a\underline{\epsilon}_g + b\underline{\mu}_g^{\mathrm{T}} = 0, \quad \underline{\xi}_g + \underline{\xi}_g^{\mathrm{T}} = 0, \quad \underline{\zeta}_g + \underline{\zeta}_g^{\mathrm{T}} = 0, \tag{4.29}$$

where the scalar coefficients a, b may have any values. These conditions define a medium studied previously in Refs. [10,11]. A plane wave in such a medium is characterized by a single wave-vector surface of the second order. This means that a plane wave in a Q-medium has no birefringence. One can show that the class of Q-media can be defined by the 4D condition [2]

$$a\underline{\mathsf{M}}_g + b\underline{\mathsf{M}}_g^{-1\mathrm{T}} \rfloor\rfloor \mathbf{e}_N\mathbf{e}_N = 0, \tag{4.30}$$

which is a compact representation of the three conditions (Equation 4.29).

4.3.3 Generalized Q-Media

An obvious generalization to Equation 4.24 is the definition

$$\underline{\mathsf{M}}_g = \underline{\mathsf{Q}}^{(2)} + \mathbf{AB}, \tag{4.31}$$

where $\mathbf{A}, \mathbf{B} \in \mathbb{E}_2$ are two bivectors. In this case we can apply the same gauge condition (Equation 4.27) for the potential $\boldsymbol{\alpha}_e$, whence the potential equation (Equation 4.12) becomes

$$\left[(\underline{\mathsf{Q}}||\mathbf{dd})\underline{\mathsf{Q}} + (\mathbf{A}\lfloor\mathbf{d})(\mathbf{B}\lfloor\mathbf{d})\right]|\boldsymbol{\alpha}_e = \mathbf{g}_e. \tag{4.32}$$

This equation still involves a dyadic operator. The corresponding inverse dyadic operator can be expressed as

$$\left[(\underline{\mathsf{Q}}||\mathbf{dd})\underline{\mathsf{Q}} + (\mathbf{A}\lfloor\mathbf{d})(\mathbf{B}\lfloor\mathbf{d})\right]^{-1} = \frac{1}{L_1(\mathbf{d})}\underline{\mathsf{Q}}^{-1} - \frac{1}{L_2(\mathbf{d})}\underline{\mathsf{Q}}^{-1}|(\mathbf{A}\lfloor\mathbf{d})(\mathbf{B}\lfloor\mathbf{d})|\underline{\mathsf{Q}}^{-1}, \tag{4.33}$$

where the two scalar operators are defined by

$$L_1(\mathbf{d}) = \underline{\mathsf{Q}}||\mathbf{dd}, \quad L_2(\mathbf{d}) = (\underline{\mathsf{Q}}||\mathbf{dd})(\underline{\mathsf{Q}} + \mathbf{BA}\lfloor\lfloor\underline{\mathsf{Q}}^{-1})||\mathbf{dd}. \tag{4.34}$$

Thus, the solution of Equation 4.32 can be written in two parts: $\boldsymbol{\alpha}_e = \boldsymbol{\alpha}_{e1} + \boldsymbol{\alpha}_{e2}$ as

$$\boldsymbol{\alpha}_{e1} = \frac{1}{L_1(\mathbf{d})}\underline{\mathsf{Q}}^{-1}|\mathbf{g}_e, \quad \boldsymbol{\alpha}_{e2} = -\frac{1}{L_2(\mathbf{d})}\underline{\mathsf{Q}}^{-1}|(\mathbf{A}\lfloor\mathbf{d})(\mathbf{B}\lfloor\mathbf{d})|\underline{\mathsf{Q}}^{-1}|\mathbf{g}_e. \tag{4.35}$$

The potential can now be found by solving two equations involving the scalar operators

$$L_1(\mathbf{d})\boldsymbol{\alpha}_{e1} = \underline{\mathsf{Q}}^{-1}|\mathbf{g}_e, \tag{4.36}$$

$$L_2(\mathbf{d})\boldsymbol{\alpha}_{e2} = -\underline{\mathsf{Q}}^{-1}|(\mathbf{A}\lfloor\mathbf{d})(\mathbf{B}\lfloor\mathbf{d})|\underline{\mathsf{Q}}^{-1}|\mathbf{g}_e. \tag{4.37}$$

$L_2(\mathbf{d})$ is of a factorized fourth-order form. The class of media defined by the condition (Equation 4.31) has been called that of generalized Q-media [2,12]. Because of the factorized operator, the plane wave is characterized by a k-vector surface which does not consist of a single quartic (fourth-order surface) but of two quadrics (second-order surfaces).

Conditions for the Gibbsian medium dyadics corresponding to a generalized Q-medium were derived in Ref. [12] after considerable algebraic work. They can be expressed in the form

$$a\underline{\epsilon}_g + b\underline{\mu}_g^{\mathrm{T}} = \mathbf{p}_1\mathbf{q}_2 + \mathbf{q}_1\mathbf{p}_2, \tag{4.38}$$

$$\underline{\xi}_g + \underline{\xi}_g^{\mathrm{T}} = \frac{1}{a}(\mathbf{p}_2\mathbf{q}_2 + \mathbf{q}_2\mathbf{p}_2), \quad \underline{\zeta}_g + \underline{\zeta}_g^{\mathrm{T}} = \frac{1}{b}(\mathbf{p}_1\mathbf{q}_1 + \mathbf{q}_1\mathbf{p}_1), \tag{4.39}$$

for some scalars a, b and vectors $\mathbf{p}_1, \mathbf{p}_2, \mathbf{q}_1, \mathbf{q}_2$. These conditions turn out to correspond to those of the "decomposable medium" defined previously in Refs. [13,14]. It is most obvious that the definition (Equation 4.31) in terms of differential forms appears much simpler than that using Gibbsian dyadics satisfying the conditions (Equations 4.38 and 4.39). Another form for the condition for $\underline{\mathsf{M}}_g$ defining a generalized Q-medium is obtained from Equation 4.30 as

$$a(\underline{\mathsf{M}}_g - \mathbf{AB}) + b(\underline{\mathsf{M}}_g - \mathbf{AB})_g^{-1\mathrm{T}}\rfloor\rfloor\mathbf{e}_N\mathbf{e}_N = 0, \tag{4.40}$$

which should be valid for some bivectors **A, B** and scalars *a, b*.

4.3.4 IB-Media

A class of media with medium dyadics $\underline{\mathsf{M}} \in \mathbb{F}_2\mathbb{E}_2$ defined in terms of a dyadic $\underline{\mathsf{B}} \in \mathbb{E}_1\mathbb{F}_1$ as

$$\underline{\mathsf{M}} = (\underline{\mathsf{I}}\wedge\underline{\mathsf{B}})^{\mathrm{T}} \tag{4.41}$$

is labeled as that of IB-media. The number of free parameters is again reduced from 36 to 16. To study its basic properties, let us first decompose

$$\underline{\mathsf{B}} = \frac{\mathrm{tr}\underline{\mathsf{B}}}{4}\underline{\mathsf{I}} + \underline{\mathsf{B}}_o, \quad \mathrm{tr}\underline{\mathsf{B}}_o = 0 \tag{4.42}$$

where $\underline{\mathsf{B}}_o$ is the trace-free part of $\underline{\mathsf{B}}$. Because of the relation

$$\mathrm{tr}\underline{\mathsf{M}} = \underline{\mathsf{I}}^{(2)}||(\underline{\mathsf{I}}\wedge\underline{\mathsf{B}})^{\mathrm{T}} = (\underline{\mathsf{I}}^{(2)}\lfloor\lfloor\underline{\mathsf{I}}^{\mathrm{T}})||\underline{\mathsf{B}}^{\mathrm{T}} = 3\mathrm{tr}\underline{\mathsf{B}}, \tag{4.43}$$

we can expand

$$\underline{\mathsf{M}} = \frac{\mathrm{tr}\underline{\mathsf{M}}}{6}\underline{\mathsf{I}}^{(2)\mathrm{T}} + \underline{\mathsf{M}}_o = \frac{\mathrm{tr}\underline{\mathsf{B}}}{2}\underline{\mathsf{I}}^{(2)\mathrm{T}} + (\underline{\mathsf{I}}\wedge\underline{\mathsf{B}}_o)^{\mathrm{T}}, \tag{4.44}$$

where $\underline{\mathsf{M}}_o$ is the trace-free part of $\underline{\mathsf{M}}$. Applying the following special case of the dyadic identity (Equation 4.A.23):

$$(\underline{\mathsf{I}}\wedge\underline{\mathsf{B}})\lfloor\lfloor\underline{\mathsf{I}}^{\mathrm{T}} = (\mathrm{tr}\underline{\mathsf{B}})\underline{\mathsf{I}} + 2\underline{\mathsf{B}}, \tag{4.45}$$

Equation 4.41 can be inverted as

$$\underline{\mathsf{B}} = \frac{1}{2}\left(\underline{\mathsf{M}}^{\mathrm{T}}\rfloor\rfloor\underline{\mathsf{I}}^{\mathrm{T}} - \frac{\mathrm{tr}\underline{\mathsf{M}}}{3}\,\underline{\mathsf{I}}\right). \tag{4.46}$$

Introducing the identity [15]

$$\underline{\mathsf{I}}^{(4)\mathrm{T}}\rfloor\rfloor\underline{\mathsf{C}} = (\mathrm{tr}\underline{\mathsf{C}})\underline{\mathsf{I}}^{(2)\mathrm{T}} - (\underline{\mathsf{C}}^{\mathrm{T}}\rfloor\rfloor\underline{\mathsf{I}})^{\wedge}_{\wedge}\underline{\mathsf{I}}^{\mathrm{T}} + \underline{\mathsf{C}}^{\mathrm{T}}, \tag{4.47}$$

valid for any dyadic $\underline{\mathsf{C}} \in \mathbb{E}_2\mathbb{F}_2$, and replacing $\underline{\mathsf{C}}$ by $\underline{\mathsf{M}}_o^{\mathrm{T}}$ with $\underline{\mathsf{I}}^{(4)} = \mathbf{e}_N\boldsymbol{\varepsilon}_N$ inserted, yields

$$\underline{\mathsf{I}}^{(4)\mathrm{T}}\rfloor\rfloor\underline{\mathsf{M}}_o^{\mathrm{T}} = \boldsymbol{\varepsilon}_N\mathbf{e}_N\rfloor\rfloor\underline{\mathsf{M}}_o^{\mathrm{T}} = \boldsymbol{\varepsilon}_N\rfloor(\mathbf{e}_N\rfloor\underline{\mathsf{M}}_o)^{\mathrm{T}} = -\underline{\mathsf{M}}_o, \tag{4.48}$$

or

$$(\mathbf{e}_N\rfloor\underline{\mathsf{M}}_o)^{\mathrm{T}} = -\mathbf{e}_N\rfloor\underline{\mathsf{M}}_o. \tag{4.49}$$

This states that the modified medium dyadic of a trace-free IB-medium is antisymmetric. The class defined by antisymmetric modified medium dyadics was labeled as that of skewon media by Hehl and Obukhov [3]. Thus, the IB-medium consists of axion and skewon components corresponding to 1 and 15 medium parameters, respectively. The 15 parameters involve those responsible for the chiral and Faraday rotation effects of the medium [3].

The condition for a medium dyadic to be of the form as in Equation 4.41 is now obtained from Equation 4.48 by inserting Equation 4.44 as

$$\underline{\mathsf{I}}^{(4)\mathrm{T}}\rfloor\rfloor\left(\underline{\mathsf{M}}^{\mathrm{T}} - \frac{\mathrm{tr}\underline{\mathsf{M}}}{6}\,\underline{\mathsf{I}}^{(2)}\right) = -\underline{\mathsf{M}} + \frac{\mathrm{tr}\underline{\mathsf{M}}}{6}\,\underline{\mathsf{I}}^{(2)\mathrm{T}}, \tag{4.50}$$

or

$$\underline{\mathsf{I}}^{(4)\mathrm{T}}\rfloor\rfloor\underline{\mathsf{M}}^{\mathrm{T}} = \frac{\mathrm{tr}\underline{\mathsf{M}}}{3}\,\underline{\mathsf{I}}^{(2)\mathrm{T}} - \underline{\mathsf{M}}. \tag{4.51}$$

If this is satisfied by $\underline{\mathsf{M}}$, the dyadic $\underline{\mathsf{B}}$ can be found from Equation 4.46.

Let us consider plane-wave propagation in an IB-medium. Substituting Equations 4.13 and 4.41 in Equation 4.12 yields

$$\mathbf{d} \wedge (\underline{\mathsf{I}}^{\wedge}_{\wedge}\underline{\mathsf{B}})^{\mathrm{T}}|(\mathbf{d} \wedge \boldsymbol{\alpha}_o)\exp(\boldsymbol{\nu}|\mathbf{x}) = 0, \tag{4.52}$$

from which we obtain

$$\boldsymbol{\nu} \wedge (\underline{\mathsf{I}}^{\wedge}_{\wedge}\underline{\mathsf{B}})^{\mathrm{T}}|(\boldsymbol{\nu} \wedge \boldsymbol{\alpha}_o) = \boldsymbol{\nu} \wedge (\underline{\mathsf{B}}^{\mathrm{T}}|\boldsymbol{\nu}) \wedge \boldsymbol{\alpha}_o = 0. \tag{4.53}$$

This is the sole condition for the one-forms $\boldsymbol{\nu}$ and $\boldsymbol{\alpha}_o$. Actually, $\boldsymbol{\nu}$ can be freely chosen. The case $\boldsymbol{\nu} \wedge (\boldsymbol{\nu}|\underline{\mathsf{B}}) = 0$ i.e., $\boldsymbol{\nu}$ being a left eigen-one-form of the dyadic $\underline{\mathsf{B}}$ is not interesting because it will eventually lead to vanishing of the field $\boldsymbol{\Phi}_o = \boldsymbol{\nu} \wedge \boldsymbol{\alpha}_o$. Thus, $\boldsymbol{\nu}$ must be chosen to satisfy $\boldsymbol{\nu} \wedge (\boldsymbol{\nu}|\underline{\mathsf{B}}) \neq 0$.

The dependence of the potential amplitude $\boldsymbol{\alpha}_o$ on $\boldsymbol{\nu}$ is now obtained from Equation 4.53 which tells us that the one-forms $\boldsymbol{\alpha}_o$, $\boldsymbol{\nu}$ and $\underline{\mathsf{B}}^{\mathrm{T}}|\boldsymbol{\nu} = \boldsymbol{\nu}|\underline{\mathsf{B}}$ are linearly dependent and one of them can be expressed in terms of the other two. Thus, the potential amplitude one-form can be written in the form

$$\boldsymbol{\alpha}_o = a\boldsymbol{\nu} + b\boldsymbol{\nu}|\underline{\mathsf{B}}, \tag{4.54}$$

where *a, b* are two arbitrary coefficients. Actually, the coefficient *a* can be ignored since it does not affect the field two-form

$$\mathbf{\Phi}_o = \boldsymbol{\nu} \wedge \boldsymbol{\alpha}_o = b\boldsymbol{\nu} \wedge (\boldsymbol{\nu}|\underline{\mathsf{B}}). \tag{4.55}$$

Example

As a concrete example of an IB-medium let us consider the simplest generalization of the PEMC (axion) medium as defined by two scalar parameters M and N in the form

$$\underline{\mathsf{B}} = \frac{M}{2}\underline{\mathsf{I}} + \frac{N}{2}(\underline{\mathsf{I}}_s - 3\mathbf{e}_4\boldsymbol{\varepsilon}_4). \tag{4.56}$$

In this case the medium dyadic becomes

$$\underline{\mathsf{M}} = (\underline{\mathsf{I}}^{\wedge}_{\wedge}\underline{\mathsf{B}})^{\mathrm{T}} = M\underline{\mathsf{I}}^{(2)\mathrm{T}} + N(\underline{\mathsf{I}}_s^{(2)\mathrm{T}} - \underline{\mathsf{I}}_s^{T\wedge}_{\wedge}\boldsymbol{\varepsilon}_4\mathbf{e}_4). \tag{4.57}$$

Obviously, for $N = 0$ we have the axion (PEMC) medium while for $M = 0$ the dyadics $\underline{\mathsf{B}}$ and $\underline{\mathsf{M}}$ are trace-free and, thus, the medium falls to the class of skewons. This kind of medium was called spatially isotropic in Ref. [2, pp. 128–129], while the skewon medium with $M = 0$ was considered in Ref. [3, pp. 261–262].

The modified medium dyadic corresponding to Equation 4.57 can be expanded as

$$\underline{\mathsf{M}}_g = (M+N)(\mathbf{e}_{34}\mathbf{e}_{12} + \mathbf{e}_{14}\mathbf{e}_{23} + \mathbf{e}_{24}\mathbf{e}_{31}) + (M-N)(\mathbf{e}_{23}\mathbf{e}_{14} + \mathbf{e}_{31}\mathbf{e}_{24} + \mathbf{e}_{12}\mathbf{e}_{34}). \tag{4.58}$$

Obviously, this dyadic is symmetric for $N = 0$ and antisymmetric for $M = 0$. The medium conditions can be represented by

$$\mathbf{D} = (M+N)\mathbf{B}, \quad \mathbf{H} = (N-M)\mathbf{E}, \tag{4.59}$$

which appear as generalizations of those of the PEMC medium [6].

Actually, we can find a Gibbsian representation similar to that in Equation 4.20 as the limit

$$\begin{pmatrix} \epsilon_g & \xi_g \\ \zeta_g & \mu_g \end{pmatrix} = q \begin{pmatrix} \sqrt{M^2 - N^2} & \sqrt{\frac{M+N}{M-N}} \\ \sqrt{\frac{M-N}{M+N}} & 1/\sqrt{M^2 - N^2} \end{pmatrix}, \quad q \to \infty \tag{4.60}$$

and it obviously reduces to the PEMC representation (Equation 4.20) for $N \to 0$. In the other case $M \to 0$, we obtain

$$\begin{pmatrix} \epsilon_g & \xi_g \\ \zeta_g & \mu_g \end{pmatrix} = q \begin{pmatrix} N & -1 \\ 1 & -1/N \end{pmatrix}, \quad q \to \infty \tag{4.61}$$

when absorbing the imaginary unit in the parameter q. Expressing

$$M = P\cosh\psi, \quad N = P\sinh\psi, \tag{4.62}$$

a more compact representation of Equation 4.60 can be obtained,

$$\begin{pmatrix} \epsilon_g & \xi_g \\ \zeta_g & \mu_g \end{pmatrix} = q \begin{pmatrix} P & e^{\psi} \\ e^{-\psi} & 1/P \end{pmatrix}, \quad q \to \infty. \tag{4.63}$$

In spite of infinite-valued parameters, they satisfy the finite conditions

$$\epsilon_g \mu_g - \xi_g \zeta_g = 0, \quad \epsilon_g / \mu_g = P^2 = M^2 - N^2 \tag{4.64}$$

for $q \to \infty$.

4.3.5 Self-Dual Media

Since any medium dyadic $\underline{\underline{\mathsf{M}}}$ corresponds to a 6×6 matrix, it always satisfies an algebraic equation of the sixth order. On the other hand, it is obvious that medium dyadics satisfying a second-order equation define a certain class of media. The general second-order equation can be written in the form

$$\underline{\underline{\mathsf{M}}}^2 - (M_+ + M_-)\underline{\underline{\mathsf{M}}} + M_+ M_- \underline{\underline{\mathsf{I}}}^{(2)\mathrm{T}} = 0 \tag{4.65}$$

for some parameters M_+, M_-. It can be shown that media satisfying Equation 4.65 are invariant in some duality transformations, which is why such media have been called self-dual in the past [16]. It is easy to see that if $\underline{\underline{\mathsf{M}}}$ satisfies Equation 4.65, the dyadic

$$\underline{\underline{\mathsf{M}}}' = \underline{\underline{\mathsf{D}}} | \underline{\underline{\mathsf{M}}} | \underline{\underline{\mathsf{D}}}^{-1} \tag{4.66}$$

also satisfies the same equation for any $\underline{\underline{\mathsf{D}}} \in \mathbb{F}_2\mathbb{E}_2$ possessing a finite inverse $\underline{\underline{\mathsf{D}}}^{-1}$.

Expressing Equation 4.65 as

$$(\underline{\underline{\mathsf{M}}} - M_+ \underline{\underline{\mathsf{I}}}^{(2)\mathrm{T}}) | (\underline{\underline{\mathsf{M}}} - M_- \underline{\underline{\mathsf{I}}}^{(2)\mathrm{T}}) = (\underline{\underline{\mathsf{M}}} - M_- \underline{\underline{\mathsf{I}}}^{(2)\mathrm{T}}) | (\underline{\underline{\mathsf{M}}} - M_+ \underline{\underline{\mathsf{I}}}^{(2)\mathrm{T}}) = 0, \tag{4.67}$$

and defining two dyadics

$$\underline{\underline{\mathsf{P}}}_+ = \frac{\underline{\underline{\mathsf{M}}} - M_- \underline{\underline{\mathsf{I}}}^{(2)\mathrm{T}}}{M_+ - M_-}, \quad \underline{\underline{\mathsf{P}}}_- = \frac{\underline{\underline{\mathsf{M}}} - M_+ \underline{\underline{\mathsf{I}}}^{(2)\mathrm{T}}}{M_- - M_+}, \tag{4.68}$$

one can see that M_+ and M_- represent eigenvalues of the eigenproblem

$$\underline{\underline{\mathsf{M}}} | \mathbf{\Phi}_\pm = M_\pm \mathbf{\Phi}_\pm, \quad \mathbf{\Phi}_\pm = \underline{\underline{\mathsf{P}}}_\pm | \mathbf{\Phi}, \tag{4.69}$$

where $\mathbf{\Phi}_+$ and $\mathbf{\Phi}_-$ are the corresponding eigenfield two-forms for some two-form $\mathbf{\Phi}$. This means that, for a self-dual medium, there exist at most two distinct eigenvalues. Let us assume $M_+ \neq M_-$ in the following.

The dyadics $\underline{\underline{\mathsf{P}}}_\pm \in \mathbb{F}_2\mathbb{E}_2$ are orthogonal projection operators, because they satisfy

$$\underline{\underline{\mathsf{P}}}_\pm^2 = \underline{\underline{\mathsf{P}}}_\pm, \quad \underline{\underline{\mathsf{P}}}_+ | \underline{\underline{\mathsf{P}}}_- = \underline{\underline{\mathsf{P}}}_- | \underline{\underline{\mathsf{P}}}_+ = 0, \tag{4.70}$$

and

$$\underline{\underline{\mathsf{P}}}_+ + \underline{\underline{\mathsf{P}}}_- = \underline{\underline{\mathsf{I}}}^{(2)T}, \quad \underline{\underline{\mathsf{M}}} = M_+ \underline{\underline{\mathsf{P}}}_+ + M_- \underline{\underline{\mathsf{P}}}_-. \tag{4.71}$$

Actually, we can decompose any given two-form $\mathbf{\Phi}$ in its eigenfields as

$$\mathbf{\Phi} = (\underline{\underline{\mathsf{P}}}_+ + \underline{\underline{\mathsf{P}}}_-) | \mathbf{\Phi} = \mathbf{\Phi}_+ + \mathbf{\Phi}_-. \tag{4.72}$$

From Equation 4.65 the inverse of the medium dyadic can be expressed as

$$\underline{\underline{\mathsf{M}}}^{-1} = \frac{1}{M_+ M_-}((M_+ + M_-)\underline{\underline{\mathsf{I}}}^{(2)\mathrm{T}} - \underline{\underline{\mathsf{M}}}) = \frac{1}{M_+}\underline{\underline{\mathsf{P}}}_+ + \frac{1}{M_-}\underline{\underline{\mathsf{P}}}_-. \tag{4.73}$$

As an example, a self-dual medium dyadic is defined by two scalars M_+, M_- and the projection dyadics

$$\underline{\mathsf{P}}_+ = \boldsymbol{\varepsilon}_{12}\mathbf{e}_{12} + \boldsymbol{\varepsilon}_{23}\mathbf{e}_{23} + \boldsymbol{\varepsilon}_{34}\mathbf{e}_{34}, \tag{4.74}$$

$$\underline{\mathsf{P}}_- = \boldsymbol{\varepsilon}_{13}\mathbf{e}_{13} + \boldsymbol{\varepsilon}_{24}\mathbf{e}_{24} + \boldsymbol{\varepsilon}_{14}\mathbf{e}_{14}, \tag{4.75}$$

in some reciprocal bases $\mathbf{e}_i, \boldsymbol{\varepsilon}_i$. The sum of the projection dyadics obviously equals $\underline{\mathsf{I}}^{(2)\mathrm{T}}$ and the eigenfields $\boldsymbol{\Phi}_+, \boldsymbol{\Phi}_-$ are any two-forms in the subspaces spanned by the respective basis two-forms $(\boldsymbol{\varepsilon}_{12}, \boldsymbol{\varepsilon}_{23}, \boldsymbol{\varepsilon}_{34})$ and $(\boldsymbol{\varepsilon}_{13}, \boldsymbol{\varepsilon}_{24}, \boldsymbol{\varepsilon}_{14})$.

After some algebra, one can show that the 3D Gibbsian medium dyadics for the self-dual medium must be of the form [16]

$$\underline{\mu}_g = \underline{\mathsf{Q}}, \quad \underline{\epsilon}_g = M_+ M_- \underline{\mathsf{Q}}, \tag{4.76}$$

$$\underline{\xi}_g = \frac{M_+ + M_-}{2}\underline{\mathsf{Q}} - \underline{\mathsf{T}}, \quad \underline{\zeta}_g = \frac{M_+ + M_-}{2}\underline{\mathsf{Q}} + \underline{\mathsf{T}}, \tag{4.77}$$

with some dyadics $\underline{\mathsf{Q}}, \underline{\mathsf{T}} \in \mathbb{E}_1\mathbb{E}_1$. The number of free medium parameters can be seen, from Equation 4.77, to be 20. The class of self-dual media was previously introduced through 3D Gibbsian analysis in Ref. [17] where it was shown that the 3D Green dyadic can be expressed in analytic form.

4.3.5.1 Almost-Complex Structure

Let us define a dyadic $\underline{\mathsf{J}} \in \mathbb{F}_2\mathbb{E}_2$ as one satisfying the equation

$$\underline{\mathsf{J}}^2 = -\underline{\mathsf{I}}^{(2)\mathrm{T}}. \tag{4.78}$$

Because dyadics $\underline{\mathsf{J}}$ appear to be similar to an imaginary unit, they are said to form an almost-complex structure in the space of medium dyadics $\underline{\mathsf{M}}$ [6,38]. In fact, expressing Equation 4.65 in the form

$$\left(\underline{\mathsf{M}}^2 - \frac{1}{2}(M_+ + M_-)\underline{\mathsf{I}}^{(2)\mathrm{T}}\right)^2 = \frac{1}{4}(M_+ - M_-)^2\underline{\mathsf{I}}^{(2)\mathrm{T}}, \tag{4.79}$$

any self-dual medium dyadic can be expressed in the form

$$\underline{\mathsf{M}} = \frac{1}{2}(M_+ + M_-)\underline{\mathsf{I}}^{(2)\mathrm{T}} + \frac{j}{2}(M_+ - M_-)\underline{\mathsf{J}}, \tag{4.80}$$

for some dyadic $\underline{\mathsf{J}}$ satisfying Equation 4.78. Another form for the medium dyadic is

$$\underline{\mathsf{M}} = M_o \exp(j\psi\underline{\mathsf{J}}), \tag{4.81}$$

with

$$M_o = \sqrt{(M_+^2 + M_-^2)/2}, \quad \tanh\psi = \frac{M_+ - M_-}{M_+ + M_-}. \tag{4.82}$$

4.3.5.2 AB Media

As a special case of self-dual media let us consider the class of AB (affine bianisotropic) media, corresponding to the case when the dyadic $\underline{\mathsf{T}}$ in Equation 4.77 is a multiple of the dyadic $\underline{\mathsf{Q}}$. The medium dyadic can then be expanded in the form [19]

$$\underline{\mathsf{M}} = \alpha\underline{\mathsf{I}}_s^{(2)\mathrm{T}} + \epsilon'\underline{\mathsf{B}} \wedge \mathbf{e}_4 + \mu^{-1}\boldsymbol{\varepsilon}_4 \wedge \underline{\mathsf{B}}^{-1} + \beta\boldsymbol{\varepsilon}_4 \wedge \underline{\mathsf{I}}_s^{\mathrm{T}} \wedge \mathbf{e}_4, \tag{4.83}$$

where $\underline{\mathsf{I}}_s = \mathbf{e}_1\boldsymbol{\varepsilon}_1 + \mathbf{e}_2\boldsymbol{\varepsilon}_2 + \mathbf{e}_3\boldsymbol{\varepsilon}_3$ denotes the spatial unit dyadic and $\underline{\mathsf{B}} \in \mathbb{F}_2\mathbb{E}_1$ is a dyadic mapping 3D one-forms to two-forms. Equation 4.83 satisfies Equation 4.65 as

$$\underline{\mathsf{M}}^2 - (\alpha - \beta)\underline{\mathsf{M}} + \left(\frac{\epsilon'}{\mu} - \alpha\beta\right)\underline{\mathsf{I}}^{(2)\mathrm{T}} = 0, \tag{4.84}$$

which corresponds to the eigenvalues

$$M_\pm = \frac{1}{2}\left(\alpha - \beta \pm \sqrt{(\alpha+\beta)^2 - (\epsilon'/\mu)}\right). \tag{4.85}$$

The AB medium is invariant in all spatial affine transformations. It corresponds to the medium whose Gibbsian medium dyadics $\underline{\epsilon}_g, \underline{\xi}_g, \underline{\zeta}_g, \underline{\mu}_g$ are all multiples of the same dyadic $\underline{\mathsf{G}} = \mathbf{e}_{123}\lfloor\underline{\mathsf{B}} \in \mathbb{E}_1\mathbb{E}_1$.

4.3.5.3 Fields

Considering fields from electric and magnetic sources in a self-dual medium, the Maxwell equations for the eigenfields become uncoupled and have the simple form

$$\mathbf{d} \wedge \boldsymbol{\Phi}_\pm = \boldsymbol{\gamma}_{m\pm}, \tag{4.86}$$

$$\mathbf{d} \wedge \boldsymbol{\Psi}_\pm = M_\pm \mathbf{d} \wedge \boldsymbol{\Phi}_\pm = \boldsymbol{\gamma}_{e\pm}. \tag{4.87}$$

To avoid contradiction, these must be the same pair of equations and the decomposed sources must satisfy

$$\boldsymbol{\gamma}_{e\pm} = M_\pm \boldsymbol{\gamma}_{m\pm}. \tag{4.88}$$

Thus, from

$$\boldsymbol{\gamma}_e = \boldsymbol{\gamma}_{e+} + \boldsymbol{\gamma}_{e-}, \tag{4.89}$$

$$\boldsymbol{\gamma}_m = \boldsymbol{\gamma}_{m+} + \boldsymbol{\gamma}_{m-}, \tag{4.90}$$

we obtain the decompositions

$$\boldsymbol{\gamma}_{m\pm} = \pm\frac{\boldsymbol{\gamma}_e - M_\mp \boldsymbol{\gamma}_m}{M_+ - M_-} = \frac{\boldsymbol{\gamma}_{e\pm}}{M_\pm}. \tag{4.91}$$

The eigenfields are defined by Equation 4.86 together with polarization restrictions of the form

$$\mathbf{A}_\mp \rfloor \boldsymbol{\Phi}_\pm = 0, \tag{4.92}$$

where the bivectors $\mathbf{A}_\pm$ are

$$\mathbf{A}_\mp = \mathbf{A}\rfloor\underline{\mathsf{P}}_\mp, \tag{4.93}$$

for an arbitrary bivector $\mathbf{A}$.

Because the eigenfields are linearly related as $\boldsymbol{\Psi}_\pm = M_\pm\boldsymbol{\Phi}_\pm$, this can be interpreted so that each of the eigenfield components sees the medium as an effective PEMC with respective PEMC admittance $M_\pm$. Since we know that there is no power propagation in a PEMC medium, the eigenfields cannot be power orthogonal. On the contrary, power propagation in a self-dual medium comes through an interaction of the eigenfields. In fact, considering the stress dyadic [2]

$$\underline{\mathsf{T}} = \frac{1}{2}(\boldsymbol{\Psi} \wedge \underline{\mathsf{I}}^{\mathrm{T}} \rfloor \boldsymbol{\Phi} - \boldsymbol{\Phi} \wedge \underline{\mathsf{I}}^{\mathrm{T}} \rfloor \boldsymbol{\Psi}), \tag{4.94}$$

after expanding in terms of eigenfields this becomes

$$\underline{T} = (M_+ - M_-)(\mathbf{\Phi}_+ \wedge \underline{I}^{\mathrm{T}} \rfloor \mathbf{\Phi}_- - \mathbf{\Phi}_- \wedge \underline{I}^{\mathrm{T}} \rfloor \mathbf{\Phi}_+), \tag{4.95}$$

which clearly shows us that the power effects are due to the interaction of $\mathbf{\Phi}_+$ and $\mathbf{\Phi}_-$.

The significance of the class of self-dual media is in that certain transformations can be made for the sources and fields without changing the medium. This allows one to find a larger number of solutions for the field problem in that medium [2]. Further discussion on the properties of the transformation does not fall in the scope of this chapter.

4.4 Conclusion

In this short overview it was demonstrated that differential-form formalism aided by suitably extended dyadic algebra can be applied to the analysis of electromagnetic fields in various bi-anisotropic media. Certain classes of media could be defined in simpler terms when compared to their definition in classical Gibbsian vector analysis. Main points in the analysis of fields in these media, treated more extensively in previous articles found in the list of references, were given and their connection to the corresponding studies using the classical Gibbsian analysis were briefly pointed out.

Appendix: Multivectors, Multiforms, and Dyadics

Application of differential forms in electromagnetic analysis requires some skill in using various identities in multivector and dyadic algebra. In the literature the notation varies slightly from author to author. The present notation is based on that in Ref. [2].

4.A.1 Notation

Differential-form formalism is based on two linear spaces: $\mathbb{E}_1$ containing vectors $\mathbf{a}$, $\mathbf{b}\ldots$ and $\mathbb{F}_1$ containing dual vectors $\boldsymbol{\alpha}, \boldsymbol{\beta}, \ldots$. Fields (functions of space and time) of dual vectors like the electric and magnetic fields **E, H** are called one-forms. Using the anticommutative exterior product $\wedge$ other linear spaces are formed: $\mathbb{E}_2$ containing bivectors $\Sigma \mathbf{a}_i \wedge \mathbf{b}_i$ and $\mathbb{F}_2$ containing dual bivectors $\Sigma \boldsymbol{\alpha}_i \wedge \boldsymbol{\beta}_i$. More complicated products like $\mathbf{a} \wedge \mathbf{b} \wedge \mathbf{c}$ and $\boldsymbol{\alpha} \wedge \boldsymbol{\beta} \wedge \boldsymbol{\gamma}$ give rise to multivectors and dual multivectors (multiforms), respectively. Dyadic algebra introduced by Gibbs as a coordinate-free representation of linear mappings in the 3D vector space [4,5] can be generalized to the algebra of differential forms, as was shown in Ref. [2]. Dyadics mapping vectors to vectors form a linear space denoted by $\mathbb{E}_1\mathbb{F}_1$. Other spaces are denoted similarly, e.g., those mapping two-forms to two-forms belong to the space $\mathbb{F}_2\mathbb{E}_2$.

4.A.2 Products

Different products of multivectors and dual multivectors are listed below.

- The exterior product (wedge product) of vectors is associative, $(\mathbf{a}\wedge\mathbf{b})\wedge\mathbf{c} = \mathbf{a}\wedge(\mathbf{b}\wedge\mathbf{c})$, and anticommutative, $\mathbf{a}\wedge\mathbf{b} = -\mathbf{b}\wedge\mathbf{a}$. For a p-vector $\mathbf{a}^p \in \mathbb{E}_p$ and a q-vector $\mathbf{b}^q \in \mathbb{E}_q$ it is either commutative or anticommutative according to the rule (superscript p in multivectors and dual multivectors is not a power but shows its grade)

$$\mathbf{a}^p \wedge \mathbf{b}^q = (-1)^{pq}\mathbf{b}^q \wedge \mathbf{a}^p \in \mathbb{E}_{p+q}. \tag{4.A.1}$$

p-vectors over an n-dimensional vector space span a linear space whose dimension is $n!/(p!(n-p)!)$. For example, in 4D vector space, bivectors ($p = 2$) form a space of six dimensions and trivectors a space of four dimensions.

- The duality product between a vector $\mathbf{a}$ and a dual vector $\boldsymbol{\alpha}$ is denoted by $\mathbf{a}|\boldsymbol{\alpha} = \boldsymbol{\alpha}|\mathbf{a}$ and the result is a scalar. For a given basis of vectors $\{\mathbf{e}_i\}$ the reciprocal basis of dual vectors $\{\boldsymbol{\varepsilon}_j\}$ satisfies the biorthogonality condition

$$\mathbf{e}_i|\boldsymbol{\varepsilon}_j = \boldsymbol{\varepsilon}_j|\mathbf{e}_i = \delta_{ij}. \tag{4.A.2}$$

Expanding $\mathbf{a} = \Sigma a_i \mathbf{e}_i$, $\boldsymbol{\alpha} = \Sigma \alpha_j \boldsymbol{\varepsilon}_j$, the duality product gives

$$\mathbf{a}|\boldsymbol{\alpha} = \sum a_i \alpha_i. \tag{4.A.3}$$

- Basis vectors and dual basis vectors generate the set of basis bivectors and dual bivectors as $\mathbf{e}_{ij} = \mathbf{e}_i \wedge \mathbf{e}_j$, $\boldsymbol{\varepsilon}_{ij} = \boldsymbol{\varepsilon}_i \wedge \boldsymbol{\varepsilon}_j$ satisfying the orthogonality $\mathbf{e}_{ij}|\boldsymbol{\varepsilon}_{k\ell} = \delta_{ik}\delta_{j\ell}$. This can be continued to p-vectors and dual p-vectors. In the n-dimensional space there is only one basis n-vector $\mathbf{e}_N = \mathbf{e}_1 \wedge \cdots \wedge \mathbf{e}_n$ and dual n-vector $\boldsymbol{\varepsilon}_N = \boldsymbol{\varepsilon}_1 \wedge \cdots \wedge \boldsymbol{\varepsilon}_n$. They satisfy $\mathbf{e}_N|\boldsymbol{\varepsilon}_N = 1$.
- The incomplete duality product, also known as contraction, between a p-vector $\mathbf{a}^p$ and a dual q-vector $\boldsymbol{\alpha}^q$ is written as $\mathbf{a}^p \lfloor \boldsymbol{\alpha}^q$ for $p > q$ and $\mathbf{a}^p \rfloor \boldsymbol{\alpha}^q$ for $p < q$ and the result is a $(p-q)$-vector or a dual $(q-p)$-vector, respectively. For $p > q$ and $\boldsymbol{\beta}^{p-q}$ being a dual $(p-q)$-vector, $\boldsymbol{\alpha}^q \wedge \boldsymbol{\beta}^{p-q}$ is a dual p-vector and we define [1], Eqn. (D.5),

$$(\mathbf{a}^p \lfloor \boldsymbol{\alpha}^q)|\boldsymbol{\beta}^{p-q} = \mathbf{a}^p|(\boldsymbol{\alpha}^q \wedge \boldsymbol{\beta}^{p-q}), \quad \boldsymbol{\beta}^{p-q}|(\boldsymbol{\alpha}^q \rfloor \mathbf{a}^p) = (\boldsymbol{\beta}^{p-q} \wedge \boldsymbol{\alpha}^q)|\mathbf{a}^p. \tag{4.A.4}$$

Because of the property (Equation 4.A.1), the incomplete duality product of a p-vector $\mathbf{a}^p$ and a dual q-vector $\boldsymbol{\alpha}^q$ obeys the rule

$$\mathbf{a}^p \lfloor \boldsymbol{\alpha}^q = (-1)^{q(p-q)} \boldsymbol{\alpha}^q \rfloor \mathbf{a}^p, \quad p > q. \tag{4.A.5}$$

4.A.3 Dyadics

- The dyadic product of a vector $\mathbf{a} \in \mathbb{E}_1$ and a dual vector $\boldsymbol{\alpha} \in \mathbb{F}_1$ is presented by the classical Gibbsian "no sign" notation as $\mathbf{a}\boldsymbol{\alpha}$ and the result is in the space of dyadics denoted by $\mathbb{E}_1\mathbb{F}_1$. It defines a mapping of a vector $\mathbf{b}$ to a multiple of $\mathbf{a}$ as

$$(\mathbf{a}\boldsymbol{\alpha})|\mathbf{b} = \mathbf{a}(\boldsymbol{\alpha}|\mathbf{b}), \tag{4.A.6}$$

as a simple associative rule. More generally, any linear mapping from vector to another vector can be expressed as a dyadic $\underline{\mathsf{A}} \in \mathbb{E}_1\mathbb{F}_1$:

$$\underline{\mathsf{A}} = \sum \mathbf{a}_i \boldsymbol{\alpha}_i. \tag{4.A.7}$$

Correspondingly, $\underline{\mathsf{A}}^{\mathrm{T}}$, the transpose of $\underline{\mathsf{A}}$ is in the space $\mathbb{F}_1\mathbb{E}_1$,

$$\underline{\mathsf{A}}^{\mathrm{T}} = \sum \boldsymbol{\alpha}_i \mathbf{a}_i, \tag{4.A.8}$$

and it maps dual vectors to dual vectors. In the same way we can define dyadic spaces $\mathbb{E}_1\mathbb{E}_1$, $\mathbb{F}_1\mathbb{F}_1$ and, more generally, spaces like $\mathbb{E}_p\mathbb{F}_p$, $\mathbb{F}_p\mathbb{E}_p$, $\mathbb{E}_p\mathbb{F}_{n-p}$, which define mappings between multivectors and/or dual multivectors of the same dimension.

- The duality product $\underline{\mathsf{A}}_1|\underline{\mathsf{A}}_2$ between two dyadics $\underline{\mathsf{A}}_1, \underline{\mathsf{A}}_2 \in \mathbb{E}_p\mathbb{F}_p$ or $\in \mathbb{F}_p\mathbb{E}_p$ gives a dyadic in the same space. In analogy to Gibbsian double-dot product [4,5], double-duality product can be defined as $(\mathbf{a}\boldsymbol{\alpha})||(\boldsymbol{\beta}\mathbf{b}) = (\mathbf{a}|\boldsymbol{\beta})(\boldsymbol{\alpha}|\mathbf{b})$ and, more generally, for dyadics $\underline{\mathsf{A}}_i \in \mathbb{E}_1\mathbb{F}_1$

as $\underline{\mathsf{A}}_1||\underline{\mathsf{A}}_2^{\mathrm{T}}$. The result is a scalar. The double-duality product $\underline{\mathsf{A}}||\underline{\mathsf{B}}$ can also be defined for dyadics $\underline{\mathsf{A}} \in \mathbb{E}_p\mathbb{E}_p$, $\underline{\mathsf{B}} \in \mathbb{F}_p\mathbb{F}_p$. Similarly, the incomplete double-duality products $\underline{\mathsf{A}}\lfloor\lfloor\underline{\mathsf{B}}$ and $\underline{\mathsf{B}}\rfloor\rfloor\underline{\mathsf{A}}$ can be defined between dyadics in certain spaces. For example, for $\underline{\mathsf{A}} \in \mathbb{E}_p\mathbb{E}_p$ and $\underline{\mathsf{B}} \in \mathbb{F}_q\mathbb{F}_q$ with $p > q$, the resulting dyadic lies in the space $\mathbb{E}_{p-q}\mathbb{E}_{p-q}$.

- The unit dyadic $\underline{\mathsf{I}}$ maps a vector to itself, $\underline{\mathsf{I}}|\mathbf{a} = \mathbf{a}$, and its transpose a dual vector to itself, $\underline{\mathsf{I}}^{\mathrm{T}}|\boldsymbol{\alpha} = \boldsymbol{\alpha}$. Its expansion

$$\underline{\mathsf{I}} = \sum \mathbf{e}_i\boldsymbol{\varepsilon}_i \tag{4.A.9}$$

  is independent of the chosen vector and reciprocal dual vector bases. In contrast, Gibbsian definition $\Sigma\mathbf{e}_i\mathbf{e}_i$ depends on the chosen basis.
- Because spaces $\mathbb{F}_p$ and $\mathbb{F}_{n-p}$ have the same dimension, dyadics $\mathbb{F}_p\mathbb{E}_{n-p}$ and $\mathbb{F}_{n-p}\mathbb{E}_p$ mapping between these two spaces have special importance and they are called Hodge dyadics. Also, dyadics mapping p-vectors to dual p-vectors and conversely are important and they are called (generalized) metric dyadics. A symmetric metric dyadic $\underline{\mathsf{G}} \in \mathbb{E}_1\mathbb{E}_1$ defines a dot product between dual vectors: $\boldsymbol{\alpha} \cdot \boldsymbol{\beta} = \boldsymbol{\beta} \cdot \boldsymbol{\alpha} = \boldsymbol{\alpha}|\underline{\mathsf{G}}|\boldsymbol{\beta}$.
- In spaces $\mathbb{E}_p\mathbb{E}_p$ and $\mathbb{F}_p\mathbb{F}_p$ transpose of a dyadic is in the same space. In these cases symmetric dyadics can be defined to satisfy, $\underline{\mathsf{A}}^{\mathrm{T}} = \underline{\mathsf{A}}$, and antisymmetric dyadics, $\underline{\mathsf{A}}^{\mathrm{T}} = -\underline{\mathsf{A}}$. The most general antisymmetric dyadic $\underline{\mathsf{A}} \in \mathbb{E}_1\mathbb{E}_1$ can be expressed in terms of a bivector $\mathbf{A}$ as

$$\underline{\mathsf{A}} = \underline{\mathsf{I}}\rfloor\mathbf{A}, \tag{4.A.10}$$

  because, from the bac-cab rule (Equation 4.A.21) below, for each term in $\mathbf{A} = \Sigma\mathbf{a}_j \wedge \mathbf{b}_j$ we can write the antisymmetric expression

$$\underline{\mathsf{I}}\rfloor(\mathbf{a}_j \wedge \mathbf{b}_j) = \sum \mathbf{e}_i\boldsymbol{\varepsilon}_i\rfloor(\mathbf{a}_j \wedge \mathbf{b}_j) = \sum \mathbf{e}_i\boldsymbol{\varepsilon}_i|(\mathbf{b}_j\mathbf{a}_j - \mathbf{a}_j\mathbf{b}_j) = \mathbf{b}_j\mathbf{a}_j - \mathbf{a}_j\mathbf{b}_j. \tag{4.A.11}$$

4.A.4 Products of Dyadics

- Denoting the 3D (Euclidean) spatial basis vectors by $\mathbf{e}_1, \mathbf{e}_2, \mathbf{e}_3$ and by $\mathbf{e}_4 = \mathbf{e}_\tau$, the temporal basis vector with regards to some observer, the reciprocal dual basis vectors $\boldsymbol{\varepsilon}_1, \boldsymbol{\varepsilon}_2, \boldsymbol{\varepsilon}_3, \boldsymbol{\varepsilon}_4 = \mathbf{d}\tau$ satisfy $\mathbf{e}_i|\boldsymbol{\varepsilon}_j = \delta_{ij}$.
- The sign $|$ denotes the scalar product between a p-vector and a dual p-vector while $\rfloor$ or $\lfloor$ denotes the contraction (incomplete duality product) between a p-vector and a dual q-vector [1]. Double products $\overset{\wedge}{\wedge}, ||, \rfloor\rfloor, \lfloor\lfloor$ follow laws similar to those defined in the Gibbsian dyadic algebra.
- The double-wedge product of two dyadics $\underline{\mathsf{A}}, \underline{\mathsf{B}} \in \mathbb{E}_1\mathbb{F}_1$ is the counterpart of the double-cross product between two Gibbsian dyadics [4,5] and it is defined as

$$(\mathbf{a}\boldsymbol{\alpha})\overset{\wedge}{\wedge}(\mathbf{b}\boldsymbol{\beta}) = (\mathbf{a} \wedge \mathbf{b})(\boldsymbol{\alpha} \wedge \boldsymbol{\beta}), \tag{4.A.12}$$

  and similarly for sums of such products:

$$\underline{\mathsf{A}}\overset{\wedge}{\wedge}\underline{\mathsf{B}} = \sum \mathbf{a}_i\boldsymbol{\alpha}_i\overset{\wedge}{\wedge}\sum \mathbf{b}_j\boldsymbol{\beta}_j = \sum(\mathbf{a}_i \wedge \mathbf{b}_j)(\boldsymbol{\alpha}_i \wedge \boldsymbol{\beta}_j). \tag{4.A.13}$$

  The result is in the dyadic space $\mathbb{E}_2\mathbb{F}_2$. Similarly we can define products $\underline{\mathsf{A}}\overset{\wedge}{\wedge}\underline{\mathsf{B}}\overset{\wedge}{\wedge}\underline{\mathsf{C}}$, etc.
- The double-wedge square of a dyadic $\underline{\mathsf{A}} \in \mathbb{E}_1\mathbb{F}_1$ is

$$\underline{\mathsf{A}}^{(2)} = \frac{1}{2}\underline{\mathsf{A}}\overset{\wedge}{\wedge}\underline{\mathsf{A}} = \frac{1}{2}\sum_i\sum_j(\mathbf{a}_i \wedge \mathbf{a}_j)(\boldsymbol{\alpha}_i \wedge \boldsymbol{\alpha}_j) = \sum_{i<j}(\mathbf{a}_i \wedge \mathbf{a}_j)(\boldsymbol{\alpha}_i \wedge \boldsymbol{\alpha}_j). \tag{4.A.14}$$

Similarly we can define $\underline{\mathsf{A}}^{(3)}$ and $\underline{\mathsf{A}}^{(4)}$ as special cases of the pth double-wedge power:

$$\underline{\mathsf{A}}^{(p)} = \frac{1}{p!}\underline{\mathsf{A}}^{\wedge}_{\wedge}\underline{\mathsf{A}}^{\wedge}_{\wedge}\cdots^{\wedge}_{\wedge}\underline{\mathsf{A}} = \frac{1}{p!}\sum_{i_1,i_2\cdots i_p}(\mathbf{a}_{i_1}\wedge\mathbf{a}_{i_2}\wedge\cdots\wedge\mathbf{a}_{i_p})(\boldsymbol{\alpha}_{i_1}\wedge\boldsymbol{\alpha}_{i_2}\wedge\cdots\wedge\boldsymbol{\alpha}_{i_p}). \quad (4.A.15)$$

For $p > n$ dimension of space, we have $\underline{\mathsf{A}}^{(p)} = 0$.

- The unit dyadic mapping any bivector to itself is

$$\underline{\mathsf{I}}^{(2)} = \frac{1}{2}\underline{\mathsf{I}}^{\wedge}_{\wedge}\underline{\mathsf{I}} = \frac{1}{2}\sum_{i,j}(\mathbf{e}_i\wedge\mathbf{e}_j)(\boldsymbol{\varepsilon}_i\wedge\boldsymbol{\varepsilon}_j). \quad (4.A.16)$$

More generally, the unit dyadic for p-vectors is $\underline{\mathsf{I}}^{(p)}$. The unit dyadic mapping a p-form to itself is the transpose $\underline{\mathsf{I}}^{(p)\mathrm{T}}$. For $p = n$ we have $\underline{\mathsf{I}}^{(n)} = \mathbf{e}_N\boldsymbol{\varepsilon}_N$. For any $\underline{\mathsf{A}} \in \mathbb{I}_1\mathbb{F}_1$ we can write $\underline{\mathsf{A}}^{(n)} = \det\underline{\mathsf{A}}\,\underline{\mathsf{I}}^{(n)}$ where the scalar $\det\underline{\mathsf{A}}$ is called the determinant of $\underline{\mathsf{A}}$. It satisfies

$$\det\underline{\mathsf{A}} = \underline{\mathsf{A}}^{(n)}\|\underline{\mathsf{I}}^{(n)\mathrm{T}} = \boldsymbol{\varepsilon}_N|\underline{\mathsf{A}}^{(n)}|\mathbf{e}_N. \quad (4.A.17)$$

- If vectors are mapped through the dyadic $\underline{\mathsf{A}}$, bivectors are mapped through $\underline{\mathsf{A}}^{(2)}$,

$$(\underline{\mathsf{A}}|\mathbf{a}_1)\wedge(\underline{\mathsf{A}}|\mathbf{a}_2) = \underline{\mathsf{A}}^{(2)}|(\mathbf{a}_1\wedge\mathbf{a}_2), \quad (4.A.18)$$

and p-vectors as

$$(\underline{\mathsf{A}}|\mathbf{a}_1)\wedge(\underline{\mathsf{A}}|\mathbf{a}_2)\wedge\cdots\wedge(\underline{\mathsf{A}}|\mathbf{a}_p) = \underline{\mathsf{A}}^{(p)}|(\mathbf{a}_1\wedge\mathbf{a}_2\wedge\cdots\wedge\mathbf{a}_p). \quad (4.A.19)$$

- The inverse of a dyadic can be formed much in the same manner as in the Gibbsian 3D case [4,5]. For example, the inverse of a dyadic $\underline{\mathsf{A}} \in \mathbb{I}_1\mathbb{F}_1$ has the form [2]

$$\underline{\mathsf{A}}^{-1} = \frac{\underline{\mathsf{I}}^{(n)}\lfloor\lfloor\underline{\mathsf{A}}^{(n-1)\mathrm{T}}}{\det\underline{\mathsf{A}}} \in \mathbb{I}_1\mathbb{F}_1. \quad (4.A.20)$$

4.A.5 Identities

An identity is an equation which is valid for any values of its arguments. Certain number of identities is essential in any analysis using differential forms because they reduce the need to expand expressions in terms of basis vectors and their basic relations. Identities can be derived by expanding multivectors, dual multivectors, and dyadics in terms of basis vectors and dual basis vectors. Here we just give some examples taken from Ref. [2].

The counterpart of the Gibbsian bac-cab rule $\mathbf{a}\times(\mathbf{b}\times\mathbf{c}) = \mathbf{b}(\mathbf{a}\cdot\mathbf{c}) - \mathbf{c}(\mathbf{a}\cdot\mathbf{b})$ can be expressed for any vector $\mathbf{a}$ and two dual vectors $\boldsymbol{\beta}$, $\boldsymbol{\gamma}$ as

$$\mathbf{a}\rfloor(\boldsymbol{\beta}\wedge\boldsymbol{\gamma}) = \boldsymbol{\beta}(\mathbf{a}|\boldsymbol{\gamma}) - \boldsymbol{\gamma}(\mathbf{a}|\boldsymbol{\beta}). \quad (4.A.21)$$

This can be generalized in many ways, for example, replacing the dual vector $\boldsymbol{\gamma}$ by the dual p-vector $\boldsymbol{\gamma}^p$:

$$\mathbf{a}\rfloor(\boldsymbol{\beta}\wedge\boldsymbol{\gamma}^p) = \boldsymbol{\beta}\wedge(\mathbf{a}\rfloor\boldsymbol{\gamma}^p) + (-1)^p\boldsymbol{\gamma}^p(\mathbf{a}|\boldsymbol{\beta}). \quad (4.A.22)$$

As an example of an identity involving dyadics let us take the following one,

$$(\underline{\mathsf{A}}^{\wedge}_{\wedge}\underline{\mathsf{B}})\lfloor\lfloor\underline{\mathsf{C}}^{\mathrm{T}} = (\underline{\mathsf{A}}\|\underline{\mathsf{C}}^{\mathrm{T}})\underline{\mathsf{B}} + (\underline{\mathsf{B}}\|\underline{\mathsf{C}}^{\mathrm{T}})\underline{\mathsf{A}} - \underline{\mathsf{A}}|\underline{\mathsf{C}}|\underline{\mathsf{B}} - \underline{\mathsf{B}}|\underline{\mathsf{C}}|\underline{\mathsf{A}}, \quad (4.A.23)$$

valid for three dyadics $\underline{A}$, $\underline{B}$, $\underline{C} \in \mathbb{F}_1\mathbb{E}_1$. The result is another dyadic in the same space $\mathbb{F}_1\mathbb{E}_1$. This identity is the counterpart of the one for Gibbsian dyadics [10]

$$(\underline{A} \overset{\times}{\times} \underline{B}) \overset{\times}{\times} \underline{C} = (\underline{A} : \underline{C})\underline{B} + (\underline{B} : \underline{C})\underline{A} - \underline{A} \cdot \underline{C}^{\mathrm{T}} \cdot \underline{B} - \underline{B} \cdot \underline{C}^{\mathrm{T}} \cdot \underline{A}. \tag{4.A.24}$$

A useful special case of Equation 4.A.23 is obtained as the special case $\underline{B} = \underline{A}$:

$$\underline{A}^{(2)} \rfloor\rfloor \underline{C}^{\mathrm{T}} = (\underline{A} : \underline{C})\underline{A} - \underline{A}|\underline{C}|\underline{A}. \tag{4.A.25}$$

The same identity is also valid for dyadics in the metric spaces $\underline{A} \in \mathbb{E}_1\mathbb{E}_1$ and $\underline{C} \in \mathbb{F}_1\mathbb{F}_1$ or $\underline{A} \in \mathbb{F}_1\mathbb{F}_1$ and $\underline{C} \in \mathbb{E}_1\mathbb{E}_1$.

References

1. G.A. Deschamps, Electromagnetics and differential forms, *Proc. IEEE*, 69(6), 676–696, June 1981.
2. I.V. Lindell, *Differential Forms in Electromagnetics*, New York: Wiley and IEEE Press, 2004.
3. F.W. Hehl and Yu.N. Obukhov, *Foundations of Classical Electrodynamics*, Boston: Birkhäuser, 2003.
4. J.W. Gibbs and E.B. Wilson, *Vector Analysis*, New York: Dover, 1960. Reprint of the 1909 edition.
5. I.V. Lindell, *Methods for Electromagnetic Field Analysis*, 2nd edn., Oxford: University Press, 1995.
6. I.V. Lindell and A.H. Sihvola, Perfect electromagnetic conductor, *J. Electromag. Waves Appl.*, 19(7), 861–869, 2005.
7. I.V. Lindell and A.H. Sihvola, Transformation method for problems involving perfect electromagnetic conductor (PEMC) structures, *IEEE Trans. Antennas Propag.*, 53(9), 3005–3011, 2005.
8. I.V. Lindell and K.H. Wallén, Wave equations for bi-anisotropic media in differential forms, *J. Electromag. Waves Appl.*, 16(11), 1615–1635, 2002.
9. I.V. Lindell and K.H. Wallén, Differential-form electromagnetics and bi-anisotropic Q-media, *J. Electromag. Waves Appl.*, 18(7), 957–968, 2004.
10. I.V. Lindell and F. Olyslager, Analytic Green dyadic for a class of nonreciprocal anisotropic media, *IEEE Trans. Antennas Propag.*, 45(10), 1563–1565, October 1997.
11. I.V. Lindell and F. Olyslager, Green dyadic for a class of nonreciprocal bianisotropic media, *Microw. Opt. Techn. Let.*, 19(3), 216–221, October 1998.
12. I.V. Lindell and K.H. Wallén, Generalized *Q*-media and field decomposition in differential-form approach, *J. Electromag. Waves Appl.*, 18(8), 1045–1056, 2004.
13. I.V. Lindell and F. Olyslager, Generalized decomposition of electromagnetic fields in bi-anisotropic media, *IEEE Trans. Antennas Propag.*, 46(10), 1584–1585, October 1998.
14. I.V. Lindell and F. Olyslager, Factorization of Helmholtz determinant operator for decomposable bi-anisotropic media, *J. Electromag. Waves Appl.*, 13, 429–444, 1999.
15. I.V. Lindell, The class of bi-anisotropic IB media, *Prog. Electromag. Res.*, 57, 1–18, 2006.
16. I.V. Lindell, Electromagnetic fields and self-dual media in differential-form representation, *Prog. Electromag. Res.*, 58, 319–333, 2006.
17. I.V. Lindell, F. Olyslager, Green dyadics for self-dual bianisotropic media, *J. Electromag Waves Appl.*, 14, 153–163, 2000.
18. D.H. Delphenich, On linear electromagnetic constitutive laws that define almost-complex structures, arXiv.org gr-qc/0610031 (14 pp.), *Ann. Phys.*, 16, 307–317, 2007.
19. I.V. Lindell, Affine transformations and bi-anisotropic media in differential-form approach, *J. Electromag. Waves Appl.*, 18(9), 1259–1273, 2004.

II

Modeling Principles of Metamaterials

5

Fundamentals of Method of Moments for Artificial Materials

Christophe Craeye
Université Catholique de Louvain

Xavier Radu
Université Catholique de Louvain

Filippo Capolino
University of California Irvine

Alex G. Schuchinsky
Queens University of Belfast

5.1 Introduction

In this chapter, the method of moments (MoM) adapted to the simulation of fields in periodic and nonperiodic structures is briefly reviewed. The integral equation (IE) techniques are known for providing accurate results when modeling conducting and dielectric structures. A drawback of the MoM is that the matrices associated to the resulting linear systems of equations (we assume here linear media) are dense, and their inversion may require significant computational resources for complex structures, or for large structures as compared to the wavelength. However, it is important to note that when the analyzed structures are composed of piecewise homogeneous media, the respective IE can be simplified by expressing the unknown fields in terms of the tangential components of electric and magnetic fields at the media interfaces only. In the following, the structures considered will be assumed piecewise homogeneous initially, and will be supposed periodic next. Hence, the surface IE for the tangential electric and magnetic fields will be primarily discussed, whereas a few references will be provided to the volumetric approaches, which enable the analysis of inhomogeneous media. Fast solutions can be obtained by either considering unit-cell approaches (i.e., assuming infinite periodic structures with periodic excitation) or specialized methods enabling efficient simulation of large finite structures, like the fast multipoles methods (FMMs) and the Green's function interpolation and fast Fourier transform (GIFFT) method, as well as the macro basis functions (MBFs) approach, all summarized in this chapter. The array scanning method (ASM), which allows for the solution for a point source excitation in an otherwise infinite passive array, will also be briefly discussed.

Implementation details will be omitted and references will be provided for further reading on each specific method. A comprehensive discussion of the MoM can be found in [1,2] and its applications to analyze the specific electromagnetic structures are illustrated, e.g., in [3,4].

5.2 Equivalence Principle

The equivalence principle [5] is frequently used for solving scattering problems by the MoM. To illustrate the concept, let us consider the example shown in Figure 5.1a, where an external incident electromagnetic field impinges on a body of volume V with permittivity ϵ^{in} and permeability μ^{in}. Fields outside the body can be represented with the help of equivalent sources, distributed either inside V or over the surface S (as shown in Figure 5.1b), enclosing the volume V. This property is extensively exploited in IE approaches based on the surface equivalence principle [5] by representing the equivalent electric and magnetic current sources in the form

$$\mathbf{J} = \hat{\mathbf{n}} \times \mathbf{H} \tag{5.1}$$

$$\mathbf{M} = \mathbf{E} \times \hat{\mathbf{n}} \tag{5.2}$$

where

$\hat{\mathbf{n}}$ is the external normal to the surface

E and **H** are the electric and magnetic fields on the surface

The field generated by **J** and **M** is such that its superposition with the incident field produces the original field outside and zero field inside the volume V. Therefore, one can virtually consider the presence of any material inside because of the absence of field. For example, one could assume a perfect conductor inside, or a homogeneous material as the one outside, so as to use the free-space Green's function (GF) to determine the field radiated outside by the equivalent currents **J** and **M**. Analogously, the equivalent currents can be used to evaluate the field inside the surface S when they radiate in the environment shown in Figure 5.1c. A discussion of the equivalence principle can be found in [5], and its use in the MoM is detailed in [1,2].

In most cases, artificial media are composed of piecewise homogeneous volumes, as in Figure 5.1, which allows for the use of a surface IE approach, with unknown field and currents at the interfaces

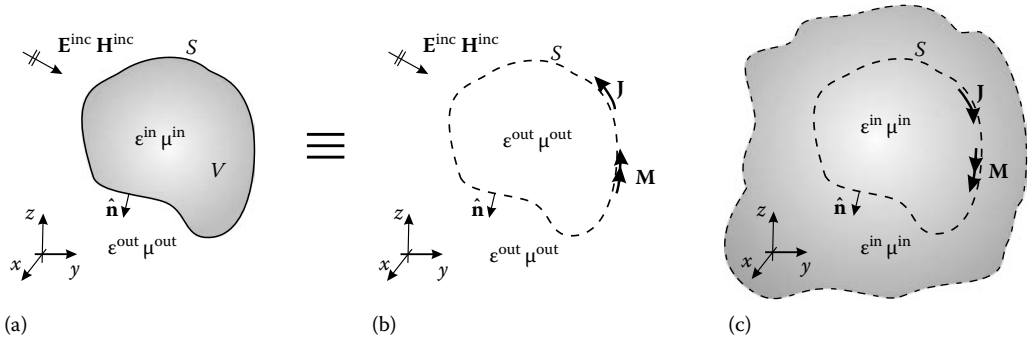

FIGURE 5.1 (a) Geometry of a scatterer of arbitrary shape with permittivity ϵ^{in} and permeability μ^{in}. (b) Equivalent surface electric **J** and magnetic **M** currents are shown on its boundary S. They radiate in a homogeneous medium, produce the original field outside and a vanishing field inside, when the incident field is added. A perfect electric conductor scatterer would have only electric currents. (c) The equivalent currents produce the original field inside the boundary S.

only. This assumption is employed below, and, in general, implies the need of a much smaller number of unknowns than required in a volumetric MoM for piecewise homogeneous media. For inhomogeneous volumes, instead, a volume IE can also be exploited [6,7]. The latter approach is based on the replacement of the dielectric contrast by an equivalent volumetric current at an arbitrary location **r** given by the relation

$$\mathbf{J}_V(\mathbf{r}) = j\omega\,(\epsilon^{\text{in}}(\mathbf{r}) - \epsilon^{\text{out}})\,\mathbf{E}(\mathbf{r}) \tag{5.3}$$

where

ω is the radian frequency
ϵ^{out} is the free-space permittivity
$\epsilon^{\text{in}}(\mathbf{r})$ is the relative permittivity of the medium at point **r**
$\mathbf{E}(\mathbf{r})$ is the electric field at the same location

A contrast magnetic current $\mathbf{M}_V = j\omega\,(\mu^{\text{in}}(\mathbf{r}) - \mu^{\text{out}})\mathbf{H}(\mathbf{r})$ can be defined similarly, based on the variation of permeability $\mu^{\text{in}}(\mathbf{r})$ versus position. An example of metamaterial analysis based on the volume IE can be found in [8]. In Section 5.3, we discuss the MoM for the solution of surface IEs. However, before proceeding further we illustrate the equivalence principle for two important particular cases. In Figure 5.2 the surface equivalence principle is illustrated for the case of a scatterer made by a perfect electric conductor (PEC). In this case, only the equivalent current on the boundary S is necessary to restore the original field outside the scatterer, since the total tangential electric field vanishes because of the PEC boundary condition, which implies $\mathbf{M} = \mathbf{E} \times \hat{\mathbf{n}} = 0$. This special case is particularly important in the RF/microwave range because metals are well approximated by PECs. In Figure 5.3 the surface equivalence principle is illustrated for the case of a scatterer made by a PEC surface with an aperture in it. The equivalent problem consists of two regions separated by a closed PEC surface. Radiation by the equivalent magnetic current $\mathbf{M} = \mathbf{E} \times \hat{\mathbf{n}}$, located just outside the scatterer at the location of the original aperture, restores the exterior field. Radiation by the equivalent magnetic current $-\mathbf{M}$, located just inside the scatterer at the location of the original aperture, restores the interior field. The opposite signs of the exterior and interior magnetic currents establish the continuity of the tangential electric field across the aperture. The continuity of the tangential magnetic field across the aperture is enforced by the IE (Section 5.3). The latter version of the equivalence principle is also used to model apertures (and periodic sets of apertures) in PEC screens of infinite extent, shown in Figure 5.3c and d.

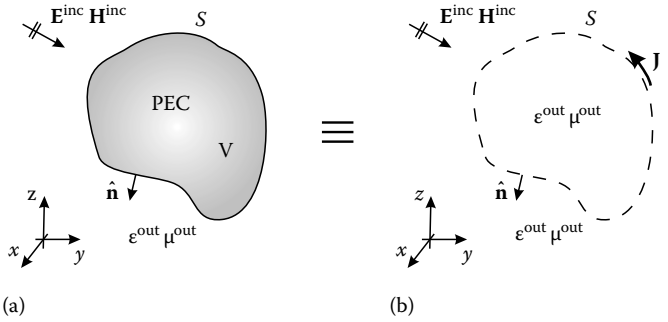

FIGURE 5.2 (a) Geometry of a PEC scatterer of arbitrary shape. (b) The equivalent surface electric **J** current is shown on its boundary S. It radiates in a homogeneous medium, produces the original field outside and a vanishing field inside, when the incident field is added.

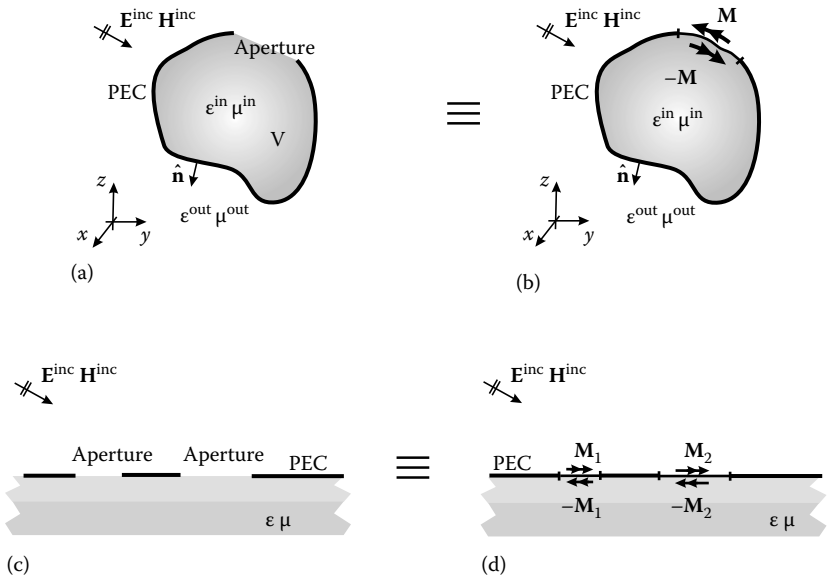

FIGURE 5.3 (a) Geometry of a PEC scatterer of arbitrary shape and aperture filled with a material with permittivity ϵ^{in} and permeability μ^{in}. (b) Closed PEC scatterer with equivalent surface magnetic currents **M** and −**M** on the exterior and interior parts of the PEC boundary *S*, respectively, at the location of the original aperture. **M** radiates outside and produces the original field when the incident field is added. −**M** radiates inside and produces the original field. The analogous problem for apertures in an infinite PEC screen is in (c), and its equivalent problem is (d). Here **M** and −**M**, just above and below the PEC screen, restore the field above and below, respectively.

5.3 Method of Moments for Surface Integral Equations

5.3.1 Spatial Domain

Electric and magnetic fields are often conveniently expressed in terms of scalar and vector potentials (see, e.g., [2,9]). The time dependence is assumed in the form $e^{j\omega t}$ and suppressed in the following. When both electric and magnetic current sources are present, the fields in the homogeneous medium with permittivity ϵ and permeability μ are represented in the frequency domain as follows:

$$\mathbf{H} = -j\omega\,\mathbf{F} + \nabla\psi + \frac{1}{\mu}\,\nabla\times\mathbf{A} \tag{5.4}$$

$$\mathbf{E} = -j\omega\,\mathbf{A} - \nabla\,\phi - \frac{1}{\epsilon}\,\nabla\times\mathbf{F} \tag{5.5}$$

Here, ϕ and ψ are the electric and magnetic scalar potentials and **F** and **A** are the electric and magnetic vector potentials. It is convenient to interrelate the vector and scalar potentials by the Lorentz gauge $\nabla\cdot\mathbf{A} = -j\omega\mu\epsilon\phi$ and $\nabla\cdot\mathbf{F} = j\omega\mu\epsilon\psi$. In this way, the knowledge of the electric and magnetic vector potentials is sufficient to determine all fields. In free space, the vector potentials can be represented as

$$\mathbf{A}(\mathbf{r}) = \mu\int_{\mathcal{D}}\mathbf{J}(\mathbf{r}')\,G\,d\mathcal{D}' \tag{5.6}$$

$$\mathbf{F}(\mathbf{r}) = \epsilon\int_{\mathcal{D}}\mathbf{M}(\mathbf{r}')\,G\,d\mathcal{D}' \tag{5.7}$$

where *G* is the free-space scalar GF

$$G = G(|\mathbf{r}-\mathbf{r}'|) = e^{-jkR}/(4\pi R) \tag{5.8}$$

where the wavenumber k is defined as $k^2 = \omega^2 \epsilon\mu$ and $R = |\mathbf{r} - \mathbf{r}'|$ is the distance between the observation and source points at $\mathbf{r}$ and $\mathbf{r}'$, respectively. $\mathbf{J}$ and $\mathbf{M}$ can be linear, and surface, or volume current densities, and the corresponding integration domain $\mathcal{D}$ can be a contour, a surface, or a volume.

With reference to the scattering problem shown in Figure 5.1a, where an external incident electromagnetic field impinges on a body of volume V with permittivity ϵ^{in} and permeability μ^{in}, the fields outside and inside the boundary S of the scatterer are represented by the radiation of the equivalent current in Figure 5.1b. In this case all the potentials $\mathbf{A}$, $\mathbf{F}$, ϕ, ψ can be expressed in terms of the scalar GF, and the electric and magnetic fields outside the surface S as follows:

$$\mathbf{E} = -j\omega\mu \int_S G\mathbf{J}dS' + \frac{1}{j\omega\epsilon}\nabla\nabla\cdot\int_S G\mathbf{J}dS' - \nabla\times\int_S \mathbf{M}GdS' + \mathbf{E}^{\text{inc}} \tag{5.9}$$

$$\mathbf{H} = -j\omega\epsilon \int_S G\mathbf{M}dS' + \frac{1}{j\omega\mu}\nabla\nabla\cdot\int_S G\mathbf{M}dS' + \nabla\times\int_S \mathbf{J}GdS' + \mathbf{H}^{\text{inc}} \tag{5.10}$$

where the superscript "inc" in the last term of both equations denotes incident fields.

In the following, since we deal with surface IEs, we need to evaluate the fields at the surface S, generated by equivalent currents located on the same surface. In this case, the integrands of the last integral terms of Equations 5.9 and 5.10 contain a singularity that needs to be treated carefully. For the electric field produced by equivalent magnetic current or for the magnetic field created by electric current (see Equations 5.4 through 5.7), a proper treatment of the field discontinuities across the equivalence surface is very important. In the last terms of Equations 5.9 and 5.10, we need to evaluate integrals of the type

$$\nabla\times\int_S G\mathbf{M}dS' = -\int_S \nabla' G\times\mathbf{M}dS' \tag{5.11}$$

where $\nabla' G$ denotes the gradient with respect to the coordinates of the source point $\mathbf{r}'$. It can be proven [10,11] that, when $\mathbf{r}$ approaches the smooth surface from outside, the limit of the integral (Equation 5.11) equals

$$-\frac{\hat{\mathbf{n}}\times\mathbf{M}}{2} + \oint_S \mathbf{M}\times\nabla' G\, dS \tag{5.12}$$

where $\oint$ denotes a principal value integral, and $\hat{\mathbf{n}}$ is a unit normal pointing toward the space containing the observation point $\mathbf{r}$. This exposes the discontinuity of fields at the surface: the fields differ depending on the side from which the surface is approached.

Thus, for components tangential to S, the fields at the exterior of surface S, where the currents are located, have the following form:

$$\mathbf{E} = -j\omega\mu \int_S G\mathbf{J}dS' + \frac{1}{j\omega\epsilon}\nabla\nabla\cdot\int_S G\mathbf{J}dS' + \frac{\hat{\mathbf{n}}\times\mathbf{M}}{2} - \oint_S \mathbf{M}\times\nabla' GdS' + \mathbf{E}^{\text{inc}} \tag{5.13}$$

$$\mathbf{H} = -j\omega\epsilon \int_S G\mathbf{M}dS' + \frac{1}{j\omega\mu}\nabla\nabla\cdot\int_S G\mathbf{M}dS' - \frac{\hat{\mathbf{n}}\times\mathbf{J}}{2} + \oint_S \mathbf{J}\times\nabla' GdS' + \mathbf{H}^{\text{inc}} \tag{5.14}$$

When the observation point lies outside the integration surface, the integrands of Equation 5.11 are no longer singular. Therefore, the fields are still given by Equations 5.13 and 5.14, where the terms $\hat{\mathbf{n}}\times\mathbf{M}/2$ and $\hat{\mathbf{n}}\times\mathbf{J}/2$ should be dropped, while all integrals are understood in the conventional sense, and all three field components can be considered.

5.3.1.1 Basis and Testing Functions

Surface electric currents on metallic sheets, as well as equivalent electric and magnetic currents on the interfaces between homogeneous media, are usually approximated by linear combinations of known basis functions $\mathbf{\Lambda}_i$,

$$\mathbf{J} \simeq \sum_{i=1}^{N_e} I_i \, \mathbf{\Lambda}_i^J \tag{5.15}$$

$$\mathbf{M} \simeq \sum_{i=1}^{N_m} V_i \, \mathbf{\Lambda}_i^M \tag{5.16}$$

where I_i and V_i are weighting coefficients. $\mathbf{\Lambda}_i^J$ and $\mathbf{\Lambda}_i^M$ denote basis functions used to approximate electric and magnetic currents, respectively. For brevity of notation, this distinction will be omitted below, also because in many practical implementations of the MoM, the same basis functions are used for both electric and magnetic currents.

Many types of basis functions have been proposed in the literature. Two major categories are usually distinguished: entire-domain basis functions and subdomain basis functions [12]. The former are particularly well suited to domains with canonical shapes. The latter have the advantage of fitting easier to surfaces with arbitrary shapes being assisted by commercially available libraries for mesh generation. The "Rao–Wilton–Glisson" (RWG, [13]) basis functions have gained particular popularity. They are defined on two triangular subdomains connected along a common edge and provide smooth approximations of the currents in the subdivided domains. Between these simple basis functions and the entire-domain basis functions, a number of higher-order basis functions have been defined. The use of higher-order functions allows the currents on larger domains to be approximated with fewer coefficients at the cost of a limited additional computational load [14].

The weighting coefficients I_i and V_i for each basis function are determined by imposing the boundary conditions at the scatterer surface S. The boundary conditions need, in principle, to be satisfied at each point of S. However, since there are $N = N_e + N_m$ unknowns, enforcing those conditions at N points ("point-matching" procedure) is sufficient, in principle, to obtain a system of N linear equations for N unknowns. These points can be chosen near the middle of the subdomain for each basis function. However, a better conditioning is generally achieved by enforcing the boundary conditions in an average sense, through multiplication of the fields by testing functions and integration of the equations over the definition domain of the testing functions [1]. It is necessary to note that when the testing function is a Dirac delta function of the surface coordinates, the testing procedure is reduced to the point-matching. The testing functions used are often chosen to be the same as the basis functions. This important special case is referred to as the Galerkin method [1,15,16], and gives rise to a symmetric system of linear algebraic equations.

5.3.1.2 The Integral Equations and Discretization

In the case of "dielectric interfaces" (Figure 5.1), the two possible types of boundary conditions to be satisfied are (1) the continuity of both the tangential electric and magnetic fields at the interface, as computed from equivalent currents on either side ("continuity" or Poggio–Miller–Chang–Harrington–Wu–Tsai (PMCHWT) formulation [10,17,18], see also [2]) and (2) the correspondence between, on one side, the equivalent currents, and on the other side, the tangential total fields, computed as a superposition of the incident field and the field radiated by the equivalent currents ("consistency" or Müller formulation [19]).

For instance, the continuity formulation for a dielectric interface S takes the form

$$\int_S \Lambda_j^t \cdot (\mathbf{E}^{\text{in}} - \mathbf{E}^{\text{out}}) \, \mathrm{d}S = 0 \tag{5.17}$$

$$\int_S \Lambda_j^t \cdot (\mathbf{H}^{\text{in}} - \mathbf{H}^{\text{out}}) \, \mathrm{d}S = 0 \tag{5.18}$$

where $\mathbf{\Lambda}_j^t$ is the jth testing function, and $\mathbf{E}^{\text{out}}$ and $\mathbf{H}^{\text{out}}$, and $\mathbf{E}^{\text{in}}$ and $\mathbf{H}^{\text{in}}$ are the total electric and magnetic fields at the opposite sides of the interface, respectively. The external fields $\mathbf{E}^{\text{out}}$, $\mathbf{H}^{\text{out}}$ are

the sums of the incident and the scattered fields created by the equivalent surface currents (assuming an infinite homogeneous medium with properties as the exterior one, see Figure 5.1b). The interior fields $\mathbf{E}^{\text{in}}$, $\mathbf{H}^{\text{in}}$ are produced by the scattered equivalent currents assuming an infinite homogeneous medium, with the parameters corresponding to the interior of the volume enclosed in S (see Figure 5.1c). The basis and testing functions chosen here have a vanishing component normal to their domain edges that allows the application of the div operator to the testing and basis functions without introducing equivalent charges at the subdomain boundaries [2,13]. The Galerkin testing procedure generally results in a better conditioned system of linear algebraic equations, which can be written as follows (the set of $\mathbf{\Lambda}_i^t$ is identical to the set of $\mathbf{\Lambda}_i^b$):

$$\begin{bmatrix} \left[Z_{mn}^{\text{in}} + Z_{mn}^{\text{out}}\right] & \left[-\beta_{mn}^{\text{in}} - \beta_{mn}^{\text{out}}\right] \\ \left[\beta_{mn}^{\text{in}} + \beta_{mn}^{\text{out}}\right] & \left[Y_{mn}^{\text{in}} + Y_{mn}^{\text{out}}\right] \end{bmatrix} \begin{bmatrix} [I_n] \\ [V_n] \end{bmatrix} = \begin{bmatrix} \left[V_m^{\text{inc}}\right] \\ \left[I_m^{\text{inc}}\right] \end{bmatrix} \tag{5.19}$$

with

$$Z_{mn}^{\text{in/out}} = \int_S \int_{S'} \left[j\omega\mu^{\text{in/out}} \; G^{\text{in/out}}(\mathbf{r},\mathbf{r}') \; \mathbf{\Lambda}_m^t(\mathbf{r}) \cdot \mathbf{\Lambda}_n(\mathbf{r}') + \frac{1}{j\omega\epsilon^{\text{in/out}}} \; G^{\text{in/out}}(\mathbf{r},\mathbf{r}') \; \nabla \cdot \mathbf{\Lambda}_m^t(\mathbf{r}) \; \nabla' \cdot \mathbf{\Lambda}_n(\mathbf{r}') \right] \mathrm{d}S' \, \mathrm{d}S \tag{5.20}$$

$$\beta_{mn}^{\text{in/out}} = \int_S \mathbf{\Lambda}_m^t(\mathbf{r}) \cdot \oint_{S'} \left[\mathbf{\Lambda}_n(\mathbf{r}') \times \nabla G^{\text{in/out}}(\mathbf{r},\mathbf{r}') \right] \mathrm{d}S' \, \mathrm{d}S \tag{5.21}$$

and $Y_{mn}^{\text{in/out}} = Z_{mn}^{\text{in/out}}/(\eta^{\text{in/out}})^2$, where $\epsilon^{\text{in/out}}$, $\mu^{\text{in/out}}$, and $\eta^{\text{in/out}} = (\mu^{\text{in/out}}/\epsilon^{\text{in/out}})^{1/2}$ represent permittivity, permeability and impedances of the medium inside/outside of the surface S, respectively. The excitation vectors are determined by projecting the incident fields on the testing functions

$$V_m^{\text{inc}} = \int_S \mathbf{E}^{\text{inc}}(\mathbf{r}) \cdot \mathbf{\Lambda}_m^t(\mathbf{r}) \mathrm{d}S \tag{5.22}$$

$$I_m^{\text{inc}} = \int_S \mathbf{H}^{\text{inc}}(\mathbf{r}) \cdot \mathbf{\Lambda}_m^t(\mathbf{r}) \mathrm{d}S \tag{5.23}$$

In the case of "perfectly conducting surfaces" (Figure 5.2), there are two possible conditions to be satisfied: (1) the tangential total (incident + scattered) electric field be zero and (2) the tangential total (incident + scattered) magnetic field ($\hat{\mathbf{n}} \times \mathbf{H} = 0$) be zero slightly inside the surface boundary of the PEC scatterer. These two boundary conditions lead to (1) the electric field integral equation (EFIE), which can be used for both open and closed PEC surfaces, and to (2) the magnetic field integral equation (MFIE), which can be used only for closed PEC surfaces [1,2]. Either equation can be employed to determine the electric current on the scatterer, and each discretization scheme based on the aforementioned testing procedures leads to a system of linear algebraic equations for the weighting coefficients in the Equation 5.15, of the surface currents only. For example, the discretized EFIE has the form

$$[Z_{mn}] \; [I_n] = \left[V_m^{\text{inc}}\right] \tag{5.24}$$

where Z_{mn} is evaluated as in Equation 5.20 considering the material parameters of the medium surrounding the PEC surface, and V_m^{inc} is given in Equation 5.22. It is noteworthy that currents on infinitesimally thin PEC sheets actually correspond to the sum of currents on both sides of the sheets.

This is why the solution of the EFIE and the MFIE on closed conducting surfaces suffers from instabilities at frequencies corresponding to interior resonances. These resonances can be generally avoided by combining the EFIE and the MFIE [1,2,20], leading to what is generally referred to as the combined field integral equation (CFIE), which is based on a weighted sum of the EFIE and the MFIE into a single equation [2].

In the case of "perfectly conducting surfaces with apertures" (Figure 5.3a), a convenient model consists of using surface magnetic currents shown in Figure 5.3b, which guarantee the continuity of the tangential electric field across the aperture. The magnetic current on the aperture S is discretized as in Equation 5.16. The IE is based on enforcing the continuity of the tangential magnetic field across the aperture S as in Equation 5.18. This leads to a linear system

$$[Y_{mn}]\ [V_n] = \left[I_m^{\text{inc}}\right] \tag{5.25}$$

where Y_{mn} is evaluated as in the text below Equation 5.20 considering the material parameters of the medium inside and outside the PEC boundary, and I_m^{inc} is given in Equation 5.23. It is important to note that in this particular case the magnetic current radiates in presence of the PEC scatterer and the GF used in Equation 5.20 should explicitly account for that. The special case of a PEC screen with apertures, shown in Figure 5.3c and d, involves less complicated GFs, since it involves the use of the free-space GF (with a factor 2 due to the image principle) or the use of the layered media GF.

When the basis and testing functions in the integral Equation 5.20 are defined on the same subdomain, the singular part $1/(4\pi R)$ of the GF is often extracted and its convolution with the basis and testing functions in Equations 5.20 and 5.21 is calculated analytically. The remaining integrals of the regular part of the GF are then evaluated using standard numerical quadratures for regular functions. The readers are referred to [21] where the corresponding expressions are presented for the low-order basis functions. Similarly, the singularity can be extracted from the terms involving the gradient of the GF [22], and respective integrals are evaluated in a similar fashion.

Recently, purely numerical quadrature schemes based upon singularity cancellation have been proposed in [23,24] for direct evaluation of GF convolutions with basis and testing functions. This approach hinges on a change of variables such that the Jacobian of the transformation cancels the singularity analytically. In contrast to the singularity subtraction approach, the resulting integrand is a regular function in the transformed variables, and hence is amenable to integration by Gauss-Legendre rules [24]. The developed scheme accurately and efficiently handles both singular and near-singular potential integrals with kernels of the form $1/R$ defined on triangular elements, which can be used as building blocks for more complex elements. The major advantage of this approach is that it provides robust and efficient computational codes without the need for explicit extraction of GF singularities.

5.3.1.3 Periodic Structures

The method described above can be applied to periodic structures as well. In this particular case, only one cell of the periodic structure needs to be analyzed numerically, and the use of the periodic GF takes into account the periodic replicas of the modeled scatterer. However, depending on the geometry considered, a few cases need to be distinguished.

First, suppose that the periodic structure is made of scatterers which are not electrically connected with those in contiguous cells. For metallic scatterers (made of perfect electric conductors as in Figure 5.2) the use of the periodic GF is sufficient to obtain a correct model. When the scattering body is made of a dielectric material (as in Figure 5.1) then, the formulation in Equation 5.19 is still valid as long as the periodic GF is considered for the exterior problem. In other words, $G^{\text{out}}(\mathbf{r}, \mathbf{r}')$ is now the periodic GF, and $G^{\text{in}}(\mathbf{r}, \mathbf{r}')$ is the homogeneous free-space GF, as it was in Equation 5.19.

Suppose instead that the periodic scattering object in the main reference cell is now electrically connected to others in adjacent cells. For perfect electric conducting scatterers, basis functions should

be placed across the boundary of the periodic cell, representing a flow of current into the next contiguous cell, and each basis function across the periodic boundary should be connected to the same one at the other side of the periodic cell ("overlapping basis function") with the proper boundary condition enforced (for example, see [25] and Fig. 4 of [26]). For dielectric objects, instead, we need to make a further distinction. When a dielectric object is located across the boundary of the periodic cell, but it is not connected to the other periodic dielectric replicas, then the "overlapping basis functions" technique is applied to the basis functions used for the interior and exterior problems.

The case of a periodic structure made by connected dielectric objects (like a chain of touching spheres, or a dielectric grating) poses a more challenging problem, and two strategies can be used, as described below. The first one, applied in [27], consists of using the free-space GF inside the dielectric medium and the 2-D periodic GF outside. However, in this case it is necessary to add unknowns at the boundaries of the periodic cell in order to explicitly enforce the periodic boundary conditions between fields in the interior domain. Also, precautions need to be taken along the lines connecting three media: outer space, the dielectric material of a given cell, and the dielectric material of a neighboring cell. The reader is referred to [28] for the treatment of junctions between multiple media. The second strategy for connected dielectric objects, applied in [29], does not use basis functions on the periodic boundary. It consists of using a periodic GF, with appropriate material parameters, for the interior problem as well, and the overlapping basis functions for the equivalent electric and magnetic currents across the periodic cell, for both the interior and exterior problems. When the structure under consideration is periodic in two directions, but the dielectric scatterers are connected to each other in one direction only (e.g., as in a linear chain of connected spheres), then, the 2-D periodic GF shall be used for the exterior problems, and the 1-D periodic GF should be used for the interior problem. If dielectric scatterers are connected in two directions, then the 2-D periodic GF should be used also for the interior problem.

5.3.2 Spectral Domain

Fields can be represented also in the spectral domain as a superposition of the spectral constituents, such as plane waves. The free-space scalar GF Equation 5.8 for a point source located at $\mathbf{r}'$ is expressed in the spectral domain as

$$G(\mathbf{r},\mathbf{r}') = \frac{1}{(2\pi)^2}\int_{-\infty}^{\infty}\int_{-\infty}^{\infty}\tilde{G}(k_x,k_y,|z-z'|)e^{-j[k_x(x-x')+k_y(y-y')]}\,\mathrm{d}k_x\mathrm{d}k_y \tag{5.26}$$

where

$$\tilde{G}(k_x,k_y,|z-z'|) = \frac{e^{-jk_z|z-z'|}}{2jk_z} \tag{5.27}$$

and $k_z = \sqrt{k^2 - k_x^2 - k_y^2}$.

When a point source is an electric current $\mathbf{J}$ of unit magnitude (1 [A/m]) located at $\mathbf{r}'$, the fields at point $\mathbf{r}$ are described by the dyadic GFs of electric $\underline{\mathbf{G}}^{EJ}$ and magnetic $\underline{\mathbf{G}}^{HJ}$ types [9,30],

$$\underline{\mathbf{G}}^{EJ}(\mathbf{r},\mathbf{r}') = \frac{1}{(2\pi)^2}\int_{-\infty}^{\infty}\int_{-\infty}^{\infty}\underline{\tilde{\mathbf{G}}}^{EJ}(k_x,k_y,|z-z'|)e^{-j[k_x(x-x')+k_y(y-y')]}\,\mathrm{d}k_x\mathrm{d}k_y \tag{5.28}$$

$$\underline{\mathbf{G}}^{HJ}(\mathbf{r},\mathbf{r}') = \frac{1}{(2\pi)^2}\int_{-\infty}^{\infty}\int_{-\infty}^{\infty}\underline{\tilde{\mathbf{G}}}^{HJ}(k_x,k_y,|z-z'|)e^{-j[k_x(x-x')+k_y(y-y')]}\,\mathrm{d}k_x\mathrm{d}k_y \tag{5.29}$$

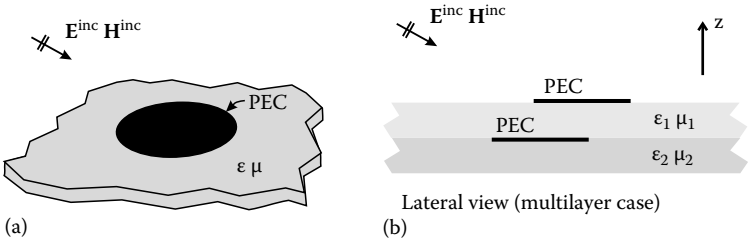

FIGURE 5.4 (a) Planar PEC scatterer of a simple shape on a dielectric layer of infinite extent. (b) The lateral view of a multilayer case.

where $\underline{\tilde{\mathbf{G}}}^{EJ}$ and $\underline{\tilde{\mathbf{G}}}^{HJ}$ are the spectral-domain counterparts of $\underline{\mathbf{G}}^{EJ}$ and $\underline{\mathbf{G}}^{HJ}$. For a homogeneous medium, the respective spectral dyads are

$$\underline{\tilde{\mathbf{G}}}_{00}^{EJ}(k_x, k_y, |z - z'|) = (j\omega\epsilon)^{-1} \left[k^2 \underline{\mathbf{I}} - \mathbf{kk}\right] \tilde{G}(k_x, k_y, |z - z'|) \tag{5.30}$$

$$\underline{\tilde{\mathbf{G}}}_{00}^{HJ}(k_x, k_y, |z - z'|) = -j \left[\mathbf{k} \times \underline{\mathbf{I}}\right] \tilde{G}(k_x, k_y, |z - z'|) \tag{5.31}$$

where $\mathbf{k} = k_x\hat{\mathbf{x}} + k_y\hat{\mathbf{y}} \pm k_z\hat{\mathbf{z}}$, and the ± signs correspond to $z > z'$ and $z < z'$, respectively.

The spectral-domain representations (Equations 5.28 and 5.29) of Green's dyads are particularly instrumental for calculating the electric and magnetic fields generated by currents located in planes normal to the z-axis (see, for example, a geometry in Figure 5.4). Indeed, the fields produced by the current $\mathbf{J}(\mathbf{r}')$ distributed, for example, on planar conductors at a certain plane z' (Figure 5.4) can be obtained as a convolution between $\mathbf{J}(\mathbf{r}')$ and the Green's dyads, cf. Equations 5.13 and 5.14. Then, making use of $\underline{\tilde{\mathbf{G}}}^{EJ}$ and $\underline{\tilde{\mathbf{G}}}^{HJ}$ in the forms of Equations 5.28 and 5.29 and integrating with respect to $\mathbf{r}'$ over the area S occupied by the current sources in the plane z' results in the field representations expressed in terms of inverse Fourier transforms or the spectral-domain convolution of Green's dyads and current density:

$$\mathbf{E}(\mathbf{r}) = \frac{1}{(2\pi)^2} \int_{-\infty}^{\infty}\int_{-\infty}^{\infty} \underline{\tilde{\mathbf{G}}}^{EJ}(k_x, k_y, |z - z'|) \cdot \tilde{\mathbf{J}}(k_x, k_y, z') e^{-j(k_x x + k_y y)}\, \mathrm{d}k_x \mathrm{d}k_y \tag{5.32}$$

$$\mathbf{H}(\mathbf{r}) = \frac{1}{(2\pi)^2} \int_{-\infty}^{\infty}\int_{-\infty}^{\infty} \underline{\tilde{\mathbf{G}}}^{HJ}(k_x, k_y, |z - z'|) \cdot \tilde{\mathbf{J}}(k_x, k_y, z') e^{-j(k_x x + k_y y)}\, \mathrm{d}k_x \mathrm{d}k_y \tag{5.33}$$

where the spectral-domain current $\tilde{\mathbf{J}}(k_x, k_y, z')$ is defined as

$$\tilde{\mathbf{J}}(k_x, k_y, z') = \int_S \mathbf{J}(\mathbf{r}')\, e^{j(k_x x' + k_y y')}\, \mathrm{d}x' \mathrm{d}y' \tag{5.34}$$

It is necessary to note that while the Fourier transform of $\mathbf{J}(\mathbf{r}')$ above is taken in infinite limits, the integral in Equation 5.34 is confined only to the finite area S occupied by the currents, in the plane z'.

In the problems of wave scattering by planar conductors, the current $\mathbf{J}(\mathbf{r}')$ is unknown a priori in Equations 5.32 and 5.33 and must be determined by enforcing the piecewise boundary conditions for the fields at planes with constant z' (note that the current sources may be placed at several interfaces in multilayered structures with various discrete values of z'). This results in the EFIE or MFIE similar to those discussed in Section 5.3.1 with the only difference that the integrands in Equations 5.32 and 5.33 are defined in the spectral domain. These equations are usually solved by the Galerkin method. The spectral-domain approach has originally been developed for analysis of printed

transmission lines and planar circuits [31–47], and later applied to the highly efficient modeling of periodic structures [48–51].

Assuming that the nth basis and mth testing functions are confined to the domains located in the planes $z = z_b$ and $z = z_t$, respectively, their spectral-domain convolutions with the GF can be expressed as an inner product, cf. Equation 5.20:

$$Z_{mn} = \frac{1}{(2\pi)^2} \int_{-\infty}^{\infty} \int_{-\infty}^{\infty} \tilde{\mathbf{\Lambda}}_m \; \underline{\tilde{\mathbf{G}}}^{EJ}(k_x, k_y, z_t, z_b) \; \tilde{\mathbf{\Lambda}}_n^{\star} \, \mathrm{d}k_x \, \mathrm{d}k_y \tag{5.35}$$

where $\underline{\tilde{\mathbf{G}}}^{EJ}(k_x, k_y, z_t, z_b)$ is a dyadic operator representing the GF in spectral-domain. It is necessary to note that while in homogeneous medium $\underline{\tilde{\mathbf{G}}}^{EJ}(k_x, k_y, z_t, z_b) = \underline{\tilde{\mathbf{G}}}^{EJ}(k_x, k_y, |z_t - z_b|)$, in general, this relationship does not hold for layered media. The terms $\tilde{\mathbf{\Lambda}}_n$ in Equation 5.35 are the Fourier transforms of the testing and basis functions, defined as

$$\tilde{\mathbf{\Lambda}}_n(k_x, k_y, z) = \int_S \mathbf{\Lambda}_n(x, y, z) \; e^{j(k_x x + k_y y)} \mathrm{d}x \; \mathrm{d}y \tag{5.36}$$

The salient feature of Equation 5.35 is that the spectral-domain Green's dyads (Equations 5.28 and 5.29) required for computations of Z_{mn} are available in closed form for a broad range of multilayered structures. For details of construction and computation of the spectral-domain GFs and their specific applications, we address the readers to the extensive literature on this topic (see, e.g., [9,52,56] and references therein).

In the case of planar stratified media, as on the right side of Figure 5.4 or in Figure 5.5, the fields can be expressed as a superposition of TE and TM waves with respect to the interface normal (z-axis) (see, e.g., [9,52,53]). The TE and TM waves independently satisfy the boundary conditions at source-free interfaces between the layers. This significantly simplifies the field representations and enables the use of the transmission matrix method to obtain the fields of each individual mode at any point of the planar stratified medium, see, e.g., [54–56] and references therein. It is necessary to note that the TE and TM waves are separable only in homogeneous planar layers, whereas they are hybridized at curvilinear interfaces, discontinuities, and in anisotropic media.

The transverse magnetic (TM) and transverse electric (TE) waves with the real wavenumber k_z in the lossless layers surrounding a source can propagate in these layers along the z-axis and carry away

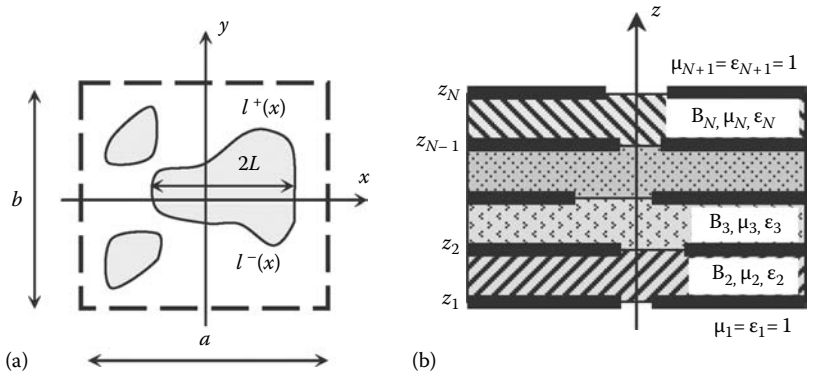

FIGURE 5.5 Unit cell of a multilayered periodic array: (a) top view showing three apertures, and (b) side view showing the apertures in the conductor screens located at the interfaces of $(N-1)$ magnetodielectric layers of thicknesses B_i with relative permittivities ϵ_i and permeabilities μ_i, $i = 2, 3, \ldots, N$. The layer stack is surrounded by free space ($\epsilon_1 = \mu_1 = 1$ and $\epsilon_{N+1} = \mu_{N+1} = 1$).

real power. Conversely, the evanescent modes with complex or purely imaginary k_z only store reactive power in the source vicinity and do not carry away real power along the z direction. Nevertheless, the evanescent part of the spectrum cannot be neglected because these modes contain the important fine details of field distributions near the sources and discontinuities. It is noteworthy that the layered medium may also guide the TE and TM eigenwaves. These traveling waves manifest themselves as the poles of the dyadic term $\underline{\tilde{\mathbf{G}}}^{EJ}(k_x, k_y)$ in the variables (k_x, k_y), which correspond to the tangential components of the wavevectors of the respective TE and TM modes.

5.3.2.1 Periodic Arrangements

Recently, periodic structures in layered media have attracted considerable attention in the context of modeling metamaterials and photonic crystals, and the study of enhanced transmission through sub-wavelength apertures in perforated screens. The spectral formulation described above can be easily adapted to the analysis of periodic structures by replacing the dyadic GF in Equation 5.35 with the dyadic GF $\underline{\tilde{\mathbf{G}}}^{p}$ (the superscripts "EJ" or "HJ" are omitted here because what follows is applicable to both cases). For example, when analyzing a doubly periodic geometry on rectangular lattices, the dyadic GF takes the form

$$\underline{\tilde{\mathbf{G}}}^{p}(k_x, k_y, z, z') = \frac{(2\pi)^2}{ab} \sum_{p,q=-\infty}^{\infty} \delta\left(k_x - k_{x,0} - p\,\frac{2\pi}{a}\right) \delta\left(k_y - k_{y,0} - q\,\frac{2\pi}{b}\right) \underline{\tilde{\mathbf{G}}}(k_x, k_y, z, z') \quad (5.37)$$

where

a and b are spacings along the x and y directions, respectively
$k_{x,0}a$ and $k_{y,0}b$ are interelement phase shifts
z' and z correspond to the source and observation points, respectively
$\underline{\tilde{\mathbf{G}}}(k_x, k_y, z, z')$ is the Green's dyad for nonperiodic structures

Besides that, $\underline{\tilde{\mathbf{G}}}(k_x, k_y, z, z')$ may contain poles in the phasing variables (k_x, k_y), which are associated with TE or TM eigenwaves.

When Equation 5.37 is substituted in Equation 5.35, the elements of the MoM impedance matrix turn into very slow convergent infinite sums. It is necessary to note that the slow convergence of the spectral integrals or sums above for z close to z' can be traced back to the spatial singularities of fields at the source, i.e., at $x \to x'$ and $y \to y'$. The convergence of these series or integrals can be significantly accelerated either by using GF representations that have an explicit singular spatial term (like in the Ewald and Kummer methods) or by isolating the spatial singularity associated with sources (for instance, through a space-domain approach). The techniques for accelerating convergence of the series in the periodic GFs are further discussed in Section 5.4.

The spectral-domain solution of the IEs is usually computationally more efficient than the respective spatial-domain procedure, provided that the proper basis and testing functions are readily available in spectral-domain. The major advantage of the spectral-domain approach is that the GFs for complex-layered structures exist in closed form. Therefore the inner products in Equation 5.35 can be efficiently calculated using the Parseval theorem for convolution of the spectral-domain GF with the respective basis and testing functions. This property is particularly beneficial for the canonical geometries, where the known entire-domain basis functions take into account the specific features of field distributions, e.g., edge singularities. The latter feature has been extensively exploited in the analysis of printed transmission lines and planar circuits (see, e.g., [31–47]), and highly efficient modeling of periodic structures [48–51,57]. Unfortunately, the spectral-domain basis functions accounting for the edge singularities of fields are available only for a few basic configurations, which considerably limits applications of the spectral-domain approach.

5.4 Green's Functions for Periodic Structures

The problem of modeling infinite periodic arrays can be reduced to the analysis of a single reference unit cell. This provides a great numerical advantage as compared to direct simulations of very large structures. The MoM techniques described above for isolated scatterers can be applied here as well, with the only difference that a periodic GF should be used instead of the GF in Equation 5.8 for a homogeneous medium.

To illustrate this approach, let us consider an infinite array on a rectangular lattice, with periodicities a and b, along the x and y directions, respectively. The periodic GF for infinite arrays can be represented as a superposition of the fields generated by an elementary source inside the reference unit cell and the source replicas in all the other unit cells. Without loss of generality we can assume that the source is placed at the origin ($\mathbf{r}' = 0$) of the reference unit cell, and all its mn-replicas are located at $\mathbf{r}'_{mn} = ma\hat{\mathbf{x}} + nb\hat{\mathbf{y}}$. The spatial representation of the periodic GF is thus given by

$$G^p = \sum_{m,n=-\infty}^{\infty} \frac{e^{-jkR_{mn}}}{4\pi R_{mn}} e^{-j(mk_{x,0}a + nk_{y,0}b)} \tag{5.38}$$

where

$k_{x,0}a$ and $k_{y,0}b$ are the phase shifts between successive cells in the x and y directions, respectively

$R_{mn} = \sqrt{(x - ma)^2 + (y - nb)^2 + z^2}$ with x and y being confined to the reference unit cell $(m = 0,\ n = 0)$

R_{mn} corresponds to the distance between the observation point at (x, y, z) and the source in the unit cell (m,n) of the infinite array. The use of the periodic GF (Equation 5.38) reduces the solution domain of the IE to a single unit cell at the expense of complexity in calculation of the GF, which includes the periodic replicas of the actual source. The convergence of the space-domain series in Equation 5.38 is very slow, and usually thousands or tens of thousands of terms must be summed up to attain acceptable accuracy. Moreover, the spatial series (Equation 5.38) does not converge for complex wavenumbers $k_{x,0}$ and $k_{y,0}$.

Alternatively, the periodic GF can be obtained with the aid of Equation 5.37 for periodically spaced sources and the spectral-domain GF, $\tilde{G}(k_x, k_y, |z - z'|)$, defined in Equation 5.27. This approach results in the spectral series expansion utilizing an infinite discrete spectrum of plane waves:

$$G^p = \frac{1}{2jab} \sum_{m,n=-\infty}^{\infty} \frac{e^{-j(k_{x,m}x + k_{y,n}y + k_{z,mn}|z|)}}{k_{z,mn}} \tag{5.39}$$

with

$$k_{x,m} = k_{x,0} + m\frac{2\pi}{a}, \quad k_{y,n} = k_{y,0} + n\frac{2\pi}{b} \tag{5.40}$$

$$k_{z,mn} = \sqrt{k^2 - k_{x,m}^2 - k_{y,n}^2} \tag{5.41}$$

The branch of $k_{z,mn}$ is chosen so that $\mathrm{Im}\{k_{z,mn}\} < 0$, unless the GF is used to model leaky waves, where the other branch should be adopted (see [58] for more details). The drawback of the series (Equation 5.39) is that it converges slowly for observation points close to the array plane, i.e., at $|z| \to 0$. Therefore, the evaluation of the GF requires acceleration of the series convergence.

Intensive research has been carried out to accelerate the GF computations, and several techniques have been developed to address this problem. Reviews on this topic can be found, for example, in [3,59–66], and references therein. In this section, only three efficient approaches are briefly outlined.

Series acceleration formulations, like the Shanks and Levin-T transforms, have been used successfully [67–71] to evaluate periodic GFs. Alternative techniques of convergence acceleration in periodic GFs, particularly Ewald and Kummer transformations, have shown excellent computational efficiency. Algorithms based upon the Ewald method [72] are extensively discussed in [61–64,73–81]. Approaches based on the Kummer method are described in [51,65,82,83]. It is necessary to mention that other efficient schemes have been reported for the periodic GF acceleration. For example in [84] the Veysoglu's transformation (see also [59,65,66]) is used to achieve exponential convergence for 2-D problems periodic in one direction.

While the numerical procedure based on Ewald's method with Gaussian convergence (cf. [73]) is faster, it suffers from breakdown when the structure period is larger than the wavelength [76]. This problem, known as the "high-frequency breakdown," can be avoided by a proper choice of the Ewald splitting parameter [61–64]. The physical reasons underlying the breakdown effect are explained in [62] in terms of emergence of propagating modes. In contrast to the Ewald method, the Kummer method provides only algebraic convergence of the GF series. Nevertheless, both these techniques exhibit excellent performance, and we briefly outline them for the reference.

Following [82], a Kummer transformation is applied to the spectral series representation of the GF (Equation 5.39)

$$G^p = \sum_{m,n=-\infty}^{\infty} F_{mn} = \sum_{m,n=-\infty}^{\infty} (F_{mn} - F^a_{mn}) + \sum_{m,n=-\infty}^{\infty} F^a_{mn} \tag{5.42}$$

where

$$F_{mn} = \frac{e^{-j(k_{x,m}x + k_{y,n}y + k_{z,mn}|z|)}}{2jabk_{z,mn}} \tag{5.43}$$

and $F^a_{mn} \sim F_{mn}$, i.e., these terms are asymptotically equal for large $|m|, |n|$. Therefore a proper choice of the asymptotic terms F^a_{mn} provides faster convergence of the difference series than the original sum of F_{mn}, while the sum of F^a_{mn} in Equation 5.42 can be efficiently computed with the aid of Poisson summation formula.

The asymptotic terms F^a_{mn} in Equation 5.42 are chosen according to [82] by representing $k_{z,mn}$ in the form, cf. Equation 5.41,

$$k_{z,mn} = -j\sqrt{k^2_{mn} - (k^2 + u^2)} \tag{5.44}$$

where

$$k^2_{mn} = k^2_{x,m} + k^2_{y,n} + u^2 \tag{5.45}$$

and u is termed "smoothing parameter." For this definition of the asymptotic form of $k_{z,mn}$, it is evident that at large m,n

$$\frac{e^{-jk_{z,mn}|z|}}{jk_{z,mn}} \sim \frac{e^{-k_{mn}|z|}}{k_{mn}} \tag{5.46}$$

Then F^a_{mn} can be represented in the following form:

$$F^a_{mn} = \frac{e^{-j(k_{x,m}x + k_{y,n}y + k_{mn}|z|)}}{2abk_{mn}} \tag{5.47}$$

Finally, substituting Equation 5.47 into Equation 5.42 and applying the Poisson summation formula to the last series in Equation 5.42 results in the following representation of the GF:

$$G^p = \frac{1}{2ab}\sum_{m,n=-\infty}^{\infty} e^{-j(k_{x,m}x+k_{y,n}y)}\left(\frac{e^{-jk_{z,mn}|z|}}{jk_{z,mn}} - \frac{e^{-k_{mn}|z|}}{k_{z,mn}}\right) + \frac{1}{4\pi}\sum_{m,n=-\infty}^{\infty} e^{-j(mk_{x,0}a+nk_{y,0}b)}\frac{e^{-uR_{mn}}}{R_{mn}} \tag{5.48}$$

The series Equation 5.48 converges faster than the original series Equation 5.39. Its convergence rate depends on the smoothing parameter u. As demonstrated in [82], the choice of the smoothing parameter has a more dramatic effect on the convergence rate of the spatial series than on the spectral sum. A reasonable choice of u, which can provide good convergence of both the spatial and spectral series in Equation 5.48 is about half the size of the maximal reciprocal lattice base vector [82].

An important result of this convergence acceleration procedure is that the singularity of GF is contained only in the single term $m = n = 0$ of the spatial series (Equation 5.48), as the distance between the source and observation points in the reference unit cell $R_{00} \to 0$

$$\frac{e^{-uR_{00}}}{R_{00}} \sim \frac{1}{R_{00}} \tag{5.49}$$

This implies that the infinite series in Equation 5.48 are regular functions and their convergence can be further accelerated by repetitive application of Kummer method or other techniques.

An alternative implementation of the Kummer method has been reported in [51,83]. Starting from the spatial representation of GF given by Equation 5.38 and explicitly extracting the singular part G_0 of G^p at $R_{mn} \to 0$, the series (Equation 5.38) can be expressed in the form of $G^p = G_0 + G_r$ where

$$G_0 = \frac{e^{-jkR_{00}}}{4\pi R_{00}} \tag{5.50}$$

and

$$G_r = \sum_{i=1}^{3}\Omega_i \tag{5.51}$$

is a regular function of x, y, z:

$$\Omega_1 = \frac{1}{2\pi b}\sum_{\substack{n\\ |k_{y,n}|>k}} e^{-jk_{y,n}y}\sum_{\substack{m=-\infty\\ m\neq 0}}^{\infty} e^{-jmk_{x,0}a}K_0\left(\sqrt{k_{y,n}^2-k^2}\sqrt{z^2+(x-ma)^2}\right) \tag{5.52}$$

$$\Omega_2 = \sum_{\substack{n=-\infty\\ n\neq 0}}^{\infty} e^{-jnbk_{y,0}}\frac{e^{-jR_{0n}}}{4\pi R_{0n}} \tag{5.53}$$

$$\Omega_3 = \sum_{\substack{n\\ |k_{y,n}|<k}}\left[\frac{j}{4b}H_0^{(2)}\left(\sqrt{k^2-k_{y,n}^2}\sqrt{z^2+x^2}\right)e^{-jk_{y,n}y} + \sum_{m=-\infty}^{\infty}\frac{e^{-j\left(k_{x,m}x+k_{y,n}y+k_{z,mn}|z|\right)}}{2jabk_{z,mn}}\right] \tag{5.54}$$

Here, $K_0(\cdot)$ is the Macdonald function, and $H_0^{(2)}(\cdot)$ is the zero-order Hankel function of second kind.

The series in Equation 5.52 converges exponentially because the summation over n is performed only for the evanescent waves with $|k_{y,n}| > k$. The external sum over n in Equation 5.54 contains only a finite number of terms which correspond to the propagating waves. But convergence of the infinite series in Equations 5.53 and 5.54 is accelerated by the Kummer method, as detailed in [51, 83]. It is necessary to emphasize that the Kummer method is applied here to a single summation in m only. Therefore Ω_2 and Ω_3 can be efficiently calculated in a robust manner with any specified rate of algebraic convergence of order N. The resulting series with the terms of order $O\left(m^{-N}\right)$ are uniformly convergent for any parameters of the structure and frequency and, in contrast to Equation 5.48, they do not require the additional smoothing parameter.

The Ewald's method has been recognized as one of the most efficient techniques for computation of periodic GFs. It is based upon representation of the GF as a sum of spatial and spectral series [73],

$$G^p = G_{\text{spatial}} + G_{\text{spectral}} \tag{5.55}$$

with

$$G_{\text{spatial}} = \sum_{m,n=-\infty}^{\infty} \frac{e^{-j\left(mk_{x,0}a + nk_{y,0}b\right)}}{8\pi R_{mn}} \left[e^{-jkR_{mn}} \text{erfc}\left(R_{mn}E - \frac{jk}{2E}\right) + e^{+jkR_{mn}} \text{erfc}\left(R_{mn}E + \frac{jk}{2E}\right)\right] \tag{5.56}$$

$$G_{\text{spectral}} = \sum_{m,n=-\infty}^{\infty} \frac{e^{-j\left(k_{x,m}x + k_{y,n}y\right)}}{4jabk_{z,mn}} \left[e^{-jk_{z,mn}|z|} \text{erfc}\left(\frac{jk_{z,mn}}{2E} - |z|E\right) + e^{jk_{z,mn}|z|} \text{erfc}\left(\frac{jk_{z,mn}}{2E} + |z|E\right)\right] \tag{5.57}$$

where

erfc is the complementary error function

E is the Ewald splitting parameter

The two series exhibit Gaussian convergence, and in most cases only the terms with $m, n = -1, 0, 1$ are sufficient to guarantee accuracy up to five or six decimal places when the so-called "optimal" choice $E = \sqrt{\pi/ab}$ is used. The optimal E implies that the same number of terms in the spatial and spectral series is used to achieve a certain rate of convergence [63,73]. When the period a or b becomes larger than the wavelength the optimal parameter E must be increased, as noted in [76], to avoid the "high-frequency breakdown." Simple algorithms for the choice of E are based on [61,62], and the details of automatic choice of E are discussed in [63,64].

Inspection of Equations 5.56 and 5.57 shows that the spatial singularity of G^p is contained only in the single term $1/R_{00}$ of G_{spatial}. This implies that the singular and regular parts of G^p can be explicitly separated within the Ewald scheme, similar to that in the Kummer method, and can be used for the analytical preconditioning of the IE kernel. It is noteworthy that the Ewald representation can be used for complex wavenumbers $k_{x,0}$ and $k_{y,0}$, and for complex frequency, i.e., for complex-valued k.

Finally, it is necessary to note that the use of Faddeeva functions instead of error functions in the series Equations 5.56 and 5.57 considerably accelerates the GF computation, e.g., in [81] a 20-fold speed up was achieved in calculating the GF with a relative error less than 10^{-4}. Indeed, some effective numerical algorithms for the evaluation of the error function are based on the use of the Faddeeva function for certain parameter values.

The Ewald method is generally more efficient than the Kummer based algorithms. However, certain implementations of the Kummer method provide uniform convergence and do not require any setup or run time modification of the parameters for internal convergence control, which are dependent on the structure dimensions and frequency. For relative errors of less than −20 dB, both acceleration techniques exhibit commensurable convergence rates [83] and can be equally used for regularization and efficient solution of the IEs with either the entire-domain or subdomain basis functions.

Another approach intimately related to the Kummer method, the so-called "line-by-line" technique, provides an efficient means for calculating the periodic GF. The spectral summation is used here in successive lines of sources, while a spatial summation is carried out to add up the contributions of successive lines [29,85–89]. This summation is carried out separately for each mode of the spectral sum, and convergence can be dramatically accelerated with the help of the Shanks and Levin-T transforms. This approach can be regarded as a reformulation of the Kummer method outlined above. Indeed, in this case, the Ω_3 term in Equation 5.54 is simply replaced by the summation of the terms corresponding to propagating cylindrical waves radiated by successive lines of sources. In other words, Ω_1 is extended to propagating modes by the new expression for Ω_3, which reads

$$\Omega_3 = \frac{1}{4jb} \sum_{\substack{n \\ |k_{y,n}|<k}} e^{-jk_{y,n}y} \sum_{\substack{m=-\infty \\ m\neq 0}}^{\infty} e^{-jmk_{x,0}a} H_0^{(2)}\left(\sqrt{(k^2 - k_{y,n}^2)(z^2 + |x - ma|^2)}\right) \tag{5.58}$$

where the inner sum can be accelerated to obtain an exponentially convergent series, as long as the source spacings are smaller than half a wavelength. In this new formulation, Equation 5.53 describes the field radiated by the closest line of sources, whereas Equations 5.52 and 5.58, both amenable to exponentially converging series with the help of the Levin accelerator, correspond to evanescent and propagating cylindrical waves radiated by the other lines of sources.

5.5 Illustrative Numerical Examples

In this section, we provide two illustrative examples of efficient simulations of periodic structures by the MoM: one is composed of dielectric spheres, the other one is formed by apertures in conducting screens in a layered medium. Subdomain basis functions are used for the former structure, and entire-domain basis functions are employed for apertures.

5.5.1 Arrays of Spheres, Using Subdomain Basis Functions

In this example, the surface equivalence principle outlined in Section 5.3.1 has been exploited with the "continuity" formulation, while the GF computation is based on the line-by-line approach presented at the end of Section 5.4.1. Simulations have been carried out for transmission of plane waves through an infinitely periodic dense array of spheres with several values of the dielectric constant. The mesh of the sphere making out the unit cell contains 612 RWG [13] basis functions. The sphere radius is 2 cm and the size of the square unit cell along the x and y axes is 4.2 cm. The magnitudes of transmission (T) and reflection (R) coefficients for normal incidence are shown in Figure 5.6, along with the sum of their squared magnitudes $|R|^2 + |T|^2$ that should equal unity (check of energy conservation). The bottom plot shows that the energy conservation is excellent: in most cases, the value of $|R|^2 + |T|^2$, expressed in dB, does not exceed a few hundredths of a dB, except for the case of $\epsilon_r = 10$ and $\lambda < 40$ cm, because in this case the domain of the basis functions $\mathbf{\Lambda}_m$ is not much smaller than the wavelength λ in the dielectric medium (in particular, it is larger than $\lambda/12.5$ when $\lambda = 40$ cm). The total computation time for each frequency point, on a 2.5 GHz desktop computer, is about 7.5 min (24 s for the tabulation of the GF and its gradients, 7 min for filling the MoM matrix, and 6 s for solution of the system of equations). It should be noted that when the unit cells are not too complex (fewer than 1500–2000

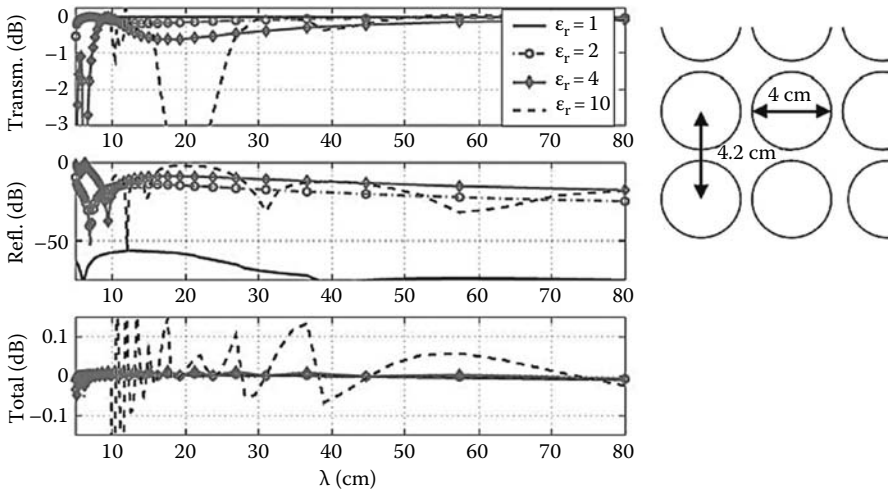

FIGURE 5.6 Reflection R (middle) and transmission T (top) coefficients through a layer of arrayed dielectric spheres. Spheres: various permittivities; 612 RWG basis functions; diameter = 4.0 cm; period = 4.2 cm. Bottom: Total = $|R|^2 + |T|^2$ for testing the conservation of energy. (From Dardenne, X. and Craeye, C., *IEEE Trans. Antennas Propagat.*, 56, 2372, 2008.)

basis functions), important time savings (a factor between 5 and 10) can be achieved by interpolating the frequency dependence of the MoM matrix.

5.5.2 Arrays of Apertures, Using Entire-Domain Basis Functions

This example illustrates the application of Galerkin method (same basis and testing functions) with entire-domain basis functions (cf. Section 5.3.1). Reflectance and transmittance are calculated for an array of 2-D periodically spaced apertures of arbitrary shapes in stacked conducting screens. As the same periodicity in x and y directions is assumed in all layers, the problem is reduced to a single unit cell $(a \times b)$, which may contain several dissimilar apertures as shown in Figure 5.5. Each aperture is defined by its length $2L$ along the x-axis and variable width $[l^+(x) + l^-(x)]$ in the y direction. The screens are assumed to be infinitesimally thin and perfectly conducting. Finite thickness of the screens is also taken into account with the aid of the effective aperture dimensions [90] and the impedance boundary conditions can alternatively be used to model imperfect conductors.

The array is illuminated by a TE (S) or TM (P) polarized plane wave incident at an arbitrary angle θ to the z-axis, so that the y components of their electric fields, E_y, are perpendicular to the aperture's larger side $(2L)$ extended along the x direction. The array reflectance and transmittance are calculated by solving a system of IEs for unknown magnetic currents on the apertures as shown in Figure 5.3d. The IE with the periodic GF has been treated by Galerkin method with the entire-domain basis and test functions, which explicitly account for the field singularities at the aperture edges. This leads to a system of linear equations similar to Equation 5.25. The convergence of GF has been accelerated by the Kummer method as detailed in Section 5.4.1. Then, the convolutions of the singular part of GF with the basis and test functions have been evaluated analytically; that resulted in a rapidly convergent computational algorithm with controllable accuracy of the numerical solution (see details in [51]). The convergence tests have shown that for calculating the scattering parameters with the relative error less than 10^{-3}, two to four basis functions are sufficient for rectangular slots and six to eight basis functions are required for apertures with substantial width variations. The simulation time per frequency point for the two-layer array with dissimilar apertures (relative error less than 0.01) was

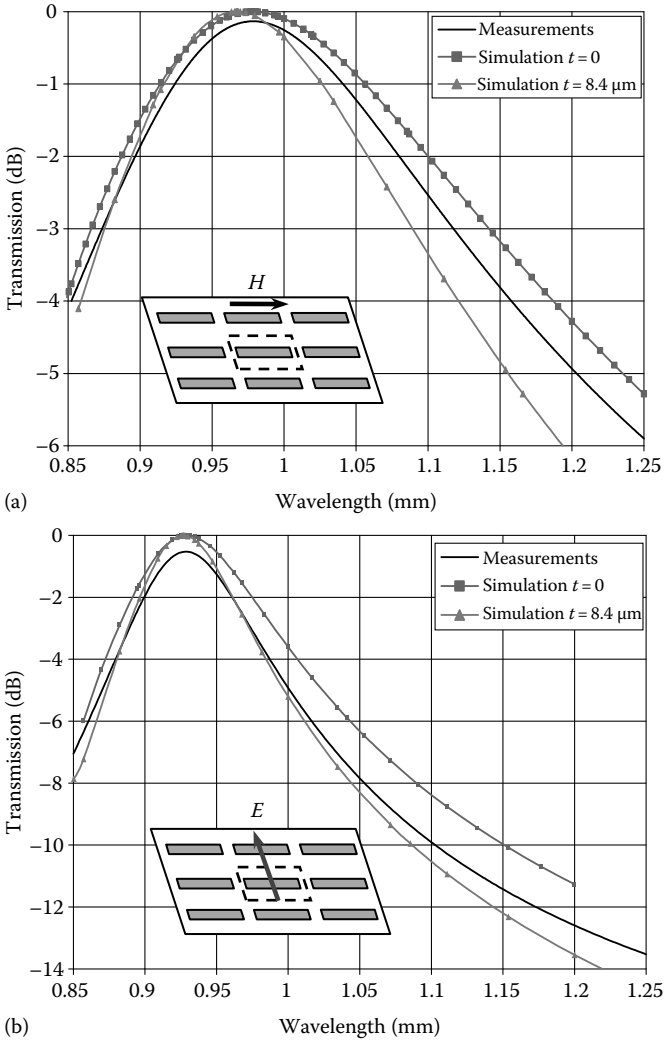

FIGURE 5.7 Comparison of measured and simulated transmittance for (a) TM and (b) TE waves incident at 45° on the slot arrays with the following dimensions: (a) $a = 0.452$ mm, $b = 0.540$ mm, $2L = 0.460$ mm, $2l = 0.016$ mm; (b) $a = 0.500$ mm, $b = 0.490$ mm, $2L = 0.458$ mm, $2l = 0.014$ mm. (From Schuchinsky, A., Zelenchuk, D., and Lerer, A., *J. Opt. A: P Appl. Opt*., 7(2), 8102, 2005.)

about 4 s when using a desktop PC with CPU Athlon XP 1600 and 400 KB RAM. Further details of the method and verification of the computational algorithm are discussed in [51].

The simulated transmission coefficients for the single layer slot arrays illuminated by TM (magnetic field in the conductor plane, see inset in Figure 5.7a) and TE (electric field in the conductor plane, see inset in Figure 5.7b) polarized plane waves incident at 45° are shown in Figure 5.7 in comparison with the measured transmittance [91–93]. The resonant wavelengths of the maximum transmittance calculated for infinitesimally thin conductors $(t = 0)$ are in excellent agreement with the measured results for both polarizations, and the simulated and measured characteristics closely follow each other in a broad range of wavelengths.

5.6 Eigenmode Analysis

Eigenmodes are waves that can propagate or resonate in the structure without distortion and interaction with other modes. This implies that they represent nontrivial solutions of the homogeneous system of algebraic equations arising from the MoM solution of the IE. Hence the determinant of the system matrix is zero, or equivalently, at least one of the matrix eigenvalues is zero. When applied to periodic structures, eigenmodes can be analyzed in the Brillouin space, appearing for particular values of phase shifts $k_{x,0}a$ and $k_{y,0}b$, that can be complex-valued for leaky modes or waves in lossy structures. Searching for zeros of the impedance matrix may be computationally intensive, since zero-searching must be carried out over a large 4-D domain. This calls for faster methods for computing the GF, for interpolating the MoM impedance matrix elements over the Brillouin space, etc. Successful implementations of the eigenmode analysis are described in [80,94–96], where, in the latter references, the procedure is accelerated thanks to a transformed IE formulation, which avoids root-searching methods by obtaining all eigenvalues at once. As an illustration, we can present the characterization of a double negative material [96], where the unit cell contains a wire section and a split-ring resonator. In Figure 5.8 the dispersion characteristics of the metamaterial are depicted (β represents the propagation wavenumber), first without the wires (solid line) and then with the wires and the split-ring resonator particle (dashed line). It can be seen that when the wires are added to the crystal, a new transparency band emerges in a frequency range previously forbidden. Furthermore, the slope of the curve is negative, showing that the mode exhibits backward propagation.

The interpretation of the resulting eigenmode loci (generally speaking, 3-D domains in a 4-D space) can be found in [97] for example. A more difficult task is the tracking of complex modes (i.e., eigenmodes with complex-valued wavenumbers $k_{x,0}$ and $k_{y,0}$, or with complex frequencies), which are important for the analysis of leaky wave structures and near field interactions. This involves evaluation of complex roots of complex-valued functions which require specialized algorithms for locating, bracketing, and refinement of the roots. The recent developments in computing complex zeros of analytical functions [98–100] provide efficient tools for analysis of such complex eigenmodes. Examples of accurate numerical complex mode analysis in periodic structures and metamaterials can be found in [26,101–103].

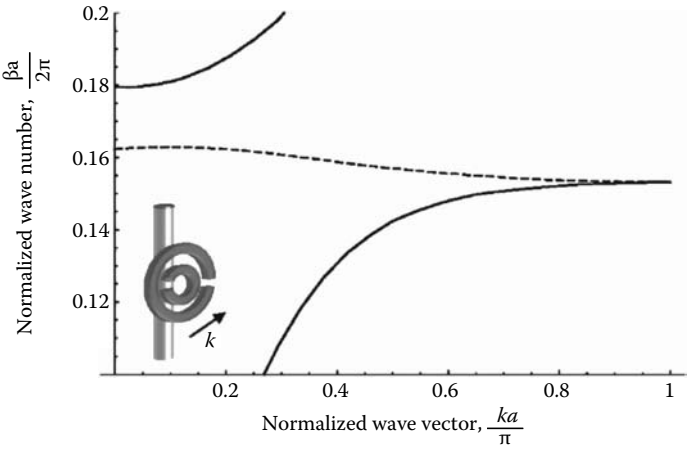

FIGURE 5.8 Dispersion characteristic of the medium with SRRs (solid line) and with SRRs and wires (dashed line). (From Silveirinha, M.G. and Fernandes, C.A., *IEEE Trans. Microwave Theory Tech.*, 52, 889, 2004.)

5.7 Array Scanning Method

The ASM (see [58,104–111] and references therein, and [112,113] for a time-domain implementation) allows for the determination of fields radiated by an isolated source in an infinite periodic structure. More details for arrays periodic in two directions are presented in Chapter 12 [58]. An explanation is provided here for the case of linear arrays of point sources along the x direction [110]. The point source at $\mathbf{r}' = 0$ can be alternatively represented by a continuous superposition of arrays of phased sources as

$$\delta(\mathbf{r}') = \delta(x')\,\delta(\mathbf{t}') = \delta(\mathbf{t}')\,\frac{1}{2\pi}\int_0^{2\pi}\sum_{m=-\infty}^{\infty}\delta(x'-ma)\,e^{-jm\psi}\,d\psi \tag{5.59}$$

where

a is the array spacing along x

$\delta(\mathbf{t}')$ is a Dirac delta function defined in the plane transverse to the x-axis and centered on it

The interelement phase shift equals $\psi = k_{x,0}a$ and varies over the Brillouin zone. Since this superposition property holds for the sources, it holds also for the generated fields. Thus, superimposing the electric field solutions, $\mathbf{E}^{\infty}$, from the infinite array of sources in the infinite periodic structure, we obtain the solution for one source at $\mathbf{r}' = 0$ only in the infinite-array structure:

$$\mathbf{E}(\mathbf{r} + na\hat{\mathbf{x}}) = \frac{1}{2\pi}\int_0^{2\pi}\mathbf{E}^{\infty}(\mathbf{r},\psi)\,e^{-jn\psi}\,d\psi \tag{5.60}$$

where $\mathbf{r} + na\hat{\mathbf{x}}$ is the coordinate of the observation point in the nth periodic cell and $\mathbf{r}$ lies within the reference unit cell (with $n = 0$). When, for numerical integration, the integral is approximated by a sum of P terms, the calculated field is the one produced by the original source at $\mathbf{r}' = 0$ plus the "images" repeated every P elements (aliasing phenomenon [58,111,114]). An estimate of the ASM numerical merit as compared to a standard plane-wave superposition for the field represented by a single source is discussed in [58,110]. When applied to 2-D periodic arrays [111], the ASM permits to determine the point-spread function (spatial impulse response), which corresponds to the field radiated by a point source through an infinite slab periodic in two directions. In [115], this technique has been used to estimate the point-spread function of a metamaterial composed of parallel wires. In three dimensions, the ASM enables the computation of fields radiated by localized sources in infinite periodic media.

5.8 Finite Arrays

In practice, periodic metamaterials will have finite size, generally limited to a few wavelengths. In view of the eigenmodes that may propagate within the structure, strong reflections at the edges of the array may take place and lead to a significantly different response of the finite structure [116,117], as compared to the infinite-array case. These effects need to be evaluated very quickly and, in doing so, the periodicity of the structure is, in general, exploited efficiently. Three main approaches are briefly outlined below.

5.8.1 Fast Multipole Methods

Fast multipoles are based on the observation that the free-space GF can be decomposed into a continuous spectrum of plane waves whose directions of propagation span the whole unit sphere. In this decomposition, the addition theorem for Bessel and Hankel functions plays a key role [118]. This decomposition leads to diagonalization of the operator standing for radiation from a given region

and testing by decomposition functions located in another, sufficiently distant, region. The required data are then the far-field patterns of basis functions and a translation operator, which depends on the relative positions of centroids of the groups. If the N basis functions are arranged into about $\sqrt{N}$ groups of about $\sqrt{N}$ basis functions, the testing by all basis functions of fields radiated from the whole current distribution can be carried out in order of $N^{3/2}$ operations instead of order N^2 [118]. When extended to a multilevel scheme, with a hierarchic decomposition of groups, the complexity asymptotically reduces to order $N \log_2 N$ [119,120]. This method has been successfully applied by different authors [121–124] to the fast simulation of fields in periodic structures. Advantage can be taken from the periodicity to reduce the amount of memory needed to store the patterns of basis functions and to compute preconditioners [121] that lead to accelerated convergence of iterative solvers based on Krylov subspace [125] methods.

5.8.2 The Fast Solver GIFFT

A new algorithm that combines the use of green's function (GF) interpolation (FFT) and fast Fourier transforms, GIFFT has been recently proposed in [126,127] to model large periodic structures of finite size. This method is similar to the adaptive integral method (AIM) [128] in the sense that it projects the solution domain onto a regular grid to enable the use of the FFT algorithm. The key difference is how the projections are done. In AIM, radiating basis and testing functions are replaced by a neighboring grid of approximately equivalent monopole sources, and the usual GF is used to compute the interactions between these groups of equivalent sources. In GIFFT, the GF is approximated on an interpolation grid, and the basis and testing function integrations are done in the usual manner using the interpolated GF. The method lends itself to efficiently handle large arrays while maintaining the generality of standard MoM. Instead of using field representation in the spectral domain as in FMM, GIFFT works entirely in the spatial domain and basis function interactions rely on point to point interactions, calculated with the proper environment GF. Therefore, multilayer GFs can be readily used in GIFFT as in the standard MoM [127].

5.8.3 Macro Basis Functions Approach

When complex unit cells of a particular artificial material, made of a periodic structure of finite extent, are considered, the solution of the IE may require a very large number of unknowns. Nevertheless, when the elements are smaller than the wavelength, which is always the case in metamaterials, the fields radiated by a given structure can be described with very few parameters [129,130]. Also, in passive periodic structures, fields (or equivalent currents) that can be excited on a given cell have relatively few physical degrees of freedom [131] for most types of excitations. In other words, the physically possible discretized solutions belong to a relatively small subspace of the space representing all possible mathematical solutions (with dimension equal to the number of unknowns). An alternative basis set for this physical subspace can be formed by the solution for a given unit cell under a few illuminations [131–134]. A relatively open problem then consists of finding a systematic way to construct such a basis. Several methods developed for antenna array applications and for metamaterials have been proposed in the literature. The first consists of exciting one cell from a number of directions [133] or from point sources located on a surface enclosing the structure [134]. The singular value decomposition (SVD) procedure then enables the reduction of the number of generated MBFs, based on their linear dependence below a certain threshold. Another method for MBF generation is based on the illumination of an isolated element (primary), which in turn, illuminates other elements (secondaries) of the array [135]. Alternative methods are based on the solutions obtained with small arrays (e.g., 3×3 arrays) [122]. Finally, another approach starts from the superposition of infinite-array solutions [114] for a given set of phasings along the periodic directions, $k_{x,0}a$ and $k_{y,0}b$, which finds its justification in the ASM. Reference [133] shows how to obtain the reduced system of

equations, whereas an accelerated technique which avoids the computation of the original system of equations, based on multipole decompositions, is described in [136].

An example for the use of MBFs in the analysis of finite metamaterials is given below [137]. The analyzed structure is composed of $3 \times 4 \times 3$ unit cells along the x, y, and z directions, respectively, as shown in the insert of Figure 5.10. Every unit cell of the array is made of the combination of a metallic (perfect electric conductor) split-ring resonator and strip, in order to realize a negative-index material [138]. Each unit cell occupies a cube with sides of 2.6 cm and is meshed with 94 RWG [13] unknowns. The array is illuminated, on one side, by a dipole fed with a delta gap excitation. On the other side, a receiving dipole is placed, in order to evaluate the transmission coefficient of the array, as shown in the inset in Figure 5.10. Both dipoles are short in comparison to the wavelength, and have a height of 1 cm.

The transmission coefficient versus frequency is shown in Figure 5.10, and it is defined as the ratio between the currents flowing at the center of the receiving and transmitting dipoles, in the presence of the metamaterial, normalized with respect to the same ratio in the absence of the metamaterial. The transmission coefficient is computed by simulating the structure in three different manners: by using MBFs obtained from a $2 \times 3 \times 2$-array solution, by using MBFs obtained from the infinite-array solution, and by a standard MoM procedure (solved with gaussian elimination). The latter solution is used as a reference solution to calculate the absolute error of the transmission obtained with the MBF methods and requires to solve a system of equations involving 3384 unknowns.

The first method based on using the MBFs from the finite-array solution represents a simple way—but also computationally expensive—for obtaining the MBFs [139]. It consists of analyzing via a standard MoM a small-scale interconnected structure, made of $2 \times 3 \times 2$ unit cells, excited by only one plane wave. The MBFs are extracted from the currents induced in each unit cell of the structure.

In the second method, based on using the MBFs from the infinite-array solution (see Figure 5.9), the primary MBF corresponds to the infinite-array solution obtained with a plane-wave excitation. The secondary MBFs [135] are obtained by placing the primary MBF in a small-scale ($2 \times 3 \times 2$ unit cells) interconnected structure and by computing on the neighboring elements, taken individually, the currents induced by the fields radiated by the primary MBF. The advantages of this approach are summarized here: (1) only two MoM impedance matrices need to be inverted, corresponding to the infinite-array and the single-element cases, respectively, and (2) the unit cells connecting to the primary MBF solution inherently exhibit continuous currents across the electric connection.

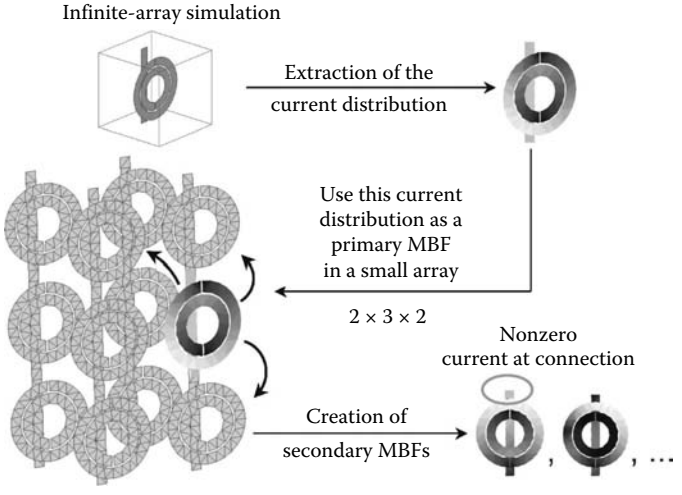

FIGURE 5.9 Scheme for creating a set of MBFs from an infinite-array solution.

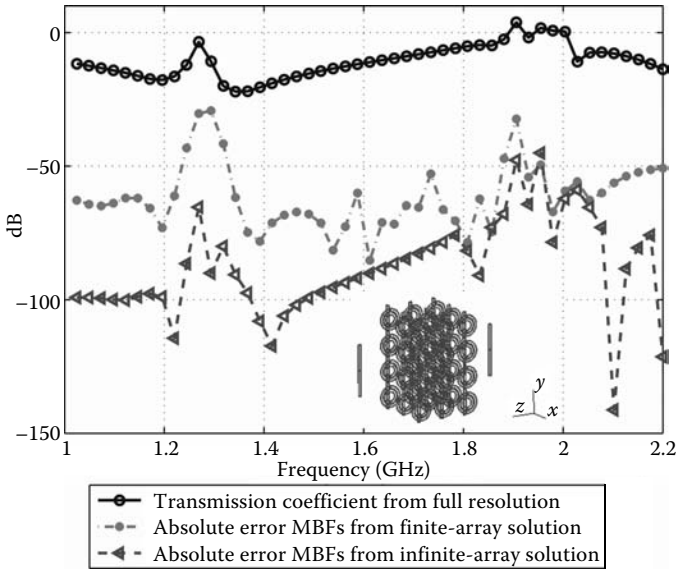

FIGURE 5.10 Transmission coefficient, as defined in Section 5.8.3, for a periodic metamaterial (see inset) made of $3 \times 4 \times 3$ unit cells.

Consequently, this method is faster and gives better results than the previous one, especially when connections are present between the unit cells of the studied structure.

Both MBF approaches allows us to reduce dramatically the number of unknowns of the complete system. Indeed, since in both methods 12 MBFs are obtained, the number of unknowns is reduced from 3384 to 432.

Figure 5.10 compares the solutions for the transmission coefficient obtained with the two MBF methods. The top line corresponds to the transmission coefficient obtained via the standard MoM with gaussian elimination for the $3 \times 4 \times 3$ array. Overall, the presence of the metamaterial leads to a certain field blockage (transmission coefficient below zero). Since the metamaterial structure is not large, compared to the wavelength, that blockage is limited. The peak near 1.9 GHz is believed to correspond to the negative-index region, where a pass-band is expected. We have verified that the peak around 1.3 GHz is related to the resonance of the wires with finite length. The two other curves represent, on the same dB scale, the absolute error in evaluating the transmission coefficient obtained by solving the problem with the two MBF-based approaches described above; the error is computed as the magnitude of the difference between the transmission coefficients obtained with the MBF-based formulation and the standard MoM solution. The curve with bullets shows the error when using the MBFs obtained from the small finite-array analysis. The curve with triangles shows the error when using the MBFs obtained from the infinite-array solution. It can be seen clearly that the error from the latter method is smaller, i.e., near −60 dB. The two methods based on the use of MBFs are much faster than the standard MoM, since they require mainly the solution of unit-cell problems only and the solution of the whole scattering problem with just a few unknowns per unit cell.

References

1. R.F. Harrington, *Field Computation by Moment Methods*. New York: Wiley-IEEE Press, 1993.
2. D.R. Wilton, Computational Methods, *Scattering: Scattering and Inverse Scattering in Pure and Applied Science*, vol. 1, chapter 1.5.5, E.R. Pike and P.C. Sabatier, Eds., Amsterdam, the Netherlands: Academic Press/Elsevier, pp. 316–365, 2002.

3. A.F. Peterson, S.L. Ray, and R. Mittra, *Computational Methods for Electromagnetics*. New York: IEEE Press, 1998.
4. B. Kolundzija and A. Djordjevic, *Electromagnetic Modeling of Composite Metallic and Dielectric Structures*: Norwood: MA Artech House, 2002.
5. R.F. Harrington, *Time-Harmonic Electromagnetic Fields*. New York: McGraw-Hill, 1961.
6. D.H. Schaubert, D.R. Wilton, and A.W. Glisson, A tetrahedral modeling method for electromagnetic scattering by arbitrarily shaped inhomogeneous dielectric bodies, *IEEE Trans. Antennas Propagat*., AP-32, 1, 77–85, January 1984.
7. N.A. Ozdemir and J.F. Lee, A nonconformal volume integral equation for electromagnetic scattering from penetrable objects, *IEEE T. Magn*., 43, 1369–1372, April 2007.
8. W.-B. Ewe, H.-S. Chu, and E.-P. Li, Volume integral equation analysis of surface plasmon resonance of nanoparticles, *Opt. Express*, 15, 18200–18208, December 2007.
9. R.E. Collin, *Field Theory of Guided Waves*, 2nd Ed. New York: IEEE Press, 1991, 864 pp.
10. A.J. Poggio and E.K. Miller, *Integral Equation Solutions of Three-Dimensional Scattering Problems*. Oxford, U.K.: Permagon, 1973, Chapter 4.
11. A. Guissard, On the surface field integral equations, *IEEE Trans. Education*, 46, 486–496, November 2003.
12. J.R. Mosig, Integral Equation Technique, *Numerical Techniques for Microwave and Millimeter Wave Passive Structures*, New York: John Wiley, 1989, Chapter 3.
13. S.M. Rao, D.R. Wilton, and A.W. Glisson, Electromagnetic scattering by surfaces of arbitrary shape, *IEEE Trans. Antennas Propagat*., 30, 409–418, May 1982.
14. M. Djordjevic and B. Notaros, Double higher order method for surface integral equation modeling of metallic and dielectric antennas and scatterers, *IEEE Trans. Antennas Propagat*., 52, 2118–2129, August 2004.
15. L.V. Kontorovich and V.I. Krylov, *Approximated Methods for Higher Analysis*, 4th Ed., translated by C.D. Bernster. New York: John Wiley & Sons, 1959, Chapter IV.
16. D.S. Jones, A critique of variational method in scattering problems, *IRE Trans*., AP-4, 3, 297–301, 1956.
17. T.K. Wu and L.L. Tsai, Scattering from arbitrarily-shaped lossy dielectric bodies of revolution, *Radio Sci*., 12, 5, 709–718, 1977.
18. J.R. Mautz and R.F. Harrington, Electromagnetic scattering from a homogeneous material body of revolution, *AEU Electron. Commun*., 33, 71–80, 1979.
19. P. Yla-Oijala and M. Taskinen, Well-conditioned Muller formulation for electromagnetic scattering by dielectric objects, *IEEE Trans. Antennas Propagat*., 53, 3316–3323, October 2005.
20. S.M. Rao and D.R. Wilton, E-field, H-field, and combined field solution for arbitrarily shaped three-dimensional dielectric bodies, *Electromagnetics*, 10, 4, 407–421, 1990.
21. D.R. Wilton, S.M. Rao, A.W. Glisson, D.H. Schaubert, O.M. Al-Bundak, and C.M. Butler, Potential integrals for uniform and linear source distributions on polygonal and polyhedral domains, *IEEE Trans. Antennas Propagat*., 32, 176–281, March 1984.
22. R.E. Hodges and Y. Rahmat-Samii, The evaluation of MFIE integrals with the use of vector triangle basis functions, *Microwave Opt. Technol. Lett*., 14, 1, 9–14, January 1997.
23. M.A. Khayat, D.R. Wilton, and P.W. Fink, An improved transformation and optimized sampling scheme for the numerical evaluation of singular and near-singular potentials, *IEEE Antennas Wireless Propagat. Lett*., 7, 377–380, 2003.
24. M.A. Khayat and D.R. Wilton, Numerical evaluation of singular and near-singular potential integrals, *IEEE Trans. Antennas Propagat*., 53, 10, 3180–3190, 2005.
25. C. Craeye, A.G. Tijhuis, and D.H. Schaubert, An efficient MoM formulation for finite-by-infinite arrays of two-dimensional antennas arranged in a three-dimensional structure, *IEEE Trans. Antennas Propagat*., 52, 271–282, January 2004.

26. P. Baccarelli, C. Di Nallo, S. Paulotto, and D.R. Jackson, A full-wave numerical approach for modal analysis of 1-D periodic microstrip structures, *IEEE Trans. Microwave Theory Tech*., 54, 1350–1362, April 2006.
27. B.C. Usner, K. Sertel, and J.L. Volakis, Doubly periodic volume-surface integral equation formulation for modelling metamaterials, *IET Microwave Antennas Propagat*., 1, 1, 150–157, February 2007.
28. P. Yla-Oijala, M. Taskinen, and J. Sarvas, Surface integral equation method for general composite metallic and dielectric structures with junctions, *Prog. Electromagnetics Res. (PIER)*, 52, 81–108, 2005.
29. X. Dardenne and C. Craeye, Method of Moments simulation of infinitely periodic structures combining metal with connected dielectric objects, *IEEE Trans. Antennas Propagat*, 56, 2372–2380, August 2008.
30. C.-T. Tai, *Dyadic Green Functions in Electromagnetic Theory*. New York: IEEE Press, 1993, pp. 343.
31. T. Itoh and R. Mittra, Spectral-domain approach for calculating the dispersion characteristics of microstrip lines, *IEEE Trans. Microwave Theory Tech*., 21, 496–499, July 1973.
32. D.M. Pozar, Input impedance and mutual coupling of rectangular microstrip antennas, *IEEE Trans. Antennas Propagat*., AP-30, 6, 1191–1196, November 1982.
33. G.F. Zargano, A.M. Lerer, V.P. Lyapin, and G.P. Sinyavskyi, *Transmission lines of complex cross-section*, (in Russian), Rostov-on-Don, USSR, Rostov State University Press, 1983, p. 320.
34. R.N. Jansen, The spectral domain approach for microwave integrated circuits, *IEEE Trans. Microwave Theory Tech*., 33, 10, 1043–1056, October 1985.
35. C.A. Olley and T. Rozzi, Systematic characterisation of the spectrum of unilateral finline, *IEEE Trans. Microwave Theory Tech*., 34, 11, 1147–1156, November 1986.
36. F. Medina, M. Horno, and H. Baudrand, Generalized spectral analysis of planar lines on layered media including uniaxial and biaxial dielectric substrates, *IEEE Trans. Microwave Theory Tech*., 37, 4, 504–511, March 1989.
37. T. Uwaro and T. Itoh, Spectral domain approach, *Numerical Techniques for Microwave and Millimeter Wave Passive Structures*, New York: John Wiley, 1989, Chapter 5.
38. F. Mesa, R. Marques, and M. Horno, An efficient numerical spectral domain method to analyze a large class of nonreciprocal planar transmission lines. *IEEE Trans. Microwave Theory Tech*., 40, 8, 1630–1641, August 1992.
39. J.C. Coetzee and J.A.G. Malherbe, Efficient matrix element calculations for the spectral domain method applied to symmetrical multiconductor transmission lines, *Appl. Computat. Electromagn. Soc. J*., 9, 1, 40–50, March 1994.
40. G. Cano, F. Messa, F. Medina, and M. Horno, Systematic computation of the modal spectrum of boxed microstrip, finline, and coplanar waveguides via an efficient SDA, *IEEE Trans. Microwave Theory Tech*., 43, 866–872, April 1995.
41. S. Amari, J. Bornemann, and R. Vahldieck, Accurate analysis of scattering from multiple waveguide discontinuities using the coupled integral-equation technique, *J. Electromag. Waves Appl*., 10, 1623–1644, December 1996.
42. S. Amari, J. Bornemann, and R. Vahldieck, Application of a coupled-integral-equations technique to ridged waveguides, *IEEE Trans. Microwave Theory Tech*., 44, 12, 2256–2264, December 1996.
43. A.I. Nosich, The method of analytical regularization in wave-scattering and eigenvalue problems: foundations and review of solutions, *IEEE Antennas Propag. Mag*., 41, 3, 34–49, June 1999.
44. M.J. Friere, F. Mesa, C. di Nallo, D.R. Jackson, and A.A. Oliner. Spurious transmission effects due to the excitation of the bound mode and the continuous spectrum on stripline with an air gap, *IEEE Trans. Microwave Theory Tech*., 47, 12, 2493–2502, December 1999.
45. C.K. Aanandan, P. Debernardi, R. Orta, R. Tascone, and D. Trinchero, Problem-matched basis functions for moment method analysis—an application to reflection gratings, *IEEE Trans. Antennas Propagat*., 48, 1, 35–40, January 2000.

46. F. Mesa, D.R. Jackson, and M.J. Freire. High-frequency leaky-mode excitation on a microstrip line, *IEEE Trans. Microwave Theory Tech*., 49, 12, 2206–2215, December 2001.
47. A.M. Lerer and A.G. Schuchinsky, Full-wave analysis of three-dimensional planar structures, *IEEE Trans. Microwave Theory Tech*., 41, 2002–2015, November 1993.
48. R. Orta, R. Tascone, and R. Zich, Efficient choice of basis functions in moment method analysis of frequency-selective surfaces, *Electronics Lett*., 23, 11, 586–587, May 1987.
49. R. Orta, R. Tascone, and R. Zich, A unified formulation for the analysis of general frequency selective surfaces, *Electromagnetics*, 5, 4, 307–329, October/December 1985.
50. R. Orta, I.P. Savi, and R. Tascone, Numerical Green's function technique for the analysis of screens perforated by multiply connected apertures, *IEEE Trans. Antennas Propagat*., 44, 6, 765–776, June 1996.
51. A.G. Schuchinsky, D. Zelenchuk, A.M. Lerer, and R. Dickie, Full-wave analysis of layered aperture arrays, *IEEE Trans. Antennas Propagat*., 54, 490–502, February 2006.
52. L.B. Felsen and N. Marcuvitz, *Radiation and Scattering of Waves*. New York: IEEE Press, 1994.
53. W.C. Chew, *Waves and Fields in Inhomogeneous Media*. New York: Van Nostrand Reinhold, 1990.
54. K.A. Michalski and J.R. Mosig, Multilayered media Green's functions in integral equation formulations, *IEEE Trans. Antennas Propagat*., 45, 508–519, March 1997.
55. M. Vrancken, G.A.E. Vandenbosch, Semantics of dyadic and mixed potential field representation for 3-D current distributions in planar stratified media, *IEEE Trans. Antennas Propagat*., 51, 2778–2787, October 2003.
56. D.L. del Ro, J.R. Mosig, On the interaction between electric and magnetic currents in stratified media, *IEEE Trans. Antennas Propagat*., AP-52, 8, 2100–2108, August 2004.
57. J. Blackburn and L.R. Arnaut, Numerical convergence in periodic method of moments analysis of frequency-selective surfaces based on wire elements, *IEEE Trans. Antennas Propagat*., 53, 3308–3315, October 2005.
58. F. Capolino, D.R. Jackson, and D.R. Wilton, Field representations in periodic artificial materials excited by a source, *Theory and Phenomena of Metamaterials*. Florida: Taylor & Francis, 2009, Chapter 12.
59. C.M. Linton, The Green's function for the two-dimensional Helmholtz equation in periodic domains, *J. Eng. Math*., 33, 377–402, 1998.
60. N. Guérin, S. Enoch, and G. Tayeb, Combined method for the computation of the doubly periodic Green's function, *J. Electromagn. Waves Appl*., 15, 2, 205–221, February 2001.
61. F. Capolino, D.R. Wilton, and W.A. Johnson, Efficient computation of the 2D Green's function for 1D periodic structures using the Ewald method, *IEEE Trans. Antennas Propagat*., 53, 2977–2984, September 2005.
62. F. Capolino, D.R. Wilton, and W.A. Johnson, Efficient computation of the 3D Green's function for the Helmholtz operator for a linear array of point sources using the Ewald method, *J. Comput. Phys*., 223, 250–261, April 2007.
63. S. Oroskar, D.R. Wilton, and D.R. Jackson, Efficient computation of the 2D periodic Green's function using the Ewald method, *J. Computational Phys*., 219, 899–911, 2006.
64. F.T. Celepcikay, D.R. Wilton, D.R. Jackson, and F. Capolino, Numerical evaluation of 1D and 2D periodic Green's functions using the Ewald method, *Radio Sci*., 43, 2008.
65. G. Valerio, P. Baccarelli, P. Burghignoli, and A. Galli, Comparative analysis of acceleration techniques for 2-D and 3-D Green's functions in periodic structures along one and two directions, *IEEE Trans. Antennas Propagat*., 55, 1630–1643, June 2007.
66. M.G. Silveirinha and C.A. Fernandes, A new acceleration technique with exponential convergence rate to evaluate periodic Green's functions, *IEEE Trans. Antennas Propagat*., 53, 1, 347–355, January 2005.

67. D. Shanks, Non-linear transformations of divergent and slowly convergent sequences, *J. Math. Phys.*, 34, 142, 1955.
68. S. Singh and R. Singh, Application of transforms to accelerate the summation of periodic free-space Greens functions, *IEEE Trans. Microwave Theory Tech.*, 38, 11, 1746–1748, November 1990.
69. S. Singh and R. Singh, On the use of Shankss transform to accelerate the summation of slowly converging series, *IEEE Trans. Microwave Theory Tech.*, 39, 3, 608–610, March 1990.
70. S. Singh and R. Singh, Efficient computation of the free-space periodic Greens function, *IEEE Trans. Microwave Theory Tech.*, 39, 7, 1226–1229, July 1991.
71. S. Singh and R. Singh, On the use of Levin's T-transform in accelerating the summation of series representing the free-space periodic Green's functions, *IEEE Trans. Microwave Theory Tech.*, 41, 884–886, 1993.
72. P.P. Ewald, Die berechnung optischer und elektrostatischen gitterpotentiale, *Ann. der Phys.*, 64, 253–287, 1921. Translated by A. Cornell, Atomics International Libray, 1964.
73. K.E. Jordan, G.R. Richter, and P. Sheng, An efficient numerical evaluation of the Green's function for the Helmholtz operator on periodic structures, *J. Comput. Phys.*, 63, 222–235, 1986.
74. A.W. Mathis, and A.F. Peterson, A comparison of acceleration procedures for the two-dimensional periodic Green's function, *IEEE Trans. Antennas Propagat.*, 44, 567–571, 1996.
75. V.G. Papanicolaou, Ewalds method revisited: Rapidly convergent series representations of certain Greens functions, *J. Comp. Anal. Appl.*, 1, 1, 105114, January 1999.
76. A. Kustepeli and A.Q. Martin, On the splitting parameter in the Ewald method, *IEEE Microwave and Guided Wave Lett.*, 10, 168–170, 2000.
77. A. Moroz, Exponentially convergent lattice sums, *Opt. Lett.*, 26, 1119–1121, 2001.
78. T.F. Eibert, J.L. Volakis, D.R. Wilton, and D.R. Jackson, Hybrid FE/BI modeling of 3D doubly periodic structures utilizing triangular prismatic elements and an MPIE formulation accelerated by the Ewald transformation, *IEEE Trans. Antennas Propagat.*, 47, 843–850, May 1999.
79. A. Moroz, Quasi-periodic Greens functions of the Helmholtz and Laplace equations, *J. Phys. A: Math. Gen.*, 39, 11247–11282, 2006.
80. I. Stevanovic and J.R. Mosig, Periodic Green's function for skewed 3-D lattices using the Ewald transformation, *Microwave Opt. Technol. Lett.*, 49, 1353–1357, June 2007.
81. G. Kobidze, B. Shanker, and D.P. Nyquist, Efficient integral-equation-based method for accurate analysis of scattering from periodically arranged nanostructures, *Phys. Rev. E*, 72, 056702, 2005.
82. S.Singh, W.F. Richards, J.R. Zinecker, and D.R. Wilton, Accelerating the convergence of series representing the free space periodic Green's functions, *IEEE Trans. Antennas Propagat.*, AP-38, 5, 1958–1962, December 1990.
83. O. Malyuskin, V.F. Fusco, and A.G. Schuchinsky, Convergence acceleration of the double periodic Green's function for the analysis of thin wire arrays, *IET Microwaves, Antennas Propagat.*, 2, 410–417, September 2008.
84. M.E. Veysoglu, H. Yueh, R. Shin, and J. Kong, Polarimetric passive remote sensing of periodic surfaces, *J. Electromagn. Waves Appl.*, 5, 3, 267–280, March 1991.
85. B.A. Munk, *Frequency Selective Surfaces: Theory and Design*, New York: Wiley, 2000.
86. C. Craeye, B. Smolders, D. Schaubert, and A. Tijhuis, An efficient computation scheme for the free space Green's function of a two-dimensional semi-infinite phased array, *IEEE Trans. Antennas Propagat.*, 51, 766–771, 2003.
87. C. Craeye and F. Capolino, Accelerated computation of the free space Green's function of semi-infinite phased arrays of dipoles, *IEEE Trans. Antennas Propagat.*, 54, 3, 1037–1040, 2006.
88. J.C. Vardaxoglou, *Frequency Selective Surfaces: Analysis and Design*, London, United Kingdom: Research Studies Press Ltd., 1997.
89. X. Dardenne, Method of Moments simulation of infinite and finite periodic structures and application to high gain metamaterial antennas, Ph.D. thesis, Université catholique de Louvain, Louvain-la-Neuve, March 2007.

90. Kh.L. Garb, I.B. Levinson, and P.Sh. Fridberg, Effect of wall thickness in slot problems of electrodynamics, *Radio Eng. Electron. Phys.* (USSR), 13, 1888–1896, December 1968.
91. A. Schuchinsky, D. Zelenchuk, and A. Lerer, Enhanced transmission in microwave arrays of periodic sub-wavelength apertures, *J. Opt. A: Pure Appl. Opt*., 7, 2, S102–S109, February 2005.
92. R. Dickie, R. Cahill, H.S. Gamble, V.F. Fusco, A.G. Schuchinsky, and N. Grant, Spatial demultiplexing in the sub-mm wave band using multilayer free-standing frequency selective surfaces, *IEEE Trans. Antennas Propagat*., 53, 6, 1904–1911, June 2005.
93. Y. Vardaxoglou, R. Lee, and A. Chauraya, Frequency selective surface (FSS) and electromagnetic bandgap (EBG) theory basics, *Theory and Phenomena of Metamaterials*, Florida: Taylor & Francis, 2009, Chapter 30.
94. M. Bozzi, S. Germani, L. Minelli, L. Perregrini, and P. de Maagt, Efficient calculation of the dispersion diagram of planar electromagnetic band-gap structures by the MoM/BI-RME method, *IEEE Trans. Antennas Propagat*., 53, 29–35, January 2005.
95. I. Nefedov, X. Dardenne, and C. Craeye, Backward waves in a waveguide filled with wire media, Special Issue on Metamaterials of Microwaves Optical and Technology Letters, 48, 2560–2564, Dec. 2006.
96. M.G. Silveirinha and C.A. Fernandes, A hybrid method for the efficient calculation of the band structure of 3-D metallic crystals, *IEEE Trans. Microwave Theory Tech*., 52, 889–902, March 2004.
97. S. Enoch, S.G. Tayeb, and B. Gralak, The richness of the dispersion relation of electromagnetic bandgap materials, *IEEE Trans. Antennas Propagat*., 51, 2659–2666, October 2003.
98. P. Kravanja and M. van Barel, A derivative-free algorithm for computing zeros of analytic functions, *Computing*, 63, 69–78, 1999.
99. P. Kravanja, T. Sakurai, and M. van Barel, Error analysis of a derivative-free algorithm for computing zeros of holomorphic functions, *Computing*, 70, 335–347, 2003.
100. C.J. Gillan, A. Schuchinsky, and I. Spence, Computing zeros of analytic functions in the complex plane without using derivatives, *Computer Phys. Commun.*, 175, 4, 304–313, August 2006.
101. P. Baccarelli, P. Burghignoli, F. Frezza, A. Galli, P. Lampariello, G. Lovat, and S. Paulotto, Modal properties of surface and leaky waves propagating at arbitrary angles along a metal strip grating on a grounded slab, *IEEE Trans. Antennas Propagat*., 53, 1, 36–46, January 2005.
102. P. Baccarelli, S. Paulotto, D.R. Jackson, and A.A. Oliner, A new Brillouin dispersion diagram for 1-D periodic printed structures, *IEEE Trans. Microwave Theory Tech*., 55, 7, 1484–1495, July 2007.
103. P. Burghignoli, G. Lovat, F. Capolino, D.R. Jackson, and D.R. Wilton, Modal propagation and excitation on a wire-medium slab, *IEEE Trans. Microwave Theory Tech*., 56, 5, 1112–1124, May 2008.
104. R. Sigelmann, A. Ishimaru, Radiation from periodic structures excited by an aperiodic source, *IEEE Trans. Antennas Propagat*., 13, 3, 354–364, May 1965.
105. R. Mailloux, Antenna and wave theories of infinite yagi-uda arrays, *IEEE Trans. Antennas Propagat*., 13, 4, 499–506, July 1965.
106. C.P. Wu and V. Galindo, Properties of a phased array of rectangular waveguides with thin walls, *IEEE Trans. Antennas Propagat*., 14, 163–173, March 1966.
107. B.A. Munk and G.A. Burrell, Plane-wave expansion for arrays of arbitrarily oriented piecewise linear elements and its application in determining the impedance of a single linear antenna in a lossy half-space, *IEEE Trans. Antennas Propagat*., 27, 331–343, May 1979.
108. H.-Y.D. Yang, Theory of antenna radiation from photonic band-gap materials source, *Electromagnetics*, 19, 3, 255–276, 1999.
109. C. Caloz, A.K. Skrivervik, and F.E. Gardiol, Comparison of two methods for the computation of Green's functions in photonic bandgap materials: The eigenmode-expansion method and the phased-array method, *Microwave Opt. Technol. Lett*., 27, 5, 323–330, December 2000.

110. F. Capolino, D.R. Jackson, and D.R. Wilton, Fundamental properties of the field at the interface between air and a periodic artificial material excited by a line source, *IEEE Trans. Antennas Propagat.*, 53, 3030–3034, January 2005.
111. F. Capolino, D.R. Jackson, D.R. Wilton, and L.B. Felsen, Comparison of methods for calculating the field excited by a dipole near a 2-D periodic material, *IEEE Trans. Antennas Propagat.*, 55, 1644–1655, June 2007.
112. Q. Rui, C. Ji, F. Capolino, D.R. Jackson, and D.R. Wilton, ASM-FDTD: A technique for calculating the field of a finite source in the presence of an infinite periodic artificial material, *IEEE Microwave Wireless Components Lett.*, 17, 4, 271–273, April 2007.
113. J. Chen, F. Yang, and R. Qiang, FDTD method for periodic structures, *Theory and Phenomena of Metamaterials*. Florida: Taylor & Francis, 2009, Chapter 6.
114. C. Craeye and R. Sarkis, Finite array analysis through combination of macro basis functions and array scanning methods, *ACES J*, 23, 3, September 2008.
115. X. Radu, X. Dardenne, and C. Craeye, Efficient analysis of the canalization effect obtained with a Fabry-Perot wire medium, *Proceedings of First International Congress on Advanced Electromagnetic Materials in Microwaves and Optics*, Rome, October 2007.
116. A.M. van de Water, B.P. de Hon, M.C. van Beurden, and A.G. Tijhuis, Linear embedding via Green's operators: A modelling technique for finite electromagnetic band-gap structures, *Phys. Rev. E*, 72, 056704, 1–11, 2005.
117. D.S. Janning and B.A. Munk, Effects of surface waves on the currents of truncated periodic arrays, *IEEE Trans. Antennas Propagat.*, 50, 1254–1265, September 2002.
118. R. Coifman, V. Rokhlin, and S. Wandzuraz, The fast multipole method for the wave equation: a pedestrian prescription, *IEEE Antennas Propagat. Mag.*, 35, 7–12, June 1993.
119. W.C. Chew, J. Jian-Ming, C.-C. Lu, E. Michielssen, and J.M. Song, Fast solution methods in electromagnetics, *IEEE Trans. Antennas Propagat.*, 45, 3, 533–543, March 1997.
120. W.C. Chew, J.-M. Jin, E. Michielssen, and J.M. Song, *Fast and Efficient Algorithm in Computational Electromagnetics*, Norwood, MA: Artech House, 2001.
121. E. Ubeda, J.M. Rius, and J. Romeu, Preconditioning techniques in the analysis of finite metamaterial slabs, *IEEE Trans. Antennas Propagat.*, 54, 1, 265–268, January 2006.
122. W.B. Lu, T.J. Cui, and H. Zhao, Acceleration of fast multipole method for large-scale periodic structures with finite sizes using sub-entire-domain basis functions, *IEEE Trans. Antennas Propagat.*, 55, 414–421, February 2007.
123. J. Song, C.C. Lu, and W.C. Chew, Multilevel fast multipole algorithm for electromagnetic scattering by large complex objects, *IEEE Trans. Antennas Propagat*, 45, 1488–1493, 1997.
124. K. Sertel and J. L. Volakis, Incomplete LU preconditioning for FMM implementation, *Microwave Opt. Technol. Lett.*, 26, 4, 158–175, August 2000.
125. A. Greenbaum, Iterative methods for solving linear systems, in *Frontiers in Applied Mathematics*, vol. 17, Philadelphia: SIAM, 1997.
126. B.J. Fasenfest, F. Capolino, D.R. Wilton, D. R. Jackson, and N. Champagne, A fast MoM solution for large arrays: Green's function interpolation with FFT, *IEEE Antennas and Wireless Propagat Lett.*, 3, 161–164, 2004.
127. B.J. Fasenfest, F. Capolino, and D.R. Wilton, Preconditioned GIFFT: A fast MoM solver for large arrays of printed antennas, *Appl. Comput. Electromagn. Soc. J*, 21, 276–283, 2006.
128. E. Bleszynski, M. Bleszynski, and T. Jaroszewicz, AIM: Adaptive integral method for solving large scale electromagnetic scattering and radiation problems, *Radio Sci.*, 31, 1225–1251, 1996.
129. L. Crocco, F. Cuomo, and T. Isernia, Generalized scattering matrix method for the analysis of two-dimensional photonic bandgap devices, *J. Opt. Soc. Am.*, 24, A12–A22, October 2007.
130. O.M. Bucci and G. Franceschetti, On the spatial bandwidth of scattered fields, *IEEE Trans. Antennas Propagat.*, 35, 1445–1455, December 1987.

131. L. Matekovits, G. Vecchi, G. Dassano, and M. Orefice, Synthetic function analysis of large printed structures: The solution space sampling approach, *2001 IEEE Antennas and Propagation Society International Symposium*, pp. 568–571, June 2001.
132. E. Suter and J.R. Mosig, A subdomain multilevel approach for the efficient MoM analysis of large planar antennas, *Microwave Opt. Technol. Lett*., 26, 270–277, March 2000.
133. V. Prakash and R. Mittra, Characteristic basis function method: A new technique for efficient solution of method of moments matrix equations, *Microwave Opt. Technol. Lett*., 36, 95–100, January 2003.
134. L. Matekovits, V.A. Laza, and G. Vecchi, Analysis of large complex structures with the synthetic-functions approach, *IEEE Trans. Antennas Propagat*., 55, 2509–2521, September 2007.
135. J. Yeo, V. Prakash, and R. Mittra, Efficient analysis of a class of microstrip antennas using the characteristic basis function method (CBFM), *Microwave Opt. Technol. Lett*., 39, 456–464, December 2003.
136. C. Craeye, Fast impedance and pattern computations in finite antenna arrays, *IEEE Trans. Antennas Propagat*., 54, 3030–3034, October 2006.
137. X. Radu and C. Craeye, Fast method to compute an efficient basis to simulate metamaterials with macro basis functions, *Ann. Rev. Appl. Comput. Electromagn. Soc*., March 19–23, 2007.
138. J.B. Pendry and D.R. Smith, Reversing light with negative refaction, *Phys. Today*, 57, 6, 37–44 June 2004.
139. X. Radu, C. Craeye, and I. Huynen, Large-scale metamaterial simulation with macro basis functions used in combination with method of moments, *Proceedings of Loughborough Antennas Propagation Conference*, Loughborough, April 11–12, 2006.

6

FDTD Method for Periodic Structures

Ji Chen
University of Houston

Fan Yang
The University of Mississippi

Rui Qiang
University of Houston

6.1 Introduction

Most metamaterials have periodic repetitions in one or more directions. Thus, it is desirable to apply periodic boundary conditions (PBCs) in electromagnetic modeling to reduce the computational cost. PBCs are formulated in the spectral domain and have been efficiently implemented by frequency domain numerical techniques. In order to develop an efficient time-domain technique for the modeling of periodic structures, spectral approaches should be explored. This chapter describes the finite-difference time-domain (FDTD) techniques developed for the modeling of periodic structures. After reviewing the basic principles of the FDTD method, we present a spectral PBC for the method, which can be used in both guided wave analysis and scattering characterization. Furthermore, the array scanning method (ASM) is integrated with the spectral FDTD method to analyze a finite source in metamaterials.

6.2 FDTD Fundamentals

The FDTD method, which discretizes Maxwell's equations in both the time and space domains, has demonstrated desirable features for the analysis of electromagnetic structures [1]. A significant advantage of the FDTD method is the versatility to solve a wide range of microwave and antenna problems.

It is flexible enough to model various media, such as conductors, dielectrics, lumped elements, active devices, and dispersive materials. Another advantage of the FDTD method is its capability in broadband characterizations. Since this method is carried out in the time domain, the transient data from one simulation can be transformed to the frequency domain to obtain a wideband response.

The FDTD method deals with the differential form of Maxwell's equations in the time domain,

$$\begin{aligned} \nabla \times \vec{E} &= -\frac{\partial \vec{B}}{\partial t}, \\ \nabla \times \vec{H} &= \frac{\partial \vec{D}}{\partial t} + \vec{J}, \\ \nabla \cdot \vec{D} &= \rho, \\ \nabla \cdot \vec{B} &= 0, \end{aligned} \tag{6.1}$$

where

$\vec{E}$ is the electric field intensity in V/m
$\vec{D}$ is the electric flux density in C/m^2
$\vec{H}$ is the magnetic field intensity in A/m
$\vec{B}$ is the magnetic flux density in Wb/m^2
$\vec{J}$ represents the electric current density in A/m^2
ρ denotes the electric charge density in C/m^3

Constitutive relations, which describe the electric and magnetic characteristics of materials, are a necessary supplement to Maxwell's equations. In a linear, isotropic, and nondispersive material, they can be simply written as follows:

$$\vec{D} = \varepsilon \vec{E}, \quad \vec{B} = \mu \vec{H}, \tag{6.2}$$

where

ε is the permittivity
μ is the permeability

It is important to point out that the four equations in Equation 6.1 are not independent of each other. Actually, the two divergence equations can be derived from the two curl equations. Therefore, only the two curl equations need to be considered in the derivation of the FDTD method.

To solve Maxwell's equations numerically, Yee introduced a cubic lattice with electric and magnetic field vectors sampled in a special manner, as shown in Figure 6.1 [2]. The cell dimensions are $(\Delta x,\ \Delta y,\ \Delta z)$ in Cartesian coordinates. It is observed that every $\vec{E}$ component is surrounded by four circulating $\vec{H}$ components, and every $\vec{H}$ component is surrounded by four circulating $\vec{E}$ components. The space domain V is then filled with these unit cells, and a grid point $(i,\ j,\ k)$ is defined as

$$(i, j, k) = (i\Delta x, j\Delta y, k\Delta z). \tag{6.3}$$

In the time domain, the electric field and magnetic field are sampled with a half time step difference, i.e., the electric field is evaluated at $t = n\Delta t$ and the magnetic field is computed at $t = (n + 1/2)\Delta t$. Here, Δt is the time increment.

With the above definitions, a central difference scheme is used to discretize the two curl equations in Equation 6.1. For example, the following six equations are obtained in free space:

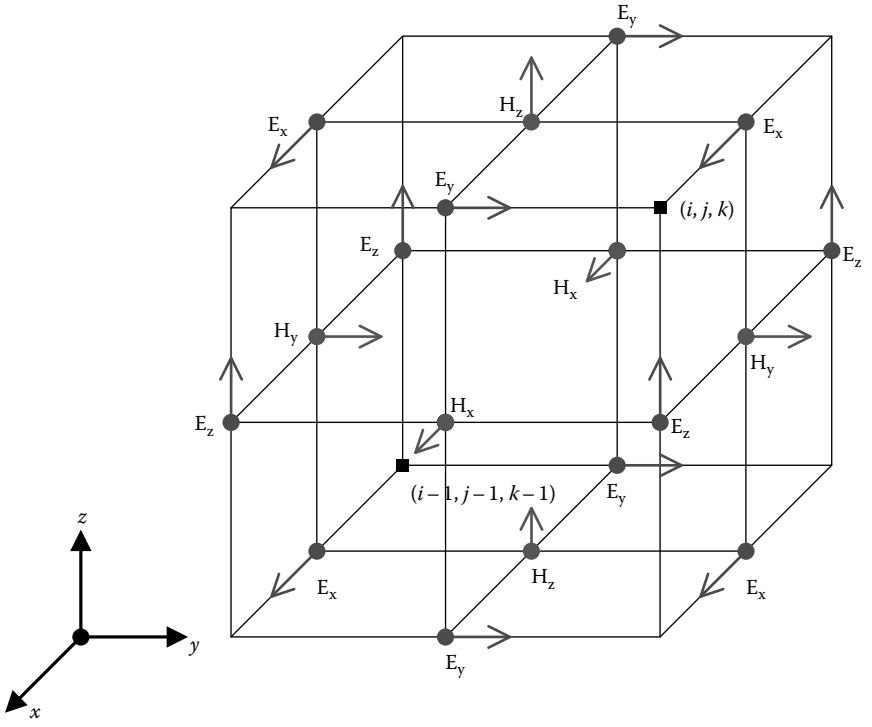

FIGURE 6.1 Electric and magnetic field vectors in a unit cell.

$$
\begin{aligned}
H^{n+1/2}_{x,i,j-1/2,k-1/2} &= H^{n-1/2}_{x,i,j-1/2,k-1/2} - \frac{\Delta t}{\mu_0}\left[\frac{E^n_{z,i,j,k-1/2} - E^n_{z,i,j-1,k-1/2}}{\Delta y} - \frac{E^n_{y,i,j-1/2,k} - E^n_{y,i,j-1/2,k-1}}{\Delta z}\right],\\
H^{n+1/2}_{y,i-1/2,j,k-1/2} &= H^{n-1/2}_{y,i-1/2,j,k-1/2} - \frac{\Delta t}{\mu_0}\left[\frac{E^n_{x,i-1/2,j,k} - E^n_{x,i-1/2,j,k-1}}{\Delta z} - \frac{E^n_{z,i,j,k-1/2} - E^n_{z,i-1,j,k-1/2}}{\Delta x}\right],\\
H^{n+1/2}_{z,i-1/2,j-1/2,k} &= H^{n-1/2}_{z,i-1/2,j-1/2,k} - \frac{\Delta t}{\mu_0}\left[\frac{E^n_{y,i,j-1/2,k} - E^n_{y,i-1,j-1/2,k}}{\Delta x} - \frac{E^n_{x,i-1/2,j,k} - E^n_{x,i-1/2,j-1,k}}{\Delta y}\right],
\end{aligned}
\tag{6.4}
$$

$$
\begin{aligned}
E^{n+1}_{x,i-1/2,j,k} &= E^n_{x,i-1/2,j,k} + \frac{\Delta t}{\varepsilon_0}\left[\frac{H^{n+1/2}_{z,i-1/2,j+1/2,k} - H^{n+1/2}_{z,i-1/2,j-1/2,k}}{\Delta y} - \frac{H^{n+1/2}_{y,i-1/2,j,k+1/2} - H^{n+1/2}_{y,i-1/2,j,k-1/2}}{\Delta z}\right],\\
E^{n+1}_{y,i,j-1/2,k} &= E^n_{y,i,j-1/2,k} + \frac{\Delta t}{\varepsilon_0}\left[\frac{H^{n+1/2}_{x,i,j-1/2,k+1/2} - H^{n+1/2}_{x,i,j-1/2,k-1/2}}{\Delta z} - \frac{H^{n+1/2}_{z,i+1/2,j-1/2,k} - H^{n+1/2}_{z,i-1/2,j-1/2,k}}{\Delta x}\right],\\
E^{n+1}_{z,i,j,k-1/2} &= E^n_{z,i,j,k-1/2} + \frac{\Delta t}{\varepsilon_0}\left[\frac{H^{n+1/2}_{y,i+1/2,j,k-1/2} - H^{n+1/2}_{y,i-1/2,j,k-1/2}}{\Delta x} - \frac{H^{n+1/2}_{x,i,j+1/2,k-1/2} - H^{n+1/2}_{x,i,j-1/2,k-1/2}}{\Delta y}\right].
\end{aligned}
\tag{6.5}
$$

The updated Equations 6.4 and 6.5 can be adjusted to model different dielectrics, conductors, thin wires, and lumped elements encountered in electromagnetic problems. In addition, active devices and dispersive materials can also be accurately characterized with proper models in the FDTD method [1].

To calculate the time evolution of the electromagnetic fields, Equations 6.4 and 6.5 are used in the following manner. Initially, all field values within the computational domain are set to zero. An excitation, which can be a lumped voltage source or a distributed plane wave source, is then introduced

at a specified location. The values of magnetic fields are computed at time $t = (n + 1/2)\Delta t$, followed by the computation of electric fields at time $t = (n + 1)\Delta t$. The time-stepping iterative procedure is repeated until the desired time response for the electromagnetic problem is obtained. Finally, a Fourier transform is performed on the time-domain data to derive the frequency characteristics of the electromagnetic problem. This implementation procedure is fully explicit, thereby avoiding the inversion of a large matrix required in other numeric methods.

As an explicit difference scheme, the FDTD algorithm requires that the time step size Δt must be smaller than a specific bound determined by the space increments Δx, Δy, and Δz in order to avoid numerical instability. For three-dimensional (3D) problems, the Courant–Friedrich–Lewy (CFL) stability condition gives the following bound in free space:

$$\Delta t \leq \frac{1}{C\sqrt{\frac{1}{\Delta x^2} + \frac{1}{\Delta y^2} + \frac{1}{\Delta z^2}}}, \tag{6.6}$$

where C is the free space wave speed.

A fundamental consideration with the FDTD method is the treatment for boundary conditions. For a closed structure with metal walls, boundary conditions can be simply handled by setting the tangential electric fields to zero. For an open structure encountered in many antenna radiation or electromagnetic scattering problems, the simulation grids must theoretically extend to infinity for a perfect representation of the actual electromagnetics scenario. Clearly, no computer can store an unlimited amount of data, and therefore, the computational domain must be truncated to a finite size. Various absorbing boundary conditions (ABCs) are developed to eliminate the reflection of outgoing waves on the perimeter of the domain as if the simulation were performed on a computational domain of infinite extent. Two popularly used boundary conditions are radiation boundary conditions based on traveling wave equations [3,4] and perfectly matched layers (PMLs) based on an appropriate design of a uniaxial lossy medium [5,6]. Modern ABCs have excellent capabilities for virtually reflection-free truncation of the computation domain with a wide dynamic range of 70 dB or more.

The aforementioned boundary conditions are used for electromagnetic structures with finite sizes. In many EM applications, especially in artificial materials, the analyzed structure is considered to be infinite in a periodic manner. Typical examples include corrugated waveguides, frequency selective surfaces (FSSs), electromagnetic bandgap (EBG) structures, and double negative materials. A direct simulation of the entire periodic structure requires prohibitively large computational resources, which is impractical for researchers and engineers. To alleviate the computational burden, PBC that models the effect of periodic replication is utilized to truncate the computational domain so that only a single unit cell needs to be simulated. In the following sections, several PBCs will be described, and their applications in a variety of artificial materials will be highlighted.

6.3 Periodic FDTD Method for Waveguide Designs

Periodic structures have been used to design various waveguides. For example, a metal ground plane with periodic corrugations is designed to guide slow waves. Recently, an EBG structure consisting of periodic patches and vias on a grounded dielectric slab are proposed to suppress surface waves within a certain frequency band. A common question behind these applications is how to accurately characterize the dispersion curve of periodic structures. More specifically, at a given frequency, the propagation constants of surface waves need to be identified. A reverse statement of this question is to find the eigenfrequencies of surface waves at a given propagation constant. The FDTD method has been successfully applied to analyze periodic waveguides. Since it is a time-domain method, the latter statement of the problem is more convenient for finding the dispersion curve.

The FDTD algorithm discussed in the previous section still applies, and the main distinction here is the setup of PBCs [7,8]. Assume that an electromagnetic wave is guided along the z-direction with a

propagation constant k_z. The period of the artificial waveguide is p_z. For the purpose of computation efficiency, the computation domain is truncated to include only a single unit of the periodic cell. In transverse directions, the traditional metal wall condition or ABC is used. In the longitude direction (z-direction), the following equations are used:

$$E(x, y, z) = E(x, y, z + p_z) \cdot \exp(jk_z p_z),$$
$$H(x, y, z) = H(x, y, z + p_z) \cdot \exp(jk_z p_z). \tag{6.7}$$

The eigenfrequencies of the system at the selected propagation constant k_z are computed from the Fourier transforms of the time-domain data of the fields. In practice, these frequencies correspond to the peaks in the frequency spectrum. To obtain a complete dispersion curve, the FDTD simulation needs to be repeated for different values of the propagation constant k_z. It is worthwhile to point out that the excitation condition and the extraction of time-domain data are critical to obtain accurate results. For example, if the excitation point is put at a null location of a specific mode, the corresponding eigenfrequency may be lost in the frequency spectrum.

Figure 6.2 shows a periodically segmented waveguide, which is analyzed using the FDTD method [8]. This waveguide is used for the quasiphase-matched second harmonic generation of blue

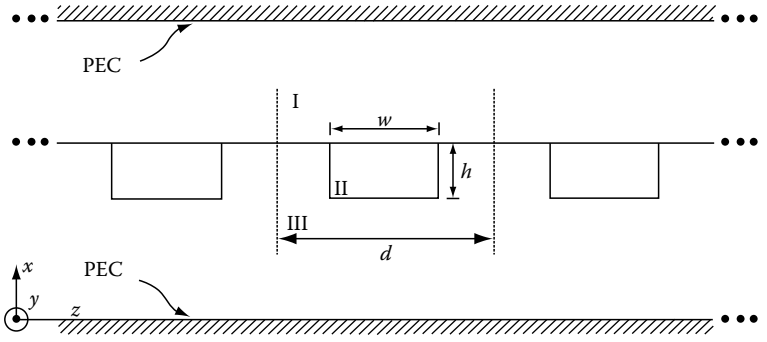

(a)

		Slab Model	This Method	
$\beta(\times 10^6\ \mathrm{m}^{-1})$	Mode	f(THz)	f(THz)	% Difference
6.75	TM_0	173.518	173.308	−0.121
13.71	TM_0	351.633	351.627	−0.002
	TM_1	352.805	352.839	+0.010
20.815	TM_0	533.540	533.680	+0.064
	TM_1	534.437	534.655	+0.041
	TM_2	535.868	536.045	+0.033
26.405	TM_0	676.692	676.966	+0.040
	TM_1	677.437	677.740	+0.045
	TM_2	678.658	678.986	+0.048
	TM_3	680.287	680.601	+0.046

(b)

FIGURE 6.2 Periodically segmented dielectric waveguide structure. (a) Waveguide geometry with dimensions: w = 2.5 μm, h = 4.0 μm, d = 5.0 μm, ε_{r1} = 1, $\varepsilon_{r2} = (1.875)^2$, and $\varepsilon_{r3} = (1.85)^2$; and (b) propagation constants and eigenfrequencies of surface wave modes. (From Cangellaris, A.C., Gribbons, M., and Sohos, G., *IEEE Microwave Guided Wave Lett.*, 3(10), 375, October 1993. With permission.)

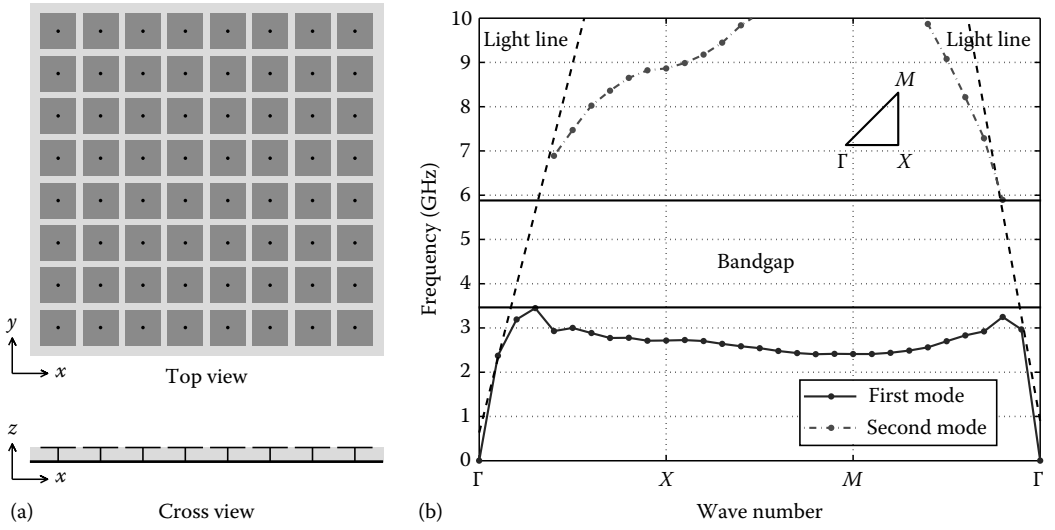

FIGURE 6.3 A mushroom-like EBG structure: (a) geometry and (b) dispersion diagram. Γ : $(k_x, k_y) = (0, 0)$, X : $(k_x, k_y) = [2\pi/(W + g), 0]$, M : $(k_x, k_y) = [2\pi/(W + g), 2\pi/(W + g)]$. (From Yang, F., Aminian, A., and Rahmat-Samii, Y., *Microwave Optical Technol. Lett.*, 47(3), 240, November 2005. With permission.)

light. In the analysis, perfect electric conductors were used 1.4 μm above the air/substrate interface and 7.0 μm below the interface for truncation. PBC is used to truncate the computation domain in the z-direction. Figure 6.2b shows a comparison of the eigenfrequencies found using a slab waveguide model and the FDTD method. Excellent agreement is observed even when multiple modes are present in the structure.

The aforementioned FDTD technique is also used to analyze a mushroom-like EBG structure [9]. The EBG structure consists of four parts: a ground plane, a dielectric substrate, periodic patches, and connecting vias, as shown in Figure 6.3a. The dimensions of an analyzed EBG structure are $W = 7.5$ mm, $g = 1.5$ mm, $h = 3$ mm, and $\varepsilon_r = 2.94$. Here W is the patch width, g is the gap width, h is the substrate thickness, and ε_r is the dielectric constant of the substrate. The vias' radius in the EBG structure is 0.375 mm. In this implementation, the structure is periodic in both x- and y-directions. To accommodate this 2D periodicity, PBCs need to be put on four side walls of the unit EBG cell. For a given pair of horizontal wave numbers (k_x, k_y), equations similar to Equation 6.7 can be derived for x and y boundary treatments. Figure 6.3b shows the dispersion diagram of the EBG structure, where the vertical axis denotes the frequency and the horizontal axis represents the values of the transverse wave numbers (k_x, k_y). One FDTD simulation outputs the eigenfrequencies of surface wave modes at a given combination of wave numbers (k_x, k_y), and the FDTD simulation is repeated for 30 different combinations of k_x and k_y in the Brillouin zone. Thus, each point in the modal diagram represents a certain surface wave mode. It is observed that no surface waves exist in the frequency range from 3.5 to 5.9 GHz regardless of the propagation directions and polarizations. This frequency region is known as a surface wave bandgap of the EBG structure.

6.4 Periodic FDTD Method for Scattering Analysis

Periodic structures have also been used to design various scatterers and antenna arrays. For example, FSSs consisting of periodic dipoles or slots are widely used as radomes and subreflectors in large antenna systems. Planar reflectarray antennas, which are built from thousands of microstrip antenna elements arranged in a periodic lattice, are utilized in the Earth remote sensing and deep space

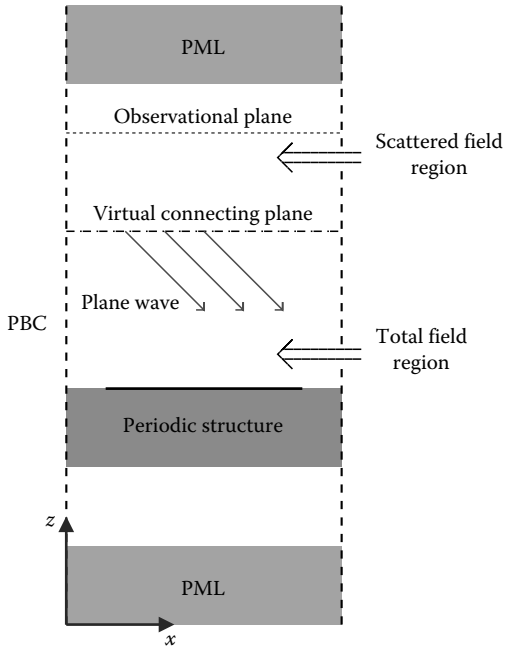

FIGURE 6.4 An FDTD model setup to simulate the scattering property of a general periodic structure.

exploration programs. More recently, artificial materials made of periodic metal wires and split rings are designed to achieve simultaneous negative permittivity and permeability, that are known as double negative metamaterials.

An FDTD model used to analyze the scattering property of a general periodic structure is plotted in Figure 6.4. The computation domain is enclosed by PMLs on the top and bottom and PBCs on four sides. A single unit cell of the periodic structure is included in the computation domain. A plane wave source is added on a virtual connection surface, which separates the entire computation domain from the scattered field region above and the total field region below. An observational plane is set in the scattered field region to extract the reflected field, and the reflection coefficient Γ is calculated by taking the ratio of the reflected field over the incident field.

According to the Floquet theory for periodic scattering problems, PBC along the x-direction is expressed in the frequency domain as below:

$$\begin{aligned} E(x, y, z) &= E(x + p_x, y, z) \exp(jk_x p_x), \\ H(x, y, z) &= H(x + p_x, y, z) \exp(jk_x p_x), \end{aligned} \tag{6.8}$$

where

p_x denotes the periodicity in the x-direction

k_x is the horizontal wave number determined by both the frequency and the incident angle θ

$$k_x = k_0 \cdot \sin\theta, \tag{6.9}$$

where $k_0 = 2\pi f\sqrt{\varepsilon_0\mu_0}$ is the free space wave number. When Equation 6.8 is transformed into the time domain,

$$\begin{aligned} E(x, y, z, t) &= E(x + p_x, y, z, t + p_x \sin\theta/C), \\ H(x, y, z, t) &= H(x + p_x, y, z, t + p_x \sin\theta/C), \end{aligned} \tag{6.10}$$

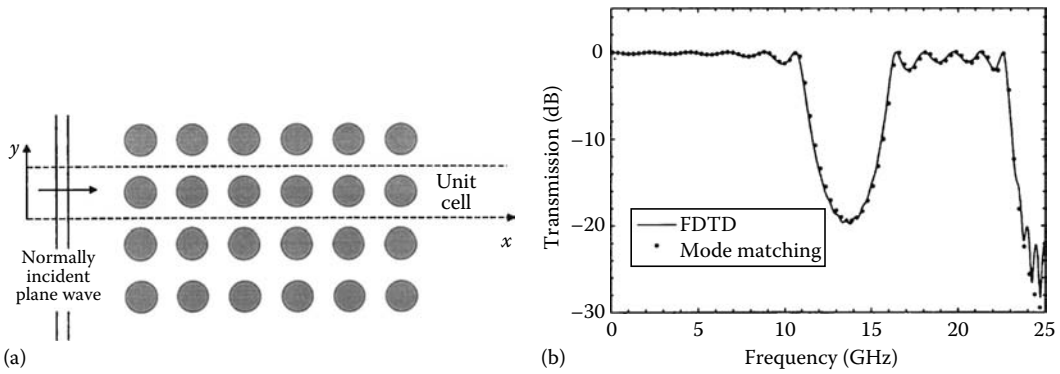

FIGURE 6.5 A PBG crystal analyzed using the FDTD method. (a) Geometry of the PBG crystal that consists of six rows of 4 mm diameter Pyrex rods ($\varepsilon_r = 4.2$) on a 9 mm square lattice; and (b) magnitude of transmission through the PBG crystal. (Reproduced from Maloney, J. and Kesler, M.P., Analysis of Periodic Structures, *Computational Electrodynamics: The Finite Difference Time Domain Method*, Artech House, Boston, MA, 2000. With permission.)

it is noticed that the field data in the *future time* $(t + p_x \sin\theta/C)$ are needed to update the electric and magnetic fields in the *current time* (t), which creates a fundamental challenge in formulating the PBCs.

6.4.1 Normal Incidence

Normal incidence is a simple but fundamental case to deal with. When a plane wave is normally incident on a periodic structure, we have $\theta = 0$ and $k_x = 0$. Therefore, Equation 6.10 is simplified to

$$\begin{aligned} E(x, y, z, t) &= E(x + p_x, y, z, t), \\ H(x, y, z, t) &= H(x + p_x, y, z, t). \end{aligned} \tag{6.11}$$

It is clear that no data in the future time is needed in this PBC. Hence, the difficulty in Equation 6.10 automatically vanishes and the PBC can be implemented easily. It should be pointed out that the stability condition and the dispersion relation of the normal incidence case remain the same as Equation 6.6.

PBCs (Equation 6.11) for normal incidence have been combined with the FDTD technique to analyze a number of scatter problems. For example, Figure 6.5a shows a photonic bandgap (PBG) crystal consisting of six rows of Pyrex rods [10]. The rods are assumed to be infinitely long in the z-direction and are periodically repeated in the y-direction. Thus, this problem is simplified into a 2D simulation, and PBCs are applied in the y-direction. A plane wave propagating along the x-direction normally illuminates on the PBG crystal. The computed transmission coefficient is shown in Figure 6.5b, where a stop band around 13.5 GHz is realized with an attenuation around −20 dB. The FDTD results agree very well with the numerical results obtained from the mode-matching method.

6.4.2 Oblique Incidence: Sine–Cosine Method

Scattering properties of a periodic structure, such as resonant frequency, reflection and transmission coefficients, vary with the incidence angle of the plane wave. Therefore, it is necessary to simulate the plane wave incidence at oblique incidence angles. Various approaches have been proposed to overcome the difficulty of PBC in Equation 6.10. Here, a Sine–Cosine method [11] is discussed first.

This technique incorporates the Floquet phase shift boundary condition (Equation 6.8) directly into the FDTD simulation instead of using its time-domain form (Equation 6.10). To this end, the

computation domain is excited by two plane waves incident simultaneously: one with a cos ωt time dependence and the other with sin ωt. The corresponding fields are denoted by $(E_1,\ H_1)$ and $(E_2,\ H_2)$. The conventional Yee's algorithm is used to update these two sets of fields separately. To apply the PBC, the fields on the boundary are first combined as follows:

$$E_c = E_1 + jE_2, \quad H_c = H_1 + jH_2. \tag{6.12}$$

It is worthwhile to emphasize that the combined fields have complex values. Since the combined fields are equivalently excited by $e^{j\omega t} = \cos\omega t + j\sin\omega t$, the phase relation in Equation 6.8 can be used directly for the combined fields:

$$\begin{aligned} E_c(x, y, z) &= E_c(x + p_x, y, z)\exp(jk_x p_x), \\ H_c(x, y, z) &= H_c(x + p_x, y, z)\exp(jk_x p_x), \end{aligned} \tag{6.13}$$

where k_x is calculated using Equation 6.9 with a known frequency ω and an incident angle θ. Finally, two sets of fields are extracted from the combined field:

$$(E_1, H_1) = \mathrm{Re}(E_c, H_c), \quad (E_2, H_2) = \mathrm{Im}(E_c, H_c). \tag{6.14}$$

This procedure is repeated in each time step until the steady state is reached. The scattering properties are then obtained from the time-domain field data.

The accuracy of this approach is validated through several FSS examples. A thick, double-concentric loop FSS is shown in Figure 6.6a with all dimensions provided in the caption. FDTD computed results for a transverse electric (TE) incident plane wave at an elevation angle of 60° are plotted in Figure 6.6b [11]. The resonant frequency is accurately computed in comparison with that from method of moment (MoM) analysis. The general behavior of the FSS near the resonance is captured.

The stability condition of the Sine–Cosine method remains unchanged regardless of the incidence angles because it uses the conventional Yee's algorithm. However, a major concern is the computational efficiency. This method deals with PBCs from a single-frequency perspective. Thus, it loses the wideband capability of the FDTD method. To improve the computation efficiency, a split-field technique is described next.

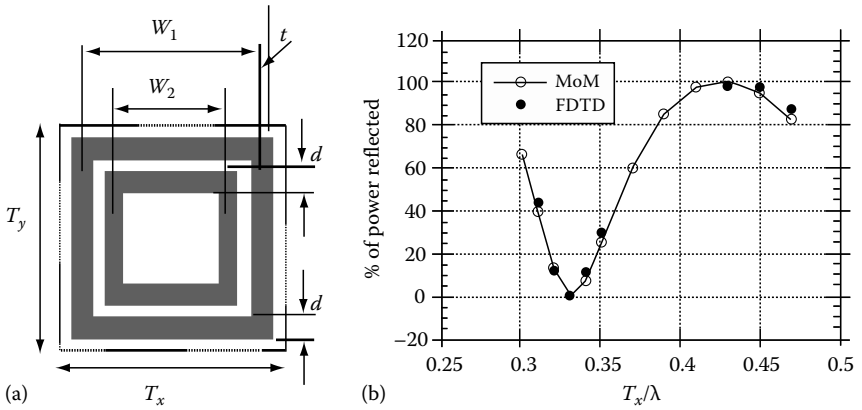

FIGURE 6.6 A thick double concentric square loop FSS analyzed using the FDTD method. (a) A single unit cell of the periodic FSS with dimensions $d = t = 1/16T_x$, $W_1 = 0.875T_x$, and $W_2 = 0.6875T_x$; and (b) reflected power from the FSS for a TE wave incident at an angle of $\theta = 60°$ and $\phi = 0°$. (From Maloney, J. and Kesler, M.P., Analysis of Periodic Structures, *Computational Electrodynamics: The Finite Difference Time Domain Method*, Artech House, Boston, MA, 2000. With permission.)

6.4.3 Oblique Incidence: Split-Field Method

Based on the field transformation technique [12], a split-field method is proposed to analyze periodic structures [13]. To explain the essence of this method, let us assume that a TM^z plane wave is incident on a 2D material that is periodic in the x-direction, as shown in Figure 6.4. To account for the phase shift along the x-direction, a set of auxiliary fields are introduced as follows:

$$\begin{aligned} P_z &= E_z e^{-jk_x x}/\eta_0, \\ Q_x &= H_x e^{-jk_x x}, \\ Q_y &= H_y e^{-jk_x x}, \end{aligned} \tag{6.15}$$

where η_0 is the wave impedance of free space. After this transformation, the boundary conditions of auxiliary fields on the opposite boundary wall are as simple as

$$\begin{aligned} P_z(x=0) &= P_z(x=p_x), \\ Q_x(x=0) &= Q_x(x=p_x), \\ Q_y(x=0) &= Q_y(x=p_x). \end{aligned} \tag{6.16}$$

Difficulties of the field transformation technique arise when substituting Equation 6.15 into Maxwell's curl equations:

$$\begin{aligned} j\omega\frac{\varepsilon_r P_z}{C} &= \frac{\partial Q_y}{\partial x} - \frac{\partial Q_x}{\partial y} + j\omega\frac{\sin\theta}{C}Q_y, \\ j\omega\frac{\mu_r Q_x}{C} &= -\frac{\partial P_z}{\partial y}, \\ j\omega\frac{\mu_r Q_y}{C} &= \frac{\partial P_z}{\partial x} + j\omega\frac{\sin\theta}{C}P_z. \end{aligned} \tag{6.17}$$

It is noticed that the time derivative ($j\omega \leftrightarrow \partial/\partial t$) appears on both sides of the equations. In addition, the right-hand sides are no longer spatially aligned to the Yee's cell. Therefore, the conventional leapfrog algorithm is not applicable now. Instead, a split-field update algorithm is proposed to solve the above equations. The auxiliary fields P and Q are each split into two parts:

$$\begin{aligned} P_z &= P_z^a + P_z^b, & Q_y &= Q_y^a + Q_y^b, \\ j\omega\frac{\varepsilon_r P_z^a}{C} &= \frac{\partial Q_y}{\partial x} - \frac{\partial Q_x}{\partial y}, & j\omega\frac{\mu_r Q_y^a}{C} &= \frac{\partial P_z}{\partial x}, \\ P_z^b &= \frac{\sin\theta}{\varepsilon_r}Q_y, & Q_y^b &= \frac{\sin\theta}{\mu_r}P_z. \end{aligned} \tag{6.18}$$

The Yee's lattice is used to discretize the computation domain, and time/spatial derivatives are calculated by the central difference scheme. It is important to point out that a dual time grid is introduced in this technique, i.e., each field component of P and Q is computed at every half time step.

The split-field method has been implemented to analyze a number of periodic structures. For example, the scattering property of a PBG structure is presented here. Figure 6.7a shows four rows of Pyrex rods illuminated by an oblique incident plane wave [13]. The parameters of the rods and lattice are the same as the one shown in Figure 6.5. Both the measured and computed transmission coefficients at a 20° incident angle are plotted in Figure 6.7b. A good agreement between simulation and experiment results is obtained. When the incident angle increases to 20°, the resonance frequency also increases as compared to Figure 6.5b.

The numerical stability of the split-field method is always a key concern. Since a new, updating algorithm is used in Equations 6.17 and 6.18 instead of the conventional leapfrog method, the stability

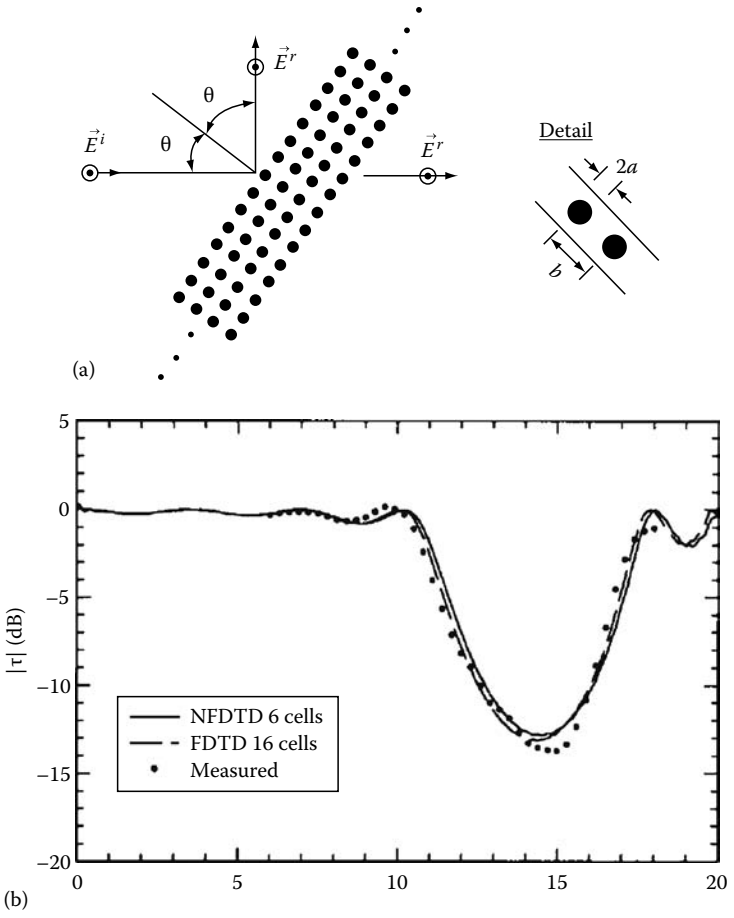

FIGURE 6.7 A PBG crystal analyzed using the FDTD method. (a) A plane wave obliquely incident on a PBG crystal that consists of four rows of Pyrex rods; and (b) magnitude of transmission coefficient at an incident angle of 20°. (From Roden, J.A., Gedney, S.D., Kesler, M.P., Maloney, J.G., and Harms, P.H., *IEEE Trans. Microwave Theory, Tech.*, 46(4), 420, 1998. With permission.)

constraint (Equation 6.6) is changed as well. A simple and conservative stability limit obtained from the maximum velocity in a cubic grid is given by

$$\frac{C\Delta t}{\Delta x} \leq \frac{1-\sin\theta}{\sqrt{D}}, \tag{6.19}$$

where D is the dimensionality of the problem. For normal incidence, this stability condition is the same as in Equation 6.6. As the incident angle increases, the required time step size must become smaller. When the incident angle is close to the grazing angles such as 85°, the time step is so tiny that the FDTD simulation time is prohibitively long. Figure 6.8 shows how the stability limits of the split-field technique vary with the incident angle [10].

Besides the aforementioned three PBCs, a number of genius ideas have been proposed in the last decade to formulate the PBC in various forms. For example, the use of multiple unit cells is one way to solve the difficulty of the requirement of future time-domain data [14]. Angle-update method is another approach based on memorizing data in a buffer [10].

In addition to the scattering analysis, PBCs are also used in antenna array designs. For example, a 6 × 9 stacked microstrip patch array is analyzed in [15] and the active reflection coefficient is

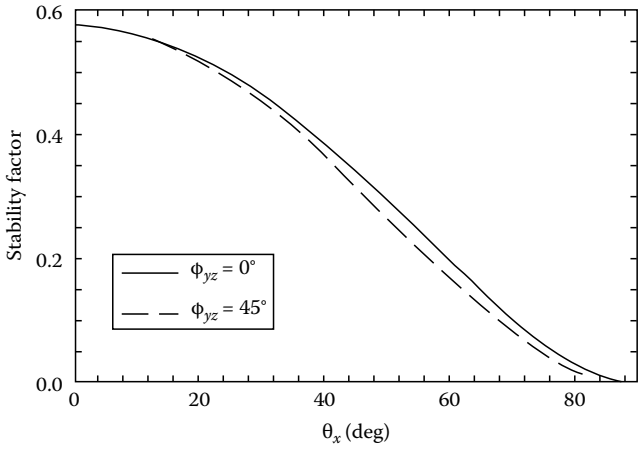

FIGURE 6.8 Stability limit of the split-field technique varies with the incident angle. (Reproduced from Taflove, A. and Hagness, S., *Computational Electrodynamics: The Finite Difference Time Domain Method*, Artech House, Inc., Norwood, MA, 2000. With permission.)

obtained. Furthermore, a finite dipole array is demonstrated in [10], and the blind scan angle is identified. Due to the page limits, these diverse PBCs and their numerous applications cannot be discussed here. Interested readers are suggested to find more information in [10].

6.5 A Unified Spectral FDTD Method

FDTD method for waveguide analysis was discussed in Section 6.3 and scattering analysis was discussed in Section 6.4. In 2004, a novel FDTD/PBC approach was introduced that was capable to simultaneously analyze both the guided wave property and the plane wave property of periodic structures in a simple and unified manner [16,17]. This section presents the basic concept and implementation issues of this unified spectral FDTD method and its applications in soft/hard surface characterizations (Figure 6.9).

6.5.1 Basic Concept of the Unified Spectral FDTD Method

Electromagnetic properties of periodic structures vary with the angle and polarization of an incident wave. For a general structure that is periodic in the x- and y-directions, let k_0 represent the free space wave number, k_x denote the propagation constant along the x-direction, and k_y denote the propagation constant along the y-direction.

1. If $k_x^2 + k_y^2 > k_0^2$, the incident wave is a guided wave along the horizontal direction and it decays in the z-direction. The eigenmodes and eigenfrequencies of the structure are of special interest.
2. If $k_x^2 + k_y^2 \le k_0^2$, the incident wave is a plane wave propagating along a direction denoted by $\vec{k} = \hat{x}k_x + \hat{y}k_y + \hat{z}k_z$, where $k_z = \sqrt{k_0^2 - k_x^2 - k_y^2}$. The reflection and transmission coefficients need to be characterized.

Therefore, if we keep $(k_x,\ k_y)$ as constants and vary the frequency from zero to a high value, the incident wave starts in the guided wave region and ends in the plane wave region. The idea of setting $(k_x,\ k_y)$ as constant has been used in Section 6.3 for guided wave analysis. However, what is the physical meaning of constant horizontal wave numbers in the scattering analysis? See Equation 6.9

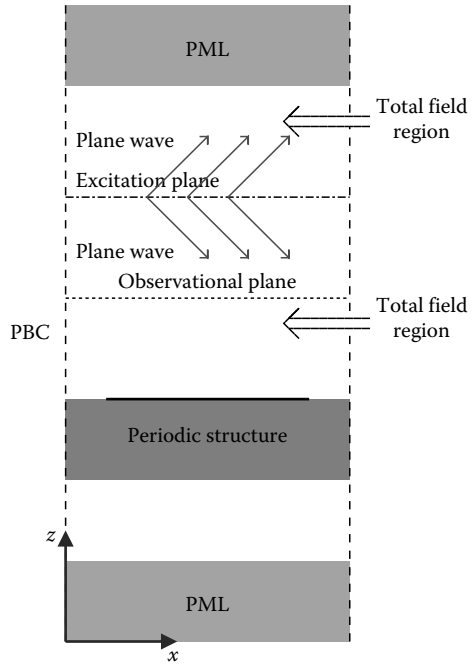

FIGURE 6.9 A new FDTD model for periodic structure analysis using the spectral FDTD technique.

to obtain the incident angle θ of a plane wave as follows:

$$\theta = \sin^{-1}\left(\frac{\sqrt{k_x^2 + k_y^2}}{k_0}\right). \tag{6.20}$$

For a fixed $(k_x,\ k_y)$, varying the frequency or k_0 in the plane wave region will result in different incident angles.

In contrast to the split-field method that calculates the electromagnetic behavior at a given incident angle but different horizontal wave numbers, the unified spectral FDTD method simulates the electromagnetic behavior at given horizontal wave numbers but different incident angles. The advantage of choosing a constant k_x is recognized from the transformation of Equation 6.8 into the time domain, while a very simple PBC is obtained:

$$\begin{aligned} E(x, y, z, t) &= E(x + p_x, y, z, t)\exp(jk_x p_x), \\ H(x, y, z, t) &= H(x + p_x, y, z, t)\exp(jk_x p_x). \end{aligned} \tag{6.21}$$

Note that $\exp(jk_x p_x)$ is a constant number in Equation 6.21 resulting in complex values for both E and H fields. It is clear from Equation 6.21 that no time delay or advancement is required in this equation. This PBC can be considered as an extension of Equation 6.7 that applies to both the guided wave region and the plane wave region [18,19]. Actually, the Sine–Cosine method is a special case of Equation 6.21, since the propagation constant is also a constant in Equation 6.13 for a given frequency and incident angle.

The applicability of this PBC can be understood using the principle of superposition. For a given k_x, the time-domain equation (Equation 6.21) is true for each frequency component. Therefore, when a wideband pulse is launched into a linear system, Equation 6.21 still holds by the superposition of all frequency components.

6.5.2 Implementation Issues

The implementation procedure of the unified spectral FDTD method is similar to the normal incidence case, which is also a special case in Equation 6.21 with $k_x = 0$. The electric and magnetic fields are computed as follows:

- In the interior of the computational domain, the conventional Yee's scheme is used to update the electromagnetic fields.
- At the periodic boundaries of the computational domain, Equation 6.21 is used to update the EM fields instead of Equation 6.11.

Several important issues need to be considered during the implementation. The first one is the plane wave excitation. In Section 6.4, the total field/scattered field (TF/SF) technique is used to excite plane waves. Both the incident electric and magnetic fields are incorporated on the virtual connecting surface that separates the computational domain into the total field region and scattered field region, as shown in Figure 6.4. When this technique is applied with constants $(k_x,\ k_y)$, a difficulty arises regarding the incident angle. For example, if a TE^z wave illuminates upon a periodic structure, the tangential incident fields E_y^{inc} and H_x^{inc} are expressed below:

$$\begin{aligned} E_y^{\text{inc}}(x, y, z_0) &= E_0^{\text{inc}}, \\ H_x^{\text{inc}}(x, y, z_0 + \Delta z/2) &= E_0^{\text{inc}}/\eta_0 \cdot e^{jk_0 \Delta z/2} \cos\theta. \end{aligned} \tag{6.22}$$

It is noticed that the H_x component depends on the incident angle. Since in the proposed algorithm, k_x, is fixed and the incident angle θ varies with frequency, it is not easy to transform H_x into the time domain. To solve the difficulty, an alternative excitation technique is used: only the E_y component is added on the excitation plane for the TE^z case. As a consequence of this one-field excitation technique, the plane wave is launched to propagate not only into $z < z_0$ region but also into $z > z_0$ region. Thus, the entire computational domain becomes the total field region, and there is no scattered field region, as shown in Figure 6.9. A similar strategy applies for the TM^z case: only the H_y component is added on the excitation plane. For general polarizations, it is required to break it up into TE and TM components, but both components can be excited and computed simultaneously.

The second issue is the parameter extraction. An observation plane is set in the computational domain to collect the tangential electric and magnetic fields. Considering the horizontal phase delay, the total E and H fields on the surface are extracted as follows:

$$\begin{aligned} E_s &= \int_S E(x, y) e^{j(k_x x + k_y y)} ds, \\ H_s &= \int_S H(x, y) e^{j(k_x x + k_y y)} ds. \end{aligned} \tag{6.23}$$

Then, the impedance on the observation plane is calculated by taking the ratio of E and H fields,

$$Z_s = \frac{E}{H}. \tag{6.24}$$

Similar to the transmission line theory, the reflection coefficient can be calculated as follows:

$$\Gamma = \frac{Z_s - Z_0}{Z_s + Z_0}, \tag{6.25}$$

where Z_0 is the tangential wave impedance of the incident plane wave in free space. For TM and TE plane waves, the wave impedances are

$$Z_0^{\text{TM}} = \frac{k_z}{k_0}\eta_0, \quad Z_0^{\text{TE}} = \frac{k_0}{k_z}\eta_0. \tag{6.26}$$

Above equations not only apply in the plane wave region, but also can be used for surface wave analysis. In the surface wave region, k_z is an imaginary number and Z_0 is also imaginary. When the calculated reflection coefficient in Equation 6.25 becomes infinity, the corresponding frequency is the eigenfrequency for the periodic structure. It is important to point out that higher Floquet modes exist in periodic structures. These modes can be extracted from Equation 6.23 by replacing $(k_x,\ k_y)$ with $(k_x + m \cdot 2\pi/p_x, k_y + n \cdot 2\pi/p_y)$.

The third issue is the eigenmode resonance [20]. When the plane wave and surface wave are analyzed simultaneously, one encounters the resonant time-domain data. At the eigenfrequencies, the surface waves are guided along horizontal directions. The energy exiting the computation domain at boundary $x = p_x$ reenters the domain at boundary $x = 0$ following the PBC in Equation 6.21. Consequently, the time-domain data does not come down to zero, and a resonance behavior is observed. As a result, the Fourier transformation cannot be used to obtain the accurate frequency domain features. To solve this problem, the auto-regressive moving average (ARMA) estimator in the signal processing area is implemented here to process the time-domain data. The analyzed structure is considered as a linear system, and the early time-domain data is used to derive the transfer function of the system. Using the ARMA estimator, the frequency domain data can be obtained accurately and efficiently. In addition, the eigenfrequencies can be directly obtained from the poles of the transfer function.

It is worthwhile to emphasize several important advantages of this new approach. First, the new algorithm is easy and straightforward to implement. In contrast to the field transformation methods that use auxiliary fields P and Q, the new approach computes E and H fields directly. No complicated discretization formulas need to be derived, and the traditional Yee's updating scheme is still valid. Another advantage of the new algorithm is the efficiency in calculating the scattering at large incident angles. The stability condition of the proposed algorithm remains unchanged regardless of the horizontal wave numbers or incident angles. Finally, this new algorithm is consistent with the guided wave analysis method, which provides an opportunity to combine the surface wave and plane wave analysis in a single FDTD simulation [20].

6.5.3 Application in Soft/Hard Surface Analysis

A corrugated surface can be realized by adding metal walls to a grounded dielectric slab, as shown in Figure 6.10. This surface operates as a soft surface and a hard surface for waves propagating along the x- and y-directions, respectively. This artificial structure has been used in waveguide designs and profiled horn antennas.

The TM and TE impedances of the surface are calculated at several k_x and k_y values. Since no loss is assumed in the FDTD simulation, the real parts of the impedances are zero and the imaginary parts are plotted in Figures 6.11 and 6.12. When the incident wave propagates along the x-direction, the TE impedance has a small value, whereas the TM impedance has a large value in a certain frequency range, which indicates a soft operation that stops the wave propagation. It is interesting to notice that both TM and TE impedances are almost independent of the wave number (incident angle). When the wave propagates along the y-direction, the TE impedance is large and the TM impedance becomes small, which represents a hard operation that allows the wave to propagate. For y-propagated waves, the wave impedances are sensitive to the wave number (incident angle) [21].

6.6 Finite Source on Periodic Structure

In previous sections, we presented techniques of using PBC in the FDTD method so that only a single periodic element needs to be modeled. However, all of the previous implementations assume that periodic structures are illuminated by planar electromagnetic signals. That is, these methods

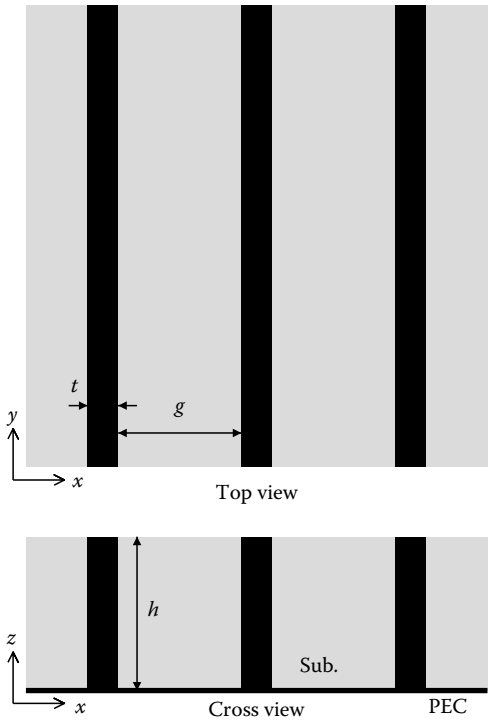

FIGURE 6.10 Geometry of a corrugated soft/hard surface. Let $g = 4\,\text{mm}$, $t = 1\,\text{mm}$, $h = 5\,\text{mm}$, and $\varepsilon_r = 4.0$. (From Aminian, A., Yang, F., and Rahmat-Samii, Y., *IEEE Trans. Antenn. Propag.*, 53(1), 18, January 2005. With permission.)

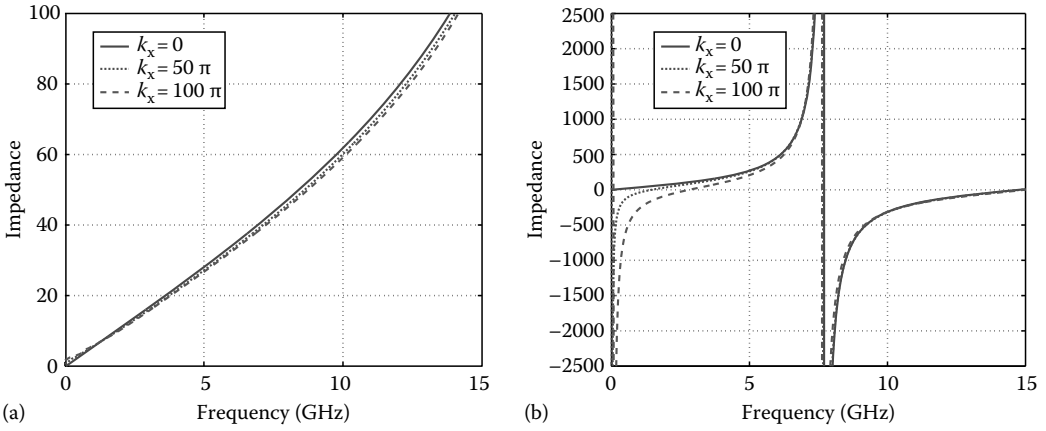

FIGURE 6.11 Surface impedances of the corrugated structure for waves propagating along the x-direction. (a) A low TE impedance and (b) a high TM impedance are obtained, which indicate a soft operation.

are valid when the incident electromagnetic signal is also periodic and infinite in nature. For some applications in which electromagnetic responses from finite-sized sources are required, "brute-force" FDTD simulations were performed [22]. In these brute-force simulations, rather than using a single periodic element, many repetitive cells are used to approximate the structure's infinite extension. Often, at least 20 unit cells are required in the directions where the infinite repetitions exist. However,

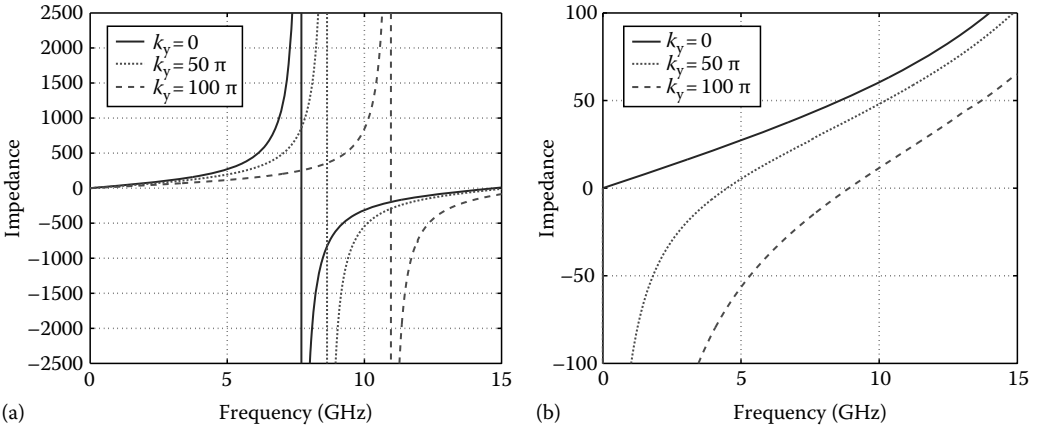

FIGURE 6.12 Surface impedances of the corrugated structure for waves propagating along the *y*-direction. (a) A high TE impedance and (b) a low TM impedance are obtained, which indicate a hard operation.

such an approximation truncates the actual domain, which could lead to a significant reflection from truncated boundaries. In addition, this approach also requires significantly more computer memory and CPU time as compared with the modeling of a single periodic element.

The purpose of this section is to present a novel FDTD method to analyze the interaction between arbitrarily finite-sized electromagnetic sources over infinite periodic structures. The approach described here is based on a spectral FDTD scheme. In this approach, the original finite-sized electromagnetic source is naturally expanded into the sum of series of periodic array sources. This technique is referred to as the ASM, and its frequency-domain approach has been well discussed in several literatures [23–28]. Instead of using complex numerical evaluation of the periodic Green's function that is performed in the frequency-domain ASM approach, we propose to use the time-domain modeling technique in combination with the spectral domain PBC.

6.6.1 ASM–FDTD Theory

Consider an arbitrary periodic structure schematic as shown in Figure 6.13, where *a* and *b* are the periodicities along the *x*- and *y*-directions of this periodic structure. A finite electromagnetic current source with a distribution of $\vec{J}\ (x, y, z, t)$ is located above the periodic structure. The unit cell where

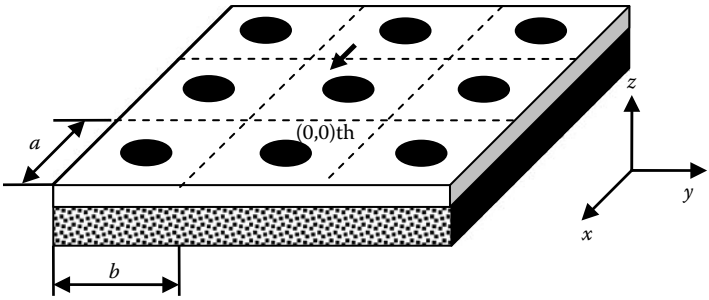

FIGURE 6.13 Planar periodic structure schematic. The distances between unit elements are *a* and *b* in the *x*- and *y*-directions, respectively. An arbitrarily shaped source is placed over a unit element, and this element is denoted as the (0,0)th unit element.

the source is located is denoted as the (0,0)th unit cell. Once this is accomplished, the solutions are obtained by the following methods.

1. Perform multiple periodic spectral FDTD simulations using the following boundary pairs to find the field $\tilde{E}^{\infty}\left(k_x, k_y, x, y, z, t\right)$ in the (0, 0)th unit element excited by the infinite periodic source array $\tilde{J}^{\infty}(x, y, z, k_x, k_y)$ corresponding to different wave numbers of k_x and k_y,

$$\begin{aligned}\vec{E}\,(x + a, y + b, z, t) &= \vec{E}\,(x, y, z, t)\exp\left(-jk_x a\right)\left(-jk_y b\right),\\ \vec{H}\,(x + a, y + b, z, t) &= \vec{H}\,(x, y, z, t)\exp\left(-jk_x a\right)\left(-jk_y b\right).\end{aligned} \tag{6.27}$$

2. Integrate all of the harmonic responses $\widetilde{E}^{\infty}\left(k_x, k_y, x, y, z, t\right)$ to obtain the total field in the (0,0)th unit cell [29],

$$\vec{E}(x, y, z, t) = \frac{ab}{(2\pi)^2}\int_{-\pi/b}^{+\pi/b}\int_{-\pi/a}^{+\pi/a}\widetilde{E}^{\infty}(k_x, k_y, x, y, z, t)\mathrm{d}k_x\,\mathrm{d}k_y. \tag{6.28}$$

3. Add a complex phase shift to the integration to find the solution in the (m, n)th element,

$$\begin{aligned}&\vec{E}\,(x + m \times a, y + n \times b, z, t)\\ &\quad= \frac{1}{(2\pi)^2}\int_{-\pi/b}^{+\pi/b}\int_{-\pi/a}^{+\pi/a}\tilde{E}^{\infty}\left(k_x, k_y, x, y, z, t\right)\exp\left(-jk_x ma\right)\exp\left(-jk_y nb\right)\mathrm{d}k_x\mathrm{d}k_y.\end{aligned} \tag{6.29}$$

6.6.2 ASM–FDTD Algorithm Properties

It is important to understand the numerical properties of this algorithm before efficiently applying it to any practical problem. In this section, the radiation field of a y-polarized electric dipole source with a current strength of 1 A in free space is first analyzed (see Figure 6.14). A sinusoid signal with

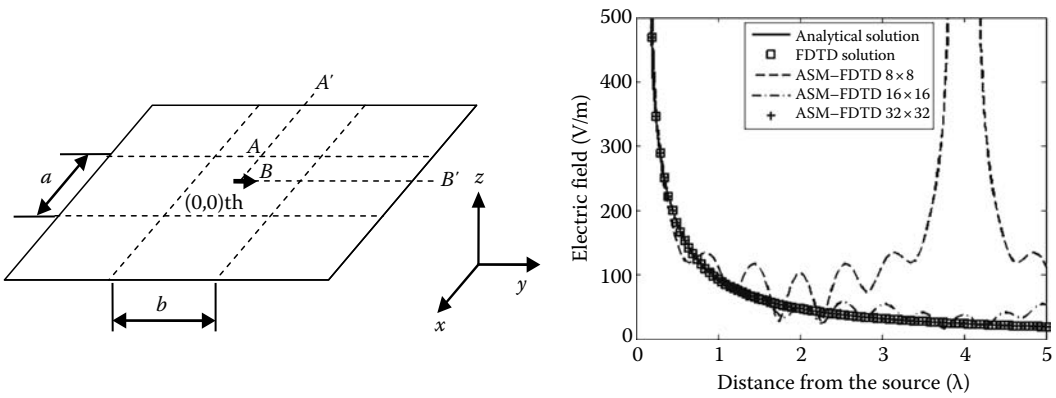

FIGURE 6.14 (Left) Periodic setup for algorithm analysis. (Right) The electric field distribution along the AA′ line calculated by different methods. 8 × 8 means that eight sampling points are used in the interval described in Equation 6.28.

an operating wavelength of $\lambda_0 = 0.1$ m is launched and placed at the origin. To apply the PBC, the computational domain is divided into a series of periodic cells in the x–y plane. The dimension of each cell in the x- and y-directions is $a = \lambda_0/2$, $b = \lambda_0/4$, and the ASM–FDTD is performed only on the (0,0)th cell, in which the source is located. For comparison, the conventional FDTD method with the same spatial resolution is also used in the same problem. In order to evaluate the far-field region, a much larger computational domain $10.5\lambda_0 \times 5.25\lambda_0$ in the x–y plane is included in the simulation of conventional FDTD.

The magnitude of the electric field radiated by this dipole source is sampled starting from the origin and moving up to $5\lambda_0$ away (see AA′ line in Figure 6.14), and this is plotted in Figure 6.14. The analytical, conventional FDTD and ASM–FDTD solutions are given here. Increasing the spectral sampling rate for both k_x and k_y by the order of power of 2 for each step, the results for three different rates are obtained (Figure 6.14). It is not surprising to find that the FDTD solution has excellent agreement with the analytical solution because the spatial sampling rates for all of the directions are $dx = dy = dz = \lambda_0/20$, and the dispersion error is already minimized. Using the same mesh grid size, when the segment number is $n = 8$ for both k_x and k_y decompositions, the field, especially in the far-field region, shows significant deviation from the analytical and FDTD solutions. When the sampling rate is doubled, the error drops dramatically, but only a few oscillations to the left in the far field. After doubling the sampling rate once more, no noticeable difference can be observed between the ASM–FDTD result and the analytical and FDTD solutions. This phenomenon can be explained by the aliasing distortion.

It is also important to see the effect of the aliasing distortion on the time-domain response. At this time, the excitation becomes a modulated Gaussian pulse function of $\exp\left(-0.5(t - t_0)^2/\sigma^2\right)$ $\sin(2\pi f_0 t)$, and the parameters are $f_0 = 3$ GHz, $\sigma = 3/(\pi \cdot \mathrm{BW})$, and $t_0 = 4\sigma$. BW here refers to the bandwidth of the Gaussian pulse with the unit hertz. The field is sampled at the point, which is $\lambda_0/4$ away from the origin on the AA′ line.

From Figure 6.15a, it can be observed that the solution of ASM–FDTD is almost identical with that of FDTD upto $t = 2.5$ ns even when the sampling rate index n is only 8. However, as the signal continues to propagate in free space, the responses excited by adjacent image sources begin to interfere with the field at $t \approx 2.5$ ns. When t is larger than 3 ns, the interference error cannot be neglected because a high level of distortion as observed in Figure 6.15b could dramatically affect the calculation

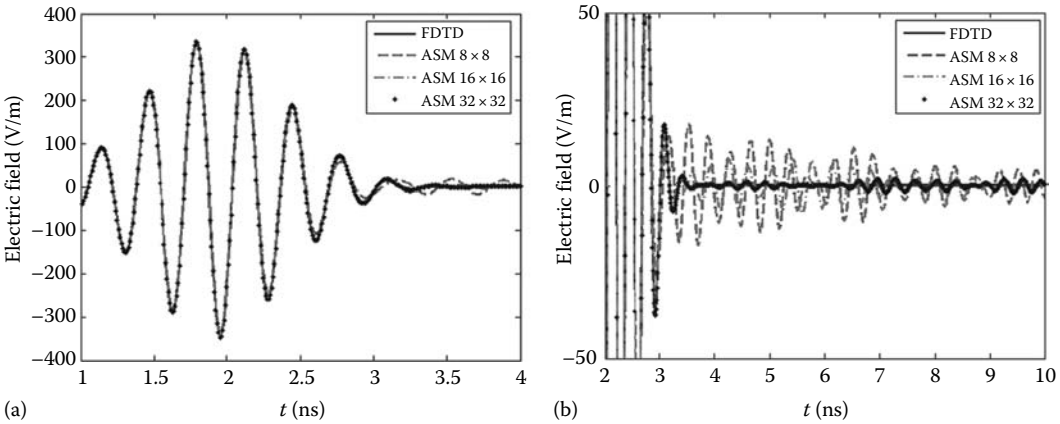

FIGURE 6.15 Time-domain waveform of electric field sampled at the point that is $\lambda_0/4$ away from the origin on the AA′ line: (a) time axis from 1 to 4 ns; and (b) time axis from 2 to 10 ns.

of frequency domain response. If we increase n to 16, the noise is obviously reduced but only after n exceeds 32, and the distortion effect from the image sources can be regarded as having the same level of background noise. This example reveals the fact that in the time-domain simulation using the ASM–FDTD method, the spectral sampling rate must be carefully selected according to the length of simulation time.

6.6.3 Numerical Examples

To validate our proposed 3D ASM–FDTD algorithm, several numerical examples are described below. We use FDTD $(m \times n)$ to denote the brute-force FDTD result that includes m unit cells in the x-direction and n unit cells in the y-direction. For the solution of the ASM–FDTD method, ASM–FDTD $(m \times n)$ refers to the sampling rates in the spectral domain.

The first example investigated here is a photonic band structure of the square lattice with a dielectric cylinder that was first reported in [30]. It consists of a periodic alumina $(\varepsilon_r = 9)$ cylinder array that is exactly filled into the holes drilled on a Styrofoam $(\varepsilon_r = 1.04)$ support plate. The whole substrate is embedded between two perfect conductor plates with a distance of 1 cm between them. Each alumina cylinder has a radius of 0.48 cm, and they are separated by $a = 1.27$ cm in both the x- and y-directions. The conductor loss in the alumina cylinder and Styrofoam support are both negligible. To observe the wave-propagation behavior, we placed an E_z-polarized, infinitesimal electric dipole in the geometry origin (0,0,0) and then sampled the electric fields at (10a,0,0) and (10a,10a,0). A wideband Gaussian pulse is excited and transmitted by the electric dipole in a 0.4 mm, discretized, uniform grid of Yee's cell space (Figure 6.16).

Figure 6.17a shows the time-domain waveform that is received at the observation point 1, obtained by the FDTD and ASM–FDTD simulations. It is clear that before $t = 3$ ns all the results match very well with each other. After this time, the solution of FDTD that includes only 32×32 unit cells in the computational space begins to deviate from the other solutions due to early boundary reflection. The same phenomenon can be observed for the FDTD (50×50) solution at the time $t = 4$ ns. We performed the Fourier transform on this waveform and normalized it to the field of free space emission, and also plotted its frequency-domain propagation characteristic in Figure 6.17b.

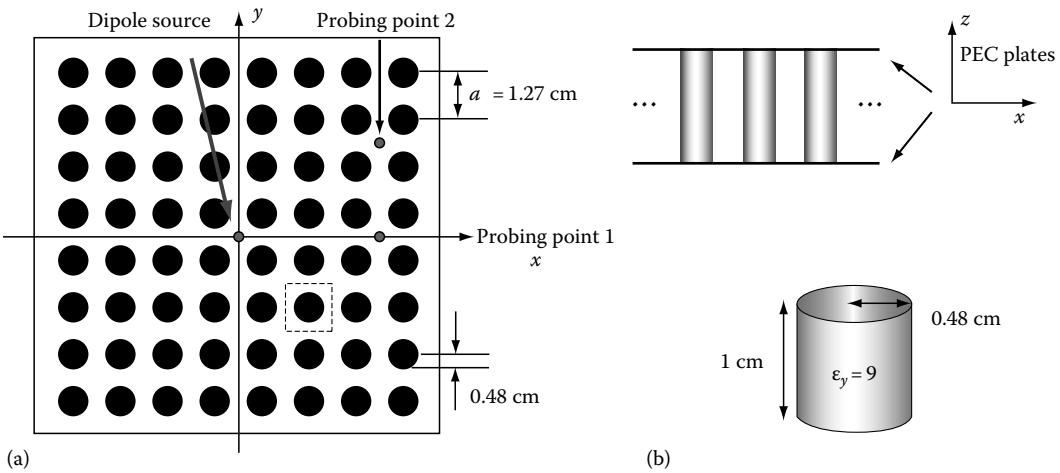

FIGURE 6.16 A 2D photonic band structure of the square lattice with dielectric cylinders. (a) Top view; and (b) side view and a single dielectric cylinder.

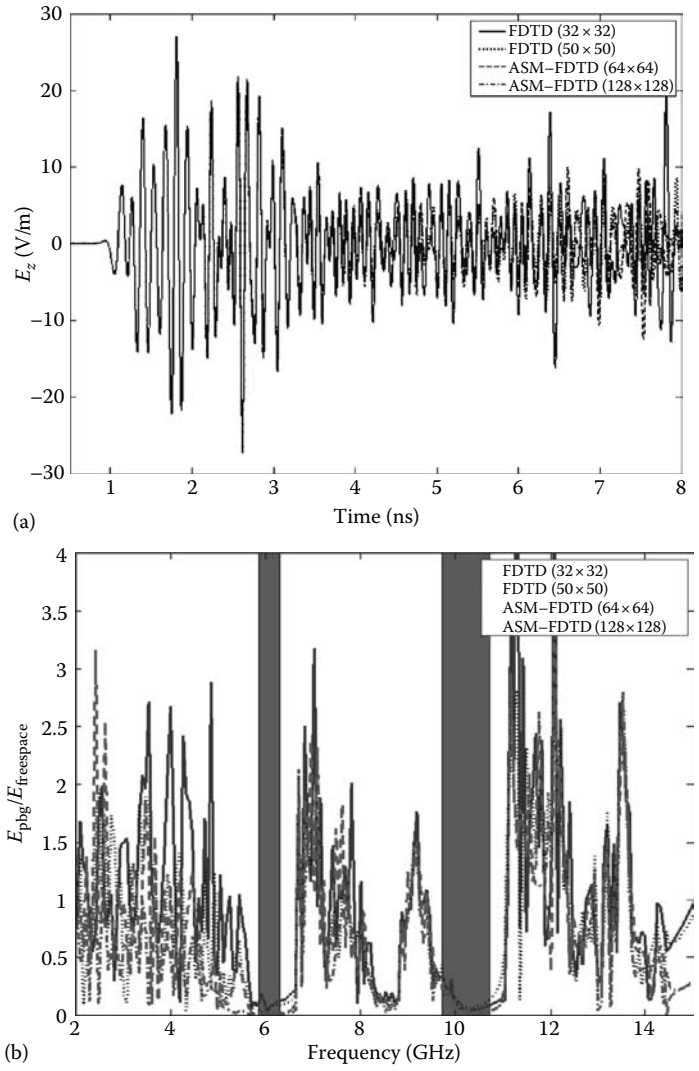

FIGURE 6.17 Comparison of simulation results by the FDTD and ASM–FDTD methods at the observation point 1. (a) Time-domain waveform; and (b) magnitude of normalized E field.

The figure reveals the fact that boundary reflection affects low-frequency energy transmission very much.

The second example is a periodic cross-dipole array shown in Figure 6.18. In this example, the length and the width of each dipole strip is 36 mm × 9 mm. The center spacing between cross-dipole elements is 45 mm in both the x- and y-directions. The structure is illuminated by an infinitesimal electric dipole source with unit strength, and polarized in the x-direction, located 120 mm above the center of the (0,0)th unit structure. In the simulation, the FDTD mesh size becomes 3 mm in the x-, y-, and z-directions. Again, a modulated Gaussian signal with a center frequency of 3 GHz and a bandwidth of 2 GHz is launched from the dipole source.

Figure 6.19 shows the time-domain waveform comparison at a receiving point that is 45 mm below the periodic structure. As we can see from the figure, in the time domain the results of all the methods agree very well at the early time instances upto $t = 4$ ns. However, the brute-force FDTD result that

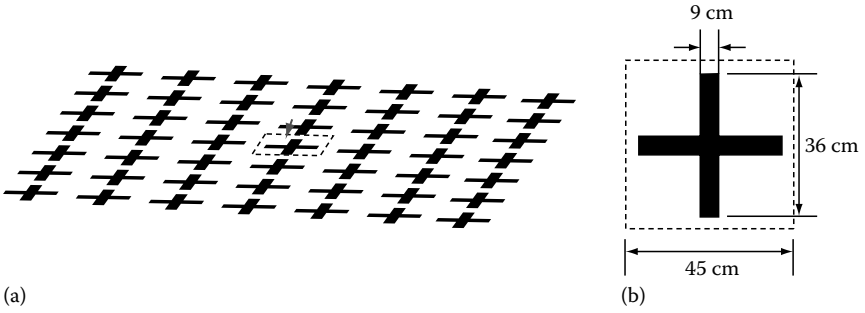

FIGURE 6.18 A periodic cross-dipole array. (a) Configuration; and (b) detailed view and parameters of a unit cell.

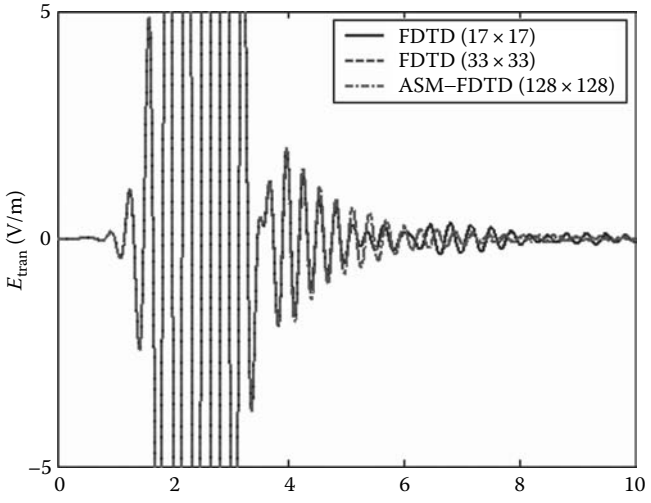

FIGURE 6.19 Comparison of time-domain FDTD and ASM–FDTD simulated waveforms at an observation point.

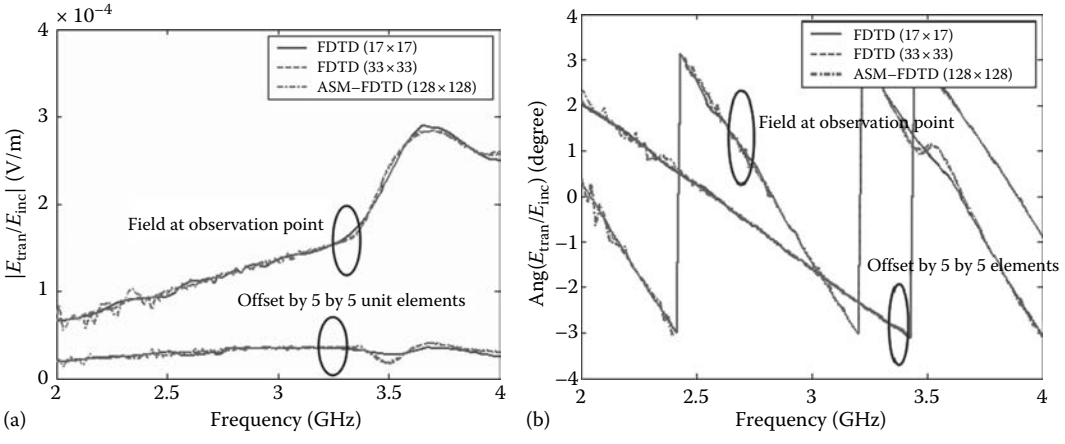

FIGURE 6.20 Comparison of normalized *E* fields of FDTD and ASM–FDTD solutions. (a) Magnitude; and (b) phase.

includes a smaller number of unit elements starts to deviate from the other two solutions significantly due to the early boundary-reflection effect.

Based on this time-domain waveform, the magnitude and the phase of the normalized transmitted electric field as a function of frequency at the observation location is shown in Figure 6.20a and b. Using Equation 6.29, the field at the location that is offset by a distance of five unit elements in both the horizontal directions is also computed and plotted. It is not surprising to see that the ASM–FDTD solution tracks with that of the brute-force FDTD, which has larger truncated space, very well again, although the difference between two FDTD solutions is small in this case. We do not observe the fluctuation in FDTD but in the ASM–FDTD result. This may be because, in this example the horizontal-resonance effect that we talked about in [19] plays a more important role than the reflection error due to the FDTD boundary termination.

6.7 Conclusions

Time-domain electromagnetic modeling techniques are presented for the analysis of periodic structures. After reviewing the basic FDTD principles, techniques for implementation of the PBC in the FDTD method are discussed. To take advantage of the periodic nature of metamaterials, novel time-domain algorithms formulated in the spectral domain are proposed. Using such implementations, simulations are carried out in the complex domain, which is particularly suitable for stable FDTD methods involving incidence angles near grazing. Some properties of these proposed algorithms are presented in this chapter. Numerical examples are used to demonstrate the effectiveness of proposed approaches. The memory usage of these methods is drastically lower than that of a standard FDTD implementation, which has to discretize a large portion of the periodic structure to avoid truncation effects.

References

1. A. Taflove and S. Hagness, Incident wave source conditions, *Computational Electrodynamics: The Finite Difference Time Domain Method*, 2nd edn., Artech House, Boston, MA, 2000.
2. K. S. Yee, Numerical solution of initial boundary value problems involving Maxwell's equations in isotropic media, *IEEE Trans. Antenn. Propag.*, 14, 302–307, 1966.
3. B. Engquist and A. Majda, Absorbing boundary conditions for the numerical simulation of waves, *Math. Comput.*, 31, 629–651, 1977.
4. G. Mur, Absorbing boundary conditions for the finite-difference approximation of the time domain electromagnetic field equations, *IEEE Trans. Electromag. Compat.*, 23, 377–382, 1981.
5. J. P. Berenger, A perfectly matched layer for the absorption of electromagnetic waves, *J. Comput. Phys.*, 114, 185–200, 1994.
6. S. D. Gedney, An anisotropic perfectly matched layer absorbing media for the truncation of FDTD lattices, *IEEE Trans. Antenn. Propag.*, 44, 1630–1639, 1996.
7. S. Xiao, R. Vahldieck, and H. Jin, Full-wave analysis of guided wave structures using a novel 2-D FDTD, *IEEE Microwave Guided Wave Lett.*, 2(5), 165–167, May 1992.
8. A. C. Cangellaris, M. Gribbons, and G. Sohos, A hybrid spectral/FDTD method for electromagnetic analysis of guided waves in periodic structures, *IEEE Microwave Guided Wave Lett.*, 3(10), 375–377, October 1993.
9. F. Yang, A. Aminian, and Y. Rahmat-Samii, A novel surface wave antenna design using a thin periodically loaded ground plane, *Microwave Opt. Technol. Lett.*, 47(3), 240–245, November 2005.

10. J. Maloney and M. P. Kesler, Analysis of periodic structures, *Computational Electrodynamics: The Finite Difference Time Domain Method*, 2nd edn., A. Taflove and S. Hagness (eds), Artech House, Boston, MA, 2000.
11. P. Harms, R. Mittra, and W. Ko, Implementation of the periodic boundary condition in the finite-difference time-domain algorithm for FSS structures, *IEEE Trans. Antenn. Propag.*, 42, 1317–1324, 1994.
12. M. E. Veysoglu, R. T. Shin, and J. A. Kong, A finite-difference time-domain analysis of wave scattering from periodic surfaces: Oblique incidence case, *J. Electromagn. Waves Appl.*, 7, 1595–1607, 1993.
13. J. A. Roden, S. D. Gedney, M. P. Kesler, J. G. Maloney, and P. H. Harms, Time-domain analysis of periodic structures at oblique incidence: Orthogonal and nonorthogonal FDTD implementations, *IEEE Trans. Microwave Theory Tech.*, 46(4), 420–427, 1998.
14. J. Ren, O. P. Gandhi, L. R. Walker, J. Fraschilla, and C. R. Boerman, Floquet-based FDTD analysis of two-dimensional phased array antennas, *IEEE Microwave Guided Wave Lett.*, 4, 109–112, 1994.
15. G. M. Turner and C. G. Christodoulou, FDTD analysis of periodic phased array antennas, *IEEE Trans. Antenn. Propag.*, 47, 661–667, April 1999.
16. A. Aminian, F. Yang, and Y. Rahmat-Samii, Surface impedance characterizations using spectral FDTD method: A unified approach to analyze arbitrary artificial complex surfaces, *2004 URSI International Symposium on Electromagnetic Theory*, Pisa, Italy, May 23–27, 2004.
17. A. Aminian, F. Yang, and Y. Rahmat-Samii, Bandwidth determination for soft and hard ground planes by spectral FDTD: A unified approach in visible and surface wave regions, *IEEE Trans. Antenn. Propag.*, 53(1), 18–28, January 2005.
18. A. Aminian and Y. Rahmat-Samii, Spectral FDTD: A novel technique for the analysis of oblique incident plane wave on periodic structures, *IEEE Trans. Antenn. Propag.*, 54(6), 1818–1825, June 2006.
19. F. Yang, J. Chen, Q. Rui, and A. Elsherbeni, A simple and efficient FDTD/PBC algorithm for periodic structure analysis, *Radio Sci.*, 42(4), RS4004, July, 2007.
20. F. Yang, A. Elsherbeni, and J. Chen, A hybrid spectral-FDTD/ARMA method for periodic structure analysis, 2007 *IEEE Antennas and Propagation Society International Symposium*, Honolulu, HI, June 10–15, 2007, pp. 3720–3723.
21. P.-S. Kildal, Artificially soft and hard surfaces in electromagnetics, *IEEE Trans. Antenn. Propag.*, 38(10), 1537–1544, Oct. 1990.
22. C. Luo, S. G. Johnson, and J. D. Joannopoulos, All-angle negative refraction without negative effective index, *Phys. Rev. Rapid Commun.*, B65, p. 201104, 2002.
23. C. P. Wu and V. Galindo, Properties of a phased array of rectangular waveguides with thin walls, *IEEE Trans. Antenn. Propag.*, 14, 163–173, 1996.
24. B. A. Munk and G. A. Burrell, Plane-wave expansion for arrays of arbitrarily oriented piecewise linear elements and its application in determining the impedance of a single linear antenna in a lossy half-space, *IEEE Trans. Antenn. Propag.*, 27, 331–343, 1976.
25. F. Capolino, D. R. Jackson, and D. R. Wilton, Mode excitation from sources in two-dimensional PBG waveguides using the array scanning method, *IEEE Microwave Wireless Comp. Lett.*, 15(2), 49–51, 2005.
26. F. Capolino, D. R. Jackson, and D. R. Wilton, Fundamental properties of the field at the interface between air and a periodic artificial material excited by a line source, *IEEE Trans. Antenn. Propag.*, 53(1), 91–99, 2005.
27. F. Capolino, D. R. Jackson, D. R. Wilton, and L. B. Felsen, Comparison of methods for calculating the field excited by a dipole near a 2-D periodic material, *IEEE Trans. Antenn. Propag.*, 55(6), 1644–1655, June 2007.
28. F. Capolino, D. R. Jackson, and D. R. Wilton, Field representations in periodic artificial materials, in *Handbook of Artificial Materials*, Chapter 12, Vol. I. Taylor & Francis/CRC Press, Boca Raton, FL.

29. J. A. C. Weideman, Numerical integration of periodic functions: A few examples, *Am. Math. Mon.*, 109(11), 29–36, 2002.
30. P. T. Suzuki, K. L. Yu, D. R. Smith, and S. Schultz, Experimental and theoretical study of dipole emission in the two-dimensional photonic band structure of the square lattice with dielectric cylinders, *J. Appl. Phys.*, 79(2), 582–594, 1995.

7

Polarizability of Simple-Shaped Particles

Ari Sihvola
Helsinki University of Technology

7.1 Introduction

In this chapter, basic material modeling questions are discussed with a focus on the polarizability of dielectric particles. Polarizability is a very important concept in the analysis of macroscopic dielectric properties of heterogeneous media. Special emphasis is given to the manner how geometric and surface characteristics affect the response of matter inclusions. This review presents results for the dielectric response and discusses the surface-geometrical parameters of various particle polarizabilities that are important in the modeling of material effects in the context of metamaterials. Because of the generality of the electric modeling results, many of the results are, *mutatis mutandis*, directly applicable to certain other fields of science, like magnetic, thermal, and even (at least analogously) mechanical responses of matter. The correspondence between different fields of physics permits such a transfer but also defines its limitations. Since many of the polarizability results are also relevant from the metamaterials point of view, the analogy also paves way to carry the whole metamaterials paradigm beyond the domain of electromagnetics.

7.2 Static Electric Response of a Simple Scatterer

The response of an individual, well-defined inclusion can be solved from the electrostatic problem when the object is placed in vacuum and exposed to a uniform static electric field. The effect of this inclusion, or scatterer, is that the uniform field becomes distorted. The perturbation of the field is concentrated into the vicinity of the scatterer.

To find order into this perturbation in the field structure, it is usually expanded in a multipolar form. There the strongest field component is due to an effective dipole, which decays with a dependence of the distance to the inverse third power. The amplitudes of the higher multipole fields (quadrupole, octopole, etc.) decrease with faster rates as the distance from the scatterer increases.

A homogeneous dielectric sphere is the basic shape in scattering problems. The response of a homogeneous, isotropic, dielectric sphere in a homogeneous, uniform electric field in vacuum is extraordinarily simple: it is a dipolar field. And the internal field of the sphere is also uniform, directed along the exciting field and of an amplitude dependent on the permittivity. No higher-order multipoles are excited.

The homogeneous internal field $\mathbf{E}_i$ as a function of the exciting, primary field $\mathbf{E}_e$ reads [1,2]

$$\mathbf{E}_i = \frac{3\epsilon_0}{\epsilon + 2\epsilon_0}\mathbf{E}_e \tag{7.1}$$

where

ϵ is the (absolute) permittivity of the spherical object
ϵ_0 is the free-space permittivity

The polarization density induced within the sphere volume is $(\epsilon - \epsilon_0)\mathbf{E}_i$ and since the dipole moment of a scatterer is the volume integral of the polarization density (dipole moment density), the dipole moment of this sphere is

$$\mathbf{p} = (\epsilon - \epsilon_0)\frac{3\epsilon_0}{\epsilon + 2\epsilon_0}\,\mathbf{E}_e V \tag{7.2}$$

where V is the volume of the sphere. Then we can write the (absolute) polarizability of the sphere α_{abs}, which is defined as the relation between the dipole moment and the incident field ($\mathbf{p} = \alpha_{abs}\mathbf{E}_e$):

$$\alpha_{abs} = 3\epsilon_0 V\frac{\epsilon - \epsilon_0}{\epsilon + 2\epsilon_0} \tag{7.3}$$

In the modeling of dielectric materials, the polarizability is a very useful concept. However, even if for a sphere with homogeneous excitation, the polarizability and the induced dipole moment fully characterize the field behavior outside the scatterer, the whole story about the response of an arbitrary scatterer is not told. In the case of inclusion of shapes other than spherical, also quadrupolic, octopolic, and even higher-order multipoles are created (and in the case of dynamic fields, the list of multipole moments is much longer, see [3] for a concise treatment of these). A more accurate name for the polarizability we are now discussing (α_{abs}) would be dipolarizability.

Nevertheless, the dipolarizability is the most important of the multipole moments. The dipole is the lowest-order multipole except the monopole, which is not present in this type of polarization problem with globally neutral particles. A monopole requires net charge.

The absolute definition of the (di)polarizability α_{abs} carries information about the following properties:

- Size of the inclusion
- Permittivity of the inclusion
- Shape of the inclusion

In addition, the dimension of the absolute polarizability includes that of the absolute permittivity. But as can be seen from Equation 7.3, the dependence on volume is trivial. The bigger the volume of the inclusions, the larger is its electrical response. A more characteristic quantity would be a normalized polarizability α, which for the sphere reads

$$\alpha = \frac{\alpha_{abs}}{\epsilon_0 V} = 3\frac{\epsilon_r - 1}{\epsilon_r + 2} \tag{7.4}$$

where the division with the free-space permittivity ϵ_0 leaves us with a dimensionless quantity. Note also the use of the relative permittivity of the sphere $\epsilon_r = \epsilon/\epsilon_0$.

With this polarizability, the response of matter distils to the very essentials. It is a response quantity of the most basic three-dimensional geometrical object with one single material parameter, permittivity. And still, this response function is by no means trivial. Some of the properties of this function are very universal.

The behavior of the polarizability as a function of the material permittivity is shown in Figure 7.1 for positive permittivity values. In the limiting cases, the normalized polarizability saturates to the value 3 for large permittivities and to the value $-3/2$ for the zero-permittivity.

Even if the behavior in Figure 7.1 looks monotonous, there is much physics inside it. In addition, very interesting phenomena can be observed when the permittivity is allowed to become negative. Figure 7.2 shows the behavior in this case.

In Figure 7.2, one phenomenon overrides all other polarizability characteristics: the singularity of the function for the permittivity value $\epsilon_r = -2$. This is also obvious from Equation 7.4. This is the electrostatic resonance that goes in the literature under several names, depending on the tradition: in electromagnetics, microwave engineering, optics, and materials science, the terminology is different. The singularity is also known as surface plasmon or Fröhlich resonance [4].

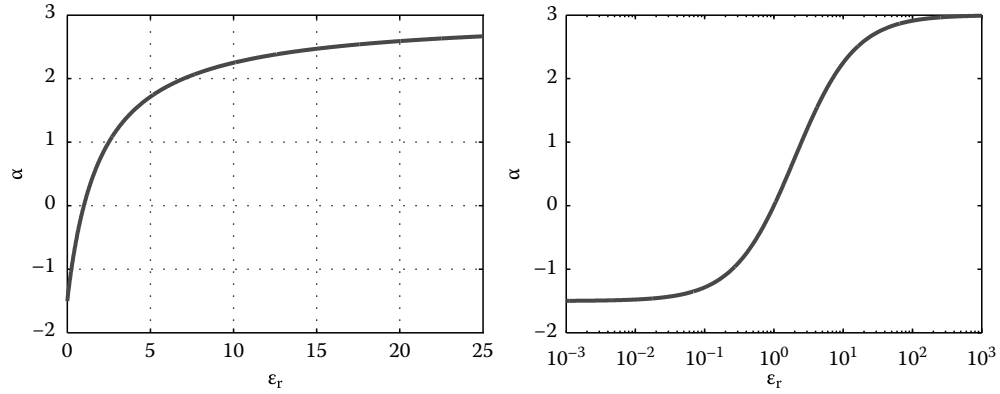

FIGURE 7.1 The polarizability of a dielectric sphere for positive values of the relative permittivity with linear and logarithmic scales. Note the negative values for the polarizability for permittivities less than that of free space. The symmetry of the polarizability behavior in the two limits (high-permittivity or "conducting", and zero-permittivity or "insulating") can be seen from the right-hand side curve.

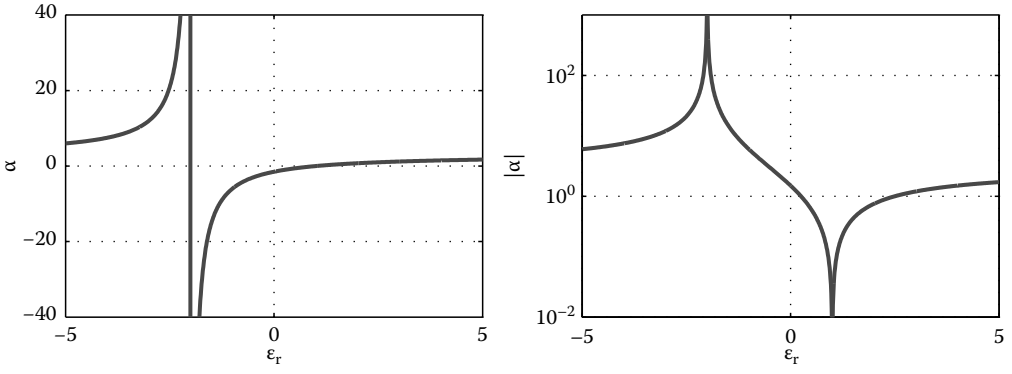

FIGURE 7.2 The polarizability of a dielectric sphere when the permittivity is allowed to be negative as well as positive. The resonance at $\epsilon_r = -2$ dominates the curve in the linear-amplitude plot (left), but if the amplitude is shown logarithmically (right), the zero-crossing at $\epsilon_r = 1$ becomes prominent.

The behavior of the negative-permittivity resonances for small-sized scatterers is an interesting topic in plasmonics [5]. Even if such media form a large class of metamaterials [6], let us focus in the following on positive permittivity values. Phenomena in the material response within this regime are also worth studying [7].

The formula for the polarizability of the sphere is enlightening in the respect that the $\alpha(\epsilon_r)$ function displays certain properties that can be easily derived from the mathematical form in Equation 7.4. Yet, these properties are universal in the sense that they also apply to dielectric objects of other shapes; at least when the three-dimensional average of the response is concerned.

From the normalized polarizability $\alpha(\epsilon_r)$, for the permittivity value $\epsilon_r = 1$, we can write down the following:

- The quasitrivial observation that transparent particles have zero polarizability:

$$\alpha = 0, \quad \text{for } \epsilon_r = 1 \tag{7.5}$$

- The slope of the function is unity at this point:

$$\frac{\partial \alpha}{\partial \epsilon_r} = 1, \quad \text{for } \epsilon_r = 1 \tag{7.6}$$

- Also there exists a condition for the second derivative:

$$\frac{\partial^2 \alpha}{\partial \epsilon_r^2} = -\frac{2}{3}, \quad \text{for } \epsilon_r = 1 \tag{7.7}$$

There are not many shapes that are less simple than the sphere, but are still analyzable in closed form. Ellipsoids are, however, such geometries. Because the internal field of a homogeneous ellipsoid in a constant electric field is also constant, the polarizability can be written as an explicit function of the shape of the ellipsoid and its permittivity. The amplitude of this field is naturally linear to the external field, but there also exists a straightforward dependence of this field on the permittivity of the ellipsoid and of a particular shape parameter, the so-called depolarization factor. Note, however, that the field "external" to the ellipsoid is no longer purely dipolar. In the vicinity of the boundary there are multipolar disturbances whose amplitudes depend on the eccentricity of the ellipsoid.

Let the semiaxes of the ellipsoid in the three orthogonal directions be a_x, a_y, and a_z. Then the internal field of the ellipsoid (with permittivity ϵ), given that the external, primary field $\mathbf{E}_e$ be x-directed, is (a generalization of Equation 7.1)

$$\mathbf{E}_i = \frac{\epsilon_0}{\epsilon_0 + N_x(\epsilon - \epsilon_0)} \mathbf{E}_e \tag{7.8}$$

where N_x is the depolarization factor of the ellipsoid in the x direction, and can be calculated from

$$N_x = \frac{a_x a_y a_z}{2} \int_0^\infty \frac{\mathrm{d}s}{(s + a_x^2)\sqrt{(s + a_x^2)(s + a_y^2)(s + a_z^2)}} \tag{7.9}$$

For the depolarization factor N_y, interchange a_y and a_x in the above integral. Similarly, in the case of N_z, interchange a_z and a_x.

The three depolarization factors for any ellipsoid satisfy

$$N_x + N_y + N_z = 1 \tag{7.10}$$

Due to symmetry, a sphere has three equal depolarization factors of 1/3. For prolate and oblate spheroids (ellipsoids of revolution), closed-form expressions can be written for the depolarization

factors [2,8]. The limiting cases of spheroids are a disk (depolarization factors (0, 0, 1)) and a needle (depolarization factors (1/2, 1/2, 0)).

The polarizability components can be written using the field relation (Equation 7.8). In this case, where the spherical symmetry is broken, the polarizabilities are different for different directions. In the x-direction the polarizability component reads

$$\alpha_x = \frac{\epsilon_r - 1}{1 + N_x(\epsilon_r - 1)} \tag{7.11}$$

and the corresponding expressions for the y- and z-components are similar with obvious replacement of N_x by the depolarization factor in the respective direction. The depolarization factor affects the amplitude of the polarizability, and indeed, this relation allows quite strong deviations from the polarizability of the spherical shape.

For a simple example, consider the limits of very large or very small permittivities. For $\epsilon_r \to \infty$, we have $\alpha_x = \frac{1}{N_x}$. And the other limit is $\alpha_x = -\frac{1}{1-N_x}$ for $\epsilon_r \to 0$. Depending on the depolarization factor values, these polarizabilities can vary in a very strong manner. Exploiting this property in a synthesis problem, it provides a possibility to design media with a very strong, effective macroscopic permittivity, using extremely squeezed ellipsoids, at least if the field direction is aligned with all the ellipsoids in the mixture.

A mixture composed of aligned ellipsoids is macroscopically anisotropic. But also an isotropic mixture can be generated from nonsymmetric elements (like ellipsoids) by mixing them in random orientations in a neutral background. Then the average response of one ellipsoid is one-third of the sum of its three polarizability components:

$$\alpha_{ave} = \frac{1}{3} \sum_{i=x,y,z} \frac{\epsilon_r - 1}{1 + N_i(\epsilon_r - 1)} \tag{7.12}$$

Figure 7.3 displays the effects of the shape of the ellipsoids on the averaged macroscopic response. One-third of the sum of the three orthogonal polarizability components is plotted against the

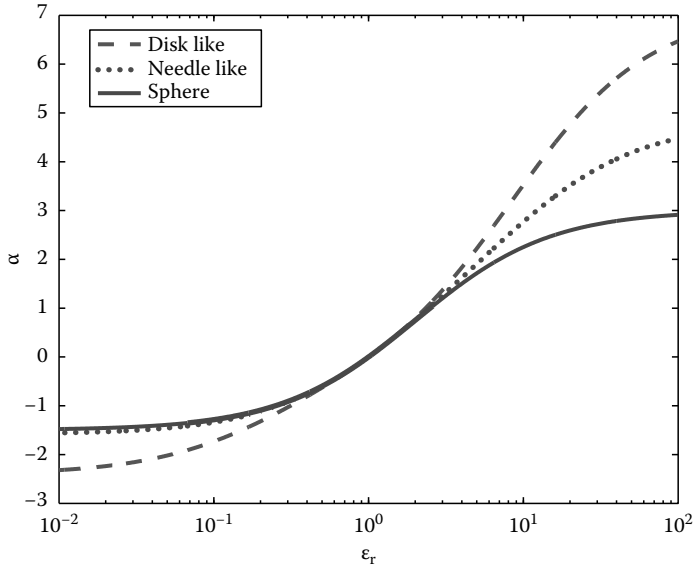

FIGURE 7.3 The average polarizability of a dielectric ellipsoid (one-third of the normalized polarizabilities in the three orthogonal directions) for spheres (smallest), elongated (depolarization factors 0.1, 0.45, 0.45; middle curve), and flattened (depolarization factors 0.8, 0.1, 0.1; highest curve).

permittivity for different ellipsoids. We can observe that the deviation from the spherical form of the inclusion enhances its dielectric response, as for high-permittivity inclusions the sphere response is smallest; then comes the elongated (needle-shaped) inclusion, and the highest response is that from a flattened spheroid. It is also worth observing that in the complementary direction (the permittivity of the inclusion is less than that of vacuum), the situation with respect to the magnitude of the response is the same; only then the polarizability is negative.

The geometry of a sphere is indeed a "minimum" geometry. In other words, with a given amount of dielectric material, in a spherical form, it creates the smallest dipole moment, and every deviation from this shape increases its polarizability. Here polarizability has to be understood in the average three-dimensional sense. Of course, some of the polarizability components of an ellipsoid may be smaller than that of the sphere of the same permittivity and volume; however, the remaining components are so large that the average overrides the sphere value. For theoretical analysis on this phenomenon in the literature, see [9,10].

A slight but perhaps essential difference can be observed in the curves of the figure. On the high-permittivity side, the curves for the needle and the disk differ strongly from the sphere curve (and would go to infinity for ideal needles and disks with depolarization factors (1/2, 1/2, 0) and (0, 0, 1), respectively). On the other hand, on the low-permittivity regime the situation is different: the disk curve separates from the sphere and needle curves. It seems that to have a strong response for zero-permittivity inclusions, it is not enough to have objects with zero curvature in one dimension (needles) but in two orthogonal dimensions (planar disks).

Polarizability is a truly powerful concept and tool in analyzing the dielectric response of single scatterers. It is also very useful in computation of the response of dielectric mixtures as a whole. The classical homogenization principles starting from Maxwell Garnett [11], following through Bruggeman [12], over to the modern refined theories take advantage of the polarizabilities of the particles that form the mixture.

7.3 Other Inclusion Shapes

It seems that for geometrical shapes other than the ellipsoid, the electrostatic solution of the particle in the external field does not have a closed-form solution. In such cases one must resort to computational approaches. With various finite-element and difference-method principles, many electrostatics and even electromagnetic problems involving small inclusions of matter can be solved with almost any desired accuracy (see, e.g., [13,14]).

For a homogeneous scatterer with an arbitrary shape, a very efficient way to solve the field problem and the polarizability is through an integral equation for the potential on the surface. Such an equation for the unknown potential function on the surface of the inclusion ϕ in this electrostatic problem reads as follows [15]:

$$\phi_e(\mathbf{r}) = \frac{\epsilon_r + 1}{2}\phi(\mathbf{r}) + \frac{\epsilon_r - 1}{4\pi}\int_S \phi(\mathbf{r}')\frac{\partial}{\partial n'}\left(\frac{1}{|\mathbf{r} - \mathbf{r}'|}\right) dS', \quad \mathbf{r} \text{ on } S \tag{7.13}$$

where

S is the surface of the inclusion
$\phi_e = -E_e z$ is the potential of the incident field
ϕ is the total potential on the surface

The outward normal to the surface is $\mathbf{n}'$ at point $\mathbf{r}'$. Equation 7.13 is a Fredholm integral equation of the second kind. Expanding the unknown function with piecewise elements, the solution can be computed with the method of moments [16]. The dipole moment comes from

$$\mathbf{p} = -(\epsilon_r - 1)\epsilon_e \int_S \phi(\mathbf{r})\mathbf{n}\, dS \tag{7.14}$$

and consequently the polarizability α can be enumerated by renormalization with E_e.

For an arbitrary object, now there are new geometrical parameters that define the inclusion and affect the polarizability, in addition to the permittivity [17]. One of the interesting questions in connection with the material design is how the specific geometrical and surface parameters correlate with the amplitude of the polarizability. A systematic study into this problem would require the numerical electrostatic analysis of many different scatterer shapes. In addition, one must remember that for nonsymmetric, anisotropic-type shapes one needs to distill the trace (or the average of the components) of the polarizability dyadic, which in the end would be a fair quantity to compare with the canonical shapes.

In the following, the polarizabilities of some important shapes are presented, for which a closed-form solution of the Laplace equation does not exist except in the form of infinite series. And again, in the normalized form of the polarizability, the linear dependence on the volume of the inclusion is taken away, and the effect of geometry is mixed with the effect of permittivity.

7.3.1 Regular Polyhedra

The five regular (Platonic) polyhedra are very symmetric shapes: tetrahedron, hexahedron (cube), octahedron, dodecahedron, and icosahedron. They all have in common with the sphere the polarizability dyadic is a multiple of the unit dyadic. In other words, the three eigenvalues of polarizability are equal. One single parameter is sufficient to describe the dipole moment response. Of course, higher-order multipolarizabilities are also present in increasing magnitudes as the sharpness of the corners of the polyhedra increases. In this sense the symmetry of Platonic polyhedra is not as complete as that of the sphere.

The dielectric response of regular polyhedra has been solved with a boundary-integral-equation principle in [16]. There, an integral equation for the potential is solved with the method of moments [18], which consequently allows many characteristic properties of the scatterer to be computed. Among them the polarizabilities of the five Platonic polyhedra have been enumerated with a very good accuracy. Also regression formulas turned out to predict the polarizabilities correct to at least four digits. These have been given in the form [16]

$$\alpha = \alpha_\infty(\epsilon_r - 1)\frac{\epsilon_r^3 + p_2\epsilon_r^2 + p_1\epsilon_r - \alpha_0}{\epsilon_r^4 + q_3\epsilon_r^3 + q_2\epsilon_r^2 + q_1\epsilon_r + \alpha_\infty} \tag{7.15}$$

where

p_1, p_2, q_1, q_2, q_3 are numerical parameters
α_∞ and α_0 are the computationally determined polarizability values for $\epsilon_r \to \infty$ and $\epsilon_r \to 0$, respectively

Of course, these parameters are different for all five polyhedra. At the special point $\epsilon_r = 1$, the conditions (Equations 7.5 through 7.7) are satisfied for all five cases. See also [7] for the connection of the derivatives of the polarizability with the virial coefficients of the effective conductivity of dispersions, and the classic study by Brown [19] on the effect of particle geometry on the coefficients.

The polarizabilities of Platonic polyhedra are shown in Figure 7.4 as functions of the permittivity.

From these results it can be observed that the dielectric response is stronger than that of the sphere, and it seems to be stronger for shapes with fewer faces (tetrahedron, cube) and sharper corners, which is intuitively to be expected. Sharp corners bring about field concentrations, which consequently lead to larger polarization densities and to a larger dipole moment.

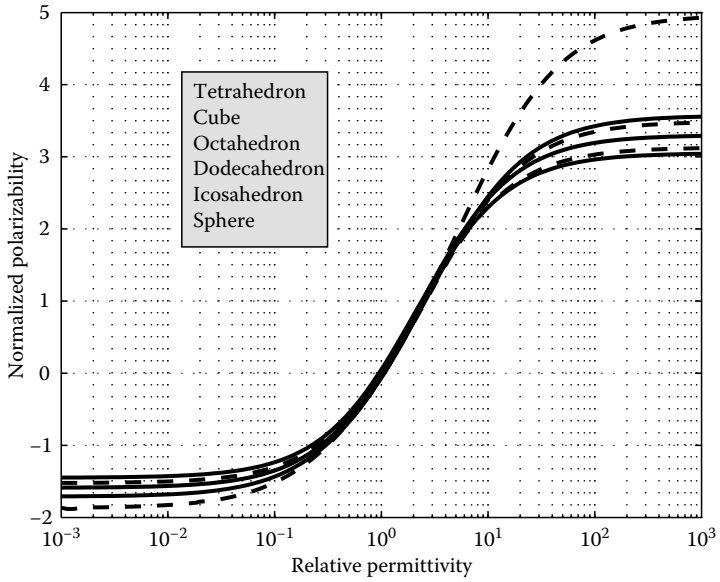

FIGURE 7.4 The polarizabilities of regular polyhedra and a sphere. Note that the curve for a sphere is always smallest in magnitude, and the order of increase is icosa, dodeca, octa, hexa, and tetra (which has the highest curve). (From Sihvola, A., *J. Nanomater.*, 2007, 9, 2007.)

7.3.2 Circular Cylinder

Another basic geometry is the circular cylinder. This shape is more difficult to analyze exhaustively for the reason that it is not isotropic. The response is dependent on the direction of the electric field. The two eigendirections are the axial direction and the transversal direction (which is degenerate as in the transverse plane no special axis breaks the symmetry). Furthermore, the description of the full geometry of the object requires one geometrical parameter (the length-to-diameter ratio), which means that the two polarizability functions are dependent on this value and the dipolarizability response of this object is a set of two families of curves depending on the permittivity.

The polarizabilities of circular cylinders of varying lengths and permittivities have been computed again with the computational approach [20]. Approximative formulas can be written to give a practical algorithm to calculate the values of the polarizabilities. In [20] these formulas are presented as differences to the polarizabilities of spheroids with the same length-to-width ratio as that of the cylinder under study. Spheroids are easy to calculate with exact formulas (Equation 7.11). Since they come close to cylinders in shape when the ratio is very large or very small, one can expect their electric response also to be similar, and the differences to vanish in the limits. Obviously the field singularities of the wedges in the top and bottom faces of the cylinder cause the main deviation of the response from that of the spheroid. Note also [21] and the early work on the cylinder problem in the U.S. National Bureau of Standards (references in [14]).

An illustrative example is the case of "unit cylinder." A unit cylinder has the height equal to the diameter [22]. Its polarizability components are shown in Figure 7.5. There, one can observe that its effect is stronger than that of a sphere (with equal volume), but not as strong as that of a cube.

7.3.3 Semisphere

One further canonical shape is a dielectrically homogeneous semisphere (a sphere cut in half gives two semispheres). However, the electrostatic problem, where two dielectrically homogeneous

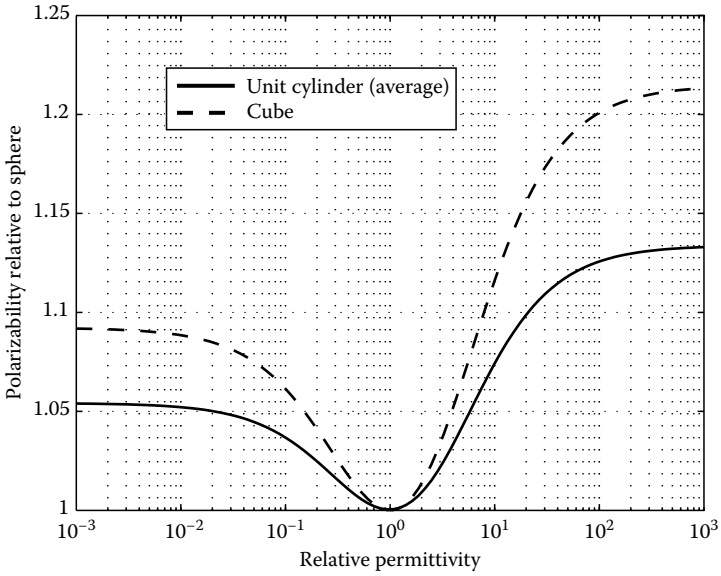

FIGURE 7.5 A comparison of the polarizability of a unit cylinder and a cube. The unit cylinder has different responses to axial and transversal excitations; here one-third of the trace of the polarizability is taken. Both curves are relative to a sphere with the corresponding volume and permittivity. (From Sihvola, A., *J. Nanomater.*, 2007, 9, 2007.)

domains are separated by semispherical boundaries, leads to infinite series with Legendre functions. The polarizability of the semisphere cannot be written in a closed form. However, by truncating the series and inverting the associated matrix, accurate estimates for the polarizability can be enumerated [23]. This requires matrix sizes of a couple of hundred rows and columns. Furthermore, a semisphere as a rotationally symmetric object has to be described by two independent polarizability components. It is nevertheless more "fundamental" than a cylinder because no geometrical parameter is needed to describe its shape.

The axial (z) and transversal (t) polarizability curves for the semisphere resemble those for the other shapes. The limiting values for low and high permittivities are the following:

$$\begin{aligned} \alpha_z &\approx \ \ 2.1894, \quad \alpha_t \approx \ \ 4.4303, \quad (\epsilon_r \to \infty) \\ \alpha_z &\approx -2.2152, \quad \alpha_t \approx -1.3685, \quad (\epsilon_r \to 0) \end{aligned}$$

Note, here the larger high-permittivity polarizability in the transversal direction compared to the longitudinal, which is explained by the elongated character in the transversal plane of the semisphere. In the $\epsilon_r = 0$ limit, the situation is the opposite: a larger polarizability for the axial case (larger in absolute value, as the polarizability is negative).

7.3.4 Double Sphere

A doublet of spheres is another important geometrical shape that is encountered in modeling of random media. When an isolated sphere in a mixture gets into the vicinity of another sphere, especially in the small scales, the interaction forces may be very strong, and the doublet of spheres can be seen as a single polarizing object. Even more, two spheres can become so close in contact that they merge and metamorphose into a cluster. Such a doublet can be described with one geometrical parameter: the distance between the center points of the spheres divided by their radius. The value

2 for this parameter divides the range into two cases: whether the doublet is clustered or separate. Again, this object is rotationally symmetric and needs to be described by two polarizabilities, axial and transversal.

A solution of the electrostatic problem with double-sphere boundary conditions is not easy [24–26]. It requires either a numerical approach or a very complicated analysis using toroidal coordinate system. Several partial results have been presented for the problem [27–29], but only recently a full solution for this problem [30] and its generalization [31] have appeared.

In both limiting cases of the double sphere (the distance of the center points of the spheres goes either to zero or very large), both the normalized polarizability components of the double sphere approach the sphere value (Equation 7.4). And obviously, the polarizability components deviate from the sphere value to the largest degree when the distance between the centers is around two radii (the distance for maximum deviation depends on the permittivity of the spheres). For the case of ϵ_r approaching infinity, the case of touching spheres has the following analytical properties [9,29]:

$$\alpha_z = 6\zeta(3) \approx 7.212, \quad \alpha_t = \frac{9}{4}\zeta(3) \approx 2.705 \tag{7.16}$$

with the Riemann Zeta function. Here the axial polarizability (z) is for the case that the electric field excitation is parallel to the line connecting the center points of the two spheres, and if the field is perpendicular to it, the transversal (t) polarizability applies.

7.4 Conclusion

A detailed knowledge of the polarizability of inclusions with basic shapes gives valuable information about the way how such building blocks contribute to the effective dielectric parameters of a continuum. Many models for the macroscopic properties of matter replace the effect of the particles in the medium fully by its polarizability. It is to be admitted that for complex scatterers this is only a part of the whole response, which also contains near-field terms due to higher-order multipoles that are characterized by stronger spatial field variation close to the scatterer. Nevertheless, dipolarizability remains the dominant term in the characteristics of the inclusion. In this respect, the results of the present chapter are hopefully helpful for modeling of complex materials.

A Web site for interactive Java-applet to calculate the depolarization factors and polarizability components for inclusions of many basic shapes is located in the URL address of the Helsinki University of Technology: http://www.tkk.fi/Yksikot/Sahkomagnetiikka/kurssit/animaatiot/dipolapplet/.

Acknowledgment

This work was supported by the Academy of Finland.

References

1. J. D. Jackson. *Classical Electrodynamics*, 3rd edn. John Wiley & Sons, New York, 1999.
2. A. Sihvola. *Electromagnetic Mixing Formulas and Applications*. IEE Publishing, London, 1999.
3. R. E. Raab and O. L. De Lange. *Multipole Theory in Electromagnetism. Classical, Quantum, and Symmetry Aspects, with Applications*. Clarendon Press, Oxford, 2005.
4. C. F. Bohren and D. R. Huffman. *Absorption and Scattering of Light by Small Particles*. Wiley, New York, 1983.
5. B. E. Sernelius. *Surface Modes in Physics*. Wiley-VCH, Berlin, Germany, 2001.

6. A. Sihvola. Electromagnetic emergence in metamaterials. In S. Zouhdi, A. Sihvola, and M. Arsalane (eds.), *Advances in Electromagnetics of Complex Media and Metamaterials*, Vol. 89. Kluwer Academic Publishers, Dordrecht, the Netherlands, 2003, pp. 1–17. NATO Science Series II: Mathematics, Physics, and Chemistry.
7. E. J. Garboczi and J. F. Douglas. Intrinsic conductivity of objects having arbitrary shape and conductivity. *Physical Review E*, 53(6):6169–6180, June 1996.
8. L. D. Landau and E. M. Lifshitz. *Electrodynamics of Continuous Media*, 2nd edn. Pergamon Press, Oxford, 1984.
9. M. Schiffer and G Szegö. Virtual mass and polarization. *Transactions on the American Mathematical Society*, 67(1):130–205, September 1949.
10. D. S. Jones. Low frequency electromagnetic radiation. *Journal of the Institute of Mathematics and Its Applications*, 23:421–447, 1979.
11. J. C. Maxwell Garnett. Colours in metal glasses and metal films. *Transactions of the Royal Society (London)*, 203:385–420, 1904.
12. D. A. G. Bruggeman. Berechnung verschiedener physikalischer Konstanten von heterogenen Substanzen. I. Dielektrizitätskonstanten und Leitfähigkeiten der Mischkörper aus isotropen Substanzen. *Annalen der Physik*, 24:636–679, 1935.
13. A. Mejdoubi and C. Brosseau. Finite-element simulation of the depolarization factor of arbitrary shaped inclusions. *Physical Review E*, 74:031405(13), 2007.
14. M. L. Mansfield, J. F. Douglas, and E. J. Garboczi. Intrinsic velocity and the electrical polarizability of arbitrarily shaped objects. *Physical Review E*, 64(6):061401(16), November 2001.
15. J. G. Van Bladel. *Electromagnetic Fields*. IEEE Press, Wiley, Piscataway, NJ, 2007.
16. A. Sihvola, P. Ylä-Oijala, S. Järvenpää, and J. Avelin. Polarizabilities of Platonic solids. *IEEE Transactions on Antennas and Propagation*, 52(9):2226–2233, September 2004.
17. A. Sihvola. Dielectric polarization and particle size effects. *Journal of Nanomaterials*, 2007:ID 45090: 1–9, 2007.
18. S. Järvenpää, M. Taskinen, and P. Ylä-Oijala. Singularity extraction technique for integral equation methods with higher order basis functions on plane triangles and tetrahedra. *International Journal for Numerical Methods in Engineering*, 58:1149–1165, 2003.
19. W. F. Brown. Solid mixture permittivities. *Journal of Chemical Physics*, 23(8):1514–1517, August 1955.
20. J. Venermo and A. Sihvola. Dielectric polarizability of circular cylinder. *Journal of Electrostatics*, 63(2):101–117, February 2005.
21. M. Fixman. Variational method for classical polarizabilities. *Journal of Chemical Physics*, 75(8): 4040–4047, October 15, 1981.
22. A. Sihvola, J. Venermo, and P. Ylä-Oijala. Dielectric response of matter with cubic, circular-cylindrical, and spherical microstructure. *Microwave and Optical Technology Letters*, 41(4):245–248, May 2004.
23. H. Kettunen, H. Wallén, and A. Sihvola. Polarizability of a dielectric hemisphere. Technical Report 482, Electromagnetics Laboratory, Helsinki University of Technology, Espoo, Finland, February 2007.
24. P. C. Chaumet and J. P. Dufour. Electric potential and field between two different spheres. *Journal of Electrostatics*, 43:145–159, 1998.
25. G. Dassios, M. Hadjinicolaou, G. Kamvyssas, and A. N. Kandili. On the polarizability potential for two spheres. *International Journal of Engineering Science*, 44:1520–1533, 2006.
26. H. Ammari, G. Dassios, H. Kang, and M. Lim. Estimates for the electric field in the presence of adjacent perfectly conducting spheres. *Quarterly Journal of Applied Mathematics*, 65(2):339–355, June 2006.
27. B. U. Felderhof and D. Palaniappan. Longitudinal and transverse polarizability of the conducting double sphere. *Journal of Applied Physics*, 88(9):4947–4952, 2000.
28. L. Poladian. Long-wavelength absorption in composites. *Physical Review B*, 44(5):2092–2107, 1991.
29. H. Wallén and A. Sihvola. Polarizability of conducting sphere-doublets using series of images. *Journal of Applied Physics*, 96(4):2330–2335, August 2004.

30. M. Pitkonen. Polarizability of the dielectric double-sphere. *Journal of Mathematical Physics*, 47:102901(10), October 2006.
31. M. Pitkonen. An explicit solution for the electric potential of the asymmetric dielectric double sphere. *Journal of Physics D: Applied Physics*, 40(5): 1483–1488, 2007.

8

Single Dipole Approximation for Modeling Collections of Nanoscatterers

Sergiy Steshenko
University of Siena

Filippo Capolino
University of California Irvine

The single dipole approximation for modeling finite and periodic collections of nanoscatterers is summarized and discussed in this chapter. Special attention is given to arrays of nanospheres periodic in one and two dimensions. Different expressions for polarizability reported in the literature are summarized, discussed, and tested against a pure numerical method. It is shown that the use of the polarizability, taken from the exact value of the Mie coefficient, provides the best comparison with full-wave results. We also consider the modeling of periodic arrays of nanoparticles excited by a plane wave and by a single dipole via the array scanning method (ASM).

8.1 Introduction

Consider a collection of N nanoscatterers (nanoparticles) placed at positions $\mathbf{r}_n$, $n = 1, \ldots, N$ shown in Figure 8.1. N can be finite or infinite. We will use bold face symbols for vectors and a hat will tag unit vectors.

We show how to model the electromagnetic response of the collection of nanoscatterers to an external source and how to determine the modes supported by the ensemble. It is known that if the size of a particle is much smaller than the wavelength, its response to an external field can be easily evaluated if the polarizability of the particle is known. The subwavelength particle can be assumed to be immersed in a locally homogeneous electromagnetic field, and its response is described in terms of

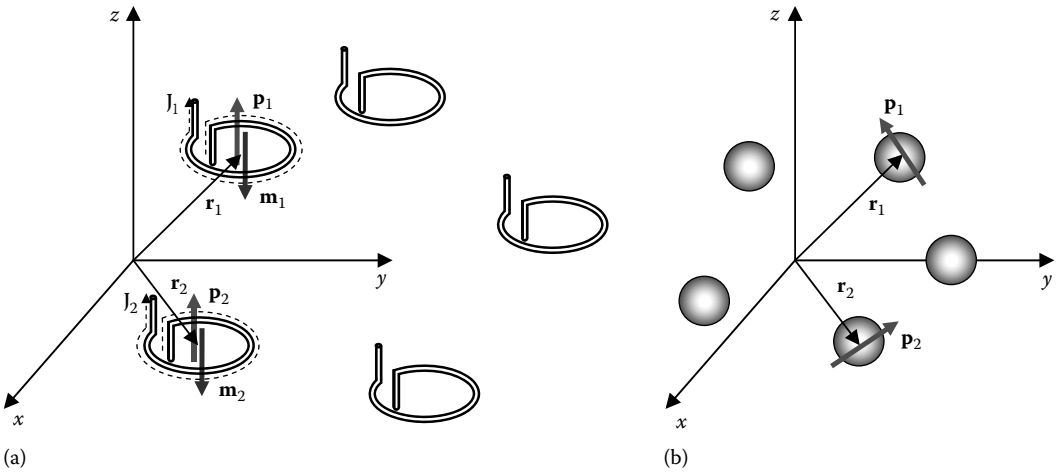

FIGURE 8.1 Structure consisting of particle. (a) Particles modeled by a couple of induced electric and magnetic dipoles; and (b) particles modeled by electric dipoles.

its induced dipole moments [1–3]. Though, in general, one assumes the field response of the particle expressed in terms of dipolar and multipolar fields, for small size scatterers one can often consider only the lower orders and neglect the higher order. Here, we use only the first (lowest) order, and thus, the field generated by the particle is represented as the combination of the electric $\mathbf{p}_n$ and magnetic $\mathbf{m}_n$ dipole moments to characterize the nth particle [4–9]:

$$\begin{aligned} \mathbf{p}_n &= \underline{\alpha}_{ee} \cdot \mathbf{E}_n^{\text{loc}} + \underline{\alpha}_{em} \cdot \mathbf{H}_n^{\text{loc}}, \\ \mathbf{m}_n &= \underline{\alpha}_{me} \cdot \mathbf{E}_n^{\text{loc}} + \underline{\alpha}_{mm} \cdot \mathbf{H}_n^{\text{loc}}. \end{aligned} \tag{8.1}$$

Here, $\mathbf{E}_n^{\text{loc}}$ and $\mathbf{H}_n^{\text{loc}}$ are the local electromagnetic fields acting on the nth particle (the field produced by all the other particles, i.e., excluding that produced by the nth particle itself), and $\underline{\boldsymbol{\alpha}}_{ij}$, $i, j = e, m$ are the polarizability tensors of the particle [10]. However, depending on the geometry and nature of the particle, one of the dipole moments can be dominant and the other can be neglected.

For example, as a first approximation, which has been recognized as satisfactory for several purposes, metallic nanospheres at optical frequencies are usually treated as electric dipoles (Figure 8.2a) [11–26]; however, consideration of both electric and magnetic dipoles would improve the accuracy of the analysis [4–8]. Due to the promising applications and simplicity of fabrication, structures made of nanoparticles have received considerable attention in the past years. Among them, the nanosphere geometry has been highly considered because of the simplicity of its modeling [4–8,11–28], as we show in this chapter. Metallic nanoellipsoid (Figure 8.2b) can also be described by an induced electric dipole [17,29,30], and its polarizability must be described by a dyadic expression. For certain scattering elements, it is the magnetic polarizability that is dominant. An example of elements with dominant-induced magnetic dipole is shown in Figure 8.3 [31,32].

The dipole approximation is an important technique for the analysis of structures made of nanoparticles, as it helps to gain physical insight into the phenomena disregarding minor features from a significantly more involved full-wave analysis. It has been widely used for the analysis of finite structures [12–17,27,30], as well as for structures periodic in one [4–6,18–22,33,34], two [7,8,23–25], and three [7,8] dimensions. The technique has also helped to discover various interesting properties of wave physics in nanostructures.

In this chapter, we consider the single dipole approximation for finite and periodic collections of spherical metallic nanoparticles at optical frequencies. Various expressions for the polarizability

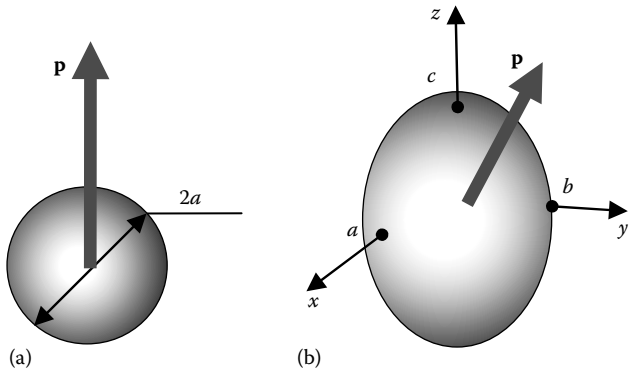

FIGURE 8.2 Metallic nanospheres and ellipsoids modeled by electric dipoles at optical frequencies.

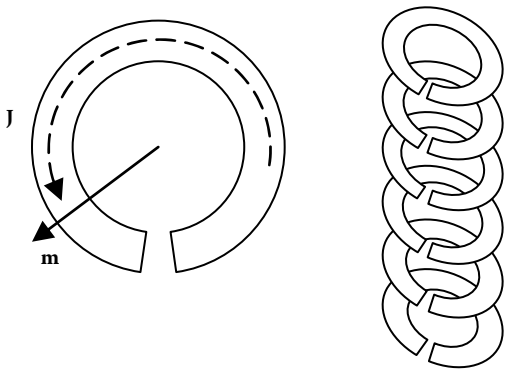

FIGURE 8.3 Loop-like nanoparticle that possesses dominant-induced magnetic dipole.

of a nanosphere are given and tested. It has been shown that the precise value of polarizability, from the Mie theory, provides the best comparison with a full-wave analysis. We provide a framework to analyze any collection of nanoscatterers, periodic and nonperiodic, considering also the case of a single dipole excitation, by using the ASM technique, shown in Chapter 12 of this book [35], and here summarized in Section 8.3.2.

8.2 Single Dipole Formulation for Modeling Collections of Spherical Nanoparticles

In an isotropic medium, spherical nanoparticles can be characterized by their induced electric dipoles:

$$\mathbf{p}_n = \alpha \mathbf{E}_n^{\text{loc}}, \tag{8.2}$$

where

α is the electric field polarizability of a spherical nanoparticle

$\mathbf{E}_n^{\text{loc}}$ is the local field acting on the nth particle, which accounts for the fields produced by all the other sources, excluding the field produced by the nth particle itself

In general, the single dipole approximation significantly simplifies the models of structures made of nanoparticles and it is an efficient tool to make initial predictions. However, it is important to understand the limitations of this approximation. Besides the restriction on the size of a modeled nanoparticle, whose overall size should be much smaller than the ambient wavelength, the distance between the scatterers is of great importance as well, as shown below and in Section 8.4. The dipolar model should not be used in the case of touching or very close particles, as in this case, the interaction of the multipolar fields of the particles becomes significant. In [28], it has been shown that the single dipolar model is appropriate when $a \leq d/3$, where a is the radius of a nanoparticle and d is the center-to-center distance between nanoparticles. For the sake of illustration, in Figure 8.4,

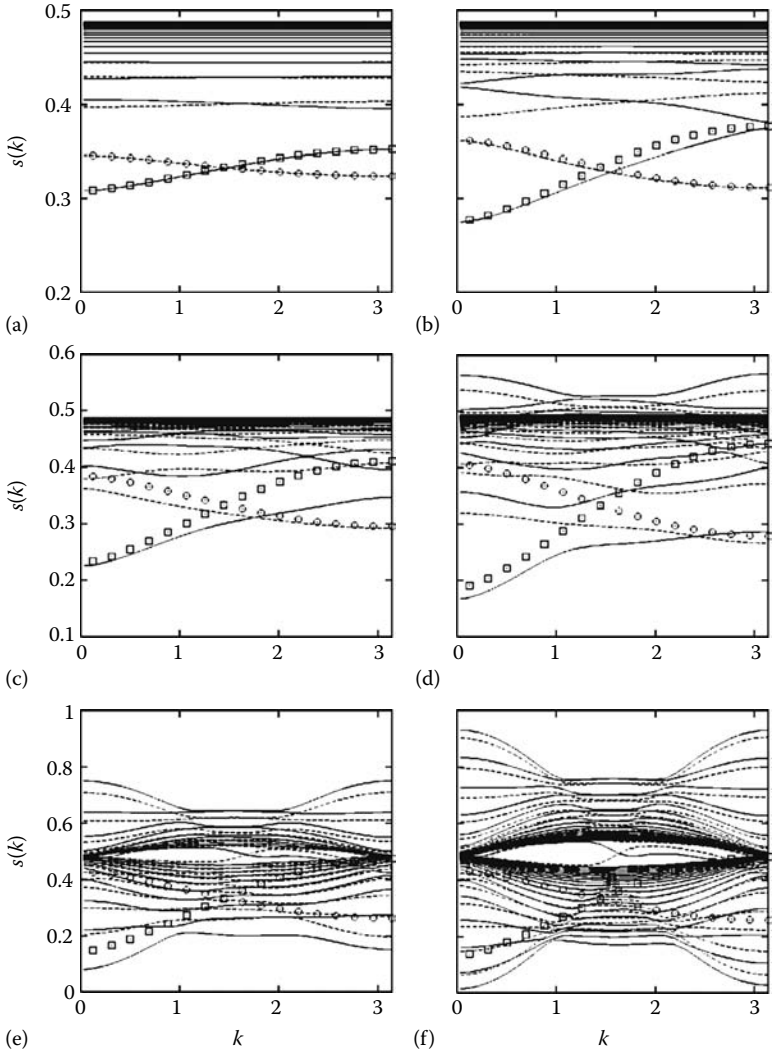

FIGURE 8.4 Dispersion curves for surface-plasmon bands propagating along a chain of spherical nanoparticles under a near-field approximation. Lines correspond to a full multipolar analysis. Open circles and squares represent results of single dipole approximation. (a) $a/d = 0.25$, (b) $a/d = 0.33$, (c) $a/d = 0.4$, (d) $a/d = 0.45$, (e) $a/d = 0.49$, and (f) $a/d = 0.5$. On the abscissa, instead of k (as in the original plot) there should be kd, the normalized longitudinal propagation wave number. (Reprinted from Park, S.Y. and Stroud, D., *Phys. Rev. B*, 69, 125418, 2004. With permission.)

a comparison of results obtained by the dipolar and multipolar approaches is shown, both evaluated with the near-field approximation (where the light velocity is set to be equal to infinity, or alternatively, the hosting material wave number, $k = \omega\sqrt{\varepsilon\mu_0}$, is set to zero, where ε and μ_0 are the permittivity and permeability of the host medium) for a linear array (chain) of nanospheres with different ratios, a/d. Although the near-field approximation used in [28] leads to significant errors, this example is useful to have an idea of the impact of the ratio, radius/distance, of the spheres on the accuracy of the results. The dispersion curves in Figure 8.4 are represented in terms of the variable, $s = \varepsilon_h/(\varepsilon_h - \varepsilon_m)$, where ε_m and ε_h are the relative permittivities of the sphere material and the host medium, versus the normalized longitudinal propagation wave number k (the abscissa in the plot in the original paper [28] is k, though it should be kd, the normalized propagation wave number). The variable s can be considered to be the frequency variable, as the relative permittivity of the metal ε_m is frequency dependent. Note that the authors of [28] use k for the longitudinal wave number (therefore k determines the propagation constant along the chain), whereas this symbol is commonly used, also in the rest of this chapter, as for the wave number in the homogeneous material hosting the nanoscatterers.

The larger the radius a of the spheres (normalized with respect to the spheres' distance d), the larger the error of the single dipole approximation technique, and it becomes inadmissible when $a/d = 0.45$, which represents the case of almost touching spheres.

We consider now a few simplified models to account for the polarizability α and to evaluate the local field $\mathbf{E}_n^{loc}$, with the aim of finding the induced dipole moments of the nanoparticles or the modes in periodic arrays of nanoparticles.

8.2.1 Polarizability Expressions for a Spherical Nanoparticle

The simplest quasistatic expression for polarizability of a spherical nanoparticle is given by the Clausius–Mossotti (Lorentz–Lorenz) relation [1,2,36–38]:

$$\alpha = 4\pi\varepsilon_0\varepsilon_h a^3\left(\frac{\varepsilon_m - \varepsilon_h}{\varepsilon_m + 2\varepsilon_h}\right), \tag{8.3}$$

where

a is the radius of the nanosphere

ε_m and ε_h are the relative permittivities of the metal and the host medium, respectively

Relative permeabilities of the metal and host media are assumed to be equal to unity. A simple representation for the relative permittivity of metal is provided by the Drude model:

$$\varepsilon_m = \varepsilon_\infty - \frac{\omega_p^2}{\omega(\omega - j\gamma)}, \tag{8.4}$$

where

ω_p is the plasma radian frequency

γ is the damping frequency

The time harmonic convention, $\exp(j\omega t)$, is assumed here and throughout the chapter. For several purposes, the dimensionless parameter ε_∞ in Equation 8.4 does not need to be the real material relative permittivity when ω tends to infinity. It can be different from unity and chosen together with the frequency parameters, ω_p and γ, to better fit the actual material permittivity [39] in the frequency range of interest.

When the dimensions of the nanoparticle are very small, the adoption of the Drude model, as in Equation 8.4, would not properly estimate the losses. Indeed, when the particle size becomes comparable with the bulk mean free path l_∞ of the conduction electrons, the scattering process is changed

by the collision of the conduction electrons with the particle surfaces [40,41, p. 79]. This process increases the losses in the nanoparticles, and it can be taken into account by introducing the size-dependent damping frequency, $\gamma(a) = v_F/l_\infty + A(v_F/a)$, in the Drude model (Equation 8.4), where v_F is the Fermi velocity and the parameter A is a theory-dependent quantity of the order of 1 [41, p. 81]. For example, some authors use $A = 1$ [29,42].

The accuracy of the polarizability expression (Equation 8.3) depends on the amount of losses and on the particle size. In the following, we discuss the accurate expressions of the polarizability α in relation to the correct electrodynamic Mie theory, and we show how Equation 8.3 can lead to contradictory results. We shall start by recalling some fundamental principles and energy constraints. The energy conservation law for a single particle is written as

$$C_{ext} = C_{sca} + C_{abs} \quad \text{or} \quad Q_{ext} = Q_{sca} + Q_{abs}, \tag{8.5}$$

where C_{ext}, C_{sca}, and C_{abs} are the extinction, scattering, and absorption cross sections, respectively [2]. It is convenient to use the extinction Q_{ext}, scattering Q_{sca}, and absorption Q_{abs} efficiencies defined as $Q_{...} \equiv C_{...}/(\pi a^2)$, i.e., by normalizing the cross sections, $C_{...}$, with the geometrical cross section, πa^2, of the nanospheres. When the polarizability α of the nanoparticle is used in the dipolar approximation, as in Equation 8.2, for lossless or lossy nanoparticles, a direct integration of the dipolar fields provides the following expressions for the scattering, extinction, and absorption efficiencies [2, p. 72, 103]:

$$Q_{sca} = \frac{k^4}{6(\varepsilon_0\varepsilon_h\pi a)^2}|\alpha|^2, \quad Q_{ext} = -\frac{k}{\varepsilon_0\varepsilon_h\pi a^2}\mathrm{Im}(\alpha), \quad Q_{abs} = Q_{ext} - Q_{sca}, \tag{8.6}$$

where $k = \omega\sqrt{\varepsilon_h}/c$ is the wave number in the homogeneous material hosting the nanospheres.

When the quasistatic expression (Equation 8.3) for the polarizability is used, a problem with the energy conservation law (Equation 8.5) is encountered, as explained in the following. Consider the limiting case of a lossless nanosphere with $\mathrm{Im}(\varepsilon_m) = 0$ and $\varepsilon_m \neq \varepsilon_h$. In this case, according to Equations 8.3 and 8.6, $Q_{sca} > 0$ and $Q_{ext} = 0$. To satisfy the energy conservation law (Equation 8.5), the absorption efficiency Q_{abs} should be negative. This would imply that the energy is being created within the nanoparticle, which is clearly a contradiction. If the quasistatic expression for the polarizability of nanoparticles (Equation 8.3) is used, the expression for the extinction efficiency in Equation 8.6 is appropriate only when the scattering is small compared to the absorption [2, p. 140].

When the quasistatic polarizability (Equation 8.3) is used, a good approximation for the scattering and absorption efficiencies, for small spheres and small losses [2, p. 136], would be provided by the expressions [2, p. 140]

$$Q_{sca} = \frac{k^4}{6(\varepsilon_0\varepsilon_h\pi a)^2}|\alpha|^2, \quad Q_{abs} = -\frac{k}{\varepsilon_0\varepsilon_h\pi a^2}\mathrm{Im}(\alpha). \tag{8.7}$$

However, as already said, the direct integration of the dipolar fields gives values represented by the expressions (Equation 8.6). As a consequence, the quasistatic polarizability (Equation 8.3) gives wrong results when used in Equation 8.6, if losses are small. And in this case, a better approximation than Equation 8.3 for the polarizability should be used if one wants to use the correct expressions (Equation 8.6). The problem of using Equation 8.3 for small or absent losses is also encountered in a variety of situations. As an illustrative example, in Section 8.4.2, we show that when a planar periodic array of nanoparticles with small or absent losses is illuminated by a plane wave, the estimated values of the reflection and transmission coefficients can be larger than unity if the quasistatic polarizability expression (Equation 8.3) is used, which is clearly a contradiction.

The energy conservation problem is overcome by considering a slight modification of the formula (Equation 8.3):

$$\alpha = 4\pi\varepsilon_0\varepsilon_h a^3\left(\frac{\varepsilon_m + 2\varepsilon_h}{\varepsilon_m - \varepsilon_h} + j\frac{2(ka)^3}{3}\right)^{-1}, \tag{8.8}$$

where the additional imaginary term in the parentheses takes into account the radiation damping [29,43]. With this value of polarizability, the energy conservation law (Equation 8.5) is exactly satisfied for lossless particles [characterized by Im $(\varepsilon_m) = 0$], as in the case of Equations 8.6 and 8.8 we have, $Q_{ext} = Q_{sca}$ and $Q_{abs} = 0$. In Section 8.4.2, we provide some examples where we show that the expression (Equation 8.8) gives satisfactory approximations.

Some authors use the value of polarizability with radiation damping correction (Equation 8.8) also for lossy nanospheres [15,20,29]. However, as it was noted in [22], Equation 8.8 with the additional radiation damping term that was obtained under the condition that Im $(\varepsilon_m) = 0$, gives an error of the same order as Equation 8.3. These concepts and approximations are clarified by considering the more accurate polarizability obtained from the Mie theory [2]:

$$\alpha = -\frac{6\pi\varepsilon_0\varepsilon_h j}{k^3}\,\frac{m\psi_1(mka)\,\psi_1'(ka) - \psi_1(ka)\,\psi_1'(mka)}{m\psi_1(mka)\,\xi_1'(ka) - \xi_1(ka)\,\psi_1'(mka)}, \tag{8.9}$$

where

$\psi_1(\rho) = \rho j_1(\rho) = \sin\rho/\rho - \cos\rho$, $\xi_1(\rho) = \rho h_1^{(2)}(\rho) = (j/\rho - 1)e^{-j\rho}$ are the Ricatti–Bessel functions

$m = k_m/k = \sqrt{\varepsilon_m/\varepsilon_h}$ is the relative refractive index

$k_m = \omega\sqrt{\varepsilon_m}/c$ is the wave number in the metal

Expanding α^{-1} in series with respect to the small parameter *ka* we have

$$\alpha = 4\pi\varepsilon_0\varepsilon_h a^3\left[\frac{m^2+2}{m^2-1} - \frac{3}{5}\frac{m^2-2}{m^2-1}(ka)^2 + j\frac{2}{3}(ka)^3 + O(ka)^4\right]^{-1}. \tag{8.10}$$

The first item in the brackets of Equation 8.10 corresponds to the quasistatic polarizability (Equation 8.3) and the third one is equal to the radiation damping correction in Equation 8.8. However, one should note that the second term is not included in Equation 8.8, and that its order $(ka)^2$ is even lower than $(ka)^3$ of the third term of Equation 8.10. The second term may be identified with a dynamic depolarization [11]. If Im $(\varepsilon_m) = 0$ (lossless spheres), this term is pure real and has no effect on the extinction efficiency (Equation 8.6). In realistic material parameters, losses should be taken into account $[\mathrm{Im}(\varepsilon_m) \neq 0]$, and the second term in Equation 8.10 contains an imaginary part as well and contributes a $(ka)^3$ term to the extinction efficiency Q_{ext}. Therefore, the use of Equations 8.3 and 8.8 implies an error of the order $(ka)^3$ in the estimation of the extinction efficiency.

The exact formula for polarizability (Equation 8.9) has been used, for example, in [21,44], and some results are also provided in this chapter.

Note that the extinction efficiency, Q_{ext}, for a lossy spherical nanoparticle is of the order of (ka). When considering the two higher spherical modes of the lossy spherical particle (magnetic dipole and electric quadrupole) in the Mie series, provided that all scattering coefficients are calculated precisely, the estimated value of the extinction efficiency, Q_{ext}, is modified by a quantity of the order of $(ka)^3$ with respect to Equation 8.9. This is exactly the order of the difference between the extinction efficiencies, Q_{ext}, calculated by using Equation 8.8 or 8.9. Thus, asymptotically, Equations 8.8 and 8.9 are both expected to give errors of the order $(ka)^3$ in the estimation of the extinction efficiency of a lossy nanoparticle. However, the accuracy of Equation 8.9 is expected to be better since it already includes the $(ka)^3$ order, not included in Equation 8.8, and the numerical results in Section 8.4.2 confirm this. Analogous considerations apply to the case of lossless nanoparticles; the error in Equation 8.8 with respect to Equation 8.9 is of the order of $(ka)^6$. The error in Equation 8.9 with respect to the inclusion of the higher order (magnetic dipole and quadrupoles) is of the order of $(ka)^8$.

For what concerns the estimation of the scattering efficiency Q_{sca}, instead, the inclusion of additional terms provided by the higher spherical (magnetic dipole and electric quadrupole) modes in the Mie series modifies the order $(ka)^8$ with respect to Equation 8.9, in both the cases of lossy and

lossless nanospheres. Note, also, that the scattering efficiency Q_{sca} calculated as in Equation 8.6 with Equation 8.8 misses the order $(ka)^6$, which is instead included when using Equation 8.9. In summary, the error in the estimation of the scattering efficiency Q_{sca} is $(ka)^8$, when using the polarizability from the Mie theory (Equation 8.9), and $(ka)^6$, when using the polarizability in Equation 8.8.

8.2.2 Calculation of the Local Field

The calculation of the local electric field $\mathbf{E}_n^{\text{loc}}$ acting on the nth particle at $\mathbf{r}_n$ depends on the type of excitation and geometry. The local field

$$\mathbf{E}_n^{\text{loc}} = \mathbf{E}^{\text{inc}}(\mathbf{r}_n) + \mathbf{E}_n^{\text{sc}} \tag{8.11}$$

includes the external incident field, $\mathbf{E}^{\text{inc}}(\mathbf{r}_n)$, and the scattered field, $\mathbf{E}_n^{\text{sc}}$, produced by all other scatterers, except for the nth one, at position $\mathbf{r}_n$:

$$\mathbf{E}_n^{\text{sc}} = \sum_{\substack{m=1 \\ m \neq n}}^{N} \underline{\mathbf{G}}(\mathbf{r}_n, \mathbf{r}_m) \cdot \mathbf{p}_m. \tag{8.12}$$

Here,

$$\begin{aligned} \underline{\mathbf{G}}(\mathbf{r}_n, \mathbf{r}_m) &= \frac{1}{\varepsilon_0 \varepsilon_{\text{h}}} \left[k^2 G(\mathbf{r}_n, \mathbf{r}_m) \underline{\mathbf{I}} + \nabla\nabla G(\mathbf{r}_n, \mathbf{r}_m) \right] \\ &= \frac{e^{-jkr_{nm}}}{4\pi\varepsilon_0\varepsilon_{\text{h}}} \left[\left(\frac{k^2}{r_{nm}} - \frac{jk}{r_{nm}^2} - \frac{1}{r_{nm}^3} \right) \underline{\mathbf{I}} - \left(\frac{k^2}{r_{nm}} - \frac{3jk}{r_{nm}^2} - \frac{3}{r_{nm}^3} \right) \hat{\mathbf{r}}_{nm} \hat{\mathbf{r}}_{nm} \right] \end{aligned} \tag{8.13}$$

is the symmetric electric-field dyadic Green's function (GF) of the homogenous medium, $\mathbf{r}_{nm} = \mathbf{r}_n - \mathbf{r}_m$, $r_{nm} = |\mathbf{r}_{nm}|$, $\hat{\mathbf{r}}_{nm} = \mathbf{r}_{nm}/r_{nm}$, and

$$G(\mathbf{r}, \mathbf{r}') = \frac{e^{-jk|\mathbf{r}-\mathbf{r}'|}}{4\pi|\mathbf{r}-\mathbf{r}'|} \tag{8.14}$$

is the scalar GF and $\underline{\mathbf{I}}$ is the identity dyadic. The expression, $\nabla\nabla G(\mathbf{r}, \mathbf{r}')$, denotes the Hessian of $G(\mathbf{r}, \mathbf{r}')$, which acts on a vector $\mathbf{p}$ as $\nabla\nabla G(\mathbf{r}, \mathbf{r}') \cdot \mathbf{p} \equiv \nabla[\nabla G(\mathbf{r}, \mathbf{r}') \cdot \mathbf{p}]$. In Cartesian coordinates, the operator $\nabla\nabla G(\mathbf{r}, \mathbf{r}')$ is given by the matrix of the second derivatives of $G(\mathbf{r}, \mathbf{r}')$ with respect to the $\mathbf{r}$ components x, y, and z.

8.2.3 Calculation of the Induced Dipole Moments of Nanoparticles

Once the polarizability (Equation 8.9) and the local field (Equation 8.11) are known, the induced dipole moments $\mathbf{p}_m$ of the nanoparticles are calculated by solving the linear system

$$\sum_{m=1}^{N} \underline{\mathbf{A}}_{nm} \cdot \mathbf{p}_m = \mathbf{E}^{\text{inc}}(\mathbf{r}_n), \tag{8.15}$$

where $n = 1, 2, \ldots N$, and

$$\underline{\mathbf{A}}_{nm} = \begin{cases} \frac{1}{\alpha}\underline{\mathbf{I}}, & n = m, \\ -\underline{\mathbf{G}}(\mathbf{r}_n, \mathbf{r}_m), & n \neq m. \end{cases} \tag{8.16}$$

8.3 Periodic Arrangements of Nanoparticles

One of the most interesting cases is represented by arrays of nanoscatterers periodic in one, two, or three dimensions. In this case, we often assume that the array of nanoparticles is linearly phased. The phasing can be fixed as in the case of an array excited by a plane wave or when the resonant frequencies of normal modes (with a real wavevector) are sought. Instead, if one is interested in determining modes with complex wavevectors, a real frequency is assigned and the complex wavevectors are sought numerically.

The ASM [35] is used when one is interested in modeling the effects of a single dipole excitation of a periodic array. The ASM technique involves the evaluation of the fields generated by linearly phased array of sources, with all possible phasings within the first Brillouin zone [45–50].

Various cases of arrays of nanoparticles periodic in one, two, or three dimensions are considered here. In the following, nanoparticles are modeled by dipole moments, $\mathbf{p}_n$, placed at positions, $\mathbf{r}_n = \mathbf{r}_0 + \mathbf{d}_n$, where n can be a single, double, or triple index for problems periodic in one, two, and three dimensions, respectively. For example, for 1D-periodic problems, $\mathbf{d}_n = n\mathrm{d}\hat{\mathbf{z}}$, $n \in \mathbb{Z}$; for 2D-periodic problems, $\mathbf{d}_n = n_1\mathbf{s}_1 + n_2\mathbf{s}_2$, $n_1, n_2 \in \mathbb{Z}$; whereas for the 3D-periodic case, $\mathbf{d}_n = n_1\mathbf{s}_1 + n_2\mathbf{s}_2 + n_3\mathbf{s}_3$, $n_1, n_2, n_3 \in \mathbb{Z}$.

8.3.1 Quasiperiodic Excitation of Periodic Arrangements of Nanoparticles

Suppose that the array of nanoparticles is excited by a plane wave or by a quasiperiodic excitation with wavevector $\mathbf{k}_B$. Accordingly, we assume that the array elements have dipole moments equal to $\mathbf{p}_n = \mathbf{p}_0 e^{-j\mathbf{k}_B\cdot\mathbf{d}_n}$.

The local field, $\mathbf{E}^{\mathrm{loc}}(\mathbf{r}_0, \mathbf{k}_B)$, acting on the nanoscatterer at position $\mathbf{r}_0$ is, thus, given by the sum

$$\mathbf{E}^{\mathrm{loc}}(\mathbf{r}_0, \mathbf{k}_B) = \mathbf{E}^{\mathrm{inc}}(\mathbf{r}_0) + \breve{\underline{\mathbf{G}}}^{\infty}(\mathbf{r}_0, \mathbf{r}_0, \mathbf{k}_B)\cdot\mathbf{p}_0, \tag{8.17}$$

where the regularized GF $\breve{\underline{\mathbf{G}}}^{\infty}$ (here, and in the following, the Mexican hat "$\smile$" denotes the regularized GF) is defined as $\breve{\underline{\mathbf{G}}}^{\infty}(\mathbf{r}, \mathbf{r}_0, \mathbf{k}_B) \equiv \underline{\mathbf{G}}^{\infty}(\mathbf{r}, \mathbf{r}_0, \mathbf{k}_B) - \underline{\mathbf{G}}(\mathbf{r}, \mathbf{r}_0)$, and

$$\underline{\mathbf{G}}^{\infty}(\mathbf{r}, \mathbf{r}_0, \mathbf{k}_B) = \sum_n \underline{\mathbf{G}}(\mathbf{r}, \mathbf{r}_0 + \mathbf{d}_n)\, e^{-j\mathbf{k}_B\cdot\mathbf{d}_n} \tag{8.18}$$

is the electric-field dyadic GF for the periodically phased array of dipoles. The summation $\boldsymbol{\Sigma}_n$ includes all periodic sources at locations, $\mathbf{r}_n = \mathbf{r}_0 + \mathbf{d}_n$. The regularized term, $\breve{\underline{\mathbf{G}}}^{\infty}(\mathbf{r}, \mathbf{r}_0, \mathbf{k}_B)$, corresponds to the dyadic GF in Equation 8.18 without the $n = 0$ term (or $n_1, n_2 = 0$, or $n_1, n_2, n_3 = 0$ for 2D- or 3D-periodic structures), and thus it is not singular at $\mathbf{r} = \mathbf{r}_0$. After substituting Equation 8.17 in Equation 8.2, we have

$$\mathbf{p}_0 = \alpha\left[\mathbf{E}^{\mathrm{inc}}(\mathbf{r}_0) + \breve{\underline{\mathbf{G}}}^{\infty}(\mathbf{r}_0, \mathbf{r}_0, \mathbf{k}_B)\cdot\mathbf{p}_0\right], \tag{8.19}$$

which leads to the linear system

$$\underline{\mathbf{A}}(\mathbf{k}_B)\cdot\mathbf{p}_0 = \mathbf{E}^{\mathrm{inc}}(\mathbf{r}_0), \tag{8.20}$$

where

$$\underline{\mathbf{A}}(\mathbf{k}_B) \equiv \frac{1}{\alpha}\underline{\mathbf{I}} - \breve{\underline{\mathbf{G}}}^{\infty}(\mathbf{r}_0, \mathbf{r}_0, \mathbf{k}_B). \tag{8.21}$$

Note that the dyadic function, $\underline{\mathbf{A}}(\mathbf{k}_B)$, does not depend on $\mathbf{r}_0$ as, in fact, the GF, $\underline{\mathbf{G}}^{\infty}(\mathbf{r}, \mathbf{r}_0, \mathbf{k}_B)$, depends on the difference, $\mathbf{r} - \mathbf{r}_0$.

The series (Equation 8.18) is slowly convergent, and it is divergent in certain important regions of the parameters k and $\mathbf{k}_B$: (1) when k is real and the components of the wavevector $\mathbf{k}_B$ are complex, (2) when $\mathbf{k}_B$ is real and Im $k > 0$. Note that the second region corresponds to the time-decaying modes. Therefore, the series (Equation 8.18) cannot be calculated directly if physical normal modes are investigated.

Various researchers have calculated the periodic GF considering the near-field (quasistatic) approximation, which takes into account the terms dominating in the near-field static part of the electric field [13,28]. According to this approximation, it is assumed that $kd << 1$ and, after setting $k = 0$ or, equivalently, $c = \infty$, in the right-hand side of Equation 8.18, we obtain

$$\underline{\mathbf{G}}^{\infty}(\mathbf{r}, \mathbf{r}_0, \mathbf{k}_B) = \frac{1}{4\pi\varepsilon_0\varepsilon_h} \sum_n \frac{e^{-j\mathbf{k}_B\cdot\mathbf{d}_n}}{|\mathbf{r} - \mathbf{r}_0 - \mathbf{d}_n|^3} \left[3(\mathbf{r} - \mathbf{r}_0 - \mathbf{d}_n)(\mathbf{r} - \mathbf{r}_0 - \mathbf{d}_n) - \underline{\mathbf{I}}\right]. \tag{8.22}$$

The series in Equation 8.22 does not depend on the wave number k, and it is convergent in the second region mentioned above. Therefore, the near-field approximation can be used to find modes with the real wavevector and complex resonance frequencies. However, the series in Equation 8.22 is still divergent for complex values of the wavevector $\mathbf{k}_B$. In summary, the near-field approximation does not allow the search for complex modes.

Another simplification that was adopted in [16,17] and denoted as the "nearest-neighbor approximation," consists in considering the dipolar field contributions arising only from a few nearest neighboring particles. In this case, the series in Equation 8.18 is truncated and there is no problem with its calculation, though, possible important long range couplings would be neglected.

In a few published cases, the rigorous calculation of Equation 8.18 for complex wavevectors $\mathbf{k}_B$ has been used. Depending on the order of periodicity, this can be possible just by using a pure spectral version of Equation 8.18, for which 2D- and 3D-periodic systems correspond to a summation of plane waves. When the periodicity is in one dimension, the pure spectral sum cannot be adopted, and some authors used the representation of the periodic GF in terms of a polylogarithm [19,20,34]. Here, we suggest the use of the Ewald summation method [51–57], which provides an analytical continuation of the series (Equation 8.18) to the complex planes for 1D-, 2D-, and 3D-periodic systems. Besides solving convergence problems (particularly, for 1D-periodic systems), the Ewald method provides series with Gaussian convergence, and therefore extremely rapid convergence rates.

8.3.2 Periodic Arrangements of Nanoparticles Excited by a Single Dipole Source

The problem of single dipole excitation of a finite array of nanoparticles can be very time-consuming when many particles need to be considered [13,15,30], because of the very large size of the matrix equation (Equation 8.15) to be solved, especially when the array is periodic in two or three dimensions.

It is more efficient to analyze the single dipole excitation of a periodic infinite array. This analysis can be performed by the ASM [35,45–50]. The assumption of an infinite array also provides a neat physical insight into certain wave excitation phenomena (modal excitation) that otherwise could be altered by truncation effects.

Assume that an array has nanoparticles located at positions, $\mathbf{r}_n = \mathbf{r}_0 + \mathbf{d}_n$. According to the ASM, the field, $\mathbf{E}(\mathbf{r}, \mathbf{r}_s)$, at an arbitrary point $\mathbf{r}$, produced by a single dipole source $\mathbf{p}_s$ at $\mathbf{r}_s$, is given by the $\mathbf{k}_B$-spectral integral

$$\mathbf{E}(\mathbf{r}, \mathbf{r}_s) = \frac{1}{A_B} \int_B \mathbf{E}^{\infty}(\mathbf{r}, \mathbf{r}_s, k_B)\mathrm{d}B, \tag{8.23}$$

where
B is the first Brillouin zone
A_B is its area

For 1D-periodic problems, $A_B = 2\pi/d$; for 2D-periodic problems, $A_B = (2\pi)^2 \big/ |\mathbf{s}_1 \times \mathbf{s}_2|$; whereas for 3D-periodic problems, $A_B = (2\pi)^3 \big/ |\mathbf{s}_1 \cdot (\mathbf{s}_2 \times \mathbf{s}_3)|$. The field, $\mathbf{E}^{\infty}(\mathbf{r}, \mathbf{r}_s, \mathbf{k}_B)$, is the total field produced by the array of nanoparticles and a periodic array of source dipoles at positions, $\mathbf{r}_{s,n} = \mathbf{r}_s + \mathbf{d}_n$, linearly phased with wavevector $\mathbf{k}_B$:

$$\mathbf{p}_{s,n} = \mathbf{p}_s e^{-j\mathbf{k}_B \cdot \mathbf{d}_n}. \tag{8.24}$$

In other words, we consider the superpositions of the array of sources, linearly phased [35], as excitations for the array of nanoparticles. The value of the total $\mathbf{k}_B$-dependent field, $\mathbf{E}^{\infty}(\mathbf{r}, \mathbf{r}_s, \mathbf{k}_B)$, is evaluated by the formula

$$\mathbf{E}^{\infty}(\mathbf{r}, \mathbf{r}_s, \mathbf{k}_B) = \underline{\mathbf{G}}^{\infty}(\mathbf{r}, \mathbf{r}_0, \mathbf{k}_B) \cdot \mathbf{p}_0^{\infty}(\mathbf{k}_B) + \underline{\mathbf{G}}^{\infty}(\mathbf{r}, \mathbf{r}_s, \mathbf{k}_B) \cdot \mathbf{p}_s, \tag{8.25}$$

where $\mathbf{p}_0^{\infty}(\mathbf{k}_B)$ is the electric dipole moment of the nanoparticle at the position $\mathbf{r}_0$, induced by the periodic array of exciting dipoles (Equation 8.24), that is determined by solving the matrix equation (Equation 8.20).

Some numerical results for the excitation of 2D-periodic finite and infinite arrays of metallic nanospheres by a single electric dipole and a couple of electric dipoles are given in [23–25] where the superlensing and near-field enhancement properties of arrays of nanoparticles are investigated.

8.4 Illustrative Examples

8.4.1 Modes

The modes in a periodic arrangement of nanoparticles are determined by looking at the homogeneous matrix equation (Equation 8.20), after setting $\mathbf{E}^{\text{inc}} = 0$. Numerically, the determinant of the matrix in Equation 8.20 is set to vanish. Modes are classified as bound and leaky modes, depending on their wavevector [35].

To illustrate the degree of accuracy of the various approximations previously discussed, in Figure 8.5 we report the dispersion curves for a linear array of silver nanospheres obtained in [13], where significant discrepancies are shown between the quasistatic analysis (using the near-field approximation (Equation 8.22) for the dipole fields and the quasistatic polarizability (Equation 8.3)) and the fully retarded analysis (including all the retarded terms as in Equation 8.13 and the polarizability with the radiation damping correction (Equation 8.8)). The dispersion equations were solved for the normal transverse and longitudinal modes, i.e., modes with induced dipole polarization directions orthogonal and parallel to the array axis, respectively. In this case, complex resonant frequencies were sought for real propagation wave numbers k along the array (though, usually, in our chapter we use a different symbol for the propagation wave number, and k represents the ambient wave number).

The radius of the spheres is $a = 25\,\text{nm}$, the period is $d = 75\,\text{nm}$, and the assumed frequency parameters of the Drude model (Equation 8.4) are $\varepsilon_\omega = 1$, $\hbar\omega_p = 6.18\,\text{eV}$ and $\hbar\gamma = 0.7\,\text{eV}$.

Quasistatic solutions, including the near-field approximation and the polarizability (Equation 8.3), were calculated for an infinite chain and a finite 20-sphere chain. Both solutions are in perfect agreement. However, a comparison between the fully retarded and the quasistatic solutions for the finite 20-sphere chain has revealed quantitative and qualitative discrepancies especially for transverse

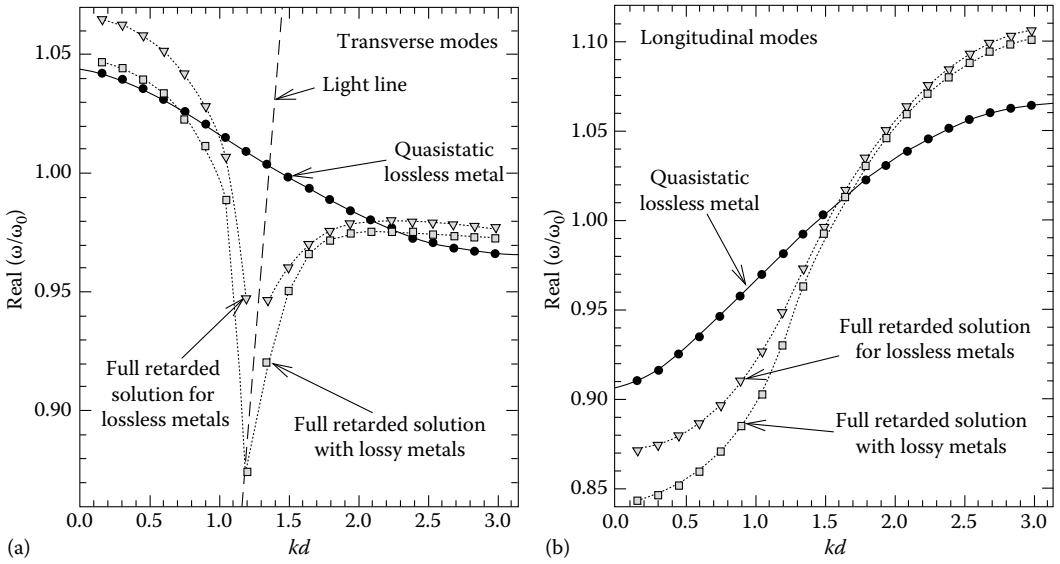

FIGURE 8.5 Comparison of the quasistatic and fully retarded solutions of the dispersion equation for an array of silver nanospheres. Solid thick lines correspond to the quasistatic solution for an infinite array of lossless nanospheres, and the superposed circles are for the quasistatic solution for a finite chain of 20 lossless nanospheres. Triangles are for the fully retarded solution for a finite chain of 20 lossless nanospheres. Squares are for the fully retarded solution for a finite chain of 20 lossy nanospheres. (a) Transverse dipolar modes and (b) longitudinal dipolar modes. (Reprinted from Weber, W. and Ford, G., *Phys. Rev. B*, 70, 125429, 2004. With permission.)

dipolar modes (Figure 8.5). There is a dramatic deviation from the quasistatic result when the light line intersects the dispersion curve of the transverse dipolar mode.

These results show the importance of considering all the retardation terms in the expression for the electric dipole field, also when dealing with subwavelength distances and radii. Note that the fully retarded solution for an infinite chain could not be found unless a special analytic continuation of the Green's function is applied, as for the polylogarithm and the Ewald methods. Even a purely spectral representation of the periodic GF could not have been used for this particular case.

Other examples of modes for planar arrays of silver nanospheres, evaluated with the technique proposed in this chapter, are included in [23–25]. There, we have assumed real frequencies and determined real wave numbers for the case of lossless nanospheres.

8.4.2 Transmission

Here, we consider the excitation of a 2D-periodic array of silver nanoparticles by a plane wave with the incidence orthogonal to the array plane. The periods of the array in the x- and y-directions are equal to 200 nm. The parameters of the Drude model for silver (Equation 8.4) are assumed as in [14], where $\varepsilon_\infty = 5$, $\omega_p = 1.37 \times 10^{16}$ rad $\cdot$ s^{-1}, and $\gamma = 27.3 \times 10^{12}$ s^{-1}. We consider different expressions (Equations 8.3, 8.8, and 8.9) for the polarizability of a nanosphere, and different nanosphere radii, a = 15, 25, and 35 nm. The results for the transmission coefficient T, the ratio between transmitted and incident power, evaluated via the fully retarded formulation (Equation 8.20) are compared with a full-wave analysis performed with CST Microwave Studio. In Figures 8.6 through 8.8, dashed lines are for the results obtained with the quasistatic polarizability (Equation 8.3), short dashed lines are for the quasistatic polarizability formula (Equation 8.8), which takes into account the radiation

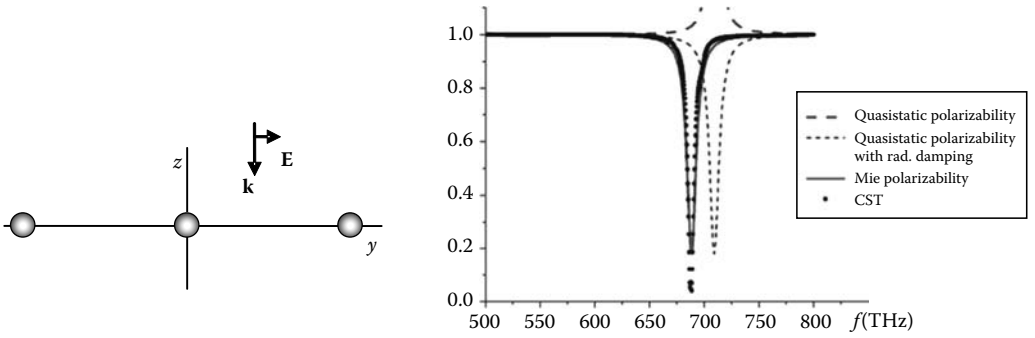

FIGURE 8.6 Transmission T through a 2D-periodic array of silver nanospheres with radius, $a = 15$ nm, and period, $d = 200$ nm. Comparison between the single dipole approximation technique with polarizability expressions as in Equations 8.3, 8.8, and 8.9, and CST Microwave Studio.

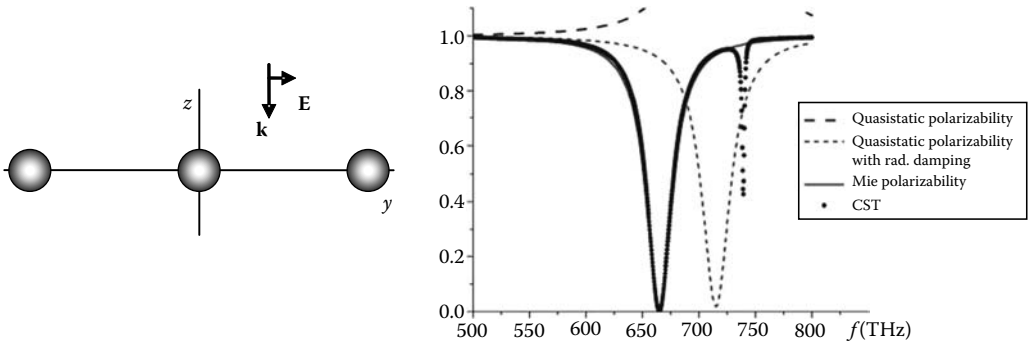

FIGURE 8.7 As in Figure 8.6, with the difference that now the nanosphere radius is $a = 25$ nm. There is a good agreement between the fully retarded solution with Mie polarizability (Equation 8.9) and the CST Microwave Studio result.

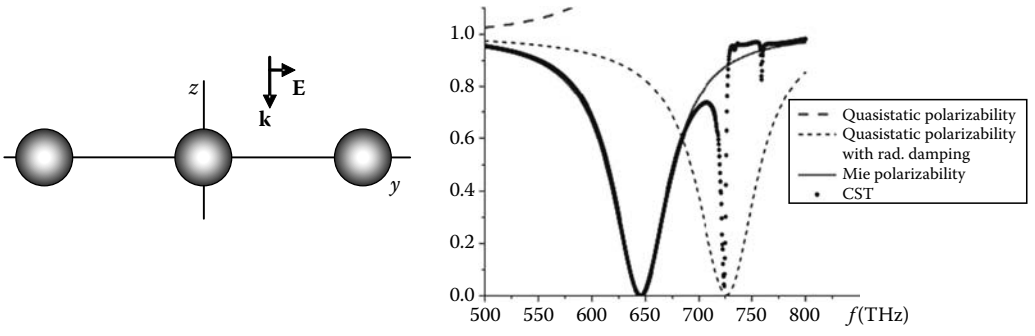

FIGURE 8.8 As in Figure 8.6, with the difference that now the nanosphere radius is $a = 35$ nm.

damping, solid lines are for the Mie polarizability (Equation 8.9), and dotted lines are for the CST results. As was noted in [11], the second term in the asymptotic formula (Equation 8.10), included in Equation 8.9, causes a redshift of the resonant frequency with respect to the quasistatic polarizability (Equation 8.8). Indeed, here, in Figures 8.6 through 8.8 we observe the same phenomena, and the results obtained with the Mie polarizability (Equation 8.9) are in good agreement with those obtained with CST, whereas results obtained with the quasistatic one in Equation 8.8 are shifted to higher frequencies. Also note that the transmission coefficients calculated with the quasistatic polarizability (Equation 8.3) are larger than 1, which contradicts the energy conservation law, as we have already discussed in Section 8.2.1.

In Figure 8.9, the single dipole approximation, using the polarizability expressions in Equations 8.3, 8.8, and 8.9, is compared with the CST Microwave Studio for an array made of pairs of tightly coupled nanospheres, also analyzed in [58]. Here, the periods of the array in the x- and y-directions are 150 nm, and the nanosphere radius is $a = 25$ nm. We assume the same Drude model for silver, as in Figure 8.6. We considered two values of the center-to-center distance between the two paired nanospheres: $h = 75$ and 60 nm. Note that the use of the quasistatic polarizability (Equation 8.3) leads to $T > 1$, which is in contradiction with the energy conservation law. We observe a good agreement of the single dipole approximation that uses the Mie polarizability (Equation 8.9) with the CST Microwave Studio for the case of nanospheres' distance' $h = 75$ nm. Note that here, $a = h/3$, and as described above we expect good approximations from the single dipole technique. Instead, for the smaller distance, $h = 60$ nm, between the paired spheres we notice a loss of accuracy of the single dipole approximation, when compared with CST, though the degree of accuracy may be enough for several purposes. When the two spheres are so close, higher order spherical harmonics or other full-wave numerical models should be used for better accuracy.

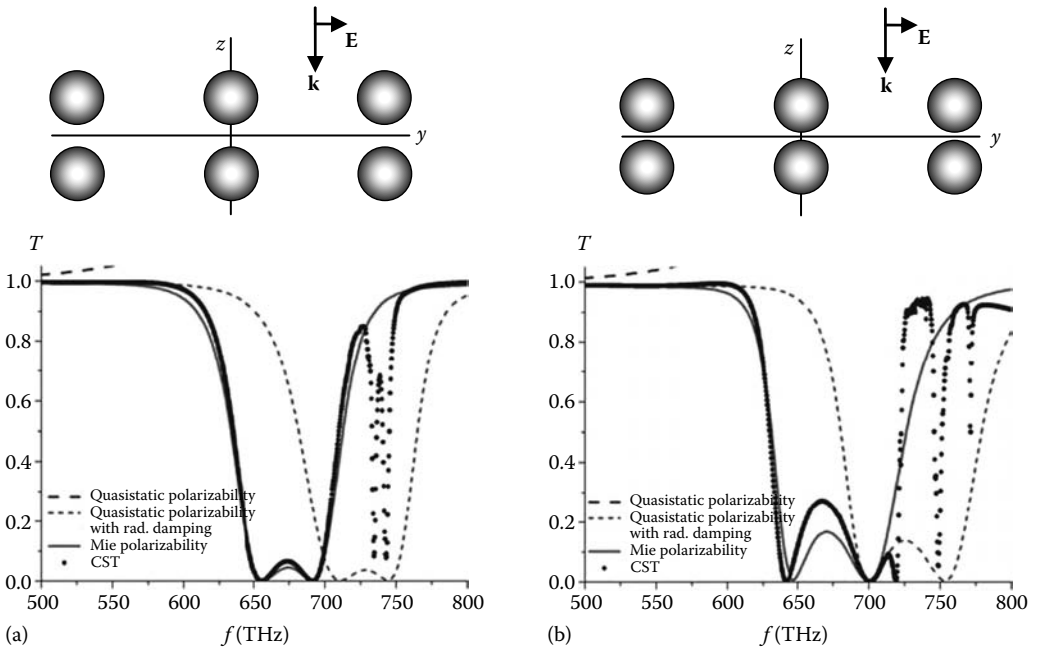

FIGURE 8.9 Transmission T through a 2D-periodic array made of pairs (aligned along z) of tightly coupled silver nanospheres with radius, $a = 25$ nm, and period, $d = 150$ nm, along x- and y-directions. The distance between the paired spheres is (a) $h = 75$ nm and (b) $h = 60$ nm. Comparison between the single dipole approximation technique with polarizability expressions as in Equations 8.3, 8.8, and 8.9, and CST.

8.5 Conclusion

We have summarized and discussed the single dipole approximation for modeling finite and periodic collections of nanospheres. We have put all cases within the same framework providing a unique formulation. The single dipole approximation is an effective tool for an approximate analysis with a degree of accuracy that depends on the nanoparticle size and the interparticle distance. The results in this chapter, and several others not reported here, show a good agreement between full-wave numerical techniques and the single dipole approximation when using the Mie polarizability expression (Equation 8.9) of a single nanosphere, which is easy to use and constitutes a better approximation than the quasistatic polarizability (Equation 8.3) and the quasistatic polarizability corrected with the radiation damping term (Equation 8.8).

References

1. Jackson, J. D. 1998. *Classical Electrodynamics*, 3rd edn. Wiley, New York.
2. Bohren, C. F. and D. R. Huffman. 1983. *Absorption and Scattering of Light by Small Particles*. Wiley, New York.
3. Van de Hulst, H. C. 1981. *Light Scattering by Small Particles*. Dover, New York.
4. Shore, R. A. and A. D. Yaghjian. 2004. Traveling electromagnetic waves on linear periodic arrays of small lossless penetrable spheres. Air Force Research Laboratory In-House Report, AFRL-SN-HS-TR-2004-044.
5. Shore, R. A. and A. D. Yaghjian. 2005. Traveling electromagnetic waves on linear periodic arrays of lossless penetrable spheres. *IEICE Transactions on Communications* E88-B: 2346–2352.
6. Shore, R. A. and A. D. Yaghjian. 2005. Travelling electromagnetic waves on linear periodic arrays of lossless spheres. *Electronics Letters* 41: 578–580.
7. Shore, R. A. and A. D. Yaghjian. 2006. Traveling waves on two- and three-dimensional periodic arrays of lossless acoustic monopoles, electric dipoles, and magnetodielectric spheres. Air Force Research Laboratory Technical Report, AFRL-SN-HS-TR-2006-0039.
8. Shore, R. A. and A. D. Yaghjian. 2007. Traveling waves on two- and three-dimensional periodic arrays of lossless scatterers. *Radio Science* 42: RS6S21-50.
9. Simovski, C., P. Belov, and M. Kondratjev. 1999. Electromagnetic interaction of chiral particles in three-dimensional arrays. *Journal of Electromagnetic Waves and Applications* 13: 189–204.
10. Sihvola, A. Polarizability of simple-shaped particles. In *Theory and Phenomena of Metamaterials*. Chapter 7. Taylor & Francis, Boca Raton, FL.
11. Meier, M. and A. Wokaun. 1983. Enhanced fields on large metal particles: Dynamic depolarization. *Optics Letters* 8: 581–583.
12. Maier, S. A., P. G. Kik, H. A. Atwater, S. Meltzer, A. A. G. Requicha, and B. E. Koel. 2002. Observation of coupled plasmon-polariton modes of plasmon waveguides for electromagnetic energy transport below the diffraction limit. *Proceedings of SPIE* 4810: 71–81.
13. Weber, W. and G. Ford. 2004. Propagation of optical excitations by dipolar interactions in metal nanoparticle chains. *Physical Review* B 70: 125429(1–8).
14. Alù, A., A. Salandrino, and N. Engheta. 2006. Negative effective permeability and left-handed materials at optical frequencies. *Optics Express* 14: 1557–1567.
15. Alitalo, P., C. Simovski, A. Viitanen, and S. Tretyakov. 2006. Near-field enhancement and subwavelength imaging in the optical region using a pair of two-dimensional arrays of metal nanospheres. *Physical Review B* 74: 235425(1–6).
16. Maier, S. A., P. G. Kik, and H. A. Atwater. 2002. Observation of coupled plasmon-polariton modes in Au nanoparticle chain waveguides of different lengths: Estimation of waveguide loss. *Applied Physics Letters* 81: 1714–1716.

17. Maier, S. A., P. G. Kik, and H. A. Atwater. 2003. Optical pulse propagation in metal nanoparticle chain waveguides. *Physical Review B* 67: 205402(1–5).
18. Simovski, C., A. Viitanen, and S. Tretyakov. 2005. Resonator mode in chains of silver spheres and its possible application. *Physical Review E* 72: 066606(1–10).
19. Alù, A. and N. Engheta. 2006. Theory of linear chains of metamaterial/plasmonic particles as subdiffraction optical nanotransmission lines. *Physical Review B* 74: 205436(1–18).
20. Koenderink, A. F. and A. Polman. 2006. Complex response and polariton-like dispersion splitting in periodic metal nanoparticle chains. *Physical Review B* 74: 033402(1–4).
21. Fung, K. H. and C. T. Chan. 2007. Plasmonic modes in periodic metal nanoparticle chains: A direct dynamic eigenmode analysis. *Optics Letters* 32: 973–975.
22. Fung, K. H. and C. T. Chan. 2008. A computational study of the optical response of strongly coupled metal nanoparticle chains. *Optics Communications* 281: 855–864.
23. Steshenko, S., F. Capolino, P. Alitalo, and S. Tretyakov. 2008. Effective analysis of arrays of nanospheres for near-field enhancement and subwavelength imaging in the optical region. *Proceedings of SPIE* 6987: 698704-1–698704-9.
24. Steshenko, S., F. Capolino, P. Alitalo, and S. Tretyakov. 2008. Effective model and investigation of the near-field enhancement and subwavelength imaging properties of multilayer arrays of plasmonic nanospheres. *Physical Review E* (submitted).
25. Steshenko, S., F. Capolino, and S. Tretyakov. Super resolution with layers of resonant arrays of nanoparticles. In *Applications of Artificial Materials*. Chapter 4. Taylor & Francis, Boca Raton, FL.
26. Hernández, J. V., L. D. Noordam, and F. Robicheaux. 2005. Asymmetric response in a line of optically driven metallic nanospheres. *Journal of Physical Chemistry B* 109: 15808–15811.
27. Quinten, M., A. Leitner, J. R. Krenn, and F. R. Aussenegg. 1998. Electromagnetic energy transport via linear chains of silver nanoparticles. *Optics Letters* 23: 1331–1333.
28. Park, S. Y. and D. Stroud. 2004. Surface-plasmon dispersion relations in chains of metallic nanoparticles: An exact quasistatic calculation. *Physical Review B* 69: 125418(1–7).
29. Wokaun, A., J. P. Gordon, and P. F. Liao. 1982. Radiation damping in surface-enhanced Raman scattering. *Physical Review Letters* 48: 957–960.
30. Alitalo, P., C. R. Simovski, L. Jylha, A. J. Viitanen, and S. A. Tretyakov. 2007. Subwavelength imaging in the visible using a pair of arrays of metal nanoparticles. *In Proceedings of Metamaterials Congress,* Rome, Italy, October 22–24, pp. 12–15.
31. Maslovski, S., P. Ikonen, I. Kolmakov, S. Tretyakov, and M. Kaunisto. 2005. Artificial magnetic materials based on the new magnetic particle: Metasolenoid. *Progress in Electromagnetics Research* 54: 61–81.
32. Sydoruk, O., O. Zhuromskyy, A. Radkovskaya, E. Shamonina, and E. Solymar. 2009. Magnetoinductive waves I: Theory. In *Theory and Phenomena of Metamaterials*. Chapter 36. Taylor & Francis, Boca Raton, FL.
33. Brongersma, M. L., J. W. Hartman, and H. A. Atwater. 2000. Electromagnetic energy transfer and switching in nanoparticle chain arrays below the diffraction limit. *Physical Review B* 62: R16 356(1–4).
34. Citrin, D. S. 2006. Plasmon-polariton transport in metal-nanoparticle chains embedded in a gain medium. *Optics Letters* 31: 98–100.
35. Capolino, F., D. R. Jackson, and D. R. Wilton. Field representations in periodic artificial materials excited by a source. In *Theory and Phenomena of Metamaterials*. Chapter 12. Taylor & Francis, Boca Raton, FL.
36. Purcell, E. M. 1965. *Electricity and Magnetism*. 1st edn. Vol. 1. MacGraw-Hill, New York.
37. Kittel, C. 1996. *Introduction to Solid State Physics*. 7th edn. Wiley, New York.
38. Draine, B. T. and P. J. Flatau. 1994. Discrete-dipole approximation for scattering calculations. *Journal of the Optical Society of America A* 11: 1491–1499.
39. Johnson, P. B. and R. W. Christy. 1972. Optical constants of the noble metals. *Physical Review B* 6: 4370(1–10).

40. Kreibig, U. and C. von Fragstein. 1969. The limitation of electron mean free path in small silver particles. *Zeitschrift für Physik* 224: 307–323.
41. Kreibig, U. and M. Vollmer. 1995. *Optical Properties of Metal Clusters*. Springer Series in Materials Science, Vol. 25. Springer, Berlin, Germany.
42. Myroshnychenko, V., J. Rodríguez-Fernández, I. Pastoriza-Santos, A. M. Funston, C. Novo, P. Mulvaney, L. M. Liz-Marzán, and F. J. García de Abajo. 2008. Modelling the optical response of gold nanoparticles. *Chemical Society Reviews* 37: 1792–1805.
43. De Vries, P., D. V. van Coevorden, and A. Lagendijk. 1998. Point scatterers for classical waves. *Reviews of Modern Physics* 70: 447–466.
44. Dungey, C. E. and C. F. Bohren. 1991. Light scattering by nonspherical particles: A refinement to the coupled-dipole method. *Journal of the Optical Society of America A* 8: 81–87.
45. Sigelmann, R. and A. Ishimaru. 1965. Radiation from periodic structures excited by an aperiodic source. *IEEE Transactions on Antennas and Propagation* 13: 354–364.
46. Wu, C. P. and V. Galindo. 1966. Asymptotic behavior of the coupling coefficients for an infinite array of thin-walled rectangular waveguides. *IEEE Transactions on Antennas and Propagation* 14: 248–249.
47. Munk, B. A. and G. A. Burrell. 1979. Plane-wave expansion for arrays of arbitrarily oriented piecewise linear elements and its application in determining the impedance of a single linear antenna in a lossy half-space. *IEEE Transactions on Antennas and Propagation* 27: 331–343.
48. Capolino, F., D. R. Jackson, D. R. Wilton, et al. 2004. Representation of the field excited by a line source near a 2D periodic artificial material. In *Fields, Networks, Computational Methods, and Systems in Modern Electrodynamics*, eds. P. Russer and M. Mongiardo, pp. 13–24. Springer-Verlag, Berlin, Germany.
49. Capolino, F., D. R. Jackson, and D. R. Wilton. 2005. Fundamental properties of the field at the interface between air and a periodic artificial material excited by a line source. *IEEE Transactions on Antennas and Propagation* 53: 91–99.
50. Capolino F., D. R. Jackson, D. R. Wilton, and L. B. Felsen. 2007. Comparison of methods for calculating the field excited by a dipole near a 2D periodic material. *IEEE Transactions on Antennas and Propagation* 55: 1644–1655.
51. Ewald, P. P. 1921. Die berechnung optischer und electrostatischer gitterpotentiale. *Annalen Der Physik* 64: 253–287.
52. Jordan, K. E., G. R. Richter, and P. Sheng. 1986. An efficient numerical evaluation of the Green's function for the Helmholtz operator on periodic structures. *Journal of Computational Physics* 63: 222–235.
53. Capolino, F., D. R. Wilton, and W. A. Johnson. 2006. Efficient computation of the 3D Green's function with one dimensional periodicity using the Ewald method. In *Proceedings of the IEEE APS Symposium*, Albuquerque, NM, July 9–14.
54. Oroskar, S., D. R. Jackson, and D. R. Wilton. 2006. Efficient computation of the 2D periodic Green's function using the Ewald method. *Journal of Computational Physics* 219: 899–911.
55. Capolino F., D. R. Wilton, and W. A. Johnson. 2007. Efficient computation of the 3D Green's function for the Helmholtz operator for a linear array of point sources using the Ewald method. *Journal of Computational Physics* 223: 250–261.
56. Steshenko, S., F. Capolino, D. R. Wilton, and Jackson, D. R. 2008. Ewald acceleration for the dyadic Green's functions for a linear array of dipoles and a dipole in a parallel-plate waveguide. In *Proceedings of the IEEE AP-S International Symposium*, San Diego, CA, July 5–11.
57. Komanduri V. R., F. Capolino, D. R. Jackson, and D. R. Wilton. 2008. Computation of the one-dimensional free-space periodic Green's function for leaky waves using the Ewald method. In *Proceedings of the URSI General Assembly*, Chicago, IL, August 7–16.
58. Valecchi, A., and F. Capolino. Metamaterials based on pairs of tightly-coupled scatterers. In *Theory and Phenomena of Metamaterials*. Chapter 19. Taylor & Francis, Boca Raton, FL.

9

Mixing Rules

Ari Sihvola
Helsinki University of Technology

9.1 Introduction

This chapter provides a theoretical background for the prediction of macroscopic dielectric properties of materials. Dielectric mixing rules are algebraic formulas with which the effective permittivity of the mixture can be calculated as a function of the constituent permittivities, their fractional volumes, and possibly some other parameters characterizing the microstructure of the mixture. The mixture can be discrete, which means that homogeneous inclusions are embedded in another homogeneous medium; otherwise the permittivity function can be continuous. The concept of effective, or macroscopic, permittivity implies that the mixture responds to electromagnetic excitation as if it were homogeneous. It may, however, be proper to remember that the dielectric constant (this term is often used synonymously with permittivity) of a material is seldom constant with respect to temperature, frequency, or any material property.

When a dielectric inclusion that is exposed to an electromagnetic field is small it can be safely assumed that its momentary internal field is the same as in the problem with a static excitation. The inclusion creates a perturbation to the field which to the lowest order, is that of an electric dipole. The polarizability of the inclusion can be enumerated by solving the Laplace equation for the field inside the scatterer; in other words, neglecting the dynamic wave processes altogether. It is not easy to give an exact upper frequency limit for the validity of the concept of effective permittivity. However, the following rule of thumb is often used: the size of an inclusion in the mixture must not exceed a tenth of the wavelength in the effective medium. In fact, this criterion is an estimate towards the conservative side.

The early history of dielectric mixing rules can be traced back to the mid-1800s [1], and some of the present-day formulas were already available in the beginning of the twentieth century [2]. For a historical overview of homogenization principles, see [3,4]. Note that the historical developments in the growth of understanding the dielectric properties of heterogeneous materials have left traces in the terminology of dielectric mixture models. As will be seen in this chapter, mixing rules are called

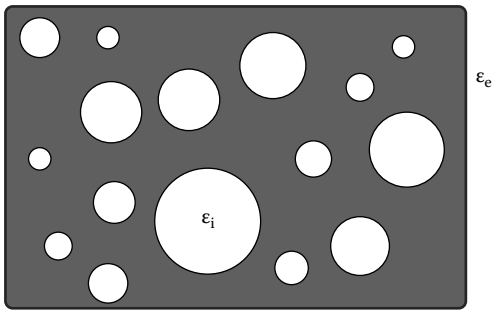

FIGURE 9.1 A simple mixture: spherical inclusions in a homogeneous background medium. The permittivity of the inclusions is ε_i and that of the environment is ε_e.

with labels like Maxwell Garnett, Rayleigh, and Bruggeman, and still earlier investigators (Mossotti, Clausius, Lorenz, and Lorentz) have their names attached to effective medium models.

9.2 Polarizability of Particles

A bottom-up type of approach to macroscopic modeling of heterogeneous media starts from the response of a single scattering element. Let us assume that the mixture to be analyzed consists of a background medium where spherical inclusions are embedded according to Figure 9.1. The two components composing the mixture are often called *phases*. The environment phase can also be termed the *matrix* or *host*, and the inclusion phase as *guest*.

The polarizability of an inclusion is a measure of its response to an incident electric field. The polarizability of a particle α is the relation between the dipole moment $\mathbf{p}$ that is induced in the inclusion by the polarization, and the external electric field $\mathbf{E}_e$:

$$\mathbf{p} = \alpha \mathbf{E}_e \tag{9.1}$$

For a sphere, the polarizability is easy to calculate. It is proportional to the internal field within the inclusion, its volume, and the dielectric contrast between the inclusion and the environment. Since the electric field $\mathbf{E}_i$ induced in a sphere in a uniform and static external field $\mathbf{E}_e$ is also uniform, static, and parallel to the external field [5, Section 4.4],

$$\mathbf{E}_i = \frac{3\varepsilon_e}{\varepsilon_i + 2\varepsilon_e}\mathbf{E}_e \tag{9.2}$$

the polarizability can be written immediately:

$$\alpha = V(\varepsilon_i - \varepsilon_e)\frac{3\varepsilon_e}{\varepsilon_i + 2\varepsilon_e} \tag{9.3}$$

where the permittivities of the inclusion and its environment are denoted by ε_i and ε_e, respectively. The volume of the sphere is V. Note that the polarizability is a scalar. This is because the inclusion material is isotropic and its shape is spherically symmetric.

9.3 Clausius–Mossotti and Maxwell Garnett Formulas

From the polarizability of a single sphere, the effective permittivity of a mixture can be calculated as a function of the density of the spheres in the background medium with permittivity ε_e.

The effective permittivity is the relation between the external field and the average electric flux density $< \mathbf{D} >$:

$$< \mathbf{D} > = \varepsilon_{\text{eff}} \mathbf{E}_e = \varepsilon_e \mathbf{E}_e + < \mathbf{P} > \tag{9.4}$$

where the average polarization $< \mathbf{P} >$ is connected to the dipole moment density in the mixture:

$$< \mathbf{P} > = n\mathbf{p} \tag{9.5}$$

where n is the density of dipole moments $\mathbf{p}$ in the mixture. Note the dimensions of the quantities in SI units: $[\mathbf{D}] = [\mathbf{P}] = \text{As/m}^2$, $[\mathbf{p}] = \text{Asm}$, $[\mathbf{E}_e] = \text{V/m}$, $[\alpha] = \text{Asm}^2/\text{V}$, and $[n] = \text{m}^{-3}$.

In a mixture, especially when it is dense, one cannot assume the field exciting one inclusion to be the external field $\mathbf{E}_e$. The surrounding polarization increases the field effect and has to be taken into account [6, pp. 366–368]. The field that excites one inclusion $\mathbf{E}_L$ is often called the *local field* or the *Lorentzian field*. It is dependent on the shape of the inclusion [7], and for a sphere it is

$$\mathbf{E}_L = \mathbf{E}_e + \frac{1}{3\varepsilon_e}\mathbf{P} \tag{9.6}$$

where the coefficient 1/3 corresponds to the depolarization factor of the sphere. Combining this equation with $\mathbf{p} = \alpha \mathbf{E}_L$ leaves us with the average polarization, and then the effective permittivity can be written (see Equation 9.4):

$$\varepsilon_{\text{eff}} = \varepsilon_e + \frac{n\alpha}{1 - \dfrac{n\alpha}{3\varepsilon_e}} \tag{9.7}$$

The equation is often seen in the form

$$\frac{\varepsilon_{\text{eff}} - \varepsilon_e}{\varepsilon_{\text{eff}} + 2\varepsilon_e} = \frac{n\alpha}{3\varepsilon_e} \tag{9.8}$$

This relation carries the name *Clausius–Mossotti formula*, although it deserves the label *Lorenz–Lorentz formula* [8] as well. The dilute-mixture approximation can be written by taking the limit of small n:

$$\varepsilon_{\text{eff}} \approx \varepsilon_e + n\alpha \tag{9.9}$$

In practical applications, quantities like polarizabilities and scatterer densities are not always the most convenient to use. Rather, one prefers to play with the permittivities of the components of the mixture. When this is the case, it is advantageous to combine the Clausius–Mossotti formula with the polarizability expression (Equation 9.3). Then we can write

$$\frac{\varepsilon_{\text{eff}} - \varepsilon_e}{\varepsilon_{\text{eff}} + 2\varepsilon_e} = f\frac{\varepsilon_i - \varepsilon_e}{\varepsilon_i + 2\varepsilon_e} \tag{9.10}$$

where $f = nV$ is a dimensionless quantity, the volume fraction of the inclusions in the mixture. This formula is called the *Rayleigh mixing formula*. Note that, because only the volume fraction and the permittivities appear in the mixing rule, the spheres need not be of the same size if all of them are small compared to the wavelength.

Perhaps the most common mixing rule is the *Maxwell Garnett formula**, which is the Rayleigh rule (Equation 9.10) written explicitly for the effective permittivity:

$$\varepsilon_{\text{eff}} = \varepsilon_e + 3f\varepsilon_e \frac{\varepsilon_i - \varepsilon_e}{\varepsilon_i + 2\varepsilon_e - f(\varepsilon_i - \varepsilon_e)} \tag{9.11}$$

* The origin of this label for the mixing formula is due to J.C. Maxwell Garnett, who presented the result in 1904 [2], and not due to the father of the Maxwell equations, James Clerk Maxwell [3].

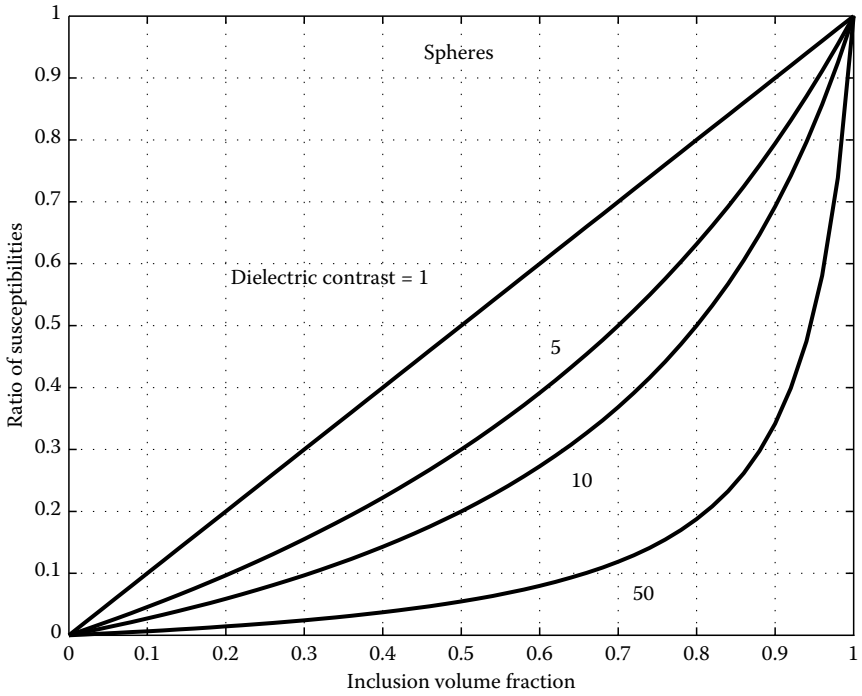

FIGURE 9.2 The susceptibility ratio $(\varepsilon_{\text{eff}} - \varepsilon_e)/(\varepsilon_i - \varepsilon_e)$ for the Maxwell Garnett prediction of the effective permittivity of a mixture with spherical inclusions of permittivity ε_i in a background medium of permittivity ε_e, as a function of the volume fraction of the inclusions f and the dielectric contrast $\varepsilon_i/\varepsilon_e$.

This formula is in wide use in diverse fields of applications. The beauty of the Maxwell Garnett formula is in its simple appearance combined with its broad applicability. It satisfies the limiting processes for the vanishing inclusion phase $f \to 0$, giving $\varepsilon_{\text{eff}} \to \varepsilon_e$, and for a vanishing background $f \to 1$ we have $\varepsilon_{\text{eff}} \to \varepsilon_i$.

The perturbation expansion of the Maxwell Garnett rule gives the mixing equation for dilute mixtures ($f \ll 1$):

$$\varepsilon_{\text{eff}} \approx \varepsilon_e + 3f\varepsilon_e \frac{\varepsilon_i - \varepsilon_e}{\varepsilon_i + 2\varepsilon_e} + 3f^2\varepsilon_e \left(\frac{\varepsilon_i - \varepsilon_e}{\varepsilon_i + 2\varepsilon_e}\right)^2 \tag{9.12}$$

Figure 9.2 shows the prediction of the Maxwell Garnett formula for different values of the dielectric contrast $\varepsilon_i/\varepsilon_e$. Shown is the susceptibility ratios,

$$\frac{\varepsilon_{\text{eff}} - \varepsilon_e}{\varepsilon_i - \varepsilon_e}$$

which vanishes for $f = 0$ and is unity for $f = 1$, independent of the inclusion-to-background contrast. The figure shows clearly the fact that the effective permittivity function becomes a very nonlinear function of the volume fraction for large dielectric contrasts.

9.4 Ellipsoids and Multiphase Mixtures

A two-phase mixture with spherical inclusions was the simplest geometry that a mixture can take. Therefore its generalization into more complicated heterogeneities is necessary. Consider a mixture where the inclusion spheres are of different permittivities. Where above the total polarization was

calculated from the individual dipole moments according to Equation 9.5, now each guest phase contributes one such term to a sum of many. The final result is (compare to Equation 9.10)

$$\frac{\varepsilon_{\text{eff}} - \varepsilon_{\text{e}}}{\varepsilon_{\text{eff}} + 2\varepsilon_{\text{e}}} = \sum_{n=1}^{N} f_n \frac{\varepsilon_{i,n} - \varepsilon_{\text{e}}}{\varepsilon_{i,n} + 2\varepsilon_{\text{e}}} \tag{9.13}$$

where

f_n is the volume fraction of the inclusions of the nth phase in the mixture
$\varepsilon_{i,n}$ is its permittivity

And of course this can be solved for the effective permittivity:

$$\varepsilon_{\text{eff}} = \varepsilon_{\text{e}} + 3\varepsilon_{\text{e}} \frac{\sum_{n=1}^{N} f_n \frac{\varepsilon_{i,n} - \varepsilon_{\text{e}}}{\varepsilon_{i,n} + 2\varepsilon_{\text{e}}}}{1 - \sum_{n=1}^{N} f_n \frac{\varepsilon_{i,n} - \varepsilon_{\text{e}}}{\varepsilon_{i,n} + 2\varepsilon_{\text{e}}}} \tag{9.14}$$

Here again, all inclusions of all phases are assumed to be spherical.

Also, the assumption of spherical shape for the inclusions needs to be relaxed because many media possess inclusions of other forms. The polarizability of small particles can of course be calculated for any shape, but in general this requires numerical effort. The only shapes for which simple analytical solutions can be found are ellipsoids. Fortunately, ellipsoids allow many practical special cases, like disks and needles for example.

The important parameters in the geometry of an ellipsoid are its depolarization factors. If the semiaxes of an ellipsoid in the three orthogonal directions are a_x, a_y, and a_z (Figure 9.3), the depolarization factor N_x (the factor in the a_x-direction) is

$$N_x = \frac{a_x a_y a_z}{2} \int_0^\infty \frac{\mathrm{d}s}{(s + a_x^2)\sqrt{(s + a_x^2)(s + a_y^2)(s + a_z^2)}} \tag{9.15}$$

For the other depolarization factor $N_y(N_z)$, interchange a_y and $a_x(a_z$ and $a_x)$ in the above integral.

The three depolarization factors for any ellipsoid satisfy

$$N_x + N_y + N_z = 1 \tag{9.16}$$

A sphere has three equal depolarization factors of 1/3. The other two special cases are a disk (depolarization factors 1, 0, 0) and a needle (0, 1/2, 1/2). For ellipsoids of revolution, prolate and oblate spheroids, closed-form expressions for the integral (Equation 9.15) can be found [9].

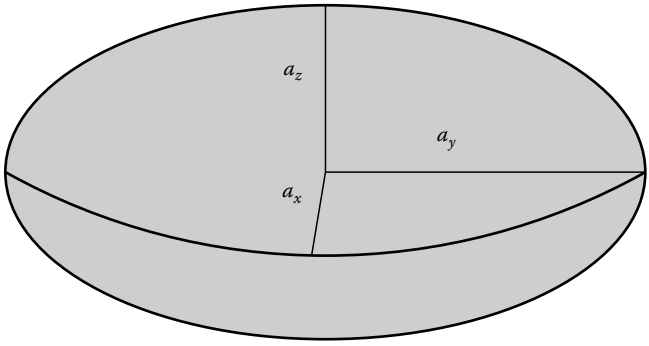

FIGURE 9.3 An ellipsoid, determined by its semiaxes a_x, a_y, and a_z.

Prolate spheroids ($a_x > a_y = a_z$) have

$$N_x = \frac{1-e^2}{2e^3}\left[\ln\left(\frac{1+e}{1-e}\right) - 2e\right] \tag{9.17}$$

and

$$N_y = N_z = \frac{1}{2}(1 - N_x) \tag{9.18}$$

where the eccentricity is $e = \sqrt{1 - a_y^2/a_x^2}$. For nearly spherical prolate spheroids, which have small eccentricity, the following hold:

$$N_x \simeq \frac{1}{3} - \frac{2}{15}e^2 \tag{9.19}$$

$$N_y = N_z \simeq \frac{1}{3} + \frac{1}{15}e^2 \tag{9.20}$$

For oblate spheroids ($a_x = a_y > a_z$),

$$N_z = \frac{1+e^2}{e^3}(e - \arctan e) \tag{9.21}$$

$$N_x = N_y = \frac{1}{2}(1 - N_z) \tag{9.22}$$

where $e = \sqrt{a_x^2/a_z^2 - 1}$. For nearly spherical oblate spheroids,

$$N_z \simeq \frac{1}{3} + \frac{2}{15}e^2 \tag{9.23}$$

$$N_x = N_y \simeq \frac{1}{3} - \frac{1}{15}e^2 \tag{9.24}$$

Figures 9.4 and 9.5 display the behaviors of the depolarization factors of these spheroids as functions of the axial ratios of the ellipsoids.

For a general ellipsoid with three different axes, the depolarization factors have to be calculated from the integral (Equation 9.15). Osborn and Stoner have tabulated the depolarization factors of a general ellipsoid [10,11], a great achievement despite the fact that today's numerical software packages like *Mathematica* [12] give these factors with very easy input efforts.

Now consider a mixture where ellipsoids of permittivity ε_i are embedded in the environment ε_e. Let all the ellipsoids be aligned. Then the effective permittivity of the mixture is anisotropic; in other words, it has different permittivity components in the different principal directions. We can write the following formula for this mixture, which generalizes the Maxwell Garnett mixing rule:

$$\varepsilon_{\text{eff},x} = \varepsilon_e + f\varepsilon_e \frac{\varepsilon_i - \varepsilon_e}{\varepsilon_e + (1-f)N_x(\varepsilon_i - \varepsilon_e)} \tag{9.25}$$

and for $\varepsilon_{\text{eff},y}$ and $\varepsilon_{\text{eff},z}$, replace N_x by N_y and N_z, respectively. This formula is sometimes termed after Bohren and Battan [13,14], and it was derived in 1919 by Burger [15].

If, on the other hand, all the ellipsoids in the mixture are randomly oriented, there is no longer any preferred direction macroscopically. The mixture is isotropic and the effective permittivity ε_{eff} is a scalar:

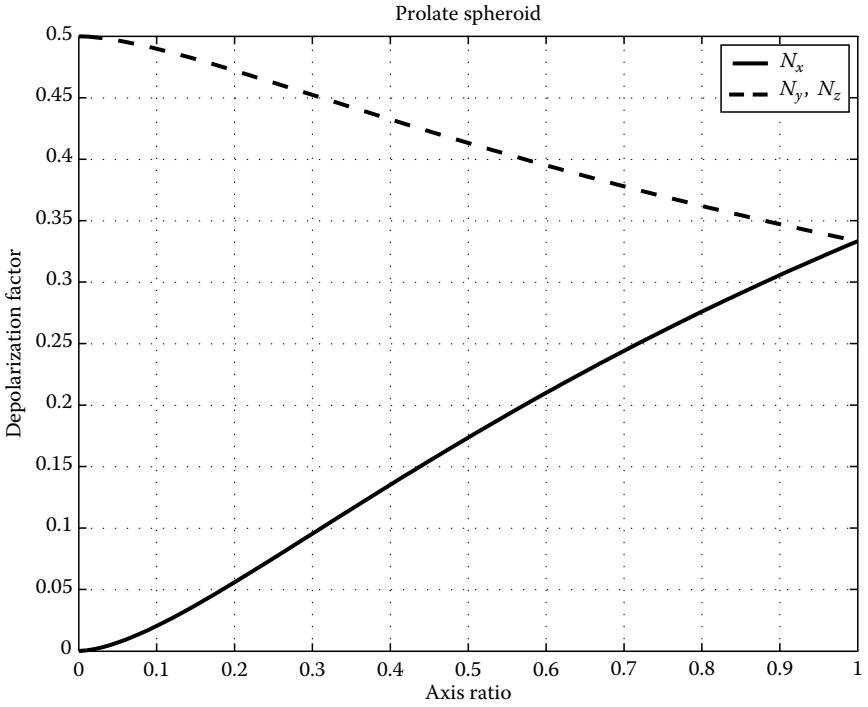

FIGURE 9.4 The depolarization factors of a prolate spheroid as a function of the axis ratio a_z/a_x. The axis of revolution is x (the longest axis of the ellipsoid compared to the two others). Obviously, $N_x + N_y + N_z = 1$, regardless of the axis ratio.

$$\varepsilon_{\text{eff}} = \varepsilon_{\text{e}} + \varepsilon_{\text{e}} \frac{\dfrac{f}{3} \sum_{j=x,y,z} \dfrac{\varepsilon_{\text{i}} - \varepsilon_{\text{e}}}{\varepsilon_e + N_j(\varepsilon_{\text{i}} - \varepsilon_{\text{e}})}}{1 - \dfrac{f}{3} \sum_{j=x,y,z} \dfrac{N_j(\varepsilon_{\text{i}} - \varepsilon_{\text{e}})}{\varepsilon_{\text{e}} + N_j(\varepsilon_{\text{i}} - \varepsilon_{\text{e}})}} \tag{9.26}$$

Figure 9.6 shows the Maxwell Garnett predictions of the effective permittivity of isotropic two-component dielectric mixtures where the inclusion shapes are varied: they are either spheres, needles, or disks. A random orientation of the inclusions guarantees that the mixture is isotropic and the permittivity a scalar. The contrast between the inclusion and background phases is $\varepsilon_{\text{i}}/\varepsilon_{\text{e}} = 30$. There is a clear effect of the shapes of the inclusions: spheres give the lowest permittivity, needles a larger permittivity, and disks provide the largest effect. However, if the contrast between the phases is smaller, the effect of the geometry decreases.

Finally, if the inclusions are neither aligned nor randomly oriented but rather follow an orientation distribution, the sums in Equation 9.26 have to be replaced by terms where the dipole moment densities are weighted by the distribution function and integrated over all relevant spatial directions.

The mixture with homogeneous isotropic ellipsoidal inclusions was only one generalization of the simplest mixture. The aligned ellipsoid case above, Equation 9.25, was an example where the geometry of the microstructure rendered the macroscopic permittivity anisotropic. But the mixing principles can also be generalized to cases where one or several of the phases are anisotropic in the first place. One of the elegant ways of achieving this goal is to generalize the Maxwell Garnett formula into dyadic domain. See [4] for details of this process.

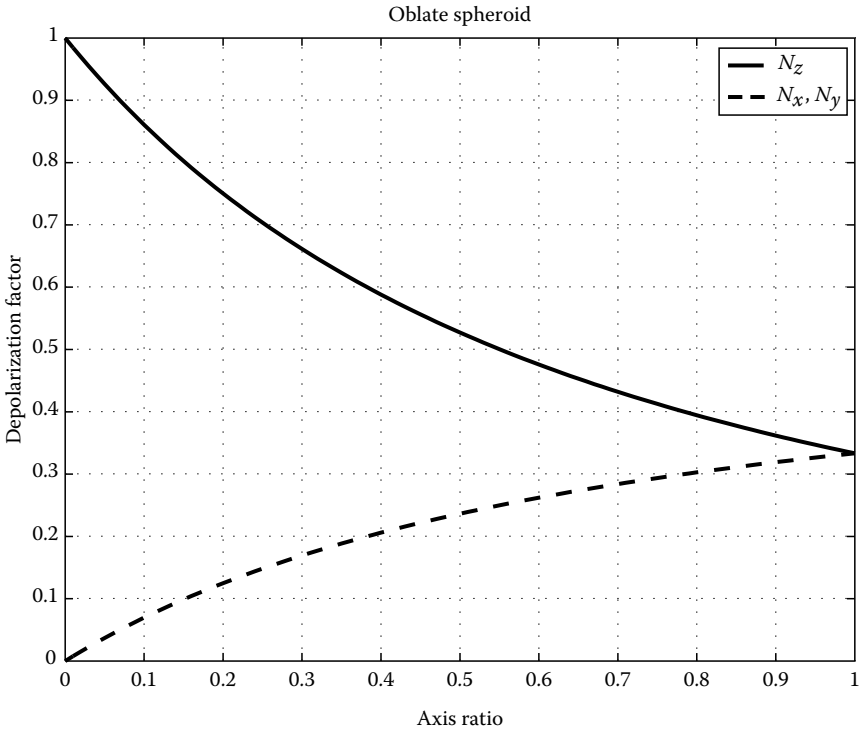

FIGURE 9.5 The depolarization factors of an oblate spheroid as a function of the axis ratio a_z/a_x. The axis of revolution is z (the shortest axis of the ellipsoid compared to the two others). Obviously, $N_x + N_y + N_z = 1$, regardless of the axis ratio.

The previous results have been derived for discrete structures. The inclusions were assumed to be dielectrically homogeneous. However, mixtures with inhomogeneous inclusions can certainly be treated within the framework of Maxwell Garnett (and not only in the basic Maxwell Garnett case but also for more complicated approaches) mixing. The challenge with nonhomogeneous scatterers is the difficulty of calculating the polarizability of such inclusions. There are, however, certain shapes for which analytical solutions can be found in the electrostatic problem.

A layered sphere is one example of such a special case. There is no restriction on the number of layers, and even the case for a radially continuous permittivity profile of the sphere has been given a solution [16]. (See also the results for mixtures with dielectrically inhomogenous ellipsoids [17].) As an example, the following is the generalization of the mixing rule (Equation 9.10) for the case when the inclusions are two-component spheres:

$$\frac{\varepsilon_{\text{eff}} - \varepsilon_e}{\varepsilon_{\text{eff}} + 2\varepsilon_e} = f\frac{(\varepsilon_1 - \varepsilon_e)(\varepsilon_c + 2\varepsilon_1) + w(\varepsilon_c - \varepsilon_1)(\varepsilon_e + 2\varepsilon_1)}{(\varepsilon_1 + 2\varepsilon_e)(\varepsilon_c + 2\varepsilon_1) + 2w(\varepsilon_c - \varepsilon_1)(\varepsilon_1 - \varepsilon_e)} \tag{9.27}$$

The inclusion sphere consists of a spherical core with permittivity ε_c that is covered by a spherical shell with permittivity ε_1. The parameter $w = (b/a)^3$ is the fraction of the volume of the core from the total inclusion volume (a is the radius of the inclusion and b is the radius of the core), and f is the volume fraction of the inclusions in the mixture, as before.

If, on the other hand, the inclusions are of such a shape that they do not have a closed-form solution for the dielectric polarizability, we cannot write down a simple Maxwell Garnett formula like in the cases of spheres and ellipsoids. However, if the polarizability is known, for example, by numerical

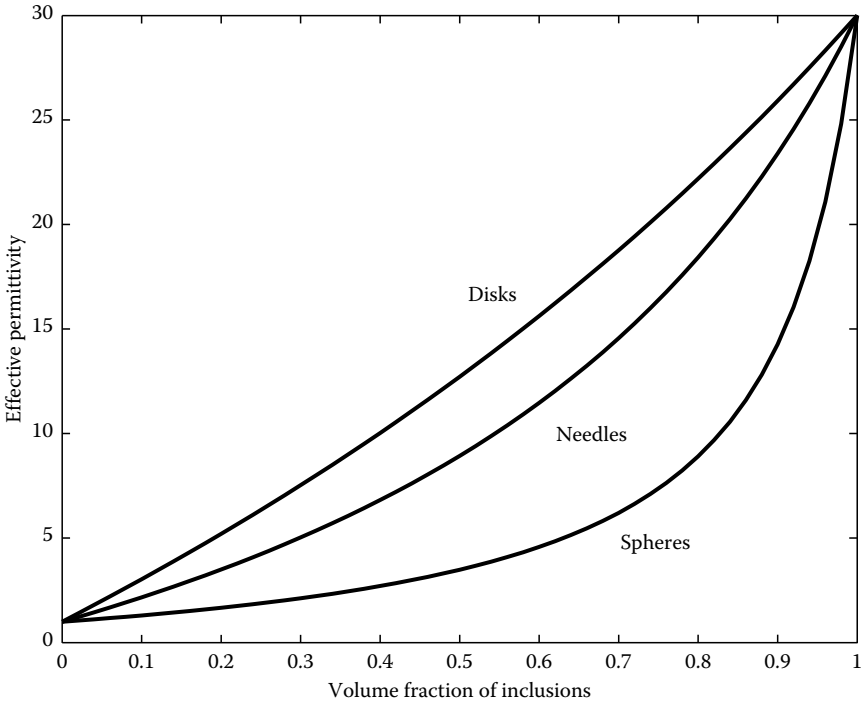

FIGURE 9.6 The effective permittivity of a mixture as a function of the volume fraction of inclusions. The inclusions are randomly oriented spheres, needles, and disks. The inclusion permittivity is 30 times that of the environment.

enumeration, the result can be used as an input in the Lorenz–Lorentz formula (Equation 9.8) to calculate the effective permittivity. For example, very accurate results have been reported for the polarizability of platonic solids (tetrahedron, cube, octahedron, dodecahedron, and icosahedron) [18]. These can be applied to model mixtures with more sharp-edged microstructures than the one shown in Figure 9.1.

9.5 Generalized Mixing Models

There is no exact result for the effective permittivity of a mixture with a random geometry. In the analysis of random media, a major difficulty comes with the problem of how to correctly take into account the interaction between the scatterers. For sparse mixtures, these effects of interaction are small and can be included by surrounding the inclusion with the average polarization <**P**>, as was done in the above derivation of the Maxwell Garnett rule. However, when dense mixtures are treated, this approach may not be correct. In the present section, mixing rules are presented for mixtures that predict different results compared to the Maxwell Garnett rule.

9.5.1 Bruggeman Mixing Rule

One important mixing rule goes under different names: *Polder–van Santen formula* [19], also called the *Bruggeman formula* [20] or the *Böttcher formula* [21], is very often encountered in material modeling studies.

The basic form of this formula for spherical scatterers is

$$(1-f)\frac{\varepsilon_e-\varepsilon_{eff}}{\varepsilon_e+2\varepsilon_{eff}}+f\frac{\varepsilon_i-\varepsilon_{eff}}{\varepsilon_i+2\varepsilon_{eff}}=0 \tag{9.28}$$

This Bruggeman formula has the special property that it treats the inclusions and the environment symmetrically. The interpretation of Equation 9.28 is that the formula balances both mixing components with respect to the unknown effective medium, using the volume fraction of each component as weight (f for the inclusions and $1-f$ for the environment). This symmetry property of Equation 9.28 makes the radical distinction between the Maxwell Garnett rule and the Bruggeman rule. The Maxwell Garnett approach is inherently nonsymmetric.

The Bruggeman formula for the case when the inclusions are randomly oriented ellipsoids is

$$\varepsilon_{eff}=\varepsilon_e+\frac{f}{3}(\varepsilon_i-\varepsilon_e)\sum_{j=x,y,z}\frac{\varepsilon_{eff}}{\varepsilon_{eff}+N_j(\varepsilon_i-\varepsilon_{eff})} \tag{9.29}$$

where now N_j are again the depolarization factors of the inclusion ellipsoids in the three orthogonal directions.

9.5.2 Coherent Potential Formula

Another well-known formula that is relevant in the theoretical studies of wave propagation in random media is the so-called *coherent potential formula* [22, p. 475]:

$$\varepsilon_{eff}=\varepsilon_e+\frac{f}{3}(\varepsilon_i-\varepsilon_e)\sum_{j=x,y,z}\frac{(1+N_j)\varepsilon_{eff}-N_j\varepsilon_e}{\varepsilon_{eff}+N_j(\varepsilon_i-\varepsilon_e)} \tag{9.30}$$

This formula for spherical inclusions is

$$\varepsilon_{eff}=\varepsilon_e+f(\varepsilon_i-\varepsilon_e)\frac{3\varepsilon_{eff}}{3\varepsilon_{eff}+(1-f)(\varepsilon_i-\varepsilon_e)} \tag{9.31}$$

It is worth noting that for dilute mixtures ($f\ll 1$), all three mixing rules, Maxwell Garnett, Polder–van Santen, and coherent potential, predict the same results. Up to the first order in f, the formulas are the same:

$$\varepsilon_{eff}\approx\varepsilon_e+3f\varepsilon_e\frac{\varepsilon_i-\varepsilon_e}{\varepsilon_i+2\varepsilon_e} \tag{9.32}$$

9.5.3 Unified Mixing Rule

A unified mixing approach [23] collects all the previous aspects of dielectric mixing rules into one family. For the case of isotropic spherical inclusions ε_i in the isotropic environment ε_e, the formula looks like

$$\frac{\varepsilon_{eff}-\varepsilon_e}{\varepsilon_{eff}+2\varepsilon_e+\nu(\varepsilon_{eff}-\varepsilon_e)}=f\frac{\varepsilon_i-\varepsilon_e}{\varepsilon_i+2\varepsilon_e+\nu(\varepsilon_{eff}-\varepsilon_e)} \tag{9.33}$$

This formula contains a dimensionless parameter ν. For different choices of ν, the previous mixing rules are recovered: $\nu=0$ gives the Maxwell Garnett rule, $\nu=2$ gives the Bruggeman formula, and $\nu=3$ gives the coherent potential approximation.

The unified mixing rule (Equation 9.33) can be generalized to the case where the inclusions are ellipsoids, all randomly oriented. Then, the scalar effective permittivity reads

$$\varepsilon_{\text{eff}} = \varepsilon_{\text{e}} + f(\varepsilon_{\text{i}} - \varepsilon_{\text{e}}) \frac{\sum_{k=1}^{3} \frac{\varepsilon_{\text{a}}}{\varepsilon_{\text{a}} + N_k(\varepsilon_{\text{i}} - \varepsilon_{\text{e}})}}{3 - f(\varepsilon_{\text{i}} - \varepsilon_{\text{e}}) \sum_{k=1}^{3} \frac{N_k}{\varepsilon_a + N_k(\varepsilon_{\text{i}} - \varepsilon_{\text{e}})}} \tag{9.34}$$

Different mixing models arise from this form by various choices of the apparent permittivity $\varepsilon_a = \varepsilon_{\text{e}} + a(\varepsilon_{\text{eff}} - \varepsilon_{\text{e}})$:

- Maxwell Garnett: $a = 0$
- Bruggeman/Polder–van Santen: $a = 1 - N_k,\ k = 1, 2, 3$
- Coherent potential: $a = 1$

9.5.4 Other Mixing Rules

Of the very large set of remaining mixing rules that are being used in the random medium theories and practical applications, the following deserve to be introduced.

A widely used class of mixing models is formed by the "power-law" approximations:

$$\varepsilon_{\text{eff}}^{a} = f\varepsilon_{\text{i}}^{\text{a}} + (1 - f)\varepsilon_{\text{e}}^{\text{a}} \tag{9.35}$$

For example, in the Birchak formula [24] the parameter is $a = 1/2$, which means that the square roots of the component permittivities add up to the square root of the mixture permittivity.

Another famous formula is the Looyenga formula [25], for which $a = 1/3$. One can also find in the literature (see, for example, [26, p. 1080]) the linear law:

$$\varepsilon_{\text{eff}} = f\varepsilon_{\text{i}} + (1 - f)\varepsilon_{\text{e}} \tag{9.36}$$

which corresponds to $a = 1$ in Equation 9.35. This mixing rule can be given theoretical confirmation if the mixture is formed of plates or other inclusions for which no depolarization is induced. If the depolarization factor is $N_x = 0$, one can recover Equation 9.36 from Equation 9.25.

Other models resulting from a differential analysis are

$$\frac{\varepsilon_{\text{i}} - \varepsilon_{\text{eff}}}{\varepsilon_{\text{i}} - \varepsilon_{\text{e}}} = (1 - f)\left(\frac{\varepsilon_{\text{eff}}}{\varepsilon_{\text{e}}}\right)^{1/3} \tag{9.37}$$

which is sometimes called the Bruggeman asymmetric formula (to distinguish it from the symmetric Bruggeman formula, Equation 9.28), and its "complement" [27], another applicable formula to predict the effective permittivity of mixtures:

$$\frac{\varepsilon_{\text{eff}} - \varepsilon_{\text{e}}}{\varepsilon_{\text{i}} - \varepsilon_{\text{e}}} = f\left(\frac{\varepsilon_{\text{eff}}}{\varepsilon_{\text{i}}}\right)^{1/3} \tag{9.38}$$

which have the common feature of one-third powers.

There are also formulas for mixtures with spherical inclusions in a cubic array in a background matrix. These formulas can be seen as successive improvements to the classical Rayleigh result, Equation 9.10. These have been presented by Runge [28]; Meredith and Tobias [29]; McPhedran, McKenzie, and Derrick [30,31]; Doyle [32]; Lam [33]; and Kristensson [34]. However, these formulas are derived for ordered mixtures, though not all necessarily for cubic-centered lattices, and from the point of view of application to random media, they suffer from the disadvantage of predicting infinite effective permittivities as the inclusions come into contact with each other.

Recently, numerical efforts also have been made to calculate the effective dielectric properties of random mixtures. There is an indication [35] that the macroscopic permittivity would fall between the Maxwell Garnett and Bruggeman predictions, and closer to Maxwell Garnett if the inclusions are forced to be separate from each other within the mixture. On the other hand, if the inclusions are allowed to touch and overlap, thus forming clusters, the Bruggeman formula seems to be more valid. These mixtures have been simulated by embedding spheres into random positions within the background matrix.

Such is the case for positive-permittivity random materials. However, in the domain of negative-permittivity inclusions, the plasmonic resonances cause particular complications in estimating the effective permittivity. In this case, only for regular lattice of inclusions we may find strong results of reliable predictions of mixing rules. For such cases the Maxwell Garnett mixing rule seems to predict well the resonances of the effective mixture [36].

Acknowledgment

This work was supported by the Academy of Finland.

References

1. Mossotti, O.F., Discussione analitica sull'influenza che l'azione di un mezzo dielettrico ha sulla distribuzione dell'elettricità alla superficie di più corpi elettrici disseminati in esso, *Memorie di matematica a di fisica della Società Italiana delle scienze, residente in Modena*, 24 (Part 2), 49–74, 1850.
2. Maxwell-Garnett, J.C., Colours in metal glasses and metal films, *Transactions of the Royal Society*, CCIII, 385–420, 1904.
3. Landauer, R., Electrical conductivity in inhomogeneous media, *American Institute of Physics Conference Proceedings* (Electrical transport and optical properties of inhomogeneous media), 40, 2–45, 1978.
4. Sihvola, A., *Electromagnetic Mixing Formulas and Applications*, IEE Publishing, London, 1999.
5. Jackson, J.D., *Classical Electrodynamics*, 2nd edn., Wiley, New York, 1975.
6. Kittel, C., *Introduction to Solid State Physics*, 6th edn., Wiley, New York, 1986.
7. Yaghjian, A.D., Electric dyadic Green's function in the source region, *Proceedings of IEEE*, 68(2), 248–263, 1980.
8. Sihvola, A., Lorenz–Lorentz or Lorentz–Lorenz? *IEEE Antennas and Propagation Magazine*, 33(4), 56, August 1991.
9. Landau, L.D. and E.M. Lifshitz, *Electrodynamics of Continuous Media*, 2nd edn., Pergamon Press, Oxford, 1984, Section 4.
10. Osborn, J.A., Demagnetizing factors of the general ellipsoid, *The Physical Review*, 67(11–12), 351–357, 1945.
11. Stoner, E.C., The demagnetizing factors for ellipsoids, *Philosophical Magazine*, Ser. 7, 36(263), 803–821, 1945.
12. http://www.wolfram.com/
13. Mätzler, C., Applications of the interaction of microwaves with the natural snow cover, *Remote Sensing Reviews*, 2, 1987, 259–387.
14. Bohren, C.F. and L.J. Battan, Radar backscattering of microwaves by spongy ice spheres, *Journal of the Atmospheric Sciences*, 39, 2623–2628, November 1982.
15. Burger, H.C., Das Leitvermögen verdünnter mischkristallfreier Legierungen, *Physikalische Zeitschrift*, 20(4), 73–75, February 15, 1919.

16. Sihvola, A. and I.V. Lindell, Polarizability and effective permittivity of layered and continuously inhomogeneous dielectric spheres, *Journal of Electromagnetic Waves Applications*, 3(1), 37–60, 1989.
17. Sihvola, A. and I.V. Lindell, Polarizability and effective permittivity of layered and continuously inhomogeneous dielectric ellipsoids, *Journal of Electromagnetic Waves Applications*, 4(1), 1–26, 1990.
18. A. Sihvola, P. Ylä-Oijala, S. Järvenpää, and J. Avelin, Polarizabilities of platonic solids. *IEEE Transactions on Antennas and Propagation*, 52(9), 2226–2233, September 2004.
19. Polder, D. and J.H. van Santen, The effective permeability of mixtures of solids, *Physica*, XII(5), 257–271, 1946.
20. Bruggeman, D.A.G., Berechnung verschiedener physikalischer Konstanten von heterogenen Substanzen, I. Dielektrizitätskonstanten und Leitfähigkeiten der Mischkörper aus isotropen Substanzen, *Annalen der Physik*, 5. Folge, Band 24, 636–664, 1935.
21. Böttcher, C.J.F., *Theory of Electric Polarization*, Elsevier, Amsterdam, the Netherlands, 1952.
22. Tsang, L., J.A. Kong, and R.T. Shin, *Theory of Microwave Remote Sensing*, Wiley, New York, 1985.
23. Sihvola, A., Self-consistency aspects of dielectric mixing theories, *IEEE Transactions Geoscience Remote Sensing*, 27(4), 403–415, 1989.
24. Birchak, J.R., L.G. Gardner, J.W. Hipp, and J.M. Victor, High dielectric constant microwave probes for sensing soil moisture, *Proceedings of the IEEE*, 62(1), 93–98, 1974.
25. Looyenga, H., Dielectric constants of mixtures, *Physica*, 31, 401–406, 1965.
26. Ulaby, F.T., R.K. Moore, and A.K. Fung, *Microwave Remote Sensing—Active and Passive*, Vol. III, Artech House, Norwood, MA, 1986.
27. Sen, P.N., C. Scala, and M.H. Cohen, A self-similar model for sedimentary rocks with application to the dielectric constant of fused glass beads, *Geophysics*, 46(5), 781–795, 1981.
28. Runge, I., Zur elektrischer Leitfähigkeit metallischer Aggregate, *Zeitschrift für technische Physik*, 6. Jahrgang, Nr. 2, 61–68, 1925.
29. Meredith, R.E. and C.W. Tobias, Resistance to potential flow through a cubical array of spheres, *Journal Applied Physics*, 31(7), 1270–1273, 1960.
30. McPhedran, R.C. and D.R. McKenzie, The conductivity of lattices of spheres. I. The simple cubic lattice, *Proceedings of the Royal Society of London*, A, 359, 45–63, 1978.
31. McKenzie, D.R., R.C. McPhedran, and G.H. Derrick, The conductivity of lattices of spheres. II. The body centred and face centred cubic lattices, *Proceedings of the Royal Society of London*, A, 362, 211–232, 1978.
32. Doyle, W.T., The Clausius–Mossotti problem for cubic array of spheres, *Journal of Applied Physics*, 49(2), 795–797, 1978.
33. Lam, J., Magnetic permeability of a simple cubic lattice of conducting magnetic spheres, *Journal of Applied Physics*, 60(12), 4230–4235, 1986.
34. Kristensson, G., Homogenization of spherical inclusions, *Progress in Electromagnetics Research*, 42, 1–25, 2003.
35. Kärkkäinen, K., A.H. Sihvola, and K.I. Nikoskinen, Analysis of a three-dimensional dielectric mixture with finite difference method, *IEEE Transactions on Geoscience and Remote Sensing*, 39(5), 1013–1018, May 2001.
36. Wallin, H., H. Kettunen, and A. Sihvola, Mixing formulas and plasmonic composites. In *Metamaterials and Plasmonics: Fundamentals, modelling, applications*, S. Zouhdi, A. Sihvola, and A. P. Vinogradov, eds, Springer, Dordrecht, pp. 91–102, 2009.

10

Nonlocal Homogenization Theory of Structured Materials

Mário G. Silveirinha
University of Coimbra

10.1 Introduction

The use of homogenization methods in characterizing the interaction of electromagnetic fields with matter has a long history. An interesting review of the pioneering works of Lorentz, Planck, Ewald, and Oseen is given in [1]. Lorentz was the first to recognize that to properly describe molecular optics it was necessary to incorporate atomic concepts into Maxwell's equations, and take into account the electric vibrations of the particles. He obtained a relation between the dielectric constant and the density of the material at optical frequencies, and established the foundations of macroscopic electromagnetism. During the last century, the theory was further developed by studies that clarified averaging procedures [2], and took into account the resonant interaction of electromagnetic radiation with dielectric crystals coupled via retarded dipole fields [3]. Classical molecular optics was also extended to optically active media and to spatially dispersive media [4,5].

In recent years, there has been a renewed interest in homogenization methods due to their application in the characterization of structured materials (metamaterials). These materials are formed by properly shaped dielectric or metallic inclusions designed to obtain a desired effective response of

the material. It has been demonstrated that metamaterials may enable anomalous phenomena, such as negative refraction [6], compression of waves through very narrow channels [7], or subwavelength imaging [8–11].

The simplest homogenization approach is based on the use of mixing formulas, such as the Clausius–Mossotti formula [12]. The Clausius–Mossotti formula requires the volume fraction of the inclusions to be small, in order that they can be accurately modeled as point dipoles. More general homogenization methods have been developed over the years [13–18], but their applications are usually restricted to the quasistatic limit or to very specific geometries, or are limited by some other factor.

A key property of novel metamaterials is that the wavelength of light is only moderately larger than the lattice constant a, typically 5–10 times. This contrasts markedly with propagation of radiation in matter where the ratio, λ/a, is several orders of magnitude larger than that value, even at optical frequencies. This property may impose some restrictions on the application of classical homogenization theories to artificial materials [19]. In particular, the role of spatial dispersion in microstructured materials has been underlined by recent works [20–28]. Spatially dispersive materials may have important applications, such as imaging with super-resolution [10] or the realization of impedance surfaces [29].

The objective of this chapter is to present the state of art of homogenization methods for spatially dispersive materials. First, in Section 10.2, we discuss the definitions of the macroscopic fields, averaging procedures, and constitutive relations in local media. In Section 10.3, the homogenization theory introduced in [30] is described. This theory enables the calculation of the nonlocal dielectric function, $\underline{\underline{\varepsilon}} = \underline{\underline{\varepsilon}}(\omega, \mathbf{k})$, of an arbitrary periodic, composite dielectric material. To illustrate the application of such a homogenization approach, in Section 10.4 the dielectric function of a crystal formed by electric dipoles is explicitly calculated. In Section 10.5, it is explained how the homogenization method can be numerically implemented using the method of moments (MoM). Then, in Section 10.6, the relation between the local effective parameters and the nonlocal dielectric function is discussed. Finally, in Section 10.7, the problem of additional boundary conditions in spatially dispersive media is studied. The time variation, $e^{j\omega t}$, is assumed in this chapter.

10.2 Macroscopic Electromagnetism and Constitutive Relations in Local Media

The homogenization theory is an attempt to describe the interaction of electromagnetic radiation with very complex systems formed by an extremely large number of atoms, or in case of microstructured materials, formed by many inclusions. Typically, homogenization concepts may be applied when the wavelength of radiation is much larger than the characteristic microscopic dimensions of the considered system. In such circumstances, it is possible to average out the microscopic fluctuations of the electromagnetic fields, and in this way obtain slowly varying and smooth macroscopic quantities, which can be used to characterize the long range variations (propagation) of the electromagnetic waves. A key concept in the homogenization theory is the notion of spatial averaging. The spatial average of a physical entity, $F(\mathbf{r})$, with respect to a test function, $f(\mathbf{r})$, is defined here as [2,12],

$$\langle F \rangle (\mathbf{r}) = \int F(\mathbf{r} - \mathbf{r}')\, f(\mathbf{r}')\, \mathrm{d}^3\mathbf{r}' \tag{10.1}$$

where

$\mathbf{r} = (x,\ y,\ z)$ is a generic point of space

$f(\mathbf{r})$ is a real-valued function, nonzero in some neighborhood of the origin, and such that its integral over all space is unity

It may also be imposed that f is nonnegative, even though this is not strictly necessary. The support of $f(\mathbf{r})$ has a radial dimension R much smaller than the wavelength, and R is typically much larger than

the characteristic length of the microscopic domain (e.g., the lattice constant). The average field is, thus, given by the spatial convolution of the corresponding microscopic field with the test function. The main advantage of the considered averaging procedure is that it preserves the structure of the Maxwell equations, as detailed next.

To be specific, consider a material formed by nonmagnetic dielectric inclusions with relative permittivity $\varepsilon_r(\mathbf{r})$, and let $\mathbf{E}$ and $\mathbf{B}$ be the electric and induction fields in the material. These fields are designated here by microscopic fields, exploring the close analogy with the propagation of electromagnetic waves in matter. The fields $\mathbf{E}$ and $\mathbf{B}$ satisfy the frequency domain Maxwell equations,

$$\begin{aligned} \nabla \times \mathbf{E} &= -j\,\omega\mathbf{B} \\ \nabla \times \frac{\mathbf{B}}{\mu_0} &= \mathbf{J}_e + \varepsilon_0\varepsilon_r j\omega\,\mathbf{E} \end{aligned} \tag{10.2}$$

where $\mathbf{J}_e$ is the applied electric current density (source of fields). The macroscopic fields, $\langle\mathbf{E}\rangle$ and $\langle\mathbf{B}\rangle$, are obtained by averaging the microscopic fields using the operator (Equation 10.1). The test function f may be rather arbitrary, and does not need to be specified in detail. It can be easily verified that the space derivatives commute with the averaging operator defined by Equation 10.1 [2,12]. Hence, the macroscopic fields satisfy the following macroscopic equations:

$$\begin{aligned} \nabla \times \langle\mathbf{E}\rangle &= -j\omega\,\langle\mathbf{B}\rangle \\ \nabla \times \frac{\langle\mathbf{B}\rangle}{\mu_0} &= \langle\mathbf{J}_e\rangle + \langle\mathbf{J}_d\rangle + j\omega\varepsilon_0\,\langle\mathbf{E}\rangle \end{aligned} \tag{10.3}$$

In the above, $\mathbf{J}_d = \varepsilon_0\,(\varepsilon_r - 1)\,j\omega,\ \mathbf{E}$ is the induced microscopic current relative to the host medium, which is assumed vacuum without loss of generality. The space averaged applied current, $\langle\mathbf{J}_e\rangle$, and the space averaged microscopic current, $\langle\mathbf{J}_d\rangle$, are defined consistently with Equation 10.1. By comparing Equations 10.2 and 10.3, it is clear that the structure of Maxwell equations is, indeed, preserved by the averaging operator.

The classical theories of macroscopic electromagnetism are based on the decomposition of the averaged microscopic currents $\langle\mathbf{J}_d\rangle$ into dipolar and higher-order contributions [12,31],

$$\langle\mathbf{J}_d\rangle \approx j\omega\mathbf{P} + \nabla \times \mathbf{M} + \cdots \tag{10.4}$$

where

$\mathbf{P}$ is the polarization vector
$\mathbf{M}$ is the magnetization vector

The terms that are omitted involve spatial derivatives of the quadrupole density and other higher-order multipole moments. The classical definition of the (macroscopic) electric displacement vector $\mathbf{D}$ and of the (macroscopic) magnetic field $\mathbf{H}$ is motivated by the decomposition (Equation 10.4) of the average microscopic current into mean and eddy currents. As is well known, $\mathbf{D}$ and $\mathbf{H}$ are related to the fundamental macroscopic fields through the textbook formulas,

$$\begin{aligned} \mathbf{D} &= \varepsilon_0\,\langle\mathbf{E}\rangle + \mathbf{P} \\ \mathbf{H} &= \frac{\langle\mathbf{B}\rangle}{\mu_0} - \mathbf{M} \end{aligned} \tag{10.5}$$

Thus, Equation 10.5 implicitly absorbs the effect of the microscopic currents into $\mathbf{D}$ and $\mathbf{H}$, and so the macroscopic Maxwell equations in the material have the same form as in vacuum, apart from the relation between $\langle\mathbf{E}\rangle$, $\mathbf{D}$, $\langle\mathbf{B}\rangle$, and $\mathbf{H}$. For linear materials, $\mathbf{P}$ and $\mathbf{M}$ may be written as a linear combination of $\langle\mathbf{E}\rangle$ and $\mathbf{H}$. Such materials form the general class of bianisotropic materials [32,33] and are characterized by the constitutive relations,

$$\mathbf{D} = \varepsilon_0 \underline{\varepsilon_r} \cdot \langle \mathbf{E} \rangle + \sqrt{\varepsilon_0 \mu_0}\, \underline{\boldsymbol{\xi}} \cdot \mathbf{H}$$
$$\langle \mathbf{B} \rangle = \sqrt{\varepsilon_0 \mu_0}\, \underline{\boldsymbol{\zeta}} \cdot \langle \mathbf{E} \rangle + \mu_0 \underline{\boldsymbol{\mu}_r} \cdot \mathbf{H} \tag{10.6}$$

where

$\underline{\varepsilon_r}(\omega)$ is the relative permittivity
$\underline{\boldsymbol{\mu}_r}(\omega)$ is the relative permeability
$\underline{\boldsymbol{\xi}}(\omega)$ and $\underline{\boldsymbol{\zeta}}(\omega)$ are (dimensionless) parameters that characterize the magnetoelectric coupling

When the structure has a center of inversion symmetry the terms $\underline{\boldsymbol{\xi}}$ and $\underline{\boldsymbol{\zeta}}$ vanish, and the material can be described using uniquely permittivity and permeability tensors.

It is stressed that the above phenomenological model is meaningful only when the approximation, $\langle \mathbf{J}_d \rangle \approx j\omega\mathbf{P} + \nabla \times \mathbf{M}$, holds, and the higher-order multipole moments are negligible. Moreover, it is implicit that the medium is local in the sense that $\mathbf{D}$ and $\mathbf{H}$ at a given point of space can be written exclusively in terms of $\langle \mathbf{E} \rangle$ and $\langle \mathbf{B} \rangle$ at the same point of space, as implied by Equation 10.6.* Otherwise the medium is characterized by spatial dispersion [4,31]. In ordinary natural materials, where the lattice constant, $a \sim 0.1\ nm$, is several orders of magnitude smaller than the wavelength of radiation, the enunciated conditions are typically verified, and thus, the model (Equation 10.6) usually describes adequately macroscopic electromagnetism. However, in common artificial materials the lattice constant is typically only marginally smaller than the wavelength of radiation, and so the nonlocal effects may not be negligible, and the approximation (Equation 10.4) may not be accurate. Moreover, the phenomenological model (Equation 10.6) may also be inadequate to characterize natural media at optical frequencies, because, as argued in [31], the "the magnetic permeability ceases to have physical meaning at relatively low frequencies." It is thus clear that more sophisticated homogenization methods and concepts are necessary to characterize novel materials. The objective of this chapter is to present a fresh overview of these methods.

10.3 Homogenization of Nonlocal Media

Spatial dispersion effects occur when the polarization and magnetization vectors at a given "point" of space cannot be related through local relations with the macroscopic fields $\langle \mathbf{E} \rangle$ and $\langle \mathbf{B} \rangle$. Nonlocal effects have been studied in crystal optics, plasma physics, and metal optics [4], and more recently in artificial materials [20–28].

The goal of this section is to describe homogenization methods in spatially dispersive media. Our analysis closely follows reference [30]. It is assumed that the artificial material is nonmagnetic and periodic, with generic geometry as in Figure 10.1. The medium is invariant to translations along the primitive vectors $\mathbf{a}_1$, $\mathbf{a}_2$, and $\mathbf{a}_3$. Hence, the permittivity of the inclusions satisfies $\varepsilon_r(\mathbf{r} + \mathbf{r_I}) = \varepsilon_r(\mathbf{r})$, where $\mathbf{r_I} = i_1\mathbf{a}_1 + i_2\mathbf{a}_2 + i_3\mathbf{a}_3$ is a lattice point and $\mathbf{I} = (i_1, i_2, i_3)$ is a generic multi-index of integers. The unit cell Ω of the periodic medium is $\Omega = \{\alpha_1\mathbf{a}_1 + \alpha_2\mathbf{a}_2 + \alpha_3\mathbf{a}_3 : |\alpha_i| \leq 1/2\}$. The permittivity may be a complex number and depend on frequency. In addition, the unit cell may contain perfectly electric conducting (PEC) metallic surfaces, which are denoted by ∂D, as illustrated in Figure 10.1. The outward unit vector normal to ∂D is $\hat{\mathbf{v}}$.

*Some authors consider that media with magnetoelectric activity are nonlocal, since such an effect may be regarded as a manifestation of the first-order spatial dispersion. Here, we follow a slightly different definition, and consider that when it is possible to relate the macroscopic fields through local relations in the space domain as in Equation 10.6, the medium is by definition local and linear.

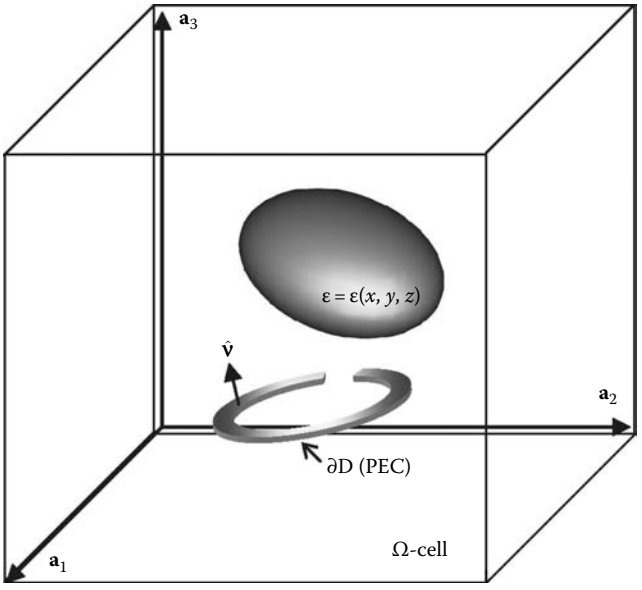

FIGURE 10.1 Geometry of the unit cell of a generic metallic-dielectric periodic material with a dielectric inclusion and a PEC inclusion. (Reprinted from Silveirinha, M.G., *Phys. Rev. B*, 75, 115104, 2007. With permission.)

10.3.1 Constitutive Relations in Nonlocal Media

In presence of strong spatial dispersion, the introduction of the effective permeability tensor $\underline{\boldsymbol{\mu}}_{\mathbf{r}}$, as well as of $\underline{\boldsymbol{\xi}}$ and $\underline{\boldsymbol{\zeta}}$, is not meaningful [31]. The problem is that splitting the mean microscopic current as in Equation 10.4 is not advantageous, because **P** and **M** cannot be related with the average fields through local relations. Due to this reason, it is common to consider alternative phenomenological constitutive relations, in which all the terms resulting from the averaging of the microscopic currents are directly included into the definition of the electric displacement **D**, without introducing a magnetization vector. In this way, for a nonlocal medium we have the following definitions [4,31] (compare with Equation 10.5):

$$\begin{aligned} \mathbf{D}_g &= \varepsilon_0 \langle \mathbf{E} \rangle + \mathbf{P}_g \\ \mathbf{H}_g &= \frac{\langle \mathbf{B} \rangle}{\mu_0} \end{aligned} \tag{10.7}$$

where, by definition, $\mathbf{P}_g = \langle \mathbf{J}_d \rangle / j\omega$. We introduced the subscript "g" to underline that the electric displacement and the magnetic field defined as in Equation 10.7 differ from the classical definition (Equation 10.5). In fact, as mentioned above, in this phenomenological model all the microscopic currents are included directly in the definition of the electric displacement. From Equation 10.4, it is evident that

$$\mathbf{P}_g = \mathbf{P} + \nabla \times \mathbf{M} / j\omega + \cdots \tag{10.8}$$

Thus, $\mathbf{P}_g$ is a generalized polarization vector that contains the effect of the dipolar moments, and in addition, the effect of all higher-order multipole moments.

The effective parameters corresponding to Equation 10.7 are completely different from the local effective parameters associated with Equation 10.6. In fact, $\mathbf{D}_g$ cannot be related with the average field $\langle \mathbf{E} \rangle$ through a local relation, since, in general, the polarization $\mathbf{P}_g$ at one point of space depends on the distribution of the macroscopic electric field in a neighborhood of the considered point. Instead,

for unbounded periodic linear materials, it is assumed that the macroscopic fields are related by a constitutive relation of the form [4,31]*

$$\mathbf{D}_g(\mathbf{r}) = \int \underline{\hat{\varepsilon}}\,(\omega, \mathbf{r} - \mathbf{r}') \cdot \langle \mathbf{E}(\mathbf{r}') \rangle \, d^3\mathbf{r}' \tag{10.9}$$

where $\underline{\hat{\varepsilon}}$ is the dielectric function of the material in the space domain. This constitutive relation establishes that the electric displacement is related to the macroscopic electric field through a space convolution. The nonlocal character of the material is clear from such a formula.

The relation between the macroscopic fields is comparatively simpler in the Fourier transform **k**-domain. The Fourier transform of the macroscopic electric field is, by definition,

$$\langle \tilde{\mathbf{E}} \rangle (\mathbf{k}) = \int \langle \mathbf{E}(\mathbf{r}) \rangle \, e^{j\mathbf{k}\cdot\mathbf{r}} d^3\mathbf{r} \tag{10.10}$$

where

"~" denotes Fourier transformation

$\mathbf{k} = (k_x, k_y, k_z)$ is the wave vector

From Equations 10.7 and 10.9, it is clear that in the spectral domain the following constitutive relations hold:

$$\begin{aligned} \tilde{\mathbf{D}}_g &\equiv \varepsilon_0 \langle \tilde{\mathbf{E}} \rangle + \tilde{\mathbf{P}}_g = \underline{\varepsilon}\,(\omega, \mathbf{k}) \cdot \langle \tilde{\mathbf{E}} \rangle \\ \tilde{\mathbf{H}}_g &= \frac{\langle \tilde{\mathbf{B}} \rangle}{\mu_0} \end{aligned} \tag{10.11}$$

where $\underline{\varepsilon}\,(\omega, \mathbf{k})$ is the dielectric function of the material, which is given by the Fourier transform of $\underline{\hat{\varepsilon}}$. The homogenized unbounded material is completely characterized by the dielectric function. When using the constitutive relations (Equation 10.7) it is not necessary to introduce a magnetic permeability tensor: all the physics is described by $\underline{\varepsilon}\,(\omega, \mathbf{k})$, including the effect of high order multipoles.

The parameters ω and **k** in the argument of the dielectric function are independent variables. This property should be obvious from the definition of $\underline{\varepsilon}$ [4]. Sometimes this may be a source of confusion, because for plane wave propagation, and in the absence of external sources, the wave vector becomes a function of frequency, $\mathbf{k} = \mathbf{k}(\omega)$. However, the key point is that the dielectric function is defined in its most general form even for ω and **k** that are not associated with plane wave normal modes. Indeed, as it is discussed in Section 10.3.3, to calculate the dielectric function the material must be excited by an external source. This makes possible the generation of microscopic fields associated with any independent values of ω and **k**.

10.3.2 Fields with Floquet Variation

Electromagnetic fields with Floquet periodicity are of special importance in the characterization of periodic media. For example, the electromagnetic properties of dielectric crystals are completely determined by the "band structure" of their Floquet eigenmodes. Thus, it is not surprising if the dielectric function of a structured material is closely related to the Floquet fields. To establish this connection in what follows, the macroscopic properties of electromagnetic fields with the Floquet

*For spatially inhomogeneous bodies, which ultimately is the case of all crystals, the dielectric function cannot be written as a function of $\mathbf{r} - \mathbf{r}'$, and is of the more general form $\underline{\hat{\varepsilon}}\,(\omega, \mathbf{r}, \mathbf{r}')$ [4, p. 87].

property are characterized. It will be shown that under suitable conditions the macroscopic fields may be identified with the amplitudes of the zero-order Floquet harmonics associated with the microscopic fields.

It is assumed that the electric field $\mathbf{E}$ is such that $\mathbf{E}(\mathbf{r})\, e^{j\mathbf{k}\cdot\mathbf{r}}$ is periodic, where $\mathbf{k}$ is the imposed wave vector. The microscopic induction field $\mathbf{B}$ and the applied current $\mathbf{J}_e$ have a similar property. Notice that $(\mathbf{E}, \mathbf{B})$ are not necessarily associated with an electromagnetic mode of the periodic material, because the applied current does not have to be zero.

In order to characterize the macroscopic fields in the spectral domain, the electric field is expanded into a Fourier series,

$$\mathbf{E}(\mathbf{r}) = \sum_{\mathbf{J}} \mathbf{E}_{\mathbf{J}}\, e^{-j\mathbf{k}_{\mathbf{J}}\cdot\mathbf{r}}, \quad \mathbf{k}_{\mathbf{J}} = \mathbf{k} + \mathbf{k}_{\mathbf{J}}^{0}$$
$$\mathbf{E}_{\mathbf{J}} = \frac{1}{V_{\text{cell}}} \int_{\Omega} \mathbf{E}(\mathbf{r})\, e^{j\mathbf{k}_{\mathbf{J}}\cdot\mathbf{r}} \mathrm{d}^3\mathbf{r} \tag{10.12}$$

where

$V_{\text{cell}} = |\mathbf{a}_1 \cdot (\mathbf{a}_2 \times \mathbf{a}_3)|$ is the volume of the unit cell
$\mathbf{J} = (j_1, j_2, j_3)$ is a multi-index of integers
$\mathbf{k}_{\mathbf{J}}^{0} = j_1\mathbf{b}_1 + j_2\mathbf{b}_2 + j_3\mathbf{b}_3$
$\mathbf{E}_{\mathbf{J}}$ is the coefficient of the $\mathbf{J}$th harmonic

The reciprocal lattice primitive vectors, $\mathbf{b}_n$, are implicitly defined by the relations, $\mathbf{a}_m \cdot \mathbf{b}_n = 2\pi\delta_{m,n}$, $m, n = 1, 2, 3$.

From the definition of the averaging operator (Equation 10.1), it is clear that $\langle\tilde{\mathbf{E}}\rangle(\mathbf{k}') = \tilde{\mathbf{E}}(\mathbf{k}')\, \tilde{f}(\mathbf{k}')$, where $\tilde{\mathbf{E}}$ is the Fourier transform of the microscopic field and $\tilde{f}$ is the Fourier transform of the test function. Hence, using Equation 10.12, it is found that in the spectral domain

$$\langle\tilde{\mathbf{E}}\rangle(\mathbf{k}') = (2\pi)^3 \sum_{\mathbf{J}} \mathbf{E}_{\mathbf{J}} \tilde{f}(\mathbf{k}_{\mathbf{J}})\, \delta(\mathbf{k}' - \mathbf{k}_{\mathbf{J}}) \tag{10.13}$$

Thus, the macroscopic electric field in the spectral domain consists of a superimposition of Dirac δ-function impulses centered at points of the form, $\mathbf{k}' = \mathbf{k}_{\mathbf{J}}$. The amplitudes of the impulses depend on the Fourier series coefficients of the microscopic field, as well as on the considered test function.

At this point it is convenient to analyze the properties of the test function f with more detail. Since f is normalized to unity, i.e., its integral over all space is unity, it follows that $\tilde{f}(\mathbf{0}) = 1$. In order to average out the microscopic fluctuations of the fields, it is sufficient that the support of f in the space domain contains the unit cell. Thus, f must be nearly constant inside Ω, and may vanish outside a neighborhood of Ω. From the properties of the Fourier transform, in principle, this implies that $\tilde{f}(\mathbf{k})$ verifies $\tilde{f}(\mathbf{k}) \approx 0$ outside the first Brillouin zone. For example, for the case of simple cubic lattice with lattice constant a, the test function may be chosen equal to

$$f(\mathbf{r}) = \left(\pi R^2\right)^{-3/2} e^{-r^2/R^2}$$
$$\tilde{f}(\mathbf{k}) = e^{-(kR/2)^2} \tag{10.14}$$

with $R \approx a$. Such a test function verifies $\tilde{f}(\mathbf{k}) \approx 0$ for points such that $k > \pi/a$.

This discussion shows that it is safe to assume that for $\mathbf{k}$, relatively close to the origin of the Brillouin zone, $\tilde{f}(\mathbf{k}_{\mathbf{J}}) \approx 0$ for $\mathbf{J} \neq 0$ and $\tilde{f}(\mathbf{k}_{\mathbf{J}}) \approx 1$ for $\mathbf{J} = 0$. Thus, by calculating the inverse Fourier transform of Equation 10.13, it follows that

$$\langle\mathbf{E}\rangle \approx \mathbf{E}_{\text{av}} e^{-j\mathbf{k}\cdot\mathbf{r}} \tag{10.15}$$

where $\mathbf{E}_{av}$ is defined as the amplitude of the zero-order Floquet harmonic:

$$\mathbf{E}_{av} = \frac{1}{V_{cell}} \int_{\Omega} \mathbf{E}(\mathbf{r})\, e^{+j\mathbf{k}\cdot\mathbf{r}} d^3\mathbf{r}. \tag{10.16}$$

Proceeding along similar lines and using Equation 10.11, it may be verified that the macroscopic fields, $\langle \mathbf{B} \rangle$ and $\mathbf{D}_g$, verify the formulas*:

$$\langle \mathbf{B} \rangle \approx \mathbf{B}_{av} e^{-j\mathbf{k}\cdot\mathbf{r}}, \quad \mathbf{D}_g \approx \mathbf{D}_{g,av} e^{-j\mathbf{k}\cdot\mathbf{r}} \tag{10.17}$$

where,

$$\mathbf{B}_{av} = \frac{1}{V_{cell}} \int_{\Omega} \mathbf{B}(\mathbf{r})\, e^{+j\mathbf{k}\cdot\mathbf{r}} d^3\mathbf{r} \tag{10.18}$$

$$\mathbf{D}_{g,av} \equiv \varepsilon_0 \mathbf{E}_{av} + \mathbf{P}_{g,av} = \underline{\boldsymbol{\varepsilon}}(\omega, \mathbf{k}) \cdot \mathbf{E}_{av} \tag{10.19}$$

and $\mathbf{P}_{g,av}$ is the generalized polarization vector:

$$\mathbf{P}_{g,av} = \frac{1}{V_{cell} j\omega} \int_{\Omega} \mathbf{J}_d(\mathbf{r})\, e^{+j\mathbf{k}\cdot\mathbf{r}} d^3\mathbf{r} \tag{10.20}$$

As mentioned in Section 10.3.1, $\mathbf{P}_{g,av}$ is closely related to the classic polarization vector. Indeed, if the exponential inside the integral is expanded in powers of the argument, the leading term corresponds exactly to the standard polarization vector (i.e., the average electric dipole moment in a unit cell). The higher-order terms can be related to the magnetization vector and other multipole moments. When the unit cell contains PEC surfaces, the polarization vector may be rewritten as

$$\mathbf{P}_{g,av} = \frac{1}{V_{cell} j\omega} \left(\int_{\partial D} \mathbf{J}_c e^{+j\mathbf{k}\cdot\mathbf{r}} ds + \int_{\Omega - \partial D} \mathbf{J}_d\, e^{+j\mathbf{k}\cdot\mathbf{r}} d^3\mathbf{r} \right) \tag{10.21}$$

where

∂D is the PEC surface

$\mathbf{J}_c = \hat{\mathbf{v}} \times [\mathbf{B}/\mu_0]$ is the surface current density (see Figure 10.1)

The previous results confirm that provided the test function is properly chosen, the macroscopic fields are completely determined by the amplitudes of the corresponding zero-order Floquet harmonics, as anticipated in the beginning of this section. Moreover, it is proven in Section 10.3.3 that the zero-order harmonics may be used to completely characterize the unknown dielectric function $\underline{\varepsilon}$.

For future reference, it can be verified from the microscopic Maxwell equations (Equation 10.2) that the average fields satisfy exactly the equations:

$$\begin{aligned} -\mathbf{k} \times \mathbf{E}_{av} + \omega \mathbf{B}_{av} &= 0 \\ \omega \left(\varepsilon_0 \mathbf{E}_{av} + \mathbf{P}_{g,av} \right) + \mathbf{k} \times \frac{\mathbf{B}_{av}}{\mu_0} &= -\omega \mathbf{P}_{e,av} \end{aligned} \tag{10.22}$$

where $\mathbf{P}_{e,av} = \frac{1}{V_{cell} j\omega} \int_{\Omega} \mathbf{J}_e e^{+j\mathbf{k}\cdot\mathbf{r}} d^3\mathbf{r}$ is the applied polarization vector.

*Equations 10.15 and 10.17 become exact for $\mathbf{k}$ in the Brillouin zone if one chooses the test function such that $\tilde{f}(\mathbf{k}) = 1$ inside the Brillouin zone and $\tilde{f}(\mathbf{k}) = 0$ outside the Brillouin zone. In such conditions the averaging operator is equivalent to a low pass spatial filter, which retains uniquely the fundamental zero-order Floquet harmonic.

10.3.3 Microscopic Theory

We now introduce a microscopic theory based on the constitutive relation (Equation 10.9) that enables the homogenization of arbitrary periodic nonmagnetic materials.

The key idea to retrieve the effective parameters of the periodic medium for fixed $(\omega, \mathbf{k})$ is to excite the structure with a periodic source $\mathbf{J}_e$ that enforces a desired phase modulation in the unit cell, so that the solution $(\mathbf{E}, \mathbf{B})$ of Maxwell equations (Equation 10.2) has the Floquet property. Thus, it is imposed that the applied $\mathbf{J}_e$ has the Floquet property, i.e., $\mathbf{J}_e e^{j\mathbf{k}\cdot\mathbf{r}}$ is periodic in the crystal, where $\mathbf{k}$ is the wave vector associated with the excitation.

From the results of Section 10.3.2 and Equation 10.19, it is known that the dielectric function must verify $\underline{\varepsilon}(\omega, \mathbf{k}) \cdot \mathbf{E}_{av} = \varepsilon_0 \mathbf{E}_{av} + \mathbf{P}_{g,av}$. Hence, for fixed $(\omega, \mathbf{k})$ the dielectric function $\underline{\varepsilon}$ can be completely determined from the previous formula, provided $\mathbf{P}_{g,av}$ is known for three independent vectors $\mathbf{E}_{av}$, e.g., for $\mathbf{E}_{av} \sim \hat{\mathbf{u}}_i$, where $\hat{\mathbf{u}}_i$ is directed along the coordinate axes. Remember that the generalized polarization vector, $\mathbf{P}_{g,av}$, can be computed from the induced microscopic currents.

The specific spatial variation of the chosen applied current $\mathbf{J}_e$, in principle, does not influence significantly the extracted effective parameters, at least if the dimensions of the unit cell are much smaller than the wavelength. However, in view of the hypotheses used in Section 10.3.2 to obtain Equations 10.15 and 10.17, it is desirable that the applied current excites mainly the zero-order Floquet harmonics, and excites as weakly as possible the remaining harmonics. Hence, it is convenient to assume that the applied density of current $\mathbf{J}_e$ is uniform, with $\mathbf{J}_e = \mathbf{J}_{e,av} e^{-j\mathbf{k}\cdot\mathbf{r}}$, where $\mathbf{J}_{e,av}$ is a constant vector independent of $\mathbf{r}$. Using the definition of $\mathbf{P}_{e,av}$, it is seen that the applied current can be written in terms of the applied polarization vector:

$$\mathbf{J}_e = j\omega \mathbf{P}_{e,av} e^{-j\mathbf{k}\cdot\mathbf{r}} \tag{10.23}$$

Thus, the recipe proposed here to calculate the dielectric function can be summarized as follows:

- For fixed $(\omega, \mathbf{k})$, solve the source-driven Maxwell equations (Equation 10.2) for an applied current, as in Equation 10.23, with $\mathbf{P}_{e,av} \sim \hat{\mathbf{u}}_i$, $i = 1, 2, 3$ (or for another equivalent independent set with a dimension three). This involves solving three different source-driven problems.
- From the computed microscopic fields calculate the corresponding macroscopic electric field, $\mathbf{E}_{av}$, and the generalized polarization vector, $\mathbf{P}_{g,av}$.
- Finally, using Equation 10.19, obtain the desired dielectric function $\underline{\varepsilon}$.

It is important to underline that the described method is not based on the solution of an eigenvalue problem, but instead only requires solving Maxwell's equations under a periodic excitation. In particular, the described homogenization procedure can be used to obtain the effective parameters even in frequency band gaps or in case of lossy materials. It should also be clear that the extracted dielectric function is completely independent of the specific test function used to define the macroscopic fields.

In the following sections, it will be illustrated how the outlined method can be applied in practice, and how it can be numerically implemented to homogenize a completely arbitrary microstructured material.

10.3.4 Plane Wave Solutions

The dielectric function $\underline{\varepsilon}$ can be used to characterize the Floquet eigenmodes supported by the structured material. In fact, the pair $(\omega, \mathbf{k})$ is associated with an electromagnetic mode of the crystal, if and only if, the Maxwell equations (Equation 10.2) support a $\mathbf{k}$-periodic solution in the absence of an external source, i.e., with $\mathbf{J}_e = 0$. In such a case, the system (Equation 10.22) has a nontrivial solution for $(\mathbf{E}_{av}, \mathbf{B}_{av})$ with an applied polarization vector such that $\mathbf{P}_e = 0$ [30]. Hence, substituting Equation 10.19 into Equation 10.22, it follows that the homogeneous system

$$-\mathbf{k}\times\mathbf{E}_{av}+\omega\mathbf{B}_{av}=0$$
$$\omega\underline{\varepsilon}\cdot\mathbf{E}_{av}+\mathbf{k}\times\frac{\mathbf{B}_{av}}{\mu_0}=0 \tag{10.24}$$

has a nontrivial solution, if and only if $(\omega,\mathbf{k})$ is associated with an electromagnetic mode of the material. This result is exact and valid for arbitrary $(\omega,\mathbf{k})$, not necessarily in the long wavelength limit. In particular, this remarkable property implies that the band structure information of an arbitrary periodic material is completely specified by its dielectric function. Hence, the dielectric function defined, as in Section 10.3.3, can be used to obtain the dispersion diagram and average fields of an arbitrary electromagnetic mode.

The nontrivial solutions of Equation 10.24 determine the plane wave normal modes supported by the homogenized medium. From the previous paragraph, it is evident that there is a one-to-one relation between the Floquet eigenmodes of a structured material and the plane wave normal modes of the corresponding homogenized medium.

From Equation 10.24, it can be proven that the average electric field verifies the characteristic system [4]:

$$\left(\left(\frac{\omega}{c}\right)^2\frac{\underline{\boldsymbol{\varepsilon}}}{\varepsilon_0}+\mathbf{k}\mathbf{k}-k^2\underline{\mathbf{I}}\right)\cdot\mathbf{E}_{av}=\mathbf{0} \tag{10.25}$$

where

$c=1/\sqrt{\varepsilon_0\mu_0}$ is the speed of light in vacuum
$k^2=\mathbf{k}\cdot\mathbf{k}$

After simple manipulations [30], it can be verified that, provided the average field is not transverse, i.e., provided $\mathbf{k}\cdot\mathbf{E}_{av}\neq 0$, the associated wave vector satisfies the characteristic equation:

$$-1=\mathbf{k}\cdot\left(\left(\frac{\omega}{c}\right)^2\frac{\underline{\boldsymbol{\varepsilon}}}{\varepsilon_0}-k^2\underline{\mathbf{I}}\right)^{-1}\cdot\mathbf{k}\quad\text{if}\quad\mathbf{k}\cdot\mathbf{E}_{av}\neq 0 \tag{10.26}$$

The solutions, $\omega=\omega(\mathbf{k})$, of Equation 10.26 yield the dispersion of the plane wave normal modes. The macroscopic average field is given by

$$\mathbf{E}_{av}\propto\left(\frac{\underline{\boldsymbol{\varepsilon}}}{\varepsilon_0}-\frac{c^2k^2}{\omega^2}\underline{\mathbf{I}}\right)^{-1}\cdot\frac{c\mathbf{k}}{\omega}\quad\text{if}\quad\mathbf{k}\cdot\mathbf{E}_{av}\neq 0 \tag{10.27}$$

10.3.5 Symmetries of the Dielectric Function

Some relevant properties of the dielectric function are enunciated next [4,30]. Below, the superscript "t" represents the transpose dyadic and the superscript "*" represents complex conjugation.

- $\underline{\varepsilon}(\omega,\mathbf{k})=\underline{\varepsilon}^*(-\omega^*,-\mathbf{k}^*)$.
- $\underline{\varepsilon}(\omega,\mathbf{k})=\underline{\varepsilon}^{\mathrm{t}}(\omega,-\mathbf{k})$.
- Let $\mathbf{T}$ represent a translation. Suppose that a given material is characterized by the dielectric function $\underline{\varepsilon}$, and that the metamaterial resulting from the application of $\mathbf{T}$ to the original structure is characterized by the dielectric function $\underline{\varepsilon}'$. Then, $\underline{\varepsilon}'(\boldsymbol{\omega},\mathbf{k})=\underline{\varepsilon}(\boldsymbol{\omega},\mathbf{k})$. In particular, the definition of the dielectric function is independent of the origin of the coordinate system.
- Let $\mathbf{S}$ be an isometry (a rotation or a reflection): $\mathbf{S}\cdot\mathbf{S}^{\mathrm{t}}=\underline{\mathbf{I}}$. Suppose that a given material is characterized by the dielectric function $\underline{\varepsilon}$, and that the material resulting from the

application of **S** to the original structure is characterized by the dielectric function $\underline{\varepsilon}'$. Then, $\underline{\varepsilon}'(\omega, \mathbf{S}\cdot\mathbf{k}) = \mathbf{S}\cdot\underline{\varepsilon}(\omega,\mathbf{k})\cdot\mathbf{S}^{t}$.

- If a material is invariant to the application of an isometry followed by a translation $\mathbf{T}\circ\mathbf{S}$, then its dielectric function satisfies $\underline{\varepsilon}(\omega,\mathbf{S}\cdot\mathbf{k}) = \mathbf{S}\cdot\underline{\varepsilon}(\omega,\mathbf{k})\cdot\mathbf{S}^{t}$. In particular, if the material has a center of inversion symmetry, i.e., the origin can be chosen such that the material is invariant to the inversion $\mathbf{S}:\mathbf{r}\to-\mathbf{r}$, then $\underline{\varepsilon}(\omega,\mathbf{k}) = \underline{\varepsilon}(\omega,-\mathbf{k})$.

10.4 Dielectric Function of a Lattice of Electric Dipoles

In order to illustrate the application of the homogenization method introduced in Section 10.3, the dielectric function of a periodic lattice of electric dipoles is characterized next. Besides being of obvious theoretical interest, this canonical problem can be solved in closed analytical form [34], and thus the study of this electromagnetic crystal gives important insights into the homogenization approach. The analysis also yields the generalized Lorentz–Lorenz and Clausius–Mossotti formulas for spatially dispersive media.

It is assumed that the medium consists of a three-dimensional periodic array of identical electric dipoles characterized by the electric polarizability $\underline{\boldsymbol{\alpha}}_{e}$. The dipoles are positioned at the lattice points, $\mathbf{r}_{\mathbf{I}} = i_1\mathbf{a}_1 + i_2\mathbf{a}_2 + i_3\mathbf{a}_3$, where $\mathbf{a}_1$, $\mathbf{a}_2$, and $\mathbf{a}_3$ are the primitive vectors of the crystal, and $\mathbf{I} = (i_1, i_2, i_3)$ is a multi-index of integers.

The microscopic electromagnetic fields induce an electric dipole moment in each particle. The dipole moment $\mathbf{p}_e$ of the particle at the origin is given by

$$\frac{\mathbf{p}_e}{\varepsilon_0} = \underline{\boldsymbol{\alpha}}_e(\omega)\cdot\mathbf{E}_{loc} \tag{10.28}$$

where $\mathbf{E}_{loc}$ is the local electric field that polarizes the inclusion, which is given by the superimposition of the fields radiated by the other particles and the external field.

To calculate the dielectric function of the periodic crystal, we need to solve the Maxwell equations (Equation 10.2) for an applied current of the form given in Equation 10.23. For a lattice of electric dipoles, Equation 10.2 may be rewritten as

$$\begin{aligned}\nabla\times\mathbf{E} &= -j\omega\mathbf{B}\\ \nabla\times\frac{\mathbf{B}}{\mu_0} &= j\omega\mathbf{P}_{e,av}e^{-j\mathbf{k}\cdot\mathbf{r}} + \mathbf{J}_{dip} + j\omega\varepsilon_0\mathbf{E}\end{aligned} \tag{10.29}$$

where $\mathbf{J}_{dip}$ represents the electric microscopic currents induced in the dipoles. Since the applied source has the Floquet property, it is clear that the induced current is such that

$$\mathbf{J}_{dip} = \sum_{\mathbf{I}}\delta(\mathbf{r}-\mathbf{r}_{\mathbf{I}})\,e^{-j\mathbf{k}\cdot\mathbf{r}_{\mathbf{I}}}\,j\omega\mathbf{p}_e \tag{10.30}$$

where

$\mathbf{p}_e$ is the electric dipole moment of the particle at the origin
$\mathbf{r}_{\mathbf{I}}$ represents a generic lattice point
δ is Dirac's distribution

The solution of Equation 10.29 can be written in a straightforward manner in terms of the lattice Green dyadic, $\underline{\mathbf{G}}_p(\mathbf{r}|\mathbf{r}') = \left(\underline{\mathbf{I}} + \frac{c^2}{\omega^2}\nabla\nabla\right)\Phi_p(\mathbf{r}|\mathbf{r}')$, where $\Phi_p = \Phi_p(\mathbf{r}|\mathbf{r}';\omega,\mathbf{k})$ is the lattice Green function [30,35,36], which verifies

$$\nabla^2\Phi_p + \left(\frac{\omega}{c}\right)^2\Phi_p = -\sum_{\mathbf{I}}\delta(\mathbf{r}-\mathbf{r}'-\mathbf{r}_{\mathbf{I}})e^{-j\mathbf{k}\cdot(\mathbf{r}-\mathbf{r}')} \tag{10.31}$$

In fact, it is simple to confirm that the solution of the problem is

$$\mathbf{E} = (-j\omega\mu_0)\,\underline{\mathbf{G}}_p(\mathbf{r}|\mathbf{0}) \cdot j\omega\mathbf{p}_e + (-j\omega\mu_0)\,V_{\text{cell}}\underline{\mathbf{G}}_{\text{av}} \cdot j\omega\mathbf{P}_{e,av}e^{-j\mathbf{k}\cdot\mathbf{r}} \tag{10.32}$$

where, by definition,

$$\underline{\mathbf{G}}_{\text{av}} = \frac{1}{V_{\text{cell}}}\int_{\Omega}\underline{\mathbf{G}}_p(\mathbf{r}|\mathbf{r}')\,e^{+j\mathbf{k}\cdot(\mathbf{r}-\mathbf{r}')}\mathrm{d}^3\mathbf{r}' \tag{10.33}$$

From [30], the dyadic $\underline{\mathbf{G}}_{\text{av}}$ and the respective inverse are equal to

$$\begin{aligned}\underline{\mathbf{G}}_{\text{av}} &= \frac{1}{V_{\text{cell}}}\frac{1}{(\omega/c)^2}\frac{(\omega/c)^2\underline{\mathbf{I}} - \mathbf{kk}}{k^2 - (\omega/c)^2}\\ \underline{\mathbf{G}}_{\text{av}}^{-1} &= -V_{\text{cell}}\left[\left((\omega/c)^2 - k^2\right)\underline{\mathbf{I}} + \mathbf{kk}\right]\end{aligned} \tag{10.34}$$

The first term on the right-hand side of Equation 10.32 corresponds to the field created by the induced electric dipoles, and the second term corresponds to the field created by the applied source, $\mathbf{P}_{e,av}$.

To obtain the full solution of Equation 10.29, it is still necessary to determine the unknown, $\mathbf{p}_e$. From Equation 10.32 it is obvious that the local electric field that polarizes the particle at the origin is

$$\mathbf{E}_{\text{loc}} = \left(\frac{\omega}{c}\right)^2\underline{\mathbf{G}}'_p(\mathbf{0}|\mathbf{0}) \cdot \frac{\mathbf{p}_e}{\varepsilon_0} + \left(\frac{\omega}{c}\right)^2 V_{\text{cell}}\underline{\mathbf{G}}_{\text{av}} \cdot \frac{\mathbf{P}_{e,av}}{\varepsilon_0} \tag{10.35}$$

where, by definition,

$$\underline{\mathbf{G}}'_p(\mathbf{r}|\mathbf{r}') = \underline{\mathbf{G}}_p(\mathbf{r}|\mathbf{r}') - \underline{\mathbf{G}}_f(\mathbf{r}|\mathbf{r}') \tag{10.36}$$

and $\underline{\mathbf{G}}_f(\mathbf{r}|\mathbf{r}')$ is the free-space Green-dyadic for a single electric dipole with the Sommerfeld radiation conditions. The electric dipole moment $\mathbf{p}_e$ can now be obtained as a function of the excitation by substituting Equation 10.28 into Equation 10.35, and solving the resulting equation for $\mathbf{p}_e$. This gives the formal solution of the microscopic equations (Equation 10.29).

To obtain the dielectric function of the crystal, it is necessary to link the polarization vector, $\mathbf{P}_{g,av}$, with the macroscopic field, $\mathbf{E}_{av}$. The vector $\mathbf{P}_{g,av}$ can be obtained by substituting Equation 10.30 into Equation 10.20. As could be expected, the following relation holds:

$$\mathbf{P}_{g,av} = \frac{\mathbf{p}_e}{V_{\text{cell}}} \tag{10.37}$$

On the other hand, the induced average electric field can be related to the applied polarization vector using the relations given in Equation 10.22. Straightforward calculations demonstrate that

$$\frac{\mathbf{P}_{e,av}}{\varepsilon_0} + \frac{\mathbf{P}_{g,av}}{\varepsilon_0} = \frac{c^2}{\omega^2}\frac{1}{V_{\text{cell}}}\underline{\mathbf{G}}_{\text{av}}^{-1} \cdot \mathbf{E}_{\text{av}} \tag{10.38}$$

Using the previous relations in Equation 10.35, it is found that the local field can be rewritten as

$$\mathbf{E}_{\text{loc}} = \mathbf{E}_{\text{av}} + \underline{\mathbf{C}}_i(\omega,\mathbf{k}) \cdot \frac{\mathbf{p}_e}{\varepsilon_0} \tag{10.39}$$

where the interaction dyadic $\underline{\mathbf{C}}_i$ is, by definition,

$$\underline{\mathbf{C}}_i(\omega,\mathbf{k}) = \left(\frac{\omega}{c}\right)^2\left(\underline{\mathbf{G}}'_p(\mathbf{0}|\mathbf{0};\omega,\mathbf{k}) - \underline{\mathbf{G}}_{\text{av}}(\omega,\mathbf{k})\right) \tag{10.40}$$

Equation 10.39 relates the local field with the macroscopic field and the induced dipole moment. This important relation is a generalization of the classical Lorentz–Lorenz formula [12]. It describes the effect of frequency dispersion, as well as of spatial dispersion, which may emerge due to the noncontinuous (discrete) nature of the material.

Using the generalized Lorentz–Lorenz formula, it is simple to obtain the dielectric function of the composite material. Substituting Equations 10.28 and 10.37 into Equation 10.39, it is found that

$$(\underline{\mathbf{I}} - \underline{\boldsymbol{\alpha}}_e \cdot \underline{\mathbf{C}}_{\mathrm{i}}) \cdot \frac{\mathbf{P}_{\mathrm{g,av}}}{\varepsilon_0} = \frac{1}{V_{\mathrm{cell}}} \underline{\boldsymbol{\alpha}}_e \cdot \mathbf{E}_{\mathrm{av}} \tag{10.41}$$

Solving the above equation for $\mathbf{P}_{\mathrm{g,av}}$ and using Equation 10.19, it clear that the dielectric function of the lattice of dipoles is given by

$$\underline{\boldsymbol{\varepsilon}}(\omega, \mathbf{k}) = \underline{\mathbf{I}} + \frac{1}{V_{\mathrm{cell}}} \left(\underline{\mathbf{I}} - \underline{\boldsymbol{\alpha}}_e \cdot \underline{\mathbf{C}}_{\mathrm{i}}(\omega, \mathbf{k})\right)^{-1} \cdot \underline{\boldsymbol{\alpha}}_e \tag{10.42}$$

This is an important result and also generalization of the classical Clausius–Mossotti formula [12]. It establishes that the dielectric function can be written in terms of the electric polarizability of the particles and of the interaction dyadic $\underline{\mathbf{C}}_{\mathrm{i}}$. It is stressed that the above result is exact within the theory described in Section 10.3. In particular, the dispersion characteristic of the electromagnetic modes may be obtained by substituting the dielectric function into Equation 10.24, and by calculating the values of $(\omega, \mathbf{k})$ for which the homogeneous system has nontrivial solutions.

It can be proven that in the quasistatic limit, the interaction dyadic of a simple cubic lattice is given by [34]

$$\underline{\mathbf{C}}_{\mathrm{i}}(\omega = 0, \mathbf{k} = \mathbf{0}) = \frac{1}{3V_{\mathrm{cell}}} \underline{\mathbf{I}} \qquad \text{(s.c. lattice)} \tag{10.43}$$

In the general dynamical case, $\underline{\mathbf{C}}_{\mathrm{i}}$ has to be evaluated numerically. For more details the reader is referred to [34]. The imaginary part of the interaction dyadic can always be evaluated in closed analytical form. Detailed calculations show that [34]

$$\mathrm{Im}\left\{\underline{\mathbf{C}}_{\mathrm{i}}(\omega, \mathbf{k})\right\} = \frac{1}{6\pi} \left(\frac{\omega}{c}\right)^3 \underline{\mathbf{I}} \tag{10.44}$$

This property implies that if the particles are lossless, the dielectric function is real-valued. In fact, it is known that in order that the balance between the power radiated by the electric dipole and the power absorbed from the local field be zero, it is necessary that the electric polarizability verifies $\mathrm{Im}\left\{\underline{\boldsymbol{\alpha}}_{\mathrm{e}}^{-1}\right\} = \frac{1}{6\pi}\left(\frac{\omega}{c}\right)^3 \underline{\mathbf{I}}$ (it is assumed without loss of generality that $\underline{\boldsymbol{\alpha}}_{\mathrm{e}}$ has an inverse). This property is sometimes reffered to as the Sipe–Kranendonk condition [3]. Using this power balance consistency condition and Equation 10.44, it follows that in the lossless care the dielectric function may be rewritten as

$$\underline{\boldsymbol{\varepsilon}}(\omega, \mathbf{k}) = \underline{\mathbf{I}} + \frac{1}{V_{\mathrm{cell}}} \left(\mathrm{Re}\left\{\underline{\boldsymbol{\alpha}}_e^{-1} - \underline{\mathbf{C}}_{\mathrm{i}}(\omega, \mathbf{k})\right\}\right)^{-1} \tag{10.45}$$

Thus, the dielectric function is real-valued, consistently with what could be expected for a lossless medium with a center of inversion symmetry, and that supports electromagnetic modes that propagate coherently with no radiation loss. An alternative proof of these properties is presented in [24]. The application of the theory to a lattice of split-ring resonators is described in [25].

10.5 Numerical Calculation of the Dielectric Function of a Structured Material

Here, it is explained how the homogenization approach introduced in Section 10.3 can be numerically implemented to characterize arbitrary microstructured materials using computational methods. To this end, we will derive an equivalent regularized formulation of the homogenization problem that is suitable for the numerical implementation of the method using MoM.

10.5.1 Regularized Formulation

The direct homogenization approach described in Section 10.3.3 may not be adequate for the numerical extraction of the dielectric function. The problem is that when $(\omega, \mathbf{k})$ is associated with an electromagnetic mode of the periodic medium, in general, the source-driven problem (Equation 10.2) cannot be solved because the corresponding homogeneous system (with $\mathbf{J}_e = 0$) has a nontrivial solution. The physical reason for the lack of solution is that when the medium is excited with a source associated with the same $(\omega, \mathbf{k})$ as an eigenmode, the amplitude of the induced fields may grow without limit due to resonant effects. Thus, the direct approach of Section 10.3.3 cannot be applied to calculate the dielectric function when $(\omega, \mathbf{k})$ belongs to the band structure of the material. This is an undesired property because the effective parameters of a composite medium are intrinsically related to the electromagnetic modes.

Since $\underline{\varepsilon}(\omega, \mathbf{k})$ is, in principle, an analytic function of its arguments, this problem could be solved by calculating the dielectric function using a limit procedure. However, in general, the band structure of the composite material is not known a priori, and even if it were known the calculation of the dielectric function at points very close to the band diagram may be numerically unstable.

To circumvent this drawback, a regularized formulation of the homogenization problem is presented next. The basic idea is to tune the applied current $\mathbf{J}_e$ in such a way that the microscopic electric field has a given desired average value $\mathbf{E}_{av}$, preventing in this way the excitation of a resonance when $(\omega, \mathbf{k})$ is associated with an eigenmode. This is possible because the amplitude of $\mathbf{J}_e$ becomes interrelated with the induced microscopic currents in the periodic medium, in such a way that depolarization effects prevent the fields in the medium to grow without limit when a resonance is approached.

To put these ideas into a firm mathematical basis, we will first relate the amplitude of $\mathbf{J}_e$ with the macroscopic field $\mathbf{E}_{av}$. To this end, we use Equation 10.22 to find that the applied polarization vector may be written in terms of the macroscopic electric field and of the polarization vector as

$$\frac{\mathbf{P}_{e,av}}{\varepsilon_0} = \frac{c^2}{\omega^2}\frac{1}{V_{cell}}\underline{\mathbf{G}}^{-1}_{av}\cdot\mathbf{E}_{av} - \frac{\mathbf{P}_{g,av}}{\varepsilon_0} \tag{10.46}$$

where $\underline{\mathbf{G}}^{-1}_{av}$ is defined as in Equation 10.34. It is convenient to rewrite the above equation in terms of two auxiliary operators $\hat{\mathbf{P}}$ and $\hat{\mathbf{P}}_{av}$. The polarization operator, $\hat{\mathbf{P}}$, transforms the electric field into the corresponding (generalized) polarization vector, $\hat{\mathbf{P}} : \mathbf{E} \to \mathbf{P}_{g,av} = \hat{\mathbf{P}}(\mathbf{E})$, where

$$\frac{\hat{\mathbf{P}}(\mathbf{E})}{\varepsilon_0} = \frac{1}{V_{cell}}\left(\frac{c^2}{\omega^2}\int_{\partial D}\hat{\mathbf{v}}\times\left[\nabla\times\mathbf{E}\right]e^{+j\mathbf{k}\cdot\mathbf{r}}ds + \int_{\Omega-\partial D}(\varepsilon_r - 1)\,\mathbf{E}\,e^{+j\mathbf{k}\cdot\mathbf{r}}d^3\mathbf{r}\right) \tag{10.47}$$

In the above, $\left[\nabla\times\mathbf{E}\right] = \nabla\times\mathbf{E}^+ - \nabla\times\mathbf{E}^-$ stands for the discontinuity of the curl of $\mathbf{E}$ at the metallic surfaces, and $\nabla\times\mathbf{E}^+$ is evaluated at the outer side of ∂D (Figure 10.1). It can be easily verified that the above definition is consistent with Equation 10.21. The second operator, $\hat{\mathbf{P}}_{av}$, acts on constant vectors (not on vector fields), $\hat{\mathbf{P}}_{av} : \mathbf{E}_{av} \to \hat{\mathbf{P}}_{av}(\mathbf{E}_{av})$, and is given by

$$\frac{\hat{\mathbf{P}}_{\text{av}}(\mathbf{E}_{\text{av}})}{\varepsilon_0} = \frac{c^2}{\omega^2}\frac{1}{V_{\text{cell}}}\underline{\mathbf{G}}_{\text{av}}^{-1}\cdot\mathbf{E}_{\text{av}} \tag{10.48}$$

Equation 10.46 is thus equivalent to

$$\mathbf{P}_{\text{e,av}} = \hat{\mathbf{P}}_{\text{av}}(\mathbf{E}_{\text{av}}) - \hat{\mathbf{P}}(\mathbf{E}) \tag{10.49}$$

Using the definition of $\mathbf{P}_{\text{e,av}}$ and Equation 10.23, it is found that applied density of current is such that

$$\mathbf{J}_{\text{e}} = j\omega\left(\hat{\mathbf{P}}_{\text{av}}(\mathbf{E}_{\text{av}}) - \hat{\mathbf{P}}(\mathbf{E})\right)e^{-j\mathbf{k}\cdot\mathbf{r}} \tag{10.50}$$

In particular, this formula shows that the applied current density can be regarded as a function of the induced macroscopic field $\mathbf{E}_{\text{av}}$. Thus, to impose the desired macroscopic field $\mathbf{E}_{\text{av}}$, we can excite the material with an applied current of the form given in Equation 10.50. Notice that in such a case $\mathbf{J}_{\text{e}}$ is also a function of the unknown microscopic field $\mathbf{E}$. Such a feedback mechanism prevents a resonance from being excited when $(\omega, \mathbf{k})$ is associated with an electromagnetic mode.

To clarify the discussion, we substitute Equation 10.50 into Maxwell's equations (Equation 10.2) to obtain

$$\begin{aligned}\nabla\times\mathbf{E} &= -j\omega\mathbf{B}\\ \nabla\times\frac{\mathbf{B}}{\mu_0} &= j\omega\left(\hat{\mathbf{P}}_{\text{av}}(\mathbf{E}_{\text{av}}) - \hat{\mathbf{P}}(\mathbf{E})\right)e^{-j\mathbf{k}\cdot\mathbf{r}} + \varepsilon_0\varepsilon_{\text{r}}j\omega\,\mathbf{E}\end{aligned} \tag{10.51}$$

The above system is, by definition, the regularized formulation of the homogenization problem. Even though it is closely related with the original set of equations (Equation 10.2), there are some important differences. First of all, unlike the direct approach (Equation 10.2), Equation 10.51 is an integral–differential system, i.e., both differential operators $(\nabla\times)$ and integral operators $(\hat{\mathbf{P}}(.))$ act on the electromagnetic fields. Note that $\hat{\mathbf{P}}(.)$ yields the generalized polarization of the unknown field $\mathbf{E}$, which involves the integration of the electric field over the unit cell.

A fundamental difference between the direct and regularized formulations is that while in the direct approach the source of fields is $\mathbf{J}_{\text{e}}$, in regularized formulation the source of fields is (from a mathematical point of view) the constant vector $\mathbf{E}_{\text{av}}$. Thus, the solutions of the homogeneous problem $(\mathbf{J}_{\text{e}} = 0)$ associated with the direct problem (Equation 10.2) are different from the solutions of the homogeneous system $(\mathbf{E}_{\text{av}} = 0)$ associated with the regularized system (Equation 10.51), i.e., the two systems have different null spaces. In particular, the electromagnetic modes of the periodic medium are, in general, associated with a nontrivial $\mathbf{E}_{\text{av}}$ and so, do not belong to the null space of the regularized problem. Thus, the regularized formulation can be used to compute the effective parameters of the composite medium even if $(\omega, \mathbf{k})$ is associated with an electromagnetic mode. In fact, when $(\omega, \mathbf{k})$ is associated with a modal solution, we have, $\hat{\mathbf{P}}_{\text{av}}(\mathbf{E}_{\text{av}}) = \hat{\mathbf{P}}(\mathbf{E})$, and thus, the amplitude of the imposed current in Equation 10.51 vanishes, avoiding the excitation of the resonance. However, since $\mathbf{E}_{\text{av}}$ is different from zero, Equation 10.51 still represents a well-formulated source-driven problem.

It is stressed that the effective parameters retrieved by solving the direct problem (Equation 10.2) are exactly the same as those obtained by solving Equation 10.51. The only difference between the two formulations is that the regularized formulation can be applied even when $(\omega, \mathbf{k})$ is associated with an electromagnetic mode. The price that we have to pay for this property is the increased complexity of integral–differential system (Equation 10.51) as compared to the simpler differential system (Equation 10.2). However, as described in Section 10.5.2, the regularized problem can be solved very efficiently using integral equation methods.

10.5.2 Integral Equation Solution

It can be verified that for given $(\mathbf{E}_{\text{av}}, \omega, \mathbf{k})$ the solution of the regularized homogenization problem (Equation 10.51) has the integral representation [30]:

$$\mathbf{E}(\mathbf{r}) = \mathbf{E}_{\text{av}} e^{-j\mathbf{k}\cdot\mathbf{r}} + \int_{\partial D} \underline{\mathbf{G}}_{p0}(\mathbf{r}|\mathbf{r}') \cdot (\hat{\mathbf{v}}' \times [\nabla' \times \mathbf{E}])\, \mathrm{d}s'$$
$$+ \int_{\Omega - \partial D} \underline{\mathbf{G}}_{p0}(\mathbf{r}|\mathbf{r}') \cdot \left(\frac{\omega}{c}\right)^2 (\varepsilon_r(\mathbf{r}') - 1)\, \mathbf{E}(\mathbf{r}')\, \mathrm{d}^3\mathbf{r}' \tag{10.52}$$

where $\underline{\mathbf{G}}_{p0}$ is the Green function dyadic defined by

$$\underline{\mathbf{G}}_{p0} = \left(\underline{\mathbf{I}} + \frac{c^2}{\omega^2}\nabla\nabla\right) \Phi_{p0}$$
$$\Phi_{p0}(\mathbf{r}|\mathbf{r}') = \Phi_p(\mathbf{r}|\mathbf{r}') - \frac{1}{V_{\text{cell}}} \frac{e^{-j\mathbf{k}\cdot(\mathbf{r}-\mathbf{r}')}}{k^2 - \omega^2/c^2} \tag{10.53}$$

and $\mathbf{\Phi}_p$ is the lattice Green function that verifies Equation 10.31. The integral representation (Equation 10.52) establishes that the microscopic field **E** can be written in terms of the induced microscopic currents and of the macroscopic electric field.

This is an important result and can be used to reduce the homogenization problem to a standard integral equation with unknowns given by the microscopic currents, $\mathbf{J}_{\text{d}} = \varepsilon_0(\varepsilon_{\text{r}} - 1)\, j\omega\mathbf{E}$, at the dielectric inclusions, $\mathbf{J}_{\text{c}} = \hat{\mathbf{v}} \times [\mathbf{B}]/\mu_0$, at the PEC surfaces. To illustrate this fact, it is considered next that the periodic medium is purely dielectric. In that case, the unknown of the integral equation may be taken equal to the vector field, $\mathbf{f} = (\varepsilon_{\text{r}} - 1)\mathbf{E}$. Notice that the vector density **f** vanishes in the host medium and is proportional to the microscopic current $\mathbf{J}_{\text{d}}$. The integral equation is obtained by imposing that Equation 10.52 is verified at the dielectric inclusions:

$$\frac{\mathbf{f}(\mathbf{r})}{\varepsilon_{\text{r}}(\mathbf{r}) - 1} = \mathbf{E}_{\text{av}} e^{-j\mathbf{k}\cdot\mathbf{r}} + \left(\frac{\omega}{c}\right)^2 \int_{\Omega} \underline{\mathbf{G}}_{p0}(\mathbf{r}|\mathbf{r}') \cdot \mathbf{f}(\mathbf{r}')\, \mathrm{d}^3\mathbf{r}' \tag{10.54}$$

The above identity is valid in the dielectric support of the inclusions, $\{\mathbf{r} : \varepsilon_{\text{r}}(\mathbf{r}) - 1 \neq 0\}$. For a given $\mathbf{E}_{\text{av}}$, this integral equation can be discretized and numerically solved with respect to **f** using standard techniques. In what follows, we briefly review the solution of the problem using MoM [37].

To apply the MoM, **f** is expanded in terms of expansion functions $\mathbf{w}_1, \mathbf{w}_2, \ldots, \mathbf{w}_n, \ldots$:

$$\mathbf{f} = \sum_n c_n \mathbf{w}_n \tag{10.55}$$

The set of expansion functions is assumed complete in $\{\mathbf{r} : \varepsilon_{\text{r}}(\mathbf{r}) - 1 \neq 0\}$. From the definition it is obvious that **f** is a Floquet field, i.e., $\mathbf{f}\exp(j\mathbf{k}\cdot\mathbf{r})$ is periodic. Thus, in general, the expansion functions must have the same property and, therefore, must depend explicitly on **k**, i.e., $\mathbf{w}_n = \mathbf{w}_{n,\mathbf{k}}(\mathbf{r})$. The dependence on **k** can be suppressed only if the inclusions are nonconnected [30].

For a given $\mathbf{E}_{\text{av}}$, the unknown coefficients, c_n, can be obtained by substituting the expansion Equation 10.55 into the integral equation (Equation 10.54), and by testing the resulting identity with appropriate test functions. Once **f** has been determined, we can compute the generalized polarization vector using Equation 10.20, and the dielectric function using Equation 10.19. The details can be read in [30]. It is found that the dielectric function can be written as

$$\frac{\underline{\boldsymbol{\varepsilon}}}{\varepsilon_0}(\omega, \mathbf{k}) = \underline{\mathbf{I}} + \frac{1}{V_{\text{cell}}} \sum_{m,n} \chi^{m,n} \left(\int_{\Omega} \mathbf{w}_{m,\mathbf{k}}(\mathbf{r})\, e^{+j\mathbf{k}\cdot\mathbf{r}} \mathrm{d}^3\mathbf{r}\right) \otimes \left(\int_{\Omega} \mathbf{w}_{n,-\mathbf{k}}(\mathbf{r})\, e^{-j\mathbf{k}\cdot\mathbf{r}} \mathrm{d}^3\mathbf{r}\right) \tag{10.56}$$

where

⊗ denotes the tensor product of two vectors

$\chi^{m,n}$ is an element of the infinite matrix $[\chi^{m,n}]$, whose inverse $[\chi_{m,n}]$ has a generic element given by

$$\chi_{m,n} = \int_{\Omega} \frac{1}{\varepsilon_r(\mathbf{r}) - 1} \mathbf{w}_{m,-\mathbf{k}}(\mathbf{r}) \cdot \mathbf{w}_{n,\mathbf{k}}(\mathbf{r})\, d^3\mathbf{r} - \left(\frac{\omega}{c}\right)^2 \int_{\Omega}\int_{\Omega} \mathbf{w}_{m,-\mathbf{k}}(\mathbf{r}) \cdot \underline{\mathbf{G}}_{p0}(\mathbf{r}|\mathbf{r}') \cdot \mathbf{w}_{n,\mathbf{k}}(\mathbf{r}')\, d^3\mathbf{r}\, d^3\mathbf{r}' \tag{10.57}$$

Since the expansion functions must vanish outside the dielectric inclusions, the integration domain in the above integrals may be replaced by $\{\mathbf{r} \in \Omega : \varepsilon_r(\mathbf{r}) - 1 \neq 0\}$. The above formulas are valid for dielectric crystals with no PEC surfaces.

Equation 10.56 establishes that the dielectric function of the periodic material can be written exclusively in terms of the expansion functions, $\mathbf{w}_{n,\mathbf{k}}$, and of the Green dyadic, $\underline{\mathbf{G}}_{p0}$. This formula is extremely useful for the numerical evaluation of the effective parameters of composite materials, and its application is illustrated in the following sections.

In case the material contains only PEC surfaces and $\varepsilon_r - 1 = 0$ in the unit cell, the unknown of the integral equation is taken equal to the vector tangential density, $\mathbf{f} = \frac{c^2}{\omega^2}\hat{\mathbf{v}}' \times [\nabla' \times \mathbf{E}]$, defined over the metallic surface ∂D. The vector field $\mathbf{f}$ is proportional to the density of current $\mathbf{J}_c$. As in the dielectric case, the unknown is expanded in terms of the complete set of vectors $\mathbf{w}_1$, $\mathbf{w}_2$, ..., except that now the expansion functions form a complete set of tangential vector fields over the metallic surface. A detailed analysis [30] shows that the dielectric function of such a material is given by

$$\frac{\underline{\boldsymbol{\varepsilon}}}{\varepsilon_0}(\omega, \mathbf{k}) = \underline{\mathbf{I}} + \frac{1}{V_{\text{cell}}} \sum_{m,n} \chi^{m,n} \left(\int_{\partial D} \mathbf{w}_{m,\mathbf{k}}(\mathbf{r})\, e^{+j\mathbf{k}\cdot\mathbf{r}} ds\right) \otimes \left(\int_{\partial D} \mathbf{w}_{n,-\mathbf{k}}(\mathbf{r})\, e^{-j\mathbf{k}\cdot\mathbf{r}} ds\right) \tag{10.58}$$

$$\chi_{m,n} = \int_{\partial D}\int_{\partial D} \left(\nabla_s \cdot \mathbf{w}_{m,-\mathbf{k}}(\mathbf{r})\, \nabla'_s \cdot \mathbf{w}_{n,\mathbf{k}}(\mathbf{r}') - \frac{\omega^2}{c^2} \mathbf{w}_{m,-\mathbf{k}}(\mathbf{r}) \cdot \mathbf{w}_{n,\mathbf{k}}(\mathbf{r}')\right) \Phi_{p0}(\mathbf{r}|\mathbf{r}')\, ds\, ds' \tag{10.59}$$

where

$\nabla_s \cdot$ represents the surface divergence of a tangential vector field

the matrix $[\chi^{m,n}]$ is the inverse of $[\chi_{m,n}]$

10.5.3 Application to Wire Media

To illustrate the versatility and usefulness of the formalism derived in Section 10.5.2, here we characterize the dielectric function of a square array of metallic rods (wire medium). Such a material is characterized by strong spatial dispersion, even in the long wavelength limit [20]. To give an intuitive physical picture of this phenomenon and understand its origin, consider an arbitrary metallic wire in an electromagnetic crystal. Since the wire is a good conductor, the current that flows along the wire at a given point, depends not only on the microscopic electric field in the immediate vicinity of the considered point, but also on the distribution of the electric field in the neighborhood of the whole wire axis. In fact, since the electric current along the wire must be continuous, it is clear that a localized fluctuation of the electric field may be propagated to a considerable distance from the perturbation point by current carriers. Hence, the radius of action of the microscopic electric field on the current along the wire may be much larger than the lattice constant, which defines the characteristic dimension of the wire medium, and possibly comparable or larger than the wavelength of

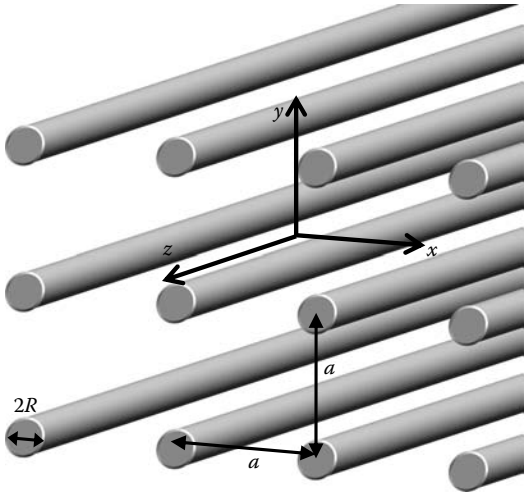

FIGURE 10.2 The wire medium is formed by a square array of infinitely long metallic rods oriented along the z-direction. (Reprinted from Silveirinha, M.G., Belov, P.A., and Simovski, C.R., *Phys. Rev. B*, 75, 035108, 2007. With permission.)

radiation. This phenomenon is, in many ways, analogous to a slow diffusion effect, because the velocity of the current carriers is much slower than the velocity of photons. Since the polarization vector **P** is proportional to the current along the wire, it follows that this long range slow diffusion effect is the origin of the nonlocal properties of the wire medium.

In order to characterize the spatial dispersion effects in wire media, we consider the geometry of Figure 10.2. The lattice constant is a and the radius of the rods is R. We suppose that $R/a \ll 1$ so that the thin-wire approximation can be used. Within such approximation, it is legitimate to assume that the surface current is uniform in the cross section of the wires and flows exclusively along the axes of the rods. Thus, since the structure is uniform along the z-direction, it follows that one single expansion function is sufficient to describe the behavior of the induced surface current density, $\mathbf{J}_c$, for an excitation with Floquet spatial variation, as in Equation 10.23. The expansion function may be taken equal to

$$\mathbf{w}_{1,\mathbf{k}}(\mathbf{r}) = \frac{e^{-j\mathbf{k}\cdot\mathbf{r}}}{2\pi R}\hat{\mathbf{u}}_z \tag{10.60}$$

Using this expression in Equation 10.58, it is found that the dielectric function of the wire medium is given by

$$\frac{\underline{\boldsymbol{\varepsilon}}}{\varepsilon_0}(\omega,\mathbf{k}) = \underline{\mathbf{I}} + \frac{1}{V_{\text{cell}}}\frac{a^2}{\chi_{11}(\omega,\mathbf{k})}\hat{\mathbf{u}}_z\hat{\mathbf{u}}_z \tag{10.61}$$

where χ_{11} is calculated using Equation 10.59, and is given by

$$\chi_{11}(\omega,\mathbf{k}) = \left(k_z^2 - \frac{\omega^2}{c^2}\right)\frac{1}{(2\pi R)^2}\int_{\partial D}\int_{\partial D}\Phi_{p0}(\mathbf{r}|\,\mathbf{r}';\omega,\mathbf{k})\,e^{j\mathbf{k}\cdot(\mathbf{r}-\mathbf{r}')}\mathrm{d}s\mathrm{d}s' \tag{10.62}$$

and $\partial D = \left\{(x,y,z) : x^2 + y^2 = R^2, -a/2 < z < a/2\right\}$ represents the surface of the metallic wire in the unit cell. Substituting the above expression into Equation 10.61, the dielectric function can be rewritten as

$$\frac{\underline{\boldsymbol{\varepsilon}}}{\varepsilon_0}(\omega,\mathbf{k}) = \underline{\mathbf{I}} - \frac{\beta_p^2}{\omega^2/c^2 - k_z^2}\hat{\mathbf{u}}_z\hat{\mathbf{u}}_z \tag{10.63}$$

where the plasma wave number β_p is such that

$$\frac{1}{\beta_p^2} = \frac{a}{(2\pi R)^2} \int_{\partial D} \int_{\partial D} \Phi_{p0}(\mathbf{r}|\mathbf{r}'; \omega, \mathbf{k})\, e^{j\mathbf{k}\cdot(\mathbf{r}-\mathbf{r}')} ds ds' \tag{10.64}$$

As it is manifest from the above expression, in general, the plasma wave number depends on both ω and **k**, or more specifically, it depends on ω, k_x, and k_y (but not on k_z). However, in the long wavelength limit, it is an excellent approximation to assume that $\beta_p \approx \beta_p\big|_{\substack{\omega=0 \\ k_x=k_y=0}}$, which may be explicitly evaluated in terms of Bessel functions as in formula (B5) of [23]. Such a formula is equivalent to the result reported in [20]:

$$(\beta_p a)^2 = \frac{2\pi}{\ln\left(\frac{a}{2\pi R}\right) + 0.5275} \tag{10.65}$$

Equations 10.63 and 10.65 determine the dielectric function of the wire medium in the long wavelength limit. For more details about the electrodynamics of wire media and the effect of strong spatial dispersion the reader is referred to [20].

The previous analysis shows that the theory described in Section 10.5.2 can be used to obtain in a very straightforward manner the homogenization model originally derived in [20] using a less direct approach. This demonstrates that the formalism of Section 10.5.2 can be applied not only to calculate the dielectric function using numerical methods, but also to derive approximate analytical models. Such a potential is further demonstrated in [38], where the dielectric function of a square array of helical wires is calculated using similar analytical methods.

10.6 Extraction of the Local Parameters from the Nonlocal Dielectric Function

Even though the formalism described in Section 10.3 deals with the characterization of spatially dispersive materials, it is possible to extract the local effective parameters associated with the model (Equation 10.6) (if meaningful) from the nonlocal dielectric function. Such ideas are developed in this section.

10.6.1 Relation between the Local and Nonlocal Effective Parameters

In most of the works on metamaterials, the composite structures are characterized using an effective permittivity and an effective permeability. It is, thus, relevant to study the relation between the nonlocal dielectric function and the local parameters. To derive such a relation, we remember that the generalized polarization vector $\mathbf{P}_g$ can be expanded as in Equation 10.8. Calculating the spatial Fourier transform of that formula and using the nonlocal constitutive relations (Equation 10.11), it is found that

$$\tilde{\mathbf{P}}_g = (\underline{\boldsymbol{\varepsilon}}(\omega, \mathbf{k}) - \varepsilon_0 \underline{\mathbf{I}}) \cdot \langle \tilde{\mathbf{E}} \rangle = \tilde{\mathbf{P}} - \frac{\mathbf{k}}{\omega} \times \tilde{\mathbf{M}} + \cdots \tag{10.66}$$

where the symbol "~" represents the Fourier transformation. The terms omitted on the right-hand side of the second identity are related to the quadrupole moment and other higher-order multipoles, and thus, are in general negligible. In a local material the polarization and magnetization vectors, **P** and **M**, can be easily related to the local effective parameters and macroscopic fields using Equations 10.5 and 10.6:

$$\mathbf{P} = \varepsilon_0 \left(\underline{\varepsilon}_r - \underline{\mathbf{I}}\right) \cdot \langle \mathbf{E} \rangle + \frac{1}{\mu_0 c}\, \underline{\boldsymbol{\xi}} \cdot \underline{\boldsymbol{\mu}}_r^{-1} \cdot \left(\langle \mathbf{B} \rangle - \frac{1}{c} \underline{\boldsymbol{\zeta}} \cdot \langle \mathbf{E} \rangle \right)$$

$$\mathbf{M} = \frac{1}{\mu_0 c}\, \underline{\boldsymbol{\mu}}_r^{-1} \cdot \underline{\boldsymbol{\zeta}} \cdot \langle \mathbf{E} \rangle + \frac{1}{\mu_0} \left(\underline{\mathbf{I}} - \underline{\boldsymbol{\mu}}_r^{-1} \right) \cdot \langle \mathbf{B} \rangle \tag{10.67}$$

Calculating the Fourier transform of the above expressions, using the relation $\langle \tilde{\mathbf{B}} \rangle = \frac{\mathbf{k}}{\omega} \times \langle \tilde{\mathbf{E}} \rangle$, substituting the resulting formulas into Equation 10.66, and noting that the obtained equation must hold for arbitrary $\langle \tilde{\mathbf{E}} \rangle$, it is found that

$$\frac{\underline{\boldsymbol{\varepsilon}}}{\varepsilon_0}(\omega, \mathbf{k}) = \left(\underline{\varepsilon}_r - \underline{\boldsymbol{\xi}} \cdot \underline{\boldsymbol{\mu}}_r^{-1} \cdot \underline{\boldsymbol{\zeta}}\right) + \left(\underline{\boldsymbol{\xi}} \cdot \underline{\boldsymbol{\mu}}_r^{-1} \times \frac{c\mathbf{k}}{\omega} - \frac{c\mathbf{k}}{\omega} \times \underline{\boldsymbol{\mu}}_r^{-1} \cdot \underline{\boldsymbol{\zeta}}\right) + \frac{c\mathbf{k}}{\omega} \times \left(\underline{\boldsymbol{\mu}}_r^{-1} - \underline{\mathbf{I}}\right) \times \frac{c\mathbf{k}}{\omega} \tag{10.68}$$

This expression gives the desired relation between the nonlocal dielectric function and the local effective parameters. Thus, a local material can be characterized using the nonlocal constitutive relations (Equation 10.11) as well as using the local constitutive relations (Equation 10.6) being the corresponding effective parameters linked as in Equation 10.68. For local materials, the two phenomenological models are perfectly equivalent: they predict exactly the same dispersion characteristic, $\omega = \omega(\mathbf{k})$, for plane wave modes, and the same macroscopic fields, $\mathbf{E}_{av}$ and $\mathbf{B}_{av}$. In particular, it is clear that the dielectric function, $\underline{\varepsilon}(\omega, \mathbf{k})$, of a local material is necessarily a quadratic function of the wave vector $\mathbf{k}$. This suggests that the local parameters are related to the first- and second-order derivatives of $\underline{\varepsilon}(\omega, \mathbf{k})$ with respect to $\mathbf{k}$. This topic is further developed in Sections 10.6.2 and 10.6.3.

The importance of the local effective parameters can be appreciated only in problems that involve interfaces between different materials. Only the local effective parameters can be used to solve boundary value problems using the classical boundary conditions (continuity of the tangential components of the macroscopic electric and magnetic fields) at an interface [39]. The reason is clear: while the local model (Equation 10.6) is valid in the spatial domain, the nonlocal model (Equation 10.11) is valid only in the Fourier domain, i.e., for unbounded homogeneous materials. The solution of boundary value problems involving spatially dispersive materials is difficult and involves the use of completely different concepts and methods [4,39]. We return to this topic in Section 10.7.

10.6.2 Spatial Dispersion Effects of First and Second Order

Equation 10.68 implies that in a local material the dyadics $\underline{\boldsymbol{\xi}}$ and $\underline{\boldsymbol{\zeta}}$ that characterize bianisotropic effects can be calculated from the first-order derivatives of the dielectric function, $\underline{\varepsilon}(\omega, \mathbf{k})$, with respect to $\mathbf{k}$, and that the magnetic permeability is completely determined by the second-order derivatives of the dielectric function. These properties suggest that it may be possible to extract the local effective parameters of a generic composite material by expanding the dielectric function in a Taylor series [31]:

$$\underline{\boldsymbol{\varepsilon}}(\omega, \mathbf{k}) \approx \underline{\boldsymbol{\varepsilon}}(\omega, \mathbf{0}) + \sum_n \frac{\partial \underline{\boldsymbol{\varepsilon}}}{\partial k_n}(\omega, \mathbf{0}) k_n + \frac{1}{2} \sum_{n,m} \frac{\partial^2 \underline{\boldsymbol{\varepsilon}}}{\partial k_n \partial k_m}(\omega, \mathbf{0}) k_n k_m \tag{10.69}$$

This expansion is meaningful only in the case of weak spatial dispersion. Otherwise, the Taylor expansion is not accurate and local parameters cannot be defined. In the above, the indices of summation are such that $m, n = x, y, z$.

Comparing Equations 10.68 and 10.69, it is evident that the local parameters must verify

$$\underline{\varepsilon}_r - \underline{\boldsymbol{\xi}} \cdot \underline{\boldsymbol{\mu}}_r^{-1} \cdot \underline{\boldsymbol{\zeta}} = \frac{\underline{\boldsymbol{\varepsilon}}}{\varepsilon_0}(\omega, \mathbf{0}) \tag{10.70}$$

On the other hand, from the symmetry property, $\underline{\varepsilon}(\omega, \mathbf{k}) = \underline{\varepsilon}^{t}(\omega, -\mathbf{k})$, enunciated in Section 10.3.5, it is clear that the first-order derivatives, $\frac{\partial \underline{\varepsilon}}{\partial k_n}(\omega, \mathbf{0})$, are antisymmetric dyadics, whereas the second-order derivatives, $\frac{\partial^2 \underline{\varepsilon}}{\partial k_n \partial k_m}(\omega, \mathbf{0})$, are symmetric dyadics. This implies that the first-order derivatives can be completely specified by 9 independent parameters, whereas the second-order derivatives can be completely specified by 36 independent parameters.

The dyadics $\underline{\boldsymbol{\xi}}$ and $\underline{\boldsymbol{\zeta}}$ are chosen so that they satisfy the symmetry relation [33]*

$$\underline{\boldsymbol{\xi}} = -\underline{\boldsymbol{\zeta}}^{t} \tag{10.71}$$

Imposing that the second terms on the right-hand side of Equations 10.68 and 10.69 are coincident, it may be proven that $\underline{\boldsymbol{\zeta}}$ must be such that

$$\underline{\boldsymbol{\zeta}} = \underline{\boldsymbol{\mu}}_{r} \cdot \frac{\omega}{c} \sum_{n} \left(j\mathbf{q}_n \hat{\mathbf{u}}_n - \frac{1}{2} j\mathbf{q}_n \cdot \hat{\mathbf{u}}_n \underline{\mathbf{I}} \right)$$

$$j\mathbf{q}_n = \frac{1}{2} \sum_{m} \frac{1}{\varepsilon_0} \hat{\mathbf{u}}_m \cdot \frac{\partial \underline{\boldsymbol{\varepsilon}}}{\partial k_n}(\omega, \mathbf{0}) \times \hat{\mathbf{u}}_m \tag{10.72}$$

where $\hat{\mathbf{u}}_n$ is a generic unit vector directed along a coordinate axis. Thus, once the magnetic permeability $\underline{\boldsymbol{\mu}}_{r}$ is determined, the remaining local parameters can be easily obtained using Equations 10.70 through 10.72.

To calculate $\underline{\boldsymbol{\mu}}_{r}$, it is necessary to impose that the third terms on the right-hand side of Equations 10.68 and 10.69 are equal for arbitrary $\mathbf{k}$. However, it is simple to verify that, in general, there is no solution for $\underline{\boldsymbol{\mu}}_{r}$ that ensures such a condition. This is a consequence of the second-order derivatives of the dielectric function being characterized by 36 independent parameters. From a physical point of view, it is possible to understand this limitation by noting that spatial dispersion of the second order (third term in the right-hand side of Equation 10.69) emerges not only due to the eddy currents associated with magnetic dipole moments, but also due to the quadrupole moment density [31]. We remind that in Equation 10.68 the effects of the quadrupole density were neglected. Despite the described difficulties, in some circumstances it may be possible to use symmetry arguments to directly extract $\underline{\boldsymbol{\mu}}_{r}$ from the second-order derivatives of the dielectric function. This is illustrated in the next section.

To illustrate the application of the described theory and the calculation of the dyadics $\underline{\boldsymbol{\xi}}$ and $\underline{\boldsymbol{\zeta}}$ in a material with strong magnetoelectric coupling, we consider next a medium formed by an array of infinitely long metallic helices [38] oriented along the z-direction, as illustrated in Figure 10.3. We restrict our attention to the case of propagation in the *xoy*-plane. Only in such conditions the effects of spatial dispersion can be considered weak, and local parameters can be defined. In reference [38], the local parameters were extracted directly from the nonlocal dielectric function using ideas analogous to those developed here. It was verified that to a good approximation, the local parameters are such that $\underline{\boldsymbol{\varepsilon}}_{r} = \varepsilon_t(\hat{\mathbf{u}}_x\hat{\mathbf{u}}_x + \hat{\mathbf{u}}_y\hat{\mathbf{u}}_y) + \varepsilon_{zz}\hat{\mathbf{u}}_z\hat{\mathbf{u}}_z$, $\underline{\boldsymbol{\zeta}} = \zeta_{zz}\hat{\mathbf{u}}_z\hat{\mathbf{u}}_z = -\underline{\boldsymbol{\xi}}^{t}$, and $\underline{\boldsymbol{\mu}}_{r} = \hat{\mathbf{u}}_x\hat{\mathbf{u}}_x + \hat{\mathbf{u}}_y\hat{\mathbf{u}}_y + \mu_{zz}\hat{\mathbf{u}}_z\hat{\mathbf{u}}_z$. In Figure 10.4 the extracted effective parameters are plotted as a function frequency for a material with radius of the helices $R = 0.4a$, radius of the wires $r_w = 0.01a$, and helix pitch $a_z = 0.5a$. It is seen that the effective permeability is less than one, and is approximately independent of frequency. Likewise, the transverse effective permittivity (not shown in the figure) is $\varepsilon_t \approx 1.77$, and is also nearly independent of frequency. On the other hand, since the helical wires are assumed infinitely long, the effective permittivity along z exhibits a plasmonic behavior being negative below a certain plasma frequency.

*This is possible because the first-order derivatives of the dielectric function can be characterized using only nine independent parameters.

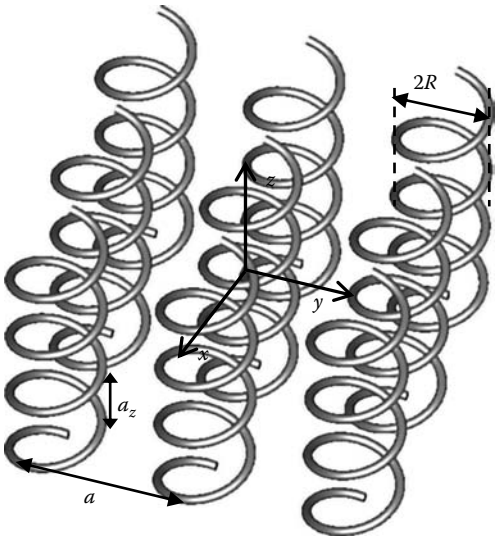

FIGURE 10.3 Geometry of a periodic array of infinitely long PEC helices arranged in a square lattice. (Reprinted from Silveirinha, M.G., *IEEE Trans. Antennas Propagat.*, 56, 390, 2008. With permission.)

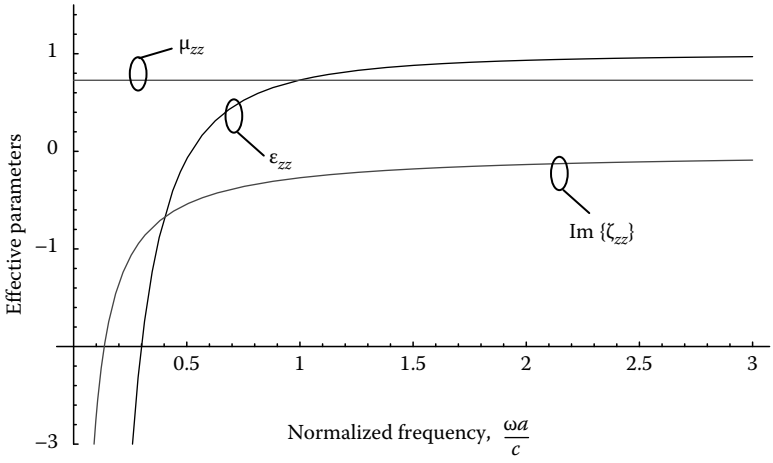

FIGURE 10.4 Effective parameters (xoy-plane propagation) for a material with $R = 0.4a$, $r_w = 0.01a$, and $a_z = 0.5a$. (Reprinted from Silveirinha, M.G., *IEEE Trans. Antennas Propagat.*, 56, 390, 2008. With permission.)

Interestingly, the chirality parameter Im $\{\zeta_{zz}\}$ has a resonant behavior near the static limit. This is a very unusual property, since in general the magnetoelectric coupling is negligible in the quasistatic limit. This property can be understood by noting that the length of the helical wires is infinite, and thus the chiral effects can be greatly enhanced at low frequencies. This anomalous phenomenon is also consistent with the analysis of [40] based on a local field approach. The strong magnetoelectric coupling characteristic of this microstructured material may be exploited to design a very efficient and thin polarization transformer; which converts a linearly polarized wave into a circularly polarized wave [38].

10.6.3 Characterization of Materials with Negative Parameters

In what follows, the formalism developed in the previous sections is applied to characterize the local parameters of complex structures formed by split-ring resonators and metallic wires. It is well known that such microstructured materials may have simultaneously negative permittivity and permeability in a certain frequency range [6].

As discussed in Section 10.6.2, the local parameters can be obtained by expanding the dielectric function $\underline{\varepsilon}(\boldsymbol{\omega}, \mathbf{k})$ in powers of the wave vector. In the examples considered here, the inclusions and the lattice have enough symmetries so that the effective medium is nongyrotropic, i.e., the first-order derivatives of $\underline{\varepsilon}(\omega, \mathbf{k})$ with respect to $\mathbf{k}$ vanish at the origin, or equivalently (see Equation 10.72), the magnetoelectric tensors $\underline{\boldsymbol{\xi}}$ and $\underline{\boldsymbol{\zeta}}$ are identically zero. This can be ensured by using a magnetic particle formed by two parallel rings with splits: the broadside coupled split-ring resonator (BC-SRR). As proven in [41], such a magnetic particle does not permit bianisotropic effects.

It is assumed here that the metallic wires are oriented along the y-direction, and that the BC-SRRs are parallel to the xoy plane (see the inset of Figure 10.6). Due to symmetry, this implies that the magnetic permeability of the artificial medium is of the form $\underline{\boldsymbol{\mu}_\mathbf{r}}(\omega) = \hat{\mathbf{u}}_x\hat{\mathbf{u}}_x + \hat{\mathbf{u}}_y\hat{\mathbf{u}}_y + \mu_{zz}\hat{\mathbf{u}}_z\hat{\mathbf{u}}_z$. Since the magnetoelectric tensors must vanish, Equation 10.70 demonstrates that the local permittivity is given by

$$\underline{\varepsilon_\mathrm{r}}(\omega) = \frac{\underline{\boldsymbol{\varepsilon}}}{\varepsilon_0}(\omega, \mathbf{0}) \tag{10.73}$$

On the other hand, substituting the formula for magnetic permeability into Equation 10.68, it is simple to verify that to obtain an identity it is necessary that

$$\mu_{zz}(\omega) = \frac{1}{1 - \left(\frac{\omega}{c}\right)^2 \frac{1}{2\varepsilon_0} \left.\frac{\partial^2 \varepsilon_{yy}}{\partial k_x^2}\right|_{\mathbf{k}=0}} \tag{10.74}$$

where $\varepsilon_{yy} = \hat{\mathbf{u}}_y \cdot \underline{\varepsilon} \cdot \hat{\mathbf{u}}_y$. Hence, provided the considered metamaterial can be characterized using a local homogenization model, its constitutive parameters are necessarily given by Equations 10.73 and 10.74. Consistently, with the discussion of Section 10.6.2, the magnetic permeability is a function of the second-order derivatives of the dielectric function with respect to the wave vector.

In the example considered here, it is assumed that the lattice spacings along the coordinate axes are $a_x = a_y \equiv a$, and $a_z = 0.5a$ (the lattice is tetragonal). The BC-SRRs have a mean radius, $R_\mathrm{med} = 0.4a$, and an angular split of 10°. To simplify the numerical implementation of the homogenization method, it was considered that the rings are formed by thin metallic wires with a circular cross section, and a radius, $0.01a$. The distance between the two rings (relative to the mid-plane of each ring) is $d = 0.125a$. The continuous metallic wires also have a radius, $0.01a$.

Using the Equations 10.58, 10.73, and 10.74, the local effective parameters $\underline{\boldsymbol{\varepsilon}_\mathbf{r}}(\boldsymbol{\omega})$ and $\mu_{zz}(\omega)$ were computed as a function of frequency. The numerical results were obtained using five expansion functions $\mathbf{w}_n = \mathbf{w}_{n,\mathbf{k}}(\mathbf{r})$ per wire/ring. The derivatives with respect to $\mathbf{k}$ in Equation 10.74 were evaluated using numerical methods. The extracted effective permittivity ε_{yy} and effective permeability μ_{zz} are depicted in Figure 10.5 for three configurations of the metamaterial. The permittivity along z, $\varepsilon_{zz} = 1$, is not shown in the figure. Consistently with the results of [6], the extracted parameters predict that there is a frequency window, $0.86 < \omega a/c < 1.04$, where the effective permittivity and permeability are simultaneously negative (curve (a)). If the continuous wires are removed and the metamaterial is formed by only BC-SRRs (curve (b)) the effective permeability is nearly unchanged, while the effective permittivity becomes positive in the indicated frequency range. If the BC-SRRs are removed the permeability becomes unity, while the effective permittivity remains negative, as shown in curve (c).

The extracted local parameters, ε_{yy} and μ_{zz}, were used to compute the dispersion characteristic $\omega = \omega(k_x)$ of the metamaterial for propagation along the x-direction. The corresponding band structure is depicted in Figure 10.6 (solid black lines). In order to confirm these results and check the

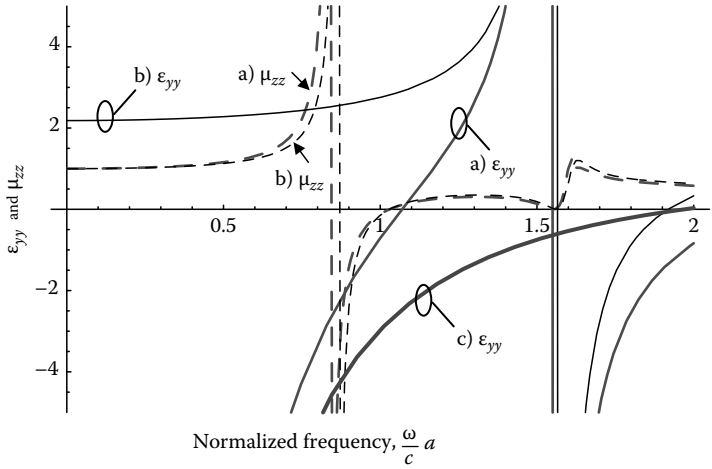

FIGURE 10.5 Extracted effective permittivity (solid lines) and effective permeability (dashed lines) for a metamaterial formed by (a) continuous wires + BC-SRRs (medium thick light gray lines), (b) only BC-SRRs (thin black lines), and (c) only continuous wires (thick dark gray line). (Reprinted from Silveirinha, M.G., *Phys. Rev. B*, 75, 115104, 2007. With permission.)

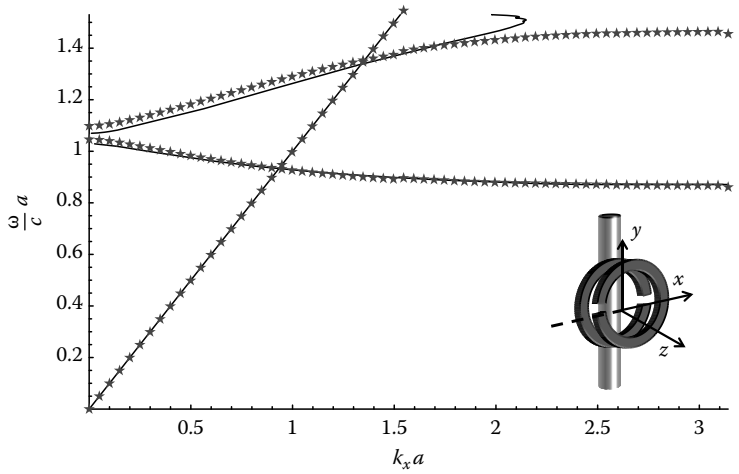

FIGURE 10.6 Band structure of a composite material formed by wires + BC-SRRs (geometry of the unit cell is shown in the inset). The solid black lines were calculated using the extracted ε_{yy} and μ_{zz}. The discrete "star" symbols were obtained using the full wave hybrid method introduced in [42]. (Reprinted from Silveirinha, M.G., *Phys. Rev. B*, 75, 115104, 2007. With permission.)

accuracy of the homogenization model, the full wave hybrid method introduced in [42] was used to compute the "exact" band structure of the composite material (star symbols in Figure 10.6). It is seen that the homogenization and full wave results compare very well, especially in the range $\omega a/c < 1.3$. In particular, the frequency band where the material has permittivity and permeability simultaneously negative is predicted with very good accuracy, even for values of k_x near the edge of the Brillouin zone. For frequencies above $\omega a/c = 1.4$, near the resonance of ε_{yy}, the agreement quickly deteriorates

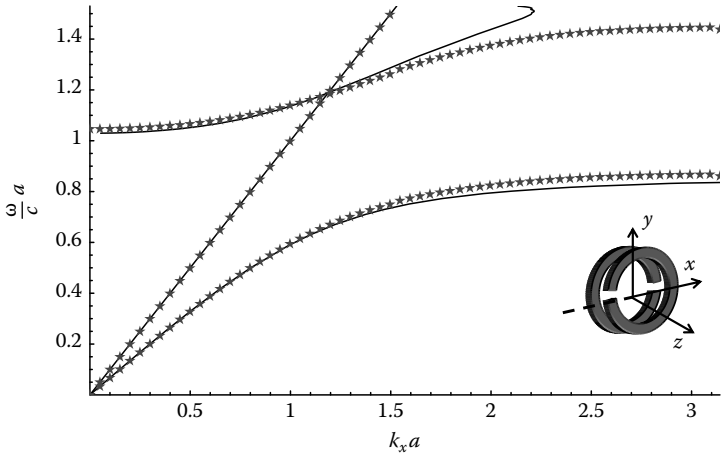

FIGURE 10.7 Band structure of a composite material formed by BC-SRRs (geometry of the unit cell is shown in the inset). The legend is as in Figure 10.6. (Reprinted from Silveirinha, M.G., *Phys. Rev. B*, 75, 115104, 2007. With permission.)

and the magnetic permeability ceases to have meaning. This can be explained by noting that ε_{yy} varies fast near the resonance, and thus, the Taylor series of the dielectric function with respect to **k** fails to describe accurately the dependence on the wave vector. Thus, spatial dispersion effects cannot be ignored near the resonance.

Similar band structure calculations were made for the case in which the continuous wires are removed, and the material is formed uniquely by BC-SRRs. These results are shown in Figure 10.7, further demonstrating the accuracy of the homogenization model. Consistently, with the results of [6], the frequency region where the composite material has simultaneously negative parameters becomes a frequency band gap when the metallic wires are removed.

10.7 The Problem of Additional Boundary Conditions

At a sharp boundary between two different materials the macroscopic fields are, in general, discontinuous due to the sudden change of the material parameters. The classical procedure to characterize the fields near the interface is to provide certain jump conditions to connect the fields on the two sides of the interface, and in this way obtain a unique solution defined in all space. For local materials, the jump conditions correspond to the continuity of the tangential components of the electric and magnetic fields. These boundary conditions are, in general, derived by considering a transition layer of infinitesimal thickness, and by using an integral formulation of Maxwell's equations [12]. Alternatively, for dielectric crystals, the classical boundary conditions can also be derived directly from the expansion of the microscopic fields into Floquet modes using the concept of transverse averaged fields [43]. The direct application of the classical boundary conditions to structured materials may not yield satisfactory results when the wavelength of the radiation is only moderately larger than the characteristic dimensions of the unit cell, say 10 times or less [44]. In these conditions, it may not be possible to regard the material as continuous, characterized by the bulk effective parameters, since its intrinsic granularity may not be neglected [43]. The discussion of strategies to overcome these difficulties is out of the scope of this chapter and can be read in [43,44].

In spatially dispersive materials the situation is even more problematic. Even the solution of a simple plane wave scattering problem may not be a trivial task when spatially dispersive materials are involved. The nonlocal character of the material response may cause the emergence of new waves, as

compared to the ordinary case in which only two plane waves can propagate along a fixed direction of space [4]. This implies that the classical boundary conditions are insufficient to relate the fields on the two sides of an interface between a spatially dispersive material and another material. In order that the problem has a unique solution it is necessary to specify also boundary conditions for the internal variables that describe the excitations responsible for the spatial dispersion effects [1]. Or in other words, to remove the extra degrees of freedom it is necessary to consider "additional boundary conditions" (ABCs) [4,5]. The ABC concept has been used in the electromagnetics of spatially dispersive media for many decades [45–48].

The simplest class of ABCs was proposed by Pekar [45], which imposes that either the polarization vector or its spatial derivatives vanish at the interface. Unfortunately, there is no general theory available to derive an ABC for a spatially dispersive material. This is a consequence of the ABCs being dependent on the internal variables of the material. The nature of the ABC depends on the specific microstructure of the material, and can be determined only on the basis of a microscopic model that describes the dynamics of these internal variables.

The objective of this section is to briefly review the theory of ABCs for wire media. This canonical problem is particularly interesting since it can be treated using analytical methods, and perfectly illustrates how ABCs can be derived and employed to characterize the refraction of waves by a spatially dispersive material. Our analysis is based on the theory derived in [43,49,50]. An alternative "ABC-free" motivated approach has been reported in [51].

10.7.1 Additional Boundary Conditions for Wire Media

In this section, the refraction and reflection of waves by a wire medium slab are investigated. The wire medium consists of an array of long metallic parallel wires arranged in a periodic lattice, as illustrated in Figure 10.8. The wires are oriented along the z direction and embedded in a host medium with permittivity ε_h. As discussed in Section 10.5.3, this material is strongly spatially dispersive, even in the long wavelength limit [20–22]. As a consequence, it supports three different families of electromagnetic modes in the long wavelength limit: transverse electric to z (TE^z) modes, transverse

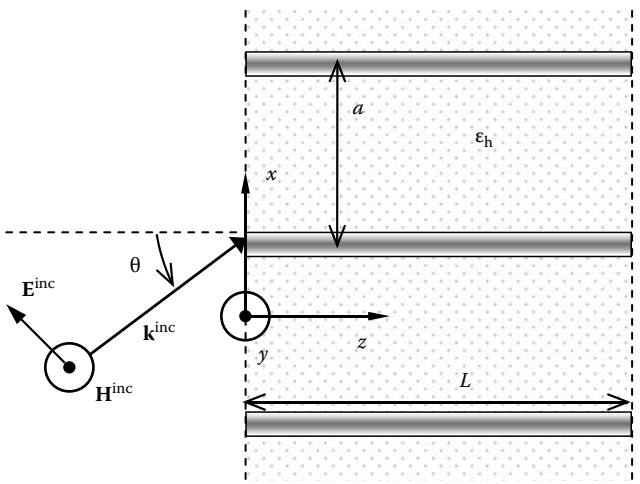

FIGURE 10.8 A wire medium slab with thickness L is illuminated by a TM^z polarized incoming plane wave. The metallic wires are arranged in a square lattice with lattice constant a, and embedded in a dielectric material with permittivity ε_h. (Reprinted from Silveirinha, M.G., Belov, P.A., and Simovski, C.R., *Phys. Rev. B*, 75, 035108, 2007. With permission.)

magnetic to z (TM^z) modes, and transverse electromagnetic (TEM) modes [20]. The existence of three different electromagnetic modes implies that the usual boundary conditions (continuity of the tangential component of the electric and magnetic fields) at an interface between the (homogenized) wire medium and another material are not sufficient to solve unambiguously a scattering problem. It can be easily verified that the associated linear system has one degree of freedom [49], and thus the need for an ABC is evident.

In order to derive the ABC, it is necessary to identify some property of the structure under study that can be used to obtain some nontrivial relation between the macroscopic/electromagnetic fields. In the case of the wire medium it is relatively simple to identify such a property. Supposing that the wire medium is adjacent to a nonconductive material (e.g., air) and that the metallic wires are thin, it is evident that the density of the electric surface current at the wires' surface must vanish at the interface:

$$\mathbf{J}_c = 0 \text{ (at the interface)} \tag{10.75}$$

It was proven in [49] that this property implies that the macroscopic electric field satisfies the following ABC at an interface with air*:

$$\varepsilon_h \, \mathbf{E} \cdot \hat{\mathbf{u}}_z \big|_{\text{wire medium side}} = \mathbf{E} \cdot \hat{\mathbf{u}}_z \big|_{\text{air side}} \tag{10.76}$$

It is important to note that the above condition is not equivalent to the continuity of the electric displacement vector, since the effective permittivity of the wire medium is not ε_h, but is instead given by Equation 10.63. The ABC is also valid in the case of wires with finite conductivity [11], and when the wires are tilted with respect to the interface with air [50].

The ABC (Equation 10.76) together with the classical boundary conditions can be used to characterize the reflection and refraction of waves by slabs of wire media. To illustrate this property and the accuracy of the described theory, in Figure 10.9 the amplitude of the reflection coefficient is plotted as a function of the normalized frequency for plane wave incidence along $\theta = 45°$. The solid lines correspond to full wave results obtained using the MoM, and the dashed lines represent the results obtained using the homogenization model and the ABC (Equation 10.76). The lattice constant is a, the radius of the wires is $r_w = 0.01a$, and the wires are embedded in air, $\varepsilon_h = 1$. It is seen that the agreement between the homogenization model and the full wave results is excellent, for both thin and thick wire medium slabs, and for normalized frequencies as large as $\omega a/c = 2.0$. It was proven in [11,52] that the proposed ABC may be used to characterize the imaging properties of wire media slabs upto infrared frequencies.

The ABC (Equation 10.76) is valid provided the material adjacent to the wire medium is nonconductive. However, in several configurations of interest the metallic wires are connected to a ground plane, as illustrated in Figure 10.10. For example, textured and corrugated surfaces have important applications in the design of high-impedance surfaces, impedance boundaries, and suppression of guided modes [29,53,54]. When the metallic wires are connected to a conductive material, it is not true that the density of current $\mathbf{J}_c$ vanishes at the interface, and thus the ABC (Equation 10.76) does not apply.

Even though Equation 10.75 does not hold at an interface of a wire medium connected to a PEC ground plane, it is relatively simple to obtain the boundary condition verified by the microscopic electric current in a such scenario. More specifically, it can be proven that the electric density of surface charge, σ_c, on the surface of a generic wire satisfies [50]

$$\sigma_c = 0 \text{ (at the interface)} \tag{10.77}$$

*In this section, the macroscopic fields, $\langle \mathbf{E} \rangle$ and $\langle \mathbf{B} \rangle / \mu_0$, are simply denoted by $\mathbf{E}$ and $\mathbf{H}$, respectively, to avoid complicating the notations unnecessarily.

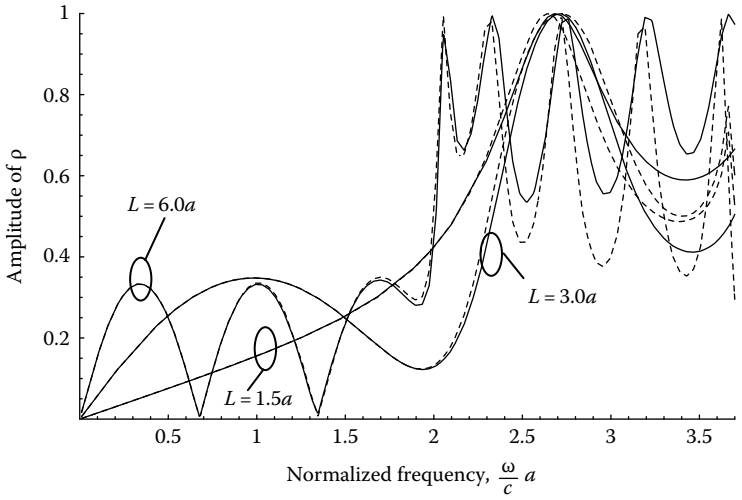

FIGURE 10.9 Amplitude of the reflection coefficient as a function of the normalized frequency for incidence along θ = 45° and different values of the slab thickness L (solid line: full wave results; dashed line: homogenization model). The wires are embedded in air and have a radius $r_w = 0.01a$. (Reprinted from Silveirinha, M.G., *IEEE Trans. Antennas Propagat.*, 54, 1766, 2006. With permission.)

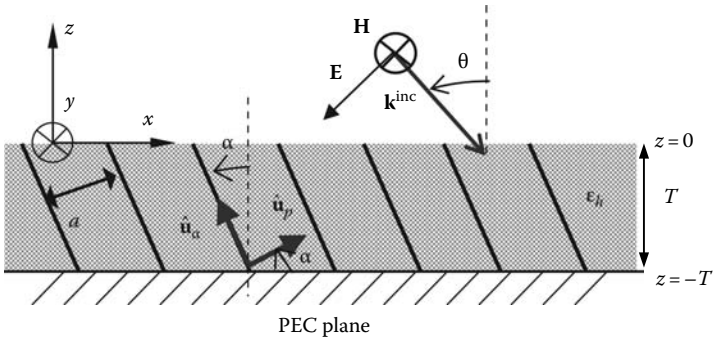

FIGURE 10.10 A wire medium slab is connected to a ground plane. The metallic wires are arranged in a square lattice with a lattice constant a. The wires may be tilted with respect to the interfaces (normal to the z-direction) by an angle α. The structure is periodic along the x and y directions. (Reprinted from Silveirinha, M.G., Fernandes, C.A., and Costa, J.R., *New J. Phys.*, 10, 053011(1–17), 2008. With permission.)

A detailed analysis demonstrates that this property, which is intrinsically related to the microstructure of the material, implies that the macroscopic fields verify the following ABC at the PEC interface [50],

$$\left(\mathbf{k}_{||}\cdot\hat{\mathbf{u}}_\alpha+\hat{\mathbf{u}}_z\cdot\hat{\mathbf{u}}_\alpha j\frac{\mathrm{d}}{\mathrm{d}z}\right)\left(\omega\varepsilon_0\varepsilon_h\hat{\mathbf{u}}_\alpha\cdot\mathbf{E}+\hat{\mathbf{u}}_\alpha\times\left(\mathbf{k}_{||}+\hat{\mathbf{u}}_z j\frac{\mathrm{d}}{\mathrm{d}z}\right)\cdot\mathbf{H}\right)=0 \tag{10.78}$$

where

$\hat{\mathbf{u}}_\alpha$ is the unit vector along the direction of the wires (see Figure 10.10)
$\hat{\mathbf{u}}_z$ is the normal to the interface
$\mathbf{k}_{||}$ is the component of the wave vector parallel to the interface

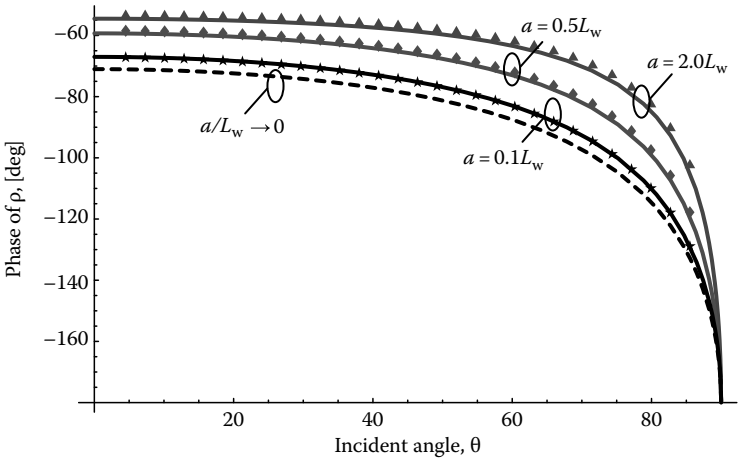

FIGURE 10.11 Reflection characteristic for a substrate formed by tilted wires ($\alpha = 45°$) connected to a PEC plane. The wires are embedded in a dielectric with $\varepsilon_h = 4.0$ and thickness T such that $T\sqrt{\varepsilon_h}\omega/c = \pi/4$. The spacing between the wires, a, associated with each curve is indicated in the figure. The radius of the wires is $r_w = 0.05a$, and the length of the wires is $L_w = T \sec \alpha$. The solid lines were obtained with the homogenization model, and the discrete symbols were obtained using the commercial simulator CST Microwave Studio. (Reprinted from Silveirinha, M.G., Fernandes, C.A., and Costa, J.R., *New J. Phys.*, 10, 053011(1–17), 2008. With permission.)

This ABC together with the classical boundary condition, $\hat{\mathbf{u}}_z \times \mathbf{E} = 0$, completely characterizes the reflection of waves by a wire medium slab connected to a ground plane. As an example of the application of such a result, we consider the geometry of Figure 10.10 where an incoming plane wave is reflected by a grounded wire medium slab. The reflection coefficient may be computed using homogenization methods by matching the fields in the air and wire medium regions at the interface $z = 0$ and using the ABC (Equation 10.76) and the classical boundary conditions, and by enforcing the ABC (Equation 10.78) and $\hat{\mathbf{u}}_z \times \mathbf{E} = 0$ at the interface with the conducting plane at $z = -T$ [50]. The calculated reflection characteristic is depicted in Figure 10.11 (solid lines) for different lattice spacings. The parameters of the microstructured substrate are given in the legend of the figure. The discrete symbols correspond to data obtained using the commercial electromagnetic simulator, CST Microwave Studio. It is seen that homogenization results compare very well with full wave simulations, both when the wires are very densely packed ($a = 0.1L_w$) and when the wires are loosely packed ($a = 2.0L_w$), where $L_w = T \sec\alpha$ is the length of the metallic wires. It can be verified that in the limit in which $a/L_w \to 0$, the wire medium behaves as a material with extreme optical properties, and the interface $z = 0$ may be characterized by an impedance boundary condition [50]. Arrays of tilted metallic wires connected to a ground plane have great potentials in the realization of high-impedance substrates.

Even though the results presented in this chapter deal exclusively with arrays of parallel wires, the described ABCs can also be applied to other more complex topologies of wire media [23,43].

References

1. J. van Kranendonk and J. E. Sipe, Foundations of the macroscopic electromagnetic theory of dielectric media, chapter 5 in *Progress in Optics XV*, (ed. by E. Wolf), New York: North-Holland, 1977.
2. G. Russakov, A derivation of the macroscopic Maxwell equations, *Am. J. Phys*, 38, 1188, 1970.

3. J. Sipe and J. V. Kranendonk, Macroscopic electromagnetic theory of resonant dielectrics *Phys. Rev. A*, 9, 1806, 1974.
4. V. Agranovich and V. Ginzburg, *Spatial Dispersion in Crystal Optics and the Theory of Excitons*, New York: Wiley-Interscience, 1966.
5. G. D. Mahan and G. Obermair, Polaritons at surfaces, *Phys. Rev*., 183, 834, 1969.
6. D. R. Smith, Willie, J. Padilla, D. C. Vier, S. C. Nemat-Nasser, and S. Schultz, A Composite medium with simultaneously negative permeability and permittivity, *Phys. Rev. Lett*., 84, 4184, 2000.
7. M. Silveirinha and N. Engheta, Tunneling of electromagnetic energy through sub-wavelength channels and bends using near-zero-epsilon materials, *Phys. Rev. Lett*., 97, 157403, 2006.
8. J. B. Pendry, Negative refraction makes a perfect lens, *Phys. Rev. Lett*., 85, 3966, 2000.
9. C. Luo, S. G. Johnson, J. D. Joannopoulos, and J. B. Pendry, Subwavelength imaging in photonic crystals, *Phys. Rev. B*, 68, 045115, 2003.
10. P. A. Belov, Y. Hao, and S. Sudhakaran, Subwavelength microwave imaging using an array of parallel conducting wires as a lens, *Phys. Rev. B*, 73, 033108, 2006.
11. M. G. Silveirinha, P. A. Belov, and C. R. Simovski, Subwavelength imaging at infrared frequencies using an array of metallic nanorods, *Phys. Rev. B*, 75, 035108, 2007.
12. J. D. Jackson, *Classical Electrodynamics*, Sect. 6.6, New York: Wiley, 1998.
13. S. Datta, C. T. Chan, K. M. Ho, and C. M. Soukoulis, Effective dielectric constant of periodic composite structures, *Phys. Rev. B*, 48, 14936, 1993.
14. W. Lamb, D. M. Wood, and N. W. Ashcroft, Long-wavelength electromagnetic propagation in heterogeneous media, *Phys. Rev. B*, 21, 2248, 1980.
15. M. G. Silveirinha and C. A. Fernandes, Effective permittivity of metallic crystals: A periodic Green's function formulation, *Electromagnetics*, 8, 647, 2003.
16. O. Ouchetto, C.-W. Qiu, S. Zouhdi, L.-W. Li, and A. Razek, Homogenization of 3-D periodic bianisotropic metamaterials, *IEEE Trans. Microwave Theory Technol*., 54, 3893, 2006.
17. D. R. Smith and J. B. Pendry, Homogenization of metamaterials by field averaging, *J. Opt. Soc. Am. B*, 23, 391, 2006.
18. D. R. Smith, S. Schultz, P. Markos, and C. M. Soukoulis, Determination of effective permittivity and permeability of metamaterials from reflection and transmission coefficients, *Phys. Rev. B*, 65, 195104, 2002.
19. C. R. Simovski, Bloch material parameters of magneto-dielectric metamaterials and the concept of Bloch lattices, *Metamaterials*, 1, 62, 2007.
20. P. A. Belov, R. Marqués, S. I. Maslovski, I. S. Nefedov, M. Silveirinha, C. R. Simovski, and S. A. Tretyakov, Strong spatial dispersion in wire media in the very large wavelength limit, *Phys. Rev. B*, 67, 113103, 2003.
21. M. G. Silveirinha, Nonlocal homogenization model for a periodic array of epsilon-negative rods, *Phys. Rev. E*, 73, 046612, 2006.
22. A. L. Pokrovsky and A. L. Efros, Nonlocal electrodynamics of two-dimensional wire mesh photonic crystals, *Phys. Rev. B*, 65, 045110, 2002.
23. M. G. Silveirinha and C. A. Fernandes, Homogenization of 3D-connected and non-connected wire metamaterials, *IEEE Trans. Microwave Theory Technol*., 53, 1418, 2005.
24. P. A. Belov and C. R. Simovski, Homogenization of electromagnetic crystals formed by uniaxial resonant scatterers, *Phys. Rev. E*, 72, 026615, 2005.
25. M. G. Silveirinha and P. A. Belov, Spatial dispersion in lattices of split ring resonators with permeability near zero, *Phys. Rev. B(BR)*, 77, 233104, 2008.
26. D. Sjoberg, Dispersive effective material parameters, *Microwave Opt. Technol. Lett*., 48, 2629, 2006.
27. J. Li and J. B. Pendry, Non-local effective medium of metamaterial, arxiv:cond-mat/0701332v1, 2007.

28. J. D. Baena, L. Jelinek, R. Marqués, and M. G. Silveirinha, Unified homogenization theory for magnetoinductive and electromagnetic waves in split-ring-metamaterials, *Phys. Rev. A*, 78, 013842, 2008.
29. M. G. Silveirinha, C. A. Fernandes, and J. R. Costa, Electromagnetic characterization of textured surfaces formed by metallic pins, *IEEE Trans. Antennas Propagat*., 56, 405, 2008.
30. M. G. Silveirinha, A metamaterial homogenization approach with application to the characterization of microstructured composites with negative parameters, *Phys. Rev. B*, 75, 115104, 2007.
31. L. D. Landau and E. M. Lifshitz, *Electrodynamics of Continuous Media*, Course of Theoretical Physics, vol. 8, Oxford: Elsevier Butterworth-Heinemann, 2004.
32. I. V. Lindell, A. H. Sihvola, S. A. Tretyakov, and A. Viitanen, *Electromagnetic Waves in Chiral and Bi-Isotropic Media*, Boston, MA: Artech House, 1994.
33. A. N. Serdyukov, I. V. Semchenko, S. A. Tretyakov, and A. Sihvola, *Electromagnetics of Bi-Anisotropic Materials: Theory and Applications*, Amsterdam, the Netherlands: Gordon and Breach Science Publishers, 2001.
34. M. G. Silveirinha, Generalized Lorentz-Lorenz formulas for microstructured materials, *Phys. Rev. B*, 76, 245117, 2007.
35. M. G. Silveirinha and C. A. Fernandes, A new acceleration technique with exponential convergence rate to evaluate the periodic green function, *IEEE Trans. Antennas Propagat*., 53, 347, 2005.
36. P. P. Ewald, Die Berechnung optischer und elektrostatistischer Gitterpotentiale, *Ann. Der Physik*, 64, 253, 1921.
37. R. E. Collin, *Field Theory of Guided Waves*, 2nd edn., New York: IEEE Press, 1991.
38. M. G. Silveirinha, Design of linear-to-circular polarization transformers made of long densely packed metallic helices *IEEE Trans. Antennas Propagat*., 56, 390, 2008.
39. A. P. Vinogradov and I. I. Skidanov, On the problem of constitutive parameters of composite materials, *Proceedings of the Bianisotropics 2000*, Lisbon, Portugal, pp. 17–22, 2000.
40. P. A. Belov, C. R. Simovski and S.A. Tretyakov, Example of bianisotropic electromagnetic crystals: The spiral medium, *Phys. Rev. E*, 67, 056622, 2003.
41. R. Marqués, F. Medina, and R. Rafii-El-Idrissi, Role of bianisotropy in negative permeability and left-handed metamaterials, *Phys. Rev. B*, 65, 144440, 2002.
42. M. G. Silveirinha and C. A. Fernandes, A hybrid method for the efficient calculation of the band structure of 3D metallic crystals, *IEEE Trans. Microwave Theory Technol*., 52, 889, 2004.
43. M. G. Silveirinha and C. A. Fernandes, Transverse average field approach for the characterization of thin metamaterial slabs, *Phys. Rev. E*, 75, 036613, 2007.
44. C. R. Simovski and S. A. Tretyakov, Local constitutive parameters of metamaterials from an effective-medium perspective, *Phys. Rev. B*, 75, 195111, 2007.
45. S. I. Pekar, Theory of the electromagnetic waves in crystals with excitons, *Sov. Phys. JETP*, 6, 785, 1958.
46. A. R. Melnyk, M. J. Harrison, Theory of optical excitation of plasmons in metals, *Phys. Rev. B*, 2, 835, 1970.
47. W. A. Davis and C. M. Krowne, The effects of drift and diffusion in semiconductors on plane wave interaction at interfaces, *IEEE Trans. Antennas Propagat*., 36, 97, 1998.
48. K. Henneberger, Additional boundary conditions: An historical mistake, *Phys. Rev. Lett*., 80, 2889, 1998.
49. M. G. Silveirinha, Additional boundary condition for the wire medium, *IEEE Trans. Antennas Propagat*., 54, 1766, 2006.
50. M. G. Silveirinha, C. A. Fernandes, and J. R. Costa, Additional boundary condition for a wire medium connected to a metallic surface, *New J. Phys*., 10, 053011(1–17), 2008.
51. I. S. Nefedov, A. J. Viitanen, and S. A. Tretyakov, Electromagnetic wave refraction at an interface of a double wire medium *Phys. Rev. B*, 72, 245113, 2005.
52. P. A. Belov and M. G. Silveirinha, Resolution of sub-wavelength transmission devices formed by a wire medium, *Phys. Rev. E*, 73, 056607, 2006.

53. D. Sievenpiper, L. Zhang, R. Broas, N. Alexopolous, and E. Yablonovitch, High-impedance electromagnetic surfaces with a forbidden frequency band, *IEEE Trans. Microwave Theory Technol.*, 47, 2059, 1999.
54. R. J. King, D. V. Thiel, and K. S. Park, The synthesis of surface reactances using an artificial dielectric, *IEEE Trans. Antennas Propagat.*, 31, 471, 1983.

11

On the Extraction of Local Material Parameters of Metamaterials from Experimental or Simulated Data

Constantin R. Simovski
Helsinki University of Technology

11.1 Introduction

Correct extraction of effective material parameters (EMP) of a metamaterial (MTM) layer formed by optically small resonant particles embedded in a dielectric matrix from the experimental data or numerical simulations is very important for the design and optimization of MTM. For MTM performed as regular lattices* it is usually done in terms of the plane-wave reflection (R) and transmission (T) coefficients of the layer. This is probably an optimal way to find the EMP of the composite medium with regular inner structure if the layer comprises the integer number of the lattice unit cells. To retrieve EMP through exact plane-wave simulations of the regular layer is much more accurate than through approximate analytical calculations involving electric and magnetic polarizabilities of individual particles, mixing rules, or other approximate algorithms of averaging. It is not simple to calculate EMP exactly using their definitions, that is, through accurate numerical averaging of numerically simulated microscopic fields and microscopic polarizations. In spite of huge computation efforts and time expenses, the researcher encounters the problem of artificial magnetism. This phenomenon in lattices of complex scatterers cannot be properly revealed using simple averaging and requires special procedures that would take into account the peculiarities of the distribution of the microscopic polarization currents in the cell [1].

* In this chapter we consider only lattices of nonbianisotropic particles without resonant, higher multipole moments.

Meanwhile, the plane-wave reflection and transmission in finite-thickness lattices evidently yield a standard cell problem. Cell problems are, as a rule, efficiently solvable using commercial packages such as the Ansoft HFSS or Microwave CST Studio. If the experimental sample of the MTM layer is built, it is much easier to measure its R and T coefficients than to measure the purely electric response of the sample to find its high-frequency permittivity or its purely magnetic response to the high-frequency permeability. Therefore, we can assert that a procedure that would allow us to relate EMP of finite-thickness lattices with R and T coefficients is of prime importance for the successful design of MTM.

In [2–12] and many others, the authors claimed that composite slabs comprising arbitrary number N of monolayers* possess the same EMP as those of infinite or semi-infinite lattices. It is, however, clear that only in the case $N \gg 1$ the refraction of the obliquely incident wave is strongly affected by lattice dipole particles, whereas in the case $N = 1$ the refraction is determined by the dielectric matrix and is not influenced by dipole particles.

What is then the meaning of the refraction coefficient retrieved for a monolayer? In addition, if it is senseless why EMP extracted for the composite layer with $N = 1$ turn out to be very often equal numerically to EMP extracted for the layer of the same composite but with $N = 4$? This coincidence cannot be occasional, and a certain physical meaning is behind material parameters retrieved in cited works, which are reviewed below.

The key point for the reader of this chapter is the insight that there is no unique mandatory method to define the EMP for composite media. Material parameters replace an array of separate particles by an "equivalent" continuous slab, and this procedure (homogenization) was never uniquely defined in any classical book. At least two pairs of EMP called here† as Bloch's and Lorentz's EMP can be extracted for many lattices from the same R and T coefficients. In fact, if one allows us to involve also mesoscopic (N-dependent) EMP, we could extract more than two pairs of EMP from the same experimental or numerical data.

Two different sets of N-independent EMP can correspond to the same R and T coefficients, because only one set of EMP allows one to express R and T directly, that is, through ε, μ, the slab thickness $d = Na$, and the frequency. The other one gives R and T only after involving additional parameters. This difference becomes visible beyond the region of very low frequencies. Well below the resonance of individual particles forming the lattice (the quasi-static limit), these two sets of EMP numerically coincide.

The additional parameters one has to involve to express R and T through material parameters ε, μ, the slab thickness d, and the frequency ω are related to the so-called transition layers whose impact was explained in the 1920s by P. Drude. Drude pointed out that when the lattice period a is still small but already not negligible compared with the wavelength in the crystal (practically when $0.1\lambda > a > 0.01\lambda$) the approximation of a sharp boundary loses validity. In other words a finite-thickness lattice of electric dipoles at these frequencies cannot be modeled as a uniform continuous dielectric with unique ε filling the space d between two sharp boundaries. The same result can be evidently expanded to magneto-dielectric lattices with both nontrivial ε and μ.

Following Drude, when the phase shift of the wave over a lattice unit cell is perhaps small but not negligible we either should refuse the idea of homogenizing this lattice or homogenize it in a way such that the interface of the effective continuous medium is spread.

P. Drude suggested to locate this transition layer at the interface of a semi-infinite crystal so that it covers the edge unit cell of the lattice. Therefore, its thickness is (in Drude's theory) equal to the

* A monolayer is a single 2D grid of particles placed in the host medium slab of thickness a, which can be treated as the lattice unit cell length.

† This terminology is not commonly adopted; it is suggested by the author of this chapter.

lattice period a. Following Drude the permittivity varies across a transition layer from its bulk value ε, which is the permittivity of the unbounded lattice to its value in free space (or surrounding medium if not free space). We can consider transition layers as uniform ones, since they are optically small, and EMP of these layers take averaged values between EMP of unbounded crystals and material parameters of the surrounding medium (e.g., free space). In this way, the finite-thickness lattice with $N \gg 1$ is modeled as a three-layer structure with two pairs of EMP: those of the inner (thick) layer and those of the transition (thin) layers. The last pair of EMP can be expressed through EMP of the inner layer.

Taking transition layers into account in this way we will extract from R and T coefficients of the slab the Lorentz material parameters of its central domain. Ignoring transition layers, that is, considering the real composite slab as a layer with a unique pair of EMP between sharp boundaries, we extract another pair of material parameters (from the same R and T coefficients). They can be dependent on N. However, there are lattices for which the pair of these directly retrieved EMP is N-independent.

In this case (see [2–12]) these extracted EMP are equivalent to the Bloch (or Ewald–Bloch) material parameters of the infinite lattice. The definitions of the Bloch EMP are given here. N-independent directly retrieved EMP can be useful, though their physical meaning is rather specific. They cannot be treated in terms of the electric (ε) or magnetic (μ) responses of the medium unit cell. One of them qualitatively describes the electric (or magnetic) response of the unit cell (however, with significant quantitative errors). Another material parameter does not describe this magnetic (electric) response at all. This assertion refers to the lattices of electric or magnetic dipoles, respectively.

There are MTM lattices for which the directly retrieved EMP are not equivalent to the Bloch material parameters. These are lattices studied, for example, in [13–18] for which the directly retrieved EMP are N-dependent and cannot be applied to any electrodynamic problem except finding R and T coefficients for the same N. However, these coefficients must be known to extract EMP from them. Only N-independent EMP extracted directly from R and T are useful.

11.2 Bloch Material Parameters Impedance: Lorentz Material Parameters and Wave Impedance

We start from the discussion of the comparative importance of the Lorentz and the Bloch sets of EMP. These sets of EMP are compared with respect to the so-called locality requirement. This requirement determines the applicability of EMP in different boundary problems with conventional boundary conditions. We see here that the violation of the locality by Bloch's EMP restricts their applicability by the only problem: reflection and transmission of a normally incident plane wave for a composite slab.

The locality is equivalent (see, in Chapter 2, and also in [19]) to a system with the following conditions:

- Passivity (for the temporal dependence $e^{-i\omega t}$ it implies $\mathrm{Im}(\varepsilon) > 0$ and $\mathrm{Im}(\mu) > 0$ simultaneously at all frequencies; for $e^{j\omega t}$ the sign of both $\mathrm{Im}(\varepsilon)$ and $\mathrm{Im}(\mu)$ should be negative).
- Causality (for media with negligible losses it corresponds to conditions $\partial(\omega\varepsilon)/\partial\omega > 1$ and $\partial(\omega\mu))/\partial\omega > 1$. This also means that in the frequency regions where losses are small material parameters obviously grow versus frequency: $\partial(\mathrm{Re}(\varepsilon))/\partial\omega > 0$ and $\partial(\mathrm{Re}(\mu))/\partial\omega > 0$).

- Absence of radiation losses in arrays with uniform concentration of particles.*
- Independence of the material parameters on the wave propagation direction. For given frequency and plane incident waves this means the independence of EMP to be extracted on the incidence angle.

It was shown in [20] that the Bloch material parameters are in this sense nonlocal within the same frequency ranges whereas the Lorentz EMP are local. This means that the nonlocality of retrieved EMP in [2–12] does not obviously mean that there is spatial dispersion in those lattices. In the frequency range where the spatial dispersion is absent, the local EMP can be introduced.

A simple procedure of the approximate extraction of Lorentz EMP for finite-thickness composite layers [20] is described here. It does not involve Drude layers. The procedure is based on the model of electromagnetic interaction in lattices containing both electric and magnetic resonant scatterers. This model was developed in [21] and [20]. In the theory it was assumed that all resonant scatterers interact as if they were point electric (p) and magnetic (m) dipoles. This approximation is accurate enough for many practical structures in the frequency range under study.† The bounds of the dipole model can always be verified by the exact numerical simulation of the plane-wave propagation in the lattice. It allows us to avoid the difficult problem of averaging the microscopic polarizations of the lattice unit cell. This difficulty (mentioned earlier) appears when the electric microscopic polarization leads to the magnetic macroscopic one [1]. The dipole model of electromagnetic interaction needs only electric and magnetic dipole moments of particles. Averaged electric and magnetic bulk polarizations referred to the cell center are simply equal to p and m dipole moments, respectively, divided by the cell volume V. Therefore, the averaging of the microscopic polarizations is not involved in the model.

Once the problem of averaging of microscopic polarizations is separated from field averaging, the problem of lattice homogenization is determined by the procedure that defines the averaging of microscopic **E** and **H** fields. The Lorentz homogenization corresponds to the simple averaging of these fields over the unit volume around the observation points.‡ Unlike the Lorentz homogenization, the Bloch homogenization§ corresponds to the treating of zeroth Bloch harmonics of **E** and **H** as if $\mathbf{E}_0$ and $\mathbf{H}_0$ were averaged fields [20].

Historically, P. Ewald was the first who shared the zeroth Bloch harmonic of a microscopic field in a semi-infinite lattice illuminated by a plane wave and treated it as the averaged field. He did it in [22,23] deriving the so-called extinction principle previously postulated by S. Oseen. This historical fact is the reason why these EMP can be called in this chapter also as Ewald–Bloch material parameters. The Ewald–Oseen extinction principle is an obvious condition for the homogenization of finite lattices [24,25]. Ewald proved the extinction of incident plane waves in semi-infinite dipole lattices at low frequencies. Recently, this principle was proved for arbitrary frequencies and lattices of arbitrary dielectric inclusions, that is, expanded also to photonic crystals in [29]. The fact of the extinction of incident waves in photonic crystals makes possible the discussion on the physical meaning of homogenization models for MTM lattices at high frequencies where they become photonic crystals. However, in this chapter we restrict the discussion to the frequency region $ka < 1$.

---

* Though this principle is often attributed in the literature to a more recent work [26], it was in fact postulated for periodic structures 100 years ago in [27], then proved for dipole lattices in [28], and was discussed in [19].

† Another approximation is neglecting the polariton waves excited at the interface of the composite layer due to its discrete structure. The higher is N and the smaller as a/λ the smaller is the error in extracted EMP associated with neglected polaritons.

‡ Perhaps, this procedure also implies the use of the so-called test or weight function F to which the microscopic field is multiplied being integrated [30]. This function choice is rather arbitrary and its introduction should serve to the further smoothing of the averaged field coordinate dependence. However, the practical influence of the test function to final results for EMP is weak, and we pick for simplicity $F \equiv 1$.

§ This terminology is not commonly adopted, however this is exactly what is implied in classical books e.g., in [24] when one introduces the permittivity as a tensor whose component depends on the wavevector in crystals.

The product of Lorentz permittivity ε_L and permeability μ_L equals the square power of the refraction index of the infinite lattice: $\varepsilon_L \mu_L = n^2$. The same holds also for Ewald–Bloch EMP: $\varepsilon_{eb}\mu_{eb} = n^2$. However, the ratio of Ewald–Bloch EMP determines the so-called Bloch impedance of the lattice (here we consider this impedance normalized to that of free space). This is not the characteristic (wave) impedance of the homogenized lattice. It is the parameter of the original discrete lattice. The wave impedance that characterizes the equivalent homogenized medium is given by the ratio of Lorentz EMP.

We have then:

$$\frac{\mu_{eb}}{\varepsilon_{eb}} = Z_B^2, \quad \frac{\mu_L}{\varepsilon_L} = Z_w^2.$$

The difference between the Bloch impedance Z_B and the wave impedances Z_w is well known for periodically loaded transmission lines (PLTL). In [41] it was emphasized that even if the PLTL can be homogenized the reflection coefficient of this semi-infinite PLTL is related to the Bloch impedance of the original PLTL and not to the wave impedance of the homogenized line. At least, it is so beyond the quasi-static limit, where these impedances are not equivalent:

$$R_\infty = \frac{\eta Z_B - \eta_0}{\eta Z_B + \eta_0} \neq \frac{\eta Z_w - \eta_0}{\eta Z_w + \eta_0}.$$

Here η and η_0 are characteristic impedances of the host transmission line and of the line from which the wave comes, respectively. The Bloch impedance of the PLTL is defined as the ratio of voltages U and currents I at the input or output of any unit cell.

For dipole lattices Z_B is the ratio of transversally averaged **E** and **H** fields calculated at central planes of gaps between crystal planes. Transversal averaging procedure [20] is defined by simple integrating of true fields around the observation point over two lattice periods a_x and a_y, orthogonal to the propagation axis z. The transversally averaged **E** and **H** are analogues, respectively, of the voltage and the current in a PLTL.

The Lorentz EMP are related to the pair Z_w and n and not to the pair Z_B and n. The wave impedance describes the ratio of volume-averaged **E** and **H** fields, where their averaging volume is centered by the particle center. In the transmission line model this impedance corresponds to the ratio $< U > / < I >$, where $< U >$ and $< I >$ are voltage and current, respectively, both averaged over the unit cell of the loaded line.

11.3 Direct Retrieval of Effective Material Parameters

Let us discuss when and why it is really possible to obtain the Lorentz and the Ewald–Bloch material parameters of an infinite lattice from plane-wave measurements of a real composite slab.

First, we discuss local material parameters. In [32] it was proved (see also [33–35]) that not only thick layers but a regular composite slab with any N, even $N = 1$,* for all angles of incidence of a plane wave can also be presented as a layer filled with a bulk homogeneous medium with two Drude transition layers at its interfaces. This result is not surprising. The locality of EMP (which implies passivity, causality, and other features listed already) means, by definition, that the electromagnetic response of the unit volume of the structure is determined by the proximity of the observation point. Practically, if the local homogenization is possible the unit cell response should be completely determined by

* However, in this case the description of the slab in terms of bulk EMP has little physical meaning, and the concept of Drude layers, though it practically works, is not justified.

this unit cell and independent of the surrounding. This speculation helps to understand the role of transition layers better. These layers "protect" the electromagnetic susceptibility of the observation point from the influence of the outer space, which is different from the medium of the slab. And the electromagnetic response of any volume inside the finite slab after introducing the Drude transition layers turns out to be the same as the response of this volume in the infinite structure. As a result, Lorentz's EMP can be extracted independently on the slab thickness $d = Na$ and are applicable for arbitrary N.

Second, we discuss EMP defined in the following formal way. Let the coefficients R and T of a composite layer comprising N monolayers be known, where the wave is normally incident. Treating (see e.g., in [3,4]) the composite slab as a uniform layer of continuous medium of same thickness d and inverting the classical Fresnel–Airy formulas

$$R = \frac{R_\infty\left(1 - e^{-2jk_0\sqrt{\varepsilon_{\text{eff}}\mu_{\text{eff}}}d}\right)}{1 - R_\infty^2 e^{-2jk_0\sqrt{\varepsilon_{\text{eff}}\mu_{\text{eff}}}d}}, \quad T = \frac{e^{-jk_0\sqrt{\varepsilon_{\text{eff}}\mu_{\text{eff}}}d}\left(1 - R_\infty^2\right)}{1 - R_\infty^2 e^{-2jk_0\sqrt{\varepsilon_{\text{eff}}\mu_{\text{eff}}}d}}, \tag{11.1}$$

we obtain

$$q = \pm\frac{1}{d}\text{acos}\left(\frac{1 - R^2 + T^2}{2T}\right) + \frac{2\pi m}{d} = k_0\sqrt{\varepsilon_{\text{eff}}\mu_{\text{eff}}}, \tag{11.2}$$

for the propagation factor and

$$Z_c = \pm\sqrt{\frac{(1+R)^2 - T^2}{(1-R)^2 - T^2}} = \sqrt{\frac{\mu_{\text{eff}}}{\varepsilon_{\text{eff}}}}, \tag{11.3}$$

for the normalized "characteristic impedance" of this "effective medium." In Equation 11.1, coefficient R_∞ is treated as the reflection coefficient from the "effective semi-infinite medium":

$$R_\infty = \left(\sqrt{\frac{\varepsilon_{\text{eff}}}{\mu_{\text{eff}}}} - \frac{\eta_0}{\eta}\right) \Big/ \left(\sqrt{\frac{\varepsilon_{\text{eff}}}{\mu_{\text{eff}}}} + \frac{\eta_0}{\eta}\right). \tag{11.4}$$

In these formulas $k_0 = \omega\sqrt{\varepsilon_0\mu_0}$ is the free space wave number, and $\eta_0 = \sqrt{\mu_0/\varepsilon_0}$ and $\eta = \sqrt{\mu_0/\varepsilon_0\varepsilon_m}$ are wave impedances of free space and of the slab host medium, respectively. Parameter m in Equation 11.2 is the integer valued function of frequency. In the region $|\text{Re}(qd)| < \pi/2$, it must be $m = 0$. Also, parameter m can be found from the requirement of smoothness for the frequency dependence of extracted parameters [4] or from the requirement of the correct sign for the imaginary part of ε_{eff} and μ_{eff}, as was suggested in [31]. Notice, however, that the requirement of the "correct sign" [31] is senseless when applied to EMP, which are by definition nonlocal.

Formal material parameters defined by relations (Equations 11.2 and 11.3) for the frequency range $qa > 0.01$ ignore both Drude's principle of the spread boundary and the difference between Bloch's and characteristic impedances. In the best case (of so-called Bloch lattices) they are equal to Ewald–Bloch material parameters. In the worst case they are senseless.

In [20] it was proved that Ewald–Bloch material parameters do not describe properly the electromagnetic response of the lattice unit cell except for the quasi-static limit $qa \ll 1$. As a result, the locality requirement does not refer to these EMP. It is not surprising that in [31] this requirement led to $m \neq 0$ even for optically thin layers, and for optically thick layers it leads to jumps of the derivative in the frequency dependence of Z_c and refraction index $n \equiv q/k_0$. Moreover, this requirement, though it attributes to the nonlocal EMP one of the features of local EMP, i.e., the apparent passivity, does not avoid the violation of the causality.

11.4 Bloch Lattices

The ABCD matrix (or transmission matrix) of the lattice unit cell $\mathbf{F_1}$ relates the transversally averaged **E** and **H** fields at the input and output. Recall that we ignore nonreciprocal and bianisotropic lattices and consider the case when the plane wave propagates along one of the lattice axes. Therefore, the field $\mathbf{E}^{\mathrm{TA}}$ (as well as $\mathbf{H}^{\mathrm{TA}}$) contains only one component. Then we can write

$$\begin{bmatrix} E^{\mathrm{TA}}(0) \\ \eta H^{\mathrm{TA}}(0) \end{bmatrix} = \begin{bmatrix} A & B \\ C & D \end{bmatrix} \begin{bmatrix} E^{\mathrm{TA}}(a) \\ \eta H^{\mathrm{TA}}(a) \end{bmatrix}, \quad D = A, \quad C = \frac{1 - A^2}{B}. \tag{11.5}$$

We see that only two components of the transfer matrix of a symmetric and reciprocal unit cell are independent [41]. These two components can be expressed through two EMP formally introduced by relations (Equation 11.1).

The electromagnetic interaction of particles exists in all lattices. However, in special lattices (here called *Bloch's lattices*) this interaction does not change the ABCD matrix of the unit cell. Then this matrix for arbitrary N is fully determined by two scalar values.* These two values are Bloch's or Ewald–Bloch's material parameters of the infinite ($N = \infty$) or finite ($N = 1, 2 \ldots$) Bloch lattice.

Consider their extraction for a monolayer. The reflection and transmission coefficients of a monolayer $R^{(1)}$ and $T^{(1)}$ uniquely determine the transfer matrix of the single monolayer:

$$\begin{bmatrix} 1 - R^{(1)} \\ 1 + R^{(1)} \end{bmatrix} = T^{(1)} \begin{bmatrix} A & B \\ \frac{1-A^2}{B} & A \end{bmatrix}. \tag{11.6}$$

The algorithm based on Equations 11.2 and 11.3 represents a real monolayer with transfer matrix $\mathbf{F_1}$ as an equivalent continuous layer described by formal material parameters $\varepsilon_{\mathrm{eff}}$, μ_{eff} keeping the same thickness and the same ABCD matrix.

Now assume that the ABCD matrix $\mathbf{F_N}$ of the slab with $N \neq 1$ (see Figure 11.1) is equal to $\mathbf{F_N} = \mathbf{F_1}^N$. It is the same so as to assume that the ABCD matrix of any unit cell in a slab of thickness Na still equals $\mathbf{F}_1$.

However, it is easy to show that the ABCD matrix of the continuous slab of thickness Na with the same material parameters $\varepsilon_{\mathrm{eff}}$, μ_{eff} is also equal to $\mathbf{F_N} = \mathbf{F_1}^N$. Therefore, the same equivalent material parameters that were extracted from coefficients $R^{(1)}$ and $T^{(1)}$ of the single monolayer still determine the ABCD matrix $\mathbf{F_N}$ and coefficients $R^{(N)}$ and $T^{(N)}$ of the slab of thickness $d = Na$. It holds also for $N \to \infty$.

In this case N-covariant case material parameters extracted directly from $R^{(N)}$ and $T^{(N)}$ for arbitrary $N = 1, 2 \ldots$ are the Ewald–Bloch EMP.

The concept of the Bloch lattice can be illustrated by analogy with a PLTL. In Figure 11.1, left panel, the composite monolayer containing p-dipoles and m-dipoles in the same plane is shown as a host transmission line of length a comprising one load (a T-circuit). It is easy to prove that the response of a dipole grid to transversally averaged fields **E** and **H** can be described in terms of shunt and serial loads Y and Z. These loads determine the jumps of E^{TA} (due to magnetic dipoles) and H^{TA} (due to electric dipoles), respectively. In the lossless case we have $Y = -jG$ and $Z = -jX$, where G and X are real. Formulas relating these grid parameters with individual electric (a_{ee}) and magnetic a_{mm} polarizabilities of particles were derived in [20]:

$$Y_0 = \frac{jka}{\left(\frac{\varepsilon_0 \varepsilon_{\mathrm{m}} V}{a_{\mathrm{ee}}}\right) - \frac{jk^3}{6\pi\varepsilon_0\varepsilon_{\mathrm{m}}} - B_0}, \quad Z_0 = \frac{jka}{\left(\frac{\mu_0 V}{a_{\mathrm{mm}}}\right) - \frac{jk^3}{6\pi\mu_0} - B_0}. \tag{11.7}$$

* Of course in anisotropic lattices the EMP determining the ABCD matrix must be two tensor values; however, for the normal propagation only two components of these tensors are essential [46].

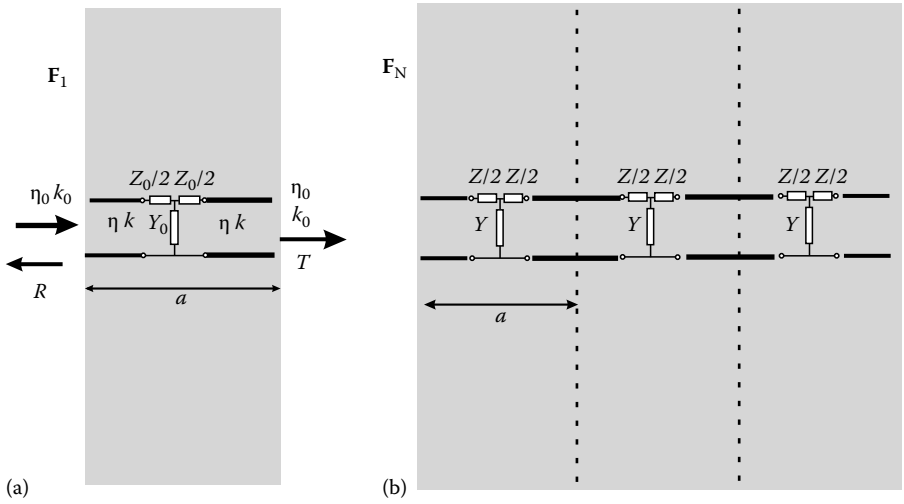

FIGURE 11.1 Extracting the Ewald–Bloch material parameters from R and T coefficients of finite-thickness lattices. (a) A monolayer ($N = 1$) and (b) a composite slab comprising N grids.

where

V is the unit cell volume

ε_m is the relative permittivity of the lattice host medium

$$B_0 = \frac{1}{2}\left(\frac{\cos kbs}{kbs} - \sin kbs\right),$$

if the lattice periods in two transverse directions are identical.

Here $s \approx 0.6954$ and b is the transverse lattice period. At very low frequencies ($kb \ll 1$) $B_0 \approx 0.36$.

The Bloch lattice is a lattice in which the equivalent loads Y and Z are not affected by the electromagnetic interaction of lattice crystal planes. Therefore for arbitrary N, Y, and Z are the same as those for a single monolayer: $Y = Y_0$, $Z = Z_0$. The meaning of Bloch's EMP for these lattices is to predict the reflection and transmission of the normally incident plane wave for composite slabs with arbitrary N if they were extracted for a slab with $N = N_1$.

11.5 Nonlocality of Bloch's Material Parameters

Now let us illustrate the violation of causality and passivity in Bloch's EMP by explicit examples. In [7] and [3] the equivalent EMP were extracted using Equations 11.2 and 11.3 for two lattices depicted in Figure 11.2. One of them was a square lattice of cylinders with high complex permittivity. In the exact numerical simulations this permittivity was picked equal to $\varepsilon_i = 200 + i5$ (the time dependence $\exp(-i\omega t)$ was used, and the imaginary part of the refraction index should be positive). The cylinders were located in free space. The lattice period was equal to 5 mm and the cylinder diameter 2 mm. An individual cylinder experiences the lowest (magnetic) Mie resonance at approximately 4.2 GHz. The electric Mie resonance holds outside the frequency range of our interest. Though the lattice of infinite cylinders is two-dimensional, all formulas derived here are valid (with the substitution of the unit surface $S = a^2$ instead of the unit volume $V = a^3$). Also, the magnetic polarizability a_{mm} is that per unit length of a cylinder.

The other lattice shown in Figure 11.2 is a cubic lattice of doubled silver split ring resonators (SRRs) paired so that to prevent the bianisotropy. The lattice period was equal to $a = 600$ nm, and the size of

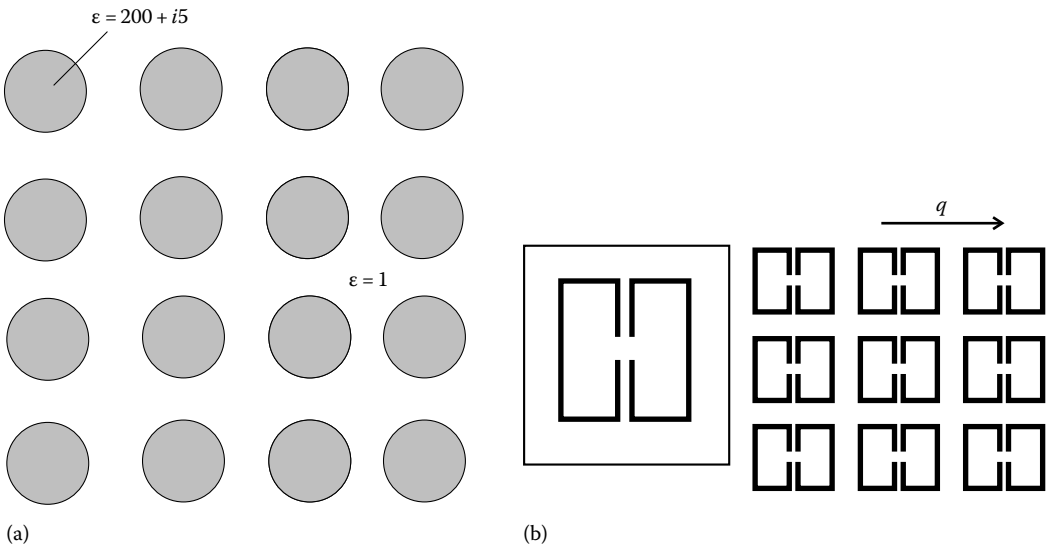

FIGURE 11.2 (a) Lattice of cylinders from oxide ceramics and (b) lattice of silver SRRs resonating in the infrared range.

the individual SRR was equal to 288 nm. These SRRs in simulations [3] resonated at 75 THz. In [3] (and some later works devoted to these SRRs) this resonance was claimed as a purely magnetic one. However, in [47] it was shown that the electric and magnetic resonances of coplanar doubled SRRs overlap. The extraction of local EMP performed here allows us to see the electric resonance of SRRs in the same frequency range as that of the magnetic resonance.

In Figure 11.3a and b the results of the extraction of the equivalent refraction index $n = q/k$ and of the effective impedance Z_c of the slab interface seen by the incident wave are shown. These results were obtained in [7] using exact numerical simulations of the reflection and transmission in the slab of $N = 10$ monolayers. It was also claimed that the same results of extraction were obtained for $N = 4,\ 8,\ 12$. This fact indicates that the lattice under study is the Bloch lattice.

The frequency region between 3.95 and 4.65 GHz corresponds to the high losses: $\mathrm{Im}(n) > 1$. For a lossless analogue of the structure these frequencies approximately correspond to the edges of the resonant stop-band (the dispersion diagram of the lossless analogue of this lattice, i.e., for $\varepsilon_i = 200$ was calculated in [8]). Therefore, in the frequency band 3.95–4.65 GHz (see in Figure 11.3) the homogenization is not allowed. Outside this frequency region the structure can be homogenized. One can see that $\mathrm{Re}(n)$ is a growing function of frequency, and the causality condition is satisfied at these frequencies. Also, $\mathrm{Im}(n) > 0$ and $\mathrm{Im}(Z) > 0$ at all frequencies. Since the time dependence was chosen as $\exp(-i\omega t)$, the equivalent refraction index and the equivalent characteristic impedance do not violate the passivity condition.

In Figure 11.3c and d the results of the direct extraction of EMP performed in [7] are presented. We see that both causality and passivity are violated in the equivalent permittivity. Therefore, it is not only inside the stop-band region where the homogenization is not allowed. The permittivity decreases versus frequency below the resonance and the sign of the electric losses is wrong everywhere.

In Figure 11.4 the analogous results are presented for the lattice of SRRs [3]. The violation of the causality and passivity for the extracted permittivity outside the "stop-band region" in this example is also evident.

If the grid parameters in the lattice are affected by the electromagnetic interaction (i.e., when the lattice under study is not a Bloch lattice), the directly retrieved equivalent material parameters of a finite-thickness slab are not Ewald–Bloch parameters. In this case these material parameters are

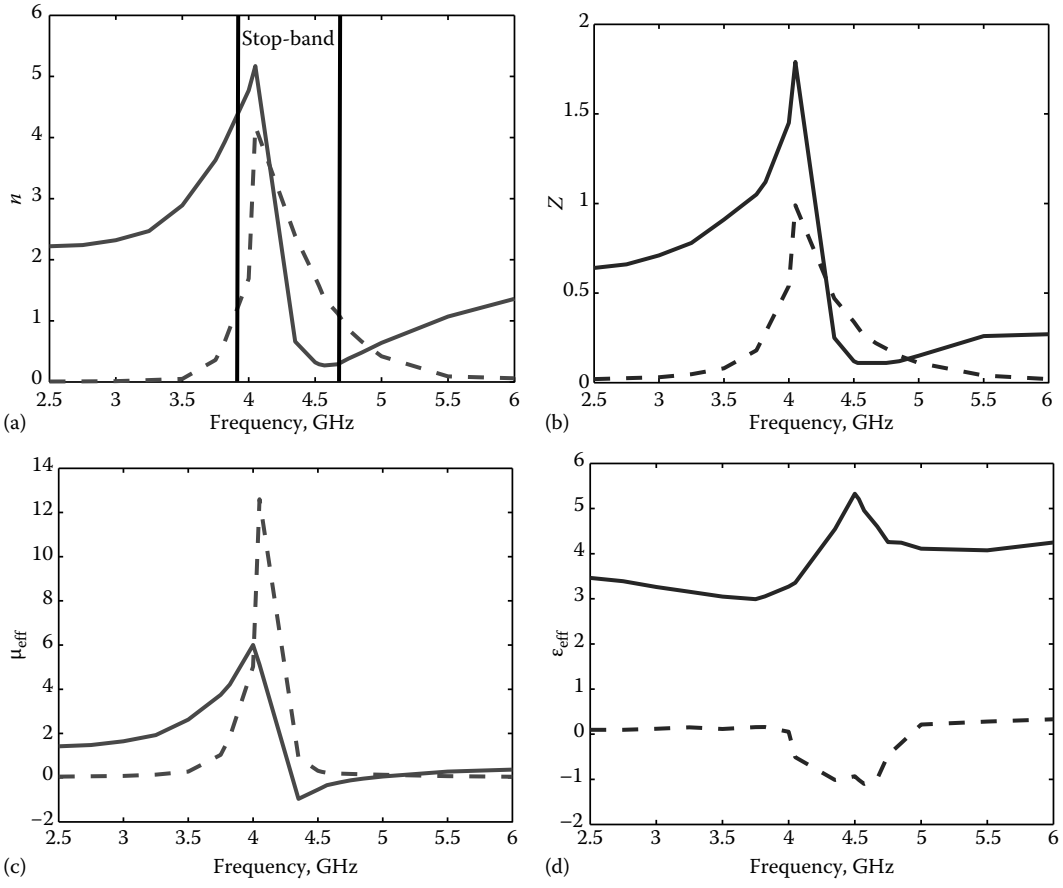

FIGURE 11.3 (a) Refraction index of the array of cylinders extracted directly from simulations of the reflection and transmission coefficients of a slab comprising $N = 10$ monolayers of ceramic cylinders. (b) Equivalent characteristic impedance Z extracted from the same simulations. (c) Permeability directly extracted from the same simulations. (d) Permittivity extracted from the same simulations. All curves repeat corresponding plots from [7]. Solid lines—real part of material parameters, dashed lines—imaginary parts.

senseless. Being nonlocal they wrongly describe the medium electromagnetic response. Being different for different N (there is no explicit dependence of these parameters on N), they cannot be used for prediction of R and T coefficients. Using these equivalent material parameters one can calculate only the same R and T from which these material parameters were extracted. The equivalent refraction index and the impedance extracted for finite-thickness non-Bloch lattices violate the causality and passivity, because they are not equal to the refraction index and Bloch impedance of the infinite lattice. The corresponding material parameters have more bizarre frequency behavior than that of the Ewald–Bloch EMP, see e.g., [13–18]. Readers can observe a typical example of extracted "refraction index" and "material parameters" of a non-Bloch layer with $N = 1$ and $N = 3$ in Figure 11.5.

11.6 How to Distinguish Bloch Lattices?

The easiest way to understand which lattices are Bloch lattices is to compare the dispersion equation derived in the theory of electromagnetic interaction of p–m lattices [20,21] and the dispersion equation of the PLTL with shunt Y and series Z loads, assuming them to be equal Y_0 and Z_0,

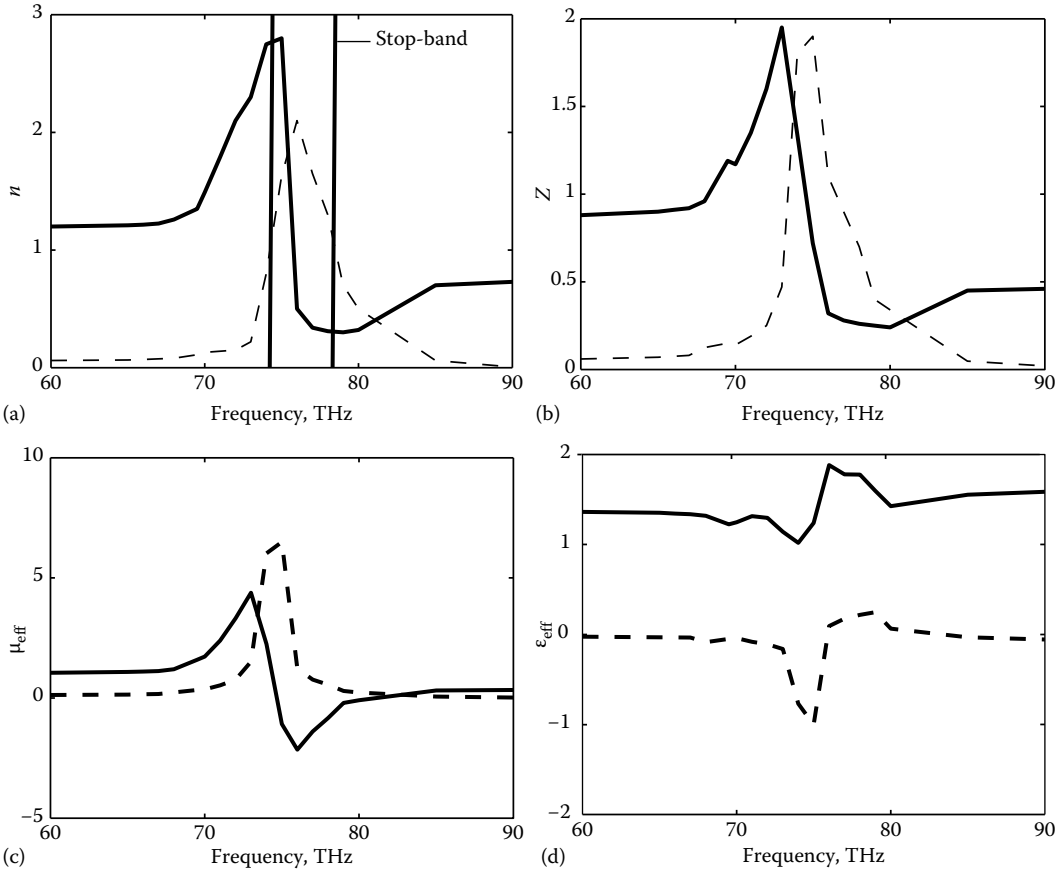

FIGURE 11.4 (a) Refraction index of the array of optical SRRs extracted from exact numerical simulations of the reflection and transmission coefficients of a slab comprising $N = 2$ or $N = 4$ monolayers of paired SRR. (b) Impedance Z extracted from the same simulations. (c) Permeability extracted from the same simulations. (d) Permittivity extracted from the same simulations. All curves reproduce corresponding plots from [3]. Solid lines—real part of material parameters, dashed lines—imaginary parts.

respectively. The idea of an equivalent PLTL is illustrated by Figure 11.1, which corresponds to two possible designs of the p–m lattice when the same crystal plane contains both p and m dipoles. These two designs are presented in Figure 11.6a and b. Scatterers are depicted as spheres schematically. The MTM based on magneto-dielectric spheres as in Figure 11.6a were studied in [36] and the MTM based on paired dielectric spheres of different radius as in Figure 11.6b were studied in [37].

The dispersion equation of the electromagnetic theory reads as [20]

$$\cos qa = \cos ka - j \sin ka \left(\frac{Y_0}{4} + \frac{Z_0}{4} \right) \pm \sqrt{\frac{Y_0 Z_0}{4} \sin^2 qa - \sin^2 ka \left(\frac{Y_0}{4} - \frac{Z_0}{4} \right)^2}. \tag{11.8}$$

The sign in front of the square root must be picked so as to keep $\mathrm{Re}\, q > 0$ for real solutions and $\mathrm{Im}\, q < 0$ for imaginary and complex solutions. The complex solution for lossless lattices is possible in the resonant stop-band only. It takes the form $qa = \pm\pi + j\mathrm{Im}q$. The sign of $\mathrm{Im}q$ depends on the choice of the sign in Equation 11.8.

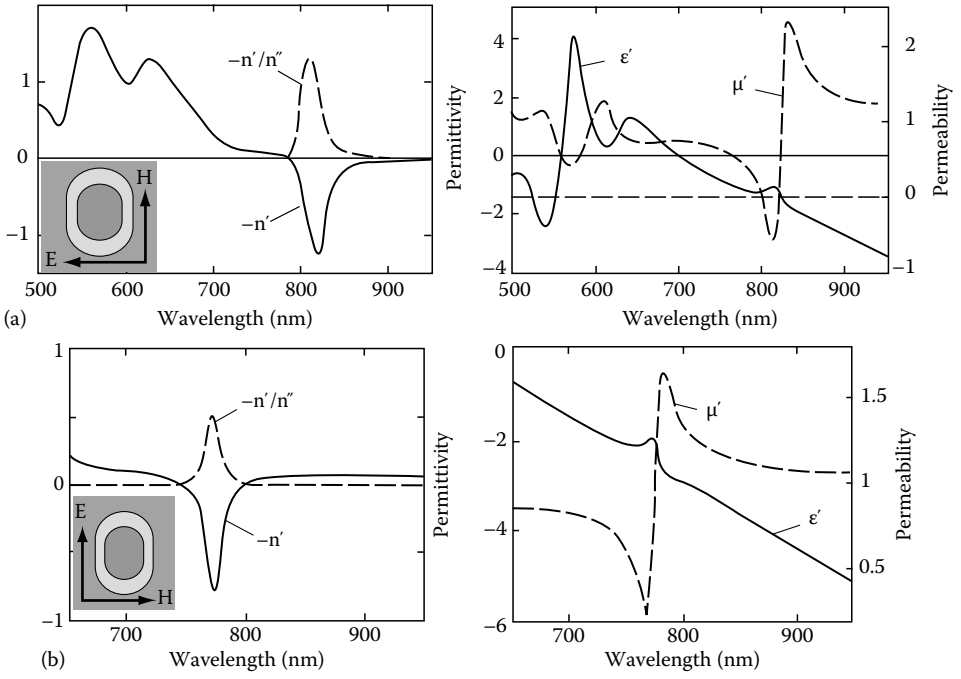

FIGURE 11.5 N-dependent and nonlocal material parameters extracted in [14]. Left, the case of a monolayer ($N = 1$). (a) Refraction index (real part n' and imaginary part n''), (b) $\varepsilon' = \mathrm{Re}(\varepsilon_{\mathrm{eff}})$ and $\mu' = \mathrm{Re}(\mu_{\mathrm{eff}})$. Imaginary parts are not shown. Right, similar plots for $N = 3$. The region 500–700 nm is not shown. The sign of $\mathrm{Im}(\varepsilon_{\mathrm{eff}})$ is wrong at all frequencies.

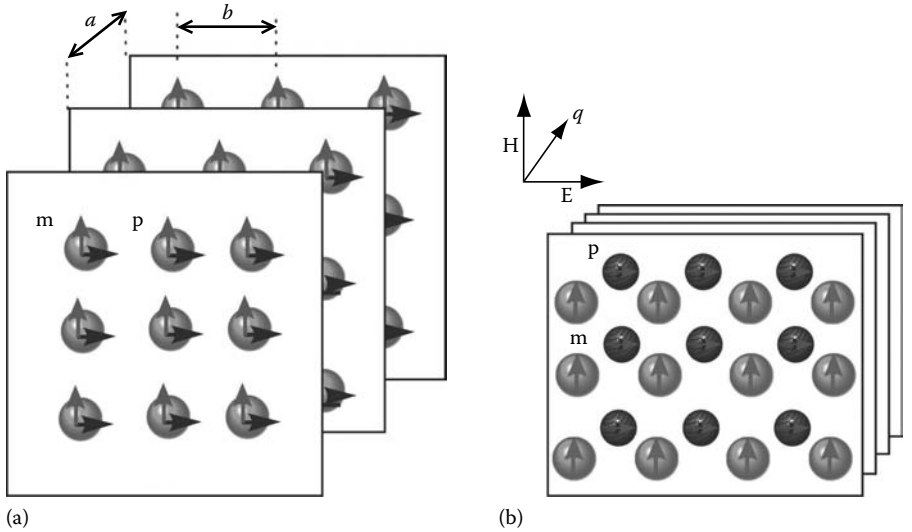

FIGURE 11.6 Presentation of a lattice of electric and magnetic dipoles as a set of crystal planes. (a) Both electric and magnetic moments are induced in every particle and resonate in the same frequency range. (b) Electric and magnetic resonant scatterers are different particles but located in the same crystal planes.

For polarizabilities of electric and magnetic dipole scatterers, the Lorentz dispersion model can be written in the form (see e.g., in [24]):

$$a_{ee} = \frac{A_e \varepsilon_0 V}{1 - \left(\frac{\omega}{\omega_e}\right)^2 + j\Gamma_e \omega}, \qquad a_{mm} = \frac{\mu_0 V A_m \omega^2}{\omega_m^2 - \omega^2 + j\Gamma_e \omega}, \tag{11.9}$$

where normalized resonance amplitudes A_e, $A_m > 0$ and resonant frequencies $\omega_{e,m}$ (electric and magnetic) can be found for explicit cases numerically or analytically. Dissipative losses that exist in real structures are neglected in this stage to observe the band structure of the lattice, which is possible only with a real-valued equation. Therefore, in this stage of the theory, parameters $\Gamma_{e,m}$ describe only the radiation damping of scatterers. Since no radiation losses exist in regular arrays, $\Gamma_{e,m}$ do not enter the dispersion equation. Really, after substituting relations (Equation 11.9) into Equation 11.7 the shunt imittance and series reactance of the individual crystal plane take the form of, respectively, imittance and reactance of lossless parallel circuits:

$$G = -jY_0 = \omega C_{\text{eff}} \left(1 - \frac{\omega_G^2}{\omega^2}\right), \tag{11.10}$$

$$X = -jZ_0 = \frac{\omega L_{\text{eff}}}{\left(1 - \frac{\omega^2}{\omega_X^2}\right)}. \tag{11.11}$$

It is easy to derive the dispersion equation of the equivalent PLTL. Following the theory of PLTL [41,44] it reads as $\cos qa = A$, where A is the element of the ABCD matrix $\mathbf{F_1}$ determined by the relation given in Equation 11.5. It is easy to calculate this ABCD matrix as the product of the transfer matrices of two host transmission lines of length $a/2$ and the transfer matrix of the loading T-circuit: $\mathbf{F_1} = \mathbf{F}_{\text{TL}}\mathbf{F}_{\text{load}}\mathbf{F}_{\text{TL}}$, where

$$\mathbf{F}_{\text{TL}} = \begin{bmatrix} \cos(ka/2) & j\frac{\eta}{\eta_0}\sin(ka/2) \\ -j\frac{\eta_0}{\eta}\sin(ka/2) & \cos(ka/2) \end{bmatrix}, \quad \mathbf{F}_{\text{load}} = \begin{bmatrix} 1 + \frac{YZ}{2} & Z\left(1 + \frac{YZ}{4}\right) \\ G & 1 + \frac{YZ}{2} \end{bmatrix}. \tag{11.12}$$

After algebraic calculations we obtain

$$\cos qa = \cos ka \left(1 + \frac{YZ}{4}\right) + \frac{j}{2}\left(Y + Z + \frac{YZ^2}{4}\right)\sin ka. \tag{11.13}$$

In the general case the loads Y and Z in Equation 11.13 cannot be identified with local admittance and impedance Y_0, Z_0 in Equation 11.8. However, in the special case when $2\sqrt{|Y_0 Z_0|} \ll \sin(ka)|Y_0 - Z_0|$ the term containing the product $Y_0 Z_0$ in the right-hand side of Equation 11.8 becomes small. Then the right-hand side of the equation is weakly dependent on q. This is the case of Bloch lattices when $Y \approx Y_0$ and $Z \approx Z_0$ (one of these values should be very small compared with the other one). Then solutions of the "p–m-lattice" dispersion Equation 11.8 and the "PLTL" dispersion Equation 11.13 are close to one another. Equations 11.8 and 11.13 perfectly coincide when $Y_0 = 0$ (only magnetic dipoles in the lattice) and when $Z_0 = 0$ (only electric dipoles). Here we list possible cases of Bloch lattices:

- Resonant p-lattices (the magnetic resonance of particles occurs outside the frequency region under study or is very weak).
- Resonant m-lattices (the electric resonance of particles occurs outside the region under study or is very weak).
- Some I–m-lattices (lattices formed by long perfectly conducting wires and magnetic scatterers as in [38]).

For the last case the approximation of Bloch lattices is applicable only within the resonance band of magnetic scatterers (metal split rings) and only when the wave propagates in the plane orthogonal to wires [39]. Then the wires are equivalent to inductive shunt loads, which are not resonant and weakly dependent on frequency. Their interaction with magnetic scatterers influences only the losses [40], and if losses are negligible the structure can be considered as a Bloch lattice [46]. Notice that in small particles possessing resonant magnetic and nonresonant electric response (for small 3D particles it is quasi-static) the electric susceptibility of the lattice can be simply added to the permittivity ε_m of host medium. Therefore, the MTM consisting of wires and SRRs can be considered as a resonant m-lattice in the modified host dielectric medium.

When p-dipoles and m-dipoles resonate at close frequencies $\omega_e \approx \omega_m$ and the resonance amplitudes are also close to one another ($A_e \approx A_m$), the approximation of the Bloch lattice is hardly adequate.

11.7 Extraction of Lorentz's Material Parameters

As already noticed the Lorentz EMP are local material parameters that can be attributed to infinite as well as to finite lattices if only the homogenization is allowed. They can be extracted from coefficients $R^{(1)}$ and $T^{(1)}$ of a monolayer without involving Drude layers. The idea of this extraction is illustrated by Figure 11.7. The case when the grid of resonant particles is located in the middle of the host medium slab is shown, but this is not mandatory, and the approach can be applied for arbitrary distances from the grid of particles to the surface of the dielectric slab (if we know this distance). Knowing the parameters k and η of host medium, we can extract the effective loads $Y = Y_0$ and $Z = Z_0$ from R–T coefficients. Knowing parameters $G = -jY$ and $X = -jZ$ and using Equation 11.7, we can find individual polarizabilities a_{ee} and a_{mm} of particles. Then one can, for example, apply the Lorentz–Lorenz formulas, i.e., find EMP in a usual quasi-static way.

Alternatively, after finding G and X we can solve the dispersion equation (Equation 11.8), find the refraction index of the infinite lattice, and find EMP from formulas relating the Lorentz EMP with dispersion characteristics of the lattice. These formulas are given in [20]. The extraction in the present symmetric geometry of the monolayer is based on Equations 11.6 and 11.12, which after the inversion

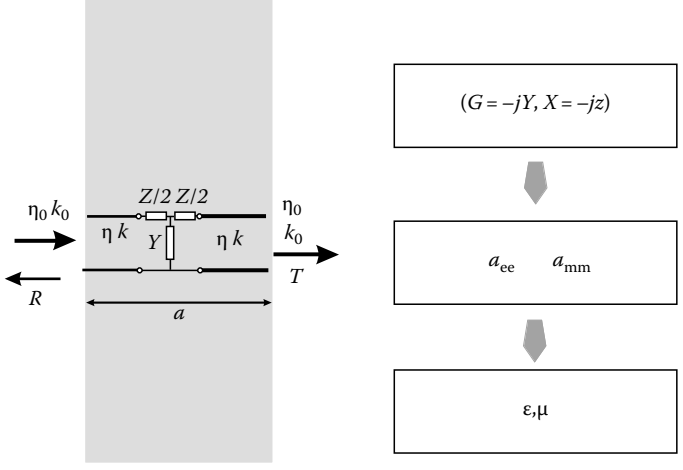

FIGURE 11.7 Idea of the extraction of Lorentz material parameters from R–T coefficients for a monolayer.

of the ABCD matrix $\mathbf{F}_{TL}$ gives the following result:

$$G = \frac{1}{\cos^2 ka}\left(\frac{j\eta_0 A}{2\eta} + \frac{\eta_0^2 C\cos^2(ka/2) - \eta^2 B\sin^2(ka/2)}{\eta_0^2}\right), \tag{11.14}$$

$$X = \frac{2}{G}\left(1 - \frac{A + j\frac{\eta_0(B-C)}{2\eta}\sin ka}{\cos^2 ka}\right), \tag{11.15}$$

where components of the ABCD matrix A, B, and C are expressed through measured or simulated $R-T$ coefficients as follows:

$$A = \frac{1 \pm \sqrt{2(R^{(1)})^2 + 2(T^{(1)})^2 - 1}}{2T^{(1)}}, \quad B = \frac{1 + R^{(1)}}{T^{(1)}} + A, \quad \text{and} \quad C = \frac{1 - A^2}{B}.$$

The same idea can be implemented for the case when the grid is located nonsymmetrically with respect to the center of the host medium slab.

It is possible to extract the Lorentz EMP from $R^{(N)}$ and $T^{(N)}$ for arbitrary N if the composite slab is a Bloch lattice. The easiest way to do it is to relate the Lorentz (wave) impedance of the homogenized medium with the Bloch impedance Z_B of the lattice. This was done in [20] for the case when the host medium is free space $\varepsilon_m = 1$. The formulas for the case when $\varepsilon_m \neq 1$ take the form [46]

$$\varepsilon_L = \frac{n(n + Z_-\varepsilon_m)}{(1 + nZ_-)}, \quad \mu_L = \frac{n(1 + nZ_-)}{(n + Z_-\varepsilon_m)}, \tag{11.16}$$

$$Z_- = \frac{Z_B - j\frac{\eta}{\eta_0}\tan\left(\frac{ka}{2}\right)}{1 - jZ_B\frac{\eta}{\eta_0}\tan\left(\frac{ka}{2}\right)}. \tag{11.17}$$

Here $n = q/k_0$ and $Z_c = Z_B$ are results of the direct extraction defined by formulas (Equations 11.2 and 11.3).

Equations 11.16 and 11.17 allow us to use graphic data presented in Figure 11.3 to calculate the Lorentz EMP for the array of oxide ceramic cylinders shown in Figure 11.2. Using similar data presented in Figure 11.4, we can do the same for the lattice of SRRs. The results are presented in Figures 11.8 and 11.9.

In both these examples the result of the extraction of Lorentz's EMP satisfies the locality requirements outside the "stop-band regions." However, we should not attribute any physical meaning to EMP extracted at the "stop-band" frequencies where the homogenization is not allowed. There is no physical reason for a strong electric resonance in the lattice of cylinders at 4 GHz. And we can see in Figure 11.8b that the frequency behavior of ε_L below the lower edge of the "stop-band" (3.9 GHz) is quasi-static. The frequency variation of the extracted permittivity at 4.7–5.5 GHz is probably due to the spatial dispersion appearing in the lattice from this frequency range.

For the lattice of SRRs we can observe in Figure 11.9 the resonance of the extracted local permittivity. It grows versus frequency below the resonant "stop-band" where the homogenization is definitely allowed. The resonance of the permittivity of SRRs holds in the same frequency range as that of the permeability. And it must be for SRRs of coplanar design [45,47]. The assertion in [3] and [8] that the resonance of these SRRs is purely magnetic was never argued about in the literature. In fact the lattice of such SRRs is the p–m lattice, and the approximation of Bloch lattices is not completely adequate for it. However, in [3] and [8] it was claimed that the extracted material parameters turned out to be almost the same for $N = 2$ and for $N = 4$. This probably means that the approximation of the Bloch lattice holds with acceptable accuracy. We can observe in Figure 11.9 that the electric resonance is twice as weaker as the magnetic one. This can be enough to neglect the influence of p-dipoles on the dispersion and to consider this lattice as a Bloch lattice, too.

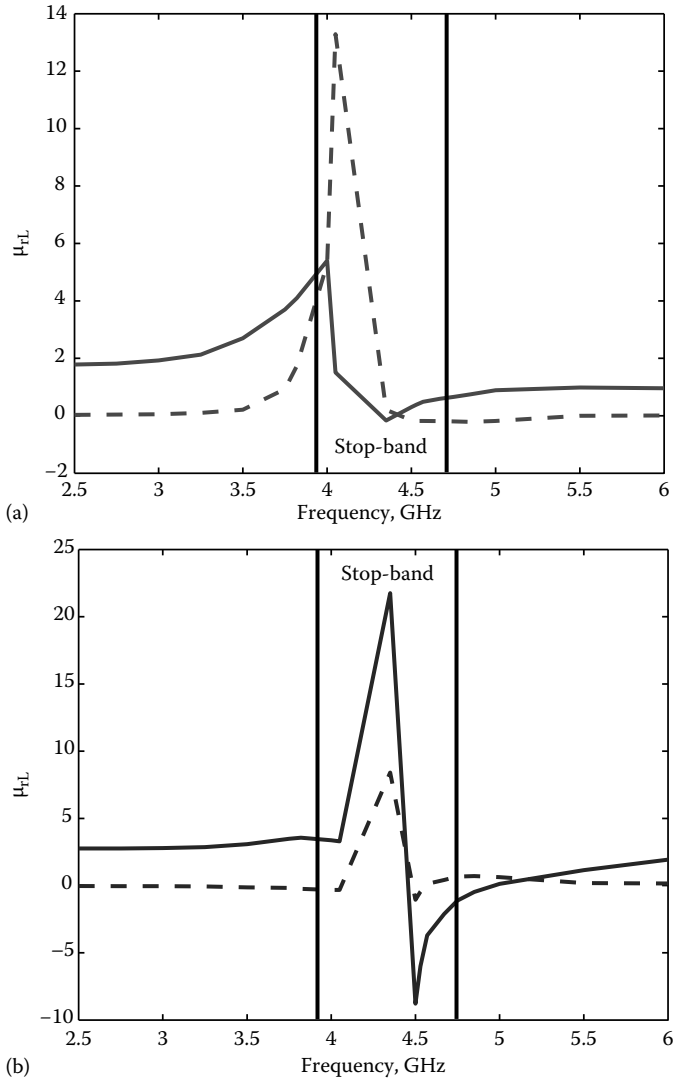

FIGURE 11.8 (a) Lorentz permeability extracted for the array of cylinders. (b) Lorentz permittivity extracted for the array of cylinders. Solid lines—real part of material parameters, dashed lines—imaginary parts.

11.8 Discussion

The use of the Lorentz EMP requires involving transition layers to calculate R and T coefficients of slabs. However, these EMP as well as parameters of the transition layer do not depend on the propagation direction. Once calculated we can apply them in the reflection problem for arbitrary angles of incidence, for wave packages, and even for real sources positioned outside the composite slab [32].

The practical importance of material parameters extracted directly using Equations 11.2 and 11.3 is much smaller. Being introduced through the refraction index and the Bloch impedance of semi-infinite crystal, the Ewald–Bloch EMP give the correct value for R of a semi-infinite crystal without

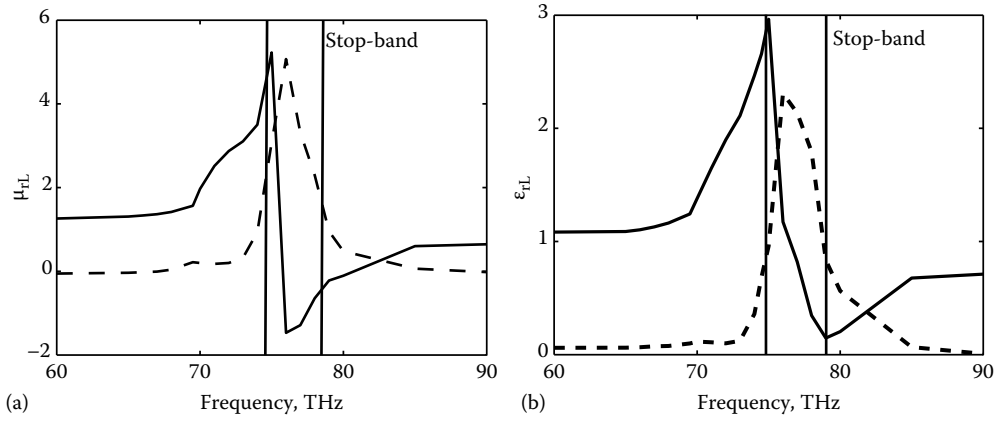

FIGURE 11.9 (a) Lorentz permeability extracted for the array of SRRs. (b) Lorentz permittivity extracted for the array of SRRs. Solid lines—real part of material parameters, dashed lines—imaginary parts.

transition layers.* If the lattice under study can be approximated as a Bloch lattice, these parameters also describe the reflection and transmission of the normally incident plane wave in a finite-thickness lattice without involving transition layers. However, this is the only advantage of these material parameters. These parameters are simple numbers and do not offer information on the eigenmodes excited in the finite lattice. They can be, probably, introduced also for the oblique incidence but will be definitely different for different angles of incidence.

The main restriction for the Ewald–Bloch EMP is that they are absolutely not applicable for evanescent waves and for any package of plane waves. If we assume that the Ewald–Bloch material parameters allow us to find the reflection coefficients for evanescent waves, we will come to the artifact of perpetuum mobile. One of material parameters extracted in works [2–12] (see also Figures 11.3, 11.4) has the imaginary part of the wrong sign.† Assume that we impinge the structure with negative electric losses $\mathrm{Im}(\varepsilon) > 0$ for time dependence $\exp(j\omega t)$ (or $\mathrm{Im}(\varepsilon) < 0$ for $\exp(-j\omega t)$) by evanescent waves, for example, by the near field of an electric antenna or simply putting the sample into a capacitor excited by alternating voltage at the frequency when the sign of the permittivity is wrong. Since the electric field in this case strongly dominates over the magnetic one, the wrong sign of $\mathrm{Im}(\varepsilon_{\mathrm{eff}})$ means the generation of the electric energy. The same artifact holds for packages of propagating waves. If we put the sample with negative electric losses into a resonator where the maximum of the electric field and the zero of the magnetic field hold at the same point, the electric energy will be also "generated."

One has to conclude that EMP directly extracted using formulas (Equations 11.2 and 11.3) cannot be applied in boundary problems with evanescent waves and plane-wave packages even for Bloch lattices. Recall that the effect of subwavelength imaging in doubly negative (left-handed) media is related with evanescent waves [42]. It is therefore impossible to design the Pendry superlens [42] using the directly retrieved material parameters. If we want to design the Pendry's perfect lens we must engineer EMP that would be meaningful for the evanescent spatial spectrum. The Lorentz material parameters

* In fact, this is the approximation in which we neglect the so-called polaritons [29–43]. If the influence of polaritons is not negligible, the Ewald–Bloch EMP give an error for R as well.

† The anomalous sign of the imaginary part for one of the EMP does not lead to a trouble if and only if we deal with an only propagating plane wave. Then the losses are determined by the product of Ewald–Bloch parameters $\varepsilon_{\mathrm{eff}}\mu_{\mathrm{eff}} = (q/k)^2 = n^2$, and this product is correct.

are meaningful in this case. Another evident conclusion is as follows: in order to design the superlens based on left-handed media one has to generalize the theory [42] taking into account the influence of Drude transition layers.

The same concerns boundary problems with packages of plane waves. To design the so-called Engheta resonator [48]* we have to engineer doubly negative Lorentz EMP and take into account the transition layers.

References

1. A. P. Vinogradov, D. P. Makhnovskiy, and K. N. Rozanov, *J. Commun. Technol. Electron.*, **44** (1999) 317.
2. I. El-Kady, M. M. Sigalas, R. Biswas, K. M. Ho, and C. M. Soukoulis, *Phys. Rev. B*, **62** (2000) 15299.
3. S. O'Brien and J. B. Pendry, *J. Phys.: Condens. Matter*, **14** (2002) 4035.
4. D. R. Smith, S. Schultz, P. Markos, and C. Soukoulis, *Phys. Rev. B*, **65** (2002) 195104.
5. D. R. Smith, P. Kolinko, and D. Schurig, *J. Opt. Soc. Am. B*, **21** (2004) 1032.
6. K. C. Huang, M. L. Povinelli, and J. D. Joannopoulos, *Appl. Phys. Lett.*, **85** (2004) 543.
7. S. O'Brien and J. B. Pendry, *J. Phys.: Condens. Matter*, **14** (2002) 6383.
8. S. O'Brien, *Artificial Magnetic Structures*, PhD thesis, Imperial College of Science, Technology and Medicine, Department of Physics, available at: http://www.imperial.ac.uk/research/cmth/research/theses/S.OBrien.pdf
9. N. Katsarakis, G. Konstantinidis, A. Kostopoulos et al., *Opt. Lett.*, **30** (2005) 1348.
10. S. O' Brien, D. McPeake, S. A. Ramakrishna, and J. B. Pendry, *Phys. Rev. B*, **69** (2004) 241101.
11. N. Katsarakis, T. Koschny, M. Kafesaki, E. N. Economou, E. Ozbay, and C. M. Soukoulis, *Phys. Rev. B*, **70** (2004) 201101(R).
12. N. Katsarakis, T. Koschny, M. Kafesaki, E. N. Economou, and C. M. Soukoulis, *Appl. Phys. Lett.*, **84** (2004) 2943.
13. G. Dolling, C. Enkrich, M. Wegener et al., *Science*, **312** (2006) 892.
14. U. K. Chettiar, A. V. Kildishev, T. A. Klar, and V. M. Shalaev, *Opt. Expr.,* **30** (2006) 7872.
15. G. Dolling, M. Wegener, S. Linden, *Opt. Lett.*, **32** (2007) 551.
16. V. M. Shalaev, W. Cai, U. K. Chettiar et al., *Opt. Lett.*, **30** (2005) 3356.
17. G. Dolling, C. Enkrich, M. Wegener et al., *Opt. Lett.*, **31** (2006) 1800.
18. G. Dolling, M. Wegener, C. Soukoulis et al., *Opt. Lett.*, **32** (2007) 53.
19. L. D. Landau and E. M. Lifshitz, *Electrodynamics of Continuous Media*, Pergamon Press, Oxford, 1960.
20. C. R. Simovski and S. A. Tretyakov, *Phys. Rev. B*, **75** (2007) 195111.
21. C. Simovski and S. He, *Phys. Lett.*, **A 311** (2003) 254.
22. P. Ewald, *Annalen der Physik*, **64** (1921) 2943.
23. P. Ewald, *ZS f. Kristallen*, **54** (1921) 129.
24. M. Born and Kun Huang, *Dynamic Theory of Crystal Lattices*, Oxford Press, Oxford, 1954.
25. M. Born and E. Wolf, *Principles of Optics*, Pergamon Press, Oxford, 1989.
26. J. Sipe and J. V. Kranendonk, *Phys. Rev.*, **A 9** (1974) 1806.
27. L. Mandelstam, *Phys. Z*, **9** (1908) 641.
28. M. Planck, *Sitzungsber. Konig. Preuss Acad.*, **24** (1902) 470; see also ibid. **24** (1904) 480.
29. P. A. Belov and C. R. Simovski, *Phys. Rev. B*, **73** (2006) 045102.
30. J. D. Jackson, *Classical Electrodynamics*, 2nd Ed., Wiley, New York, 1998.
31. X. Chen, T. Grzegorczyk, B.-E. Wu, J. Pacheko, and J. A. Kong, *Phys. Rev., E*, **70** (2004) 016608.

* It is a very thin resonator based on the paired slabs of doubly negative medium and of usual medium, for example, simple dielectric.

32. C. R. Simovski, *Weak Spatial Dispersion in Composite Media*, Politekhnika Publishers, St. Petersburg, 2003 (in Russian).
33. C. R. Simovski, S. He, and M. Popov, *Phys. Rev. B*, **62** (2000) 13718.
34. C. R. Simovski, S. A. Tretyakov, A. H. Sihvola, and M. Popov *Eur. Phys. J.: Appl. Phy.*, **9** (2000) 195.
35. C. R. Simovski, B. Sauviac, *Eur. Phys. J.: Appl. Phys.*, **17** (2002) 11.
36. C. L. Holloway, E. F. Kuester, J. Baker-Jarvis, and P. Kabos., *IEEE Trans. Antenn. Propag.*, **51** (2003) 2596.
37. L. Jylhä, I. Kolmakov, S. Maslovski, and S. Tretyakov, *J. Appl. Phys.*, **99** (2006) 043102.
38. R. A. Shelby, D. R. Smith, and S. Schultz, *Science*, **292** (2001) 77.
39. C. Simovski, P. A. Belov, and S. He, *IEEE Trans. Antenn. Propag.*, **51** (2003) 2582.
40. C. Simovski and B. Sauviac, *Phys. Rev. E*, **70** (2004) 046607.
41. C. Caloz and T. Itoh, *Electromagnetic Metamaterials: Transmission Line Theory and Microwave Applications*, John Wiley and Sons, New York, 2006.
42. J. B. Pendry, *Phys. Rev. Lett.*, **85** (2000) 3966.
43. G. Mahan and G. Obermair, *Phys. Rev.*, **183** (1969) 834.
44. G. Eleftheriades and K. G Balmain, *Negative-Refraction Metamaterials: Fundamental Principles and Applications*, Wiley, New York, 2006.
45. S. Anantha Ramakrishna, *Rep. Prog. Phys.*, **68** (2005) 449.
46. C. R. Simovski, *Metamaterials*, **1** (2007) 62.
47. B. Sauviac, C. Simovski, and S. Tretyakov, *Electromagnetics*, **24** (2004) 317.
48. N. Engheta, *IEEE Trans. Antenn. Wireless Propag. Lett.*, **1** (2002) 10.

12

Field Representations in Periodic Artificial Materials Excited by a Source

Filippo Capolino
University of California Irvine

David R. Jackson
University of Houston

Donald R. Wilton
University of Houston

12.1 Introduction

This chapter aims to provide a simple framework for field representation in infinite periodic structures that are excited by a single (nonperiodic) source. This chapter thus complements well the other chapters in this book, since most artificial materials are periodic. For simplicity and for the sake of brevity, we deal with the most common case of a structure that is periodic in two directions and composed of one or more layered arrays of three-dimensional (3D) elements. The case of 3D periodicity

or the case of two-dimensional (2D) or 3D elements with one-dimensional (1D) periodicity is an extension of what is treated here.

The use of periodic artificial materials (PAMs) has been investigated for antennas, microwave devices [1–21], and many other applications in the optical regime. Examples include the creation of artificial magnetism [18–21] and superlens devices (see Part I of *Applications of Metamaterials*), as well as electromagnetic bandgap (EBG) materials that are used to suppress surface-wave propagation [3–6]. A periodic wire medium has also been used as an artificial dielectric [7–9]. In other applications, a PAM has been used to create an artificial magnetic conductor (AMC) (see [10–12] and references therein), and placing an antenna near the AMC has been used to create low-profile antennas [11,12]. Also, it has been demonstrated that a PAM can be used to create directed beams [11–17]. Enhanced directivity has been related to leaky-wave excitation, whereby a periodic leaky-wave antenna is created, which is periodic and is excited by a simple source such as a dipole or line source within the periodic structure [13–17]. Other applications of PAMs at microwave and optical frequencies can be seen in most of the chapters of this handbook, and we suggest the reader to look at these and their reference lists for completeness.

We aim at keeping this chapter as general as possible, so that the fundamental principles discussed here can be applied to any problem involving the field due to a single (nonperiodic) source in the presence of an infinite 2D PAM (including structures composed of metal or dielectric elements). Some of the related numerical implementation issues are also discussed. Although the general case of a skewed lattice could be treated, the discussion is limited here to a rectangular lattice with periods a and b along the x- and y-axes, respectively. A typical periodic structure (with a metallic cross element in the unit cell) is shown in Figure 12.1, which presents the dipole source location $\mathbf{r}_0 = (x_0, y_0, z_0)$ and the observation point $\mathbf{r} = (x, y, z)$.

The discussion of field representations provided here has two purposes: to provide an efficient numerical scheme for the field calculation and to gain physical insight into the field species in a PAM excited by a source. Accordingly, we first review how the field produced by a dipole source in the presence of an infinite PAM may be calculated by a direct plane-wave expansion method. Although this method is well known and (as shown here) is not the most efficient method, it is useful as a benchmark for comparison.

We also review the array scanning method (ASM) for calculating the field due to a single dipole source near an infinite PAM. This method has been introduced previously and used in the analysis of

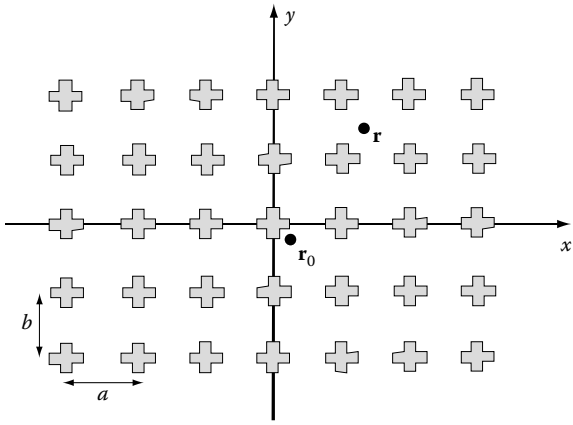

FIGURE 12.1 2D periodic structure made of a rectangular lattice of scatterers with a dipole source at $\mathbf{r}_0$ and an observation point at $\mathbf{r}$. (From Capolino, F., Jackson, D.R., Wilton, D.R., and Felsen, L.B., *IEEE Trans. Antennas Propag.*, 55(6), 1644, June 2007. With permission.)

phased arrays [22–25] and also successively used in the context of EBG materials and metamaterials [26–30]. The method has also been discussed recently in the context of analyzing the fields and their properties near 1D or 2D PAM structures [31–33]. The ASM has been used in various applications in recent years [34–45].

In the ASM method, the PAM (supposed here to be 2D periodic) is excited by an infinite periodic array of dipole sources that have the same period as the PAM and which are phased with variable transverse wave numbers (k_x, k_y). An integration in (k_x, k_y) (i.e., scanning the phased dipole array) over the Brillouin region, $-\pi/a < k_x < \pi/a$ and $-\pi/b < k_y < \pi/b$, recovers the field produced by the single dipole source near the infinite PAM.

In addition to providing a very efficient method for calculating the field of a dipole source near a PAM, it is shown how the ASM may be used to efficiently calculate the Fourier transform of the field at any aperture plane of interest. This is useful for performing asymptotic analysis, since such analyses often start with the assumption that the relevant integrals that describe the field are in the form of an inverse transform integral (i.e., a spectral-domain representation). Having the field expressed in this form is also useful for complex path deformations to identify the types of wave phenomena that are present and to determine the launching amplitude of surface and leaky waves. The ASM provides a more efficient calculation of the transform of the field than does the direct plane-wave expansion method or an alternative reciprocity-based method [33].

An understanding of the nature of the k_x and k_y planes in the ASM is important for an asymptotic evaluation of the field along the interface of the PAM. It is shown that, due to the periodic nature of the problem, there is an infinite periodic set of branch-point loci. Furthermore, there is also an infinite set of periodic pole loci that lead to surface and leaky waves. A discussion of these issues is given so that the numerical aspects in the implementation of the ASM can be understood.

Based on the discussion of the important singular points in the wave number plane, an asymptotic description of the field near the PAM boundary excited by a single dipole source is given for large source-observer distances. The field is composed of a spatial wave, similar to the field excited by the source without the PAM, plus modal field contributions that can be bound or leaky (radiating) modes. The modal field terms have either forward or backward propagation.

In this chapter, a time-harmonic variation $\exp(j\omega t)$ is assumed, unless otherwise stated (as in the sections dealing with time-domain field expansions). If $f(\mathbf{r})$ is a time-harmonic field value relative to $\exp(j\omega t)$, the corresponding field value relative to $\exp(-i\omega t)$ is $f^*(\mathbf{r})$, where "*" denotes phase conjugation.

12.2 Quasiperiodic Fields in Periodic Structures

The standard Floquet (space harmonic) representation of the field in a PAM is briefly summarized here, and this serves as a background for the succeeding sections. For simplicity, we consider only the case of a PAM that is periodic in 2D; the 1D and 3D cases are analogous. Consider the problem illustrated in Figure 12.1 where the PAM is periodic along the two directions x and y, with periods a and b, respectively, and layered along the z-direction (i.e., there may be multiple layers of the periodic elements). We start by assuming that a field is present in the PAM, either excited by an incident plane wave or due to a guided mode on the structure. The electric field $\mathbf{E}$ is "quasiperiodic," which means that it is periodic except for an interelement phase shift, so that $\mathbf{E}(\mathbf{r} + a\hat{\mathbf{x}} + b\hat{\mathbf{y}}, \mathbf{k}_t) = \mathbf{E}(\mathbf{r}, \mathbf{k}_t)e^{-j(k_x a + k_y b)}$, where $\mathbf{r} = x\hat{\mathbf{x}} + y\hat{\mathbf{y}} + z\hat{\mathbf{z}}$ is an arbitrary observation position. (Here and in the following, boldface symbols are used to identify vector quantities and the caret "$\wedge$" identifies unit vectors.) The terms k_x and k_y are the propagation wave numbers along the x- and y-directions, and these constitute the transverse wave number vector $\mathbf{k}_t$ as

$$\mathbf{k}_t = k_x\hat{\mathbf{x}} + k_y\hat{\mathbf{y}}. \tag{12.1}$$

It is easy to recognize that $\mathbf{E}^p(\mathbf{r},\mathbf{k}_t) \equiv \mathbf{E}(\mathbf{r},\mathbf{k}_t)e^{j(k_x x+k_y y)}$ is periodic along the x- and y-directions, with periods a and b, respectively, and thus can be represented in terms of a Fourier series expansion. Accordingly, the electric field $\mathbf{E}$ at any position is represented in terms of a superposition of "Floquet spatial harmonics" as

$$\mathbf{E}(\mathbf{r},\mathbf{k}_t) = \sum_{p=-\infty}^{\infty}\sum_{q=-\infty}^{\infty} e^{-j(k_{xp}x+k_{yq}y)}\mathbf{e}_{pq}(z,\mathbf{k}_t), \tag{12.2}$$

where

$$k_{xp} = k_x + F_{xp}, \quad F_{xp} = \frac{2\pi p}{a} \tag{12.3}$$

$$k_{yq} = k_y + F_{yq}, \quad F_{yq} = \frac{2\pi q}{b}. \tag{12.4}$$

The terms k_{xp}, k_{yq} are the Floquet wave numbers, and $\mathbf{e}_{pq}(z,\mathbf{k}_t)$ is the amplitude of the pqth harmonic that accounts for all the z-variation of the field. Analogous expressions hold for the magnetic field and also for the potential fields. Usually, by convention, the transverse wavevector $\mathbf{k}_t = \hat{\mathbf{x}}k_{x0} + \hat{\mathbf{y}}k_{y0}$ corresponds to the transverse wave number of the incident field.

12.3 Field Produced by a Single Source in the Presence of a Periodic Medium: Standard Plane-Wave Expansion

The case of a PAM excited by a single dipole source, as shown in Figure 12.1, is important for many applications, and it provides physical insight into wave propagation in source-excited PAMs. The PAM structure in Figure 12.1 is periodic along x and y, with periods a and b, respectively. The structure may also be periodic along z, truncated after a finite number of layers, thereby constituting a slab of artificial material. In this case, the term "supercell" is used to denote a unit cell in the x- and y-directions (which contains multiple conductors spaced along z). For simplicity, we treat here only the case of electric dipole excitation. The impressed unit-amplitude electric dipole source at $\mathbf{r}_0 = x_0\hat{\mathbf{x}} + y_0\hat{\mathbf{y}} + z_0\hat{\mathbf{z}}$ is represented by the direction vector $\hat{\mathbf{p}}_0$ (which may be $\hat{\mathbf{x}}$, $\hat{\mathbf{y}}$, $\hat{\mathbf{z}}$, or any other direction), with units [Cm]. Mathematically, the dipole moment polarization density is represented as

$$\mathbf{P}^i(\mathbf{r}') = \hat{\mathbf{p}}_0\delta(\mathbf{r}' - \mathbf{r}_0), \tag{12.5}$$

where $\delta(\mathbf{r}' - \mathbf{r}_0) = \delta(x' - x_0)\delta(y' - y_0)\delta(z' - z_0)$.

In [33], we have considered the analogous case of an electric current density excitation $\mathbf{J}$ $[\mathrm{A/m^2}]$ that is related to the one in this chapter by the equivalence $\mathbf{J} = j\omega\mathbf{P}$ with $\mathbf{P}$ $[\mathrm{C/m^2}]$, the volume dipole polarization density.

In what follows, we represent a general observation point (which may be located in the (m,n)th unit cell) as $\mathbf{r} + ma\hat{\mathbf{x}} + nb\hat{\mathbf{y}}$, where $\mathbf{r}$ is assumed to lie within the (0,0)th unit cell.

12.3.1 Calculation of the Field

The field in free space at $\mathbf{r}$ radiated by a single unit-amplitude dipole source at $\mathbf{r}_0$ without the presence of PAM is denoted by $\mathbf{E}_{\mathrm{inc}}(\mathbf{r},\mathbf{r}_0)$, and it can be represented in terms of a standard plane-wave superposition as

$$\mathbf{E}_{\mathrm{inc}}(\mathbf{r},\mathbf{r}_0) = \frac{-j}{8\pi^2}\int_{-\infty}^{\infty}\int_{-\infty}^{\infty}\frac{1}{k_z}\underline{\mathbf{G}}(\mathbf{k}_t)\cdot\hat{\mathbf{p}}_0 e^{-j[k_x(x-x_0)+k_y(y-y_0)+k_z|z-z_0|]}\mathrm{d}k_x\mathrm{d}k_y, \tag{12.6}$$

$$\underline{\mathbf{G}}(\mathbf{k}_t) = \frac{1}{\varepsilon}\left[k^2\underline{\mathbf{I}} - \mathbf{kk}\right], \tag{12.7}$$

where $\mathbf{k} = k_x\hat{\mathbf{x}} + k_y\hat{\mathbf{y}} \pm k_z\hat{\mathbf{z}}$, $k_z = (k^2 - k_x^2 - k_y^2)^{1/2}$, and $\mathbf{k}_t = k_x\hat{\mathbf{x}} + k_y\hat{\mathbf{y}}$ is the transverse part of $\mathbf{k}$. The term $\underline{\mathbf{I}}$ is the identity dyad. The square root that defines k_z is chosen such that Im $k_z \leq 0$. For lossless media k_z can also be real, in which case the choice is Re $k_z \geq 0$. The plus (minus) sign is used when the observation point is above (below) the source point. (We note here for the benefit of the readers that in [33, (2–3)] there are three sign errors.)

Assuming, for simplicity, that the dipole source is above the periodic structure, the incident field from the dipole source that illuminates the periodic structure is a continuum of plane waves of the form

$$\mathbf{E}_{\text{inc}}^{\text{PW}}(\mathbf{r}, \mathbf{r}_0, \mathbf{k}_t) = \hat{\mathbf{e}}_{\text{inc}}(\mathbf{k}_t)\, W_{\text{inc}}(\mathbf{k}_t, \mathbf{r}_0)\, e^{-j[k_x x + k_y y - k_z z]}, \tag{12.8}$$

with

$$W_{\text{inc}}(\mathbf{k}_t, \mathbf{r}_0) = \frac{-j}{8\pi^2}\frac{1}{k_z}\hat{\mathbf{e}}_{\text{inc}} \cdot \underline{\mathbf{G}}(\mathbf{k}_t) \cdot \hat{\mathbf{p}}_0 e^{j[k_x x_0 + k_y y_0 - k_z z_0]}. \tag{12.9}$$

Each incident plane wave in the spectrum is polarized in a direction $\hat{\mathbf{e}}_{\text{inc}}(\mathbf{k}_t) = \underline{\mathbf{G}}(\mathbf{k}_t) \cdot \hat{\mathbf{p}}_0 / |\underline{\mathbf{G}}(\mathbf{k}_t) \cdot \hat{\mathbf{p}}_0|$. The total field due to a unit-amplitude incident plane wave $\overline{\mathbf{E}}_{\text{inc}}^{\text{PW}}(\mathbf{r}, \mathbf{k}_t) = \hat{\mathbf{e}}_{\text{inc}}(\mathbf{k}_t)\, e^{-j[k_x x + k_y y - k_z z]}$ with transverse wave number $\mathbf{k}_t$ is denoted as $\overline{\mathbf{E}}_{\text{tot}}^{\text{PW}}(\mathbf{r}, \mathbf{k}_t)$. (A bar over a quantity is used here to signify that the quantity is either a unit-amplitude incident plane wave or is produced by such an incident wave.) Similarly, the scattered field due to a unit-amplitude incident plane wave is denoted as $\overline{\mathbf{E}}_{\text{sca}}^{\text{PW}}(\mathbf{r}, \mathbf{k}_t)$.

The scattered $\overline{\mathbf{E}}_{\text{sca}}^{\text{PW}}(\mathbf{r}, \mathbf{k}_t)$ or total $\overline{\mathbf{E}}_{\text{tot}}^{\text{PW}}(\mathbf{r}, \mathbf{k}_t)$ electric fields produced by a unit-amplitude incident plane wave $\overline{\mathbf{E}}_{\text{inc}}^{\text{PW}}(\mathbf{r}, \mathbf{k}_t)$ may be found by using a full-wave method within the $(m,n) = (0,0)$ supercell. Several methods could be used, such as the method of moments (MoM) [46,47], the FDTD method [43,48], or other techniques. Once a numerical procedure is applied, suppose that the dipole moment density $\overline{\mathbf{P}}_D^{\text{PW}}(\mathbf{r}', \mathbf{k}_t)$ is found on the domain D_0 comprising the scattering elements within the $(m, n) = (0, 0)$ supercell. The field scattered by the PAM is then given as (for isolated dipoles, the integral should be replaced by a sum)

$$\overline{\mathbf{E}}_{\text{sca}}^{\text{PW}}(\mathbf{r}, \mathbf{k}_t) = \int_D \underline{\mathbf{G}}^{\infty}(\mathbf{r}, \mathbf{r}', \mathbf{k}_t) \cdot \overline{\mathbf{P}}_D^{\text{PW}}(\mathbf{r}', \mathbf{k}_t)\, d\mathbf{r}'. \tag{12.10}$$

The free-space periodic Green's function is

$$\underline{\mathbf{G}}^{\infty}(\mathbf{r}, \mathbf{r}', \mathbf{k}_t) = \frac{1}{2jab}\sum_{p=-\infty}^{\infty}\sum_{q=-\infty}^{\infty} e^{-j(k_{xp}x + k_{yq}y)}\frac{1}{k_{zpq}}\underline{\mathbf{G}}(\mathbf{k}_{t,pq})\, e^{+j(k_{xp}x' + k_{yq}y' - k_{zpq}|z-z'|)}, \tag{12.11}$$

where the dyad $\underline{\mathbf{G}}(\mathbf{k}_{t,pq})$ is given by Equation 12.7 with $\mathbf{k}_t = \mathbf{k}_{t,pq}$ and the wavevector for each Floquet wave is $\mathbf{k}_{pq} = k_{xp}\hat{\mathbf{x}} + k_{yq}\hat{\mathbf{y}} + k_{zpq}\hat{\mathbf{z}}$, with a transverse wavevector

$$\mathbf{k}_{t,pq} = k_{xp}\hat{\mathbf{x}} + k_{yq}\hat{\mathbf{y}}. \tag{12.12}$$

The longitudinal Floquet wave number along z is

$$k_{zpq} = \sqrt{k^2 - k_{xp}^2 - k_{yq}^2}, \tag{12.13}$$

where k is the free-space wave number. We chose a representation that exhibits the singularity $1/k_{zpq}$ explicitly in Equation 12.11. Branch points are defined by $k_{xp}^2 + k_{yq}^2 = k^2$, corresponding to $k_{zpq} = 0$, and hence the branch-point singularity is evident in Equation 12.11.

The scattered field $\overline{\mathbf{E}}_{\text{sca}}^{\text{PW}}(\mathbf{r}, \mathbf{k}_t)$ radiated by the scattering structure when illuminated by a unit-amplitude incident plane wave can be expressed as a Floquet expansion as in Equation 12.2:

$$\overline{\mathbf{E}}_{\text{sca}}^{\text{PW}}(\mathbf{r}, \mathbf{k}_t) = \sum_{p=-\infty}^{\infty}\sum_{q=-\infty}^{\infty} e^{-j(k_{xp}x + k_{yq}y)}\overline{\mathbf{e}}_{\text{sca},pq}^{\text{PW}}(z, \mathbf{k}_t), \tag{12.14}$$

where the terms

$$\bar{\mathbf{e}}^{\mathrm{PW}}_{\mathrm{sca},pq}(z,\mathbf{k}_t) = \frac{-j}{2ab}\frac{1}{k_{zpq}}\underline{\mathbf{G}}\left(\mathbf{k}_{t,pq}\right)\cdot\int_D \bar{\mathbf{P}}^{\mathrm{PW}}_D(\mathbf{r}',\mathbf{k}_t)e^{+j\left[k_{xp}x'+k_{yq}y'-|z-z'|k_{zpq}\right]}\mathrm{d}\mathbf{r}' \tag{12.15}$$

are found by substituting Equation 12.11 in Equation 12.10. Note that Equation 12.14 represents the Floquet wave expansion of the scattered field. The term $\bar{\mathbf{e}}^{\mathrm{PW}}_{\mathrm{sca},pq}$ physically represents the amplitude of the (p,q)th Floquet mode scattered by the PAM due to a unit-amplitude incident plane wave.

The Floquet wave numbers k_{xp} and k_{yq} are given in Equations 12.3 and 12.4, and the expression $\bar{\mathbf{e}}^{\mathrm{PW}}_{\mathrm{sca},pq}(z,\mathbf{k}_t)$ has an infinite set of branch-point loci defined by $k_{xp}^2 + k_{yq}^2 = k^2$. This is evident from Equation 12.14. An explicit expression for a PAM composed of perfect conductors may be found in [33] for 2D-periodic structures, and in [32] for 1D-periodic structures.

The circular pq-branch-point loci in the real k_x, k_y plane are shown in Figure 12.2.

From superposition, the total field produced by the single dipole source $\mathbf{p}^i(\mathbf{r}')$ in the PAM environment is evaluated by summing all the fields produced by each plane wave in Equation 12.6 as the total field produced is

$$\mathbf{E}_{\mathrm{tot}}(\mathbf{r},\mathbf{r}_0) = \int_{-\infty}^{\infty}\int_{-\infty}^{\infty} W_{\mathrm{inc}}(\mathbf{k}_t,\mathbf{r}_0)\ \bar{\mathbf{E}}^{\mathrm{PW}}_{\mathrm{tot}}(\mathbf{r},\mathbf{k}_t)\,\mathrm{d}k_x\mathrm{d}k_y \tag{12.16}$$

and similarly for $\mathbf{E}_{\mathrm{sca}}$. The total field produced by a unit-amplitude plane wave is found to be $\bar{\mathbf{E}}^{\mathrm{PW}}_{\mathrm{tot}}(\mathbf{r},\mathbf{k}_t) = \bar{\mathbf{E}}^{\mathrm{PW}}_{\mathrm{sca}}(\mathbf{r},\mathbf{k}_t) + \bar{\mathbf{E}}^{\mathrm{PW}}_{\mathrm{inc}}(\mathbf{r},\mathbf{k}_t)$. Besides the infinite set of branch-point loci, the integrand in Equation 12.16 may also exhibit sets of real or complex poles in the complex k_x, k_y plane; some of them represent the physical modes that are excited by the source.

When the total field is evaluated by a numerical analysis, quite a large numerical effort is required to evaluate the 2D infinite integral in Equation 12.16 and the 2D infinite sum in Equation 12.14. A more efficient method for calculating the scattered field, using the ASM, is discussed in Section 12.4.

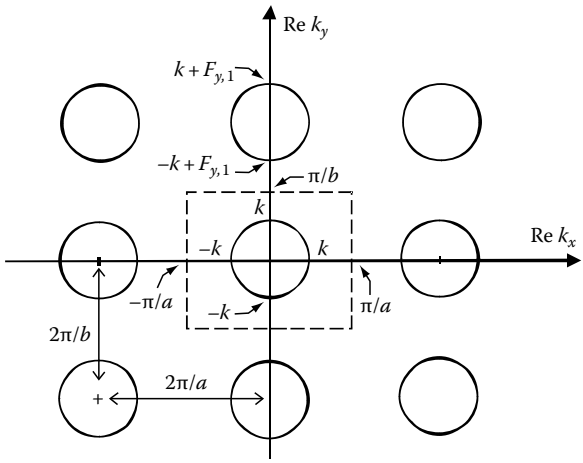

FIGURE 12.2 Periodic branch-point locus in the plane Re k_x, Re k_y. The area contained within the dashed line represents the Brillouin zone, which is used in the ASM. (From Capolino, F., Jackson, D.R., Wilton, D.R., and Felsen, L.B., *IEEE Trans. Antennas Propag.*, 55(6), 1644, June 2007. With permission.)

12.3.2 Calculation of the Fourier Transform of the Field

The total field in Equation 12.16 may be put in terms of an inverse Fourier transform integral by "collecting the spectrum." That is, all of the plane waves that have a wave number $\mathbf{k}_t$ are summed together, as shown in [33], which results in the following expression for the inverse Fourier transform:

$$\mathbf{E}_{\text{tot}}(\mathbf{r},\mathbf{r}_0) = \frac{1}{4\pi^2}\int_{-\infty}^{\infty}\int_{-\infty}^{\infty} e^{-j(k_x x+k_y y)}\,\tilde{\mathbf{E}}_{\text{tot}}\left(z,\mathbf{r}_0,\mathbf{k}_t\right)\mathrm{d}k_x\mathrm{d}k_y, \tag{12.17}$$

where

$$\tilde{\mathbf{E}}_{\text{tot}}\left(z,\mathbf{r}_0,\mathbf{k}_t\right) = 4\pi^2\sum_{p=-\infty}^{\infty}\sum_{q=-\infty}^{\infty} W_{\text{inc}}\left(\mathbf{k}_{t,pq},\mathbf{r}_0\right)\bar{\bar{\mathbf{e}}}^{\text{PW}}_{\text{tot},(-p)(-q)}\left(z,\mathbf{k}_{t,pq}\right) \tag{12.18}$$

is the Fourier transform of the field at a specified z. The integrand term $\tilde{\mathbf{E}}_{\text{tot}}$ has an infinite set of branch-point loci such that $k_{xp}^2 + k_{yq}^2 = k^2$, seen from the definition of the W_{inc} function in Equation 12.9 (see [33] for more details).

It is numerically intensive to compute the Fourier transform of the field at any z-value via Equation 12.18, since it requires the numerical solution of an infinite number of scattering problems involving an incident plane wave (i.e., an infinite number of incidence angles corresponding to wave numbers $\mathbf{k}_{t,pq}$). In Section 12.4, a more efficient method for obtaining the Fourier transform using the ASM is presented.

12.4 Field Produced by a Single Source in the Presence of a Periodic Medium: The Array Scanning Method

Before representing the field via the ASM [22–33], we show how the single dipole source $\mathbf{P}^i(\mathbf{r}')$ in Equation 12.5, oriented along the direction $\hat{\mathbf{p}}_0$, can be synthesized using this technique, that is, by synthesizing the single dipole source from a superposition of infinite phased arrays of identical point sources located at $\mathbf{r}_{mn} = \mathbf{r}_0 + ma\hat{\mathbf{x}} + nb\hat{\mathbf{y}}$, as shown in Figure 12.3. In mathematical terms, the single dipole can be obtained by integrating over the Brillouin zone, shown in Figure 12.2:

$$\mathbf{p}^i\left(\mathbf{r}'\right) = \frac{ab}{(2\pi)^2}\int_{-\pi/a}^{\pi/a}\int_{-\pi/b}^{\pi/b}\mathbf{p}^{i,\infty}\left(\mathbf{r}',\mathbf{k}_t\right)\mathrm{d}k_x\mathrm{d}k_y. \tag{12.19}$$

The phased array of dipole sources, with a phase-gradient $\mathbf{k}_t$, is represented mathematically as

$$\mathbf{p}^{i,\infty}\left(\mathbf{r}',\mathbf{k}_t\right) = \hat{\mathbf{p}}_0\sum_{m=-\infty}^{\infty}\sum_{n=-\infty}^{\infty}\delta\left(\mathbf{r}'-\mathbf{r}_{mn}\right)e^{-j\left(k_x ma+k_y nb\right)}. \tag{12.20}$$

The wave numbers k_x and k_y are the phasing gradients along the x- and y-directions, respectively. Physically, Equation 12.19 represents the fact that when the phased-array currents $\mathbf{p}^{i,\infty}\left(\mathbf{r}',\mathbf{k}_t\right)$ are integrated in $\mathbf{k}_t$ over the Brillouin zone, all of the dipoles located at $\mathbf{r}_{mn}$ in the phased array integrate to zero except the one that is located at $(m,n) = (0,0)$. This follows from the fact that an integral of an exponential function of the form $\exp(jk_x ma)$ over the interval $(-\pi/a,\ \pi/a)$ is zero unless $m = 0$.

Since the ASM representation in Equations 12.19 and 12.20 is valid for the dipole source, in a linear PAM environment, the ASM is able to represent also the field produced by such a source. Accordingly, we write

$$\mathbf{E}_{\text{tot}}(\mathbf{r},\mathbf{r}_0) = \frac{ab}{(2\pi)^2}\int_{-\pi/a}^{\pi/a}\int_{-\pi/b}^{\pi/b}\mathbf{E}^{\infty}_{\text{tot}}(\mathbf{r},\mathbf{r}_0,\mathbf{k}_t)\mathrm{d}k_x\mathrm{d}k_y. \tag{12.21}$$

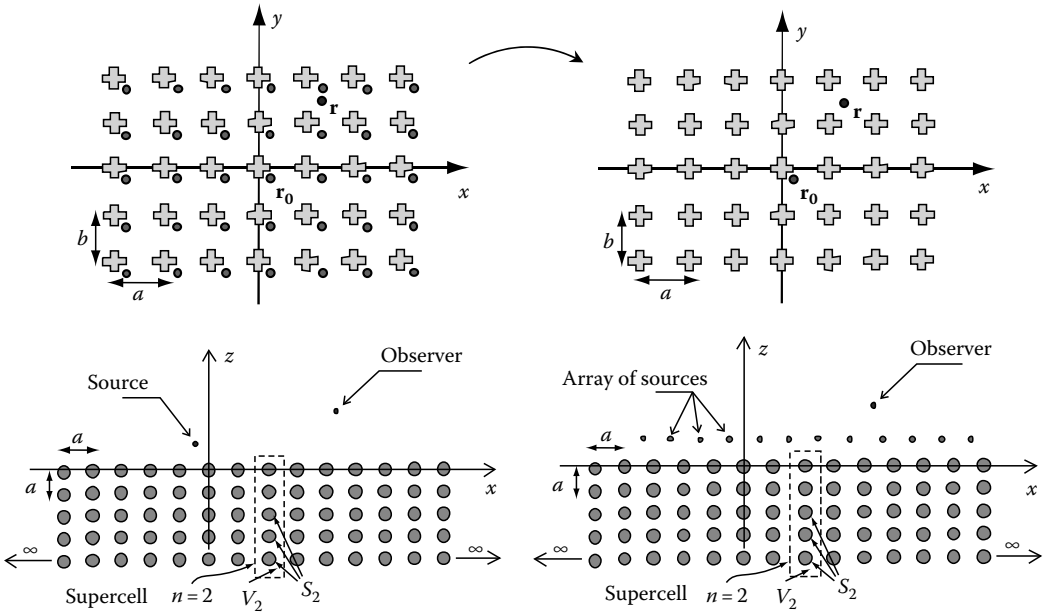

FIGURE 12.3 Left, Periodic structure excited by an infinite array of phased dipole sources at locations $\mathbf{r}_{mn} = \mathbf{r}_0 + ma\hat{\mathbf{x}} + nb\hat{\mathbf{y}}$. The original dipole source is located at $\mathbf{r}_0$. Right, The ASM integration over the Brillouin zone synthesizes the single dipole source. (From Capolino, F., Jackson, D.R., and Wilton, D.R., *IEEE Trans. Antennas Propag.*, 53(1), 91, Jan. 2005; Capolino, F., Jackson, D.R., Wilton, D.R., and Felsen, L.B., *IEEE Trans. Antennas Propag.*, 55(6), 1644, June 2007. With permission.)

More generally, we have

$$\mathbf{E}(\mathbf{r},\mathbf{r}_0) = \frac{ab}{(2\pi)^2}\int_{-\pi/a}^{\pi/a}\int_{-\pi/b}^{\pi/b}\mathbf{E}^{\infty}(\mathbf{r},\mathbf{r}_0,\mathbf{k}_t)\mathrm{d}k_x\mathrm{d}k_y, \tag{12.22}$$

where $\mathbf{E}(\mathbf{r},\mathbf{r}_0)$ denotes either $\mathbf{E}_{\mathrm{inc}}(\mathbf{r},\mathbf{r}_0)$, $\mathbf{E}_{\mathrm{sca}}(\mathbf{r},\mathbf{r}_0)$, or $\mathbf{E}_{\mathrm{tot}}(\mathbf{r},\mathbf{r}_0)$ produced by the dipole source at $\mathbf{r}_0$. Any field $\mathbf{E}(\mathbf{r},\mathbf{r}_0)$ is thus obtained by the spectral integration over the Brillouin zone of $\mathbf{E}^{\infty}(\mathbf{r},\mathbf{r}_0,\mathbf{k}_t)$, which denotes either the incident field $\mathbf{E}^{\infty}_{\mathrm{inc}}(\mathbf{r},\mathbf{r}_0,\mathbf{k}_t)$, the scattered field $\mathbf{E}^{\infty}_{\mathrm{sca}}(\mathbf{r},\mathbf{r}_0,\mathbf{k}_t)$, or the total field $\mathbf{E}^{\infty}_{\mathrm{tot}}(\mathbf{r},\mathbf{r}_0,\mathbf{k}_t)$ produced by the periodic phased array of sources $\mathbf{p}^{i,\infty}(\mathbf{r}',\mathbf{k}_t)$.

The incident field generated by $\mathbf{p}^{i,\infty}(\mathbf{r}',\mathbf{k}_t)$ is represented as $\mathbf{E}^{\infty}_{\mathrm{inc}}(\mathbf{r},\mathbf{r}_0,\mathbf{k}_t) = \underline{\mathbf{G}}^{\infty}(\mathbf{r},\mathbf{r}_0,\mathbf{k}_t)\cdot\hat{\mathbf{p}}_0$, where the periodic dyadic Green's function $\underline{\mathbf{G}}^{\infty}(\mathbf{r},\mathbf{r}_0,\mathbf{k}_t)$ is given in Equation 12.11. The incident field is thus rewritten as

$$\mathbf{E}^{\infty}_{\mathrm{inc}}(\mathbf{r},\mathbf{r}_0,\mathbf{k}_t) = \sum_{p=-\infty}^{\infty}\sum_{q=-\infty}^{\infty} e^{-j(k_{xp}x+k_{yq}y)}\mathbf{e}^{\infty}_{\mathrm{inc},pq}(z,\mathbf{r}_0,\mathbf{k}_t), \tag{12.23}$$

with

$$\mathbf{e}^{\infty}_{\mathrm{inc},pq}(z,\mathbf{r}_0,\mathbf{k}_t) = \frac{1}{2jab}\frac{1}{k_{zpq}}\underline{\mathbf{G}}\left(\mathbf{k}_{t,pq}\right)\cdot\hat{\mathbf{p}}_0\; e^{+j(k_{xp}x_0+k_{yq}y_0-k_{zpq}|z-z_0|)}, \tag{12.24}$$

where the dyad $\underline{\mathbf{G}}\left(\mathbf{k}_{t,pq}\right)$ is found from Equation 12.7. The incident field representation exhibits an infinite set of (pq)-indexed branch-point loci in the (k_x,k_y) plane defined by the equation $k_{xp}^2+k_{yq}^2 = k^2$. The scattered field can then be represented as a sum of scattered Floquet waves as

$$\mathbf{E}^{\infty}_{\text{sca}}\left(\mathbf{r},\mathbf{r}_0,\mathbf{k}_t\right)=\sum_{p=-\infty}^{\infty}\sum_{q=-\infty}^{\infty}e^{-j(k_{xp}x+k_{yq}y)}\mathbf{e}^{\infty}_{\text{sca},pq}\left(z,\mathbf{r}_0,\mathbf{k}_t\right), \tag{12.25}$$

where

$$\mathbf{e}^{\infty}_{\text{sca},pq}\left(z,\mathbf{r}_0,\mathbf{k}_{t,pq}\right)=\frac{1}{2jab}\frac{1}{k_{zpq}}\underline{\mathbf{G}}\left(\mathbf{k}_{t,pq}\right)\cdot\int_D\mathbf{P}^{\infty}_D\left(\mathbf{r}',\mathbf{r}_0,\mathbf{k}_t\right)e^{+j\left[k_{xp}x'+k_{yq}y'-|z-z'|k_{zpq}\right]}\mathrm{d}\mathbf{r}', \tag{12.26}$$

and $\mathbf{P}^{\infty}_D\left(\mathbf{r}',\mathbf{r}_0,\mathbf{k}_t\right)$ is the dipole moment density on the scatterer domain D within the (0,0) supercell, when excited by the infinite phased array of dipoles. This dipole moment density may be obtained, for example, from a numerical solution of the electric field integral equation on the (0,0) supercell using a periodic moment-method code. The dipole moment density $\mathbf{P}^{\infty}_D\left(\mathbf{r}',\mathbf{r}_0,\mathbf{k}_t\right)$ is a periodic function of the spectral variable $\mathbf{k}_t$, with periods $2\pi/a$ and $2\pi/b$ in k_x and k_y, respectively, since the phased array of dipole sources is periodic in k_x and k_y.

The field $\mathbf{E}^{\infty}_{\text{tot}}\left(\mathbf{r},\mathbf{r}_0,\mathbf{k}_t\right)=\mathbf{E}^{\infty}_{\text{inc}}\left(\mathbf{r},\mathbf{r}_0,\mathbf{k}_t\right)+\mathbf{E}^{\infty}_{\text{sca}}\left(\mathbf{r},\mathbf{r}_0,\mathbf{k}_t\right)$ may be conveniently represented as a sum of Floquet waves, as

$$\mathbf{E}^{\infty}_{\text{tot}}\left(\mathbf{r},\mathbf{r}_0,\mathbf{k}_t\right)=\sum_{p=-\infty}^{\infty}\sum_{q=-\infty}^{\infty}e^{-j(k_{xp}x+k_{yq}y)}\mathbf{e}^{\infty}_{\text{tot},pq}\left(z,\mathbf{r}_0,\mathbf{k}_t\right), \tag{12.27}$$

where

$$\mathbf{e}^{\infty}_{\text{tot},pq}\left(z,\mathbf{r}_0,\mathbf{k}_t\right)=\mathbf{e}^{\infty}_{\text{inc},pq}\left(z,\mathbf{r}_0,\mathbf{k}_t\right)+\mathbf{e}^{\infty}_{\text{sca},pq}\left(z,\mathbf{r}_0,\mathbf{k}_t\right). \tag{12.28}$$

The integrands $\mathbf{E}^{\infty}_{\text{inc}}(\mathbf{r},\mathbf{r}_0,\mathbf{k}_t)$, $\mathbf{E}^{\infty}_{\text{sca}}(\mathbf{r},\mathbf{r}_0,\mathbf{k}_t)$, and $\mathbf{E}^{\infty}_{tot}(\mathbf{r},\mathbf{r}_0,\mathbf{k}_t)$ in Equation 12.22 are periodic functions of k_x and k_y with periods $2\pi/a$ and $2\pi/b$, respectively. The singularities of the integrands, given by Equations 12.23, 12.25, and 12.27, are discussed in Section 12.7; they are important to know for proper numerical treatment of the integral in Equation 12.21. (See [33] for more details and [31,32] for a similar problem with 1D periodicity.)

12.4.1 Fourier Transform of Aperture Field via the Array Scanning Method

It is possible to "unfold" the integration path from the Brillouin zone shown in Figure 12.2 to the entire (k_x,k_y) plane. Doing so allows for a convenient identification and calculation of the Fourier transform of the field at any fixed height z. The path unfolding is done by first substituting Equation 12.27 in Equation 12.21 and then recalling that the term $\mathbf{P}^{\infty}_D\left(\mathbf{r}',\mathbf{r}_0,\mathbf{k}_t\right)$, appearing in the expression for $\mathbf{e}^{\infty}_{\text{sca},pq}\left(z,\mathbf{r}_0,\mathbf{k}_t\right)$ in Equation 12.26, is periodic in k_x and k_y. The shift of variables $k_x+F_{xp}\rightarrow k_x$ and $k_y+F_{yq}\rightarrow k_y$ is applied for every (p,q) term of the sum, leading to

$$\mathbf{E}_{\text{tot}}(\mathbf{r},\mathbf{r}_0)=\frac{ab}{(2\pi)^2}\int_{-\infty}^{\infty}\int_{-\infty}^{\infty}e^{-j(k_xx+k_yy)}\mathbf{e}^{\infty}_{\text{tot},00}\left(z,\mathbf{r}_0,\mathbf{k}_t\right)\mathrm{d}k_x\mathrm{d}k_y, \tag{12.29}$$

where $\mathbf{e}^{\infty}_{\text{tot},00}\left(z,\mathbf{r}_0,\mathbf{k}_t\right)$ is calculated using Equation 12.28 along with Equations 12.26 and 12.24 and the supercell dipole moment density $\mathbf{P}^{\infty}_D\left(\mathbf{r}',\mathbf{r}_0,\mathbf{k}_t\right)$. By comparing Equation 12.29 with Equation 12.17, the Fourier transform of the total field is identified as

$$\tilde{\mathbf{E}}_{\text{tot}}\left(z,\mathbf{r}_0,\mathbf{k}_t\right)=ab\,\mathbf{e}^{\infty}_{\text{tot},00}\left(z,\mathbf{r}_0,\mathbf{k}_t\right). \tag{12.30}$$

Equation 12.30 indicates that the Fourier transform of the aperture field is (within the constant ab) the same as the amplitude of the (0,0) Floquet wave radiated by the PAM, when it is excited by the phased array of dipole sources. It is straightforward to extract the amplitude of this fundamental Floquet wave from a periodic moment-method solution, when a phased array of dipole sources is used as the excitation.

The same derivation holds for the incident and scattered fields, and in general

$$\mathbf{E}(\mathbf{r},\mathbf{r}_0) = \frac{ab}{(2\pi)^2}\int_{-\infty}^{\infty}\int_{-\infty}^{\infty} e^{-j(k_x x+k_y y)}\mathbf{e}_{00}^{\infty}(z,\mathbf{r}_0,\mathbf{k}_t)\,\mathrm{d}k_x\mathrm{d}k_y, \tag{12.31}$$

where,

$\mathbf{E}(\mathbf{r},\mathbf{r}_0)$ denotes either $\mathbf{E}_{\mathrm{inc}}(\mathbf{r},\mathbf{r}_0)$, $\mathbf{E}_{\mathrm{sca}}(\mathbf{r},\mathbf{r}_0)$, or $\mathbf{E}_{\mathrm{tot}}(\mathbf{r},\mathbf{r}_0)$

$\mathbf{e}_{00}^{\infty}(z,\mathbf{r}_0,\ \mathbf{k}_t)$ denotes the field of the (0,0) Floquet wave for the incident, scattered, or total field in the phased-array problem, denoted as $\mathbf{e}_{\mathrm{inc},00}^{\infty}(z,\mathbf{r}_0,\mathbf{k}_t)$, $\mathbf{e}_{\mathrm{sca},00}^{\infty}(z,\mathbf{r}_0,\mathbf{k}_t)$, or $\mathbf{e}_{\mathrm{tot},00}^{\infty}(z,\mathbf{r}_0,\mathbf{k}_t)$, respectively

12.4.2 Numerical Considerations

Various considerations arise when performing the numerical integration (Equation 12.22) over the Brillouin zone, depending on the integration rule used and the spectral singular points. Both branch-point and pole singularities may be encountered. Branch points occur in the complex transverse wave number k_t plane at $k_t^2 = \mathbf{k}_t\cdot\mathbf{k}_t = k_x^2 + k_y^2 = k^2$. This gives rise to a periodic set of branch-point circles in the (k_x, k_y) plane, as shown in Figure 12.2. The circular branch-point loci in the principal Brillouin zone are highlighted in Figure 12.2. Following what has been reported in [32, 33], in Figure 12.4, we summarize the behavior of the singularity that is present in the various field terms (incident, scattered, and total) when the spectral wave numbers approach the branch-point circle. One should note that the integrands (Equations 12.24 and 12.26) for the incident and scattered fields have a strong singularity on the branch-point circle at $k_x^2 + k_y^2 = k^2$, due to the $k_{z,pq}$ term in the denominator of Equations 12.24 and 12.26. The total field, being the sum of the two, as in Equation 12.28, also has a branch-point singularity but of a lower order, with the integrand remaining finite at the singularity. The behaviors are shown in Figure 12.4. The branch-point contribution to the fields is called the "space-wave contribution" and is discussed in more detail later. As shown in Section 12.6 and in the numerical results in Section 12.7, the less singular behavior of the integrand for the total field results in a faster rate of decay in the total space-wave field $\mathbf{E}_{\mathrm{tot}}^{\mathrm{sp}}(\mathbf{r},\mathbf{r}_0)$ compared with the scattered space-wave field $\mathbf{E}_{\mathrm{sca}}^{\mathrm{sp}}(\mathbf{r},\mathbf{r}_0)$, as the horizontal radial distance ρ from the source

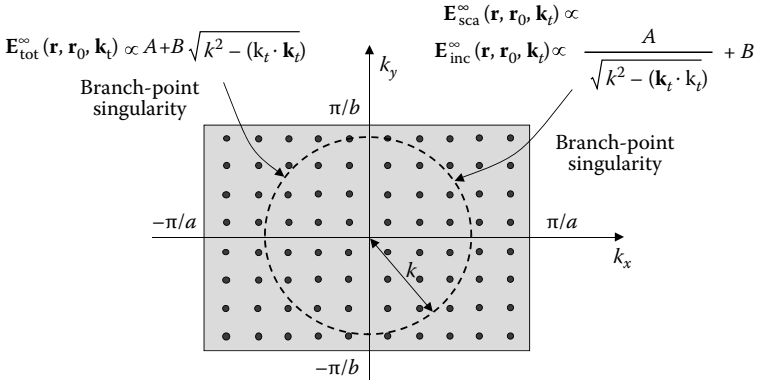

FIGURE 12.4 The Brillouin zone in the $(k_x,\ k_y)$ plane, showing the branch-point circle that lies within this region. The type of singularities present in the integrand of Equation 12.22 is shown for the calculation of the incident, scattered, and total fields. Note that for observation points near the PAM boundary, the integrand for the total field calculation is less singular than that for the scattered field.

increases for a fixed value of z. In particular, as $\rho = |\boldsymbol{\rho}| \to \infty$, with $\boldsymbol{\rho}$ the transverse (in the x–y plane) component of the vector $\mathbf{r} - \mathbf{r}_0$, the main singular terms in Equations 12.24 and 12.26 cancel out so that the total space-wave field has a faster asymptotic rate of decay, behaving as $1/\rho^2$ instead of $1/\rho$. (There may also be guided waves present that are excited by the source; these are discussed later.)

When losses are present in the ambient (host) medium, the branch points in the complex $\mathbf{k}_t$ plane move from the real axes into the complex plane, and the numerical integration is easier in this case because of a smoother integrand in Equation 12.22.

In some applications, such as the superlens (see the book *Applications of Metamaterials*) or for waveguides, a pole singularity may exist very near the real axis, posing a challenge for the numerical integration. In this case, a path deformation in both variables is suggested, leading to the results in [45].

In general, various integration schemes can be used to numerically evaluate Equation 12.22, including integration path deformation in one or both variables. Here we mention that because the integrand in Equation 12.22 is a periodic function, the trapezoidal rule is advantageous [49] and there is no particular advantage in using Gauss–Legendre rules, as demonstrated in [33] through a few simple numerical examples.

Recognizing that the trapezoidal rule is coincident with the "midpoint rectangle" integration rule for periodic functions leads to an interesting physical interpretation of the error in the numerical integration. Using this rule of integration, the integrand is sampled at the points

$$k_x = \xi_p \equiv -\frac{\pi}{a} + \frac{2\pi}{aP}\left(p - \frac{1}{2}\right), \tag{12.32}$$

$$k_y = \eta_q \equiv -\frac{\pi}{b} + \frac{2\pi}{bQ}\left(q - \frac{1}{2}\right), \tag{12.33}$$

with $p = 1, \ldots, P$ and $q = 1, \ldots, Q$, that is, at the center of each of the $(P,\ Q)$ intervals. It can be shown that the error in approximating the field at a location $\mathbf{r}$ due to a dipole source at $\mathbf{r}_0$, introduced via the numerical integration with a finite number of sample points P and Q in k_x and k_y, is equivalent to summing the field produced by an infinite number of dipole source "images" located at $\mathbf{r}_0 + mPa\hat{\mathbf{x}} + nQb\hat{\mathbf{y}}$ for $m, n = \pm 1, \pm 2 \ldots$. The numerical approximation of the integral is thus satisfactory when the nearest images (those with $m = \pm 1,\ n = \pm 1$) are located sufficiently far away from the observation point, that is, P and Q are large enough to result in a large spatial field decay from the nearest images (Figure 12.5). For a lossy host medium, there is exponential decay of the fields from the images, and hence, P and Q need not be as large as in the lossless case.

As shown later in Section 12.6, the field excited by a source is composed of the so-called spatial wave $\mathbf{E}_{\text{tot}}^{\text{sp}}(\mathbf{r}, \mathbf{r}_0)$ plus modal field terms $\mathbf{E}_n^{\text{mode}}(\mathbf{r}, \mathbf{r}_0)$. Spatial waves decrease geometrically away from their sources, and, therefore, spatial waves from the distant images generally do not contribute much to the error in the numerical evaluation of Equation 12.21. However, modes excited by their sources (the images) may decay slowly along the structure; therefore, even distant images may significantly limit the accuracy of Equation 12.21. This physical picture is consistent with the mathematical fact that for a lossy medium the branch points are located below the real axis of the (k_x, k_y) plane, and hence, no singularities are encountered when integrating over the Brillouin zone of the (k_x, k_y) plane in Figure 12.2.

12.5 Relation between the ASM and the Plane-Wave Superposition Method

The incident field $\mathbf{E}_{\text{inc}}^{\infty}(\mathbf{r}, \mathbf{r}_0, \mathbf{k}_t)$ in Equation 12.23, produced by the infinite phased array of dipoles $\mathbf{P}^{i,\infty}(\mathbf{r}', \mathbf{k}_t)$ in the ASM, can be viewed as a weighted superposition of plane waves. The relation between the scattered field $\mathbf{E}_{\text{sca}}^{\infty}(\mathbf{r}, \mathbf{r}_0, \mathbf{k}_t)$, produced by $\mathbf{p}^{i,\infty}(\mathbf{r}', \mathbf{k}_t)$ and the field $\overline{\mathbf{E}}_{\text{sca}}^{\text{PW}}(\mathbf{r}, \mathbf{k}_t)$,

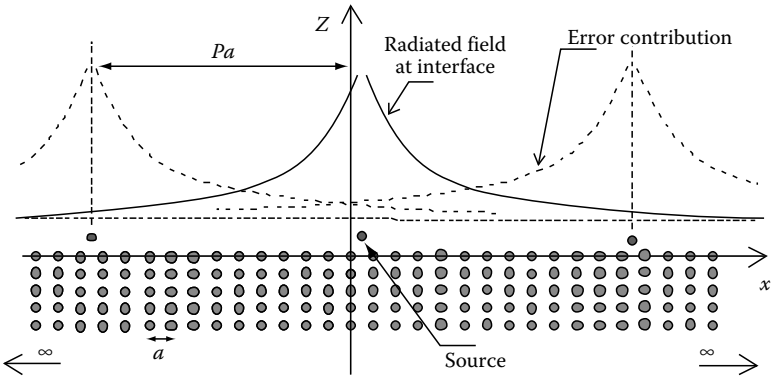

FIGURE 12.5 Physical interpretation of the numerical error in evaluating Equation 12.21 when using a midpoint rectangle rule of integration. For simplicity, we show only the *xz* plane cut. Due to the numerical integration with a finite number of sample points, the field at a certain location is the superposition of the field due to the actual source plus that due to "images" located at distances $m(Pa)$, where P is the total number of spectral points used to perform the k_x integration in Equation 12.21.

produced by a unit-amplitude incident plane wave, may be written as (assuming the dipole to be above the structure)

$$\mathbf{E}_{\text{sca}}^{\infty}\left(\mathbf{r},\mathbf{r}_0,\mathbf{k}_t\right)=\sum_{p=-\infty}^{\infty}\sum_{q=-\infty}^{\infty}\frac{1}{2jab}\frac{c_{pq}}{k_{zpq}}\overline{\mathbf{E}}_{\text{sca}}^{\text{PW}}\left(\mathbf{r},\mathbf{k}_{t,pq}\right), \tag{12.34}$$

with

$$c_{pq}=\hat{\mathbf{e}}_{\text{inc}}\left(\mathbf{k}_{t,pq}\right)\cdot\underline{\mathbf{G}}\left(\mathbf{k}_{t,pq}\right)\cdot\hat{\mathbf{p}}_0 e^{+j\left(k_{xp}x_0+k_{yq}y_0-k_{zpq}z_0\right)}. \tag{12.35}$$

Similarly, the current $\mathbf{P}_D^{\infty}\left(\mathbf{r}',\mathbf{r}_0,\mathbf{k}_{t,pq}\right)$ on the (0,0) supercell induced by $\mathbf{p}^{i,\infty}\left(\mathbf{r}',\mathbf{k}_t\right)$ is

$$\mathbf{P}_D^{\infty}\left(\mathbf{r},\mathbf{r}_0,\mathbf{k}_t\right)=\sum_{p=-\infty}^{\infty}\sum_{q=-\infty}^{\infty}\frac{1}{2jab}\frac{c_{pq}}{k_{zpq}}\overline{\mathbf{P}}_D^{\text{PW}}\left(\mathbf{r},\mathbf{k}_{t,pq}\right). \tag{12.36}$$

The scattered field calculated by the ASM may then be cast into the form

$$\mathbf{E}_{\text{sca}}\left(\mathbf{r},\mathbf{r}_0\right)=\frac{ab}{\left(2\pi\right)^2}\int_{-\pi/b}^{\pi/b}\int_{-\pi/a}^{\pi/a}\frac{1}{2jab}\sum_{p=-\infty}^{\infty}\sum_{q=-\infty}^{\infty}\frac{c_{pq}}{k_{zpq}}\overline{\mathbf{E}}_{\text{sca}}^{\text{PW}}\left(\mathbf{r},\mathbf{k}_{t,pq}\right)\,dk_x dk_y. \tag{12.37}$$

Mathematically, Equation 12.37 is equivalent to Equation 12.16, since the integration over the Brillouin zone of the infinite series of terms is equivalent to a single integration over the entire wave number plane. More details are in [33].

The integrand $\mathbf{E}_{\text{sca}}^{\infty}\left(\mathbf{r},\mathbf{r}_0,\mathbf{k}_t\right)$ in Equation 12.22 for the scattered field can, in principle, be calculated using Equation 12.34. However, doing so requires the solution of an infinite number of plane-wave scattering problems. A much more efficient method is to directly calculate $\mathbf{E}_{\text{sca}}^{\infty}\left(\mathbf{r},\mathbf{r}_0,\mathbf{k}_t\right)$ by numerically solving the problem of an infinite set of phased dipole sources above the periodic structure. This numerical solution requires a periodic moment-method analysis, which is essentially no more numerically intensive than that for a single plane-wave scattering problem.

The advantage of the ASM over the direct plane-wave superposition method is that Equation 12.21 requires a spectral integration that is carried out *only* over the Brillouin zone, in contrast to Equation 12.16, which requires an integration over the entire (k_x,k_y) plane. Furthermore, the ASM

provides a much more efficient method for calculating the Fourier transform of the field at any horizontal (constant z) plane of interest, as discussed in the next section. The calculation of the transform of the field is important for performing asymptotic analysis and for identifying the launching amplitude of surface and leaky waves.

12.6 Wave Species in Periodic Media: Spatial and Modal Waves

12.6.1 Total Field Representation

We show here that the total field at $\mathbf{r}$ excited by a source at $\mathbf{r}_0$ may be represented in terms of two types of wave "species": a "spatial wave" that is denoted as $\mathbf{E}^{\text{sp}}_{\text{tot}}(\mathbf{r}, \mathbf{r}_0)$ and modal field terms $\mathbf{E}^{\text{mode}}_n(\mathbf{r}, \mathbf{r}_0)$ corresponding to guided waves [32,33]. That is,

$$\mathbf{E}_{\text{tot}}(\mathbf{r}, \mathbf{r}_0) = \sum_n \mathbf{E}^{\text{mode}}_n(\mathbf{r}, \mathbf{r}_0) + \mathbf{E}^{\text{sp}}_{\text{tot}}(\mathbf{r}, \mathbf{r}_0). \tag{12.38}$$

Although such a mathematical representation always exists, the physical interpretation of the two types of wave fields is the most direct for observation points that are at least several wavelengths distant from the source. Equation 12.38 is an asymptotic representation of the total field derived from the Fourier transform representation given in Equation 12.17 or (more efficiently) by that given in Equation 12.29. The asymptotic representation is obtained by the following steps. As shown in Appendix A, Figure 12.A.1a, the original integration path on the real axis may be deformed around the singular points in the wave number plane, that is, the branch points and poles, to highlight the space-wave and modal contributions. The nth modal field $\mathbf{E}^{\text{mode}}_n(\mathbf{r}, \mathbf{r}_0)$ arises from the residue evaluations at the nth periodic set of poles, in which the residue at each pole location, followed by an asymptotic evaluation, determines the amplitude of the corresponding Floquet mode contribution to the nth guided mode.

The space-wave field $\mathbf{E}^{\text{sp}}_{\text{tot}}(\mathbf{r}, \mathbf{r}_0)$ arises from the evaluation of the integral around each branch point in one variable (say k_x) followed by an asymptotic evaluation in the other spectral variable k_y. This involved procedure leads to an expression for both wave species in terms of Floquet spatial harmonics. The field of a guided mode is represented as

$$\mathbf{E}^{\text{mode}}(\mathbf{r}, \mathbf{r}_0) = \sum_{p,q=-\infty}^{\infty} e^{-j\mathbf{k}^{\text{mode}}_{t,pq}\cdot\boldsymbol{\rho}} \mathbf{e}^{\text{mode}}_{pq}(z, \mathbf{k}_t), \tag{12.39}$$

where

$$\mathbf{k}^{\text{mode}}_{t,pq} = \mathbf{k}^{\text{mode}}_t + F_{xp}\hat{\mathbf{x}} + F_{yq}\hat{\mathbf{y}} = k^{\text{mode}}_{xp}\hat{\mathbf{x}} + k^{\text{mode}}_{yq}\hat{\mathbf{y}}, \tag{12.40}$$

$$k^{\text{mode}}_{xp} = \beta_x + F_{xp}, k^{\text{mode}}_{yq} = \beta_y + F_{yq}, \tag{12.41}$$

and $\mathbf{k}^{\text{mode}}_t = \boldsymbol{\beta} - j\boldsymbol{\alpha}$ is the wavevector of the (00)th harmonic that may have either real or complex values, corresponding to a surface-wave type of mode or a leaky type of mode [50,56]. The final asymptotic expression for the total spatial field at a point $\mathbf{r}$ along or near the interface of the periodic structure is [33]

$$\mathbf{E}^{\text{sp}}_{\text{tot}}(\mathbf{r}, \mathbf{r}_0)\frac{1}{\rho^2} \sum_{pq=-\infty}^{\infty} e^{-j\mathbf{k}^{\text{sp}}_{t,pq}\cdot\boldsymbol{\rho}}\, \mathbf{e}^{\text{sp}}_{pq}(z, \mathbf{k}_t), \tag{12.42}$$

where

$$\mathbf{k}^{\text{sp}}_{t,pq} = k\hat{\boldsymbol{\rho}} + F_{xp}\hat{\mathbf{x}} + F_{yq}\hat{\mathbf{y}} = k^{\text{sp}}_{xp}\hat{\mathbf{x}} + k^{\text{sp}}_{yq}\hat{\mathbf{y}}, \tag{12.43}$$

$$k^{\text{sp}}_{xp} = k\cos\phi + F_{xp}, k^{\text{sp}}_{yq} = k\sin\phi + F_{yq}, \tag{12.44}$$

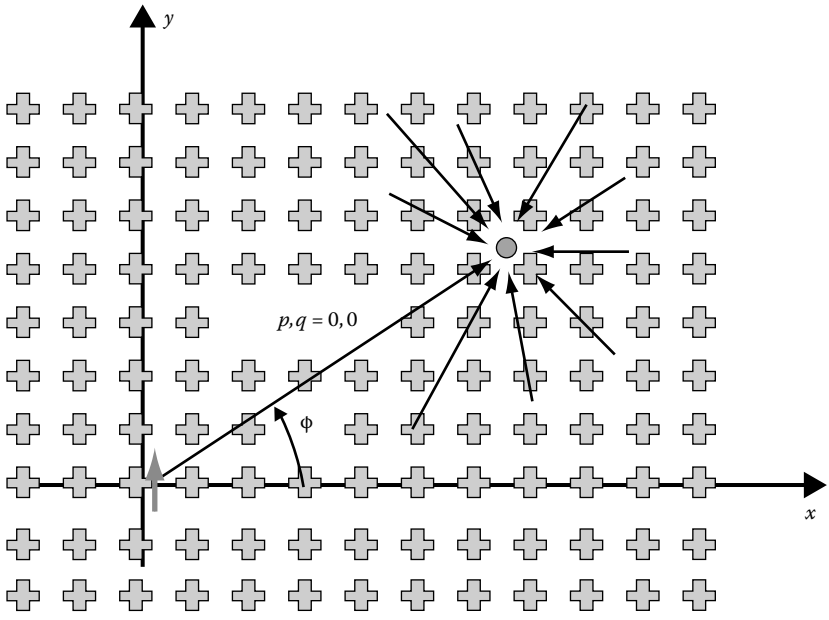

FIGURE 12.6 Wavevectors of the spatial harmonics that reach the observation point. The term $(p, q) = (0, 0)$ is the fundamental harmonic with wavevector $k\hat{\boldsymbol{\rho}}$. The other wavevectors are present because of the periodicity.

and $\rho = |\boldsymbol{\rho}|$, with $\boldsymbol{\rho}$ the transverse (in the x–y plane) component of the vector $\mathbf{r} - \mathbf{r}_0$. Here, it is interesting to note that even if the spatial wave is excited by a localized source, it is still represented in terms of Floquet harmonics $e^{-j\mathbf{k}_{t,pq}^{\mathrm{sp}}\cdot\boldsymbol{\rho}}$ with weights $\mathbf{e}_{pq}^{\mathrm{sp}}$. It is also interesting to note that all the pq-spatial harmonics decrease with distance ρ with the same geometrical spreading factor $1/\rho^2$. In Figure 12.6, we illustrate the harmonics of the spatial field $\mathbf{E}_{\mathrm{tot}}^{\mathrm{sp}}$ impinging on the observer at $\mathbf{r}$, produced by a source at the origin. The arrows represent the directions of the wavefronts. The $(p, q) = (0, 0)$ term is the direct contribution that would exist even in a homogenous (nonperiodic) problem such as a source over a dielectric layer, and the wavevector $k\hat{\boldsymbol{\rho}}$ represents a direct propagation from the source to the observer. All the other higher-order pq-harmonics are represented as wavefronts impinging from other directions, produced by the scatterers surrounding the observation point. Locally, the spatial field at the observation point behaves as a spatial wave propagating along the interface of a homogeneous interface, with the periodic structure setting up high-order Floquet waves, produced by the discrete nature of the scattering structure. The group velocity of all of the Floquet waves is in the radial direction.

The total field

$$\mathbf{E}_{\mathrm{tot}}(\mathbf{r}, \mathbf{r}_0) = \mathbf{E}_{\mathrm{inc}}(\mathbf{r}, \mathbf{r}_0) + \mathbf{E}_{\mathrm{sca}}(\mathbf{r}, \mathbf{r}_0) \tag{12.45}$$

is the superposition of the incident field $\mathbf{E}_{\mathrm{inc}}$, the field in the absence of the PAM produced by the source at $\mathbf{r}_0$, and of the scattered field $\mathbf{E}_{\mathrm{sca}}$, which is the field produced by the PAM (more specifically by the equivalent sources representing the PAM). The asymptotic total field representation (Equation 12.38) has been obtained via the asymptotic steps, a brief description of which follows Equation 12.38 and is described in Appendix B, applied to the radiation integral (Equation 12.31) transformed as in Equation 12.53. An analogous treatment could be performed for the scattered field, also represented in Equation 12.38, which would lead to the following asymptotic representation of the scattered field:

$$\mathbf{E}_{\mathrm{sca}}(\mathbf{r}, \mathbf{r}_0) = \sum_n \mathbf{E}_n^{\mathrm{mode}}(\mathbf{r}, \mathbf{r}_0) + \mathbf{E}_{\mathrm{sca}}^{\mathrm{sp}}(\mathbf{r}, \mathbf{r}_0). \tag{12.46}$$

The modal terms $\mathbf{E}_n^{\text{mode}}$ in Equations 12.38 and 12.46 are exactly the same. After insertion of Equation 12.46 into Equation 12.45, and a comparison with Equation 12.38, it is noted that the spatial field $\mathbf{E}_{tot}^{\text{sp}}$ in Equation 12.38 is made up of two contributions:

$$\mathbf{E}_{\text{tot}}^{\text{sp}}(\mathbf{r},\mathbf{r}_0) = \mathbf{E}_{\text{inc}}(\mathbf{r},\mathbf{r}_0) + \mathbf{E}_{\text{sca}}^{\text{sp}}(\mathbf{r},\mathbf{r}_0), \tag{12.47}$$

which is the sum of the incident field and the "spatial wave" part of the scattered field $\mathbf{E}_{\text{sca}}$. Mathematically, the term $\mathbf{E}_{\text{sca}}^{\text{sp}}$ arises from the asymptotic evaluation of the branch-point contributions of the scattered field integrand in Equation 12.31. Away from the source, and for observation points not close to the interface of the PAM, all three terms $\mathbf{E}_{\text{tot}}^{\text{sp}}$, $\mathbf{E}_{\text{inc}}$, and $\mathbf{E}_{\text{sca}}^{\text{sp}}$ decrease as $1/|\mathbf{r}-\mathbf{r}_0|$ away from the PAM, just as the fields do in a diffraction problem when the observation point is located away from a shadow boundary [54,57]. Near the PAM, but far away from the source, the $1/|\mathbf{r}-\mathbf{r}_0|$ spreading factors of $\mathbf{E}_{\text{inc}}$ and $\mathbf{E}_{\text{sca}}^{\text{sp}}$ cancel out, and the total spatial field $\mathbf{E}_{\text{tot}}^{\text{sp}}$ decreases as in Equation 12.42 [33,58,59].

12.6.1.1 1D Structure Excited by a Line Source

Although the preceding discussion was focused on a 2D periodic PAM excited by a dipolar source, here, we briefly report the field representation when a y-directed line source excites a 1D periodic structure of y-invariant scatterers that are periodic in the x-direction (i.e., we are considering a 2D problem), as this important case also arises frequently in the excitation of periodic structures. For this particular case, all the field expressions are analogous to those given previously in this chapter. The total field representation (Equation 12.38), in which the total field is represented as the sum of a spatial wave plus modal fields, is still valid. Modal fields still have the expression (Equation 12.39), with one summation index suppressed. The spatial field for points far away from the source but not too far from the PAM is now given by the expression [32]

$$\mathbf{E}_{\text{tot}}^{\text{sp}}(\mathbf{r},\mathbf{r}_0)\frac{1}{x^{3/2}}\sum_{p=-\infty}^{\infty} e^{-jk_{x_p}^{\text{sp}}x}\,\mathbf{e}_p^{\text{sp}}(z,k_x)\,. \tag{12.48}$$

In this case, the spatial field has a different spreading factor than for the dipole case. Also, the incident and scattered fields now decrease as $1/x^{1/2}$.

12.6.2 Leaky and Bound Modes

The modal field $\mathbf{E}^{\text{mode}}(\mathbf{r},\mathbf{r}_0)$ in Equation 12.39 at the observation point can be further classified into a few cases depending on its complex propagation wave number, which is written as

$$\mathbf{k}_t^{\text{mode}} = \boldsymbol{\beta} - j\boldsymbol{\alpha}, \tag{12.49}$$

(when the $\exp(-i\omega t)$ time convention is used, the transverse wave number is defined as $\mathbf{k}_t^{\text{mode}} = \boldsymbol{\beta} + i\boldsymbol{\alpha}$, and all considerations on the sign of $\boldsymbol{\alpha}$ are maintained.) The guided mode at the observation point does not need to have the phase and attenuation vectors in the same direction, and in general, neither one has to be in the radial direction. However, if the PAM acts approximately as a homogenous material, then $\mathbf{k}_t^{\text{mode}} = \boldsymbol{\beta} - j\boldsymbol{\alpha} = (\beta - j\alpha)\hat{\boldsymbol{\rho}}$. The pqth Floquet wavevector of the guided mode in Equation 12.39 can be written as

$$\mathbf{k}_{t,pq}^{\text{mode}} = \boldsymbol{\beta}_{pq} - j\boldsymbol{\alpha}, \text{ with } \boldsymbol{\beta}_{pq} = \boldsymbol{\beta} + F_{xp}\hat{\mathbf{x}} + F_{yq}\hat{\mathbf{y}}. \tag{12.50}$$

The z-directed pqth Floquet wave number is thus

$$k_{z,pq}^{\text{mode}} = \sqrt{k^2 - \left(\mathbf{k}_{t,pq}^{\text{mode}}\cdot\mathbf{k}_{t,pq}^{\text{mode}}\right)} = \beta_{z,pq} - j\alpha_{z,pq}. \tag{12.51}$$

TABLE 12.1 Properties of Physical Complex Waves, According to Their Classification

	Forward Wave $\boldsymbol{\beta}_{pq} \cdot \boldsymbol{\alpha} > 0$	Backward Wave $\boldsymbol{\beta}_{pq} \cdot \boldsymbol{\alpha} < 0$
Slow wave	$\lvert\boldsymbol{\beta}_{pq}\rvert > k$, $\alpha_{z,pq} > 0$ (proper, bound)	$\lvert\boldsymbol{\beta}_{pq}\rvert > k$, $\alpha_{z,pq} > 0$ (proper, bound)
Fast wave	$\lvert\boldsymbol{\beta}_{pq}\rvert < k$, $\alpha_{z,pq} < 0$ (improper, leaky)	$\lvert\boldsymbol{\beta}_{pq}\rvert < k$, $\alpha_{z,pq} > 0$ (proper, leaky)

Depending on the value of the phase and attenuation constants, we distinguish among a few cases categorized in Table 12.1. Bound and leaky modes can be forward or backward, depending on whether the phase vector $\boldsymbol{\beta}_{pq}$ is in the same or opposite direction as the attenuation vector $\boldsymbol{\alpha}$, that is, when $\boldsymbol{\beta}_{pq} \cdot \boldsymbol{\alpha} > 0$ or $\boldsymbol{\beta}_{pq} \cdot \boldsymbol{\alpha} < 0$, respectively.

Bound (nonradiating) modes are surface-wave-like modes that do not radiate into the upper $(z > 0)$ and lower $(z < 0)$ regions, and, therefore, must have $\left|\boldsymbol{\beta}_{pq}\right| > k$ for all pq Floquet indices; their attenuation in the array plane (the transverse xy plane) is dictated only by the losses present in the materials. For a bound mode on a lossless structure, $\boldsymbol{\alpha} = 0$. For a bound mode, all of the Floquet waves decay exponentially away from the structure, so that $\alpha_{z,pq} > 0$.

Leaky modes are modes that radiate power away from the transverse plane containing the periodic structure, because at least one Floquet wave has a phase velocity faster than that of light in the surrounding medium, that is, $\left|\boldsymbol{\beta}_{pq}\right| < k$. In this case, it is important to note that the vertical wavevector $k_{z,pq}$ may be located on the bottom Riemann sheet of the complex $\mathbf{k}_t$ plane, which is defined by the improper (exponentially growing) choice of branch in Equation 12.51, that is, $\boldsymbol{\alpha}_{pq} < 0$, so that this Floquet wave grows exponentially away from the periodic structure for increasing $|z|$. A leaky mode with one or more improper Floquet waves may be physical (discussed below). However, in this case, an asymptotic analysis reveals that its region of existence is limited, and, indeed, we never have a physical field that grows exponentially as $z = \pm\infty$ in a practical problem, where the guiding structure is excited by a finite source. More details on the asymptotic analysis and the improper nature of leaky modes can be found in [33,50–57].

When solving for leaky guided modes on a structure, one may find various mathematical solutions, but depending on the structure and the frequency range, the guided modes may be physical or nonphysical. We define a physical solution as one that can actually be significantly measured when the structure is excited by an appropriate finite source located in proximity to the structure. The overall mode is considered to be physical if all of its Floquet waves are physical. Otherwise, if one or more Floquet waves are nonphysical, the overall mode is considered to be nonphysical.

All bound (surface-wave-like) modes with a real wave number are considered to be physical, but leaky modes with a complex wave number may be either physical or nonphysical, just as for leaky modes on 1D guiding structures (e.g., leaky-wave antennas). In the 1D case of propagation in the x-direction on a periodic structure, where $k_{xp} = \beta_p - j\alpha$, a forward Floquet wave is defined as one where $\beta_p > 0$ whereas a backward wave is one where $\beta_p < 0$ (assuming here that $\alpha > 0$, so that power is flowing in the positive x-direction). A forward leaky Floquet wave is physical if it is a fast wave $(0 < \beta_p < k_0)$ and it is improper $(\alpha_z < 0)$. A backward leaky Floquet wave is physical if it is a fast wave $(-k_0 < \beta_p < 0)$ and it is proper $(\alpha_z > 0)$.

Extending the above discussion to the case of a 2D guiding structure such as a PAM, a forward leaky Floquet wave is defined as one where $\boldsymbol{\beta}_{pq} \cdot \boldsymbol{\alpha} > 0$ whereas a backward wave is defined by $\boldsymbol{\beta}_{pq} \cdot \boldsymbol{\alpha} < 0$. Table 12.1 presents a summary of the properties of physical Floquet waves for a leaky mode, depending on the classification (slow or fast and forward or backward) of the wave, adopted from [56].

Mathematically, in a spectral integral representation for the field radiated by a source near a periodic structure, the physical modes are those for which the corresponding poles in the complex plane

are captured in the path deformation from the original to the steepest descent path, as shown in appendix. See [32,33,50,53,54,57] for more details.

12.7 Examples of Field Species in a PAM Excited by a Single Source

Consider an array of scatterers made of perfectly conducting, x-directed, resonant strip dipoles with length $L = 0.5\lambda$ and width $W = 0.07\lambda$, where $\lambda = 1\,\text{m}$ is the free-space wavelength (corresponding to a frequency of 300 MHz). Results for the electric field at any other frequency may be found by dividing the results obtained at 300 MHz by λ^2. (Equivalently, the results for the electric field at 300 MHz may be conveniently interpreted as being those for the *normalized* electric field at any arbitrary frequency, where the normalized field is the product of the field and λ^2 and has units of Vm.) In the first example, for simplicity, the current on the strip dipoles is assumed to be x-directed, and only one cosine basis function $B(x, y) = \cos(\pi x/L)$ for the x-directed current is used, with $x \in (-L/2, L/2)$ and $y \in (-W/2, W/2)$. The array is a square lattice with element spacings $a = b = 1.4\lambda$. The source is an elementary x-directed electric dipole with unit amplitude ($Il = 1\,\text{Am}$), which is located at $\mathbf{r}_0 = 0.7\lambda\hat{\mathbf{x}} + 0.7\lambda\hat{\mathbf{y}} + 0.5\lambda\hat{\mathbf{z}}$ (the origin is at the center of one of the metal strip dipoles). Figure 12.7 shows the magnitude of the total and scattered fields generated by the source, evaluated at locations $\mathbf{r} + nb\hat{\mathbf{y}}$, with $n = 0, 1, 2, \ldots 40$, calculated via the ASM. The observer location is at $\mathbf{r} = 0.01\lambda\hat{\mathbf{z}}$ (close to the metallic dipoles, directly above the dipole center). Both the total and scattered fields have been

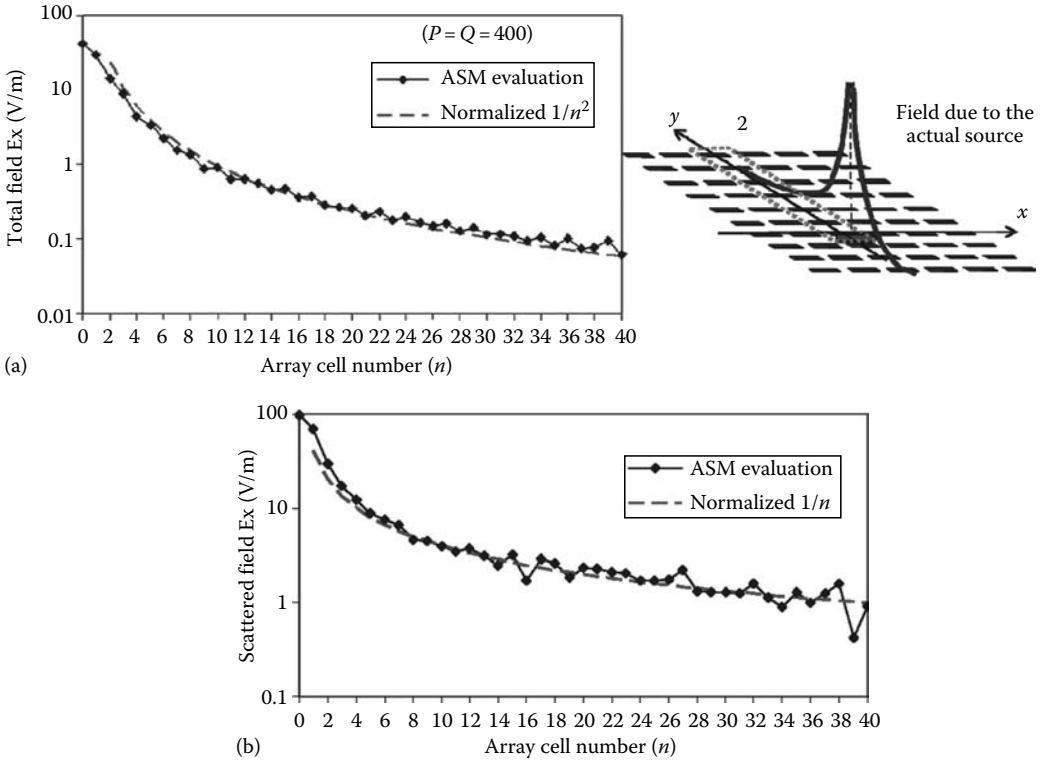

FIGURE 12.7 Total (a) and scattered (b) electric fields evaluated via the ASM at locations $\mathbf{r} + nb\hat{\mathbf{y}}$, versus n, generated by a single dipole source. The total field decays as $1/n^2$ away from the source, whereas the scattered field decays as $1/n$.

evaluated from Equation 12.21, with the integration performed numerically with the "midpoint rule" using $P = Q = 400$ (see Equations 12.32 and 12.33), yielding a total number of $P \times Q = 1.6 \times 10^5$ spectral sampling points. The large number of sampling points is required since we are observing the field in lossless free space for large y, up to $y = 40b = 64\lambda$, and thus the exponential function in Equation 12.25 or in Equation 12.27 is rapidly varying with k_y, requiring a fine sampling. One should note that the error in the evaluation of the scattered field is larger than that for the total field, for the reasons explained in Section 12.3.2 (the behavior of the integrands near the branch-point circle). The purpose of Figure 12.7 is to show numerically the expected $1/n^2$ decay for the total field and $1/n$ decay for the scattered field. In this example, modal fields are not excited, and the only field species in Equation 12.38 is the spatial field. Furthermore, Figure 12.7 demonstrates the effect of the image sources (explained in Section 12.6.2) that are responsible for the oscillations observed for large n (the nearest image source is in cell $n = 400$). The oscillations in the scattered field are larger than those of the total field, because the scattered field produced by each image source decays as $1/D$, where D is the distance from the image source, as opposed to $1/D^2$ for the total field. If the plots were extended to much larger distances, they would show that the calculated field actually repeats at $n = 400$, due to the image source effect. (The exact field continues to decrease as the distance increases.)

In the second example, the same perfectly conducting dipole in the (0,0) unit cell is divided into 10 rectangular subdomains of length $d = 0.05\lambda$, and 9 rectangular rooftop basis functions are used. The array is a square lattice with an element spacing that is now $a = b = 0.7\lambda$. The source is an elementary x-directed electric dipole with unit amplitude ($I\,l = 1\,\text{Am}$) located at $\mathbf{r}_0 = -0.2\lambda\hat{\mathbf{x}} - 0.2\lambda\hat{\mathbf{y}} + 0.0\lambda\hat{\mathbf{z}}$ [the origin is at the center of the (0,0) metal strip dipole]. The magnitude of the current I (in amperes) is calculated on the metal dipoles at a distance d from the left end of each dipole for a free-space wavelength of $\lambda = 1\,\text{m}$ (the results for the current I at any other frequency may be found by dividing the results presented here by the corresponding free-space wavelength λ). Results are presented for the current on dipole $(0, n)$ centered at $(x, y) = (0,\ nb)$, where n is varied. In Figure 12.8, the current is plotted over the first 40 metal dipoles along the y-direction (n varies from 0 to 40). The field decay follows the expected behavior $1/r^2$ as seen by the addition of the normalized $1/n^2$ curve. The curve has noticeable oscillations, which in this case are not due to numerical error ($P = Q = 600$ is sufficient to

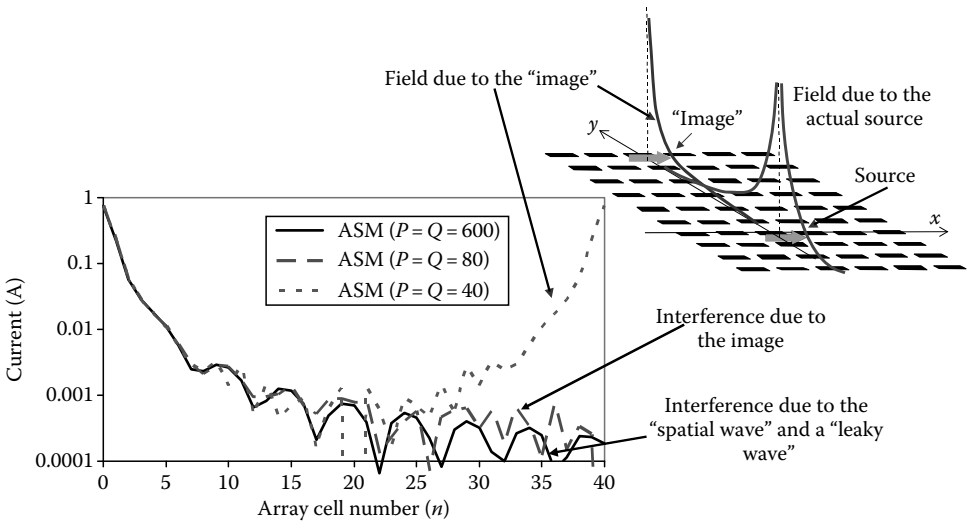

FIGURE 12.8 The current on the metal dipoles calculated by using the ASM versus the number of cells away from the (0,0) cell in the y-direction. Results are shown for various numbers of integration points.

guarantee accurate results). Evidently, this is due to interference between the main space wave and a weaker mode (perhaps a leaky mode) propagating along the PAM interface. The field is also compared with that obtained using $P = Q = 80$ and $P = Q = 40$. Using fewer integration points causes a loss of accuracy away from the source. For $P = Q = 40$ points the effect of the nearest "image" source in cell $n = 40$ is clearly visible. The null at $n = 20$ is caused by the cancellation of the field produced by the source and this image.

Other examples of ASM field calculations are given in [44,45]. There, the field in a 2D array of plasmonic nanospheres excited by a single dipole is shown, with the aim of determining subwavelength resolution and near-field enhancement.

In Figure 12.9, we show results for a 2D problem (invariant in y), namely, the excitation of an artificial material EBG slab consisting of three layers of periodic, infinitely long, perfectly conducting cylinders with a normalized radius of $0.2a$ in free space, where a is the period of the lattice in the x- and z-directions. The structure is excited by a unit-amplitude, y-directed electric line source of current $I = 1$A placed over it. The axes of the cylinders in the top row are located at z = 0. The source is located at $\mathbf{r}_0 = 0.5a\,\hat{\mathbf{z}}$. In the MoM calculations, each cylinder has been discretized using 16 subdomain surface pulse basis functions. In Figure 12.9, the operating frequencies correspond to $a/\lambda = 0.3$, 0.48, and 0.57. The lowest frequency $(a/\lambda = 0.3)$ corresponds to the 0th bandgap $(0 < a/\lambda < 0.48)$ of the infinite EBG material [8], whereas the second frequency $(a/\lambda = 0.48)$ is at the band edge, and the third one $(a/\lambda > 0.48)$ is in the propagation band of the EBG material. The normalized total field (normalized by multiplying by the period a) is plotted versus the distance from the line source parallel to the EBG interface at points $\mathbf{r}_n = na\hat{\mathbf{x}} + a\hat{\mathbf{z}}$, with n denoting the supercell index. (The normalized field does not depend on frequency, since dimensions have been specified in terms of wavelength.) For $a/\lambda = 0.3$ and 0.48, the total field is dominated by the spatial wave, and it, therefore, decreases as $1/n^{3/2}$ (see Equation 12.48) as clearly shown in Figure 12.9, where the reference $1/n^{3/2}$ curve, properly normalized, is shown with dots. This demonstrates that no significant modal fields are excited along the structure. However, at the higher frequency $a/\lambda = 0.57$ a leaky mode propagates along the interface, as can be seen from the interference between the spatial wave and the leaky wave in Figure 12.9

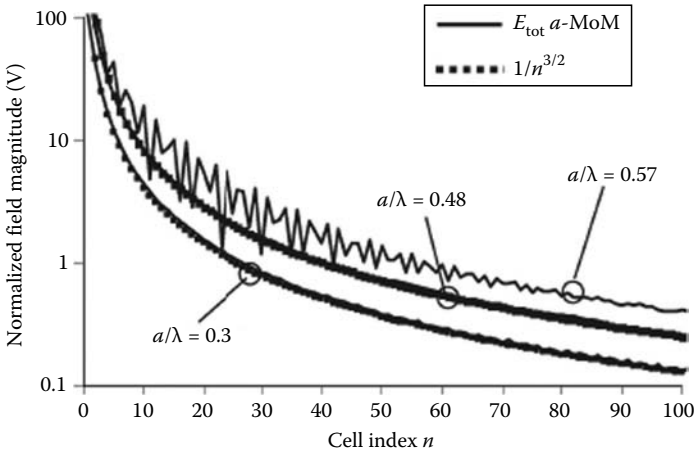

FIGURE 12.9 Spatial decay of the total field produced by a line source over a 2D periodic EBG material made of three periodic layers of infinitely long conducting cylinders. The field is evaluated at points $\mathbf{r}_n = na\hat{\mathbf{x}} + a\hat{\mathbf{z}}$, where n denotes the supercell index. The fields match well with a simple $1/n^{3/2}$ factor (normalized to the exact fields for large n) for the two lower frequencies. At the higher frequency, the spatial wave interferes with a leaky mode. (From Capolino, F., Jackson, D.R., and Wilton, D.R., *IEEE Trans. Antennas Propag.*, 53(1), 91, Jan. 2005. With permission.)

(the interference subsides for larger distances, due to the exponential decay of the leaky mode). The presence of a leaky mode has been confirmed by a numerical search in the complex plane of the zeros of the determinant of the MoM linear system, and it has been found that the wave number of the leaky-wave pole (corresponding to the pole location in the zeroth Brillouin zone) is approximately given by $\beta = 0.26k$ and $\alpha = 0.017k$.

When PAMs are properly designed, the field along the PAM is dominated by a leaky mode and the spatial field is much weaker. This property is used to design leaky-wave antennas with very narrow radiated beams [15].

12.8 Conclusions

We have provided the field representation for a single dipole source in the presence of an infinite periodic material (PAM) that is periodic in two dimensions (x and y) and finite in the third (z) dimension. This has been done in two different ways: by employing a direct plane-wave expansion and by using the array scanning method (ASM). In the ASM, a periodic "phased array" of dipole sources is used to excite the PAM. The solution of the periodic phased array problem is efficient since it involves the analysis of only a single unit cell, for example, using a periodic Green's function in a moment-method solution (although the ASM is not limited to a moment-method analysis). The fields produced by the single dipole source in the presence of the PAM are then constructed by numerically integrating the fields of the phased-array problem over the Brillouin zone of the wave number (k_x, k_y) plane. As shown in [33], the ASM is numerically much more efficient than the direct plane-wave expansion method, since it requires an integration only over the Brillouin zone rather than over the entire wave number plane.

For some purposes, such as asymptotic analysis and calculation of surface-wave and leaky-wave excitation amplitudes, it is also important to be able to calculate the Fourier transform of the field on an aperture plane. We have shown how the Fourier transform of the field at an aperture plane z = constant can be evaluated via the direct plane-wave expansion and the ASM. Again, the ASM is the more efficient method. In the ASM, the Fourier transform of the field is given directly by the (0,0) Floquet wave in the phased-array problem and is thus relatively easy to numerically calculate, involving a single periodic moment-method solution. In contrast, the direct plane-wave expansion method requires the solution of an infinite number of plane-wave excitation problems (an infinite number of different incident angles) to calculate the Fourier transform of the field for a fixed set of transform wave numbers (k_x, k_y).

This chapter has also discussed some of the basic mathematical and numerical issues encountered when implementing the ASM. It was shown that because of branch-point singularities in the complex transverse wave number $\mathbf{k}_t$ plane, a periodic set of "branch-point circles" appears in the (k_x, k_y) plane. The integrand for the total field is less singular on these circles than is the integrand for the scattered field, and, hence, it is numerically more efficient to calculate the total field. When numerically implementing the ASM, a simple midpoint rectangle rule of integration works quite well for evaluating the k_x and k_y integrals due to the periodic nature of the integrand. When using this simple integration rule, it is possible to develop a simple physical interpretation of the error that is incurred when using a finite number of sample points. This simple interpretation shows that the error is due to an infinite number of periodically located "image" sources that appear further away from the original source as the number of sample points increases. This interpretation makes it clear that the integrals converge much faster in the case of a lossy medium due to the exponential decay of the fields from the image sources.

This chapter has also summarized the basic field behavior for the field excited by a single source located in proximity to a PAM. It has been shown that the total field consists of two parts, a spatial field and a sum of guided modes that propagate outward from the source along the PAM. The spatial

field arises from the branch-point circle, and it decays radially with distance ρ from the source along the PAM as $1/\rho^2$. In the far-zone region near the PAM, this field consists of a cylindrical wavefront together with an infinite set of Floquet waves induced by the periodicity. The guided modes may be of two types, bound modes and leaky modes. The bound modes are surface-wave-like modes for which all of the Floquet waves (space harmonics) decay exponentially away from the PAM and the wavevector of the guided mode is purely real. All the Floquet waves of the bound modes are slow waves (phase velocity slower than the speed of light). In contrast, a leaky mode is a guided wave for which at least one of the Floquet waves is fast with respect to the speed of light and hence is a radiating wave. The leaky mode has a wavevector that is complex, due to the leakage. In order for a leaky mode to be physical (and therefore significantly excitable by a practical source), all of the constituent Floquet waves must be physical, which means that the correct choice of branch for the vertical wave number must be used for each Floquet wave. The vertical wave number of a Floquet wave is improper if the wave is a forward wave (the dot product of the phase and attenuation vectors is positive) that is fast with respect to the speed of light.

Appendices: Spectral Singularities and Asymptotic Evaluation

We assume that the spectral integrals in Equation 12.16 or 12.29 are performed sequentially, and in particular, we consider the k_x integration to be performed first as the inner integral, followed by the k_y integration. Such integrations could be performed numerically to calculate the field or evaluated asymptotically as in Section 12.6.1 or Appendix B to highlight the physical nature of the excited wave species. The classification in Section 12.6.2 follows from an asymptotic evaluation. Here, we first describe the critical spectral points, and then we summarize the steps in the asymptotic evaluation.

Appendix A: Spectral Singularities

The path for the k_x integration stays on the top Riemann sheet of all the branch points, and the wave number k_{zpq} in Equation 12.13, for real k_x and k_y, is chosen as either purely real and positive or purely imaginary with a negative imaginary part. Physically, the location of the branch points for a given value of k_y is determined by the intersection of a horizontal line (constant k_y) with the circles shown in Figure 12.2. Although the integrations in Equations 12.22 and 12.31 are equivalent (and the form shown in Equation 12.22 is numerically more efficient, involving integrations with finite limits), the form shown in Equation 12.31 is preferred here for a discussion of path deformation, since the limits are infinite.

In performing the k_x integration in Equation 12.31, for each value of k_y, branch-point singularities may be encountered on the real axis of the k_x plane. Branch points are defined by $k_{xp}^2 + k_{yq}^2 = k^2$, corresponding to $k_{zpq} = 0$. Therefore, for a fixed value of k_y, there is a doubly infinite set of branch points in the k_x plane at

$$k_{xb,pq}^{\pm}(k_y) = \pm\sqrt{k^2 - k_{yq}^2} - F_{xp}, \tag{12.A.1}$$

as shown in Figure 12.A.1. The branch points are periodic in k_x, with a period $2\pi / a$. In the central Brillouin zone, defined as $-\pi/a < \text{Re}\, k_x < \pi/a$, there are an infinite number of branch points along the imaginary axis. We refer the reader to [33] for a detailed description of all possible cases.

In many practical cases the frequency is low enough so that $kb < \pi$, and there will be at most one pair of branch points on the real k_x axis within the integration region $-\pi/a < k_x < \pi/a$; all the others will lie on the imaginary k_x axis. This is the case shown in Figure 12.A.1a. The integration in the complex k_x plane in the region $-\pi/a < k_x < \pi/a$ can be deformed off the real axis to avoid the branch points on the real axis. When $ka > \pi$, branch cuts may overlap on the real k_x axis as shown in Figure 12.A.1b.

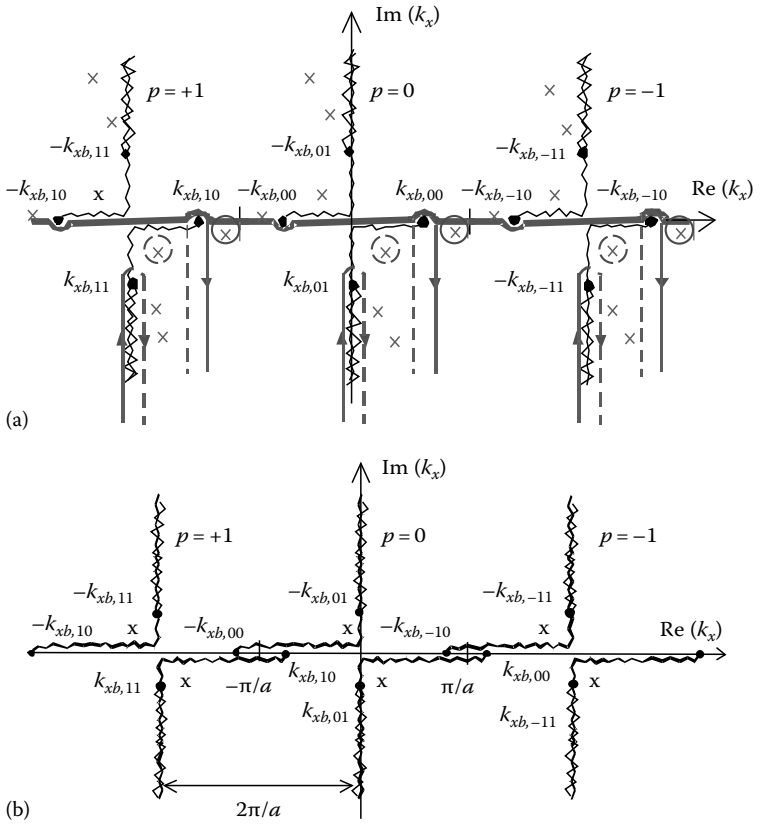

FIGURE 12.A.1 The complex k_x plane, for a fixed k_y value. (a) Case for $ka < \pi$ or equivalently $a/\lambda < 1/2$. (b) Case for $ka > \pi$. The poles (the **x** points below the branch cuts) and branch points are periodic in the k_x plane, with period $2\pi/a$. The integration path in the k_x plane is shown on the real axis (detouring around the branch-point singularities). The path may be deformed around the branch points as shown in part (a), yielding vertical paths that represent the harmonics of the spatial wave and poles whose residues represent the Floquet harmonics of the modal waves. (From Capolino, F., Jackson, D.R., Wilton, D.R., and Felsen, L.B., *IEEE Trans. Antennas Propag.*, 55(6), 1644, June 2007. With permission.)

As mentioned in Section 12.4.2, in performing the integration in Equation 12.31 for observation points along the PAM interface, the integrand $\mathbf{E}^{\infty}_{\text{sca}}(\mathbf{r}, \mathbf{r}_0, \mathbf{k}_t)$ is more singular at the branch points than is the integrand $\mathbf{E}^{\infty}_{\text{tot}}(\mathbf{r}, \mathbf{r}_0, \mathbf{k}_t)$. Physically, this is because the scattered field from the source decays more slowly with distance along the PAM than does the total field. The decay of the scattered field is $1/\rho$, which matches that of the incident field (the two must cancel on the conducting surfaces of the PAM). However, the total field has a more rapid decay of $1/\rho^2$ far away from the source, typical of the behavior observed in any interface problem, including, for example, a source over a dielectric layer. Hence, especially when evaluating the scattered field, care must be taken to integrate accurately near the branch points or to deform around them if possible (easily doable for the case of Figure 12.A.1a). The behavior of the fields has been verified numerically in Figure 12.7.

As described in Section 12.6.1, there may also appear bound-wave poles if the PAM allows for the guidance of such waves. In the absence of losses, they are located on the real axis, whereas with loss present, they will be below the real axis. In the case of Figure 12.A.1a, where $ka < \pi$, deforming the path off the real axis will avoid such poles. In the case of Figure 12.A.1b, where $ka > \pi$, it is not

possible to deform the path entirely off the real axis. However, in this case, all guided modes must be leaky modes [55] because at least one Floquet wave is a radiating fast wave for all k_x values within the Brillouin zone. The leaky-wave poles will lie below the real k_x axis.

Leaky modes may also exist in addition to bound modes. In the case of Figure 12.A.1a, the leaky-mode poles are denoted by crosses; for one of them, $Rek_x < k_{xb,00}$, so that the (0,0) Floquet wave is a forward wave that is improper (exponentially increasing vertically) and is located on the bottom Riemann sheet of the (0,0) branch point but is physical. The pole is located on the top Riemann sheet with respect to all the other branch points, so that only the (0,0) Floquet wave is improper. The leaky modes may cause numerical difficulty in performing the integration if they are close to the real axis, but this is an unusual situation unless the PAM has been specifically designed to form a leaky-wave antenna type of structure.

Appendix B: Asymptotic Evaluation of the Spectral Integral (Equation 12.31)

The analytic result (Equation 12.38) for the wave species excited by a source within the PAM is obtained by two sequential asymptotic evaluations of the integral (Equation 12.31), first in the k_x plane (inner integral), followed by second in the k_y plane. We limit our description to observation points near the PAM interface; for locations not close to it, the procedure outlined below must be changed, and the field representation requires the concept of shadow boundaries, which for periodic structures are rather complicated. We refer the reader to [58,59] for more details and to [60,61] for an analogous problem (fields arising at an array edge-truncation) where a detailed asymptotic analysis has been carried out for the scattered fields.

When the observation point is not far from the PAM boundary and is electrically distant from the source ($\rho \to \infty$), the k_x integration path on the real axis, shown in Figure 12.A.1a, is deformed onto the vertical paths around the branch points. These are steepest descent paths that represent collections of plane waves arriving at the observation point with the same phase. Each steepest descent path represents a certain wave species, since it provides a wave field that has a well-defined wave number. In the k_x-plane path deformation, certain poles may be encountered; their residues, which represent modal excitation amplitudes, must be added to the total field. The sum of the steepest descent integrations $\mathbf{I}_{pq}^{\text{branch}}(k_y)$ from the vertical paths descending from the branch points and the residues from the integrations $\mathbf{I}_{pq}^{\text{pole}}(k_y)$ around the poles leads to the following representation:

$$\mathbf{E}_{\text{tot}}(\mathbf{r}, \mathbf{r}_0) = \sum_{pq=-\infty}^{\infty} \int_{-\infty}^{\infty} \left[\mathbf{I}_{pq}^{\text{branch}}(k_y) + \mathbf{I}_{pq}^{\text{pole}}(k_y) \right] e^{-jk_y y} dk_y. \tag{12.B.1}$$

Each term of the pq-sum is thus split into two integrals that, when asymptotically evaluated via their saddle-point contributions, lead to the final field representation in Equation 12.38.

References

1. P.-S. Kildal, Artificially soft and hard surfaces in electromagnetics, *IEEE Transactions on Antennas Propagation*, 38(10), 1537–1544, Oct. 1990.
2. Z. Ying and P.-S. Kildal, Improvements of dipole, helix, spiral, microstrip patch and aperture antennas with ground planes by using corrugated soft surfaces, *Microwaves, Antennas and Propagation, IEE Proceedings*, 143(3), 244–248, June 1996.

3. D. Sievenpiper, L. Zhang, R. Broas, N. Alexopoulos, and E. Yablonovitch, High-impedance electromagnetic surfaces with a forbidden frequency band, *IEEE Transactions on Microwave Theory and Techniques*, 47(11), 2059–2074, Nov. 1999.
4. R. Gonzalo, P. de Maagt, and M. Sorolla, Enhanced patch-antenna performance by suppressing surface waves using photonic-bandgap substrates, *IEEE Transactions on Antennas and Propagation*, 47(11), 2131–2138, Nov. 1999.
5. H. Y. D. Yang, R. Kim, and D. R. Jackson, Design considerations for modeless integrated circuit substrates using planar periodic patches, *IEEE Transactions on Microwave Theory and Techniques*, 48(12), 2233–2239, Dec. 2000.
6. R. B. Hwang and S. T. Peng, Surface-wave suppression of resonance-type periodic structures, *IEEE Transactions on Antennas and Propagation*, 51(6), 1221–1229, June 2003.
7. P. A. Belov, S. A. Tretyakov, and A. J. Viitanen, Dispersion and reflection properties of artificial media formed by regular lattices of ideally conducting wires, *Journal of Electromagnetic Waves and Applications*, 16(8), 1153–1170, 2002.
8. E. I. Smirnova, C. Chen, M. A. Shapiro, J. R. Sirigiri, and R. J. Temkin, Simulation of photonic band gaps in metal rod lattices for microwave applications, *Journal of Applied Physics*, 91(3), 960–968, Feb. 2002.
9. I. Nefedov and A. J. Viitanen, Wire media, in *Theory and Phenomena of Metamaterials*, Taylor & Francis, Boca Raton, FL, Chapter 15, 2009.
10. G. Goussetis, A. Feresidis, A. Yakovlev, and C. Simovski, High impedance surfaces, in *Theory and Phenomena of Metamaterials*, Taylor & Francis, Boca Raton, FL, Chapter 31, 2009.
11. Y. C. Vardaxoglou, R. D. Seager, J. A. Flint, A. Chauraya, G. K. Palikaras, and C.B. Mulenga, Metamaterials antenna applications, in *Applications of Metamaterials*, Taylor & Francis, Boca Raton, FL, Chapter 20, 2009.
12. A. Feresidis, G. Goussetis, A. Yakovlev, and C. Simovski, High-impedance surfaces: Applications, in *Applications of Metamaterials*, Taylor & Francis, Boca Raton, FL, Chapter 21, 2009.
13. S. Enoch, G. Tayeb, P. Sabouroux, N. Guérin, and P. Vincent, A metamaterial for directive emission, *Physical Review Letters*, 89(21), 213902-1–213902-4, Nov. 2002.
14. P. Burghignoli, G. Lovat, F. Capolino, D. R. Jackson, and D. R. Wilton, Analysis of directive radiation from a line source in a metamaterial slab with low permittivity, *IEEE Transactions on Antennas and Propagation*, 54(3), 1017–1030, March 2006.
15. G. Lovat, P. Burghignoli, F. Capolino, D. R. Jackson, and D. R. Wilton, Enhancement of directivity by using metamaterial substrates, in *Applications of Metamaterials*, Taylor & Francis, Boca Raton, FL, Chapter 19, 2009.
16. T. Zhao, D. R. Jackson, J. T. Williams, H. Y. Yang, and A. A. Oliner, 2-D periodic leaky-wave antennas—Part I: Metal patch design, *IEEE Transactions on Antennas and Propagation*, 53(11), 3505–3514, Nov. 2005.
17. T. Zhao, D. R. Jackson, and J. T. Williams, 2-D periodic leaky-wave antennas—Part II: Slot design, *IEEE Transactions on Antennas and Propagation*, 53(11), 3515–3524, Nov. 2005.
18. V. M. Shalaev, W. Cai, U. Chettiar, H. -K. Yuan, A. K. Sarychev, V. P. Drachev, and A. V. Kildishev, Negative index of refraction in optical metamaterials, *Optical Letters*, 30, 3356–3358, 2005.
19. S. Zhang, W. Fan, N. C. Panoiu, K. J. Malloy, R. M. Osgood, and S. R. J. Brueck, Experimental demonstration of near-infrared negative-index metamaterials, *Physical Review Letters*, 95(13), 137404, 2005.
20. N. Katsarakis, G. Konstantinidis, A. Kostopoulos, R. S. Penciu, T. F. Gundogdu, M. Kafesaki, E. N. Economou, Th. Koschny, and C. M. Soukoulis, Magnetic response of split-ring resonators in the far-infrared frequency regime, *Optical Letters*, 30, 1348–1350, 2005.
21. K. Aydin, K. Guven, C. M. Soukoulis, and E. Ozbay, Observation of negative refraction and negative phase velocity in left-handed metamaterials, *Applied Physics Letters*, 86, 124102, 2005.

22. R. Sigelmann and A. Ishimaru, Radiation from periodic structures excited by an aperiodic source, *IEEE Transactions on Antennas and Propagation*, 13(3), 354–364, May 1965.
23. R. J. Mailloux, Excitation of a surface wave along an infinite yagi-uda array, *IEEE Transactions on Antennas and Propagation*, 13, 719–724, 1965.
24. C. P. Wu and V. Galindo, Properties of a phased array of rectangular waveguides with thin walls, *IEEE Transactions on Antennas and Propagation*, 14, 163–173, March 1966.
25. B. A. Munk and G. A. Burrell, Plane-wave expansion for arrays of arbitrarily oriented piecewise linear elements and its application in determining the impedance of a single linear antenna in a lossy half-space, *IEEE Transactions on Antennas and Propagation*, 27, 331–343, May 1979.
26. H.-Y. D Yang, Theory of antenna radiation from photonic band-gap materials source, *Electromagnetics*, 19(3), 255–276, 1999.
27. H.-Y. D Yang and D. R. Jackson, Theory of line-source radiation from a metal-strip grating dielectric slab structure, *IEEE Transactions on Antennas and Propagation*, 48, 556–564, 2000.
28. C. Caloz, A. K. Skrivervik, and F. E. Gardiol, Comparison of two methods for the computation of Green's functions in photonic bandgap materials: The eigenmode-expansion method and the phased-array method, *Microwave and Optical Technology Letters*, 27(5), 323–330, Dec. 2000.
29. C. Caloz, Green's functions in a PC-PPWG structure, *Microwave and Optical Technology Letters*, 29(6), 405–408, June 2001.
30. C. Caloz, A. K. Skrivervik, and F. E. Gardiol, An efficient method to determine Green's functions of a two-dimensional photonic crystal excited by a line source—The phased-array method, *IEEE Transactions on Antennas and Propagation*, 50, 1380–1391, May 2002.
31. F. Capolino, D. R. Jackson, D. R. Wilton, and L. B. Felsen, Representation of the field excited by a line source near a 2D periodic artificial material, in *Fields, Networks, Computational Methods, and Systems in Modern Electrodynamics*, P. Russer and M. Mongiardo, Eds., Springer-Verlag, Berlin, ISBN 3540-23929-4, pp. 13–24, 2004.
32. F. Capolino, D. R. Jackson, and D. R. Wilton, Fundamental properties of the field at the interface between air and a periodic artificial material excited by a line source, *IEEE Transactions on Antennas and Propagation*, 53(1), 91–99, Jan. 2005.
33. F. Capolino, D. R. Jackson, D. R. Wilton, and L. B. Felsen, Comparison of methods for calculating the field excited by a dipole near a 2-D periodic material, *IEEE Transactions on Antennas and Propagation*, 55(6), 1644–1655, June 2007.
34. H.-Y. D Yang, Analysis of microstrip dipoles on planar artificial periodic dielectric structures, *Journal of Electromagnetic Waves and Applications*, 18(10), 1373–1388, 2004.
35. F. Capolino, D. R. Jackson, and D. R. Wilton, Mode excitation from sources in two-dimensional PBG waveguides using the array scanning method, *IEEE Microwave on Wireless Components Letters*, 15(2), 49–51, Feb. 2005.
36. P. C. Chaumet and A. Sentenac, Numerical simulations of the electromagnetic field scattered by defects in a double-periodic structure, *Physical Review B*, 72, 205437, 2005.
37. S. Wilcox, L. C. Botten, R. C. McPhedran, C. G. Poulton, and C. Martijn de Sterke, Modeling of defect modes in photonic crystals using the fictitious source superposition method, *Physical Review E*, 71, 056606, 2005.
38. X. Dardenne and C. Craeye, ASM based method for the study of periodic metamaterials excited by a slotted waveguide, in *Proceedings of the IEEE Symposium on Antennas and Propagation*, 3–8 July, Washington, D.C., 2005, pp. 692–695.
39. I. Thompson and C. M. Linton, On the excitation of a closely spaced array by a line source, *IMA Journal of Applied Mathematics*, 72, 476–497, Aug. 2007.
40. V. Jandieri, K. Yasumoto, and H. Toyama, Radiation from a line source placed in two-dimensional photonic crystals, *International Journal of Infrared Millimeter Waves*, 28(12), 1161–1173, 2007.

41. G. Valerio, P. Baccarelli, P. Burghignoli, A. Galli, R. Rodríguez-Berral, and F. Mesa, Analysis of periodic shielded microstrip lines excited by monperiodic sources through the array scanning method, *Radio Science*, 43, RS1009, 2008.
42. R. Qiang, J. Chen, F. Capolino, D. R. Jackson, and D. R. Wilton, ASM–FDTD: A technique for calculating the field of a finite source in the presence of an infinite periodic artificial material, *IEEE Microwave on Wireless Components Letters*, 17(4), 271–273, April 2007.
43. J. Chen, F. Yang, and R. Qiang, FDTD method for periodic structures, in *Theory and Phenomena of Metamaterials*, Taylor & Francis, Boca Raton, FL, Chapter 6, 2009.
44. S. Steshenko and F. Capolino, Single dipole approximation for collections of nanoscatterers, in *Theory and Phenomena of Metamaterials*, Taylor & Francis, Boca Raton, FL, Chapter 8, 2009.
45. S. Steshenko, F. Capolino, S. Tretyakov, and C. S. Simovski, Super resolution and near-field enhancement with layers of resonant arrays of nanoparticles, in *Applications of Metamaterials*, Taylor & Francis, Boca Raton, FL, Chapter 4, 2009.
46. D. R. Wilton, Computational methods, in *Scattering: Scattering and Inverse Scattering in Pure and Applied Science*, vol. 1, E. R. Pike and P. C. Sabatier, Eds., Academic Press/Elsevier, Amsterdam, the Netherlands, 2002, pp. 316–365, Chapter 1.5.5.
47. C. Craeye, X. Radu, F. Capolino, and A. G. Schuchinsky, Fundamentals of method of moments for article materials, in *Theory and Phenomena of Metamaterials*, Taylor & Francis, Boca Raton, FL, Chapter 5, 2009.
48. A. Taflove and S. Hagness, *Computational Electrodynamics: The Finite Difference Time Domain Method*, 2nd edn., Artech House, Boston, MA, 2000.
49. J. A. C. Weideman, Numerical integration of periodic functions: A few examples, *American Mathematical Monthly*, 109, 21–36, Jan. 2002.
50. T. Tamir and A. A. Oliner, Guided complex waves—Part I: Fields at an interface, *Proceedings of the Institute of Electrical Engineers (London)*, 110, 310–324, Feb. 1963.
51. T. Tamir and A. A. Oliner, Guided complex waves—Part II: Relation to radiation patterns, *Proceedings of the Institute of Electrical Engineers (London)*, 110, 325–334, Feb. 1963.
52. T. Tamir and A. A. Oliner, The spectrum of electromagnetic waves guided by a plasma layer, *Proceedings of the IEEE*, 51(2), 317–332, Feb. 1963.
53. A. Hessel, General characteristics of traveling wave antennas, in *Antenna Theory*, R. E. Collin and F. J. Zucker, Eds., McGraw-Hill, New York, 1969, Chapter 19.
54. T. Tamir, Leaky wave antennas, in *Antenna Theory*, R. E. Collin and F. J. Zucker, Eds., McGraw-Hill, New York, 1969, Chapter 20.
55. A. A. Oliner and D. R. Jackson, Leaky-wave antennas, in *Antenna Engineering Handbook*, J. L. Volakis, Ed. McGraw-Hill, New York, 2007, Chapter 11.
56. P. Baccarelli, S. Paulotto, and C. Di Nallo, Full-wave analysis of bound and leaky modes propagating along 2D periodic printed structures with arbitrary metallisation in the unit cell, *IET Microwave Antennas and Propagation*, 1(1), 217–225, 2007.
57. L. B. Felsen and N. Marcuvitz, *Radiation and Scattering of Waves*, Prentice-Halls, Englewood Cliffs, NJ, 1973 (also IEEE Press, 1994).
58. D.-H. Kwon, High-frequency ray behavior of floquet modes arising from electromagnetic scattering by periodic structures with line-source excitation, private communication.
59. V. Lomakin and E. Michielssen, Beam transmission through periodic sub-wavelength hole structures, *IEEE Transactions on Antennas and Propagation*, 55(6), 1564–1581, 2007.
60. F. Capolino, M. Albani, S. Maci, and L. B. Felsen, Frequency domain Green's function for a planar periodic semi-infinite phased array. Part I: Truncated Floquet wave formulation, *IEEE Transaction on Antennas and Propagation*, 48(1), 67–74, Jan. 2000.
61. F. Capolino, M. Albani, S. Maci, and L. B. Felsen, Frequency domain Green's function for a planar periodic semi-infinite phased array. Part II: Phenomenology of the diffracted waves, *IEEE Transactions on Antennas and Propagation*, 48(1), 75–85, Jan. 2000.

13

Modal Properties of Layered Metamaterials

Paolo Baccarelli
Sapienza University of Rome

Paolo Burghignoli
Sapienza University of Rome

Alessandro Galli
Sapienza University of Rome

Paolo Lampariello
Sapienza University of Rome

Giampiero Lovat
Sapienza University of Rome

Simone Paulotto
Sapienza University of Rome

Guido Valerio
Sapienza University of Rome

13.1 Introduction

This chapter addresses modal properties of layered structures composed by metamaterials and their basic applications in waveguiding and radiating devices.

In Section 13.2 an overview of results that appeared in the literature on this topic is presented, without aiming for completeness, to provide the reader some background information. The attention is then focused on a specific structure, that is, a grounded metamaterial slab, which, as is well known, constitutes a basic building block in a variety of planar microwave components. This is described in Section 13.3, where the theoretical approach used for its analysis and the models adopted for the metamaterial parameters are illustrated. In Section 13.4, the surface-wave propagation on a grounded metamaterial slab is discussed and simple sufficient conditions for surface-wave suppression are given, showing their application to reduce edge-diffraction effects in planar antennas and to achieve unimodal propagation in nonradiative dielectric waveguides. In Section 13.5, complex (leaky) waves supported by the same reference structure are studied, illustrating some of their peculiar radiative properties.

13.2 Background

The study of modal properties of layered structures characterized by possibly negative effective parameters has been a topic of interest since the 1960s: in [1] the discrete spectrum of a slab with plasma-like permittivity in air is investigated, including a discussion on contributions to the total field arising from complex improper (leaky) waves. The analysis in [2] is focused on surface waves guided by an interface between air and a half-space filled with a uniaxial ferromagnetic and plasmonic permittivity. In [3] guidance properties are studied in a slab with negative permittivity surrounded by double positive (DPS, i.e., with positive ε and μ) slabs and in a DPS slab surrounded by two negative-permeability slabs.

More recently, within the frame of the great amount of research in the field of negative-index materials (NIMs), several analyses have been carried out about modal properties of layered media with both electric and magnetic parameters assuming negative values (double negative, DNG) or with only one negative parameter (single negative, SNG), with either $\varepsilon < 0$ (epsilon-negative, ENG) or $\mu < 0$ (mu-negative, MNG). Different models for these parameters have been considered: e.g., a simple scalar plasma-like temporal-dispersive behavior, anisotropic effective media, and anisotropic with both temporal and spatial dispersive features. New dispersive phenomena have been found, such as monomodal propagation with an unusual range of physical or geometrical parameters and contradirectional flows of power in media with different handedness. Moreover, different kinds of waves (surface polaritons, surface plasmons, or surface evanescent waves [4]) are present with respect to DPS slabs. These surface waves, previously known at a metal–dielectric interface, are attenuated in both media at the boundary of the guiding interface.

Surface waves along the interface between an NIM and a DPS half-space are studied in [5]. The effects of these waves on the performance of the perfect lens proposed in [6] are discussed in [7], where it is shown that a realistic transition modeling the interface between a DPS and a DNG gives rise to surface waves, which could deteriorate the perfect lens behavior. In [8] it is found that the spatial dispersion of the slab limits the achievable resolution in such a structure. In [9], a graphical method is proposed to study evanescent surface waves along an NIM slab in a DPS medium. In [10] an NIM half-space is in contact with a DPS medium or with an SNG media (with either $\varepsilon < 0$ or $\mu < 0$).

In [11] the propagation of ordinary waves (attenuated only in air) for an NIM slab in air is studied; in [12] a DNG and an SNG slab surrounded by a DPS dielectric are studied, and relevant energy issues are discussed. In [13] the discrete spectrum of an NIM slab sandwiched between different DPS dielectrics is considered.

Nonlinear effects in the propagation of surface waves along DNG–DPS interfaces between nonlinear metamaterials are studied in [14] through an ad hoc formulation of the electromagnetic problem, with energy considerations similar to the linear case.

A rich collection of results on possible applications of layered metamaterial structures is given in [15]: several reference structures, here only briefly mentioned, are examined through both dispersive and excitation analyses with details about energy propagation. For more details, the bibliography of that chapter is suggested. A parallel-plate waveguide inhomogenously filled with two DPS/SNG/DNG media is investigated. An ENG–MNG pair of slabs is seen to allow for a monomodal propagation of a surface plasmon along the interface with an arbitrarily large waveguide section, thus improving coupling with waves impinging on the waveguide. Furthermore, particular choices of the two media can give rise to interesting dispersive behaviors: monomodal propagation can occur with an arbitrarily thin distance between the metallic plates, or the fundamental mode can present an arbitrarily large value of its wavenumber. These phenomena can lead to the possibility of miniaturized waveguides or resonators. The case of a DNG slab in air is also treated: while the thinner is a DPS slab the larger is its effective cross-section, a DNG slab can be made as thin as possible, thus increasing the confinement of the field of its fundamental mode. Finally, a design of a backward coupler is shown by means of the

well-known contradirectional power flow in media with different handedness, by properly placing a DPS slab near a DNG slab.

In [16] dispersive studies of a DNG slab in air are shown to be useful to investigate its reflection and transmission properties. In [17] surface waves at the interface between two general kinds of media are studied: details on energy transport, inverse Cherenkov radiation, and Doppler shift are shown, with results analogous to those obtained with bulk waves.

In [18] the leaky regimes of the same structure are studied to characterize their spectral nature and to show the possibility to obtain a leaky-wave antenna by exciting these leaky waves through an elementary dipole source. A similar analysis has also been carried out in [19] considering a line-current excitation. In [20] the spectrum of the surface waves of a grounded NIM slab in air is studied, with the aim of deriving sufficient conditions for their suppression in a given range of frequency. A dispersive analysis of a grounded metamaterial slab can also be found in [21], with reference to guided waves only. More details on these topics are given in the following sections.

Different models have been adopted for the parameters of the layers. In [22] guided waves are studied in a grounded wire medium slab, taking into account its anisotropy and its temporal and spatial dispersion. In [23] it is shown that in such a structure the spatial dispersion surprisingly determines an isotropic modal propagation along the slab, despite the inherent anisotropy of the microscopic arrangement of the wires. For more details on antenna applications of wire media see Chapter 19 of *Applications of Metamaterials*.

More complex structures are analyzed, for example, in [24], where a discontinuity in DNG slabs is studied with the mode-matching method. In [25] the electromagnetic coupling is studied both between DNG slabs and between a DNG and a DPS slab, surrounded by air. The dispersive properties of a surface-terminated photonic bandgap (PBG) are studied in [26], where comparisons are shown with the dispersion behavior of an infinite PBG. The surface evanescent waves of a multilayer structure are investigated in [27], with layers alternatively made by isotropic DPS and ferromagnetic materials. The analysis is performed by means of the transmission-matrix formalism. The presence of several interfaces allows for the propagation of different kinds of surface polaritons, which affect the transmission properties of the structure.

13.3 Grounded Metamaterial Slabs: Structure Description

In the following sections the attention is focused on a specific reference structure, namely a grounded metamaterial (isotropic) slab. A sketch of the structure is provided in Figure 13.1, along with the relevant transverse network representation from which the dispersion equation for transverse electric (TE) and transverse magnetic (TM) modes (with respect to the transverse direction y) can easily be derived.

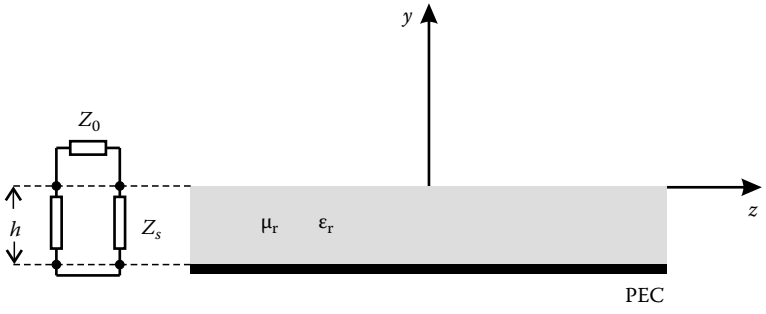

FIGURE 13.1 The reference structure of a grounded metamaterial slab and its transverse equivalent network.

A time-harmonic dependence $e^{j\omega t}$ is assumed and suppressed throughout. No variation of the electromagnetic field is assumed along the x direction, thus the two-dimensional nature of the problem allows us to study TE and TM modes separately. As is well known, a transverse equivalent network in the y direction can be associated to each TE or TM mode [28], as shown in Figure 13.1. The expressions of the relevant characteristic impedances for the two polarizations in the air and slab regions (subscripts 0 and s, respectively) are as follows:

$$\begin{aligned} Z_0^{\mathrm{TE}} &= \frac{\omega\mu_0}{k_{y0}}, \quad Z_{\mathrm{s}}^{\mathrm{TE}} = \frac{\omega\mu_0\mu_{\mathrm{r}}}{k_{ys}} \\ Z_0^{\mathrm{TM}} &= \frac{k_{y0}}{\omega\varepsilon_0}, \quad Z_{\mathrm{s}}^{\mathrm{TM}} = \frac{k_{ys}}{\omega\varepsilon_0\varepsilon_{\mathrm{r}}}, \end{aligned} \tag{13.1}$$

where

$$k_{y0} = \sqrt{k_0^2 - k_z^2}, \quad k_{ys} = \sqrt{k_{\mathrm{s}}^2 - k_z^2} \tag{13.2}$$

are the vertical wavenumbers in air and in the slab, respectively, with $k_0^2 = \omega^2\mu_0\varepsilon_0$ and $k_{\mathrm{s}}^2 = k_0^2\mu_{\mathrm{r}}\varepsilon_{\mathrm{r}}$.

The dispersion equation for TE and TM modes can be obtained by enforcing the transverse-resonance condition, for example, at $y = 0$, on the relevant equivalent network. The result is

$$jZ_{\mathrm{s}}\tan(k_{ys}h) + Z_0 = 0. \tag{13.3}$$

The metamaterial slab will be assumed homogeneous, isotropic, and lossless, with permeability $\mu_{\mathrm{s}} = \mu_0\mu_{\mathrm{r}}$ and permittivity $\varepsilon_{\mathrm{s}} = \varepsilon_0\varepsilon_{\mathrm{r}}$, where relative permeabilities and permittivities, μ_{r} and ε_{r}, respectively, will be modeled as simple, scalar plasma-like, temporal-dispersive behaviors. In particular, relative permeabilities will be chosen as in [29]:

$$\mu_{\mathrm{r}}(\omega) = 1 - \frac{\omega_{\mathrm{mp}}^2 - \omega_{\mathrm{m0}}^2}{\omega^2 - \omega_{\mathrm{m0}}^2} \tag{13.4}$$

or as in [30]:

$$\mu_{\mathrm{r}}(\omega) = 1 - \frac{F\omega^2}{\omega^2 - \omega_{\mathrm{m0}}^2}, \tag{13.5}$$

where ω_{m0} is the magnetic resonance angular frequency, ω_{mp} is the magnetic plasma angular frequency, and F is an adimensional factor, while relative permittivities will be chosen as in [29].

$$\varepsilon_{\mathrm{r}}(\omega) = 1 - \frac{\omega_{\mathrm{ep}}^2}{\omega^2}, \tag{13.6}$$

with ω_{ep} the electronic plasma angular frequency. These expressions will allow us to obtain either DNG or SNG slabs in certain frequency ranges, provided that appropriate values are chosen for the relevant resonance and plasma frequencies.

13.4 Grounded Metamaterial Slabs: Surface Waves

The problem addressed here is the study of guided modes supported by this structure, propagating along the longitudinal z direction with a real propagation constant $k_z = \beta_z$. The dispersion equation (Equation 13.3) will be studied in Sections 13.4.1 and 13.4.2 for TE and TM modes, by considering DNG and SNG slabs separately.

Since the grounded slab is a transversely open structure, its modes can be either proper, that is, attenuating at infinity in the transverse y direction ($\mathrm{Im}(k_{y0}) < 0$), or improper, that is, diverging at infinity ($\mathrm{Im}(k_{y0}) > 0$) [28]. In particular, surface waves have a purely imaginary transverse wavenumber in air, with $k_{y0} = -j\alpha_{y0}$ for proper surface waves and $k_{y0} = +j\alpha_{y0}$ for improper surface waves ($\alpha_{y0} > 0$).

In addition to this, when one (or both) of the constitutive parameters is negative, two kinds of real solutions, corresponding to surface waves supported by the structure, have to be considered, that is, ordinary surface waves, with a real transverse wave number $k_{ys} = \beta_{ys}$ inside the slab, and evanescent surface waves, with an imaginary wave number $k_{ys} = j\,\alpha_{ys}$ inside the slab. It is known that ordinary surface waves cannot exist in SNG slabs, whereas evanescent surface waves cannot exist in a grounded DPS isotropic slab, although they are known to be present in SNG and DNG slabs [9,12], and in other specific (anisotropic) structures, for example, ferrite slabs [31,32].

13.4.1 TE Surface Waves

Ordinary TE surface waves

In this case, the dispersion equation (Equation 13.3) for proper real modes can be written as

$$\tan(\beta_{ys}h) = \frac{1}{|\mu_r|}\frac{\beta_{ys}}{\alpha_{y0}}. \tag{13.7}$$

By taking into account that $\alpha_{y0}^2 = (k_s^2 - k_0^2) - \beta_{ys}^2$, Equation 13.7 becomes

$$\tan(\beta_{ys}h) = \frac{1}{|\mu_r|}\frac{\beta_{ys}h}{\sqrt{k_0^2h^2(\mu_r\varepsilon_r - 1) - \beta_{ys}^2h^2}}. \tag{13.8}$$

The condition $k_0 < \beta_z < k_s$ implies that ordinary TE surface waves cannot exist if $\mu_r\varepsilon_r < 1$ (which would imply $k_s < k_0$). Therefore, only the case $\mu_r\varepsilon_r > 1$ has to be considered if this type of waves is studied.

Evanescent TE surface waves

In this case, $\beta_z > k_s$ and the dispersion equation (Equation 13.3) for proper real modes can be written as

$$\tanh(\alpha_{ys}h) = \frac{1}{|\mu_r|}\frac{\alpha_{ys}}{\alpha_{y0}} = \frac{1}{|\mu_r|}\frac{\alpha_{ys}h}{\sqrt{k_0^2h^2(\mu_r\varepsilon_r - 1) + \alpha_{ys}^2h^2}}. \tag{13.9}$$

Both the cases $\mu_r\varepsilon_r \lessgtr 1$ have to be considered.

13.4.2 TM Surface Waves

Ordinary TM surface waves

In this case, the dispersion equation (Equation 13.3) for proper real modes can be written as

$$\tan(\beta_{ys}h) = -|\varepsilon_r|\frac{\alpha_{y0}}{\beta_{ys}} = -|\varepsilon_r|\frac{\sqrt{k_0^2h^2(\mu_r\varepsilon_r - 1) - \beta_{ys}^2h^2}}{\beta_{ys}h}. \tag{13.10}$$

As for the TE case, the condition $k_0 < \beta_z < k_s$ implies that ordinary surface waves cannot exist if $\mu_r\varepsilon_r < 1$. Only the case $\mu_r\varepsilon_r > 1$ has to be examined.

Evanescent TM surface waves

In this case, $\beta_z > k_s$ and the dispersion equation (Equation 13.3) for proper real modes can be written as

$$\tanh(\alpha_{ys}h) = |\varepsilon_r|\frac{\alpha_{y0}}{\alpha_{ys}} = |\varepsilon_r|\frac{\sqrt{k_0^2h^2(\mu_r\varepsilon_r - 1) + \alpha_{ys}^2h^2}}{\alpha_{ys}h}. \tag{13.11}$$

Both the cases $\mu_r\varepsilon_r \lessgtr 1$ have to be considered.

13.4.3 Surface-Wave Suppression in Grounded DNG Slabs

By means of a simple graphical analysis it can be shown that for each kind of proper surface wave supported by a grounded DNG slab, conditions may be found that inhibit its propagation. However, it is necessary to ascertain if simultaneous suppression of all kinds of such waves can be obtained. In this connection, the cases of $\mu_r\varepsilon_r \lessgtr 1$ will be considered separately.

Sufficient conditions to avoid propagation of proper surface waves in the case $\mu_r\varepsilon_r < 1$ are summarized in Table 13.1, where $b = k_0h\sqrt{1 - \mu_r\varepsilon_r}$. In particular, the condition reported for TE modes is also a necessary condition, whereas the condition for TM modes is only sufficient.

By examining Table 13.1, it can be concluded that, to inhibit the propagation of every kind of surface wave (both ordinary and evanescent) when $\mu_r\varepsilon_r < 1$, a sufficient condition is that the following set of inequalities is satisfied:

$$\begin{cases} |\mu_r| < 1 \\ |\varepsilon_r| < 1 \end{cases} \tag{13.12}$$

provided that

$$b > \tanh^{-1}(|\varepsilon_r|). \tag{13.13}$$

In particular the last inequality can be satisfied, at a fixed frequency f, by choosing the slab thickness h sufficiently large; in fact, the condition on b in Equation 13.13 can also be expressed as

$$h > \tanh^{-1}(|\varepsilon_r|)\frac{c}{2\pi f\sqrt{1 - \mu_r\varepsilon_r}}, \tag{13.14}$$

where c is the speed of light in a vacuum.

Sufficient conditions to avoid propagation of proper surface waves in the case $\mu_r\varepsilon_r > 1$ are collected in Table 13.2, where $a = k_0h\sqrt{\mu_r\varepsilon_r - 1}$. In particular, the condition reported for TM evanescent waves is also a necessary condition, whereas the other conditions are only sufficient ones. By examining the alternative conditions for TE-mode suppression, it can be deduced that the only consistent pairs are

TABLE 13.1 Summary of Conditions for Suppression of Proper Surface Waves of Different Kinds on Grounded DNG Slabs with $\mu_r\varepsilon_r < 1$

TE		TM	
Ordinary	Evanescent	Ordinary	Evanescent
–	$\lvert\mu_r\rvert < 1$	–	$\begin{cases} \lvert\varepsilon_r\rvert < 1 \\ b > \tanh^{-1}(\lvert\varepsilon_r\rvert) \end{cases}$

Source: Baccarelli, P., Burghignoli, P., Frezza, F., Galli, A., Lampariello, P., Lovat, G., and Paulotto, S., *IEEE Trans. Microw. Theory Tech.* 53(4), 1431, 2005. With permission.

Notes: The condition for evanescent TE waves is necessary and sufficient; the condition for evanescent TM waves is only sufficient. Ordinary waves cannot exist in this case.

TABLE 13.2 Summary of Conditions for Suppression of Proper Surface Waves of Different Kinds on Grounded DNG Slabs with $\mu_r\varepsilon_r > 1$

TE	
Ordinary	Evanescent
(o1) $\begin{cases} \dfrac{1}{a\lvert\mu_r\rvert} > 1 \\ a < \tan^{-1}\left(\dfrac{1}{\lvert\mu_r\rvert}\right) \end{cases}$ or	(e1) $\begin{cases} \lvert\mu_r\rvert < 1 \\ a < \sqrt{\dfrac{1}{\lvert\mu_r\rvert^2} - 1} \end{cases}$ or
(o2) $\sqrt{\dfrac{1}{\lvert\mu_r\rvert^2} + \left(\dfrac{\pi}{2}\right)^2} < a < \pi$	(e2) $\begin{cases} \lvert\mu_r\rvert > 1 \\ a > \tanh^{-1}\dfrac{1}{\lvert\mu_r\rvert} \end{cases}$
TM	
Ordinary	Evanescent
$a < \dfrac{\pi}{2}$	$\lvert\varepsilon_r\rvert > 1$

Source: Baccarelli, P., Burghignoli, P., Frezza, F., Galli, A., Lampariello, P., Lovat, G., and Paulotto, S., *IEEE Trans. Microw. Theory Tech.* 53(4), 1431, 2005. With permission.
Notes: The condition for evanescent TM waves is necessary and sufficient; the other conditions are only sufficient.

(o1)–(e1) or (o2)–(e2). However, it can easily be seen that the only pair compatible with the reported conditions for TM-mode suppression is the (o1)–(e1) pair.

Therefore, to inhibit the propagation of every kind of surface wave (both ordinary and evanescent) when $\mu_r\varepsilon_r > 1$, a sufficient condition is given by the following set of inequalities:

$$\begin{cases} \lvert\mu_r\rvert < 1 \\ \lvert\varepsilon_r\rvert > 1 \\ a < \tan^{-1}\left(\dfrac{1}{\lvert\mu_r\rvert}\right) \\ a < \sqrt{\dfrac{1}{\lvert\mu_r\rvert^2} - 1} \end{cases} \tag{13.15}$$

which can also be written as

$$\begin{cases} \lvert\mu_r\rvert < 1 \\ \lvert\varepsilon_r\rvert > 1 \end{cases} \tag{13.16}$$

provided that

$$a < \eta = \min\left\{\tan^{-1}\left(\frac{1}{\lvert\mu_r\rvert}\right), \sqrt{\frac{1}{\lvert\mu_r\rvert^2} - 1}\right\}. \tag{13.17}$$

In this case the condition on a can be achieved, at a fixed frequency f, by choosing the slab thickness h sufficiently small; in fact, the inequality in Equation 13.17 can be expressed as

$$h < \eta \frac{c}{2\pi f\sqrt{\mu_r\varepsilon_r - 1}}. \tag{13.18}$$

Similar results can be obtained for grounded SNG slabs as reported in Table 13.3.

For the case of grounded MNG slabs, surface-wave suppression is achieved if and only if $\lvert\mu_r\rvert < 1$, without any additional condition on the slab thickness. For the case of grounded ENG slabs, a sufficient condition to achieve surface-wave suppression is that $\lvert\varepsilon_r\rvert < 1$, provided that the slab thickness h satisfies the inequality

$$h > \tanh^{-1}(\lvert\varepsilon_r\rvert)\frac{c}{2\pi f\sqrt{1 + \lvert\mu_r\varepsilon_r\rvert}}. \tag{13.19}$$

TABLE 13.3 Summary of Conditions for Suppression of Proper Surface Waves on Grounded MNG and ENG Slabs

MNG		ENG	
TE	TM	TE	TM
$\lvert\mu_r\rvert < 1$	–	–	$\begin{cases} \lvert\varepsilon_r\rvert < 1 \\ b > \tanh^{-1}(\lvert\varepsilon_r\rvert) \end{cases}$

Source: Baccarelli, P., Burghignoli, P., Frezza, F., Galli, A., Lampariello, P., Lovat, G., and Paulotto, S., *IEEE Trans. Microw. Theory* Tech. 53(4), 1431, 2005. With permission.

In order to verify the possibility to achieve suppression of proper surface waves, numerical results are presented for the dispersion properties of TE and TM modes supported by a grounded DNG slab with thickness $h = 5$ mm and a metamaterial medium modeled as in [29], with relative permeabilities and permittivities given by Equations 13.4 and 13.6, where $\omega_{m0}/2\pi = 21$ GHz, $\omega_{mp}/2\pi = 24.5$ GHz, and $\omega_{ep}/2\pi = 28$ GHz. The region of simultaneously negative permeability and permittivity in this case ranges from $f = 21$ GHz to 24.5 GHz.

In Figure 13.2a, the values of the relative permeability (solid line with circles) and permittivity (solid line with diamonds) are reported in a frequency range from $f = 21$ GHz to 25 GHz, together with the values of the product $\mu_r\varepsilon_r$ (light-gray solid line). For the considered medium model, when $\mu_r\varepsilon_r > 1$,

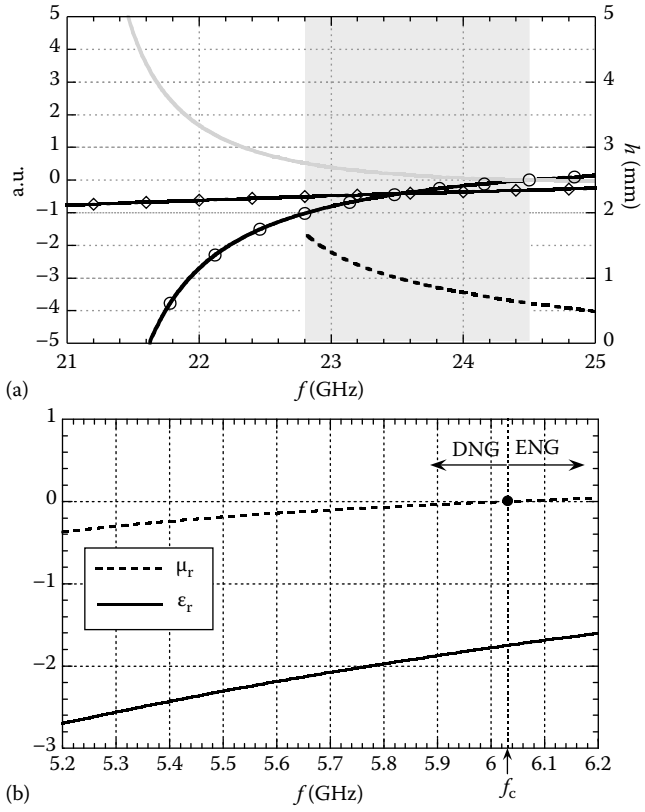

FIGURE 13.2 Illustrations of material parameters. (a) Examples discussed in Section 13.4. (From Baccarelli, P., Burghignoli, P., Frezza, F., Galli, A., Lampariello, P., Lovat, G., and Paulotto, S., *IEEE Trans. Microw. Theory Tech.* 53(4), 1431, 2005. With permission.). (b) Example discussed in Section 13.5. (From Baccarelli, P., Burghignolli, P., Frezza, F., Galli, A., Lampariello, P., Lovat, G., and Paulotto. S., *IEEE Trans. Microw. Theory Tech.* 53(1), 32, 2005. With permission.)

the conditions expressed in Equation 13.16 are never satisfied, whereas when $\mu_r \varepsilon_r < 1$ the conditions in Equation 13.12 hold in the range of frequencies from $f = 22.82$ GHz to 24.5 GHz, represented as a shaded area in the figure. In order to have surface-wave suppression inside this range of frequencies, the additional condition in Equation 13.14, which fixes a lower limit for the slab thickness, has to be satisfied. Such a limit is also reported in Figure 13.2a as a function of frequency (dashed line). Since the slab thickness has been chosen as $h = 5$ mm, by inspection of Figure 13.2a it can be concluded that, when the medium is DNG, the range of surface-wave suppression is the whole interval from $f = 22.82$ GHz to 24.5 GHz.

In the same figure, the shown range from $f = 24.5$ GHz to 25 GHz is a part of the frequency interval where the medium is ENG. According to the results reported in Table 13.3, to achieve surface-wave suppression a sufficient condition is that $|\varepsilon_r| < 1$, provided that the slab thickness is higher than the lower limit expressed in Equation 13.19. Such a lower limit has been also reported in Figure 13.2a, and it is seen to be the continuation of the lower limit valid for the DNG case. Therefore, since $h = 5$ mm and the relative permittivity is less than one in absolute value in all the ENG range (although it is not completely shown in Figure 13.2a), it can be concluded that no surface waves may also exist in the ENG range.

The condition of surface-wave suppression will be illustrated by means of the dispersion diagrams of the relevant TE and TM modes. In Figure 13.3a, the dispersion curves of three TE modes, conventionally labeled TE_1, TE_2, and TE_3, are reported in a frequency range between $f = 21$ GHz and $f = 25$ GHz, together with the line $\beta_z = k_s$; the shaded area represents again the predicted range of surface-wave suppression for the DNG range. It has to be noted that the mode TE_1 is improper real [28] below cutoff and proper real above cutoff. Moreover, the proper real branch of the TE_1 mode is ordinary at lower frequencies and evanescent at upper frequencies; its normalized phase constant tends to infinity at $f = 22.82$ GHz.

In Figure 13.3b, the dispersion curves of three TM modes, conventionally labeled TM_1, TM_2, and TM_3, are reported in the same frequency range as in Figure 13.3a, again with the line $\beta_z = k_s$ and the shaded area of predicted surface-wave suppression in the DNG range. The three modes have a similar behavior, the only difference being that the proper real branch of the TM_1 mode is evanescent, whereas the proper real branches of the TM_2 and TM_3 modes are ordinary.

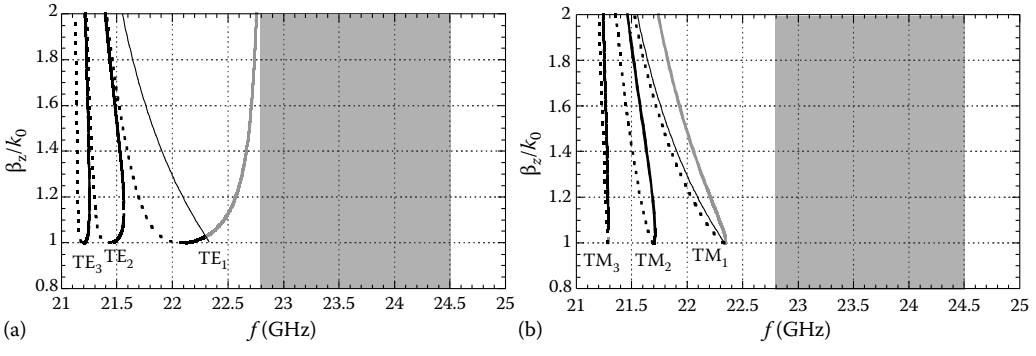

FIGURE 13.3 Dispersion curves for (a) TE and (b) TM modes supported by a grounded metamaterial slab with slab medium as in Figure 13.2a and thickness $h = 5$ mm. The shaded area represents the predicted range of surface-wave suppression for both TE and TM modes. Legend: Normalized phase constants β_z/k_0: solid lines, proper real ordinary waves; dotted lines, improper real ordinary waves; *light-gray* solid line, proper real evanescent wave, thin solid line, $\beta_z = k_s$. (Adapted from Baccarelli, P., Burghignoli, P., Frezza, F., Galli, A., Lampariello, P., Lovat, G., and Paulotto, S., *IEEE Trans. Microw. Theory Tech.* 53(4), 1431, 2005. With permission.)

Finally, it can be observed that the region of surface-wave suppression, in the DNG range, is exactly predicted, being limited on the left by the frequency $f = 22.82$ GHz at which the phase constant of one evanescent TE mode tends to infinity, whereas on the right by the frequency $f = 24.5$ GHz, at which the material ceases to be DNG, becoming SNG. In fact, with reference to Table 13.1, the condition for TE proper evanescent surface-wave suppression is a necessary and sufficient one.

13.4.4 Magnetic Dipole Excitation

In order to verify surface-wave suppression and to show its effects on radiation patterns, the far field radiated by a point source in the presence of a finite-size DNG slab is considered. A magnetic dipole source is assumed to be placed on the ground plane of a DNG slab along the x axis, to model radiation from a short and narrow slot; the finite-size slab is assumed to be circular, with radius R (see Figure 13.4). Comparisons will be presented between the far fields radiated in the presence of an infinite- and a finite-size DNG slab, whereas in the latter case the radiated field may be calculated through a physical-optics approximation of the aperture field on the air–slab interface.

In Figure 13.4, a DNG slab with physical parameters as in Figure 13.3 is considered; the radius of the finite structure is $R = 10\lambda_0$, where λ_0 is the free-space wavelength. In Figure 13.5 the radiation patterns of the infinite (black line with diamonds) and of the finite (gray line) structures are presented in the elevation plane $\phi = 0°$, where the far field is mostly due to TE waves. At $f = 22.5$ GHz the effect of TE surface-wave diffraction at the edges of the finite structure is clearly evident, whereas at $f = 23.5$ GHz no diffraction effects are found since neither TE nor TM surface waves are present.

13.4.5 Nonradiative Dielectric Waveguides

The basic analysis just presented for surface waves in metamaterial slabs can be useful to argue novel behaviors also in other guiding structures: among them, we illustrate here some interesting features concerning metamaterial nonradiative dielectric (NRD) waveguides. The "standard" NRD guide [33] is usually constituted by a nonmagnetic, dielectric, rectangular rod sandwiched between wide metal plates, spaced at a distance that is less than half a free-space wavelength (see Figure 13.6).

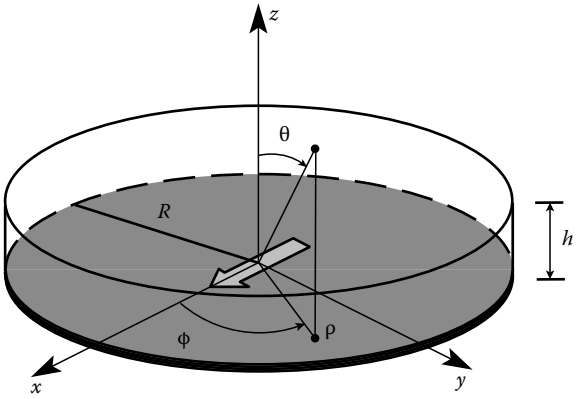

FIGURE 13.4 Truncated grounded metamaterial slab with relevant physical and geometrical parameters as in Figure 13.3. A finite-size slab is assumed to be circular with radius $R = 10\lambda_0$. (From Baccarelli, P., Burghignoli, P., Frezza, F., Galli, A., Lampariello, P., Lovat, G., and Paulotto, S., *IEEE Trans. Microw. Theory Tech.* 53(4), 1431, 2005. With permission.)

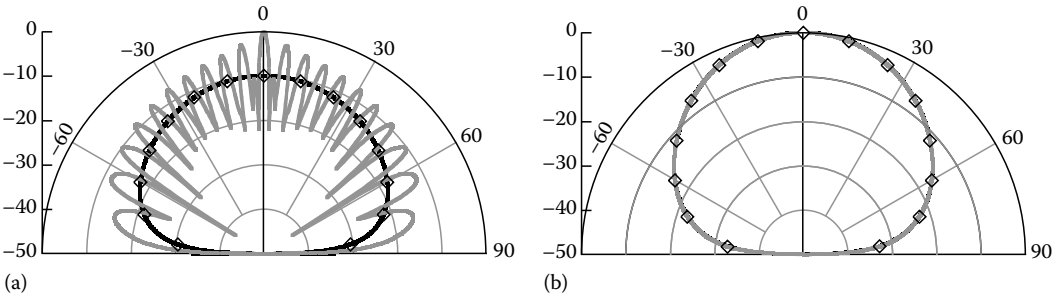

FIGURE 13.5 Normalized radiation patterns (in dB) of a magnetic dipole placed on the ground plane of a DNG slab along the x axis, in the elevation plane $\phi = 0$ at (a) $f = 22.5$ GHz and (b) $f = 23.5$. Physical parameters: as in Figure 13.3. Legend: infinite structure: black line with diamonds; circular finite structure (radius $R = 10\lambda_0$): gray line. (From Baccarelli, P., Burghignoli, P., Frezza, F., Galli, A., Lampariello, P., Lovat, G., and Paulotto, S., *IEEE Trans. Microw. Theory Tech.* 53(4), 1431, 2005. With permission.)

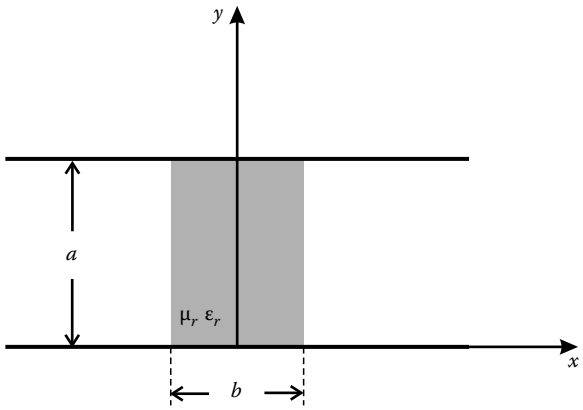

FIGURE 13.6 Cross-section of the metamaterial NRD guide considered here, with the relevant physical and geometrical parameters. (From Baccarelli, P., Burghignoli, P., Frezza, F., Galli, A., Lampariello, P., and Paulotto, S., *Microwave Opt. Tech. Lett.* 48, 2557, 2006. With permission.)

The operating mode is the so-called LSM_{01}, which is an odd mode with respect to the transverse horizontal (x) direction (short-circuit bisection at $x = 0$) and presents a half-wave variation with respect to the vertical (y) direction (open-circuit bisection at $y = a/2$). The structure is typically aimed at reducing both ohmic and radiation losses in high-frequency applications (usually at the higher microwave ranges and at millimeter waves). In fact, the operating mode, which has an electric field prevalently parallel to the metal plates, presents limited ohmic losses; moreover, due to the suitably reduced spacing between the plates, each discontinuity that preserves the horizontal-plane symmetry can furnish only a reactive effect and no lateral radiation occurs from the plates (such radiation has to be avoided in guiding components but could be desired in leaky-wave structures [34]). In standard NRD guides, the unimodal operation band can negatively be limited not only by the presence of higher-order modes of the same LSM type (e.g., the LSM_{11}) [33,34], but also by the possible excitation of additional above-cutoff modes of LSE type (e.g., the LSE_{00} mode, if the horizontal-plane symmetry is no longer preserved, and the LSE_{01} mode, when the vertical-plane symmetry is broken). An original possibility of avoiding such band limitations in NRD guide is briefly illustrated

here, based on the use of a metamaterial rod instead of a standard dielectric one [35]. Various other investigations on the peculiarities of NRD guides based on metamaterials can be found in the references of [35]. In the following, the above-introduced assumptions for the metamaterial models are obviously maintained.

At first it should be reminded that, in general, a strict correspondence exists between the TE/TM modal spectrum of a slab guide and the LSE/LSM spectrum of an NRD guide, since the NRD structure can be viewed as an equivalent slab, which is transversely limited by the pair of metal plates at the distance a apart in the direction where the slab fields were assumed to be constant (i.e., along the x axis of the slab, according to the reference coordinate system presented in the previous subsections, which corresponds to the y axis for the coordinate system chosen here in Figure 13.6 for the NRD guide) [33–35]. For the same slab width ($2h$) and NRD width ($b = 2h$), the eigenvalues of the slab ($k_t^2 = k_y^2$) correspond to the horizontal wavenumbers (here denoted k_x^2) of the NRD guide; thus, the presence of the metal plates in the NRD guide furnishes only an additional contribution to the transverse wavenumber of the simple type $k_y^2 = (m\pi/2)^2$, with $m = 0, 1, \ldots$ (as said, $m = 1$ is chosen on usual NRD applications): $k_{t,\mathrm{NRD}}^2 = k_{t,\mathrm{slab}}^2 + (m\pi/a)^2$. As a consequence, from the separation condition, the propagation constant k_z for the NRD guide can easily be calculated, based on the knowledge of the relevant slab wavenumbers; e.g., for the $m = 1$ case, it results in the following:

$$k_{z,\mathrm{NRD}} = \sqrt{k_{z,\mathrm{slab}}^2 - (\pi/a)^2} \tag{13.20}$$

On this ground, the first step to furnish the wished suppression of NRD-guide undesired modes can consist simply in the use of an ENG metamaterial slab, which, as seen in the previous subsections, automatically avoids the propagation of any TE slab mode and consequently of any LSE NRD-guide mode. Once the NRD-guide LSE modes are suppressed with the simple choice of ENG rods, the remaining problem concerns with the possible achievement of a suitable band of unimodal LSM-mode propagation.

The modal analysis in ENG slabs emphasizes that for $\varepsilon_r < 0$ (i.e., for $f < f_p$) generally a pair of TM modes is present (conventionally labeled as TM_0 and TM_1), whose dispersion behaviors are strongly dependent on the choice of the involved physical parameters. An example is illustrated in Figure 13.7a and b for two different ("high" and "low") values of the slab width b, respectively.

From a simple analysis of the dispersion equations for ENG-slab TM modes with even/odd symmetries [35], it is possible to show that the slab TM_1 mode (which can give rise to the undesired

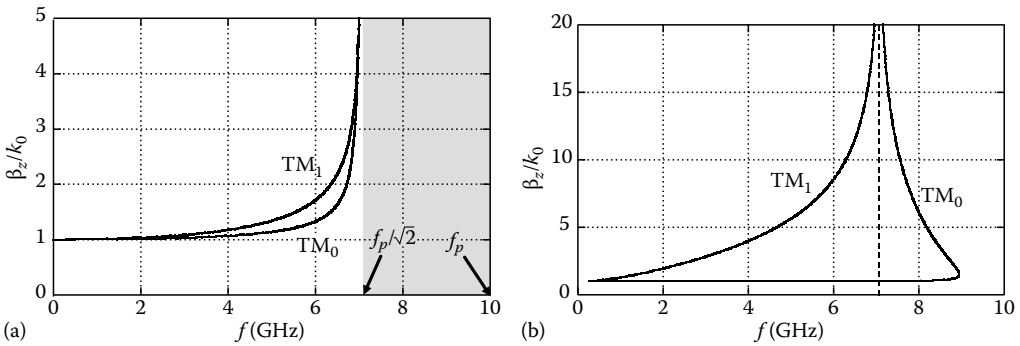

FIGURE 13.7 (a) Dispersion diagram for TM modes supported by a slab in free space made of a plasma-like ENG medium. Parameters: $b = 10$ mm, $f_p = 10$ GHz. (b) Dispersion diagram for TM modes supported by a slab in free space made of a plasma-like ENG medium. Parameters: $b = 1.2$ mm, $f_p = 10$ GHz. (From Baccarelli, P., Burghignoli, P., Frezza, F., Galli, A., Lampariello, P., and Paulotto, S., *Microwave Opt. Tech. Lett.* 48, 2557, 2006. With permission.)

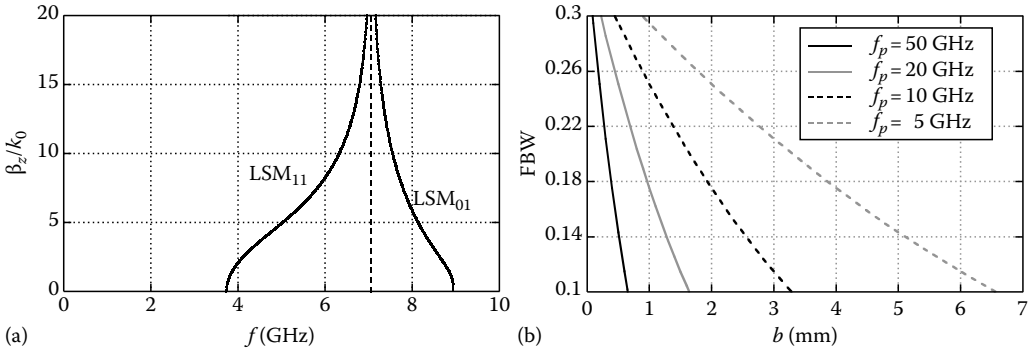

FIGURE 13.8 (a) Dispersion diagram for LSM modes supported by an NRD waveguide with a plasma-like ENG medium. Parameters: a = 11.4 mm, b = 1.2 mm, f_p = 10 GHz. (b) Fractional bandwidth of unimodal propagation as a function of the slab width for different values of the plasma frequency. (From Baccarelli, P., Burghignoli, P., Frezza, F., Galli, A., Lampariello, P., and Paulotto, S., *Microwave Opt. Tech. Lett.* 48, 2557, 2006. With permission.)

NRD-guide LSM$_{11}$ mode) cannot exist at all when $|\varepsilon_r| < 1$ (necessary and sufficient condition), that is in the range between $f_p/\sqrt{2}$ and f_p. On the contrary, in this range between $f_p/\sqrt{2}$ and f_p, it is possible to have propagation of the slab TM$_0$ mode (which can give rise to the operating NRD-guide LSM$_{01}$ mode), provided that the metamaterial width b is sufficiently reduced [35]. In Figure 13.7, it is confirmed that, with a "high" value of b, both the TM modes exist in the range of $f < f_p/\sqrt{2}$; if b is suitably decreased, only the TM$_0$ can propagate in the range between $f_p/\sqrt{2}$ and f_p, even though such a mode generally presents the undesirable feature of possessing two different branches, which tend to coalesce as frequency is increased (by further increasing frequencies, this mode assumes a complex proper nature and is no longer purely bound). Nevertheless, these two TM$_0$ branches typically show rather different propagation (phase) constants in a wide frequency range; in the related NRD guide, it is, therefore, possible to find a sufficiently low value of the metal-plate spacing (cf. Equation 13.20) that is able to change into an imaginary quantity the real contribution of the propagation constant of only the TM$_0$ branch with the lower longitudinal wave number (while maintaining real the contribution to the propagation constant of the other branch with the higher longitudinal wavenumber). In this way, the "lower" modal branch is suppressed (i.e., it becomes attenuated), and the desired unimodal propagation of the NRD guide (related to the "higher" modal branch) is achieved. For given slab width and permittivity, it is always possible to find a maximum value of the thickness a of the NRD guide, which gives the largest possible frequency band of unimodal propagation. An example of such behavior is illustrated in Figure 13.8a, where only one branch is now present between $f_p/\sqrt{2}$ and f_p, as desired for the unimodal NRD-guide LSM$_{01}$ operation. The operating mode possesses in this case a backward highly dispersive behavior and a transversely evanescent field configuration, as is typical of ENG slab modes. The other parameters being fixed, the bandwidth of unimodal propagation can be increased monotonically as b is decreased. An example is shown in Figure 13.8b for the maximal attainable fractional bandwidth (FBW) as a function of the width b for different values of the metamaterial plasma frequency f_p.

13.5 Grounded Metamaterial Slabs: Leaky Waves

In this section properties of leaky modes in grounded metamaterial slabs are discussed. As is well known, leaky modes are complex modes, that is, their propagation wave number $k_z = \beta - j\alpha$ is complex. A nonzero attenuation constant α is present, also in lossless structures, due to radiation losses

associated with the propagation of the mode in a transversely open environment. An important issue in connection with leaky modes is their spectral character, which is established by their behavior at infinity in the transverse plane: if a leaky mode satisfies the radiation condition at infinity, it is termed proper, otherwise improper. This is in turn related to the nature of leaky-mode radiation, which is backward for proper modes and forward for improper modes. We recall here that modal solutions in waveguiding structures correspond to pole singularities of the waveguide Green's function in the complex plane of the relevant spectral variable (for grounded slabs, such a variable can be k_z for 1D modal propagation along the z axis or k_ρ for 2D propagation along the radial axis ρ); the spectral Green's function has also square-root branch points at the wavenumbers $\pm k_0$ of the air medium, and the proper or improper character of a mode is related to the location of the corresponding pole in different Riemann sheets with respect to that branch point [28].

In lossless grounded DPS slabs complex proper modes cannot exist, whereas complex improper modes do exist and they may come into play in a nonspectral, steepest-descent representation of the field radiated by sources [28]; under appropriate conditions, a single, complex improper (leaky) mode can provide an accurate representation of the continuous-spectrum part of the field at the air–slab interface, thus affording a compact representation of the far field via a Fourier transform [28,36,37]. In grounded DNG slabs, it can be seen by inspection that the dispersion equations for proper modes on a DNG slab are the same as those for improper modes on a DPS slab, and vice-versa [20]. It can be concluded that, in grounded DNG slabs, only complex proper modes may exist, whereas complex improper modes are forbidden. Considering now grounded SNG slabs, it can be seen that for grounded MNG slabs, the dispersion equation for TE waves is the same as that for DNG slabs, whereas the dispersion equation for TM waves is the same as that for DPS slabs. The opposite is true for grounded ENG slabs. Therefore, it can be concluded that on grounded MNG slabs proper complex TE waves and improper complex TM waves may exist, whereas on grounded ENG slabs improper complex TE waves and proper complex TM waves may exist. The spectral properties of complex modes for different kinds of lossless, metamaterial grounded slabs are summarized in Figure 13.9.

As is well known, the electric field at the air–slab interface may be represented as an inverse Hankel transform of the relevant spectral Green's function with respect to the spectral variable k_ρ. According to the above discussion, the complex poles of the spectral Green's function for a DNG slab may be located only on the *proper* Riemann sheet defined by the Sommerfeld branch cut; in Figure 13.10 the location of singularities in the complex k_ρ plane is illustrated, showing, for example, two complex proper leaky-wave poles (LW_1 and LW_2) and one proper real bound-wave pole (BW).

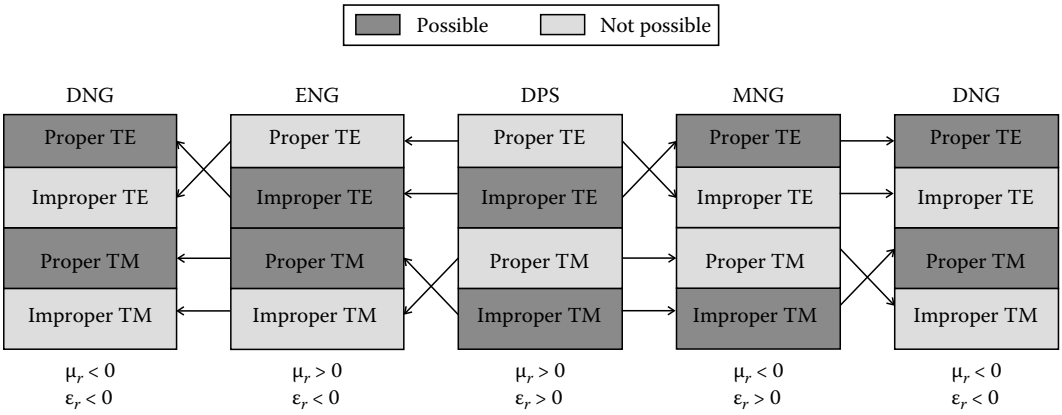

FIGURE 13.9 Spectral properties of complex modes in grounded DPS, DNG, and SNG metamaterial slabs.

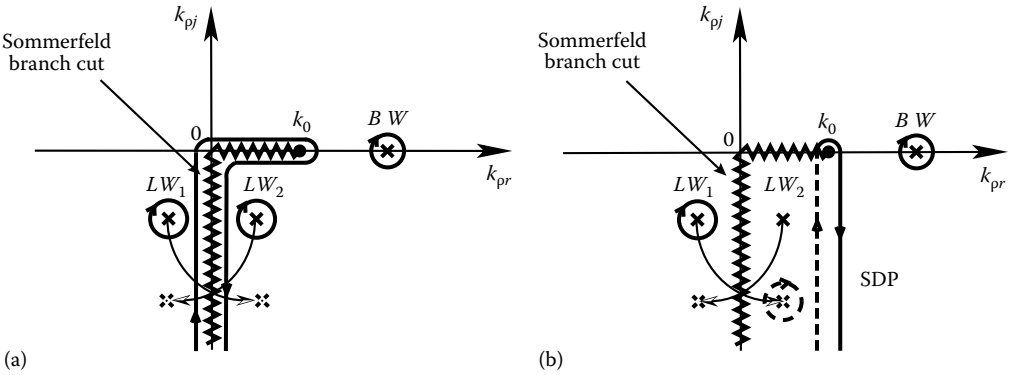

FIGURE 13.10 (a) Singularities of the spectral Green's function and path deformation that leads to the spectral representation of the field at the air–slab interface. (b) Path deformation that leads to the nonspectral representation of the field at the air–slab interface. (From Baccarelli, P., Burghignoli, P., Frezza, F., Galli, A., Lampariello, P., Lovat, G., and Paulotto, S., *IEEE Trans. Microw. Theory Tech.* 53(1), 32, 2005. With permission.)

Alternative field representations can be obtained by performing different deformations of the original integration path along the real axis. For example, by adopting a path that runs along the two sides of the Sommerfeld branch cut in the lower half plane and applying the residue theorem to take into account the contribution of the captured poles, the spectral representation of the field at the air–slab interface is obtained: the total field is thus represented as the sum of a discrete spectrum (sum of the residue contributions of BW and of the pair (LW_1, LW_2), neglecting higher-order proper leaky contributions) and a continuous spectrum (integral along the branch cut) (see Figure 13.10a). On the other hand, by deforming the integration path to the steepest-descent path (SDP) running vertically along the two Riemann sheets through the k_0 branch point, a nonspectral representation of the field is obtained, in which the field is represented as the sum of the contributions of BW, LW_1, and the integral along the steepest descent path (SDP) (named residual wave (RW)) (see Figure 13.10b). Under suitable conditions, the BW and RW contributions to the radiated field may be neglected, so that an accurate representation of the field is provided by only one complex proper leaky pole, responsible for radiation at an angle in the backward quadrant, as observed in other structures, for example, a nonreciprocal ferrite slab [38]; in the same fashion, improper leaky modes give rise to directive forward radiation on DPS slabs [36].

To illustrate the typical shape of dispersion curves in grounded DNG slabs, in Figure 13.11 dispersion diagrams (for normalized phase and attenuation constants vs. frequency) are reported for (a) TE and (b) TM modes supported by a grounded slab modeled through Equations 13.5 and 13.6 (with $F = 0.56$, $\omega_0/2\pi = 4$ GHz, and $\omega_p/2\pi = 10$ GHz, see Figure 13.2b) and slab thickness $h = 60$ mm, in a frequency range between $f = 4.8$ GHz and 6.2 GHz. At $f = f_c$ the metamaterial changes from DNG to ENG; thus all the TE modes have to change their spectral nature from proper to improper, that is, the associated poles in the k_ρ plane cross the Sommerfeld branch cut; this occurs by crossing the imaginary axis as shown with arrows in Figure 13.10a and b, so that the phase constants of the TE modes simultaneously become zero and change their sign at f_c (see Figure 13.11a).

It can be observed that the normalized phase constants of all the shown leaky modes span the range almost completely $(0,1)$ (in the case of TE modes this range is completely covered down to 0 because the TE phase constants become zero at $f_c = 6.03$ GHz). Moreover, the low values of the normalized attenuation constants of the TE_1 and TM_1 modes give rise to radiation of a directive beam in a wide angular range. However, the most striking feature of Figure 13.11 is that the phase constants of the TE_1

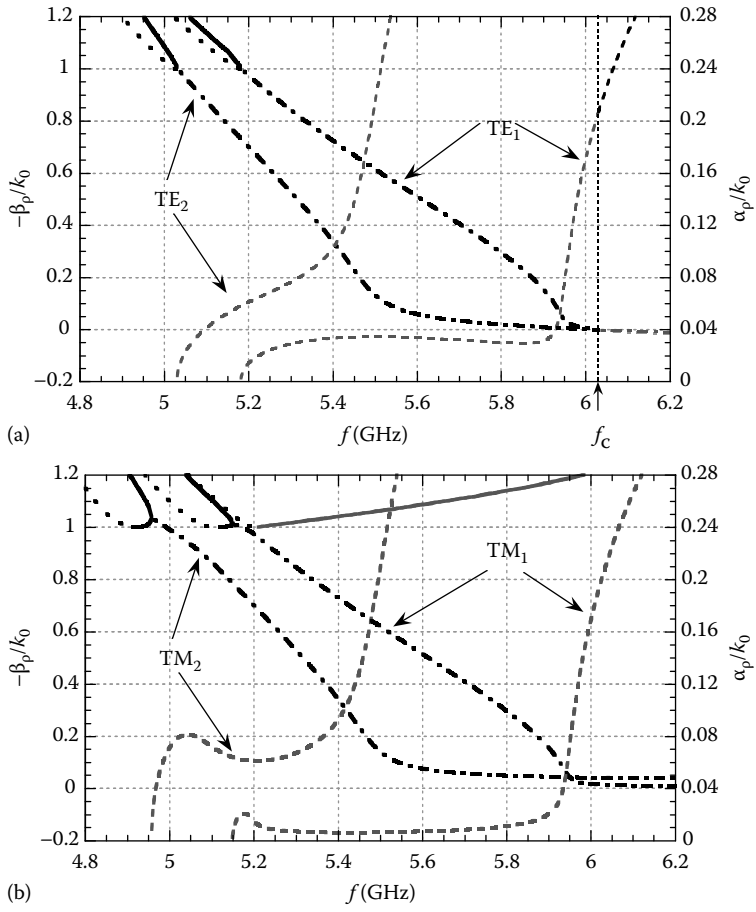

FIGURE 13.11 Dispersion diagrams for (a) TE and (b) TM modes on a grounded metamaterial slab with parameters as in Figure 13.2b and thickness $h = 60$ mm. Legend: Normalized phase constants: real proper ordinary modes (black solid lines); real proper evanescent modes (gray solid lines); real improper ordinary modes (black dotted lines); complex proper modes (black dashed–dotted lines); complex improper modes (gray dashed–dotted lines). Normalized attenuation constants: complex proper modes (gray dashed lines); complex improper modes (black dashed lines). (From Baccarelli, P., Burghignoli, P., Frezza, F., Galli, A., Lampariello, P., Lovat, G., and Paulotto, S., *IEEE Trans. Microw. Theory Tech.* 53(1), 32, 2005. With permission.)

and TE_2 modes are almost superimposed to those of the TM_1 and TM_2 modes, respectively, in a very wide frequency range. This TE–TM phase-constant equalization has been observed for various slab thicknesses, becoming more pronounced and extending over wider frequency ranges, by increasing the slab thickness.

In order to investigate the effects of the presence of the grounded metamaterial slab on radiation properties, we have studied the beam-scanning features of the far field radiated by a finite source as in Section 13.4.4, namely, a horizontal magnetic dipole placed along the x axis on the ground plane of an infinite metamaterial slab. Since the pointing angle of the beam in the E plane is known to be primarily determined by TM leaky modes when the beam points off broadside, whereas the pointing angle of the beam in the H plane is instead primarily determined by TE leaky modes [39],

a conical beam with almost equal pointing angles in all the elevation planes can be expected. This is confirmed by the plots reported in Figure 13.12, which represent the normalized radiation patterns at two different frequencies on a gray-scale map for the same structure as in Figure 13.11; in these plots, the distance from the origin is proportional to the spherical angle θ (elevation), whereas the angular coordinate is equal to the spherical angle ϕ (azimuth).

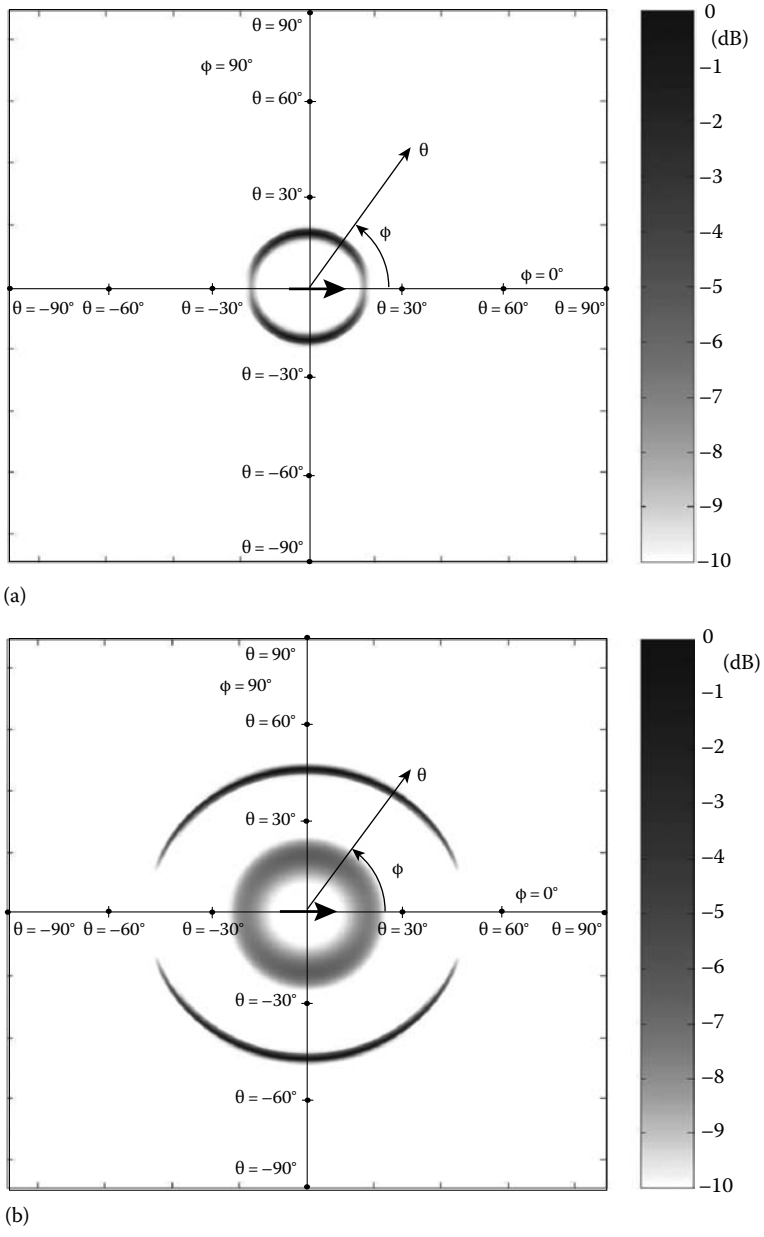

FIGURE 13.12 Radiation of conical beams from a horizontal magnetic dipole in a grounded metamaterial slab at (a) $f = 5.8$ GHz and (b) $f = 5.4$ GHz. (Adapted from Baccarelli, P., Burghignoli, P., Frezza, F., Galli, A., Lampariello, P., Lovat, G., and Paulotto, S., *IEEE Trans. Microw. Theory Tech.* 53(1), 32, 2005. With permission.)

References

1. Tamir, T. and A. A. Oliner. 1963. The spectrum of electromagnetic waves guided by a plasma layer. *Proc. IEEE* 51(2):317–332.
2. Camley, R. E. and D. L. Mills. 1982. Surface polaritons on uniaxial antiferromagnets. *Phys. Rev. B* 26(3):1280–1287.
3. Prade, B., J. Y. Vinet, and A. Mysyrowicz. 1991. Guided optical waves in planar heterostructures with negative dielectric constant. *Phys. Rev. B* 44(24):13556–13572.
4. Barnes, W. L., A. Dereux, and T. W. Ebbesen. 2003. Surface plasmon subwavelength optics. *Nature* 424:824–830.
5. Ruppin, R. 2000. Surface polaritons of a left-handed medium. *Phys. Lett. A* 277:61–64.
6. Pendry, J. B. 2000. Negative refraction makes a perfect lens. *Phys. Rev. Lett.* 85(18):3966–3969.
7. Feise, M. W., P. J. Bevelacqua, and J. B. Schneider. 2002. Effect of surface waves on the behavior of perfect lenses. *Phys. Rev. B* 66:035113.
8. Haldane, F. D. M. 2002. Electromagnetic surface modes at interface with negative refractive index make a "not-quite-perfect" lens. arXiv:cond-mat/0206420v3.
9. Wu, B.-I., T. M. Grzegorczyk, Y. Zhang, and J. A. Kong. 2003. Guided modes with imaginary transverse wave number in a slab waveguide with negative permittivity and permeability. *J. Appl. Phys.* 93(11): 9386–9388.
10. Darmanyan, S. A., M. Nevière, and A. A. Zakhidov. 2003. Surface modes at the interface of conventional and left-handed media. *Opt. Commun.* 225:233–240.
11. Cory, H. and A. Barger. 2003. Surface-wave propagation along a metamaterial slab. *Microw. Opt. Tech. Lett.* 38(5):392–395.
12. Shadrivov, I. V., A. A. Sukhorukov, and Y. S. Kivshar. 2003. Guided modes in negative-refractive-index waveguides. *Phys. Rev. E* 67: 057602 (4 pages).
13. He Y., Z. Cao, and Q. Shen. 2004. Guided optical modes in asymmetric left-handed waveguides. *Opt. Commun.* 245:125–135.
14. Darmanyan. S. A., M. Nevière, and A. A. Zakhidov. 2005. Nonlinear surface waves at the interfaces of left-handed electromagnetic media. *Opt. Commun.* 245:125–135.
15. Alú, A. and N. Engheta. 2005. An overview of salient properties of planar guided-wave structures with double-negative (DNG) and single-negative (SNG) layers. In *Negative-Refraction Metamaterials: Fundamental Principles and Applications.* G. V. Eleftheriades and K. G. Balmain (eds.), pp. 339–380. Hoboken, NJ: IEEE Press.
16. Park, K., B. J. Lee, C. Fu, and Z. M. Zhang. 2005. Study of the surface and bulk polaritons with a negative index metamaterial. *J. Opt. Soc. Am. B* 22(5):1016–1023.
17. Kats, A. V., S. Savelev, V. A. Yampolskii, and F. Nori. 2007. Left-handed interfaces for electromagnetic surface waves. *Phys. Rev. Lett.* 98:073901 (4 pages).
18. Baccarelli, P., P. Burghignoli, F. Frezza, A. Galli, P. Lampariello, G. Lovat, and S. Paulotto. 2005. Effects of leaky-wave propagation in metamaterial grounded slabs excited by a dipole source. *IEEE Trans. Microw. Theory Tech.* 53(1):32–44.
19. Kampitakis, M. E. and N. K. Uzunoglu. 2007. Analysis of guided and leaky waves excited by an infinite line source in metamaterial substrates. *IET Microw. Antennas Propag.* 1(1):129–136.
20. Baccarelli, P., P. Burghignoli, F. Frezza, A. Galli, P. Lampariello, G. Lovat, and S. Paulotto. 2005. Fundamental modal properties of surface waves on metamaterial grounded slabs. *IEEE Trans. Microw. Theory Tech.* 53(4):1431–1442.
21. Kim, K. Y., Y. K. Cho, H.-S. Tae, and J.-H. Lee. 2006. Guided mode propagations of grounded double-positive and double-negative metamaterial slabs with arbitrary material indexes. *J. Korean Phys. Soc.*, 49(2):577–584.
22. Nefedov, I. S. and A. J. Viitanen. 2005. Guided waves in uniaxial wire medium slab. *Prog. Electromagn. Res.* 51:167–185.

23. Burghignoli, P., G. Lovat, F. Capolino, D. R. Jackson, and D. R. Wilton. 2008. Modal propagation and excitation on a wire-medium slab. *IEEE Trans. Microw. Theory Tech.* 58(5):1112–1124.
24. Dong, H. and T. X. Wu. 2003. Analysis of discontinuities in double-negative (DNG) slab waveguide. *Microwave. Opt. Tech. Lett.* 39(6):483–388.
25. Cory, H. and O. Skorka. 2004. Metamaterial slabs coupling. *Microwave Opt. Tech. Lett.* 39(6):483–388.
26. Hwang, R. 2007. Surface waves and volume waves in a photonic crystal slab. *Microwave Opt. Tech. Lett.* 15(13):7913–7921.
27. Gao, L., Y. Huang, and C. Tang. 2007, Surface polaritons and transmission in multi-layer structures containing anisotropic left-handed materials. *Appl. Phys. A* 87:199–204.
28. Collin, R. E. 1991. *Field Theory of Guided Waves*, 2nd edn., Piscataway, NJ: IEEE Press.
29. Shelby, R. A., D. R. Smith, and S. Schultz. 2001. Experimental verification of a negative index of refraction. *Science* 292:77–79.
30. Pendry, J. B., A. J. Holden, D. J. Robbins, and W. J. Stewart. 1999. Magnetism from conductors and enhanced nonlinear phenomena. *IEEE Trans. Microw. Theory Tech.* 47(11):2075–2084.
31. Damon, R. W. and J. R. Eshbach. 1999. Magnetostatic modes of a ferromagnetic slab. *J. Phys. Chem. Solids* 19(3/4):308–320.
32. Baccarelli, P., C. Di Nallo, F. Frezza, A. Galli, and P. Lampariello. 1996. Novel behaviors of guided and leaky waves in microwave ferrite devices. *Proceedings of MELECON 1996*, Bari, Italy, 1:587–590.
33. Yoneyama, T. and S. Nishida. 1981. Nonradiative dielectric waveguide for millimeter-wave integrated circuits. *IEEE Trans. Microw. Theory Tech.* 29(11):1188–1192.
34. Di Nallo, C., F. Frezza, A. Galli, P. Lampariello, and A. A. Oliner. 1994. Properties of NRD-guide and H-guide higher-order modes: physical and nonphysical ranges. *IEEE Trans. Microw. Theory Tech.* 42(12):2429–2434.
35. Baccarelli, P., P. Burghignoli, F. Frezza, A. Galli, P. Lampariello, and S. Paulotto. 2006. Unimodal surface-wave propagation in metamaterial nonradiative dielectric waveguides. *Microwave Opt. Tech. Lett.* 48:2557–2560.
36. Tamir, T. and A. A. Oliner. 1963. Guided complex waves. Part I: Fields at an interface. Part II: Relation to radiation patterns. *Proc. IEE* 110(2):310–334.
37. Felsen, L. B. 1986. Real spectra, complex spectra, compact spectra. *J. Opt. Soc. Am. A, Opt. Phys. Image Sci.* 3:486–496.
38. Baccarelli, P., C. Di Nallo, F. Frezza, A. Galli, and P. Lampariello. 1997. The role of complex waves of proper type in radiative effects of nonreciprocal structures. *Digest Int. Microw. Symp. 1997* 2:491–494.
39. Ip, A. and D. R. Jackson. 1990. Radiation from cylindrical leaky waves. *IEEE Trans. Antennas Propagat.* 38(4):482–488.

III

Artificial Magnetics and Dielectrics, Negative Index Media

14

RF Metamaterials

M. C. K. Wiltshire
Imperial College London

14.1 Introduction

Metamaterials are effective media [PHSY96,PHRS98,PHRS99] that can provide an engineered response to electromagnetic radiation that is not available from the range of naturally occurring materials. They consist of arrays of structures in which both the individual elements and the unit cell are small compared with the wavelength of operation; homogenization of the structures then allows them to be described as effective media with the conventional electromagnetic constants of permittivity (ϵ) and permeability (μ) but with values that could not previously be obtained. For example, material with simultaneously negative ϵ and μ can be built to have a negative refractive index [SPV$^+$00,SSS01,PGL$^+$03], and much attention has been given to the behavior of such media [SPW04].

Most of the work on metamaterials has been concentrated in the microwave regime and above (gigahertz to terahertz frequencies), and the majority of these metamaterials has been constructed from a combination of fine wire grids [PHSY96,PHRS98] to give a dielectric response and split ring resonators (SRRs) [PHRS99] to provide the magnetic response. These are simple to fabricate [SRSNN04] and are active in the microwave regime, providing negative permeability typically over a bandwidth of some 10% [SSMS02]. In the first examples (see Figure 14.1), the fine wire grid was constructed from a 20 μm diameter gold-coated tungsten wire [PHSY96], which showed a plasma frequency at 9 GHz, whereas the SRR array was made by etching a conventional FR4 circuit board with patterns that were approximately 5 mm in diameter; these had a resonant frequency of about 3 GHz.

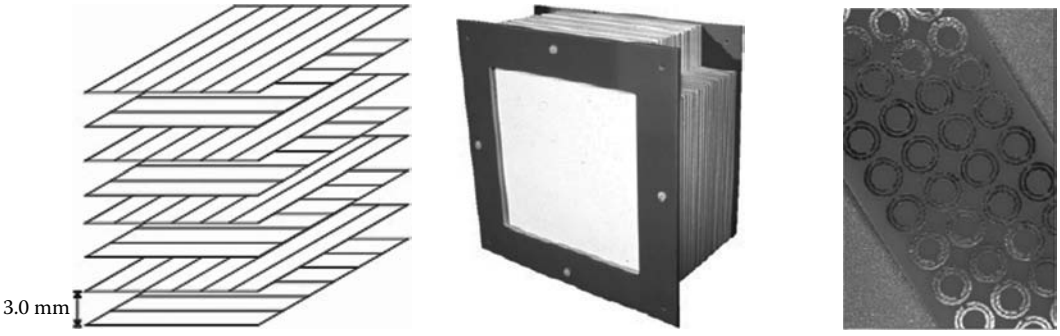

FIGURE 14.1 Early examples of metamaterials: (a) schematic of the fine wire grid structure; (b) its implementation; and (c) the split ring resonator structure.

In a seminal series of articles, Smith and coworkers [SPV+00,SSNNS01] combined the wires and SRRs into a composite structure etched on a circuit board and were able to demonstrate negative refractive index behavior [SSS01]. More recent work has built on this approach, and metamaterials have now been made that operate at terahertz [YPF+04], infrared [LEW+04], and even optical frequencies [EWL+05]. These have all used the SRR structure or modifications thereof.

There is much to be gained, however, from working at lower frequencies—in the radiofrequency (RF) regime [Wil07]. The wavelength of the electromagnetic radiation is extremely long, so the condition that the structure should be much smaller than a wavelength is easily met. Moreover, all distances are very small compared with the wavelength, so all measurements are made in the very near field, where the electric and magnetic fields are essentially independent [Pen00,Str41a], thus simplifying both the material requirements and the interpretation of measurements. Finally, there are potential applications for these materials in magnetic resonance imaging (MRI), which operates at radiofrequencies (RF). At these lower frequencies, however, the SRR structure becomes impractically large, and different structures are required; in particular, the so-called Swiss roll [PHRS99] has proved to be very effective.

In this chapter, we first review RF metamaterial development. We then consider how they can be described by the effective medium approximation, develop the mean field description of how electromagnetic radiation propagates through them, and compare these predictions with experimental results. We then describe how these materials can be used to produce high-resolution images with RF radiation and conclude with an overview of some potential devices and applications.

14.2 RF Metamaterials Design

For metamaterials in the microwave regime and at higher frequencies, the building blocks have been the SRR and fine wire structure, and much of the practical considerations have focused on making these small compared with a wavelength. However, when working at lower frequencies (and we select a frequency of about 64 MHz, the operating frequency of a 1.5 Tesla MRI system, as a specific example), a different set of issues arises. The concern that the structure is much smaller than the wavelength, now ≈5 m *in vacuo*, becomes trivial, but the individual elements still need to be physically small in order first that the materials can be handled in the laboratory and second that they may be used in RF applications. Thus we need to drive the critical frequency of the components down without making them physically larger. In the following sections, we discuss the suitability first of the fine

wire structure and then of the SRR structure and its derivatives for use at RF. We then briefly discuss the use of discrete capacitors within these structures and finally introduce the Swiss roll structure, which turns out to be ideally suited to this frequency range.

14.2.1 Dielectrics

The plasma frequency ω_p of the fine wire grid structure [PHSY96] is given by

$$\omega_p^2 = \frac{2\pi c_0^2}{a^2 \ln(a/r)} \tag{14.1}$$

where
- r is the wire radius
- a is the grid spacing
- c_0 is the speed of light *in vacuo*

so that 20 μm wires placed on a 5 mm grid show a plasma frequency of ≈9.5 GHz [PHRS98]. Using Equation 14.1 as a scaling relation to design material active at 64 MHz shows that, once the wire diameter is much smaller than the unit cell size ($r \ll a$), the frequency depends most strongly on the unit cell size a, so we would need to have very thin wires (say 10 μm diameter) spaced on a very sparse grid ($a \approx 600$ mm), which would not constitute a feasible material.

Smith et al. [SVP+99] suggested forming the wire into a loop in a plane normal to its length (see Figure 14.2): this increases the self-inductance and hence reduces the resonant frequency to

$$\omega_p^2 = \frac{2\pi c_0^2}{a^2 \left(ln(a/r) + (2\pi R/l)\left[ln(8R/r) - 7/4\right]\right)}, \tag{14.2}$$

where
- R is the radius of the loop
- l is the length of the wire

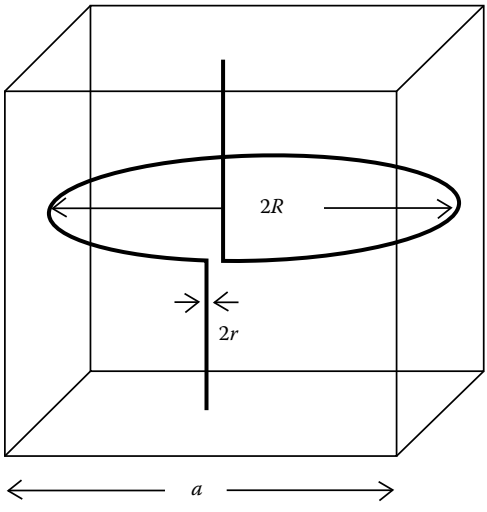

FIGURE 14.2 Schematic diagram of the loop-wire dielectric structure: the self-inductance of the thin wire is enhanced by forming a loop of radius R in the unit cell, thus reducing the effective plasma frequency.

This lowers the resonant frequency significantly but not sufficiently to provide viable material in the 10's of MHz range. For example, taking the same 10 μm diameter wire as above and assuming that the loop size is equal to the spacing ($R = a/2$) and that there is one loop per unit cell ($l = a$), we require a wire spacing of 200 mm. This is substantially smaller than the 600 mm found for the straight wire but is still not a viable material option. Thus far, no dielectric metamaterial has been reported that operates in this range. However, as pointed out earlier (see Section 14.1), at RF frequencies and working in the very near field (i.e., at distances of a few cm), the electric and magnetic field components are essentially independent, and so to manipulate the fields from magnetic sources, the most common requirement at RF, only requires control of the permeability. Thus good progress can be made without having access to dielectric metamaterials.

14.2.2 Split Ring Resonators

The conventional SRR structure has a resonant frequency of [PHRS99]

$$\mu_{\text{eff}} = 1 - \frac{\frac{\pi r^2}{a^2}}{1 - \frac{3lc_0^2}{\pi^2\omega^2 r^3 ln(2w/d)} + i\frac{2l\sigma}{\omega r\mu_0}}, \tag{14.3}$$

where

d is the gap between the rings
w is the width of the rings
r is the radius of the inner ring
a is the size of the unit cell
l is the inter layer spacing

To obtain a resonant frequency of 60 MHz while maintaining a gap of 0.1 mm and ring width of 0.5 mm requires a radius of 200 mm. Although this is still small compared with the wavelength of 10 m, the element is impractically large. To make a viable element, we have to increase either the self-capacitance or self-inductance of the structure or, ideally, both.

We consider several approaches. First, we note that the self-capacitance of the conventional, edge-coupled SRR described above (Figure 14.3a) is small; this can be increased by using the broadside SRR (Figure 14.3b), in which the two rings are on opposite sides of a (thin) membrane. This structure has been discussed in some detail by Marques and coworkers [MMMM03,MMREI02], who show that an element size of $\approx\lambda/25$ can be achieved using a substrate of 100 μm thickness with permittivity $\epsilon = 10$ at a frequency of 10 GHz. Thinner substrates are available, so this size could be further reduced. Despite this, however, a structure to operate at, say, 60 MHz would be rather large (60 mm radius), albeit much smaller than the edge-coupled case discussed above, and so this structure will not be further discussed.

14.2.3 Spiral Resonators

To increase the self-inductance of the resonator, a spiral structure can be considered for which the self-inductance scales as approximately the number of turns in the spiral [MHBL99]. Baena et al. [BMMM04,BJMZ06] have considered two- and three-turn elements and have shown that the frequency for a three-turn spiral is approximately $2\sqrt{2}$ times smaller than that of a commensurate SRR structure; however, even the three-turn structure is still resonant in the GHz regime for an element size of ≈4 mm, and so to achieve a 64 MHz response would require it to have ≈70 mm radius. Wiltshire [Wil00] has considered a hexagonal, eight-turn double-spiral structure with an element

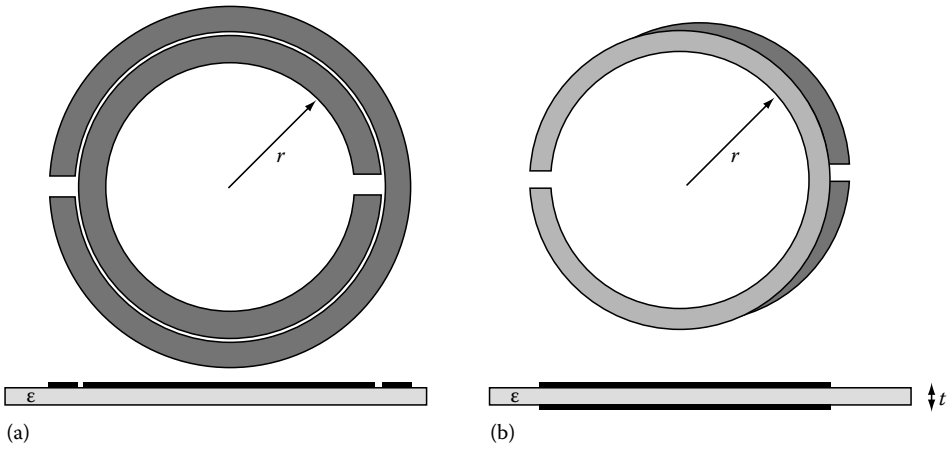

FIGURE 14.3 Schematic diagram of split ring resonator structures: (a) the edge-coupled structure consists of two concentric split rings on a dielectric substrate, whereas (b) the broadside-coupled form has the two rings disposed on opposite sides of the (thin) substrate thus enhancing the self-capacitance of the structure.

size of ≈40 mm, which is resonant at around 100 MHz. Thus using spiral structures does give a magnetic response from a planar structure in the required frequency range, but the elements are still too big to be incorporated in a material.

14.2.4 Ring Resonators

Adding a discrete capacitance to the ring structure produces a simple LC resonant loop [SKRS02a, SKRS02b] whose frequency and size can be selected at will. One such element, investigated by Wiltshire et al. [WSYS03] consisted simply of two turns of 1 mm diameter copper wire, wound on a 9.6 mm diameter Delrin rod, with a 100 pF capacitor connected across the ends of the wire to produce an element that was resonant at ≈60 MHz. In a similar way, Sydoruk et al. [SRZ+06] connected 330 pF capacitors to a 20 mm diameter split pipe to produce resonators at 46 MHz. Both these elements are constructed macroscopically, but there is no *a priori* reason why circuit board technology cannot be used to fabricate elements, and this was in fact done by Syms et al. [SYS06], who constructed miniature spirals combined with surface-mounted capacitors to produce 8 mm diameter elements resonant at 150 MHz. The behavior of ring resonator structures is fully described in the chapters by Sydoruk et al., and so will not be further discussed here.

14.2.5 Swiss Rolls

The Swiss roll structure [PHRS99] (see Figure 14.4) is particularly suitable for use at RF frequencies up to ≈200 MHz, because it has inherently large self-inductance and self-capacitance. The elements consist of a number of turns N of insulated conductor wound onto a central mandrel. In practice, this is achieved by using a metal–dielectric laminate that is wound spirally onto a dielectric rod. The self-inductance is governed by the number of layers of conductor, whereas the self-capacitance is determined by the thickness and permittivity of the dielectric. For a compact, low-frequency element, we require the dielectric layer to be thin and of low loss.

The magnetic permeability of an array of such rolls is given by [PHRS99]

$$\mu(\omega) = 1 - \frac{\frac{\pi r^2}{a^2}}{\left(1 - \frac{d c_0^2}{2\pi^2 \epsilon r^3 (N-1)\omega^2}\right) + i \frac{2\rho}{\omega r \mu_0 (N-1)}} \tag{14.4}$$

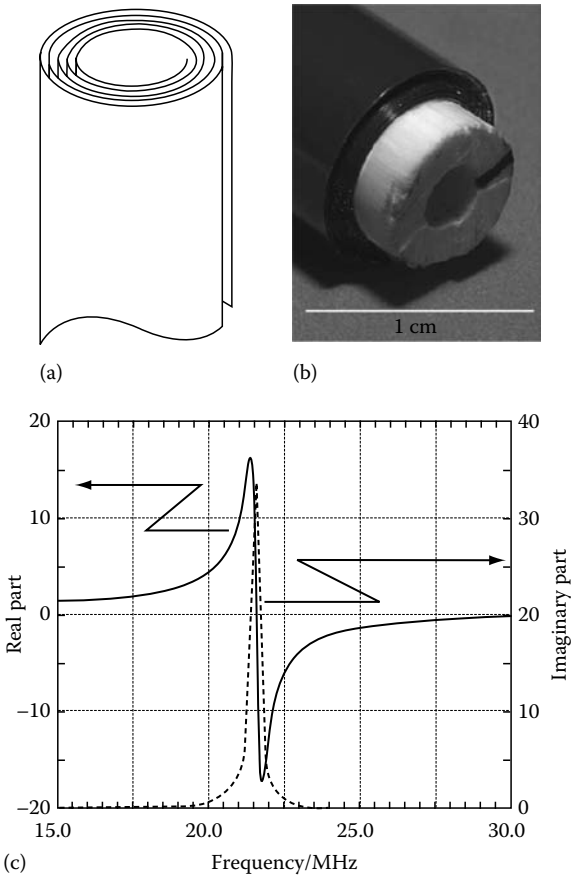

FIGURE 14.4 The Swiss roll metamaterial: (a) schematic diagram of an individual element, showing the spiral-wound structure; (b) a photograph of an element; and (c) the measured permeability of a material designed to operate near 21.3 MHz. Full line and left-hand scale show the real part; dashed line and right-hand scale show the imaginary part.

where

N is the number of turns in each roll of diameter r

ϵ is the (complex) permittivity of the dielectric between the conducing layers

ρ is the resistivity of the conductor

The rolls are packed with a unit cell spacing of a. Typical values for resonance at 21.3 MHz are r = 5 mm, N = 11, using the material Espanex, which consists of a 12.5 μm polyimide sheet with 18 μm of copper laminated to it, manufactured as a flexible printed circuit board (PCB) material. The polyimide has a permittivity of $\epsilon \approx 2.3$ and a loss tangent of ≈0.01, and the resonance has $Q \approx 60$ [WHP+03].

The frequency-dependent permeability (Equation 14.4) is anisotropic and usually written [WHP+03]

$$\mu_{zz}(\omega) = 1 - \frac{F}{\left(1 - \frac{\omega_0^2}{\omega^2}\right) + i\frac{\Gamma}{\omega}}, \quad \mu_{xx} = \mu_{yy} = 1 \tag{14.5}$$

in which

F is the filling factor, given as $\pi r^2/a^2$ in Equation 14.4

ω_0 is the resonant angular frequency, given by

$$\omega_0 = \sqrt{\frac{dc_0^2}{2\pi^2 \epsilon r^3 (N-1)}} \tag{14.6}$$

and is determined by the construction of the element

Γ is the damping, and includes both the resistance of the conductive layer and the dissipative part of the permittivity of the dielectric layer.

The damping plays a critical role in determining the performance of these materials: strong damping leads to broad resonances with low quality factor Q and weak magnetic effects. In the very first system studied [WPY+01], the metal layer was extremely thin and the resistivity term dominated the loss. For all other systems, based on flexible PCB materials, the dielectric loss dominates. It has therefore been important to seek flexible PCB systems that are adhesiveless and based on low-loss dielectric. In most of the work discussed here, the Swiss rolls had a $Q \approx 60$ at a resonant frequency near 21.5 MHz. An optimized Kapton base (Novaclad) can provide a $Q \approx 100$, whereas a Teflon based material (CuFlon) has a $Q \approx 300$.

14.3 Effective Medium Description

There are two approaches to describe the behavior of ensembles of the metamaterial elements: the microscopic and the macroscopic. In the microscopic approach the ensemble is considered as an array of coupled resonators, each with a resonant frequency and coupled to neighboring elements (or indeed to all other elements). The currents and voltages flowing in the elements can then be calculated explicitly, given some excitation, and the resulting current distribution in the ensemble found. It is found that there are wave-like solutions for the current equations, which describe magneto-inductive waves [SKRS02a,SKRS02b,WSYS04]. From this analysis, the field distributions may be obtained for comparison with measurement [ZSS05]. This approach is described in detail in the chapters by Sydoruk et al. and will not be discussed further here.

In the macroscopic view, on the other hand, we assert that, since the element size is much smaller than the wavelength at the frequency of operation, we can ignore the detail in the material and describe it as a homogeneous, effective medium whose electromagnetic response is defined by an effective permittivity and permeability whose values need not be confined to those available in natural materials. Based on these parameters within the effective medium approach, we investigate the interaction of the medium with electromagnetic fields and calculate their behavior either analytically or numerically.

14.3.1 Permeability

The effective medium prescription was given by Pendry et al. [PHRS99] for a variety of structures, and considered in more detail by Smith and Pendry [SP06]. The effective medium parameters arise from consideration of average fields:

$$\mathbf{B_{ave}} = \mu_{\text{eff}} \mu_0 \mathbf{H_{ave}} \quad \text{and} \quad \mathbf{D_{ave}} = \varepsilon_{\text{eff}} \varepsilon_0 \mathbf{E_{ave}} \tag{14.7}$$

We write Maxwell's equations in integral form:

$$\int_C \mathbf{H} \bullet d\mathbf{l} = +\frac{\partial}{\partial t} \int \int_S \mathbf{D} \bullet d\mathbf{S} \quad \text{and} \quad \int_C \mathbf{E} \bullet d\mathbf{l} = -\frac{\partial}{\partial t} \int \int_S \mathbf{B} \bullet d\mathbf{S}, \tag{14.8}$$

where the line integral is taken along the curve C, which bounds the surface S. Then when the magnetic fields are very inhomogeneous, and vary rapidly within the structure, the averages for **H** and **B** are quite different so that μ_{eff} becomes significantly different from unity. This situation arises in the resonant structures discussed here, and following this prescription, Pendry et al. [PHRS99] calculated the effective permeability of the Swiss roll structure to be that given in Equation 14.4.

Whereas the permeability of SRR metamaterials has to be derived from the inversion of transmission and reflection data in the microwave regime, it can be measured directly for the Swiss roll structure because the elements are long, thin, needle-like elements. Accordingly, the demagnetizing factor (see e.g., [Str41b]) for a single roll or a small bundle of long rolls is quite small and can be approximated to that of an ellipsoid with the same axial ratio. The material is inserted into a solenoid, and the change in its self-inductance and resistance is measured. The complex permeability is then obtained by applying a volume correction and the demagnetizing factor. An alternative method is to modify the mutual inductance between two loops by introducing a material sample along their common axis. By this means, the effective permeability of the medium can be obtained and is shown in Figure 14.4 for the material based on Espanex (see above). It is clear that this has the resonant form of Equation 14.5, and the values of ω_0 and Γ can be obtained from a least-squares fit to the data. Furthermore, by measuring samples with different numbers of turns, it is possible [WPY+01] to deduce both the permittivity of the dielectric (taken as unity in the theory above) and the effective radius of the roll expressed as $r = r_0 + \alpha N$, where α is a parameter to take into account the thickness of the laminate (the theory assumes that the layers are infinitesimally thin so that $Nd << r_0$, whereas in reality the thickness of the winding Nd and the radius r may be comparable).

14.3.2 Propagation

We consider the behavior of electromagnetic fields in a highly anisotropic effective medium and describe the fields by a Fourier expansion of the form [WHP+03]:

$$\mathbf{E}(\mathbf{r}, t) = \sum_{\mathbf{k}} \mathbf{E}(\mathbf{k}) \exp i\left[\mathbf{k}\cdot\mathbf{r} - \omega t\right] \tag{14.9}$$

with an analogous expression for **H**. Maxwell's equations for a monochromatic field with angular frequency ω and wavevector **k** are

$$i\mathbf{k}\times\mathbf{E} = i\omega\mu\mu_0\mathbf{H}, \quad i\mathbf{k}\times\mathbf{H} = -i\omega\varepsilon\varepsilon_0\mathbf{E}. \tag{14.10}$$

The medium is magnetically active but dielectrically inactive, so on eliminating **E** we find

$$-\mathbf{k}\times\mathbf{k}\times\mathbf{H} = \omega^2 c_0^{-2}\mu\mathbf{H} \quad \text{or} \quad -\mathbf{k}\left(\mathbf{k}\cdot\mathbf{H}\right) + k^2\mathbf{H} = k_0^2\mu\mathbf{H}, \tag{14.11}$$

where k_0 is the free-space wavevector, ω/c_0.

The effective medium is isotropic in the $x-y$ plane, so we can confine our calculations to the $x-z$ plane without loss of generality. It is convenient to rewrite Equation 14.11 in terms of **B**, whereupon expanding gives

$$\begin{bmatrix} k_z^2/\mu_{xx} & -k_x k_z/\mu_{zz} \\ -k_x k_z/\mu_{xx} & k_x^2/\mu_{zz} \end{bmatrix}\begin{bmatrix} B_x \\ B_z \end{bmatrix} = k_0^2\begin{bmatrix} B_x \\ B_z \end{bmatrix}. \tag{14.12}$$

The condition for solution is

$$\frac{k_x^2}{\mu_{zz}} + \frac{k_z^2}{\mu_{xx}} = k_0^2 = \frac{\omega^2}{c_0^2} \tag{14.13}$$

and the associated eigenvectors are

$$\begin{bmatrix} B_x \\ B_z \end{bmatrix} = \begin{bmatrix} k_x^2/\mu_{zz} - k_0^2 \\ k_x k_z/\mu_{xx} \end{bmatrix}. \tag{14.14}$$

Equations 14.13 and 14.14 allow us to explore the behavior of fields both inside the medium and at its interfaces. In free space, the eigenvalue equation becomes

$$k_x^2 + k_z^2 = k_0^2 = \frac{\omega^2}{c_0^2} \tag{14.15}$$

so that $k_z = \sqrt{\omega^2/c_0^2 - k_x^2}$, and only those fields with $k_x < k_0$ can propagate; for $k_x > k_0$ the fields decay evanescently along the propagation direction, z.

Within the medium, however, consideration of Equation 14.13 shows that there are several possibilities of interest:

1. In what Smith et al. [SKS04] have termed an indefinite medium, that is one with opposite signs of μ_{xx} and μ_{zz}, propagation is not restricted to $k_x < k_0$. If $\mu_{zz} < 0$, Equation 14.13 has real solutions for k_z for all values of k_x.
2. In the very near field in an indefinite medium, when $k_x, k_z >> k_0$, Equation 14.13 reduces to

$$k_z = \frac{k_x}{\sqrt{|\mu_{zz}|}} \tag{14.16}$$

   so that the fields propagate with a conical wavefront [Bal64,BLK03].
3. In the limiting case on resonance, $\mu_{xx} = 1$ and $\mu_{zz} \to \infty$. Then the eigenvalues (Equation 14.13) reduce to

$$k_z = \pm k_0 \tag{14.17}$$

   and the eigenvectors (Equation 14.14) become

$$\begin{bmatrix} B_x \\ B_z \end{bmatrix} = \begin{bmatrix} -k_0 \\ \pm k_x \end{bmatrix}. \tag{14.18}$$

   We see that k_z is now independent of k_x, so all the transverse Fourier components of an object propagate along the z-axis with the same relative phase: if we measure the intensity we see a perfect image. In the electric field equivalent of this situation [RPWS03], an incident electric field distribution is transported through the material as if the faces of the slab were connected by perfectly conducting wires. By analogy in the present case, we can imagine magnetic "wires," composed of a perfect magnetic conductor, transporting the magnetic image information across the material slab.

14.3.3 Transmission

The eigenvectors from Equation 14.14 (after using Equation 14.13 and removing the redundant factors) are found to be

$$\begin{bmatrix} B_x \\ B_z \end{bmatrix} = \begin{bmatrix} -k_z \\ k_x \end{bmatrix}, \tag{14.19}$$

so we can match the fields at the boundaries between the prism and free space to obtain the interface transmission and reflection coefficients, t_{k_x} and r_{k_x}, as a function of the transverse wavevector k_x.

Hence the transmission of a semi-infinite slab can be calculated in the conventional manner [PP64] to obtain

$$B_z(r,z) = 2\pi \int_0^\infty \left[c^+_{k_x} J_0(k_x r) \exp(ik_z (z-d))\right] \mathrm{d}k_x, \tag{14.20}$$

where

$$c^+_{k_x} = \left[\cos(k_z d) + \frac{1}{2}\left[\frac{\mu_{xx}k_x}{k_z} - \frac{k_z}{\mu_{xx}k_x}\right]\sin(k_z d)\right]^{-1} \tag{14.21}$$

is the overall transmission coefficient of the semi-infinite slab as a function of k_x and $J_0(k_x r)$ is the zeroth-order Bessel function of the first kind.

To take into account the finite size of the sample, we note that there are internal reflections at the entrance and exit surfaces and also at the sides of the material. For the square prism, this can be treated by considering a unit cell with periodic boundary conditions and folding all the higher-order components back into the central zone to deduce the total field. We combine this with Equations 14.20 and 14.21 for the transmission coefficient to calculate the output pattern, which should consist of a central ring whose radius is given by Equation 14.16 along with an additional structure arising from internal reflections [WPWH07,Wil05].

14.3.4 Numerical modeling

No numerical modeling of the individual elements has yet been carried out. Unlike the SRR structure, where the minimum feature size (i.e., the gap between the rings or in the ring itself) is typically 1/1000 of the wavelength and detailed modeling can be performed, in the Swiss roll, this ratio is nearer 1/500,000 and the gridding problem is formidable. Accordingly, the only simulations that can be performed treat the sample as a homogeneous effective medium with an anisotropic, frequency dispersive permeability. Numerical simulations can then be carried out using, for example, the transient solver of CST MicroWave Studio (MWS). Here, a short pulse of radiation is launched into the model, whose time evolution is calculated. This is then Fourier transformed to provide the frequency response of the system. The transverse permeabilities are set to unity, and the axial permeability can be described using the Lorentzian dispersion in MWS, which sets

$$\mu(f) = \mu_s + \frac{(\mu_s - \mu_\infty) f_0^2}{(f_0^2 - f^2) - if\gamma}, \tag{14.22}$$

where

- μ_s and μ_∞ are the low-frequency and high-frequency limiting values, respectively, of the permeability
- f_0 is the resonant frequency
- γ is the damping

By comparing this with Equation 14.4, we see that the metamaterial requires $\mu_s = 1$ and $\mu_\infty = 1 - F$; the resonant frequency and the damping have the same values in both equations.

The source of the magnetic field in the calculation can be a plane wave or, to model realistic situations, a 5 mm diameter wire loop placed in the space behind the slab and excited by a current source in the loop acts as a point source. The metamaterial is embedded in a background medium, typically vacuum, and so-called "open"boundaries (i.e., perfectly matched layers) were placed approximately $\lambda/8$ away from the region of interest, this distance being set by the software itself. Although this can lead to an extremely large model, the gridding is required to be fine only across the metamaterial

region; away from the material, quite a coarse grid can be used so that the overall model is a manageable size.

14.3.5 Comparison with Experiments in the Negative μ Regime

To explore the behavior of magnetic RF metamaterials in the regime above their resonant frequency, when the permeability is negative, transmission experiments have been performed [WHP+03, WPWH07]. In this work, Swiss rolls were assembled into either a square or a hexagonal prism, and their transmission was measured by placing a small loop acting as a magnetic dipole point source on one face while scanning a similar loop acting as a detector across the other face. It is clear from the theoretical discussion here that the transmission is not just a simple number: it depends on the transverse wavevector, and so a variety of field patterns are created on the output face. The challenge for a mean field theory is to reproduce these.

Accordingly, detailed comparisons between measured, analytical calculations and numerical modeling needs to be made [WPWH07]. An early observation was that the calculated results showed much finer detail than was observed experimentally. In part, this difference is a consequence of the finite size of the elements in the metamaterial: no component of the field pattern with a spatial wavelength smaller than the size of an element can be sustained, so there is an effective cutoff at high transverse spatial frequency or wavevector. Moreover, the finite size of the prism itself leads to a minimum for the transverse wavevector. Thus for accurate modeling, the range of wavevector needs to be restricted. This can be implemented in the analytical model with some success, but it is not possible to impose such limits directly in the numerical model, so the effect of the upper limit on the wavevector was approximated by moving the source further away from the prism, thus making the incident field pattern more diffuse and reducing the high spatial-frequency components of the field on the input face.

14.3.5.1 The Square Prism

The measured results for the magnetic field patterns on the output face of the square prism are shown in the central column of Figure 14.5, starting at the highest frequency. The first point to note is that in the negative μ_z regime, the boundary conditions at the edges of the prism require $H_z = 0$. Thus, at the highest frequency (28.5 MHz), where we observe a uniform mode, it has $H_z = 0$ at the edges. As the frequency is reduced, all intensity fades and then a sequence of resonant patterns appear, with first five and then nine high-intensity spots, and then increasingly complicated patterns evolve as the frequency is reduced toward f_0. We also note in Figure 14.5 that the measured patterns have a granularity: this is due to the size of the individual elements of the metamaterial, and we cannot expect any calculation based on an effective medium model to reproduce this.

In the left-hand column of Figure 14.5, we show the field patterns calculated using the analytical theory of Section 14.3.3, along with the periodic boundary conditions discussed there, implemented for the situation when the source was taken to be 20 mm behind the rear face of the prism and the wavevector integral in Equation 14.20 truncated at a spatial frequency corresponding to the roll diameter. First, we note that this model does not produce a result at the highest frequency. Here $\mu_z \approx 0$, so there is an extremely large mismatch between the medium and the vacuum and hence little field penetration. Thus the predicted transmission in this frequency region is essentially zero. The correlation between the other calculated and measured patterns is better than when the source lies 5 mm behind the prism, and we can clearly see that the basic structure of the field patterns is correctly produced. However, the agreement is not particularly good: overall, the features are rather smaller and sharper than those observed.

In the right-hand column are the results of the numerical simulation, for the case when the source is 20 mm behind the prism. Here we see an excellent agreement between the model and the measured data: not only is the basic structure of the patterns correctly given but also the size and shape of the

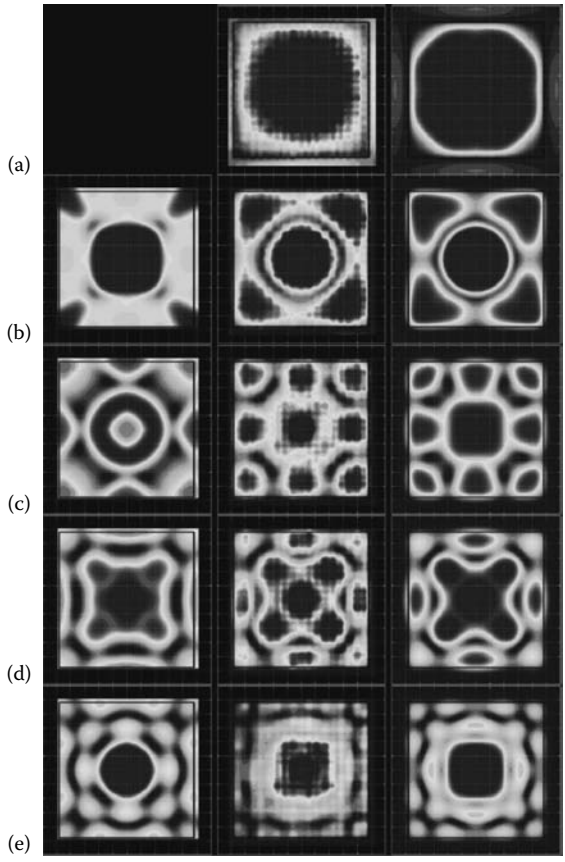

FIGURE 14.5 Comparison of (center column) the field patterns observed 5 mm from the exit face of the square metamaterial prism at (a) 28.50 MHz, (b) 24.70 MHz, (c) 23.65 MHz, (d) 23.25 MHz, and (e) 22.50 MHz, with the patterns calculated using the analytical model (left column) and the numerical model (right column).

high-intensity regions are well described. This model is able to calculate the correct pattern at the high-frequency end (Figure 14.5a, 28.5 MHz). Between the two highest resonances, however, some extra structure was calculated except when a plane wave source was used. At the lower frequencies, below 25 MHz, the agreement between the measured and calculated field patterns is extremely good, and the whole progression from one pattern to another down and through the resonance frequency is correctly described by the numerical simulation. The results are shown for 24.7, 23.65, 23.25, and 22.50 MHz as in Figure 14.5b through d, respectively.

14.3.5.2 The Hexagonal Prism

Magnetic field patterns have also been measured for a hexagonal prism, for both the axial and radial fields. At the highest frequency, 29.7 MHz, a simple drum-head-like resonance is observed, with H_z being maximum at the center and zero at the edges of the prism. Conversely, the radial field is zero at the center and maximum at the edges and points uniformly outward. As the frequency is reduced, the intensity fades until the next resonance at 24.7 MHz, where a central peak and a ring of intensity is seen in which the sign of H_z is reversed. In the radial field, we see the complementary pattern. As the frequency is further reduced, additional "rings" of intensity, modulated by the hexagonal symmetry of the prism, appear. The results are shown in Figure 14.6, as the left-hand frames in each set of data.

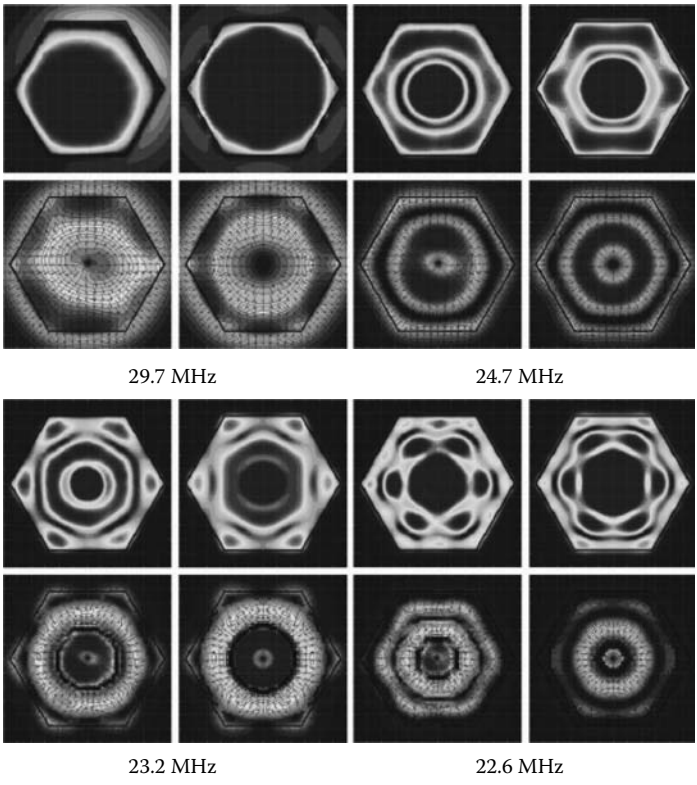

FIGURE 14.6 Comparison of measured and modeled resonant field patterns for the hexagonal prism sample. In each frequency group, the left frames are the measured patterns and the right frames are calculated. The upper pair of frames in each case show the axial field amplitude, $|H_z|$, whereas the lower pair show the radial field amplitude, $|H_{rad}|$, whose direction is shown by the arrows.

The right-hand frames of the data sets in Figure 14.6 show the results of the numerical simulation, again with the source placed 20 mm behind the prism, as described in the previous section. It is clear that the agreement between the measured patterns and the simulated results is extremely good, both for the axial and radial field components. As for the square prism, in the high-frequency regime, between the first two resonances (at 29.7 and 24.7) the numerical simulation shows an additional structure that is not observed in the measurements. As pointed out earlier, this region is better described by simulations using a plane wave source rather than a finite-sized loop source. As the frequency is reduced toward the resonance of the individual rolls, however, the sequence of patterns and the progression from one to another are well described by the numerical simulation.

14.3.6 Discussion

The results above show that a numerical simulation based on an effective medium description of a magnetic metamaterial is able to give a very good description of the observed spatial resonances in the field patterns around the material samples. However, this was achieved by modifying the actual experimental layout: with the field source in its correct position, additional structure was present in the calculations that did not appear in the measurements. This indicated that high spatial-frequency components arising from the finite size of the source continued to be present in the calculation, although they were not observed in the measurements. Clearly, spatial frequencies greater than that

set by the unit cell cannot be sustained in the real material but are present in the model—there is no cutoff mechanism in an effective medium model. To some extent, this restriction on high spatial frequencies was simulated by moving the source further away from the sample, to a distance several times the source diameter, so that the highest spatial components were attenuated before impinging on the material. As shown above, this approach has been very successful in the lower-frequency regime but less so between the first two resonances; here the plane-wave excitation (i.e., launching a uniform magnetic field in the model) gives the best result.

We have also considered an analytical approach within the effective medium framework, but again there is an additional, sharper structure in the calculation than is observed in experiment. Attempts to impose a spatial frequency cutoff in the analytical models (e.g., by constraining the upper limit of integration in Equation 14.20) have been partially successful: the pattern details are indeed smeared out, and the characteristic features of the spatial resonances are reproduced, but the details of the patterns are not correct. Nevertheless, overall this simple model gives a surprisingly good account of the experiments.

The alternative description of the Swiss roll medium as an array of coupled resonators has been investigated by Zhuromskyy and coworkers [ZSS05], using data extracted from a linear array of these rolls [WSYS04], and the response of a hexagonal prism as a function of frequency was calculated. This calculation showed very similar features to those described here. In particular, as the frequency is reduced from well above f_0, a first, uniform resonance is predicted. As the frequency is reduced, the intensity falls, rising again at the next resonance; this has the central peak and a further ring of intensity, as seen in our hexagonal prism at 24.7 MHz. There is no structure in the pattern between these two resonances. Similarly, no extra structure is predicted between here and the next resonance, corresponding to the measured pattern at 23.2 MHz. Thereafter, however, much detailed structure is predicted: indeed, this persists below f_0, and this is not observed experimentally. Thus, the situation regarding additional structure is reversed: whereas in the effective medium model this appears at the higher frequencies and the behavior near f_0 is correctly predicted, in the coupled resonator approach the reverse is true.

A possible explanation for these observations may be seen by considering the dispersion relation, which is plotted over the frequency region of interest as Figure 14.7, for two values of the transverse wavevector, k_x, corresponding to the prism size and to the element size. This figure shows that at a given frequency, a higher k_x demands higher k_z. However, one might expect that the effective medium models would not be accurate for very large k_z, especially for those values corresponding to wavelengths much smaller than the thickness of the prism, that is, $k_z \approx 50$ or $\pi/0.06$, shown as the dashed vertical line in Figure 14.7.

Although the effective medium can certainly support large k_z, the actual Swiss rolls probably cannot: no variations in amplitude or phase were observed along the length of 200 mm long rolls excited by a loop at one end as was done in [WPY$^+$01]. The impact of such a restriction is that the effective medium model is good for the lower k_z, and hence for the lower frequencies, but breaks down at higher frequencies when there is no mechanism within the model to restrict the k_z and hence the k_x. The converse appears to be the case for the coupled resonator description.

Finally, because the wavelength of electromagnetic radiation at these frequencies is so long compared with any length scale in the experiment, we expect the electric and magnetic fields to be essentially independent of one another. Accordingly, an equivalent dielectric model, with the same dispersion parameters but with an electric dipole excitation, should show the same results. This situation, of course, corresponds to the better known plasmon resonances but on an interface that lies between a dielectric (ϵ positive) and a metal (ϵ negative). We have carried out the MWS calculations for such a system and indeed find that the results for the electric field are the same as those for the magnetic system. Accordingly, we can think of the resonances that we measure in the field patterns as caused by magnetic plasmons [PO02].

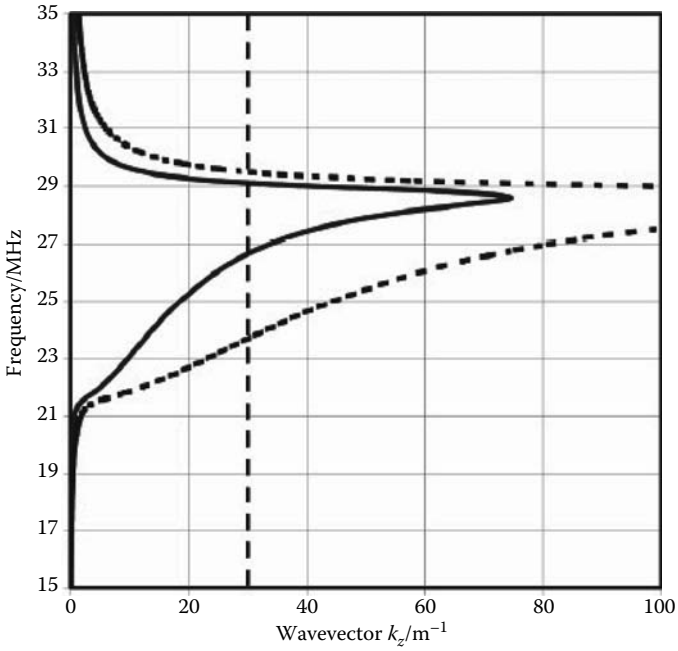

FIGURE 14.7 Dispersion curves of frequency vs. k_z plotted for $k_x = 5\pi$ (full line) and 12π (dashed line), corresponding to the two limiting values imposed by the roll diameter and the sample size. The vertical dashed line corresponds to the prism thickness being half a wavelength.

14.4 RF Imaging

There are two approaches to imaging with RF metamaterials, which we denote as nonfocusing (the endoscope) and focusing (the lens). In the former case, the material is used on resonance, so that the permeability is very large, and signal is guided according to Equations 14.17 and 14.18 from one face of the material to the other, so that the image of the flux pattern on the entrance face appears on the exit face. In the second case, the material is used at the frequency where $\mu = -1$, the prescription for the "perfect lens" [Pen00], and an image (that would be perfect if the material were lossless) is formed in free space at a distance from the object equal to twice the metamaterial thickness. Both approaches have been reported and will be discussed below.

14.4.1 Flux Guiding—Initial Demonstration

In the first demonstration of Swiss rolls used for flux guiding [WPY$^+$01], the bulk material was made up of a bundle of 19 rolls in a hexagonal close-packed array. These initial Swiss roll structures were constructed using "ProFilm Chrome" [a proprietary aluminized mylar film, about 50 μm thick, with a thermosetting glue layer], which was wound on mandrels 200 mm long, made of glass-reinforced plastic (GRP) rod. Following initial characterization, a material was designed and made for use at the 21.3 MHz operating frequency of a Marconi Medical Systems (Cleveland, Ohio) Apollo 0.5T MRI machine.

The coupling (S_{21}) between two short coils, linked by one of the Swiss rolls, was measured as a function of their separation. Figure 14.8 shows the coupling between the coils (S_{21}) at 21.3 MHz, plotted as a function of the separation of the two coils. The dashed line shows the result without the Swiss roll present. When a Swiss roll was inserted so that the drive coil was 25 mm from the end of the roll, the full line was obtained. It is clear that the Swiss roll acts as a flux-guiding medium, providing

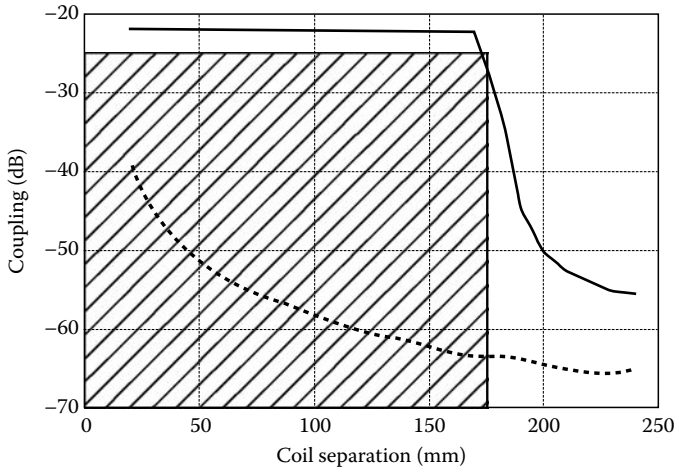

FIGURE 14.8 Measured coupling, S_{21}, as a function of the separation of two coils with a Swiss roll inserted between them (solid line) and with the Swiss roll removed (dashed line). The fixed coil was placed 25 mm from one end of the Swiss roll; the extent of the Swiss roll is indicated by the shading.

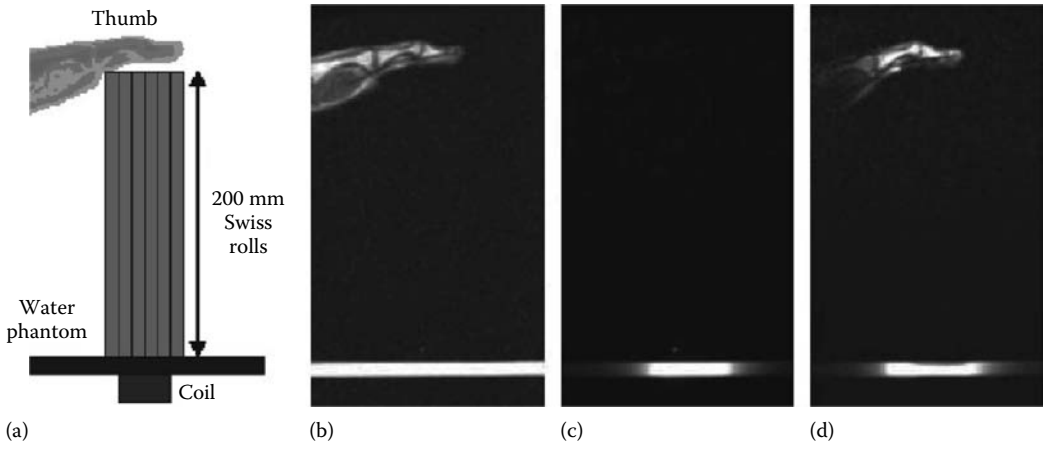

FIGURE 14.9 The MRI imaging experiment: (a) Schematic of setup. A small coil (diameter 37 mm) acts as the receiver, and a thumb is the object to be imaged. The water phantom provides a reference plane. The 200 mm space between the phantom and the thumb is filled either with an inert plastic block (not shown) or with Swiss rolls. (b) A reference image obtained with the "body coils" that are built into the structure of the magnet, showing the thumb and the reference plane. (c) The image from the small receiver coil when the thumb is supported on an inert plastic block. Only the phantom is visible. (d) The image from the same coil when the Swiss rolls are inserted. Now the image of the thumb can be clearly seen.

linkage between coils that may be up to 150 mm apart in this case. Note that there is little flux leakage along the length of the core, which is qualitatively different from what would be observed for a conventional magnetic core with the same permeability of $\mu \approx 2$.

This Swiss roll metamaterial was then applied in the MRI environment [WPY+01]. The bundle of rolls was used to duct flux from an object to a remote detector; the results are shown in Figure 14.9. Since the metamaterial used in these experiments was lossy, all the positional information in the

image was provided by the spatial encoding system of the MRI machine (see also Section 14.5.1). Nevertheless, it was clear from this work that such metamaterials could perform a potentially useful and unique function.

14.4.2 Flux Guiding—High-Performance Material

To improve the flux-guiding performance, a material with a lower loss is necessary. To achieve this, a thicker metal layer is required, along with a low loss dielectric, and hence adhesiveless construction. Very thin flexible PCB provides a good material for this purpose, and Swiss rolls have been made with a $Q \approx 60$ at a resonant frequency near 21.5 MHz, by rolling approximately 11 turns of the material Espanex SC-18-12-00-FR, which consists of an adhesiveless laminate of an 18 μm copper sheet with a 12.5 μm polyimide layer, onto a 10 mm diameter Delrin mandrel. The effective permeability of the Swiss roll medium was determined as described in Section 14.3.1 by inserting a roll into a long solenoid and measuring the changes in the complex impedance that result. On resonance the peak imaginary value of $\mu'' = 35$ was found. These rolls were assembled as a hexagonal array in a balsawood box to create the prism of material whose behavior above resonance was described in Section 14.3.5.

At 21.3 MHz, the wavelength *in vacuo* is about 14 m, so the length scales are much less than a wavelength and the losses will dominate in Equation 14.13. At resonance, we can write the permeability as

$$\mu_z(\omega_{\text{res}}) = i\beta^2. \tag{14.23}$$

Assuming that $k_x^2/\beta^2 >> k_0^2$, Equation 14.13 gives

$$k_z^2 \approx ik_x^2/\beta^2. \tag{14.24}$$

Thus for finite loss, k_z has an imaginary component, and the material does not transport the image perfectly: the higher Fourier components degrade faster with distance. For a material thickness d the attenuation will become significant when $\text{Im}(k_z)d \approx 1$ or, using Equation 14.24 , when $k_x(\max) \approx \beta/d$. The resolution is therefore limited to

$$\Delta \approx 1/k_x(\max) \approx d/\beta. \tag{14.25}$$

In the present case, $\beta \approx 6$ and $d = 60$ mm, so that $\Delta \approx 10$ mm, approximately equal to the diameter of the individual rolls. Thus, we do not expect loss effects to degrade the resolution of any transmitted structure beyond the intrinsic granularity of the Swiss rolls.

Figure 14.10 shows both the cross-section and the plane view of both the measured and simulated results. These plots demonstrate convincingly that the face-plate behavior is obtained in a homogeneous (but strongly anisotropic) effective medium and is not just due to guiding through the individual Swiss rolls. Moreover, in Figure 14.10e, we plot a comparison of the measured profile (dots) with an analytic calculation based on the effective medium formalism that we reported previously (dashed line) and the profile obtained from the present numerical calculation (full line). The detailed structure in the measured data arises because we sample discrete rolls, and flux is trapped inside the individual elements. Clearly, this effect cannot be represented in an effective medium approximation, so the comparison should be made between the envelope of the data points and the calculated profiles. The agreement between the two calculated profiles is very good over a wide intensity range (note the logarithmic scale), and both are accurate envelopes for the measured points.

To test the two-dimensional (2D) imaging performance of the material, an antenna was constructed from a pair of antiparallel wires, bent into the shape of the letter M (Figure 14.11a). This generated a line of magnetic flux, thus providing a characteristic field pattern for imaging. It was

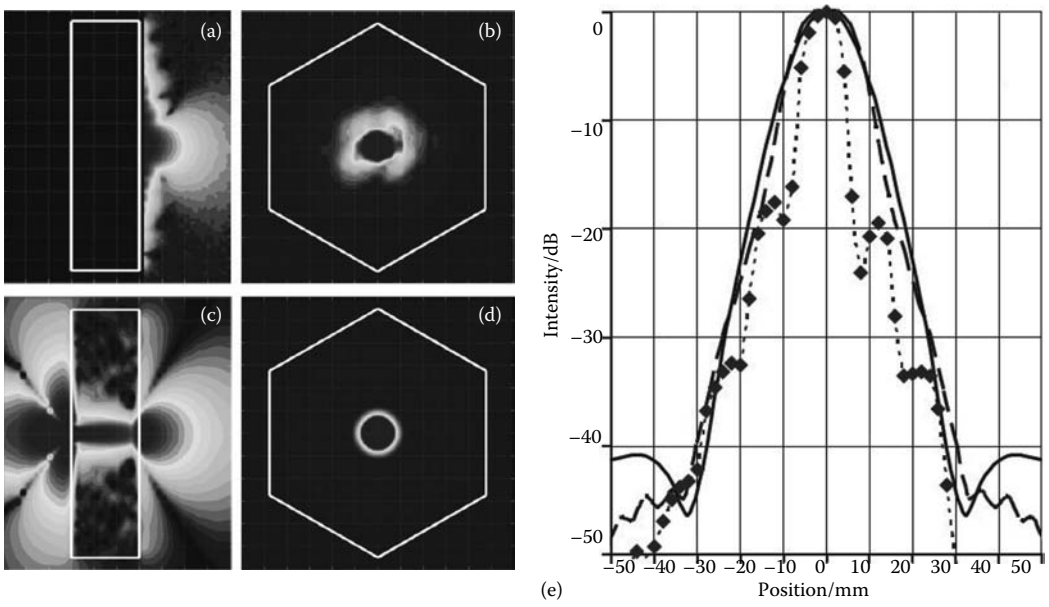

FIGURE 14.10 Axial magnetic field ($|H_z|$) patterns from the hexagonal prism on resonance: (a) measured intensity (dB) in the XZ plane; (b) amplitude in the XY plane, 5 mm above the prism; (c) modeled intensity (dB) in the XZ plane, showing the jet of flux propagating through the material; (d) amplitude in the XY plane, 5 mm from the prism; and (e) comparison of measured and calculated profiles: the points are measured data with the dotted line being a guide to the eye, the dashed line the analytical profile, and the full line the profile from the numerical calculation.

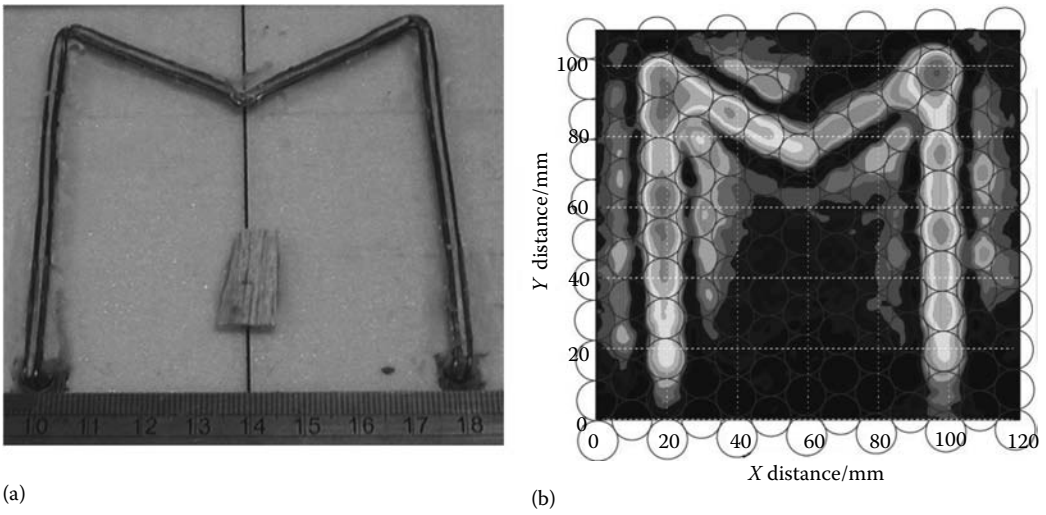

FIGURE 14.11 (a) The M-shaped antenna, constructed from two antiparallel wires held 1 mm apart, and (b) the field pattern observed at 21.3 MHz in a plane approximately 2 mm above the surface of the metamaterial slab. The Swiss roll structure is overlaid.

placed horizontally, and the material was positioned on top of it. The transmitted field was measured by scanning a small probe above the surface of the material, and the pattern thus observed at 21.3 MHz is shown in Figure 14.11b, in which the Swiss roll structure is overlaid on the field pattern [WHP+03].

Figure 14.11 clearly shows that the material does indeed act as an image transfer device for the magnetic field. The shape of the antenna is faithfully reproduced in the output plane, both in the distribution of the peak intensity and in the "valleys"that bound the M. These mimic the minima in the input field pattern either side of the central line of flux. The upper-right arm of the M itself was twisted, so that the flux pattern was launched with a much reduced vertical component. This is reproduced in the weaker intensity observed in this region.

14.4.3 RF Focusing

To observe focusing effects [Pen00], the material should be isotropic and have a refractive index $n = -1$. If we confine our attention to the (x, z) plane (where z is the direction of propagation and x is a transverse direction), such material can be constructed by stacking alternate layers axially and transversely to make a 2D log pile [WPH06]. Moreover, it was also pointed out in [Pen00] that when all relevant lengths are much less than the wavelength, the electric and magnetic components of electromagnetic radiation are decoupled. In this near field regime, therefore, a magnetic signal can be focused using material with permeability $\mu = -1$, but materials with this property are not found in nature, so this focusing has not previously been observed. However, using metamaterials allows us to construct materials with the specified $\mu = -1$, and, by working at radiofrequency (RF), the requirements that both the material elements and the measurement distance should be much smaller than a wavelength are readily satisfied.

The resolution enhancement, R, that can be achieved with a negative index slab was calculated analytically in [PR02,Ram05,SSR+03], where it was shown that the limit of resolution, Δ, is determined by the loss in the material, which here is μ'', and by the length of the sample, d, to be

$$R = \frac{\lambda}{\Delta} = -\frac{1}{2\pi} \ln\left(\mu''/2\right) \frac{\lambda}{d} \quad \text{or} \quad \Delta = \frac{2\pi d}{|\ln\left(\mu''/2\right)|}. \tag{14.26}$$

Using the measured values, we obtain $\mu'' = 0.14$ when $\mu = -1$, so that $\Delta \approx 140$ mm and $R \approx 90$. A log pile was made [WPH06] from Swiss rolls, arranged so that the transverse and axial permeabilities were equal. Magnetic field sources consisting of long thin loops that each generated a line of magnetic flux were placed 20 mm behind the slab, and a similar loop was used to measure the magnetic field, H_z, in the output space [WPH06].

The experimental data were analyzed to determine the frequency at which $\mu' = -1$; this was found to be 24.55 MHz. The data were then plotted to show the spatial distribution of the magnetic field in the image space. This is shown in Figure 14.12. Here, Figure 14.12a shows the distribution of $|H_z|$ arising just from the two sources, spaced 100 mm apart. We note that there is no discernible structure at 120 mm from the source plane. When the slab of metamaterial is introduced in the position indicated, the fields in the image plane are enhanced by a factor of ≈ 15, and significant structure is obtained (Figure 14.12b). Near the surface of the metamaterial, there are strong fields with rapid spatial variation—note that the intensity scale is the same in both frames. In the image plane, indicated by a dashed line in Figure 14.12a and b, distinct modulation can be seen. Plotting the field magnitude as a function of position in the image plane shows two peaks (Figure 14.12c). As the source separation is increased, the weakly modulated peak observed at the lowest value of 100 mm is split into two peaks with appropriate spacing and increasing contrast. This confirms that the structure in the image plane does indeed arise from imaging the sources.

The performance of an imaging system is defined by the transfer function, which describes the (complex) transmission of the system as a function of the spatial frequency. The formula of [SSR+03]

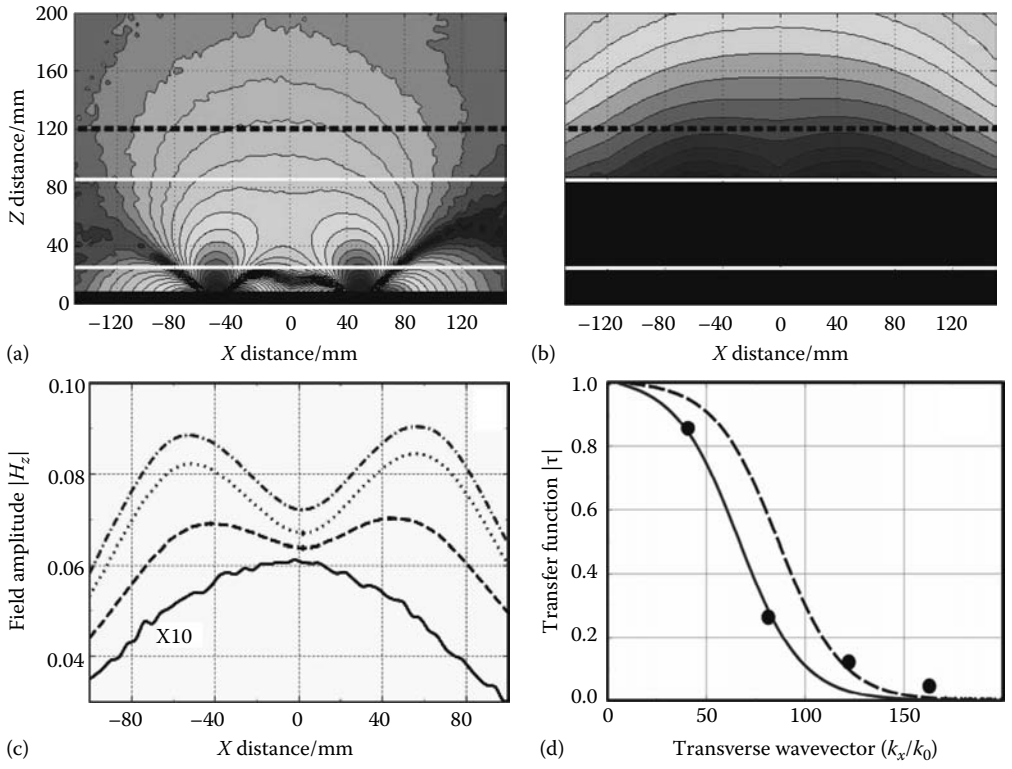

FIGURE 14.12 Measured distributions of H_z field intensity (dB) at 24.55 MHz: (a) From two sources spaced 100 mm apart in free space; (b) as (a) but with the metamaterial slab in place. In these frames, the position of the metamaterial is indicated by the thin white line and the image plane by the dashed black line. (c) The variation of the field amplitude in the image plane $z = 120$ mm without the metamaterial (full line, X10) and with the metamaterial when the sources are spaced 100 mm (dashed line), 120 mm (dotted line), and 140 mm (dash-dot line) apart. (d) Measured (points) and calculated (lines) transfer function for a 60 mm slab of metamaterial with $\mu' = -1$ at 24.55 MHz: dashed line $\mu'' = 0.14$, full line $\mu'' = 0.26$.

was used to calculate the transfer function using the predicted value of $\mu'' = 0.14$. This is shown as the dashed curve in Figure 14.12d. The transfer function was measured and the resulting points were also plotted in Figure 14.12d. It is clear that the actual value of μ'' is rather larger than that estimated from measurements of a single element. A least-squares fitted value is $\mu'' = 0.26$, and the transfer function for this value is plotted as the full line in Figure 14.12d. The Rayleigh criterion was applied to estimate the resolution as $\approx\lambda/64$, although the measurements actually display a rather higher resolution, as indicated by the high spatial-frequency tail in Figure 14.12d.

14.4.4 Discussion

The first point that should be noted for these imaging mechanisms is that the resolution Δ is independent of the wavelength of operation; see Equations 14.24 and 14.25. Thus by working at a long wavelength in the RF, it is simple to achieve massively subwavelength resolution. The absolute resolution (i.e., Δ itself) depends critically on the loss in the material: the smaller the loss, the better the resolution. In the case of the flux guiding endoscope, the achievable resolution is also limited by the finite size of the individual elements, because the image is formed at the surface of the material. In the case of the lens, on the other hand, the image is removed from the surface, so that the effect of

granularity, which only persists to a distance about equal to the element size, is smeared out. Thus, to achieve improved performance of the endoscope, the material needs to be made from smaller elements with lower loss, whereas to improve the lens just needs lower loss in the material. However, the improvement that can be achieved in the case of the lens is limited because of the logarithmic dependence of the resolution on the imaginary part of the permeability.

It should also be noted that these mechanisms show focusing only in the transverse plane: there is no focusing in the longitudinal direction, and conventional three-dimensional image formation does not occur. This is self-evident in the case of the endoscope, in which the image is formed on the output face. For the lens, the subwavelength features in the image arising from the presence of the evanescent field components, which are "amplified" by the material in such a way that they combine to form the image observed. Thus the field distribution between the lens and the image plane is complicated and shows no longitudinal focusing. Such longitudinal focusing has been obtained [FM05,MFMB05], but it relies on the detector perturbing the output field, which does not occur here, and, indeed, is generally undesirable.

14.5 Applications

There are many potential applications of RF metamaterials, but the key feature that will govern how well they perform is their dispersion: their permeability is a strong function of frequency. Therefore, the most promising applications are those with narrow bandwidth demands. One possible use is in antenna applications, where the ability to tailor the permeability of the substrate opens up a wide range of novel antenna concepts; these are explored elsewhere in this handbook. Another application area is magnetic resonance, where the signal bandwidth is small, but there are other magnetic fields present that must not be perturbed. MRI is a particularly promising area in which metamaterial components might be used.

In an MRI system, the main magnetic field (typically 0.5–3 Tesla) needs to be homogeneous to a few parts per million, thus ruling out the introduction of any conventional magnetic material. Nevertheless, it would be very useful to have access to magnetic materials with which to manipulate the RF signals (in the range 20–120 MHz). Functions such as guiding, focusing, and screening could substantially enhance the performance of MRI systems. Metamaterials can achieve this, because they offer a means of obtaining magnetic properties at RF (for example large positive or negative permeability) without affecting the other magnetic fields in the system: here we describe work on a faceplate, a yoke, waveguides, and flux compressors, all of which could have application in an MRI environment.

14.5.1 RF Endoscope/Faceplate

The first demonstration of RF metamaterials used in an MRI environment [WPY$^+$01] was described earlier (Section 14.4.1). Further experiments on this concept have been carried out with the improved material described in Section 14.4.2. To do this, the M-shaped antenna was tuned and used to excite localized field patterns in an NMR-visible polymer sheet (Spenco™), as shown in Figure 14.13. The NMR signal from the Spenco sheet was detected by using the M-antenna in transmit-receive mode. In the control experiment (Figure 14.13a), the RF excitation level was set so that signals were received only from locations close to conductors, so that the conductor pattern was directly visualized in the image using multislice spin echo imaging performed in planes parallel to the sheet surface, and these revealed the expected flux patterns (Figure 14.13c). When the metamaterial was placed between the excitation coil and Spenco sheet (Figure 14.13b), no change of RF excitation amplitude was required to maximize the signal, and the flux pattern was directly transferred with geometry preserved (Figure 14.13d) [WPL$^+$03].

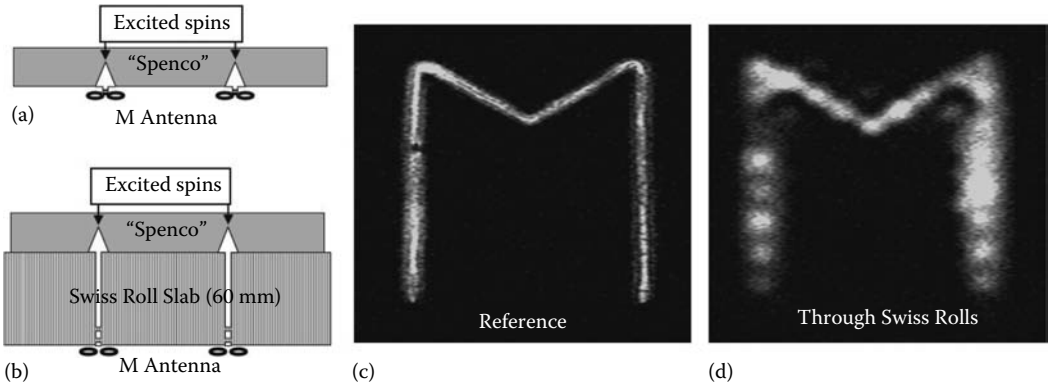

FIGURE 14.13 The MRI experiment with the metamaterial faceplate. (a) The reference layout with the "Spenco" placed directly on the M-antenna; the measured image is shown in (c). (b) The Swiss roll prism is inserted between the antenna and the "Spenco"; the image obtained using the M in a transmit-receive mode through the Swiss rolls is shown in (d).

Behr et al. [BHJ04] also used a Swiss roll as a flux guide in an NMR system. It was used to couple a small solenoid that acted as both source and detector for the RF signal, in this case from the $_{31}$P resonance at 34.25 MHz in a 2 T field. They found that the signal was transmitted with minimal propagation loss, although there was a significant insertion loss. The potential advantage of using such a guide is that the signal coils do not have to be optimized for each different sample geometry.

14.5.2 Yoke

A metamaterial yoke made of Swiss rolls could provide a low reluctance pathway, which might assist in excitation delivery or signal reception in MRI and spectroscopy applications [WHYH04].

A set of Swiss rolls designed to resonate at 21.5 MHz with a Q of ≈30 were made with the Dupont material Pyralux, and used in the first experiments. Preliminary tests were made on single rolls, by injecting a signal through a coupling loop at one end and recording the detected signal through a second loop that could be moved along the roll. As shown in Figure 14.8, the detected signal was independent of the position of the receiver. However, it did depend on the length of the roll, being smaller for longer rolls. Thus the rolls act as good magnetic flux conductors, and the signal is determined by the reluctance (i.e., the length) of the flux return path.

Joining the individual rolls together introduces extra loss, so a yoke constructed from butt-coupled single rolls would not be viable. To reduce the corner losses, bundles of seven rolls of different lengths were used, so that the corners were mitered at 45 degree, as shown in Figure 14.14a. This arrangement was much less sensitive to alignment and significantly reduced the corner losses, so that a full yoke became viable.

The performance of the yoke was tested by using a remote receiver loop to detect flux circulating through the metamaterial bundles from a source loop placed between the pole pieces. The reference level was defined when the two loops were in a coplanar configuration without the metamaterial, and the signal being guided around the yoke was then measured (Figure 14.14b). At first sight, this result shows perfect coupling, but it must be recalled that this is a resonant system, so we expect the signal on resonance to be much higher than the reference. Therefore, although this result is encouraging, it also shows that the device must be improved to be truly useful.

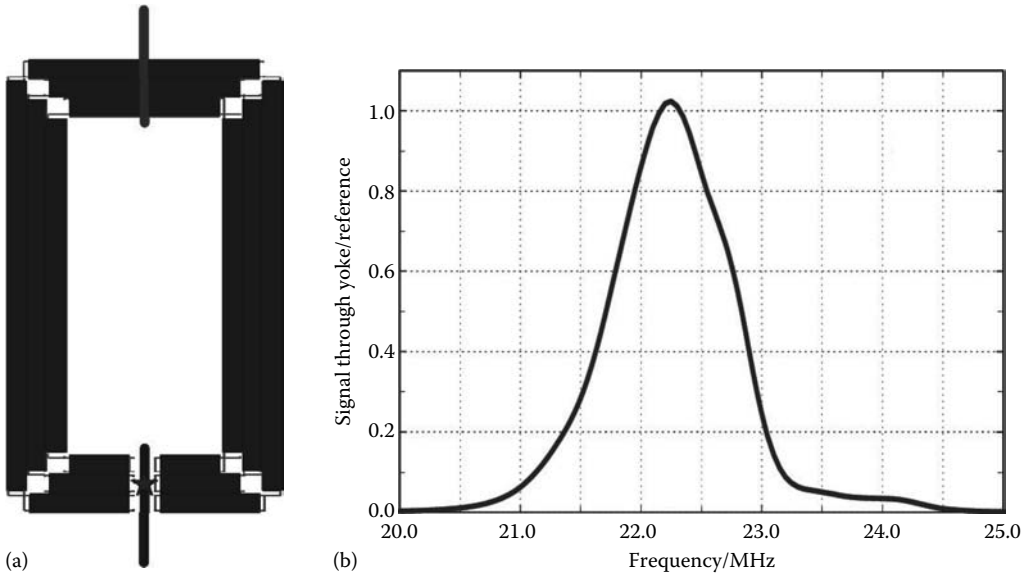

FIGURE 14.14 (a) Schematic diagram of an RF yoke, constructed from bundles of Swiss rolls; the bottom arm consists of two sets of pole pieces with the sample volume between them. The star in the sample volume denotes either the source point or the required excitation volume within a sample, and the lines on the top and bottom arms represent alternative positions for exciting or receiver coils. (b) The signal recorded by the remote detector demonstrates that the flux is being guided from the source through the Swiss roll bundles.

TABLE 14.1 Comparison of Junction Losses for Straight and 90° Joints in Pyralux, Espanex, and Coupled Systems

Signal (dB)	Straight Joint	90° Joint
Pyralux	−5.9	−11.3
Espanex	2.7	−6.8
Espanex + coupler	−1.1	−0.9

The higher-performance material described in Section 14.4.2 has also been tested. This has a permeability and Q that are at least a factor of 2 higher than those in the Pyralux material above. The signal down a 200 mm roll was increased, showing much improved flux ducting. However, the losses at joints, while reduced compared with those in the Pyralux system, are still unacceptable (see Table 14.1), so the effect of additional couplers in the form of two connected loops that link the end of one roll with the next was investigated. This significantly improves the flux linkage, as shown in Table 14.1, but further work is necessary to optimize this approach.

Allard et al. [AWHH05] modeled the performance of such a yoke in an MRI system using an effective medium model. These calculations showed that significant signal gain should be obtained when the yoke cross-section is approximately the same as the width of the gap in the yoke, and the permeability is as large as possible. With achievable values of the permeability ($\mu \approx 100$), a signal gain of 2–3 dB was predicted. In further work [AH06], they used a finite difference time domain (FDTD) approach to calculate the currents in a circuit model of the Swiss roll structure and concluded that there would in fact be little gain due mostly to the finite Q of the rolls. They did point out, however, that there is almost no leakage of magnetic flux from the rolls, a point noted in [WPY+01] even for low-Q material.

14.5.3 Waveguides

The concept of the magneto-inductive waveguide was introduced by Shamonina et al. [SKRS02a], who derived the dispersion relations and considered the current distribution and power flow through the line. The impact of unmatched ends and the coupling between two guides was treated by Shamonina and Solymar [SS04], and further waveguide device concepts were presented by Syms et al. [SSS06].

Syms et al. [SYS06] discuss the performance of waveguides constructed from arrays of up to 70 metamaterial elements, formed into a planar ring resonator at 150 MHz, and reduce the propagation loss to 0.12 dB per element. Consideration also has to be given to the termination of such guides [SSS05], so that the insertion loss is minimized. Sydoruk et al. [SRZ+06] built waveguide structures from their split-pipe elements and considered the coupling between the lines. By assembling the elements in a ring, Solymar et al. [SZS+06] proposed a device with a rotational resonance, which could be potentially used in the detection of NMR signals.

14.5.4 Flux Compressor

To use our metamaterials successfully in the MRI environment, it will be necessary to develop various components that can be incorporated into the metamaterial assemblies. One such component, a flux compressor, is intended to collect a signal from a significant area and output it to a much smaller one or *vice versa*. A prototype device [WSSY04], shown in Figure 14.15a, was made from 19 turns of 1 mm diameter wire, and wound on a tapered mandrel, with maximum and minimum diameters of 10 and 3 mm, respectively. Its length was 20 mm. The compressor was tuned with 6.8 pF to give a frequency of ≈67 MHz. The quality factor was $Q \approx 165$.

The compressor was tested by placing the wide end on a 10 mm diameter transmitter loop and measuring the transmission to a receiver loop (3 or 10 mm in diameter) at the other end. The difference between the 3 and 10 mm loop measurements at the compressor tip was only ≈1 dB, whereas the difference in reference signal in this plane was ≈17 dB. Thus it is clear that the flux was confined to the 3 mm exit diameter and the compressor concept is valid. On resonance, we see a significant enhancement of the compressed signal, and such a device could play a role in coupling elements of unequal size (for example coupling a pole piece to an MM yoke).

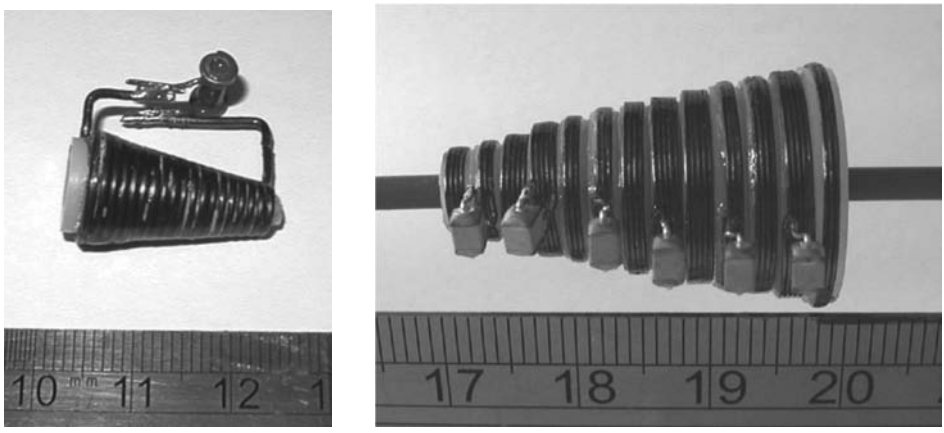

(a) (b)

FIGURE 14.15 Prototype flux compressors: (a) The tapered solenoid device and (b) the resonant ring structure.

An alternative device can be built from a sequence of resonant loops, wound on different diameter formers and all tuned to the same frequency (see Figure 14.15b). Coil–Coil interactions result in magneto-inductive (MI) waves, which propagate along the coupled coils. Measurements show that the device can operate over an appreciable bandwidth and that the overall transmission levels are little affected by the precise spacing of the coils, so the design of these devices appears quite robust.

14.6 Conclusion

In this chapter, we have reviewed the development and properties of metamaterials in the RF band. At these low frequencies, the wavelength of electromagnetic radiation is very long, so that the condition for homogenization, that is, that the structure and its unit cell should be much smaller than the wavelength, is easily satisfied. Moreover, because measurements can be performed in the very near field, it is necessary to manipulate only the permeability of the material to control the behavior of RF magnetic fields.

The basic magnetic element that is used at higher frequency, the split ring resonator, is not suitable for use at RF, but an alternative structure, the Swiss roll, is ideal. It is compact, can be made to resonate at frequencies as low as 5 MHz, and displays intense magnetic activity: when assembled into a bulk material, the negative permeability region extends to a bandwidth $\Delta\omega/\omega_0 \approx 40\%$. Moreover, there is a wide range of permeability, from large positive values through zero to large negative values, to explore.

The applicability of the mean field or effective medium approach has been tested by measuring the field patterns that are induced on the surface of metamaterial prisms when excited by a point source on the opposite surface and comparing the data to those calculated assuming the prism to be a homogeneous block of material with an effective permeability derived from measurements. At high spatial frequency, mean field theory breaks down, because the material is granular and the theory contains no mechanism for limiting the spatial frequencies that propagate. For all other cases, the agreement between the measured and the calculated distributions is excellent.

The materials have been used to demonstrate subwavelength imaging, both as an endoscope/faceplate and as a lens. In the former case, the material is anisotropic and used on resonance, when the permeability is large, and acts to transfer the field pattern from the input face faithfully to the output face. The lens requires an isotropic material with a permeability of $\mu = -1$ that focuses both the propogating and evanescent waves to produce a "perfect" image. The performance of both mechanisms is in accord with the theory and is dominated by the losses in the material.

Finally, possible applications in the fields of MRI have been explored, and potential device prototypes have been tested, to show that metamaterials can indeed perform useful functions. However, there is much work still to be done before fully practical devices can be realized.

References

[AH06] M. Allard and R. M. Henkelman. Using metamaterial yokes in nmr measurements. *Journal of Magnetic Resonance*, 182(2):200–207, 2006.

[AWHH05] M. Allard, M. C. K. Wiltshire, J. V. Hajnal, and R. M. Henkelman. Improved signal detection with metamaterial magnetic yokes. *Proceedings of International Society for Magnetic Resonance in Medicine*, 13:871, 2005.

[Bal64] K. G. Balmain. The impedance of a short dipole in a magnetoplasma. *IEEE Transactions on Antennas and Propagation*, AP-12:605–617, 1964.

[BHJ04] V. C. Behr, A. Haase, and P. M. Jakob. Rf flux guides for excitation and reception in (31)p spectroscopic and imaging experiments at 2 tesla. *Concepts in Magnetic Resonance Part B-Magnetic Resonance Engineering*, 23B(1):44–49, 2004.

[BJMZ06] J. D. Baena, L. Jelinek, R. Marques, and J. Zehentner. Electrically small isotropic three-dimensional magnetic resonators for metamaterial design. *Applied Physics Letters*, 88(13):134108, 2006.

[BLK03] K. G. Balmain, A. E. A. Luttgen, and P. C. Kremer. Power flow for resonance cone phenomena in planar anisotropic metamaterials. *IEEE Transactions on Antennas and Propagation*, 51(10):2612–2618, 2003.

[BMMM04] J. D. Baena, R. Marques, F. Medina, and J. Martel. Artificial magnetic metamaterial design by using spiral resonators. *Physical Review B*, 69(1):014402, 2004.

[EWL+05] C. Enkrich, M. Wegener, S. Linden, S. Burger, L. Zschiedrich, F. Schmidt, J. F. Zhou, T. Koschny, and C. M. Soukoulis. Magnetic metamaterials at telecommunication and visible frequencies. *Physical Review Letters*, 95:203901, 2005.

[FM05] M. J. Freire and R. Marques. Planar magnetoinductive lens for three-dimensional subwavelength imaging. *Applied Physics Letters*, 86(18):182505, 2005.

[LEW+04] S. Linden, C. Enkrich, M. Wegener, J. F. Zhou, T. Koschny, and C. M. Soukoulis. Magnetic response of metamaterials at 100 terahertz. *Science*, 306(5700):1351–1353, 2004.

[MFMB05] F. Mesa, M. J. Freire, R. Marques, and J. D. Baena. Three-dimensional superresolution in metamaterial slab lenses: Experiment and theory. *Physical Review B*, 72(23):235117, 2005.

[MHBL99] S. S. Mohan, M. D. Hershenson, S. P. Boyd, and T. H. Lee. Simple accurate expressions for planar spiral inductances. *IEEE Journal of Solid-State Circuits*, 34(10):1419–1424, 1999.

[MMMM03] R. Marques, F. Mesa, J. Martel, and F. Medina. Comparative analysis of edge- and broadside-coupled split ring resonators for metamaterial design—theory and experiments. *IEEE Transactions on Antennas and Propagation*, 51(10):2572–2581, 2003. Part 1.

[MMREI02] R. Marques, F. Medina, and R. Rafii-El-Idrissi. Role of bianisotropy in negative permeability and left-handed metamaterials. *Physical Review B*, 65(14):144440, 2002.

[Pen00] J. B. Pendry. Negative refraction makes a perfect lens. *Physical Review Letters*, 85(18):3966–3969, 2000.

[PGL+03] C. G. Parazzoli, R. B. Greegor, K. Li, B. E. C. Koltenbah, and M. Tanielian. Experimental verification and simulation of negative index of refraction using snell's law. *Physical Review Letters*, 90(10):107401, 2003.

[PHRS98] J. B. Pendry, A. J. Holden, D. J. Robbins, and W. J. Stewart. Low frequency plasmons in thin-wire structures. *Journal of Physics-Condensed Matter*, 10:4785–4809, 1998.

[PHRS99] J. B. Pendry, A. J. Holden, D. J. Robbins, and W. J. Stewart. Magnetism from conductors and enhanced nonlinear phenomena. *IEEE Transactions on Microwave Theory and Techniques*, 47:2075–2084, 1999.

[PHSY96] J. B. Pendry, A. J. Holden, W. J. Stewart, and I. Youngs. Extremely low frequency plasmons in metallic mesostructures. *Physical Review Letters*, 76:4773–4776, 1996.

[PO02] J. B. Pendry and S. O'Brien. Very-low-frequency magnetic plasma. *Journal of Physics-Condensed Matter*, 14(32):7409–7416, 2002.

[PP64] W. K. H. Panofsky and M. Phillips. *Classical Electricity and Magnetism*, 2nd edn, Chapter 5.8. Addison-Wesley Reading, MA, 1964.

[PR02] J. B. Pendry and S. A. Ramakrishna. Near-field lenses in two dimensions. *Journal of Physics-Condensed Matter*, 14(36):8463–8479, 2002.

[Ram05] S. A. Ramakrishna. Physics of negative refractive index materials. *Reports on Progress in Physics*, 68(2):449–521, 2005.

[RPWS03] S. A. Ramakrishna, J. B. Pendry, M. C. K. Wiltshire, and W. J. Stewart. Imaging the near field. *Journal of Modern Optics*, 50(9):1419–1430, 2003.

[SKRS02a] E. Shamonina, V. A. Kalinin, K. H. Ringhofer, and L. Solymar. Magneto-inductive waveguide. *Electronics Letters*, 38(8):371–373, 2002.

[SKRS02b] E. Shamonina, V. A. Kalinin, K. H. Ringhofer, and L. Solymar. Magnetoinductive waves in one, two, and three dimensions. *Journal of Applied Physics*, 92(10):6252–6261, 2002.

[SKS04] D. R. Smith, P. Kolinko, and D. Schurig. Negative refraction in indefinite media. *Journal of the Optical Society of America B-Optical Physics*, 21(5):1032–1043, 2004.

[SP06] D. R. Smith and J. B. Pendry. Homogenization of metamaterials by field averaging (invited paper). *Journal of the Optical Society of America B-Optical Physics*, 23(3):391–403, 2006.

[SPV+00] D. R. Smith, W. J. Padilla, D. C. Vier, S. C. Nemat-Nasser, and S. Schultz. Composite medium with simultaneously negative permeability and permittivity. *Physical Review Letters*, 84:4184–4187, 2000.

[SPW04] D. R. Smith, J. B. Pendry, and M. C. K. Wiltshire. Metamaterials and negative refractive index. *Science*, 305(5685):788–792, 2004.

[SRSNN04] A. F. Starr, P. M. Rye, D. R. Smith, and S. Nemat-Nasser. Fabrication and characterization of a negative-refractive-index composite metamaterial. *Physical Review B*, 70(11):113102, 2004.

[SRZ+06] O. Sydoruk, A. Radkovskaya, O. Zhuromskyy, E. Shamonina, M. Shamonin, C. J. Stevens, G. Faulkner, D. J. Edwards, and L. Solymar. Tailoring the near-field guiding properties of magnetic metamaterials with two resonant elements per unit cell. *Physical Review B*, 73(22):224406, 2006.

[SS04] E. Shamonina and L. Solymar. Magneto-inductive waves supported by metamaterial elements: components for a one-dimensional waveguide. *Journal of Physics D-Applied Physics*, 37(3):362–367, 2004.

[SSMS02] D. R. Smith, S. Schultz, P. Markos, and C. M. Soukoulis. Determination of effective permittivity and permeability of metamaterials from reflection and transmission coefficients. *Physical Review B*, 65(19):195104, 2002.

[SSNNS01] R. A. Shelby, D. R. Smith, S. C. Nemat-Nasser, and S. Schultz. Microwave transmission through a two-dimensional, isotropic, left-handed metamaterial. *Applied Physics Letters*, 78:489–491, 2001.

[SSR+03] D. R. Smith, D. Schurig, M. Rosenbluth, S. Schultz, S. A. Ramakrishna, and J. B. Pendry. Limitations on subdiffraction imaging with a negative refractive index slab. *Applied Physics Letters*, 82(10):1506–1508, 2003.

[SSS01] R. A. Shelby, D. R. Smith, and S. Schultz. Experimental verification of a negative index of refraction. *Science*, 292:77–79, 2001.

[SSS05] R. R. A. Syms, L. Solymar, and E. Shamonina. Absorbing terminations for magneto-inductive waveguides. *IEE Proceedings-Microwaves Antennas and Propagation*, 152(2):77–81, 2005.

[SSS06] R. R. A. Syms, E. Shamonina, and L. Solymar. Magneto-inductive waveguide devices. *IEE Proceedings-Microwaves Antennas and Propagation*, 153(2):111–121, 2006.

[Str41a] J. A. Stratton. *Electromagnetic Theory*, Chapter 8. McGraw-Hill, New York, 1941.

[Str41b] J. A. Stratton. *Electromagnetic Theory*, Chapter 3.27-8. McGraw-Hill, New York, 1941.

[SVP+99] D. R. Smith, D. C. Vier, W. Padilla, S. C. Nemat-Nasser, and S. Schultz. Loop-wire medium for investigating plasmons at microwave frequencies. *Applied Physics Letters*, 75(10):1425–1427, 1999.

[SYS06] R. R. A. Syms, I. R. Young, and L. Solymar. Low-loss magneto-inductive waveguides. *Journal of Physics D-Applied Physics*, 39(18):3945–3951, 2006.

[SZS+06] L. Solymar, O. Zhuromskyy, O. Sydoruk, E. Shamonina, I. R. Young, and R. R. A. Syms. Rotational resonance of magnetoinductive waves: Basic concept and application to nuclear magnetic resonance. *Journal of Applied Physics*, 99(12):123908, 2006.

[WHP+03] M. C. K. Wiltshire, J. V. Hajnal, J. B. Pendry, D. J. Edwards, and C. J. Stevens. Metamaterial endoscope for magnetic field transfer: near field imaging with magnetic wires. *Optics Express*, 11(7):709–715, 2003.

[WHYH04] M. C. K. Wiltshire, R. M. Henkelman, I. R. Young, and J. V. Hajnal. Metamaterial yoke for signal reception—an initial investigation. *Proceedings of International Society for Magnetic Resonance in Medicine*, 12:43, 2004.

[Wil00] M. C. K. Wiltshire. Structure with switchable magnetic properties. UK Patent Application GB2360132A, 2000 (also unpublished work).

[Wil05] W. Williams. *Bessl Beams, Resonances and Meatamaterials*. PhD thesis, Department of Physics, Imperial College, London, 2005.

[Wil07] M. C. K. Wiltshire. Radio frequency (rf) metamaterials. *Physica Status Solidi B-Basic Solid State Physics*, 244(4):1227–1236, 2007.

[WPH06] M. C. K. Wiltshire, J. B. Pendry, and J. V. Hajnal. Sub-wavelength imaging at radio frequency. *Journal of Physics-Condensed Matter*, 18(22):L315–L321, 2006.

[WPL+03] M. C. K. Wiltshire, J. B. Pendry, D. J. Larkman, D. J. Gilderdale, D. Herlihy, I. R. Young, and J. V. Hajnal. Geometry preserving flux-duxcting by magnetic metamaterials. *Proceedings of International Society for Magnetic Resonance in Medicine*, 11:713, 2003.

[WPWH07] M. C. K. Wiltshire, J. B. Pendry, W. Williams, and J. V. Hajnal. An effective medium description of 'swiss rolls', a magnetic metamaterial. *Journal of Physics-Condensed Matter*, 19:456216, 2007.

[WPY+01] M. C. K. Wiltshire, J. B. Pendry, I. R. Young, D. J. Larkman, D. J. Gilderdale, and J. V. Hajnal. Microstructured magnetic materials for rf flux guides in magnetic resonance imaging. *Science*, 291(5505):849–851, 2001.

[WSSY04] M. C. K. Wiltshire, E. Shamonina, L. Solymar, and I. R. Young. Development of metamaterial components for use in mri and nmr systems. *Proceedings of International Society for Magnetic Resonance in Medicine*, 12:1582, 2004.

[WSYS03] M. C. K. Wiltshire, E. Shamonina, I. R. Young, and L. Solymar. Dispersion characteristics of magneto-inductive waves: comparison between theory and experiment. *Electronics Letters*, 39(2):215–217, 2003.

[WSYS04] M. C. K. Wiltshire, E. Shamonina, I. R. Young, and L. Solymar. Experimental and theoretical study of magneto-inductive waves supported by one-dimensional arrays of "swiss rolls". *Journal of Applied Physics*, 95(8):4488–4493, 2004.

[YPF+04] T. J. Yen, W. J. Padilla, N. Fang, D. C. Vier, D. R. Smith, J. B. Pendry, D. N. Basov, and X. Zhang. Terahertz magnetic response from artificial materials. *Science*, 303:1494–1496, 2004.

[ZSS05] O. Zhuromskyy, E. Shamonina, and L. Solymar. 2d metamaterials with hexagonal structure: spatial resonances and near field imaging. *Optics Express*, 13(23):9299–9309, 2005.

15

Wire Media

I. S. Nefedov
Helsinki University of Technology

A. J. Viitanen
Helsinki University of Technology

15.1 Introduction

The wire medium (or the rodded medium) consisting of a two-dimensional (2D) or three-dimensional (3D) rectangular lattice of low-loss wire grids (Figure 15.1) has been known for a long time, and it has been extensively studied in microwave lens design [1–7] and for the synthesis of surface reactance [8]. The grids of resistive wires were considered in [9]. The single-wire medium (WM) (Figure 15.1a) is usually described at low frequencies as a uniaxial material, whose relative permittivity dyadic can be written as (the wires are in the z-direction)

$$\overline{\overline{\epsilon}} = \epsilon_h(u_x u_x + u_y u_y) + \epsilon_z u_z u_z, \tag{15.1}$$

where ϵ_z is expressed by the plasma formula:

$$\epsilon_z = \epsilon_h\left(1 - \frac{\omega_p^2}{\omega^2 \epsilon_h}\right) = \epsilon_h\left(1 - \frac{k_p^2}{k^2}\right). \tag{15.2}$$

Here ϵ_h is the permittivity of the host medium, $k = \omega/c\sqrt{\epsilon_h} = k_o\sqrt{\epsilon_h}$, and c is the speed of light. The constant ω_p (or the corresponding k_p) is an equivalent "plasma frequency" that gives grounds to call the wire medium as "artificial plasma." Different models exist for the plasma frequency, which are discussed Section 15.2.

Interest in wire media was renewed at the end of the last decade in connection with engineering of materials with negative parameters, sometimes called double-negative materials (DNM).

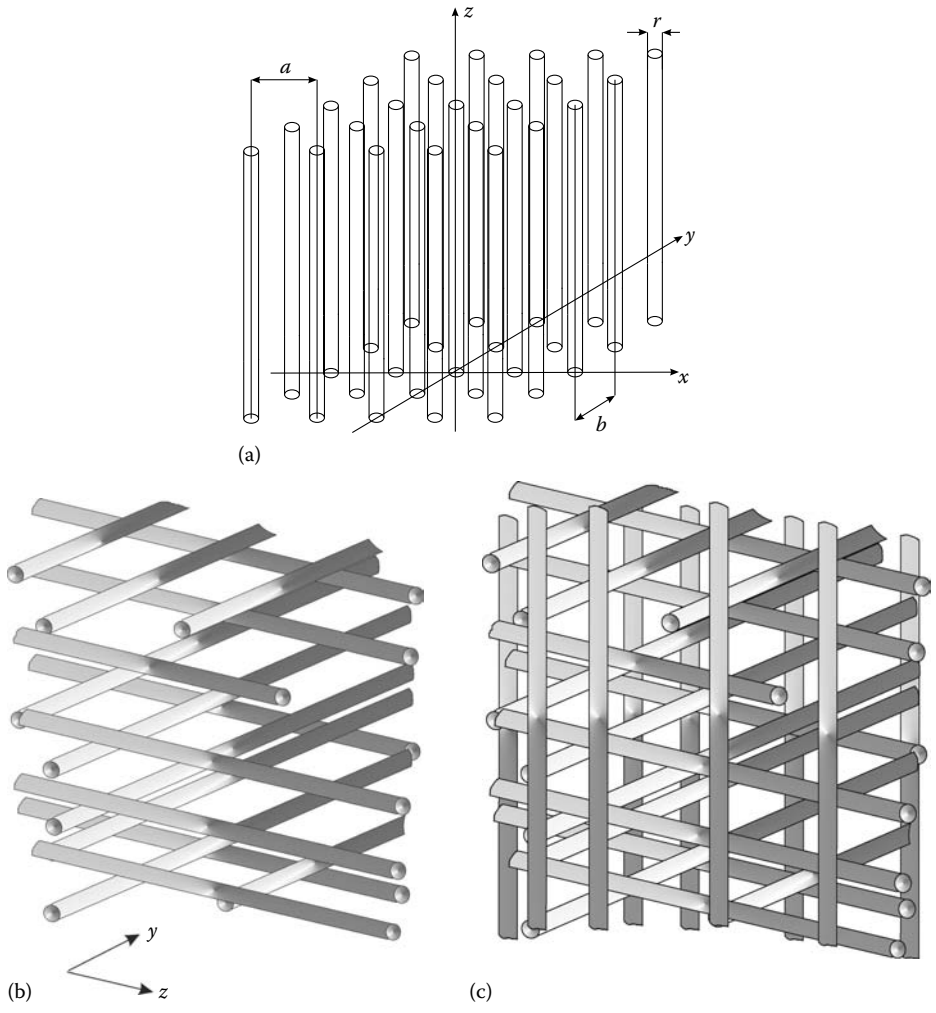

FIGURE 15.1 The wire media. (a) Two-dimensional lattice (a single WM), electric field in z-direction. (b) Three-dimensional lattice (a double WM), electric field in y–z plane. (c) Three-dimensional lattice (a triple WM), arbitrary polarization.

The first DNM proposed by Smith et al. consists of a lattice of long metal strips and split-ring resonators [10]. Now the wire medium is a commonly used component of artificial metamaterials for microwave and optical applications [11]. Despite the conventional Drude formula (Equation 15.2) examined experimentally in early works, only waves propagating normally to the wires were investigated. However, it has been shown that if the wave vector in a wire medium has a nonzero component along the wires, the plasma model (Equation 15.2) gives nonphysical results [12]. The plasma model has been corrected introducing terms describing the spatial dispersion (SD) into Equation 15.2.

A series of works were devoted to three-dimensional lattices of wires as a continuation of investigations implemented in 1950s. An artificial structure, composed of infinite wires arranged in a cubic lattice joined at the corners of the lattice, was considered in [13]. Such a medium is expected to behave as an isotropic electromagnetic crystal, with a negative permittivity at low frequencies given by Equation 15.2. This model does not take into account SD, which may be expected there

in analogy with the 1D case. Also at the same time, a 3D wire mesh grid with covalently bonded diamond structure was studied in [14]. Last years double and triple wire media formed of connected and disconnected 3D lattices have been studied in [16–19], where wave properties and effects of SD were investigated.

The chapter is organized as follows. In Section 15.2 we discuss a nonlocal model, which takes into account SD. Important consequences of the SD are appearance of additional waves and necessity to use additional boundary conditions (ABC) for solution of any boundary-value problems. We demonstrate that application of the local model leads to appearance of nonphysical effects even for simple cases. In Section 15.3 we consider electromagnetic properties of unbounded double-wire medium (DWM) using effective medium (EM) theory. Applicability of this approach was repeatedly confirmed by numerical simulations for different situations. The Poynting vector and the group velocity in DWM are discussed. In Section 15.4, the spectrum of eigenmodes in a rectangular waveguide, filled with WM, is considered, and in Section 15.5 we offer an overview of some applications of wire media.

Where it is possible, we use simple analytical models for description of structures, based on WM, and consider their applicability comparing with results of numerical simulations. Details of special numerical methods developed for WM can be found in referred articles.

15.2 Effective Medium Model and Strong Spatial Dispersion in Wire Media

In this section we show that the Drude formula (Equation 15.2) for effective permittivity leads to unphysical results and must be substituted by a nonlocal dispersive relation [12].

15.2.1 Plasma Frequency for Wire Media

The plasma frequency corresponding to collective oscillations of electron density is expressed as

$$\omega_p^2 = \frac{ne^2}{\epsilon_0 m_{\text{eff}}}, \tag{15.3}$$

where n, e, and m_{eff} are the density, charge, and effective mass of the electron, respectively. For metals ω_p typically is in the ultraviolet region. It seems to be reasonable to reduce the plasma frequency to the microwave range cutting thin wires, forming a 2D periodic structure, from a bulk metal. Then we obtain collective oscillations of electrons along wires. The density of these active electrons will be

$$n_{\text{eff}} = n\frac{\pi r^2}{a^2}, \tag{15.4}$$

where a and r are the lattice constant and radius of a wire, respectively. It turned out that in contrast to the case of natural plasma, a restoring force acting on the electron not only has to work against the rest mass of the electrons but also against self-inductance of the wire structure [13]. Moreover, the effect of self-inductance considerably exceeds the effect of the rest mass, and one can neglect the last one for high-conductive metals in the microwave range. After that both the electron density and the effective mass drop from the final expression for the plasma frequency. The most generally used formulas for the plasma frequency were proposed in [13,20,21]:

1. Formula from [13]:

$$k_p^2 = \frac{2\pi}{a^2 \ln(a/r)}. \tag{15.5}$$

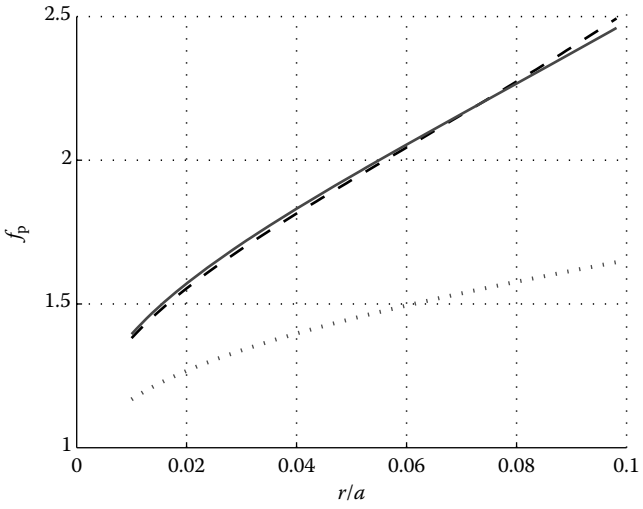

FIGURE 15.2 Plasma frequency f_p in GHz, calculated using Equation 15.5: dotted line, Equation 15.6: solid line, and Equation 15.7: dashed line.

2. Formula from [20]:

$$k_p^2 = \frac{2\pi}{a^2(\ln(a/2\pi r) + 0.5275)}. \tag{15.6}$$

3. Formula from [21]:

$$k_p^2 = \frac{2\pi}{a^2}\frac{1}{\ln(a^2/4r(a-r))}. \tag{15.7}$$

Derivation of the first formula was outlined earlier, and this formula does not take into account interaction between wires. The second formula is derived from consideration of WM as a photonic crystal, and in the third case a quasistatic model was used. Figure 15.2 illustrates comparison between the f_p, calculated using different formulas for thin wires ($r/a < 0.1$) and $a = 1$ cm.

15.2.2 Spatial Dispersion

In fact, assuming that the medium can be described by the uniaxial dyadic (Equation 15.1), the dispersion equation for extraordinary plane waves ($E_z \neq 0$) with the wave vector $(q_x, q_y, q_z)^T$ in this uniaxial dielectric reads [22,23]

$$\epsilon_h(q_x^2 + q_y^2) = \epsilon(k^2 - q_z^2). \tag{15.8}$$

On the other hand, these extraordinary waves correspond to the well-known TM (to z) set of modes, allowed by the invariance of the boundary conditions along z. Thus, for any extraordinary wave traveling with a phase constant q_z along the z-axis, the E_z field must satisfy the Helmholtz equation:

$$\left\{\frac{\partial}{\partial x^2} + \frac{\partial}{\partial y^2} + (k^2 - q_z^2)\right\} E_z = 0, \tag{15.9}$$

with the boundary condition $E_z = 0$ on the wires. It is clear from this equation that any "plane" extraordinary wave must satisfy

$$k(q_x, q_y, q_z) = \sqrt{k^2(q_x, q_y, 0) + q_z^2}. \tag{15.10}$$

This result is incompatible with Equations 15.2 and 15.8, as can be easily seen by substitution of Equation 15.2 into Equation 15.8. However, if we choose

$$\epsilon(k, q_z) = \epsilon_h \left(1 - \frac{k_p^2}{k^2 - q_z^2}\right) \tag{15.11}$$

instead of Equation 15.2, then Equation 15.8 becomes compatible with Equation 15.10, giving the following dispersion equation for the plane wave:

$$q^2 \equiv q_x^2 + q_y^2 + q_z^2 = k^2 - k_p^2, \tag{15.12}$$

where we have assumed that $q_z \neq k$ (the case with $q_z = k$ is analyzed below). The above rationale suggests that the considered wire media can still be described by the permittivity dyadic (Equation 15.1), but the axial permittivity ϵ must be a nonlocal parameter of the form given in Equation 15.11. The conventional expression (Equation 15.2) would only be a particular case of Equation 15.11, valid for wave propagation in the x–y plane.

Note that Equation 15.11 was proposed first by Shvets [24]. The main difference between the local uniaxial model, Equation 15.2, and the nonlocal model, Equation 15.11, for the parallel WM is that the nonlocal model predicts a stop band (at frequencies below $\omega_0 = \omega_p/\sqrt{\epsilon_h \mu_h}$) for extraordinary waves propagating along any direction in the media. On the contrary, Equations 15.2 and 15.8 predict propagation of extraordinary waves at any frequency provided $q_z > k = \omega\sqrt{\epsilon_h \mu_h}$. Thus, both models predict qualitatively very different behaviors, even near the cutoff plasma frequency ω_0, where $q^2 \to 0$ i.e., $a/\lambda \to 0$). That is, the nonlocality of the proposed constitutive relations affects the electromagnetic response of the medium even in the very large wavelength limit, thus being important for any values of the a/λ ratio inside the medium. Other relevant differences between the predictions of both models are developed along this paper.

The rigorous proof of Equation 15.11 is based on the local-field approach, which is described in detail in [20]. There it was shown that in the thin WM and for $q_z \neq k$, two sets of modes can propagate: ordinary (with $E_z = 0$) and extraordinary (with $E_z \neq 0$) waves. The ordinary waves do not interact with the wires and propagate in the host media. For extraordinary waves, an explicit dispersion equation connecting the wave vector $q = (q_x, q_y, q_z)^T$ with the wave number of the host isotropic matrix k has been derived in [20].

Let us consider the modes in WM, following from the EM theory. Assuming for simplicity $q_x = 0$ (this restriction does not change the spectrum of modes) and substituting Equation 15.1 into the Maxwell equations, we can separate them into two subsystems, describing ordinary and extraordinary waves. For the ordinary waves, the equations are

$$\begin{aligned} -q_z H_y + \frac{k^2 - q_y^2}{k_0 \eta} E_x &= 0, \\ q_z E_x - k_0 \eta H_y &= 0, \end{aligned} \tag{15.13}$$

(denoting η as the free-space wave impedance), which results in the propagation factor for the ordinary wave: $q_z^2 = k^2 - q_y^2$. There are no effects due to wires for ordinary waves.

Assuming $q_z \neq 0$ for the fields of extraordinary waves, which is the most interesting case, the following equations are obtained:

$$\begin{aligned} q_z E_y + \frac{k_0^2 \epsilon_z - q_y^2}{k_0 \epsilon_z} \eta H_x = 0, \\ q_z H_x + \frac{k_0 \epsilon_h}{\eta} E_y = 0 \end{aligned} \tag{15.14}$$

which give the wave equation for the magnetic field H_x after eliminating E_y and E_z:

$$\left[k^2 - \frac{q_y^2}{\epsilon_z} - q_z^2 \right] H_x = 0. \tag{15.15}$$

Since $\epsilon_z = \epsilon_h \left(1 - k_p^2 / k^2 - q_z^2\right)$, the wave equation reads

$$\left[k^2 - q_z^2\right]\left[k^2 - q_y^2 - q_z^2 - k_p^2\right] H_x = 0. \tag{15.16}$$

Thus we have obtained two dispersion relations:

$$k^2 = q_z^2, \quad k^2 = q_y^2 + q_z^2 + k_p^2, \tag{15.17}$$

which determine two separate independent solutions, denoted by the TEM wave and the TM wave, respectively. It follows from Equation 15.17 that propagation (or attenuation) of the TM mode is isotropic in the y–z plane, which is rather surprising since the medium is strongly anisotropic (according to its geometry). However, it can be shown from the very fundamental facts summarized in Equations 15.8 and 15.10.

Due to the presence of two waves with the same polarization, ABC are needed for the solution of any boundary-value problem for TM-polarized waves. It was pointed out first by Pekar [25] (1956) that the well-known Maxwell's boundary conditions (Equation 15.18) are not sufficient to connect the amplitudes of the incident and transmitted waves in adjoining media, if more than one independent wave can propagate in any medium. Let us illustrate it with the simplest problem of a plane-wave refraction at an air–WM interface. Assuming the y-component of the electric field of the incident wave to be equal to unity and applying the continuity conditions for the tangential field components results in following formulation of the reflection problem:

$$\begin{aligned} 1 + R_E &= E_+ + E_- \\ (1 - R_E)/Z_0 &= E_+/Z_+ + E_-/Z_-, \end{aligned} \tag{15.18}$$

where

R_E is the unknown reflection coefficient for the electric field
E_+, E_- are unknown amplitudes of refracted waves in the wire medium
Z_0 is the wave impedance (TM) in free space
$Z_\pm$ is the wave impedances of refracted waves

Obviously the system is undetermined. Thus the problem becomes similar to one appearing in crystallooptics, where excitons arise and SD cannot be neglected [26]. Unfortunately, universal ABCs are absent, and they should be derived in each particular case based on physical considerations. ABCs for the WM were derived by Silveirinha from the condition of zero current on wires at the interface [27]. This ABC is the continuity of $\epsilon_h E_n$ at the interface, where E_n is the normal component of the electric field.

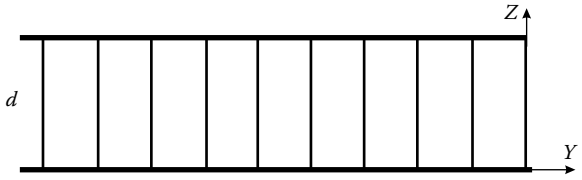

FIGURE 15.3 Parallel-plate waveguide, filled with WM.

15.2.3 Inconsistence of the Local Model

Despite the model in Equation 15.8, taking into account SD, was proposed in 2003 and successfully used in many publications on WM, there still appear works where the old local model is used and it is even declared that the local model better describes some situations. Here we demonstrate how the application of the local model predicts nonexisting effects and analyze the origin of unphysical solutions.

First, consider the guidance of electromagnetic waves in a parallel-plate waveguide infinite in the x- and y-directions and bounded by parallel, perfectly conducting planes orthogonal to the z-axis (see Figure 15.3). Separation between the conducting walls is d. We assume that this waveguide is filled with a WM with the wires along the z-direction. We consider eigenwave propagation along the x-axis (orthogonal to the figure plane) of the TM_{0m} mode (H_y, E_x, $E_z \neq 0$). For waveguides filled by a local uniaxial dielectric with anisotropy axis along the z-direction, we have from Equation 15.8

$$\epsilon_h q_x^2 = \epsilon\left(k^2 - q_z^2\right) \quad q_x = \sqrt{\frac{\epsilon}{\epsilon_h}\left[k^2 - \left(\frac{m\pi}{d}\right)^2\right]}, \tag{15.19}$$

where ϵ is expressed by Equation 15.2. Let $m = 1$. If $\epsilon > 0$, Equation 15.19 gives a cutoff for $k < \pi/d$ and propagation for $k > \pi/d$. In contrast, if $\epsilon < 0$, propagation is allowed when $k < \pi/d$ (and forbidden for $k > \pi/d$). Within this passband a backward wave ($dq/d\omega < 0$) propagates. Moreover, for high-order "modes" the larger the m the lower the cutoff frequency! This amazing effect disappears if one fills the waveguide with the analyzed nonlocal WM. Using Equation 15.12, we have in this case

$$q_x^2 + q_z^2 = k^2 - k_p^2 \quad q_x = \sqrt{k^2 - k_p^2 - \left(\frac{m\pi}{d}\right)^2}, \tag{15.20}$$

and we obtain the usual frequency behavior: cutoff of mth mode for $k < \sqrt{(m\pi/d)^2 + k_p^2}$ and propagation for $k > \sqrt{(m\pi/d)^2 + k_p^2}$. An increase in the cutoff frequency is observed compared with the case when there is no filling medium.

Next consider a plane wave reflection from a grounded WM slab (see Figure 15.4), and compare the results given by the local and nonlocal models, taking into account SD and ABC. Parameters of the WM slab are the following: $a = 5$ mm, $r = 0.05$ mm, $d = 10$ mm, and $\epsilon_h = 1$. The incidence angle equals 60°. Then the plasma frequency of WM equals 14.3 GHz.

We do not give here trivial formulas describing this process in one-wave (local) theory but pay attention to the normal component of a wave vector in the WM slab:

$$q_z = \sqrt{k^2 - \frac{\epsilon_h}{\epsilon} q_y^2}. \tag{15.21}$$

It is important that $q_z \to \infty$ if $k \to k_p$. It causes an infinite (countable) number of oscillations of the phase of reflected wave near the plasma frequency (see Figure 15.5). At the same time, the SD causes propagation of TEM and TM waves where q_z are expressed by formulas given in Equation 15.17, and both of them do not tend to infinity near the plasma frequency. Solution of the wave reflection

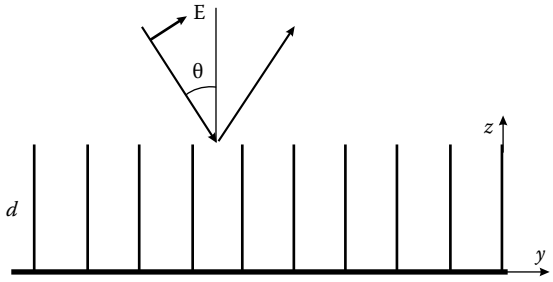

FIGURE 15.4 Plane wave reflection from a grounded WM slab.

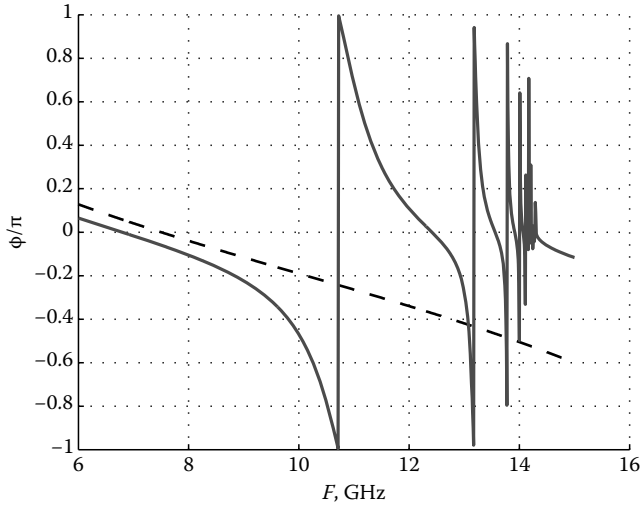

FIGURE 15.5 Phase of the reflected wave. The solid curve corresponds to the local model and the dashed curve corresponds to the nonlocal model.

problem using a nonlocal model and ABC is similar to the one described in [28] for transmission through a finite-thickness WM slab. The problem is reduced to a five-order system of linear equations because TEM and TM modes are coupled at the interface with air only. The results given by local and nonlocal models do not differ much at low frequencies, but oscillations are not obtained from the nonlocal model. Of course, there may be a question: Which model gives more accurate results? However, we do not see physical reasons for $q_z \to \infty$ near the plasma frequency. The accuracy of the nonlocal model was confirmed numerically for the problem of a wave transmission through a WM slab [27]. Comparison of the results given by the nonlocal model and full-wave simulations for the DWM, performed in [16,18,30], shows applicability of this theory for even more complex media.

15.2.4 Nonlocal Model for a Periodic Array of ϵ-Negative Rods

In the previous section, we discussed WM composed of perfectly conducting wires and exhibiting negative ϵ below the plasma frequency. The interesting question is about effective permittivity of WM composed of rods whose ϵ_m is already negative. This class of materials includes periodic arrays of metal rods in the optical range and metal wires with finite conductivity. Homogenization of such a medium was implemented in Ref. [29] (see also [28]). The following expressions have been obtained for the effective permittivity dyadic components:

$$\epsilon_t = \epsilon_{xx} = \epsilon_{yy} = 1 + \frac{2}{\frac{1}{f_V}\frac{\epsilon_m+\epsilon_h}{\epsilon_m-\epsilon_h} - 1} \tag{15.22}$$

$$\epsilon_{zz}(\omega, q_z) = 1 + \frac{1}{\frac{\epsilon_h}{(\epsilon_m-\epsilon_h)f_V} - \frac{k^2-q_z^2}{k_p^2}}, \tag{15.23}$$

where $f_V = \pi r^2/a^2$ is the volume fraction of the rods, k_p is the plasma wave number defined for perfectly conducting wires, and ϵ_m is defined by the Drude model:

$$\epsilon_m(\omega) = \epsilon_0\left(\epsilon_\infty - \frac{\omega_m^2}{\omega^2 - j\omega\Gamma}\right). \tag{15.24}$$

Here ω_m and Γ are the plasma and damping frequencies of the material, respectively.

Substitution of this dyadic into Maxwell's equations gives the following expression for wave number in unbounded medium:

$$q_z^2 = \frac{1}{2}\left\{\epsilon_h(k^2 - k_\parallel^2) + (k^2 + \beta_c^2 - k_p^2) \pm \sqrt{\left[\epsilon_t(k^2 - k_\parallel^2) - (k^2 + \beta_c^2 - k_p^2)\right]^2 + 4\epsilon_t k_\parallel^2 k_p^2}\right\}, \tag{15.25}$$

where

$$\beta_c^2 = -\frac{\epsilon_h k_p^2}{(\epsilon_m - \epsilon_h)f_V}, \quad k_\parallel^2 = \epsilon_{zz}\left(k^2 - q_z^2\right). \tag{15.26}$$

This expression determines two eigenwaves propagating in both directions, one of which may be evanescent. The eigenwave, corresponding to the sign "+" in Equation 15.26, can be referred to as a quasi-TEM mode. It propagates at any low frequencies, but unlike proper TEM mode its propagation constant q_z depends on geometry, frequency, and transversal wave number $k_\parallel$.

Figure 15.6 illustrates the dependence of the slow-wave factor on the propagation direction. Silver is taken as a material at 30 THz ($\lambda = 10\,\mu$m), $\epsilon_m = 1$ and $\epsilon_m \approx -5143 - j746$, as in [28]. The imaginary part grows with the slow-wave factor.

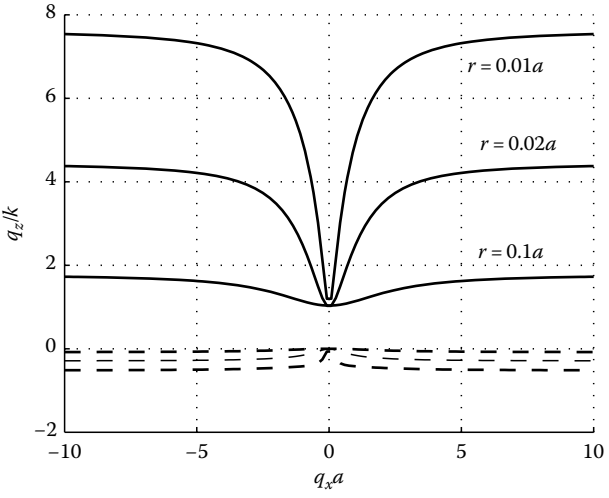

FIGURE 15.6 Slow-wave factor of quasi-TEM mode q_z/k versus the normalized transversal wave number $q_z a$ calculated at $a = 0.25\,\mu$m and different r/a. Real and imaginary parts of q_z/k are shown by solid and dashed lines, respectively.

15.3 Effective Medium Theory in Unbounded Double-Wire Medium

In the EM approach the dense 2D wire grid is considered as a homogeneous anisotropic medium with SD. For considering a DWM let us take a case where the wires are along y and z directions and are nonconnected. We consider waves in unbounded space filled with such medium, assuming $e^{j(\omega t - q_x x - q_y y - q_z z)}$ space–time dependence of the fields. Because of the SD the crystal is anisotropic in the yz-plane even for a square cell, i.e., the DWM is a biaxial crystal with the permittivity dyadic:

$$\bar{\bar{\epsilon}} = \epsilon_h u_x u_x + \epsilon_y u_y u_y + \epsilon_z u_z u_z, \tag{15.27}$$

where [12,15–18]

$$\epsilon_y = \epsilon_h \left(1 - \frac{k_p^2}{k^2 - q_y^2}\right), \quad \epsilon_z = \epsilon_h \left(1 - \frac{k_p^2}{k^2 - q_z^2}\right). \tag{15.28}$$

It is important to note that the model in Equation 15.28 works both for real and imaginary q_y and q_z, i.e., for propagating and evanescent waves, respectively [12].

Considering an arbitrary direction of wave propagation in space, the wave vector is $\mathbf{q} = q_x \mathbf{u}_x + q_y \mathbf{u}_y + q_z \mathbf{u}_z$. Substituting the expressions for the permittivity dyadic (Equations 15.27 and 15.28) into the Maxwell equations results in the following eigenvalue equation:

$$\det = \begin{vmatrix} k^2 - q_y^2 - q_z^2 & q_x q_y & q_x q_z \\ q_x q_y & k^2\left(1 - \frac{k_p^2}{k^2 - q_y^2}\right) - q_x^2 - q_z^2 & q_y q_z \\ q_x q_z & q_y q_z & k^2\left(1 - \frac{k_p^2}{k^2 - q_z^2}\right) - q_x^2 - q_y^2 \end{vmatrix} = 0. \tag{15.29}$$

The determinant in Equation 15.29 results in a fourth-order equation for k^2 for a fixed set q_x, q_y, and q_z. To illustrate the dispersion surfaces we denote $q_x = q\cos\theta$, $q_y = q\sin\theta\cos\varphi$, and $q_z = q\sin\theta\sin\varphi$. The surface of the normalized frequency k/k_p versus θ and φ consists of separate branches corresponding to different propagating modes or passbands as illustrated in Figure 15.7. Especially, at the plane $\theta = \pi/2$ the lowest and two higher-order modes are the extraordinary modes and the second one is the ordinary mode. It forms the second passband when $q_x \neq 0$. Both first and second modes cannot propagate in the x-direction, i.e., at $\theta = 0$, when the electric field vector lies in the plane of wires. Also the first and the second mode cannot propagate at any θ if $\varphi = 0$ or $\varphi = \pi/2$, where the vector of the electric field is parallel to the wires of one of the lattices. In these special cases the eigenvalue equation reduces to $k^2 = q_x^2 + q_y^2 + k_p^2$ (propagation in the xy-plane) and $k^2 = q_x^2 + q_z^2 + k_p^2$ (propagation in the xz-plane), respectively. Third and fourth passbands lie in the region above the plasma resonance and are presented by surfaces, merged at $\varphi = 0$ and $\varphi = \pi/2$ for identical wire arrays (having the same plasma frequencies).

15.3.1 Modes in the *yz*-Plane

Let us consider in more detail the propagation in the (yz-) plane. The wave vector is $q = q_y u_y + q_z u_z$, and the determinant Equation 15.29 splits into two parts. This is also found when inserting the permittivity dyadic in the Maxwell equations when they separate into two subsystems, describing ordinary and extraordinary waves as presented Section 15.2. For the ordinary wave the equation for the propagation factor is $q_z^2 = k^2 - q_y^2$. There are no effects due to wires for the ordinary wave.

For extraordinary waves, which is the most interesting case, solving the eigenvalue equation using the effective medium model, we have the permittivities (Equations 15.27 and 15.28). In general, the plasma numbers k_p may be different due to different dimensions and placements of wires in

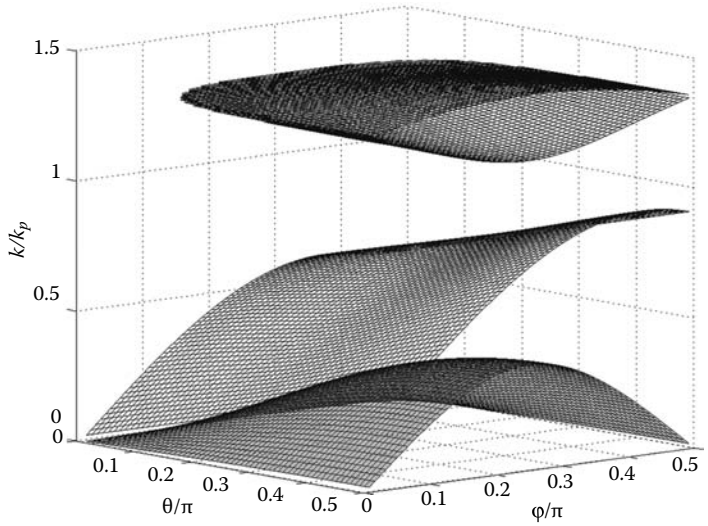

FIGURE 15.7 Surface of the normalized frequency k/k_p versus the angles θ and φ calculated for $qa = 0.4\pi$ and $k_p a = 1.38$. (From Nefedov, I.S., Viitanen, A.J., and Tretyakov, S.A., *Phys. Rev. E*, 71, 046612, 2005. With permission.)

y- and z-directions. Here, for simplicity, we assume the same plasma numbers. After evaluating the dispersion relation, we have a cubic equation for k^2:

$$k^6 - 2(q_y^2 + q_z^2 + k_p^2)k^4 + [(q_y^2 + q_z^2 + k_p^2)^2 + q_y^2 q_z^2]k^2 - q_y^2 q_z^2(q_y^2 + q_z^2 + 2k_p^2) = 0. \tag{15.30}$$

Writing $q_y = q\cos\varphi$ and $q_z = q\sin\varphi$, the cubic equation (Equation 15.30) gives three different real solutions for k, indicating three existing eigenwaves. One mode is at very low frequencies, and the two other ones exist a little above the plasma frequency. The EM model is applicable both at low and at quite high frequencies above the plasma resonance.

Figure 15.8 demonstrates the dispersion characteristics of the propagating modes, calculated using the EM approach and compared with the results of [16]. Parameters of the WM are taken the same as in [16]: the wire radius $r = 0.01a$, $q = 0.1\pi/a$, and $\delta = a/2$ where a is the lattice constant. The plasma wave number calculated according to the model [20] equals $k_p a \approx 1.38$ for this geometry (in [16] $k_p a \approx 1.37$ is used).

15.3.2 Evanescent Modes

When considering the evanescent modes in the DWM we assume $q_y = jq\cos\varphi$ and $q_z = jq\sin\varphi$ with $q = 0.1\pi/a$. The EM equation (Equation 15.30) gives three real solutions for k, which are illustrated in Figure 15.9a and b. In these figures the results are given using the EM and the full-wave theories. Two modes were found a little below the plasma resonance (see Figure 15.9b), and the third one within the same spectral range as the lowest propagating mode (compare with Figures 15.8a and 15.9a).

Further, if we fix the normalized frequency k and calculate the corresponding propagation constants q_z and q_y, the EM theory gives four solutions, two for each propagation direction. Figure 15.9 illustrates such dependence, calculated at $ka = 0.2\pi$ and using both EM theory and the electrodynamical models. One mode can propagate at very low frequencies under conditions $q_y > k$, $q_x = 0$ [17] (see Figure 15.9), the curve marked by q'_{z1} ($q'_{z1} = |\mathrm{Re}(q_{z1})|$, $\mathrm{Im}(q_{z1}) = 0$). Since this solution is a real one, the respective hyperbolic-type dispersion line can be called isofrequency. At the same time, the second solution, shown by the curve q''_{z2} ($q''_{z2} = \mathrm{Im}(q_{z2})$, $\mathrm{Re}(q_{z2}) = 0$), is pure imaginary at $q_y > k$.

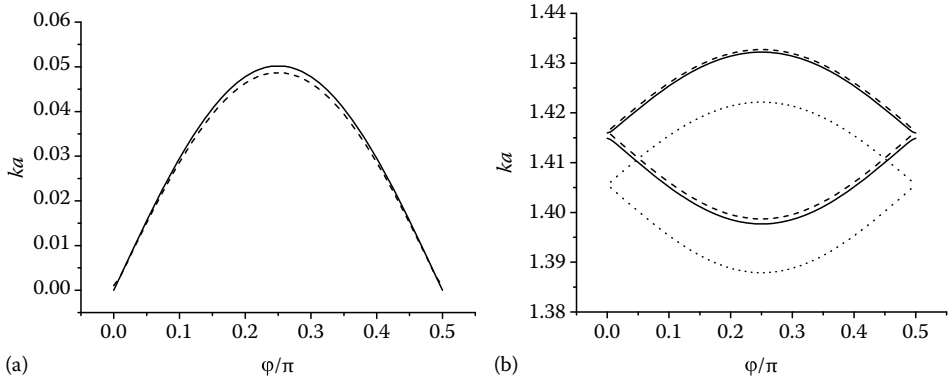

FIGURE 15.8 Dispersion of low-order propagating modes, calculated using electrodynamical and EM models in comparison with numerical results [16]. Normalized frequency for the propagating modes versus the angle φ. The solid curves correspond to our numerical results, the dashed curves correspond to the EM model, and the dotted curves show results [16] excluding the dispersionless mode. (a) The low-frequency mode and (b) the two modes above the plasma resonance.

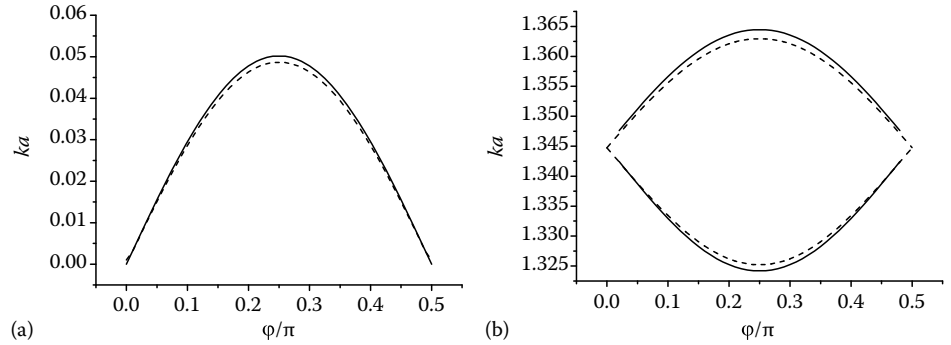

FIGURE 15.9 Dispersion of evanescent modes, electrodynamical calculation (solid curves), and the EM theory (dashed curves).

At $q_y < k$ there are four complex solutions:

$$q_{z1} = q_z' + jq_z'', \quad q_{z2} = -q_z' + jq_z'', \quad q_{z3} = q_z' - jq_z'', \quad q_{z4} = -q_z' - jq_z'', \tag{15.31}$$

where $q_z' = |\mathrm{Re}(q_z)|$, $q_z'' = |\mathrm{Im}(q_z)|$. The real and imaginary parts of q_{z1} are shown in Figure 15.10. If we consider an eigenvalue problem, these four solutions are independent, but such solutions are unphysical because the amplitude of the Poynting vector will increase or decrease along the propagation direction, which is impossible in a lossless medium. However, if we combine the solutions in the form of standing waves with complex amplitudes,

$$\begin{aligned} E_1(z) &= e_1 e^{-q_z'' z} \cos q_z' z, \quad E_2(z) = e_2 e^{-q_z'' z} \sin q_z' z, \\ E_3(z) &= e_3 e^{q_z'' z} \cos q_z' z, \quad E_4(z) = e_4 e^{q_z'' z} \sin q_z' z, \end{aligned} \tag{15.32}$$

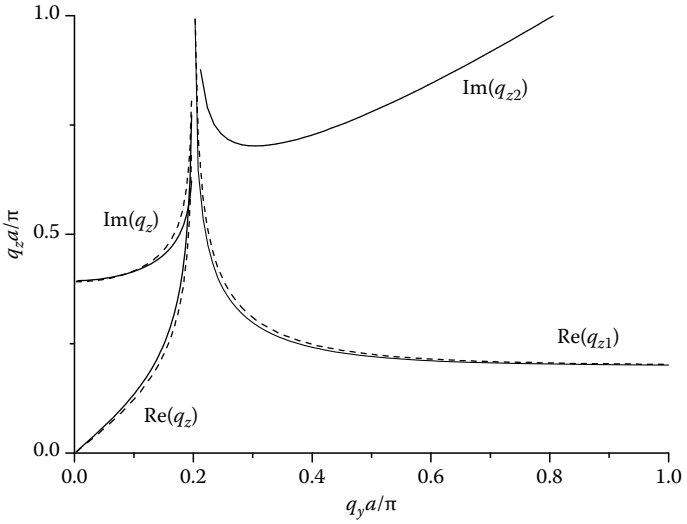

FIGURE 15.10 Dispersion diagram q_z versus q_y. The real and imaginary parts of q_z calculated using the electrodynamical model (solid curves) and the EM theory (dashed curves).

this difficulty disappears because the time-averaged Poynting vector is zero at any z. That is why the basis in Equation 15.32 is more appropriate than the exponential one at least for the solution of problems of wave reflection from an interface of DWM. These solutions also suggest a possibility for existence of localized electromagnetic fields near inhomogeneities.

15.3.3 Propagation in the *z*-Direction

Let us consider an important case when k and q_y are fixed real numbers and we have to determine the respective q_z. Such a problem arises when we solve the problem of wave reflection from a medium interface. The propagation factor in the z-direction is obtained from Equation 15.30. Solutions for q_z^2 have the form

$$q_{z1,2}^2 = \frac{2k^4 - 2k^2k_p^2 - 3k^2q_y^2 + 2k_p^2q_y^2 + q_y^4 \mp q_y\sqrt{(q_y^2 - k^2)((2k_p^2 + q_y^2)^2 - k^2(4k_p^2 + q_y^2))}}{2(k^2 - q_y^2)}. \quad (15.33)$$

Thus, there exist four solutions for q_z, which are, in general, complex numbers describing propagating or evanescent waves in the z-direction.

In the reflection from the interface of the WM, the wave vector component q_y has the fixed value $q_y = k\sin\theta$, where θ is the incidence angle. Although the waves can propagate in the DWM at very low frequencies, we always have the case $q_y < k$ and obtain complex solutions for q_z. In this example $\epsilon_h = 1$ is assumed. Two waves propagating or attenuating in both directions follow from the EM theory (Equation 15.33). The conventional isotropic plasma model leads to only one wave for a certain direction, namely, $q_z = \sqrt{k_o^2\epsilon - q_y^2}$, where $\epsilon = \epsilon_h(1 - k_p^2/k_o^2\epsilon_h)$.

Real and imaginary parts of q_z versus the normalized frequency k/k_p are presented in Figure 15.11 for $\theta = \pi/4$. In the conventional model (dotted curve) q_z is imaginary when $k < K_2 = k_p/\cos\theta$, and it is real when $k > K_2$. The solution of the conventional plasma model differs essentially from the solution obtained from the EM theory between K_1 and K_2, because it gives an imaginary value of q_z

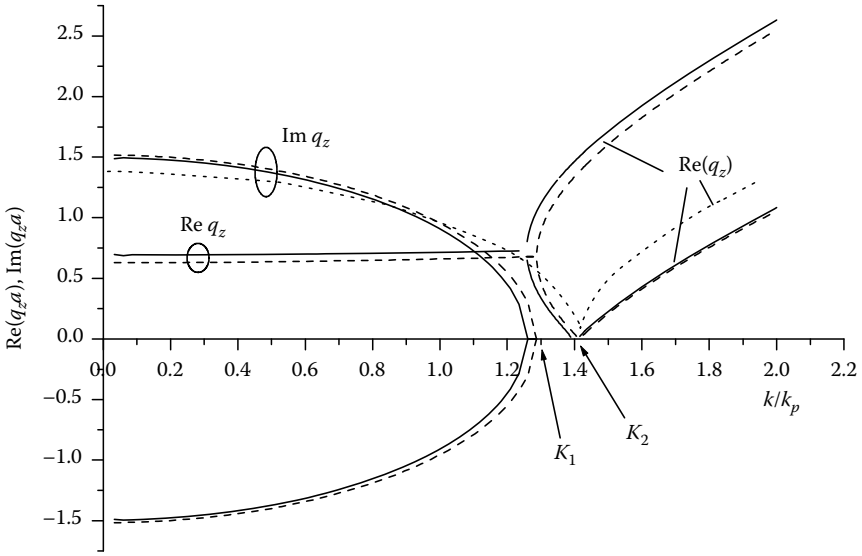

FIGURE 15.11 Real and imaginary parts of q_z, calculated using the electrodynamical model (solid curves) and the EM theory (dashed curves). The dotted curve shows q_z given by the conventional plasma model.

instead of a real one of the EM model. Analyzing Equation 15.33 one can see that there exist three frequency regions, corresponding to different kinds of solution.

The first one is at the low-frequency band, $k < K_1$, where

$$K_1 = k_p \frac{\sqrt{2}}{\sin\theta}\sqrt{\frac{1-\cos\theta}{\cos\theta}}. \tag{15.34}$$

There the propagation constant q_z is complex despite the fact that we have assumed the lossless medium (Figure 15.11). Actually, there are two complex conjugate solutions for each $\mathrm{Re}(q_z) > 0$. The complex waves in lossless media do not transfer energy, and they are found in stop-band regions of periodic structures, ferrite films, and other complex media.

The second frequency band is $K_1 < k < K_2$. In this region the eigenwaves are propagating. At point K_2 one of the solutions is zero, and within the range $K_1 < k < K_2$ we have a forward wave and a backward wave with respect to the interface that follows from the analysis of the isofrequencies, presented in Figure 15.12 with the value $\theta = \pi/4$. It means that one wave has the negative projection of the wave vector to the interface inner normal (i.e., the wave vector makes the negative angle to the interface) and another wave has the positive projection of the wave vector to the interface inner normal (i.e., the wave vector makes the positive angle to the interface). Directions of the refracted waves can also be found from these isofrequencies. In both these waves the group velocity makes the positive angle with the interface. Similar isofrequencies are presented in [17]. In the cases $\theta = \pi/15$ and $\theta = 0$ both a positive and a negative refraction takes place for different waves.

Finally, for $k > K_2$ both waves are propagating forward waves. Electrodynamical calculations confirm the results of the EM theory with a high accuracy in a wide spectral range, including the regions of evanescent and propagating waves as shown in Figure 15.11. Note that point K_2 corresponds to the edge of the passband in the conventional plasma model. Thus, the model taking into account SD leads to a considerably more complicated structure of eigenwaves than the conventional model of isotropic plasma, and it is in very good agreement with the results of the full-wave analysis.

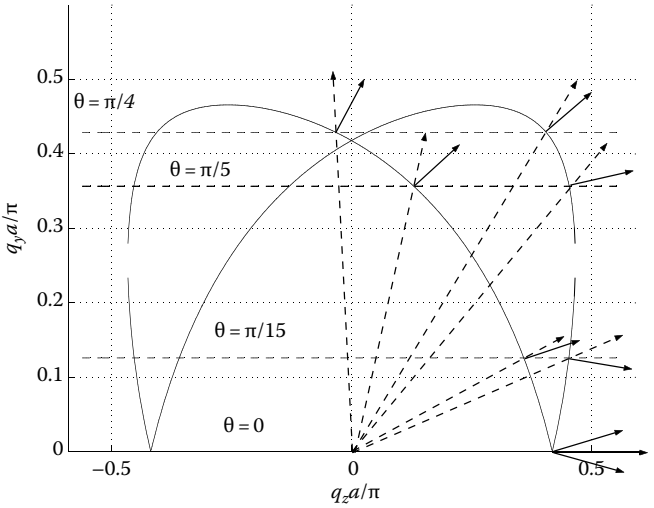

FIGURE 15.12 Isofrequencies, calculated at $k/k_\mathrm{p} = 1.35$ and their sections by the lines $q_y = k \sin\theta$ are shown for the different θ. Dashed and solid arrows show directions of the phase and group velocities, respectively.

15.3.4 Group Velocity and Poynting Vector in DWM

In this section we consider the group velocity and Poynting vectors of waves in the yz-plane in a DWM. It is well known that the group velocity is defined as

$$\mathbf{v}_\mathrm{g} = \mathrm{grad}_\mathbf{q}\,\omega. \tag{15.35}$$

The Poynting vector that determines the energy density flow in media with SD has the form [32]:

$$S = \frac{1}{2}\mathrm{Re}\{EH^*\} - \frac{\omega}{4}\frac{\partial \epsilon_{ik}}{\partial q}E_i^* E_k. \tag{15.36}$$

Because of SD, the Poynting vector, in addition to the conventional cross-product term, also has an additional term with derivatives with respect to the wave vector components. The permittivity dyadic components are expressed by Equation 15.28 for DWM. Their partial derivatives read [33]:

$$\frac{\partial \epsilon_x}{\partial q_x} = 0, \quad \frac{\partial \epsilon_y}{\partial q_y} = -\frac{2k_\mathrm{p}^2 q_y}{(k^2 - q_y^2)^2}, \quad \frac{\partial \epsilon_z}{\partial q_z} = -\frac{2k_\mathrm{p}^2 q_z}{(k^2 - q_z^2)^2}. \tag{15.37}$$

We apply this expression to find the Poynting vector of the two eigenwaves in WM. The Poynting vector of each wave consists of the cross-product term (the first term):

$$\mathbf{S}^0 = \frac{|H_x|^2}{2\omega\epsilon_\mathrm{o}}\left[\frac{q_y(k^2 - q_z^2)}{k^2 - q_z^2 - k_\mathrm{p}^2}\mathbf{u}_y + \frac{q_z(k^2 - q_y^2)}{k^2 - q_y^2 - k_\mathrm{p}^2}\mathbf{u}_z\right] \tag{15.38}$$

and the spatial dispersive term (the second term)

$$\mathbf{S}^\mathrm{d} = \frac{|H_x|^2}{2\omega\epsilon_\mathrm{o}}\left[\frac{q_y q_z^2 k_\mathrm{p}^2}{(k^2 - q_y^2 - k_\mathrm{p}^2)^2}\mathbf{u}_y + \frac{q_z q_y^2 k_\mathrm{p}^2}{(k^2 - q_z^2 - k_\mathrm{p}^2)^2}\mathbf{u}_z\right]. \tag{15.39}$$

The group velocity describes the energy flow of the electromagnetic field. The direction of the group velocity must coincide with the direction of the Poynting vector. It is shown that the direction of the

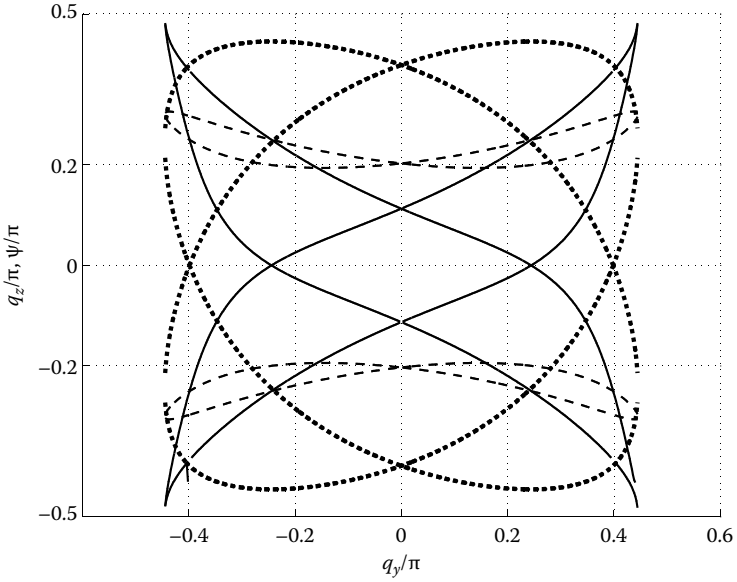

FIGURE 15.13 Solid curves show the angle ψ between the group velocity and the z-axis versus q_y. Dashed curves show the angle between S^0 and the z-axis versus q_y. Dotted curves show the isofrequencies.

Poynting vector of each eigenwave coincides exactly with the direction of the group velocity when the term due to SD is included. In framework of EM theory the group velocity and the energy density w were found analytically. Strict accuracy of the identity $\mathbf{v}_g = \mathbf{S}/w$ was checked. Otherwise, the group velocity vector and the Poynting vector are not parallel. The calculations in Figure 15.13 are done at the frequency corresponding to $k/k_p = 1.35$. In Figure 15.13 it is also shown that disregarding the term due to SD leads to a strongly incorrect result.

15.4 Eigenmodes in a Waveguide Filled with Wire Medium

Recently J. Esteban et al. [34] have shown that if one inserts a WM sample into a rectangular waveguide (see Figure 15.14), the propagation of backward waves below TM mode cutoff becomes possible. Thus, it is not necessary to be in the presence of a double-negative metamaterial; a negative permittivity is sufficient. The following explanation, based on the EM model, was given in [34] for the existence of backward waves in such a structure. If mutually perpendicular wires are identical, the medium inside the waveguide can be considered as a uniaxial crystal with permittivity dyadic components $\epsilon_t = \epsilon_{xx} = \epsilon_{yy}, \epsilon_{zz} = \epsilon_h$, where ϵ_t is expressed by the conventional Drude formula (Equation 15.2) and is negative at low frequencies. Then the known formula for the propagation constant γ of guided TM modes in a waveguide filled with a uniaxial crystal is used:

$$\gamma^2 = \epsilon_t \left[k_0^2 - (q_z^2 + q_y^2)/\epsilon_h \right], \tag{15.40}$$

where for a square cross-section and TM_{11} mode, $q_z = q_y = \pi/a$. Obviously, Equation 15.40 predicts propagating waves below cutoff and plasma resonance. Moreover, it gives a countable spectrum of propagating waves in any rectangular waveguide at low frequencies, which can be seen if one substitutes $q_z = m\pi/a$, $q_y = n\pi/a$. For arbitrary low k_0, we can find m and n such that wave propagation becomes possible, which looks weird.

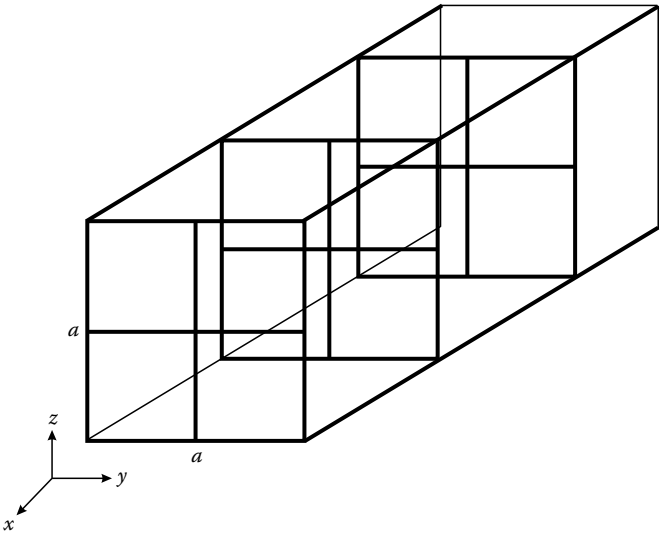

FIGURE 15.14 Double-wire medium in a square cross section waveguide. (From Nefedov, I. S., Dardenne, X., Craeye, C., and Tretyakov, S. A., *Microwave Opt. Technol. Lett*., 48, 2560, 2006. With permission.)

This structure was examined by Nefedov et al. [30] revising the explanation given by the authors of [34] for the effect of backward wave propagation. As was shown earlier, similar unphysical effects disappear if one uses a nonlocal model that takes into account SD. Namely, application of Equation 15.11 yields the following expression for γ, assuming that $q_y = q_z = \pi/a$ [18]:

$$\gamma^2 = k_0^2\epsilon_h - k_p^2 \pm \frac{q_z^2 k_p^2}{k_0^2\epsilon_h - q_z^2} - 2q_z^2. \tag{15.41}$$

This formula does not allow propagation of a countable spectrum of propagating modes, in opposition to Equation 15.40. However, Equation 15.41 relates to the nonconnected geometry, and in [34] the connected topology was considered (see Figure of [34]). The applicability of Equations 15.40 and 15.41 for both geometries as well as the difference between their spectra of modes is discussed hereunder.

We first consider a waveguide, loaded by wires as shown in Figure 15.15 (one lattice period within the cross-section and the period d of the WM in the x-direction are the same, equal to a). The ratio $r/a = 0.01$ leads to the plasma wave number $k_p a \approx 1.38$, and the wires are assumed not to be connected. In Figure 15.15 we compare the results given by Equation 15.40, which was used by the authors of [34], with the results obtained in the framework of the corrected EM theory (Equation 15.41) and those of the Green's function method, described in [18]. We can see a good agreement between the results of the corrected EM and full-wave simulations. A similar structure was simulated by using full-wave MoM [31]. In those simulations, the wires have been taken as thin strips whose width w satisfies the condition $w = 4r$, which approximately gives the same plasma frequency for strip-based WM as that for circular cross-section WM with the radius of wires r (in the case of thin wires and narrow strips). Thus the strip-based WM with $w/a = 0.04$ is equivalent to the circular WM with $r/a = 0.01$. The obtained results are in good agreement with both the analytical and Green's function [18] methods for the two lowest modes (see Figure 15.15b). What is drawn is the determinant of the MoM impedance matrix. Dark lines correspond to low values and are denoting eigenmodes, whereas white lines correspond to high values of the determinant. The black horizontal line between the dispersion curves for the forward and backward modes corresponds to the cutoff of the TE_{10} mode.

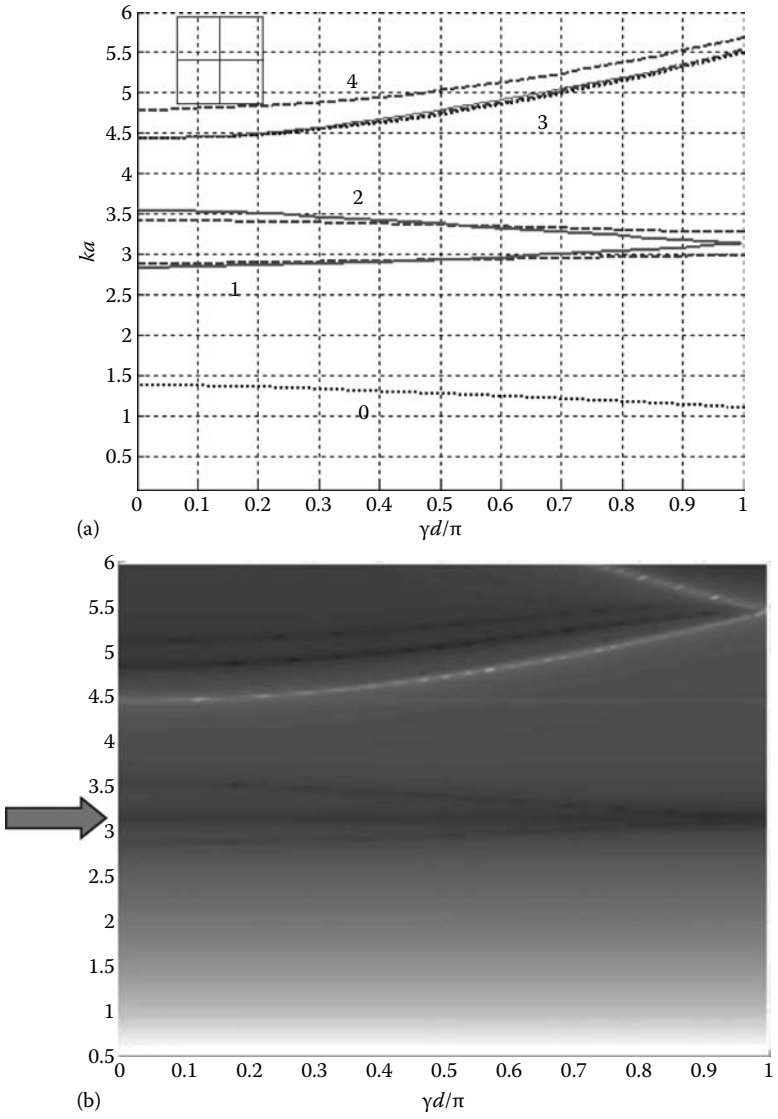

FIGURE 15.15 (a) Spectrum of modes for circular wires and nonconnected geometry. Inset shows the cross-section geometry. Dotted curve: dispersion, calculated using Equation 15.40 as in [34]; dashed curves: results obtained from Equation 15.41, solid curves: numerical results of Green's function method. (b) Spectrum of modes for the strip-based WM and nonconnected geometry. Map of the determinant of the MoM impedance matrix. Nulls are black (eigenmodes), whereas peaks are white. The horizontal black line at $ka = \pi$ represents the TE_{10} mode cutoff.

It is remarkable that two low-order passbands lie above the plasma wave number, which is equal to $1.38/a$ for the chosen parameters of the wires, though below the cutoff wave number, which is equal to $4.44/a$ for the TM_{11} mode. The first passband lies even below the cutoff for the dominant TE_{10} mode at $ka = \pi$. In addition, under assumed parameters and geometry, the backward wave belongs to the second passband and the lowest mode is a forward wave. Also two higher-order modes, propagating above the cutoff, are shown in Figure 15.15. On the other hand, the results, obtained from

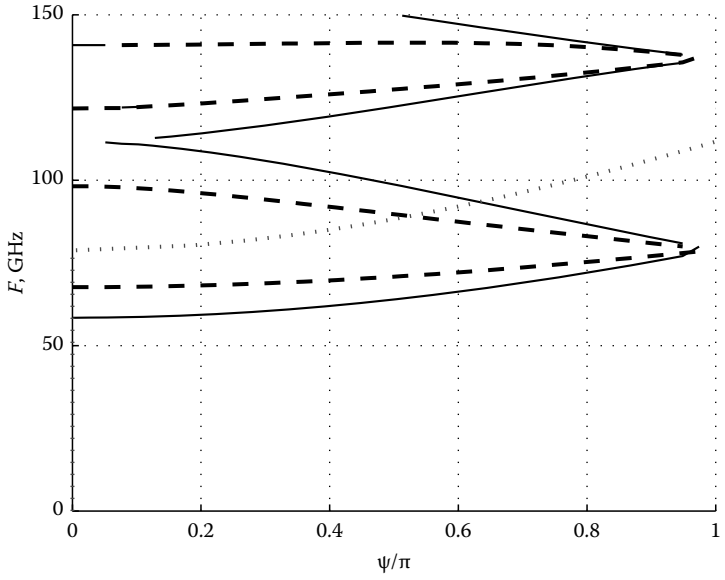

FIGURE 15.16 Spectrum of modes, calculated at different plasma frequencies: $f_p = 86$ GHz (solid line); $f_p = 49.3$ GHz (dashed line). Dotted line shows dispersion of TE_{10} mode of the empty waveguide. ψ is the phase shift per period.

Equation 15.40 (the curve marked '0'), strongly differ from the ones described above and give a wave propagating below plasma frequency.

Figure 15.16 illustrates how the plasma frequency of the WM, filling the waveguide, influences the spectrum of modes. One can see that an increase in r, causing an increase in f_p, broadens passbands of all eigenmodes.

Connected wires, filling the waveguide, have also been considered in [30] as well as two and three wires of each direction in the waveguide cross-section. Experimental study of waveguides, filled with DWM [35], confirms the effects of the SD.

15.5 Applications of Wire Media

15.5.1 Coupling Reduction in Antenna Arrays

The problem of reduction of mutual coupling between radiating elements in antenna arrays remains very important for many applications despite much work done for its solution. Spurious coupling can be caused by the following carriers: near (electrostatic) fields; TM-polarized waves; TE-polarized waves; and surface waves (if the radiating elements are placed on a substrate). Utilization of electromagnetic band gap (EBG) [or photonic band gap (PBG)] structures is considered now as one of the most promising ways for antenna element decoupling. An approach, alternative to EBG (PBG) structures and based on a WM slab, was proposed by Nefedov et al. [36]. Figures 15.17 and 15.18 illustrate reduction of the mutual coupling using the WM slab. The Parameters of the structure are the following: $r = 0.8$ mm, $a = 5$ mm, the thickness of WM slab is the same as the distance between patches and ground plane, $h = 20$ mm, the distance between patches equals 50 mm, and the space between patch and WM equals 5 mm. We have achieved a reduction of the mutual coupling to −38 dB for TM and to −40 dB for TE excitation. It is important that a single WM slab effectively reduces coupling for the TM excitation but, at the same time, considerably increases the coupling for TE excitation.

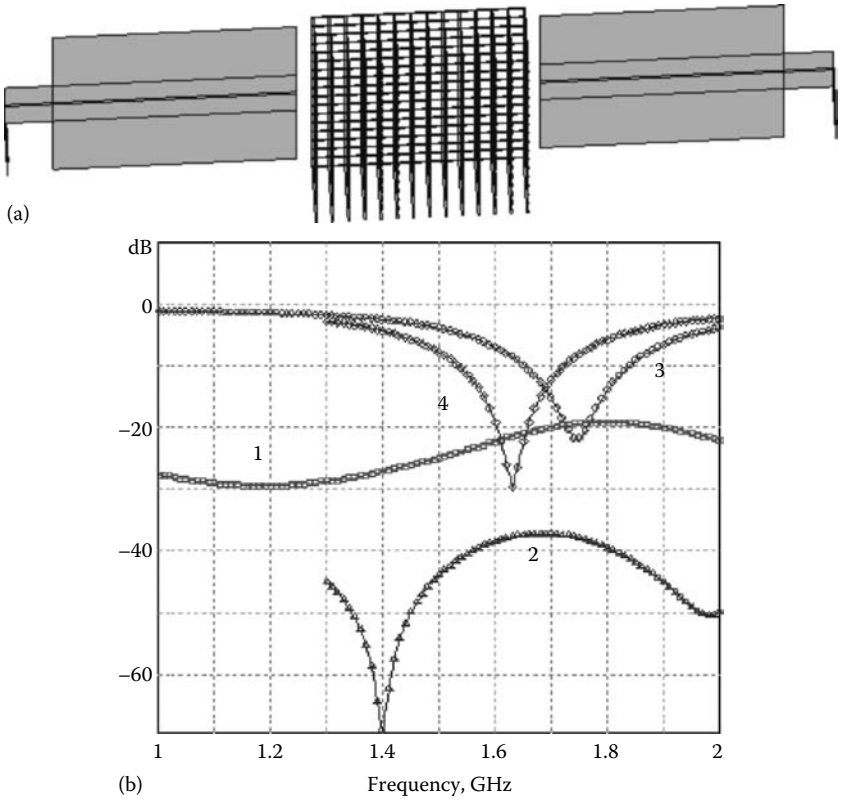

FIGURE 15.17 Geometries of decoupling structures for TM excitation (a). *S*-parameters (b): curve 1—S_{21} for the structure without WM; 2—S_{21}, with WM; 3—S_{11}, without WM, 4—S_{11}, with WM. (From Nefedov, I. S., Tretyakov, Säily, J., Xu Liangge, Mynttinen, T., and Kaunisto, M., "Application of wire media layers for coupling reduction in antenna arrays and microwave devices, *2007 Loughborough Antennas and Propagation Conference*, Loughborough, United Kingdom, 2–3 April 2007, pp. 39–44. With permission.)

Therefore, we connect vertical wires by horizontal arches. Actually we use 3D mesh similar to that studied in [13]. It allows to suppress a parasitic coupling for the TE polarization and even improve it for the TM polarization. It is interesting that the nonlocal model that takes into account coupled TM and TEM modes predicts the existence of guided waves in a WM slab [37]. The nonlocal model, which neglects the TEM mode, does not give propagating waves, which [38] is in agreement with above-described results. This problem needs in further study.

Thus, WM can be efficiently used for decoupling of antenna elements. In contrast to other known EBG structures WM has the following explicit advantages:

- Nonresonant nature of a stop-band gap and, hence, a much wider operational frequency band
- Relative simplicity in implementation
- Capability to use for any polarization
- Insensibility to deviation of parameters. It is enough if the plasma frequency exceeds operating frequencies but not too much

Results of numerical simulations were confirmed experimentally for both polarizations [36].

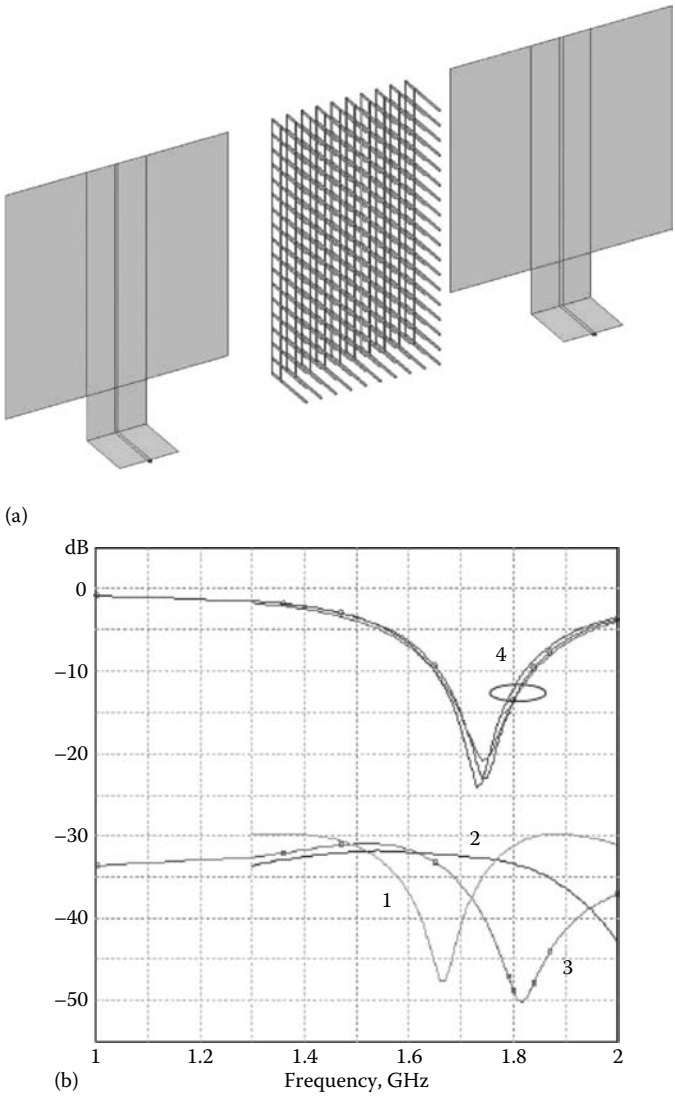

FIGURE 15.18 Geometries of decoupling structures for TE excitation (a). *S*-parameters (b): curve 1—S_{21} for the structure without wires; 2—S_{21}, wires with 2D top grid; 3—S_{21}, wires with two-level grids, 4—S_{11} with and without WM. (From Nefedov, I. S., Tretyakov, S. A., Säily, J., Liangge Xu, Mynttinen, T., and Kaunisto, M., Application of wire media layers for coupling reduction in antenna arrays and microwave devices, *2007 Loughborough Antennas and Propagation Conference*, Loughborough, 2–3 April 2007, pp. 39–44, United Kingdom. With permission.)

15.5.2 Antenna Lenses and Other Applications

Besides first applications of WM in antenna lenses [1,2], new ideas have been developed in recent years. Hereafter we give a brief description of two of them. One is based on capacitively loaded WM [39,41], which exhibits a positive permittivity. Strip-like wires can be printed on a thin low-permittivity substrate (see Figure 15.19, taken from [41]). Parameters of WM, taken from [40,41], provide effective relative permittivity 2–4, which depends on an angle of transmission. An antenna lens made of such a medium has a light weight compared with a similar one made of a bulk dielectric.

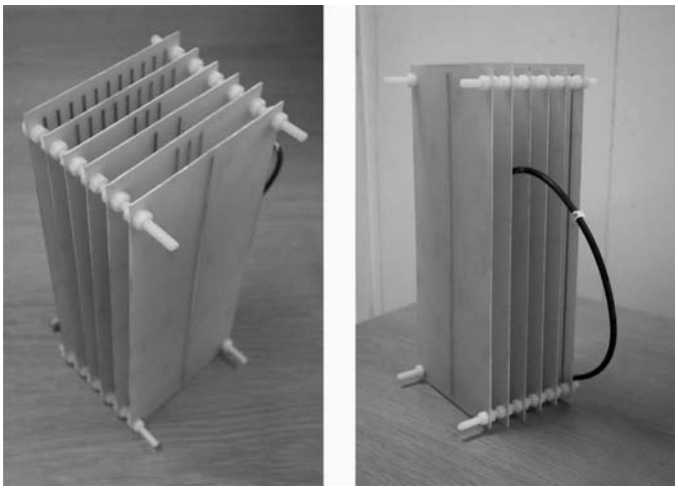

FIGURE 15.19 Photograph showing the implemented prototype with the wide lens. (From Ikonen, P., Simovski, C., and Tretyakov, S., *Microwave Opt. Technol. Lett.*, 43(6), 467, 2004. With permission.)

The second idea is creation of a metamaterial for directive emission [42]. If a source is placed in a slab of metamaterials whose ϵ or μ is positive but close to zero, then all points of the slab interface are excited in phase, and high directive emission can be obtained. The simplest way to realize near-zero permittivity is to use wire media near the plasma frequency. This approach was studied in many articles; see, for example, [43–46].

Capacitively loaded DWM is promising for the creation of controllable microwave devices and antennas [47]. A controllable phase shifter, based on a metal waveguide, filled with capacitively loaded WM, was proposed in [48]. A similar structure can be a base for an electrically controllable leaky-wave antenna [49].

A series of articles, where the idea of transfer of images with subwavelength resolution by the TEM modes in WM is developed, have been published during the last 2 years [28,37,50,51]. We do not discuss them here, because this topic is the subject of a special chapter in this book.

15.6 Conclusion

The authors were not able to refer to and discuss all articles devoted to wire media, published during recent years, so a choice of selected material for this overview relates to the scientific interests of authors. The most important result, achieved in this area is the understanding of the role of SD in electromagnetic properties of WM. The main consequence of the SD is that the TM and the TEM waves with similar polarizations can propagate in WM, and they can be coupled at interfaces of WM and other media. However, we have no certain answers to some questions. One is the applicability of the local model to very thin layers of WM especially embedded into a high-permittivity substrate. Next one concerns SD in double and triple WM with connected wires. Effects of SD are predicted in [52] for waves propagating in all directions in double and triple WM with connected wires. However, numerical simulations, implemented in [19] for DWM, did not show the influence of the SD on wave propagation in a plane of wire lattices. At the same time, dispersion characteristics for the waves, propagating orthogonally to the wires, certainly are in agreement with the nonlocal model [30].

References

1. J. Brown, *Prog. Dielect.*, 2, 195, 1960.
2. J. Brown, Artificial dielectrics having refractive indices less than unity, *Proceedings of the IEEE*, Monograph No. 62R, 100, 4, 51–62, May 1953.
3. J. Brown and W. Jackson, The properties of artificial dielectrics at centimetre wavelengths, *Proceedings of the IEEE*, paper no. 1699R., 102B, 11–21, January 1955.
4. A. Carne and J. Brown, Theory of reflections from the rodded-type artificial dielectric, *Proceedings of the IEEE*, paper no. 2742R, 105C, 105–115, November 1958.
5. J.S. Seeley, The quarter-wave matching of dispersive materials, *Proceedings of the IEEE*, paper no. 2736R, IO5C, 103–106, November 1958.
6. J.S. Seeley and J. Brown, The use of dispersive artificial dielectrics in a beam scanning prism, *Proceedings of the IEEE*, paper no. 2735R, 105C, 93–102, November 1958.
7. A.M. Model, Propagation of plane electromagnetic waves in a space which is filled with plane parallel grids, *Radiotekhnika*, 10, 52–57, June 1955 (In Russian.)
8. R.J. King, D.V. Thiel, and K.S. Park, The synthesis of surface reactance using an artificial dielectric, *IEEE Trans. Antennas Propag.*, AP-31, 3, pp. 471–476, May 1983.
9. W. Rotman, Plasma simulation by artificial dielectrics and parallel-plate media, *IRE Trans. Antennas Propag.*, 10, 82–95, January 1962.
10. D.R. Smith, W.J. Padilla, D.C. Vier, S.C. Nemat-Nasser, and S. Schultz, *Phys. Rev. Lett.*, 84, 4184, 2000.
11. S. Tretyakov, *Analytical Modeling in Applied Electromagnetics*, Artech House, Boston, MA London, 2003.
12. P.A. Belov, R. Marques, S.I. Maslovski, I.S. Nefedov, M. Silveirinha, C.R. Simovski, and S.A. Tretyakov, Strong spatial dispersion in wire media in the very large wavelength limit, *Phys. Rev. B*, 67, 113103, 2003.
13. J.B. Pendry, A.J. Holden, W.J. Stewart, and I. Youngs, Extremely low frequency plasmons in metallic mesostructures, *Phys. Rev. Lett.*, 76, 4773–4776, 1996.
14. D.F. Sievenpiper, M.E. Sickmiller, and E. Yablonovitch, 3D wire mesh photonic crystals, *Phys. Rev. Lett.*, 76, 2480, 1996.
15. I.S. Nefedov and A.J. Viitanen, Electromagnetic wave reflection from the wire medium, formed by two mutually orthogonal wire lattices, *27th ESA Antenna Technology on Innovative Periodic Antennas: Electromagnetic Bandgap, Left-handed Materials, Fractal and Frequency Selective Surfaces*, March 9–11, 2004, Santiago de Compostela, Spain, pp. 265–271.
16. M.G. Silveirinha and C.A. Fernandes, A hybrid method for the efficient calculation of the band structure of 3-D metallic crystals, *IEEE Trans. Microwave Theory Tech.*, 52, 889–902, March 2004.
17. C.R. Simovski and P.A. Belov, Low-frequency spatial dispersion in wire media, *Phys. Rev. E*, 70, 046616, 2004.
18. I.S. Nefedov, A.J. Viitanen, and S.A. Tretyakov, Propagating and evanescent modes in two-dimensional wire media, *Phys. Rev. E*, 71, 046612, 2005.
19. M. Hudlička, J. Macháč, and I. Nefedov, A triple wire medium as an isotropic negative permittivity metamaterial, *Progress in Electromagnetics Research, PIER*, 65, 233–246, EMW Publishing, Cambridge, MA.
20. P.A. Belov, S.A. Tretyakov, and A.J. Viitanen, Dispersion and reflection properties of artificial media formed by regular lattices of ideally conducting wires, *J. Electromagn. Waves Appl.*, 16, 1153–1170, August 2002.
21. S.I. Maslovski, S.A. Tretyakov, and P.A. Belov, Wire media with negative effective permittivity: A quasi-static model, *Microwave Opt. Technol. Lett.*, 35, 47–51, October 2002.
22. V. Ginzburg, *The Propagation of Electromagnetic Waves in Plasmas*, Pergamon, Oxford, 1964.
23. I.V. Lindell, S. Tretyakov, K. Nikoskinen, and S. Ilvonen, BW media–media with negative parameters, capable of supporting backward waves, *Microwave Opt. Technol. Lett.*, 31, 129–133, 2001.

24. G. Shvets, Photonic approach to making a surface wave accelerator, *CP647, in Advanced Accelerator Concept: Tenth Workshop*, C.E. Clayton and P. Muggli (eds.), American Institute of Physics, pp. 371–382, 2002.
25. S.I. Pekar, *Zh. Eksp. Teor. Fiz*., 33, 1022, 1957 [*Soviet Phys. JETP*, 6, 785, 1958].
26. V.M. Agranovich and V.L. Ginzburg, *Crystal Optics with Spatial Dispersion and Excitons*, 2nd edn., Springer, New York, 1984.
27. M.G. Silveirinha, Additional boundary condition for the wire medium, *IEEE Trans. Microwave Theory Technol.*, 54, 1766–1780, June 2006.
28. M.G. Silveirinha, P.A. Belov, and C.R. Simovski, Subwavelength imaging at infrared frequencies using an array of metallic nanorods, *Phys. Rev. B*, 75, 03508, 2007.
29. M.G. Silveirinha, Nonlocal homogenization model for a periodic ϵ-negative rods, *Phys. Rev. E*, 73, 046612, 2006.
30. I. S. Nefedov, X. Dardenne, C. Craeye, and S.A. Tretyakov, Backward waves in a waveguide, filled with wire media, *Microwave Opt. Technol. Lett*., 48, 2560–2564, 2006.
31. I. Huynen, A. Saib, J.P. Raskin, X. Dardenne, and C. Craeye, Periodic metamaterials combining ferromagnetic, dielectric and/or metallic structures for planar circuits applications, *Proceedings of the Bianisotropics 2004 Conference*, Ghent, Belgium, September 2004.
32. L.D. Landau and E.M. Lifshitz, *Electrodynamics of Continuous Media (Course of Theoretical Physics, Volume 8),* 2nd edn., Ed by E.M. Lifshitz and L.P. Pitaevskii, Pergamon, Oxford, 1984.
33. I.S. Nefedov, A.J. Viitanen, and S.A. Tretyakov, Electromagnetic wave refraction at an interface of a double wire medium, *Phys. Rev. B*, 72, 245113, 2005.
34. J. Esteban, C. Camacho-Penalosa, J.E. Page, T.M. Martin-Guerrero, and E. Marquez-Segura, Simulation of negative permittivity and negative permeability by means of evanescent waveguide modes–theory and experiment, *IEEE Trans. Microwave Theory Technol.*, 53, 1506–1514, April 2005.
35. S. Hrabar, A. Vuckovic, M. Vidalina, and M. Masic, Influence of spatial dispersion on properties of waveguide filled with wire media—an experimental investigation, in *Proceedings of Metamaterials*, Rome, pp. 259–262, October 22–24, 2007.
36. I.S. Nefedov, S.A. Tretyakov, J. Säily, Xu Liangge, T. Mynttinen, and M. Kaunisto, Application of wire media layers for coupling reduction in antenna arrays and microwave devices, in: *2007 Loughborough Antennas and Propagation Conference*, Loughborough, United Kingdom, April 2–3, pp. 39–44, 2007.
37. P.A. Belov and M.G. Silveirinha, Resolution of subwavelength transmission devices formed by a wire medium, *Phys. Rev. E*, 73, 056607, 2006.
38. I.S. Nefedov and A.J. Viitanen, Guided waves in uniaxial wire medium slab, *Prog. Electromagn. Res., PIER*, 51, 167–185, 2005.
39. C.R. Simovski and S. He, Antennas based on modified metallic photonic bandgap structures consisting of capacitively loaded wires, *Microwave Opt. Technol. Lett*., 31(5), 214–221, 2001.
40. P. Ikonen, C. Simovski, and S. Tretyakov, Compact directive antennas with a wire-medium artificial lens, *Microwave Opt. Technol. Lett*., 43(6), 467–469, 2004.
41. P. Ikonen, M. Kärkkäinen, C. Simovski, P. Belov, and S. Tretyakov, Light-weight base-station antenna with artificial wire medium lens, *IEE Proc. Microwave Antennas Propagat*., 153, 163–170, February 2006.
42. S. Enoch, G. Tayeb, P. Sabourougx, N. Guéerin, and P. Vincent, A metamaterial for directive emission, *Phys. Rev. Lett*., 89(21), 213902, 2002.
43. G. Lovat, P. Burghignoli, F. Capolino, D.R. Jackson, and D.R. Wilton, Analysis of directive radiation from a line source in a metamaterial slab with low permittivity, *IEEE Trans. Antennas Propagat*., 54, 1017–1030, March 2006.
44. G. Lovat, P. Burghignoli, F. Capolino, and D.R. Jackson, High directivity in low-permittivity metamaterial slabs: Ray-optic vs. leaky-wave models, *Microwave Opt. Technol. Lett*., 48, 2542–2548, December 2006.

45. G. Lovat, P. Burghignoli, F. Capolino, and D.R. Jackson, Combinations of low/high permittivity and/or permeability substrates for highly directive planar metamaterial antennas, *IET Microwaves, Antennas Propagat.*, 1, 177–183, February 2007.
46. A. Della Villa, F. Gapolino, V. Galdi, S. Enoh, V. Pierro, and G. Taeb, Analysis of modal propagation in slabs of photonic quasicrystals with penrose-type lattice, in: *Proceedings of Metamaterials*, Rome, pp. 154–157, October 22–24, 2007.
47. I.S. Nefedov and S.A. Tretyakov, Electromagnetic waves in electrically controllable metamaterials based on loaded wire media, *European Microwave Week*, Paris, France, *WSEuMC05, Ferroelectrically Tuneable Microwave Devices*, pp. 119–126, October 3–7, 2005.
48. I. Nefedov, P. Alitalo, and S. Tretyakov, Tunability and losses in metamaterials based on loaded wire media, *Presentation tue1s3 in Nanometa'2007 Conference*, Seefeld, Tirol, Austria, January 8–11, 2007.
49. I.S. Nefedov, P. Alitalo, and S.A. Tretyakov, High-frequency scanning leaky-wave antenna based on a waveguide filled with controllable wire media, in: *Proceedings of 29th ESA Antenna Workshop on Multiple Beam and Reconfigurable Antennas*, Noordwijk, the Netherlands, pp. 334–337, April 18–20, 2007.
50. P.A. Belov, Y. Hao, and S. Sudhakaran, Subwavelength microwave imaging using an array of parallel conducting wires as a lens, *Phys. Rev. B*, 73, 033108, 2006.
51. I.S. Nefedov and A.J. Viitanen, Effective medium approach for subwavelength resolution, *Electronics Lett.*, 43, 22, October 25, 2007.
52. M.G. Silveirinha and C.A. Fernandes, Homogenization of 3-D-connected and nonconnected wire metamaterials, *IEEE Trans. Microwave Theory Technol.*, 53, 1418–1430, April 2005.

16

Split Ring Resonators and Related Topologies

Ricardo Marqués
University of Sevilla

Ferran Martín
Universidad Autónoma de Barcelona

16.1 Introduction

Diamagnetic properties of conducting rings have been known for long. In 1852, W. Weber invoked *Faraday's* law to suggest that natural diamagnetism could be produced by currents induced in microscopic conducting closed loops, which would be present inside matter [1]. In fact, it can be easily shown that a single and lossless metallic ring presents a negative magnetic polarizability given by

$$m_z = \alpha_{zz}^{mm} B_z^{\text{ext}}; \quad \alpha_{zz}^{mm} = -\frac{\pi^2 r^4}{L}, \tag{16.1}$$

where
z has been assumed to be the ring axis
r is the ring radius
L is the ring inductance

Thus, a random or periodic arrangement of closed metallic rings will exhibit a diamagnetic behavior provided the wavelength of the incident radiation is much smaller than periodicity. However, this negative polarizability is not very high and is not enough to provide an effective negative permeability. In 1952 S.A. Shelkunoff proposed to introduce a capacitor to enhance the magnetic response of the ring [2]. Still neglecting losses, this would lead to a magnetic polarizability given by

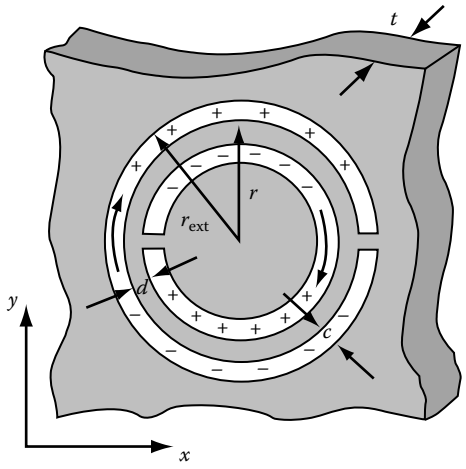

FIGURE 16.1 The split ring resonator (SRR) configuration proposed in [3] for magnetic metamaterial design. Metallizations are in white and dielectric substrate is in gray. Charges and currents induced at resonance on the upper and lower SRR halves are sketched.

$$\alpha_{zz}^{mm} = \frac{\pi^2 r^4}{L} \frac{\omega^2}{\omega_0^2 - \omega^2}, \tag{16.2}$$

where $\omega_0 = 1/\sqrt{LC}$ is the frequency of resonance of the LC circuit. It is apparent from the above formula that introducing a capacitor results in a strong magnetic response near the resonance, which is paramagnetic/diamagnetic below/above this resonance. Although this proposal works at low frequencies, at higher frequencies (for instance at microwave frequencies), low-loss chip capacitors may become unavailable, and the task of mounting hundredths or perhaps thousands of these capacitors to manufacture a metamaterial may become unapproachable. At such frequencies it may be better to substitute the wire ring by a strip ring photo etched on a dielectric board and the chip capacitor by a distributed capacitance. This was essentially the proposal made by Pendry et al. in 1999 [3] for manufacturing artificial magnetic media at microwave frequencies. The split ring resonator (SRR) proposed in [3] consists of two concentric split rings etched on a dielectric circuit board and separated by some distance, as shown in Figure 16.1. Although there can be found some precedents in the scientific literature of this and other similar designs, this was the first time that this configuration was proposed as the basic "atom" for building up magnetic metamaterials at microwave frequencies.

Along this contribution, the physics and the main characteristics of SRRs and other related configurations are analyzed. We start by describing the behavior of SRRs at microwave frequencies, where metals can be considered good conductors. A circuit model is developed for this analysis, and closed expressions for the frequency of resonance and polarizabilities of such structures are derived. The main advantages and disadvantages of the different SRR geometries proposed in the literature for metamaterial design, including the "complementary" SRR [4], will be discussed. Finally, the behavior of SRRs at infrared and optical frequencies is analyzed. More information on these and other related topics can be found in [5].

16.2 Nonbianisotropic SRR

Before analyzing Pendry's SRR design, it will be convenient to analyze the simpler structure shown in Figure 16.2. It is a small modification of Pendry's SRR proposed in [6] in order to avoid SRR bianisotropy (see below, Section 16.4). Figure 16.3 shows the equivalent circuit as well as a sketch of currents and voltages on a non-bianisotropic SRR (NB-SRR) operating near the first resonance.

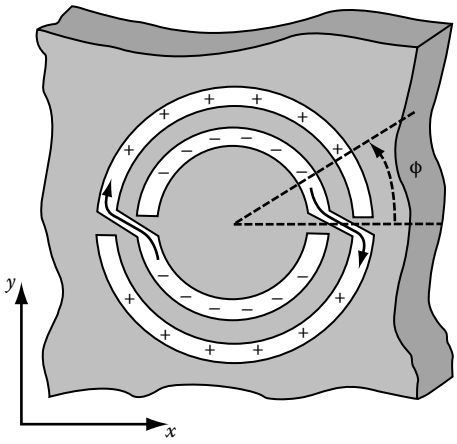

FIGURE 16.2 Nonbianisotropic split ring resonator (NB-SRR). As in Figure 16.1, metallizations are in white and dielectric substrate is in gray. NB-SRR parameters (not shown in the figure) r, r_{ext}, c, d, and t are defined as in Figure 16.1.

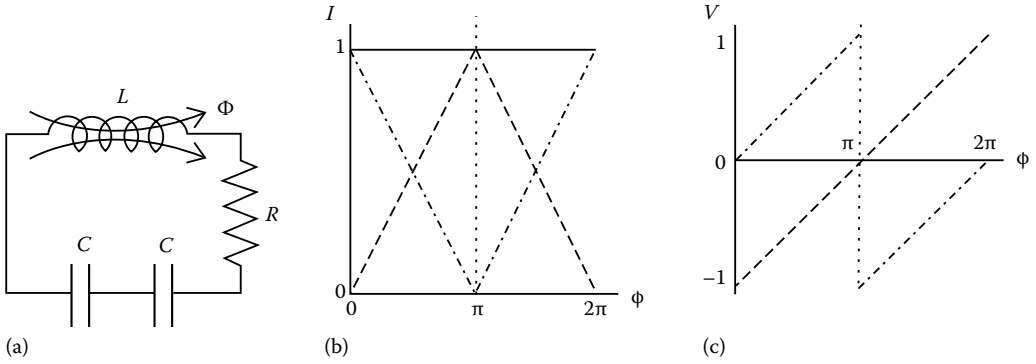

FIGURE 16.3 Quasi-static circuit model for the NB-SRR; (a) Equivalent circuit for the determination of the frequency of resonance (L is the NB-SRR self-inductance and C is the capacitance across the slots on the upper and lower halves of the NB-SRR). (b) Plots of the angular dependence (ϕ is the angle with the x-axis) of currents on the rings (dashed and dash–dotted lines), and of the total current on both rings (solid line). (c) Plots of the angular dependence of the voltage on the rings (dashed and dash–dotted lines).

For electrically small NB-SRR, currents on each ring vary linearly from zero (the capacitance of the gaps on the rings can be neglected in a first-order approximation) to a maximum value, as shown in Figure 16.3b. However, the total current on the whole NB-SRR (i.e., the summation of currents on both rings) is uniform (i.e., angle independent) around the NB-SRR [7]. In order to maintain this uniform total current around the NB-SRR, current must pass from one ring to another through the slot between them, as an electric displacement current. Therefore, the slots between the rings act as distributed capacitances, and the equivalent circuit for the NB-SRR first resonance is that shown in Figure 16.3a, where C is the capacitance of each slot. Voltage distribution around the rings is shown in Figure 16.3c. The capacitance of the slots C can be calculated as $C = \pi r C_{pul}$, where r is the average radius of the NB-SRR and C_{pul} the per unit length capacitance through the slots. Therefore, the frequency of the NB-SRR first resonance is given by

$$\omega_0 = \sqrt{\frac{2}{LC}} = \sqrt{\frac{2}{\pi r C_{\text{pul}} L}}\,, \tag{16.3}$$

where L can be approximated as the inductance of a closed ring of average radius r and width c [8,9]. Closed expressions for the evaluation of C_{pul} and L can be found in [8] or in [5].

Let us now examine the NB-SRR polarizabilities. These polarizabilities are defined by the tensor equations:

$$\mathbf{p} = \overline{\overline{\alpha}}^{ee} \cdot \mathbf{E}^{\text{ext}} + \overline{\overline{\alpha}}^{em} \cdot \mathbf{B}^{\text{ext}} \tag{16.4}$$

$$\mathbf{m} = \overline{\overline{\alpha}}^{me} \cdot \mathbf{E}^{\text{ext}} + \overline{\overline{\alpha}}^{mm} \cdot \mathbf{B}^{\text{ext}}\,, \tag{16.5}$$

where

$\mathbf{p}$ and $\mathbf{m}$ are the electric and magnetic moments induced on the NB-SRR by the external fields $\mathbf{E}^{\text{ext}}$ and $\mathbf{B}^{\text{ext}}$

$\overline{\overline{\alpha}}^{ee}$, $\overline{\overline{\alpha}}^{em}$, $\overline{\overline{\alpha}}^{me}$, and $\overline{\overline{\alpha}}^{mm}$ are the NB-SRR tensor polarizabilities.

From Onsager symmetry relations it can be deduced that [10]

$$\overline{\overline{\alpha}}^{ee} = \left(\overline{\overline{\alpha}}^{ee}\right)^{\text{t}} \tag{16.6}$$

$$\overline{\overline{\alpha}}^{mm} = \left(\overline{\overline{\alpha}}^{mm}\right)^{\text{t}} \tag{16.7}$$

$$\overline{\overline{\alpha}}^{em} = -\left(\overline{\overline{\alpha}}^{me}\right)^{\text{t}}, \tag{16.8}$$

where the subscript $(\cdot)^{\text{t}}$ indicates "transpose." That is, $\overline{\overline{\alpha}}^{ee}$ and $\overline{\overline{\alpha}}^{mm}$ are symmetic tensors, whereas $\overline{\overline{\alpha}}^{em}$ and $\overline{\overline{\alpha}}^{me}$ are related through Equation 16.8. For lossless systems the whole (6×6) tensor polarizability must be hermitian. Therefore, for lossless NB-SRRs $\overline{\overline{\alpha}}^{ee}$ and $\overline{\overline{\alpha}}^{me}$ are real tensors, whereas $\overline{\overline{\alpha}}^{em}$ and $\overline{\overline{\alpha}}^{me}$ are purely imaginary quantities. It may be worth mentioning that the above equations are completely general and valid for any linear polarizable system.

Regarding the NB-SRR, the number of nonvanishing elements of the above tensor polarizabilities are drastically reduced due to particle symmetries. First of all, the NB-SRR has inversion symmetry. Since the sign of electric quantities ($\mathbf{p}$ and $\mathbf{E}^{\text{ext}}$) changes after inversion, whereas magnetic quantities ($\mathbf{m}$ and $\mathbf{B}^{\text{ext}}$) remain unchanged [11], any tensor relating these quantities must vanish in systems invariant by inversion. Thus, the NB-SRR cross-polarizability tensors $\overline{\overline{\alpha}}^{em}$ and $\overline{\overline{\alpha}}^{me}$ vanish. On the other hand, since the NB-SRR is a planar particle, only electric moments along the x- and y-axis (p_x and p_y) and magnetic moments along the z-axis (m_z) are allowed. That is, only the polarizabilities $\alpha^{mm}_{z,z}$, $\alpha^{ee}_{x,x}$, $\alpha^{ee}_{x,y}$, and $\alpha^{ee}_{y,y}$ can be different from zero.

Once the effect of particle symmetries on the tensor polarizabilities has been analyzed, these polarizabilities will be calculated. When an external magnetic field B^{ext}_z illuminates the particle, an external electromotive force $-j\omega\pi r^2 B^{\text{ext}}_z$ acts on the equivalent circuit of Figure 16.3a. Therefore, the equation for the total current on the NB-SRR is

$$\left(\frac{2}{j\omega C} + j\omega L + R\right) I = -j\omega\pi r^2 B^{\text{ext}}_z\,, \tag{16.9}$$

where R is the NB-SRR resistance (which can be estimated as in [8]). From this equation and from $m_z = \pi r^2 I$, the magnetic polarizability of the NB-SRR can be found as

$$\alpha^{mm}_{zz} = \frac{\pi^2 r^4}{L}\left(\frac{\omega^2}{\omega_0^2 - \omega^2 + j\omega R/L}\right). \tag{16.10}$$

Since the magneto-electric polarizabilities $\bar{\bar{\alpha}}^{me}$ vanish, no other dipolar moment is associated with the NB-SRR first resonance. That is, the only resonant polarizability of the particle is the magnetic polarizability (Equation 16.10).* The nonresonant electric polarizabilities can be estimated as those of a metallic disk with the same external radius as the NB-SRR:

$$\alpha_{xx}^{ee} = \alpha_{yy}^{ee} = \varepsilon_0 \frac{16}{3} r_{\text{ext}}^3, \tag{16.11}$$

$$\alpha_{xy}^{ee} = 0, \tag{16.12}$$

where $r_{\text{ext}} = r + c + d/2$.

The NB-SRR is perhaps the simpler SRR configuration providing a resonant magnetic polarizability near its first resonance. Since no cross-polarization effects are present in the NB-SRR, this particle provides metamaterials with a resonant magnetic response only. This property simplifies the design and the interpretation of the experimental results and usually can be considered as an advantage. However, this does not imply that the nonresonant electric polarizabilities (Equation 16.12) are not important for the final characterization of the metamaterial. They usually take non-negligible values, providing a nonvanishing electric susceptibility for the metamaterial.

16.3 Other SRR Configurations with Inversion Symmetry

As shown in Section 16.2, the frequency of resonance of SRRs depends on the SRR self-inductance L and on the per unit length capacitance between the rings C_{pul}. The self-inductance of the SRRs cannot be substantially increased without increasing its size: it is always $L \sim \mu_0 r$. For the analyzed NB-SRR, as well as for the original Pendry's SRR design, the per unit length capacitance cannot be made very high, due to the edge-coupling between the metallic strips making the SRR. Thus, the electrical size at the resonance of this configuration can hardly be made smaller that $\lambda/10$. Therefore, the ratio between wavelength λ and periodicity a of metamaterials made with these atoms cannot be made very high.† By comparing with the values of this ratio for natural materials at optical frequencies, $\lambda/a \sim 10^3$, it becomes apparent that SRR-made magnetic metamaterials are in the very limit of applicability of the continuous medium approximation. However, the SRR per unit length capacitance can be easily increased by substituting the edge coupling by a broadside coupling as well as a thin substrate of high dielectric constant. This broadside coupling SRR (BC-SRR) was proposed in [13] and is shown in Figure 16.4. It can be easily realized that the BC-SRR equivalent circuit as well as its current and voltage distributions are still given by Figure 16.3. Moreover, as the NB-SRR, this BC-SRR configuration also shows inversion symmetry. Therefore, there are no cross-polarization effects in such a design. In summary, the frequency of resonance and polarizabilities of the BC-SRR shown in Figure 16.4 are still formally given by Equations 16.3, 16.10, and 16.11. However, in practice, the per unit length capacitances C_{pul} of BC-SRRs can be made much higher than those of the NB-SRR. Therefore, electrical sizes one order of magnitude smaller than those of the NB-SRR can be achieved by using commercial microwave dielectric substrates [8], and even smaller electrical sizes could be achieved by using more specific technologies, such as ferroelectric substrates or thin-layer technologies.

There are many other modifications of Pendry's original design showing inversion symmetry. For instance, by adding two additional cuts to the design shown in Figure 16.1, a new SRR structure invariant can be obtained by inversion. This double-split SRR (2-SRR), along with its equivalent

* This statement is valid only for the first NB-SRR resonance. Higher-order NB-SRR resonances can be associated to other polarizabilities (electric or magnetic) [12] that will not be analyzed here.

† See [5] for a more complete discussion on this topic including the role of the internal wavelength.

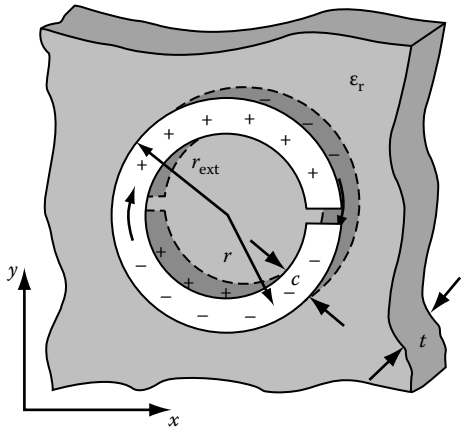

FIGURE 16.4 Broadside-coupled split ring resonator (BC-SRR).

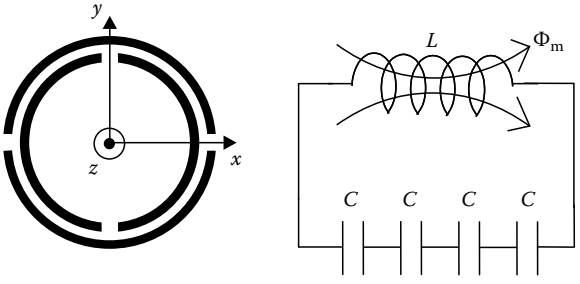

FIGURE 16.5 Sketch of a double-split SRR (2-SRR) and its equivalent circuit.

circuit is shown in Figure 16.5. In this circuit C is now the capacitance of a quarter of circumference $C = \pi r C_{\text{pul}}/2$. Therefore, the frequency of resonance of the 2-SRR is twice the frequency of resonance of the NB-SRR of the same size and characteristics. Since the 2-SRR exhibits inversion symmetry, its polarizabilities are still formally given by Equations 16.10 and 16.11. However, the electrical size at resonance for the 2-SRR is twice than that for the NB-SRR of similar size and design. Thus, this configuration is not by itself of much practical interest. However, the broadside-coupled version of the 2-SRR has been useful for the design of isotropic three-dimensional SRR configurations [14] with small electrical sizes.

16.4 Bianisotropic Effects in SRRs

The SRR configuration shown in Figure 16.1 is topologically equivalent to the NB-SRR configuration shown in Figure 16.2. Therefore, its frequency of resonance is still given by Equation 16.3, and currents and voltages across the SRR are still described by Figure 16.3. However, the SRR of Figure 16.1 is not invariant by inversion. Therefore, cross-polarization effects can be present in this structure [13]. Nevertheless, the SRR symmetries substantially reduce the number of nonvanishing cross-polarizabilities. First of all, as the NB-SRR, the SRR is a planar configuration. Therefore, only electric moments along the x- and y-axis (p_x and p_y) and magnetic moments along the z-axis (m_z) are allowed. This reduces the possible nonvanishing polarizabilities to $\alpha_{z,z}^{mm}$, $\alpha_{x,x}^{ee}$, $\alpha_{x,y}^{ee}$, $\alpha_{y,y}^{ee}$, $\alpha_{z,x}^{me} = -\alpha_{x,z}^{em}$, and $\alpha_{z,y}^{me} = -\alpha_{y,z}^{em}$. Moreover, the SRR is invariant by reflection on the $y = 0$ plane. Since, by this

symmetry, the sign of B_z^{ext} changes whereas p_x remains invariant, it results in $\alpha_{zx}^{me} = 0$. This finally reduces the possible nonvanishing polarizabilities to $\alpha_{z,z}^{mm}$, $\alpha_{x,x}^{ee}$, $\alpha_{x,y}^{ee}$, $\alpha_{y,y}^{ee}$, and $\alpha_{z,y}^{me} = -\alpha_{y,z}^{em}$.

If the SRR is excited by an external magnetic field, the equation for the total current is Equation 16.17; therefore, the magnetic polarizability of the SRR is the same as that for the NB-SRR and is given by Equation 16.10. However, a careful consideration of the SRR behavior shows that the SRR also exhibits a resonant electric dipole when it is magnetically excited. In fact, when the SRR is excited at resonance, charges in the upper half of the EC-SRR must be the images of charges at its lower half, as sketched in Figure 16.1. Therefore, two parallel electric dipoles directed along the y-axis are generated on each SRR half. The total electric dipole induced by the external field component B_z^{ext} can be computed as

$$p_y = 2\int_0^{\pi} p_{\text{r}} r \sin\phi \, d\phi = 4 r p_{\text{r}}, \tag{16.13}$$

where p_{r} is the radial per unit length electric dipole created along the slot between the rings in the upper SRR half. This quantity can be written as $p_{\text{r}} = q_{\text{t}} d_{\text{eff}}$, where q_{t} is the per unit length total charge (i.e., free and polarization charge*) on the outer ring, and d_{eff} some effective distance $d_{\text{eff}} \simeq c + d$. The radial per unit length electric dipole can now be estimated as

$$p_{\text{r}} = q_{\text{t}} d_{\text{eff}} = C_{0,\text{pul}} V d_{\text{eff}}, \tag{16.14}$$

where $C_{0,\text{pul}}$ and V are the "in vacuo" per unit length capacitance and the voltage difference across the slot between the outer and the inner rings, respectively. This voltage can be calculated from $2V = \oint \mathbf{E} \cdot \mathbf{dl}$, where the field integral is taken along a path going on the rings and passing from one to another ring across the slots. From Faraday's law $2V = -j\omega\left(LI + \pi r B_z^{\text{ext}}\right) + RI$. Therefore, taking into account Equations 16.13 and 16.14,

$$p_y = -2j\omega r C_{0,\text{pul}} d_{\text{eff}} \left(LI + \pi r^2 B_z^{\text{ext}}\right), \tag{16.15}$$

and taking into account Equation 16.9,

$$p_y = -4j \frac{r^2 d_{\text{eff}}}{\omega L} \left(\frac{C_{0,\text{pul}}}{C_{\text{pul}}}\right) \left(\frac{\omega^2}{\omega_0^2 - \omega^2 + j\omega R/L}\right) B_z^{\text{ext}}, \tag{16.16}$$

which directly gives the cross-polarization α_{yz}^{em}.

Let us now consider the behavior of the SRR under an electric excitation. The equation for the total current is now

$$\left(\frac{2}{j\omega C} + j\omega L + R\right) I = 2 < V^{\text{ext}} >, \tag{16.17}$$

where $< V^{\text{ext}} >$ is the average voltage created by the external field on one of the SRR halves. This external voltage can be estimated as†

$$< V^{\text{ext}} > = \frac{1}{\pi} \int_0^{\pi} \left(\frac{C_{0,\text{pul}}}{C_{\text{pul}}}\right) E_y^{\text{ext}} d_{\text{eff}} \sin\phi \, d\phi = \frac{2}{\pi} d_{\text{eff}} \left(\frac{C_{0,\text{pul}}}{C_{\text{pul}}}\right) E_y^{\text{ext}}. \tag{16.18}$$

* See [5] for a more complete discussion on this topic.

† The factor $C_{0,\text{pul}}/C_{\text{pul}}$ appears because the voltage induced by an external electric field E^{ext} in a capacitor partially filled by a dielectric is approximately given by $C_0/C\, E^{\text{ext}} d$, where d is the distance between the plates. See [5] for a more complete discussion of this topic.

After substitution in Equation 16.17, the total current on the SRR can be found as

$$I = j\frac{4d_{\text{eff}}}{\pi\omega L}\left(\frac{C_{0,\text{pul}}}{C_{\text{pul}}}\right)\left(\frac{\omega^2}{\omega_0^2 - \omega^2 + j\omega R/L}\right)E_y^{\text{ext}}. \tag{16.19}$$

This current creates a magnetic moment $m_z = \pi r^2 I$, which can be written as

$$m_z = 4j\frac{r^2 d_{\text{eff}}}{\omega L}\left(\frac{C_{0,\text{pul}}}{C_{\text{pul}}}\right)\left(\frac{\omega^2}{\omega_0^2 - \omega^2 + j\omega R/L}\right), \tag{16.20}$$

which together with Equation 16.16 satifies the Onsager symmetry (Equation 16.8). Moreover, when the EC-SRR is under this excitation, the resonant current generated around the rings also creates an electric moment, due to the radial polarization (Equation 16.14) along the slots. It is easier to obtain the per unit length total charge on the outer ring from the current on this ring and from charge conservation:

$$j\omega q_{\text{t}} = -\left(\frac{C_{0,\text{pul}}}{C_{\text{pul}}}\right)\frac{1}{r}\frac{\text{d}I_{\text{out}}}{\text{d}\phi}, \tag{16.21}$$

where I_{out} is the current on the outer ring. Since, according to the model sketched in Figure 16.3b, there is a linear dependence of I_{out} on ϕ, and I_{out} takes a maximum $I_{\text{out}} = I$ at $\phi = 0$, and a minimum $I_{\text{out}} = 0$ at $\phi = \pi$, the derivative in (Equation 16.21) can be evaluated as $\text{d}I_{\text{out}}/\text{d}\phi = -I/\pi$. Therefore, taking into account Equation 16.19

$$q_{\text{t}} = \left(\frac{C_{0,\text{pul}}}{C_{\text{pul}}}\right)\frac{I}{j\omega\pi r} = \frac{4d_{\text{eff}}}{\pi^2\omega^2 rL}\left(\frac{C_{0,\text{pul}}}{C_{\text{pul}}}\right)^2\left(\frac{\omega^2}{\omega_0^2 - \omega^2 + j\omega R/L}\right)E_y^{\text{ext}}. \tag{16.22}$$

The resonant electric dipole on the SRR is evaluated by substitution in Equations 16.13 and 16.14:

$$p_y = \frac{16d_{\text{eff}}^2}{\pi^2\omega^2 L}\left(\frac{C_{0,\text{pul}}}{C_{\text{pul}}}\right)^2\left(\frac{\omega^2}{\omega_0^2 - \omega^2 + j\omega R/L}\right)E_y^{\text{ext}}. \tag{16.23}$$

Finally, the nonresonant polarizabilities (Equation 16.11) are still present in the SRR. Therefore, the final SRR polarizabilities can be written as

$$\alpha_{zz}^{mm} = \frac{\pi^2 r^4}{L}\left(\frac{\omega^2}{\omega_0^2 - \omega^2 + j\omega R/L}\right) \tag{16.24}$$

$$\alpha_{xx}^{ee} = \varepsilon_0\frac{16}{3}r_{\text{ext}}^3 \tag{16.25}$$

$$\alpha_{yz}^{em} = -\alpha_{zy}^{me} = -4j\frac{r^2 d_{\text{eff}}}{\omega L}\left(\frac{C_{0,\text{pul}}}{C_{\text{pul}}}\right)\left(\frac{\omega^2}{\omega_0^2 - \omega^2 + j\omega R/L}\right) \tag{16.26}$$

$$\alpha_{yy}^{ee} = \varepsilon_0\frac{16}{3}r_{\text{ext}}^3 + \frac{16d_{\text{eff}}^2}{\pi^2\omega^2 L}\left(\frac{C_{0,\text{pul}}}{C_{\text{pul}}}\right)^2\left(\frac{\omega^2}{\omega_0^2 - \omega^2 + j\omega R/L}\right). \tag{16.27}$$

Cross-polarization effects produce a bianisotropic behavior in metamaterials made from SRRs [13]. These effects can be considered as small corrections in some cases. However, in other cases, they are crucial for the understanding of the physics of the metamaterial. SRR-made metasurfaces [4] are an example of this last possibility.

16.5 Chirality in SRRs

Bi-isotropic and racemic mixtures of resonant particles [15–17], as well as mixtures of chiral particles with wires [18] or other elements, are of interest for the development of negative refractive index metamaterials. A small modification of the NB-SRR (Section 16.2) proposed in [19] fulfills these requirements. This particle is shown in Figure 16.6. It is the broadside-coupled version of the NB-SRR. Here it will be called chiral-SRR (Ch-SRR). Since the Ch-SRR has no inversion symmetry, cross-polarization effects are present in it. However, the Ch-SRR still has symmetries that substantially reduce the number of nonvanishing polarizabilities. First of all the Ch-SRR is invariant by rotation of 180° around the z-axis. From this symmetry it directly follows that $\ddot{\alpha}_{zx} = \ddot{\alpha}_{zy} = 0$. The Ch-SRR also has 180° rotation symmetry around the x-axis, which implies that $\ddot{\alpha}_{xy} = 0$. Therefore, all polarizability tensors in Equations 16.4 and 16.5 are diagonal.

Since the Ch-SRR is only a modification of the basic topology of the NB-SRR, its equivalent circuit as well as the current and voltage distributions on the rings are still described by Figure 16.3. The main Ch-SRR polarizabilities can be obtained following a similar procedure as that already followed in Section 16.4. The final result is [19]

$$\alpha_{zz}^{mm} = \frac{\pi^2 r^4}{L} \frac{\omega^2}{\omega_0^2 - \omega^2 + j\omega R/L} \tag{16.28}$$

$$\alpha_{zz}^{em} = \pm j \frac{2\pi r^2 t}{\omega L} \left(\frac{C_{0,\text{pul}}}{C_{\text{pul}}} \right) \frac{\omega^2}{\omega_0^2 - \omega^2 + j\omega R/L} \tag{16.29}$$

$$\alpha_{zz}^{ee} = \frac{4t^2}{\omega^2 L} \left(\frac{C_{0,\text{pul}}}{C_{\text{pul}}} \right)^2 \frac{\omega^2}{\omega_0^2 - \omega^2 + j\omega R/L} \tag{16.30}$$

$$\alpha_{xx}^{ee} = \alpha_{yy}^{ee} = \varepsilon_0 \frac{16}{3} r_{\text{ext}}\,, \tag{16.31}$$

where the sign in Equation 16.29 depends on the helicity of the Ch-SRR.

From Equations 16.28 through 16.30 it follows that

$$\alpha_{zz}^{mm} \alpha_{zz}^{ee} + \left(\alpha_{zz}^{em}\right)^2 = 0\,, \tag{16.32}$$

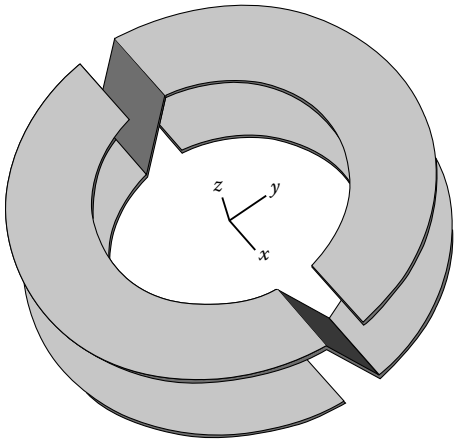

FIGURE 16.6 Chiral-SRR (Ch-SRR). The substrate has been removed for a better understanding of the configuration. In practice, besides the substrate between the rings, the connections can be substituted by holes.

which is a general property arising from the *LC* nature of the model [16]. In order to obtain metamaterials with wider left-handed bandwidths, it is convenient a balanced design for the particle [19]:

$$\alpha_0^{ee} = \mu_0 \varepsilon_0 \alpha_0^{mm}. \tag{16.33}$$

This condition is satisfied provided

$$t\lambda_0 = \frac{C_{\text{pul}}}{C_{0,\text{pul}}} (\pi r)^2, \tag{16.34}$$

where λ_0 is the wavelength at the resonance.

16.6 Spirals and Helices

Spirals are well-known designs, widely used in planar microwave circuits as small-size inductors and resonators. They have also been succesfully used for metamaterial design [20]. The frequency of resonance of a two-turns spiral is approximately half the frequency of resonance of an NB-SRR or SRR of the same size, and further reduction in the frequency of resonance can be achieved by adding more turns to the spiral [20]. Therefore, spiral resonators can provide an useful alternative to SRRs if smaller electrical sizes are required. However, spirals are low-symmetry structures and, in particular, they do not show inversion symmetry. Therefore, in spite of the fact that a quasi-static analysis does not predict them, bianisotropy and other cross-polarization effects can be present in metamaterials made from spiral resonators. This fact has been confirmed by experiments [21] and may preclude the use of spirals as metamaterial elements if these effects are not desired. Moreover, the reduction in the electrical size achieved by spiral resonators is not comparable with the reduction that can be obtained from the BC-SRR already analyzed in Section 16.3.

The broadside-coupled version of the two-turns spiral is the quasi-planar helix analyzed in [17,19]. This design is obviously a chiral particle, so as a racemic and a bi-isotropic mixture of these particles can provide a negative refractive index metamaterial [17,19]. In fact, the diagonal terms of the polarizability tensors of this design show a behavior very similar to that reported in Section 16.5 for the Ch-SRR [19]. However, owing to its low symmetry, the polarizability tensors of the helix are not diagonal.

16.7 Complementary SRRs

The complementary SRR (CSRR), shown in Figure 16.7, is the complementary screen [11] of the SRRs. Babinet principle [11] imposes the condition that the behavior of SRRs and CSRRs must be approximately dual (small deviations from this duality may arise from the effects of the dielectric substrate on which the SRR and the CSRR are printed). We have already shown in Section 16.4 that, in the most general case, when it is illuminated by some external fields $\mathbf{E}^0$, $\mathbf{B}^0$, a single SRR shows a set of electric and magnetic dipolar moments given by

$$m_z = \alpha_{zz}^{mm} B_z^0 - \alpha_{yz}^{em} E_y^0 \tag{16.35}$$

$$p_y = \alpha_{yy}^{ee} E_y^0 + \alpha_{yz}^{em} B_z^0, \tag{16.36}$$

$$p_x = \alpha_{xx}^{ee} E_x^0, \tag{16.37}$$

where the polarizabilities in Equations 16.35 and 16.36 are given by Equations 16.24 through 16.27. The effect of an incident electromagnetic field on a single SRR is illustrated in Figure 16.8a. The magnetic and electric dipolar moments (Equations 16.35 through 16.37) are generated in the SRR, and they

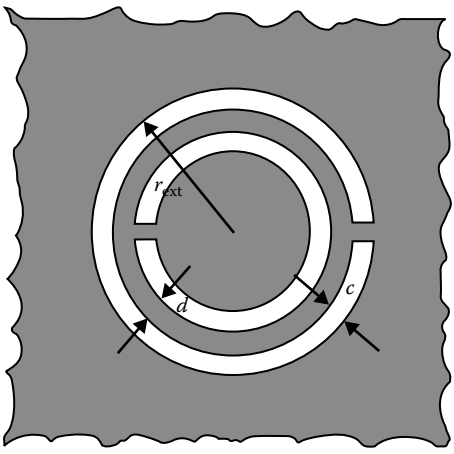

FIGURE 16.7 Complementary SRR (CSRR).

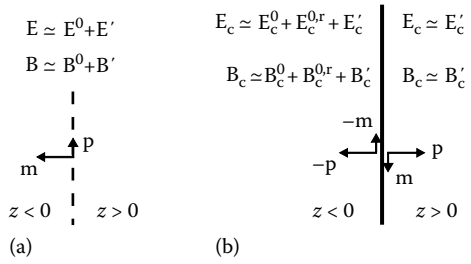

FIGURE 16.8 Illustration of the behavior of an SRR (a) and a CSRR (b) when they are illuminated by an external field $\mathbf{E}^0$; $\mathbf{B}^0$ (a) or $\mathbf{E}_c^0 = c\mathbf{B}^0$; $\mathbf{B}_c^0 = -(1/c)\mathbf{E}^0$ (b) incident from $z < 0$.

produce the scattered fields $\mathbf{E}'$ and $\mathbf{B}'$. The total fields are the superposition of the incident and the scattered fields. Let us consider the complementary screen, that is, the complementary resonator (CSRR). If the screen is a perfect conductor of negligible thickness, and the effects of the dielectric substrate are ignored (or it has a negligible dielectric susceptibility), the behavior of this CSRR can be deduced from classical diffraction theory and the Babinet principle [11]. The CSRR behavior when it is illuminated by the complementary fields is as follows:

$$\mathbf{E}_c^0 = c\mathbf{B}^0; \quad \mathbf{B}_c^0 = -(1/c)\mathbf{E}^0, \tag{16.38}$$

where c is the velocity of light in vacuum, incident from the left ($z < 0$) as illustrated in Figure 16.8b. At the right-hand side of the screen ($z > 0$), the fields are those produced by the electric and magnetic dipoles **m** and **p**. These electric and magnetic dipoles are given by

$$p_z = \beta_{zz}^{ee} E_z^0 - \beta_{yz}^{em} B_y^0 \tag{16.39}$$

$$m_y = \beta_{yy}^{mm} B_y^0 + \beta_{yz}^{em} E_z^0 \tag{16.40}$$

$$m_x = \beta_{xx}^{mm} B_x^0, \tag{16.41}$$

where, from the Babinet principle [11] and from the well-known expressions for the electromagnetic fields of the electric and magnetic dipoles, it follows that [22]

$$\beta_{xx}^{mm} = -c^2 \alpha_{xx}^{ee} \tag{16.42}$$

$$\beta_{yy}^{mm} = -c^2 \alpha_{yy}^{ee} \tag{16.43}$$

$$\beta_{yz}^{em} = -\alpha_{yz}^{em} \tag{16.44}$$

$$\beta_{zz}^{ee} = -\frac{1}{c^2} \alpha_{zz}^{mm}. \tag{16.45}$$

According to the diffraction theory [11], the fields at the left-hand side of the screen ($z < 0$) are the superposition of the incident field (Equation 16.38), the field that would be reflected by a perfect metallic screen at $z = 0$ ($\mathbf{E}_c^{0,r}$, $\mathbf{B}_c^{0,r}$), and the field created by some magnetic and electric dipoles, which are the opposite of Equations 16.39 through 16.41. Note that this change of sign for the induced dipoles at the right- and left-hand sides of the screen ensures that both the total magnetic polarization parallel to the screen and the total electric polarization perpendicular to the screen vanish, as it must be for a plane screen. Therefore, CSRRs will not be useful for three-dimensional negative-ε metamaterial design. However, CSRRs and related geometries (such as the complementary of the NB-SRR) can be useful for the design of one- and two-dimensional negative-ε metamaterials [4]. They can be also useful for the design of planar frequency-selective surfaces [4,22]. When the effect of the dielectric circuit board that supports the SRR and the CSRR is not neglected, Equations 16.42 through 16.45 are only approximate, although the qualitative behavior of the CSRR still remains the same. The main quantitative difference between Equations 16.42 through 16.45 and the actual CSRR behavior is a small change in the frequency of resonance, which can be obtained from the equivalent circuit models reported in [7].

16.8 SRR Behavior at Infrared and Optical Frequencies

At infrared and optical frequencies metals cannot be characterized as good conductors but as lossy solid-state plasmas, with a complex dielectric permeability of negative real part. This complex permittivity is given by

$$\hat{\varepsilon} = \varepsilon_0 \left(1 - \frac{\omega_p^2}{\omega(\omega - j f_c)}\right), \tag{16.46}$$

where

ω_p is the plasma frequency
f_c is the collision frequency of the electrons

Near the plasma frequency, which for most metals is in the ultraviolet, it is $|\varepsilon|/\varepsilon_0 \sim 1$, and the analysis of the electromagnetic behavior of SRRs becomes a very complex electromagnetic problem. However, at infrared and, in many cases, also at optical frequencies, most metals satisfy the inequalities $|\varepsilon|/\varepsilon_0 \gg 1$ and $|\mathrm{Re}(\varepsilon)| \gg |\mathrm{Im}(\varepsilon)$ [23]. When these conditions are satisfied, it is still possible to develop a circuit model for the SRR, similar to that devoloped in the previous sections [5,24]. Now we consider the simplified SRR geometry shown in Figure 16.9, which is probably the simpler SRR configuration invariant by inversion. However, the analysis developed in this section can be applied to many other similar configurations. If $|\varepsilon|/\varepsilon_0 \gg 1$ (Equation 16.46) can be approximated as

$$\hat{\varepsilon} \simeq -\varepsilon_0 \frac{\omega_p^2}{\omega(\omega - j f_c)}. \tag{16.47}$$

Also, from the continuity of the normal component of $j\omega\hat{\varepsilon}\mathbf{E}$ at the metal–air interface, it directly follows that $\mathbf{n} \cdot \mathbf{E}_{SRR} \approx 0$, where $\mathbf{E}_{SRR}$ is the electric field inside the SRR and $\mathbf{n}$ the unit vector normal to the SRR boundary. Thus, the electric lines of force are strongly confined inside the SRR, forming

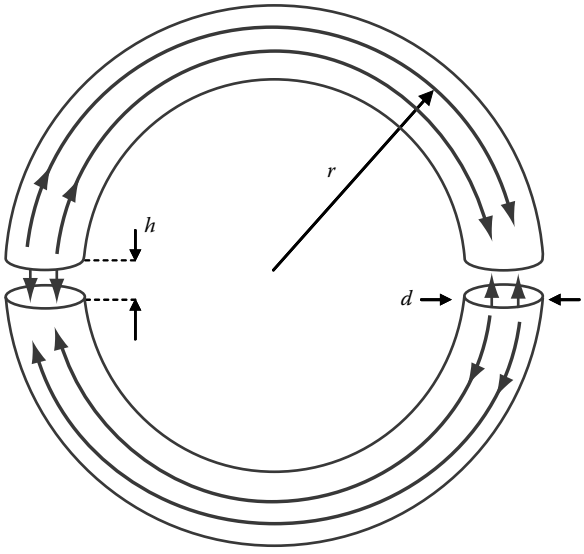

FIGURE 16.9 Split ring resonator made from a wire with two capacitive gaps, the simpler SRR configuration with inversion symmetry. The electric field lines of force at infrared/optical frequencies are also sketched. Note the field confinement in the SRR and the change of sign of the electric field in the gap, due to the change of sign in the permittivity.

closed loops, as illustrated in Figure 16.9. Therefore, it makes sense to define a *total* current inside the ring as

$$I_t = j\omega\hat{\varepsilon}E_{SRR}\,S\,, \tag{16.48}$$

where S is the SRR wire section. This current includes both ohmic and displacement currents and is approximately uniform along the SRR. Therefore, it is still possible to define the ring magnetic inductance, L_m, as usual, i.e.,

$$L_m \equiv \frac{\Phi(I_t)}{I_t}\,, \tag{16.49}$$

where $\Phi(I_t)$ is the magnetic flux across the ring. Since the magnetic flux is related to the total current through Ampère's law, L_m is approximately given by [10]

$$L_m = \mu_0 r\left[\ln\left(\frac{16d}{r}\right) - \frac{7}{4}\right], \tag{16.50}$$

where

r is the SRR radius
d is the diameter of the wire

Taking into account Equations 16.47 and 16.48, the electromotive force around the ring $\mathcal{E} = \oint \mathbf{E}\,d\mathbf{l} \simeq 2\pi r E_r$ can be written as [24]

$$\mathcal{E} \simeq \left(\frac{1}{j\omega C} + R + j\omega L_k\right) I_t\,, \tag{16.51}$$

where
C is the total capacitance provided by the series connection of the gaps (i.e., $C = C_g/2$, where C_g is the capacitance of each gap)
R is the ohmic resistance of the SRR

$$R = \frac{2\pi r f_c}{S\omega_p^2 \varepsilon_0}, \tag{16.52}$$

L_k is a magnitude with dimensions of inductance given by

$$L_k = \frac{2\pi r}{S\omega_p^2 \varepsilon_0}. \tag{16.53}$$

This inductance can be interpreted as caused by the kinetic energy of the electrons [25]. Therefore, the final equation for the current I_t on the ring is

$$\left\{\frac{1}{j\omega C} + R + j\omega(L_m + L_k)\right\} I_t = -j\omega\pi r^2 B_z^{ext}, \tag{16.54}$$

where B_z^{ext} is the external magnetic field. Therefore, as far as $|\varepsilon|/\varepsilon_0 \gg 1$ and $|\mathrm{Re}(\varepsilon)| \gg |\mathrm{Im}(\varepsilon)$, the SRR can still be described by the equivalent circuit shown in Figure 16.3.a, provided the kinetic inductance L_k is added to the magnetic inductance L_m [24]. From Equations 16.50 and 16.53, it follows that [5]

$$\frac{L_m}{L_k} \sim \frac{2\pi S}{\lambda_p^2}, \tag{16.55}$$

where $\lambda_p = 2\pi c/\omega_p$ is the plasma wavelength, i.e., the free-space wavelength at the plasma frequency. In particular, the magnetic polarizability of the ring is

$$\alpha_{zz}^{mm} = \alpha_0 \left(\frac{\omega^2}{\omega_0^2 - \omega^2 + j\omega\gamma}\right); \quad \alpha_0 = \frac{\pi^2 r^4}{L_m + L_k}, \tag{16.56}$$

where
$\omega_0 = \sqrt{1/(L_m + L_k)C}$ is the frequency of resonance
$\gamma = R/(L_m + L_k)$.

This equation differs from Equation 16.10 only by the presence of the kinetic inductance L_k.
Let us now consider the behavior of the SRR polarizability (Equation 16.56) when the SRR is scaled down to increase its frequency of resonance without changing its electrical size. Since according to Equation 16.53 L_k scales as $L_k \propto 1/r$, for small SRR sizes it dominates over L_m, which scales as $L_m \propto r$. On the other hand, C scales as $C \propto r$. Therefore, for sufficiently small ring sizes $L_k \gg L_m$, the frequency of resonance saturates [25] to the value

$$\omega_0 = \sqrt{\frac{1}{L_k C}}, \tag{16.57}$$

which does not depend on the SRR size. Also, the loss factor saturates to

$$\gamma_s = \frac{R}{L_k} = f_c. \tag{16.58}$$

Finally, the amplitude of the magnetic polarizability scales down as [24]

$$\alpha_0 \to \frac{\pi^2 r^4}{L_k} = \omega_p^2 \varepsilon_0 r^3 S \propto r^5. \tag{16.59}$$

Since the magnetic susceptibility of a bulk metamaterial is proportional to the polarizability and to the specific volume per particle $V_{SRR} \propto r^{-3}$, Equation 16.59 implies that the amplitude of the magnetic susceptibility scales down as r^2. The above discussion shows that scaling down SRR media to achieve a negative magnetic permeability at infrared and optical frequencies has two main limitations: saturation of frequency of resonance and decrease in the magnetic response.* Such effects appear when the key parameter S/λ_p^2 becomes small, which, according to Equation 16.55, makes the kinetic inductance dominant over the magnetic one.

16.9 Synthesis of Metamaterials and Other Applications of SRRs

SRRs have been succesfully used as magnetic metamaterial elements at microwave frequencies. Combined with wires [26,27] or with metallic waveguides [28] or plates [29], they provide left-handed effective media in one, two, and three dimensions. Usually, the well-known Lorentz local field theory provides adequate homogenization formulae for magnetic SRR media [30]. In [5] explicit expressions for the computation of metamaterial parameters in some relevant cases are given. These expressions make use of the polarizabilities developed in the previous sections, combined with Lorentz local field theory. It must be stressed that, in general, SRR-based magnetic metamaterials are bianisotropic media [28], thus showing the most general linear constitutive relations:

$$\mathbf{D} \equiv \varepsilon_0 \mathbf{E} + \mathbf{P} = \varepsilon_0 \left(1 + \bar{\bar{\chi}}_e\right) \cdot \mathbf{E} + j\sqrt{\varepsilon_0 \mu_0}\, \bar{\bar{\kappa}} \cdot \mathbf{H} \tag{16.60}$$

$$\mathbf{B} \equiv \mu_0 (\mathbf{H} + \mathbf{M}) = -j\sqrt{\varepsilon_0 \mu_0}\, (\bar{\bar{\kappa}})^T \cdot \mathbf{E} + \mu_0 \left(1 + \bar{\bar{\chi}}_m\right) \cdot \mathbf{H}\,. \tag{16.61}$$

Nevertheless, SRRs can be arranged to provide small magnetic resonators with an isotropic response [14], thus opening the way to the design of isotropic magnetic effective media with negative permeability. When combined with conventional transmission lines, SRRs provide one- and two-dimensional metamaterials with negative parameters, including left-handed transmission line metamaterials [31]. As already mentioned, unlike SRRs, CSRRs do not provide a net polarizability in three dimensions. Therefore, they are not useful for the design of bulk three-dimensional metamaterials. However, they are useful for the design of one- and two-dimensional structures with negative electric permittivity. In particular, when combined with conventional planar transmission lines they provide effective negative-ε and left-handed metamaterials [4]. An alternative and interesting path to the design of negative refractive index metamaterials is the use of racemic and bi-isotropic mixtures of chiral SRRs and other related geometries (Sections 16.5 and 16.6). This possibility has been theoretically explored in [17,19]. The most relevant advantage of such designs is that negative refraction can be obtained in metamaterials made from a single kind of inclusion. Wide negative refractive index bandwidth and good matching to free space are additional advantages of bi-isotropic mixtures of chiral SRRs [19].

The equivalent circuits of SRRs and CSRRs coupled to microwave transmission lines have been developed in [7], opening the way for the design of miniaturized planar microwave circuit components, such as filters, couplers, diplexers, and controllable transmission lines, as well as antennas and other microwave devices (see [5] and references therein). Linear chains of SRRs, as well as two- and three-dimensional SRR arrays support magneto-inductive waves [32], which are useful for the design of miniaturized slow-wave waveguides [33], delay lines [34], and superlenses [35]. Electro-inductive waves are also supported by chains of CSRRs etched on metallic plates [36]. Two-dimensional arrays of SRRs and CSRRs show promising frequency and polarization-selective characteristics [22], which

* In the RF and microwave range, however, since L_m scales down as r, the amplitude of the magnetic polarizability scales down as r^3, and the amplitue of the magnetic susceptibility does not vary substantially when the structure is scaled down.

can be useful for the design of frequency-selective surfaces, radomes, and polarization converters. The resonant magnetic activity of SRRs has also been detected at terahertz and infrared frequencies [37,38]. However, practical applications of SRRs at infrared and optical frequencies are limited by the considerations made in Section 16.8.

16.10 Conclusion

SRRs provide a simple and effective way for designing magnetic metamaterials with negative parameters. At microwave and millimeter wave frequencies they can be effectively characterized by a quasi-static *LC* circuit model which provides analytical expressions for the SRR first frequency of resonance and polarizabilities. This analysis can be extended to other related topologies, including complementary (CSRRs) and chiral (Ch-SRRs) configurations. Although SRRs are highly anisotropic configurations (actually bianisotropic in most cases), isotropic arrangements of SRRs can be designed to develop three-dimensional magnetic metamaterials with an isotropic response. SRRs and related topologies can be combined with conventional transmission lines to provide negative-ϵ, negative-μ, and left-handed transmission line metamaterials with interesting applications in microwave technology. Other SRR applications may come from the ability of SRR arrays of guiding magneto-inductive slow waves and from the frequency and polarization selectivity of SRR and CSRR arrays. Finally, the behavior of SRRs at infrared and optical frequencies can be obtained from a straightforward extension of the aforementioned *LC* circuit model. The main effects at these frequencies are the saturation in the SRR frequency of resonance and a strong decrease in the SRR magnetic response. These effects appear when the SRR wire/strip section approaches the square of the plasma wavelength.

Acknowledgments

This work has been partially supported by the Spanish Ministry of Science and Education under contract projects TEC2007-68013-C02-01 and TEC2007-68013-C02-02 as well as by Junta de Andalucia under contract project P06-TIC-01368 and by Generalitat de Catalunya under project contract SGR2005-0624. Authors are in debted to people from the Microwave Group of the University of Sevilla and the GEMMA Group and CIMITEC of the Universitat Autònoma de Barcelona for many hours of helpful discussions and joint research on this topic.

References

1. W. Weber, On the relationship of the science of the diamagnetism with the sciences of magnetism and electricity, *Ann. Phys*., 87, 145–189, 1852.
2. S.A. Shelkunoff and H.T. Friis, *Antennas. Theory and Practice*. John Wiley & Sons, New York, 1952.
3. J.B. Pendry, A.J. Holden, D.J. Robbins, and W.J. Stewart, Magnetism from conductors and enhanced nonlinear phenomena, *IEEE Trans. Microwave Theory Tech*., 47, 2075–2084, 1999.
4. F. Falcone, T. Lopetegi, M.A.G. Laso, J.D. Baena, J. Bonache, M. Beruete, R. Marqués, F. Martín, and M. Sorolla, Babinet principle applied to metasurface and metamaterial design, *Phys. Rev. Lett*., 93, paper 197401, 2004.
5. R. Marquś, F. Martín, and M. Sorolla, *Metamaterials with Negative Parameters. Theory, Design and Microwave Applications*. Wiley, Hoboken, NJ, 2008.
6. R. Marqués, J.D. Baena, J. Martel, F. Medina, F. Falcone, M. Sorolla, and F. Martín, Novel small resonant electromagnetic particles for metamaterial and filter design, *Proc. ICEAA'03*, pp. 439–442, Torino, Italy, 2003.

7. J.D. Baena, J. Bonache, F. Martín, R. Marqués, F. Falcone, T. Lopetegi, M.A.G. Laso, J. García-García, I. Gil, M. Flores, and M. Sorolla, Equivalent circuit models for split rings resonators and complementary split rings resonators coupled to planar transmission lines, *IEEE Trans. Microwave Theory Tech*., 53, 1451–1461, 2005.
8. R. Marqués, F. Mesa, J. Martel, and F. Medina, Comparative analysis of edge and broadside coupled split ring resonators for metamaterial design. Theory and experiment, *IEEE Trans. Antennas Propagat*., 51, 2572–2581, 2003.
9. M. Shamonin, E. Shamonina, V. Kalinin, and L. Solymar, Resonant frequencies of a split-ring resonator: analytical solutions and numerical simulations, *Microwave Opt. Technol. Lett.*, 44, 133–137, 2005.
10. L.D. Landau, E.M. Lifshitz, and L.P. Pitaevskii, *Electrodynamics of Continuous Media*. Pergamon, New York, 1984.
11. J.D. Jackson, *Classical Electrodynamics*. Wiley, New York, 1999 (3rd. ed.).
12. J. García-García, F. Martín, J.D. Baena, R. Marqués, and L. Jelinek, On the resonances and polarizabilities of split ring resonators, *J. Appl. Phys.*, 98, paper 033103, 2005.
13. R. Marqués, F. Medina, and R. Rafii-El-Idrissi, Role of bianisotropy in negative permeability and left handed metamaterials, *Phys. Rev. B*, 65, paper 144441, 2002.
14. J.D. Baena, L. Jelinek, R. Marqués, and J. Zehentner, Electrically small isotropic three-dimensional magnetic resonators for metamaterial design, *Appl. Phys. Lett.*, 88, paper 134108, 2006.
15. S.A. Tretyakov, *Analytical Modelling in Applied Electromagnetics*, Artech House, Norwood, MA, 2003.
16. S.A. Tretyakov, A. Sihvola, and L. Jylh, Backward-wave regime and negative refraction in chiral composites, *Photonics Nanostruct. Fund. Appl.*, 3, 107–115, 2005.
17. R. Marqués, F. Mesa, and L. Jelinek, Negative refraction from balanced quasi-planar chiral inclusions, *Microwave Opt. Technol. Lett.*, 49, 2006–2009, 2006.
18. J.B. Pendry, A chiral route to negative refraction *Science*, 306, 1353–1355, 2004.
19. R. Marqués, F. Mesa, L. Jelinek, and J.D. Baena, Balanced right/left-handed mixtures of quasi-planar chiral inclusions *Proceedings of Metamaterials 2007 Conferences*, pp. 214–217, 22–24 October 2007, Rome, Italy.
20. J.D. Baena, R. Marqués, F. Medina, and J. Martel, Artificial magnetic metamaterial design by using spiral resonators, *Phys. Rev. B*, 69, paper 014402, 2004.
21. J.D. Baena. Private communication.
22. M. Beruete, M. Sorolla, R. Marqués, J.D. Baena, and M. Freire, Resonance and cross-polarization effects in conventional and complemenmtary split ring resonator periodic screens, *Electromagnetics*, 26, 247–260, 2006.
23. M.A. Ordal, L.L. Long, R.J. Bell, S.E. Bell, R.R. Bell, R.W. Alexander Jr., and C.A. Ward, Optical properties of the metals Al, Co, Cu, Au, Fe, Pb, Ni, Pd, Pt, Ag, Ti, and W in the infrared and far infrared, *Appl. Optica*, 22, 1099–1120, 1983.
24. R. Marqués and M.J. Freire, On the usefulness of Split Ring Resonators for magnetic metamaterial design at infrared and optical frequencies, *Proceedings of the 13th IEEE Mediterranean Electrochemical Conference (MELECON 2006)*, pp. 122–124. May 16–19, Benalmádena (Málaga), Spain, 2006.
25. J. Zhou, Th. Koschny, M. Kafesaki, E.N. Economou, J.B. Pendry, C.M. Soukoulis, Saturation of the magnetic response of split ring resonators at optical frequencies, *Phys. Rev. Lett.*, 95, paper 223902, 2005.
26. D.R. Smith, W.J. Padilla, D.C. Vier, S.C. Nemat-Nasser, and S. Schultz, Composite medium with simultaneously negative permeability and permittivity, *Phys. Rev. Lett.*, 84, 4184–4187, 2000.
27. R.A. Shelby, D.R. Smith, and S. Schultz, Experimental verification of a negative index of refraction, *Science*, 292, 77–79, 2001.
28. R. Marqués, J. Martel, F. Mesa, and F. Medina, Left-handed-media simulation and transmission of EM waves in subwavelength split-ring-resonator-loaded metallic waveguides, *Phys. Rev. Lett.*, 89, paper 183901, 2002.

29. R. Marqués, J. Martel, F. Mesa, F. Medina, A new 2D isotropic left-handed metamaterial design: Theory and experiment, *Microwave Opt. Technol. Lett.*, 35, 405–4088, 2002.
30. J.D. Baena, R. Marqués, J. Martel, F. Medina, Experimental results on metamaterial simulation using SRR-loaded waveguides, *Proceedings of the IEEE-AP/S International Symposium on Antennas and Propagation*, Columbus, OH, pp. 106–109, 2003.
31. F. Martín, J. Bonache, F. Falcone, M. Sorolla, R. Marqués, Split ring resonator-based left-handed coplanar waveguide, *Appl. Phys. Lett.*, 83, 4652–4654, 2003.
32. E. Shamonina, V.A. Kalinin, K.H. Ringhofer, L. Solymar, Magneto-inductive waves in one, two and three dimensions, *J. Appl. Phys.*, 92, 6252–6261, 2002.
33. E. Shamonina, L. Solymar Magneto-inductive waves supported by metamaterials elements: Components for a one-dimensional waveguide, *J. Phys. D: Appl. Phys.*, 37, 362–367, 2004.
34. M.J. Freire, R. Marqués, F. Medina, M.A.G. Laso, F. Martin, Planar magnetoinductive wave transducers: Theory and applications, *Appl. Phys. Lett.*, 85, 4439–4441, 2004
35. M.J. Freire, R. Marqués, Planar magnetoinductive lens for three-dimensional subwavelength imaging, *Appl. Phys. Lett.*, 86, paper 182505, 2005.
36. M. Beruete, F. Falcone, M.J. Freire, R. Marqués, J.D. Baena, Electroinductive waves in chains of complementary metamaterial elements, *Appl. Phys. Lett.*, 88, paper 083503, 2006.
37. T.J. Yen, W.J. Padilla, N. Fang, D.C. Vier, D.R. Smith, J.B. Pendry, D.N. Basov, X. Zhang, Terahertz magnetic response from artificial materials, *Science*, 303, 1494–1496, 2004.
38. S. Linden, C. Enkrich, M. Wegener, J. Zhou, T. Koschny, C.M. Soukoulis, Magnetic response of metamaterials at 100 terahertz, *Science*, 306, 1351–1353, 2004.

17

Designing One-, Two-, and Three-Dimensional Left-Handed Materials

Maria Kafesaki
Foundation for Research and Technology Hellas (FORTH)

Th. Koschny
Iowa State University and Foundation for Research and Technology Hellas (Forth)

C. M. Soukoulis
Iowa State University, FORTH, and University of Crete

E. N. Economou
Foundation for Research and Technology Hellas and University of Crete

17.1 Introduction

Left-handed materials (LHMs) or negative index materials (NIMs), i.e., materials with simultaneously negative electrical permittivity, ε, and magnetic permeability, μ, and therefore negative index of refraction, n^*, (over a common frequency range) have received considerable attention over the last years; this is mainly due to their novel and unique properties, which provide a huge potential and novel capabilities in the manipulation of electromagnetic waves (for recent reviews see [1,2]). These properties include backward propagation (i.e., opposite phase and energy velocities), negative

* The negative real part of n results by requiring a positive imaginary part, i.e., an attenuated rather than an exponentially growing wave $e^{i(\omega/c)nz}$, where z is the propagation direction.

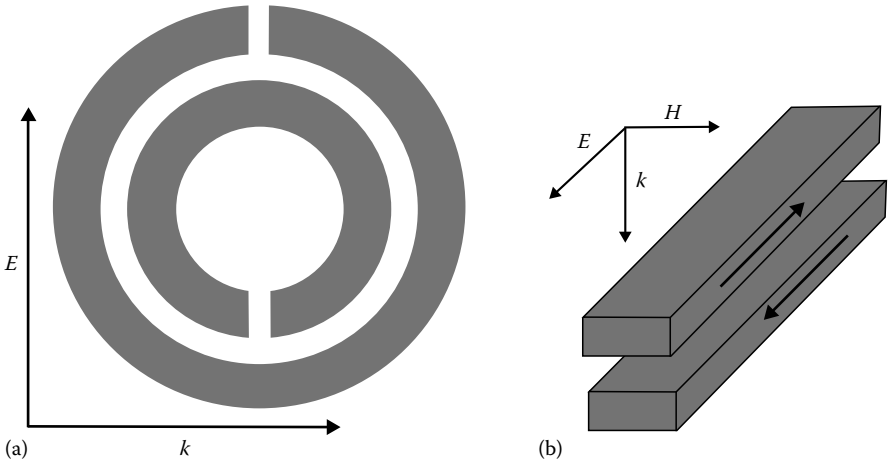

FIGURE 17.1 Two of the major designs employed for the achievement of negative permeability response: the SRR (a) and the pair of slabs (b). The SRR design of panel (a) is the original design proposed by Pendry et al. The figure shows also the direction of the incident electromagnetic field which excites the negative permeability response in the designs shown.

refraction, reversed Doppler effect; and Cherenkov radiation, evanescent wave amplification [3], etc.; and open new ways in applications such as imaging, lithography, antenna systems, transmission lines, and various microwave components and devices, etc.

Although many of the theoretical capabilities of LHMs have been described long ago [4], the first practical implementation of an LHM came only in 2000 [5], by Smith et al., following ideas by Sir J. Pendry et al. [6,7]; this first LHM was a periodic combination of metallic rings with gaps (see Figure 17.1a), known as split-ring resonators (SRRs), providing negative permeability [7], and continuous wires, providing negative permittivity [6].

Since Smith's demonstration of the first LHM, several left-handed (LH) structures have been demonstrated (see e.g., [8–10]), most of them being combinations of SRRs and wires, operating in the microwave regime, and intensive efforts to understand their behavior, to optimize them (as to achieve a wide LH band with high transmittance), and to raise their frequency of operation were carried out. Moreover, alternative ways to achieve LH behavior were investigated, such as employing photonic crystals [11], chiral media [12], polaritonic media [13], etc.

Although some of those ways look promising and constitute a subject of intense further investigations, still the most common way to achieve LH behavior is to follow Smith's approach of combining resonant permeability elements (for the achievement of negative permeability response), such as SRRs, with negative permittivity elements, such as thin metallic wires.

The resonant permeability elements are all characterized by the generation of resonant loop-like currents, under the influence of an external alternating magnetic field. These loop currents lead to a resonant magnetic dipole moment and thus to a resonant permeability in a collection of such "magnetic dipoles," which has the form [2,7]

$$\mu = \mu_0 \left(1 - \frac{F\omega^2}{\omega^2 - \omega_m^2 + i\omega\gamma_m}\right), \tag{17.1}$$

where

ω_m is the frequency of the magnetic resonance,

γ_m is a factor representing the losses,

the parameter F, determining the strength of the magnetic resonance and the width of the negative permeability regime, is a geometrical factor that is approximately equal to the volume fraction of the loop-current element within the system unit cell.

Since the loop-current element is a resonant electromagnetic system, it is very often described as an inductor–capacitor (LC) circuit, with the frequency ω_m given as $\omega_m = 1/\sqrt{LC}$.

The resonant permeability (loop-current) elements that have received most attention up to now are the SRR (of various designs—the original (Pendry's) one is shown in Figure 17.1a) and the slab-pair design [14,15], i.e., a pair of two parallel slabs (or stripes or wires), like the one shown in Figure 17.1b. This slab pair is characterized by a resonant current mode with antiparallel currents in the two slabs of the pair, which generate a resonant magnetic moment, thus making the pair to behave like an SRR (it can be seen as a modification of a single-ring SRR with two gaps). The slab-pair design presents certain advantages compared with the SRR (see Section 17.6), especially in small-length-scale structures aimed to give THz and/or optical LHMs.

Concerning the negative permittivity structures, the most common one is the periodic system of thin metallic wires. Thin metallic wires behave as a dilute free electron plasma (whose kinetic energy is greatly enhanced by the addition of the magnetic energy), described by a Drude type ε, of the form (in lossless case)

$$\varepsilon = \varepsilon_0 \left(1 - \frac{\omega_p^2}{\omega^2}\right), \tag{17.2}$$

which is characterized by a broad negative regime terminated at a reduced plasma frequency [6], ω_p. ω_p depends on the geometrical system parameters, namely the cross-section of the wires and the periodicity of the medium. For mm scale wires the frequency $f_p = \omega_p/2\pi$ falls in the few GHz regime.

Although there are additional negative permittivity elements that have been proposed in the literature (e.g., see [16]), in most of them the negative permittivity results from a Lorentz-type permittivity resonance. Thus they are characterized by a narrow negative ε band and relatively high losses. Therefore, the thin continuous wires still remain the optimum negative permittivity component for the creation of left-handed materials.

Since both SRRs and metallic wires have been described in detail elsewhere in this handbook (see, e.g., Chapters 15 and 16), we do not proceed here to a detailed analysis of their properties; we comment only on the aspects of their behavior that are essential for their use as components of LHMs, which is the central topic of this chapter.

Specifically, in this chapter we discuss some of our efforts to understand the behavior of metamaterials composed of SRRs and wires, slab pairs, and slab pairs and wires (in both GHz and optical regimes) and to arrive at conditions for the achievement of optimized LHMs, both planar and two dimensional (2D) or three dimensional (3D), employing those structures. The properties of the different media discussed here have been examined and analyzed by transmission (T) and reflection (R) simulations and/or measurements and, when required, by inversion of the transmission and reflection data to obtain the effective material parameters ε, μ, refractive index, n, and impedance, $z = \sqrt{\mu/\varepsilon}$. For the inversion of the R/T data the standard retrieval procedure [17] has been employed, which treats a metamaterial as a homogeneous effective medium.

The chapter is organized as follows: In Section 17.2 we examine the conditions to achieve LH behavior in combined systems of SRRs and wires; in addition, we present some considerations related to the presence of SRR asymmetries or with the resonant electric, dipole-like SRR response. We also present a criterion to unambiguously identify the LH regimes in SRRs and wire transmission spectra, which is based on the above considerations. Employing the results described in Section 17.2, we examine in Section 17.3 the conditions for the achievement of a homogeneous-like, 3D LH material employing SRRs and wires, and we propose SRR designs appropriate for the

achievement of 3D LHMs. We note here that many of the proposed applications of LHMs (especially superlensing applications) require 3D isotropic, homogeneous-like structures.

Since many of the conclusions of our study have been obtained through the retrieval procedure based on the homogeneous effective medium (HEM) approach, which is fully justified if the characteristic units of the structures are of deep subwavelength scale, a condition that is not always fulfilled in the SRRs and wire media (and even less in slab pairs and wires media), we comment on the applicability of this approach in Section 17.4. Specifically, we discuss the artifacts appearing in the form of the HEM-obtained effective $\varepsilon(\omega)$ and $\mu(\omega)$ due to the influence of the periodicity; these artifacts have been analyzed and understood mainly by comparing the HEM results with those of a periodic effective medium approach.

Finally, closing the first part of this chapter, which concerns SRR-based LHMs, we discuss in Section 17.5 the possibility to achieve optical SRR-based LH materials and the frequency limitations of the LH behavior in SRR systems.

One of the most common approaches for obtaining optical LH materials is scaling-down known LH microwave designs. SRRs, though, do not offer an optimized solution in that respect due to the fact that negative permeability response requires in-plane propagation and thus multistack SRR samples. A better solution is offered by the slab-pair design, which exhibits a negative permeability response for incidence normal to the plane of the pairs. For that reason, in the second part of this chapter we discuss slab pairs and slab-pair-based LH materials, mostly in microwaves but also in THz and optical frequencies. In Section 17.6 we discuss the possibility to obtain LH behavior using only slab pairs and exploiting the simultaneous presence of resonant magnetic and resonant electric response in the pair at neighboring frequencies. In Section 17.7 we examine LH materials based on slab pairs and continuous wires, emphasizing the so-called fishnet design, i.e., wide slab pairs, connected with wires. Finally, in Section 17.8 we discuss the properties of the slab-pair-based designs as the designs are scaled down to give optical LHMs.

17.2 One-Dimensional Microwave Left-Handed Materials Employing SRRs and Wires

Since in an LH material of SRRs and wires the major element for the achievement of negative μ it is the SRR while for the achievement of negative ε it is the wires, the only condition that was sought in the construction of the first and many of the subsequent LHMs was "the negative μ regime of the SRRs to be within the negative ε regime of the wires"; thus, the negative μ and ε regimes of the SRRs and wires, respectively, have been determined by measuring the transmission properties of the SRRs alone and of the wires alone (the lowest frequency dip in the SRR transmission spectra was considered as originating from a negative μ response, while the first transition from zero to high transmission in the wires system was considered as the transition from negative to positive ε response).

This approach does not provide any safe way to identify unambiguously the presence of negative μ and, moreover, it neglects any effects coming from the interaction of SRRs and wires or any additional effects that may result from the complexity (e.g., bianisotropy) of the SRR particles [18].

Such effects, which are discussed below, are (a) the influence of the electric dipole-like response of the SRRs on the effective ε of the SRR and wire systems, and (b) the effect of the SRR asymmetries on the LH behavior of an SRR and wire medium.

17.2.1 Electric Response of the SRRs and Its Role in the Electric Response of LHMs

SRRs have been widely studied and used up to now as magnetic elements. Apart from their magnetic response though, they also present a resonant electric-dipole-like response, such as all metallic

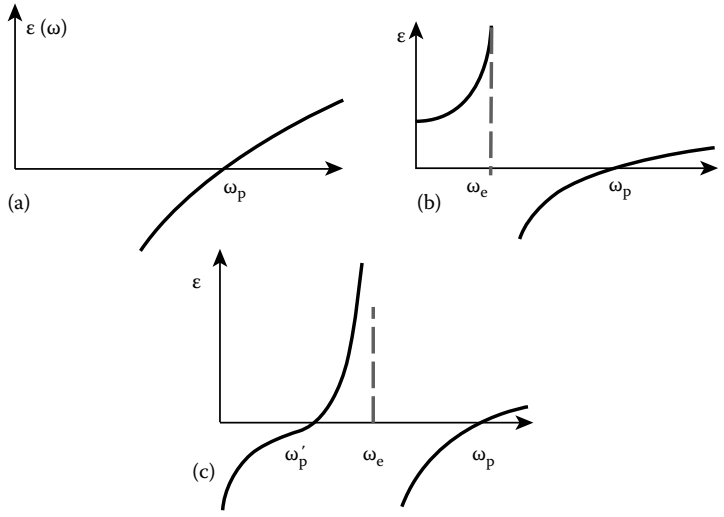

FIGURE 17.2 Frequency dependence of the effective permittivity, ε, of a system of infinitely long wire (a) (Drude-type response, characterized by a "plasma-like" frequency $\omega_p = \omega_{p-w}$), and of a system of lossless short wires or SRRs, (b) (Lorentz-type response, characterized by a resonance frequency ω_e and a "plasma-like" frequency $\omega_p = \omega_{p-SRR}$). In panel (c) the $\varepsilon(\omega)$ resulting from the addition of the ε of panels (a) and (b) is shown. Note that the new plasma frequency ω'_p is lower than the wires' plasma frequency, ω_{p-w}.

systems that are finite along the external electric field direction. This resonant electric response, which can be described with a Lorentz-type effective permittivity involving also negative permittivity values, is associated with strong homoparallel currents at the external electric field parallel to the (**E**) sides of the SRR.

In the cases where the magnetic response of the SRR is not in the deep sub-wavelength regime, like, e.g., in simple SRR designs or multigap SRRs, the electric response frequency of the SRR is not far above its magnetic resonance frequency and contributes to the low-frequency electric response of the combined system of SRRs and wires. Detailed studies of this contribution [19] have shown that the total effective ε of an SRR and wire medium is the one resulting from the addition of a Drude-like ε response (coming from the wires—see Figure 17.2a) with the a Lorentz-like ε response (coming from the SRRs—see Figure 17.2b) and has the form shown in Figure 17.2c.

The result of this addition that is more relevant for the construction of an LHM is a downward shift of the effective plasma frequency of the system, ω'_p, compared with that of only the wires, ω_p. This shift poses stringent requirements for the achievement of LH behavior: for an SRR and wire medium to be LH the magnetic SRR resonance frequency, ω_m, should lie not only below ω_p but also below the new cutoff frequency, ω'_p. (Note that if $\omega_p < \omega_m < \omega'_p$, a case very common in practical implementations, ignoring the SRR electric response and its effect, it may result in wrong identification of the character of the transmission peaks [20].)

Another observation of great practical importance is the following: By closing the gap/gaps of the SRR, its magnetic response is switched off (since the resonance of the loop-like currents is destroyed), but the electric SRR response is entirely preserved [2,19,21] (this is valid though only for SRRs with mirror symmetry with respect to the external electric field). Therefore, the closing of the SRR gaps can lead to the identification of both the negative μ and the negative ε regimes of an SRR system, as shown in Figure 17.3a, and also of an SRR and wire system, as shown in Figure 17.3b, offering hence an easy way to unambiguously identify the LH regimes. This way is extremely valuable in experimental studies, as it provides an easy to apply criterion to unambiguously conclude if a structure is LH or not.

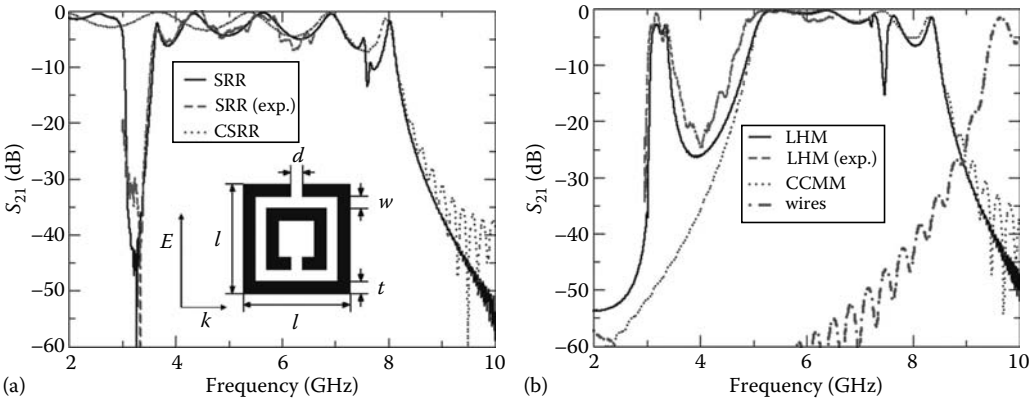

FIGURE 17.3 (a) Simulated (solid line) and measured (dashed line) transmission amplitude (S_{21}) of a 5-unit cell (uc) along propagation direction periodic arrangement of square SRRs. The dotted line shows the simulated S_{21} after closing the gaps of the SRRs. Notice that by closing the SRR gaps the dip at ~3 GHz disappears whereas the rest of the spectrum remains unaffected. This indicates that the ~3 GHz dip is magnetic in origin, whereas the dip after 8 GHz is due to negative ε behavior. (b) Simulated (solid line) and measured (dashed line) transmission (S_{21}) spectra of a left-handed material composed of SRRs (like the ones described in panel (a)) and wires, in a periodic arrangement (5 uc). The dotted line shows the S_{21} of the combined material of closed-SRRs and wires (CCMM) and the dotted-dashed line the S_{21} for the wires only. Notice than the plasma frequency of the CCMM (at ~5 GHz) is much lower than the plasma frequency of wires only, which is at ~9 GHz. Notice also that the only difference between the transmission of LHM and CCMM is the left-handed peak at ~3 GHz, showing that the CCMM carries all the electric response of the LHM. The geometrical parameters of the system are: uc size 8.8 × 8.8 × 6.5 mm^3, l = 7 mm, d = w =0.2 mm, t = 0.9 mm (see inset), metal depth = 30 μm, wires width = 0.9 mm. The SRRs and wires are printed on opposite sides of a FR-4 dielectric board of thickness 1.6 mm and ε = 2.8. The wires are placed symmetrically to the SRRs, along the imaginary line connecting the two SRR gaps. (From Kafesaki, M., Koschny, Th., Zhou, J., Katsarakis, N., Tsiapa, I., Economou, E.N., and Soukoulis, C.M., *Physica B*, 394, 148, 2007. With permission.)

17.2.2 Bianisotropy of SRR and Its Influence on the LH Behavior

Investigating the effect of the SRR orientation on the LH behavior of an SRR and wire system, for various SRR types [22,23], we found that another aspect of the electromagnetic response of the SRR, which is crucial for its ability to create LHMs, comes from its bianisotropy [18,24], which gives the possibility of excitation of its magnetic resonance (i.e., the resonant oscillation of the circular currents around its rings) by the external electric field, **E**. This electric field-induced excitation of the magnetic resonance (EEMR effect) occurs whenever the SRR does not present mirror symmetry with respect to **E**, as shown and explained in Figure 17.4b; it occurs even for incidence normal to the SRR plane [22]. One result, among others, of the resonant circular currents excited in the asymmetric SRR is the nonzero average polarization induced, which is translated to a resonant permittivity response (in a homogeneous effective medium description) at the magnetic resonance frequency [21–23].

A resonant permittivity response at the magnetic resonance frequency can be detrimental for the achievement of LH behavior in SRR and wire systems, as it imposes strong positive ε regimes where negative ε is required. The effect is even more detrimental in two-dimensional (2D) and three-dimensional (3D) SRR and wire systems designed to create LHMs, where one requires that the SRRs that do not contribute to the magnetic response of the medium to be also electrically inactive. In such systems, especially in 3D, EEMR can be avoided only by employing symmetric SRR designs, like, e.g., multigap SRRs [23]. (Note that in 1D or even 2D systems the effect can be avoided by orienting the SRRs properly.)

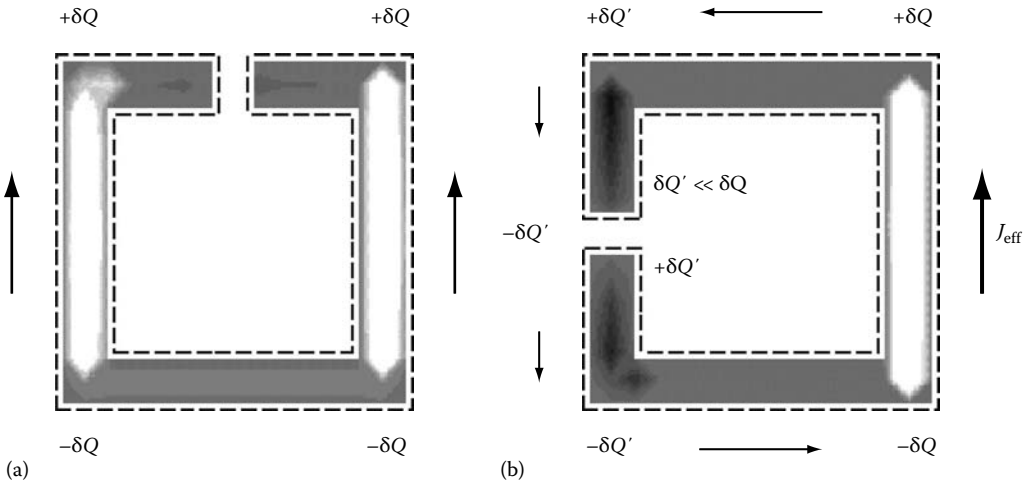

FIGURE 17.4 Simple drawing for the charge and current for a symmetric (a) and a nonsymmetric (b) single-ring SRR in an external electric field, **E** (pointing upward). The interior of the ring shows simulation data for the polarization current component $J||E$ at a fixed time for normal incidence; white color indicates upward current and black downward current. The asymmetry of the SRR in the case of panel (b) leads to different electric-field-induced charges at the two top and bottom corners of the SRR and thus to a potential difference, which is compensated by a circular current. (From Katsarakis, N., Koschny, T., Kafesaki, M., Economou, E.N., and Soukoulis, C.M., *Appl. Phys. Lett*., 84, 2943, 2004. With permission.)

Despite the detrimental influence of the EEMR effect on the achievement of LH behavior in SRR and wire systems, this effect presents an important advantage in the study of small (micrometer and nm scale) SRR systems, since it offers an indirect way to trace the SRR magnetic resonance regime in transmission experiments, i.e., by using normal incidence in one or few SRR layers. This advantage has been exploited very extensively recently, as it was used to demonstrate experimentally the occurrence of a magnetic SRR resonance in the 6 THz [25], 100 THz [26], and 1.5 mm [27] regimes.

17.3 Two-Dimensional and Three-Dimensional Left-Handed Materials from SRRs and Wires

Since many of the proposed applications of LHMs, such as the superlensing-based applications, require 2D or 3D isotropic, homogeneous-like materials, many attempts have been made to realize such metamaterials (see e.g., [28–33]). Besides the practical problems though in such a realization, there are many fundamental considerations that should be taken into account for the achievement of a 3D homogenous-like and isotropic LHM using SRRs and wires.

One impeding factor, which was discussed in the previous section, is the presence of the SRR's asymmetries, which produce electric resonances (resonances in ε) at the magnetic resonance frequency regimes, destroying the negative ε response required for the achievement of LH behavior. Therefore, for the achievement of 2D and mainly 3D LHMs it is essential to employ fully symmetric SRR structures. An example of such a structure is a symmetric four-gap SRR, as the one shown in Figure 17.5a [31]. The presence of many gaps though, as in the design of Figure 17.5a, leads to an upward shift of the magnetic resonance frequency [23,32] (gaps act like capacitors in series, reducing the total capacitance of the structure and thus increasing the magnetic resonance frequency, $\omega_m = 1/\sqrt{LC}$); as a result, it is difficult for the magnetic resonance frequency to fall in the negative ε regime of the

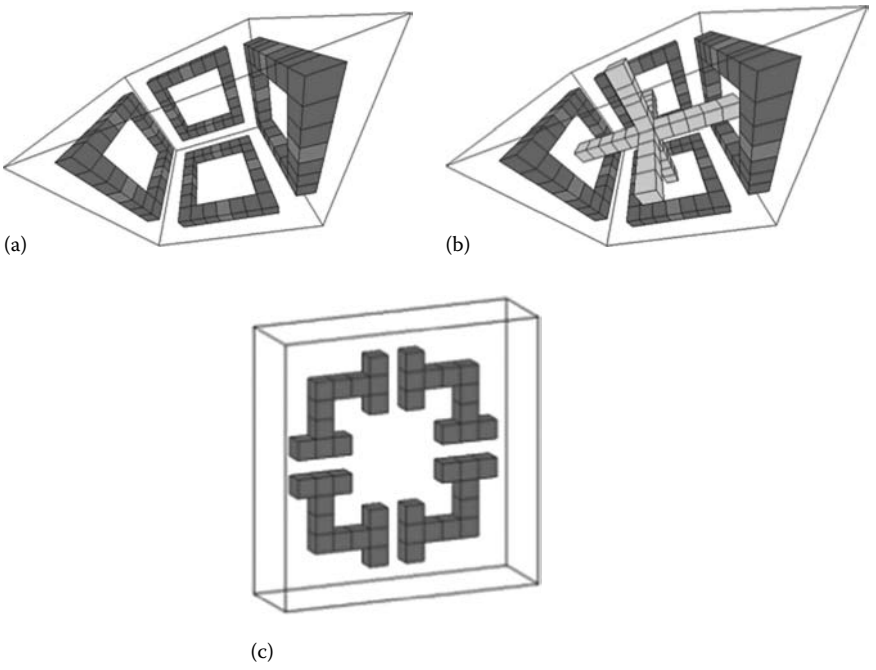

FIGURE 17.5 The design of a fully symmetric unit cell (uc) for a one unit-cell-thick slab of an isotropic four-gap SRR (a) and an LHM (b). The uc interfaces are parallel to the left and right SRR. The SRR gaps are filled with a material of high dielectric constant (light-gray) to reduce the magnetic resonance frequency. An alternative way to reduce the magnetic resonance frequency is to design extensions in the SRR gaps, as shown in panel (c), which increase the gap capacitance. (From Koschny, Th., Zhang, L., and Soukoulis, C.M., *Phys. Rev. B*, 71, 036617, 2005. With permission.)

system, although it may be pushed close to the periodicity-induced band gaps; hence, design modifications are essential in this structure. Such modifications can be achieved through the introduction of a high-index material in the SRR gaps (as in the case of Figure 17.5a) [31] or through the introduction of proper extensions in the gaps [23], so as to increase the gap capacitance (e.g., overleaf capacitors, extra branches—see Figure 17.5c, etc.) or by using, instead of single rings, ring pairs with broad-side (face to face) coupling.

Apart from the requirement of symmetric and of subwavelength-scale SRR structures though, there are additional conditions required for a structure to approach the isotropic, homogeneous, effective medium behavior. Such conditions, which are described in detail in [31], are the inversion symmetry of the unit cell along propagation direction, the inversion symmetry in at least one of the two directions perpendicular to that of the propagation (to avoid cross-polarization effects), and a proper choice of the relative position of SRRs and wires an to minimize the cross-talk between them; such optimum position was found to be the one in Figure 17.5b, with the wires aligned in the middle of the SRRs.

17.4 Effects of Periodicity in the Homogeneous Effective Medium Retrieved Parameters in SRRs and Wire Metamaterials

Most proposals for applications based on the unique physical properties of LHMs rely on the homogeneity of the material, in addition to specific values and dispersion of the metamaterial's

impedance and refractive index. For instance, a perfect lens, even with exact parameters $n = -1$ and $z = 1$, will only amplify evanescent wave components with momenta smaller than the inverse unit cell size of the LHM [34]. Similar restrictions apply to all super resolution imaging and even cloaking applications of metamaterials.

Homogeneous-like effective medium behavior occurs in metamaterials when the structural length scale of the material becomes much smaller than the wavelength of the electromagnetic radiation propagating through it. Under this condition the metamaterial will behave like a homogeneous medium characterized by just two (in the absence of magnetoelectric coupling) frequency-dependent parameters: the effective permeability, $\mu(\omega)$, and the effective permittivity, $\varepsilon(\omega)$. (Both of them may be tensors if the material is anisotropic.)

One of the key benefits of metamaterials is that we have—in principle—full control over both their magnetic and electric response, such that achieving an LHM with large wavelength to unit cell size ratio becomes possible (current state of the art is about 70–200 for microwave metamaterials).

If homogenization of a metamaterial, i.e., the description as an effective homogeneous medium, is possible, we expect the effective parameters $\mu(\omega)$ and $\varepsilon(\omega)$ to be only functions of the frequency and not of the wave vector. The effective parameters then can be derived by a simple retrieval procedure [17,35], essentially equating the plain wave scattering amplitudes of a metamaterial slab with those of a finite homogeneous slab of same thickness and solving for the $\mu(\omega)$ and $\varepsilon(\omega)$ or, equivalently, refractive index, $n(\omega)$, and impedance, $z(\omega)$, of the slab. If these parameters can be chosen independent of the length of the metamaterial, they constitute effective homogeneous medium parameters describing the scattering properties and the propagation inside the metamaterial.

Early microwave metamaterials and all recent metamaterials in the THz and optical regime suffer from the difficulty in reducing the structural size to vacuum wavelength ratio beyond the range of 5–10, while maintaining reasonable response amplitudes and losses. In this region, the effective parameters retrieved for the metamaterials show strong artifacts [36], which were not expected from the simple analytic theory. They indicate the beginning of the breakdown of the homogeneous medium behavior and the transition into a multiple scattering dominated regime, as in a photonic crystal. These artifacts include the following: (a) the resonant index of refraction is cut off close to the resonance, at values for which the wavevector inside the material approaches the Brillouin zone edge; (b) the discontinuities marking the position of the resonance as retrieved from the effective refractive index and impedance (or ε and μ) do not coincide but are shifted in frequency; (c) the expected Lorentzian shape of the magnetic resonance is strongly deformed, usually with the positive part cut off; (d) an unexpected antiresonant behavior in $\varepsilon(\omega)$ is found whenever $\mu(\omega)$ is resonant, and vice versa; and (e) seemingly unphysical negative imaginary parts occur in the effective medium parameters $\mu(\omega)$ and $\varepsilon(\omega)$.

All those artifacts can be understood and quantitatively predicted taking the inherent periodicity of the metamaterial into account [37]. In the long wavelength limit all of these artifacts vanish (except in very close proximity to a strong, low-loss resonance) and the expected behavior of a Lorentz-like resonant $\mu(\omega)$ and a smooth plasmonic $\varepsilon(\omega)$ are recovered. For a typical microwave SRR and wire LHM this would require a wavelength to unit cell ratio of the order of 50.

These periodicity artifacts are usually strongly detrimental to the desired metamaterial properties, and their avoidance constitutes an additional constraint for metamaterial design. Further, also the symmetry of the unit cell and the metamaterial sample places some constraints on the effective medium behavior [35] (see Section 17.3), which need to be accounted for in LHMs design.

17.5 SRRs and Wire Metamaterials toward Optical Regime

The novel and unique properties of LHMs, which result in new capabilities in the manipulation of EM waves, have as a result a strong effort worldwide to achieve such materials not only in the

microwaves, where they were initially demonstrated, but also in the THz and optical regimes [38], targeting applications such as imaging, security, sensing, and lithography, etc.

One of the most straightforward approaches to achieve THz and optical LHMs is the scaling of established microwave LH structures, like the SRRs and wires structures. Although the properties of the metal, which is the main constituent of most of today's metamaterials, are drastically different in the optical regime compared with those in the microwaves (there, the metal practically behaves as a perfect conductor), scaling of the structures is not expected to always produce proportional scaling of the resulting properties; thus a detailed examination of the scaling behavior of both SRRs and wires is essential.

Such an examination of the scaling properties of the SRRs [39,40] revealed that by scaling the structures the magnetic resonance frequency, which in microwaves scaled inversely proportional to the structure size, close to the optical regime saturates to a constant value (see Figure 17.6a), which depends mainly on the SRR design (geometrical characteristics). Moreover, the magnetic permeability resonance becomes weaker and weaker as we approach the submicron scale, and after some length scale it ceases to reach negative values (see Figure 17.6b). Both of these effects can be explained by taking into account the kinetic energy of the current-carrying electrons inside the SRR rings, besides the magnetic energy produced by those current-carrying electrons. This kinetic energy, which in microwaves is negligible compared with the magnetic energy and is usually ignored, in higher frequencies becomes more and more important, mainly due to the large reduction of the magnetic energy as the SRR becomes smaller and smaller.

Considering the electrons, kinetic energy through an equivalent inductance, L_e, (added to the magnetic field inductance, L) in an LC circuit description of the SRR [39–41] and examining the

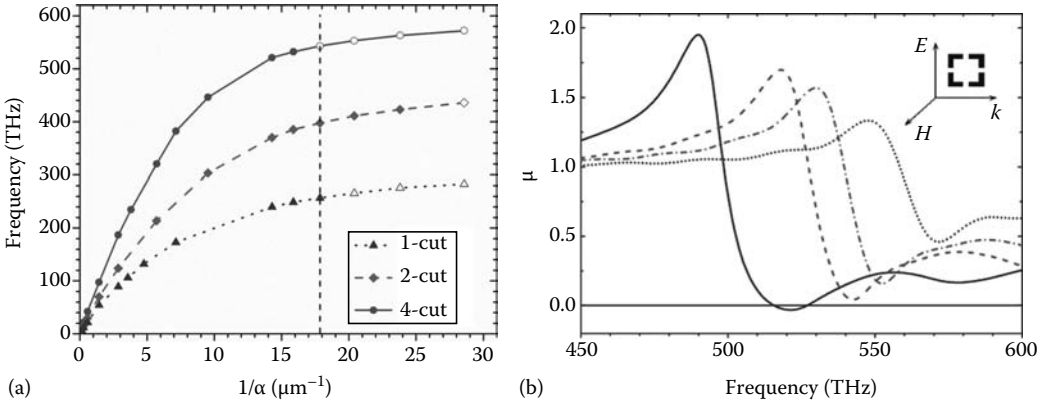

FIGURE 17.6 (a) The scaling of the simulated magnetic resonance frequency, $f_m = \omega_m/2\pi$, as a function of the linear size, a, of the SRR unit cell, for single-ring SRRs of one, two, and four gaps (cuts). Up to lower THz region the scaling is linear. The maximum attainable frequency is strongly increased with the number of gaps in the SRR ring. The hollow symbols and the vertical line at $1/a = 17.9$ μm^{-1} indicate that no negative μ is reached beyond this value. For the SRR designs employed the unit cell has dimensions $a \times a$ in the SRRs plane and $0.614a$ perpendicular to it. The SRR is made of Aluminum, simulated with a Drude-type permittivity. (b) Simulated Re μ for a single-ring four-gap SRRs system, for unit cell sizes a = 70 nm (solid line), 56 nm (dashed line), 49 nm (dotted-dashed line), and 35 nm (dotted line). (From Zhou, J., Koschny, Th., Kafesaki, M., Economou, E.N., Pendry, J.B., and Soukoulis, C.M., *Phys. Rev. Lett.*, 95, 223902, 2006. With permission.)

scaling behavior of L_e (resulting to be $\propto 1/\text{size}$), L ($\propto$ size), and C ($\propto$ size), one obtains for the magnetic resonance frequency the form

$$\omega_m = \frac{1}{\sqrt{(L + L_e)C}} \propto \frac{1}{\sqrt{\text{size}^2 + \text{const.}}}, \tag{17.3}$$

which leads to a constant value as the SRR size tends to zero.

Accurate numerical simulations employing practically achievable SRRs [39,40,43] have demonstrated this saturation behavior and have shown negative permeability up to 500 THz (600 nm) (in four-gap SRRs—see Figure 17.6b), i.e., the visible range, indicating the possibility of achieving LHMs even in the visible range, by employing SRRs.

If one also takes into account the potential energy of electrons inside the SRR [42], it can be concluded that the theoretical absolute upper limit for the magnetic resonance frequency (assuming the "optimum" SRR design) is the plasma frequency of the bulk metal. In practical cases though, the upper limit that can be achieved is much below that frequency. We have to mention finally that the saturation of the magnetic resonance frequency in nm-scale SRRs has also been demonstrated experimentally [43], for a single-ring, single-gap SRR system.

17.6 Slab Pairs and Slab-Pair-Based Left-Handed Materials

Although the SRR and wire geometry proposed by Pendry has become very widely used in the microwaves regime, this topology presents certain disadvantages in the THz and optical regime requiring micron and submicron length-scale structures. Its major disadvantage comes from the fact that the negative permeability SRR response is achieved for propagation parallel to the SRR plane (so as to have magnetic field perpendicular to that plane), which makes essential the fabrication of multilayer samples, somehow difficult to achieve with the current technological limitations.

An alternative design that overcomes the above impediment is the slab-pair design (see Figure 17.1b), which was proposed by the Purdue group in 2002 [14]. As can be concluded from Figure 17.1b, the slab-pair design responds as a resonant magnetic dipole for propagation normal to the plane of the structure, which makes possible the demonstration of negative permeability response with a single or very few structure layers. Moreover, the design is very simple and relatively easy to be fabricated in the micro- and nano-scale.

Besides the resonant magnetic mode associated with resonant antiparallel currents at the two slabs of the pair, the slab-pair design also allows a resonant electric mode, associated with parallel currents at the slabs, resulting in a resonant electric dipole moment. Therefore, besides the resonant and negative permeability response, there is also a strong resonant (and with negative values) permittivity response in slab-pair systems, which can occur in frequencies close to the magnetic resonance frequency.

The simultaneous existence of negative ε and μ at nearby frequencies in slab-pair systems has led to many attempts to achieve LH behavior employing only slab pairs [15] and tuning properly the negative μ regime to fall within the negative ε regime (which is much broader, due to the stronger electric resonance [44]).

Detailed theoretical studies, though [44], have shown that such a "coincidence" can be achieved only under very extreme conditions, whereas it is impossible for isolated pairs (where the magnetic resonance frequency is always below that of electric resonance). The factor that makes a "coincidence" possible in a periodic system of pairs is the capacitive interaction of neighboring pairs along the electric field direction, which can lead to a large downward shift of the electric resonance, bringing it below the magnetic one. Modifications of the slab-pair design to increase this interaction give

additional possibilities for the achievement of LH behavior using only slab pairs. Such design modifications (T-shape extensions) have been exploited recently for the demonstration of LH behavior in slab pairs at the GHz regime [45].

The difficulty in achieving electric and magnetic resonances at nearby frequencies in only slab-pair systems is based to a large degree on the fact that both the electric and the magnetic resonances result from the splitting of a "single particle dipole resonance" (single-slab resonance), due to the interaction of the slabs of the pair. This is confirmed further by the fact that the dominant parameter determining both resonance frequencies (in GHz slabs) is the length of the slabs. The magnetic resonance frequency, in particular, seems to be almost independent of all the other geometrical parameters, i.e., slab width, thickness of metal, and separation of the slabs [44]. (This result that can be easily explained through an *LC* description of the system.)

Closing this section, we have to mention that the achievement of LH behavior only from slab pairs, besides the disadvantage of being possible only under very extreme conditions, has the additional disadvantage that it stems from the involvement of two resonances, which is associated with large induced losses.

17.7 Left-Handed Behavior from Slab Pairs and Wires—The Fishnet Design

Another approach for the achievement of LH behavior that seems to overcome the above-mentioned disadvantages of the slab pair-only LHMs is to combine the slab pairs with continuous wires, as shown, e.g., in Figure 17.7a, using only the resonant magnetic response of the pairs and making use of the broad negative ε regime offered by the wires. This approach has been exploited recently for the demonstration of LH behavior in both the GHz and the THz regimes [46–48].

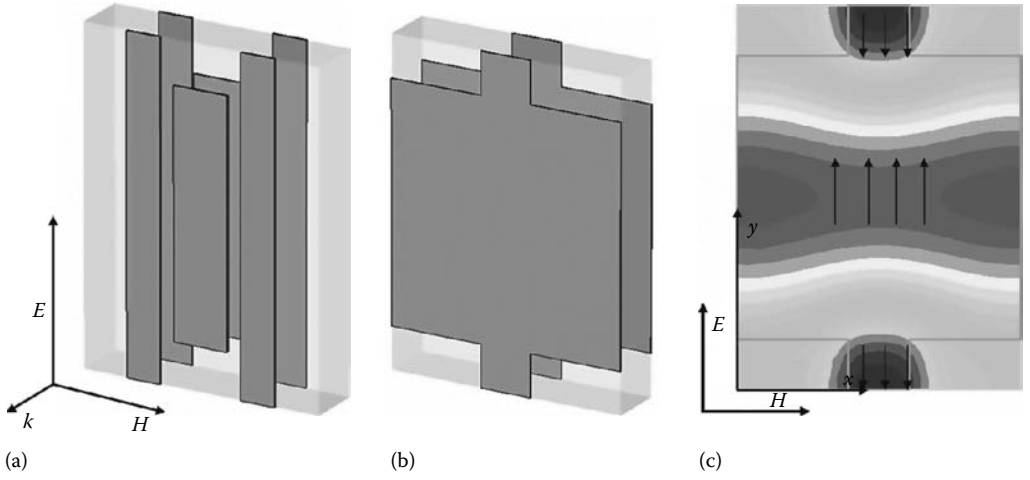

FIGURE 17.7 (a) The unit cell of an LH metamaterial design based on combination of slab pairs and continuous wires. The picture also shows the orientation of the external electromagnetic (EM) field that excites the left-handed response of the structure. (b) One unit cell of the fishnet design. The external EM field for the excitation of the LH behavior of the design is as shown in panel (a). (c) The magnetic field component H_x at the magnetic resonance frequency of the fishnet design. The field is plotted at the $x-y$ (or **H**–**E**) plane, which lies in the middle (along the z direction) of the two metallic sheets of the structure. Dark color indicates large field amplitude and light color, low amplitude. (From Kafesaki, M., Tsiapa, I., Katsarakis, N., Koschny, Th., Soukoulis, C.M., and Economou, E.N., *Phys. Rev. B*, 75, 235114, 2007. With permission.)

Despite the fact that the addition of wires offers an easier and safer approach compared with the only-slabs one, certain considerations should be taken into account here, stemming mainly from the presence of the electric resonance of the slabs at frequencies close to that of the magnetic resonance. As described in Section 17.2 for SRRs and wires, in slabs and wire systems the electric response of the slabs modifies the effective permittivity of the system (compared with that of only the wires), leading to a new plasma frequency, ω_p', below that of the wires and below the electric resonance frequency of the slabs, ω_e. The influence of the slab's electric resonance though, besides the dramatic in some cases lowering of the plasma frequency in some cases, also results in a very abrupt ε dispersion close to the new plasma frequency. This comprises a serious impediment for the achievement of a good impedance match of the structure with its environment and thus for the achievement of LH behavior with high transmittance.

Studying in detail the dependence of the characteristic frequencies of the system on the various system parameters [44], it can be seen that to ensure a negative μ regime below the new plasma frequency ω_p', one needs relatively isolated slabs (i.e., short slabs compared with the corresponding unit cell side), to ensure magnetic resonance below the electric one.

Moreover, to minimize the destructive influence of the electric resonance on the system's impedance one needs to push the electric resonance not just above the magnetic one but at frequencies as further up as possible. Examining the dependence of the electric resonance frequency on the various system parameters it was found [49] that a large upwards shift of the electric resonance without affecting much the magnetic resonance frequency can be achieved by widening the slabs, reducing thus their inductance. (This widening, despite the fact that it does not affect the magnetic resonance frequency, has a positive influence on the magnetic resonance strength, reinforcing it—due to the increase in the volume available for the induced magnetic field.)

Another factor that leads to upward shift of ω_e is to physically connect the slabs with the wires, as shown in Figure 17.7b, which results in a design known as fishnet [49–51]. Fishnet design, which is described here, seems to offer an optimized solution for the achievement of LH behavior, both in microwaves [49] and the optical regime [52,53].

17.7.1 The Fishnet Design

The fishnet design [49–51], shown in Figure 17.7b, combines strong magnetic response and high enough electric (ε) resonance frequency, due to the wide slabs and the physical connection of slabs and wires.

Detailed numerical simulations [49] and corresponding experiments for the fishnet design in the GHz regime [54,55] have shown LH behavior with high transmittance for a wide range of geometrical parameters, making it an optimized design for the achievement of LH behavior. The superior performance of the design has been revealed also in the optical regime, where fishnet has given the highest in frequency [53] and the highest in transmittance levels of [52] LHM up to now.

The strong magnetic response (as a result of the wide slabs) seems to be responsible for this superior performance of the fishnet, combined with the smooth, Drude-like electric response (as a result of the high electric resonance frequency) [49]. This smooth electric response results in a good impedance match with the environment for a wide range of geometrical parameters of the structure and thus to high LH transmittance (if the material losses are also low).

The high electric resonance frequency together with all the other characteristics of the structure behavior can be understood through examination of the current and the electric and magnetic fields at the resonances of the structure. Such an examination has revealed a strong inductive response not only at the slabs of the pair but also at the joints connecting the neighboring slabs along the external **E** direction (see Figure 17.7c). This response, taken into account through an equivalent inductance, parallel to the slab's inductance, can account for all the aspects of the behavior of the structure. Taking into account the joint's inductance and employing simple analytic formulas for the capacitances and

inductances of the structure, one can reproduce and explain the dependence of both the magnetic and electric resonance frequency from all the geometrical and material parameters of the fishnet design [49].

Another characteristic of the fishnet worth mentioning is the slightly higher magnetic resonance frequency compared with the magnetic resonance frequency of only the slabs. This feature, which can also be explained through the joints' loop inductance, although it is not desired in the GHz regime (as it makes the structure less subwavelengh in scale), is highly desired in the optical regime, as we discuss below.

17.8 Slab-Pair-Based Systems toward Optical Regime

As it has been mentioned in Section 17.5, where we discussed the scaling behavior of SRRs, the nonscalability of the metal properties as one goes from microwaves to the optical regime results to nonscalability of the properties of the artificial magnetic and of the LH structures.

This nonscalability observed in the SRRs is repeated (as is expected) also for the structures based on slab-pairs [42,56], including the fishnet design.

Figure 17.8a shows the magnetic and the electric resonance frequency for a pair of relatively narrow slabs (as the ones of Figure 17.7a—without the wires) and Figure 17.8b the same frequencies, with the addition of the plasma frequency, $f_p = \omega_p'/2\pi$, for the fishnet design. Both results show the saturation of all the characteristic metamaterial frequencies. Calculations of the magnetic permeability close to the saturation regime show also here the weakening of the permeability resonance going to higher and higher frequencies [56].

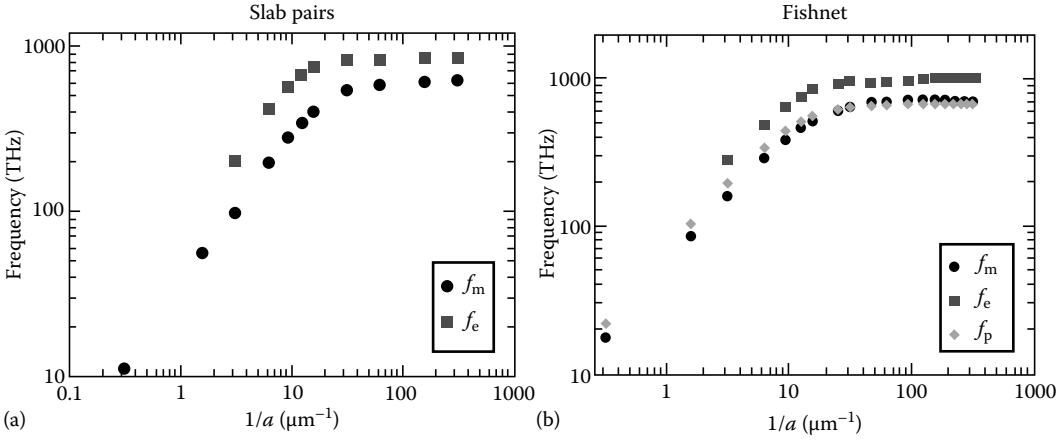

FIGURE 17.8 The scaling of the simulated magnetic resonance frequency, $f_m = \omega_m/2\pi$, and the electric resonance frequency, $f_e = \omega_e/2\pi$, as a function of the inverse unit cell size, a, (a here is the unit cell side along propagation direction) for a system of slab pairs (panel (a)) and for a fishnet structure (panel (b)—for the design see Figure 17.7b). Panel (b), in addition, shows the scaling of the "plasma" frequency, $f_p = \omega_p'/2\pi$ (i.e., the frequency of the first transition from negative to positive real part of the structure permittivity) for the fishnet design. The structures have been simulated using the Drude model for the permittivity of the metallic components, with the Aluminum parameters for the plasma frequency (3570 THz) and the collision frequency (19.4 THz), while the dielectric spacer between the metallic elements has been chosen to be glass, with a permittivity of 2.8. The unit cell parameters are $2.97a \times 2.19a \times a$, along the external **E**, **H**, and **k** direction, respectively (for the designs and axes see Figure 17.7), the slab's thickness is $0.25a$, the width (along **H**) of the joints is $0.47a$, the board thickness (along **k**) is $0.5a$, the slab's length is $2.19a$ and the narrow-slab's width is $0.47a$. (From Penciu, R.S., et al., Slab-pairs and fishnet design: Limits of size scaling (in preparation).)

Both the saturation of the magnetic and the electric resonance frequencies as well as the weakening of the resonance strength can be explained, like for SRRs, through the "kinetic inductance" of the electrons inside the metal. (Note that the involvement of the kinetic inductance results in the involvement of additional geometrical parameters in the determination of the magnetic resonance frequency, which in the gigahertz range was found to be determined almost exclusively by the length of the slabs.)

Comparing the saturation values of the magnetic resonance frequency of the pairs with those of single-ring single-gap SRRs, one can observe higher saturation values for the pairs. This is due to the decreased capacitance (because of the two gaps) and inductance (because of the reduced area) of the pair compared with single-ring, single-gap SRR.

From Figures 17.8 it is worth mentioning also that

1. Fishnet maintains the observed in microwaves of higher magnetic resonance frequency (compared with only slab pairs) also close to the saturation regime.
2. Electric resonance frequency, both for slab pairs and fishnet, maintains its higher values compared with magnetic resonance frequency in all frequency ranges, including the saturation regime.
3. The plasma frequency for the fishnet, f_p, although it is higher than the magnetic resonance frequency in the microwaves, does not maintain its higher values in the saturation regime; thus design modifications are required for the structure to maintain its LH behavior as it is scaled down. This shows that an optimized LH microwave design is not necessarily the preferred LH design at the optical regime.

Finally, we have to mention that consideration of the kinetic inductance of the slab electrons can explain all the above features and can give simple approximate analytical formulas for the various saturation values [56], which can be very useful for structure optimizations.

An overall structure optimization, though, should take into account not only the effects associated with the kinetic inductance but also the other important factor for the achievement of functional optical LH materials: the minimizations of the resistive losses, unavoidable in such materials. The proposed solutions for such a minimization include not only changes in designs [57] and optimization of the quality of the constituent materials (e.g., using silver for the metallic components) but also incorporation of gain media into LHMs, to compensate for the losses [58]. This last solution has been studied extensively recently and might constitute one of the most promising ways for achievement of functional optical LHMs.

17.9 Conclusions

The unique properties and capabilities of LHMs have led to a widespread recognition of them and to exponentially increasing research efforts devoted to their study and exploitation. In this chapter, we attempted a summary of basic design considerations aiming at the achievement of optimized LHMs in one-, two-, and three dimensions and in frequency regimes ranging from microwaves to optics.

This kind of structures will be capable of fully demonstrating all the unique properties and abilities of LHMs, such as (a) the ability to match the vacuum impedance, which is a unique property of LHMs with many applications (e.g., in stealth technology); (b) the possibility of coupling with the magnetic component of an electromagnetic field without the presence of any magnetic material (this is a new capability of fundamental importance, especially in the terahertz region where no natural magnetic materials exist); (c) the possibility of miniaturizing devices and components such as antennas and waveguide structures, leading to very important potential system weight and size savings; and (d) the negative refraction and the subwavelength resolution capability, which open up the possibility of new applications in optics and communications.

References

1. D. R. Smith, J. B. Pendry, and M. Wiltshire, Metamaterials and negative refractive index, *Science* **305**, 788 (2004).
2. C. M. Soukoulis et al., Negative index materials: New frontiers in optics, *Adv. Matter* **18**, 1941 (2006).
3. J. B. Pendry, Negative refraction makes a perfect lens, *Phys. Rev. Lett*. **85**, 3966 (2000).
4. V. G. Veselago, The electrodynamics of substances with simulatenous negative values of ε and μ, *Sov. Phys. Usp*. **10**, 509 (1968) [*Usp. Fiz. Nauk* **92**, 517 (1967)].
5. D. R. Smith et al., Composite medium with simultaneously negative permeability and permittivity, *Phys. Rev. Lett.* **84**, 4184 (2000).
6. J. B. Pendry, A. T. Holden, W. J. Stewart, and I. Youngs, Extremely low frequency plasmons in metallic mesostructures, *Phys. Rev. Lett.* **25**, 4773 (1996); J. B. Pendry, A. J. Holden, D. J. Robbins, and W. J. Stewart, Low frequency plasmons in thin wire structures, *J. Phys. Cond. Matter* **10**, 4785 (1998).
7. J. B. Pendry et al., Magnetism from conductors and enhanced non-linear phenomena, *IEEE Trans. MIT* **47**, 2075 (1999).
8. R. A. Shelby, D. R. Smith, and S. Schultz, Experimental verification of a negative index of refraction, *Science* **292**, 77 (2001).
9. C. G. Parazzoli et al., Experimental verification and simulation of negative index of refraction using Snell's law, *Phys. Rev. Lett.* **90**, 107401 (2003); K. Li et al., Free-space focused-beam characterization of left-handed materials, *Appl. Phys. Lett*. **82**, 2535 (2003).
10. M. Bayindir et al., Transmission properties of composite metamaterials in free space, *Appl. Phys. Lett*. **81**, 120 (2002); K. Aydin et al., Experimental observation of true left-handed transmission peak in metamaterials, *Opt. Lett*. **29**, 2623 (2004).
11. M. Notomi, Negative refraction in photonic crystals, *Phys. Rev. B* **62**, 10696 (2000); E. Cubukcu et al., Negative refraction by photonic crystals, *Nature* **423**, 604 (2003); Subwavelength resolution in 2D photonic crystal-based superlens, *Phys. Rev. Lett*. **91**, 207401 (2003); S. Foteinopoulou and C. M. Soukoulis, Negative refraction and left-handed behavior in 2D photonic crystals, *Phys. Rev. B* **67**, 235107 (2003).
12. J. B. Pendry, A chiral route to negative refraction, *Science* **306**, 1353 (2004).
13. S. O'Brien and J. B. Pendry, Photonic band gap effects and magnetic activity in dielectric composites, *J. Phys: Condens. Matter* **14**, 4035 (2002); K. C. Huang, M. L. Povinelli, and J. D. Joannopoulos, Negative effective permeability in polaritonic photonic crystals, *Appl. Phys. Lett.* **85**, 543 (2004).
14. V. A. Podolskiy, A. K. Sarychev, and V. M. Shalaev, Plasmon modes in metal nanowires and left-handed materials, *J. Nonlinear Opt. Phys. Mater.* **11**, 6574 (2002).
15. V. M. Shalaev et al., Negative index of refraction in optical metamaterials, *Opt. Lett.* **30**, 3356 (2005).
16. W. J. Padilla et al., Electrically resonant terahertz metamaterials: Theoretical and experimental investigations, *Phys. Rev. B* **75**, 041102(R) (2007).
17. D. R. Smith, S. Schultz, P. Markos, and C. M. Soukoulis, Determination of permittivity and permeability of metamaterials from scattering data, *Phys. Rev. B* **65**, 195104 (2002).
18. R. Marques, F. Medina, and R. Rafii-El-Idrissi, Role of bianisotropy in negative permeability and left-handed metamaterials, *Phys. Rev. B* **65**, 144440 (2002).
19. T. Koschny, M. Kafesaki, E. N. Economou, and C. M. Soukoulis, Effective medium theory of left-handed materials, *Phys. Rev. Lett.* **93**, 107402 (2004).
20. N. Katsarakis, T. Koschny, M. Kafesaki, E. N. Economou, E. Ozbay, and C. M. Soukoulis, Left- and right-handed transmission peaks near the magnetic resonance frequency in composite metamaterials, *Phys. Rev. B*. **70**, 201101(R) (2004).
21. M. Kafesaki, Th. Koschny, J. Zhou, N. Katsarakis, I. Tsiapa, E. N. Economou, and C. M. Soukoulis, Electromagnetic behavior of left-handed materials, *Physica B* **394**, 148 (2007).

22. N. Katsarakis, T. Koschny, M. Kafesaki, E. N. Economou, and C. M. Soukoulis, Electric coupling to the magnetic resonance of split ring resonators, *Appl. Phys. Lett.* **84**, 2943 (2004).
23. M. Kafesaki, Th. Koschny, R. S. Penciu, T. F. Gundogdu, E. N. Economou, and C. M. Soukoulis, Left-handed metamaterials: Detailed numerical studies of the transmission properties, *J. Opt. A: Pure Appl. Opt.* **7**, S12 (2005).
24. P. Gay-Balmaz and O. J. F. Martin, Electromagnetic resonances in individual and coupled split-ring resonators, *J. Appl. Phys.* **92**, 2929 (2002).
25. N. Katsarakis et al., Magnetic response of split-ring resonators in the far infrared frequency regime, *Opt. Lett.* **30**, 1348 (2005).
26. S. Linden et al., Magnetic response of metamaterials at 100 THz, *Science* **306**, 1351 (2004).
27. C. Enkrich et al., Magnetic metamaterials at telecommunication and visible frequencies, *Phys. Rev. Lett.* **95**, 203901 (2005).
28. P. Gay-Balmaz and O. J. F. Martin, Efficient isotropic magnetic resonators, *Appl. Phys. Lett.* **81**, 939 (2002).
29. J. D. Baena, L. Jelinek, R. Marqus, J. Zehentner, Electrically small isotropic three-dimensional magnetic resonators for metamaterial design, *Appl. Phys. Lett.* **88**, 134108 (2006).
30. I. Bulu, H. Caglayan, and E. Ozbay, Experimental demonstration of labyrinth-based left-handed metamaterials, *Opt. Expr.* **13**, 10238 (2005).
31. Th. Koschny, L. Zhang and C. M. Soukoulis, Isotropic 3d left-handed and related metamaterials of the split-ring resonator and wire type, *Phys. Rev. B* **71**, 036617 (2005).
32. K. Aydin, I. Bulu, K. Guven, M. Kafesaki, C. M. Soukoulis, and E. Ozbay, Investigation of magnetic resonances for different split-ring resonator parameters and designs, *New J. Phy*. **7**, 168 (2005).
33. N. Katsarakis, M. Kafesaki, I. Tsiapa, E. N. Economou, and C. M. Soukoulis, High transmittance left-handed materials involving symmetric split-ring resonators, *Photonics Nanostruct*. **5**, 149 (2007).
34. Th. Koschny, R. Moussa, and C. M. Soukoulis, Limits on the amplification of evanescent waves in left-handed materials, *J. Opt. Soc. Am. B* **23**, 485 (2006).
35. D. R. Smith, D. C. Vier, Th. Koschny, and C. M. Soukoulis, Electromagnetic parameter retrieval from inhomogeneous metamaterials, *Phys. Rev. E* **71**, 121103 (2005).
36. T. Koschny, P. Markoš, D. R. Smith, and C. M. Soukoulis, Resonant and anti-resonant frequency dependence of the effective parameters of metamaterials, *Phys. Rev. E* **68**, 065602 (2003).
37. Th. Koschny, P. Markoš, E. N. Economou, D. R. Smith, D. C. Vier, and C. M. Soukoulis, Impact of inherent periodic structure on effective medium description of left-handed and related metamaterials, *Phys. Rev. B* **71**, 245105 (2005).
38. V. M. Shalaev, Optical negative-index materials, *Nat. Photonics* **1**, 41 (2007); C. M. Soukoulis, S. Linden, and M. Wegener, Negative index metamaterials at optical wavelengths, *Science* **315**, 47 (2007); S. Linden et al., Photonic metamaterials: Magnetism at optical frequencies, *IEEE J. Quant. Electr.* **12**, 1097 (2006).
39. J. Zhou, Th. Koschny, M. Kafesaki, E. N. Economou, J. B. Pendry, and C. M. Soukoulis, Saturation of the magnetic response of split-ring resonators at optical frequencies, *Phys. Rev. Lett.* **95**, 223902 (2006).
40. C. M. Soukoulis, Th. Koschny, J. Zhou, M. Kafesaki, and E. N. Economou, Magnetic response of split-ring resonators at terahertz frequencies, *Phys. Stat. Sol. (b)* **244**, 1181 (2007).
41. L. Solymar, *Lectures on Electromagnetic Theory* (Oxford University Press, Oxford, 1976).
42. S. Tretyakov, On geometrical scaling of split-ring and double-bar resonators at optical frequencies, *Metamaterials* **1**, 40 (2007).
43. M. W. Klein, C. Enkrich, M. Wegener, C. M. Soukoulis, and S. Linden, Single-slit split-ring resonators at optical frequencies: Limits of size scaling, *Opt. Lett*. **31**, 1259 (2006).
44. J. Zhou, E. N. Economou, Th. Koschny and C. M. Soukoulis, A unifying approach to left handed materials design, *Opt. Lett.* **31**, 3620 (2006).
45. J. Zhou et al., Negative index materials using simple short wire pairs, *Phys. Rev. B* **73**, 041101 (2006).

46. J. Zhou et al., Experimental demonstration of negative of index of refraction, *Appl. Phys. Lett.* **88**, 221103 (2006).
47. K. Guven, et al., Bilayer metamaterial: Analysis of left-handed transmission and retrieval of effective medium parameters, *J. Opt. A: Pure Appl. Opt.* **9**, S361 (2007).
48. T. F. Gundogdu et al., Negative index short-slab pair and continuous wires metamaterials in the far infrared regime, *Opt. Expr.*, 11, 9173 (2008).
49. M. Kafesaki, I. Tsiapa, N. Katsarakis, Th. Koschny, C. M. Soukoulis, and E. N. Economou, Left-handed metamaterials: The fishnet structure and its variations, *Phys. Rev. B* **75**, 235114 (2007).
50. S. Zhang et al., Experimental demonstration of near-infrared negative-index metamaterials, *Phys. Rev. Lett.* **95**, 137404 (2005); S. Zhang et al., Mid-infrared resonant magnetic nanostructures exhibiting a negativity permeability, *Phys. Rev. Lett*. **94**, 37402 (2005).
51. R. Ulrich, Far infrared properties of metallic mesh and its complementary structure, *Infrared Phys.* **7**, 37 (1967).
52. G. Dolling, C. Enkrich, M. Wegener, C. M. Soukoulis, and S. Linden, A low-loss negative index metamaterial at telecommunication wavelengths, *Opt. Lett.* **31**, 1800 (2006).
53. U. K. Chettiar et al., Dual-band negative index metamaterials: Double-negative at 813 nm and single negative at 772 nm, *Opt. Lett.* **32**, 1671 (2007).
54. N. Katsarakis et al., Optimized left-handed behavior in microwaves, employing the fishnet design, in preparation.
55. K. B. Alici and E. Ozbay, A planar metamaterial: Polarization independent fishnet structure, *Photonics Nanostr*. **6**, 102 (2008).
56. R. S. Penciu et. al., Slab-pairs and fishnet design: Limits of size scaling, in preparation.
57. G. Dolling, M. Wegener, C. M. Soukoulis, and S. Linden, Design-related losses of of double-fishnet negative-index photonic metamaterials, *Opt. Expr.* **15**, 1153 (2007).
58. A. K. Popov and V. M. Shalaev, Compensating losses in negative-index metamaterials with optical parametric amplification, *Opt. Lett.* **31**, 2169 (2006).

18

Composite Metamaterials, Negative Refraction, and Focusing

Ekmel Ozbay
Bilkent University

Koray Aydin
Bilkent University

18.1 Introduction

In recent years, left-handed metamaterials (LHMs) have become a remarkable research area and have received a considerable amount of interest due to their exotic electromagnetic properties that are not attainable from common materials. The left-handed media phenomenon was brought to the attention of the scientific community by Veselago four decades ago [1] and has received great attention in recent years since the first experimental demonstration of LHMs by Smith et al. [2,3].

The dielectric permittivity (ε) and the magnetic permeability (μ) are both positive for natural materials. In fact, it is possible to obtain negative values for ε and μ by using proper designs of metamaterials. An array of split ring resonators (SRRs) exhibits negative effective permeability (μ_{eff}) values for frequencies close to the magnetic resonance frequency (ω_m) of the SRRs [3]. Combining negative permittivity media together with negative permeability media results in a metamaterial with a negative refractive index provided that the negative values of permittivity and permeability coincide at certain range of frequencies [2]. Metamaterials offer novel properties, such as negative refraction, subwavelength imaging, and cloaking.

In this study, we review our research efforts in the field of metamaterials and report on the transmission, reflection, refraction, and imaging properties of two-dimensional (2D) LHMs composed of SRRs and thin-wire media. A left-handed transmission band is observed within the frequency region where both ε and permeability μ are negative. The refractive index is verified to be negative at these frequencies by using three independent measurement methods, such as refraction from prism-shaped LHMs, slab-shaped LHMs, and phase measurements. Consequently, imaging and resolution beyond the diffraction limit are observed for a 2D LHM superlens.

18.2 Left-Handed Metamaterial

The response of materials to the incident magnetic field is determined by magnetic permeability. Magnetic permeability is positive in usual materials. The absence of the negative values of magnetic permeability provided little motivation for studying negative-index materials (NIM). Pendry et al. [4] proposed SRR structures to obtain negative permeability values. The resonant behavior of SRRs is due to the capacitive elements (gaps and splits), which in turn result in rather high positive and negative values of permeability near the magnetic resonance frequency (ω_m).

SRRs under investigation are built from concentric metal rings on a dielectric printed circuit board with a thickness of 1.6 mm and $\varepsilon = 3.85$ [5]. To obtain negative permeability, we arranged SRR structures periodically with the parameters given in Ref. [6].

Figure 18.1 displays the measured and simulated transmission spectra of periodic SRRs. Two band gaps are observed throughout the frequency range of interests. The first band gap is between 3.55 and 4.05 GHz, and the second gap is from 8.15 to 11.95 GHz. The simulation results validate the experimental data as seen in the figure. In order to check the reason for the band gap formation, we proposed a test structure in which the splits are no longer present. The resulting structure is two complete rings without the splits, which we name as closed ring resonator (CRR) [4]. The splits in the SRR structure play a key role in obtaining magnetic resonance. Removing the splits prevents the current from flowing between the inner and outer rings, and, therefore, the magnetic resonance is no longer present. The measured transmission data are also given in Figure 18.1 with a black dotted line. The first band gap is not present for the CRR structure; however, the second band gap remains. We can claim that the stop bands of SRR media cannot be assumed as a result of "negative μ" behavior. Some of the observed gaps (such as the second band gap in this measurement) in the transmission spectra could also originate from the electrical response of the SRRs or from Bragg gaps due to periodicity. The band gap between 3.55 and 4.05 GHz is due to the magnetic response of SRRs. However, the stop band 8.15–11.95 GHz appeared due to the electrical response of the concentric rings.

We then combined SRR media with a proper thin-wire media, which provides the negative permittivity that is required for left-handed type of propagation [5]. Figure 18.2 shows the measured transmission spectra of SRR array (dashed line), wire array (dashed-dotted line), and LHM array (solid line). The wire array does not transmit EM waves at the frequency range of interest. This is

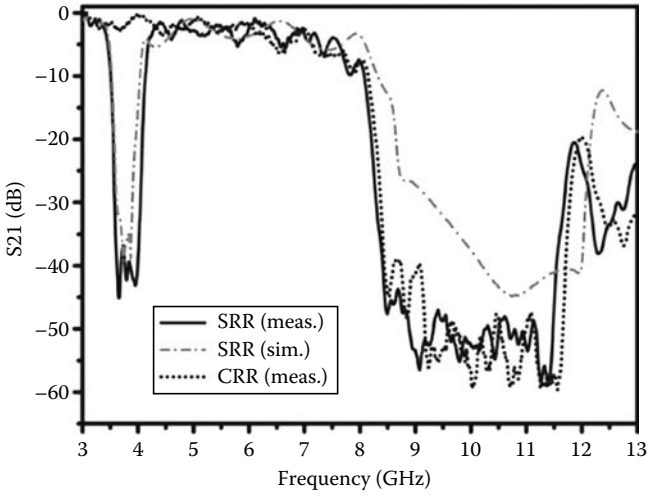

FIGURE 18.1 Measured and simulated transmission spectra of SRR and CRR arrays.

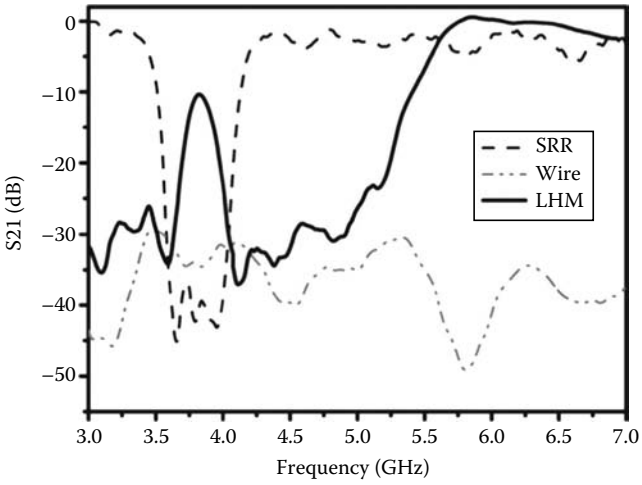

FIGURE 18.2 Measured transmission spectra of periodic SRR (dashed line), wire (dashed-dotted line), and LHM (black line) arrays.

to the negative values of dielectric permittivity. The plasma frequency of wire media is 8.0 GHz (not shown here), and below that frequency the dielectric permittivity becomes negative. One should observe a transmission band within the frequency region where both permittivity and permeability are negative. It is worthy of note that the effective plasma frequency reduces down to 5.4 GHz, when wire arrays are combined with the SRR arrays [4]. As seen in the figure, a transmission band is observed between 3.65 and 4.05 GHz, where the effective permeability and effective permittivity of LHM are simultaneously negative. The peak value within this transmission band is −7.6 dB. This measurement was performed for an LHM with three layers along the propagation direction.

We also measured transmission from a five-layer LHM. The result is given with a dashed line in Figure 18.3b. The peak value reduces to −9.9 dB for LHM with five layers. The reduction in the

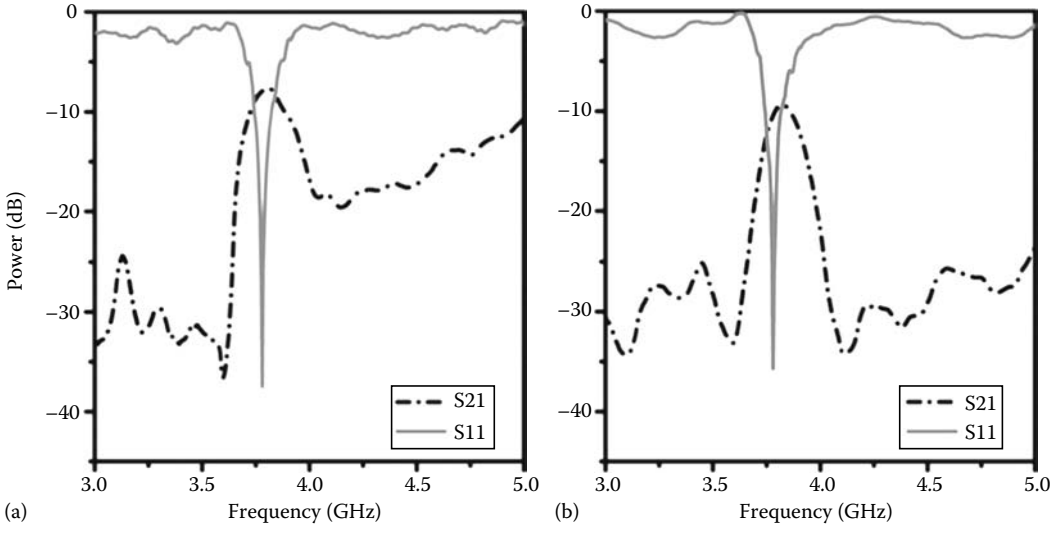

FIGURE 18.3 Measured transmission (dashed line) and reflection (solid line) spectra of (a) three-layer and (b) five-layer 2D LHM.

transmission peak could be attributed to the increased loss that is caused by the increased amount of metal and lossy substrate in the system.

We also measured reflection from three- and five-layered LHMs. The reflection spectra of three and five layer LHMs are shown by solid lines in Figure 18.3a and b, correspondingly [7]. For both structures, we observed a dip in the reflection spectra at 3.78 GHz. The reflection is very low around −35 dB, which means that the incident EM waves do not face significant amount of reflection at the LHM surface.

The low reflection from the surface can be attributed to either matched impedance at the interface or to the thickness resonance of the slab. Since the frequency for lowest reflection did not change for three- and five-layered LHMs, such a behavior could not be due to the thickness resonance. The effective parameters of the LHM structure are calculated in a recent work, and impedance is found to be matched with that of free space [7].

18.3 Negative Refraction

For materials with a negative refractive index, the phase velocity points toward the source, i.e., the phase velocity and energy flow are antiparallel inside an LHM [6]. By measuring the transmission phases for LHMs with varying thicknesses, one can verify that the phase velocity is indeed negative. We have constructed four different 2D LHM slabs with 5, 6, 7, and 8 layers. The transmitted phases are plotted in the frequency range 3.70–4.00 GHz, which is within the left-handed transmission region. It has been recently shown that increasing the number of layers of LHM results in a decrease at the phase of the transmitted EM wave. This is a typical left-handed behavior [6]. We measured the average phase shift between LHMs with the consequent number of layers.

The index of refraction in terms of wavelength, phase shift, and change in the length of left-handed material is given by [6]

$$n = \frac{\Delta\phi}{\Delta L}\frac{\lambda}{2\pi}.$$

We constructed a prism-shaped 2D composite metamaterial (CMM) structure (with a wedge angle of $\theta = 26°$) for negative refraction. Figure 18.4 shows the transmission spectrum as a function of

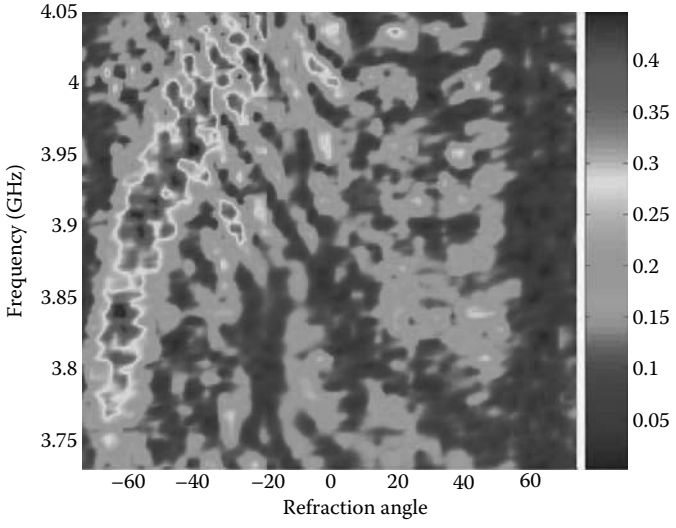

FIGURE 18.4 Transmission spectra as a function of frequency and refraction angle.

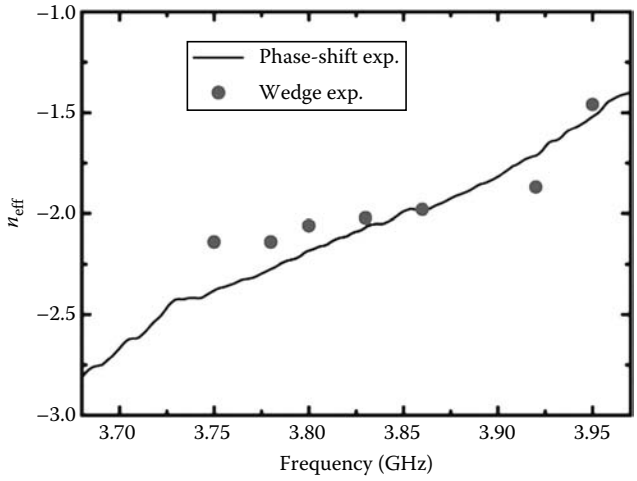

FIGURE 18.5 Measured effective refractive indices as a function of frequency, which are obtained from the phase-shift experiments (black line) and wedge experiments (•).

frequency and refraction angle. The transmitted EM waves are refracted toward the negative side of the surface normal within the frequency range of 3.73–4.05 GHz. At lower frequencies, the EM waves are refracted at higher negative refraction angles, which results in a higher negative refractive index. On the other hand, the refraction index is lowered with increasing frequencies. By employing Snell's law ($n_{CMM} \sin\theta_i = n_{air} \sin\theta_r$), an effective refractive index can be defined for the CMM. At $f = 3.92$ GHz, the incidence angle is $\theta_i = 26°$ and EM wave is refracted at an angle of $\theta_r = 55°$; then from Snell's law, we obtain $n_{eff} = -1.87 \pm 0.05$ at 3.92 GHz.

Figure 18.5 shows the measured refractive index values calculated by using the phase shift between the consecutive numbers of negative index material (NIM) layers that are reported in [6]. The symbol (•) corresponds to the refractive indices obtained from wedge experiments at some other frequencies (data not shown here). There is a good agreement between the results obtained from the two different methods.

At $f = 3.78$ GHz, the wavelength of the EM wave is $\lambda = 7.96$ cm. The average phase shift per unit cell ($\Delta L = 8.8$ mm) obtained from the experimental results is $\Delta\Phi = -0.51 \pm 0.04\pi$. Inserting these values in Equation 18.1, the index of refraction at 3.78 GHz is found to be $n_{eff} = -2.31 \pm 0.18$.

18.4 Subwavelength Imaging

A perfect lens is one of the most important applications of materials with a negative refractive index. The term, perfect lens, was coined by Pendry owing to the ability of such lenses to reconstruct a perfect image by recovering the evanescent components of EM waves [8]. In conventional optics, the lenses are constructed from positive-index materials and require curved surfaces to bring EM waves into focus. Positive-index lenses suffer from the diffraction limit and can only focus objects with sizes in the order of or greater than a half-wavelength.

The imaging measurements are performed at 3.78 GHz, where the reflection is considerably low and the losses due to reflection are negligible. The impedance is matched at 3.78 GHz for perpendicular normal incidence; however, the reflection will still affect the performance of LHM superlens for oblique incidence. In the imaging experiments, we employed monopole antennae to imitate the point source. The exposed center conductor acts as the transmitter and receiver and has a length of 4 cm ($\sim \lambda/2$). First, we measured the beam profile in free space that is plotted in Figure 18.6 with

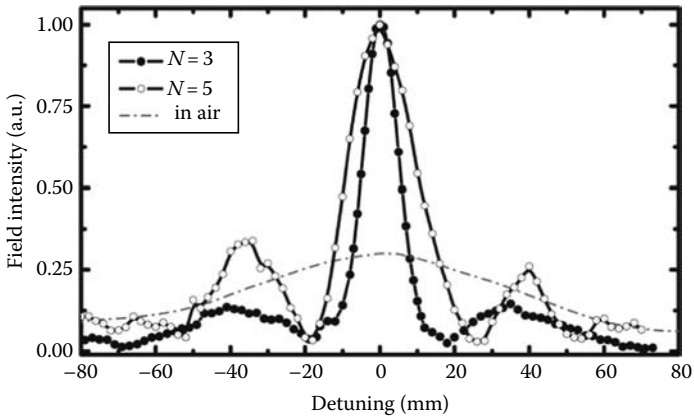

FIGURE 18.6 The measured power distributions at the image plane with three- and five-layer LHM superlenses. Gray dashed-dotted line corresponds to the power distribution in free space. Normalized intensity in free space is multiplied with 0.3.

a dashed line. The full width at half maximum (FWHM) of the beam is 8.2 cm (1.03λ). Then, we inserted LHM superlens and measured the spot size of the beam as 0.13λ, which is well below the diffraction limit. The LHM superlens consists of three layers along the propagation direction. The source is located d_s = 1.2 cm away from the first boundary, and the image forms d_i = 0.8 cm away from second boundary of the superlens. The intensity of the electric field at the image plane is scanned by the receiver monopole antenna with Δx = 1 mm steps.

We also performed additional measurements to check the influence of the lens thickness on the resolution of the superlens. The thicker LHM superlens has higher losses due to the increased amount of lossy substrate and the metal. Thus, one would expect the resolution to decrease for a thicker superlens. We performed imaging measurements for five-layer superlens, and the beam profile at the image plane is plotted within Figure 18.6 (–o–). As seen in the figure, the resolution is decreased and the FWHM of the beam is measured as 0.25λ.

18.5 Conclusions

In conclusion, we have successfully demonstrated a left-handed transmission band for 2D LHM in free space. Impedance matching condition is satisfied at a certain frequency regime where a sharp dip in the reflection spectra of LHMs is observed. Refractive index is calculated to be negative at the frequency region where both permittivity and permeability are negative. Phase shift and therefore the phase velocity are shown to be negative. Finally, an impedance-matched, low-loss, negative-index metamaterial superlens is demonstrated, which is capable of resolving subwavelength features with a record-level 0.13λ resolution. This is the highest resolution achieved from a negative-index metamaterial superlens. Moreover, two sources separated with a distance of λ/8 are clearly resolved. The effect of thickness on the subwavelength resolution is also verified, where a thicker superlens substantially reduced the resolution down to 0.25λ.

Acknowledgments

This work was supported by the European Union under the projects EU-NoE-METAMORPHOSE, EU-NoE-PHOREMOST, EU-PHOME, EU-ECONAM, and TUBITAK under the Project Numbers

105E066, 105A005, 106E198, 106A017, and 107A012. One of the authors (E.O.) also acknowledges partial support from the Turkish Academy of Sciences.

References

1. V. G. Veselago, *Sov. Phys. Usp*. **10**, 509 (1968).
2. D. R. Smith, W. J. Padilla, D. C. Vier, S. C. Nemat-Nasser, and S. Schultz, *Phys. Rev. Lett*. **84**, 4184–4187 (2000).
3. R. A. Shelby, D. R. Smith, and S. Schultz, *Science* **292**, 77–79 (2001).
4. J. B. Pendry, A. J. Holden, D. J. Robbins, and W. J. Stewart, *IEEE Trans. Microw. Theory Tech*. **47**, 4785 (1999).
5. K. Aydin, K. Guven, M. Kafesaki, L. Zhang, C. M. Soukoulis, and E. Ozbay, *Opt. Lett*. **29**, 2623–2625 (2004).
6. K. Aydin, K. Guven, C. M. Soukoulis, and E. Ozbay, *Appl. Phys. Lett*. **86**, 124102 (2005).
7. K. Aydin, I. Bulu, and E. Ozbay, *Appl. Phys. Lett*. **90**, 254102 (2007).
8. J. B. Pendry, Negative refraction makes a perfect lens, *Phys. Rev. Lett*. **85**, 3966–3969 (2000).

19

Metamaterials Based on Pairs of Tightly Coupled Scatterers

Andrea Vallecchi
University of Siena

Filippo Capolino
University of California Irvine

19.1 Introduction

In this chapter we describe the development of a few negative refractive index (NRI) metamaterials with periodic structure whose unit cells are based on the concept of pairing two suitably shaped conductors, for microwave and optical frequencies. Such configurations are shown to support both antisymmetric (magnetic) and symmetric (electric) resonance modes, whose interaction, when properly engineered, results in simultaneous negative permittivity and permeability, and, accordingly, NRI. The presented metamaterial structures can be considered as generalizations of the short-wire or strip-pair design, which have been demonstrated to provide a magnetic response and negative permeability and to constitute an effective alternative to split ring resonators (SRRs).

The organization of the chapter is as follows. In Section 19.2 the state of the art in the field of NIMs is briefly summarized, without aiming for completeness, to provide the reader some background information. Then, the designs of a few fully planar metamaterial media suitable for microwaves and millimetre-wave frequencies are presented. These fully printed designs using a single dielectric sheet are very simple to fabricate and constitute alternative implementations for either single-polarization or isotropic left-handed materials (LHMs). Furthermore, as a main advantage, the presented geometries provide several parameters to control the electric and magnetic resonances. In the second part of this chapter, the attention is focused on metamaterials based on plasmonic nanostructures. In particular, we analyze the properties of certain metamaterials whose constitutive unit cell simply consists of a pair of nanospheres or a cluster of four nanospheres. We show that one of the local resonance modes of these closely packed nanospheres constituting the metamaterial unit cell is associated with a magnetic dipole and thus can lead to artificial magnetism.

19.2 Background

Realization of NRI materials loomed as a challenge since the late 1960s when Veselago analytically investigated the electrodynamics of substances exhibiting simultaneous negative dielectric permittivity and magnetic permeability, showing that in such media waves behave in a reversed manner and exhibit many peculiar effects, including negative refraction, reversed Doppler shift, and Cherenkov radiation [1]. Indeed, a main obstacle to the practical implementation of metamaterials was represented by the fact that at microwave frequencies the magnetic susceptibility of all natural materials tails off and losses start to be significant. To overcome such fundamental limitations, the original approach proposed by Pendry et al. [2] was to exploit the inductive response from structured nonmagnetic materials to obtain high-frequency magnetism. This concept has found successful implementations through the use of arrays of copper SRRs which generate an effective magnetic response at frequencies up to hundreds of terahertz [3–6]. In this range of frequencies, SRRs combined with wires have been used as the constituent particles of artificial media in which NRI can be observed for plane waves with fixed polarization impinging at certain angles [7–9].

However, the direct scaling of the demonstrated SRR microwave media to visible-light frequencies, where one can expect most exciting applications, appears to be impracticable because of both technological issues (structures with critical features and extremely small sizes) and different electromagnetic responses of materials to visible light and microwaves, including the impact of inherent losses, which were predicted to limit the SRR approach to frequencies well below optical [10]. Furthermore, a major disadvantage of SRR-based materials is that to achieve a LH behavior one has to employ an incident magnetic field perpendicular to the SRRs' plane and thus a propagation direction parallel to the SRRs' plane; this requires multilayer samples that must be assembled in a nonplanar way, with very tight tolerances. Therefore, the manufacturing of such material faces enormous difficulties, especially at terahertz and optical frequencies. Accordingly, a great deal of effort has been recently focused on the development and fabrication of increasingly more efficient metamaterial media, and the search of novel physical structures of the constituent particles still remains an acute problem, especially at optical frequencies.

Indeed, a variety of designs have been devised to overcome the technological impairments related to the fabrication and assembling of SRRs. Many of these alternative approaches are summarized in this handbook; for instance, in [11,12] an example of metamaterial at microwave frequencies made by a planar assembly of metallic disks or holes in metallic screens is presented; moreover, see [13] (and references therein) for a description of a class of metamaterials using electrically dense spheres.

In the rest of this chapter we restrict our focus to a class of metamaterials that exploit the occurence of an antisymmetric resonance mode (the so-called magnetic resonance mode) in *pairs* of tightly coupled particles, at both microwave and optical frequencies.

19.3 From SRR and Wire Media to Planar Metamaterials: Short-Strip Pairs and Related Structures

An alternative to the SRR and wire design that seems to overcome most of the aforementioned impairments is based on a simplified structure composed by a pair of short wires or strips [14–16] (Figure 19.1). The capability of a pair of metallic nanorods to provide a diamagnetic response and, most importantly, NRI was first demonstrated in [17,18]. As illustrated in Figure 19.1, a magnetic field oriented perpendicularly to the plane of the rods causes antiparallel currents in the two rods, which in turn provide a resonant magnetic response of the system analogous to that of the SRRs. A similar mechanism works also for strip pairs. This substantial equivalence between the magnetic response of wire or strip pairs and SRRs is further clarified in Figure 19.2a through c, which shows how by continuous transformation an SRR can be reduced to a pair of aligned strips separated by a dielectric spacer.

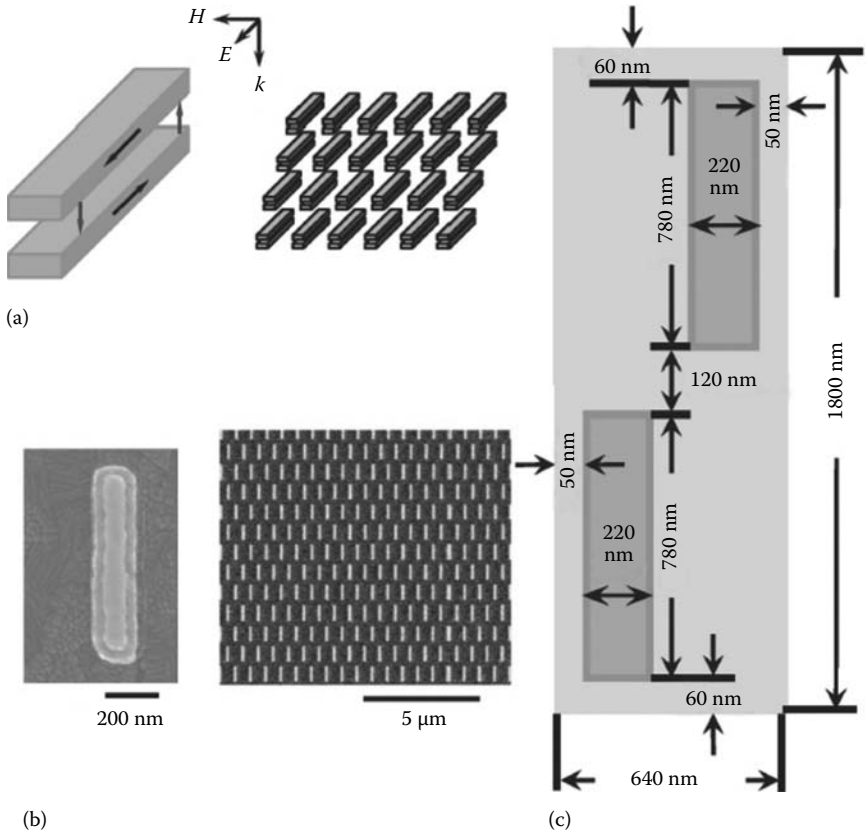

FIGURE 19.1 (a) Schematic for the array of nanorod pairs supporting antiparallel current modes. (b) Field-emission scanning electron microscope images of the fabricated nanorod pairs array where a negative refractive index is achieved at telecommunication wavelengths. (c) Elementary cell. (Reprinted from Shalaev, V.M., Cai, W., Chettiar, U.K., Yuan, H.-K., Sarychev, A.K., Drachev, V.P., and Kildishev, A.V., *Opt. Lett.*, 30(24), 3356, 2005. With permission.)

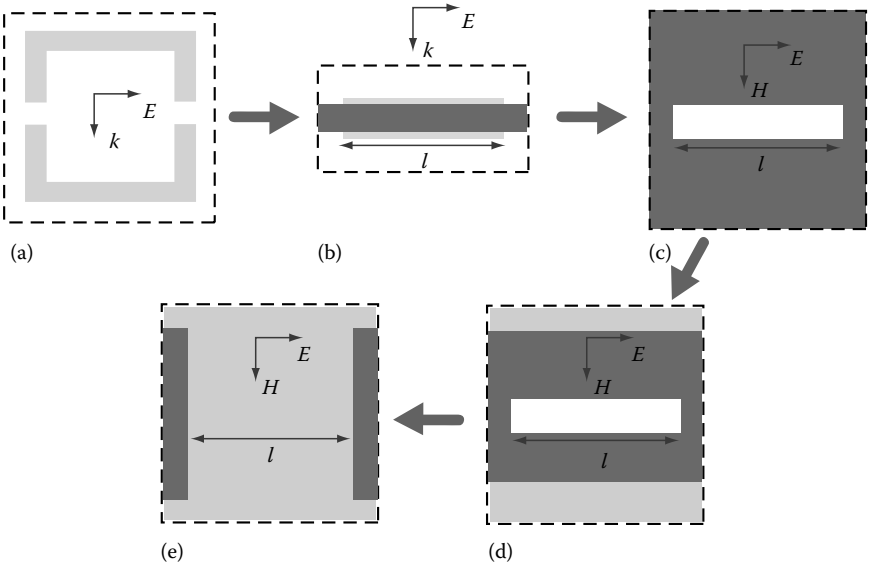

FIGURE 19.2 The two-cut single metallic SRR (a) can be transformed to a pair of parallel metallic bars separated by a dielectric; (b) view in $(\boldsymbol{E}, \boldsymbol{k})$ plane; (c) view in $(\boldsymbol{E}, \boldsymbol{H})$ plane. Adding continuous wires results in design (d) [view in $(\boldsymbol{E}, \boldsymbol{H})$ plane], which can be modified to (e) a fully connected one on both sides of the thin dielectric board. The dashed squares define unit cells with dimensions a_x (parallel to $\boldsymbol{H}$), a_y (parallel to $\boldsymbol{E}$), and a_z (parallel to $\boldsymbol{k}$). (Reprinted from Zhou, J., Economon, E.N., Koschny, T., and Soukoulis, C.M., *Opt. Lett.*, 31(24), 3620, 2006. With permission.)

Differently from SRRs, the antisymmetric or loop mode in the strip pairs can be excited by an incident EM field propagating perpendicularly to the layer where such pairs are printed, as also indicated in Figure 19.1, such that a strong magnetic response and demonstration of negative permeability can be obtained with only one layer of short-strip pairs. In addition to this magnetic mode, short-strip pairs also support a symmetric mode, corresponding to parallel currents in the strips associated with a resonant electric response and a negative permittivity regime. Accordingly, as a further advantage of using pairs of finite-length wires or strips, besides replacing the SRRs as magnetic resonators, one could simultaneously obtain a negative permittivity in the same frequency range, and, therefore an NRI, without the need for additional continuous wires.

However, it must be pointed out that the condition for obtaining simultaneous negative permeability and negative permittivity by pairs of short metallic strips is subject to some restrictions [19,20]. Indeed, the difficulty of obtaining NRI with short-strip pairs originates from the fact that the electric resonance is generally stronger and wider than the magnetic one; thus, if the electric resonance of the strips is well above the magnetic resonance frequency, simultaneous negative permittivity and permeability cannot be achieved. As a consequence, one usually needs to locate the magnetic resonance within the negative permittivity region (unless the region of negative permeability can be made wide enough to overlap, at least partially, the negative permittivity region). Yet employing simple short-strip pairs, the separate tuning of these two resonances to achieve an NRI is not feasible, because the frequencies of both the electric and magnetic resonances are controlled by a single geometrical parameter, i.e., the length of the wires (both frequencies are approximately proportional to the inverse length) [21].

A convenient approach to achieve LH behavior from short-strip pairs is to combine them with continuous wires (cf. Figure 19.2d), which provide a large negative permittivity band due to their plasmonic response, and one can exploit only the negative permeability produced by the pair [19,22].

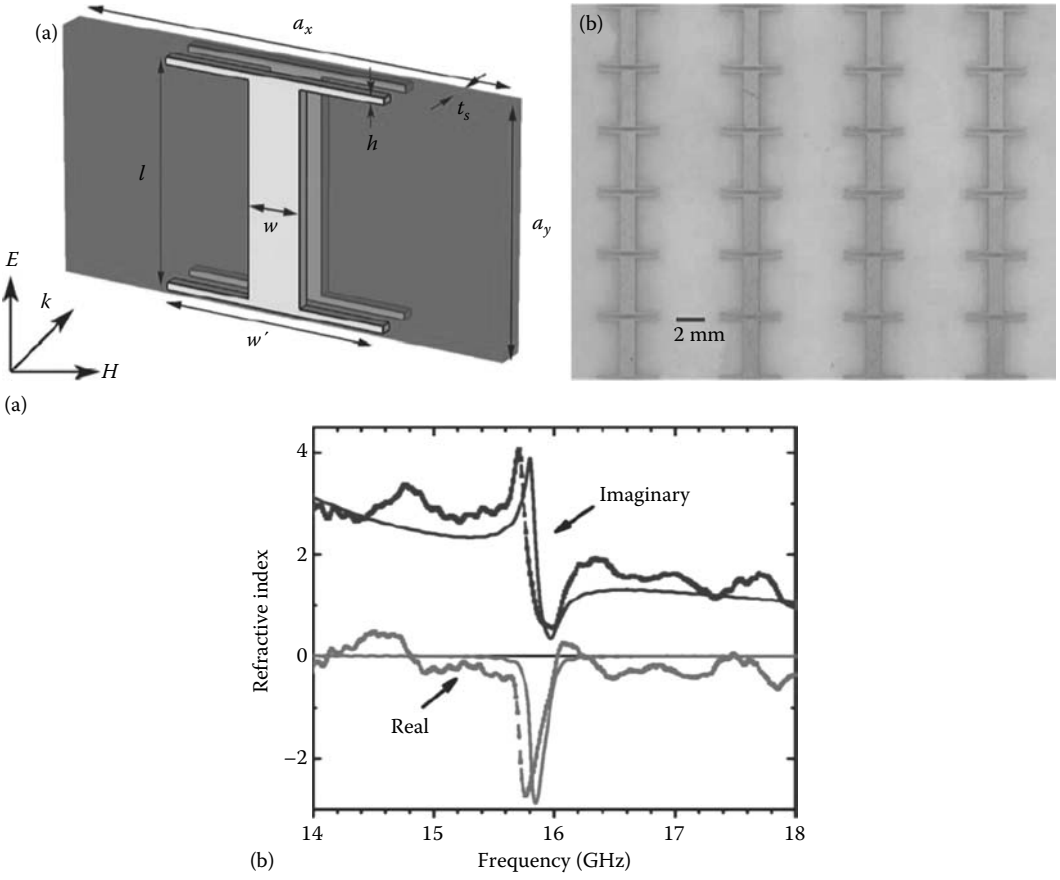

FIGURE 19.3 (a) Schematic representation of one unit cell of the wire-pair structure. (b) Photograph of fabricated microwave-scale wire-pair sample. (b) Extracted refractive index n of a periodic array of wire-pair unit cells, using the simulated (solid curves) and measured (dotted curves) transmission and reflection data. The black and gray curves show the real and imaginary parts of n, respectively. (Reprinted from Zhou, J., Koschny, T., Zhang, L., Tuttle, G., and Soukoulis, C. M., *Appl. Phys. Lett.*, 88(22), 221. 103/1–3, 2006. With permission.)

A further possibility to accomplish an electric resonance lower than the magnetic one is to increase the interparticle capacitance by reducing the distance between the pairs or increasing the width of the strips at their ends as shown in Figure 19.3, that is, by choosing for each strip an "H" shape (in the following also referred to as "dogbone" shape), as first suggested in [20].

The same concept of pairs of strips or slabs underlies the so-called fishnet structure, which was originally introduced in [23]. Indeed, the fishnet design can be thought of as obtained from the strip-pair and continuous-wire design by increasing the width of the strips until they join the infinite wires, thus producing a continuous connected network that can be constructed by opening periodically placed rectangular or circular holes in uniform metallic films covering both sides of a dielectric sheet [22,24–28]. The fishnet has been proven as one of the effective structures for obtaining NRI behavior; however, its properties are described in detail elsewhere in this handbook [29], and, therefore, they will not be repeated herein. Instead, in this chapter we focus on the description of metamaterials featuring alternative configurations of the constitutive resonant particles.

It is noted that most of successful designs for NRI materials at both microwaves and optical frequencies have so far used the idea of creating a negative magnetic permeability by means of the excitation of antisymmetric currents in pairs of either rods or strips, following the original idea in [17]. The negative permittivity in such structures originates from resonant or off-resonant oscillations of electrons in metals.

As a generalization of this design approach, we have developed a few sample metamaterials with periodic structure whose unit cells are based on the concept of pairing two substantially arbitrarily, though suitably, shaped conductors. Analogously to short-strip pairs, such configurations are shown to support both antisymmetric (magnetic) and symmetric (electric) resonance modes, whose interaction, when properly engineered, can reflect in simultaneous negative permittivity and permeability, and, accordingly, NRI behavior.

The main reason prompting this investigation is that modifications of the basic structures previously recalled and materials with significantly different geometries, though based on the same coupled-particle approach, may lead to NIMs with altered and possibly improved NRI properties.

In particular, the tightly coupled particle pair concept is first applied to the development of planar metamaterial designs, also taking inspiration, in the choice of the unit cell configuration, from the geometries elaborated in the context of frequency selective surfaces [30]. These fully printed structures using a single dielectric sheet are simple to fabricate and provide alternative implementations for single polarization and isotropic NIMs. The NRI properties of these planar metamaterials are demonstrated at microwave frequencies. These structures present the same level of complexity of simple cut-wire pairs, which have already found experimental confirmations at optical wavelengths [14], therefore, extension to terahertz and optical frequencies is conceivable provided that the change of the metal behavior from lossy conductors at gigahertz frequencies to lossy, negative permittivity dielectrics in the higher terahertz region is adequately taken into account. Then, in the second part of this chapter, we focus on metamaterials for optical frequencies based on plasmonic nanostructures. In particular, we analyze the electromagnetic response of certain metamaterials whose constitutive unit cell simply consists of a pair of nanospheres or a cluster of four nanospheres. We show that one of the local resonance modes of these closely packed nanospheres constituting the metamaterial unit cell is associated with a magnetic dipole and thus can lead to artificial magnetism at optical frequencies.

The properties of the different media discussed here have been examined through transmission (T) and reflection (R) simulations and, when required, by inversion of the transmission and reflection data to obtain the effective material parameters ϵ, μ, refractive index, n, and impedance, $z = \sqrt{\mu/\epsilon}$. For the inversion of the R/T data a standard retrieval procedure [31] has been employed, which treats a metamaterial as a homogeneous effective medium.

19.4 Negative Refractive Index Behavior from Loaded Strip Pairs: The Dogbone-Pair Design

As mentioned above, independent tuning of the electric and magnetic resonances of a short-strip pair medium may become possible by strengthening the interaction of the pairs belonging to the neighboring unit cells along the electric field direction [32]. The additional interpair capacitance, resulting from this enhanced interaction, has more effect on the electric resonance frequency than the magnetic one, when the pair distance H is small. Instead, the magnetic resonance is strongly affected by the capacitance between the top and bottom conductors. In summary, the modification of the cut-wire topology by the adoption of the dogbone shape, whose lateral arms contribute to both these capacitances, leads to the possibility of separating the control of the electric and magnetic resonance frequencies as required for the achievement of a LH behavior. Indeed, the achievement of NRI behavior by adopting dogbone-shaped conductor pairs in place of simple short-wire pairs has been

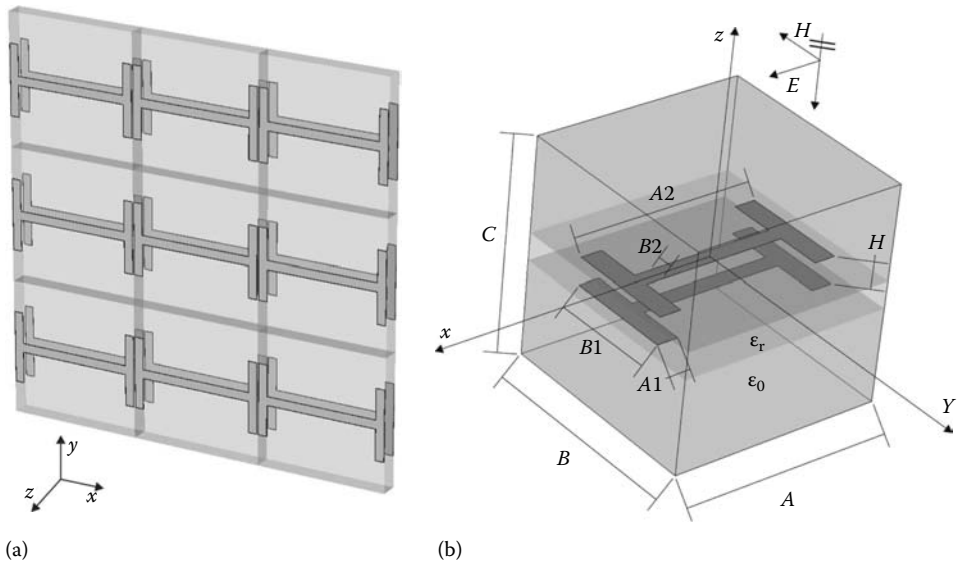

FIGURE 19.4 (a) Perspective view of a layer of the metamaterial formed by a periodic arrangement of tightly coupled pairs of dogbone-shaped conductors printed on a dielectric substrate. (b) Metamaterial elemental particle (unit cell) with geometrical parameters quoted. The polarization of the incident electric field is along the x-direction. (From Markley, L. and Eleftheriades, G.V., *Antennas Wireless Propagat. Lett.*, 6(11), 28, 2007. With permission.)

demonstrated in Ref. [20], from which the sample result of Figure 19.3b is taken. The dogbone particle configuration also exhibits the attractive feature of a reduced unit cell size due to the additional capacitive loading provided by the dogbone lateral arms.

19.4.1 The Dogbone-Pair Design

The objective of this section is to introduce a planar doubly periodic structure, which has the potential to act as an effective anisotropic NRI medium. The constitutive periodic unit cell of this metamaterial structure consists of a pair of tightly coupled dogbone-shaped conductors, as illustrated in Figure 19.4. Such resonant particles are arranged in a regular rectangular lattice that is illuminated by a normally incident (along the z-axis) plane wave with the electric field polarized along the x-direction, parallel to the central segment of the dogbones.

The mechanisms of the resonance formation and field interactions in this periodic structure have been thoroughly investigated [33], and extensive parametric analyses have been carried out to highlight the influence of various geometrical and electrical features of the dogbone unit cell on the response of the metamaterial; major findings that emerged from these analyses are summarized in the following section.

19.4.2 Phenomena Involved in Dogbone Pairs

The resonance properties of a periodic array of dogbone conductor pairs have been investigated through numerical simulation of the field transmission coefficient $|T|$ by using the commercial software Ansoft HFSS [34]. The accuracy of the obtained results was verified through comparison with a further set of simulated data calculated by CST Microwave Studio [35], which were found to be in good agreement with HFSS results.

For the sake of simplicity, we first consider the dogbone particles in free space, i.e., we assume that the dielectric substrate between the top and bottom conductors of the pair has permittivity $\epsilon_r = 1$. Moreover, since we aim at discovering the basic operation features of the dogbone-pair structure, such as resonance frequency locations and NRI capability, conductors are assumed lossless and infinitesimally thin, which is a reasonable approximation at microwave frequencies.

Simulations were performed at a few different values of the unit cell size along the x-direction A, namely $A = 7.5, 7.6, 7.7$ mm, to gain a first insight into the structure resonances. The remaining geometrical parameters (quoted in Figure 19.4) are set to the following default values (in millimeters): $B = 7.5$, $B1 = 4$, $A2 = 7.4$, $B2 = 0.8$, $A1 = 1.0$, and $H = 0.2$. The simulated field transmission coefficient $|T|$ for a doubly periodic layer of dogbone particles with such unit cell configuration is shown in Figure 19.5a. These plots illustrate the first two resonances in the considered structure. The highest resonances at $f \approx 10.9$–11.2 GHz appear to be very slightly affected by variations of A, thus indicating that the fields are confined to the close proximity of the dogbone pairs and are loosely coupled to the adjacent cells. This resonance is usually referred to as the magnetic resonance; its frequency f_m mainly depends on the dogbone-particle dimensions and is associated with the so-called transmission line (TL) mode, which creates an equivalent magnetic dipole moment. The other resonance, denoted as electric resonance, is associated with a dipole-like symmetric mode, which creates an electric dipole moment. It exhibits a much wider stopband, and its frequency f_e ($\approx$9.2, 10.3, 10.9 GHz) more strongly depends on the lattice constant A. This implies that the capacitive coupling between the dogbone particles in the adjacent cells dominates similarly to that in the frequency selective surfaces (FSS) of capacitive type, made, for example, of dipoles or Jerusalem crosses [30].

In order to verify such a definition of the resonant modes, the same dogbone particle was simulated when its lateral arms were short circuited (see inset, Figure 19.5b). Comparison of the corresponding plots in Figure 19.5a and b shows that the magnetic resonance at 10.9–11.25 GHz is suppressed in the structure with the short-circuited arms, whereas the electric resonance at f_e remains nearly unchanged. This confirms that the resonance at 10.9–11.25 GHz in Figure 19.5a is indeed the magnetic-type resonance produced by the antisymmetric mode, with oppositely directed currents flowing on the top and bottom parts of each dogbone pair, and these currents are strongly affected when the arms are short circuited. Conversely, the electric resonance at f_e is weakly perturbed by the short circuits, because it is produced by a symmetric mode whose currents flow in the same direction on both the top and bottom parts of the dogbone particle.

The proposed interpretation of the resonance modes has also been supported by the simulation results for variable cell size B (the period along the y-axis), which is found to similarly influence the structure resonances (although the shift of the electric resonance associated to variations of B is smaller than that observed for variable A, because the particle mutual coupling in the y-direction is weak as long as $(B - B1) >> H$ [33]).

To further illustrate the features of the electric and magnetic resonances, the current distributions on the top and bottom conductors of the unit cell of the dogbone structure considered above, with the period along x, A, set to 7.5 mm, is presented in Figure 19.6 at the frequencies $f \approx 9$ GHz and $f \approx 10.9$ GHz, that is, near the electric f_e and magnetic f_m resonances, respectively. These plots clearly demonstrate that the currents on the top and bottom conductors are antisymmetric at the magnetic resonance, thus justifying the TL model associated with the magnetic dipole discussed in Section 19.4.3. Conversely, near the electric resonance, the currents are in-phase on both conductors and no artificial magnetism can be produced. Note also that the currents on the central parts of the dogbone conductors have more or less the same intensity. At frequencies above f_e, the symmetric mode stores magnetic energy (also due to elements intercouplings), whereas electric energy prevails at low frequencies.

Once the resonance types have been identified and the lattice constant effect is understood, we have evaluated how the resonance frequencies are affected by the dielectric layer parameters, to which the magnetic resonance is expected to be particularly sensitive [33]. The transmission characteristics in

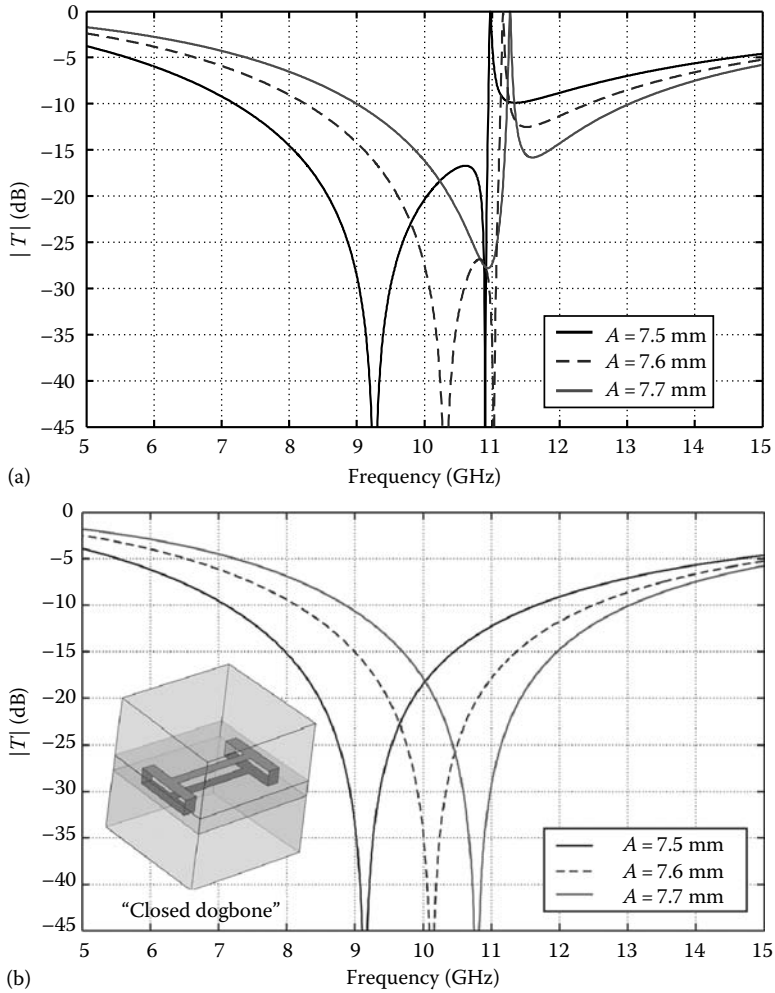

FIGURE 19.5 Field transmission coefficient versus frequency for a doubly periodic layer of dogbone particles (Figure 19.4) in free space at different values of the unit cell size along x (A = 7.5, 7.6, 7.7 mm). (a) The broad electric resonance occurs at $f_e \approx 9.2, 10.3, 10.9$ GHz; the magnetic resonance is at $f_m \approx 10.9, 11.15, 11.25$ GHz; (b) dogbone particles with short-circuited arms in free space ("closed dogbone", in the inset): the electric resonance is still present at $f_e \approx 9.2, 10.3, 10.9$ GHz, whereas the magnetic resonance at $f_m \approx 10.9$–11.25 GHz was suppressed by the short circuits.

Figure 19.7a are simulated for different values of the dielectric substrate permittivity ϵ_r, whereas the geometrical parameters of the dogbone unit cell are set to the default values $A = 7.5, B = 7.5, B1 = 4, A2 = 7.4, B2 = 0.8, A1 = 1.0, H = 0.2$ (in millimeters) reveal that variation of ϵ_r causes interchange of the magnetic and electric resonance positions with respect to each other. Both types of resonances shift toward lower frequencies at higher ϵ_r, albeit f_e and f_m vary with substantially different rates. Indeed, the magnetic resonance appears to be more sensitive to ϵ_r, because its fields are predominantly confined to the dielectric spacer between the dogbone conductors. The electric resonance is less affected, because the electric field of the symmetric mode is mainly located outside the thin dielectric substrate.

Finally, Figure 19.7b demonstrates the effect of the separation H between the top and bottom dogbone conductors. Simulations refer to the same unit cell configuration of Figure 19.5a, except that

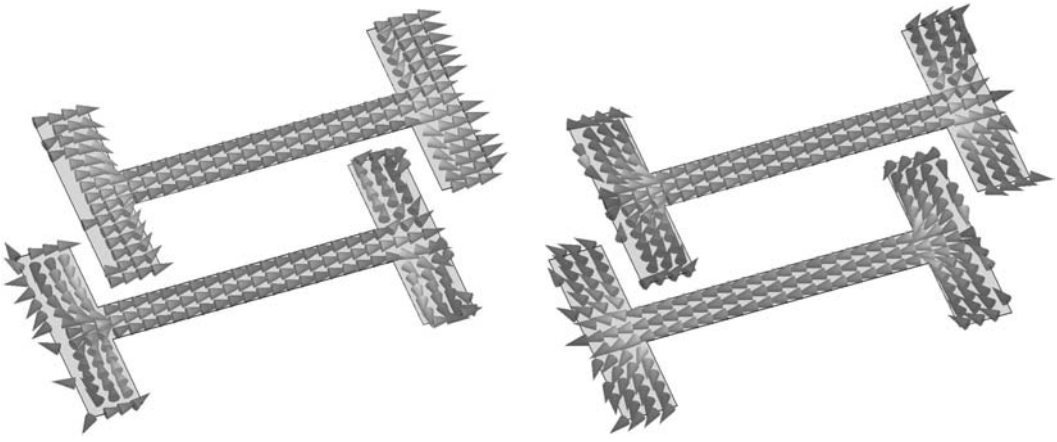

FIGURE 19.6 Current distributions on a pair of tightly coupled dogbone conductors: (a) symmetric current distribution at $f = 9$ GHz, near the electric resonance f_e; (b) antisymmetric current distribution at $f = 10.9$ GHz, near the magnetic frequency f_m. Note that the distance between the conductors is not shown to scale in order to improve the clarity of the representation (in the simulation $H = 0.2$ mm).

H is a variable parameter ($H = 0.4, 0.6, 1.4, 2.6$ mm) and A is fixed to $A = 7.5$ mm. As apparent, f_m decreases with H and also f_e undergoes considerable changes. Namely, at small H (0.4–0.6 mm) $f_m > f_e$, and the magnetic resonance is readily identifiable. But when H further increases to 1.4–2.6 mm, it not only becomes $f_m < f_e$ but also the magnetic resonance exhibits a lower Q-factor.

These changes of the magnetic resonance behavior cannot be explained in terms of a single-mode model, because the capacitive coupling between the top and bottom conductors in a pair may become weaker than capacitive interaction with the particles in the adjacent cells. Under these circumstances, the coupling between contiguous dogbone particles also affects the magnetic resonance as the distance between the contiguous conductors $(A - A2) = 0.1$ mm becomes significantly smaller than the separation H between the top and bottom parts (in this geometry $A = 7.5$ mm and $A2 = 7.4$ mm). Moreover, with larger H, the fringing field effects also become more significant as the stripe separation of $H = 1.4$ mm is even larger than the stripe widths $A1 = 1$ mm or $B2 = 0.8$ mm.

It is noted that for this free-space configuration the size of the induced magnetic dipoles, at the magnetic resonance frequency $f_m \approx 11$ GHz, is less than $A = B = \lambda/3.65$. In spite of the absence of a dielectric substrate, the cell size miniaturization, with respect to the wavelength, still represents a dogbone cell with size considerably smaller than the free-space wavelength, owing to the capacitive coupling between the top and bottom parts of the dogbone particle. Of course, by adopting a denser dielectric substrate, the electrical size of the unit cell can be further reduced [33].

The presented analysis (and additional results in [33]) has demonstrated that the dogbone particles provide for the capability of control over the positions of the electric and magnetic resonances. This property is of particular importance for the implementation of an artificial medium with NRI. In Section 19.4.5 we show that dogbone pairs can be used to realize a medium supporting backward-wave propagation in a frequency band near f_m. If homogeneization is allowed, backward-wave propagation occurs when both the effective permittivity and permeability are negative. This double-negative requirement can be satisfied near f_m, as long as $f_m > f_e$, because the magnetic resonance is generally much narrower than the electric one. (However, as Figure 19.7b shows, the magnetic resonance becomes broader for larger H, and in this case the condition $f_m > f_e$ may not be strictly required for obtaining an NRI.) To fulfill the condition $f_m > f_e$, it is necessary either to increase f_m or to decrease f_e. The f_e can be reduced either by increasing the capacitance between the contiguous

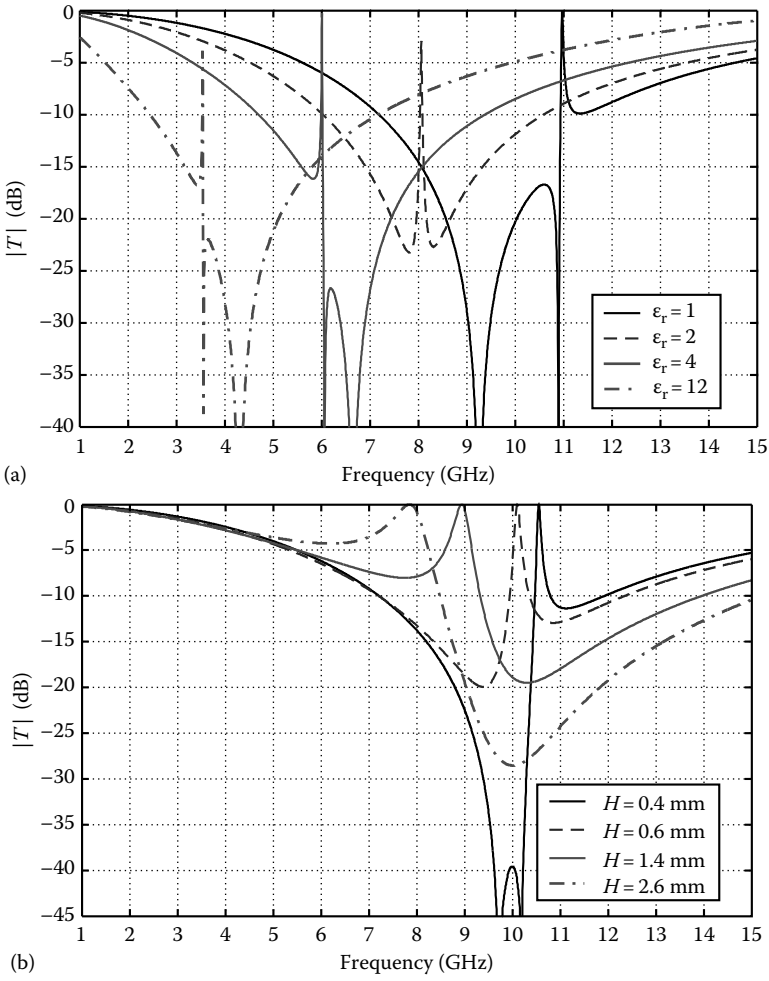

FIGURE 19.7 Field transmission coefficient versus frequency for a double periodic layer of dogbone particles (Figure 19.4) at the default geometrical parameter values (in millimeters): $A = 7.5, B = 7.5, B1 = 4, A2 = 7.4, B2 = 0.8, A1 = 1.0$. In (a) the curves correspond to different values of the permittivity ϵ_r of the dielectric substrate supporting the conductor pairs ($\epsilon_r = 1, 2, 4, 12$), whereas the substrate thickness is fixed to $H = 0.2$ mm. In contrast in (b) the spacing H between the top and bottom conductors is a variable parameter ($H = 0.4, 0.6, 1.4, 2.6$ mm), whereas the substrate permittivity is assumed to be $\epsilon_r = 1$ (dogbone particles in free space).

dogbones or by making the dogbones longer (cf. Figure 19.5a). Alternatively, f_m can be increased by thinning the dogbone lateral arms or by using thinner or lower permittivity dielectric spacers between the top and bottom parts of the dogbone particles (Figure 19.7a and b). In order to qualitatively evaluate the physical structures suitable for realization of the dogbone particles with the required characteristics, a TL model of the dogbone pairs has been developed and is discussed in Section 19.4.3.

19.4.3 Approximate Transmission Line Model for Magnetic Resonances

We provide here an approximate method to predict the magnetic resonances f_m based on a TL model of the antisymmetric mode in the pair of dogbone conductors.

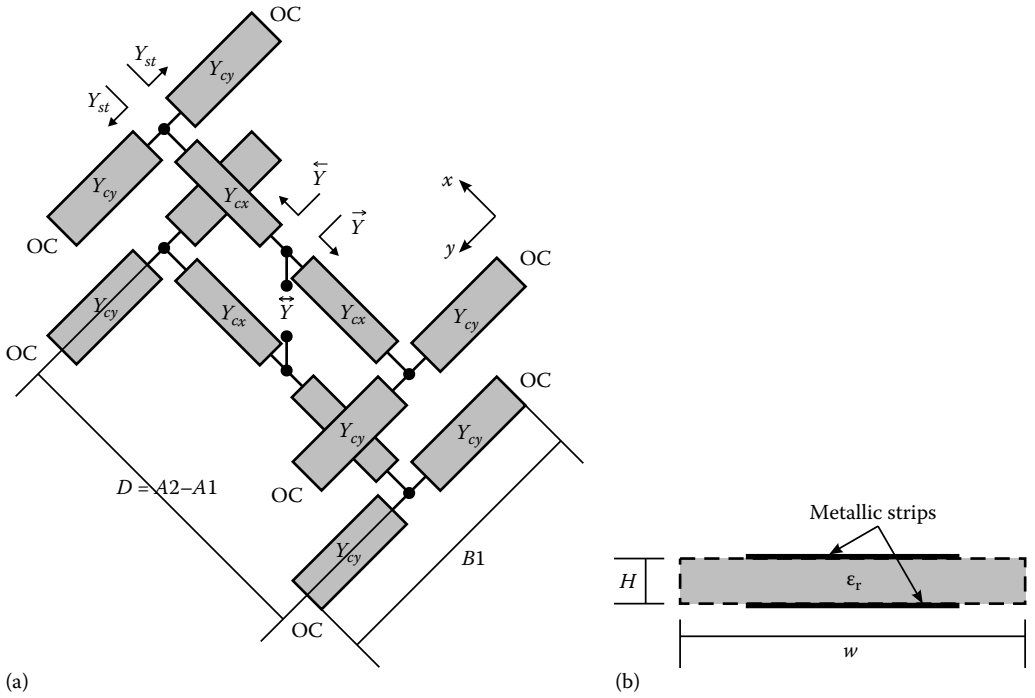

FIGURE 19.8 (a) TL model for the antisymmetric current distribution on a single dogbone-pair particle. (b) Cross-section of the TL. The stripes have width $w = B2$ or $w = A1$ and are separated by a dielectric slab of permittivity ϵ_r and thickness H.

The dogbone "arms" are represented as open-circuited (OC) stubs with characteristic admittance Y_{cy} and wave number β_y, where the subscript "y" is used to denote propagation along the y-direction (Figures 19.4 and 19.8). When using the time convention $\exp(j\omega t)$, these stubs provide the shunt admittances $Y_{st} = jY_{cy}\tan(\beta_y B1/2)$, at the reference ports where they are connected to the TL segment of length $D = (A2 - A1)$ along the x-direction, with the characteristic admittance Y_{cx} and wave number β_x (cf. Figure 19.8). The length D of the central TL segment is defined as the distance between the two mid points in the arms of the dogbone.

To evaluate the characteristic admittances Y_c and wave numbers β of the TLs and stubs, it is convenient to express them in terms of the capacitance C_l and the inductance L_l per unit length (subscripts x, y are temporarily omitted here since the same expressions are used for both the central TL and stubs):

$$Y_c = \sqrt{\frac{C_l}{L_l}}, \quad \beta = \omega\sqrt{C_l L_l} = \frac{\omega}{v_p}, \tag{19.1}$$

where

ω is the angular frequency

$v_p = 1/\sqrt{C_l L_l}$ is the phase velocity of the quasi-TEM (transverse electric and magnetic) wave (purely TEM when the dielectric substrate has $\epsilon_r = 1$)

Then, C_l and L_l can be evaluated for the TL with the cross-section shown in Figure 19.8b by using the standard approximations for microstrip lines with quasi-TEM waves [36]. For the quasi-TEM wave, v_p is alternatively defined as $v_p = c/\sqrt{\epsilon_r^{\text{eff}}}$, where $c = 1/\sqrt{\epsilon_0\mu_0}$ is the speed of light in free space,

ϵ_0 and μ_0 are the permittivity and permeability of free space, and ϵ_r^{eff} is a relative *effective* permittivity of the equivalent homogeneous medium filling the TL cross-section, which may differ for a TL along the x- or y-direction. For a quasi-TEM mode traveling along the TL shown in Figure 19.8b, ϵ_r^{eff} can be approximated as follows cf. [36]:

$$\epsilon_r^{\text{eff}} \approx \frac{\epsilon_r + 1}{2} + \frac{\epsilon_r - 1}{2} \frac{1}{\sqrt{1 + 6/r}}, \tag{19.2}$$

where

$r = w/H$ is the TL aspect ratio
w is the width of stripe conductors
H is the separation between them, as shown in Figure 19.8b
w is either $B2$ (for a TL along x) or $A1$ (for a TL along y)

Making use of the effective permittivity ϵ_r^{eff}, the capacitance per unit length C_l is represented as follows:

$$C_l \approx \epsilon_r^{\text{eff}} \epsilon_0 \overline{C}, \tag{19.3}$$

where $\overline{C}$ is the capacitance per unit length of the stripe conductors in free space, normalized to ϵ_0. Several approximations are available to calculate $\overline{C}$, cf. [36,37], and the following closed-form expressions with relative error less than ±1% at any aspect ratio r is used:

$$\overline{C} \approx \begin{cases} r + 1.21 - \dfrac{0.11}{r} + \dfrac{1}{2}\left(1 - \dfrac{1}{2r}\right)^6, & 2r \geq 1, \\ \dfrac{\pi}{\ln(4/r + r/2)}, & 2r \leq 1. \end{cases} \tag{19.4}$$

The inductance per unit length L_l is expressed in terms of $\overline{C}$ making use of Equations 19.1 and 19.3:

$$L_l = \frac{1}{v_p^2 C_l} = \frac{\mu_0}{\overline{C}}. \tag{19.5}$$

Then the characteristic admittance Y_c takes the form

$$Y_c = \sqrt{\frac{C_l}{L_l}} \approx \frac{\sqrt{\epsilon_r^{\text{eff}}}}{\eta_0} \overline{C}, \tag{19.6}$$

where $\eta_0 = \sqrt{\mu_0/\epsilon_0} = 120\pi\,\Omega$ is the free-space impedance, and the parameters ϵ_r^{eff}, $\overline{C}$ are given by Equations 19.2 and 19.4.

The resonance f_m associated with the TL circuit shown in Figure 19.8 is found by evaluating the total input admittance $\overleftrightarrow{Y} = \overleftarrow{Y} + \overrightarrow{Y}$ at a certain location on the composite TL, where $\overleftarrow{Y}$ and $\overrightarrow{Y}$ are the admittances of the TL facing opposite directions from the reference port (at the center of the dogbone $\overleftarrow{Y} = \overrightarrow{Y}$ for symmetry reasons). Here we are interested in the lowest resonance f_m, whose mode has a maximum current at the center of the dogbone TL that maximizes the strength of the magnetic dipole moment. Therefore, at this resonance $\overleftrightarrow{Y} = \infty$, which requires the denominator of $\overleftrightarrow{Y}$ to vanish, so that the magnetic resonance can be determined by solving

$$Y_{cx} + 2Y_{\text{st}}\, j \tan(\beta_x D/2) = 0, \tag{19.7}$$

whose solutions can be obtained either numerically or approximately as detailed here. Note that in this model we neglect fringe capacitances at open circuits at the TL ends and reactances at the TL bends and junctions. In most cases such approximations are found to be satisfactory and give adequate results.

Approximate Resonance Condition

The above equations can be simplified to determine approximate values of f_m. In the case of $\beta_x D/2 \ll \pi/2$ and $\beta_y B1/2 \ll \pi/2$, with $D = A2 - A1$, we use the following approximations: $\tan(\beta_x D/2) \approx \beta_x D/2$ and $Y_{st} \approx jY_{cy} B1\, \beta_y/2$. Accordingly, the resonance condition (Equation 19.7) takes the form $Y_{cx} - Y_{cy}\, \beta_y\, \beta_x\, B1\, D/2 = 0$, which gives the magnetic resonance angular frequency:

$$\omega_m = \sqrt{\frac{\overline{C}_x}{\overline{C}_y}} \sqrt{\frac{2}{B1\, D}}. \tag{19.8}$$

It is interesting to note that this same result could be obtained by using electrostatic and magnetostatic approximations for the capacitance and inductance of the dogbone [33]. The former is associated with the charge accumulated on the dogbone lateral arms, whereas the latter can be approximated by assuming that the current on the central part of the dogbone is uniform. As a result, we have the following approximations for the capacitance and inductance of the dogbone:

$$C_{\text{eff}} = \epsilon_0 \epsilon_{r,y}^{\text{eff}} \frac{A1\, B1}{H}, \quad L_{\text{eff}} = \mu_0 \frac{H}{B2} D, \tag{19.9}$$

where we have neglected the fringing effects (this is a satisfactory approximation for $w >> H$). Then, taking into account the capacitive contributions of both dogbone arms, the magnetic resonance frequency is given by

$$\omega_m = \frac{1}{\sqrt{L_{\text{eff}} C_{\text{eff}}/2}} = \frac{c}{\sqrt{\epsilon_{r,y}^{\text{eff}}}} \frac{\sqrt{2\, B2}}{\sqrt{B1\, A1\, D}}, \tag{19.10}$$

which is identical to Equation 19.8 when the characteristic impedances are equal, $Y_{cx} = Y_{cy}$ (and thus $B2 = A1$) and $v_{p,x} = v_{p,y}$.

Accuracy and Limitations of the TL Model

The relative accuracy and applicability of the TL approximations developed earlier to evaluate the magnetic resonance f_m of the dogbone particle have been carefully examined, especially in connection with the dependence of f_m on the parameters of the dielectric substrate, namely, its permittivity ϵ_r and thickness H [33].

In Figure 19.9, f_m was calculated at several values of permittivity ϵ_r, whereas the dogbone geometrical parameters assumed the default values (in millimeters): $A = B = 7.5, C = 8, B1 = 4, A2 = 7.4, B2 = 0.8, A1 = 1, H = 0.2$. The reference data for f_m (black curve) have been retrieved from the transmission response of a doubly periodic array of dogbone particles simulated numerically at $\epsilon_r = 1, 2, 4, 8, 12, 16$. The other curves represent the f_m estimates obtained from Equations 19.7, 19.8, and 19.10. It appears that for the considered configuration with a small separation between the top and bottom conductors in the dogbone particle, all the approximations based on a TL model of the antisymmetric mode provide an accurate prediction of the magnetic resonance frequency. Furthermore, they exhibit the same trend previously observed in Figure 19.7a of f_m rapidly decreasing with ϵ_r, thus reconfirming the fact that the fields of the antisymmetric mode are tightly confined to the dielectric substrate between the dogbone conductors.

However, it must be pointed out that when the distance H increases, the estimates of f_m provided by the TL formulas tend to be less accurate [33]. This is indeed not surprising since these approximate formulas completely neglect the fringe capacitances at the TL ends and bends and the capacitance between contiguous dogbone particles. Yet, for larger H, the fringing effects and coupling between adjacent cells become even more pronounced. The latter interaction affects not only the electric but also the magnetic resonance in the case of large separation H between the top and bottom conductors compared with the distance $(A - A1)/2$ between contiguous conductors. Thus, at large values

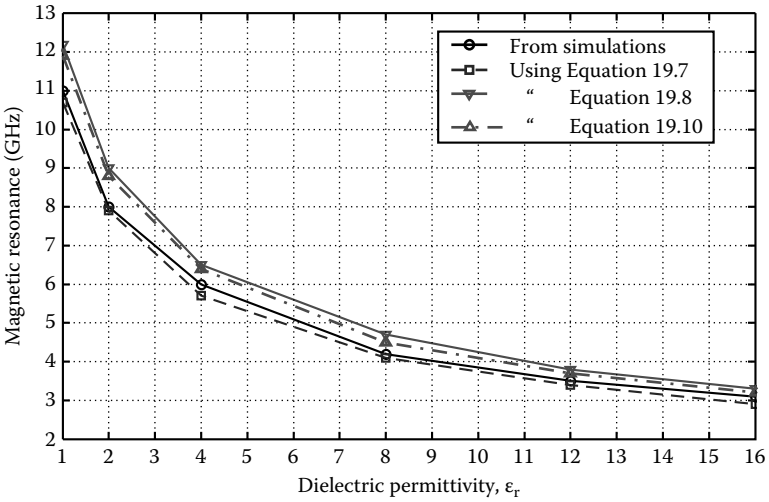

FIGURE 19.9 Magnetic resonance frequency f_m versus permittivity of the dielectric substrate supporting the dogbone particle (thickness is fixed to $H = 0.2$ mm). Data obtained from rigorous numerical simulations (assuming a periodic structure) are compared with the approximate formulas (Equations 19.7, 19.8, and 19.10) based on the TL model for the dogbone antisymmetric mode.

of H, because the rapid variation of f_m cannot be explained in terms of a simple TL model for a single isolated particle since the fringing effects and coupling between particles strongly influence the collective response of the whole array.

In spite of this limitation, the results presented in Figure 19.9 allow one to conclude that, for a broad range of dogbone configurations, the developed approximate analytical models provide an adequate qualitative description which can be instrumental in the initial design of the constituent dogbone particles when the magnetic resonance at a particular frequency is required.

19.4.4 Transverse Equivalent Circuit Network

A more accurate description of the behavior of a metamaterial made of a periodic arrangement of dogbone conductor pairs, or, more generally, of a metamaterial layer made of pairs of conductors, can be derived in the context of a plane-wave transmission line model, which is an effective tool to predict propagation through a number of layers. Indeed, by postprocessing the field reflection and transmission coefficients of a metamaterial layer obtained by simulations, a lumped element network can be synthesized, which exhibits the same frequency response when inserted in the plane-wave equivalent transmission line. The presence in the metamaterial response of both an electric (symmetric) and a magnetic (antisymmetric) resonance finds its correspondence in two respective resonant L–C groups arranged in an equivalent balanced X-network. This equivalent network is useful for a quick numerical characterization of the layer, but it also provides a neat physical description in terms of transmission lines and lumped elements of the operating mechanism of the metamaterial dictated by particle interactions. Furthermore, this network description offers the possibility to evaluate Bloch wave numbers and characteristic impedances and to match metamaterials formed by stacked layers to the free-space impedance.

For the sake of simplicity, we consider here reflection and transmission through just one layer of dogbone pairs, and we assume that the metallic conductors are separated by air (dielectric spacer

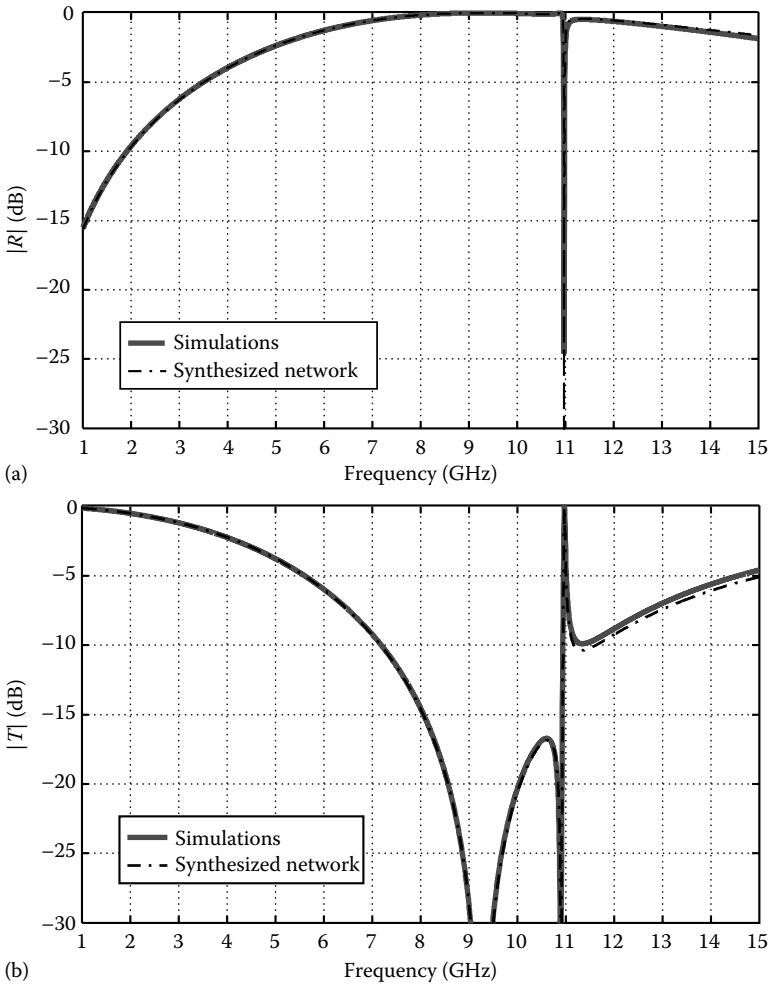

FIGURE 19.10 (a) Reflection and (b) transmission coefficients versus frequency for a layer of dogbone pairs: the magnetic resonance is at $f = 11$ GHz, whereas the electric resonance is at $f = 9.3$ GHz. Data from a numerical analysis are compared with those from the synthesized equivalent network in Figure 19.11.

with $\epsilon_r = 1$). The various geometrical parameters characterizing the unit cell of the considered metamaterial (cf. Figure 19.4) are as follows (in millimeter): $A = 7.5, B = 7.5, A1 = 1.0, B1 = 4, A2 = 7.4, B2 = 0.8, H = 0.2$. The field reflection and transmission coefficients $|R|$ and $|T|$ as obtained by numerical simulations are plotted in Figure 19.10. As can be inferred from the examination of these plots and in accordance with the dogbone-pair particle phenomenology previously discussed, the magnetic resonance occurs at $f = 11$ GHz, whereas the electric resonance is at $f = 9.3$ GHz.

We derive here a z-transmission line model that is able to predict propagation through a layered structure along the z-direction by replacing the thin pairs by an equivalent network of lumped circuital elements, as shown in Figure 19.11a. We assume absence of losses in the metals and in the ambient; therefore, we use only L–C elements. We already know that the magnetic resonance should be described by an L–C resonator (cf. Section 19.4.3) and that the usual stop band of capacitive FSS is described by an L–C series resonance. We synthesize the equivalent X-network in Figure 19.11b for

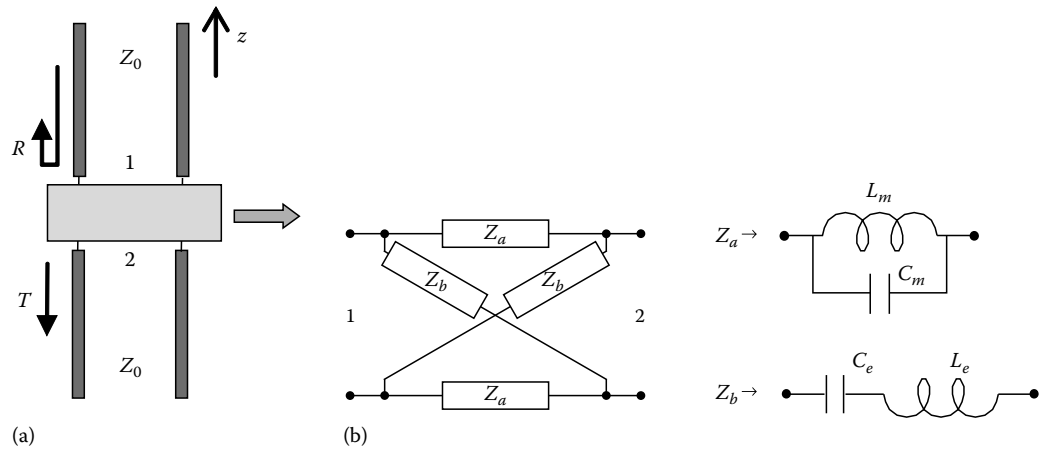

FIGURE 19.11 (a) Plane-wave equivalent z-transmission line with interposed metamaterial diaphragm. (b) Synthesized symmetric X-network reproducing the metamaterial layer frequency response, which comprises two L–C groups associated to the metamaterial electric and magnetic resonances.

the two-port circuit in the z-TL model in Figure 19.11a. The impedances appearing in the synthesized network are simply expressed as

$$Z_a = \frac{1}{j\omega C_m + \dfrac{1}{j\omega L_m}} = \frac{j\omega L_m}{1 - \omega^2 C_m L_m}, \quad Z_b = j\omega L_e + \frac{1}{j\omega C_e} = \frac{1 - \omega^2 C_e L_e}{j\omega C_e}, \tag{19.11}$$

where $C_m = 29.04$ pF, $L_m = 0.072$ nH, $C_e = 6.70$ pF, and $L_e = 4.45$ nH. The L, C values are found by data matching, and one can see in Figure 19.10 that reflection and transmission in the z-transmission line model perfectly match the numerical results.

19.4.5 Backward-Wave Propagation in Media Formed by Stacked Dogbone Particle Layers

Here we show that metamaterials composed of stacked layers of dogbone particles made of tightly coupled pairs of conductors, as shown in Figure 19.4, can support backward-wave propagation in certain frequency bands. In particular, we consider as an example the case of dogbone particles printed on the opposite faces of a dielectric substrate with permittivity $\epsilon_r = 2.2$, such as commercial microwave laminates Rogers RT/Duroid 5880 or Taconic TLY-5. The dogbone dimensions (in millimeters) are $A = B = 7.5$, $B1 = 4$, $A2 = 7.4$, and $A1 = B2 = 0.5$. The simulated magnitude of the field transmission coefficient $|T|$ of a single layer of particles made of such paired dogbone conductors is shown in Figure 19.12a, for two different values of the separation H between the top and bottom conductors, which coincides with the thickness of the dielectric substrate. A narrow passband, which corresponds to the magnetic resonance of the dogbone pair and strongly depends on H, is clearly seen in the plots.

The dispersion diagrams for an infinite periodic arrangement along z, with period $C = 3$ mm, of the stacked layers of the arrayed dogbone particles printed on opposite faces of the dielectric substrate, with two different thicknesses of $H = 0.5$ and 1 mm are presented in Figure 19.12b. The negative slope of the dispersion curves indicates backward-wave propagation along the z-axis, for both considered substrate thicknesses. The passband associated with the magnetic resonance is narrow and further decreases at higher permittivity and/or smaller thickness of the dielectric substrate.

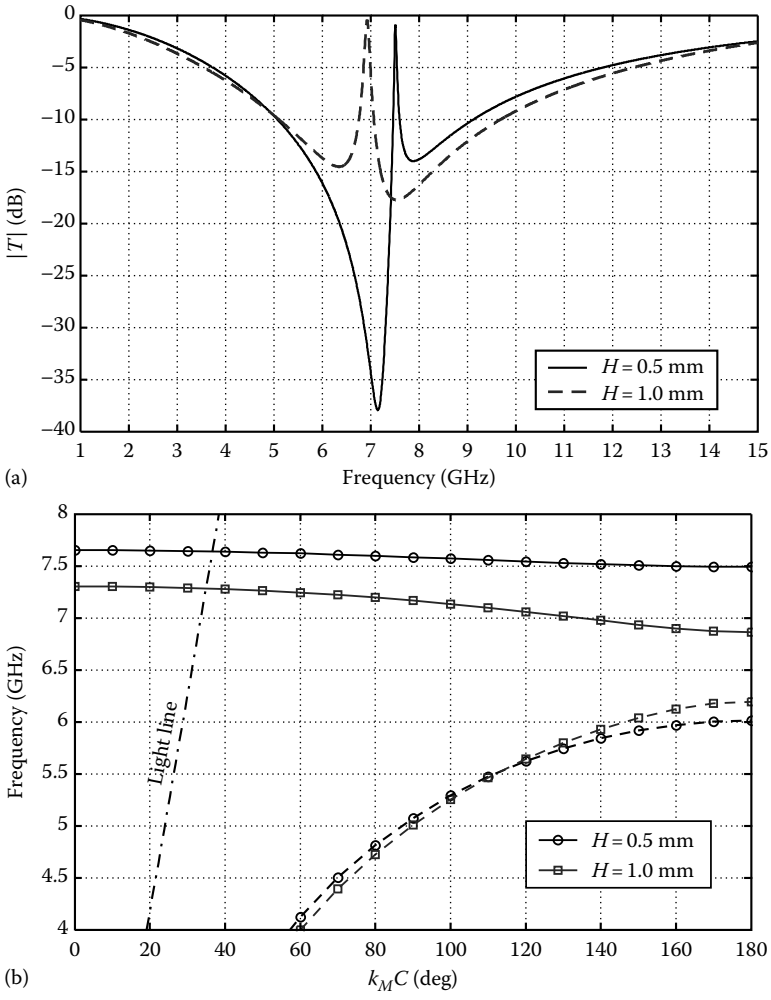

FIGURE 19.12 (a) Amplitude of the field transmission coefficient $|T|$ for a doubly periodic layer of dogbone particle arrays printed on a dielectric substrate with permittivity $\epsilon_r = 2.2$. The thickness of the dielectric substrate H is a variable parameter ($H = 0.5, 1$ mm). The conductor dimensions are $A = B = 7.5$, $B1 = 4$, $A2 = 7.4$, and $A1 = B2 = 0.5$ (in mm). (b) Dispersion curves for a wave with the propagation constant k_M in the infinite periodic stack (period $C = 3$ mm) of layers made of the tightly coupled dogbone pairs from Figure 19.4, printed on a dielectric substrate with permittivity $\epsilon_r = 2.2$ and of variable thickness $H = 0.5, 1$ mm.

19.5 Planar 2D Isotropic Negative Refractive Index Metamaterial

Most of the previously designed NIMs are anisotropic, i.e., their properties are polarization dependent. For example, in cut-wire pairs the aforementioned magnetic and electric resonances are observed only for an incident electric field parallel and magnetic field perpendicular to the plane containing the two wires. Such polarization dependence of the effective medium is undesired in potential applications, such as, for example, the perfect lens.

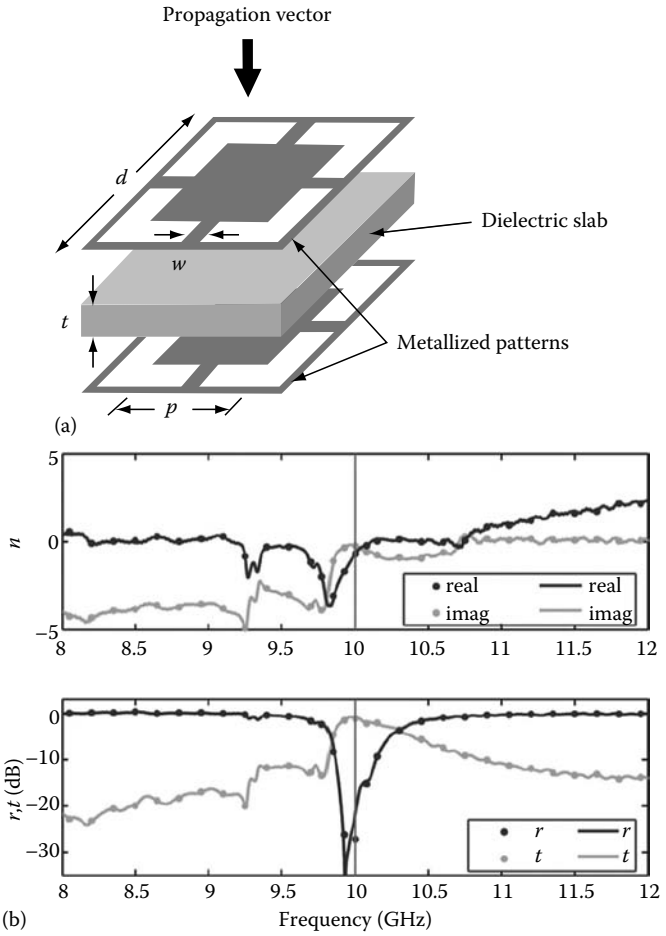

FIGURE 19.13 (a) Schematic representation of the unit cell of the structure presented in [39]. (b) Extracted refractive index *n* and scattering parameters from the experimental data relevant to the same metamaterial structure at horizontal polarization (lines) and diagonal polarization (markers). (Reprinted from Markley, L. and Eleftheriades, G.V., *Antennas Wireless Propagat. Lett*., 6(11), 28, 2007. With permission.)

Fully printable NIMs responsive to arbitrary linear incident polarization have been recently proposed in [38], as an extension of the cut-wire pair structure, and in [28,39] by modification of the "fishnet" design introduced in [24]. The unit cell configuration for the metamaterial proposed in [39] is shown in Figure 19.13 along with experimental data confirming the NRI behavior.

A further structure suitable for arbitrarily polarized incident waves has been developed in [40] starting from the dogbone-pair design, which was presented in [20,33] and is summarized in Section 19.4.1. In the following, we discuss in detail the characteristics of this latter 2D isotropic NIM that, similarly to the dogbone-pair structure from which it is descended, provides enhanced control of the particle resonances as compared with the simple cut-wire pair topology and its extension to couple with incoming plane waves of any linear polarization [38].

The original dogbone-pair particle can be converted into a symmetrical configuration by simply combining two orthogonal "dogbone" pairs, thus forming a pair of tightly coupled Jerusalem crosses. By virtue of this symmetric arrangement of the unit cell, the resulting material exhibits an

LH behavior for any linear polarization of the incident wave, in contrast to [33], where the composite medium is sensitive to a single polarization only. The effect of substrate losses is also examined, showing their negligible effect unless the magnetic resonance is very narrowband.

19.5.1 The Jerusalem-Cross-Pair Design

The proposed metamaterial structure is composed of a doubly periodical arrangement of pairs of face-coupled Jerusalem crosses, as illustrated in Figure 19.14. Owing to its unit cell symmetry, such metamaterial provides an isotropic response to any linearly polarized incident wave. The conductor pairs are made of 10 μm-thick copper foils deposited on both sides of a dielectric substrate with permittivity $\epsilon_r = 2.2$ and loss tangent 0.0009, such as commercially available microwave laminates Rogers RT/Duroid 5880 or Taconic TLY-5. The constitutive periodic unit cell has a square cross-section with side length $A = B = 7.5$ mm, whereas the size C in the longitudinal direction as well as the thickness H of the dielectric substrate are variable parameters. The default values of the remaining geometrical parameters used for the design are $A1 = B2 = 0.5$ mm, $A2 = 7.4$ mm, and $B1 = 4$ mm.

Since the pair of Jerusalem crosses can be seen as the superposition of two dogbone-shaped conductor pairs [33], the phenomenology of the particle response is substantially similar in both structures except the polarization sensitivity. Indeed, at any orientation of the incident magnetic field, its components perpendicular to the area between the central arms of the Jerusalem crosses induce a current loop closed by the displacement currents at the external arms. These loops, associated with antiparallel currents in the pair of stacked crosses and opposite sign charges accumulated at the corresponding ends, give rise to the magnetic resonance, which in turn results in an effective permeability of the patterned substrate. The cross pairs also exhibit an electric resonance due to the

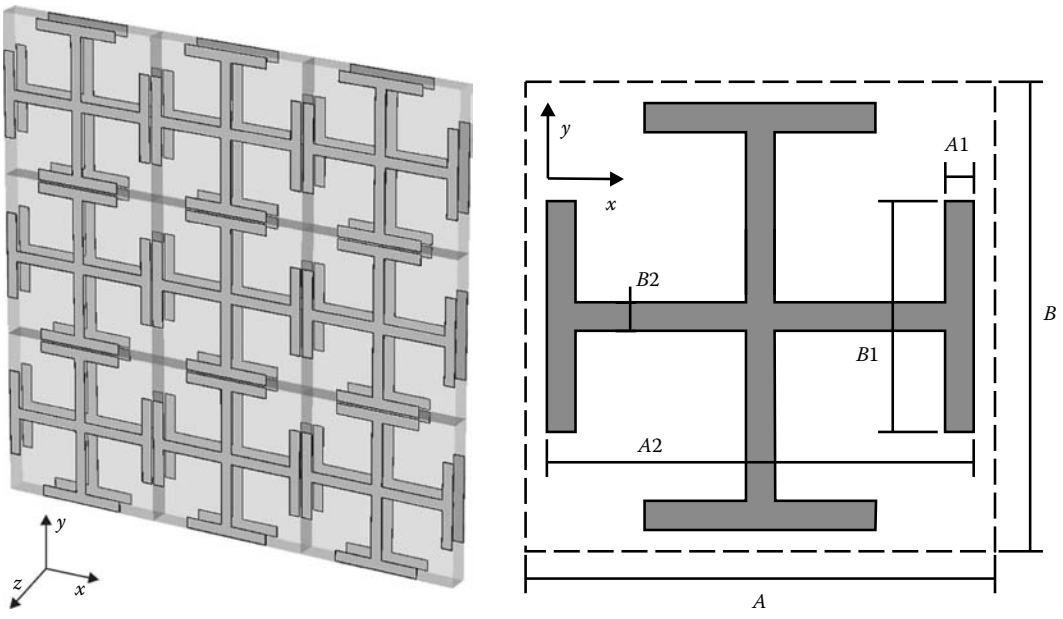

FIGURE 19.14 (a) Perspective view of a layer of the 2D isotropic metamaterial formed by a periodic arrangement of tightly coupled pairs of Jerusalem crosses, which exhibit an antisymmetric (magnetic) resonance for both orthogonal incident linear polarizations. (b) Top view of the metamaterial unit cell with geometrical parameters quoted. In all simulations, we have set $A = B = 7.5$ mm, $A1 = B2 = 0.5$ mm, $A2 = 7.4$ mm, and $B1 = 4$ mm.

excitation of parallel currents in the central stripes and charges of the same sign accumulated by the external arms. This latter resonance can be associated with an effective negative permittivity, and when it is superimposed with the above-mentioned magnetic resonance, the composite medium is expected to exhibit an effective NRI behavior in a certain frequency band.

19.5.2 Left-Handed Transmission in Jerusalem-Cross-Pair Media

The properties of the metamaterial whose unit cell particle consists of the Jerusalem cross-pair of Figure 19.14 have been simulated with the aid of the commercial software CST Microwave Studio. The reflection and transmission characteristics of a layer with periodically arranged particles were modeled using a single unit cell with double periodical boundary conditions in the layer plane, xy. In the numerical analysis we considered a single linear polarization along the x-axis because, due to the structure symmetry, the response to the orthogonal y-directed polarization is identical, and arbitrarily linearly polarized waves at normal incidence can be represented as a superposition of two waves with orthogonal polarizations. The magnitudes of the simulated reflection and transmission coefficients at normal incidence for three different values of H ($H = 0.5, 1$, and 2 mm) are shown in Figure 19.15 for both the cases of lossy and lossless structures. Resonance transmission peaks can be observed, which, similarly to those in the "dogbone" pairs [33], are attributed to the magnetic-type resonance. As apparent with thicker substrates, the transmission resonance occurs at lower frequencies and its bandwidth increases.

It is noted that the transmission is slightly lower and attenuation is slightly higher in the structures with thinner substrates, which is the result of a stronger concentration of the electric field between the conductors that in turn causes an increased absorption of the incident wave by the lossy dielectric substrate. Away from the magnetic resonance, the transmission characteristics of the lossy and lossless structures are almost coincident. Therefore, for the sake of simplicity, both dielectric and conductor losses are not considered in the subsequent analyses.

In Figure 19.16, we show the surface current distribution on the conductor pairs of the unit cell of the structure presented in Figure 19.14, with $C = 4$ mm and $H = 2$ mm, calculated at the frequency $f = 6.4$ GHz, just above the transmission peak occurring at 6.3 GHz (cf. Figure 19.15). This plot clearly demonstrates that the currents on the two conductors are antisymmetric at the resonance, thus forming a current loop that can be represented by an equivalent magnetic dipole moment. This magnetic moment is responsible for the artificial magnetism of the structure, and, therefore, such a resonance is referred to as a magnetic resonance, similarly to the case of dogbone pairs [33].

In the subsequent simulations we have examined the effect of tilting the incoming plane wave to off-normal incidence on the transmission properties of the Jerusalem cross-pair structure of Figure 19.14 with $C = 4$ mm and $H = 1.5$ mm. A transverse-electric (TE) polarized wave was considered under incidence angles ranging from $\theta_i = 0°$ to $\theta_i = 45°$, and the results are displayed in Figure 19.17. It can be seen that the transmission characteristics barely change at increasingly off-normal incidence and the only effect seems to be a low reduction of the resonance bandwidth; this implies that the structure can still provide an NRI behavior when illuminated at skew incidence angles.

Effective Material Parameters

In order to obtain further evidences that the transmission characteristics presented above are associated with a backward-wave phenomenon, the effective material parameters describing the behavior of the Jerusalem cross-pair structure in Figure 19.14 at normal incidence have been determined by following the procedure proposed in [31]. The effective impedance Z, refractive index n, permittivity ϵ, and permeability μ retrieved from the simulated transmission and reflection characteristics for one layer of Jerusalem cross-pairs are shown in Figure 19.18. These results correspond to the same set of

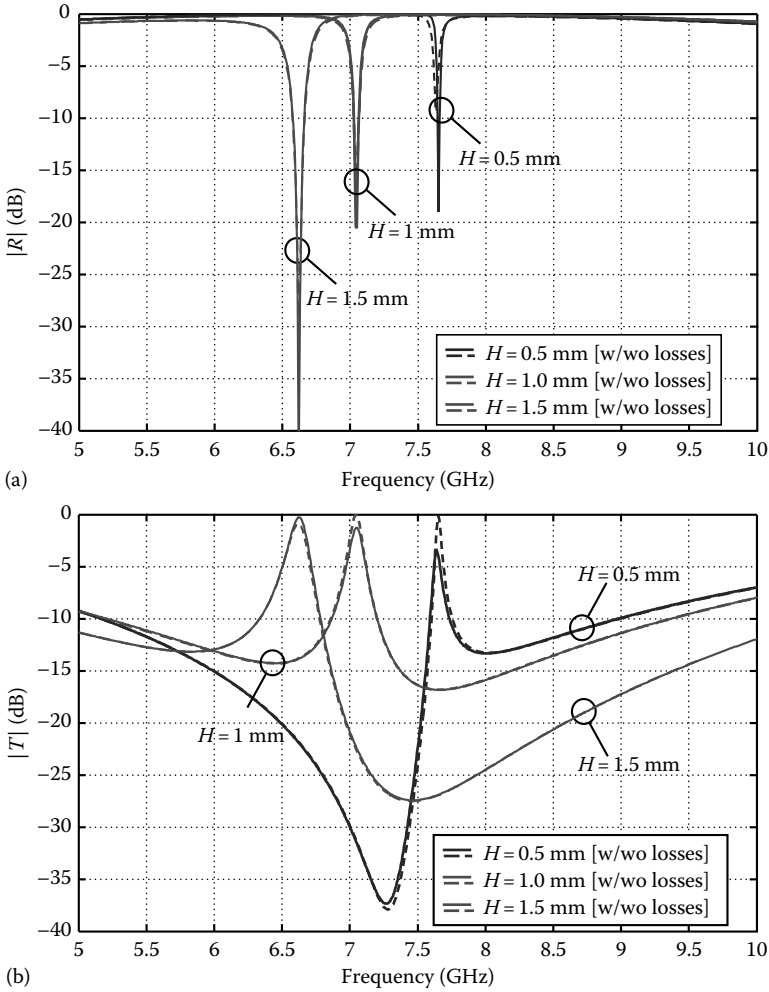

FIGURE 19.15 Simulated reflection and transmission coefficients versus frequency for a layer of periodically arranged Jerusalem cross-pairs (Figure 19.14); various curves correspond to different thicknesses H of the dielectric substrate supporting the top and bottom conductors, whereas the size of the unit cell along the propagation direction is fixed to $C = 4$ mm. Solid and dashed lines correspond to lossy and lossless structures, respectively.

different substrate thicknesses H considered in Figure 19.15, whereas the size of the unit cell along the propagation direction is fixed to $C = 4$ mm. The plots show that the real part of the permittivity is negative over most of the simulated frequency range (for $f > 5.6$–5.8 GHz) for all thickness values. Contrastingly, the real part of the permeability is negative only over a resonance band that becomes more narrow at smaller substrate thicknesses. (The imaginary parts of both the permittivity and permeability are zero due to the assumption of absence of losses). At any rate, the magnetic resonance always falls within the negative region of ϵ; as a consequence, in the frequency band just above the magnetic resonance the metamaterial presents a double-negative behavior and the extracted real part of the effective refractive index is found to be negative. This confirms the LH nature of the transmission peaks observed in Figure 19.15. The NRI bands, which are highlighted by different shaded areas in Figure 19.18, are separated from the relative transmission bands with positive refractive index at low frequencies by a band gap where transmission is forbidden. As apparent, the frequency extension

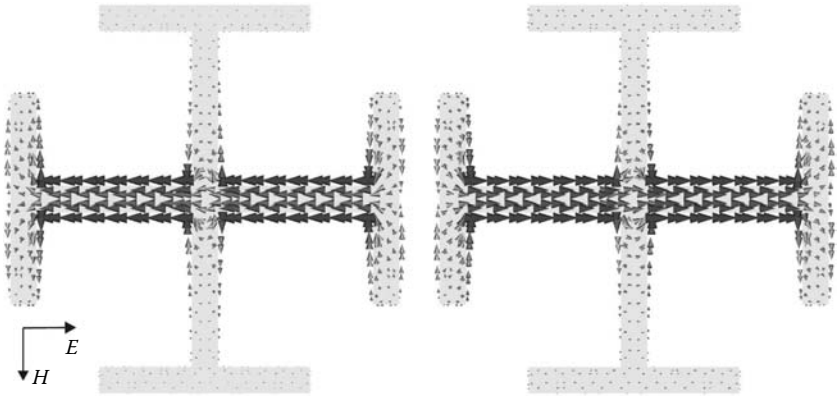

FIGURE 19.16 Surface current distribution on the top and bottom conductors (left- and right hand side plots, respectively) of the Jerusalem cross-pair structure of Figure 19.14 ($C = 4$ mm, $H = 2$ mm) at the frequency $f = 6.4$ GHz just above the magnetic resonance $f_m = 6.3$ GHz. The illuminating plane wave is normally incident on the structure with the electric field horizontally polarized.

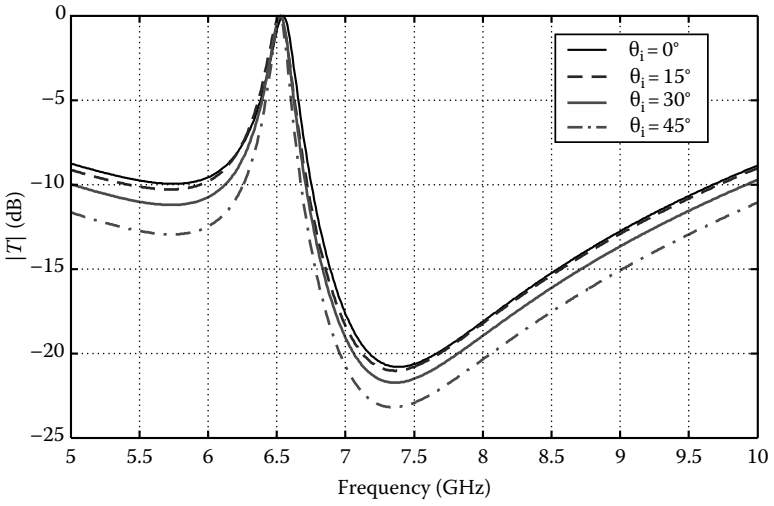

FIGURE 19.17 Simulated field transmission coefficients versus frequency for a layer of periodically arranged Jerusalem cross-pairs (Figure 19.14) illuminated by a TE-polarized plane wave at off-normal incidence angles $\theta_i = 0°, 15°, 30°$, and 45°. The thickness of the dielectric substrate is $H = 1.5$ mm, and the size of the unit cell along the propagation direction is $C = 4$ mm.

of these bandgaps gradually reduces for larger substrate thicknesses, whereas the NRI bandwidths increase.

Modal Dispersion Analyses

The existence of an effective NRI band can be further demonstrated by calculating the dispersion characteristics of the eigenmodes in the infinitely extended metamaterial formed by stacking with period C along the z-axis the structure of Figure 19.14 with the same parameters as in Figure 19.15 ($H = 0.5, 1$, and 2 mm). Figure 19.19 shows the calculated one-dimensional dispersion diagram ω

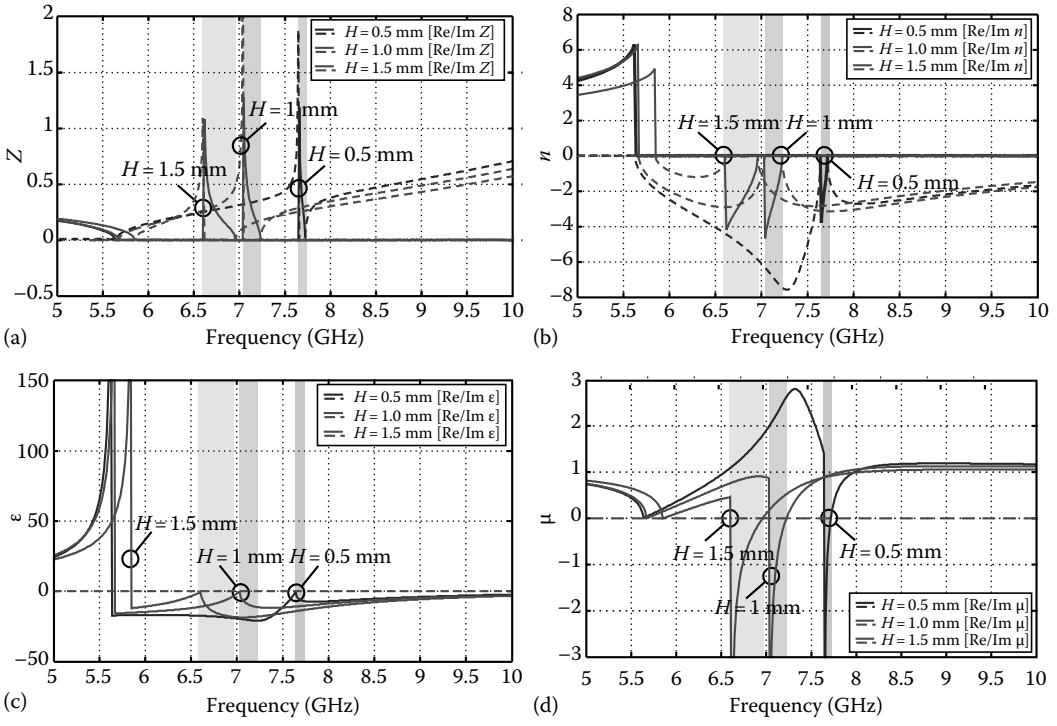

FIGURE 19.18 Effective material parameters for the Jerusalem cross-pair structure of Figure 19.14 under normal incidence and fixed polarization calculated at different thicknesses H of the dielectric substrate supporting the top and bottom conductors. The size of the unit cell along the propagation direction is set to $C = 4$ mm. The real and imaginary parts of the effective parameters are plotted in solid and dashed lines, respectively. Shaded areas highlight double-negative, i.e., NRI transmission, frequency bands for the considered dielectric substrate thicknesses. (a) Effective impedance; (b) effective refractive index; (c) effective permittivity; and (d) effective permeability.

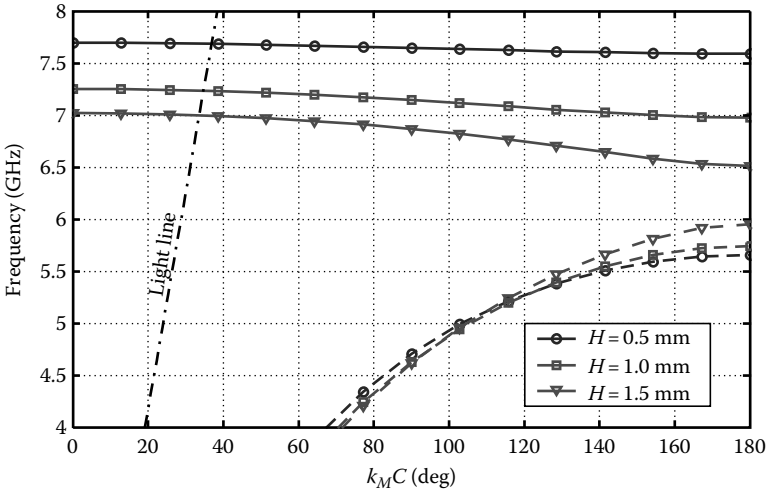

FIGURE 19.19 Dispersion curves for a wave with the propagation constant k_M in the infinite periodic stack (period $C = 4$ mm) of layers made of the pairs of tightly coupled Jerusalem crosses from Figure 19.14. (From Gunnarsson, L., Rindzevicius, T., Prikulis, J., Kasemo, B., Kall, M., Zou, S., and Schatz, G., *J. Phys. Chem. B.*, 109(3), 1079, 2005. With permission.)

versus the Bloch wave number k_M along the z-direction, normalized with respect to the period $C = 4$ mm; the light line $\omega = k_0 c$ (dashed-dotted line), where c is the speed of light and k_0 denotes the free-space wave number, is also plotted in Figure 19.19 for reference. The negative slope of the dispersion curves at frequencies above 6.3 GHz conclusively confirms backward-wave propagation for all three thicknesses H. The passband associated with the magnetic resonance decreases for smaller H. In particular, for $H = 2$ mm, predictions of the dispersion characteristics are fully consistent with the retrieved refractive index in Figure 19.18b. The central frequency and the percentage width of the NRI transmission band deduced from these dispersion diagrams are plotted in Figure 19.20 versus H and for a few values of C. As apparent from these plots, the transmission band progressively shifts toward lower frequencies for a larger H, it has its lowest values for $H = C/2$, and it moves toward higher frequencies for even larger values of H. It is found that $H \approx C/2$ generally corresponds to the optimal NRI bandwidth in addition to the lowest frequency of the magnetic resonance.

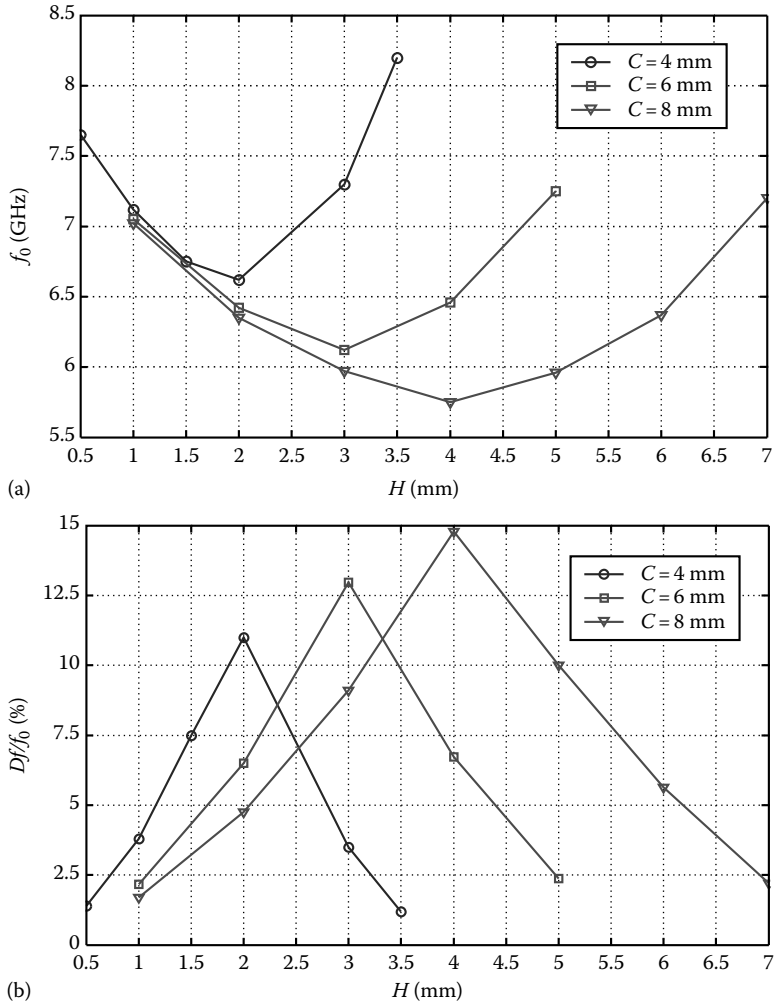

FIGURE 19.20 Center frequency and percentage width of the left-handed transmission band for the structure of Figure 19.14 versus thickness H of the dielectric substrate supporting the Jerusalem cross-pairs at a few values of the unit cell size C along the propagation direction. (From Gunnarsson, L., Rindzevicius, T., Prikulis, J., Kasemo, B., Kall, M., Zou, S., and Schatz, G., *J. Phys. Chem. B.*, 109(3), 1079, 2005. With permission.)

This is clearly illustrated in Figure 19.20b, which also shows that as long as $H \approx C/2$ the percentage width of the NRI band steadily increases for increasing lengths C of the unit cell in the propagation direction.

Finally, it is important to note that in the NRI frequency band, the ratio of wavelength to the lattice constant A is of the order of $\lambda/A = 6$.

19.5.3 The Tripole-Pair Design

As a further demonstration of the concept of using pairs of tightly coupled conductors as elemental constituents of a periodic medium exhibiting an NRI behavior, in this section we present another fully printable metamaterial design. The developed structure is composed of a double periodical arrangement of pairs of face-coupled, loaded tripoles as shown in Figure 19.21. Due to its threefold symmetry, such metamaterial provides an isotropic response to any linearly polarized incident wave, and one could expect that its transmission properties would be somehow preserved when the incident plane wave is tilted far from normal incidence. As for the case of the Jerusalem cross-pairs, the conductor pairs are made of 10 μm thick copper foils deposited on both sides of a dielectric substrate with permittivity $\epsilon_r = 2.2$ and loss tangent 0.0009. The constitutive periodic unit cell has a hexagonal cross-section with side lengths $A = 5$ mm; the size C in the longitudinal direction is fixed to $C = 4$ mm, whereas the thickness H of the dielectric substrate is a variable parameter. The default values of the remaining geometrical parameters used for the design are $A1 = 0.722$ mm, $B2 = 0.5$ mm, $A2 = 4.885$ mm, and $B1 = 4$ mm.

19.5.4 Left-Handed Transmission in Tripole-Pair Media

The electromagnetic behavior of the tripole-pair metamaterial from Figure 19.21 has been characterized by calculating its reflection and transmission spectra and then analyzing the dispersion

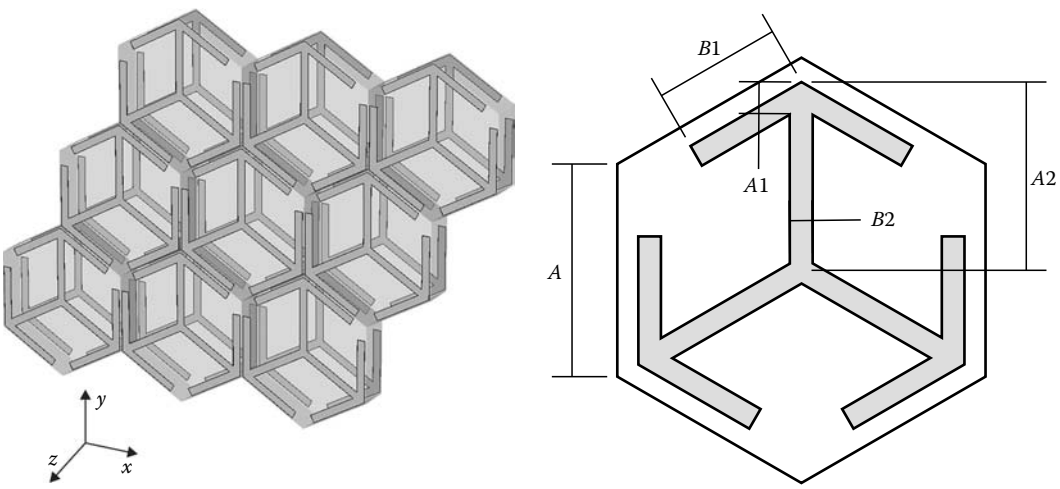

(a) (b)

FIGURE 19.21 (a) Perspective view of a layer of the 2D isotropic metamaterial formed by a periodic arrangement of tightly coupled pairs of loaded tripoles, which exhibit an antisymmetric (magnetic) resonance for any incident linear polarizations. (b) Top view of the metamaterial unit cell with geometrical parameters quoted. In the simulations, we have set $A = 5$ mm, $A1 = 0.722$ mm, $B2 = 0.5$ mm, $A2 = 4.885$ mm, and $B1 = 4$ mm.

properties of the eigenmodes in the infinitely extended structure formed by stacking the layer of Figure 19.21a with period C along the z-axis. The magnitude of the simulated field transmission coefficient $|T|$ at normal incidence for two different values of H (H = 1 and 2 mm) is plotted in Figure 19.22a. In close analogy with corresponding results obtained for the Jerusalem cross-pair structure (cf. Figure 19.15), the resonance transmission peaks are attributed to the magnetic type or antisymmetric mode resonance and are associated with backward-wave propagation. Furthermore, it appears again that for thicker substrates the transmission resonance occurs at lower frequencies and its bandwidth increases. A definite assessment of the nature of the transmission peaks in Figure 19.22a can be made by examining Figure 19.22b, which shows the calculated one-dimensional dispersion diagram ω versus the Bloch wave number k_M along the z-direction, normalized with respect to the period C = 4 mm. In fact, the negative slope of the dispersion curves at frequencies above 4.5 GHz

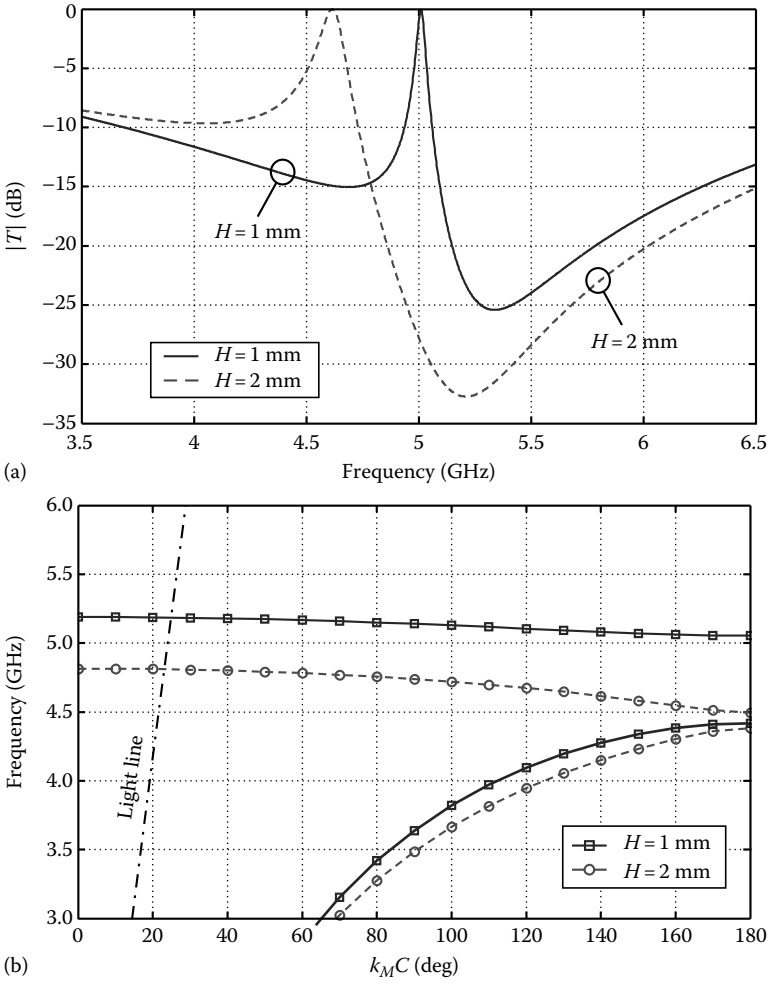

FIGURE 19.22 (a) Simulated field transmission coefficients versus frequency for a layer of periodically arranged tripoles pairs (Figure 19.21); the two curves correspond to different thicknesses H = 1 and 2 mm of the dielectric substrate supporting the top and bottom conductors, whereas the size of the unit cell along the propagation direction is fixed to C = 4 mm. (b) Dispersion curves for a wave with the propagation constant k_M in the infinite periodic stack (period C = 4 mm) of layers made of the pairs of tightly coupled tripoles from Figure 19.21.

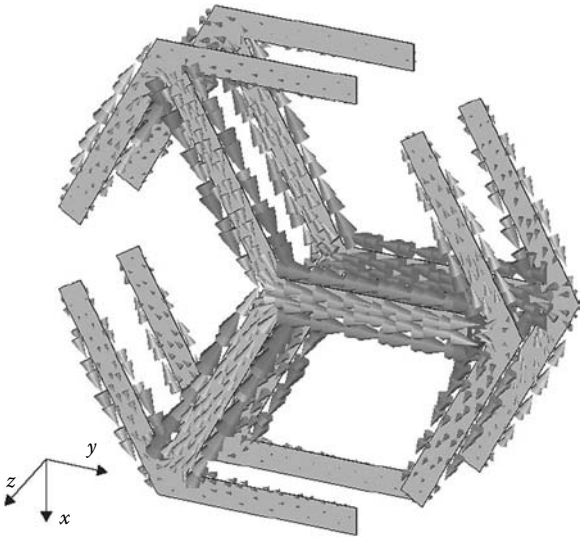

FIGURE 19.23 Surface current distribution on the unit cell of the tripole pair structure of Figure 19.21 (C = 4 mm, H = 2 mm) at the the magnetic resonance f_m = 4.6 GHz. The illuminating plane wave is normally incident on the structure with the electric field polarized along the y-axis.

confirms backward-wave propagation for both the considered substrate thicknesses H; moreover, it is noteworthy that the width of the NRI passband decreases for a smaller H, as previously noticed also for the Jerusalem cross-pair design.

In Figure 19.23, we show the surface current distribution for the unit cell of the tripole pairs in Figure 19.21, with H = 2 mm, calculated at the frequency f = 4.6 GHz, corresponding to the transmission peak observed in Figure 19.22a. As expected, the currents on the two conductors are antisymmetric at the resonance and form a loop, which can be represented as an equivalent magnetic dipole moment. This magnetic moment is responsible for the artificial magnetism of the structure, which in turn results in an effective negative permeability of the substrate printed with the pairs of tripoles. This magnetic resonance is superimposed with the electric resonance corresponding to the excitation of a symmetric mode on the two tripoles, which is associated with an effective negative permittivity; this superimposition yields the effective NRI behavior of the composite medium in the frequency bands highlighted by the transmission and dispersion plots of Figure 19.22.

Finally, it is important to note that in the NRI frequency band the ratio of wavelength to the lattice constant A is of the order $\lambda/A \approx 6.5$. Thus, the NRI band should not be confused with the usual high-order Brillouin zones of a photonic crystals, because the latters do not usually satisfy the $A << \lambda$ condition.

19.6 Plasmonic Nanopairs and Nanoclusters

Gold and silver nanoparticles have been used since Roman times to embellish stained glass windows, ceramics, enamel pottery, and clothes with brilliant red and yellow colors [41]. However, it was not until the middle of the nineteenth century that first insight into the underlying mechanisms that give rise to the spectacular colors of small metal particles was provided by the pioneering work of Faraday [42]. Then came the results of Maxwell Garnett [43,44] explaining the scattering effects and color changes, and Mie's theory [45] quantitatively describing the size-dependent optical properties

of metal spheres, which is still of great importance because it is the only simple exact solution to Maxwell's equations relevant to particles.

The field of metallic nanoparticles has recently witnessed a strong resurgence of interest due to the development of nanofabrication techniques, such as electron-beam lithography (EBL), ion-beam milling, nanochemistry, and self-assembly, together with modern nanocharacterization techniques, such as dark-field and near-field optical microscopies and the emergence of quantitative electromagnetic simulation tools. Advances in particle synthesis and nanofabrication technology have made it possible to produce well-defined metal nanostructures. Sample transmission electron microscopy (TEM) images of pairs of particles of two different sizes prepared by EBL are shown in Figure 19.24a.

These progresses have generated the expectation that metallic nanoparticles will play a crucial role in the development of several new applications and devices, especially in the field of photonic

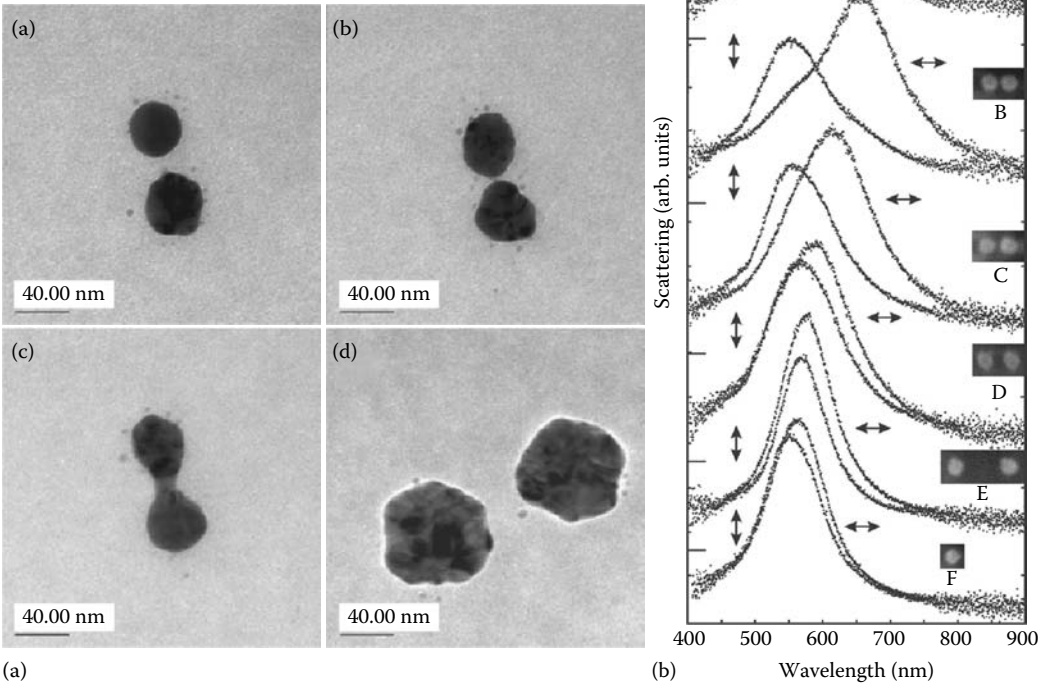

FIGURE 19.24 (a) TEM images of pairs of particles of two different sizes prepared by EBL [50]. The particle diameter is 50 nm for the upper pairs and lower-left pair and 80 nm for the pair at the lower-right corner. The particle separation (gap) is 15 nm for the upper pairs and approximately 20 nm for the pair at the lower-right corner. The particles at the lower-left corner are in contact instead. (b) Scattering spectra from isolated pairs of oblate spheroids with a diameter of 95 nm and height of 25 nm at variable separations in parallel and perpendicular polarizations, as indicated by arrows. The separations (gaps) between particles are 10, 15, 25, 50, and 250 nm for particle pairs A, B, C, D, and E, respectively. Spectrum F from a single particle is included for comparison. (Reprinted from Gunnarsson, L., Rindzevicius, T., Prikulis, J., Kasemo, B., Kall, M., Zou, S., and Schatz, G., *J. Phys. Chem. B.*, 109(3), 1079, 2005.)

circuitry and optical communications, where they could enable the creation of radically new, metal-based, subwavelength, optical components with broad technological potential and miniaturized size dimensions [46].

The fascinating optical properties of metallic nanoparticles arise from the excitation of localized surface plasmon (LSP) resonances, which can be interpreted as collective resonant oscillations of all the conduction electrons of the nanoparticle in response to an incident optical field. A nanoparticle supports a range of LSPs, but the optical response is usually dominated by dipolar modes. LSPs lead to increased absorption and scattering cross-sections for electromagnetic waves as well as to a strongly enhanced near field in the immediate vicinity of the particle surface [47]. It is the combination of these properties with the tunability of plasmon resonances by varying the particle constituent material, size, geometry, and the dielectric function of the surrounding host from which most of the promising applications of metal nanoparticles stem, such as optical waveguides [47–49], biosensors [50], subwavelength imaging [51], and surface-enhanced Raman scattering [52,53].

A significant amount of research effort has been devoted to using metal (gold or silver) nanoparticle chains as subwavelength optical waveguides in which wave propagation is mediated by coupled plasmonic resonances [48,49]. At the same time, there have also been some interesting experimental [54,55] and theoretical [56] results on two-dimensional (2D) arrays of nanoparticles or dipolar scatterers. In particular, a red shift of the dipole coupled mode has been observed when the electric field is oriented along the interparticle axis and a blue shift of the dipole coupled mode when the electric field is perpendicular to the pair axis [50,57]. This is illustrated in Figure 19.24 showing scanning electron microscopy (SEM) images and the scattering spectra from individual particle pairs measured in the two orthogonal polarization configurations. As apparent, the dipolar LSP resonance observed for the parallel polarization case (E field parallel to the pair axis) shifts dramatically to the near-infrared region when the interparticle distance is decreased.

Arrays of metal nanoparticles can also provide the opportunity of developing new NRI metamaterials operating at optical frequencies. Indeed, at near-infrared and visible frequencies, the design of NRI metamaterials with both negative dielectric permittivity and negative magnetic permeability is a rather intricate matter and involves several challenges. The direct scaling to visible optics of the NRI media demonstrated in the microwave range [7] is nearly infeasible. In fact, at microwaves frequencies the realization of an NIM is usually accomplished by embedding in a host medium some suitably shaped metallic resonant inclusions with both electric and magnetic responses. Yet the electromagnetic behavior of metals drastically changes from microwaves to visible frequencies: at microwaves metals possess a very high (imaginary) permittivity and behave as nearly perfect conductors, whereas at optical frequencies their permittivity can be comparable to that of the host material. Moreover, the extension of the above approach to higher frequencies also raises technological issues, as previously mentioned. Since negative permittivity is inherent to plasmonic structures at resonance, efforts have recently focused on developing structures with a strong magnetic response. Means to achieve artificial magnetism with negative permeability at visible frequencies in nanostructure assemblies have recently been suggested, for example, in [58,59]. In [58] a simple plasmonic system composed of a pair of gold nanodisks illuminated in the end-fire configuration has been shown to provide a magnetic response due to the excitation of a magnetic dipole resonance. In [59] the design of subwavelength inclusions exhibiting a negative effective magnetic dipole moment at optical frequencies is addressed by exploiting the collective resonance of an array of plasmonic nanoparticles arranged in a circular pattern. It is noteworthy that resonant inclusions synthesized at higher frequencies usually exploit the resonance of the circulating displacement current rather than of the conduction current. Further alternative concepts for NRI materials in the visible range using ensembles of metallic nanospheres have been proposed and analyzed in [60,61].

Basic ingredients for an NRI material recipe at optical frequencies are as follows [16]: (a) ease of fabrication, (b) inversion symmetry (to avoid bianisotropy), (c) availability of both magnetic and electric resonances close to each other in frequency, and (d) small unit cell electrical size. Bearing in

mind these considerations, and somewhat inpsired by promising results from [59], we investigated a particular class of metamaterials, whose constitutive elements simply consist of either a pair of tightly coupled silver nanospheres or a cluster of four nanospheres. We show that due to interparticle coupling these structures support an antisymmetric (or loop) electromagnetic oscillation, which is associated with a magnetic dipole and thus can lead to artificial magnetism. This oscillation is initially revealed from the analysis of the resonance modes of an isolated pair or cluster of nanospheres by using an approximated dipolar model for the particles and then for periodical structures of coupled silver nanospheres through finite-difference simulations [35].

19.6.1 Resonance Modes of a Pair of Tightly Coupled Metallic Nanospheres

To understand the electromagnetic coupling between resonant nanoparticles, it is advantageous to investigate first the basic coupled structure, a pair of nanospheres. The two nanospheres are supposed to be made of silver, a noble metal that at optical frequencies exhibits a negative real part of dielectric permittivity. Specifically, in this range of frequency the permittivity of silver can be described by the Drude model:

$$\epsilon_m = \epsilon_\infty - \frac{\omega_p^2}{\omega\left(\omega + i\gamma\right)}, \tag{19.12}$$

where the parameters can be defined by matching experimental data in the interested frequency range. Here $\epsilon_\infty = 5$, the plasma angular frequency ω_p and the damping angular frequency γ are chosen as $\omega_p = 1.37 \times 10^{16}$ rad/s and $\gamma = 27.3 \times 10^{12}$ s^{-1}, respectively, following [59,62].

Previous investigations of coupled particle dimers have shown that there are several different behavior regimes based on the separation between particles [63,64]. When the pair of particles are illuminated by a beam and they are widely spaced apart, they respond to the field independently, and the only effect of their interaction is the oscillatory variation of the dimer response with interparticle distance due to interference between the two nanoparticles. As the particle separation is reduced, it was observed that for illumination by a plane wave with the electric field parallel to the dimer axis the dimer far-field scattering response redshifts, whereas the far-field intensity initially weakens, because the effective dipole of the coupled particles is diminished, due to localization at the dimer gap of the charge induced by the incident field [63]. For even smaller separations, the scattering response of the dimer continues to redshift, there is a strong buildup of charge at the gap, near-fields in the gap are enhanced, and the far-field scattering begins to increase again [63]. Two additional regimes of distinctly different behavior occur when the particles are separated but nearly touching and when the nanoparticles overlap [64]. At very small separations, the multipoles associated to each sphere become important, and fully retarded calculations in large neighboring spheres could be performed by using multiple multipole methods [65].

Here we are interested in examining the case of nanospheres with relatively small radius r_p and finite separation d between them. Therefore, to investigate the interparticle coupling we can resort to the single dipole per particle approximation (SDA), which is a simplified approach consisting in modeling each particle with just one electric dipole (see, for example, [66,67] and references therein). Dipole interactions among particles are modeled correctly, and the SDA is accurate for particles that are small and well separated, in which case the field of each particle at any of its nearest neighbors is well represented by a dipole field. Proper implementation of the method requires an appropriate choice of the dipole polarizability expression for each particle [67].

We aim at finding the resonance modes and resonance frequencies of the isolated nanosphere pair system illustrated in Figure 19.25. In the SDA, this corresponds to finding the eigenvalues of the

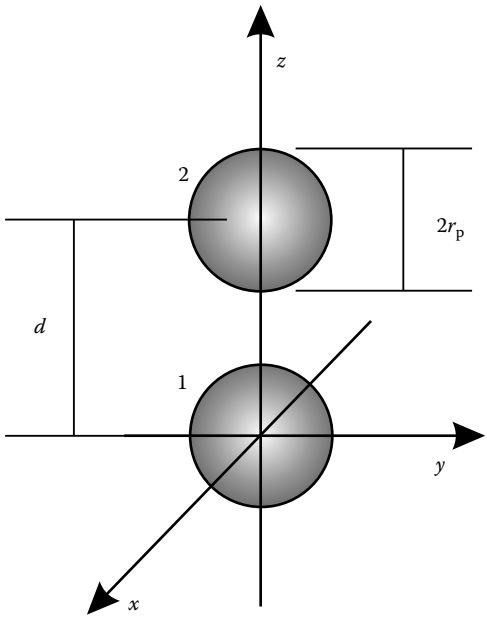

FIGURE 19.25 Configuration of the isolated nanosphere pair.

following system of two coupled equations (electromagnetic fields are assumed to be time harmonic with an $e^{-i\omega t}$ time variation):

$$\begin{aligned} \boldsymbol{E}(\boldsymbol{r}_2) &= \underline{\boldsymbol{G}}(\boldsymbol{r}_2, \boldsymbol{r}_1) \cdot \boldsymbol{p}_1, \\ \boldsymbol{E}(\boldsymbol{r}_1) &= \underline{\boldsymbol{G}}(\boldsymbol{r}_1, \boldsymbol{r}_2) \cdot \boldsymbol{p}_2, \end{aligned} \tag{19.13}$$

with the information that $\boldsymbol{p}_{1,2} = \alpha \boldsymbol{E}(\boldsymbol{r}_{1,2})$. Here, boldface symbols denote vectors, whereas dyads are underlined; therefore, $\boldsymbol{r}_1$, $\boldsymbol{r}_2$ denote the position vectors of the nanospheres, which are treated as electric dipoles with dipole moments $\boldsymbol{p}_1$ and $\boldsymbol{p}_2$, respectively; $\underline{\boldsymbol{G}}(\boldsymbol{r}_1, \boldsymbol{r}_2)$ is the dyadic Green's function:

$$\underline{\boldsymbol{G}}(\boldsymbol{r}_1, \boldsymbol{r}_2) = \left[c_1 \underline{\boldsymbol{I}} + c_2 \underline{\boldsymbol{\Psi}}(\boldsymbol{r}_{21}) \right], \tag{19.14}$$

where

$\underline{\boldsymbol{I}}$ is the identity dyad

$\underline{\boldsymbol{\Psi}}(\boldsymbol{r}_{21})$ is the dyadic

$$\underline{\boldsymbol{\Psi}}(\boldsymbol{r}_{21}) = \frac{1}{r^2} \boldsymbol{r}_{21} \boldsymbol{r}_{21}, \tag{19.15}$$

and

$$c_1 = \frac{e^{ikr}}{4\pi\epsilon_0\epsilon_h} \left(\frac{k^2}{r} + \frac{ik}{r^2} - \frac{1}{r^3} \right), \quad c_2 = -\frac{e^{ikr}}{4\pi\epsilon_0\epsilon_h} \left(\frac{k^2}{r} + \frac{3ik}{r^2} - \frac{3}{r^3} \right), \tag{19.16}$$

with $r = |\boldsymbol{r}_{21}|$; ϵ_h and μ_h are the relative permittivity and permeability of the host media and $k = \omega\sqrt{\epsilon_h}/c = k_0\sqrt{\epsilon_h}$ is its wave number; k_0 is the free-space wave number. Furthermore, α is the scalar

sphere polarizability, which may be given in closed form as a function of silver permittivity by the expression [67,68]

$$\alpha = \left[\frac{\epsilon_m + 2\epsilon_h}{\epsilon_0 \epsilon_h 4\pi r_p^3 (\epsilon_m - \epsilon_h)} - i \frac{k^3}{6\pi\epsilon_0 \epsilon_h} \right]^{-1}. \tag{19.17}$$

We anticipate that the interesting frequency range is one in which the first plasmon resonance in each sphere is excited, which implies that the relative permittivity ϵ_m of each nanosphere is such that $\epsilon_m \approx -2\epsilon_h$. Indeed, as it is clear from the expression of the polarizability (Equation 19.17), in this frequency range each nanosphere produces a strong electric dipole when excited by an electric field. Combining the equations (Equation 19.13) one obtains

$$\begin{aligned} \boldsymbol{p}_2 &= \alpha \underline{\boldsymbol{G}}(\boldsymbol{r}_2, \boldsymbol{r}_1) \cdot \boldsymbol{p}_1, \\ \boldsymbol{p}_1 &= \alpha \underline{\boldsymbol{G}}(\boldsymbol{r}_1, \boldsymbol{r}_2) \cdot \boldsymbol{p}_2. \end{aligned} \tag{19.18}$$

It can be easily shown that this system admits independent antisymmetric ($\boldsymbol{p}_2 = -\boldsymbol{p}_1$) and symmetric solutions ($\boldsymbol{p}_2 = \boldsymbol{p}_1$), which leads to two sets of solutions of the equation:

$$\left[\underline{\boldsymbol{G}}(\boldsymbol{r}_1, \boldsymbol{r}_2) \pm \frac{\underline{\boldsymbol{I}}}{\alpha} \right] \cdot \boldsymbol{p}_1 = 0, \tag{19.19}$$

where ± signs hold for antisymmetric and symmetric solutions, respectively. The eigenvectors associated to the four possible resonance configurations are shown in Figure 19.26. The eigenfrequencies $f_{t,1}$ and $f_{t,2}$ are associated to the two transverse (with respect to the particle pair axis) resonances shown in Figure 19.26a and b, respectively. The two eigenfrequencies $f_{\ell,1}$ and $f_{\ell,2}$ are relevant to the two longitudinal (parallel to the particle-pair axis) resonances shown in Figure 19.26c and d, respectively. The real and imaginary parts of the four resonance frequencies are plotted against spheres radius r_p (Figure 19.27), keeping the distance between the spheres fixed at $d = 75$ nm.

It appears that $f_{t,2}$ and $f_{\ell,2}$, the resonances of the symmetric modes in Figure 19.26b and d, have a larger imaginary part than $f_{t,1}$ and $f_{\ell,1}$, the resonances of the antisymmetric modes in Figure 19.26a and c. This is because of the larger radiation losses for the symmetric modes, as the pair of spheres radiate like two parallel dipoles. Instead, the radiation associated to an antisymmetric mode is weaker than the previous symmetric case, which results in a lower imaginary part of the resonant frequency. Indeed, the radiations of the two dipoles tend to cancel each other, and the antisymmetric dipole pair tends to radiate like a quadrupole. Equivalently, the antisymmetric mode is associated to a current

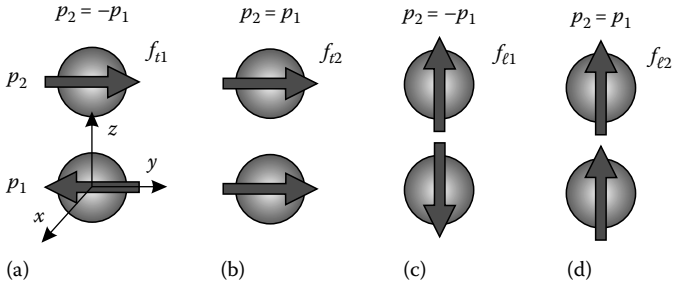

FIGURE 19.26 Nanosphere pairs and resonance configurations: two resonance modes are along the direction orthogonal to the particle-pair axis (transverse resonance modes), whereas two other resonance modes are oriented parallelly to the particle-pair axis (longitudinal resonance modes). The vectors on each particle indicate the electric dipole moments.

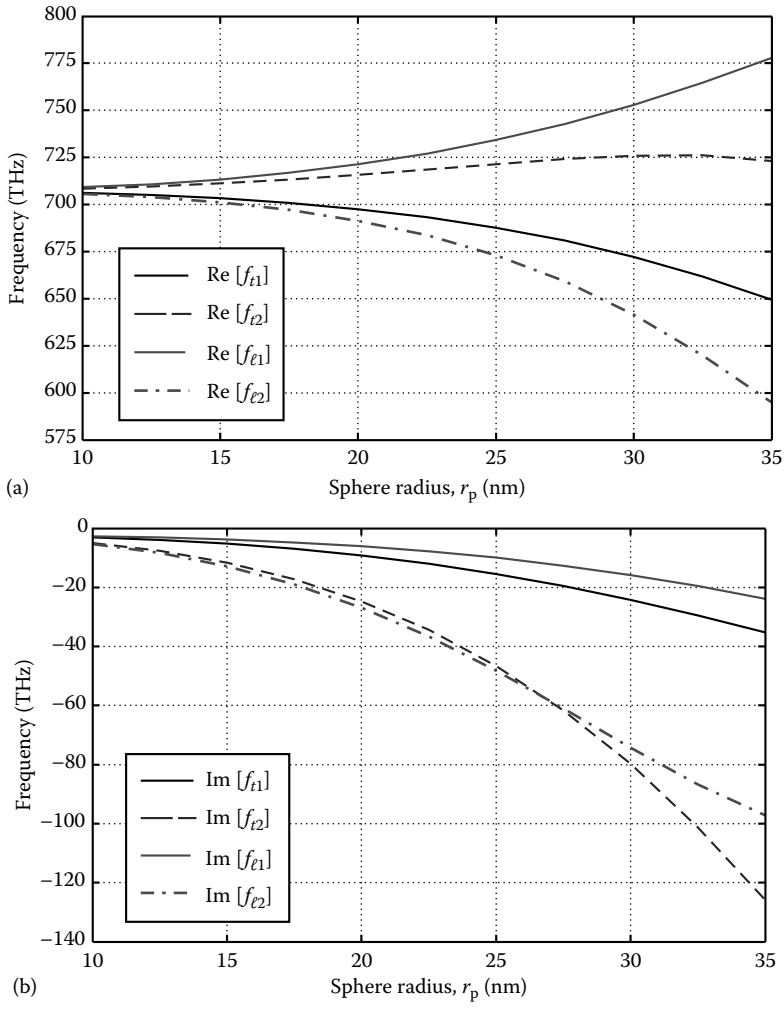

FIGURE 19.27 (a) Real and (b) imaginary parts of the four resonance frequencies for a pair of nanospheres, in a glass host ($\epsilon_h = 2.25$), with varying radius r_p, and for a fixed distance between the spheres $d = 75$ nm, evaluated using (19.19).

loop, and it is a classic result of antenna theory that a small loop radiates less than a small dipole. It is also noted that the antisymmetric resonance $f_{t,1}$ is smaller than the symmetric one $f_{t,2}$, for all the considered cases; generally, the resonances are ordered as $f_{\ell,2} < f_{t,1} < f_{t,2} < f_{\ell,1}$, as shown in Figure 19.28. Moreover, for large distance-to-radius ratios d/r_p the real part of the four resonance frequencies tends to be similar due to the reduced coupling between spheres.

19.6.2 Quasistatic Resonance Modes of Two Coupled Metallic Nanospheres

If the particles are small compared with the wavelength of light, then it is possible to replace some electrodynamic terms by electrostatic ones. In SDA calculations, this is equivalent to setting $k = 0$ in Equation 19.16 (see also [67]) but keeping the correct frequency-dependent dielectric constant. The electrostatic approximation is especially useful in the treatment of particles with special shapes such

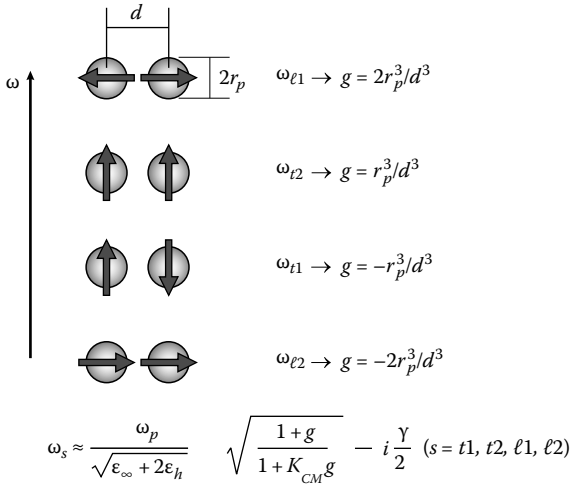

FIGURE 19.28 Quasi-static resonance modes of two interacting nanospheres as derived from the eigenfrequencies of the two-particle SDA equations. The mode frequencies are given by the formula at the bottom, with values of f, depending on the radius of the particles r_p and their center-to-center separations d, shown on the right-hand side.

as spheroids, since it can provide an analytical solution to the Laplace's equation. This approximation applies specifically to the dynamics of a single particle, but it can also be combined with the SDA method to describe the electromagnetic behavior of a particle cluster [66].

Here we are interested in deriving the analytical expressions of the nanosphere pair resonances, estimated in Section 19.6.1 by solving Equation 19.19 numerically. After neglecting the dynamic terms in Equation 19.16, and by taking into account that $\gamma \ll \omega_p$, Equation 19.19 is solved analytically for the resonant angular frequencies, leading to the expressions

$$\omega_{t1} \approx \frac{\omega_p}{\sqrt{\epsilon_\infty + 2\epsilon_h}} \sqrt{\frac{1 - r_p^3/d^3}{1 - K_{CM} r_p^3/d^3}} - i\frac{\gamma}{2} \tag{19.20a}$$

$$\omega_{t2} \approx \frac{\omega_p}{\sqrt{\epsilon_\infty + 2\epsilon_h}} \sqrt{\frac{1 + r_p^3/d^3}{1 + K_{CM} r_p^3/d^3}} - i\frac{\gamma}{2} \tag{19.20b}$$

for the transverse modes and

$$\omega_{\ell 1} \approx \frac{\omega_p}{\sqrt{\epsilon_\infty + 2\epsilon_h}} \sqrt{\frac{1 + 2r_p^3/d^3}{1 + K_{CM} 2r_p^3/d^3}} - i\frac{\gamma}{2} \tag{19.20c}$$

$$\omega_{\ell 2} \approx \frac{\omega_p}{\sqrt{\epsilon_\infty + 2\epsilon_h}} \sqrt{\frac{1 - 2r_p^3/d^3}{1 - K_{CM} 2r_p^3/d^3}} - i\frac{\gamma}{2} \tag{19.20d}$$

for the longitudinal modes. Here, K_{CM} denotes the Clausis–Mossotti factor $K_{CM} = (\epsilon_\infty - \epsilon_h)/(\epsilon_\infty + 2\epsilon_h)$ [69]. By choosing $\epsilon_h = 1$, these expressions are found to coincide with those given in [70]. The quasi-static modes of two interacting nanospheres are illustrated in Figure 19.28. These expressions are particularly useful for an initial design of the pairs, when one needs to have a preliminary guess of the particle dimensions.

19.6.3 Array of Pairs of Tightly Coupled Nanospheres

Now that certain properties related to an isolated pair of nanospheres have been shown, we analyze some characteristics of an array of such pairs, which is sketched in Figure 19.29. It consists of an infinite, two-dimensional periodic distribution, in the xy plane, of pairs of tightly coupled spheres. In other words, each array element is made of a pair of nearby metallic spheres, like that shown in Figure 19.26. The lattice constants of the array are a and b along x and y, respectively. The origin of the coordinate system coincides with the position of a sphere in the lower array. The positions of the lower spheres are thus $\boldsymbol{\rho}_{mn} = ma\hat{\boldsymbol{x}} + nb\hat{\boldsymbol{y}}$, with $m, n = 0, \pm 1, \pm 2, \ldots$. Those in the upper array are located at a distance d, from the lower one.

We now analyze certain properties pertaining to an array of pairs of tightly coupled spheres, assuming a plane wave coming from the positive z-direction, as shown in Figure 19.29. The magnitude of the field reflection R and transmission T coefficients shown in Figure 19.30, for $d = 60$ nm, $r_p = 25$ nm, and $a = b = 150$ nm, are obtained by finite-difference simulations [35]. For symmetry reasons, only the transverse resonance modes of Figure 19.26a and b are excited. Indeed, the sphere pair array shows two distinct resonances around $f = 642$ and 701 THz, corresponding to the antisymmetric and symmetric modes, respectively. The values of the resonances are approximatively related to the reflection/transmission peaks, though their exact values should be determined via an eigenvalue numerical analysis. The absorption $1-|T|^2-|R|^2$ is also shown in Figure 19.30, which peaks in the proximity of the magnetic resonance. It is noteworthy that these values of the resonance frequencies are in satisfactory agreement with the estimates provided by the quasi-static expressions of the antisymmetric and symmetric mode resonances given in Section 19.6.2, which read as $f_{t1} = 688$ THz and $f_{t2} = 725$ THz. To further strengthen this classification of the resonances, we have looked at the field locally, for a single pair, which is illustrated in Figure 19.31. These plots confirm that a normally incident plane wave at $f = 642$ THz excites antiphase currents flowing mostly along the x-axis (the arrows in Figure 19.31a), which is characteristic of the antisymmetric mode. A current loop is effectively created in the yz-plane, which in turn generates strong magnetic fields, shown also in the figure with gray tones, in the region between the spheres and produces a substantial magnetic moment contributing to an effective permeability.

In Figure 19.31b we also show that an incident plane wave at $f = 701$ THz excites currents mostly in-phase, flowing along the x-direction, which are regarded as a symmetric mode, similar to that in Figure 19.26b, and do not produce a significant enhancement of the magnetic field.

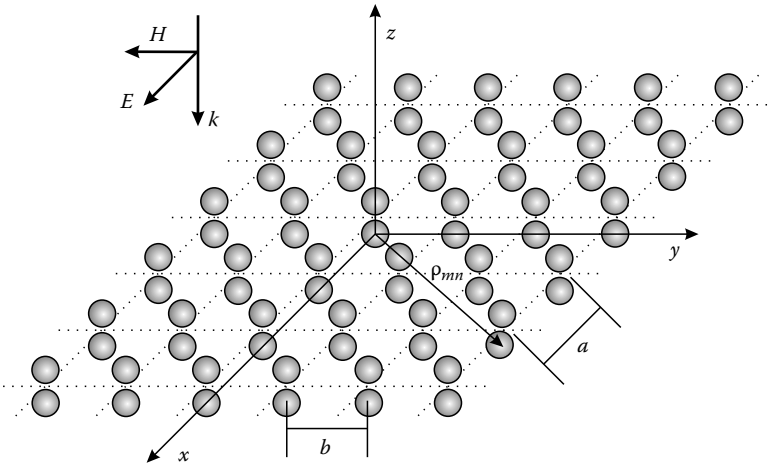

FIGURE 19.29 Doubly periodic array of pairs of tightly coupled spheres.

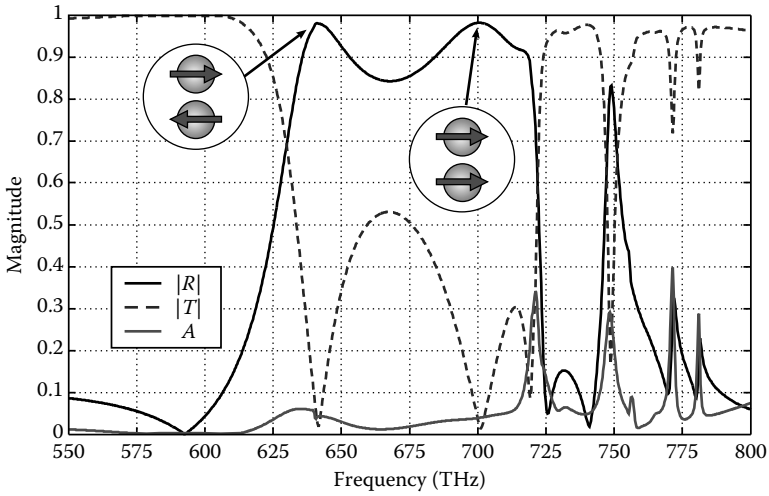

FIGURE 19.30 Field reflection and transmission through a periodic array of silver nanosphere pairs, in a glass host ($\epsilon_h = 2.25$), with $r_p = 25$ nm, center-to-center vertical distance $d = 60$ nm, and transverse periods $a = b = 150$ nm. The absorption $1 - |T|^2 - |R|^2$ is related to the nanospheres losses and peaks in the proximity of the magnetic frequency.

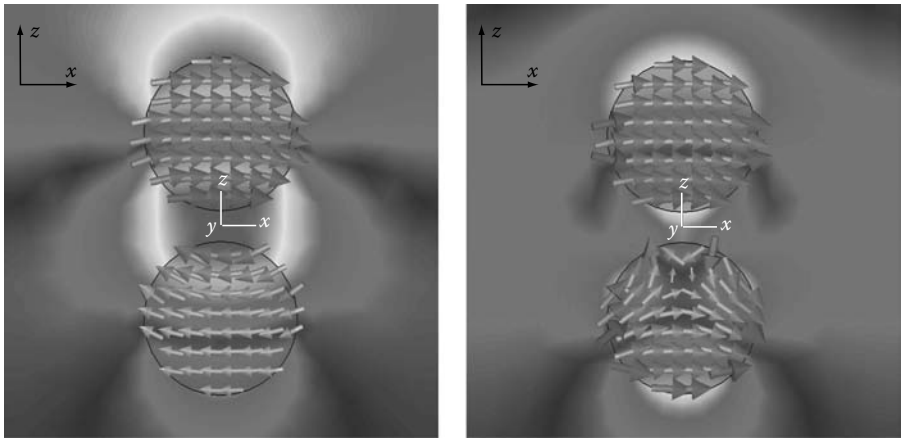

FIGURE 19.31 Current (arrows) and magnetic field amplitude (gray tones) distributions for an array of sphere pairs, in a glass host ($\epsilon_h = 2.25$), with $r_p = 25$ nm, $d = 60$ nm, and $a = b = 150$ nm: (a) antisymmetric resonance mode at $f = 642$ THz; note the strong magnetic field between the two spheres; (b) symmetric resonance mode at $f = 701$ THz.

19.6.4 Effective Magnetic Permeability for a Two Coupled Nanosphere System

Since we have shown that a pair of nanospheres is able to generate a magnetic moment, we estimate here the artificial magnetism produced by a collection of pairs, neglecting their interaction. To this aim, we use here the formula

$$\alpha_{mm}^{-1} = \frac{2\epsilon_0\epsilon_h}{k^2(d/2)^2}\alpha^{-1} - i\left[\frac{4k^3}{15\pi} - \frac{k}{3\pi(d/2)^2}\right] - \frac{1}{16\pi k^2(d/2)^5} \tag{19.21}$$

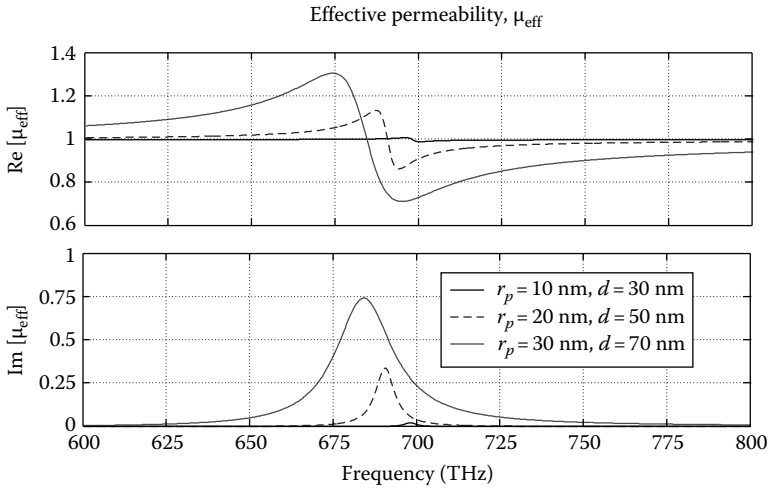

FIGURE 19.32 Effective relative magnetic permeability μ_{eff} for a bulk periodic medium of silver nanosphere pairs with the following parameters: $r_p = 10, 20, 30$ nm, $d = 30, 50, 70$ nm, respectively, and $N_d = (150\,\text{nm})^{-3}$. The permittivity of silver is described by the Drude model in Equation 19.12 with the same parameters specified above [59,62]. The background material is glass with $\epsilon_h = 2.25$.

which is a specialization of the general expression for the magnetic polarizability of a loop of spherical particles developed in [59,71] to the case of only two nanospheres (we recall here that $k = k_0\sqrt{\epsilon_h}$). The polarizabilty is used to determine the magnetic dipole moment associated to a pair, as a function of the local magnetic field as $\boldsymbol{m} = \alpha_{mm}\boldsymbol{H}^{\text{loc}}$, with $\boldsymbol{m}$ and $\boldsymbol{H}$ along a direction orthogonal to the pair axis. Then, the effective permeability of a 3D periodic arrangement of nanopair inclusions can be obtained through the effective medium theory [72] and can be expressed as

$$\mu_{\text{eff}} = 1 + \frac{1}{N_d^{-1}\left[\alpha_{mm}^{-1} + ik^3/(6\pi)\right] - 1/3}, \tag{19.22}$$

where N_d is the number density of nanosphere pairs per unit volume. Figure 19.32 shows the behavior of μ_{eff} for a periodic lattice of silver nanopairs embedded in a glass host with $\epsilon_h = 2.25$. The density of inclusions is $N_d = (150\,\text{nm})^{-3}$ and the particle pair geometry is characterized by the sphere radius $r_p = 10, 20, 30$ nm and distance $d = 30, 50, 70$ nm, respectively. It can be seen that the material presents a significant magnetic response and that the strength of the magnetism is larger for increasing particle size.

It is also noted that the prediction of the frequency at which magnetism is exhibited, provided by the analytical model (Equation 19.22), is blue-shifted when compared with the magnetic response calculated by the full-wave simulations previously discussed. However, this shift is due on the one side to the fact that the spheres are in very close proximity and thus they may interact in a more complex manner than described by the SDA [59,73]; furthermore, a better agreement between theory and simulations could be obtained by using in place of Equation 19.17 an alternative expression of the electric dipole polarizability as determined through the Mie theory [67,74]. In this referenced work, it has been shown that the use of the quasi-static polarizability expression causes a blue shift.

19.6.5 Electromagnetic Modes of Four Coupled Metallic Nanospheres

We consider here an isolated cluster of four silver nanospheres placed at the vertices of a square with side length d, as illustrated in Figure 19.33. This nanoparticle configuration exhibits several

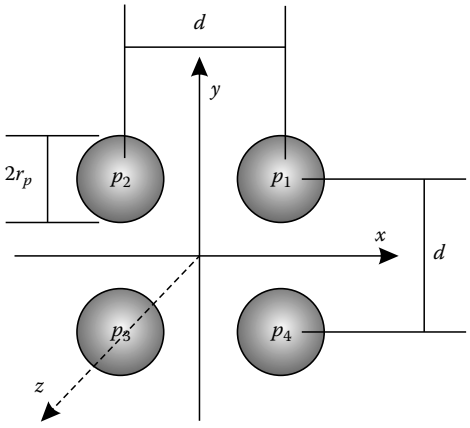

FIGURE 19.33 Configuration of the isolated cluster of four silver nanospheres.

resonances that in the context of an SDA for the considered nanosphere system can be schematically described as shown in Figure 19.34. It is pointed out that the dipoles in the resonance modes from Figure 19.34b, c, f, and g are not necessarily oriented at ±45° directions, but their orientations rather depend on the specific geometrical and material parameters characterizing the cluster configuration, and they are simultaneously rotated by a given angle, as suggested by the superimposed rotating arrows.

As already stated in [59], clusters made by several nanospheres may lead to stronger artificial magnetism than the structures based on pairs shown in the previous sections, besides providing a more isotropic performance. We are particularly interested in the resonance configuration shown in Figure 19.34e, since it is the one that is associated with artificial magnetism, as can be envisaged from the loop disposition of the dipoles. Following the same procedure described in Section 19.6.2, where the electrodynamic terms have been dropped, and by taking into account that $\gamma \ll \omega_p$, a quasi-static approximation for the resonance angular frequency relative to the magnetic mode in Figure 19.34e is given by

$$\omega_{\text{loop}} = \omega_p \sqrt{\frac{4\,d^3 - \left(12+\sqrt{2}\right) r_p^3}{\left[8\,d^3 + \left(12+\sqrt{2}\right) r_p^3\right] \epsilon_h + \left[4\,d^3 - \left(12+\sqrt{2}\right) r_p^3\right) \epsilon_\infty}} - i\frac{\gamma}{2}, \tag{19.23}$$

which provides a useful initial design tool for the dimensions of such a cluster when a specific operational frequency is desired. Similar expressions can be derived also for the resonant frequencies corresponding to the other resonance modes of the four-sphere system tabulated in Figure 19.34.

In the next section, we show that when the nanosphere cluster of Figure 19.33 is used as the constitutive element of a 2D periodic metamaterial, the excitation of the above loop resonance mode by means of an incident wave with a suitable polarization clearly affects the reflection and transmission properties of the composite metamaterials and provides the opportunity to realize artificial magnetism, as first elaborated in [59].

19.6.6 Array of Four Tightly Coupled Nanospheres

We consider here certain electromagnetic properties of a periodic array whose unit cell is made by a cluster of four nanospheres with radius $r_p = 25$ nm, placed in the xz-plane by the vertices of a square

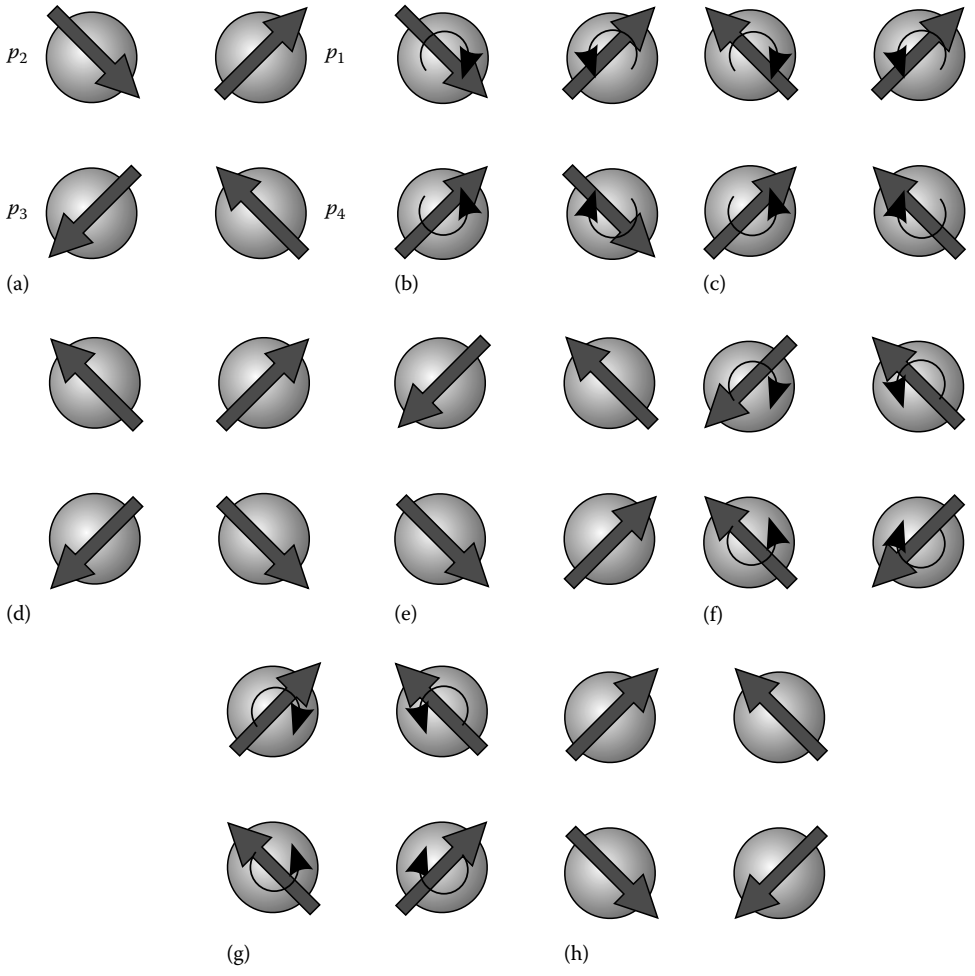

FIGURE 19.34 Resonance modes of four spheres arranged in the double-symmetric configuration shown in Figure 19.33.

with side length $d = 60$ nm (Figure 19.35). The array is periodic along the x and y directions with periods equal to 150 nm.

In Figure 19.36 we show the magnitude of the field transmission T, reflection R, and absorption $1 - |T|^2 - |R|^2$, relative to such an array computed with CST Microwave Studio. As apparent, there are two resonant frequencies of maximum reflection ($f = 563$ and 669 THz) and two resonant frequencies of maximum transmission ($f = 581$ and 662.5 THz). In the inset of Figure 19.36 are shown the directions of the electric dipoles modeling the nanospheres at the first frequency of maximum reflection $f = 563$ THz. Note that the electric field direction at each sphere mainly coincides with the orientation of the dipole modeling the sphere. The reflection arises because the current loop creates a magnetic mismatch for the incoming plane wave, which can be explained in terms of equivalent transmission lines.

To confirm the identification of the loop (magnetic) resonance, we have examined the local field distribution in the unit cell, which is illustrated in Figure 19.37. This graph confirms that a normally incident plane wave at $f = 563$ THz excites a circulating current (arrows) and produces a strong magnetic field enhancement, shown with gray tones in the inside region of the cluster. In this

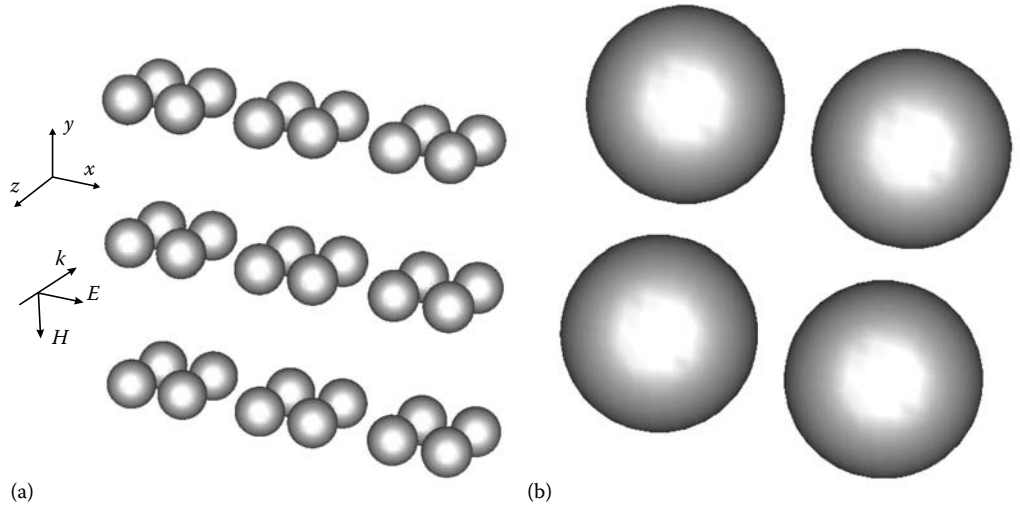

FIGURE 19.35 (a) Perspective view of a layer of the metamaterial formed by a periodic arrangement of four tightly coupled silver nanospheres. (b) Metamaterial elemental particle (unit cell). The polarization of the incident electric field is along the x-direction.

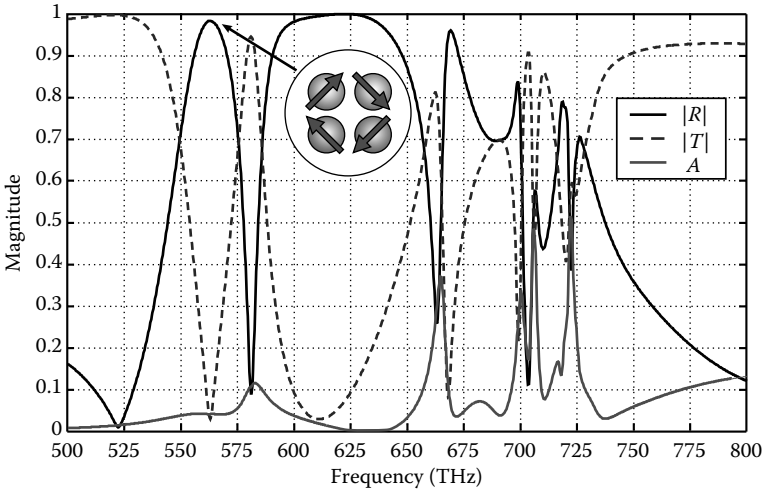

FIGURE 19.36 Frequency response of an array of four tightly coupled nanospheres in the $x-z$-plane with $r_p = 25$ nm and $d = 60$ nm: magnitude of transmission T, reflection R, and absorption $A = 1 - |T|^2 - |R|^2$ versus frequency. In the inset is shown the orientations of the dipoles modeling the nanospheres at the first resonance frequency $f = 563$ THz, corresponding to a maximum of reflection.

antisymmetric oscillation of the four-nanosphere array, the electric dipole moments form a displacement current loop corresponding to an equivalent magnetic dipole oriented along the y-direction, parallel to the incident magnetic field. This phenomenon could be interpreted as artificial magnetism, although more investigation is required to establish the limits of this equivalence (cf. [59,73]). It is noted that absorption is relatively small for this configuration.

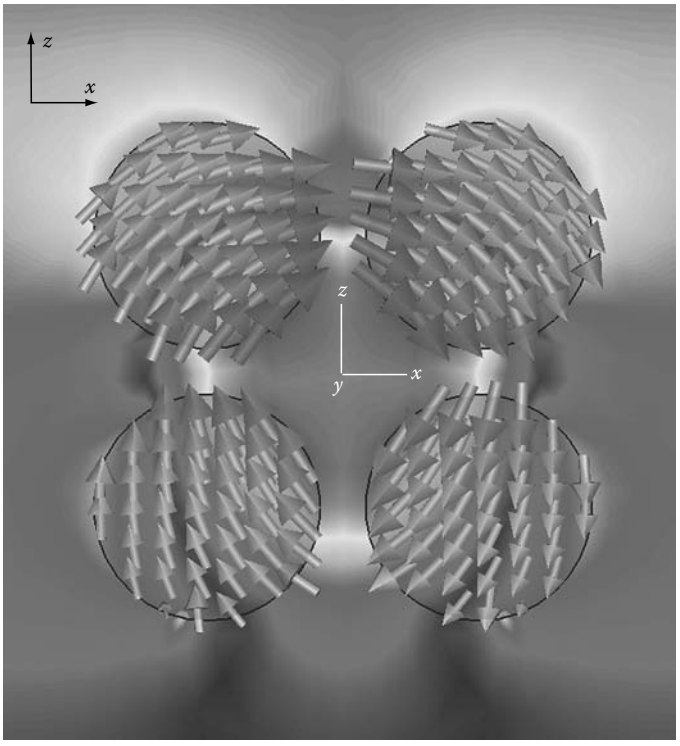

FIGURE 19.37 Current density (arrows) and magnetic field amplitude distribution (gray tones) for the array of four silver nanospheres shown in Figure 19.33, with $r_p = 25$ nm, $d = 60$ nm, and periods along the x- and y-directions $a = b = 150$ nm, and at the first frequency of maximum reflection $f = 563$ THz. The particles are embedded in a host glass with $\epsilon_h = 2.25$. Note the strong magnetic field at the center of the cluster.

The quasi-static approximation (Equation 19.23) provides an estimate of the loop resonance frequency of $f = 638$ THz, which is higher than the actual loop frequency $f = 563$ THz, shown in Figure 19.36. Analogously to what was discussed for the pairs of nanospheres, the disagreement is based on the fact that the nanospheres are very close to each other, and so the minimum distance requirement implied by the SDA is not satisfied for this case, and that a more accurate polarizability expression should be used [67]. Nevertheless, the quasi-static resonance formula (Equation 19.23) is a useful tool for an initial design also for this particular case. The quasi-static formula is expected to be accurate when the center-to-center distance between the spheres is at least $3r_p$ and the spheres are much smaller than the wavelength.

The realization of such clusters is made possible by recent developments in the field of nanochemistry [75,76]. Indeed, it has been shown that it is possible to make clusters of metallic nanospheres around a central nanoparticle of a different material. Here we consider an illustrative example consisting of an array distribution of clusters made of four nanospheres with radius $r_p = 25$ nm, supported by a central silica particle with radius 17.4 nm and $\epsilon_r = 2.25$ (Figure 19.38). The nanoparticles are embedded in free space. The electromagnetic response of this metamaterial to a normally incident plane wave with the electric field polarized along the x-direction is shown in Figure 19.39. As apparent, the response of this array configuration is analogous to that illustrated in Figure 19.36 apart from the shift of the resonances toward higher frequencies. Accordingly, the very same phenomena discussed above are expected to underlie such an electromagnetic behavior: the cluster exhibits a strong magnetic field created by the current loop around $f = 725$ THz, parallel to the incident

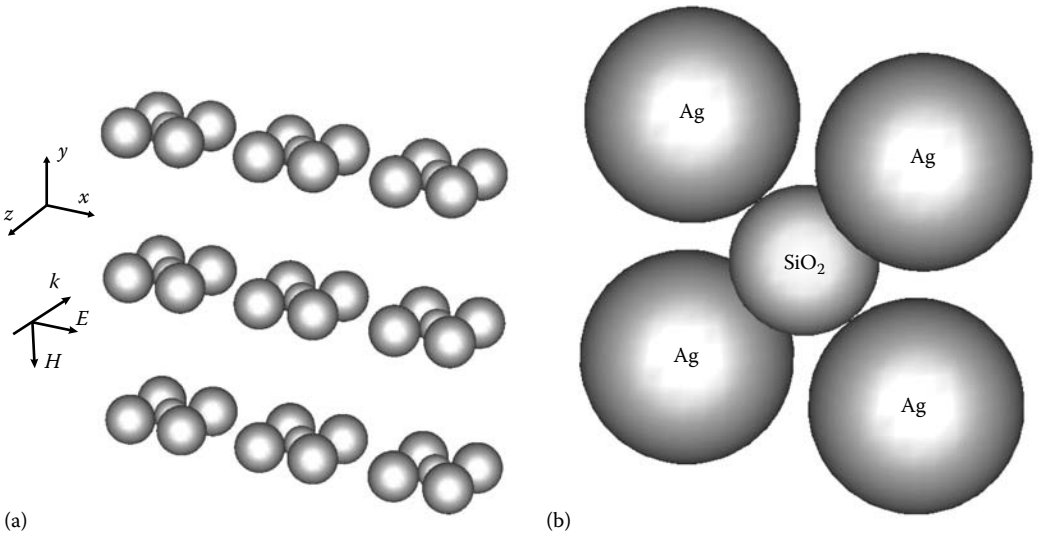

FIGURE 19.38 (a) Perspective view of a layer of the metamaterial formed by a periodic arrangement of four tightly coupled silver nanospheres supported by a central silica particle ($\epsilon_r = 2.25$). (b) Metamaterial elemental particle (unit cell). The polarization of the incident electric field is along the x-direction.

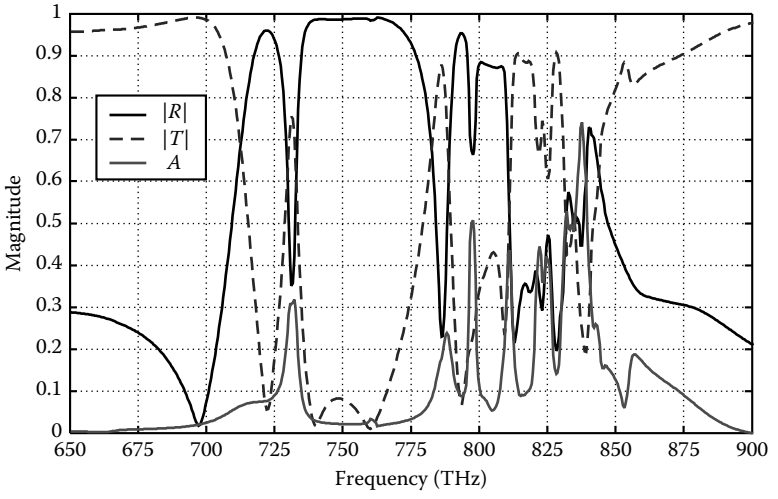

FIGURE 19.39 Frequency response of an array of four tightly coupled silver nanospheres, with $r_p = 25$ nm and $d = 60$ nm, supported by a central silica particle $\epsilon_r = 2.25$: magnitude of transmission T, reflection R, and absorption $A = 1 - |T|^2 - |R|^2$ versus frequency.

magnetic field, which may be interpreted as artificial permeability. The loop resonance frequency is now higher because in the previous case the spheres were embedded in a dielectric host with $\epsilon_h = 2.25$, whereas in this case, besides the presence of the central nanosphere, the host is assumed to have $\epsilon_h = 1$.

19.7 Conclusions

We have presented a few NRI metamaterial designs based on the concept of pairing two suitably shaped conductors. Such configurations have been demonstrated to support both antisymmetric and symmetric resonance modes, whose interaction can lead to simultaneous negative permittivity and permeability, and, accordingly, to an NRI. This design approach can be considered as a generalization of the short-wire or strip-pair designs; however, as a major advantage of this approach, it has been shown that an appropriate choice of the resonant inclusions can provide additional degrees of freedom to control the separation of electric and magnetic resonances, in contrast to simple short-strip-pair media, where these resonances are mainly determined by the length of the wires or strips so that the achievement of an NRI behavior is more difficult.

The ease of fabrication of the presented designs is expected to facilitate their scaling to achieve an NRI response in the terahertz region, provided that the change of the metal behavior from lossy conductors at gigahertz frequencies to lossy, negative permittivity dielectrics in the higher terahertz region is adequately taken into account. Furthermore, extension to the optical range is also conceivable, as the developed metamaterials present the same level of complexity of simple cut-wire or strip pairs, which have already found experimental confirmations at optical wavelegths [14].

Materials based on coupled-particle arrangements with significantly different geometries may lead to negative index materials as well. In particular, the tightly coupled particle pair concept proposed here can be profitably applied to the development of novel metamaterials by taking inspiration from the choice of the unit cell configuration from the plenty of geometries that have been developed in the context of frequency-selective surfaces to address specific electromagnetic responses [30]; indeed, simply pairing such kinds of structures may constitute the starting point to accomplish a range of metamaterial designs with enhanced capabilities.

Furthermore, in the second part of this chapter we have investigated the properties at optical frequencies of certain plasmonic metamaterials whose constitutive unit cell generally consists of a cluster of metallic nanospheres. We have shown that macroscopic effects in the response of these metamaterials are caused by the electromagnetic coupling between the metallic nanospheres closely packed in the metamaterial unit cell. As a consequence of such coupling, these structures support antisymmetric or loop modes. From an electromagnetic point of view, these modes could be interpreted as effective magnetic dipoles, oriented perpendicularly to the plane containing the nanospheres, and could be used in designing metamaterials that support backward propagation or have equivalent high/low characteristic wave impedance.

References

1. V. G. Veselago, The electrodynamics of substances with simultaneously negative values of ϵ and μ, *Sov. Phys. Usp.*, 10, 509–514, 1968.
2. J. B. Pendry, A. J. Holden, D. J. Robbins, and W. J. Stewart, Magnetism from conductors and enhanced nonlinear phenomena, *IEEE Trans. Microw. Theory Technol.*, 47(11), 2075–2084, November 1999.
3. J. B. Pendry and S. O'Brien, Magnetic activity at infrared frequencies in structured photonic crystals, *J. Phys. Condens. Matter*, 14, 6383–6394, 2002.
4. T. J. Yen, W. J. Padilla, N. Fang, D. C. Vier, D. R. Smith, J. B. Pendry, D. N. Basov, and X. Zhang, Magnetic activity at infrared frequencies in structured photonic crystals, *Science*, 303, 5663, 1494–1496, 2004.
5. S. Linden, C. Enkrich, M. Wegener, J. Zhou, T. Koschny, and C. M. Soukoulis, Magnetic response of metamaterials at 100 terahertz, *Science*, 306(5700), 1351–1353, 2004.
6. N. Katsarakis, G. Konstantinidis, A. Kostopoulos, R. S. Penciu, T. F. Gundogdu, M. Kafesaki, E. N. Economou, T. Koschny, and C. M. Soukoulis, Magnetic response of split-ring resonators in the far-infrared frequency regime, *Opt. Lett.*, 30, 1348–1350, 2005.

7. D. R. Smith, W. J. Padilla, D. C. Vier, S. C. Nemat-Nasser, and S. Schultz, Composite medium with simultaneously negative permeability and permittivity, *Phys. Rev. Lett.*, 84, 4184–4187, 2000.
8. R. A. Shelby, D. R. Smith, S. C. Nemat-Nasser, and S. Schultz, Microwave transmission through a two-dimensional, isotropic, left-handed metamaterial, *Appl. Phys. Lett.*, 78, 489–491, 2001.
9. M. Bayindir, K. Aydin, E. Ozbay, P. Markos, and C. M. Soukoulis, Transmission properties of composite metamaterials in free space, *Appl. Phys. Lett.*, 81(1), 120–122, 2002.
10. J. O. Dimmock, Losses in left-handed materials, *Opt. Express*, 11, 2397–2402, 2003.
11. N. G. Alexopoulos, C. A. Kyriazidou, and H. F. Contopanagos, Effective parameters for metamorphic materials and metamaterials through a resonant inverse scattering approach, *IEEE Trans. Microw. Theory Tech.*, 55(2), 254–267, February 2007.
12. N. G. Alexopoulos, C. A. Kyriazidou, and H. F. Contopanagos, Theory and design of metamorphic metamaterials, in *Theory and Phenomena of Metamaterials*, Taylor & Francis, Boca Raton, Florida, 2009, Chapter 20.
13. I. Vendik, O. Vendik, and M. Odit, Isotropic DNG materials, in *Theory and Phenomena of Metamaterials*, Taylor & Francis, Boca Raton, Florida, 2009, Chapter 21.
14. V. M. Shalaev, W. Cai, U. K. Chettiar, H.-K. Yuan, A. K. Sarychev, V. P. Drachev, and A. V. Kildishev, Negative index of refraction in optical metamaterials, *Opt. Lett.*, 30(24), 3356–3358, 2005.
15. G. V. Eleftheriades and K. G. Balmain, *Negative-Refraction Metamaterials: Fundamental Principles and Applications*, New York: Wiley-Interscience, June 2005.
16. G. Shvets and Y. A. Urzhumov, Negative index meta-materials based on two-dimensional metallic structures, *J. Opt. A: Pure Appl. Opt.*, 8, S122–S130, 2006.
17. V. A. Podolskiy, A. K. Sarychev, and V. M. Shalaev, Plasmon modes in metal nanowires and left-handed materials, *J. Nonlinear Opt. Phys.*, 11, 65–74, 2002.
18. V. Podolskiy, A. Sarychev, and V. Shalaev, Plasmon modes and negative refraction in metal nanowire composites, *Opt. Express*, 11(7), 735–745, 2003.
19. J. Zhou, L. Zhang, G. Tuttle, T. Koschny, and C. M. Soukoulis, Negative index materials using simple short wire pairs, *Phys. Rev. B*, 73(4), 041 101/1–4, 2006.
20. J. Zhou, T. Koschny, L. Zhang, G. Tuttle, and C. M. Soukoulis, Experimental demonstration of negative index of refraction, *Appl. Phys. Lett.*, 88(22), 221 103/1–3, 2006.
21. J. Zhou, E. N. Economon, T. Koschny, and C. M. Soukoulis, Unifying approach to left-handed material design, *Opt. Lett.*, 31(24), 3620–3622, 2006.
22. G. Dolling, C. Enkrich, M. Wegener, C. M. Soukoulis, and S. Linden, Simultaneous negative phase and group velocity of light in a metamaterial, *Science*, 312(5775), 892–894, 2006.
23. S. Zhang, W. Fan, N. C. Panoiu, K. J. Malloy, R. M. Osgood, and S. R. J. Brueck, Experimental demonstration of near-infrared negative-index metamaterials, *Phys. Rev. Lett.*, 95(13), 137404, 2005.
24. S. Zhang, W. Fan, K. J. Malloy, S. Brueck, N. C. Panoiu, and R. M. Osgood, Near-infrared double negative metamaterials, *Opt. Express*, 13(13), 4922–4930, 2005.
25. G. Dolling, C. Enkrich, M. Wegener, C. M. Soukoulis, and S. Linden, Low-loss negative-index metamaterial at telecommunication wavelengths, *Opt. Lett.*, 31(12), 1800–1802, 2006.
26. G. Dolling, M. Wegener, C. M. Soukoulis, and S. Linden, Design-related losses of double-fishnet negative-index photonic metamaterials, *Opt. Express*, 15(18), 11 536–11 541, 2007.
27. G. Dolling, M. Wegener, C. M. Soukoulis, and S. Linden, Negative-index metamaterial at 780 nm wavelength, *Opt. Lett.*, 32(1), 53–55, 2007.
28. M. Kafesaki, I. Tsiapa, N. Katsarakis, T. Koschny, C. M. Soukoulis, and E. N. Economou, Left-handed metamaterials: The fishnet structure and its variations, *Phys. Rev. B*, 75(23), 235 114/1–9, 2007.
29. M. Kafesaki, T. Koschny, C. M. Soukoulis, and E. N. Economou, Designing one-, two- and three-dimensional left-handed materials, in *Theory and Phenomena of Metamaterials*, Taylor & Francis, Boca Raton, Florida, 2009, Chapter 17.
30. B. A. Munk, *Frequency Selective Surfaces: Theory and Design*. New York: Wiley, 2000.

31. X. Chen, T. M. Grzegorczyk, B.-I. Wu, J. Pacheco, and J. A. Kong, Robust method to retrieve the constitutive effective parameters of metamaterials, *Phys. Rev. E*, 70(1), 016 608/1–7, July 2004.
32. M. Kafesaki, T. Koschny, J. Zhou, N. Katsarakis, I. Tsiapa, E. N. Economou, and C. M. Soukoulis, Electromagnetic behaviour of left-handed materials, *Physica B*, 394, 148–154, May 2007.
33. G. Donzelli, A. Vallecchi, F. Capolino, and A. Schuchinsky, Metamaterial made of paired planar conductors: Particle resonances, phenomena and properties, *Metamaterials*, 3(1), 2009.
34. *High Frequency Structure Simulator (HFSS), Ver. 10.0*, Ansoft Corporation, Pittsburgh, PA, 2006.
35. *CST Microwave Studio, User Manual Ver. 5*, CST GmbH, Darmstadt, Germany, February 2004.
36. D. M. Pozar, *Microwave Engineering*. Reading, MA: Addison-Wesley, 1990.
37. M. A. R. Gunston, *Microwave Transmission-Line Impedance Data*. London: Van Nostrand Reinhold, 1972.
38. C. Imhof and R. Zengerle, Pairs of metallic crosses as a left-handed metamaterial with improved polarization properties, *Opt. Express*, 14(18), 8257–8262, 2006.
39. L. Markley and G. V. Eleftheriades, A negative-refractive-index metamaterial for incident plane waves of arbitrary polarization, *Antennas Wireless Propagat. Lett.*, 6(11), 28–32, 2007.
40. A. Vallecchi, F. Capolino, and A. G. Schuchinsky, 2-D isotropic effective negative refractive index metamaterial in planar technology, *Microw. Wireless Comp. Lett.*, 19(2), 2009.
41. L. Hunt, The oldest metallurgical handbook, *Gold Bull.*, 9(1), 24–32, January 1976.
42. M. Faraday, Experimental relations of gold (and other metals) to light, *Philos. Trans. Royal Soc. London*, 147, 145–181, 1857.
43. J. C. Maxwell Garnett, Colours in metal glasses, in metallic, and in metallic solutions. I, *Philos. Trans. Royal Soc. London*, 203, 385–420, 1904.
44. —, Colours in metal glasses, in metallic films, and in metallic Solutions. II, *Philos. Trans. Royal Soc. London*, 205, 237–288, 1906.
45. G. Mie, Beiträge zur optik trüber medien, speziell kolloidaler metallösungen, *Leipzig, Ann. Phys.*, 330, 377–445, 1908.
46. W. L. Barnes, A. Dereux, and T. W. Ebbesen, Surface plasmon subwavelength optics, *Nature*, 424, 824–830, August 2003.
47. S. A. Maier and H. A. Atwater, Plasmonics: Localization and guiding of electromagnetic energy in metal/dielectric structures, *J. Appl. Phys.*, 98(1), 011 101/1–10, 2005.
48. W. H. Weber and G. W. Ford, Propagation of optical excitations by dipolar interactions in metal nanoparticle chains, *Phys. Rev. B*, 70(12), 125 429/1–8, September 2004.
49. K. H. Fung and C. T. Chan, Plasmonic modes in periodic metal nanoparticle chains: A direct dynamic eigenmode analysis, *Opt. Lett.*, 32(8), 973–975, 2007.
50. L. Gunnarsson, T. Rindzevicius, J. Prikulis, B. Kasemo, M. Kall, S. Zou, and G. Schatz, Confined plasmons in nanofabricated single silver particle pairs: Experimental observations of strong interparticle interactions, *J. Phys. Chem. B*, 109(3), 1079–1087, 2005.
51. P. Alitalo, C. Simovski, A. Viitanen, and S. Tretyakov, Near-field enhancement and subwavelength imaging in the optical region using a pair of two-dimensional arrays of metal nanospheres, *Phys. Rev. B*, 74(23), 235 425/1–6, 2006.
52. H. Xu, E. J. Bjerneld, M. Käll, and L. Börjesson, Spectroscopy of single hemoglobin molecules by surface enhanced raman scattering, *Phys. Rev. Lett.*, 83(21), 4357–4360, November 1999.
53. J. Jiang, K. Bosnick, M. Maillard, and L. Brus, Single molecule raman spectroscopy at the junctions of large ag nanocrystals, *J. Phys. Chem. B*, 107(37), 9964–9972, 2003.
54. T. Jensen, M. Malinsky, C. Haynes, and R. Van Duyne, Nanosphere lithography: Tunable localized surface plasmon resonance spectra of silver nanoparticles, *J. Phys. Chem. B*, 104(45), 10 549–10 556, 2000.
55. C. Haynes, A. McFarland, L. Zhao, R. Van Duyne, G. Schatz, L. Gunnarsson, J. Prikulis, B. Kasemo, and M. Kall, Nanoparticle optics: The importance of radiative dipole coupling in two-dimensional nanoparticle arrays, *J. Phys. Chem. B*, 107(30), 7337–7342, 2003.

56. L. Zhao, K. Kelly, and G. Schatz, The extinction spectra of silver nanoparticle arrays: Influence of array structure on plasmon resonance wavelength and width, *J. Phys. Chem. B*, 107(30), 7343–7350, 2003.
57. W. Rechberger, A. Hohenau, A. Leitner, J. R. Krenn, B. Lamprecht, and F. R. Aussenegg, Optical properties of two interacting gold nanoparticles, *Opt. Commun.*, 220, 137–141, May 2003.
58. T. Pakizeh, M. S. Abrishamian, N. Granpayeh, A. Dmitriev, and M. Käll, Magnetic-field enhancement in gold nanosandwiches, *Opt. Express*, 14(18), 8240–8246, 2006.
59. A. Alù, A. Salandrino, and N. Engheta, Negative effective permeability and left-handed materials at optical frequencies, *Opt. Express*, 14(4), 1557–1567, 2006.
60. A. Alù and N. Engheta, Three-dimensional nanotransmission lines at optical frequencies: A recipe for broadband negative-refraction optical metamaterials, *Phys. Rev. B*, 75(2), 024 304/1–20, 2007.
61. E. V. Ponizovskaya and A. M. Bratkovsky, Ensembles of plasmonic nanospheres at optical frequencies and a problem of negative index behavior, *Appl. Phys. A-Mat.*, 87(2), 175–179, January 2007.
62. I. El-Kady, M. M. Sigalas, R. Biswas, K. M. Ho, and C. M. Soukoulis, Metallic photonic crystals at optical wavelengths, *Phys. Rev. B*, 62(23), 15 299–15 302, December 2000.
63. J. Aizpurua, G. W. Bryant, L. J. Richter, F. J. García de Abajo, B. K. Kelley, and T. Mallouk, Optical properties of coupled metallic nanorods for field-enhanced spectroscopy, *Phys. Rev. B*, 71(23), 235 420/1–13, June 2005.
64. I. Romero, J. Aizpurua, G. W. Bryant, and F. J. G. D. Abajo, Plasmons in nearly touching metallic nanoparticles: Singular response in the limit of touching dimers, *Opt. Express*, 14(21), 9988–9999, 2006.
65. F. J. García de Abajo, Interaction of radiation and fast electrons with clusters of dielectrics: A multiple scattering approach, *Phys. Rev. Lett.*, 82(13), 2776–2779, March 1999.
66. T. Jensen, L. Kelly, A. Lazarides, and G. Schatz, Electrodynamics of noble metal nanoparticles and nanoparticle clusters, *J. Cluster Sci.*, 10, 295–317, June 1999.
67. S. Steshenko and F. Capolino, Single dipole approximation for modeling collections of nanoscatterers, in *Theory and Phenomena of Metamaterials*, Taylor & Francis, Boca Raton, Florida, 2009, Chapter 8.
68. F. Bohren and D. R. Huffman, *Absorption and Scattering of Light by Small Particles*. New York: Wiley, 1983.
69. J. D. Jackson, *Classical Electrodynamics*. New York: Wiley, 1998.
70. V. Myroshnychenko, J. Rodrguez-Fernndez, I. Pastoriza-Santos, A. M. Funston, C. Novo, P. Mulvaney, L. M. Liz-Marzn, and F. J. G. de Abajo, Modelling the optical response of gold nanoparticles, *Chem. Soc. Rev.*, 37(9), 1792–1805, July 2008.
71. A. Alù and N. Engheta, Dynamical theory of artificial optical magnetism produced by rings of plasmonic nanoparticles, *Phys. Rev. B*, 78(8), 085 112/1–10, August 2008.
72. S. Tretyakov, *Analytical Modeling in Applied Electromagnetics*. Norwood, MA: Artech House, 2003.
73. A. Alù, and N. Engheta, Negative refraction in infrared and visible domains, in *Theory and Phenomena of Metamaterials*, Taylor & Francis, Boca Raton, Florida, 2009, Chapter 23.
74. W. T. Doyle, Optical properties of a suspension of metal spheres, *Phys. Rev. B*, 39(14), 9852–9858, May 1989.
75. A. Perro, S. Reculusa, E. Bourgeat-Lami, E. Duguet, and S. Ravaine, Synthesis of hybrid colloidal particles: from snowman-like to raspberry-like morphologies, *Colloids Surf. A*, 14(4), 78–83, 2006.
76. V. Ponsinet, A. Aradian, P. Barois, and S. Ravaine, Self-assembly and nanochemistry techniques for the fabrication of metamaterials, in *Theory and Phenomena of Metamaterials*, Taylor & Francis, Boca Raton, Florida, 2009, Chapter 32.

20

Theory and Design of Metamorphic Materials

Chryssoula A. Kyriazidou
University of California Irvine and Broadcom Corporation Irvine

Harry F. Contopanagos
National Center for Scientific Research "Demokritos"

Nicólaos G. Alexopóulos
University of California Irvine and Broadcom Corporation Irvine

20.1 Introduction

Composite electromagnetic media have long been the subject of interest for a variety of theoretical and practical reasons and in a variety of physical realizations as amorphous mixtures, ordered media, frequency-selective surfaces, photonic crystals, etc. A wide range of interesting physical phenomena is revealed in several of these realizations, most importantly frequency-modulated reflection and transmission.

In this chapter, we present the newly defined metamorphic materials, which are artificial metallo-dielectric structures composed of passive elements and switches, and which exhibit bulk electromagnetic transitions among a set of dinstinct electromagnetic states, each characterized by a specific range of values of the reflected electromagnetic field. According to the interconnect topologies of the metallic inclusions, a metamorphic material behaves, at a single frequency, as an electric conductor, a passive or active magnetic conductor, an absorber, or an amplifier.

Early investigations of electromagnetic scattering from objects and interfaces characterized by an equivalent variable surface impedance [1,2] reveal the presence of a set of universally defined, distinct electromagnetic states at a given frequency. For smooth curvilinear scatterers, backscattering is dominated locally, within a factor accounting for curvilinear effects, by the reflection coefficient from a planar interface of the same material composition [3]. Further, by applying the Whittaker–Shannon Theorem, the surface impedance continuum can be replaced with a discrete array of elements with the same locally variable electromagnetic properties, thus yielding the same result. This may be a discrete array of antennas terminated at a variable impedance load [4]. As a corollary, bulk reflection from a

homogeneous medium as well as reflection from printed photonic crystals may also be described by a similar formula. Given this universal set of metamorphic states, it is interesting to develop practical electromagnetically metamorphic structures that realize a number of these states. In the present overview, we realize this with the use of photonic crystals.

A formal statement that allows us to unify these properties and define generally the metamorphic states of a scattering object when this scatterer is modeled as a terminating obstacle that reflects a propagating mode of characteristic impedance Z_0 follows by casting the reflection coefficient in the form of a transmission line equivalent:

$$\Gamma = \frac{Z - Z_0}{Z + Z_0} = \frac{\dfrac{R}{Z_0} + i\dfrac{X}{Z_0} - 1}{\dfrac{R}{Z_0} + i\dfrac{X}{Z_0} + 1} \tag{20.1}$$

where, the load impedance is $Z = R + iX$. Similarly, a half-space filled with homogeneous material that can be described in the bulk by relative permittivity and permeabilitty functions $\varepsilon_d = \varepsilon_d^r + i\varepsilon_d^i$, $\mu_d = \mu_d^r + i\mu_d^i$ has a corresponding reflection coefficient for normal plane-wave incidence:

$$\Gamma_\infty = \frac{\eta_d - \eta_0}{\eta_d + \eta_0} = \frac{\dfrac{\eta_d}{\eta_0} - 1}{\dfrac{\eta_d}{\eta_0} + 1} = \frac{\mathrm{Re}\,(\eta) + i\mathrm{Im}\,(\eta) - 1}{\mathrm{Re}\,(\eta) + i\mathrm{Im}\,(\eta) + 1}, \tag{20.2}$$

where

$\eta_0 = \sqrt{\mu_0/\varepsilon_0} = 120\pi\Omega$ is the wave impedance of air
η_d is the wave impedance of the dielectric material
η is the relative complex wave impedance of the material

Equations 20.1 and 20.2 are otherwise identical, and we imagine a material in which we can vary $\mathrm{Re}\{\eta\}$ for fixed $\mathrm{Im}\{\eta\}$. The corresponding circuit analogy in Equation 20.1 is that we vary the load resistance. The induced variation on the reflection coefficient is shown in Figure 20.1, where $\mathrm{Im}\{\eta\}$ is varied parametrically. The region $\mathrm{Re}\{\eta\} < 0$ corresponds to an active material (amplifier) for which $|\Gamma_\infty| > 1$.

In accordance with Figure 20.1, we define metamorphic materials as composite materials whose bulk reflection coefficient Γ (or slab reflection coefficient S_{11} for physical realizations) can transition under electromagnetic excitations, among two or more values from Table 20.1 [5].

One main issue we address in Sections 20.2 through 20.4 is how to physically realize artificial materials that exhibit transitions between these electromagnetic states using electronic reconfigurability. We show that metallo-dielectric photonic crystals can be used to realize several metamorphic states [5] depicted in Figure 20.1. The metamorphic material should perform these transitions at the same frequency, without changing the geometry of the scatterers or any other geometrical features. The only agent creating these transitions should be a lattice of switches affecting the topology of the conducting path of the induced currents between the scatterers. The switch lattice can be electronically reconfigured, but the physical size of the switches should have negligible scattering cross-section. In this chapter, we examine several realizations of such materials as metallo-dielectric photonic crystals, where the metallic scatterers form a lattice. On this lattice, we envision a second lattice of switches, to be realized in practice as solid-state or micro-electro-mechanical (MEM) switches, that can be on or off and otherwise with negligible physical size. In this chapter, we cover only passive metamorphic states. A complete set of metamorphic states, including active ones, may be realized by employing an actively loaded perfect electric conductor (PEC) circular ring array within a lossy host material [6]. In [6], a negative index of refraction metamaterial is achieved as a subclass of a metamorphic material.

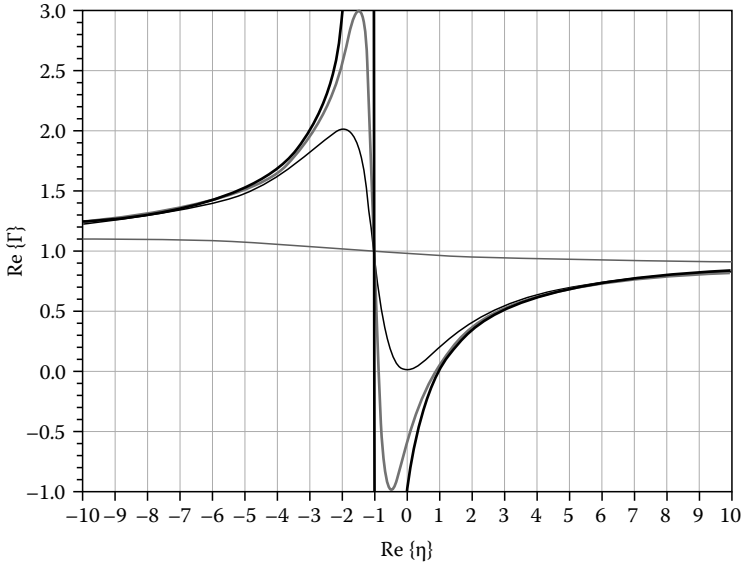

FIGURE 20.1 Variation of the real part of bulk reflection coefficient according to the theoretical variations of the relative complex wave impedance. Im{η} is varied parametrically at values ±0.1 (thick black), ±0.5 (thick gray), ±1 (thin black), and ±10 (thin gray). (From Kyriazidou, C.A., Contopanagos, H.F., and Alexopoulos, N.G., *J. Opt. Soc. Am. A*, 23(11), 2961, November 2006. With permission.)

TABLE 20.1 Definition of Metamorphic States

Definition of Metamorphic States		
Γ	Re{η}	Function
$-1 + i0$	0	Perfect electric conductor
$+1 + i0$	$+\infty$	Perfect passive magnetic conductor
$+1 + i0$	$-\infty$	Perfect active magnetic conductor
0	+1	Passband filter/absorber[a]
$-\infty$	$-1 + \delta$	Perfect electric amplifier
$+\infty$	$-1 - \delta$	Perfect magnetic amplifier

Source: Kyriazidou, C.A., Contopanagos, H.F., and Alexopoulos, N.G., *J. Opt. Soc. Am. A*, 23(11), 2961, November 2006. With permission.

[a] The functions passband filter/absorber are distinguished for a slab by the transmission coefficient.

The second main issue concerns the extraction of an effective description of these materials, which we address in Sections 20.5 and 20.6. Each metamorphic state realized corresponds to a certain artificial periodic lattice of metallic scatterers, i.e., a distinct photonic crystal. In general, a photonic crystal may be characterized in the bulk by an effective parameter theory that yields equivalent effective response functions similar to homogeneous dispersive materials [7–15]. Such approaches are covered extensively, in Part I of this book, but we briefly summarize an alternative view on the subject of power loss. Further, we use the resonant inverse scattering approach [14] to extract the effective parameters of the specific metamorphic materials we present. This is useful to reclassify the metamorphic structures in terms of transitions among fundamental values of their effective parameters, instead of just their backscattering response presented in [5]. In this sense, it promotes the physical intuition and application space and simplifies the design of metamorphic crystals. The effective description makes each metamorphic state equivalent to a metamaterial state; hence, a metamorphic material is an electronically reconfigurable collection of metamaterials. A time-harmonic dependence $\exp(-i\omega t)$ is assumed throughout this chapter.

20.2 Physical Realization of Metamorphism through Babinet Complementarity

In this work, metamorphism is achieved by taking advantage of the frequency dependence and the highly resonant behavior of the reflection coefficient of metallo-dielectric crystals. The switch lattice will then modulate that frequency dependence according to certain complementarity principles of electromagnetic scattering of metallic targets. To be specific, we apply Babinet's principle of complementary screens to achieve a fundamental two-state metamorphism in the reflection coefficient. We first start with the disk medium, which has been solved analytically in [7,8,15]. In [14,15], we have shown that the analytical solution agrees well with finite-element numerical simulations performed with the commercial full-wave simulator HFSS (high-frequency structure simulator) and with measured prototypes. Given the validation, we use HFSS for most of the analysis.

Two main ideas lead us to the development of our metamorphic medium. The first is the anticipated electromagnetic inversion that follows from the Babinet principle. When we compare, at a specific frequency, the response of a lattice of printed elements to that of its dual printing, we expect a maximal metamorphic inversion. For instance, at a specific frequency where we have an electric wall, characterized by large effective permittivity and negligible effective permeability values, in the dual system we expect a magnetic wall, characterized by near-zero effective permittivity and large effective permeability values. The second notion is that the basic characteristics of the frequency response do not change for small variations in the shape of the implants. In this section, we derive these properties focusing on a specific set of design geometries D_{ij}, summarized in Table 20.2.

Each entry D_{i1} in Table 20.2 has a Babinet-complementary structure D_{i2}, and we show specific metamorphic relations in the electromagnetic response of each pair. As a second step, it has been shown [5] that the second and third entries in a given column show the same metamorphic behavior as the first entry of the opposite column, i.e., the structures $\{D_{11}, D_{22}, D_{32}\}$ and $\{D_{12}, D_{21}, D_{31}\}$

TABLE 20.2 Summary of Geometries Used and Their Complementarity Properties

Composite Medium	Babinet-Complementary Medium
D_{11}: Circular metal disks	D_{12}: Metal screen with circular holes
D_{21}: Overlapping metal disks	D_{22}: Metal screen with overlapping holes
D_{31}: Metal disks connected with metal strips	D_{32}: Metal screen with connected holes

Source: Kyriazidou, C.A., Contopanagos, H.F., and Alexopoulos, N.G., *J. Opt. Soc. Am. A*, 23(11), 2961, November 2006. With permission.

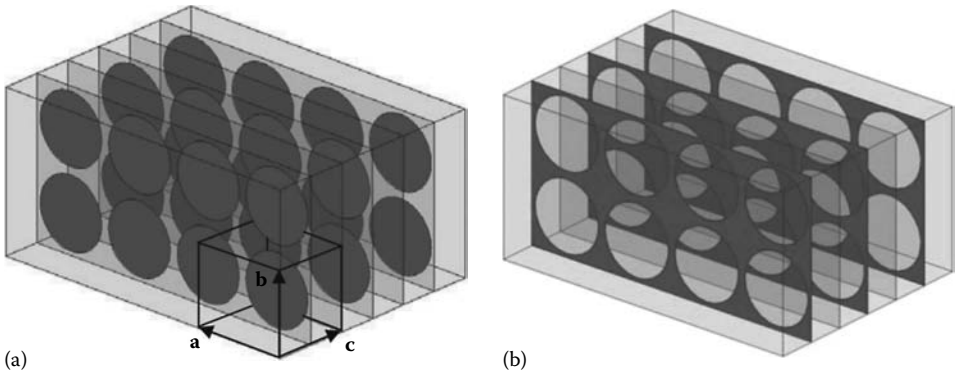

FIGURE 20.2 (a) D_{11}: Circular metal disks. (b) D_{12}: Metal screen with circular holes. (From Kyriazidou, C.A., Contopanagos, H.F., and Alexopoulos, N.G., *J. Opt. Soc. Am. A*, 23(11), 2961, November 2006. With permission.)

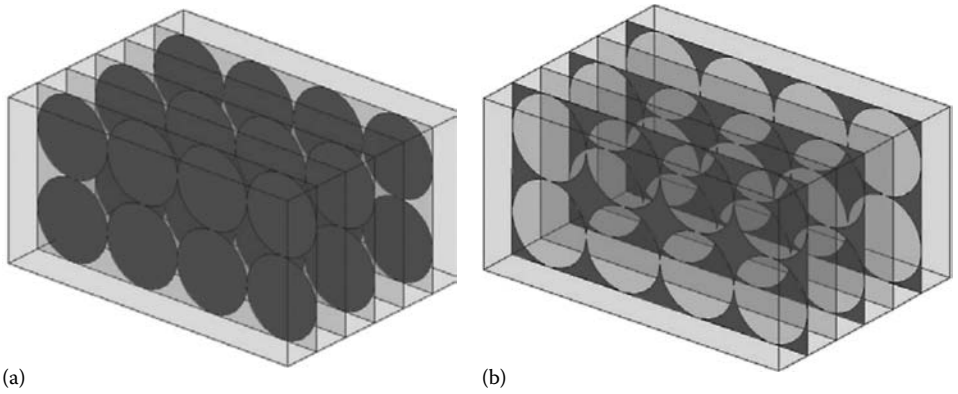

FIGURE 20.3 (a) D_{21}: Overlapping metal disks. (b) D_{22}: Metal screen with overlapping holes. (From Kyriazidou, C.A., Contopanagos, H.F., and Alexopoulos, N.G., *J. Opt. Soc. Am. A*, 23(11), 2961, November 2006. With permission.)

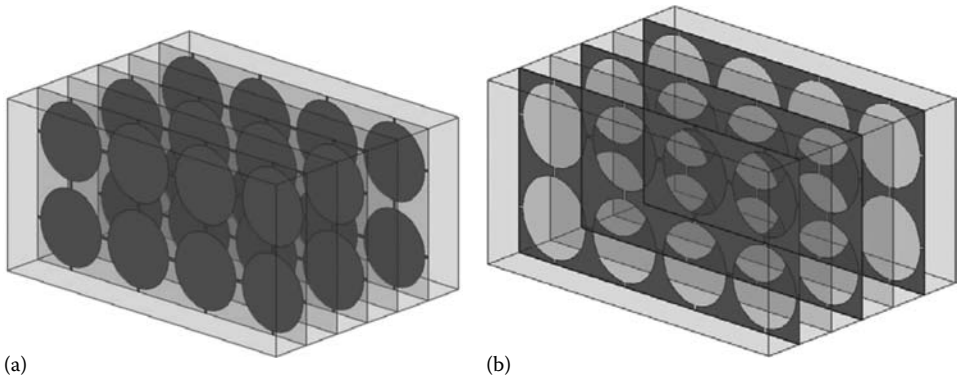

FIGURE 20.4 D_{31}: Metal disks shorted with metal strips. (b) D_{32}: Metal screen with connected holes. (From Kyriazidou, C.A., Contopanagos, H.F., and Alexopoulos, N.G., *J. Opt. Soc. Am. A*, 23(11), 2961, November 2006. With permission.)

in Table 20.2 have similar electromagnetic response. It is clear that the third row of entries can be realized by electronic switching of the first row, as it involves metallization with localized electrical connectivity, which can be accomplished by either open or closed electrical switches. Hence, it follows that the two behaviors of the sets $\{D_{11}, D_{22}, D_{32}\}$ and $\{D_{12}, D_{21}, D_{31}\}$ in Table 20.2 can be realized by electronic switching of either D_{11} or D_{12} without any further change in the photonic crystal geometry. In Section 20.3, we illustrate how this works in practice, for a specific set of designs reflecting the structures of Table 20.2 and shown in Figures 20.2 through 20.4. In Figure 20.4, the shorting metal strips have been chosen to have a negligible cross-section, and their electromagnetic function is equivalent to a point-like connector (short), which can be realized by an electronic switch.

20.3 Realization and Design of a Two-State Metamorphic Material

We choose a host material, unit cell dimensions, and disk size identical to those in [15], which produced optimized passband filtering properties in the Ka frequency band, and was also validated by

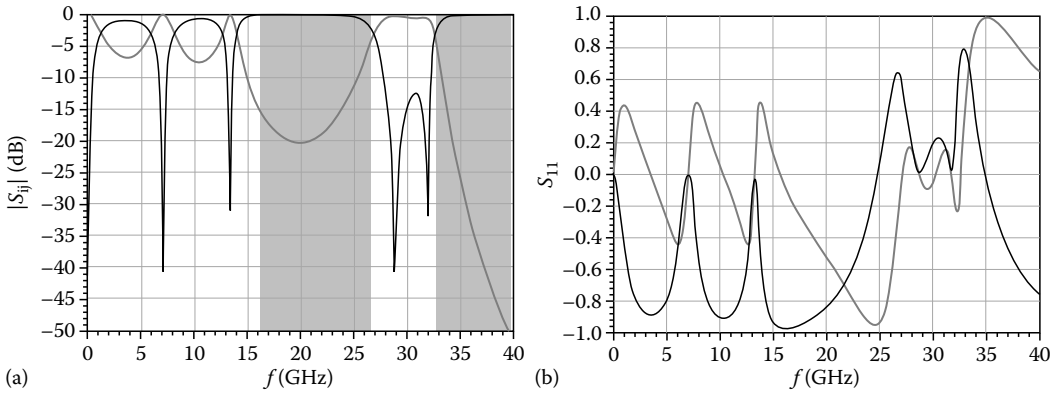

FIGURE 20.5 Normal plane-wave incidence on D_{11} (disk medium): (a) Reflected (black) and transmitted (gray) power and the first two PBG regions. (b) Real (black) and imaginary (gray) parts of the reflection coefficient. (From Kyriazidou, C.A., Contopanagos, H.F., and Alexopoulos, N.G., *J. Opt. Soc. Am. A*, 23(11), 2961, November 2006. With permission.)

prototype measurements. The passive lattice consists of an orthogonal unit cell $(a, b, c) = (1.75\,\text{mm},\ 1.75\,\text{mm},\ 1.7\,\text{mm})$ of host dielectric relative complex permittivity $\varepsilon = 11.1(1 + i0.0028)$ in which the size of the circular scatterers (metal disks or holes) is $r/a = 0.45$.

In Figure 20.5, we summarize the properties of the power spectrum and reflection coefficient of three layers of design D_{11}, i.e., the disk medium, obtained analytically or through HFSS simulations and the results being in excellent agreement, [14,15].

1. At DC and low frequencies the material is a homogeneous dielectric slab, and the reflection coefficient is that of a Fabry–Perot resonator.
2. At the first electromagnetic band gap (EBG), which is the left shaded area, the reflection coefficient starts as an electric wall in the first half of the band gap and transforms to a magnetic wall in the second half of the band gap.
3. At the second band gap (right shaded area), the material transitions in the opposite sense: First it becomes a magnetic wall and then an electric wall.
4. The frequency region between two successive magnetic walls is a "zero reflection region," where the material can operate as a passband filter. It can also operate as a perfect absorber, if the host loss tangent is increased.

In Figure 20.6, we show the corresponding response for the Babinet-complementary material D_{12}. Contrasting this with Figure 20.5, we see that the material behaves as a perfectly reflecting screen at DC and low frequencies, because the holes have negligible size at these long wavelengths. Further, in the frequency region where D_{11} has its first EBG, D_{12} has a passband, whereas in the higher frequency region where D_{11} has its passband, D_{12} has its second band gap [5,14].

In Figure 20.7, we show the response of material D_{31}, which is made of disks interconnected by very thin metal strips. We have checked that the strip width is of negligible cross-section as the same response is obtained by strips of half the width as well as a quarter of the width shown. These strips can be realized as connectors operated by electronic switches or MEMs switches. Notice that despite the fact that designs D_{12} and D_{31} are geometrically very different, they are topologically similar, and the corresponding responses are also very similar all the way up to the second photonic band gap. Design D_{21} shows a behavior very similar to D_{31}. Hence, topology predetermines metamorphic properties much more than specific scatterer shapes (of comparable electrical size).

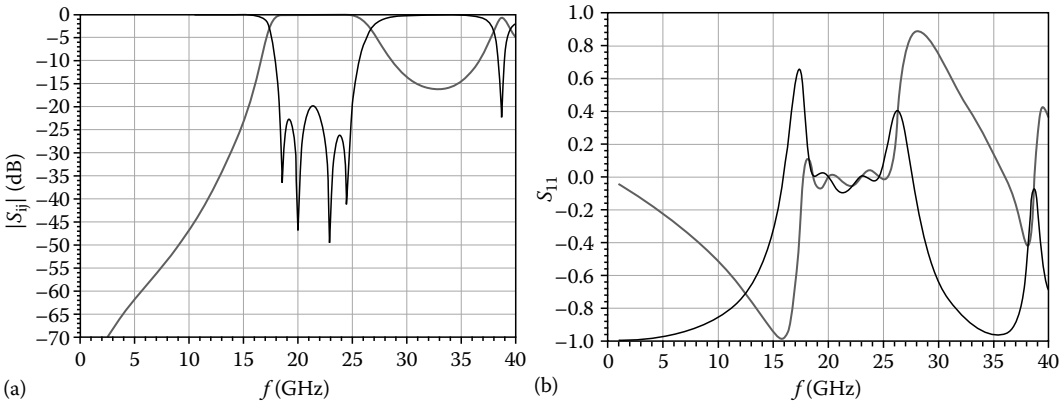

FIGURE 20.6 Normal plane-wave incidence on Babinet-complementary material D_{12}. (a) Reflected (black) and transmitted (gray) power. (b) Real (black) and Imaginary (gray) parts of S_{11}. (From Kyriazidou, C.A., Contopanagos, H.F., and Alexopoulos, N.G., *J. Opt. Soc. Am. A*, 23(11), 2961, November 2006. With permission.)

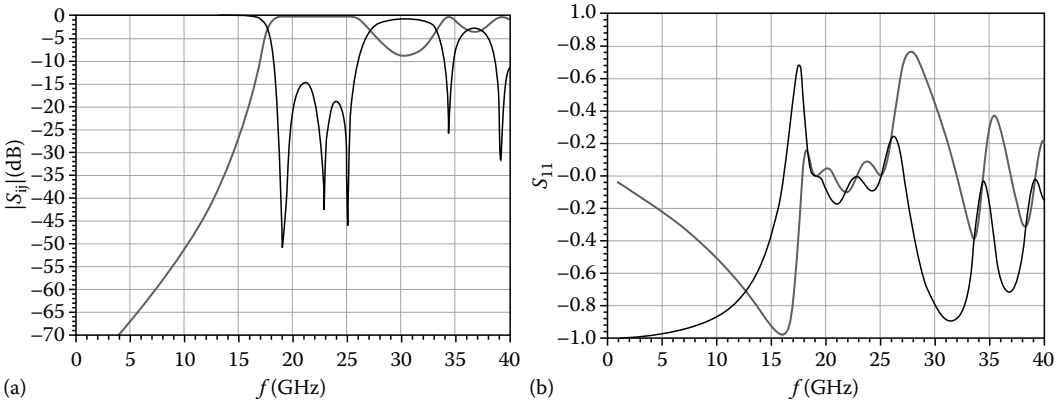

FIGURE 20.7 Normal plane-wave incidence on material D_{31}. (a) Reflected (black) and transmitted (gray) power. (b) Real (black) and imaginary (gray) parts of S_{11}. (From Kyriazidou, C.A., Contopanagos, H.F., and Alexopoulos, N.G., *J. Opt. Soc. Am. A*, 23(11), 2961, November 2006. With permission.)

In Figure 20.8, we show the two-state metamorphic transitions (shaded bands) between D_{11} (disks) and D_{31} (shorted disks). D_{11} has a broadband passband at around 31 GHz and can be reconfigured to an electric conductor by shorting the disks and becoming D_{31}. The reverse metamorphic transition at the much lower frequency of 19 GHz is observed between the media D_{11} and D_{31} as a consequence of Babinet's principle. This is important for applications where low-frequency metamorphism for small electrical sizes is desired. We note also a narrow-band transition at 17 GHz, where the magnetic wall state is not close to perfect. Its value can approach +1 by increasing the number of layers. A behavior identical to the above and at the same frequencies (17–20 GHz) can be observed for the designs D_{12} (holes) and D_{32} ("shorted" holes) as Figures 20.5 and 20.6 indicate, but the metamorphic states are reversed [5].

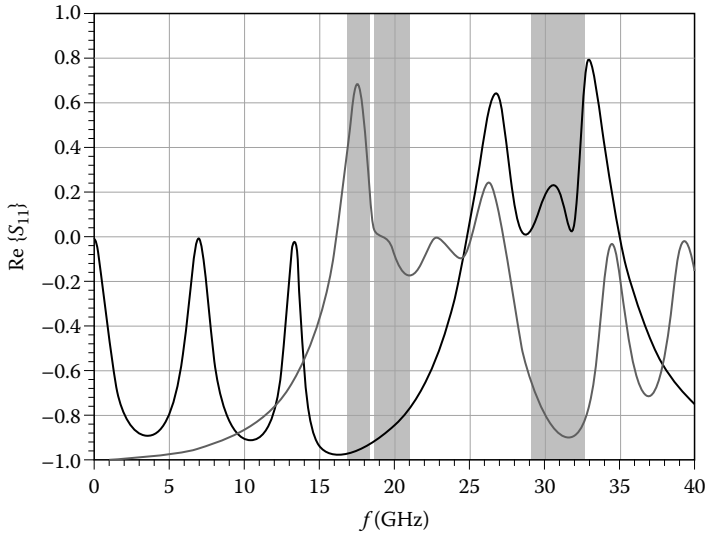

FIGURE 20.8 Two-state metamorphic material under normal plane-wave incidence. The two electronically reconfigurable states are D_{11} (black) and D_{31} (gray). (From Kyriazidou, C.A., Contopanagos, H.F., and Alexopoulos, N.G., *J. Opt. Soc. Am. A*, 23(11), 2961, November 2006. With permission.)

20.4 Realization and Design of a Three-State Metamorphic Material

In this section, we summarize how to physically realize a three-state metamorphism in a similar manner [5]. In Figure 20.9, we show the design of a third reconfigurable state complementing the two-way metamorphism of Figure 20.8. We observe that in the frequency region of 31 GHz and with an appreciable bandwidth, the system of Figure 20.9 behaves as a magnetic conductor while D_{11} is a passband filter (or an absorber) and the shorted disk medium is an electric conductor. Notice that this

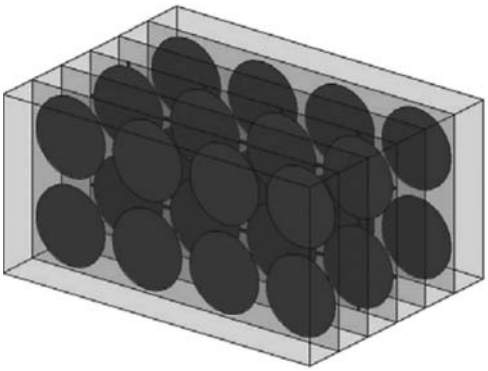

(a)

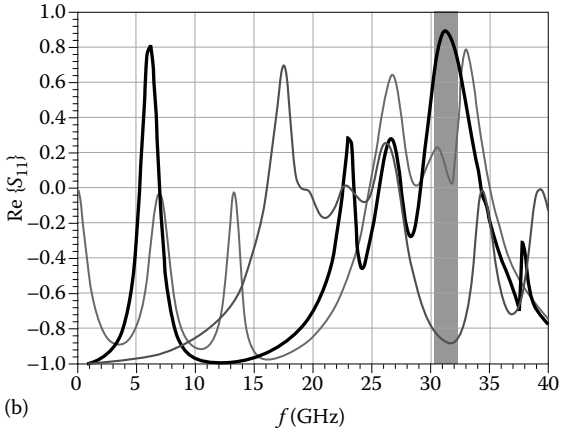

(b)

FIGURE 20.9 Three-state metamorphic material. The three electronically reconfigurable states are D_{11} (thin black), D_{31} (Figure 20.7, thick gray), and this figure (thick black). (From Kyriazidou, C.A., Contopanagos, H.F., and Alexopoulos, N.G., *J. Opt. Soc. Am. A*, 23(11), 2961, November 2006. With permission.)

TABLE 20.3 Active Lattice of Switches Applied on Design D_{11} (Metal Disk Medium) and Corresponding Metamorphic States at 31 and 21 GHz

Switch State (Active Lattice)			Metamorphic State at 31 GHz	Metamorphic State at 21 GHz
(0,1,0)	Layer 1	Open	Magnetic conductor	
	Layer 2	Closed		
	Layer 3	Open		
(0,0,0)	Layer 1	Open	Passband filter/absorber	Electric conductor
	Layer 2	Open		
	Layer 3	Open		
(1,1,1)	Layer 1	Closed	Electric conductor	Passband filter/absorber
	Layer 2	Closed		
	Layer 3	Closed		
(1,0,1)	Layer 1	Closed		Magnetic conductor
	Layer 2	Open		
	Layer 3	Closed		

Source: Kyriazidou, C.A., Contopanagos, H.F., and Alexopoulos, N.G., *J. Opt. Soc. Am. A*, 23(11), 2961, November 2006. With permission.

system also shows a narrowband two-way metamorphism (an electric-to-magnetic wall transition) at the very low frequency of 6.5 GHz, providing a metamorphism with a material of very small physical thickness $\approx \lambda_0/10$ or an optical thickness $\approx \lambda_0/3$.

We can describe in general the three-way transitions implemented with electronic or MEMs switches in Table 20.3. The first three rows of the table describe the switch states corresponding to the metamorphism of Figure 20.9b. In the last row of this table, we have also included a different configuration, where a switch state (1,0,1) indicates that the terminating layers are D_{31} (shorted disks), whereas the middle layer is D_{11}. This also presents a three-way metamorphism at the much lower frequency of 21 GHz, of similar bandwidth. For more details, the interested reader may refer [5].

20.5 Metamaterial Characterization of Photonic Crystals and Their Metamorphic States

In this section, we describe the bulk material characterization of metamorphic structures in terms of a pair of complex functions $\{\eta(\omega), n(\omega)\}$ (effective or intrinsic wave impedance and refractive index) or in terms of a pair $\{\varepsilon(\omega), \mu(\omega)\} = \left\{\frac{n(\omega)}{\eta(\omega)}, n(\omega)\cdot\eta(\omega)\right\}$ (effective permittivity and permeability). Apart from being simply a restatement or an alternative description, the reduction of each photonic crystal, and in the present context each metamorphic state, to a pair of basic parameters is useful to reveal unusual dispersive properties not found in natural media, such as permittivities, permeabilities, and refractive indices less than one or negative. In this sense, it promotes the physical intuition in the design of metamorphic crystals targeting specific applications. The method has been used to characterize photonic crystals and extract their metamaterial properties, even in the resonant regime. For structures that can be solved analytically, it provides analytical expressions for the effective parameters in terms of the polarizabilities of the metallic scatterers [7,8,15]. For general shapes, it relies on inverse scattering [9,12–14]. We refer to the method of [13] as a resonant inverse scattering method. The resonant inverse scattering method allows us to distinguish the structures that have a bulk description as well as to obtain their unambiguous characterization regarding its electromagnetic parameters as follows:

First, we assume that a structure is equivalent to a macroscopically homogeneous medium. Consequently, it may be described in terms of dispersive effective response functions. In such systems, the scattering parameters (S_{11}, S_{21}), i.e., the reflection and transmission coefficients for a slab, assume the form of the corresponding formulas for a macroscopically homogeneous medium. S_{11} and S_{21} are the inputs in this approach and may be obtained through analytical solutions, simulations, or measurements. We treat structures that are electromagnetically symmetric, i.e., $S_{11} = S_{22}$, and hence the illumination side is immaterial.

Second, we invert algebraically the system of equations for the complex quantities S_{11}, S_{21}, in accordance with the experimental extraction of material parameters [16]. In this manner, we obtain a pair of effective parameters.

The question may arise, however, whether the derived parameters provide an effective description of the medium, *for the specific metal scatterer shapes/topologies used in simulations or measurements*, which may be quite complicated. Not every complex structure accepts an effective description, and moreover, those that do may not maintain it for the entire frequency regime. This leads us to formulate a third step, which should be viewed as a general criterion.

Consistency criterion: A *periodic or random* structure *does* have a bulk description in a specific frequency regime, only when it yields the *same* effective parameters for a slab of *any thickness*. A successful homogeneous description of a slab of any thickness is, in our view, the *most fundamental and physically transparent* phenomenological description of a composite material, because it involves the most fundamental aspects of macroscopic scattering, i.e., (a) transmission through the bulk, (b) diffraction by two terminating interfaces, and (c) a three-way power balance (reflection, transmission, and loss). If the effective parameters are uniquely determined, *independently of the slab thickness*, then, obviously, they represent the correct effective parameters of the system. What we do in practice is to take two cuts of the various structures we treat [14]. Given that the input S-parameters for these two cuts are *extremely different and still yield identical parameters*, the chance that the bulk description does not hold for some other cuts is *really* minimal. Equivalently, we may produce the effective parameters for one specific slab, use them to predict the scattering matrix for a slab of different thickness, and finally compare these to measured or simulated results. This criterion is therefore a consistency test, functioning as a necessary and sufficient condition, which will obviously reject the structures that do not accept a bulk description. For periodic structures, the slab thickness, d, should be an integer multiple of the monolayer period, c, i.e., $d = N \times c$.

The starting point is the slab reflection and transmission complex coefficients under normal incidence, which assume the form of the corresponding formulas for a macroscopically homogeneous medium:

$$S_{11} = \frac{\eta - 1}{\eta + 1} \frac{1 - x^2}{1 - \left(\dfrac{\eta - 1}{\eta + 1}\right)^2 x^2}, \quad S_{21} = \frac{4\eta x}{(\eta + 1)^2} \frac{1}{1 - \left(\dfrac{\eta - 1}{\eta + 1}\right)^2 x^2}, \; x = \exp\left(ik_0 dn\right). \tag{20.3}$$

This is an algebraic system of two equations with two unknowns: the wave impedance η and the refractive index n. The known inputs are the complex quantities S_{11}, S_{21} obtained through analytical solutions, simulations, or measurements. Exact algebraic inversion of the system (Equation 20.3) provides the effective parameters:

$$\eta = \frac{1 + A}{1 - A} =, \quad A = V \pm \sqrt{V^2 - 1}, \quad V = \frac{1 + S_{11}^2 - S_{21}^2}{2S_{11}}, \quad \mathrm{Re}\{\eta\} > 0 \tag{20.4}$$

$$n = \frac{\arccos(\mathrm{Re}\{x\}/|x|)}{k_0 d} - i\frac{\ln|x|}{k_0 d}, \quad x = \frac{S}{1 + R - ASR}, \quad S = S_{11} + S_{21}, \; R = \frac{S_{11}}{S_{21}}. \tag{20.5}$$

The inversion formulas of Equations 20.4 and 20.5, although exact, will only be as accurate as the fundamental inputs, which will carry measurement or computational uncertainties. For further details on the method and many results, the reader may consult [14]. In this report, we illustrate the method as applied on the photonic crystal of the hole medium D_{12} of Figure 20.2b or the equivalent metamorphic state D_{31} of the shorted disk medium, Figure 20.4a. The hole medium can also be solved analytically [17], based on Booker's formulation of Babinet's principle [18] and our analytical solution for the disk medium [7,15]. The results are in excellent agreement with the HFSS simulations of Figure 20.6, (see [17]), just as they were for the disk medium within the same frequency range [14].

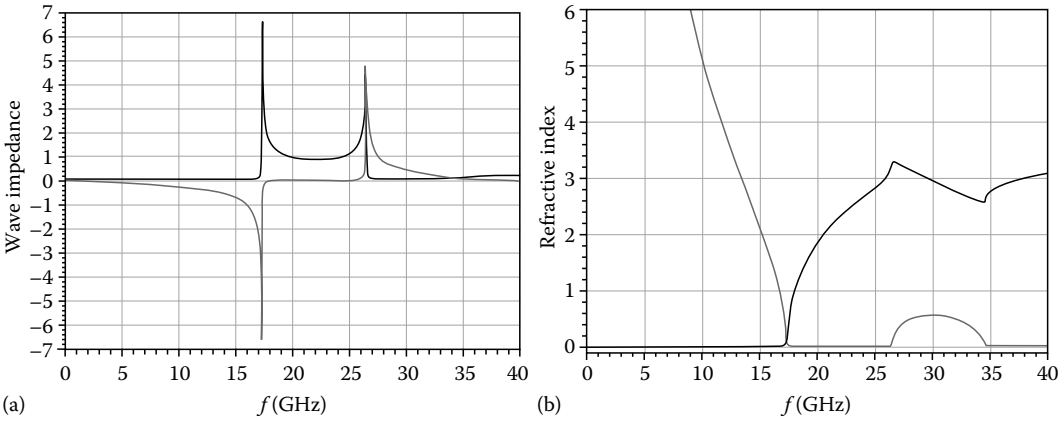

FIGURE 20.10 Wave impedance (a) and refractive index (b) under normal plane-wave incidence. Real parts, black; imaginary parts, gray. (From Kyriazidou, C.A., Contopanagos, H.F., and Alexopoulos, N.G., Effective description and power balance of metamaterials, in *ACES 2007 Conference Proceedings*, Verona, Italy, March 19–23, 2007, pp. 260–264. With permission.)

For the plots below, we use the S-parameters of Figure 20.6a but generated analytically with a very dense frequency sweep (4000 points). All functions appearing below are analytic, i.e., smooth at their extrema (which have been examined by local magnification) and differentiable at all points in these regions. The corresponding results using HFSS-generated S-parameters are in [14].

We see from Figure 20.10b that the hole medium behaves as a metal from DC up to 17 GHz, as the huge values of the imaginary part of the refractive index reveals. This is also evident from the transmittivity of Figure 20.6a. For these frequencies, the holes are too small for the field to pass through. Near 17 GHz, we have a transition to transparency, and the hole medium behaves as a low-loss dielectric, while the first band gap appears centered at 30 GHz, as revealed again by Figure 20.10b.

In Figure 20.11a, we see that the permittivity has a negative real part up to 17 GHz, where it reaches zero. This is obviously an artificial plasma frequency, above which the material becomes

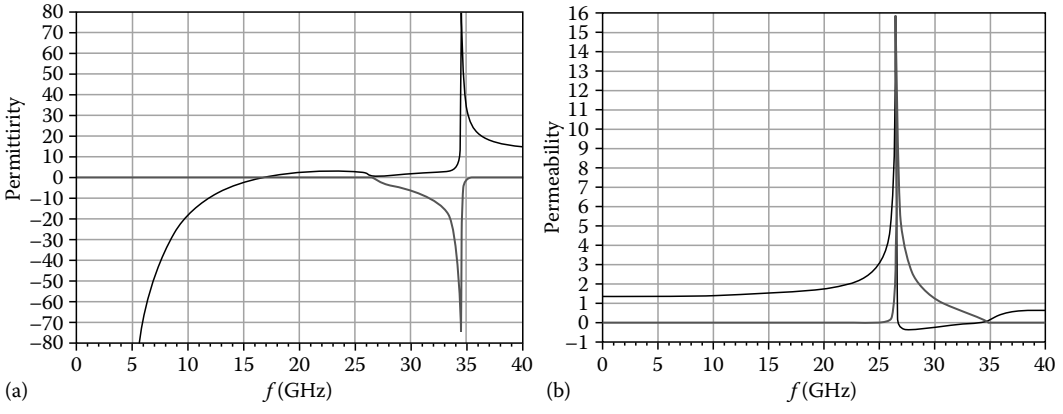

FIGURE 20.11 Permittivity (a) and permeability (b) under normal plane-wave incidence. Real parts, black; imaginary parts, gray. (From Kyriazidou, C.A., Contopanagos, H.F., and Alexopoulos, N.G., Effective description and power balance of metamaterials, in *ACES 2007 Conference Proceedings*, Verona, Italy, March 19–23, 2007, pp. 260–264. With permission.)

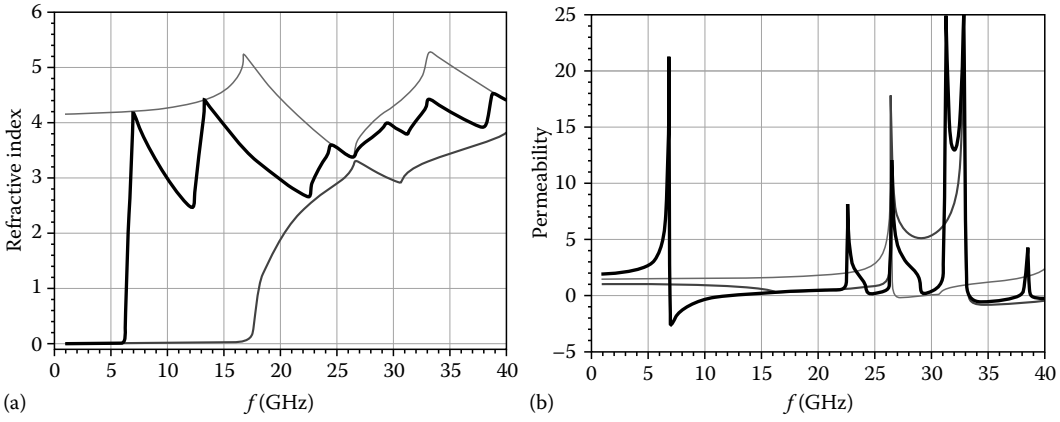

FIGURE 20.12 Three-state metamorphism of real parts of refractive index (a) and permeability (b). (0,0,0), Thin black; (1,1,1), thick gray; (0,1,0): thick black. (From Alexopoulos, N.G., Kyriazidou, C.A., and Contopanagos, H.F., *IEEE Trans. Microw. Theory Tech.*, 55(2), 254, February 2007. With permission.)

very transparent, as seen in Figure 20.6a. The physical diameter of the holes at that frequency is $\approx \lambda_0/11$, whereas the optical diameter in the host dielectric is $\approx \lambda_0/3.4$. We therefore see very high transmission at substantially subwavelength holes, consistent with earlier work [19–23] and explanations based on an artificial plasma frequency [22]. The reason we have a broadband passband in Figure 20.6a, rather than isolated transmission resonances, is because we have optimized the design of the material so that stacked monolayers provide such a passband. The design shown is ideal for passband filter applications.

In Figure 20.12, we have extracted the effective parameters for the three-state metamorphic material shown in Figure 20.9b and Table 20.3. As expected, the results show the possibility of very strong modulation of the effective parameters with the underlying electronic reconfigurability. We notice in particular the metamorphic effective permeability of Figure 20.12b. We see that very high resonant permeability values develop for all three metamorphic states of the photonic crystal, despite the fact that the constituent materials are nonmagnetic, as had been observed some time ago [7,24]. The resonant permeabilities indicate magnetic wall behavior in the corresponding reflection coefficients of Figure 20.9b. In particular, we emphasize the low-frequency resonant permeability at around 6 GHz [14] exhibited by the (0,1,0) metamorphic state of Figure 20.9a, which provides an electronically reconfigurable magnetization realized for a very thin metamaterial slab, as discussed at the beginning of Section 20.4.

20.6 Power Balance, Loss, and Usefulness of the Resonant Effective Description

We conclude this chapter with a few remarks regarding the signs of the effective parameters one obtains for such periodic structures and their relation to the power balance of any macroscopic slab of material. As has been shown in early publications [7,8] and can be verified from Equation 20.2, $\mathrm{Re}\{\eta\}$ must be positive for the medium to be passive, because the wave impedance is directly connected to the reflectivity of a semiinfinite bulk medium, which must be less than unity. $\mathrm{Im}\{\eta\}$ can alternate in sign [7,8], signifying an inductive (negative) or capacitive (positive) medium. It was also shown early on for the disk medium [7], and later for other structures [25,26], that one can obtain negative $\mathrm{Im}\{\varepsilon\}$ and/or $\mathrm{Im}\{\mu\}$, something that is not found in natural materials, and further, that the negative behavior of these quantities is multiplexed in frequency. More specifically [7], the disk medium has

$\mathrm{Im}\{\varepsilon\} > 0$, $\mathrm{Im}\{\mu\} < 0$ in the first band gap, $\mathrm{Im}\{\varepsilon\} < 0$, $\mathrm{Im}\{\mu\} > 0$ in the second, etc. The hole medium behaves analogously, as shown in Figure 20.11 where the only first EBG above the plasma frequency is shown.

Questions have been raised about the physical meaning of such results, as they may lead to negative power-loss density, which would be an unphysical result for passive media [13,27,28]. The reader may refer to the extensive documentation in this book [29] for alternatives based on this criticism. In this section, we would like to justify the use of the above effective description and offer a more different outlook than that suggested by the above objections, on how to interpret these effective parameters in the frequency regimes questioned. We consider our approach both physically and mathematically straightforward and, further, useful at all frequencies including the resonant regimes. This outlook was indeed built in [7] where the issue, to the best of our knowledge, appeared first.

Our view is that these effective parameters have to be interpreted as characterizing a slab of the material, and their meaning should not be extrapolated to local densities and point-like, submonolayer scales. To illustrate this view explicitly, imagine a laterally infinite slab of a material or a metamaterial, such as the ones in Figure 20.2, with z the stacking (finite thickness) direction, under monochromatic normal plane-wave incidence. The material or metamaterial can be arbitrarily dispersive, but let us assume that it is described by scalar (effective) parameters, as the issue can be fully discussed within this framework. Let us consider the field density term existing at any point z inside the slab, for "monochromatic" normal incidence [30]:

$$P \equiv 2i\omega\left[w_{\mathrm{e}} - w_{\mathrm{m}}\right] = i\omega\left(\varepsilon_0\varepsilon^*\left|\mathbf{E}\right|^2 - \mu_0\mu\left|\mathbf{H}\right|^2\right)\Big/2, \tag{20.6}$$

where **E**, **H** are the total fields at that point and the star denotes complex conjugation. For single-frequency (time-harmonic) fields, this is the only term that provides dissipation even for a dispersive material [31,32], where derivative terms in the general field density are traditionally included. This dissipation is quantified as the time-average power-loss density inside the material, which is provided by

$$\mathrm{Re}\{P\} = \omega\left(\varepsilon_0\ \mathrm{Im}\{\varepsilon\}\left|\mathbf{E}\right|^2 + \mu_0\ \mathrm{Im}\{\mu\}\left|\mathbf{H}\right|^2\right)\Big/2. \tag{20.7}$$

The objection to having effective parameters for a metamaterial where $\mathrm{Im}\{\varepsilon\} < 0$ or $\mathrm{Im}\{\mu\} < 0$ for a certain frequency ω_0 is related to Equation 20.7. As we scan the interior slab coordinate z, we may (and will) find regions within the slab where the sum of the two terms above, i.e., the total power-loss density, becomes negative. Some researchers may also find that even a single term in the sum of Equation 20.7 being negative is intolerable, as they tend to ascribe a precise magnetic and electric physical meaning to the two loss terms separately. In any case, our argument applies to either objection. Before we discuss this issue, we stress that regarding the effective parameters extracted, in addition to having $\mathrm{Re}\{\eta\} > 0$, we also have $\mathrm{Im}\{n\} > 0$ in the disputed frequency regions, which shows attenuation and therefore a passive medium. However, our discussion applies to the physical interpretation of the field density in Equation 20.7, which involves the total field at any point inside the slab, which is the sum of a left-going and a right-going wave.

Imagine a cylindrical pillbox whose axis is aligned with the z-axis running perpendicularly to the slab interfaces and which terminates exactly on them. Taking the real part of the sourceless time-harmonic Poynting Theorem applied on this pillbox, we get

$$\int_V \mathrm{Re}\{P\}d^3r + \oiint_S \mathrm{Re}\{\mathbf{S}\cdot\mathbf{n}\}\mathrm{d}S = 0, \tag{20.8}$$

where

$\mathbf{S} = \mathbf{E}\times\mathbf{H}^*/2$ is the time-harmonic Poynting vector

$\mathbf{n}$ is the unit pillbox surface outward normal

If we number the incidence region, slab region, and output region by 1, 2, and 3, respectively, we can write the solution of Maxwell's equations in these regions as

$$\mathbf{E}^{(1)} = \hat{\mathbf{x}}\left(E_0 e^{ik_0 z} + E_-^{(1)} e^{-ik_0 z}\right),\ \mathbf{H}^{(1)} = \hat{\mathbf{y}}\frac{1}{\eta_0}\left(E_0 e^{ik_0 z} - E_-^{(1)} e^{-ik_0 z}\right)$$

$$\mathbf{E}^{(2)} = \hat{\mathbf{x}}\left(E_+^{(2)} e^{ink_0 z} + E_-^{(2)} e^{-ink_0 z}\right),\ \mathbf{H}^{(2)} = \hat{\mathbf{y}}\frac{1}{\eta_0\eta}\left(E_+^{(2)} e^{ink_0 z} - E_-^{(2)} e^{-ink_0 z}\right)$$

$$\mathbf{E}^{(3)} = \hat{\mathbf{x}}\left(E_+^{(3)} e^{ik_0 z}\right),\ \mathbf{H}^{(3)} = \hat{\mathbf{y}}\frac{1}{\eta_0}\left(E_+^{(3)} e^{ink_0 z}\right), \tag{20.9}$$

where

$\{n, \eta\}$ are the (effective) dispersive complex refractive index and relative wave impedance, respectively

$E_0,\ E_\pm^{(j)}$ are constant complex amplitudes

The Poynting vector is along $\hat{\mathbf{z}}$ everywhere, and the fields only have z-variation; hence, Equation 20.8 becomes

$$\int_0^d \mathrm{Re}\{P\}\mathrm{d}z + \left(\mathrm{Re}\{\mathbf{S}\cdot\mathbf{n}\}\big|_{z=d} + \mathrm{Re}\{\mathbf{S}\cdot\mathbf{n}\}\big|_{z=0}\right) = 0. \tag{20.10}$$

We can consider the two pillbox faces that sit on the two interfaces as having the fields of regions 1 and 3. Even if we considered the two faces as having the limiting values of the fields of region 2, continuity of the fields at those two interfaces, which follow from the boundary conditions of Maxwell's equations, would guarantee the above fact. Therefore,

$$\mathbf{S}\big|_{z=d} = \frac{1}{2}\hat{\mathbf{x}}E_+^{(3)} e^{ik_0 d} \times \hat{\mathbf{y}}\frac{1}{\eta_0}E_+^{(3)^*}\left(e^{ik_0 d}\right)^* = \frac{1}{2\eta_0}\hat{\mathbf{z}}\left|E_+^{(3)}\right|^2 \tag{20.11}$$

$$\mathbf{S}\big|_{z=0} = \frac{1}{2}\hat{\mathbf{x}}\left(E_0 + E_-^{(1)}\right) \times \hat{\mathbf{y}}\frac{1}{\eta_0}\left(E_0 - E_-^{(1)}\right)^* = \frac{1}{2\eta_0}\hat{\mathbf{z}}\left[|E_0|^2 - \left|E_-^{(1)}\right|^2 - 2i\mathrm{Im}\left\{E_0 E_-^{(1)^*}\right\}\right]. \tag{20.12}$$

Now, by definition of the complex reflection and transmission coefficients *for the whole slab*, we have

$$E_-^{(1)} \equiv S_{11}E_0, \quad E_+^{(3)} \equiv S_{21}E_0 \tag{20.13}$$

and Equations 20.11 and 20.12 become

$$\mathbf{S}\big|_{z=L} = \frac{1}{2\eta_0}\hat{\mathbf{z}}\,|E_0|^2\,|S_{21}|^2, \quad \mathbf{S}\big|_{z=0} = \frac{1}{2\eta_0}\hat{\mathbf{z}}\,|E_0|^2\left(1 - |S_{11}|^2 + 2i\mathrm{Im}\{S_{11}\}\right). \tag{20.14}$$

Therefore, Equation 20.10 is equivalent to

$$\int_0^d \mathrm{Re}\{P\}\,\mathrm{d}z = \frac{|E_0|^2}{2\eta_0}\left(1 - |S_{11}|^2 - |S_{21}|^2\right). \tag{20.15}$$

According to Equation 20.15, no matter what the individual signs of $\mathrm{Im}\{\varepsilon\}$, $\mathrm{Im}\{\mu\}$ and therefore $\mathrm{Re}\{P\}$ are the integral of $\mathrm{Re}\{P\}$ throughout the whole slab thickness and will always have the sign of the dimensionless normalized quantity $\overline{PL} \equiv 1 - |S_{11}|^2 - |S_{21}|^2$. Hence, an average power-loss density (in this one-dimensional case per unit thickness) defined through this total integrated point-like power loss (by dividing by the total slab thickness) would be both the following: A meaningful effective characterization of the loss of the slab and *also* would be positive definite, provided $\overline{PL} > 0$.

Equation 20.15 stands to reason since the quantity $\overline{PL} = 1 - |S_{11}|^2 - |S_{21}|^2$ would be exactly the percentage power loss deriving from energy conservation, for any slab of passive material, when the slab is viewed macroscopically and quite independently of any effective characterization. We think that the above statement is quite uncontroversial, since it is hard to imagine anyone disagreeing with the statement that the total slab loss (in this configuration) is what is missing from the total reflectivity and transmittivity collected outside the slab, independently of any slab details or any theory attempting to characterize it (the slab can be considered a black box, i.e., an unknown passive two-port network). Any correct measurement or calculation of $\overline{PL}$ for a slab of passive composite medium of any thickness should produce a positive result.

Focusing on the effective description of passive photonic crystals, we have summarized here, for example, for the hole medium in Figures 20.10 and 20.11, the average power loss for a slab of an arbitrary number N of monolayers, defined through the integral (Equation 20.15), which would be positive if the S-parameters given in Equation 20.3 and fed by the effective parameters of that material provide $\overline{PL} > 0 \; \forall N$. In all the instances we have examined, this turned out to be the case. We remind the reader that according to our consistency criterion, the effective parameters will be extracted just once, for a slab of a fixed number N_0 of monolayers, whereas $\overline{PL} > 0$ has to follow for *any arbitrary number of monolayers.* Therefore, the procedure is not cyclical. We illustrate this in Figure 20.13, where we plot $\overline{PL}$ for a slab of 1 monolayer (thick black), 3 monolayers (gray), and 10 monolayers (thin black), using effective parameters extracted from 1 monolayer. In Figure 20.13a, the input is obtained analytically from [17], whereas Figure 20.13b contains HFSS inputs. All curves are positive for the whole frequency range; hence, the corresponding effective parameters do not lead to unphysical power loss, if that quantity is interpreted in an average sense over the bulk of the whole metamaterial slab. For completeness, let us compare directly a 10-monolayer HFSS simulation to the corresponding analytical methods of [7,15,18]. This comparison, shown in Figure 20.14, has nothing to do with the effective description; it simply examines the analytical approach. We see that the agreement is excellent, as alluded to in Section 20.5.

Let us compare the above approach to one that belongs to the objecting literature and is often quoted, for example, [12]. The authors of [12] impose the condition that $\mathrm{Im}\{\varepsilon\} > 0$, $\mathrm{Im}\{\mu\} > 0$ as a constraint to their extraction of effective parameters. This results in their inability to obtain effective parameters for a resonant metamaterial (the SRR material) wherever this condition is not satisfied, which they term as the "resonant" region. Such an approach clearly does not have analytic effective parameters that could be used to predict the reflectivity and transmittivity spectrum of a slab for all

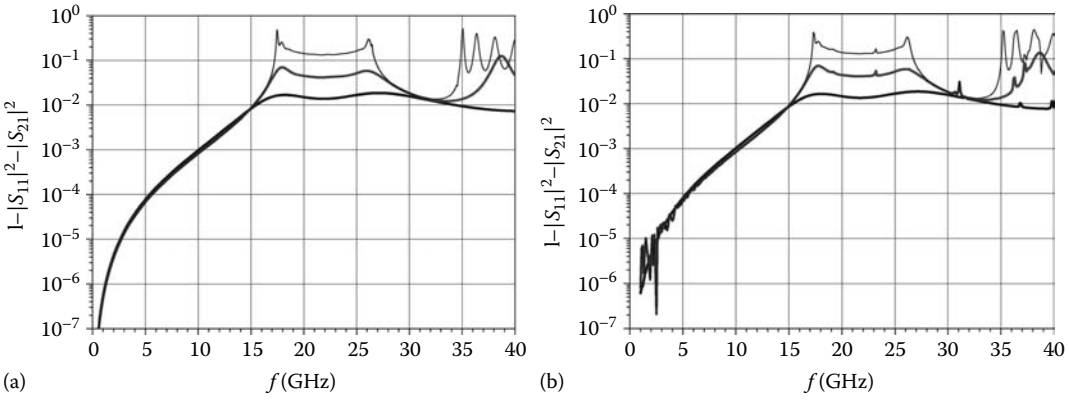

FIGURE 20.13 Power loss for a hole medium slab containing various numbers of monolayers, with effective parameters extracted from one-monolayer S-parameter inputs.

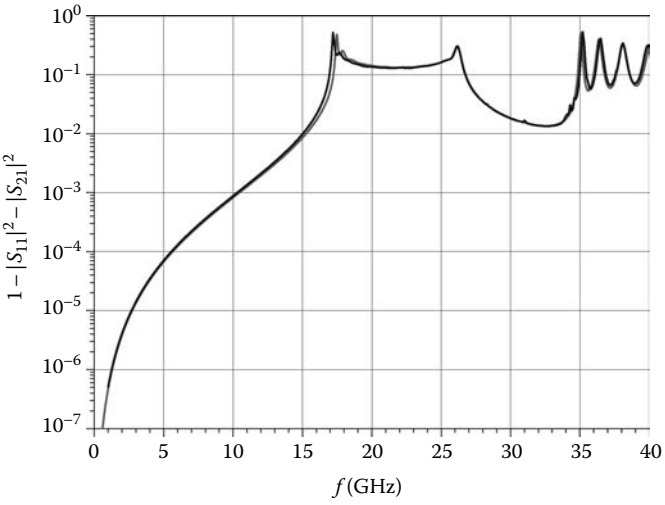

FIGURE 20.14 Power loss for a 10-monolayer hole medium slab calculated monolithically: HFSS (black) versus analytical (gray) calculations.

frequencies, including band edges and band gaps, since it explicitly excludes the "resonant" regions. For photonic crystals, it is precisely near the band edges and inside the band gaps that one would be interested in having an effective description. Further, if one has a resonant metamaterial that does not exhibit the negativities objected to, the authors would presumably claim their approach valid. How is the latter resonance fundamentally different from the former "resonance," except for the tautological feature of having the good signs and therefore being acceptable?

In the end, accepting or rejecting an effective description such as the one we presented in Section 20.5 depends on the decision to either interpret it microscopically beyond the validity scale this description intended (i.e., to demand a positive definite point-like loss density, Equation 20.7) or not. In the latter case, the macroscopic result of Equation 20.15 restores a valid physical interpretation within the length scales intended in the first place. However, we believe the resonant effective description we summarized here has some additional distinct advantages. It still provides on average useful physical interpretation of properties of arrayed materials that can create valid theoretical intuition, including effective resonant magnetization, without preconditioning which resonances are "appropriate." Are there any additional practical advantages? The answer is that it can predict the whole reflection and transmission spectrum, i.e., the macroscopically relevant observable quantities for a metamaterial composed of an arbitrary number of monolayers. It is also interesting to notice that the extraction of effective parameters from these observable quantities imposes the following hierarchy: The wave impedance and refractive index are directly extracted from the observed S-parameters. In this sense, these should be considered as the fundamental effective parameters as opposed to ε and μ, which are derived at a secondary level from η and n.

Let us demonstrate explicitly this predictive power, with an example we hope the reader will find entertaining: Let us assume that there exists a scientist who is interested in making a photonic crystal using the hole medium, Figure 20.2b, but has no idea where the first EBG is or how to design the monolayer in order to have an EBG tuned to the frequency band one desires. Let us also assume one cannot afford many expensive and time-consuming prototypes involving many stacked monolayers and sensitive corresponding measurements (a situation not impossible to imagine) but instead

a single monolayer, in order to decide on the final design. Finally, the scientist cannot afford a good expensive computer.* The scientist can proceed as follows:

1. Take one monolayer, for example, from Figure 20.2b.
2. Simulate on an inexpensive computer or measure a prototype of this single monolayer. Note that, because there is only one monolayer, the *S*-parameters (obtained numerically, analytically, or by direct measurements) do not by inspection provide any clue of whether there exists a band gap; see Figure 20.15a. This is unlike Figure 20.6a for three monolayers, where the band gap has already formed around 30–35 GHz, but even then it is not clear where the band edges are.
3. Extract the effective $n(\omega)$ using the approach presented here, for one monolayer. The scientist will obtain Figure 20.10b. By immediate inspection of $\mathrm{Im}\{n(\omega)\}$ he/she will

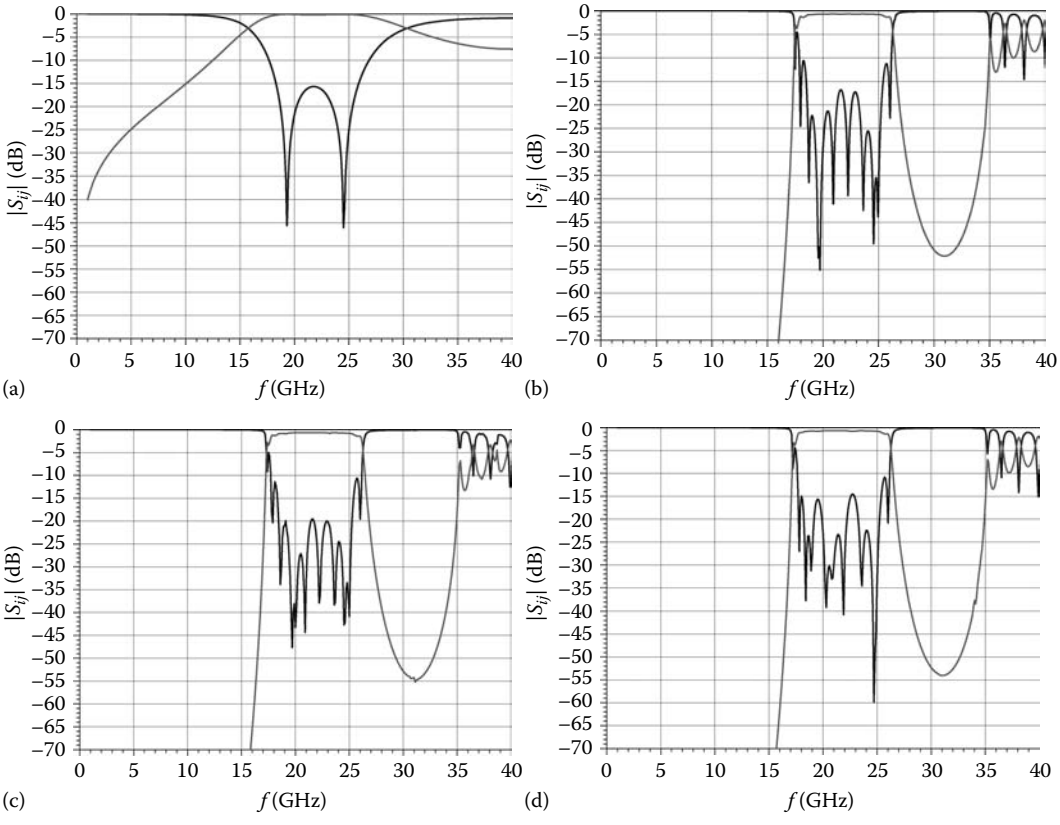

FIGURE 20.15 (a) HFSS *S*-parameters for a one-monolayer hole medium slab; (b) *S*-parameters for a 10-monolayer slab obtained from the homogeneous formulas and the effective parameters extracted from analytical one-monolayer *S*-parameters; (c) *S*-parameters for a 10-monolayer slab obtained from the homogeneous formulas and the effective parameters extracted from HFSS 1-monolayer *S*-parameters, Figure 20.15a; and (d) HFSS simulation results for a 10-monolayer slab.

*Regarding full-wave simulators, this is not simply a joke but hinges on numerical convergence issues.

notice not only that there is a band gap but also its precise band edges, located at 26.5 and 34.5 GHz, respectively. Now the scientist knows that stacking several monolayers will always prohibit transmission in that band. Note that even if one could obtain results for three monolayers, without the effective description but based only on Figure 20.6a, one might consider the band gap to be more broadband, extending up to 38 GHz. Can one produce a precise prediction of the *S*-parameters for any number of monolayers?

4. Take Equation 20.3, insert the extracted $\{\eta(\omega), n(\omega)\}$ for one monolayer ($d = c$ in Equation 20.5) and use a total slab thickness $d_{\text{slab}} = Nc$ with N an arbitrary number of monolayers. Now, the scientist can predict the spectra and performance of the corresponding designs for any number of stacked monolayers by writing a simple script.

We demonstrate this procedure in Figure 20.15b, where a 10-monolayer spectrum has been produced, using, in step 2, analytical one-monolayer *S*-parameter inputs (4000 points). The EBG band and band edges are now clearly formed and are found exactly as predicted by Figure 20.10b. In Figure 20.15c, we reproduce the same 10-monolayer spectrum using, in step 2, HFSS one-monolayer *S*-parameter inputs (391 points). The agreement between the results of Figure 20.15b and c is quite excellent. The predictive power of the procedure is apparent by the excellent agreement between Figure 20.15b, c and d, which depicts the results of a direct HFSS simulation for the 10-monolayer material. Notice also that this simulation is computationally very intensive, requiring 41,000 tetrahedra for a convergence better than 5×10^{-3}, 620 Mb of memory, and a CPU time of 15 h on a Pentium IV processor. For comparison, the computational requirements for generating the results of Figure 20.15a for the one monolayer were 4800 tetrahedra, 85 Mb of memory, and 50 min of CPU time.

20.7 Conclusions

We have summarized the features and functionalities of a new category of composite electromagnetic materials according to their ability to change the value of their reflection coefficient at the same frequency by electronically reconfiguring the interconnection of the conducting implants within them. We have shown how this can be designed in practice and provided physical realizations of materials exhibiting transitions of the reflection coefficient among two and three states and have shown the corresponding electrical functionality of such systems, in a variety of frequencies. Many more designs and functions are possible. We have further extracted their effective parameters through a resonant inverse scattering formalism and have presented a macroscopic physical meaning of the various ranges of values of these parameters as they relate to the total material power loss.

References

1. N.G. Alexopoulos, G.A. Tadler, and F.W. Schott, Scattering from an elliptic cylinder loaded with active or passive continuously variable surface impedance, *IEEE Trans. Antennas Propag.*, 22, 132–134 (1974).
2. N.G. Alexopoulos, P.L.E. Uslenghi, and G.A. Tadler, Antenna beam scanning by active impedance loading, *IEEE Trans. Antennas Propag.*, 22, 722–723 (1974).
3. T.B.A. Senior and J.L. Volakis, *Approximate Boundary Conditions in Electromagnetics*, *IEE Electromagnetic Waves Series 41*, IEE Publications, London, 1995.
4. N.G. Alexopoulos and P.B. Katehi, *On the Theory of Active Surfaces*, J.D. Damaskos, Inc. Report, Philadelphia, PA, 1980.
5. C.A. Kyriazidou, H.F. Contopanagos, and N.G. Alexopoulos, Metamorphic materials: Bulk electromagnetic transitions realized in electronically reconfigurable composite media, *J. Opt. Soc. Am. A*, 23(11), 2961–2968 (2006).

6. Y. Liu and N.G. Alexopoulos, Negative index of refraction: A subclass of electromagnetically metamorphic materials, *Appl. Phys. Lett*., 89, 144109 (2006).
7. H.F. Contopanagos, C.A. Kyriazidou, W.M. Merrill, and N.G. Alexopoulos, Effective response functions for photonic band gap materials, *J. Opt. Soc. Am*., 16(7), 1682–1699 (1999).
8. C.A. Kyriazidou, H.F. Contopanagos, W.M. Merrill, and N.G. Alexopoulos, Artificial versus natural crystals: Effective wave impedance for printed photonic bandgap materials, *IEEE Trans. Antennas Propag*., 48(1), 95–106 (2000).
9. D.R. Smith, S. Schultz, P. Marcos, and C.M. Soukoulis, Determination of effective permittivity and permeability of metamaterials from reflection and transmission coefficients, *Phys. Rev., B* 65, 195104 (2002).
10. S. O'Brien and J.B. Pendry, Magnetic activity at infrared frequencies in structured metallic photonic crystals, *J. Phys.: Condens. Matter*, 14, 6383–6394 (2002).
11. R.W. Ziolkowski, Design, fabrication and testing of double negative metamaterials, *IEEE Trans. Antennas Propag.*, 51, 1516–1529 (2003).
12. X. Chen, T.M. Grzegorczyk, B.I. Wu, J. Pacheco, and J.A. Kong, Robust method to retrieve the constitutive effective parameters of metamaterials, *Phys. Rev. E*, 70, 016608 (2004).
13. D.R. Smith, D.C. Vier, Th. Koschny, and C.M. Soukoulis, Electromagnetic parameter retrieval from inhomogeneous materials, *Phys. Rev. E*, 71, 036617 (2005).
14. N.G. Alexopoulos, C.A. Kyriazidou, and H.F. Contopanagos, Effective parameters for metamorphic materials and metamaterials through a resonant inverse scattering approach, *IEEE Trans. Microw. Theory Tech*., 55(2), 254–267 (2007).
15. C.A. Kyriazidou, H.F. Contopanagos, and N.G. Alexopoulos, Monolithic waveguide filters using printed photonic band gap materials, *IEEE Trans. Microw. Theory Tech.*, 49(2), 297–307 (2001).
16. W.B. Weir, Automatic measurement of complex dielectric constant and permeability at microwave frequencies, *Proc. IEEE*, 62(1), 33–36 (1974).
17. C.A. Kyriazidou, H.F. Contopanagos, and N.G. Alexopoulos, Effective description and power balance of metamaterials, *ACES 2007 Conference Proceedings*, Verona, Italy, March 19–23, 2007, pp. 260–264.
18. H.G. Booker, Slot aerials and their relation to complementary wire aerials, *J. IEE*, 93, 620–626 (1946).
19. T.W. Ebbesen, H.J. Lezec, H.F. Ghaemi, T. Thiot, and P.A. Wolff, Extraordinary optical transmission through subwavelength hole arrays, *Nature*, 391, 667–669 (1998).
20. L. Martin-Moreno, F.J. Garcia-Vidal, H.J. Lezec, K.M. Pellerin, T. Thio, J.B. Pendry, and T.W. Ebbesen, Theory of extraordinary optical transmission through subwavelength hole arrays, *Phys. Rev. Lett*., 86, 1114–1117 (2001).
21. W.L. Barnes, A. Dereux, and T.W. Ebbesen, Surface plasmon subwavelegth optics, *Nature*, 424, 824–830 (2003).
22. J.B. Pendry, L. Martin-Moreno, and F.J. Garcia Vidal, Mimicking surface plasmons with structured surfaces, *Science*, 305, 847–848 (2004).
23. P. Hibbins, B.R. Evans, and J.R. Sambles, Experimental verification of designer surface plasmons, *Science*, 308, 670–772 (2005).
24. J.B. Pendry, A.J. Holden, D.J. Robbins, and W.J. Stewart, Magnetism from conductors and enhanced nonlinear phenomena, *IEEE Trans. Microw. Theory Tech.*, 47(11), 2075–2084 (1999).
25. S. O'Brien and J.B. Pendry, Photonic band-gap effects and magnetic activity in dielectric composites, *J. Phys.: Condens. Matter*, 14, 4035 (2002).
26. T. Koschny, P. Marcos, D.R. Smith, and C. Soukoulis, Resonant and antiresonant frequency dependence of the effective parameters of metamaterials, *Phys. Rev. E*, 68, 065602(R), (2003).
27. A.L. Efros, Comments II on "Resonant and antiresonant frequency dependence of the effective parameters of metamaterials", *Phys. Rev. E*, 70, 048602 (2004).
28. R.A. Depine and A. Lakhtakia, Comments I on "Resonant and antiresonant frequency dependence of the effective parameters of metamaterials", *Phys. Rev., E* 70, 048601 (2004).

29. C. Simovski and S. Tretyakov, Material parameters and field energy in reciprocal composite media, *Theory and Phenomena of Metamaterials*, Part I, Taylor & Francis, Boca Raton, FL, 2008.
30. J.D. Jackson, *Classical Electrodynamics*, John Wiley & Sons, New York, 1975.
31. L.D. Landau and E.M. Lifshitz, *Electrodynamics of Continuous Media*, Section 61, Pergamon Press, Oxford, 1st edn., 1960, 2nd edn., 1984.
32. A.D. Yaghjian, Internal energy, Q-energy, Poynting's Theorem and the stress dyadic in dispersive material, *IEEE Trans. Antennas Propag.*, 55(6), 1495–1505 (2007).

21

Isotropic Double-Negative Materials

Irina Vendik
St. Petersburg Electrotechnical University

Orest G. Vendik
St. Petersburg Electrotechnical University

Mikhail Odit
St. Petersburg Electrotechnical University

21.1 Introduction

Media with single-negative (SNG) permittivity or SNG permeability and simultaneously negative permittivity and permeability, which is called double-negative (DNG) media, are under relentless interest of physicists and microwave engineers [1–12]. These artificial materials are known as metamaterials. It has been shown that application of SNG materials can sufficiently improve the characteristics of many microwave devices. However, more interesting properties can be realized using DNG structures. In a limited frequency band, such materials exhibit anomalous properties: lensing beyond the diffraction limit, wave propagation in subwavelength guiding structures, resonant enhancement of the power radiated by electrically small antennas, etc.

Most theoretical and practical investigations in this area are related to one-dimensional (1D) or two-dimensional (2D) structures. The well-known metamaterial structure suggested in [5] and experimentally examined in [6] is a combination of two lattices: a lattice of split-ring resonators (SRRs) and a lattice of infinitely long parallel wires. The wires produce the effective negative permittivity, and the SRRs are responsible for the effective negative permeability. A combination of SRRs and metal wires provides an artificial material with simultaneously negative effective permeability and permittivity [5,6,12]. This structure is anisotropic and reveals the negative permittivity and permeability, if the propagation direction of the electromagnetic wave is orthogonal to the axes of the wires and belongs to the plane of the SRRs. The unusual electromagnetic properties originate from these artificial structures rather than arising directly from the materials. It is interesting and useful for practical applications to realize a DNG medium using the intrinsic electromagnetic properties of artificial inclusions forming the material. In many cases, isotropic DNG structures are very attractive for practical uses. For this purpose, structures with embedded three-dimensional (3D) resonant inclusions are very promising.

Different ways to create a 2D and 3D isotropic DNG medium based on a regular lattice of resonant inclusions are discussed in this chapter: (a) SNG or DNG metamaterial formed as a rectangular lattice of cubic unit cells of plane resonant particles on the faces of the cube; (b) a 2D DNG medium formed as an array of dielectric cylindrical resonators; and (c) a 3D DNG medium formed as a regular lattice of spherical resonant inclusions.

The characteristic feature of the structures considered is the isotropy of the effective permittivity and permeability. In the case of the cubic symmetry pertaining to the class $m3m$, the second rank tensors of electromagnetic parameters of the media are diagonal [13,14]. Thus, the permittivity and permeability tensors of particles arranged in the cubic structure are scalars, ε_{eff} and μ_{eff}. Body-centered and face-centered structures are characterized by the same forms of the second-order tensor as the simple cubic structure. Hence, the 3D isotropic metamaterial can be realized as artificial structures designed in form of a regular array of particles. The symmetry class of the unit cells arranged in the periodical structure provides the isotropy of the metamaterial.

In this chapter, we discuss isotropic 2D and 3D metamaterials, which differ in the properties of the constitutive resonant particles. The following isotropic structures are under consideration:

1. SNG and DNG metamaterial formed by a rectangular/random lattice of isotropic cubic unit cells of particles: SRRs, Ω-particles, and a combination of the SRRs and wire/dipole particles
2. 3D DNG metamaterial based on transmission lines (TL)
3. 2D DNG medium formed by an array of dielectric resonators (DRs), providing excitation of the electric and magnetic dipoles
4. 3D DNG medium formed by a regular lattice of spherical resonant inclusions, providing excitation of the electric and magnetic dipoles

21.2 Two-Dimensional and Three-Dimensional Isotropic Metamaterials Formed by an Array of Cubic Cells with Metallic Planar Inclusions

The first 3D SNG magnetic structure with high isotropy was described in [15]. An array of single cells composed of two intersecting SRRs normal to each other is suggested to demonstrate isotropic metamaterial. The single cell is formed by crossed SRRs (CSRRs). Each SRR is made of two aluminum (Al) strips deposited on the inner and outer faces of the foam ring made from the dielectric with low permittivity. The dielectric foam has a form of strip of 4 mm width; the inner radius is 15 mm and

the outer radius is 20 mm, and the separation between the inner and outer Al strips is $t = 5$ mm. It is machined from a foam plate to obtain two open rings that are then fitted into each other. The 4 mm wide Al strips are cut from the 50 mm thick self-adhesive Al foil. The gaps at the extremities of the two CSRRs are located at the same pole of the spherical structure. The width of these gaps is 6 mm. Rotating the CSRR in the waveguide around its z-axis does not affect the transmission coefficient S_{21} measured. The structure is isotropic in the plane perpendicular to the z-axis. A possibility to obtain a material with effective isotropic magnetic properties by building up an array of CSRRs with periodic or random orientations was experimentally confirmed.

The idea of using cubic cells with planar metallic inclusions on the cube faces is very promising. Each unit cell is formed by printing perfectly conducting plane resonant particles on the faces of a cubic unit cell: SRRs [16], Ω-particles [17], spider dipoles [18], and a combination of SRRs and dipoles [19].

The symmetric SRR was suggested to be used as part of 3D isotropic structure, which can be considered as an isotropic μ-negative material (Figure 21.1a) [16]. The single cell is made of six planar SRRs exhibiting 90° rotational symmetry, placed on the faces of the cube so that the whole particle is invariant with respect to 90° rotations around all Cartesian axes. The unit cell provides a distinct magnetic SNG response. The isotropy is experimentally confirmed by the measurement of the transmission coefficient of the waveguide loaded with one 3D particle in different orientations. The experimental investigation confirmed the isotropy of the μ-negative material (Figure 21.2a) [17,19–21].

The same symmetry exhibits the cubic structure based on spider dipoles (Figure 21.1b) providing an ε-negative response. A periodical spatial arrangement of the cells forms the bulk of the isotropic magnetic or electric metamaterials. The negative permeability/permittivity of the single magnetic/electric particle placed in a rectangular waveguide was extracted from the measured scattering parameters. The 3D regular arrangement of the cubic particles is a sophisticated technological problem. The concept of randomly distributed magnetic particles was therefore checked first on 2D and then on 3D structures [19]. The experiments demonstrated that better isotropy and a wider frequency band of the metamaterial can be achieved by a quasiperiodical location and a higher density of the particles [20].

The electrical dipole loaded by a loop inductance (inset in Figure 21.2c) was suggested to provide effective negative permittivity of the media. The isotropy of one 3D cubic unit cell with a single dipole is documented by its measured transmission coefficient (Figure 21.2c). Experiments with random distributions of these particles also exhibited promising results. Measured transmission coefficients of 147 particles inserted in the polystyrene slices consecutively rotated by 90° provided very good isotropy of the cubic sample, as follows from the small dispersion shown in Figure 21.2d.

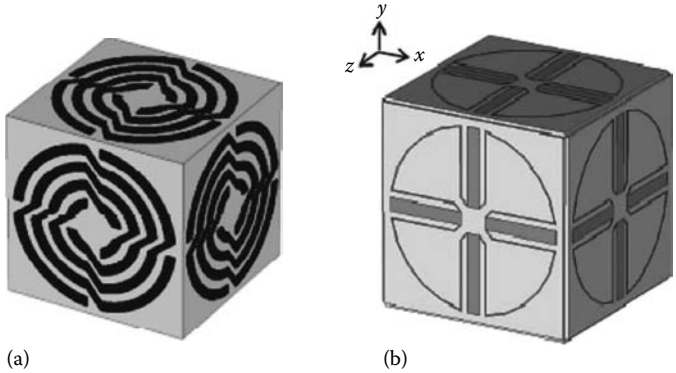

FIGURE 21.1 (a) Volumetric μ-negative particles composed of C4-SRRs and (b) volumetric ε-negative particles composed of C4-dipoles. (Taken from Baena, J.D., Jelinek, L., Marques, R., and Zehentner, J., *Appl. Phys. Lett.*, 88, 134108, 2006. With permission.)

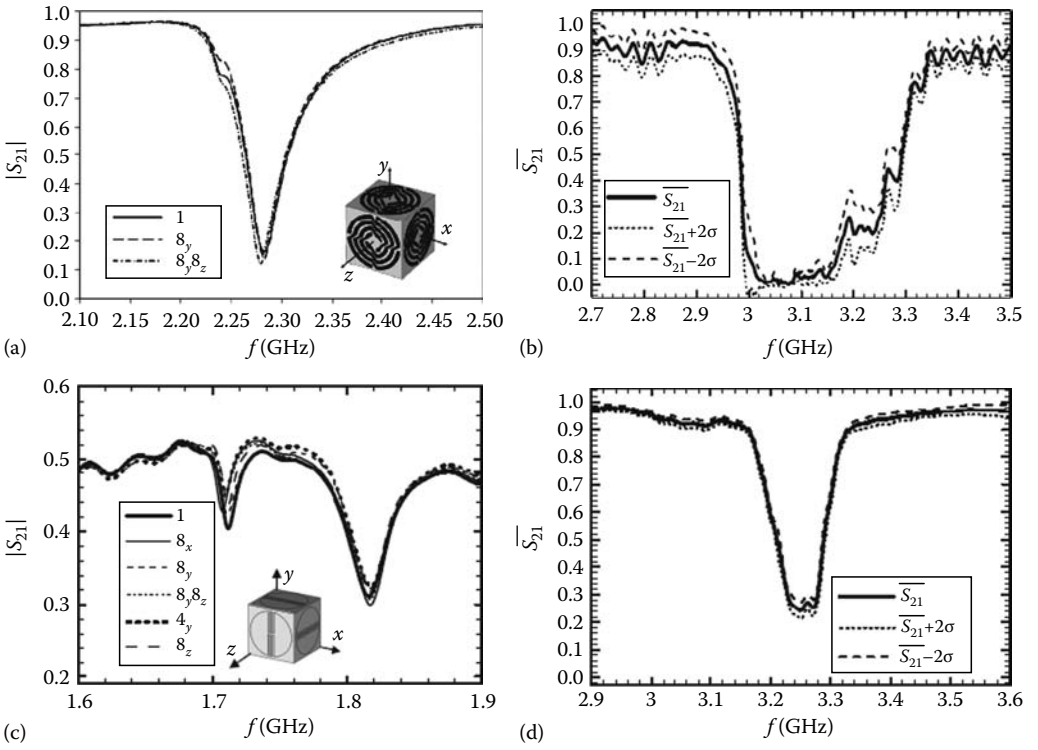

FIGURE 21.2 (a) Transmission through the waveguide loaded by quaternary split spirals; (b) transmission through 64 cubic samples and its dispersion when the resonators are in the nodes of the squared net and are randomly oriented; (c) measured transmission coefficient of one cubic unit cell with the electric dipoles in the parallel plate waveguide for different orientations; and (d) transmission coefficients of 147 periodically distributed and randomly oriented electric SNG particles.

In order to integrate the SRR and wire in one particle, Ω-particles can be introduced [17]. The DNG metamaterial is formed by a rectangular lattice of isotropic cubic unit cells of Ω-particles (Figure 21.3). Each isotropic cubic cell is made by putting six Ω-shaped perfectly conducting particles on the cube faces. A single cubic cell can be described approximately as an isotropic resonant scatterer. The effective permittivity ε_{eff} and permeability μ_{eff} of the media are calculated from electric and magnetic polarizabilities by an analytical model. The dispersion diagram for the cubic lattice of isotropic scatterers shows negative dispersion within a limited frequency range between two stop bands. The frequency range, in which both the effective permittivity and the permeability are negative, corresponds to the mini band of backward waves (BWs) within the resonant band of the individual isotropic scatterer.

The Ω-particles-based, 3D isotropic structure has been investigated experimentally [22]. The electromagnetic properties of 3D homogeneous structures can be described by a set of averaged effective parameters, such as the electric permittivity and the magnetic permeability. The measurements were done in free space, with two dipole antennas, one used as a point source and the other as a probe. The source was placed at a distance less than the thickness of the layer to verify the possible "super" lens properties of the device: the thickness was 40 mm, corresponding to six unit cells across the layer. The transmission coefficient of the structure reveals a narrow pass band between 5.9 and 6.3 GHz, which corresponds to the superlensing effect of the slab (Figure 21.3c).

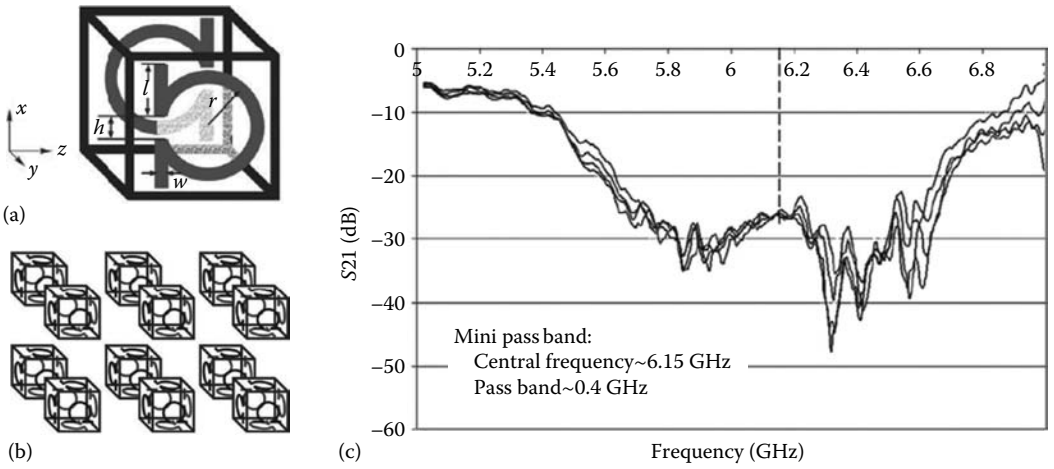

FIGURE 21.3 (a) Geometry of a cubic unit cell of Ω-particles. For graphic clearness, only one pair of Ω-shaped perfectly conducting particles is shown on two opposite faces of the cubic unit cell. (b) A rectangular lattice of isotropic cubic unit cells of Ω-particles. (From Simovski C.R. and He, S., *Phys. Lett. A*, 311, 254, 2003. With permission.) (c) Mini pass band between 5.9 and 6.3 GHz for four different distances of the source. (Taken from Verney, E., Sauviac, B., and Simovski, C.R., *Phys. Lett. A*, 331(3–4), 244, October 2004. With permission.)

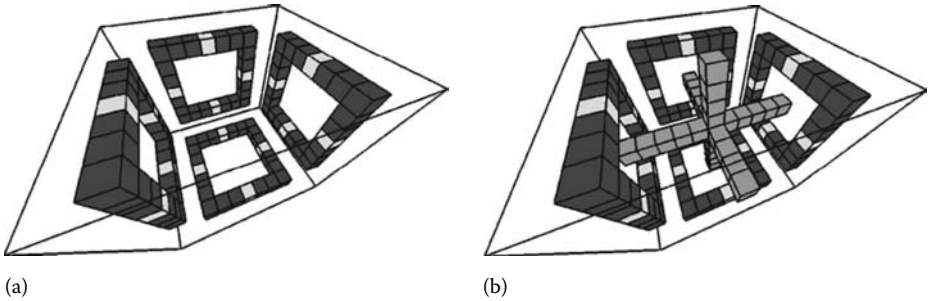

FIGURE 21.4 The design of a fully symmetric unit cell for a one-unit-cell thick slab of an isotropic SRR (a) and a left-handed (b) metamaterial. The interfaces are parallel to the left and right SRRs. (Taken from Koschny, Th., Zhang, L., and Soukoulis, C.M., *Phys. Rev. B*, 71, 121103 (R), 2005. With permission.)

The DNG metamaterial based on the 3D configuration of SRRs and the continuous wires (Figure 21.4) is another 3D isotropic metamaterial [23]. The isotropic unit cell is based on the four-gap SRRs (Figure 21.4a). The SRR gaps are filled with a high permittivity dielectric with a relative permittivity $\varepsilon_{gap} = 300$ to lower the magnetic resonance frequency.

The design of this type of metamaterial minimizes the mutual interaction of SRRs and wires, a coupling of the electric field to the magnetic resonance, and the cross-polarization scattering amplitudes and effects of the periodicity. The transmission and reflection coefficients for a slab of the isotropic SRR and the corresponding isotropic left-handed metamaterial (LHM) of 1- and 10-unit-cell thickness have been calculated. The simulated transmission coefficients for 1 unit cell and a slab of 10 cells have been plotted for different incident angles θ and polarizations φ (Figure 21.5). Despite the square shape of the SRR, the absolute independence of the scattering amplitudes on the orientation φ of

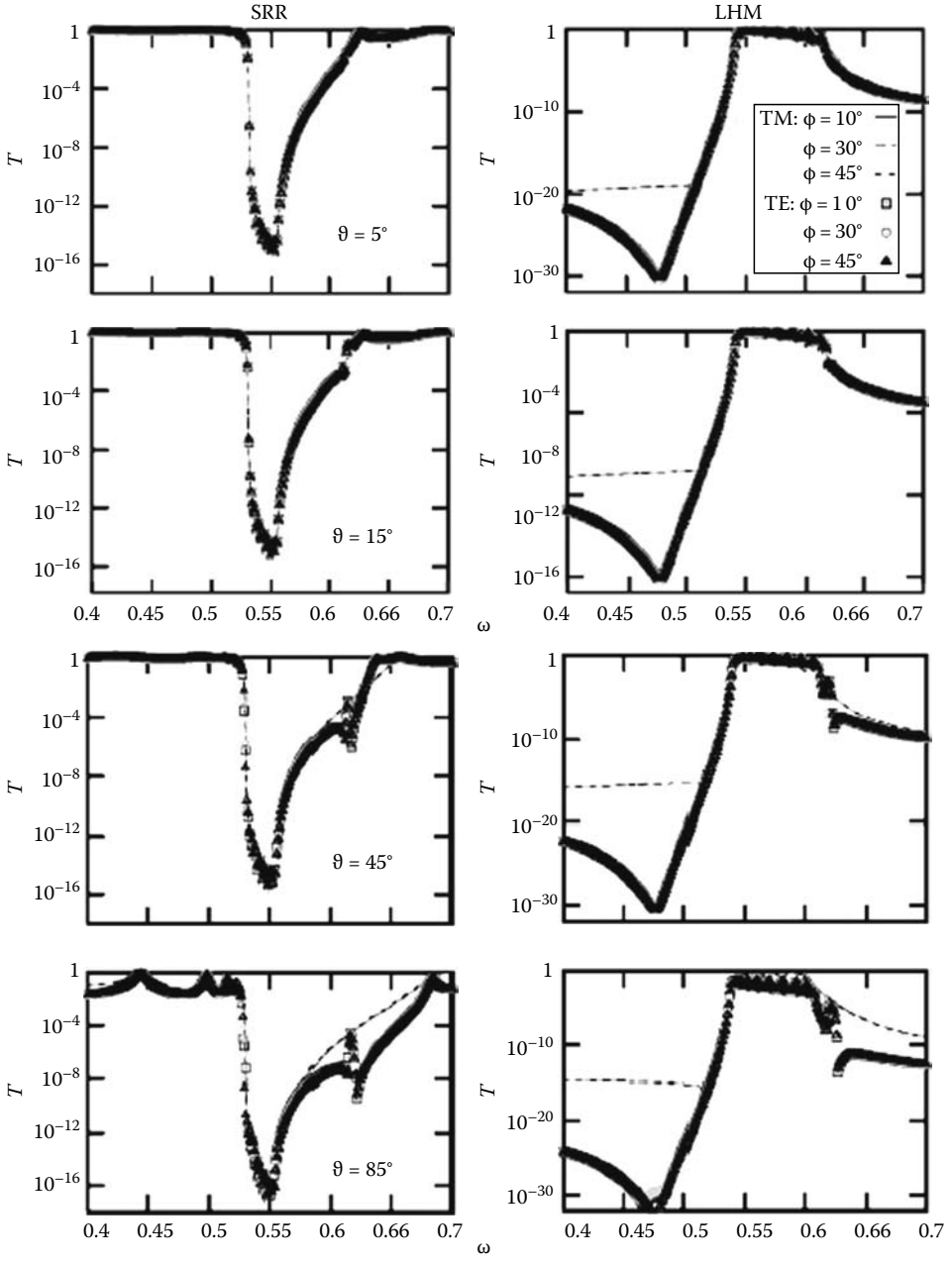

FIGURE 21.5 Transmission spectra $T = |t(\omega)|^2$ for a 10-unit-cell thick slab of the SRR and the LHM metamaterial for various angles of incidence (θ) and polarizations (φ, TE and TM modes). (Taken from Koschny, Th., Zhang, L., and Soukoulis, C.M., *Phys. Rev. B*, 71, 121103 (R), 2005. With permission.)

the incidence plane for both the transverse electric (TE) and transverse magnetic (TM) modes, arbitrary θ, SRR, and LHM metamaterial slabs of any thickness is confirmed. Analysis of the 10-unit-cell thick slab of the SRR and the LHM metamaterial revealed the isotropic behavior.

21.3 TL-Based Metamaterials

Among other kinds, the metamaterials based on TLs are of high interest. The use of loaded TL networks allows the realization of wide-band and low-loss BW materials in the microwave region [24,25]. 3D isotropic, TL-based, BW materials have been proposed in [26–28].

In [28], a rotated TL method (TLM) scheme [29] was used to produce a unit cell of isotropic metamaterial. In the TLM representation of discrete electrodynamics, a 12-port scattering matrix, representing the TLM cell, contains all the information of the discretized Maxwell's equations. The 12-port cell can be decomposed into two independent six-port cells by a coordinate transformation. The two independent half-cell six ports described by scattering matrices S and $-S$ [28] are called "A" and "$\bar{\text{A}}$" cells, respectively. A TLM cell that completely samples the electromagnetic field can be established by either nesting the six-port structures of the A and $\bar{\text{A}}$ half-cells or by a cluster of eight half-cells with alternating A and $\bar{\text{A}}$ cells. The lumped-element circuit for an A cell contains series elements Z and shunt elements Y. An elementary metamaterial cell may be conceived on the basis of rotated TLM cells by inserting reactances in series to the six cell ports and four admittances connecting the series reactances at a central node, forming a virtual ground. Both half-cells can be connected at the virtual ground.

In the general case, the unit cell is composed of composite right-/left-handed (CRLH) TL sections. In a CRLH unit cell, the impedance Z is a series resonator $(L_R,\ C_L)$, whereas Y is a parallel resonator $(L_L,\ C_R)$. The right-handed components account for unavoidable parasitics [1]. The corresponding unit cell for the rotated TLM metamaterial is shown in Figure 21.6a.

The proposed realization of the CRLH rotated TLM metamaterial, corresponding to the lumped-element network of Figure 21.6a, is depicted in Figure 21.6b. Shunt inductors are implemented by wires connected to a common center point, and series capacitors are implemented by metal–insulator–metal (MIM) plates located between the adjacent unit cells. Figure 21.6b shows a cluster of $2 \times 2 \times 2$ nested unit cells. The plate capacitors are realized in printed circuit board (PCB) with patches on both sides of the substrate, which ensures accurate C_L values. The inductors are realized by rigid wires. The unit-cell length is 2 cm, the substrate is Rogers 4350B 10 mil, and the left-handed values are $L_L \approx 17.3$ nH and $C_L \approx 5.4$ pF.

Figure 21.6c shows the unit-cell prototype of the CRLH rotated TLM metamaterial. This prototype was measured with a two-port vector network analyzer through baluns (microstrip to parallel-strip transitions) connected at two arbitrary nonaligned ports, whereas the remaining ports are terminated with the resistors. The dispersion diagram depicted in Figure 21.6d shows a good agreement with circuit simulation results up to 2.2 GHz. The expected two left-handed and two right-handed frequency bands are clearly visible, therefore verifying the behavior of the rotated TLM metamaterial. A simplified planarized implementation, preserving the same network topology, can also be realized for practical applications.

The idea of a superlens based on the TL-metamaterial has been discussed in [30]. The proposed structure of a 3D super-resolution lens consists of two forward-wave (FW) regions and one BW region. The 3D FW networks can be realized with simple TLs and the 3D BW network with inductively and capacitively loaded TLs. One unit cell of the BW network is shown in Figure 21.7 (the unit cell is shown by the dotted line). In the 3D structure, there are impedances $Z/2$ and TLs also along the z-axis (not shown in Figure 21.7). In view of potential generalizations, the loads are represented by series impedances $Z/2$ and shunt admittances Y, although for the particular purpose of realizing a BW network, the loads are simple capacitances and inductances. The unit cell of the FW network

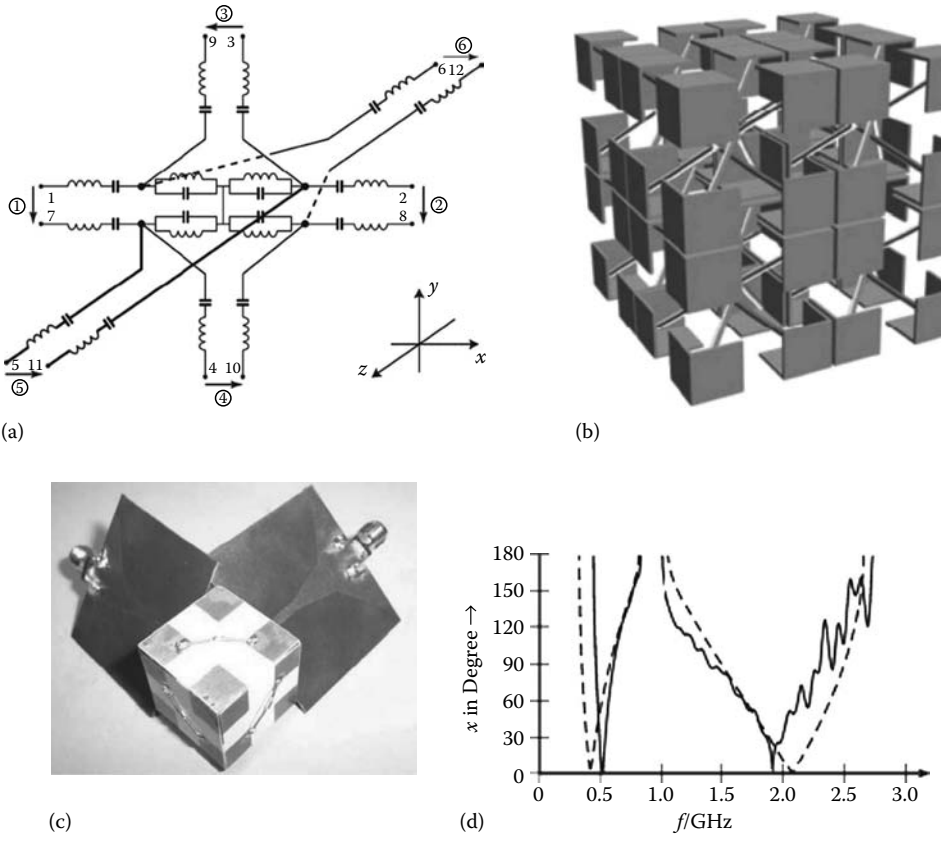

FIGURE 21.6 (a) CRLH rotated, TLM metamaterial, half-unit cell [29]; (b) 3D CRLH rotated, TLM metamaterial realization, complete 2 × 2 × 2 structure; (c) 3D CRLH rotated, TLM unit cell with its input and output baluns required for the differential excitation of the measurement setup; (d) dispersion diagram: measured (solid line) and simulated (dashed line). (Taken from Zedler, M., Caloz, C., and Russer, P., Circuital and experimental demonstration of a 3D isotropic LH metamaterial based on the rotated TLM scheme, *Microwave Symposium, 2007 IEEE/MTT-S International*, Honolulu, HI, June 3–8, 2007, pp. 1827–1830. With permission.)

is the same as in Figure 21.7 but without the series impedances $Z/2$ and shunt admittance Y. In a simplified case, $Z = 1/j\omega C$ and $Y = 1/j\omega L$.

The derived dispersion equations and analytical expressions for the characteristic impedances for waves in the FW and BW regions make it possible to find the condition for a design of such structures. The full-wave simulations revealed the subwavelength resolution characteristics of a realizable design with commercially available lossy materials and components. There is a special problem of impedance and refraction index matching of the FW and BW regions. From the derived dispersion equations, it has been seen that there exists such a frequency at which the corresponding isofrequency surfaces for FW and BW regions coincide. Theoretically, this can provide distortionless focusing of the propagating modes, if the wave impedances of the FW and BW regions are also well matched. Impedance matching becomes even more important when the evanescent modes are taken into account. Theoretically, it was shown that the wave impedances can be matched at least within 1% accuracy or better, if the characteristic impedances of the TLs are properly tuned. However, from a practical point of view, accuracy better than 1% is hardly realizable. It has been shown that decreasing the thickness of the

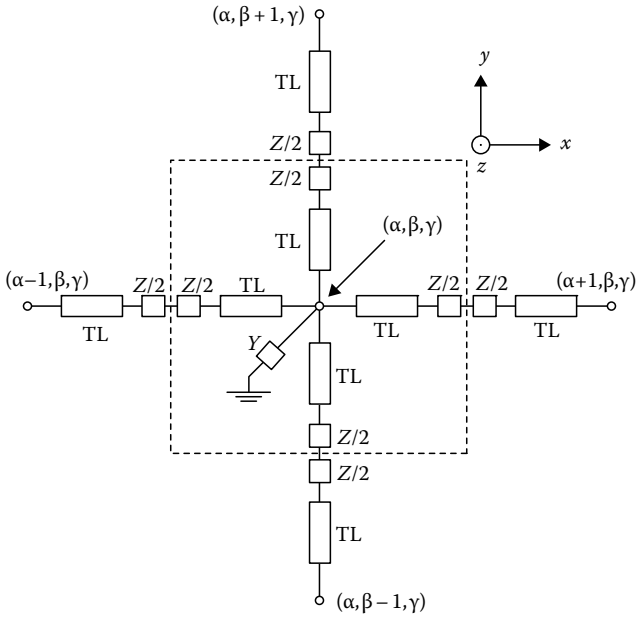

FIGURE 21.7 Unit cell of a 3D BW TL network (enclosed by the dotted line). The TLs and impedances along the z-axis are not shown. TLs have the characteristic impedance Z_0 and the length $d/2$ (d is the period of the structure). (Taken from Alitalo, P., Maslovski, S., and Tretyakov, S., *J. Appl. Phys.*, 99, 064912, 2006. With permission.)

BW region reduces the negative effect of the impedance mismatch, whereas the amplification of the evanescent modes is preserved.

In [31], the design and experimental realization of a 3D superlens based on LC-loaded TLs were presented. A 2D prototype was designed (Figure 21.8a). The structure was excited by a coaxial feed (SMA connectors) connected with the edge of the first FW region, as shown at the bottom of Figure 21.8b. To change the position of the excitation, four SMA connectors were soldered to the structure.

The measured electric field distributions on the top of the structure are shown in Figure 21.9. The maximum values of the amplitude occur at the back edge of the BW region (as expected from the

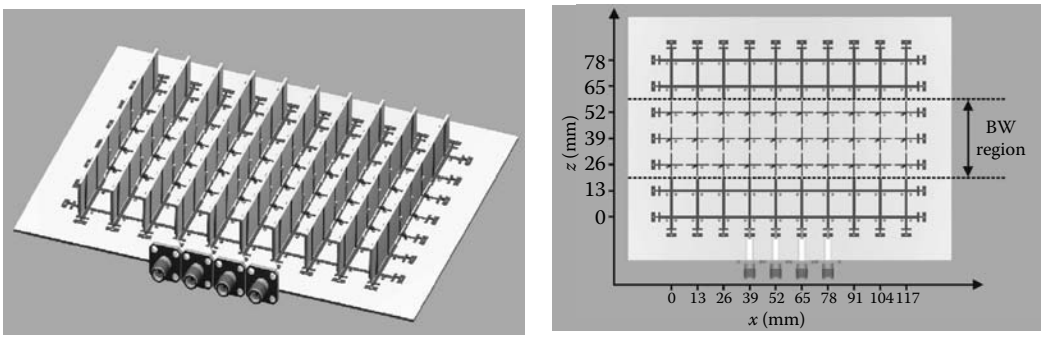

(a) (b)

FIGURE 21.8 (a) 2D prototype of TL-based metamaterial; (b) 3D prototype of TL-based metamaterial. (Taken from Alitalo, P., Maslovski, S., and Tretyakov, S., *J. Appl. Phys.*, 99(12), 2006. With permission.)

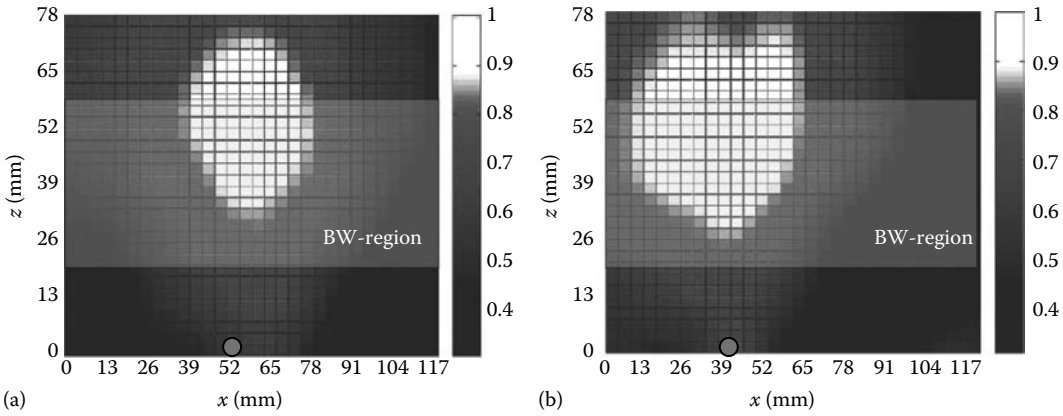

FIGURE 21.9 Measured amplitude of the vertical component of electric field on top of the 2D structure at $f = 900$ MHz. Fields are normalized to the maximum value. (a) Symmetrical excitation by two sources at $x = 52$ mm, $z = -6.5$ mm, and $x = 65$ mm, $z = -6.5$ mm. (b) One source at $x = 39$ mm, $z = -6.5$ mm. (Taken from Alitalo, P., Maslovski, S., and Tretyakov, S., *J. Appl. Phys.*, 99(12), 2006. With permission.)

theory). In Figure 21.9b, the point of excitation is displaced from the middle to show that the effects seen are not caused by reflections from the side edges. It is clear that both propagating and evanescent modes are excited in the structure, because the fields do not reveal a significant decay in the first FW region (evanescent modes decay exponentially). There is a remarkable growth of the amplitude in the BW region, since only evanescent modes can be "amplified" in a passive structure like this. The experiment did not show any noticeable reflections at the FW/BW interfaces, which implies a good impedance matching between the two types of networks.

To realize a 3D structure, a combination of two and three previously observed 2D structures was manufactured. To connect these layers, 10 vertical sublayers of height 12.2 mm were soldered between them. In Figure 21.8b, the geometry of the structure is presented: only 1 bottom horizontal layer and 10 vertical sublayers are shown. The resulting 3D structure is isotropic with respect to the waves propagating inside the TLs. The distance between adjacent horizontal and vertical nodes remains the same, and the vertical microstrip lines are also loaded with capacitors in the BW region.

The experiments with prototypes show BW propagation and amplification of evanescent waves in the TL-based structures.

21.4 Two-Dimensional Structure of DNG Metamaterial Based on Resonant Inclusions

Attempts to create an isotropic metamaterial resulted in the idea of using resonant inclusions as constituent particles arranged in a regular structure [32–36]. A medium composed of a periodic lattice of resonant particles considered as scatterers generates dielectric polarization and magnetization according to the distribution of the scatterers and their polarizabilities. A mixture consisting of an array of scatterers embedded in a host media is an effective medium relative to the propagating wave. When the size of the scatterers is small compared with the wavelength in the host material and is not small in the material of the scatterers, the effective medium parameters become frequency dependent. Within a limited frequency range, electric and/or magnetic polarizabilities of inclusions exhibit a characteristic resonant behavior, and the media yield effective negative permittivity and permeability.

As a 2D isotropic metamaterial, a regular array of dielectric rods is considered. In order to obtain dielectric and magnetic dipoles, one has to excite electric and magnetic resonances into the DRs [32]. The 2D isotropic DNG material consists of an array of dielectric rods with different radii, so that two different types of resonances lead to the DNG response of the medium. The magnetic resonance is excited in the roads of smaller diameter, which behave as magnetic dipoles. The electric resonance is excited in the roads of larger diameter, which behave as electric dipoles. The simplified structure of the regular array of the DRs placed between the perfect magnetic walls (PMW) and the perfect electric walls (PEW) is shown in Figure 21.10a. The dispersion diagram has been calculated by analytical full-wave simulation (Figure 21.10c). The negative slope of the dispersion characteristic demonstrates the DNG properties of the designed medium. The transmission coefficient of the structure (Figure 21.10b) reveals a pass band in a limited frequency range conditioned by the resonant characteristics of the two cylindrical resonators.

Dielectric cylinders can also be placed in a cutoff parallel plate waveguide [33]. In this case, the collective macroscopic behavior of the DR lattice under TE resonance gives negative effective permeability, whereas the parallel plate waveguide below the cutoff frequency for the fundamental TE modes shows negative effective permittivity, which leads to the left-handedness. The 2D triangular prism of the proposed left-handed waveguide that is sandwiched by the right-handed parallel plate waveguides provides the numerical and experimental demonstrations of the negative refraction for the propagated waves. Dispersion diagrams obtained show the 2D isotropic and left-handed propagation characteristics of the proposed structure.

Resonance phenomena in metamaterials constructed as an array of dielectric rods are studied in [34] by means of numerical modeling using the finite-difference time-domain (FDTD) method.

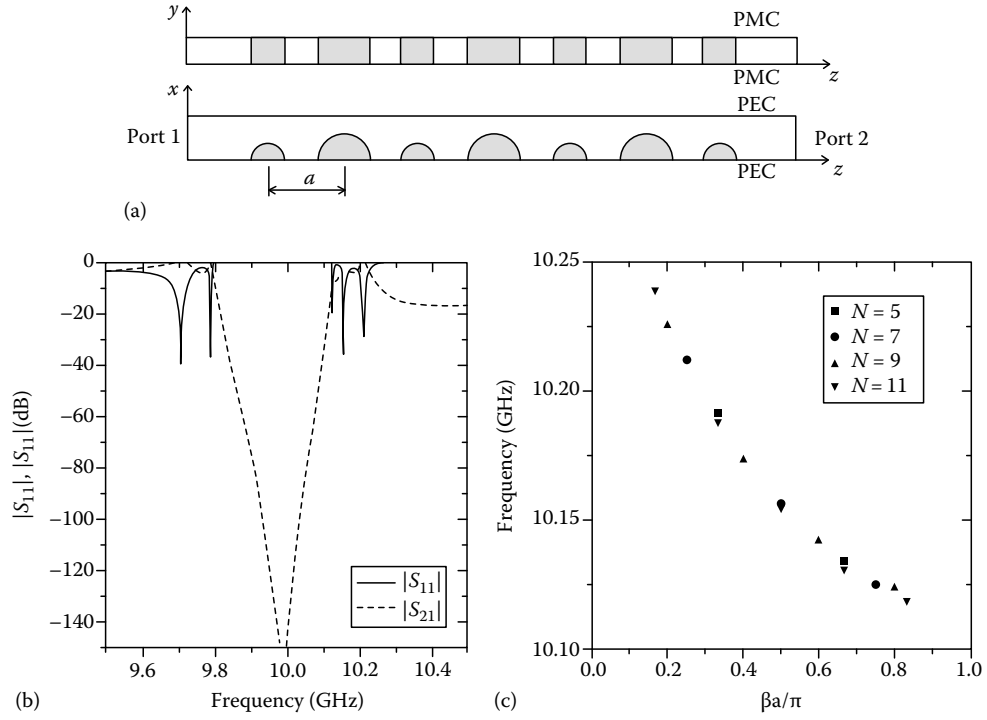

FIGURE 21.10 (a) Cross-section of simulation domain. (b) Numerically calculated S-parameters of a lattice of cylinders $[\varepsilon_p = 44(1 - j1.25 \times 10^{-4})$, $\varepsilon_h = 1$, $a_1 = 2.71\,\text{mm}$, $a_2 = 1.73\,\text{mm}$, lattice constant $s = 15\,\text{mm}]$. (c) Dispersion curves for a lattice of cylinders calculated for different numbers of cylinders (N).

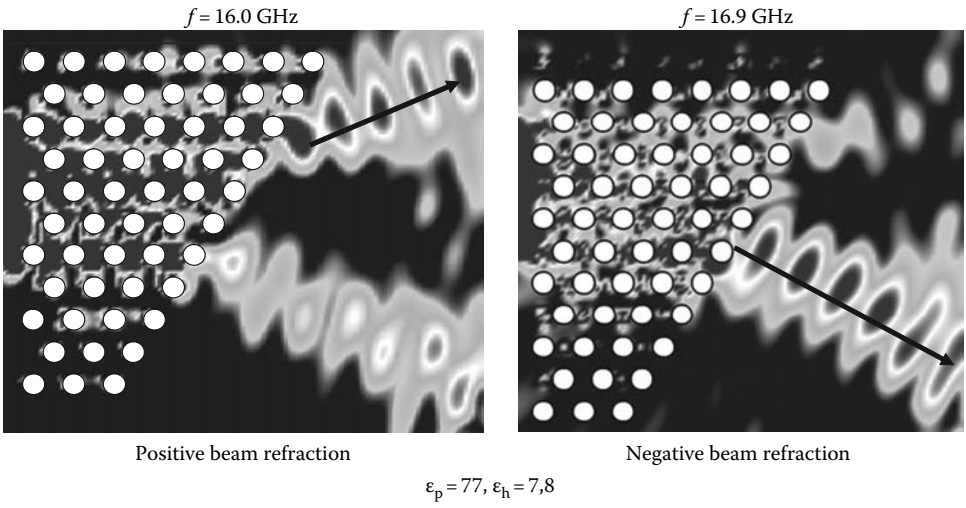

FIGURE 21.11 Wave propagation through the prism formed by a regular array of dielectric cylindrical resonators. (Taken from Semouchkina, E.A., Semouchkin, G.B., Lanagan, M., and Randall, C.A., *IEEE Trans. Microwave Theory Technol.*, 53, 1477, April 2005. With permission.)

The authors suggested that coupling between the resonators could affect the EM response of the metamaterial in a way similar to that observed at the BW propagation in DNG media. Coupling between resonators causes resonant mode splitting and promotes the channeling of electromagnetic energy by coupled fields, which contributes to the formation of the bands with enhanced transmission. The all-dielectric metamaterial consists of closely positioned dielectric cylinders embedded in a low-permittivity matrix. The ability of the all-dielectric metamaterial to provide negative refraction has been demonstrated by EM simulation of the wave propagation through the prism of metamaterial with a rhombus lattice at frequencies close to the first higher-order resonance of the DRs (Figure 21.11): the negative beam refraction is observed at $f = 16.9$ GHz.

There is one more way to provide simultaneous negative effective permittivity and permeability of artificial media: mutual constitutive particle interaction [35]. As an example, the clustered dielectric particle (CDP) metamaterial, constituted by the periodic repetition of a molecule-like cluster of dielectric atom-like particles, is explored. The structure consists of clusters of coupled DRs (cubes, for example) arranged along a periodic lattice. The clusters may be seen as molecules, whereas the DRs may be seen as atoms or particles, by analogy with natural materials. It is therefore expected that this CDP structure could exhibit some properties identical to those of natural materials, such as electromagnetic homogeneity, and in addition metamaterial properties, such as negative refraction, under appropriate design conditions.

21.5 Three-Dimensional Isotropic DNG Metamaterial Based on Spherical Resonant Inclusions

Isotropy of a DNG structure is provided by the symmetry of the structure and by the symmetry of the components constituting the structure.

21.5.1 Symmetry of the Bispherical DNG Structure

Let us consider two sets of the spherical particles arranged in the NaCl structure (Figure 21.12). This structure is a member of the cubic system of symmetry and pertains to the class $m3m$. In the case

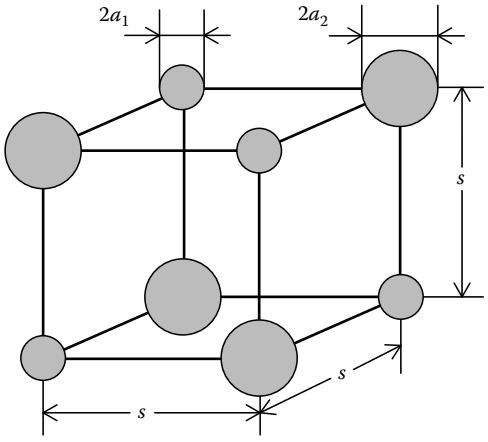

FIGURE 21.12 A cell of the periodic composite medium consisting of two sublattices of dielectric spherical particles with different radii embedded in a host.

of cubic symmetry, the second-rank tensors of all physical parameters of the media are diagonal and characterized by the components of the same values [14]. Thus, the permittivity and permeability tensors have the following forms:

$$\varepsilon = \begin{vmatrix} \varepsilon_{\text{eff}} & 0 & 0 \\ 0 & \varepsilon_{\text{eff}} & 0 \\ 0 & 0 & \varepsilon_{\text{eff}} \end{vmatrix}, \quad \mu = \begin{vmatrix} \mu_{\text{eff}} & 0 & 0 \\ 0 & \mu_{\text{eff}} & 0 \\ 0 & 0 & \mu_{\text{eff}} \end{vmatrix}, \tag{21.1}$$

where the subindices "eff" are introduced to stress that the permittivity and permeability are obtained as a result of averaging the electric and magnetic polarizations of spherical particles embedded in the matrix. Body-centered and face-centered structures are characterized by the same form of the second-order tensor as the simple cubic structure [14]. For averaging the polarization of spherical particles embedded in the matrix, one needs to find the volume of the matrix falling on each particle considered. For a lattice of cubic symmetry, the volume of the unit cell is evaluated as s^3, where s is the distance between the nearest neighbors of the two-component "crystal lattice" (Figure 21.12).

We should stress that the isotropy of the media considered is valid only for the second-rank tensors. If one considers phenomena like dielectric nonlinearity or electrostriction, which are described by fourth-rank tensors, the specific anisotropy of the media formed by the embedded spherical particles should be taken into account.

The idea of using magnetodielectric spherical particles as constitutive particles for artificial metamaterial belongs to Holloway [36]. The modeling of the electromagnetic response of spherical inclusions embedded in a host material (Figure 21.13a) is based on the generalized Lewin's model [37]. The spherical particles with radius a are arranged in a cubic lattice with the lattice constant s.

The incident electromagnetic plane wave with wavelength λ propagating in the host material excites certain modes in the particles. These modes are not strongly eigenmodes of spherical DRs, but they can be specified as H or E modes at the frequencies that are close to the spherical cavity eigenfrequencies.

In 2004, the isotropic structure suitable for a practical realization was introduced in [38] (Figure 21.13b). It was suggested that the artificial material is composed of two sets of dielectric spheres embedded in a host dielectric material. The spheres are made from the same dielectric material and have different radii. The dielectric constant of the spherical particles is much larger than that of the host material. The wavelength inside the sphere is comparable with the diameter of

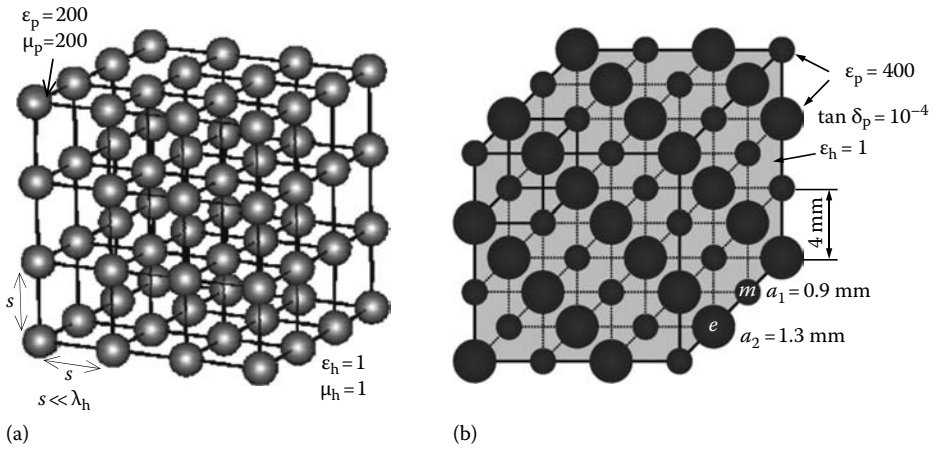

FIGURE 21.13 (a) Composite structure containing magnetodielectric spherical particles; and (b) isotropic media composed of dielectric spheres with different radii.

the sphere, and at the same time the wavelength outside the sphere is large compared with the sphere dimensions. By combining two sets of spheres with suitable radii, different modes can be simultaneously excited in the spheres: the magnetic resonance mode in one set of spheres and the electric resonance mode in the other set.

21.5.2 DNG Medium Composed of Magnetodielectric Spherical Inclusions

The model introduced by Holloway is based on Lewin's derivation of expression for the effective properties of an array of spherical particles embedded in a background matrix [36]. Let us consider the spherical particles with radius a arranged in a cubic lattice with the lattice constant s. The incident electromagnetic wave propagating in the host material is the plane-polarized wave. The relative effective permittivity ε_{eff} and effective permeability μ_{eff} of such a structure are written as

$$\varepsilon_{eff} = \varepsilon_h \left(1 + \frac{3v}{\frac{F(\theta)+2K_e}{F(\theta)-K_e} - v} \right), \tag{21.2}$$

$$\mu_{eff} = \mu_h \left(1 + \frac{3v}{\frac{F(\theta)+2K_m}{F(\theta)-K_m} - v} \right), \tag{21.3}$$

where

$F(\theta) = \frac{2(\sin\theta - \theta\cos\theta)}{(\theta^2-1)\sin\theta + \theta\cos\theta}$

$v_f = \frac{4}{3}\frac{\pi a^3}{s^3}$ is the fraction volume defined as the ratio of the volume of particles in the mixture and the total volume of the mixture

$\theta = k_0 a \sqrt{\varepsilon_p \mu_p}$, k_0 is the wave number in free space

$K_e = \frac{\varepsilon_h}{\varepsilon_p}$

$K_m = \frac{\mu_h}{\mu_p}$

ε_p and μ_p are the relative permittivity and relative permeability of the inclusions

ε_h and μ_h are the relative permittivity and permeability of the host (matrix) medium

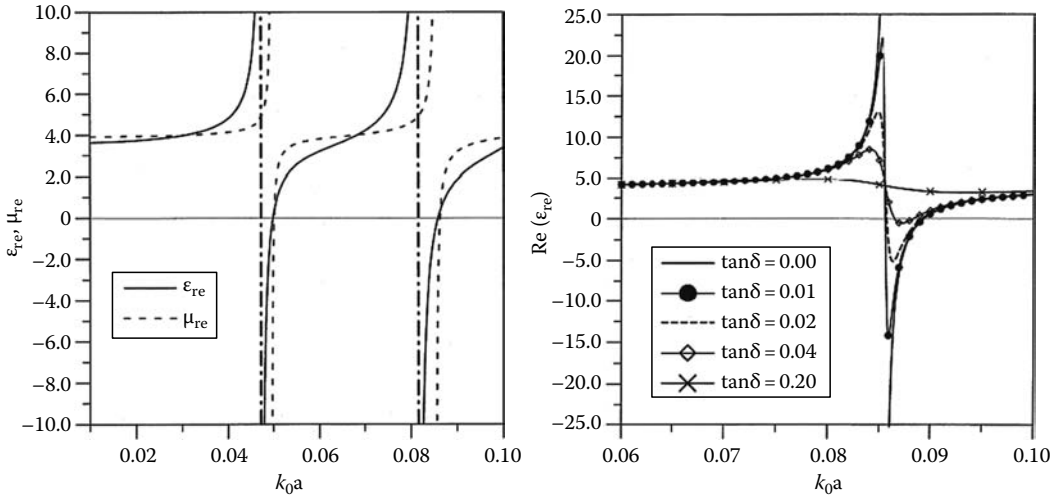

FIGURE 21.14 (a) ε_{eff} and μ_{eff} for $\nu_f = 0.5$, $\varepsilon_h = \mu_h = 1$, $\varepsilon_p = 40$, $\mu_p = 200$. The dashed-dotted lines are the asymptotes. (b) ε_{eff} for $\nu_f = 0.5$, $\varepsilon_h = \mu_h = 1$, $\varepsilon_p = 50$, $\mu_p = 50$. (Taken from Holloway, C. and Kuester, E., *IEEE Trans. Antennas Propag.*, 51, 2596, October 2003. With permission.)

The function $F(\Theta)$ has a resonance nature. It becomes negative at some frequencies and in some ranges of Θ. Negative values of function $F(\Theta)$ are necessary (but not sufficient) demand for ε_{eff} and μ_{eff} to be negative (for real values of ε and μ of the matrix media and spheres in them) (Figure 21.14a). Decreasing the inclusion volume fraction ν_f has the effect of narrowing the band of frequencies, for which ε_{eff} and μ_{eff} become negative. Besides ν_f, the product of ε_p and μ_p influences the bandwidth and location of the resonance. By making this product smaller, the first resonance of ε_{eff} and μ_{eff} is moved to larger values of the product $k_0 \cdot a$ and the frequency bandwidth over which the permittivity and permeability are negative increases.

Losses in material of particles decreases the effect of resonance behavior on the composite. This effect is shown in Figure 21.14b. In this figure, the dependence of the real part of the effective permittivity on a normalized frequency is shown for several different values of the dielectric loss tangent of the inclusions defined as $\tan\delta = \frac{\varepsilon_p''}{\varepsilon_p'}$. The dielectric loss tangent of the matrix as well as the magnetic loss tangents of both materials are taken to be zero. Notice that, for this example, the real part of the effective permittivity can still be negative for loss tangents of the inclusions, as large as 0.04. However, for larger values, the resonance is damped out and the real part of the effective permittivity remains positive. This shows that if the inclusion (i.e., the spherical particle) becomes too lossy, the DNG properties cannot be realized.

21.5.3 DNG Medium Composed of Dielectric Spheres with Different Radii (Garnet–Maxwell Mixing Rule)

The particles used in artificial isotropic media on electromagnetic resonance spheres [36] are impractical because of their simultaneous high values not only of permittivity but of permeability as well. Another model suitable for practical realization has been introduced by Vendik and Gashinova [38]. In that case, two types of spheres were used with different radii but made from the same material (Figure 21.13b). In such a structure, one can observe the resonance of the TE_{111} mode in one type of spherical particles and the resonance of the TM_{111} mode in other types of spherical particles at the

same given frequency. In this case, it is possible to realize the negative dielectric permittivity as a result of a contribution of the resonance of the TM_{111} mode and the negative magnetic permeability as a result of a contribution of the resonance of the TE_{111} mode. The diameters of the spheres must be much smaller than the wavelength in the matrix (host material) but comparable to the wavelength in the material of the spheres. Ferroelectric single crystal or ceramic samples with dielectric constants 100–400 can be used as a material for manufacturing the spherical particles.

The numerical simulation of two-lattice structures by eigenmode analysis and FDTD analysis has also been implemented in [38]. The resonant behavior of a single sphere embedded in a host material was investigated. The cell under simulation with two pairs of PEW and PMW bounding a propagation region is shown in the inset of Figure 21.15. The field pattern of the exiting plane wave is equivalent to a waveguide excitation of the structure. This definition of the elementary cell allows us to obtain a scattering parameter (Figure 21.15a and b) of a two-port device. Extraction of the effective dielectric permittivity and magnetic permeability is based on the transformation of Z-parameters of such an effective TL section. The DNG behavior is observed at $f = 66.4$ GHz (Figure 21.15c and d).

In [36,38], Lewin's equations were applied directly to the system of two sets of spheres, and the electric polarizability of spheres in the magnetic resonant mode was not taken into account. However, the electrical properties of these spheres can have a significant effect on the effective permittivity of the composite. This affects especially the low-frequency limit, which then approaches the classical Maxwell–Garnett mixing rule. In [39], a new model was presented, which takes this effect into account. Equations are validated both analytically and numerically. Scattering from a single sphere was calculated both analytically from the full Mie theory and numerically.

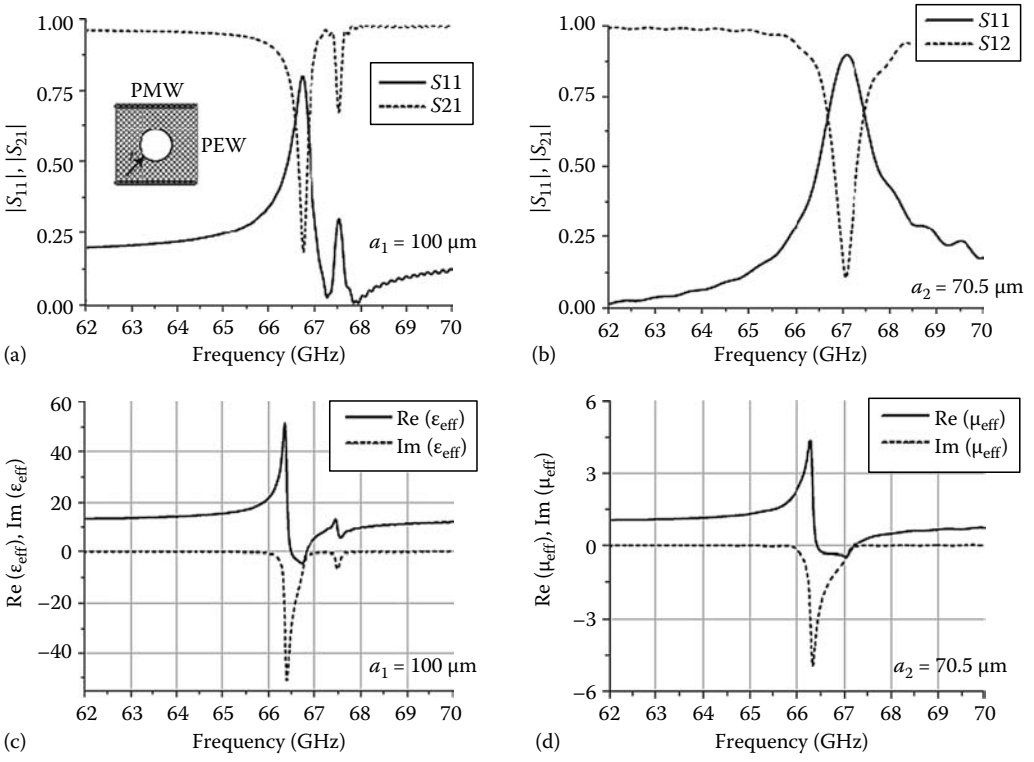

FIGURE 21.15 Scattering parameters and extracted effective permittivity (ε_{eff}) and effective permeability (μ_{eff}) of a single sphere with $\varepsilon = 1000$, radius $a_1 = 100\,\mu$m (a,c), and $a_2 = 70.5\,\mu$m (b,d).

An effective medium model for a composite consisting of two sets of resonating spheres is defined by

$$\frac{\varepsilon_{\text{eff}} - \varepsilon_{\text{h}}}{\varepsilon_{\text{eff}} + 2\varepsilon_{\text{h}}} = \frac{f_{\text{e}}}{\varepsilon_{\text{h}}}\left(\frac{2\varepsilon_{\text{h}} + \varepsilon_{\text{p}}F(\theta_1)}{\varepsilon_{\text{h}} - \varepsilon_{\text{p}}F(\theta_1)}\right) + \frac{f_{\text{m}}}{\varepsilon_{\text{h}}}\left(\frac{2\varepsilon_{\text{h}} + \varepsilon_{\text{p}}F(\theta_2)}{\varepsilon_{\text{h}} - \varepsilon_{\text{p}}F(\theta_2)}\right), \tag{21.4}$$

$$\frac{\mu_{\text{eff}} - 1}{\mu_{\text{eff}} + 2} = f_{\text{m}}\left(\frac{2 + F(\theta_2)}{1 - F(\theta_2)}\right), \tag{21.5}$$

$$f_{\text{e}} = \frac{4}{3}\pi a_1^3 \frac{1}{s^3}, \quad f_{\text{m}} = \frac{4}{3}\pi a_2^3 \frac{1}{s^3}, \tag{21.6}$$

$$F(\theta) = \frac{2(\sin\theta - \theta\cos\theta)}{(\theta^2 - 1)\sin\theta + \theta\cos\theta}, \tag{21.7}$$

where

$\theta_1 = k_0 a_1 \sqrt{\varepsilon_{\text{p}}\mu_{\text{p}}}$
$\theta_2 = k_0 a_2 \sqrt{\varepsilon_{\text{p}}\mu_{\text{p}}}$
a_1 is the radius of spheres with the electric resonance
a_2 is the radius of spheres with the magnetic resonance
f_{e} and f_{m} are the volume fractions for the corresponding spheres

In Figure 21.16, an example of effective permittivity as a function of the volume fraction of spheres is shown. The solid line represents ε_{eff} given by Equation 21.4, and the dashed line, $\varepsilon'_{\text{eff}}$, is calculated using the method in [36,38], where the electric polarizability of spheres in the magnetic resonance

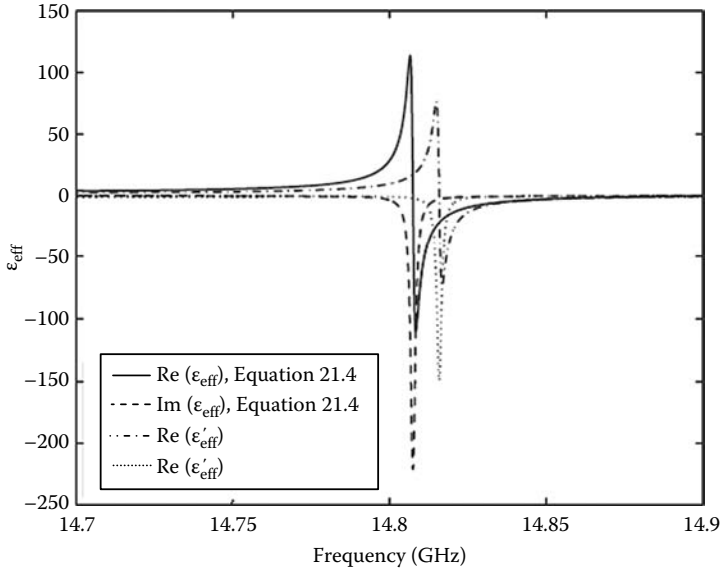

FIGURE 21.16 The effective permittivity ε_{eff} as a function of the frequency calculated by Equation 21.4 compared with the effective permittivity $\varepsilon'_{\text{eff}}$ calculated without taking into account the electrical polarizability of spheres in the magnetic resonance. In this case, the second term on the right-hand side of Equation 21.4 is zero. $\varepsilon_{\text{p}} = 100(1 - j1.25 \cdot 10^{-4})$, $\varepsilon_{\text{h}} = 1$, $f_e = 0.15$, $f_m = 0.15$, $a_1 = 3.18 \cdot 10^{-3}$ mm, $a_2 = 2.18 \cdot 10^{-3}$ mm. (Taken from Jylhä, L., Kolmakov, I., Maslovski, S., and Tretyakov, S., *J. Appl. Phys.*, 99(4), 043102–043102-7, 2006. With permission.)

mode is not taken into account. It can be seen that the resonant frequency slightly shifts when the improved mixing equation is used.

21.5.4 DNG Medium Composed of Dielectric Spheres with Different Radii (Electromagnetic Wave Diffraction Model)

A numerical analysis of a bispherical structure [38] revealed that the interference of the adjacent spherical particles is negligibly small. This makes it possible to solve the electromagnetic problem for each sphere independent of the influence of all others. We consider the diffraction of a plane electromagnetic wave on a dielectric sphere using the approach of Stratton [40]. Some results of solving this problem as applied to the bispherical structure were presented in [41,42].

Let us consider the diffraction of a plane electromagnetic wave with the amplitude of electric field E_0 linearly polarized along the x-axis. The wave propagates along the z-axis (Figure 21.17):

$$\vec{E}(z,t) = \vec{e}_x E_0 \cdot e^{i(\omega t - k_2 z)}, \quad \vec{H}(z,t) = \vec{e}_y \frac{k_2}{\omega \mu_o} E_0 \cdot e^{i(\omega t - k_2 z)}. \tag{21.8}$$

The wave number k_2 is defined later.

In order to fulfill the boundary conditions on the surface of the spherical particle with respect to the tangential components of the electric and magnetic fields, expansion of the incident plane wave in terms of the spherical function is used. The spherical modes inside the sphere and the spherical modes propagating in open space outside the sphere are taken into consideration as well. The boundary conditions give rise to two pairs of nonhomogeneous equations with respect to the complex amplitudes of the spherical functions inside and outside the spherical particle.

The fields inside the spherical particle are presented in the following forms:

$$\vec{E}^{(\text{in})} = E_0 e^{i\omega t} \sum_{n=1}^{\infty} i^n \frac{2n+1}{n(n+1)} \left(a_n^{(\text{in})} \vec{m}_{o/n} - i b_n^{(\text{in})} \vec{n}_{e/n} \right), \tag{21.9}$$

$$\vec{H}^{(\text{in})} = -\frac{k^1}{\omega \mu_0} E_0 e^{i\omega t} \sum_{n=1}^{\infty} i^n \frac{2n+1}{n(n+1)} \left(b_n^{(\text{in})} \vec{m}_{e/n} + i a_n^{(\text{in})} \vec{n}_{o/n} \right), \tag{21.10}$$

where $\vec{m}_{o/n,m,n}$ and $\vec{n}_{o/e,m,n}$ are spherical wave functions (odd and even) [40]. As far as the incident wave in open space is linearly polarized, the number $m = 1$ is taken in Equations 21.9 and 21.10. The wave numbers are defined as

$$k_1 = \omega \sqrt{\varepsilon_0 \varepsilon_p \mu_0}, \quad k_2 = \omega \sqrt{\varepsilon_0 \varepsilon_h \mu_0}, \tag{21.11}$$

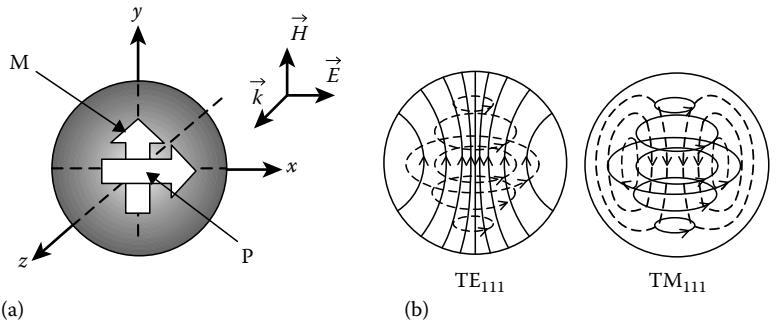

FIGURE 21.17 Spherical particle in the field of a linearly polarized electromagnetic wave and field distribution in the equatorial plane. (a) Dipole momentum of electric polarization of the particle P and dipole momentum of magnetization of the particle M. (b) Mode charts of the dominant TE_{111} and TM_{111} modes in a spherical resonator with magnetic walls. Solid and dashed lines show the magnetic and electric field lines, respectively.

where ε_0 and μ_0 are the dielectric permittivity and permeability of free space. The diffracted field outside the spheres is given in [40].

The solutions of the system of equations specified by the boundary conditions define the amplitudes of the waves inside the spherical particle in the following forms:

1. For the waves of magnetic (transverse electric) type ($E_r = 0$, Figure 21.17b, left),

$$a_n^{(\text{in})} = -\frac{j_n(\rho)[\rho h_n^{(1)}(\rho)]' - h_n^{(1)}(\rho)[\rho j_n(\rho)]'}{j_n(N\rho)[\rho h_n^{(1)}(\rho)]' - h_n^{(1)}(\rho)[N\rho j_n(N\rho)]'} \tag{21.12}$$

2. For the waves of electric (transverse magnetic) type ($H_r = 0$, Figure 21.17b, right),

$$b_n^{(\text{in})} = -\frac{j_n(\rho)[\rho h_n^{(1)}(\rho)]' - h_n^{(1)}(\rho)N[\rho j_n(\rho)]'}{N^2 j_n(N\rho)[\rho h_n^{(1)}(\rho)]' - h_n^{(1)}(\rho)[N\rho j_n(N\rho)]'} \tag{21.13}$$

where

$\rho = k_2 a$, a is the radius of the spherical particle
$j_n(z)$ is the spherical Bessel function
$h_n^{(1)}(z)$ is the spherical Hankel function of the first order
the sign $[]'$ means the differentiation with respect to ρ or $N\rho$
$N = k_1/k_2$

Figure 21.18 represents the distribution of the electromagnetic field components in line with Equations 21.8 through 21.10 for the spheres with the dielectric permittivity $\varepsilon_p = 400$ surrounded by the air ($\varepsilon_h = 1$). Diagrams were plotted for values of polar angles $\theta = \pi/4$ and $\varphi = \pi/4$.

Analysis of Equations 21.12 and 21.13 is followed by the two important conclusions:

1. At certain frequencies, the modulus of the denominators of the fractions (Equations 21.12 and 21.13) become minimum and corresponds to the resonance phenomena, but because of the complex nature of the Hankel functions, they do not lead to singularities.
2. The imaginary components of the Hankel functions determine the quality factor of the resonator, which is finite even in the case of lossless material of the spheres. Physically this can be explained by the loss caused by the radiation of the diffracted waves outside the sphere.

21.6 Effective Permittivity and Permeability of the Bispherical Lattice

For the model of a DNG composite arranged from the magnetodielectric spherical inclusions introduced by Holloway, the effective permittivity and permeability are determined on the effective medium theory of the electromagnetic response of inclusions embedded in a host material developed by Lewin (see Section 21.5.2). In Section 21.5.3, the effective permittivity and permeability were found by application of the classical Maxwell–Garnet mixing rule. Now, we consider the framework of the electromagnetic wave diffraction model. The effective permittivity and permeability of the bisphere lattice are determined.

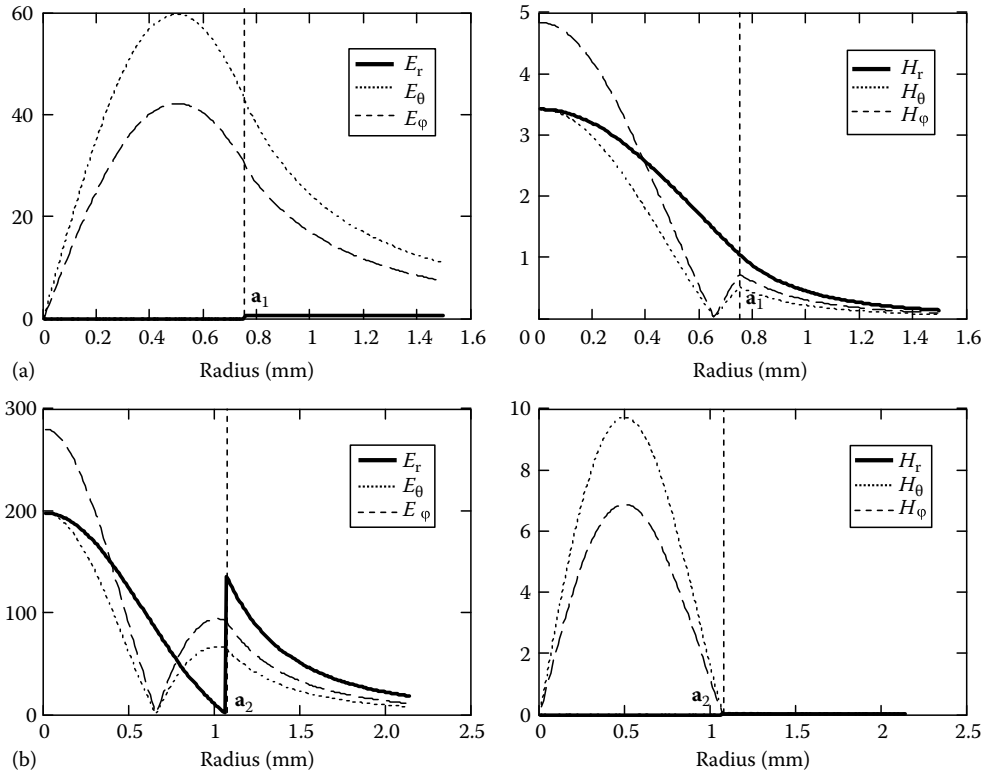

FIGURE 21.18 (a) Electromagnetic field components distribution for magnetic type waves; $E_r = 0$ inside the sphere. (b) Electromagnetic field components distribution for electric type waves; $H_r = 0$ inside the sphere.

21.6.1 Electric and Magnetic Dipole Moments of Spherical Resonators

The spherical particle electric dipole momentum $D_x^{(E)}$ oriented along the x-axis and the magnetic dipole momentum $D_y^{(M)}$ oriented along the y-axis (Figure 21.17a) are calculated as follows:

$$D_x^{(E)} = \varepsilon_0 \varepsilon_p \int_{V_{sph}} \left(\vec{E}^{(in)}(r, \theta, \varphi) \cdot \vec{e_x} - E_0 \right) dv, \tag{21.14}$$

$$D_y^{(M)} = \mu_0 \int_{V_{sph}} \left(\vec{H}^{(in)}(r, \theta, \varphi) \cdot \vec{e_y} - \frac{k_1}{\omega \mu_0} \cdot E_0 \right) dv. \tag{21.15}$$

While integrating the scalar product of basis vectors $\vec{e}_r, \vec{e}_\theta,$ and $\vec{e}_\varphi$, $\vec{e}_x$ and $\vec{e}_y$ should be taken into account.

The averaged macroscopic magnetization and averaged macroscopic electric polarization can be found as the corresponding dipole momentum divided by the volume of the cell containing the dipoles [43]. Thus, one obtains the relative effective permittivity and permeability:

$$\varepsilon_r^{(eff)}(\omega) = \frac{D_x^{(E)}(\omega)}{s^3 \varepsilon_0 E_0} + \varepsilon_h, \tag{21.16}$$

$$\mu_r^{(eff)}(\omega) = \frac{D_y^{(M)}(\omega)}{s^3 E_0 \frac{k_2}{\omega}} + 1 \tag{21.17}$$

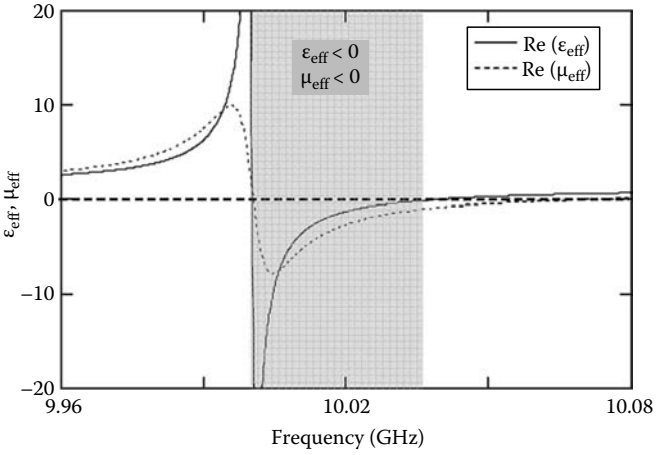

FIGURE 21.19 The effective permittivity and permeability of bispherical medium versus frequency.

After calculating the integrals in Equations 21.14 and 21.15 in accordance with Equations 21.9 and 21.10, where the spherical wave functions should be used [40], one obtains

$$\varepsilon_r^{(\mathrm{eff})}(\omega) = \frac{4}{3}\pi a_2^3 \cdot \frac{1}{s^3}\varepsilon_p \cdot b_1^{(\mathrm{in})}(k_1 a_2) \cdot I(k_1 a_2), \tag{21.18}$$

$$\mu_r^{(\mathrm{eff})}(\omega) = \frac{4}{3}\pi a_1^3 \cdot \frac{1}{s^3}\sqrt{\varepsilon_p} \cdot a_1^{(\mathrm{in})}(k_1 a_1) \cdot I(k_1 a_1). \tag{21.19}$$

Here, $I(\xi)$ is the result of integration over the volume of the particle, a_1 and a_2 are radii of the particles, $a_2 > a_1$. The function $I(\xi)$ has been approximated in the region $3 < \xi < 5$ by the following simple formula:

$$I(\zeta) = 0.1852(4.5 - \zeta) + 0.0438(4 - \zeta)^2. \tag{21.20}$$

The frequency dependence of the wave amplitude for the excited modes $a_1^{(\mathrm{in})}$ and $b_1^{(\mathrm{in})}$ determines the frequency dependence of $\varepsilon_r^{(\mathrm{eff})}(\omega)$ and $\mu_r^{(\mathrm{eff})}(\omega)$. Considering the structure composed by two sublattices of the dielectric spherical particles with different radii, we can adjust these radii to obtain the same resonant frequencies for the H_{111} mode in the smaller sphere and the E_{111} mode in the larger sphere. Figure 21.19 presents the simulated frequency dependence of $\varepsilon_r^{(\mathrm{eff})}(\omega)$ and $\mu_r^{(\mathrm{eff})}(\omega)$ for $a_1 = 0.748$ mm, $a_2 = 1.069$ mm, $s = 4$ mm, dielectric permittivity of the particle $\varepsilon_p = 400$ and $\tan\delta = 10^{-3}$, and permittivity of the matrix $\varepsilon_h = 1$.

One may see that at the frequency slightly above $f = 10$ GHz both the permittivity $\varepsilon_r^{(\mathrm{eff})}$ and the permeability $\mu_r^{(\mathrm{eff})}$ are negative. Thus, in the rather narrow frequency band around $f = 10$ GHz, the existence of isotropic DNG has been theoretically substantiated. A negative refraction bandwidth depends on the permittivity of the spherical particles. The smaller the value of permittivity of the dielectric spherical particles, the wider is the frequency range, where both the effective permittivity and permeability are negative. The dependence of the negative refraction index bandwidth on the permittivity of the material constituent particles is presented in Figure 21.20.

21.6.2 Comparison of the Effective Permittivity and Permeability Obtained with Different Models

Different analytical models for the DNG medium description were introduced to describe the structures with sets of spherical particles [36,38,39,41,42,44]. The modeling of the electromagnetic

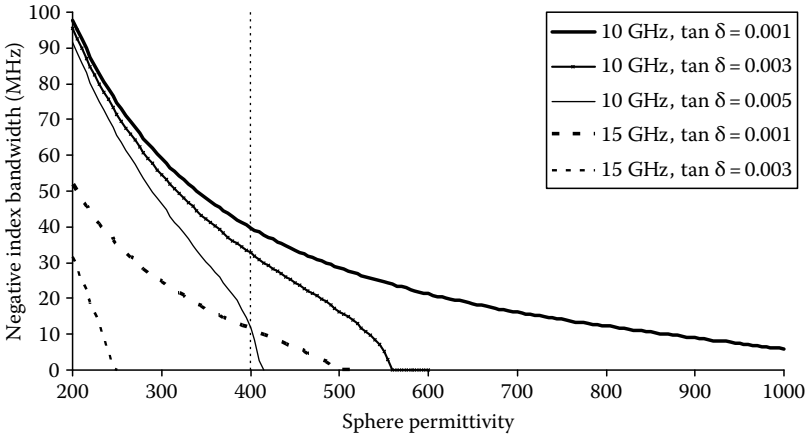

FIGURE 21.20 Dependence of negative refractive index bandwidth on spherical particle permittivity for two resonance frequencies, f_1 = 10 GHz f_2 = 15 GHz, and different loss levels.

response of spherical inclusions embedded in a host material [36,38,39] is based on the generalized Lewin's model [37]. Originally, the Lewin's model has been specified only for spherical particles with the same radius a arranged in a cubic lattice with the lattice constant s. The spheres are assumed to resonate either in the first or second resonance mode of the Mie theory [45]. Expansion of the model for the case of two sublattices of dielectric spherical particles with different radii makes possible the description of the DNG media [41,44]. The properties of DNG media required could be observed in the frequency region, where the resonance of the E mode in one set of particles and the resonance of the H mode in another set of particles are excited simultaneously. The improved model of the bispherical structure was presented in [39]. The effective permittivity ε_{eff} for a material with two types of inclusions having two different electric polarizabilities was calculated from the generalized Claussius–Mossotti relation, taking into account the electric polarizabilities of the spheres in the magnetic resonance and in the electric resonance mode. Consideration of the remaining static electric polarizability of spheres in the magnetic resonance modes, which is not equal to zero as in [38], is important.

Let us compare the frequency dependences of both the effective dielectric permittivity and the effective magnetic permeability calculated by using different models. Figure 21.21 presents an example of effective permittivity and permeability as a function of the frequency for three different analytical models: (1) Lewin's model [37], (2) the improved mixing rule model [39], taking into account the electrical polarizability of spheres in the magnetic resonance, and (3) the diffraction model [44].

The parameters of the constituent materials are $\varepsilon_p = 400$, $\varepsilon_h = 1$, $\tan\ \delta = 10^{-4}$, $\mu_p = \mu_h = 1$, a_1 = 0.747 mm, $a_2 = 1.069$ mm, and $s = 4$ mm. The results are in general similar, but they differ in the resonant frequency and the magnitude of effective electromagnetic parameters of the medium. The resonant frequency is slightly shifted in comparison with Lewin's model when the improved mixing equation is used and is shifted more remarkably for the diffraction model.

21.6.3 Results of the Full-Wave Analysis

After analytical calculations based on the diffraction model, the structure was simulated by full-wave analysis [46]. The simulated structure consists of quarters of spheres placed in the dielectric material (Figure 21.22). In the case of appropriate boundary conditions, simulation of this model should give the same results as those for the infinite 3D structure. Four quarters of the spheres of different radii were placed in a host medium with the permittivity and the permeability equal to unity bounded with

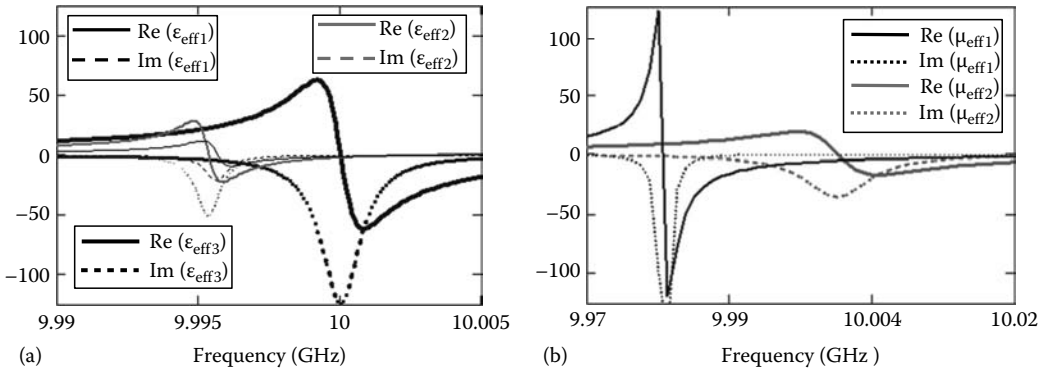

FIGURE 21.21 (a) The effective permittivity as a function of the frequency for three different analytical models: (1) Lewin's model [37] ε_{eff1}; (2) the improved mixing rule model (taking into account the electrical polarizability of spheres in the magnetic resonance), [39] ε_{eff2}; and (3) the diffraction model. (b) The effective permeability as a function of the frequency for the three different analytical models: (1) the mixing rule model [37,39], μ_{eff1}; and (2) diffraction model, μ_{eff2}. The parameters of the constituent materials are as follows: $\varepsilon_p = 400$, $\tan\delta = 10^{-4}$, $\varepsilon_h = 1$; $\mu_p = \mu_h = 1$, $a_1 = 0.748$ mm, $a_2 = 1.069$ mm, and $s = 4$ mm.

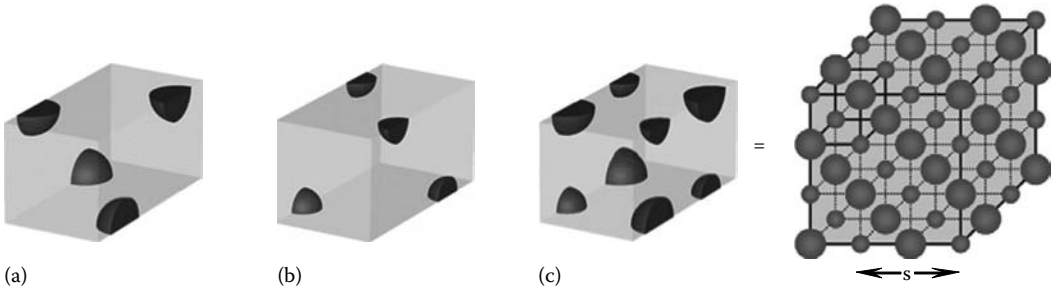

FIGURE 21.22 Single cells of single spherical and bispherical structures. Boundary conditions are two PEWs and two PMWs on opposite sides: (a) large spheres, (b) small spheres, and (c) mixed structure.

two PEWs and two PMWs on the opposite sides, respectively. First, four quarters of the larger sphere (radius $r = 1.069$ mm, permittivity of particle $\varepsilon_p = 400$, and loss factor $\tan\delta = 0.0001$) and then four quarters of the smaller sphere ($r = 0.747$ mm, $\varepsilon_p = 400$, $\tan\delta = 0.0001$) were modeled. Then, the structure consisting of sets of spheres of two radii was modeled.

The results for scattering matrix elements $|S_{11}|$ and $|S_{21}|$ are shown in Figure 21.23. The stop band is observed near the frequency 10 GHz in case of negative permittivity or permeability only. For the medium with the set of both spheres, a narrow pass band near the frequency 10 GHz is observed. The frequency range of the electromagnetic wave with an enhanced transmission coefficient corresponds to the DNG characteristics of the structure. The resonance frequency has the same value as the one calculated analytically.

Field patterns inside the unit cells are presented in Figure 21.24. The magnetic field distribution on the side plane of the structure (Figure 21.24a) and the electric field distribution on the top plane of the structure (Figure 21.24b) represent the TM mode in a larger sphere (electric dipole momentum) and the TE mode (magnetic dipole momentum) in a smaller sphere.

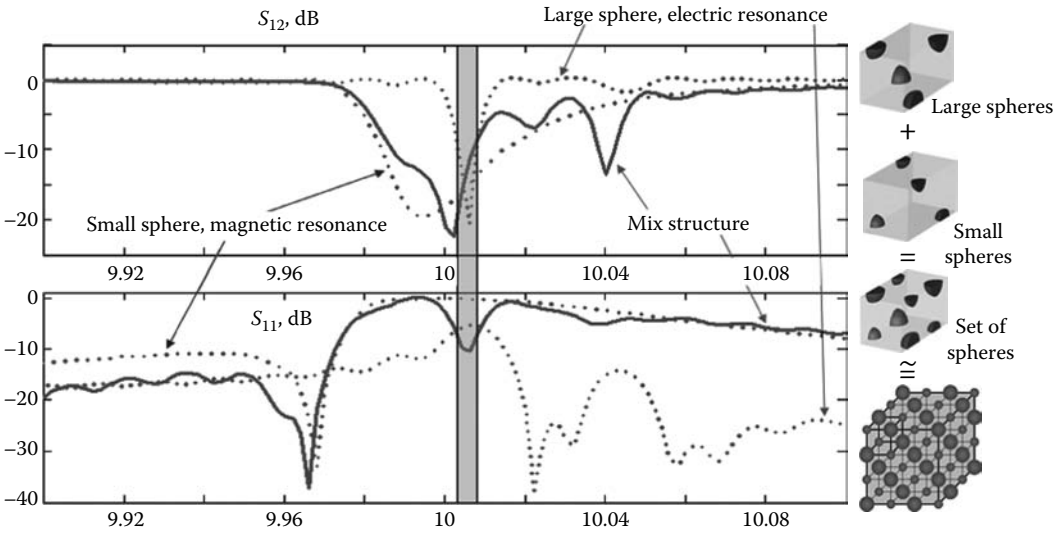

FIGURE 21.23 Simulation results for a mixed structure with the following parameters: $\varepsilon_p = 400$, $\varepsilon_h = 1$; $a_1 = 1.065$ mm, $a_2 = 0.747$ mm, $s = 4$ mm, and $\tan\delta = 0.0001$.

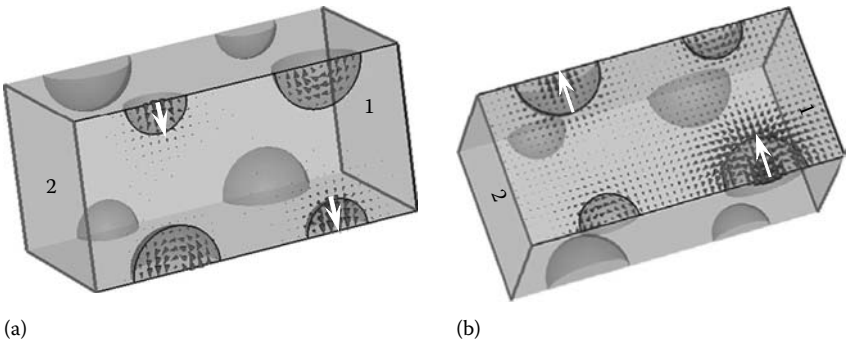

FIGURE 21.24 Field patterns inside the unit cell of a structure: (a) magnetic field distribution on the side plane (magnetic dipoles) and (b) electric field distribution on the top plane (electric dipoles).

21.6.4 Results of the Experiment

In order to verify the resonance behavior of the spheres, an experiment was conducted [46]. The Network Analyzer Agilent 8720ES was used for the measurement of *S*-parameters of the spheres. A spherical particle was placed inside the rectangular waveguide. Different samples were used in the experiment (two large spheres with radius 0.65 mm and two small spheres with radius 0.45 mm). The results of the experiment were compared with the data obtained previously by modeling. The transmission and reflection coefficients for the small sphere (Figure 21.25) reveal the resonance behavior at the frequency 17.17 GHz. Here, the gray solid and dashed lines represent the measured $S_{11(22)}$ and $S_{12(21)}$ parameters, and the black line corresponds to the simulated results. The transmission and reflection coefficients for the large sphere exhibit two resonances (Figure 21.26): magnetic resonance at the frequency 11.89 GHz and electric resonance at 16.8 GHz.

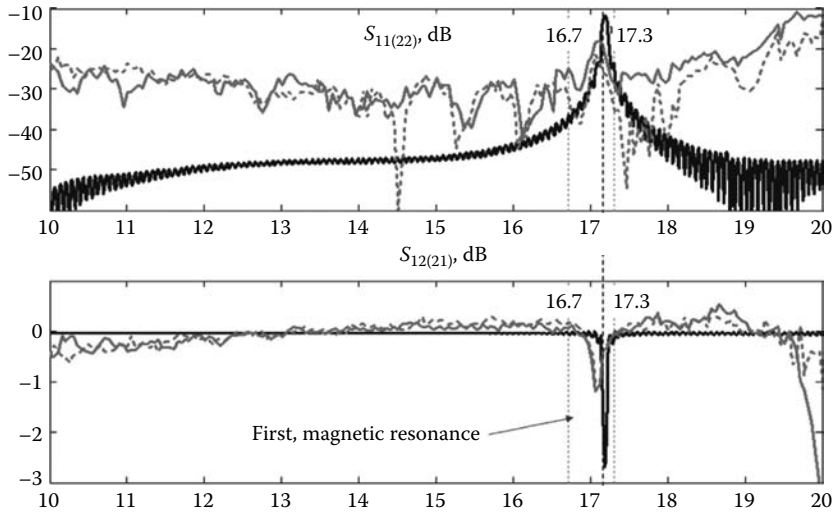

FIGURE 21.25 *S*-parameters for the small sphere. The solid black line represents the simulation results, and the gray solid and dashed lines correspond to the measured characteristics. $\varepsilon_p = 378$, $r = 0.451$ mm, $\tan\delta \approx 0.004$.

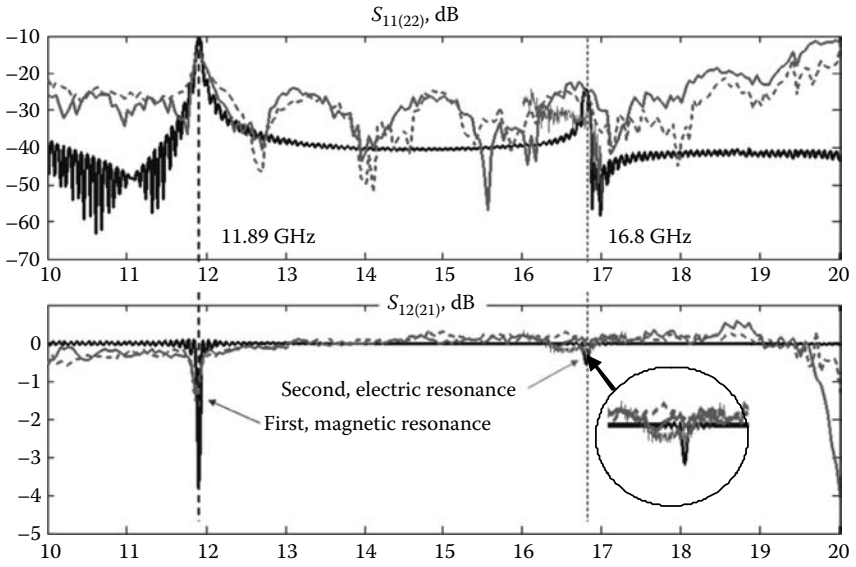

FIGURE 21.26 *S*-parameters for the large sphere. The solid black line represents the simulation result, and the gray solid and dashed lines correspond to the measured characteristics. $\varepsilon_p = 378$, $r = 0.65$ mm, $\tan\delta \approx 0.004$.

In the experiment, the magnetic resonance frequency in the small sphere does not coincide with the electric resonance frequency in the large sphere, because the radii were not adjusted accurately, and the possible DNG behavior of the structure consisting of these samples was not observed. Nevertheless, the experiment proved the validity of an analytical diffraction model describing the resonance behavior of the dielectric spheres [42].

21.6.5 Influence of Distribution of Size and Permittivity of Spherical Particles on DNG Characteristics

Let us consider a DNG medium composed of dielectric spheres with different radii described by the Maxwell–Garnet mixing rule (see Section 21.5.3). It has been shown in [32,39] that the random distribution of the spherical particle sizes caused by manufacturing inaccuracy may affect the values of the effective permittivity and permeability of the DNG medium.

In order to take into account the random size distribution of the spheres, one should rewrite Equation 21.5 in the form [39]

$$\frac{\varepsilon_{\text{eff}} - \varepsilon_{\text{h}}}{\varepsilon_{\text{eff}} + 2\varepsilon_{\text{h}}} = \frac{1}{\varepsilon_{\text{h}}} \left(\sum_{k=1}^{K} \frac{f_{ek}}{G(\theta_{1k})} + \sum_{l=1}^{L} \frac{f_{ml}}{G(\theta_{2l})} \right), \tag{21.21}$$

where

k is the number of spheres in the electric resonance

l is the number of spheres in the magnetic resonance, $G(\theta) = \frac{\varepsilon_{\text{h}} - \varepsilon_{\text{p}} F(\theta)}{2\varepsilon_{\text{h}} + \varepsilon_{\text{p}} F(\theta)}$

This is the solution for the effective permittivity of the structure with two sets of spheres, where one set of spheres is in the magnetic resonance and the other set is in the electric resonance. The effective permeability can be calculated in a similar way.

An example of how a normal size distribution, $N = \frac{1}{\sigma\sqrt{2\pi}} \exp\left(\frac{(r-r')^2}{2\sigma^2}\right)$ of spheres with half-value widths $\sigma = \sigma_{\text{e}}$ and $\sigma = \sigma_{\text{m}}$ and expectation values $r' = a_1$ and $r' = a_2$ affects the effective material parameters is presented in Figure 21.27. The left-hand side of Figure 21.27 describes the spheres that are normally distributed with the half-value widths $\sigma_{\text{m}} = \sigma_{\text{e}} = 1\,\mu\text{m}$. The expected values of the sphere radii are $a_1 = 3.18$ mm and $a_2 = 2.28$ mm. The size distribution N for σ_{e} is also shown. On the right-hand side, everything is the same, except the half-value widths $\sigma_{\text{e}} = \sigma_{\text{m}} = 10\,\mu\text{m}$.

The half-value width $\sigma_{\text{e}} = \sigma_{\text{m}} = 1\,\mu\text{m}$ (Figure 21.27, left) does not increase the loss factor of the structure significantly, but in the case of the half-value width of $\sigma_{\text{e}} = \sigma_{\text{m}} = 10\,\mu\text{m}$ (Figure 21.27, right), the imaginary part becomes remarkably larger and μ_{eff} does not exhibit negative values.

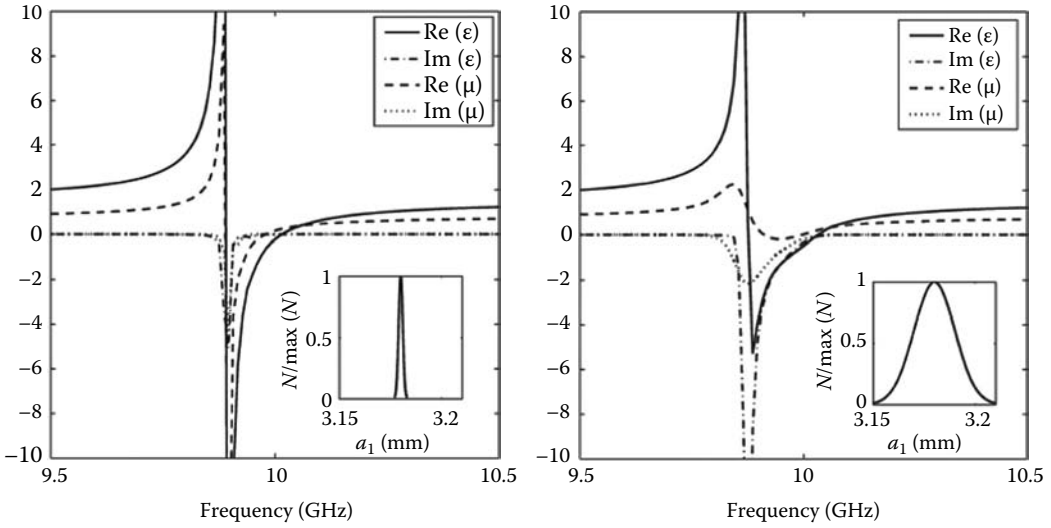

FIGURE 21.27 The effective permittivity as a function of the frequency calculated using Equation 21.21 with $\varepsilon_{\text{p}} = 44 \cdot (1 - j1.25 \cdot 10^{-4})$, $\varepsilon_{\text{h}} = 1$, and filling ratios $f_{\text{e}} = 2\%$, $f_{\text{m}} = 14\%$. (Taken from Jylhä, L., Kolmakov, I., Maslovski, S., and Tretyakov, S., *J. Appl. Phys.*, 99(4), 043102–043102-7, 2006. With permission.)

Now, we consider the influence of the size distribution for the DNG medium model using the model of the electromagnetic wave diffraction on dielectric spheres with different radii. According to Equations 21.18 and 21.19, the spherical particle radius influences the values of the effective permittivity and permeability. Dielectric sphere radius variation affects the value of the resonance frequency, which corresponds to the low-frequency threshold of the negative index range. Let us estimate how the resonant frequency depends on the radius of the constituent spherical particles. The electrical radius of the sphere was defined previously as

$$N\rho = k_1 a, \tag{21.22}$$

where $k_1 = \omega\sqrt{\varepsilon_0 \varepsilon_p \mu_0}$ is the propagation constant. Let us rewrite Equation 21.22 in this way:

$$f = \frac{N\rho}{2\pi \cdot a \cdot \sqrt{\varepsilon_0 \varepsilon_p \mu_0}}, \tag{21.23}$$

where f is the frequency of the electromagnetic wave.

Values of the electrical radius of the resonant spheres can be calculated from Equations 21.12 and 21.13 for the minimum modulus of the denominator in Equations 21.12 and 21.13. For a given a, the values of the electrical radius providing magnetic or electric resonance the resonance frequency can be calculated using Equation 21.23.

Dependence of the resonant frequency on the sphere radius is shown in Figure 21.28. This graph represents the dependence of the resonant frequency on the spherical particle radius for two values of particle permittivity, 400 and 1000. According to Figure 21.20, the negative index bandwidth for a DNG medium with spherical inclusions permittivity equal to 400 should be 16 MHz for a 10 GHz resonant frequency. This implies that the spherical particle radius accuracy should be ±1.5 μm in this case.

In line with Equation 21.23, the resonance frequency is also influenced by the permittivity of the dielectric material of the particles. Figure 21.29 represents the dependence of the resonant frequency on the spherical particle permittivity for two different values of radii, 1 and 0.5 mm. To avoid frequency spreading beyond the negative index bandwidth of 32 MHz, the tolerance of the permittivity of material should be ±0.5%.

With regard to the possibility of the practical realization of such an artificial metamaterial, we should mention that recent technologies allow the production of dielectric spheres with accuracy

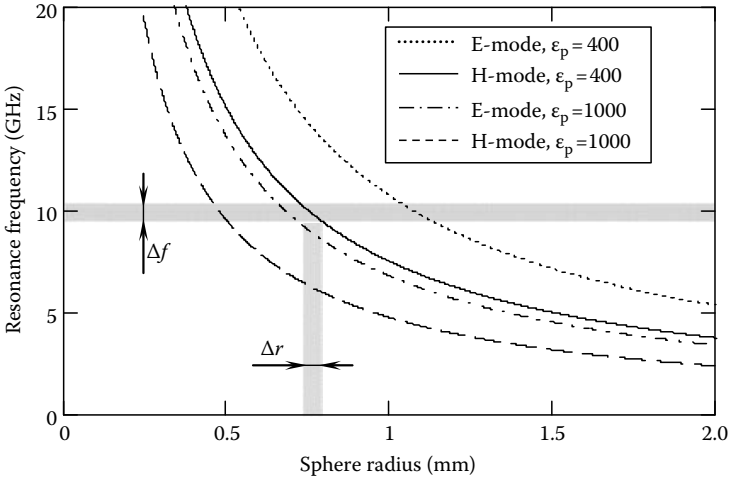

FIGURE 21.28 Dependence of resonance frequency on sphere radius for particles with $\varepsilon_p = 400$ and $\varepsilon_p = 1000$, $\Delta f = 32$ MHz, $\Delta r = 3$ μm.

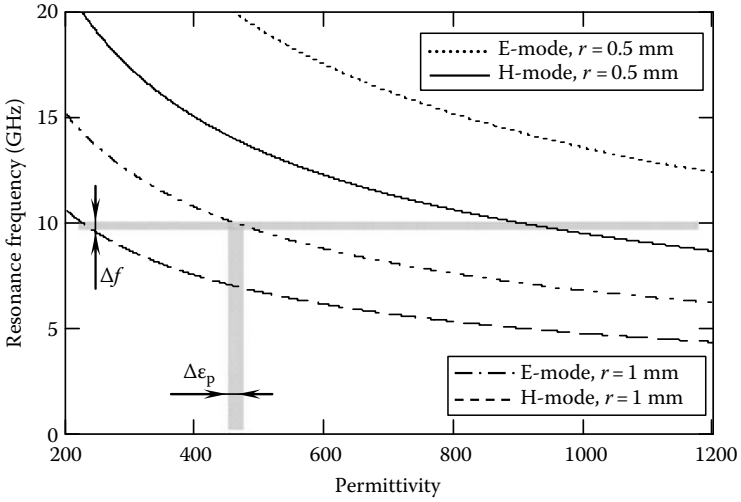

FIGURE 21.29 Dependence of resonance frequency on spherical particle permittivity for particles with $r = 0.5$ mm and $r = 1$ mm; $\Delta f = 32$ MHz, $\Delta\varepsilon_p = 3$.

$\Delta r = 1\,\mu$m. At the same time, the achievable accuracy of permittivity of the dielectric material with $\varepsilon_r > 200$ is about 5%–20%. Despite this, it is really possible to select samples with desired values of permittivity among a large number of manufactured samples.

21.6.6 Isotropic Medium of Coupled Dielectric Spherical Resonators

When dielectric spherical resonators are placed close to each other, they begin to interact. The coupling between resonators leads to the formation of new electromagnetic field distribution in the media outside the spheres. It becomes possible to get electric and magnetic dipole responses using only one type of sphere. The magnetic dipole comes from the first Mie resonance in a dielectric sphere. The electric dipole is formed by the sphere interaction. Electric and magnetic dipole existence provides a DNG response of the media [47].

A 2D plane structure consisting of 24 closely positioned dielectric spheres has been modeled. If the distance between the spheres is large, there is no wave propagation on a resonant frequency (Figure 21.30a). By decreasing the spacing between the spheres, splitting of the resonance curve occurs (Figure 21.30b). The pass band appears near the resonant frequency.

Figure 21.31 represents the phase diagram of the structure considered. The transverse magnetic field component in the free space is shown on the left side of the picture. The right side represents the magnetic field pattern for the structure containing the regular array of dielectric spheres. It is clearly

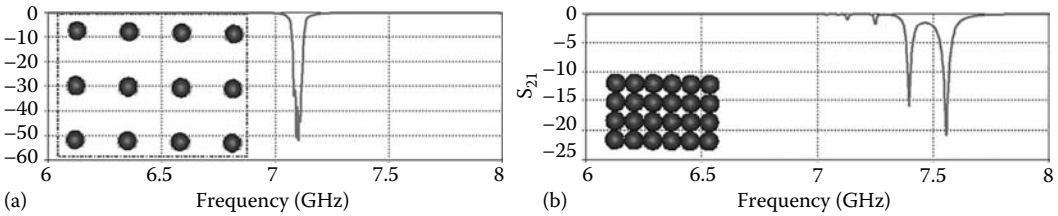

FIGURE 21.30 Transmission coefficient for (a) far and (b) closely positioned spheres.

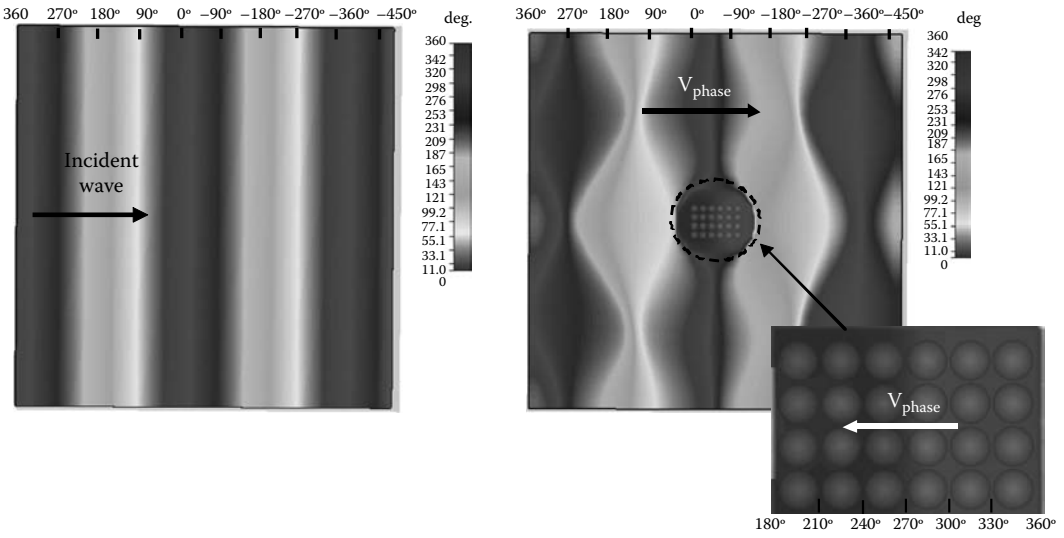

FIGURE 21.31 Phase distribution in a 2D plane of dielectric spheres.

seen from the magnified part of the picture that the phase response of the propagated electromagnetic inside the array of the spheres is positive, whereas the phase response outside the structure is negative. This means that there is BW propagation in the structure considered.

21.7 Metamaterials for Optical Range

Definitely, one of the most challenging problems is producing a metamaterial for the optical frequency range. Invisibility, superlenses, and light rays manipulation—these properties in the optical range are extremely promising. A model of metamaterial that can exhibit a negative refractive index band in excess of 6% in a broad frequency range from the deep infrared to the terahertz region, has been investigated in [48]. The favored realization of the structure considered is a "periodic" crystal wherein polaritonic spheres and Drude-like or plasma spheres are arranged on two interpenetrating "simple cubic" lattices. When the differences between the spheres are ignored, the resulting structure is a face-centered cubic structure. The sublattice of polaritonic spheres possesses negative magnetic permeability in certain frequency regions, whereas the sublattice of the Drude-like spheres possesses negative electric permittivity. Both phenomena are the results of the strong single-sphere Mie resonances. By a suitable choice of materials and parameters, a common region can be found, within a broad frequency range from the deep infrared to the terahertz region, where both functions are negative and the structure exhibits a negative refractive index band in excess of the 6% bandwidth.

A new concept of metafluids—liquid metamaterials based on clusters of metallic nanoparticles or artificial plasmonic molecules (APMs)—has been introduced in [49]. APMs comprising four nanoparticles in a tetrahedral arrangement have isotropic electric and magnetic responses and are analyzed using the plasmon hybridization method, an electrostatic eigenvalue equation, and vectorial finite-element, frequency-domain, electromagnetic simulations. It has been demonstrated that a colloidal solution of plasmonic tetrahedral nanoclusters can act as an optical medium with very large, small, or even negative effective permittivity, ε_{eff}, and substantial effective magnetic susceptibility, $\chi_{eff} = \mu_{eff} - 1$, in the visible or near-infrared bands. The electric and magnetic responses of the tetramer allow one to construct an effective medium with a completely isotropic electric and magnetic

response. Electromagnetic simulations indicate that achieving $\varepsilon_{eff} < 0$ and $\mu_{eff} < 0$ in colloidal solutions of "artificial molecules" should be possible using either sufficiently high concentrations of gold clusters or materials with low-loss negative permittivity.

References

1. C. Caloz and T. Itoh, *Electromagnetic Metamaterials: Transmission Line Theory and Microwave Applications*, Wiley, New York, 2004.
2. G. V. Eleftheriades and K. G. Balmain, *Negative Refraction Metamaterials: Fundamental Principles and Applications*, John Wiley & Sons Inc., Hoboken, NJ, 2005.
3. N. Engheta and R. W Ziolkowski (eds.), *Metamaterials: Physics and Engineering Explorations*, Wiley-IEEE Press, Hoboken, NJ, 2006.
4. R. Marqués, F. Martín, and M. Sorolla, *Metamaterials with Negative Parameters: Theory, Design and Microwave Applications*, John Wiley & Sons, Inc., Hoboken, NJ, 2008.
5. D. R. Smith, W. J. Padilla, D. C. Vier, S. C. Nemat-Nasser, and S. Schultz, A composite media with simultaneously negative permeability and permittivity, *Appl. Phys. Lett*., 84, 4184–4187, May 2000.
6. R. A. Shelby, D. R. Smith, and S. Schultz, Experimental verification of a negative index of refraction, *Science*, 292, 77, April 2001.
7. J. B. Pendry, Negative refraction makes a perfect lens, *Phys. Rev. Lett*., 85, 3966–3969, 2000.
8. R. A. Shelby and D. R. Smith, Microwave transmission through a two-dimensional, isotropic, left-handed metamaterial, *Appl. Phys. Lett*., 78, 489–491, 2001.
9. D. R. Fredkin and A. Ron, Effective left-handed (negative index) composite material, *Appl. Phys. Lett*., 81(10), 1753–1755, September 2002.
10. A. Alu and N. Engheta, Pairing an epsilon-negative slab with a mu-negative slab: Resonance, tunneling and transparency, *IEEE Trans. Antennas Propag*., 51(10), 2558–2571, October 2003.
11. A. Alù, N. Engheta, A. Erentok, and R. W. Ziolkowski, Single-negative, double-negative, and low-index metamaterials and their electromagnetic applications, *IEEE Trans. Antennas Propag. Mag*., 49(1), 23–36, February 2007.
12. R. S. Penciu, M. Kafesaki, T. F. Gundogdu, E. N. Economou, and C. M. Soukoulis, Theoretical study of lefthanded behavior of composite metamaterials, *Photon. Nanostruct. Fund. Appl*., 4(1), 12–16, 2006.
13. J. F. Nye, *Physical Properties of Crystals*, Clarendon Press, Oxford, 1964.
14. N. W. Ashcroft and N. D Mermin, *Solid State Physics*, Holt, Rinehart & Winston, New York, London, 1976.
15. P. Gay-Balmaz and O. J. F. Martin, Efficient isotropic magnetic resonators, *Appl. Phys. Lett*. 81, 939, 2002.
16. J. D. Baena, L. Jelinek, R. Marques, and J. Zehentner, Electrically small isotropic three-dimensional magnetic resonators for metamaterial design, *Appl. Phys. Lett*., 88, 134108, 2006.
17. C. R. Simovski and S. He, Frequency range and explicit expressions for negative permittivity and permeability for an isotropic medium formed by a lattice of perfectly conducted particles, *Phys. Lett. A*, 311, 254–263, 2003.
18. J. Machac, P. Protiva, and J. Zehentner, Isotropic epsilon-negative particles, *Proceedings—2007 IEEE Antennas and Propagation Society International Symposium*, Piscataway, NJ, June 2007, pp. 1831–1834.
19. J. Zehentner and J. Machac, Volumetric single negative metamaterials, *Proceedings of Metamaterials 2007 Congress*, Rome, October 22–24, 2007, pp. 617–620.
20. L. Jelinek, J. Machac, and J. Zehentner, A magnetic metamaterial composed of randomly oriented SRRs, *Proceedings PIERS 2007*, Beijing, China, 2007, pp. 474–477.
21. P. Protiva, J. Macháč, and J. Zehentner, Particle for an isotropic metamaterial with negative permittivity, *Proceedings of EMTS 2007, International URSI Commission B, Electromagnetic Theory Symposium*, Ottawa, Ontario, Canada, July 26–28, 2007.

22. E. Verney, B. Sauviac, and C. R. Simovski, Isotropic metamaterial electromagnetic lens, *Phys. Lett. A* 331(3–4), 244–247, October 18, 2004.
23. Th. Koschny, L. Zhang, and C. M. Soukoulis, Isotropic three-dimensional left-handed metamaterials, *Phys. Rev. B*, 71, 121103 (R), 2005.
24. C. Caloz, H. Okabe, T. Iwai, and T. Itoh, Transmission line approach of left-handed (LH) materials, *Proceedings of the USNC/URSI National Radio Science Meeting*, vol. 1, San Antonio, TX, June 2002, p. 39.
25. G. V. Eleftheriades, A. K. Iyer, and P. C. Kremer, Planar negative refractive index media using periodically L-C loaded transmission lines, *IEEE Trans. Microw. Theory Tech.*, 50(12), 2702–2712, December 2002.
26. A. Grbic and G. V. Eleftheriades, An isotropic three-dimensional negative-refractive-index transmission-line metamaterial, *J. Appl. Phys.*, 98, 043106, 2005.
27. W. J. R. Hoefer, P. P. M. So, D. Thompson, and M. M. Tentzeris, Topology and design of wide-band 3D metamaterials made of periodically loaded transmission line arrays, *2005 IEEE MTT-S International Microwave Symposium Digest*, Long Beach, CA, June 2005, pp. 313–316.
28. M. Zedler, C. Caloz, and P. Russer, Circuital and experimental demonstration of a 3D isotropic LH metamaterial based on the rotated TLM scheme, *Microwave Symposium, 2007 IEEE/MTT-S International*, Honolulu, HI, June 3–8, 2007, pp. 1827–1830.
29. M. Zedler and P. Russer, Investigation on the dispersion relation of a 3D LC-based metamaterial with an omnidirectional left-handed frequency band, *2006 International Microwave Symposium Digest*, San Francisco, CA, 2006, p. 1477.
30. P. Alitalo, S. Maslovski, and S. Tretyakov, Three-dimensional isotropic perfect lens based on LC-loaded transmission lines, *J. Appl. Phys.*, 99, 064912, 2006.
31. P. Alitalo, S. Maslovski, and S. Tretyakov, Experimental verification of the key properties of a three-dimensional isotropic transmission line based superlens, *J. Appl. Phys.*, 99(12), 124910–124910-6, 2006.
32. I. A. Kolmakov, L. Jylhä, S. A. Tretyakov, and S. Maslovski, Lattice of dielectric particles with double negative response, *XXVIIIth General Assembly of International Union of Radio Science (URSI)*, New Delhi, India, paper BCD.5(0109).pdf, October 23–29, 2005.
33. T. Ueda, A. Lai, and T. Itoh, Negative refraction in a cut-off parallel-plate waveguide loaded with two-dimensional lattice of dielectric resonators, *Proceedings of EuMC36*, Manchester, 2006, pp. 435–438.
34. E. A. Semouchkina, G. B. Semouchkin, M. Lanagan, and C. A. Randall, FDTD study of resonance processes in metamaterials, *IEEE Trans. Microw. Theory Technol.*, 53, 1477–1487, April 2005.
35. A. Rennings, C. Caloz, and M. Coulombe, Unusual wave phenomena in a guiding/radiating clustered dielectric particle metamaterial (CDP-MTM), *Proceedings of the 36th European Microwave Conference*, Univ. Duisburg, Manchester, September 2006, pp. 439–442.
36. C. Holloway and E. Kuester, A double negative composite medium composed of magnetodielectric spherical particles embedded in a matrix, *IEEE Trans. Antennas Propag.*, 51, 2596–2603, October 2003.
37. L. Lewin, The electrical constants of a material loaded with spherical particles, *Proc. Inst. Elec. Eng.*, 94, 65–68, 1947.
38. O. G. Vendik and M. S. Gashinova, Artificial double negative (DNG) media composed by two different dielectric sphere lattices embedded in a dielectric matrix, *Proceedings of EuMC34*, Paris, France, October 2004, pp. 1209–1212.
39. L. Jylhä, I. Kolmakov, S. Maslovski, and S. Tretyakov, Modeling of isotropic backward-wave materials composed of resonant spheres, *J. Appl. Phys.*, 99(4), 043102–043102-7, 2006.
40. A. Stratton, *Electromagnetic Theory*, McGraw-Hill Book Co., Inc., New York, 1941.
41. I. Vendik, O. Vendik, and M. Gashinova, Artificial dielectric medium possessing simultaneously negative permittivity and magnetic permeability, *Tech. Phys. Lett.*, 32, 429–433, May 2006.
42. I. Vendik, O. Vendik, M. Odit, M. Gashinova, and I. Kolmakov, Isotropic artificial media with simultaneously negative permittivity and permeability, *Microw. Opt. Technol. Lett.*, 48, 2553–2556, December 2006.

43. C. Kittel, *Introduction to Solid State Physics*, 5th edn., Wiley, New York, 1976.
44. I. Vendik, O. Vendik, I. Kolmakov, and M. Odit, Modeling isotropic DNG media for microwave applications, *Opto-Electron. Rev*., 14(3), 179–186, September 2006.
45. J. A. Kong, *Electromagnetic Wave Theory*, EMW Publishing, Cambridge, MA, 2005.
46. M. Odit, I. Vendik, and O. Vendik, 3D Isotropic metamaterial based on dielectric resonant spheres, *Proceedings of 1st Metamaterial Congress*, Rome, Italy, October 2007.
47. I. Vendik, M. Odit, and O. Vendik, 3D isotropic DNG material based on a set of coupled dielectric spheres with Mie resonance, *Proceeding of 2nd Metamaterial Congress*, Pamplona, Spain, September 2008, pp. 18–20.
48. V. Yannopapas and A. Moroz, Negative refractive index metamaterials from inherently non-magnetic materials for deep infrared to terahertz frequency ranges, *J. Phys.: Condens. Mat*., 17(25), 3717–3734(18), 2005.
49. Y. A. Urzhumov, G. Shvets, J. A. Fan, F. Capasso, D. Brandl, and P. Nordlander, Plasmonic nanoclusters: A path towards negative-index metafluids, *Opt. Exp*., 15(21), 14129–14145, 2007.

22

Network Topology-Derived Metamaterials: Scalar and Vectorial Three-Dimensional Configurations and Their Fabrication

P. Russer
Munich University of Technology

M. Zedler
University of Toronto

22.1 Introduction

In this chapter we show that space-discretizing algebraic schemes describing discrete fields can be considered the unifying framework behind metamaterials. Physical realizations of these schemes lead to either Drude or Lorentz dispersion with their immanent properties and hence limitations. Next, this perspective on metamaterials being physical realizations of space-discretizing schemes is extended to two-dimensional (2D) and three-dimensional (3D).

So far five different topologies for 3D, left-handed, isotropic metamaterials have been proposed: A finite-differences-derived (FDTD)-derived structure independently proposed in Refs. [1,2], a structure derived from the rotated transmission-line-matrix (TLM) scheme [3,4], a structure consisting of dielectric spheres [5], a 3D extension of the wire/split-ring approach [6,7], and a scalar

3D structure [8,9] in shunt configuration. The latter was the first 3D, left-handed, metamaterial demonstrated experimentally.

This contribution is organized as follows: Section 22.2 shows that a unifying framework for metamaterials can be given on the basis of network models and their topological structure. These results are then used in Section 22.3 and 22.4 to present 2D and 3D scalar metamaterials. Section 22.4 also contains a novel scalar 3D structure, which can be physically implemented obeying inversion symmetry. Section 22.5 presents a vectorial, 3D metamaterial structure that was first proposed by the authors of this chapter in Ref. [3] and experimentally verified in Ref. [4]. Section 22.6 considers the crucial point in 3D metamaterials, i.e., how to build these structures. Section 22.6.1 proposes a decomposition of the metamaterial cells into polyhedrons, allowing for fabrication techniques such as (2-component)-injection molding, 3D-molded interconnect device technology (3D-MID), hot embossing, plasma activation and printing, physical vapor deposition, laser direct structuring, and rapid prototyping. Section 22.6.2 discusses topology-invariant planarizations of the two 3D metamaterial structures, yielding anisotropic behavior along one axis but offering compatibility with standard planar fabrication techniques.

22.2 Topological Description of Discrete Electrodynamics

Metamaterials are compound artificial materials tailored to achieve a particular type of dispersion for permittivity and/or permeability. In the following subsections we show that due to these properties metamaterials can be more easily derived by dividing the task of finding a structure yielding the desired metamaterial behavior into four subtasks: First a suitable topology, i.e., a network, is deduced using symmetry considerations [10]. Next, the desired type of dispersive behavior is chosen. Then, a physical realization for this desired network is synthesized. Finally, the physical realization is characterized using group-theoretical considerations for determining (bi/an)isotropy [11,12].

The advantage of first making topological analyses is that the search for new physical realizations of metamaterials becomes comparatively easy, as will be shown in Section 22.4 and Section 22.5.

22.2.1 One-Dimensional Metamaterials

In order to deduce a topological analysis of metamaterials let us first examine Maxwell's equations in the one-dimensional (1D) case within a homogeneous, uniform medium describing an x-polarized wave propagating in the $+z$-direction

$$\partial_z E_x(z) = -\mathrm{j}\omega\mu_0\mu_r H_y(z) \quad \partial_z H_y(z) = -\mathrm{j}\omega\epsilon_0\epsilon_r E_x(z). \tag{22.1}$$

The network-theory analogous to Equation 22.1, which constitutes the step for a topological description, is

$$\partial_z V(z) = -Z'\, I(z) \quad \partial_z I(z) = -Y'\, V(z), \tag{22.2}$$

which is the step for a topological description and is considered a formal substitution within the scope of this chapter. A rigorous analysis of the relationship between the field description and the network description can be performed using structure functions.* Obviously the network theory

*A derivation and detailed analysis of structure functions can be found in Ref. [13]. Within this approach propagation of transverse electric (TE) and transverse magnetic (TM) waves is considered separately. The transverse fields of each mode are factored into a complex scalar amplitude—which depends only on the direction of propagation—and a field distribution—which depends only on the transverse coordinates. Written formally the ansatz is $E = V(z) \cdot e(x, y)$, $H = I(z) \cdot h(x, y)$. The transverse field distributions of each mode are called structure functions. $e(x, y)$ and $h(x, y)$ form a bi-orthonormal system. Structure functions fulfill the Helmholtz equation, allowing for a transformation of the Helmholtz equation in E, H into the transmission line equation in V, I. Power transmission properties are unchanged,

analogon does not reduce the manifold of solutions to the wave equation. Both Equations 22.1 and 22.2 have continuous translation symmetry as they describe wave propagation in a homogeneous, uniform medium. The impedance per unit length Z' and the admittance per unit length Y' obey

$$Z' \propto \mathrm{j}\omega\mu_r \quad Y' \propto \mathrm{j}\omega\epsilon_r. \tag{22.3}$$

Hence Z' and Y' are proportional to the—possibly dispersive—material parameters and can thus model dispersion, too. A first-order space-discretizing numerical scheme for Equation 22.2, resulting in discrete translational symmetry, is

$$V(z+\Delta z) - V(z) = -Z \cdot I(z) \quad I(z+\Delta z) - I(z) = -Y \cdot V(z), \tag{22.4}$$

with $Z = Z'\Delta z$ and $Y = Y'\Delta z$. The corresponding circuit for Equation 22.4 is depicted in Figure 22.1a. For structures with continuous translational symmetry Equation 22.4 is an approximation. For metamaterials, however, these equations are exact, because metamaterials are composite artificial structures of finite size and hence with inherent discrete translation symmetry. From Equation 22.4 the resulting dispersion relation and Bloch impedance of the symmetrized cell are

$$\sin^2\frac{\chi}{2} = \tfrac{1}{4}ZY. \tag{22.5a}$$

$$Z_{\mathrm{Bloch}} = \sqrt{Z/Y}\cdot\sqrt{1+\tfrac{1}{4}ZY} = \sqrt{Z/Y}\cdot\cos\frac{\chi}{2}, \tag{22.5b}$$

with the phase shift across a unit cell $\chi = k\Delta z$. For the metamaterial frequency range, where the unit cell is small compared with the wavelength, i.e., $|\chi| \ll 1$, the dispersion relation reads $\chi^2 = -ZY$ (Figure 22.1a).

22.2.1.1 Implementation of Dispersion Models

The choice of the series element Z and shunt element Y determines the type of dispersion, Drude dispersion or Lorentz dispersion being the two most common types. This is shown in Figure 22.1b.

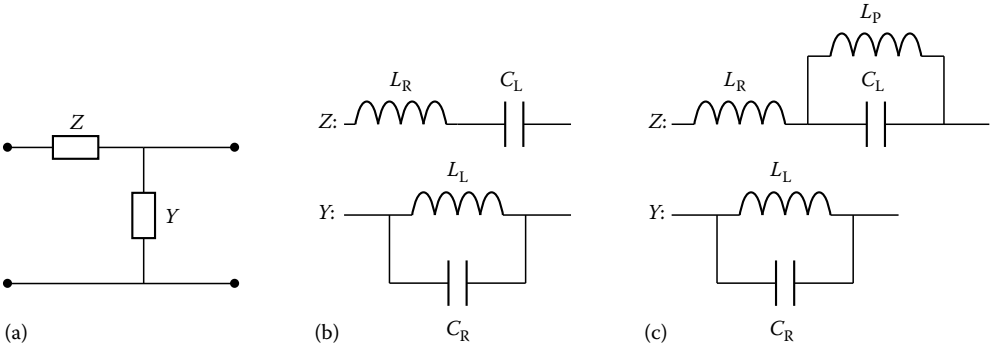

FIGURE 22.1 (a) Unit cell due to the first-order discretization of the telegrapher's equation, (b) unit cell elements implementing Drude dispersion (CRLH) for both ϵ_r and μ_r and (c) unit cell elements implementing ϵ_r following Drude dispersion, μ_r following Lorentz dispersion, as, e.g., in split-ring resonator (SRR)/wire-grid arrangements.

(continued) $\iint E \times H^* \,\mathrm{d}A = Z_\mathrm{F}^{-1}\iint |E|^2\,\mathrm{d}A = Z_\mathrm{F}\iint |H|^2\,\mathrm{d}A = VI^* = Z_\mathrm{F}^{-1}|V|^2 = Z_\mathrm{F}|I|^2$, using the characteristic impedance Z_F for both the field description and the network description.

In the case of plane wave propagation in free space as described by Equation 22.1, the structure functions reduce to $e(x,y) = h(x,y) = 1$. For the TE/TM wave propagation one obtains that the longitudinal field components are expressed in the equivalent network topology by effective Z' and Y' with $\partial^2_{\omega\omega}Z' \neq 0$ and/or $\partial^2_{\omega\omega}Y' \neq 0$. Comparing this result with the remainder of this section, this behavior describes dispersion.

Using series resonators for Z and parallel resonators for Y results in the composite right/left-handed (CRLH) approach [14–16], yielding Drude dispersion for both the effective permeability and permittivity [17]

$$Z = \mathrm{j}\omega\mu_{r,\mathrm{eff}} = \mathrm{j}\omega\mu_\infty\left(1-\omega_{0,\mu}^2/\omega^2\right) \tag{22.6a}$$

$$Y = \mathrm{j}\omega\epsilon_{r,\mathrm{eff}} = \mathrm{j}\omega\,\epsilon_\infty\left(1-\omega_{0,\epsilon}^2/\omega^2\right), \tag{22.6b}$$

where

μ_∞ and ϵ_∞ are the permeability and permittivity for $\omega \to \infty$, respectively
$\omega_{0,\mu}$ and $\omega_{0,\epsilon}$ denote the magnetic and electric plasmon resonance frequencies, respectively

The correspondence between Equation 22.6 and Figure 22.1b is

$$\mu_\infty = L_\mathrm{R} \qquad \epsilon_\infty = C_\mathrm{R} \qquad \omega_{0,\mu}^2 L_\mathrm{R} C_\mathrm{L} = 1 \qquad \omega_{0,\epsilon}^2 L_\mathrm{L} C_\mathrm{R} = 1. \tag{22.7}$$

The motivation to use the terminology of Equation 22.6 is that dispersion of effective material parameters is treated in this chapter.

For the synthesis of physical structures it is possible and common to directly incorporate the network, as in Figure 22.1a and Figure 22.1b, using lumped elements, i.e., series capacitors connected to shunt inductors. These elements together with their unavoidable parasitics then physically realize double-Drude dispersion. It shall be emphasized that with this type of structure incident free-space waves can also interact. In the case of a free-space wave setup it needs to be ensured that at the operational frequency the metamaterial structure is monomodal [18], see also Section 22.5.3.

Apart from these lumped element physical realizations, structures based on purely distributed elements have been proposed. Examples are the mushroom structure [19] and a structure consisting of stacked thick metallic screens operating below cutoff [20], with the holes realizing the shunt inductance [21] and the interplate capacitance the series capacitance in the double-Drude topology. Details of wave propagation in double-Drude metamaterials are given in, e.g., Refs. [15,16].

Lorentz dispersion for the permeability and Drude dispersion for the permittivity result in

$$Z = \mathrm{j}\omega\mu_{r,\mathrm{eff}} = \mathrm{j}\omega\mu_\infty\left(1-\frac{\omega_{0,\mu}^2}{\omega^2-\omega_{\infty,\mu}^2}\right) \tag{22.8a}$$

$$Y = \mathrm{j}\omega\epsilon_{r,\mathrm{eff}} = \mathrm{j}\omega\,\epsilon_\infty\left(1-\omega_{0,\epsilon}^2/\omega^2\right). \tag{22.8b}$$

The network elements to Figure 22.1a modeling this type of dispersion are shown in Figure 22.1c. Their relation to Equation 22.8a modelling is

$$\mu_\infty = L_\mathrm{R} \qquad \omega_{0,\mu}^2 L_\mathrm{R} C_\mathrm{L} = 1 \qquad \omega_{\infty,\mu}^2 L_\mathrm{P} C_\mathrm{L} = 1. \tag{22.9}$$

As expected, Lorentz dispersion passes into Drude dispersion for $\omega_\infty \to \infty$ and hence in the equivalent circuit of Figure 22.1c for $L_P \to 0$.

Physical realizations of Lorentz/Drude dispersion are, for example, the split-ring resonator (SRR)/wire-grid configuration as well as Mie-resonant dielectric resonators [5,22].

An illustration showing the correspondences between the contents of the SRR/wire-grid unit cell and the related equivalent circuit is shown in Figure 22.2. This equivalent circuit is valid only in the quasi-static approximation, i.e., the unit cell is small compared with the wavelength. The electric field of an incident wave is parallel to the wire grid, which loads the effective permittivity inductively with L_L. The SRR is modeled by C_L', L_P'. This resonator is probed by the magnetic field, which is parallel to the SRR plane normal vector. Due to the coupling of the magnetic field with the resonator, the effective permeability is modified. Last, the free space between the split rings is modeled by a ladder network with the elements L_R and C_R. The equivalent circuit of Figure 22.2b shows a direct

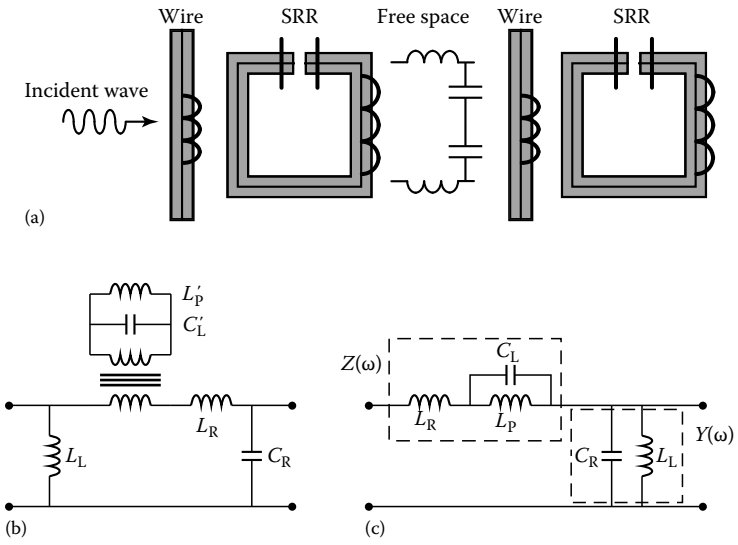

FIGURE 22.2 Wave traveling through an SRR/wire-grid metamaterial: (a) Correspondence of unit cell contents with network elements. (b) equivalent circuit, and (c) simplified equivalent circuit.

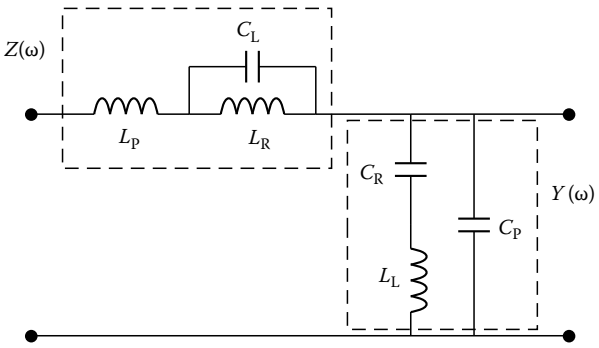

FIGURE 22.3 Equivalent circuit of a metamaterial where the dispersion of both the permittivity and the permeability are of Lorentz type.

correspondence to Figure 22.2a. The coupling of the magnetic field to the resonator is modeled by an ideal transformer. Simplifying and rearranging the network in Figure 22.2b yields Figure 22.2c. Here the elements C'_L and L'_P are transformed into the elements C_L and L_P by virtue of the transformer ratio. The resulting network is of the type shown in Figure 22.1c, which describes mixed Lorentz/Drude dispersion.

Reexamining Equation 22.8a it is desirable to enlarge $\omega_{\infty,\mu}$ while keeping $\omega_{0,\mu}$ and the unit cell size constant in order to improve the bandwidth of a left-handed operation. This translates into the requirement of solely reducing L_P, which can unfortunately be achieved only to a small degree with the SRR approach. Further, the resonance within the SRR is particularly prone to losses.

If SRR are combined with cut wires this yields Lorentz dispersion for the permittivity and the permeability. This can be seen from Figure 22.2a by substituting the inductance L_L with a series resonator, where the series capacitance is modeling the capacitive gap between the cut wires. The corresponding equivalent circuit is shown in Figure 22.3.

Similar to the above discussion, one obtains Drude dispersion for the permeability and Lorentz dispersion for the permittivity with the complementary SRR configuration [23]. In this configuration

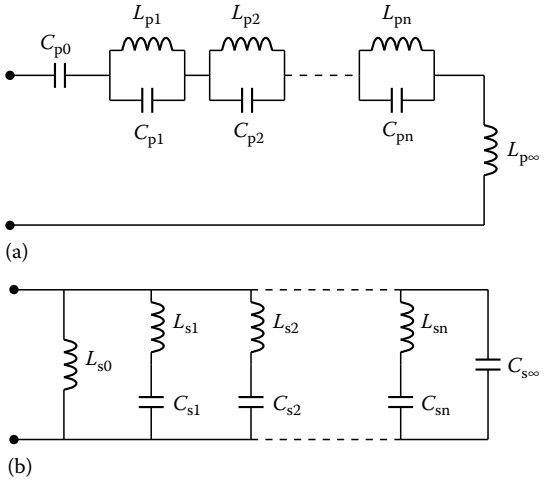

FIGURE 22.4 Canonical Foster equivalent circuit: (a) Foster impedance representation and (b) Foster admittance representation.

the SRR geometry is etched periodically into a ground plane and forms the metamaterial together with a microstrip line with periodic series gap capacitors.

Arbitrary types of dispersion can be obtained by performing the canonical fractional expansion representation of the one-ports Z, Y. These Foster representations of Z and Y are given by [24–26]

$$Z(\omega) = \frac{1}{\mathrm{j}\omega C_{\mathrm{p}0}} + \sum_{n=1}^{\infty} \frac{1}{j\left(\omega C_{\mathrm{p}n} - \frac{1}{\omega L_{pn}}\right)} + \mathrm{j}\omega L_{\mathrm{p}\infty} \tag{22.10a}$$

$$Y(\omega) = \frac{1}{\mathrm{j}\omega L_{\mathrm{s}0}} + \sum_{n=1}^{\infty} \frac{1}{j\left(\omega L_{\mathrm{s}n} - \frac{1}{\omega C_{sn}}\right)} + \mathrm{j}\omega C_{\mathrm{s}\infty}. \tag{22.10b}$$

The lumped element equivalent circuits of Foster impedance and admittance representations are shown in Figure 22.4. The advantage of this type of dispersion-engineering approach based on equivalent circuits and thus on networks is that causality is unconditionally preserved, which may pose a problem in other formulations [16,27,28].

22.2.2 Scattering Matrix Representation of Metamaterial Cells

Although in Section 22.2.1 the discretization by means of a finite-difference scheme to the wave equation was carried out to derive the foundation of metamaterials, now a scattering matrix-based approach is presented. This approach will prove useful for the extension to multidimensional metamaterials.

The scattering matrix of a transmission line segment of length Δz normalized to its characteristic impedance Z_0 is

$$\mathbf{S} = \exp(-j\phi) \begin{pmatrix} 0 & 1 \\ 1 & 0 \end{pmatrix} = \exp(-j\phi)\ (\mathbf{1} - \mathbf{I}), \tag{22.11}$$

where

ϕ is the phase shift across a unit cell

$\mathbf{I}$ denotes the unity matrix

$\mathbf{1}$ is a matrix with all elements equal to 1

Its impedance matrix representation is

$$\mathbf{Z} = -jZ_0 \begin{pmatrix} \frac{1}{\tan\phi} & \frac{1}{\sin\phi} \\ \frac{1}{\sin\phi} & \frac{1}{\tan\phi} \end{pmatrix}. \tag{22.12}$$

The aim is to find network circuits realizing Equation 22.12. The circuit depicted in Figure 22.1a models a segment of a 1D material. We note that such a 1D material is equivalent to a transmission line. Symmetrizing Figure 22.1a to a "T" form, the circuit has the impedance matrix

$$Z = \tfrac{1}{2}Z \cdot \mathbf{I} + \frac{1}{Y} \cdot \mathbf{1}. \tag{22.13}$$

Comparing Equations 22.13 and 22.12 yields

$$Z/Z_0 = j2\tan\tfrac{1}{2}\phi \quad Y \cdot Z_0 = j\sin\phi. \tag{22.14}$$

A first-order expansion in $\phi \propto \omega$ of Equation 22.14 yields the expected result of a series inductance and a shunt capacitance. This is the well-known ladder-network approximation of a short piece of transmission line. Certain types of dispersion, which, for example, yield metamaterial behavior, can then be implemented as discussed in Section 22.2.1. In summary, a scattering matrix-based approach enables an abstract view on network topologies for metamaterial cells.

22.3 Two-Dimensional Metamaterials

In Section 22.2 we showed that a scattering matrix-based representation of a metamaterial cell can be used to find metamaterial structures. Let us now consider the 2D case: The scattering matrix of a symmetrical, reciprocal, and lossless 2D metamaterial has the form

$$\mathbf{S} = \tfrac{1}{2}\exp(-j\phi)\ (\mathbf{1} - 2\cdot\mathbf{I})\,. \tag{22.15}$$

In fact, Equation 22.15 is the foundation of the 2D space-discretizing numerical scheme TLM [29]. Like in the previous Section 22.2.2, a lumped element representation can be obtained by converting to impedance or admittance matrix representation and doing a first-order expansion in ϕ. Doing so yields two network topologies, shown in Figure 22.5: The shunt node describes the TM polarization in 2D space, and the series node describes the TE polarization [29]. The impedance and admittance

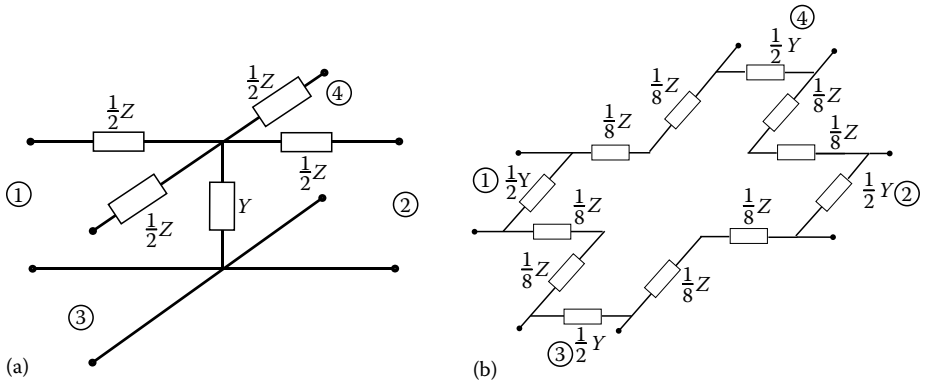

FIGURE 22.5 Lumped element implementations of the 2D TLM scattering matrix: (a) Shunt node and (b) series node [10].

representations are, respectively

$$\mathbf{Z}_{\text{shunt node}} = \tfrac{1}{2}Z \cdot \mathbf{I} + \frac{1}{Y} \cdot \mathbf{1} \tag{22.16a}$$

$$\mathbf{Y}_{\text{series node}} = \tfrac{1}{2}Y \cdot \mathbf{I} + \frac{1}{Z} \cdot \mathbf{1}, \tag{22.16b}$$

leading to the same dispersion relation for both types of nodes

$$\sin^2 \frac{\chi}{2} + \sin^2 \frac{\eta}{2} = \tfrac{1}{4}ZY. \tag{22.17}$$

Similar to the 1D case the dispersion relation reads for the case if the metamaterial cell is small compared with the wavelength $\chi^2 + \eta^2 = -ZY$, i.e., the metamaterial is isotropic. Physical realizations of the shunt-node structure yielding Drude dispersion are, e.g., mushroom structures [19,30] and their derivatives, including anisotropic variations [31]. The series-node structure was analyzed in Ref. [32]. Both types of structures can be stacked to yield a "volumetric" metamaterial [18]. Two-dimensional arrangements of split-ring/wire-grid setups [33] are physical realizations of Lorentz dispersion for the permeability within the shunt-node configuration.

In summary, the 2D materials proposed in the literature so far can be considered physical realizations of a scattering matrix-based discretization scheme.

22.4 Three-Dimensional Scalar Isotropic Metamaterials

In analogy to the derivations in the 2D case, let us consider a symmetric, reciprocal scattering matrix describing a lossless system for a scalar 3D scattering matrix. It has the form

$$\mathbf{S} = \tfrac{1}{3}\exp(-j\phi)\ (\mathbf{1} - 3 \cdot \mathbf{I})\,. \tag{22.18}$$

Conversion to impedance and admittance matrices yields

$$\mathbf{Z}_{\text{shunt}} = \tfrac{1}{2}Z \cdot \mathbf{I} + \frac{1}{Y} \cdot \mathbf{1} \tag{22.19a}$$

$$\mathbf{Y}_{\text{series}} = \tfrac{1}{2}Y \cdot \mathbf{I} + \frac{1}{Z} \cdot \mathbf{1}, \tag{22.19b}$$

leading to the same dispersion relation for both types of nodes

$$\sin^2 \frac{\chi}{2} + \sin^2 \frac{\eta}{2} + \sin^2 \frac{\xi}{2} = -\tfrac{1}{4}ZY. \tag{22.20}$$

If the metamaterial cell is small compared with the wavelength, the dispersion relation simplifies to $\chi^2 + \eta^2 + \xi^2 = -ZY$, i.e., the metamaterial is isotropic. The realization proposed in Ref. [8] implements Equation 22.19a. It has two extra series elements attached to the shunt element of the shunt-node TLM configuration (see Figure 22.6). These are then routed to the top and bottom. The drawback of this approach is that its physical realizations cannot be symmetric, as this would require an inductance of zero spatial extension.

A topological network representation of Equation 22.19b is shown in Figure 22.7 [34]. It is a series configuration of shunt elements $\frac{1}{2}Y$ and series elements $\frac{1}{6}Z$ along a closed loop. Ports ① to ⑥ span across the shunt elements. This loop of elements is wrapped around a cube symmetrically, exposing the ports at the faces of the cube. Coupling to adjacent cells is accomplished through these ports.

A physical realization yielding Drude dispersion for ϵ and μ is shown in Figure 22.8. It consists of six partially metallized pyramids, each having a thin strip running diagonally along a pyramid's base, realizing $\frac{1}{2}Y$, and two plates, which are separated by a gap. Each plate forms with the neighboring

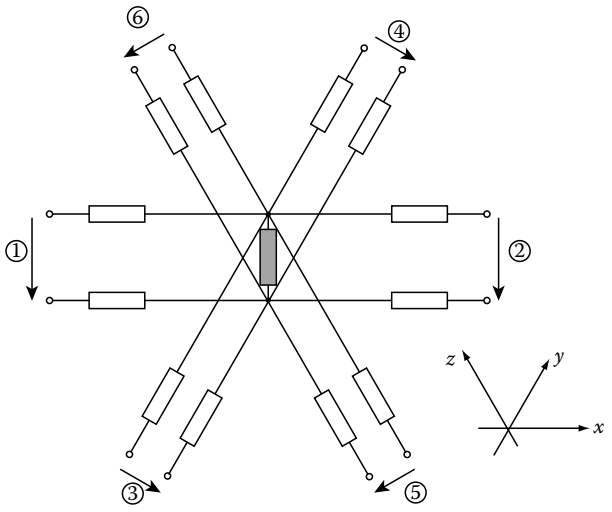

FIGURE 22.6 Shunt-node configuration of the scalar 3D metamaterial. Shunt element Y shown filled in gray, series elements $\frac{1}{4}Z$ shown unfilled.

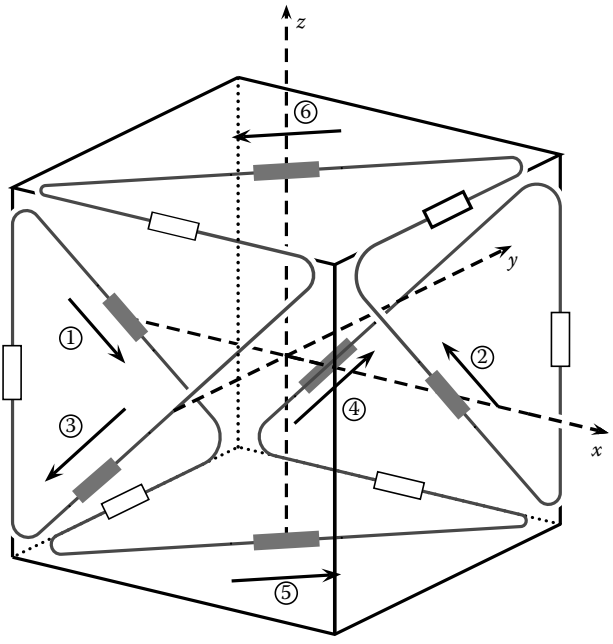

FIGURE 22.7 Series node configuration of a scalar 3D metamaterial implementing Equation 22.19b. Shunt elements $\frac{1}{2}Y$ shown in gray and series elements $\frac{1}{6}Z$ interconnecting shunt elements shown as white boxes. Two adjacent cells are connected at the ports spanning over the shunt elements, denoted by circled numbers.

pyramid's plate a capacitance, realizing $\frac{1}{6}Z$. The structure's geometry fulfills the symmetry of the point group T_h [35], following Schoenflies notation. This point group is defined as having inversion symmetry and $4_x \cdot 4_y$ symmetry, where n_p is the n-fold rotation around the p-axis, describing rotations along diagonals of the cube. The T_h symmetry ensures isotropic behavior of the cell [12].

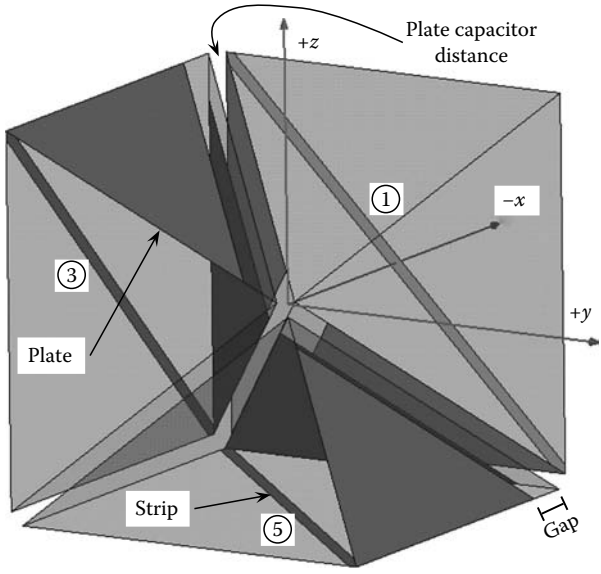

FIGURE 22.8 Realization of a scalar 3D metamaterial in series configuration; three of six partially surface-metallized pyramids shown, the remaining three pyramids are determined by inversion symmetry. Port labels ① to ⑥ and axis definitions correspond to Figure 22.7. Metal shown as dark gray. Dielectric shown as transparent light gray.

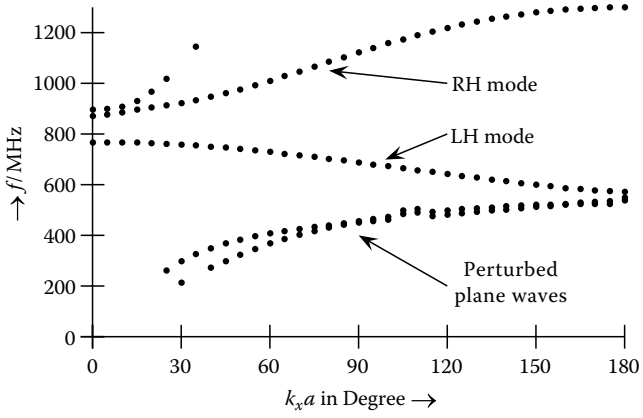

FIGURE 22.9 Dispersion diagram obtained by full-wave eigenmode simulation using the commercial FEM package HFSS. Each dot represents a numerical solution.

Full-wave simulations were carried out using the commercial FEM package HFSS. The geometry parameters used in the simulation are unit cell size 20 mm, capacitor plate distance 280 μm, inductor strip width 270 μm, and separation gap between capacitor plates 2 mm. No dielectric was included in the simulation, and conductors have copper conductivity 5.8×10^7 S/m.

Full-wave eigenmode results for the Γ–X part of the Brillouin zone are shown in Figure 22.9. The lowest two eigenmodes correspond to perturbed plane wave modes [36], which have their origin at $(k = 0, f = 0)$. A left-handed band, i.e., a band with negative effective refractive index, extends from 570 MHz up to the electric plasmon resonance frequency 767 MHz, yielding a 30 % relative bandwidth of left-handed operation. At the magnetic plasmon resonance frequency of 872 MHz,

a right-handed band starts, extending up to 1301 MHz. An additional mode not predicted by network theory spans the right-handed mode, but the frequency range of the left-handed operation is monomodal. Quality factors of the left-handed eigenmodes are ≈ 80. For the frequency range of the left-handed operation the unit cell size is smaller than $\lambda/20$, fulfilling the common metamaterial definitions [15,27,37]. The T_h symmetry of the structure ensures isotropic behavior for operation in the vicinity of the Γ-point.

It is important to note that this 3D isotropic metamaterial supports only one polarization, as can be seen both from the derivation as well as the full-wave simulations, in which the left-handed and right-handed modes are not degenerate. Anisotropy of the structure can easily be achieved by varying the strips and plates of each of the six pyramids making up a unit cell or by compressing the unit cell unevenly along different principal axes.

22.5 Three-Dimensional Vectorial Isotropic Metamaterial Based on the Rotated TLM Method

While Section 22.4 discusses scalar 3D metamaterial structures, this section treats a vectorial structure, i.e., one in which two polarizations independently propagate. The foundation of this structure is the symmetric condensed-node TLM representation of discrete electrodynamics, which contains all the information of the discretized Maxwell's equations [13,38–40]: Space is discretized into cubes, and at each face the tangential fields are sampled at the center of each cube surface. Hence each face has two electrical and two magnetic field components, which can be formulated as two incident and two scattered waves per cubic face [13,40,41]. The scattering can therefore be described as a 12-port depicted in Figure 22.10. It can be represented by a scattering matrix **S**; its structure is well known and was, e.g., derived by the method of moments [40]. In Ref. [4] it was also shown that

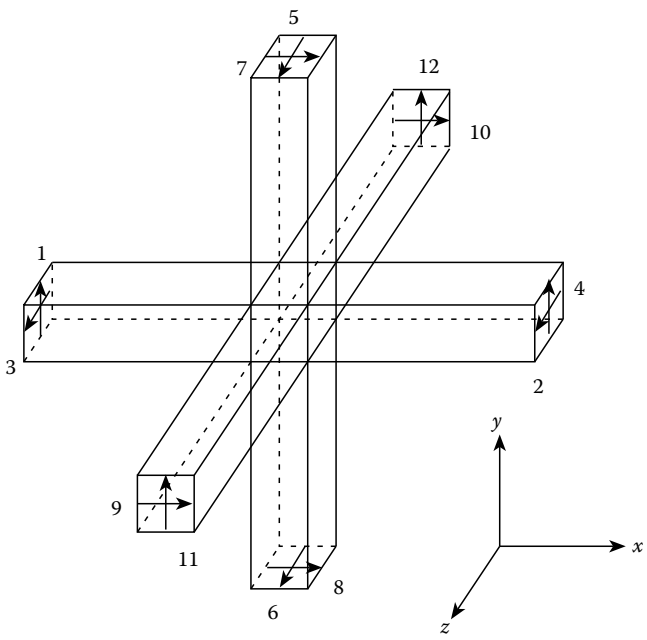

FIGURE 22.10 General space-discretizing TLM 12-port. (From Zedler, M., Caloz, C., and Russer, P., *IEEE Trans. Microw. Theory Technol.*, IMS Special Issue, 55(12), 2930, 2007. With permission.)

using only symmetry, reciprocity, and losslessness considerations one can also derive the symmetric condensed-node TLM scattering matrix

$$\mathbf{S} = \exp(-j\phi)\begin{bmatrix} \mathbf{0} & \mathbf{S}_A & \mathbf{S}_A^T \\ \mathbf{S}_A^T & \mathbf{0} & \mathbf{S}_A \\ \mathbf{S}_A & \mathbf{S}_A^T & \mathbf{0} \end{bmatrix} \quad \text{with } \mathbf{S}_A = \frac{1}{2}\begin{bmatrix} 0 & 0 & 1 & -1 \\ 0 & 0 & -1 & 1 \\ 1 & 1 & 0 & 0 \\ 1 & 1 & 0 & 0 \end{bmatrix}. \tag{22.21}$$

In order to be able to synthesize a metamaterial, i.e., a physical realization of the computing scheme, a transformation of the symmetric condensed-node TLM scheme needs to be applied. The 12-port cell can be decomposed into two independent six-ports $\tilde{\mathbf{S}}$ and $-\tilde{\mathbf{S}}$ by the coordinate transformation [41,42]

$$\mathbf{P}^T \cdot \mathbf{S} \cdot \mathbf{P} = \begin{bmatrix} \tilde{\mathbf{S}} & 0 \\ 0 & -\tilde{\mathbf{S}} \end{bmatrix} \quad \mathbf{P} = \begin{bmatrix} \mathbf{P}_{0a} & \mathbf{0} & \mathbf{0} & \mathbf{P}_{0b} & \mathbf{0} & \mathbf{0} \\ \mathbf{0} & \mathbf{P}_{0a} & \mathbf{0} & \mathbf{0} & \mathbf{P}_{0b} & \mathbf{0} \\ \mathbf{0} & \mathbf{0} & \mathbf{P}_{0a} & \mathbf{0} & \mathbf{0} & \mathbf{P}_{0b} \end{bmatrix} \tag{22.22a}$$

$$\mathbf{P}_{0a}^T = \begin{bmatrix} 1 & 0 & -1 & 0 \\ 0 & 1 & 0 & 1 \end{bmatrix} \quad \mathbf{P}_{0b}^T = \begin{bmatrix} 1 & 0 & 1 & 0 \\ 0 & 1 & 0 & -1 \end{bmatrix}. \tag{22.22b}$$

This corresponds to a rotation of the polarizations by 45°, as shown in Figure 22.11. The transformed scattering matrix is given by

$$\tilde{\mathbf{S}} = \exp(-j\phi)\begin{bmatrix} \mathbf{0} & \tilde{\mathbf{S}}_0 & \tilde{\mathbf{S}}_0^T \\ \tilde{\mathbf{S}}_0^T & \mathbf{0} & \tilde{\mathbf{S}}_0 \\ \tilde{\mathbf{S}}_0 & \tilde{\mathbf{S}}_0^T & \mathbf{0} \end{bmatrix} \quad \tilde{\mathbf{S}}_0 = \tfrac{1}{2}\begin{bmatrix} -1 & -1 \\ 1 & 1 \end{bmatrix}. \tag{22.23}$$

In this contribution the two independent, half-cell six-ports described by $\tilde{\mathbf{S}}$ and $-\tilde{\mathbf{S}}$ are called "A" and "$\bar{\text{A}}$" cells, respectively. A TLM cell that represents both polarizations at each surface can be established by either nesting the six-port structures of the "A" and "$\bar{\text{A}}$" half-cells or by a cluster of eight half-cells with alternating "A" and "$\bar{\text{A}}$" cells [41].

An elementary metamaterial cell may be conceived on the basis of rotated TLM cells, by inserting reactances in series to the six cell ports and four admittances connecting the series reactances at a

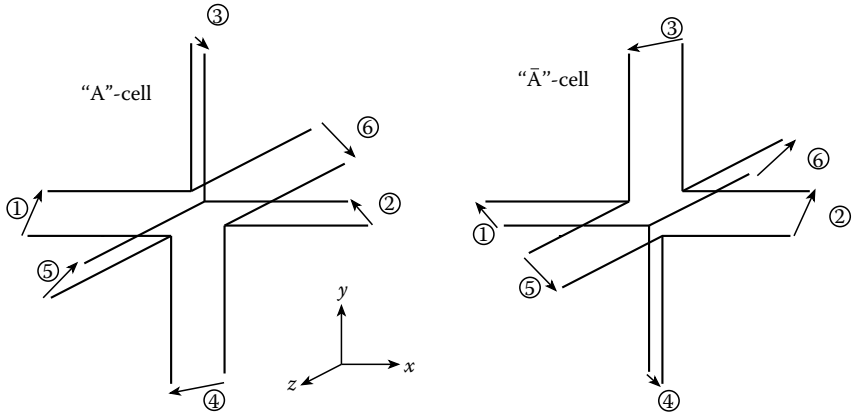

FIGURE 22.11 Rotated TLM half unit cells implementing $\tilde{\mathbf{S}}$. The complete unit cell is constituted by the merging of both half-cells. (From Zedler, M. and Russer, P., *International Microwave Symposium Digest*, San Francisco, CA, 2006, pp. 1477–1480. With permission.)

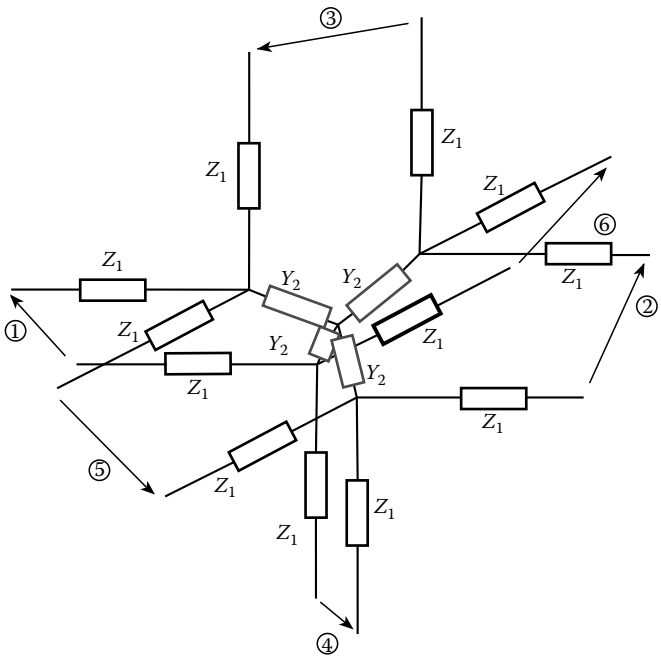

FIGURE 22.12 Lumped element model of a rotated TLM half unit cell implementing the structure shown in Figure 22.11. Shunt elements Y_2 are shown in gray, and series elements denoted are by Z_1. (From Zedler, M., Caloz, C., and Russer, P., *IEEE Trans. Microw. Theory Technol.*, IMS Special Issue, 55(12), 2930, 2007. With permission.)

central node, as shown in Figure 22.12. The formal proof of equivalence between this topology and the topology required by Equation 22.23 was given in Ref. [3]. Further details can be found in Ref. [4].

22.5.1 Dispersion Behavior

The dispersion relation of a rotated TLM metamaterial consisting of only "A"-cells is [3]

$$\tfrac{1}{4}(3 - \cos\chi\cos\eta - \cos\chi\cos\xi - \cos\eta\cos\xi) = (1 + Z_1 Y_2)^2 . \tag{22.24}$$

For small wave numbers the left-hand side of Equation 22.24 simplifies to $(\chi^2 + \eta^2 + \xi^2)/4$, i.e., the metamaterial is isotropic. Comparing the dispersion relation of Equation 22.24 with that of a 1D/2D/scalar 3D metamaterial (Equations 22.5a, 22.17, and 22.20), one notes that the right-hand side in the rotated TLM case contains terms Z^2 and Y^2, which leads to a doubling of the number of frequency bands. The Bloch impedance of the rotated TLM cell equals that of the 1D double-Drude (CRLH) cell

$$Z_{\text{Bloch}} = \sqrt{Z_1 Y_2^{-1}}\sqrt{2 + Z_1 Y_2}. \tag{22.25}$$

This shows that there is no angular dispersion, as Equation 22.25 is independent on χ, η, and ξ. This property is unique to 3D TLM and FDTD schemes and is not achievable with scalar discretizations.

Using a double-Drude unit cell (see Section 22.2.1.1) one obtains the unit cell for the rotated TLM metamaterial as shown in Figure 22.13. Its dispersion diagram is depicted in Figure 22.14 for the resonance-balanced and resonance-unbalanced cases, yielding two left-handed and two right-handed bands. A discussion of the frequency behavior of the Bloch impedance for these two cases can be found in Ref. [4].

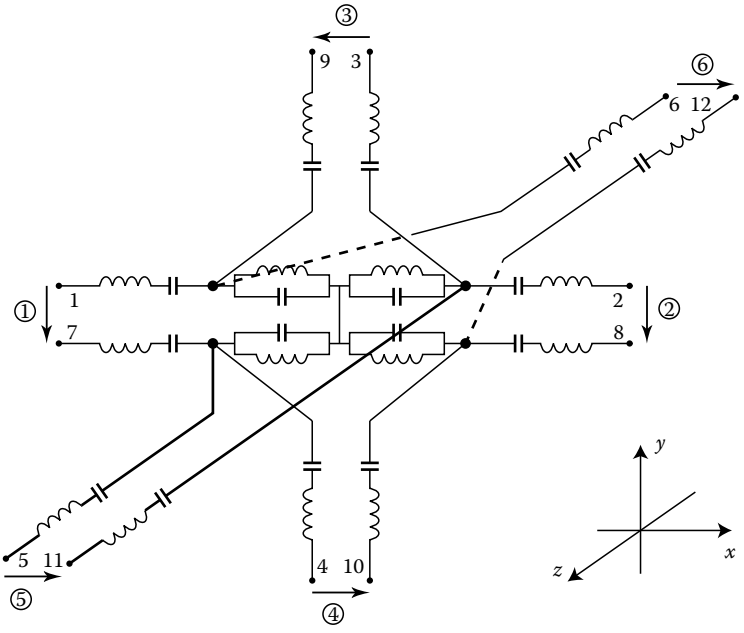

FIGURE 22.13 Double-Drude-rotated TLM metamaterial half unit cell. (From Zedler, M. and Russer, P., *International Microwave Symposium Digest*, San Francisco, CA, 2006, pp. 1477–1480. With permission.)

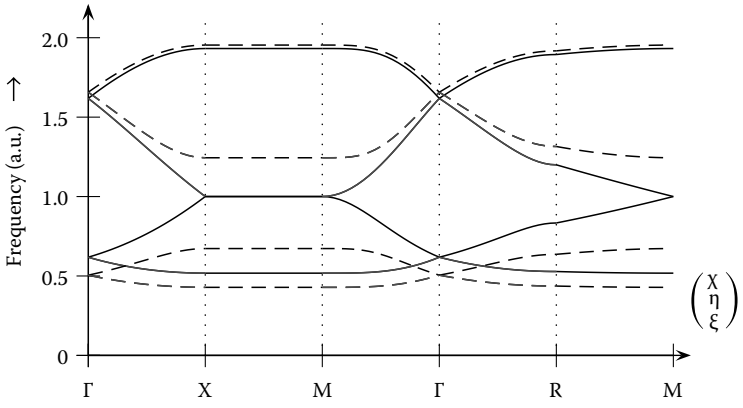

FIGURE 22.14 Dispersion diagram for the 3D, double-Drude-rotated, TLM metamaterial for the balanced-resonance case (solid line) and unbalanced-resonance (dashed line) case. (From Zedler, M., Caloz, C., and Russer, P., *IEEE Trans. Microw. Theory Technol.*, IMS Special Issue, 55(12), 2930, 2007. With permission.)

22.5.2 Physical Realization of the Rotated TLM Metamaterial

The proposed realization of the double-Drude-rotated, TLM metamaterial, corresponding to the lumped element network of Figure 22.13, is depicted in Figure 22.15. Shunt inductors are implemented by wires connected to a common center point, and series capacitors are implemented by metal–insulator–metal plates located between adjacent unit cells. Figure 22.15a shows the two half

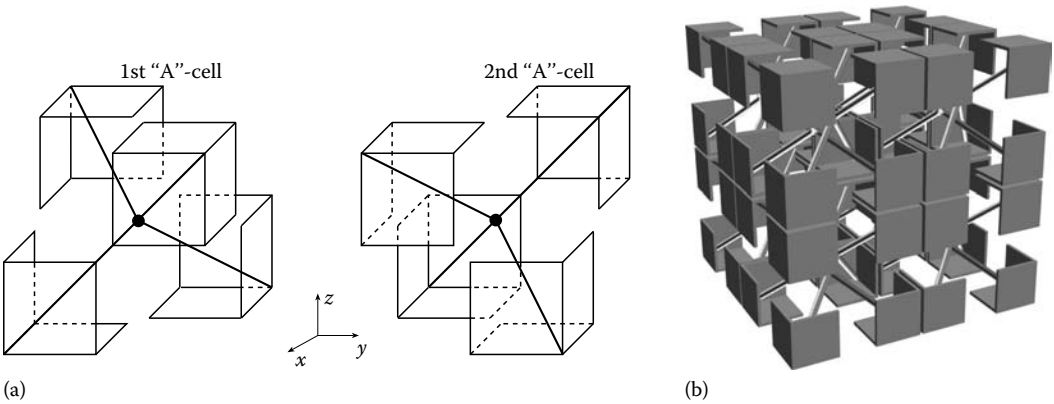

FIGURE 22.15 3D, double-Drude-rotated, TLM metamaterial realization. (a) "A"-type half unit cells and (b) a complete 2 × 2 × 2 structure. (From Zedler, M., Caloz, C., and Russer, P., *IEEE Trans. Microw. Theory Technol.*, IMS Special Issue, 55(12), 2930, 2007. With permission.)

unit cells in the proper orientation to be then nested. Figure 22.15(b) shows a cluster of 2 × 2 × 2 nested unit cells.

22.5.3 Parasitic Modes

Unconnected metamaterial structures may allow the wave propagation of an additional mode within the structure, usually referred to as the perturbed plane wave mode [43] and sometimes also referred to as "acoustic branch" due to analogy with solid-state physics. In order to avoid mode splitting and coupling to this parasitic mode, the unit cell can either be scaled appropriately to have the metamaterial mode and the parasitic mode reside at different frequencies [18,36]. In 2D configurations it is also possible to inhibit the parasitic mode by appropriate modifications to the unit cell [18].

22.5.4 Signal Propagation through the Cell

The unit cell is a balanced structure: It has a virtual ground that is a zero voltage point due to the symmetry of the structure rather than due to physical connection to a physical ground. It consists of two nested cells, the two cells shown in Figure 22.15a. These two cells are electromagnetically decoupled in the sense that they support electromagnetic waves of independent orthogonal polarizations in each of the directions of space, x, y, and z.

To explain wave propagation through the structure, let us consider in some detail the example of a $-xz$-polarized (electric field along the $z = -x$ direction) plane (transverse) wave propagating along the y-direction and incident on the structure at the level of a unit cell.

Consider the first "A" half-cell (left-hand side of Figure 22.15a), displayed in Figure 22.16. In this cell, the incident plane wave produces a symmetric voltage difference ($+V$ and $-V$) between the two patches at the input face of the half-cell (left-hand side of the structure in Figure 22.15a). These two patches form capacitors, with the patches printed on the opposite faces of the thin substrate slabs, which store electric energy and provide the required series capacitance C_L corresponding to negative permeability. Due to these capacitors, the incident transverse electric field becomes locally longitudinal between the two plates of the capacitors. The voltages at the plates inside the structure are $V' = V - ZI$, where I is the current flowing into the incident port. From this point, the wave "sees" the wire environment. Due to the symmetry of the structure and the symmetrical incident

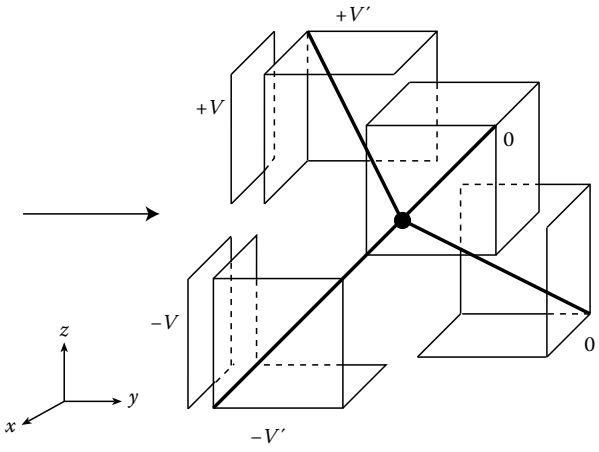

FIGURE 22.16 Signal Propagation through the cell. (From Zedler, M., Caloz, C., and Russer, P., *IEEE Trans. Microw. Theory Technol.*, IMS Special Issue, 55(12), 2930, 2007. With permission.)

voltages, propagation is prohibited along the straight (y) direction, since the field is short-circuited at the center node (virtual ground), consistently with the fact that the scattering parameter $\tilde{s}_{21}$ is zero in Equation 22.23.

Although propagation in the axial direction is not allowed, off-axis propagation occurs through the four lateral faces of the unit cell, along the positive and negative x- and z-directions. Figure 22.16 shows how this is realized in the 3D cell as a result of the differential voltages and symmetry of the structure, which lead to the voltage difference $\pm V'$ at the off-axis ports. Since the wave is deflected toward the four lateral faces in the unit cell, the magnetic flux circulates around the two wire branches extending from the corner voltage points to the virtual ground point, which corresponds to magnetic energy storage and generates the required shunt inductance L_L corresponding to negative permittivity. Note that the directions of the fields indicated in Figure 22.16 correspond to the other four independent scattering parameters of Equation 22.23.

Consider next the second "A" half-cell (right-hand side of Figure 22.15a). In this cell, the incident $-xz$-polarized electric field does not encounter any metallization at the input plane of the cell, which is therefore transparent to it. The plates with the same polarization at the output plane belong to the next "A" half-cell.

When many cells are nested, "A-A" are cascaded along the three directions of space. Plane wave propagation is obtained by meander-like scattering between unit cells, which is in agreement with the scattering-type propagation in the numerical technique TLM.

22.5.5 Experimental Verification

The proposed unit cell prototype was fabricated as shown in Figure 22.17. Plate capacitors are realized in PCB technology with patches on both sides of the substrate, which ensures accurate C_L values. Inductors are realized by rigid wires. The unit cell edge length is 2 cm, the substrate is Rogers 4350B 10 mil, and the left-handed values are $L_L \approx 17.3$ nH and $C_L \approx 5.4$ pF.

This unit cell prototype was measured using a two-port vector network analyzer connected via baluns (microstrip to parallel-strip transitions) to two arbitrary nonaligned ports, whereas the remaining ports are terminated with $Z_L = 50\,\Omega$ resistors. Note that this excitation corresponds to wave propagation through the structure, because the rotated TLM structure is a network with

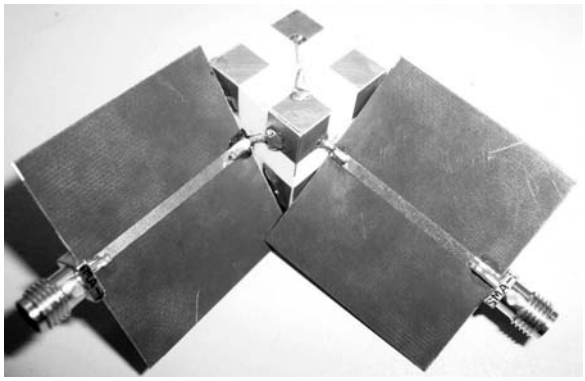

FIGURE 22.17 3D double-Drude-rotated TLM unit cell with the input and output baluns required for the differential excitation of the measurement setup. (From Zedler, M., Caloz, C., and Russer, P., *IEEE Trans. Microw. Theory Technol.*, IMS Special Issue, 55(12), 2930, 2007. With permission.)

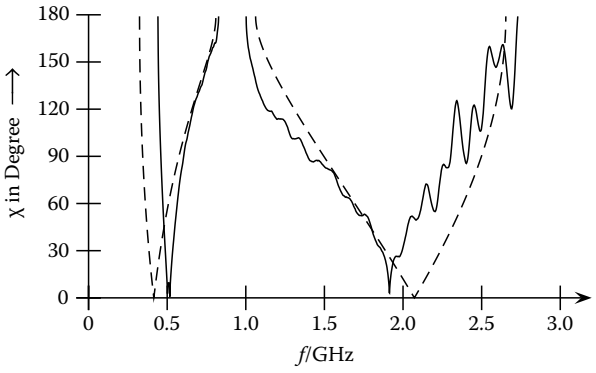

FIGURE 22.18 Dispersion diagram for propagation along a principal axis extracted from a measurement of the setup shown in Figure 22.17. Solid line: measurements, dashed line: circuit simulator results using lumped elements only. (From Zedler, M., Caloz, C., and Russer, P., *IEEE Trans. Microw. Theory Technol.*, IMS Special Issue, 55(12), 2930, 2007. With permission.)

well-defined ports. On the basis of the rotated TLM metamaterial, it suffices to verify experimentally that the metamaterial cell indeed acts like the lumped circuit of Figure 22.12. Under this assumption the behavior of the entire structure can be inferred from the response of a single unit cell; details on the extraction procedure can be found in Refs. [4,44].

A comparison of the measured dispersion relation and that of a lumped element circuit model is depicted in Figure 22.18. It shows good agreement, with circuit simulation results up to 2.2 GHz. The expected two left-handed and two right-handed frequency bands are clearly visible, therefore verifying the behavior of the rotated TLM metamaterial.

The interested reader can find further information on the rotated TLM metamaterial in Refs. [45, 46]; in the former full-wave simulation results of a finite slab consisting of 24 × 24 × 6 illuminated by a Hertzian dipole are presented, the latter describes an efficient approach to simulate large-scale structures containing "normal" materials and metamaterials.

22.6 Fabrication of 3D Metamaterials

Three-dimensional metamaterials are challenging to fabricate; on one hand the unit cells are more complex compared with the 1D and 2D case, and on the other hand the number of cells required for a setup increases: Assuming ten metamaterial cells per wavelength and a structure size of five wavelength, this yields $50^3 = 125,000$ cells. In order to overcome these problems we present two approaches: decomposition of the unit cell into polyhedrons and topology-invariant planarization.

22.6.1 Decomposition into Polyhedrons

Three-dimensional metamaterials proposed so far in the literature all use cubic cells to discretize space [2,4–7,9]. These unit cells can be decomposed into polyhedrons [47] so that all metal parts lie on polyhedron surfaces. These structures can be fabricated with technologies such as (2-component)-injection molding [48], 3D-molded interconnect device technology (3D-MID) [49], hot embossing [50], plasma activation and printing [51], physical vapor deposition [52], and laser direct structuring [53]. For prototyping 3D printers can be used. As shown subsequently, the polyhedrons are primarily a mechanical supporting structure. Electric field penetration into the polyhedrons is low, making the metamaterial behavior insensitive to substrate losses within the polyhedrons. The above mentioned fabricational approaches limit the achievable cell size to the order of millimeters, but one may also envision polyhedron decomposition for micro/nanostructuring.

In the following we present decomposition into polyhedrons for the rotated TLM structure [3], the Kron structure [2], and the scalar 3D structure in series configuration (see Section 22.4).

22.6.1.1 Rotated TLM Unit Cell

The unit cell depicted in Figure 22.15 can be decomposed into pyramids (see Figure 22.19) and compounds of pyramids (see Figures 22.20 through 22.23). Each of these offer specific advantages and disadvantages:

- A single pyramid offers the simplest casting mold (see Figure 22.19).
- Two compound pyramids offer a simple casting mold and require solely planar metallization techniques (see Figure 22.20).

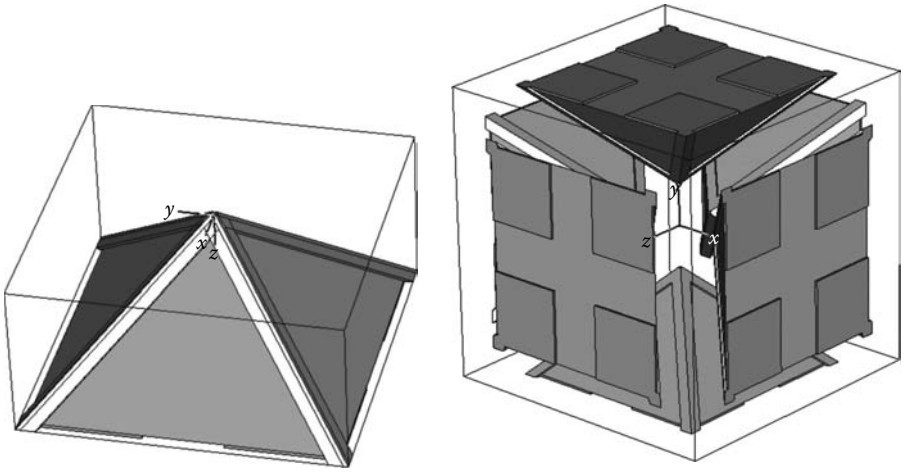

(e) (f)

FIGURE 22.19 Decomposition of a rotated TLM unit cell into pyramids. Spacing between cells achieved through, e.g., thin dielectric sheets and a mechanical press fit.

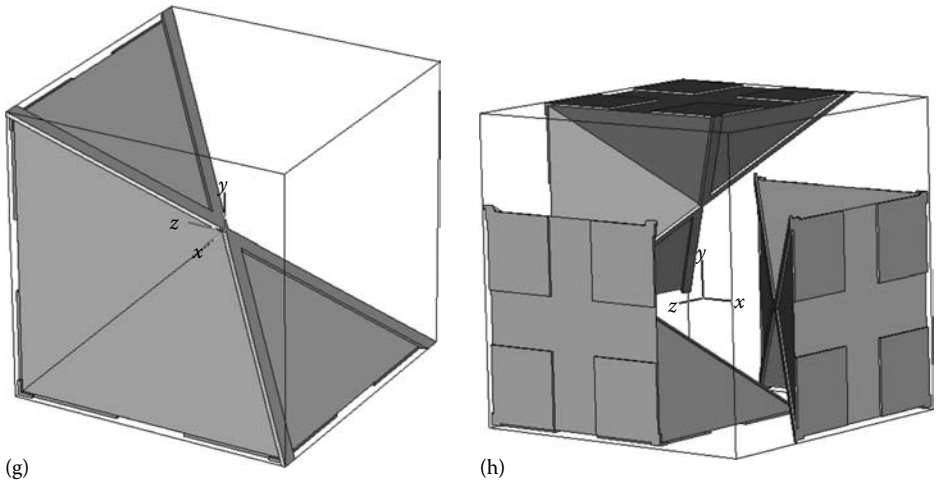

(g) (h)

FIGURE 22.20 Compound polyhedron consisting of two pyramids.

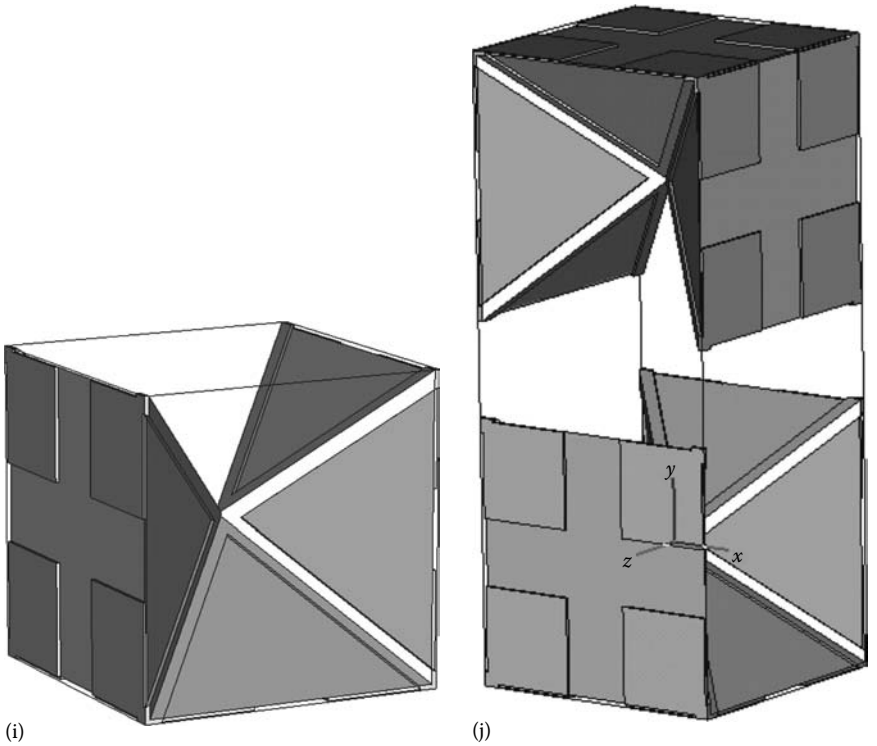

(i) (j)

FIGURE 22.21 Compound polyhedron consisting of three pyramids, yielding a mechanically self-aligning structure.

- Three compound pyramids forming a half-cell, offering a self-aligning structure when two half-cells are set into each other (see Figure 22.21).
- Merging half-cells to form a half-cell line (see Figure 22.22), with intercell capacitive coupling realized using capacitive coupling patches. The latter approach is described in detail in Section 22.6.2.

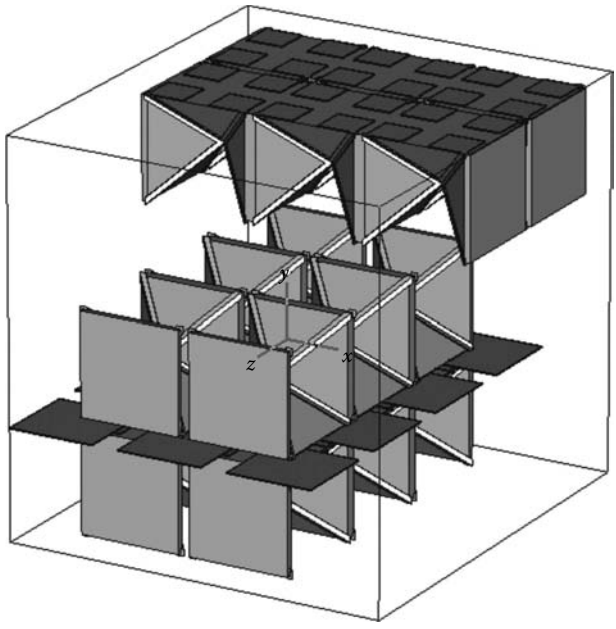

FIGURE 22.22 Half-cells as in Figure 22.21 merged to yield a half-cell line.

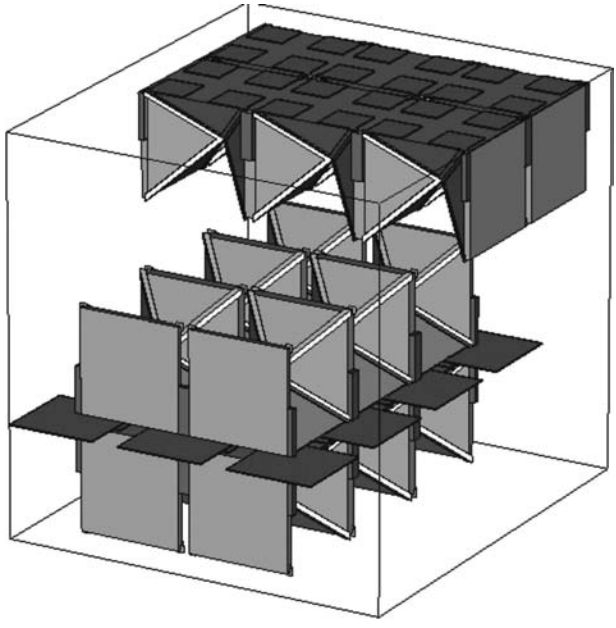

FIGURE 22.23 Several half-cell lines mechanically connected by dielectric element connected to form a half-cell plane.

- Merging half-cell lines to half-cell planes, as shown in Figure 22.23. In this figure the additional dielectric elements compared with Figure 22.22 are shown in a darker shade of gray. These extra elements serve only mechanical connection purposes.
- Inductive connections may be lay out as a meander to decrease the magnetic plasma frequency (see Figure 22.24).

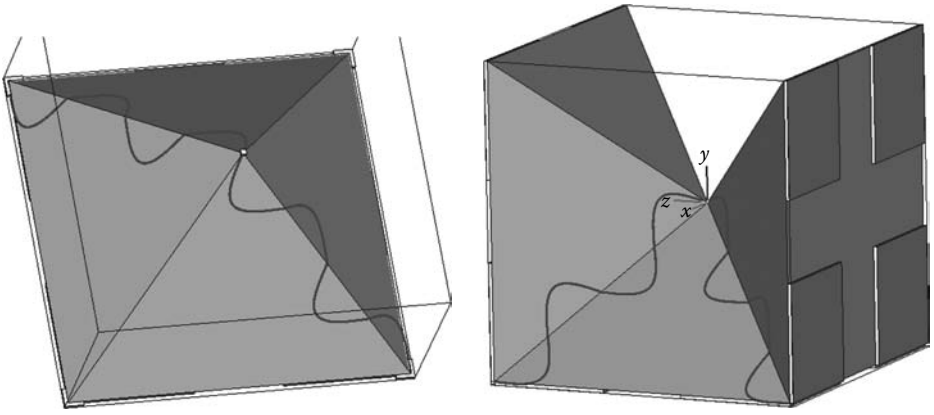

FIGURE 22.24 Variations of inductive connections.

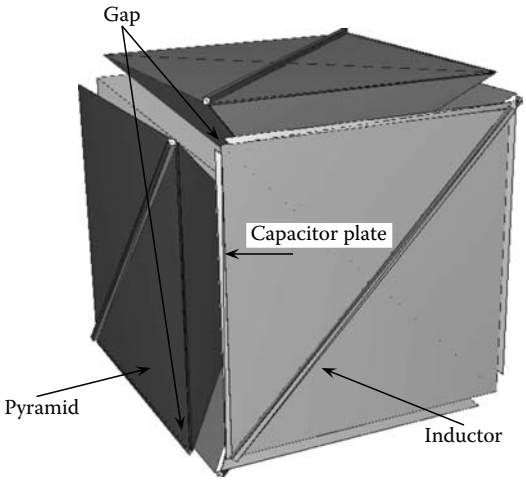

FIGURE 22.25 Pyramidal decomposition of the scalar 3D metamaterial cell in series configuration.

22.6.1.2 Scalar 3D Metamaterial Cell in Series Configuration

A physical realization of the scalar 3D metamaterial in series configuration is shown in Figure 22.25. This geometry has inversion symmetry and can be decomposed into pyramids. Different from the rotated TLM structure, six pyramids forming a unit cell need to be assembled with a thin spacer in order not to short cut the capacitive coupling.

22.6.1.3 Kron's Unit Cell

Another vectorial metamaterial was proposed in Ref. [2] which is based on Kron's equivalent circuit representation of free space [39]. The inverted configuration yielding left-handed behavior is shown in Figure 22.26a, and its physical realization is shown in Figure 22.26b. Wires along the edges of the unit cell implement inductors, which are interconnected by diagonal plate capacitors. Although this unit cell is seemingly highly complicated, in fact a shift of the unit cell boundaries by half a cell along

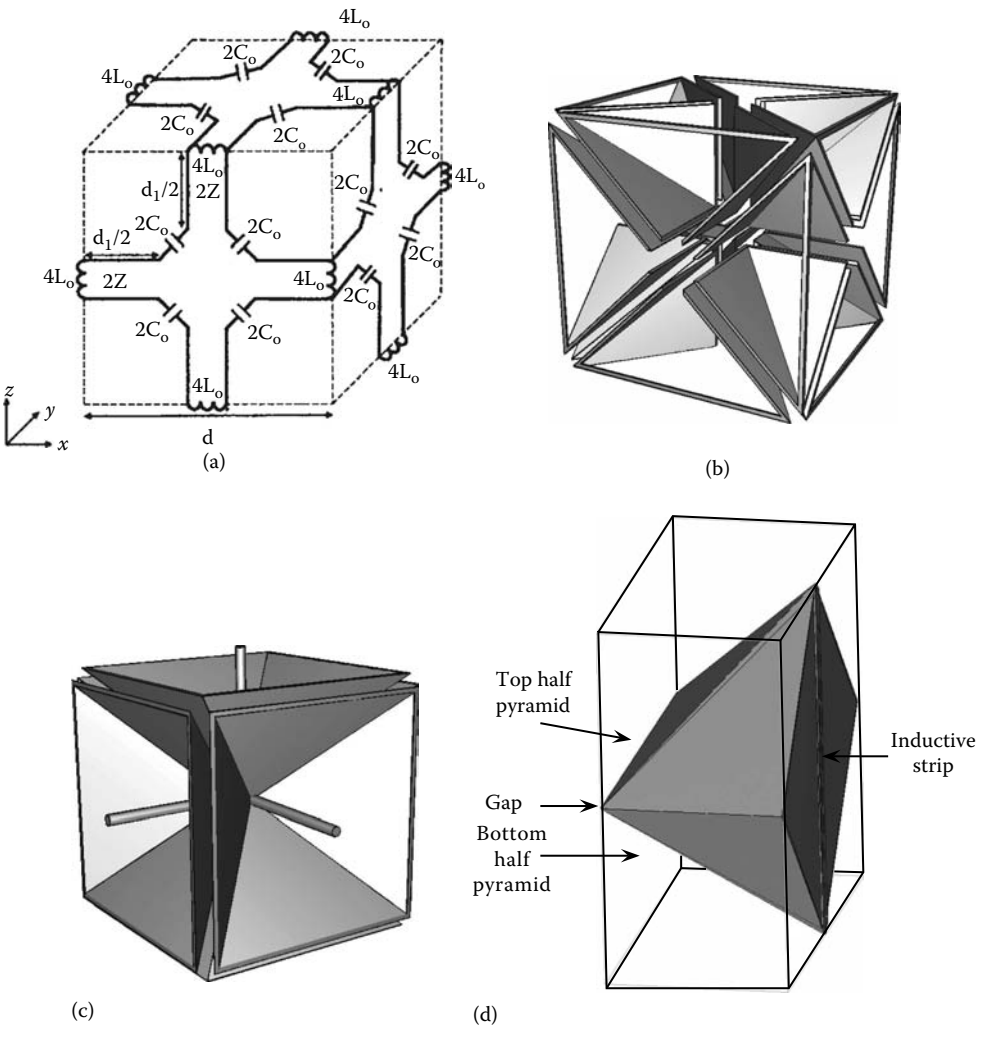

FIGURE 22.26 Decomposition of Kron's cell into polyhedrons. (a) Kron's cell-based metamaterial, (b) physical implementation of Kron's cell. Inductors along the edges implemented by wires and capacitive coupling between inductors by diagonally oriented plate capacitors, (c) identical structure to Figure 22.26b, but unit cell boundaries shifted along all directions by half a cell, (d) decomposition of Kron's unit cell elementary polyhedron consisting of two half pyramids. (Reprinted from Grbic, A. and Eleftheriades, G., *J. Appl. Phys.*, 98, 043 106–1, 2005. With permission.)

all directions yields the simpler appearing structure shown in Figure 22.26c. This structure can be decomposed into polyhedron as shown in Figure 22.26d, which is a symmetrically cut octaeder. On the cut face rests an inductive strip, connecting the tips of the half pyramids. The remaining faces of the cut octaeder are metallized, leaving a gap between the half pyramids. Another approach is a fully surface metallized octaeder with a drilled metallized hole connecting the tips.

22.6.2 Topology-Invariant Planarization

Although fully 3D fabrication, as proposed in Section 22.6.1, offers the highest level of isotropy and design flexibility, planar fabrication techniques are much more widespread. In Refs. [4,54,55]

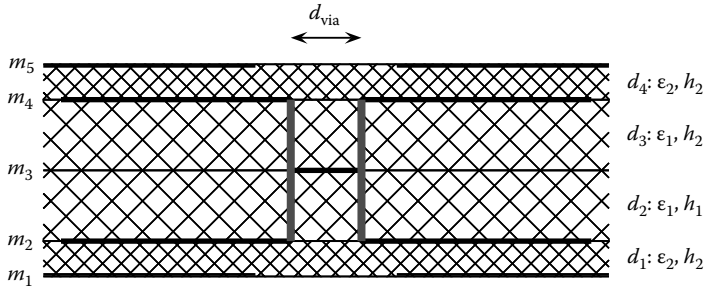

FIGURE 22.27 Cross-sectional view of the planarized double-Drude-rotated TLM metamaterial. ϵ_1: low permittivity; ϵ_2: high permittivity; h_2 as thin as possible. Vertical thick lines: buried via. Via distance d_{via} as small as possible. m_i denotes the metallization layers in the unit cell. If multiple cells are stacked then the adjacent top and bottom layers m_1 and m_5 can be merged into one layer. (From Zedler, M., Caloz, C., and Russer, P., *IEEE Trans. Microw. Theory Technol.*, IMS Special Issue, 55(12), 2930, 2007. With permission.)

topology-invariant planarized geometries of the rotated TLM metamaterial were proposed and analyzed numerically as well as algebraically, yielding design guidelines for this geometry. These are presented here and extended to also cover the novel scalar 3D structure described in Section 22.4.

22.6.2.1 Rotated TLM Structure

Figure 22.27 shows the cross-sectional view of the planarized, rotated, TLM metamaterial cell. Figure 22.28a shows the corresponding metal layers. The layers m_1 and m_5 at the bottom and top correspond to the patches in the cell corners in Figure 22.15. Layer m_5 is identical with layer m_1 of the overlying cell. Each of the four patches of the layers m_1 and m_5, respectively, is continued into the four neighboring cells at every corner. These patches produce the capacitive coupling with the neighboring cells via the patches of layers m_1 and m_4. In the layers m_2 and m_4 the strips are connected to the patches with insets that increase the inductance. Together with the through-connections through layers d_2 and d_3 these strips produce the required inductive coupling. The vertical capacitive coupling is achieved through two series capacitances $m_4 \rightarrow m_5 \rightarrow m_2'$ (where the prime denotes the next unit cell). In-plane capacitive coupling is achieved through two series capacitances $m_4 \rightarrow m_5 \rightarrow m_4'$.

An alternative configuration requiring no metal–insulator–metal patches is depicted in Figure 22.28b: Here the vertical capacitive coupling is $m_4 \rightarrow m_2'$. The in-plane capacitive coupling is achieved by interdigital capacitors $m_4 \rightarrow m_4'$. In addition to the advantage of requiring less layers per unit cell, this configuration also alleviates fabrication tolerances with respect to dielectric layer thicknesses, as the two layers d_1/d_4 are merged into one layer. This advantage comes at a cost; both C_{L} and L_{R} of the vertical plate capacitors and the in-plane interdigital capacitors need to be carefully matched.

22.6.2.2 Scalar 3D Metamaterial in Series Configuration

The network topology of the scalar 3D metamaterial in series configuration is shown in Figure 22.7. A planarized physical realization of this topology yielding Drude dispersion for the permeability and permittivity is depicted in Figure 22.32: Layer m_1 provides the in-plane elements of the 2D scalar series configuration (see also Figure 22.5b). Black parts denote metallization, hatches denote interdigital capacitors, and red circles are connection points of vias. The stubs connecting to the edge of the unit cell form half of the shunt inductance, IDC the series capacitance. Two vias located in the bottom left connect to layer m_2, and the two vias in the top right connect to the above cell layer m_4. In layer m_2 vias connect to metal plates. These form together with plates in layer m_3 two

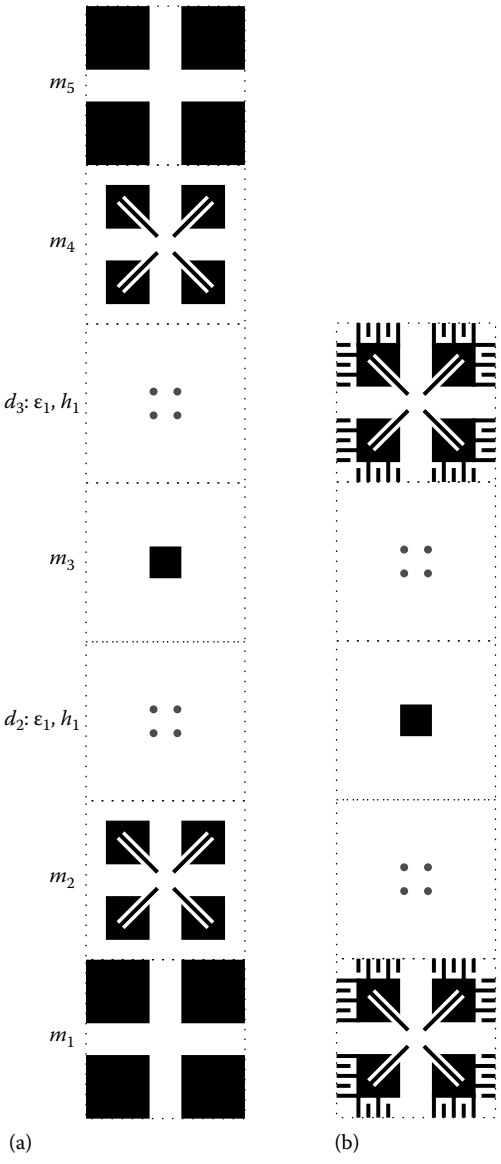

FIGURE 22.28 Exploded top view of the different metal layers for the structure of Figure 22.27: (a) MIM capacitor implementation and (b) interdigital capacitor implementation. (From Zedler, M., Caloz, C., and Russer, P., *IEEE Trans. Microw. Theory Technol.*, IMS Special Issue, 55(12), 2930, 2007. With permission.)

series plate capacitors. In layer m_3 inductive coupling is implemented by a thin strip, shown in red for clarity. Metallic plates in layer m_4 form a series capacitance with those in layer m_3 toward the next cell located below the current cell. There two vias connect to the next cell's layer m_1 in the top right.

The shape of the metallic layers m_2, m_3, and m_4 can be varied to tune the shunt inductance of layer m_3 and the vertical series capacitance. Thus together with the choice of layer dielectrics and layer thicknesses, the anisotropy of the planarized structure can be well controlled.

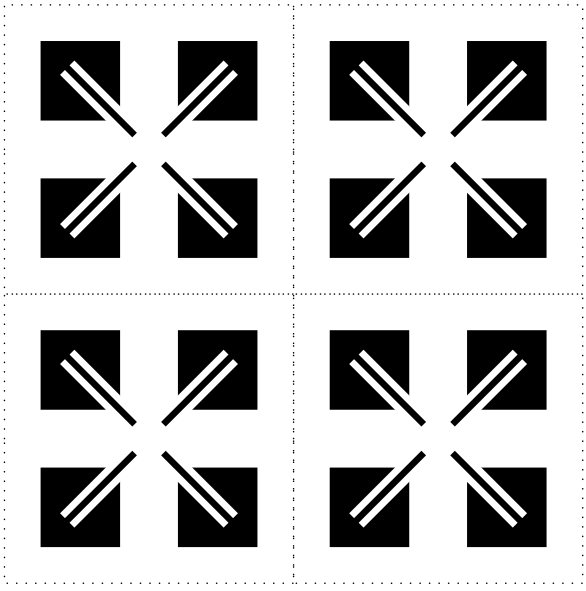

FIGURE 22.29 Top view of layer m_2/m_4 of 2×2 cells of the structure depicted in Figure 22.28a. (From Zedler, M., Caloz, C., and Russer, P., *IEEE Trans. Microw. Theory Technol.*, IMS Special Issue, 55(12), 2930, 2007. With permission.)

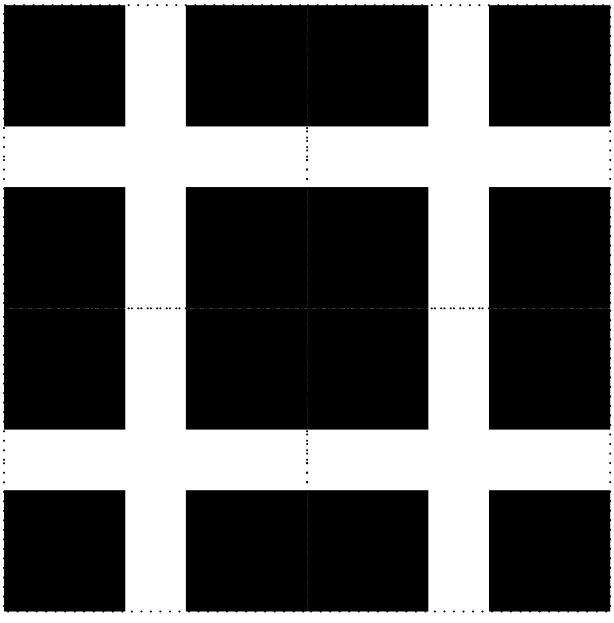

FIGURE 22.30 Top view of layer m_1/m_5 of 2×2 cells of the structure depicted in Figure 22.28a. The coupling patches provide the series capacitive coupling between in-plane adjacent cells. (From Zedler, M., Caloz, C., and Russer, P., *IEEE Trans. Microw. Theory Technol.*, IMS Special Issue, 55(12), 2930, 2007. With permission.)

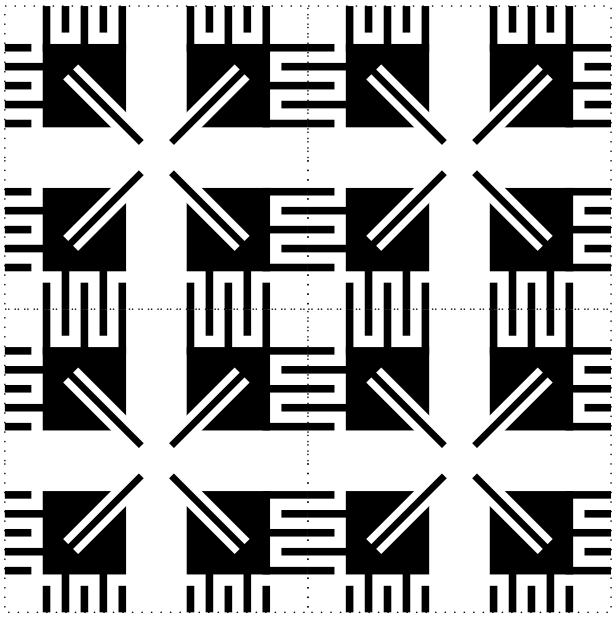

FIGURE 22.31 Top view of layer m_2/m_4 of 2 × 2 cells of the structure depicted in Figure 22.28b. (From Zedler, M., Caloz, C., and Russer, P., *IEEE Trans. Microw. Theory Technol.*, IMS Special Issue, 55(12), 2930, 2007. With permission.)

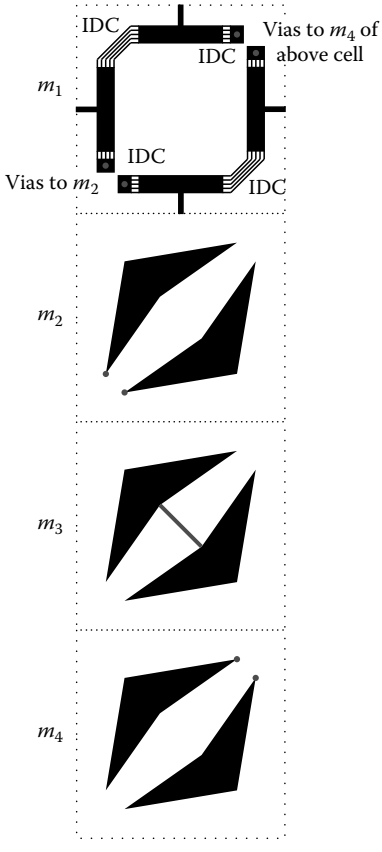

FIGURE 22.32 Planarized realization of the scalar 3D metamaterial in series configuration.

22.7 Conclusions and Outlook

In this chapter we presented a network-based topological framework for the systematic study of metamaterials, derived from the assumption that metamaterials are compound structures implementing dispersion.

It was shown that the synthesis of metamaterial structures can be subdivided into four steps: topological analysis, choice of dispersion type, synthesis of physical realization, and last, group theoretical analysis. Structures presented so far in the literature are shown to be covered by this approach. In addition a novel scalar (single polarization supporting) 3D metamaterial was derived using this approach. A physical realization of the new topology with inversion symmetry and implementing Drude dispersion for the permeability and permittivity was presented.

A vectorial, i.e., two polarizations supporting 3D isotropic metamaterial, was discussed. It was derived from the topological analysis of the discretized 3D space supporting two polarizations, essentially rederiving the TLM computational scheme and its network representation. A symmetrical physical realization was synthesized and experimentally verified.

Last, fabrication aspects of 3D metamaterial structures were discussed. A polyhedron decomposition approach and its application to the rotated TLM cell, the Kron cell, and the scalar series configuration cell were presented. Using this decomposition scheme, 3D fabrication techniques and rapid prototyping techniques can be used.

A second fabrication approach based on topology-invariant planarization was presented as an alternative to polyhedral decomposition. Using the network topology of the unit cell, a physical realization is synthesized, which offers compatibility with planar fabrication techniques at the price of anisotropic behavior.

The theoretical framework and the fabricational approaches presented in this chapter allow one to use the various applications proposed for 3D metamaterials, including imaging systems [56] and novel antenna concepts [15,16,27]. The topology-based concept as well as the polyhedral decomposition and the topology-invariant planarization can be extended to achieve anisotropic graded material parameters, enabling 3D, radar cross-section modifications [57].

Acknowledgments

The authors thank the Deutsche Forschungsgemeinschaft for supporting this research project. In addition we would like to thank Susanne Hipp née Hofmann for performing simulations of the scalar 3D structure, Pascal Hofmann for his expertise on fabrication aspects, and Uwe Siart, Rania Issa, and Christian Neumair for proofreading and figure generation.

References

1. W. Hoefer, P. So, D. Thompson, and M. Tentzeris, Topology and design of wide-band 3D metamaterials made of periodically loaded transmission lines, *Int. Microwave Symposium Digest*, Long Beach, CA, pp. 1443–1446, 2005.
2. A. Grbic and G. Eleftheriades, An isotropic three-dimensional negative-refractive-index transmission-line metamaterial, *J. Appl. Phys.*, 98, 043 106–1–043 106–5, 2005.
3. M. Zedler and P. Russer, Investigation on the dispersion relation of a 3D LC-based metamaterial with an omnidirectional left-handed frequency band, *Int. Microwave Symposium Digest*, San Francisco, CA, pp. 1477–1480, 2006.
4. M. Zedler, C. Caloz, and P. Russer, A 3D isotropic left-handed metamaterial based on the rotated transmission line matrix (TLM) scheme, *IEEE Trans. Microw. Theory Technol, IMS Special Issue*, 55(12), 2930–2941, 2007.

5. O. Vendik and M. Gashinova, Artificial double negative (DNG) media composed by two different dielectric sphere lattices embedded in a dielectric matrix, *Proc. European Microwave Conf.*, Amsterdam, the Netherlands, pp. 1209–1212, 2004.
6. P. K. Mercure, R. P. Haley, A. Bogle, and L. Kempel, Three-dimensional isotropic meta-materials, *Int. Antennas and Propagation Society Symposium Digest*, Washington DC, pp. 623–626, 2005.
7. T. Koschny, L. Zhang, and C. Soukoulis, Isotropic three-dimensional left-handed metamaterials, *Phys. Rev. B*, 71, 121 103–1–121 103–4, 2005.
8. P. Alitalo, S. Maslovski, and S. Tretyakov, Three-dimensional isotropic perfect lens based on LC-loaded transmission lines, *J. Appl. Phys.*, 99, 064 912–1–064 912–8, 2006.
9. P. Alitalo, S. Maslovski, and S. Tretyakov, Experimental verification of the key properties of a three-dimensional isotropic transmission-line superlens, *J. Appl. Phys.*, 99, 124 910–1–124 910–6, 2006.
10. M. Zedler, U. Siart, and P. Russer, Circuit theory unifying description for metamaterials, *Proc. URSI GA 2008*, Chicago.
11. W. Padilla, Group theoretical description of artificial electromagnetic metamaterials, *Opt. Expr.*, 15(4), 1639–1646, 2007.
12. J. Baena, L. Jelinek, and R. Marqués, Towards a systematic design of isotropic bulk magnetic metamaterials using the cubic point groups of symmetry, *Phys. Rev. B*, 76(24), 245115, 2007.
13. P. Russer, *Electromagnetics, Microwave Circuit and Antenna Design for Communications Engineering*. Boston, MA: Artech House, 2006.
14. A. A. Oliner, A periodic-structure negative-refractive-index medium without resonant elements, *USNC/URSI Nat. Radio Science Meeting*, San Antonio, TX, p. 41, 2002.
15. G. Eleftheriades and K. Balmain, (Eds.), *Negative-Refraction Metamaterials*. Weinheim, Germany: Wiley, 2005.
16. C. Caloz and T. Itoh, *Electromagnetic Metamaterials*. Hoboken, NJ: John Wiley & Sons, 2006.
17. M. Zedler, C. Caloz, and P. Russer, 3D composite right-left handed metamaterials with lorentz-type dispersive elements, *ISSSE 2007*, Montréal, Canada, 2007.
18. A. K. Iyer and G. Eleftheriades, Mechanism of subdiffraction free-space imaging using transmission-line metamaterial superlens: An experimental verification, *Appl. Phys. Lett.*, 92, 131105, 2008.
19. D. Sievenpiper, L. Zhang, R. Jimenez-Broas, N. Alexópolous, and E. Yablonovitch, High-impedance electromagnetic surfaces with a forbidden frequency band, *IEEE Trans. Microw. Theory Technol.*, 47, 2059, 1999.
20. M. Beruete, I. Campillo, M. Navarro-Cía, F. Falcone, and M. S. Ayza, Molding left- or right-handed metamaterials by stacked cutoff metallic hole arrays, *IEEE Trans. Microw. Theory Technol.*, 55(6), 1514–1521, 2007.
21. N. Marcuvitz, *Waveguide Handbook*. London: IEEE Press, 1986.
22. D. Gaillot, C. Croenne, and D. Lippens, An all-dielectric route for terahertz cloaking, *Opt. Expr.*, 16(6), 3986, 2008.
23. J. Baena, J. Bonache, F. Martín, R. Marqués-Sillero, F. Falcone, T. Lopetegi, M. Laso et al., Equivalent-circuit models for split-ring resonators and complementary split-ring resonators coupled equivalent circuit models for split-ring resonators and complementary split-ring resonators coupled to planar transmission lines, *IEEE Microw. Theory Technol.*, 53(4), 1451–1460, 2005.
24. W. Cauer, *Theorie der linearen Wechselstromschaltungen*. Berlin: Akademie-Verlag, 1954.
25. V. Belevitch, *Classical Network Theory*. San Francisco, CA: Holden-Day, 1968.
26. P. Russer, *Electromagnetics, Microwave Circuit and Antenna Design for Communications Engineering*, 2nd edn. Boston, MA: Artech House, 2006.
27. N. Engheta and R. Ziolkowski, *Electromagnetic Metamaterials*. Hoboken, NJ: Wiley, 2006.
28. M. Zedler and P. Russer, Three-dimensional CRLH metamaterials for microwave applications, *Proc. Eur. Microw. Assoc.*, Munich, Germany, 3, 151–162, 2007.
29. T. Itoh, *Numerical Techniques for Microwave and Millimeter-Wave Passive Structures*. New York: John Wiley & Sons, 1989.

30. M. Stickel, F. Elek, J. Zhu, and G. Eleftheriades, Volumetric negative-refraction-index metamaterials based upon the shunt-node transmission-line configuration, *J. Appl. Phys.*, 102, 094903, 2007.
31. K. Balmain, A. Lüttgen, and P. Kremer, Power flow for resonance cone phenomenon in planar anisotropic metamaterials, *IEEE Trans. Antennas Propagat.*, 51(10), 2612, 2003.
32. A. Iyer and G. Eleftheriades, A volumetric layered transmission-line metamaterial exhibiting a negative refractive index, *J. Opt. Soc. Am. (JOSA-B)*, 23, 553, 2006.
33. R. A. Shelby, D. R. Smith, and S. Schultz, Experimental verification of a negative index of refraction, *Science*, 292, 77–79, April 2001.
34. M. Zedler, System Topological Design of Metamaterials, Phd thesis, Munich University of Technology, Munich, Germany, 2008. http://mediatum2.ub.tum.de/node?id=653119.
35. N. Ashcroft and N. Mermin, *Solid State Physics*. Philadelphia, PA: Saunders College, 1988.
36. I. Tsukerman, Negative refraction and the minimum lattice cell size, *J. Opt. Soc. Am. B*, 25, 927–936, 2008.
37. S. Tretyakov, *Analytical Modeling in Applied Electromagnetics*. Morwood, MA: Artech House, 2003.
38. W. J. R. Hoefer, The transmission line matrix (TLM) method, in *Numerical Techniques for Microwave and Millimeter Wave Passive Structures*, T. Itoh (Ed.), New York: John Wiley & Sons, 1989, pp. 496–591.
39. G. Kron, Equivalent circuits to represent the electromagnetic field equations, *Phys. Rev.*, 64(3), 126–128, 1943.
40. M. Krumpholz and P. Russer, On the dispersion in TLM and FDTD, *IEEE Trans. Microw. Theory Technol.*, 42(7), 1275–1279, 1994.
41. P. Russer, The alternating rotated transmission line matrix (ARTLM) scheme, *Electromagnetics*, 16(5), 537–551, 1996.
42. A. Wlodarczyk, Representation of symmetrical condensed TLM node, *Electron. Lett.*, 28(18), 1686–1687, 1992.
43. R. E. Collin, *Field Theory of Guided Waves*, 2nd edn. New York: IEEE Press, 1990.
44. M. Zedler, C. Caloz, and P. Russer, Circuital and experimental demonstration of a 3D isotropic LH metamaterial based on the rotated TLM scheme, *Int. Microwave Symposium Digest*, Honolulu, HI, pp. 1827–1830, 2007.
45. M. Zedler and P. Russer, A three-dimensional left-handed metamaterial based on the rotated TLM method, *Proc. of SPIE*, 6987(58), 69 871M1–69 871M14, 2008.
46. M. Zedler, P. So, C. Caloz, and P. Russer, IIR approach for the efficient computation of large-scale 3D RTLM CRLH metamaterials, *Proc. ACES*, Niagara Falls, Canada, p. 978, 2008.
47. P. Hofmann, M. Zedler, and P. Russer, Dekomposition dreidimensionaler Metamaterialien in Polyeder und Verfahren zu deren Herstellung, Patent filed, 2008.
48. K. Murphy, Development of integrated electrical and mechanical assemblies using two shot moulding and selective metallization technique, 5th *International Congress Molded Interconnect Devices*, pp. 35–39, 2002.
49. W. Eberhardt, D. Ahrendt, U. Keßler, D. Warkentin, and H. Kück, Polymer based multifunctional 3d-packages for microsystems, *Proceedings of the 2nd International Conference on Multi-Material Micro Manufacture (4M)*, 2006.
50. C. Pein, W. Eberhardt, and H. Kück, Process optimization for hot embossing, 6th *International Congress Molded Interconnect Devices*, pp. 241–245, 2004.
51. A. Möbius, D. Elbick, E. Weidlich, K. Feldmann, F. Schüßler, J. Borris, M. Thomas, A. Zänker, and C. Klages, Plasma-printing and galvanic metallization hand in hand—a new technology for the cost-efficient manufacture of flexible printed circuits, *Electrochimica Special Issue of the Euro-Interfinish 2007, Athens*, 2008.
52. Forschungsvereinigung Räumliche Elektronische Baugruppen 3-D MID e.V., Ed., *3D-MID Technologie, Räumliche elektronische Baugruppen*. Hanser, Munich, 2004.
53. LPKF Laser & Electronics AG, LDS process description, http://www.lpkfusa.com/datasheets/mid/lds.pdf, Tech. Rep., 2008.

54. M. Zedler, C. Caloz, and P. Russer, Analysis of a planarized 3D isotropic LH metamaterial based on the rotated TLM scheme, *EuMC*, 2007.
55. M. Zedler, C. Caloz, and P. Russer, Numerical analysis of a planarized 3D isotropic LH metamaterial based on the rotated TLM scheme, *Eurocon*, pp. 24–27, 2007.
56. J. Pendry, Negative refraction makes a perfect lens, *Phys. Rev. Lett.*, 85, 3966–3969, 2000.
57. J. Pendry, D. Schurig, and D. Smith, Controlling electromagnetic fields, *Science*, 312, 1780–1782, 2006.

23

Negative Refraction in Infrared and Visible Domains

Andrea Alù
University of Texas, Austin

Nader Engheta
University of Pennsylvania

23.1 Introduction

The research on negative refraction has considerably grown in the past several years, as extensively discussed in this handbook and in recent books, special issues, and reviews [1–10]. This is mainly due to the recent interest in the unconventional properties of composite "metamaterials" with both negative permittivity and permeability, also known as left-handed (LH) or double-negative (DNG) materials [11]. In particular, the theoretical possibility of subwavelength focusing and perfect lensing has fostered this sudden increase in interest, starting from the seminal work of Pendry on this topic [12]. It is clear how a major breakthrough in the metamaterial technology will be experienced when these concepts are readily applied to the visible frequencies, for which subwavelength focusing and imaging are primary applications [13–19].

In the microwave regime, negative-index metamaterials have been constructed in two distinct ways: (a) by embedding arrays of metallic split-ring resonators (SRRs) and wires in a host medium (see, e.g., [20]) and (b) by realizing loaded dual transmission lines with backward-wave behavior (see, e.g., [4,5]). In both cases, some of the predicted anomalous properties of negative-index materials have already been experimentally demonstrated in this regime of frequency.

In the near-infrared (IR) and visible regimes, however, synthesizing such LH materials poses relevant challenges, mainly due to the fact that in these frequency regimes, the magnetic polarization due to the microscopic molecular currents in a natural material tends to be negligible, and therefore, the corresponding magnetic permeability in these frequency regimes approaches that of free space [21]. The electric permittivity of materials, on the other hand, may become naturally resonant at these frequencies, and a relatively wide range of plasmonic and polaritonic materials are known at THz, IR, and visible frequencies [22].

In this sense, the straightforward scaling of the metallic SRR in order to induce a suitable resonant permeability, as the first of the previous options for realizing negative permeability down to the optical wavelength, encounters related challenges [23]. In addition to the problems in nanofabrication of ring or loop resonators and small gaps, it should be mentioned that the electric conductivity of metals, upon which the resonance of SRR at microwave frequencies depends, behaves differently as the frequency is increased in the IR and visible domains.

Similarly, loading optical nanotransmission lines with lumped inductors and capacitors at these high frequencies may be limited by current technology, since the same conventional definition of circuit elements practically loses its standard meaning at these frequencies, where the conduction properties of materials are modified in such a way as to forbid the presence of a significant conduction current flowing across the elements.

Following these issues, several novel ideas have been put forward by other researchers to achieve LH materials in the IR and visible regimes. They include the possibility of using coupled plasmonic parallel nanowires and nanoplates [24–26], coupled nanocones [15], anisotropic waveguides [27], modified SRR in the near-IR region [16–19,28], closely packed inclusions with negative permittivity and their electrostatic resonances [29], and defects in regular photonic band gap structures [30].

Our group has also offered and developed various ideas, concepts, and proposals for overcoming the current limitations in the realization of negative refraction at optical frequencies. One of the ways we have proposed to realize optical metamaterials with negative permeability, and more in general negative refraction, follows the techniques that employ resonant inclusions, proposing a novel design of a macroinclusion in the shape of a loop (or ring) composed of properly arranged nanoparticles, which may resemble the behavior of an SRR at these high frequencies. In this sense, some theoretical results have been proposed in Refs. [31,32]. As a different way of realizing negative refraction at visible frequencies, we have proposed to extend the concepts of loaded transmission lines to the visible frequencies, envisioning backward-wave nanotransmission lines in the form of plasmonic planar nanolayers [33] and periodic arrays of nanoparticles in one [34] and three dimensions [35].

All these solutions rely on, and may be explained in terms of, the nanocircuit paradigm, which we have recently presented in Refs. [36,37] and properly extended in Ref. [38–44]. In the framework of this paradigm, the role of conduction current $J_c = \sigma E$ (σ being the local material conductivity and E the local electric field), which is at the basis of the functionalities of circuits at lower frequencies, but which is less available at optical frequencies, may be replaced (or dominated) by the displacement current $J_d = j\omega\varepsilon E$ (ε being the local permittivity, under an $e^{j\omega t}$ time convention). In this case, the role of inductors and capacitors may be taken by nanoparticles with negative and positive real part of the permittivity, respectively, whereas the role of "good" or "bad" conductors (connectors and insulators, respectively) is taken by materials with large or near-zero permittivity, respectively. The flexibility in design that optical materials may exhibit in their permittivity at IR and optical frequencies may be exploited for tailoring the functionalities of nanocircuits. As we have extensively shown in our recent articles, such concepts may be employed to realize the typical functions of circuit elements at IR and optical frequencies, i.e., nanofiltering [43], nanoguiding optical signals [34], and loading and tuning optical nanoantennas [44].

As we review and discuss in the following sections, these same concepts may turn out to be essential in understanding and explaining our ideas, concepts, and proposals for achieving negative refraction at optical frequencies. This would allow us to draw some analogies among the different concepts that we discuss in the following sections, as interpreted through nanocircuit concepts.

However, the distinctions among the different solutions we propose are evident, and their individual limitations are related to the different ways in which they have been conceived. For instance, when resonant nanoloops (i.e., nanorings) with dominant magnetic response are embedded in an optical metamaterial, as described in Section 23.3, some limitations in the bandwidth of operation are expected, similarly to the analogous drawbacks that SRR metamaterials show at microwave

frequencies. These limitations may be overcome, or reduced, by employing the transmission-line concepts, applied in Sections 23.4 and 23.5, for which the operation, both in our concepts at optical frequencies and in the microwave regime, shows wider bandwidth and more robustness to losses. These features are described in more detail in the following sections of this chapter, underlining analogies of and differences in these different techniques and providing insights into these concepts in terms of our nanocircuit interpretation.

The results reviewed here may open interesting doors to the realization of LH metamaterials at optical frequencies, with potential applications in imaging and nanooptics.

23.2 Nanocircuit Elements at IR and Optical Frequencies

Extending the concept of lumped circuit elements, i.e., capacitors, inductors, and resistors, to IR and visible wavelengths, as already anticipated in the introduction, is possible in terms of our nanocircuit paradigm [36,37]. Here, we review the main concepts associated with this theory, which would be useful for the discussions in the following sections.

Following the results of Ref. [36], an isolated nanoparticle illuminated by a uniform electric field $\mathbf{E}_0$ may be regarded as a lumped nanocircuit element with complex impedance Z_{nano}, as depicted schematically in Figure 23.1.

Such nanoimpedance Z_{nano} may be defined, analogously to the classic concept of impedance in circuit theory, as the ratio of the optical voltage V across the "ends" (or the "terminals") of the nanoelement and the total displacement current I_{pol} circulating across it. Such impedance is a fixed quantity, depending only on the geometry of the particle and its constituent materials and possibly on the

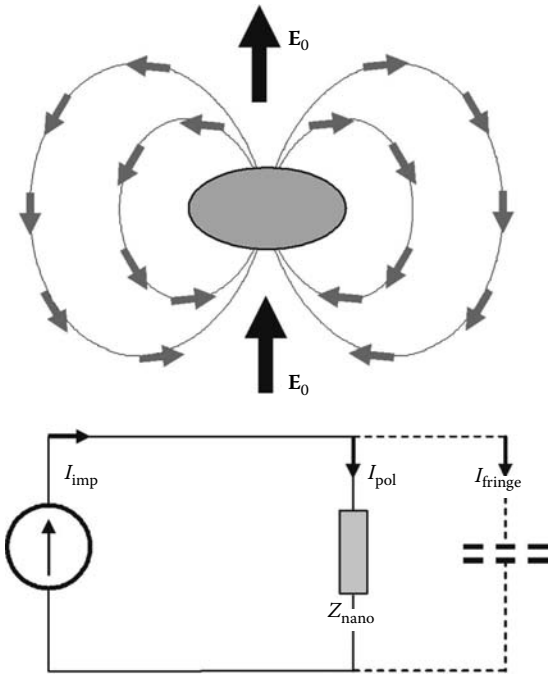

FIGURE 23.1 A nanoparticle illuminated by a uniform electric field $\mathbf{E}_0$ (thicker arrows) may be viewed [36] as a lumped impedance Z_{nano} excited by the impressed current generator I_{imp} and loaded with the fringe capacitance associated with its fringe dipolar fields (thinner arrows). (From Alù, A., Salandrino, A., and Engheta, N., *Opt. Exp.*, 15(21), 13865, October 2007. Copyright (2007) by the optical society of America.)

orientation of the applied field in the case of nonsymmetric particles. Following the calculations reported in Ref. [36], we obtain, for a spherical nanoparticle, the expressions

$$Z_{\text{nano}} = \left(-i\omega\varepsilon\pi R\right)^{-1}$$
$$I_{\text{imp}} = -i\omega\left(\varepsilon - \varepsilon_0\right)\pi R^2 \left|\mathbf{E}_0\right|$$
$$Z_{\text{fringe}} = \left(-i\omega 2\pi R\varepsilon_0\right)^{-1}, \tag{23.1}$$

where

ε is the nanosphere permittivity
R is the radius
ε_0 is the background permittivity

This description is consistent with the circuital model of Figure 23.1, and it implies that a nonplasmonic (plasmonic) isolated nanoparticle may act as a lumped nanocapacitance (nanoinductance) due to the positive (negative) sign of the real part of its permittivity (see Equation 23.1). In this analogy, the presence of material loss corresponds to a nanoresistor.

These concepts may be easily extended to a more complex shape for the nanoparticles, whose polarizability affects the expression and the isotropy of the corresponding impedance. The expressions for an ellipsoid nanoparticle, for instance, have been evaluated in Ref. [41].

In the case of isolated particles, the three basic lumped elements of any linear circuit, R, L, and C, which are at the core of a complex circuit board, may therefore be considered available at IR and optical frequencies following this paradigm due to the abundance of plasmonic and nonplasmonic materials in these frequency regimes.

Clearly, however, the complexity of a full circuit board requires much more efforts than just establishing the nanocircuit theory for an isolated nanoparticle, particularly because, as Figure 23.1 shows, the behavior of the lumped nanoelement is strictly related to the external dipolar fields induced by the excitation. According to the discussion in the previous section, the displacement current flowing across the element closes itself in the dipolar fields outside it, and this is very distinct from what usually happens in a classic lumped circuit.

As a first attempt to generalize this theory to a more complex situation in which multiple nanocircuit elements are closely put together, we developed an analytical model to take into account the coupling among closely spaced nanoparticles. This may be rigorously done in terms of controlled (i.e., "dependent") generators, extending the circuit model in Figure 23.1 to an arbitrary configuration of nanoparticles. For the case of two nanoparticles, the corresponding circuit scheme is reported in Ref. [41]. Although viable, this technique has two main drawbacks: its inherent complexity, for which the number of dependent sources would grow large when the closely spaced nanocircuit elements grow in quantity, and the corresponding lack of intuitive functionality. The advantage of classic radio-frequency (RF) circuits is in that the connections among different elements may be easily achieved by metallic wires and thus "printed" on the circuit board, obtaining complex functionalities with a simple application of standard circuit formulas.

As we anticipated in the introduction, however, the nanocircuit paradigm is based on the formal analogy between the classic circuit theory and our nanocircuit paradigm, for which the conductivity σ is conceptually substituted by the factor $j\omega\varepsilon$, which takes into account the functional equivalence between conduction and displacement currents. Where does the functional difference between classic circuits and optical nanocircuits, which seems to make difficult the analysis of a complex nanocircuit board, reside then? The answer is fairly straightforward: conventional background materials, i.e., free space or simple dielectrics, in classic circuits are inherently poorly conductive ($\sigma \simeq 0$) with respect to the lumped elements, whereas in the analogous nanocircuit the background permittivity is not necessarily different from that of the lumped elements that reside in the background material. This implies that the displacement current may easily "flow" or "leak" anywhere in the

nanocircuit board, coupling the elements that should not be necessarily coupled and not ensuring good connection among elements that should be placed in a specific series or parallel combination.

To solve these issues, in the design of our nanocircuit boards, we introduced the presence of ε-near-zero (ENZ) materials with the role of nanoinsulators, ε-very-large (EVL) materials with the role of nanoconnectors [38], and optical "shorting" nanowires for connecting relatively distant nanocircuit elements with low voltage drops and phase delay [42].

Moreover, we have fully envisioned the configurations for obtaining series and parallel combinations of nanocircuit elements, which are different from the classic circuit theory and are strongly affected by the orientation of the optical electric field vector with respect to the pair of elements. In particular, two adjacent nanoparticles may be considered in "series" when the electric field is normal to their common interface, so that the displacement current flowing in one element flows into the adjacent one, as ensured by the boundary conditions, whereas they may be considered in "parallel" if the electric field vector is parallel with their common interface, ensuring that the voltage drop at their terminals is the same [39]. These conditions allow further degrees of freedom in the realization of a nanocircuit board, with the possibility of modifying the functionality of the connection of two or more elements by varying the polarization of the field. On the other hand, a wise use of nanoinsulators and nanoconnectors allows the possibility of tailoring the desired connection among relatively distant elements at will.

Figure 23.2, as an example, shows the design of an interconnection between a lumped nanoinductor and a lumped nanocapacitor. It is evident how the proper use of EVL and ENZ materials allow us to confine the displacement current flow through the nanoelements, ensuring an oppositely directed electric field at the resonance in the two series elements, as expected in an LC resonant series (oppositely signed voltage drop across the elements and same current flow).

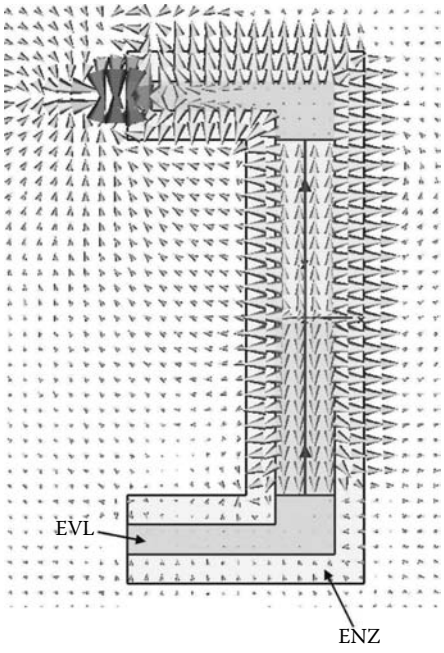

FIGURE 23.2 An example of series interconnection between a lumped nanoinductor and a lumped nanocapacitor. In this case, the proper use of connectors and insulators ensures a proper series connection whatever the polarization of the impinging field. The figure shows the electric field distribution in the nanocircuit at the LC resonance.

Combining all these results, we recently presented some designs for more complex functionalities, to show the inherent possibility of nanofiltering at optical frequencies [43] and of loading optical nanoantennas for tuning and matching purposes [44]. In the next sections, using these tools, we show how proper combinations of nanoinductors and nanocapacitors may constitute a viable way to design negative-refractive metamaterials at optical frequencies and to interpret their anomalous electromagnetic features.

23.3 Negative Permeability and DNG Metamaterials at IR and Optical Frequencies

As mentioned in Section 23.1, various groups have offered several different approaches to achieve negative refraction at IR and optical frequencies [13–35]. Here, we review our different method that relies on the design of subwavelength nanoloops exhibiting a "pure" magnetic dipolar resonant response and thus provide the possibility of having negative effective magnetic dipole moment, at optical frequencies [31,32]. We highlight some of the inherent advantages of this geometry for the inclusion compared with the other recent attempts to realize optical negative-refractive materials.

Our idea is based on the collective resonance of a circular array of plasmonic nanoparticles arranged in a specific pattern (e.g., in a circular pattern) to form a single subwavelength "ring inclusion." As in the nanocircuits described in the previous section, in this nanoring the conventional conduction current (as also in the SRR at microwave frequencies) does not produce the magnetic dipole moment, but instead the plasmonic resonant feature of every nanoparticle induces a circulating resonant "displacement" current around the nanoloop. Unlike the case of the conventional metallic loops or SRRs at the microwave frequencies, here the size of this loop does not directly influence the resonant frequency of the induced magnetic dipole moment, but rather the plasmonic resonant frequency of each nanoparticle is the main determining factor for this resonance to happen.

Consider the geometry depicted in Figure 23.3, i.e., N identical nanoparticles with radius a arranged to have their centers located symmetrically on a circle of radius R. The figure refers to two different possible excitations of the array: a magnetic excitation with a uniform magnetic field at the center of the loop (Figure 23.3a) and an electric excitation (Figure 23.3b). The nanospheres are small compared with the wavelength, and they are characterized by a complex permittivity ε, whose real part may be negative when plasmonic materials are employed, and a permeability equal to that of free space μ_0. The material in which the particles are embedded has permittivity ε_b. Such a setup is realistic at IR and optical frequencies within the limitations of current nanotechnology.

The electric and magnetic polarizabilities of this nanoloop may be extracted by evaluating its response to the two different types of excitation. A local magnetic field, as in Figure 23.3a, is in fact expected to induce a magnetic response from the nanoloop, since the electric dipoles induced on each particle are expected to cancel out their electric response for symmetry. On the other hand, one expects to have a strong electric response to an electric excitation, and therefore the complex response of the nanoloop may be conveniently described in terms of its complex electric and magnetic polarizabilities. The details of our results can be found in Refs. [31,32].

The magnetic polarizability of the nanoloop is obtained by evaluating its response to a uniform magnetic field excitation $\mathbf{H}_{\text{imp}} = H_{\text{imp}}\hat{\mathbf{z}}$ directed along the axis of the loop. Since we are assuming that each nanosphere is small compared with the wavelength, we may conveniently describe its electromagnetic behavior in terms of its electric polarizability α_p. The hypothesis of describing the electromagnetic interaction of the particles composing the loop only through their electric polarizability is justified by the subwavelength size of each of the particles and by the fact that they are nonmagnetic at optical frequencies. This implies that each of the particles responds solely to the local electric field $\mathbf{E}_{\text{loc}}$ impinging on it and not directly to $\mathbf{H}_{\text{imp}}$.

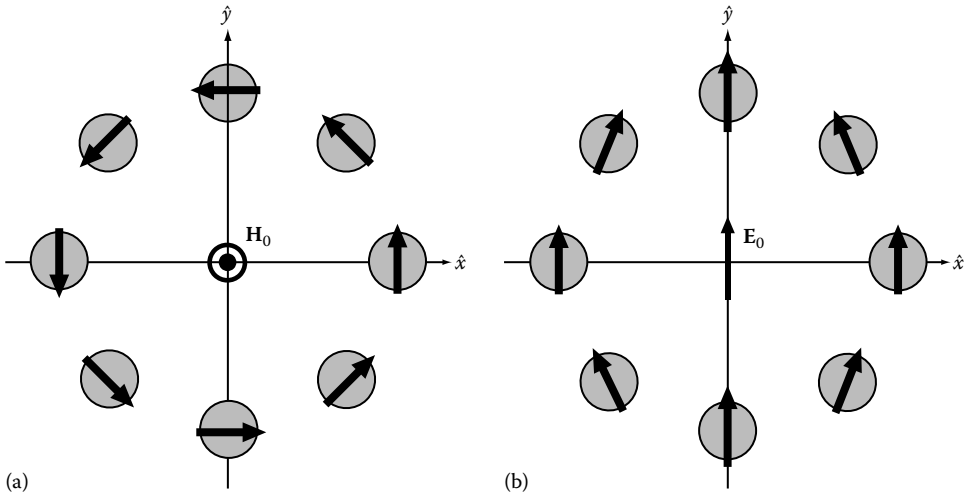

FIGURE 23.3 A circular array of equi-spaced nanospheres in the x–y plane excited by (a) a local time-varying magnetic field directed along z, (b) a local time-varying electric field directed along y. The vectors on each particle indicate the induced electric dipole moments in the two cases. (From Alù, A., Salandrino, A., and Engheta, N., *Opt. Exp.*, 14(4), 1557, February 2006.)

Integrating Maxwell equation $\nabla \times \mathbf{E}_{\text{imp}} = -j\omega\mu_0 \mathbf{H}_{\text{imp}}$ under the assumption of a uniform quasi-static (but time-varying) magnetic field over the volume occupied by the loop and subwavelength dimensions, we find that at the location of the particles the following relation holds:

$$\mathbf{E}_{\text{imp}} = \frac{-j\omega\mu_0 R H_{\text{imp}}}{2}\hat{\boldsymbol{\varphi}}. \tag{23.2}$$

Notice how Equation 23.2 derives the amplitude of the electric field impressed on each particle, relating the magnetic response of the loop in its entirety to the local variation, i.e., the curl, of the impressed electric field on each constituent of the nanoloop. This is consistent with the sketch in Figure 23.3a. In Ref. [31], we derived the same result as that in Equation 23.2 by launching a bunch of plane waves, each impinging in the direction of one of the nanoparticles and with phases chosen in such a way as to excite a local quasi-uniform magnetic field on the nanoloop. In the limit $R \ll \lambda_0$, which is required for employing the nanoloop as the basic inclusion for an optical metamaterial, the results of these two approaches yield the same quantitative value.

It is interesting to note how Equation 23.2 relates the electric response of each of the nanoparticles to the magnetic form of excitation—the first step to obtain the magnetic polarizability of the nanoloop structure is by showing that the induced electric dipole moments on each particle collectively lead to an overall magnetic effect. This is a clear consequence of tailoring the weak spatial dispersion, inherent property of the nanoloop, to achieve at these high frequencies a nonnegligible magnetic response from a nonmagnetic subwavelength inclusion. This is consistent with the more general discussion on the magnetic response in optical metamaterials provided in Ref. [45].

As formally derived in Ref. [31] and consistent with Equation 23.2, each of the nanoparticles composing the loop is excited in this case by an impressed electric field directed along the tangent to the loop and proportional to the uniform magnetic field on the loop. Owing to the symmetry of geometry and excitation, the electric dipoles induced over the particles are also directed along $\hat{\boldsymbol{\varphi}}$, as sketched in Figure 23.3a. The induced dipole amplitude is proportional (through the proportionality factor α_p) to the local electric field at each particle when its self-polarization contribution is not considered, which is $\mathbf{E}_{\text{loc}} = \mathbf{E}_{\text{imp}} + \sum_{j \neq j'} \mathbf{E}_{jj'} = E_{\text{loc}}\hat{\boldsymbol{\varphi}}$. In this expression $\mathbf{E}_{jj'}$ is the electric field induced by the

dipole j on the position where the particle j' is placed. Each one of the N particles, therefore, can be represented as an effective dipole moment $\mathbf{p} = p\hat{\boldsymbol{\varphi}} = \alpha_p E_{loc}\hat{\boldsymbol{\varphi}}$. Since $\mathbf{E}_{jj'} = p\underline{\mathbf{Q}}_{jj'} \cdot \hat{\boldsymbol{\varphi}}(\mathbf{r}_{j'})$, where

$$\underline{\mathbf{Q}}_{jj'} = \frac{e^{-jk_b|\mathbf{r}_j - \mathbf{r}_{j'}|}}{4\pi\varepsilon_b |\mathbf{r}_j - \mathbf{r}_{j'}|} \left\{ k_b^2 \left[\bar{\mathbf{I}} - \bar{\mathbf{D}}_{jj'}\right] + \left(\frac{1}{|\mathbf{r}_j - \mathbf{r}_{j'}|^2} + \frac{jk_b}{|\mathbf{r}_j - \mathbf{r}_{j'}|} \right) \left[3\bar{\mathbf{D}}_{jj'} - \bar{\mathbf{I}}\right] \right\} \tag{23.3}$$

is the 3D dyadic Green's function as usually defined [46], with $\bar{\mathbf{D}}_{jj'} = \frac{\mathbf{r}_j - \mathbf{r}_{j'}}{|\mathbf{r}_j - \mathbf{r}_{j'}|} \frac{\mathbf{r}_j - \mathbf{r}_{j'}}{|\mathbf{r}_j - \mathbf{r}_{j'}|}$, $\bar{\mathbf{I}}$ being the identity dyadic, $k_b = \omega\sqrt{\varepsilon_b \mu_0} = 2\pi/\lambda_b$, and $\hat{\boldsymbol{\varphi}}(\mathbf{r}_{j'})$ is the spherical unit vector $\hat{\boldsymbol{\varphi}}$ at the location $\mathbf{r}_{j'}$, and the final closed-form expression for p is given by

$$p = \frac{-j\omega\mu_0 R H_{imp}/2}{\alpha_p^{-1} - \sum_{j \neq j'}^{N-1} \underline{\mathbf{Q}}_{jj'} \cdot \hat{\boldsymbol{\varphi}}(\mathbf{r}_j) \cdot \hat{\boldsymbol{\varphi}}(\mathbf{r}_{j'})}. \tag{23.4}$$

As descried in detail in Ref. [32], the quasi-static multipole expansion of the total current density $\mathbf{J} = j\omega p \sum_{j=0}^{N-1} \hat{\boldsymbol{\varphi}}(\mathbf{r}_j)\delta(\mathbf{r} - \mathbf{r}_j)$ induced by this form of excitation gives rise to electric and magnetic multipoles of order n with the following unusual properties:

- Electric multipoles are zero for any order $n \leq N - 1$.
- Amplitude of the residual, nonvanishing, higher-order, electric multipoles is proportional to R^{n-1}.
- The electric multipoles of order $N + 1$ are identically zero, and for even N, all the odd electric multipoles vanish.
- Magnetic multipoles are zero for any order $2n \leq N$.
- Odd magnetic multipoles are always nonzero, proportional to NR^n.
- Even magnetic multipoles are all identically zero when N is even.

In particular, the dominant magnetic dipole moment, the one that is of more interest for the present discussion, has the amplitude

$$\mathbf{m}_H^{(1)} = \frac{j\omega pNR}{2}\hat{\mathbf{z}}. \tag{23.5}$$

The result represented by Equation 23.5, consistent with the derivations in Refs. [31,32], confirms analytically to which extent the magnetic response of the nanoloop may be considered effectively a magnetic dipolar response when its geometrical parameters are varied. It is clear that, by increasing N and reducing R, more multipoles may be canceled or diminished, and therefore, the ratio between the nonvanishing multipole amplitudes and the magnetic dipole moment may be made sufficiently small to be neglected.

In particular, it is worth underlining that when the particles related to the nanoloop are only two, as in the cases usually considered in the literature, the field scattered by this nanopair is dominated not only by the magnetic dipole moment, with the expression given by Equation 23.5, i.e., $\mathbf{m}_H^{(1)} = j\omega pR\hat{\mathbf{z}}$, but also by an electric quadrupole moment $\mathbf{p}_H^{(2)} = 2pR(\hat{\mathbf{x}}\hat{\mathbf{y}} + \hat{\mathbf{y}}\hat{\mathbf{x}})$, as expected from the geometry. The two contributions are of the same order with respect to R, and therefore, the quadrupolar contribution cannot be reduced by changing the size of the nanoloop. This should be clearly taken into account when such pairs are embedded in a bulk metamaterial, as many recent articles have proposed in realizing optical metamaterials [13–16,24–26]. As we show in the following paragraph, this directly affects the magnetic response of the metamaterial by introducing extra scattering losses.

Following the previous analysis, it may be underlined that when the number of particles is low and/or the loop is not electrically very small, so that higher-order multipoles weigh significantly on the purity of the magnetic dipole response of the inclusion, it is preferable to employ an even number

of particles, rather than an odd one—a choice that cancels the contribution from even magnetic and odd electric multipoles.

The corresponding magnetic polarizability α_m of the nanoloop of Figure 23.3, which satisfies the relation $\mathbf{m}_H^{(1)} = \alpha_m \mathbf{H}_{imp}$, reads, after comparing Equations 23.5 and 23.4:

$$\alpha_m^{-1} = \frac{4\varepsilon_b}{N(k_b R)^2}\left[\alpha_p^{-1} - \sum_{j\neq j'}^{N-1} \underline{\mathbf{Q}}_{jj'} \cdot \hat{\boldsymbol{\varphi}}(\mathbf{r}_j) \cdot \hat{\boldsymbol{\varphi}}(\mathbf{r}_{j'})\right]. \tag{23.6}$$

It is interesting to underline how a careful consideration of the imaginary part of this expression α_{mloss}, which should be properly taken into account to design an inclusion robust to absorption and radiation losses, gives rise to the following expression [32]:

$$\begin{aligned} \alpha_{mloss} &= \frac{4\varepsilon_b \alpha_{loss}}{N(k_b R)^2} + \frac{k_b^3}{10\pi} + o(k_b R)^2 \quad \text{for } N = 2, \\ \alpha_{mloss} &= \frac{4\varepsilon_b \alpha_{loss}}{N(k_b R)^2} + o(k_b R)^2 \quad \text{for } N > 2, \end{aligned} \tag{23.7}$$

where $\alpha_{loss} = \mathrm{Im}\left[\alpha_p^{-1}\right]$, taking into account the material absorption in each particle.

This expression shows how intrinsically the pair of nanoparticles is characterized by higher radiation losses, represented by the contribution $k_b^3/10\pi$, due to the quadrupole radiation, whereas the robustness to absorption can be improved in both cases with a larger loop or a larger number of nanoparticles.

A resonant magnetic dipole moment may be obtained when $\mathrm{Re}\left[\alpha_m^{-1}\right] = 0$, which happens near the resonant frequency of each of the particle composing the nanoloop (arising at $\mathrm{Re}\left[\alpha_p^{-1}\right] = 0$), but slightly shifted by the coupling term represented by the summation in Equation 23.6. It is worth emphasizing that this magnetic resonance depends mainly on the resonant characteristics of the plasmonic particles composing the loop, rather than on the loop geometry, implying that a subwavelength magnetic resonance can, in principle, be achieved independently of the total size of the nanoloop. This is of particular importance for synthesizing a subwavelength inclusion to be embedded in a metamaterial for homogenization purposes.

We can interpret this anomalously resonant magnetic response in terms of the nanocircuit paradigm discussed in the previous section: in order to have each nanoparticle near its resonance, we certainly need to have plasmonic nanoparticles composing the loop in this subwavelength regime. The gaps between the two neighboring nanoparticles, which are essential in this geometry, provide "series" nanocapacitances, due to the specific orientation of the electric field, that may provide a lumped resonance with the nanoinductance of the plasmonic nanoparticles. It is clear how, under proper conditions, the nanoloop may enter into resonance independently of the size of the nanoring, in some ways analogous to a resonant SRR. Here, however, the circulating displacement current is responsible for such resonance, rather than the conduction current circulating in the SRR geometry.

In order to verify numerically these predictions and the applicability of this circuit interpretation, we conducted some numerical simulations for this problem, using CST Microwave Studio [47]. Figure 23.4 reports some plots of our numerical simulation, which clearly shows the resonant behavior of a nanoring of four particles at the resonant frequency. The figure shows the field distributions for a 4-nanosphere ring, for the same geometry simulated analytically in Ref. [31] (Figure 23.2b) at the frequency of 655 THz. In this case, the structure has been excited by two counterpropagating plane waves with frequency near the resonant frequency predicted by our analytical models (the slight shift between this frequency in our full-wave simulations, and the resonant frequency predicted by our analytical model is clearly due to the fact that the spheres, due to their close proximity, may interact in a slightly more complex way than just with a simple dipolar field contribution. However, our

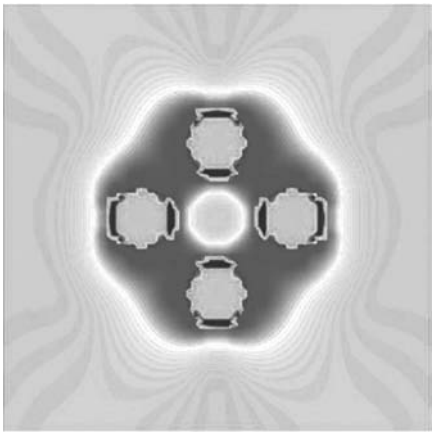

(a)

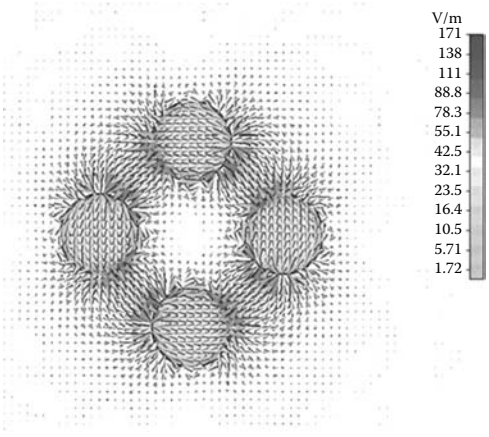

(b)

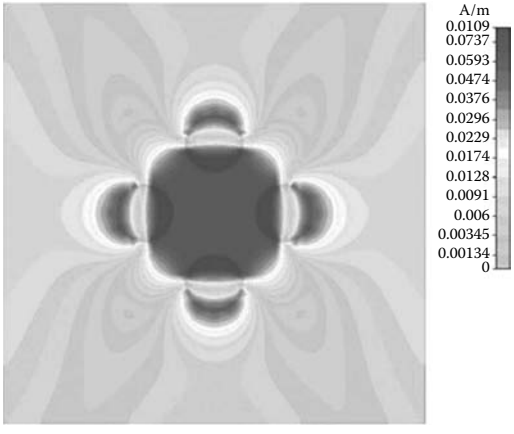

(c)

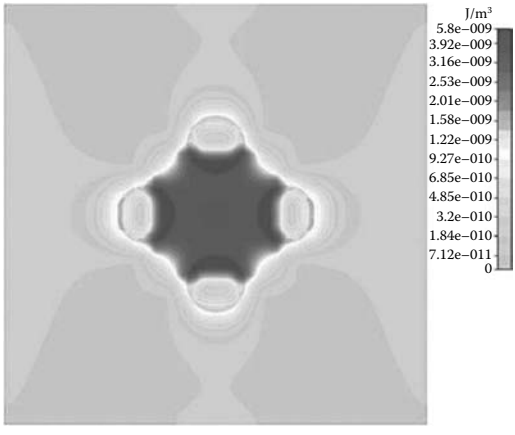

(d)

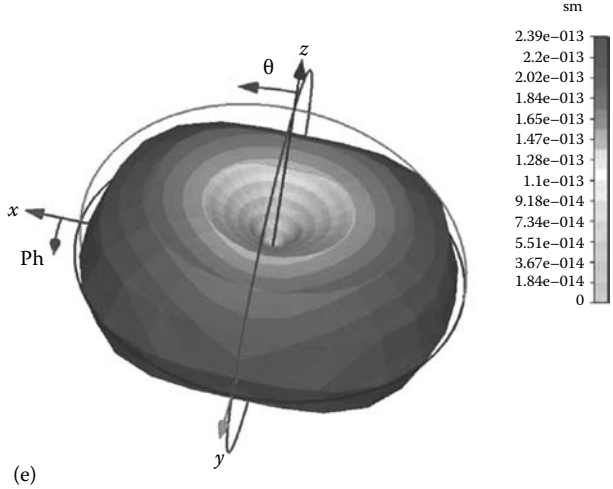

(e)

FIGURE 23.4 Field distributions for a magnetic excitation of a nanoring with geometry following Ref. [31], Figure 23.2b, i.e., $R = 38\,\text{nm}$, $a = 16\,\text{nm}$, $N = 4$, and $N_d = 95^{-3}\,\text{nm}$ for silver particles with realistic permittivity dispersion. Parts (a) through (e) are described in the text.

model works reasonably well and accurately predicts the magnetic resonance verified here with full-wave simulations). Figure 23.4a shows the electric energy density, which relates to the distribution of the "displacement" current around the ring, confirming the phenomenon that our analytical model predicts. The following figures depict for the same geometry the distribution of the instantaneous electric field vector (Figure 23.4b), of the magnetic field amplitude (Figure 23.4c), of the magnetic energy density (Figure 23.4d), and of the scattering radiation pattern (Figure 23.4e). All these plots confirm numerically the analytical predictions of a strong magnetic resonance present around the nanoloop, caused by a circulating resonant displacement current, and the circuit interpretation that we just provided.

Once the magnetic polarizability of the nanoloop is evaluated, the effective permeability of a composite made of an infinite 3D lattice of such inclusions can be calculated with the classic Clausius–Mosotti homogenization formulas. For instance, in the case of a regular cubic lattice, whose periodicity compensates the radiation losses due to the magnetic dipole radiation from each nanoloop, the effective permeability is given by

$$\mu_{\text{eff}}^{(p)} = \mu_0 \left(1 + \left\{ N_{\text{d}}^{-1} \left[\alpha_{\text{m}}^{-1} + i \left(\frac{k_0^3}{6\pi} \right) \right] - \frac{1}{3} \right\}^{-1} \right), \tag{23.8}$$

with N_{d} being the density of loops in the lattice.

The electric response of the nanoinclusion of Figure 23.3 may be calculated by exciting the inclusion with a "quasi-uniform" time-varying electric field, i.e., with the excitation of Figure 23.3b. In order to do that, in this case, we may launch two oppositely directed plane waves that sum their electric fields in phase at the center of the nanoloop, canceling their magnetic field contribution at that point. In this case, we are able to isolate the electric response of the nanoloop for evaluating its electric polarizability. The composed excitation, following, Ref. [31], has the expression

$$\begin{aligned} \mathbf{E}_0 &= E_0 \cos\left(k_{\text{b}} x\right) \hat{\mathbf{y}} \\ \mathbf{H}_0 &= \frac{-jE_0 \sin(k_{\text{b}} x)}{\eta_{\text{b}}} \hat{\mathbf{z}}. \end{aligned} \tag{23.9}$$

For small loops, the induced total electric dipole moment is proportional to the electric polarizability α_{ee}^{y} of the loop. In the cases in which there is a lack of symmetry, the loop exhibits an anisotropic response for its electric polarizability even in the x–y plane. By increasing the number N of nanoparticles composing the loop, however, this planar anisotropy diminishes.

The dipole moment induced on the nth sphere may be evaluated through the vectorial relation:

$$\mathbf{p}_n = \alpha \mathbf{E}_{\text{loc}} = \alpha \left[\mathbf{E}_0 \left(\mathbf{r}_n \right) + \sum_{l \neq n}^{N} \underline{\mathbf{Q}}_{\text{ln}} \cdot \mathbf{p}_l \right]. \tag{23.10}$$

A system of N (Equation 23.10), for $n = 1 \cdots N$, may be solved numerically to derive the induced dipole moments $\mathbf{p}_n$, as proposed in Ref. [31]. In the limit $k_{\text{b}} R \ll 1$, the multipole expansion of such a distribution is dominated by the effective dipole moment $\mathbf{p}_{\text{E}}^{(1)} = \sum_{n=1}^{N} \mathbf{p}_n$, which, due to the symmetry, is parallel to the applied field $\mathbf{E}_0$. The induced dipole distribution for this case is sketched in Figure 23.1b. The related polarizability factor α_{ee}^{y}, which satisfies the relation $\mathbf{p}_{\text{E}} = \alpha_{\text{ee}}^{y} \mathbf{E}_0(0)$, may be straightforwardly calculated numerically, and analogous results may be obtained for the quantity α_{ee}^{x}, for an electric field excitation polarized along $\hat{\mathbf{x}}$. The two quantities are expected to be the same for N

as a multiple of four and increasingly more similar for higher values of N. The effective permittivity for the bulk medium is given by Clausius–Mosotti expressions analogous to Equation 23.8.

Several numerical simulations for this nanoloop geometry have been reported in Refs. [31,32], showing how a metamaterial composed of regular collections of nanoloops may support effective negative permeability and permeability. A judicious design for obtaining the resonant response for the two parameters in the same range of frequencies may yield a negative index of refraction at optical frequencies. Here, we report some additional numerical simulations that underline the functionalities of this negative-index optical metamaterial and highlight how a variation in the background substrate may be employed to tune the resonance frequency of the metamaterial.

Figure 23.5, as a first example, shows the dispersion of the effective parameters for a regular cubic lattice with the number density $N_d = (95)^{-3}$ nm of nanoloops of radius $R = 38$ nm made of silver nanospheres with radius $a = 16$ nm in a glass (SiO_2) background medium. In the calculations, realistic ohmic losses and frequency dispersion of the silver have been considered, following a Drude model with $\varepsilon_{Ag} = \varepsilon_0\left(\varepsilon_\infty - \frac{f_p^2}{f(f-j\gamma)}\right)$ and $\varepsilon_\infty = 5$, $f_p = 2175$ THz, $\gamma = 4.35$ THz, and $f = \omega/2\pi$. The number of nanoparticles per loop in this geometry is $N = 4$, which is the minimum number to achieve cancellation of the quadrupolar electric moment with an even number of particles. An advantage of few particles per loop, as in this case, resides in the possibility of making the nanoparticles relatively large for a given nanoloop size, which increases the robustness to losses.

In particular, the figure shows how we can achieve simultaneously the resonant electric and magnetic polarizability for the nanoloop of Figure 23.3, obtaining a negative index of refraction at optical frequencies with realistic materials. It is evident how the resonance of the effective permeability is shifted by the mutual coupling between the particles composing the loop, as predicted by Equation 23.6, and the magnetic resonance is drastically enhanced by an increase in the number of particles composing the loop. Employing just a pair of particles for each loop in this geometry would create a weak magnetic resonance around the antisymmetric resonant frequency of the pair, but the effective permeability would not yield negative values for the parameters we considered above and would be mainly dominated by losses (as a sum of the ohmic losses of silver and the scattering losses due to quadrupole radiation from each pair). If the number of particles per loop is increased, the situation drastically changes and the sensitivity to losses is reduced, together with a corresponding increase in the frequency range where the effective permeability of the composite may have a negative real part.

Figure 23.6 shows a similar geometry, but obtained with silver nanoparticles in a silicon carbide background, in order to shift the resonance frequency downwards (in this case, in fact, $\varepsilon_{SiC} = 2.55^2\varepsilon_0$). The other parameters for this case are $N_d = 55^{-3}$ nm, $R = 22$ nm, $a = 9.5$ nm, and $N = 4$.

It is interesting to see how the resonant frequency of the nanoring and, consequently, the region of negative refraction for the metamaterial may be tuned by varying the background permittivity for the same material composing the ring.

The metamaterials studied numerically in Figures 23.5 and 23.6, as some of those designed in Refs. [31,32], show a range of visible optical frequencies over which both effective permittivity and permeability simultaneously have negative real parts. This happens due to the fact that the small number of nanospheres per loop (four in the example) does not sensibly shift the resonance frequency for the magnetic permeability. Therefore, the two resonances might happen around the plasmonic resonance of the single nanospheres (around $\varepsilon = -2\varepsilon_b$ for the sphere). This overlapping of the two resonances provides us with the possibility of synthesizing an effective DNG (or LH) material in this frequency regime. We notice how there is a range of frequency in which this metamaterial may have negative refraction with reasonably low losses.

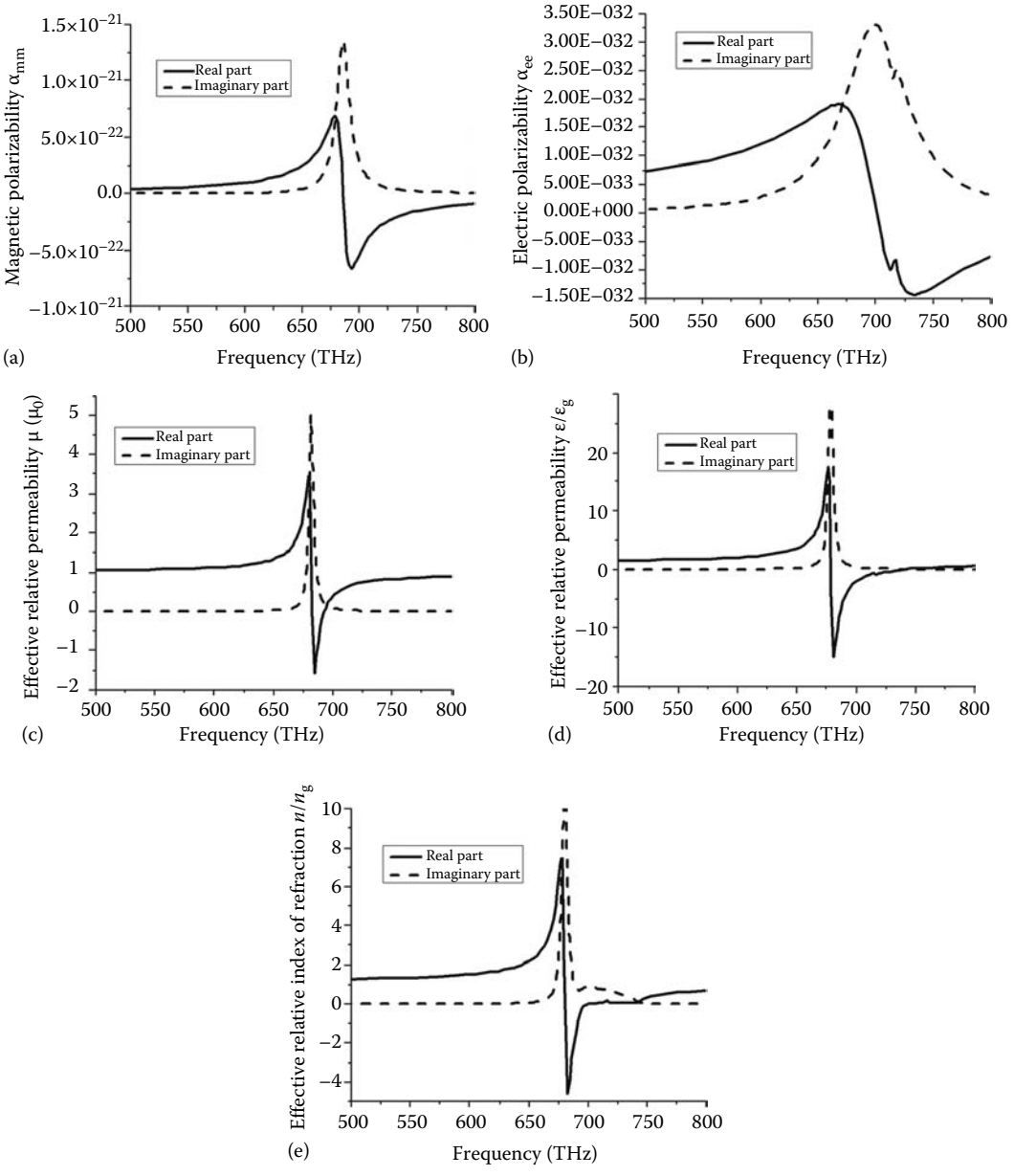

FIGURE 23.5 Magnetic (a) and electric (b) polarizability of a single nanoloop and effective permeability (c), permittivity (d), and index of refraction (e) for a metamaterial with $N_d = 95^{-3}$ nm, $R = 38$ nm, $a = 16$ nm, and $N = 4$.

23.4 Optical Nanotransmission Lines as One-Dimensional and Two-Dimensional Photonic Metamaterials with Positive or Negative Index of Refraction

Although the technique described in the previous section may indeed provide an interesting way to achieve negative index of refraction at optical frequencies, such behavior may be limited in bandwidth

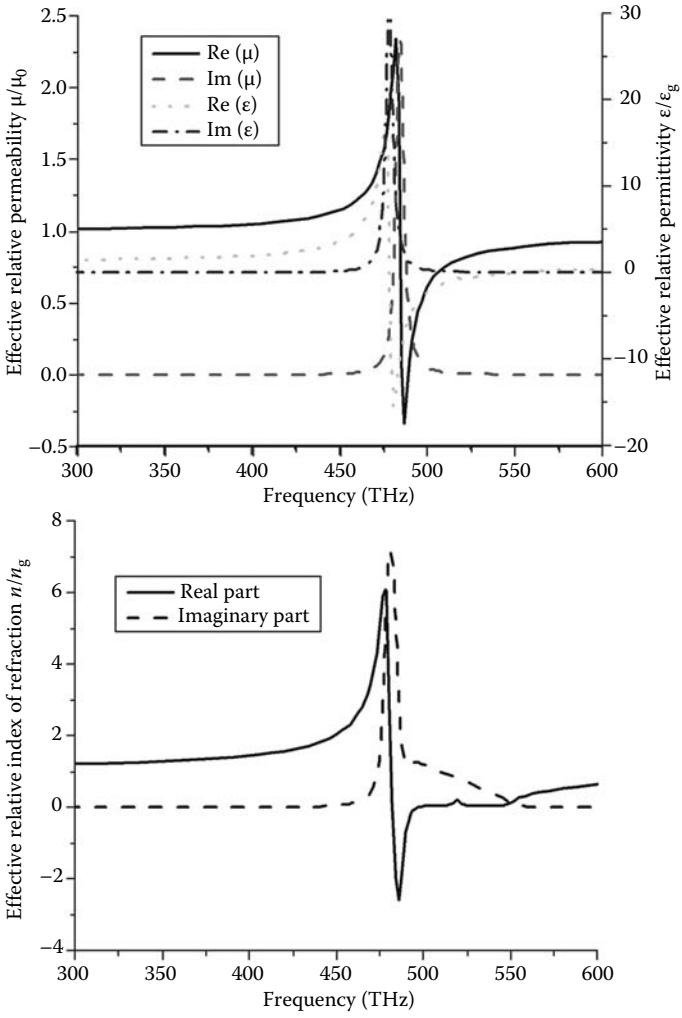

FIGURE 23.6 Effective constitutive parameters for a metamaterial made of silver nanorings embedded in a SiC background. In this case, $N_d = 55^{-3}$ nm, $R = 22$ nm, $a = 9.5$ nm, and $N = 4$.

and robustness to losses by the inherent resonances of the small nanoparticles involved. In order to overcome these limitations, we have investigated the possibility of applying the transmission-line concepts to the optical frequencies, as highlighted in Section 23.2, which may avoid the necessity to rely on individual nanoresonances.

Extending the findings of the transmission-line metamaterials at microwave frequencies developed in the groups of Eleftheriades, Caloz, and Itoh [4,5], the goal is to design an LH transmission line supporting backward propagation at optical frequencies. The circuit model of a "right-handed (RH)" (standard) transmission line, depicted in Figure 23.7 (top row, left column), consists of the cascade of distributed series inductors and shunt capacitors. It is well known that interchanging the role of inductors and capacitors, one may synthesize an LH transmission line, as depicted in Figure 23.7 (top row, right column). This circuit supports LH (backward-wave) propagation, which constitutes an alternative route to design negative-refraction metamaterials. By cascading nanoinductors and nanocapacitors, one may have an analogous behavior at optical frequencies, as Figure 23.7 (middle row) suggests. Consistent with what we have shown in the previous section, the role of the

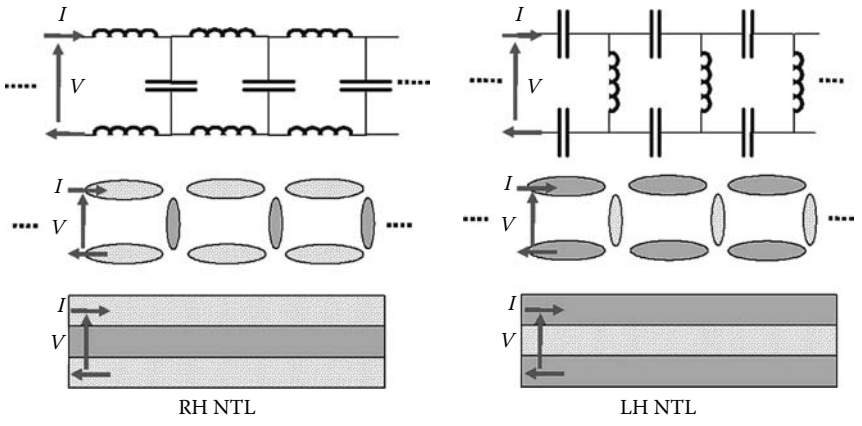

FIGURE 23.7 Synthesis of RH and LH nanotransmission lines at optical frequencies. Top row, conventional circuit model of RH and LH lines using distributed inductors and capacitors; middle row, plasmonic and nonplasmonic nanoparticles may play the role of nanoinductors and nanocapacitors; bottom row, closely packed nanoparticles, in the limit, become plasmonic and dielectric layers, which may be employed in a way similar to that of a nanotransmission line. A sketch of the voltage (V) and current (I) symbols along the lines is also depicted. (From Alù, A., Engheta, N., *J. Opt. Soc. Am. B*, 23(3), 571, 2006.)

nanocapacitors may be even taken by the background gaps between plasmonic particles, provided that the electric field has the correct orientation. This is consistent with what we found in our exact analysis of arrays of plasmonic nanoparticles [34], which we review in detail in the next section.

In this section, however, we analyze a simpler situation, considering the fact that arrays of closely spaced nanoparticles eventually resemble stacks of planar layers of dielectric and plasmonic materials (bottom row in Figure 23.7), which correspond to the simple planar geometry. As we have reported extensively in Ref. [33], under the proper polarization of the field, such stacks of plasmonic and nonplasmonic materials may constitute effective, layered, negative-refractive, optical metamaterials in the form of LH nanotransmission lines.

The geometry in the last row of Figure 23.7 may be easily analyzed theoretically, as in Ref. [33]. If we consider a planar slab with permittivity $\varepsilon_{in}(\omega)$ and thickness d sandwiched between two half-spaces with permittivity $\varepsilon_{out}(\omega)$, the guided modes of this structure propagating along the x direction with a factor $e^{-j\beta x}$ may be split into even and odd modes with respect to the transverse variation along the y axis and into transverse electric (TE) and transverse magnetic (TM) modes with respect to the direction of propagation. In this case, all quantities are therefore independent of the z variable.

The dispersion relations for such modes, as derived in Ref. [33], are given by

$$\text{even:} \quad \tanh\left[\sqrt{\beta^2-\omega^2\varepsilon_{in}\mu_0}\frac{d}{2}\right] = -\frac{\varepsilon_{in}}{\varepsilon_{out}}\frac{\sqrt{\beta^2-\omega^2\varepsilon_{out}\mu_0}}{\sqrt{\beta^2-\omega^2\varepsilon_{in}\mu_0}}$$

$$\text{odd:} \quad \coth\left[\sqrt{\beta^2-\omega^2\varepsilon_{in}\mu_0}\frac{d}{2}\right] = -\frac{\varepsilon_{in}}{\varepsilon_{out}}\frac{\sqrt{\beta^2-\omega^2\varepsilon_{out}\mu_0}}{\sqrt{\beta^2-\omega^2\varepsilon_{in}\mu_0}}. \tag{23.11}$$

The TE mode equations may be easily obtained by duality.

In the limit at which the thickness of the inner layer is small compared with the wavelength (this is an important requirement to apply the "quasi-static" analysis required for the nanocircuit interpretation), this structure still supports a guided mode, even if its wave number may become very high, corresponding to a slow-mode operation. In this case, approximate forms for the TM-guided wave

number are given by the following formulas:

$$\text{even: } |\beta| = -\frac{2}{d}\tanh^{-1}\frac{\varepsilon_{in}}{\varepsilon_{out}}$$
$$\text{odd: } |\beta| = -\frac{2}{d}\coth^{-1}\frac{\varepsilon_{in}}{\varepsilon_{out}}. \tag{23.12}$$

We note from Equation 23.12 that, since $d > 0$ and β is real, in this subwavelength lossless case the constraint $-1 < \varepsilon_{in}/\varepsilon_{out} < 0$ for even modes and $\varepsilon_{in}/\varepsilon_{out} < -1$ for odd ones holds. Even in the case of moderate ohmic losses (of interest here), similar considerations hold on the real part of the permittivities involved. This implies that in any case it is necessary to involve in this setup both plasmonic and nonplasmonic materials to achieve subdiffraction propagation in the sense described in Figure 23.7.

As far as the power flow along these layers is concerned, it may be rigorously shown, as reported in Ref. [33], that the guided modes support an anomalous power flow composed of two oppositely directed power channels in the oppositely signed materials composing the waveguide. For positive β, i.e., phase velocity parallel to the positive x axis, it may be shown that $\text{sgn } P_{out} = \text{sgn } \varepsilon_{out}$ and $\text{sgn } P_{in} = \text{sgn } \varepsilon_{in}$, where P_{in} and P_{out} are, respectively, the integrated power flows inside and outside the slab. This shows how the two fluxes flow in opposite directions (since $\text{sgn } \varepsilon_{in} = -\text{sgn } \varepsilon_{out}$).

The net power flux evidently consists of the algebraic sum $P_{net} = P_{in} + P_{out}$, which in magnitude is less than $\max(|P_{in}|, |P_{out}|)$. For positive β, when we get $P_{net} > 0$, the corresponding mode is a forward mode, since its phase velocity is parallel with the net power flow (and thus with its group velocity); if instead $P_{net} < 0$, we are dealing with a backward mode, with antiparallel phase and group velocities.

As rigorously shown in Ref. [33], a positive group velocity, and therefore a forward mode, is obtained when $\varepsilon_{ENG} < -\varepsilon_0$, and a backward mode is supported for $-\varepsilon_0 < \varepsilon_{ENG} < 0$ for both even and odd modes. This is justified by the fact that when $|\varepsilon_{ENG}| > \varepsilon_0$, the mode is less distributed in the epsilon-negative (ENG) material and more "available" in the double-positive (DPS) layer, independent of their relative position. As a result, the negative power flow present in the ENG material is also less than the positive one in the DPS and the net power remains positive, i.e., parallel to the phase velocity. For backward modes, the situation is reversed, since $|\varepsilon_{ENG}| < \varepsilon_0$. This interesting feature confirms our heuristic prediction based on nanocircuit analogy of Figure 23.7, following which we envisioned this planar geometry. In particular, the transmission-line model of Figure 23.7 holds directly for the even mode, due to the electric field polarization consistent with the voltage and current orientations in the figure, since the electric field polarization in this mode places in "series" configuration the outer layer and in "parallel" the inner layer. In this case, we indeed require $-1 < \varepsilon_{in}/\varepsilon_{out} < 0$, and therefore, a metal–insulator–metal waveguide would have $\varepsilon_{ENG} < -\varepsilon_0$, and therefore, a forward-wave behavior as predicted by Figure 23.7a, whereas an insulator–metal–insulator waveguide will have $-\varepsilon_0 < \varepsilon_{ENG} < 0$, and therefore, a backward behavior, as in Figure 23.7b. As described in Ref. [33], and consistent with the slow-wave features of these modes, in these subwavelength structures the field distributions are very much concentrated around the interfaces $y = \pm d/2$, in some sense indeed resembling a transmission line made of conducting wires running along $y = \pm d/2$ at lower frequencies. The odd modes behave in a dual way, due to the different orientation of the electric field, consistent with our intuitions in Ref. [39]. This is consistent with the discussion by Shvets [48] for the plasmonic–air–plasmonic waveguide supporting an odd backward mode.

It is interesting to notice that the modal propagation along the planar interfaces that we have just described provides an "effective" index of refraction, which may be positive or negative depending on the properties of the excited mode, i.e., on the forward or backward nature of the corresponding power flow. This opens the possibility to develop the concept of a "flatland" nanooptics, for which the concepts of negative-refractive materials may be translated into the plane of propagation. The advantage of this configuration, which is analogous to the planar transmission-line propagation at

microwave frequencies analyzed in Refs. [4,5], relies just on the combinations of plasmonic and nonplasmonic layers, consistent with our nanocircuit paradigm.

Varying the geometrical parameters of the waveguide along the direction orthogonal to the plane of propagation directly affects the effective properties in the flatland plane, and, in particular, the effective index of refraction. It is worth underlining an important property of these planar metamaterials: unlike the other common ways of constructing LH metamaterials with resonant inclusions, like the one suggested in Section 23.3, here these effective 2D planar metamaterials do not rely on an individual resonant phenomenon, similar to their microwave counterparts synthesized with printed microstrip lines and lumped circuit elements [4,5]. This allows better robustness to losses and larger bandwidth of operation, i.e., better possibility for demonstrating some of the unconventional loss-sensitive features of negative-index metamaterials in the IR and visible frequency domains.

In Ref. [33], we defined a proper metric for describing the propagation properties of this optical transmission-line metamaterials. In particular, it is possible to define effective (i.e., equivalent) permittivity and permeability for the propagating mode. In the even operation, which is the one consistent with Figure 23.7 and with the nanocircuit analogy, the effective constitutive parameters "sensed" by the modes are given by the following formulas [33]:

$$\varepsilon_{\text{eff}}^{\text{even}} \equiv \varepsilon_{\text{in}}$$
$$\mu_{\text{eff}}^{\text{even}} \equiv \mu_0 + \frac{\partial E_x/\partial y|_{y=0}}{i\omega\, H_z|_{y=0}}. \tag{23.13}$$

In other words, the longitudinal component of the electric field (which is interestingly the one associated with the circulating displacement current) directly affects the effective permeability of the metamaterial, providing the possibility of having effective DNG properties and therefore negative-index propagation, for $\varepsilon_{\text{in}} < 0$.

In order to provide some insight into the equivalence between the transmission-line propagation and this optical nanotransmission-line metamaterial, Figure 23.8 sketches the displacement current

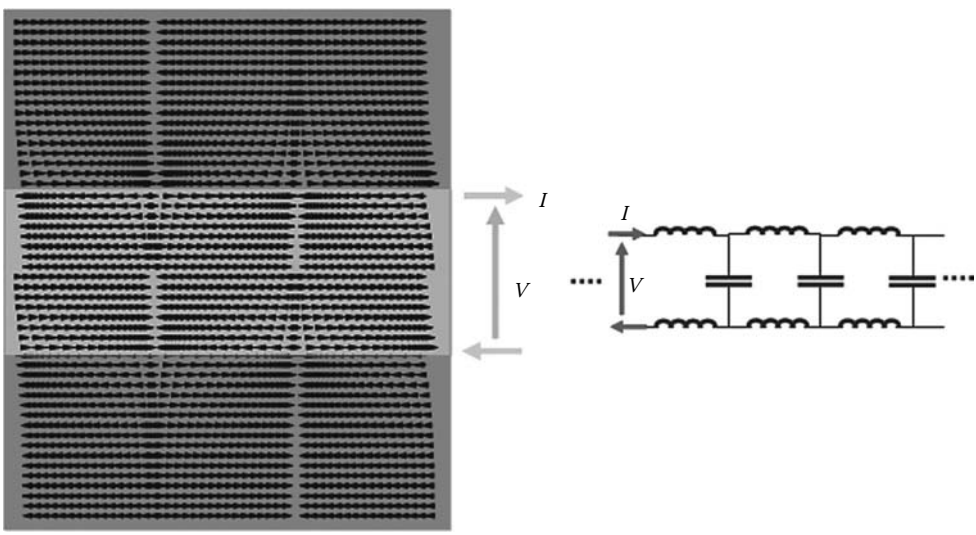

FIGURE 23.8 Analogy between current and voltage in a standard transmission line and those flowing in the nanotransmission-line metamaterials at optical frequencies. The panel on the left plots the displacement current distribution in the layered nanotransmission line of Figure 23.7, highlighting the roles of current and voltage flow along the line, analogous to those in a low-frequency transmission-line segment modeled with lumped inductors and capacitors.

flow in such a metamaterial, comparing it with the currents and voltages flowing along a standard transmission-line model. It can be seen how the even mode of operation resembles the same functionalities as the transmission-line counterpart, noticing however that there are differences in supporting two oppositely directed power and current flows at the two sides of the plasmonic interfaces. The figure supports also our heuristic intuition in terms of the nanocircuit paradigm for the realization of optical positive-index and negative-index metamaterial, consistent with Figure 23.7.

In the dispersion of these optical nanotransmission-line metamaterials, an important role is taken by the necessary frequency dispersion of the involved plasmonic material. Supposing to employ the Drude model (including realistic losses) for silver, as the one we already used in the previous section, we have derived in Ref. [33] some important plots showing the dispersion of forward and backward modes versus frequency for glass–silver combinations. Fixing the core slab thickness at $d = 14\,\text{nm}$ and assuming glass with $\varepsilon_{SiO_2} = 2.19\varepsilon_0$ as the insulating material, Figures 23.9 and 23.10 show the plots of the variation of $\text{Re}[\beta]$ and $\text{Im}[\beta]$ versus frequency for even and odd modes in the

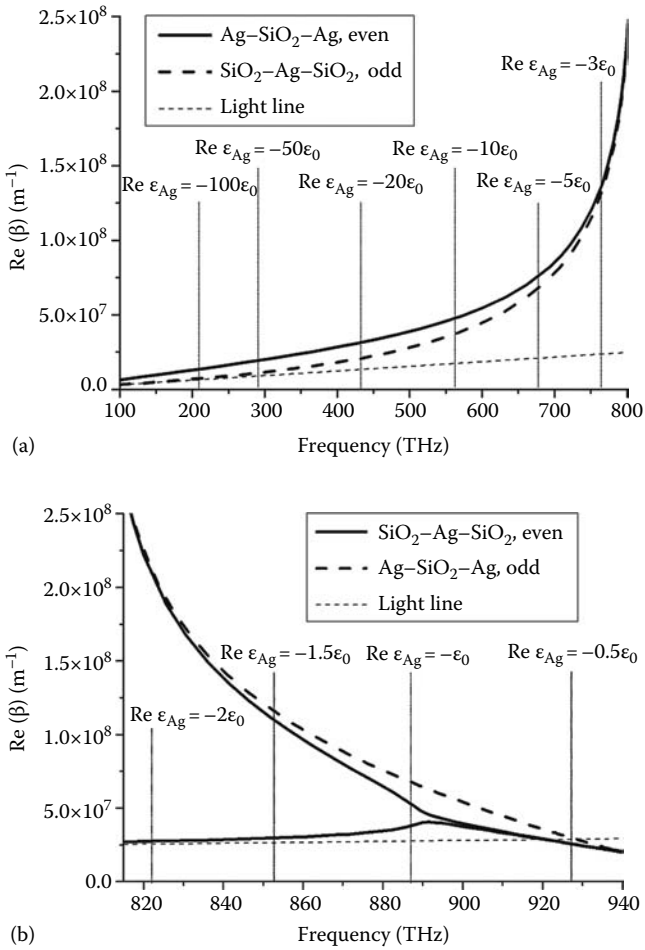

FIGURE 23.9 Dispersion plots taking into account the Drude model for silver (including loss): (a) the positive slope confirms a positive index of propagation (in the even mode this corresponds to the structure of Figure 23.7a); (b) the negative slope indicates negative-index behavior (consistent for the even mode with Figure 23.7b). (From Alù, A., Engheta, N., *J. Opt. Soc. Am. B*, 23(3), 571, 2006.)

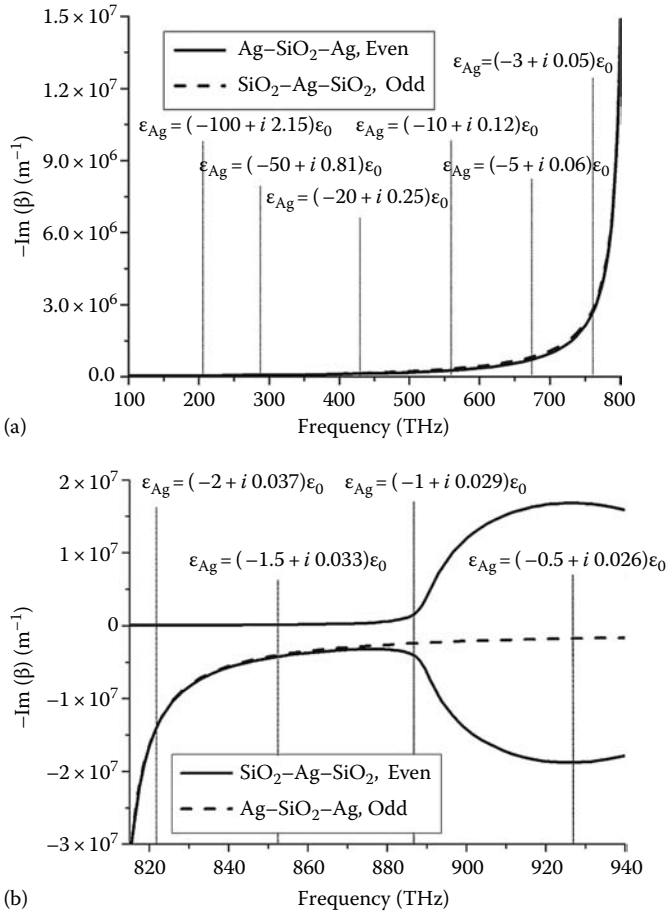

FIGURE 23.10 Damping factors (Im β) corresponding to the dispersion plots of Figure 23.9, due to the presence of absorption in silver. (From Alù, A., Engheta, N., *J. Opt. Soc. Am. B*, 23(3), 571, 2006.)

two configurations of SiO_2–Ag–SiO_2 and Ag–SiO_2–Ag waveguides. The slope of these plots again confirms our prediction regarding the RH and LH behavior of the modes, depending on the value of the real part of the permittivity as a function of frequency (as indicated at certain selected frequencies).

In particular, Figures 23.9b and 23.10b refer to the behavior of these layered metamaterials as negative-index optical metamaterials. At high frequencies, the permittivity of silver is indeed higher than $-\varepsilon_{SiO_2}$, and therefore, in this regime, the SiO_2–Ag–SiO_2 waveguide operates in its negative-refractive even mode, as predicted in Figure 23.7b, whereas the dual geometry has its backward operation with an odd mode. We note that in the even case, for which the background region allows propagation, there are two possible modes supported at the same frequency, one backward and one forward. This is consistent with our general findings for propagation along periodic arrays of plasmonic particles, for which the propagation in the background region adds a spurious forward mode with phase velocity close to that in the background. This mode is not described by our nanocircuit analogy and is not of interest for the present purposes.

The imaginary part of β, reported in Figure 23.10 for the corresponding cases, represents the damping factor for these modes, due to the material losses in the silver. In the figure, the sign of Im β is

positive for the forward modes and negative for the backward modes, since in Figure 23.9 we considered solutions with positive Re β in the $+x$ direction [and therefore for the backward case, one should have a power flow in the opposite direction (i.e., $-x$ direction)]. Considering that we used realistic values for material losses and that the cross-section of the guided beam is very small (the core thickness is just 14 nm), this example shows that highly confined guided modes can propagate along this structure without diffraction for some noticeable distance both in the even and odd mode of operation. The effective index of refraction for these modes may attain negative values and maintain a reasonably low level of absorption, arguably better than that achievable with the geometry of Section 23.3 or any other solution involving resonant inclusions. This is due to the inherent robustness achievable with the transmission-line concepts, since the negative refraction is not achieved by individual resonances of electrically small inclusions, but rather by the distributed resonance of the whole metamaterial. This solution, analogous with the microwave transmission-line metamaterial counterparts, ensures larger bandwidth and more robustness to losses, as clearly seen in Figure 23.10.

The corresponding effective parameters for this geometry, as calculated from Equation 23.13, are reported in Figure 23.11. The possibility of obtaining effectively negative permittivity and permeability is clearly shown, confirming the results of Figures 23.9 and 23.10 and our previous discussion.

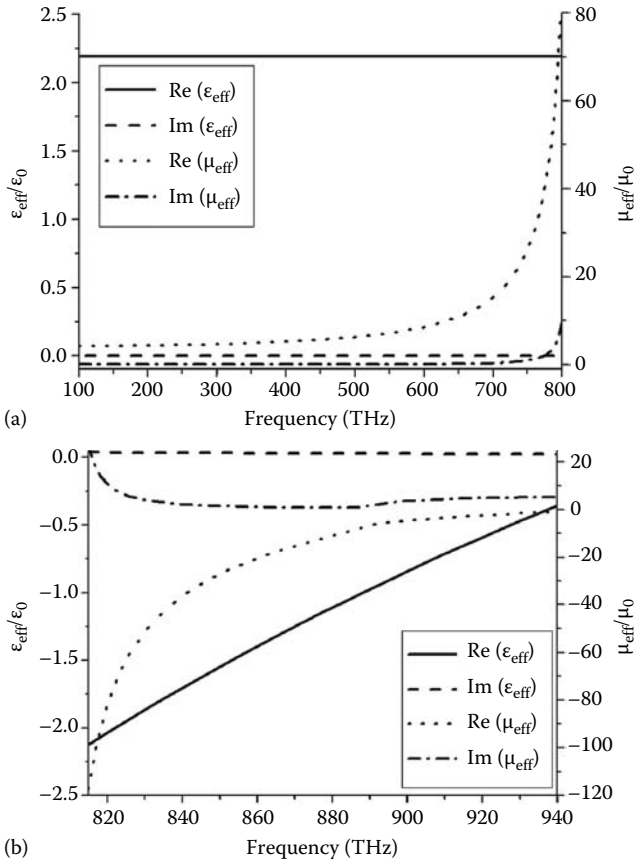

FIGURE 23.11 The effective material parameters for the geometry of Figures 23.9 and 23.10, calculated following Equation 23.13. (From Alù, A., Engheta, N., *J. Opt. Soc. Am. B*, 23(3), 571, 2006.)

In Ref. [33], we have applied these concepts to prove negative refraction and subwavelength focusing in this flatland geometry. Our full-wave simulations, obtained with a mode-matching technique, demonstrate that it is indeed possible to build two matched metamaterials at optical frequencies with positive-index and negative-index properties and experience highly subwavelength focusing and negative refraction. Experimental results, obtained by the Atwater group, although for a nonmatched interface, have recently shown the realistic possibility of obtaining negative refraction at optical frequencies [49], following similar considerations and employing silver and gold plasmonic layers.

23.5 Three-Dimensional Optical Negative-Index Metamaterials

As we have pointed out in the previous section, for a linear array of plasmonic nanoparticles (the 1D analog to the planar array of nanoparticles as in the middle row of Figure 23.7), when excited with an electric field vector orthogonal to the array axis, one may expect to see, under proper conditions, a confined guided mode with negative index of refraction supported by this array. As we have reported in our full-wave analysis of this 1D problem [34], this is indeed the case: linear plasmonic arrays of nanoparticles may support a transmission-line mode consistent with the heuristic interpretation of Figure 23.7, as another interesting possibility to realize backward-wave materials at optical frequencies exploiting plasmonic effects. It is interesting to note that the transverse polarization is required to achieve backward-wave propagation in this 1D setup, consistent with the field distribution inside a transmission line at lower frequencies (see Figure 23.7).

In the nanocircuit analogy, each plasmonic nanoparticle would correspond to a lumped nanoinductor, and the free-space (or dielectric) gaps between and around them correspond to the nanocapacitors. Such a cascade of inductors and capacitors is capable of guiding and transmitting the wave energy [34]. Even though such linear chains may represent an alternative route for realization of backward-wave propagation at optical frequencies, it is evident that to realize negative refraction we need the 2D materials, and the ideal situation would be to have an isotropic 3D response.

To this end, we have proposed an optical metamaterial that generalizes our 1D chain results to a 3D geometry, showing how it may indeed be possible to obtain an isotropic metamaterial, at least in the two dimensions, but possibly also in three dimensions, with negative-refraction properties. The 3D LH nanotransmission-line metamaterial introduced in Ref. [35] is therefore envisioned as a metamaterial composed of plasmonic nanoparticles, of polarizability α, interleaved by gaps in a background medium with permittivity $\varepsilon_0 > 0$. Once again, as in Section 23.3, due to the small dimensions of the inclusions and their nonmagnetic nature, we assume that their electromagnetic response is adequately described by the polarizability model.

As shown rigorously in Ref. [35], a regular lattice of densely packed and properly designed plasmonic particles may indeed support a nanotransmission-line propagating mode in three directions and thus may act as an effective negative-index metamaterial, even though no direct magnetic response is present in the materials of each nanoparticle under consideration (i.e., at the frequencies of interest all the magnetic permeabilities of the constituent materials are equal to free-space permeability μ_0, and due to the small size of the inclusions the magnetic polarizability of each of them is negligible). Following the same analogy described in the previous section, for the same transverse polarization of the electric field, the dual lattice, i.e., a dense array of "voids" in a plasmonic host medium, would correspond to a DPS metamaterial with forward-wave behavior.

The dispersion properties of such a metamaterial have been obtained analytically in Ref. [35] by considering the eigenvalue problem associated with this crystal lattice and searching for the self-sustained solutions for the phase vector $\boldsymbol{\beta} = \beta_x \hat{\mathbf{x}} + \beta_y \hat{\mathbf{y}} + \beta_z \hat{\mathbf{z}}$.

The dispersion relation for these modes is given by the following equation [35]:

$$\sum_{(l,m,m)\neq(0,0,0)} \mathrm{Re}\left(\frac{e^{i\left(\bar{r}+l\bar{\beta}_x\bar{d}_x+m\bar{\beta}_y\bar{d}_y+n\bar{\beta}_z\bar{d}_z\right)}}{\bar{r}^3}\left[(1-i\bar{r})\,\frac{2l^2\overline{\mathrm{d}_x^2}-m^2\overline{\mathrm{d}_y^2}-n^2\overline{\mathrm{d}_z^2}}{\bar{r}^2}+m^2\bar{d}_y^2+n^2\bar{d}_z^2\right]\right) = \frac{2}{3}\mathrm{Re}\left[\bar{\alpha}^{-1}\right] \tag{23.14}$$

where $\bar{\boldsymbol{\beta}} = \boldsymbol{\beta}/k_0$, $\bar{d} = k_0 d = 2\pi d/\lambda_0$, $\bar{r} = \sqrt{l^2\overline{\mathrm{d}_x^2}+m^2\overline{\mathrm{d}_y^2}+n^2\overline{\mathrm{d}_z^2}}$, $\bar{\alpha} = k_0^3\alpha/(6\pi\varepsilon_0)$, and d_i are the lattice distances in the three directions and λ_0 is the wavelength in the background host. This real-valued (in the lossless limit, as shown in Ref. [35]) and completely general dispersion relation, which is written in terms of normalized dimensionless quantities, relates the propagating modal solutions for a lattice of particles embedded in a transparent background to the normalized geometrical and electromagnetic properties of the lattice. In the limit of closely spaced (but not touching) particles, this dispersion relation may be simplified by assuming that the main interaction among the particles happens in the nearest-neighbor limit. In this case, a good approximation for Equation 23.14 is given by

$$\frac{2\cos\left(\bar{\beta}_x\bar{d}_x\right)}{\overline{\mathrm{d}_x^3}}-\frac{\cos\left(\bar{\beta}_y\bar{d}_y\right)}{\overline{\mathrm{d}_y^3}}-\frac{\cos\left(\bar{\beta}_z\bar{d}_z\right)}{\overline{\mathrm{d}_z^3}}=\frac{\mathrm{Re}\left[\bar{\alpha}^{-1}\right]}{3}. \tag{23.15}$$

In this scenario, consistent with the 1D results, it may be shown that Equation 23.15 implies backward-wave propagation for the transverse polarization, i.e., the transverse electric waves supported by this collection of closely spaced plasmonic nanoparticles, under proper conditions on the polarizability of the particles, supports negative-refractive properties.

Two important requirements have been found to be essential for obtaining this LH propagation in an optical metamaterial composed of regular lattices of plasmonic nanoparticles: (1) the particles should be relatively close to their individual resonance and (2) the distance among them should be electrically small, i.e., that the optical metamaterial is densely packed. The latter condition ensures the "transmission-line" condition on the collection of lumped nanoinductors constituting the 3D transmission line, in some sense analogous to the 3D metamaterial at microwave frequencies [50]. The first condition requires the nanoparticles to be plasmonic and relatively close to their resonance. The interesting point that arises from our analysis, however, is that the tight and strong coupling among the individual nanoresonances widens enormously the bandwidth of operation when compared with the individual resonances of the single nanoparticle. This is consistent with the inherent transmission-line behavior: even in its basic circuit model, an infinitely long cascade of infinitely small LC cells has, in the limit, an infinite bandwidth of operation, even though the basic cell itself would represent a filter with a small bandwidth.

This concept is clear in the theoretical result shown in Figure 23.12, which reports the regions of operation for a metamaterial made of homogeneous nanoparticles with permittivity ε as a function of the center-to-center distance among them. It is evident how for narrow spacing (which indirectly implies a smaller size for each individual nanoparticle) the bandwidth of operation, in terms of the allowed values of permittivity, increases, even though it is well known that the resonant condition for an individual nanosphere narrows down dramatically around the value $\varepsilon = -2\varepsilon_0$ when its radius gets smaller and smaller.

The result is a relatively broad range of permittivities for which backward-wave propagation is possible, and this value saturates to a finite range of permittivities even when the single particle size tends to zero (of course at some point, approaching the atomic size, quantum effects should be considered in the description of the particle interaction, and this classic approach would not be adequate any more).

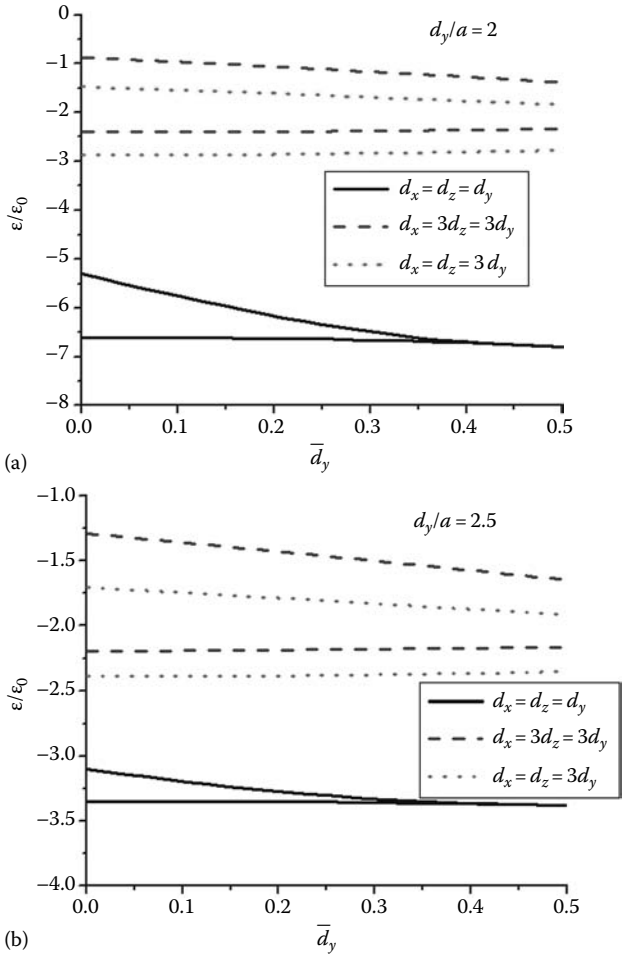

FIGURE 23.12 Regions of negative-index operation in terms of the permittivity of the spherical particle and their relative spacing factors in the three directions. (From Alù, A. and Engheta, N., *Phys. Rev. B*, 75, 024304 (20 pages), January 2007.)

As we have shown with rigorous analytical proof in Ref. [35], the robustness to losses is also much higher than that of a single individual nanoresonance, again due to the tight coupling among the closely spaced plasmonic nanoparticles. This provides a clear advantage with respect to the scenarios for negative refraction at optical frequencies employing resonant inclusions, as those proposed in Section 23.2 and in the referenced literature.

As an example of the proposed LH metamaterial employing simple homogeneous silver particles, we show here some numerical simulations, as reported in Ref. [35], using realistic data for the permittivity of bulk silver, including material dispersion and realistic material losses in the material. Figure 23.13a shows the frequency dispersion for a lattice of silver particles of radius $a = 15$ nm and center-to-center spacing between the particles $d_z = d_y = 33$ nm and $d_x = 3d_y$ in a glass background ($\varepsilon_{SiO_2} = 2.14\varepsilon_0$). In this case, the resonance $\mathrm{Re}\,\alpha^{-1} = 0$ is for $f_0 \simeq 750$ THz, $\lambda_0 \simeq 400$ nm, and the spacing is $\overline{d}_y = 0.7$ at this frequency, which is in the range of minimum losses, as optimized with fully analytical proofs in Ref. [35]. The solid lines report real (darker) and imaginary (lighter) parts of the wave number $\overline{\beta}_y$. The dashed lines also show the behavior that such dispersion curves would

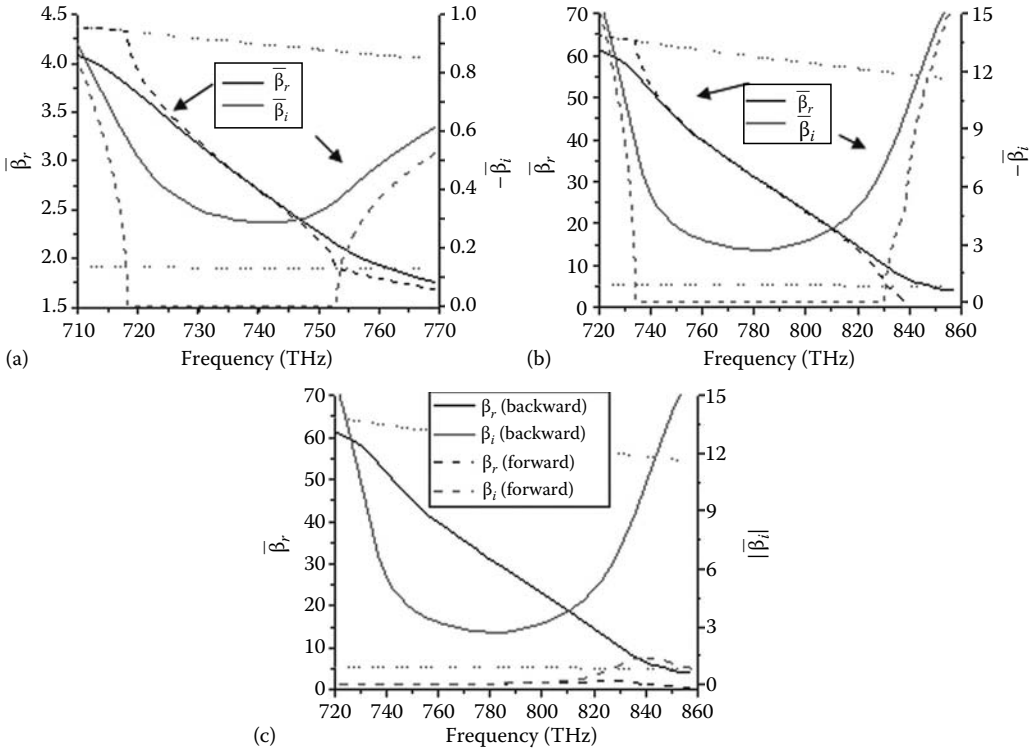

FIGURE 23.13 Dispersion plots of the negative-index operation versus frequency for a metamaterial made of silver particles, using silver material parameters (including losses) from experimental data for its bulk properties in a glass background ($\varepsilon_{SiO_2} = 2.14\varepsilon_0$). The solid lines correspond to realistic data with losses, the dashed lines neglect the losses in the silver, and the thin dotted lines bound the region of backward-wave operation in the ideal lossless case. (a) $a = 15$ nm, $d_z = d_y = 33$ nm, and $d_x = 3d_y$; (b) $a = 1$ nm and $d_z = d_y = 2.2$ nm; (c) the backward-wave mode for (b) is compared with the forward-wave mode, showing the difference in the sensitivity to losses in the two cases. In (a) and (b), the forward-wave mode, although present, is not shown here to avoid crowding the plots. (From Alù, A. and Engheta, N., *Phys. Rev. B*, 75, 024304, 2007. Copyright (2007) by the American Physical Society.)

have had, if the silver losses in the particles had been neglected. The thin red dotted lines plot the ideal boundaries that limit such dispersion curves, i.e., $\pi/\overline{d}_y$ and $\overline{\beta}_{\min}$, as defined in Ref. [35].

For comparison, Figure 23.13b also includes the results for the same setup but for hypothetically much smaller particles ($a = 1$ nm), maintaining the same aspect ratio with the spacing, i.e., $d_z = d_y = 2.2$ nm. In this case, $\overline{d}_y = 0.05$ at the central frequency. As one can see when comparing the two cases, the smaller spacing has definitely increased the bandwidth of backward-wave behavior for this setup, together with a corresponding increase in its loss factor, as predicted in the previous section. In addition, the real part of $\overline{\beta}$ has increased, giving rise to a slower phase propagation, due to the reduced distance between neighboring particles. The level of losses in this configuration is lower than any other solutions proposed in the literature involving resonant nanoinclusions, consistent with our previous discussion. The price to be paid is the simultaneous presence of another mode of propagation, forward in nature, that coexists at the same frequency and for the same polarization, consistent with the results of the previous section. This is related to the strong spatial dispersion inherently present in such densely packed arrays of plasmonic particles. Figure 23.13c, for completeness, reports the dispersion of this extra forward mode, which is not of interest to our purposes. We

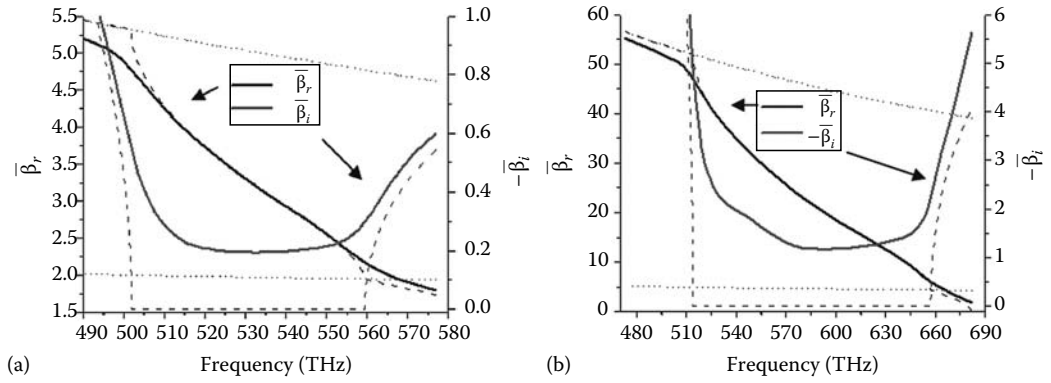

FIGURE 23.14 Similar to Figure 23.13 but with a SiC background ($\varepsilon_{SiC} = 6.52\varepsilon_0$). (a) $a = 10$ nm, $d_z = d_y = 22$ nm, and $d_x = 3d_y$; (b) $a = 1$ nm and $d_z = d_y = 2.2$ nm. (From Alù, A. and Engheta, N., *Phys. Rev. B*, 75, 024304 (20 pages), January 2007.)

are currently studying configurations and solutions to overcome the presence of this spurious mode and isolate the negative-index response for this optical metamaterial.

Figure 23.14 shows analogous results obtained with a silicon carbide background ($\varepsilon_{SiC} = 6.52\varepsilon_0$). In this case, the frequency of operation is shifted down, since $\mathrm{Re}\,\alpha^{-1} = 0$ for $f_0 \simeq 550$ THz, $\lambda_0 \simeq 550$ nm. In Figure 23.14a, the radius of each particle is fixed at $a = 10$ nm and spacing between the particles $d_z = d_y = 22$ nm and $d_x = 3d_y$. The normalized spacing in this case is again around $\overline{d}_y = 0.6$, ensuring minimum attenuation for this configuration. Employing smaller particles, as in Figure 23.10b, i.e., $a = 1$ nm, $d_y = 2.2$ nm, and $\overline{d}_y \simeq 0.06$, the bandwidth is sensibly increased, but the attenuation factors are higher, consistent with the previous section and Figure 23.13.

The numerical results reported here all refer to 3D optical metamaterials that are isotropic in two dimensions in the y–z plane since $d_z = d_y \neq d_x$, eventhough in Ref. [35] we have also studied the case of 3D isotropy. The major limitation of a fully isotropic metamaterial resides in the fact that the tight coupling in the direction of polarization of the electric field actually deteriorates the performance of the metamaterial, both in terms of bandwidth and robustness to losses. In other words, full isotropy may be obtained only at the expense of an increase in the Q factor of the structure, which may not be desirable for these configurations. At least for the isotropy in two dimensions, this solution, however, provides a viable and interesting way to obtain negative-refraction behavior at optical frequencies within the limitations of natural plasmonic materials. In Ref. [35], applying these concepts and exploiting the anomalous dispersion features of these 3D optical metamaterials, we have presented some full-wave numerical simulations producing subwavelength focusing in the canalization regime.

As a last numerical result, which summarizes the main features of the nanotransmission-line solution to the design of negative-index metamaterials, Figure 23.15 shows a comparison between the planar waveguide of the previous section and the 3D lattice metamaterial of this section in terms of robustness to ohmic losses in their negative-index regime.

Figure 23.15 shows the distance that a negative-index beam may travel before its field amplitude reaches e^{-1} of the original value for a cross-section of the planar waveguide, or of the cylindrical array of particles along which the mode is traveling, with $2a = 50$ nm. In the lattice case, the longitudinal period has been assumed to be $2.1a$. The figure compares four cases: the two modal distributions (even and odd) for the planar waveguide, which following the previous section supports backward-wave propagation respectively for the insulator–metal–insulator case (named regular in the caption) and metal–insulator–metal (named dual in the caption) and the two lattice configurations, i.e., the regular one made of plasmonic nanoparticles and the dual one made of insulating

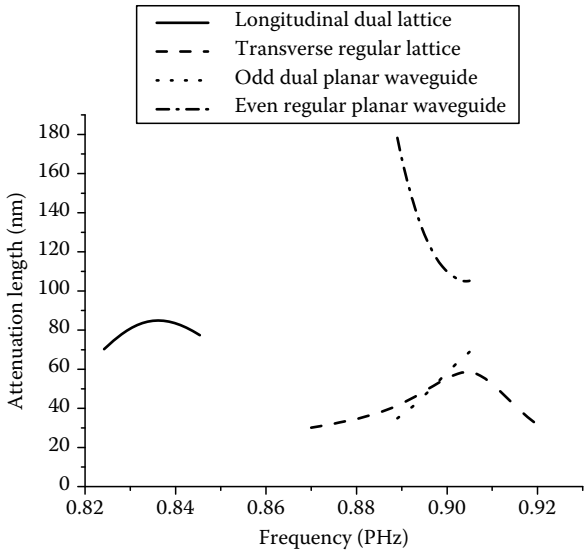

FIGURE 23.15 Comparison of the attenuation length traveled by a negative-index mode along planar layers or lattices, consistent with our results in this section and the previous one. In both cases, we assume the plasmonic material to be silver with realistic parameters and the insulating material to be free space. The thickness of each layer or planar array composing the lattice is $2a = 50$ nm.

voids in a plasmonic background. These last two geometries support backward-wave propagation for transverse and longitudinal electric modes, respectively.

Figure 23.15 shows how it is possible to guide backward modes with subwavelength cross-sections over a relatively long distance, providing some hope for the possible methods of experimental verification of these results. The possibility of enlarging the modal distribution (which anyway poses a limit to the transverse resolution of these devices when used as super-resolving lenses) and/or using lower loss materials may represent a viable way to improve these performances. It is interesting to see how the two pairs of curves are strictly related to each other in their functionalities and field polarization, consistent with the nanocircuit analogy that drew us to envision both geometries.

23.6 Conclusions

In light of our recently proposed theory for extending the circuit concepts to optical frequencies, here we reviewed our recent results on multiple scenarios and possibilities for designing negative-refraction metamaterials in the IR and visible domain. We focused on three of our theoretical proposals in this regard: the use of properly designed nanoinclusions made of loops of plasmonic nanoparticles that may exhibit a resonant magnetic response, the use of plasmonic nanolayers, and the use of periodic lattices of nanoparticles. All these geometries have been shown to potentially guide backward-wave modes and provide a negative-refraction behavior at optical frequencies exploiting naturally available plasmonic materials. Our nanocircuit interpretation explains all these different mechanisms, showing how plasmonic materials are essential to provide the required compact resonances in these different geometries. These results may provide interesting possibilities for subwavelength focusing, compact waveguiding devices, and enhanced imaging at optical frequencies.

References

1. N. Engheta and R. W. Ziolkowski, guest editors, *IEEE Transactions on Antennas and Propagation, Special Issue on Metamaterials*, 51, 2546–2750, October 2003.
2. N. Engheta and R. W. Ziolkowski, eds., *Electromagnetic Metamaterials: Physics and Engineering Explorations*, IEEE-Wiley, New York, 2006.
3. N. Engheta and R. W. Ziolkowski, A positive future for double-negative metamaterials, *IEEE Transactions on Microwave Theory and Techniques*, 53, 1535–15556, April 2005.
4. G. V. Eleftheriades and K. G. Balmain, eds., *Negative Refraction Metamaterials: Fundamental Properties and Applications*, IEEE Press, John Wiley & Sons Inc., Hoboken, NJ, 2005.
5. C. Caloz and T. Itoh, eds., *Electromagnetic Metamaterials*, Wiley, New York, 2005.
6. A. K. Sarychev and V. M. Shalaev, *Electrodynamics of Metamaterials*, World Scientific Publishing Company, Singapore, 2007.
7. R. Marqués, F. Martín, and M. Sorolla, *Metamaterials with Negative Parameters: Theory, Design and Microwave Applications*, Wiley Series in Microwave and Optical Engineering, John Wiley & Sons, New York, 2008.
8. V. M. Shalaev, Optical negative-index metamaterials, *Nature Photonics*, 1, 41–48, 2007.
9. J. B. Pendry, Metamaterials in the sunshine, *Nature Materials*, 5, 599–600, August 2006.
10. J. B. Pendry and D. R. Smith, Reversing light with negative refraction, *Physics Today*, 57, 37, 2004.
11. R. W. Ziolkowski and E. Heyman, Wave propagation in media having negative permittivity and permeability, *Physical Review E* 64, 056625, 2001.
12. J. B. Pendry, Negative refraction makes a perfect lens, *Physical Review Letters*, 85(18), 3966–3969, 2000.
13. V. M. Shalaev, W. Cai, U. K. Chettiar, H.-K. Yuan, A. K. Sarychev, V. P. Drachev, and A. V. Kildishev, Negative index of refraction in optical metamaterials, *Optics Letters*, 30, 3356–3358, 2005.
14. G. Dolling, C. Enkrich, M. Wegener, J. F. Zhou, C. M. Soukoulis, and S. Linden, Cut-wire pairs and plate pairs as magnetic atoms for optical metamaterials, *Optics Letters*, 30, 3198–3200, 2005.
15. A. N. Grigorenko, A. K. Geim, H. F. Gleeson, Y. Zhang, A. A. Firsov, I. Y. Khrushchev, and J. Petrovic, Nanofabricated media with negative permeability at visible frequencies, *Nature*, 438, 335–338, 2005.
16. C. Enkrich, M. Wegener, S. Linden, S. Burger, L. Zschiedrich, F. Schmidt, J. F. Zhou, Th. Koschny, and C. M. Soukoulis, Magnetic metamaterials at telecommunication and visible frequencies, *Physical Review Letters* 95, 203901, 2005.
17. S. Zhang, W. Fan, K. J. Malloy, S. R. J. Brueck, N. C. Panoiu, and R. M. Osgood, Near-infrared double negative metamaterials, *Optics Express*, 13, 4922–4930, 2005.
18. N. Fang, H. Lee, C. Sun, and X. Zhang, Sub-diffraction-limited optical imaging with a silver superlens, *Science*, 308, 534–537, 2005.
19. T. J. Yen, W. J. Padilla, N. Fang, D. C. Vier, D. R. Smith, J. B. Pendry, D. N. Basov, and X. Zhang, Terahertz magnetic response from artificial materials, *Science*, 303, 1494–1496, 2004.
20. R. A. Shelby, D. R. Smith, and S. Schultz, Experimental verification of a negative index of refraction, *Science*, 292, 77–79, 2001.
21. L. Landau and E. M. Lifschitz, *Electrodynamics of Continuous Media*, Elsevier, New York, 1984.
22. C. F. Bohren and D. R. Huffman, *Absorption and Scattering of Light by Small Particles*, Wiley, New York, 1983.
23. J. Zhou, T. Koschny, M. Kafesaki, E. N. Economou, J. B. Pendry, and C. M. Soukoulis, Saturation of the magnetic response of split-ring resonators at optical frequencies, *Physical Review Letters*, 95, 223902, 2005.
24. V. A. Podolskiy, A. K. Sarychev, and V. M. Shalaev, Plasmon modes in metal nanowires and left-handed materials, *Journal of Nonlinear Optical Physics & Materials*, 11, 65–74, 2002.
25. A. K. Sarychev and V. M. Shalaev, Magnetic resonance in metal nanoantennas, in *Complex Mediums V: Light and Complexity*, *Proc. SPIE*, 5508, 128–137, 2004.

26. A. K. Sarychev and V. M. Shalaev, Plasmonic nanowire metamaterials, in *Negative Refraction Metamaterials: Fundamental Properties and Applications*, G. V. Eleftheriades and K. G. Balmain, eds., John Wiley & Sons, Inc., Hoboken, NJ, 2005, Chapter 8, pp. 313–337.
27. V. A. Podolskiy and E. E. Narimanov, Strongly anisotropic waveguide as a nonmagnetic left-handed system, *Physical Review B*, 71, 201101, 2005.
28. S. O'Brien, D. McPeake, S. A. Ramakrishna, and J. B. Pendry, Near-infrared photonic band gaps and nonlinear effects in negative magnetic metamaterials, *Physical Review B*, 69, 241101, 2004.
29. G. Shvets and Y. A. Urzhumov, Engineering electromagnetic properties of periodic nanostructures using electrostatic resonance, *Physical Review Letters*, 93, 243902, 2004.
30. M. L. Povinelli, S. G. Johnson, J. D. Joannopoulos, and J. B. Pendry, Towards photonic crystal metamaterials: Creating magnetic emitters in photonic crystals, *Applied Physics Letters*, 82, 1069–1071, 2003.
31. A. Alù, A. Salandrino, and N. Engheta, Negative effective permeability and left-handed materials at optical frequencies, *Optics Express*, 14(4), 1557–1567, February 20, 2006.
32. A. Alù and N. Engheta, Dynamical theory of artificial optical magnetism produced by rings of plasmonic Nanoparticles, *Physical Review, B*, 78, 085112, August 2008.
33. A. Alù and N. Engheta, Optical nano-transmission lines: Synthesis of planar left-handed metamaterials in the infrared and visible regimes, *Journal of the Optical Society of America B, Special Focus Issue on Metamaterials*, 23(3), 571–583, March 2006.
34. A. Alù and N. Engheta, Theory of linear chains of metamaterial/plasmonic particles as sub-diffraction optical nanotransmission lines, *Physical Review B*, 74, 205436 (18 pages), November 2006.
35. A. Alù and N. Engheta, Three-dimensional nanotransmission lines at optical frequencies: A recipe for broadband negative-refraction optical metamaterials, *Physical Review B*, 75, 024304 (20 pages), January 2007.
36. N. Engheta, A. Salandrino, and A. Alù, Circuit element at optical frequencies: nanoinductors, nanocapacitors and nanoresistors *Physical Review Letters*, 95, 095504, August 2005.
37. N. Engheta, Circuits with light at nanoscales: Optical nanocircuits inspired by metamaterials, *Science*, 317, 1698–1702, 2007.
38. M. G. Silveirinha, A. Alù, J. Li, and N. Engheta, Nanoinsulators and nanoconnectors for optical nanocircuits, *Journal of Applied Physics*, 103, 064305 (24 pages), March 2008.
39. A. Salandrino, A. Alù, and N. Engheta, Parallel, series, and intermediate interconnections of optical nanocircuit elements—Part 1: Analytical solution, *Journal of the Optical Society of America B*, 24(12), 3007–3013, December 2007.
40. A. Alù, A. Salandrino, and N. Engheta, Parallel, series, and intermediate interconnections of optical nanocircuit elements—Part 2: Nanocircuit and physical interpretation, *Journal of the Optical Society of America B*, 24(12), 3014–3022, December 2007.
41. A. Alù, A. Salandrino, and N. Engheta, Coupling of optical lumped nanocircuit elements and effects of substrates, *Optics Express*, 15(21), 13865–13876, October 2007.
42. A. Alù and N. Engheta, Optical 'Shorting Wires', *Optics Express*, 15(21), 13773–13782, October 2007.
43. A. Alù, M. Young, and N. Engheta, Design of nanofilters for optical nanocircuits, *Physical Review B*, 77, 144107 (12 pages), April 2008.
44. A. Alù and N. Engheta, Tuning the scattering response of optical nanoantennas with nanocircuit loads, *Nature Photonics*, 2, 307–310, April 2008.
45. C. R. Simovski and S. A Tretyakov, Local constitutive parameters of metamaterials from an effective-medium perspective, *Physical Review B*, 75, 195111, 2007.
46. J. D. Jackson, *Classical Electrodynamics*, Wiley, New York, 1998.
47. CST Design Studio 2006B, www.cst.com.
48. G. Shvets, Photonic approach to making a material with a negative index of refraction, *Physical Review B*, 67, 035109, 2003.
49. H. J. Lezec, J. A. Dionne, and H. A. Atwater, Negative refraction at visible frequencies, *Science*, 316, 430–432, 2007.
50. A. K. Iyer and G. V. Eleftheriades, *Journal of the Optical Society of America B: Optical Physics*, 23, 553, 2006.

IV

Artificial Chiral, Bianisotropic Media, and Quasicrystals

24

A Review of Chiral and Bianisotropic Composite Materials Providing Backward Waves and Negative Refractive Indices

Cheng-Wei Qiu
National University of Singapore

Saïd Zouhdi
Université Paris

Ari Sihvola
Helsinki University of Technology

24.1 Introduction

In a broad sense, the word *composite* means *made of two or more different parts*. The different natures of constituents allow us to obtain a material in which the set of performance characteristics is greater than that of the components taken separately. The properties of composite materials result from the properties of the constituent materials, the geometrical distribution, and their interactions. Thus to describe a composite material it will be necessary to specify the nature of constituents, the geometry of the distribution, and macroscopic response. In the field of electrical engineering, the electromagnetics in composite materials are more important, since the electromagnetic behavior of rather complicated structures has to be understood in the design of new devices or in the exploration of new findings. In the last few years, there has been an increasing interest in the research community in the modeling and characterization of negative-index materials. Negative-index materials are a class of composite materials artificially constructed to exhibit exotic electromagnetic properties not readily found in naturally occurring materials. This type of composite materials refract light in a way that is contrary to the normal right-handed rules of electromagnetism. Researchers hope that the peculiar properties will lead to superior lenses and might provide a chance to observe some kind of negative analog of other prominent optical phenomena, such as reversal of the Doppler shift and Cerenkov radiation. When the dielectric constant (ϵ) and magnetic permeability (μ) are both negative, waves can still propagate in such a medium. In this case, the refractive index in the Snell's law is negative, an incident wave experiences a negative refraction at the interface, and we have a backward wave whose phase velocity is in the direction opposite to the direction of the energy flow.

The first study of general properties of wave propagation in such a negative-index medium (NIM) has been usually attributed to the work of Russian physicist Veselago [1]. In fact, related work can be traced up to 1904 when physicist Lamb [2] suggested the existence of backward waves in a mechanical system. However, the first person who discussed the backward waves in electromagnetics was Schuster [3]. In his book, he briefly notes Lamb's work and gives a speculative discussion of its implications for optical refraction. He cited the fact that within the absorption band of, for example, sodium vapor a backward wave will propagate. However, because of the high absorption region in which the dispersion is reversed, he was pessimistic about the applications of negative refraction. Around the same time, Pocklington [4] showed that in a specific backward-wave medium, a suddenly activated source produces a wave whose group velocity is directed away from the source, while its velocity moves toward the source. Several decades later, negative refraction and lens application (not perfect yet) was rediscovered [5–7]. However, it is the translation of Veselago's paper into English that brought about the revival of the negative-index materials, which are also referred to as left-handed material (LHM) or metamaterials. Very influential were the papers by Pendry [8–10]. The interest was further renewed due to the arrival of existence of NIM was experimentally confirmed by Smith and Shelby [11–14]. A further boost to the field of NIM came when the applicability of lensing was proposed to avoid the diffraction limit [15] by using both periodic and evanescent electromagnetic waves. The field keeps expanding owing to the fact that the Maxwell equations are scalable; thus, practically the same strategies can be employed in the microwave and optical regions.

24.2 Fundamentals of NIM

In order to realize the negative refraction [16,17], the composite material must have effective permittivity and permeability that are negative over the same frequency band. When the real parts of permittivity and permeability possess the same sign, the electromagnetic waves can propagate. If those two signs are opposite, waves cannot propagate unless the incident wave is evanescent. Historically, the development of artificial dielectrics [19] was the first electromagnetic NIM by the design of a composite material. If both ϵ and μ are negative, the refractive index of the given composite is defined as

$$n = \sqrt{|\epsilon||\mu|}\sqrt{e^{2j\pi}} = -\sqrt{|\epsilon||\mu|}. \tag{24.1}$$

More detailed investigation on the causality of negative-index materials can be found in Ref. [20]. Usually, the solution of $n < 0$ consists of waves propagating toward the source, rather than plane waves propagating away from the source. Since such a solution would normally be rejected by the principles of causality, the physical proof of the solution of $n < 0$ can be supplied by the concept *average work* [12]. The work done by the source on the fields is

$$P = \Omega W = \pi \frac{\mu}{cn} j_0^2, \tag{24.2}$$

where

Ω and j_0 represent the oscillation frequency and magnitude of the source current
W is the average work done by the source on the field

It can be found that the solution of $n < 0$ leads to the correct interpretation that the current performs positive work on the fields because of $\mu < 0$ for negative-index materials. Because the work done by the source on the fields is positive, energy propagates outward from the source, in agreement with Veselago's work [1].

No known material has naturally negative permittivity and permeability, and hence NIM has to be a composite of at least two kinds of materials, which individually possess $\epsilon < 0$ and $\mu < 0$ in an

overlapped frequency band. In order to create negative permittivity at the microwave region, the approach of an array of metallic rods with the electric field along with the axis is used [10]. Such structures act as a plasma medium, and if the frequency is below the plasma frequency, the permittivity is negative. The Drude–Lorentz model can be used to characterize the wire medium with periodic cuts

$$\epsilon(\omega) = 1 - \frac{\omega_p^2 - \omega_{0e}^2}{\omega(\omega + j\Gamma_e) - \omega_{0e}^2}, \tag{24.3}$$

where ω_p, ω_{0e}, and Γ_e denote plasma frequency, resonant frequency, and damping constant, respectively. If the wires are continuous, the resonant frequency $\omega_{0e} = 0$.

Pendry proposed the resonant structures of loops of conductors with a gap inserted to realize the negative permeability [8]. The gap in the structure introduces capacitance and gives rise to a resonant frequency determined only by the geometry of the element. It is also known as the split-ring resonator (SRR), which could be described as

$$\mu(\omega) = 1 - \frac{F\omega^2}{\omega(\omega + j\Gamma_m) - \omega_{0m}^2}, \tag{24.4}$$

where F, Γ_m, and ω_{0m} are the filling fraction, resonant damping, and resonant frequency, respectively. New designs of SRR medium have been explored numerically and experimentally to overcome the narrow-band property, such as broadside SRR, complementary SRR, omega SRR, deformed SRR, and S-ring SRR [21–27]. Current designs can yield a large bandwidth, low loss, and small size, which make the application of SRR wider.

The combination of wire medium and SRR medium would present negative refraction due to the electric and magnetic responses [18,28–30]. However, such designs are normally anisotropic or bianisotropic, and the bianisotropic role and extraction of those bianisotropic parameters are thus discussed [21,31]. Efforts to create isotropic composite NIM are made by ordering SRRs in three dimension [32], and the design is further scaled to IR frequencies [33]. However, at the wavelength approaching the optical region, the inertial inductance caused by the electron mass and the currents through SRRs determines the plasma frequency and becomes dominant for scaled-down dimensions, which further makes the negative effects of permittivity and permeability totally disappear [34]. To overcome this, it is proposed to add more capacitive gaps to the original SRR [35]. Among the most recent results of experimental NIM structures with near-infrared response are those on NIM metamaterials for 1.5 nm range with a double periodic array of pairs of parallel gold nanorods [36], with a negative refractive index of about −0.3.

It is true that the conventional SRR's resonant structures are lossy and narrow-banded, and alternative approaches apart from exploring new designs may be of particular interest. Thus, the transmission line (TL) approaches are proposed by a group in the University of Toronto to support negative refraction and backward waves [37–40]. Their basic idea is to use a two-dimensional TL network with lump elements to achieve a high-pass filter, in which the backward wave can propagate. Thus, effective negative permittivity and permeability can be realized by suitable changes in configuration. The group in UCLA has further explored the TL approaches to realize the composite right- and left-handed structures [41–44]. The TL approach may provide a broader band for negative refraction than SRR and wire medium, but obviously it is more difficult to be implemented in practical application than the latter.

Another approach to generate negative refraction is to use photonic or electromagnetic bandgap structures (PBGs or EBGs) [45–47]. PBGs or EBGs, first initiated by Yablonovitch [48] in 1987, are constructed typically from periodic high dielectric materials and possess frequency band gaps eliminating electromagnetic wave propagation. Under certain circumstances, the Bloch/Floquet modes will lead to negative refraction. However, the negative-refraction behavior is different from that of the negative-index materials, in which the group velocity and phase vector are exactly antiparallel.

Electrically tunable nonreciprocal bandgap materials in the axial propagation along the direction of magnetization were considered in Ref. [49] to study cubic lattices of small ferrimagnetic spheres. Electromagnetic crystals (ECs) [50,51] operating at higher frequencies exhibit dynamic interaction between inclusions. ECs are artificial periodical structures operating at the wavelengths comparable with their period, whereas artificial dielectrics [19] operate only at long wavelengths compared with the lattice periods. In the optical frequency range they are called photonic crystals (PCs) [52]. In some particularly designed PCs, negative refraction is present [53–55], and the application of open resonators with PCs of negative refraction [56–58] is also proposed in Ref. [59].

24.3 Material Routes to NIMs via Chiral/Bianisotropic Media

Although the method of stacking metal resonators to achieve NIMs would macroscopically exhibit the magnetoelectric couplings and bianisotropy due to the periodic metal microstructures in the artificial media, this section focuses on the exploration of the material physics of chiral and bianisotropic media as promising candidates for NIMs, not only in the microwave but also in optical regions.

Composite materials may suffer bulkiness and difficulty in fabrication, which is a limiting factor in electromagnetic applications. Composites with the ability for magnetoelectric coupling may help alleviate some of those problems. The magnetoelectric composites are characterized by the cross-coupling between electricity and magnetism inherently from the optical activity, and composites can be isotropic or anisotropic, which depends on the existence of external biased fields. The phenomenon of optical activity was first discovered via experimentation by French scientists. In 1811, Arago found that quartz crystals rotate the plane of polarization of linearly polarized light, which is transmitted in the direction of its optical axis [60]. Later, this property was further demonstrated by various experiments by Biot [61,62], and it was found that optical activity is not restricted to crystal solids but exhibits in other materials such as boiling turpentine. Formal discussion of the concept of polarization was proposed in 1822 by Fresnel [63] who constructed a prism of rotatory quartz to separate two circularly polarized components from a linearly polarized ray. The time dependence $e^{j\omega t}$ was used but suppressed.

24.3.1 Isotropic Chiral Materials

In contrast to the argument that the optical activity was due to molecules, recent studies have used microwaves and wire spirals (Figure 24.1) to achieve a macroscopic model for such phenomenon instead of using light and chiral molecules [64].

From a macroscopic view, a chiral medium can be regarded as a continuous medium composed of chiral composites, which are uniformly distributed and randomly placed. It is a subclass of bianisotropic (magnetoelectric) composites. Scientists have made extensive research efforts to study bi-isotropic materials, such as the wave properties and interaction [65–67], light reflection and propagation through chiral interfaces [68], novel structures exhibiting cross-coupling [69], mixing formula to get effective parameters [70], and chiral patterns for antennas [71]. However, it appears that the application of chiral materials may be limited to the case of polarization converters, which can be used as polarizator shields and absorbing coating in RCS reduction such as Salisbury screens. More recently, there has been a renewed interest in the community of chiral materials, especially in the realm of negative-index materials. Pendry proposed a chiral route by wounding a metal plate into coils stacked by log pile [72].

Based on the work by the scientists in Helsinki, chiral materials have been proved to be a good alternative approach to realize negative refraction, since the backward wave could be supported [73,74]. The negative refraction can be easily obtained by properly mixing chiral particles [75] and arranging dipoles to minimize electric/magnetic response [76]. More recently, the negative reflection in a strong chiral medium and huge gyrotropy in planar chiral metamaterials were discovered [77,78].

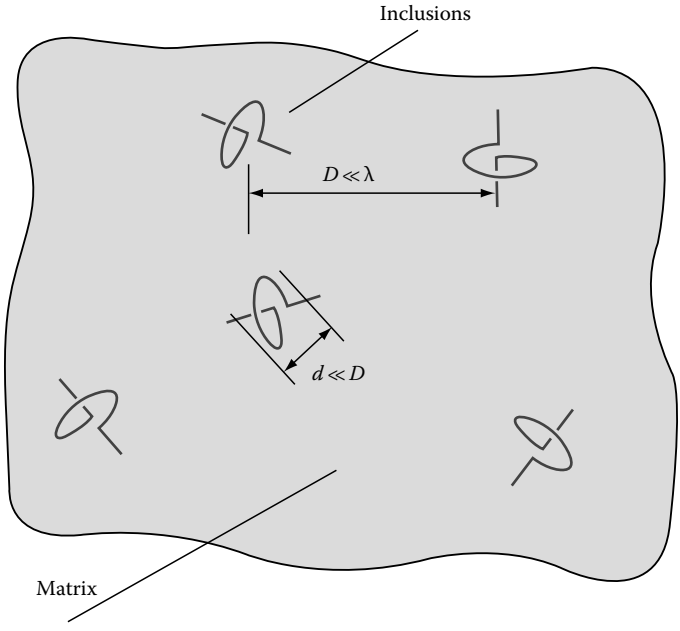

FIGURE 24.1 The typical configuration of a chiral medium composed of the same handed wire-loop inclusions distributed uniformly and randomly.

Two definitions are widely used to describe chiral media: Post's relations

$$D = \epsilon_P E + j\xi_c B \tag{24.5a}$$

$$H = j\xi_c E + (1/\mu_P)B \tag{24.5b}$$

and Tellegen's relations

$$D = \epsilon_T E + j\kappa\sqrt{\mu_0\epsilon_0}H \tag{24.6a}$$

$$B = -j\kappa\sqrt{\mu_0\epsilon_0}E + \mu_T H, \tag{24.6b}$$

where

ϵ_0/μ_0 is the permittivity/permeability in free space
P/T denotes the permittivity and permeability under Post/Tellegen constitutive relations
κ/ξ_c is the chirality used in the Post/Tellegen constitutive relations

These two constitutive relations were found to be applicable to chiral media composed of short wire helices as well as reciprocal chiral objects of arbitrary shape.

In order to force chiral materials to fall in the backward-wave regime, one only needs to make either permittivity or permeability resonant, which will produce a very small value of the product of $\epsilon\mu$. On the other hand, the effect of the chirality should be another solution, where the big chirality also favors the realization of backward waves and negative refraction. The optical activity and circular dichroism has been studied for chiral media, and the chirality of the medium's molecules can be seen as the cause of optical activity. Born [79] put forward the interpretation of optical activity for a particular molecular model, in which a coupled-oscillator model was used. Condon [80] gave a single-oscillator model in dissymmetric field for optically active material, based on the molecular theories of Drude, Lorentz, and Livens. The constitutive relations were suggested as follows:

$$D = \epsilon E + \frac{j\omega\alpha}{c_0} H$$
$$B = -\frac{j\omega\alpha}{c_0} E + \mu H, \tag{24.7}$$

where
c_0 is the light velocity in free space
α is the rotatory parameter

The parameter of α for rotatory power is frequency dependent:

$$\alpha(\omega) \sim \sum_b \frac{R_{ba}}{\omega_{ba}^2 - \omega^2 + j\omega\Gamma_{ba}} \tag{24.8}$$

where
a, b stand for quantum states
ω_{ba} is the frequency of the light absorbed in the jump $a \to b$
R_{ba} means the rotational strength of the absorbed line
the damping term of Γ_{ba} has been included for the consideration of the absorption

Finally, by comparing Tellegen's relations and Condon's model, the dispersion of the dimensionless chirality κ can be expressed in such a way that

$$\kappa(\omega) = \frac{\omega\omega_c}{\omega_c^2 - \omega^2 + jd_c\omega\omega_c}, \tag{24.9}$$

where
ω_c represents the characteristic frequency
d_c means the damping factor

Note that Equation 24.9 is valid for the one-phase transition, in which only one rotatory term in Equation 24.8 is counted due to the assumption that each transition between quantum states lies far off the others. Using the wavefield theory [70], a chiral medium can be characterized as two sets of equivalent dielectric parameters $\epsilon_\pm$ and $\mu_\pm$, given as

$$\epsilon_\pm(\omega) = \epsilon\left(1 \pm \frac{\kappa(\omega)\sqrt{\mu_0\epsilon_0}}{\sqrt{\mu\epsilon}}\right) \tag{24.10a}$$

$$\mu_\pm(\omega) = \mu\left(1 \pm \frac{\kappa(\omega)\sqrt{\mu_0\epsilon_0}}{\sqrt{\mu\epsilon}}\right). \tag{24.10b}$$

The imaginary parts of $(\epsilon_\pm,\ \mu_\pm)$ are also studied but not included, which are almost zero over the whole region except in the vicinity of ω_c. From Figure 24.2, one can find that $(\epsilon_+,\ \mu_+)$ becomes a double-negative (DNG) material in the frequency band [10, 13.3]GHz. When the frequency drops below ω_c or exceeds, it turns to a double-positive (DPS) medium. In Figure 24.3, such DNG–DPS reversion also happens. In the frequency band of [7.52, 13.3]GHz, the negative refraction occurs to + and − effective mediums, alternatively.

Hence, the electromagnetic fields within the chiral media can be obtained by the superposition of components as follows:

$$E = E_+ + E_-$$
$$H = H_+ + H_-, \tag{24.11}$$

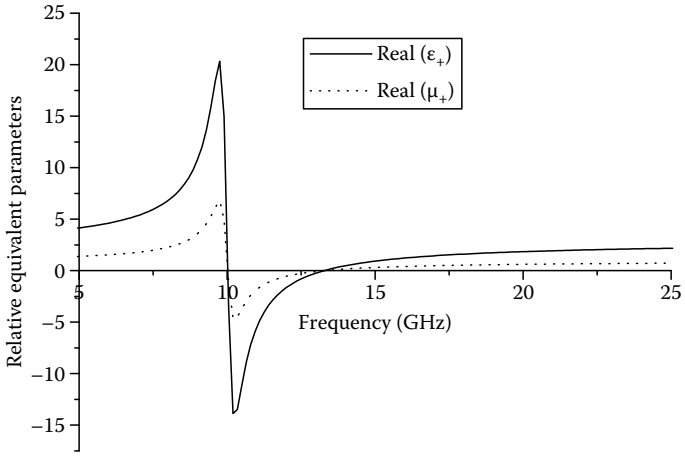

FIGURE 24.2 The frequency dependence of relative (ϵ_+, μ_+) in the range of [5, 25]GHz, the chirality's characteristic frequency $\omega_c = 2\pi 10^9$ (rad/s), $d_c = 0.05$, $\epsilon = 3\epsilon_0$, and $\mu = \mu_0$.

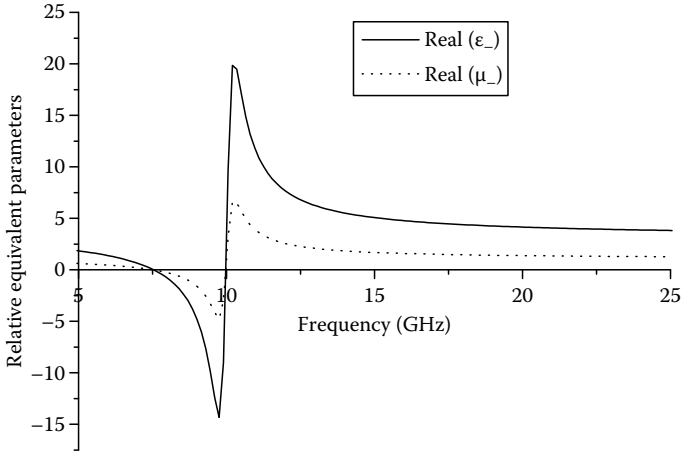

FIGURE 24.3 The same as Figure 24.2, for the frequency dependence of relative (ϵ_-, μ_-).

where ± fields correspond to the results calculated from two separate sets of effective materials (ϵ_+, μ_+) and (ϵ_-, μ_-), respectively. Interestingly, if we consider the case of a plane wave impinged upon an air–chiral interface, two frequencies where no chirality is actually present are particular: (1) if $f_l = 7.52$ GHz, the chiral medium is only characterized by the + equivalent medium composed of (ϵ_+, μ_+), which results in that only half of the power can be transmitted from the air to the chiral medium; and (2) if $f_h = 13.3$ GHz, only the pair of (ϵ_-, μ_-) remains. It can be observed that their geometrical mean is the characteristic frequency of chirality (i.e., $f_c = \omega_c/2\pi$), demonstrating the symmetric relation:

$$f_l f_h = f_c^2. \tag{24.12}$$

To summarize, the chirality dispersion in Condon's model, based on the molecular theory for quantum mechanics, can lead to negative-index media (i.e., $n_\pm = Re\left[\sqrt{\epsilon_\pm}\sqrt{\mu_\pm}\right]$) at certain frequency

bands. One, however, has to mind that $n_{\pm}$ cannot be simultaneously negative within the region of $(f_l,\ f_h)$. The plus and minus signs of refractive indices will be exchanged when the working frequency oversteps resonant frequency f_c.

In view of Equations 24.5 and 24.6, both constitutive relations are applicable to reciprocal media only. When the nonreciprocity is present in chiral magnetoelectric materials, the constitutive relations are expressed for Post's relations

$$\begin{aligned} D &= \epsilon_P E + (j\xi - \nu)B \\ H &= (j\xi + \nu)E + (1/\mu_P)B \end{aligned} \tag{24.13}$$

and for Tellegen's relations

$$\begin{aligned} D &= \epsilon_T E + (\chi + j\kappa)\sqrt{\mu_0\epsilon_0}H \\ B &= (\chi - j\kappa)\sqrt{\mu_0\epsilon_0}E + \mu_T H, \end{aligned} \tag{24.14}$$

where χ and ν denote the nonreciprocity parameters used in these two commonly used constitutive relations. The conversion between these two relations is given as follows:

$$\begin{aligned} \epsilon_T &= \epsilon_P + \mu_P(\xi^2 + \nu^2) \\ \chi &= \mu_P \nu c_0 \\ \kappa &= \mu_P \xi c_0 \\ \mu_T &= \mu_P. \end{aligned} \tag{24.15}$$

In particular, we consider only the Tellegen's relations as a nonreciprocal example, since such a condition can be transformed to Post's relations in an isotropic case. The dispersion of nonreciprocity has not been clearly worked out independently so far, but from general considerations it can be envisioned that the dispersion relation of χ and κ in Equation 24.14 would be a similar alteration of Condon's model:

$$\chi(\omega) = \frac{d_c\omega^2\omega_c^2}{\omega^4 + \omega_c^4 - (2 - d_c^2)\omega^2\omega_c^2} \tag{24.16a}$$

$$\kappa(\omega) = \frac{(\omega_c^2 - \omega^2)\omega\omega_c}{\omega^4 + \omega_c^4 - (2 - d_c^2)\omega^2\omega_c^2}. \tag{24.16b}$$

The refractive indices can be expressed by reading from the corresponding eigenwave

$$n_{\pm} = \sqrt{\epsilon\mu/\epsilon_0\mu_0 - \chi^2} \pm \kappa. \tag{24.17}$$

The frequency dependence and the role of damping are shown in Figure 24.4, noting that the indices for "−" effective medium carries a similar fashion by mirroring the curves of "+" medium along the vertical line at $f = 10$ GHz. When the damping factor $d_c = 1$, the refractive index varies limitedly against the frequency even in the characteristic frequency of ω_c, and it can be proved that high damping of the chiral material will hold back the power rotatory and the curve appears more flat (approaching $\sqrt{3}$ over all frequencies), which means that the chirality does not resonate for chiral media of high damping. When the damping factor becomes smaller, more power is rotated and the resonant phenomenon becomes fairly clear. The resonance will further induce negative refraction of eigenmodes within certain frequency bands. Those negative-index bands are inversely proportional to the damping factor.

Due to the wide application potentials of chiral materials in negative refraction, planar structures and focusing devices, magnetoelectric composites, including but not limited to chiral materials, are receiving further investigation, not only in theory but also in application. Zheludev's group has made

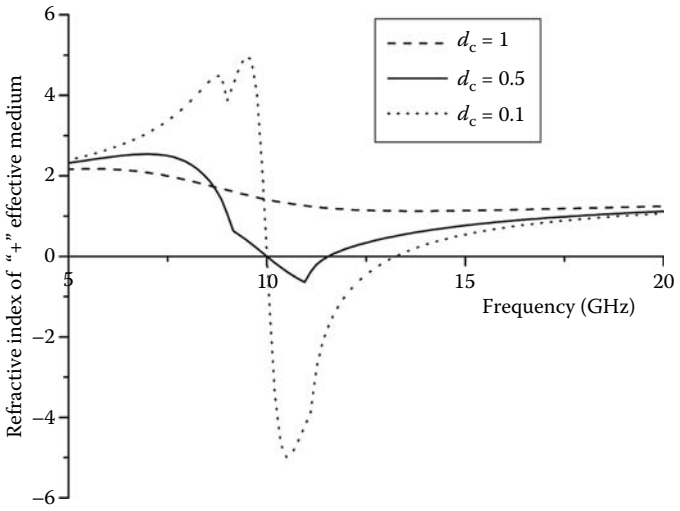

FIGURE 24.4 The frequency dependence of refractive indices for "+" effective medium in the range of [5, 20]GHz, with the same parameters as in Figure 24.2 except d_c.

intensive study on the planar chiral metamaterials, such as light transmission/focusing through chiral holes in a metallic screen [81], planar chiral metastructures for optical application [82], and chiral fish-scale structures to break the polarization symmetry [83]. Another stream in the chiral metamaterial study is to tailor the conventional numerical techniques to computation needs of the chiral metamaterials, such as the bi-FDTD [84] and new uniaxial PML [85].

24.3.2 Gyrotropic Chiral Materials

As suggested by Zhuledev's findings of symmetry break and giant gyrotropy in chiral structures, we find that the gyrotropic chiral composites are found to be a better candidate than normal chiral composites according to the following merits: (1) negative index of refraction in a gyrotropic chiral medium can be realized with less restrictions, while chiral material requires a small permittivity at a working frequency to obtain negative-refractive index; (2) two backward eigenwaves are found due to the effects of the gyroelectric and gyromagnetic parameters; and (3) all parameters in permittivity and permeability tensors as well as chirality admittance can be positive when negative refraction occurs.

The optical rotation exhibited by the chiral composites can be called natural optical activity, and there is another similar phenomenon of rotation by gyrotropic chiral composites with different mechanism, which is called Faraday rotation, induced by external biased fields. The former is independent of the propagation direction and invariant under time reversal, whereas the latter is dependent on propagation and invariant under spatial inversion. A biased magnetic field leads to the gyrotropy in permeability, and crossed external electric and magnetic fields perpendicular to the direction of propagation create gyrotropy in both permittivity and permeability. In this section, instead of conceptual bianisotropic materials whose parameters are manually set, those gyrotropic chiral composites, which can be practically manufactured, are studied.

The constitutive relations of gyrotropic chiral materials in Post formalism are shown as

$$D = \overline{\boldsymbol{\epsilon}} \cdot E + j\xi_c B \tag{24.18a}$$

$$H = j\xi_c E + \overline{\boldsymbol{\mu}}^{-1} \cdot B. \tag{24.18b}$$

The permittivity and permeability tensors are

$$\overline{\boldsymbol{\epsilon}} = \begin{bmatrix} \epsilon & -jg & 0 \\ jg & \epsilon & 0 \\ 0 & 0 & \epsilon_z \end{bmatrix} \tag{24.19a}$$

$$\overline{\boldsymbol{\mu}} = \begin{bmatrix} \mu & -jl & 0 \\ jl & \mu & 0 \\ 0 & 0 & \mu_z \end{bmatrix}, \tag{24.19b}$$

where g and l are the electric and magnetic gyrotropic parameters, respectively. This kind of material includes a chiroplasma consisting of chiral objects embedded in a magnetically biased plasma or a chiroferrite made from chiral objects immersed into a magnetically biased ferrite. Substituting Equation 24.18 into Maxwell equations, one finally has

$$\nabla \times \left[\overline{\boldsymbol{\alpha}} \cdot \nabla \times E\right] - 2\omega\xi_c \nabla \times E - \omega^2 \overline{\boldsymbol{\epsilon}} \cdot E = j\omega J, \tag{24.20}$$

where J is the current excitation

$$\overline{\boldsymbol{\alpha}} = \overline{\boldsymbol{\mu}}^{-1} = \begin{bmatrix} \alpha_t & j\sigma & 0 \\ -j\sigma & \alpha_t & 0 \\ 0 & 0 & \alpha_z \end{bmatrix} \tag{24.21}$$

and

$$\alpha_t = \frac{\mu}{\mu^2 - l^2} \tag{24.22a}$$

$$\sigma = \frac{l}{\mu^2 - l^2} \tag{24.22b}$$

$$\alpha_z = \frac{1}{\mu_z}. \tag{24.22c}$$

Assuming waves of the form $E_0 e^{-jk\cdot r}$ (where k is the wave vector), plane wave propagation in gyrotropic magnetoelectric composites can be examined by setting J zero. Under these conditions, the electric field satisfies

$$\overline{\boldsymbol{\Phi}} \cdot E = 0, \tag{24.23}$$

with $[\Phi]$ defined as

$$[\Phi] = \left[\Phi_1\ \Phi_2\ \Phi_3\right], \tag{24.24}$$

where

$$[\Phi_1] = \begin{bmatrix} \omega^2\epsilon - \alpha_z k_y^2 - \alpha_t k_z^2 \\ j\omega^2 g + \alpha_z k_x k_y + j\sigma k_z^2 + 2j\xi_c \omega k_z \\ \alpha_t k_x k_z - 2j\xi_c \omega k_y + j\alpha_z k_y k_z \end{bmatrix} \tag{24.25a}$$

$$[\Phi_2] = \begin{bmatrix} -j\omega^2 g + \alpha_z k_x k_y - j\sigma k_z^2 - 2j\xi_c \omega k_z \\ \omega^2\epsilon - \alpha_z k_x^2 - \alpha_t k_z^2 \\ \alpha_t k_y k_z + 2j\xi_c \omega k_x - j\alpha_z k_x k_z \end{bmatrix} \tag{24.25b}$$

$$[\Phi_3] = \begin{bmatrix} \alpha_t k_x k_z + j\sigma k_y k_z + 2j\xi_c \omega k_y \\ \alpha_t k_y k_z - j\sigma k_x k_z - 2j\xi_c \omega k_x \\ \omega^2\epsilon_z - \alpha_t k_x^2 - \alpha_t k_y^2 \end{bmatrix}. \tag{24.25c}$$

Equation 24.23 has only nontrivial solutions if the determinant of $[\Phi]$ is zero. Note that the obtained polynomial expression for k is tedious to solve. However, a certain case can still be solved, which gives much insight into the physical properties of the magnetoelectric composites. Considering the waves are propagating along z-direction, one can solve $\det\overline{\mathbf{\Phi}} = 0$ and obtain the wavenumbers supported by the medium. By reducing Equation 24.24, one finally obtains

$$k_{p\pm} = \omega \frac{\pm\xi_c + \sqrt{\xi_c^2 + (\alpha_t \mp \sigma)(\epsilon \pm g)}}{\alpha_t \mp \sigma} \tag{24.26a}$$

$$k_{a\pm} = \omega \frac{\mp\xi_c - \sqrt{\xi_c^2 + (\alpha_t \pm \sigma)(\epsilon \mp g)}}{\alpha_t \pm \sigma}, \tag{24.26b}$$

where p and a represent the parallel and antiparallel directions of energy flow (i.e., real part of the Poynting's vector) and the ± signs refer to the right-circular polarization (RCP) and left-circular polarization (LCP), respectively. Note that the k_{p-} and k_{a-} could represent the wavenumbers for backward eigenwaves under some situations as shown in Table 24.1, which is discussed later. The helicity and polarized state of each wavenumber can be obtained by inserting Equation 24.26 into Equation 24.23. It can be found that the helicity of k_{p+} and k_{a-} is positive and the helicity of k_{p-} and k_{a+} is negative, provided that negative helicity is defined as left-handedness to positive z-direction and right-handedness to negative z-direction. The refraction indices of k_{p-} and k_{a-} are obtained:

$$n_{R1} = \frac{c_0}{(\alpha_t + \sigma)}\left[\sqrt{\xi^2 + (\alpha_t + \sigma)(\epsilon - g)} - \xi\right] \tag{24.27a}$$

$$n_{R2} = \frac{c_0}{(\alpha_t - \sigma)}\left[\sqrt{\xi^2 + (\alpha_t - \sigma)(\epsilon + g)} - \xi\right], \tag{24.27b}$$

where

c_0 is the light's velocity in vacuum
the subscript of R denotes RCP
the subscripts of 1 and 2 correspond to k_{p-} and k_{a-}, respectively

The chirality under Post's relations appear twice in the final expressions of refractive indices. By amplifying the gyrotropic parameter or increasing the chirality, negative refraction can be achieved.

24.3.2.1 Chiroplasma

The constitutive relations of chiroplasma are shown:

$$\begin{aligned} D &= \epsilon_0\epsilon_r \begin{bmatrix} \epsilon & -jg & 0 \\ jg & \epsilon & 0 \\ 0 & 0 & \epsilon_z \end{bmatrix} \cdot E + j\xi_c B, \\ H &= j\xi_c E + \frac{1}{\mu_0\mu_r} B \end{aligned} \tag{24.28}$$

where

$$\epsilon = \left(1 - \frac{\omega_p^2(\omega + j\omega_{eff})}{\omega\left[(\omega + j\omega_{eff})^2 - \omega_g^2\right]}\right) \tag{24.29a}$$

$$g = \frac{\omega_p^2\omega_g}{\omega\left[(\omega + j\omega_{eff})^2 - \omega_g^2\right]} \tag{24.29b}$$

$$\epsilon_z = 1 - \frac{\omega_p^2}{\omega^2}. \tag{24.29c}$$

where ω_{eff}, ω_g, and ω_p represent collision frequency, electron gyrofrequency, and plasma frequency [86], respectively. Such gyroelectric chiral media can be managed by distributing chiral objects into a controllable biasing magnetic field, which is applied externally. The wave equations can be expressed as

$$k \times (k \times E) + 2j\omega\mu_r\mu_0\xi_c k \times E + k_0^2\mu_r\epsilon_r \begin{bmatrix} \epsilon & -jg & 0 \\ jg & \epsilon & 0 \\ 0 & 0 & \epsilon_z \end{bmatrix} \cdot E = 0, \tag{24.30}$$

where k_0 represents the wavenumber in free space. Algebraically, wavenumbers corresponding to parallel and antiparallel eigenmodes for two mutually perpendicular polarizations can be obtained from nontrivial solutions in terms of a quartic polynomial, which would be cumbersome to solve. Thereafter, to yield some physical insight, longitudinal waves with respect to the external biasing field are considered with the interest in backward waves and negative phase velocity. For the longitudinally propagating eigenwaves along the biasing plasma, one can obtain four wavenumbers corresponding to eigenmodes

$$k_{\frac{1}{2}} = \omega\left[\mp\mu_0\mu_r\xi_c \pm \sqrt{\mu_0^2\mu_r^2\xi_c^2 + \mu_0\mu_r\epsilon_0\epsilon_r(\epsilon \mp g)}\right] \tag{24.31}$$

$$k_{\frac{3}{4}} = \omega\left[\pm\mu_0\mu_r\xi_c \pm \sqrt{\mu_0^2\mu_r^2\xi_c^2 + \mu_0\mu_r\epsilon_0\epsilon_r(\epsilon \pm g)}\right]. \tag{24.32}$$

With reference to the energy transportation direction, eigenwaves corresponding to eigen wavenumbers k_1 and k_2 may become backward waves, because the handedness of these two eigenwaves will change within certain frequency bands. Note that the k_1 eigenwave is parallel to the energy transportation while k_2 eigenwave is opposite, and in backward-wave frequency bands both eigenwaves are right-circular polarized [87]. In particular, the phase velocity against the frequency is studied to observe characteristics of LHM. In Figure 24.5a, it can be observed that when no magnetoelectric coupling is present the phase velocity of k_2 eigenmode is always negative and that of k_1 eigenmode is positive. Substituting those two eigenmodes into Equation 24.30, one can note that negative phase velocity in Figure 24.5a does not mean backward-wave phenomenon. Instead, when $\xi_c = 0$, negative phase velocity represents that k_2 eigenmode is left-handed with reference to the opposite direction of the external magnetic field, and positive velocity shows that the k_1 eigenmode is left-handed along the direction of the external field. When slight magnetoelectric coupling exists (e.g., $\xi_c = 10^{-3}$ in Figure 24.5b), backward-wave phenomena arise for both k_1 and k_2 eigenmodes, in which resonances can be observed. In what follows, a gyroelectric chiral medium is considered with bigger magnetoelectric coupling effect as shown in Figure 24.5c. Compared with the case shown in Figure 24.5b, one can note that the shift of resonant frequencies is neglectable, whereas resonant amplitudes in Figure 24.5c are drastically enhanced. In both weak-coupling and strong-coupling cases, it can be found that backward-wave regions arise before respective resonances. After passing the resonant frequency, the handedness and polarization status of those eigenmodes become an analogy to the nonmagnetoelectric case.

24.3.2.2 Generalized Gyrotropy

Generalized gyrotropy can be either regarded as a generalization of the gyrotropic (chiral) media without the assumption of $H : H = B$ [88,89] or an advanced mixture of chiroplasma and chiroferrite due to the crossed biased fields.

- *Wave impedance:*

One parallel LCP (i.e., k_{p-}) and one antiparallel LCP (i.e., k_{a-}) can backward propagate with opposite directions of phase and energy velocities. The directions of the energy velocities are identical with those of Poynting's vectors, which can be verified using the Maxwell equations:

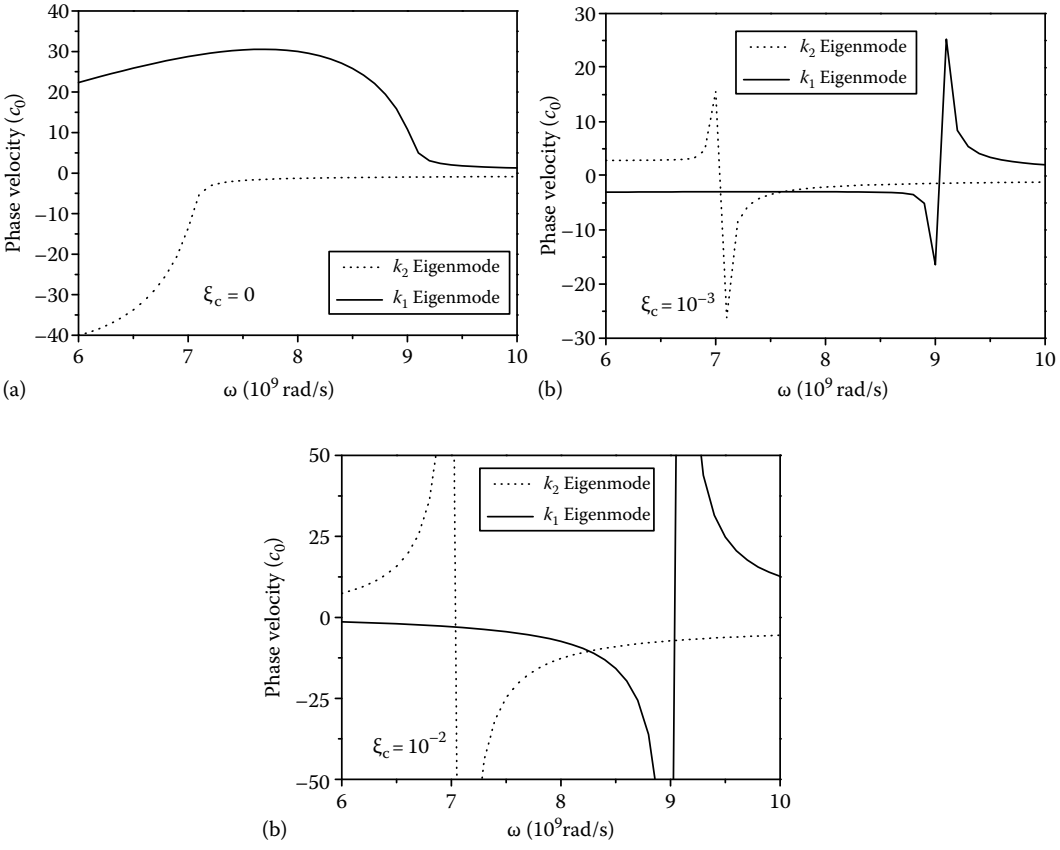

FIGURE 24.5 Phase velocities for backward-wave eigenmodes as a function of frequency near plasma frequency, with parameters $\omega_p = 8 \times 10^9$ rad/s, $\omega_{eff} = 0.1 \times 10^9$ rad/s, and $\omega_g = 2 \times 10^9$ rad/s under different degrees of magnetoelectric couplings: (a) decoupling plasma $\xi_c = 0$; (b) ξ_c=0.001; and (c) $\xi_c = 0.01$.

$$S_{p+} = \hat{\boldsymbol{z}} \frac{|E_0|^2}{2\eta_1} \tag{24.33a}$$

$$S_{a-} = -\hat{\boldsymbol{z}} \frac{|E_0|^2}{2\eta_1} \tag{24.33b}$$

$$S_{p-} = \hat{\boldsymbol{z}} \frac{|E_0|^2}{2\eta_2} \tag{24.33c}$$

$$S_{a+} = -\hat{\boldsymbol{z}} \frac{|E_0|^2}{2\eta_2}, \tag{24.33d}$$

where η_1 and η_2 denote the wave impedances of the positive and negative helicities, respectively.

In view of the above equations, the z-axis component of the Poynting vector can be shown as

$$S_z = \frac{1}{2}\left[E_x H_y^* - E_y H_x^*\right], \tag{24.34}$$

where the transverse magnetic fields can be obtained

$$\begin{bmatrix} H_x \\ H_y \end{bmatrix} = \begin{bmatrix} j\left(\xi_c + \frac{k_z}{\omega}\sigma\right)E_x - \frac{k_z}{\omega}\alpha_t E_y \\ j\left(\xi_c + \frac{k_z}{\omega}\sigma\right)E_y + \frac{k_z}{\omega}\alpha_t E_x \end{bmatrix}. \tag{24.35}$$

Before solving η_1 and η_2, one condition should be noted

$$\left(2\xi_c + \frac{\omega}{k_z}g + \frac{k_z}{\omega}\sigma\right)^2 = \left(\frac{\omega}{k_z}\epsilon - \frac{k_z}{\omega}\alpha_t\right)^2. \tag{24.36}$$

Substituting Equation 24.35 into Equation 24.34 with the aid of the solution in Equation 24.36, we finally obtain

$$\eta_1 = \frac{1}{\sqrt{\xi_c^2 + (\alpha_t - \sigma)(\epsilon + g)}} = \frac{1}{\sqrt{\xi_c^2 + \dfrac{\epsilon + g}{\mu + l}}} \tag{24.37a}$$

$$\eta_2 = \frac{1}{\sqrt{\xi_c^2 + (\alpha_t + \sigma)(\epsilon - g)}} = \frac{1}{\sqrt{\xi_c^2 + \dfrac{\epsilon - g}{\mu - l}}}. \tag{24.37b}$$

Alternatively, by applying the Beltrami fields [90], $\epsilon_\pm$ and $\mu_\pm$ of the eigenmodes can also be obtained as below:

$$\begin{aligned} \epsilon_\pm = & \sqrt{\xi_c^2 + \frac{\epsilon \pm g}{\mu \pm l}}\Big[\pm \xi_c(\mu \pm l) \\ & + \sqrt{[\xi_c(\mu \pm l)]^2 + (\epsilon \pm g)(\mu \pm l)}\Big] \end{aligned} \tag{24.38a}$$

$$\begin{aligned} \mu_\pm = & \sqrt{\frac{\mu \pm l}{\xi_c^2(\mu \pm l) + \epsilon \pm g}}\Big[\pm \xi_c(\mu \pm l) \\ & + \sqrt{[\xi_c(\mu \pm l)]^2 + (\epsilon \pm g)(\mu \pm l)}\Big]. \end{aligned} \tag{24.38b}$$

Thus, the wave impedances of those eigenmodes can be verified by using $\eta_\pm = \sqrt{\mu_\pm/\epsilon_\pm}$, which agrees with the η_1 and η_2, respectively.

These findings are of importance in phase compensation and compact resonator [91], since a good impedance matching can be achieved at the interface between a gyrotropic chiral slab and the adjacent spaces. Note that the elements in the permittivity and the permeability tensors involve frequency, plasma frequency, electron gyrofrequency, gyromagnetic response frequency, and saturation magnetization frequency [86,92], and the realization of the backward wave depends on the frequency selection. Within certain frequency ranges, k_{p-} and k_{a-} could be wavenumbers of the backward wave simultaneously or only one of them could. Configurations of conventional and subwavelength cavity resonators are proposed using gyrotropic chiral slabs, when the working frequency is properly chosen to arrive at the negative-refractive index.

In Figure 24.6, it can be seen that, if a plane wave propagates in the direction penpendicular to the interfaces at a certain frequency range, its phase increased in the conventional medium can be decreased by the gyrotropic chiral medium, which falls into the backward-wave region. It is noted that, the backward eigenmodes possess two impedances. Hence, by properly controlling the parameters and the external biased fields, $\eta_+ = \eta_0$ or $\eta_- = \eta_0$ could be chosen to match the wave

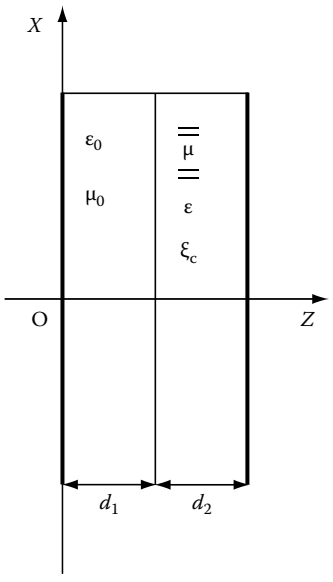

FIGURE 24.6 Compact resonator formed by a 2-layer structure consisting of air and gyrotropic chiral media backed by two ideally conducting planes.

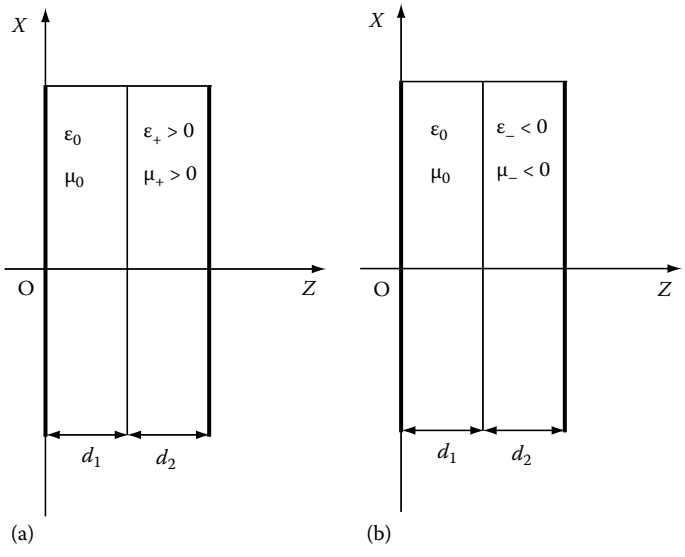

FIGURE 24.7 Equivalent configuration of 1-D cavity resonator made of gyrotropic chiral materials.

impedance η_0 of the air, which means that two kinds of cavity resonators can be created as shown in Figure 24.7.

The resonance condition for a cavity takes the following form [91]:

$$\frac{n_2}{\mu_2}\tan(n_1 k_0 d_1) + \frac{n_1}{\mu_1}\tan(n_2 k_0 d_2) = 0, \tag{24.39}$$

where the subscripts of 1 and 2 correspond to the layer on the left-handed and right-handed side, respectively. As in the case shown in Figure 24.7a when the η_+ is matched, it turns out to be the conventional cavity resonator, and thus Equation 24.39a becomes

$$n_+ d_2 + d_1 = \frac{m}{2}\lambda_0, \quad m = 0, 1, 2..., \tag{24.40}$$

where λ_0 is the wavelength in the air.

Of particular and practical interest is the case of subwavelength cavity resonators, in which the arguments on the tangential functions can be assumed small. If η_- is matched as shown in Figure 24.7b, the resonant condition in Equation 24.39 is reduced to

$$\frac{d_1}{d_2} \cong \frac{|\mu_-|}{|\mu_0|}. \tag{24.41}$$

It can be observed that to have simultaneously negative permittivity and permeability is not necessary to satisfy the above condition, because only the first term in the Taylor expansion in tangent function is kept for the thin layer on metal surfaces. The definition of $n_\pm$ is given in the following part.

- *Negative refraction:*

The k_{p-} and k_{a-} are of particular interest because they represent the properties of backward waves under specific cases, as shown in Table 24.1. The quantities ϵ and g given in Ref. [86] are as follows:

$$\epsilon = \epsilon_0\left(1 - \frac{\omega_p^2(\omega + j\omega_{eff})}{\omega\left[(\omega + j\omega_{eff})^2 - \omega_g^2\right]}\right) \tag{24.42a}$$

$$g = \epsilon_0 \frac{\omega_p^2 \omega_g}{\omega\left[(\omega + j\omega_{eff})^2 - \omega_g^2\right]}, \tag{24.42b}$$

where ω_p, ω_g, and ω_{eff} are the plasma frequency, electron's gyrofrequency, and the collision frequency of the electrons, respectively.

It should also be noted that the positive/negative helicity is defined as right-/lefthandedness to positive/negative z-axis. The helicity and polarized states can be found by inserting Equation 24.26 into Equation 24.20. When k_{p-} or k_{a-} becomes backward waves, the handedness changes.

A collisionless case is considered here (i.e., $\omega_{eff} = 0$). Two quantities are introduced first.

$$\omega_{c1} = \frac{1}{2}\left[-\omega_g + \sqrt{\omega_g^2 + 4\omega_p^2}\right] \tag{24.43a}$$

$$\omega_{c2} = \frac{1}{2}\left[\omega_g + \sqrt{\omega_g^2 + 4\omega_p^2}\right]. \tag{24.43b}$$

As shown in Table 24.1, in order to realize the backward eigenmode k_{a-}, one can see that $\epsilon + g < 0$ should be satisfied (i.e., $0 < \omega < \omega_{c1}$ should be held). To form the backward eigenmode k_{p-}, it shows $g > \epsilon$, which means $\omega_g < \omega < \omega_{c2}$. Note that if

$$\omega_p < \sqrt{2}\omega_g$$

TABLE 24.1 Helicity and Polarization States of k_{p-} and k_{a-} in Three Cases, under the Conditions of $|l| < \mu$ and $\xi_c > 0$

	$g < -\epsilon$		$-\epsilon < g < \epsilon$		$g > \epsilon$	
	HEL	POL	HEL	POL	HEL	POL
k_{p-}	$\ominus$	LCP	$\ominus$	LCP	*$\ominus$	*RCP
k_{a-}	*$\oplus$	*RCP	$\oplus$	LCP	$\oplus$	LCP
ω	$(0, \omega_{c1})$		—		(ω_g, ω_{c2})	

*Backward wave regions.

is satisfied, there is no overlapping of the two intervals regarding the frequency condition in Table 24.1. If one chooses

$$\omega_p > \sqrt{2}\omega_g,$$

then both k_{p-} and k_{a-} are backward wavenumbers, and two impedances will be presented in any one layer of slabs in Figure 24.6. In that case, it would be impossible to match those two impedances simultaneously at the material–air interface. However, we can choose one impedance equal to that of air, and correspondingly the backward wave associated with that impedance can propagate through the slabs as shown in Figure 24.7.

One can further split the external *dc* magnetic field into two parts as

$$B_{dc} = \mu_0(H_{dc} + M_{dc}), \tag{24.44}$$

where M denotes the magnetic moment in the whole volume occupied by gyrotropic chiral material, and the H field has taken into account the demagnetizing field. Then the permeability tensor in Equation 24.19b can be characterized

$$\mu = \mu_0\left(1 - \frac{\omega_0\omega_M}{\omega^2 - \omega_0^2}\right) \tag{24.45a}$$

$$l = \mu_0\frac{\omega\omega_M}{\omega^2 - \omega_0^2}, \tag{24.45b}$$

where

$$\omega_0 = \frac{e}{m_e}\mu_0 H_{dc} \tag{24.46a}$$

$$\omega_M = \frac{e}{m_e}\mu_0 M_{dc}. \tag{24.46b}$$

Therefore, it can be shown that the restriction $|l| < \mu$ (as stated in Table 24.1) can be maintained by choosing a proper external *dc* magnetic field and the number of electrons. Further study reveals that $l + \mu > 0$ as always. Thus the restriction $l < \mu$ becomes

$$\frac{\omega_M}{\omega - \omega_0} < 1. \tag{24.47}$$

With the conditions clearly stated, the negative refractive indices of a generalized gyrotropic chiral medium can be obtained. Taking into account Equation 24.26, for respective polarization states and helicities, one can finally obtain two refraction indices for those backward eigenwaves:

$$n_\pm = \frac{c_0}{(\alpha_t \mp \sigma)}\left[\sqrt{\xi_c^2 + (\alpha_t \mp \sigma)(\epsilon \pm g)} - \xi_c\right], \tag{24.48}$$

where plus and minus signs refer to as k_{a-} and k_{p-}, respectively.

It can be seen that n_+ is negative when $g < -\epsilon$ and n_- possesses a minus sign when $g > \epsilon$ (which means that a backward wave propagates in such a medium). It also shows that a negative-refraction index may be easily achieved even if the chirality admittance ξ_c is very small. Note that one can use all positive parameters (i.e., ϵ, g, μ, w, and ξ_c) to achieve a negative index of refraction (i.e., n_-). In addition, $g > \epsilon$ can be realized with some advanced technology in future based on the theory of off-diagonal parameter amplification in artificially gyrotropic media.

In what follows, Equation 24.48 is analyzed in detail to discuss the possibility of backward waves. We can further rewrite Equation 24.48 as

$$n_{\pm} = c_0\left[\sqrt{(\mu \pm w)^2\xi_c^2 + (\mu \pm w)(\epsilon \pm g)} - (\mu \pm w)\xi_c\right]. \tag{24.49}$$

It is found that the negative-refractive indices may be easily achieved if $\epsilon \pm g < 0$, and it has been pointed out how the frequency shall be selected so as to give rise to negative refraction indices in Figure 24.6.

Then what is of particular interest turns out to be the case of $n_{\pm} = 0$ (i.e., $\epsilon \pm g = 0$). It follows that this case can be realized at two specific frequencies as given below:

$$\omega_1 = -\frac{\omega_g}{2} + \sqrt{\left(\frac{\omega_g}{2}\right)^2 + \omega_p^2} \tag{24.50a}$$

$$\omega_2 = \frac{\omega_g}{2} + \sqrt{\left(\frac{\omega_g}{2}\right)^2 + \omega_p^2} \tag{24.50b}$$

where $\omega = \omega_1$ and $\omega = \omega_2$ lead to $\epsilon + g = 0$ and $\epsilon - g = 0$, respectively.

Therefore, one can come up with an equivalent cover for patch antennas (Figure 24.8a) with zero refractive index and a positive wave impedance $1/\xi_c$ which is composed of a gyrotropic chiral medium. Only normal incident waves are transmitted into the slab, and the phases in any planes between $z = 0$ and $z = d$ will be kept unchanged. Hence, potential application includes a radome of antennas, which will greatly enhance the directivity of the antennas. No reflected waves interfere with antennas if impedance matching at the material–air interface has been done. In addition, the existence of the slab has no influence on the phase of the propagating waves.

Alternatively, in Figure 24.8b, if some sources are placed in such a substrate made from a gyrotropic chiral slab, which has $n = 0$ and finite impedance, all the transmitted waves will be perpendicular with the upper surface no matter what the form of the source would be. This property is attributed to the Snell's law when one of the material has zero refractive index. Due to the property of zero or nearly zero refractive index, gyrotropic chiral materials at two particular frequencies provide potentials in quantum devices because the discrete quantized field will be greatly enhanced. For instance, the critical field is assumed to be E_c. If the field strength has the same order of magnitude of E_c or less than E_c, the field can be viewed as a quantized one or a fluctuation of quantum vacuum. It is obvious that the critical field strength becomes very large when the refractive index is almost zero. Hence, the quantum vacuum fluctuation field becomes strong.

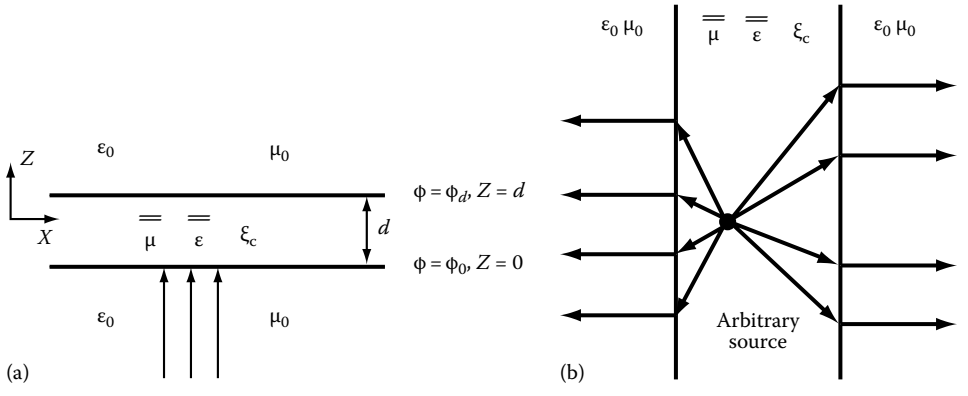

FIGURE 24.8 Application of a gyrotropic chiral slab with zero index but finite impedance.

24.3.3 Chiral Nihility Routes

As is known, the NIMs in the microwave region have been measured and confirmed. However, realizing negative permeability from metallic structures as well as achieving low-loss negative-index media at much higher frequencies is a very difficult task. Negative values can even be obtained simultaneously for the real parts of the permeability and the permittivity without achieving a negative index of refraction due to high values of the imaginary part of the permeability in the visible region [93]. Hence, the impact of NIM would be more far-reaching if negative refraction is realized at optical frequencies. In this connection, chiral composites have been proposed as a potential candidate to acheive negative refraction [72] in the optical region, since it is not necessary to create artificial magnetic media any more. In chiral materials with long helices, backward wave can be excited along the helix that acts as a delay line. An electric or magnetic excitation will produce simultaneously both the electric and magnetic polarizations.

However, the chirality cannot be very large in nature so as to satisfy the backward-wave condition $\sqrt{\epsilon_r \mu_r} - \kappa < 0$. Thus, a special type of chiral materials with extremely small permittivity and permeability (termed as *chiral nihility* (CN) firstly by Tretyakov et al.) helps a lot in enlarging the impact of chiral materials in the realm of negative-index materials. As a complementary counterpart of gyrotropic chiral materials that make use of gyrotropic parameters to reduce refractive indices, CN is based on the suppression of permittivity and permeability by appropriate wire-loop models [76].

Initially, the concept of nihility was conjectured by Lakhtakia [94] for the mixtures of DPS and DNG dielectric materials, which gives null parameters to the permittivity and permeability of the mixture. It can be found that this nihility is not physical since the Maxwell equations have no nontrivial solutions. However, this concept is still of use, based on which CN is generalized. The physical definition of CN is that the two eigenwaves have the opposite propagation constants and that the wave impedance is a finite number. In such exotic materials, the electromagnetic wave propagates and negative refraction occurs. By the model in Figure 24.1 ordered in arrays, it has been validated that CN is realizable if the radius of the loop and the length of the dipole are advisably chosen.

In contrast to previous studies on CN, the original work in this section focuses on the macroscopic characterization of electromagnetic wave interaction with CN. First, the wave scattering and transmission through an air–CN interface are characterized, which yields many exciting phenomena such as a wide range of Brewster angle and power transport control. Next, we tend to explore different mechanisms of CN and how to realize those CN. Previously, the CN is for isotropic reciprocal chiral materials. In the following parts, different medium formalisms for such CN are discussed to find discrepancy. Furthermore, nonreciprocal CN and gyrotropic CN are proposed, and chirality control is studied to meet the conditions of respective nihilities.

24.3.3.1 Brewster Angles and Chirality Effects in Semi-Infinite Chiral Nihility

A plane wave incidence upon the interface between a dielectric and a chiral medium is considered as shown in Figure 24.9.

The homogeneous reciprocal chiral material has been defined in Equation 24.6, with only slight changes in notations here (i.e., $\epsilon_T \to \epsilon_r \epsilon_0$ and $\mu_T \to \mu_r \mu_0$). The wavenumbers of the two eigenwaves in the chiral medium then read

$$k_{1,2} = k_0(\sqrt{\mu_r \epsilon_r} \pm \kappa), \tag{24.51}$$

which corresponds to two eigenmodes respectively

$$E_1 = E_{01}(e_x + je_y)e^{-jk_1 z} \tag{24.52a}$$

$$E_2 = E_{02}(e_x - je_y)e^{-jk_2 z}. \tag{24.52b}$$

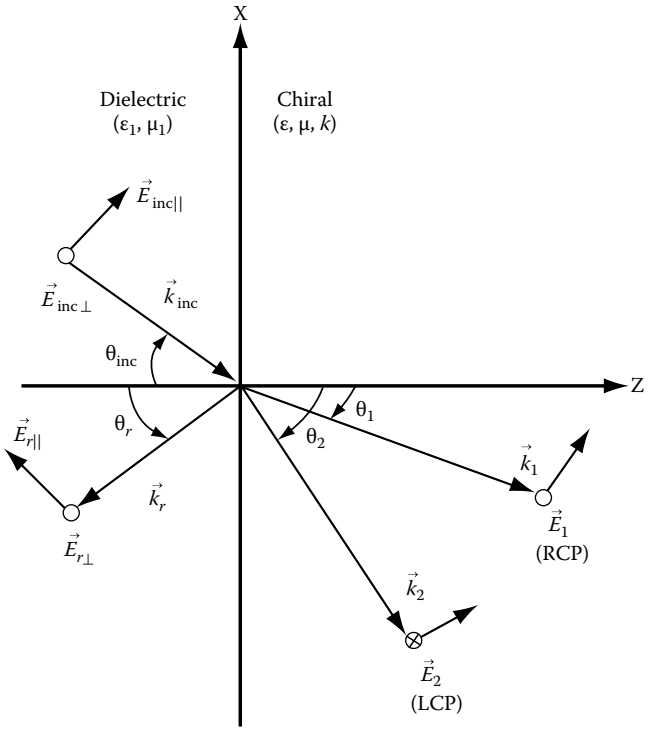

FIGURE 24.9 Orientation of the wave vectors at an oblique incidence on a dielectric–chiral interface. The subscripts ∥ and ⊥ respectively stand for parallel and perpendicular with respect to the plane of incidence.

The refractive indices are thus given as

$$n_{1,2} = \sqrt{\mu_r \epsilon_r} \pm \kappa. \tag{24.53}$$

Potential applications in phase compensator and quantum devices can also be envisaged similarly as the gyrotropic cases. In order to study the reflected power at the interface between the dielectric and the chiral medium, the boundary condition has to be satisfied.

$$\hat{z} \times [E_{inc} + E_r] = \hat{z} \times [E_1 + E_2] \tag{24.54a}$$

$$\hat{z} \times [H_{inc} + H_r] = \hat{z} \times [H_1 + H_2] \tag{24.54b}$$

from which the method to retrieve Fresnel reflection and transmission coefficients [95] is adopted and further transformed into the Tellegen formalism. In Figure 24.10, the reflected power is drawn versus the angle of incidence for two different configurations.

The first case deals with a chiral medium where the permittivity is greater than that of the dielectric. It then has a Brewster angle for an incidence at about 65° for the parallel polarization, as shown in Figure 24.10a. For the second case (Figure 24.10b), the chiral medium has a lower permittivity compared with that of the surrounding dielectric. For the value of $\kappa = 0.25$, no Brewster angle can be observed for either polarization of the incident field. However, when $\theta = 22°$, the reflected power of P_{pa} has a minimum, which is close to zero. The total reflection starts from 40° incidence for both P_{pa} (∥) and P_{pe} (⊥) polarizations. Further investigation shows that the permittivity ratio (i.e., permittivity of dielectrics over permittivity of chiral medium) plays an important role in the zero and total reflection characteristics. As for the zero reflection, it only occurs in parallel polarization, which

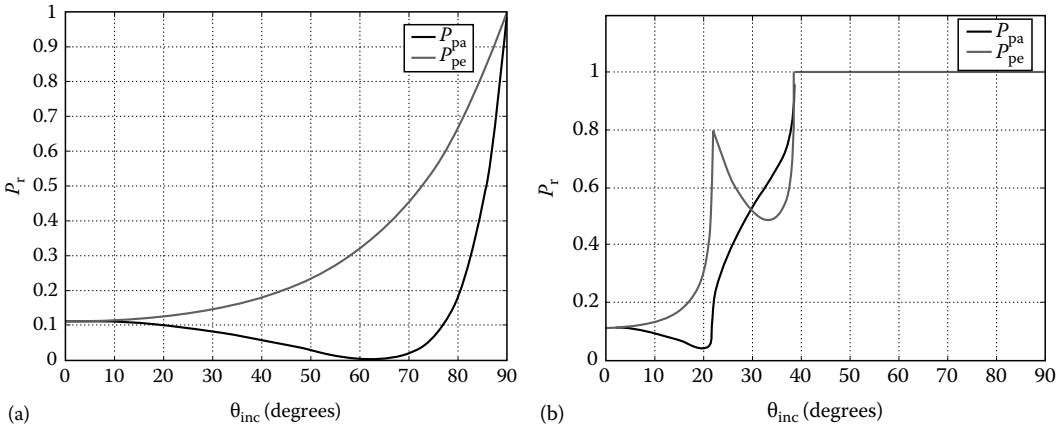

FIGURE 24.10 Reflected power as a function of the incidence with unit permeability, same chirality but different permittivity.

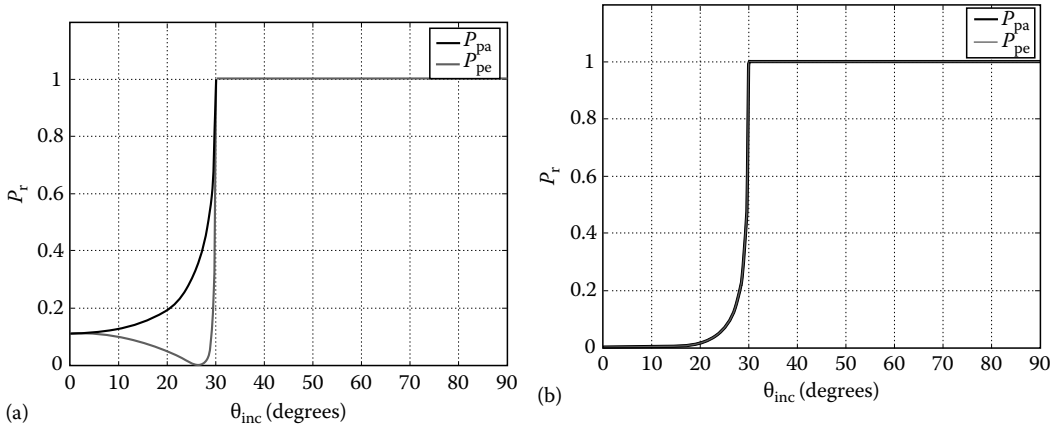

FIGURE 24.11 Reflected power as a function of the incidence with different cases of chiral nihility: (a) $\epsilon_1 = \mu_1 = 1$, $\epsilon = 4e - 5$, $\mu = 1e - 5$, and $\kappa = 0.5$; (b) $\epsilon_1 = \mu_1 = 1$, $\epsilon = \mu = 1e - 5$, and $\kappa = 0.5$.

is consistent with the results of the conventional dielectric–dielectric interface. It is interesting to observe that the total reflection happens over a wide range of incidence angles, and a secondary total-reflection angle at $\theta = 22°$ appears for perpendicular polarization.

Next, the energy transport from the dielectric to the CN is investigated, where some interesting phenomena arise. Two cases of CNs are considered (i.e., with/without impedance matching to the air).

Comparing Figure 24.11a with Figure 24.10a, it is seen that zero-reflection angle occurs in perpendicular polarization rather than parallel polarization, which is in contrast to the situation for normal chiral or dielectric materials. It is shown that the reflected power dependence on the incident angle varies drastically within a certain range. The zero-reflection angle at 27° is quite close to the lowest total reflection angle at 30°, which means that this range is quite angle sensitive. More surprisingly, the dependence of reflected power on the incidence becomes identical for both polarizations when the impedance of CN is matched to that of the free space. In this special case as shown in Figure 24.11b, the Breswter angle is a range rather than a single angle, and total reflection happens

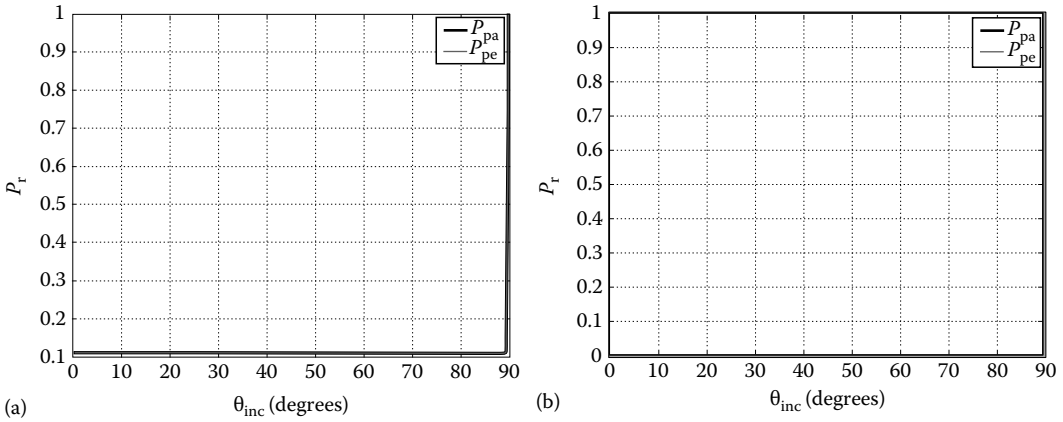

FIGURE 24.12 Reflected power as a function of the incidence with same permittivity and permeability as Figure 24.11 but with higher chirality: (a) $\epsilon_1 = \mu_1 = 1$, $\epsilon = 4e-5$, $\mu = 1e-5$, and $\kappa = 1$; (b) $\epsilon_1 = \mu_1 = 1$, $\epsilon = 4e-5$, $\mu = 1e-5$, and $\kappa = 1$.

when the incidence angle is greater than 30° though the impedance matching is achieved. It is due to the mismatch of the refractive indices.

As one can see, the chirality in each case in Figure 24.11 is doubled in Figure 24.12, keeping other parameters unchanged. As such, the chirality effects in CN can be presented. In Figure 24.12, the reflected powers of both polarizations carry similar dependence on incidence, while the magnitude of reflected power significantly differs from that in Figure 24.11. In Figure 24.12, the value is quite stable over the whole region except at 90°. If the impedance of CN is matched, the value will be further reduced to zero (Figure 24.12b), which means that the Brewster angle almost covers the whole range of incidence angles. Therefore, under such circumstances, all the energy will be transmitted to the CN if the incident angle is smaller than 90°. It may be of great importance to realize imaging characteristics without much loss of information of a point source or a line source, since one of the refractive indices of CN is very close to −1.

Figure 24.13 shows the reflected power versus the chirality for the two same configurations as above at an oblique incidence of 45°. When the chiral medium is denser than the dielectric (Figure 24.13a)

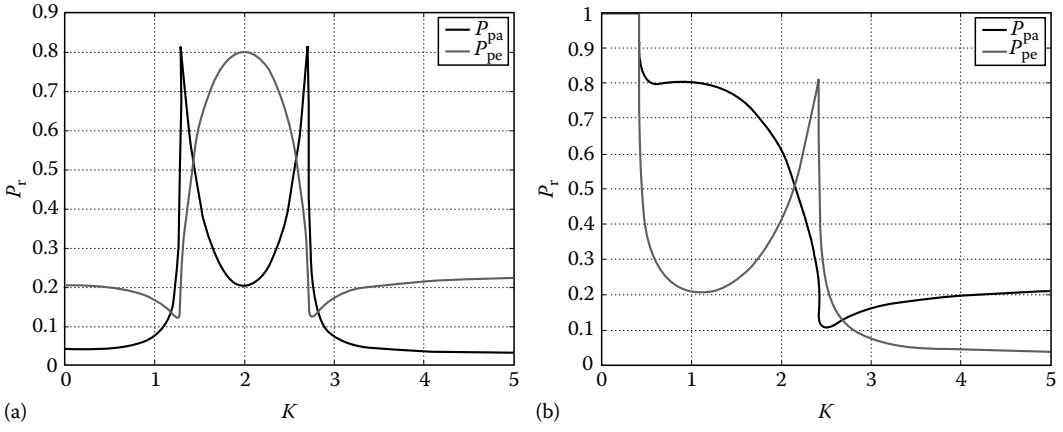

FIGURE 24.13 Reflected power as a function of the chirality for a $\theta_{inc} = 45°$ oblique incidence.

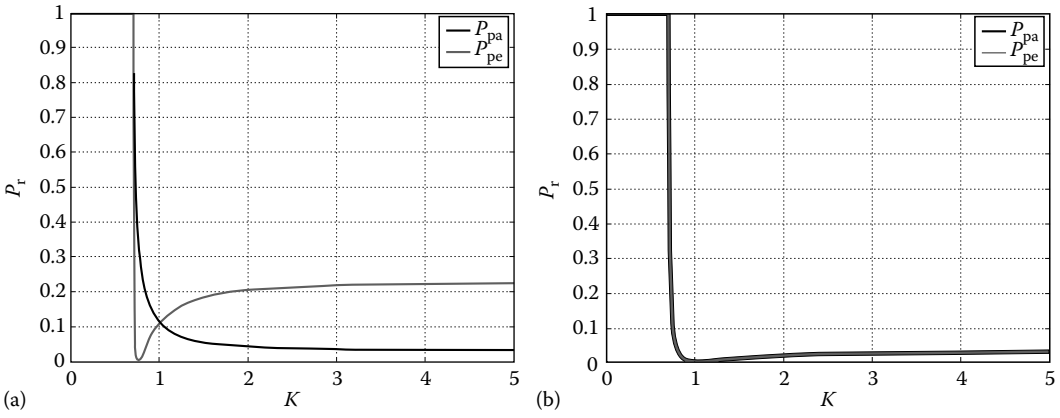

FIGURE 24.14 Reflected power as a function of the chirality for a $\theta_{inc} = 45°$ oblique incidence in different cases of chiral nihility.

and for a perpendicular polarization of the incident field, the reflected power shows a maximum of 0.8 for $\kappa = 2$ and tends to stable value of 0.22 for $\kappa > 4$. Concerning the parallel polarization, two maxima are obtained (Pr = 0.8) at $\kappa = 1.29$ and $\kappa = 2.71$, respectively. In order to have a good transmission through the interface, the chirality must be either lower than 1.29 or greater than 2.71. On the contrary, when the dielectric is denser than the chiral medium (Figure 24.13b), total reflection is observed for both polarizations for chirality smaller than 0.42. Concerning the case of parallel polarization, the reflected power decreases to a stable value of 0.22 as chirality increases. For the perpendicular polarization of the incident field, a minimum is first observed for $\kappa = 1$ and then a maximum for $\kappa = 2.41$. For $\kappa > 3$, the reflected power tends to 0.04. If one further increases the mismatch of the permittivity between the dielectric and the chiral medium, the plots observed in Figure 24.13 shift to the right (higher values of chirality) and the amplitude of the reflected power increases.

In contrast to the normal chiral slab, CN slabs for an oblique incidence are also studied in Figure 24.14. Similarly, particular values of chirality will lead to zero reflection, which is the so-called critical chirality κ_c. In Figure 24.14a, $\kappa_c \approx 0.75$, which exists only for perpendicular polarization. If the chirality is lower than κ_c, total reflection happens and no power can be transmitted to the CN slab. When the chirality is sufficiently large, the reflected powers are approaching their respective stable values, and it is found that the stable reflected power of P_{pa} is about seven times larger than that of P_{pe}. If the chirality nihility slab has its impedance matched to the free space, both P_{pa} and P_{pe} have identical performance against chirality, and κ_c can be observed for both cases. It suggests that a bigger chirality would be a better choice if energy transport is desired.

24.3.3.2 Constraints and Conditions of Isotropic/Gyrotropic Chiral Nihility

Since the CN is so promising in realizing negative refraction, it is of particular interest to explore the physics of CN and the conditions to satisfy not only isotropic CN but also the nonreciprocal and gyrotropic CN.

- *Isotropic chiral nihility:*

1. **Tellegen:**

Tellegen's formalism has been given in Equation 24.6. When $\epsilon_T \mu_T \to 0$, the nihility condition of isotropic chiral media can be represented by

$$k_\pm = \omega\left(\sqrt{\epsilon_T \mu_T} \pm \kappa\sqrt{\epsilon_0 \mu_0}\right) \to \pm k_0 \kappa, \tag{24.55}$$

where k_0 is the wave number in free space. Hence, one of the waves becomes a backward wave and has the negative refractive index of $n = -\kappa$.

In the meantime, the wave impedance of the chiral medium $\eta = \sqrt{\mu_T/\epsilon_T}$ should remain finite, which means

$$\lim\{\mu_T/\epsilon_T\} \to \text{const} \neq 0, \infty. \tag{24.56}$$

The combination of this relation with the nihility condition implies that $\epsilon_T \to 0$ and $\mu_T \to 0$.

2. **Post:**

In the Post's notation, the constitutive relations are shown in Equation 24.5. The mapping relations between Tellegen and Post formalism are given below:

$$\mu_P = \mu_T \tag{24.57a}$$

$$\epsilon_P = \epsilon_T - \frac{\epsilon_0\mu_0}{\mu_T}\kappa^2 \tag{24.57b}$$

$$\xi_c = \frac{\sqrt{\epsilon_0\mu_0}}{\mu_T}\kappa. \tag{24.57c}$$

The eigenwave numbers in Post formalism are found to be

$$k_\pm = \omega\left(\sqrt{\mu_P\epsilon_P + \mu_P^2\xi_c^2} \pm \mu_P\xi_c\right). \tag{24.58}$$

Thus, the nihility condition is

$$\mu_P\epsilon_P + \mu_P^2\xi_c^2 \to 0. \tag{24.59}$$

The condition in Equation 24.59 is satisfied if $\epsilon_T\mu_T \to 0$, because the terms containing the chirality parameter κ cancel out.

The impedance

$$\eta = \frac{\sqrt{\mu_P\epsilon_P + \mu_P^2\xi_c^2}}{\epsilon_P + \mu_P\xi_c^2} \tag{24.60}$$

remains finite if

$$\epsilon_P + \mu_P\xi_c^2 \to 0. \tag{24.61}$$

Substituting the Post parameters expressed via the Tellegen parameters, one sees that if the nihility condition in the Post formalism Equation 24.59 is satisfied, then the Tellegen permittivity

$$\epsilon_T = \epsilon_P + \mu_P\xi_c^2 \to 0, \tag{24.62}$$

which is consistent with the CN requirements in terms of the Tellegen parameters.

3. **Drude-Born-Fedorov:**

The Drude-Born-Fedorov (DBF) constitutive relations are

$$D = \epsilon_{DBF}(E + \beta\nabla \times E) \tag{24.63a}$$

$$B = \mu_{DBF}(H + \beta\nabla \times H), \tag{24.63b}$$

where β denotes the chirality in DBF formalism. The wavenumbers obtained for the two eigenmodes are given by

$$k_{\pm} = \frac{\omega\sqrt{\epsilon_{DBF}\mu_{DBF}} \pm \omega^2\epsilon_{DBF}\mu_{DBF}\beta}{1 - \omega^2\epsilon_{DBF}\mu_{DBF}\beta^2} \tag{24.64}$$

and the wave impedance

$$\eta = \sqrt{\mu_{DBF}/\epsilon_{DBF}}. \tag{24.65}$$

In this case, the conditions of CN look the same as in the Tellegen notation:

$$\epsilon_{DBF} \to 0, \qquad \mu_{DBF} \to 0 \tag{24.66}$$

However, if Equation 24.66 is satisfied, then $k_{\pm} = 0$ unless the DBF chirality parameter $\beta \to \infty$. This is, however, consistent with the known relation between the chirality parameters in the Tellegen notation and the DBF formalism:

$$\epsilon_T = \frac{\epsilon_{DBF}}{1 - k_{DBF}^2\beta^2} \tag{24.67a}$$

$$\mu_T = \frac{\mu_{DBF}}{1 - k_{DBF}^2\beta^2} \tag{24.67b}$$

$$\kappa = \frac{\omega\mu_{DBF}\epsilon_{DBF}\beta}{\sqrt{\epsilon_0\mu_0}(1 - k_{DBF}^2\beta^2)}, \tag{24.67c}$$

where $k_{DBF}^2 = k_0^2\epsilon_{DBF}\mu_{DBF}$. Apparently, if $\mu_{DBF}\epsilon_{DBF} \to 0$, κ can remain finite only if $\beta \to \infty$. Inversely, if Tellegen's nihility is fulfilled ($\epsilon_T \to 0$, $\mu_T \to 0$), we will have zero μ_{DBF} and zero ϵ_{DBF}. Thus, the Tellegen chirality κ will be forced to zero in Equation 24.67c, which is also the reason why such $\epsilon = \mu = 1e-5$ instead of zero is set.

Therefore, Tellegen and Post notations are equivalent and equally convenient to describe isotropic CN, whereas the DBF formalism is less suitable due to the requirement of $\beta \to \infty$.

- *Nonreciprocal condition:*

The constitutive relations for general bi-isotropic nonreciprocal chiral media in Tellegen's notation can be written in the following form:

$$D = \epsilon_T E + (\chi + j\kappa)\sqrt{\epsilon_0\mu_0}H \tag{24.68a}$$

$$B = \mu_T H + (\chi - j\kappa)\sqrt{\epsilon_0\mu_0}E, \tag{24.68b}$$

where χ is the nonreciprocity parameter. Let us see how the introduction of the nonreciprocity parameter would modify to the nihility condition. The expression of the propagation constants of the two eigenwaves is found to be [70]

$$k_{\pm} = \omega\left(\sqrt{\epsilon_T\mu_T - \chi^2\epsilon_0\mu_0} \pm \kappa\sqrt{\epsilon_0\mu_0}\right). \tag{24.69}$$

Thus, the nihility condition is

$$\sqrt{\epsilon_T\mu_T - \chi^2\epsilon_0\mu_0} \to 0. \tag{24.70}$$

When this condition is satisfied, then

$$k_{\pm} = \omega\left(\sqrt{\epsilon_T\mu_T - \chi^2\epsilon_0\mu_0} \pm \kappa\sqrt{\epsilon_0\mu_0}\right) \rightarrow \pm k_0\kappa. \tag{24.71}$$

Apparently, the nonreciprocal nihility is easier to achieve than the CN $\epsilon_T\mu_T \rightarrow 0$ due to the role of the nonreciprocity parameter, which further reduces the value of the product of permittivity and permeability.

The wave impedances for a bi-isotropic nonreciprocal medium are found to be

$$\eta_{\pm} = \frac{\mu_T}{\sqrt{\epsilon_T\mu_T - \chi^2\epsilon_0\mu_0} \mp j\chi\sqrt{\epsilon_0\mu_0}}, \tag{24.72}$$

which are independent on the chirality parameter κ. If the CN condition Equation 24.70 is satisfied, then the expressions of the impedances reduce to

$$\eta_{\pm} = \pm j\frac{\mu_T}{\chi\sqrt{\epsilon_0\mu_0}} = \pm j\frac{\mu_T}{\epsilon_T}, \tag{24.73}$$

which is a purely imaginary number for lossless media.

It is also found that if Equation 24.70 is exactly zero, the effective permittivity and permeability seen by the LCP and RCP waves also become purely imaginary numbers (for lossless media)

$$\mu_T^{\pm} = j\mu_T\frac{\kappa}{\chi} \tag{24.74a}$$

$$\epsilon_T^{\pm} = -\frac{\mu_0}{\mu_T}j\kappa\chi\epsilon_0. \tag{24.74b}$$

Let us now consider the case of dispersive bi-isotropic media with a single-resonance dispersion. The expressions of the permittivity and permeability in Equation 24.68 read

$$\epsilon_T(\omega) = \epsilon_0\left[1 - \frac{\omega_{pe}^2}{\omega(\omega + j\Gamma_e\omega_{pe})}\right] \tag{24.75a}$$

$$\mu_T(\omega) = \mu_0\left[1 - \frac{\omega_{pm}^2}{\omega(\omega + j\Gamma_m\omega_{pm})}\right], \tag{24.75b}$$

where the plasma frequency and damping terms are assumed to be equal for both polarization and magnetization: $\omega_{pe} = \omega_{pm} = \omega_p$ and $\Gamma_e = \Gamma_m = \Gamma$. The nonreciprocity parameter and the chirality can be described in terms of a quantum mechanical model analogue to the classical lossy Drude model:

$$\chi(\omega) = \frac{\Gamma_c\omega^2\omega_c^2}{\omega^4 - (2 - \Gamma_c^2)\omega^2\omega_c^2 + \omega_c^4} \tag{24.76a}$$

$$\kappa(\omega) = \frac{(\omega_c^2 - \omega^2)\omega\omega_c}{\omega^4 - (2 - \Gamma_c^2)\omega^2\omega_c^2 + \omega_c^4}, \tag{24.76b}$$

where ω_c is the characteristic frequency for the single-resonance model, and the damping term Γ_c is consistent with the one for polarization/magnetization (i.e., $\Gamma_c = \Gamma$). Let us call the real part of $\sqrt{\epsilon_T(\omega)\mu_T(\omega)/\epsilon_0\mu_0 - \chi^2(\omega)}$ the nonreciprocal nihility parameter (NNP).

In Figure 24.15, it appears that for $\omega = 9.95 \times 10^9$ rad/s, NNP is of the order of 10^{-6} only; the nonreciprocal CN would then be realized. On the other hand, the imaginary part for NNP is of the order of 0.1 at this frequency. As a consequence, the forward and backward waves propagating in

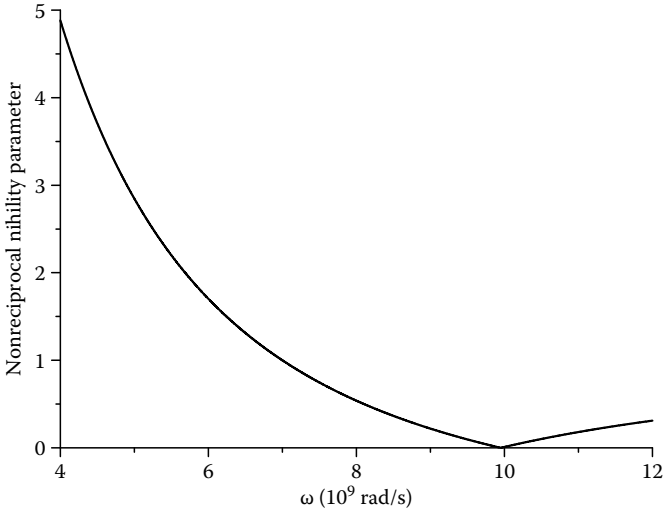

FIGURE 24.15 Nonreciprocal nihility parameter versus frequency for nonreciprocal chiral material: $\omega_p = 10 \times 10^9$ rad/s, $\omega_c = 1 \times 10^9$ rad/s, and $\Gamma = 0.1$.

the medium would be decaying waves. Thus, the nonreciprocity parameter χ might be used as an additional parameter to achieve CN. It is also worth noting that if the bi-isotropic medium has no dispersion and is lossless, the limiting case of $\chi = \sqrt{\epsilon_T \mu_T}/\sqrt{\epsilon_0 \mu_0}$ implies that this medium carries zero power [70]. However, due to the dispersion, the lossy chiral medium can still convey some power even if the NNP is very close to zero. Thus, it can be concluded that dispersive nonreciprocal CN material has properties that are quite different from that of the reciprocal CN media.

- *Gyrotropic chiral nihility:*

Although the nonreciprocity parameter in general bi-isotropic media offers an additional degree of freedom to achieve CN, the nihility condition is still a challenge to satisfy in practice due to the difficulty of realizing artificial nonreciprocal bi-isotropic media. In this section, another possibility of creating CN is investigated. It concerns gyrotropic chiral media with gyrotropy [87,89,96], either in permittivity/permeability or in magnetoelectric parameters. Introduction of certain anisotropy or gyrotropy may provide methods to control chirality. This category of chiral media has three subsets: (1) Ω–medium, (2) chiroplasma medium, and (3) chiroferrite medium. Although the Ω–medium can exhibit negative refraction and most probably nihility, the investigation is mainly restricted to chiroplasma and chiroferrite [97]. Chiroplasma can be realized by embedding chiral inclusions in a magnetically biased plasma, which results in the gyrotropic tensor in permittivity, while chiroferrites can be made from chiral inclusions immersed into ferrites with biased magnetic fields, which leads to a gyrotropic tensor in permeability. An example of such media is the generalized form of Faraday chiral media.

Based on the viewpoint of practical application, Post notations are employed to describe such media as Equation 24.18 and the parameters are defined as Equations 24.29 and 24.45. Looking back into the result of refractive indices as shown in Equation 24.48, one can further rewrite as

$$n_{\pm} = c_0 \left[\sqrt{\xi_c^2 (\mu \pm l)^2 + (\epsilon \pm g)(\mu \pm l)} - \xi_c (\mu \pm l) \right]. \tag{24.77}$$

Therefore, the condition for achieving gyrotropic nihility is

$$\xi_c^2 = -(\epsilon \pm g)/(\mu \pm l). \tag{24.78}$$

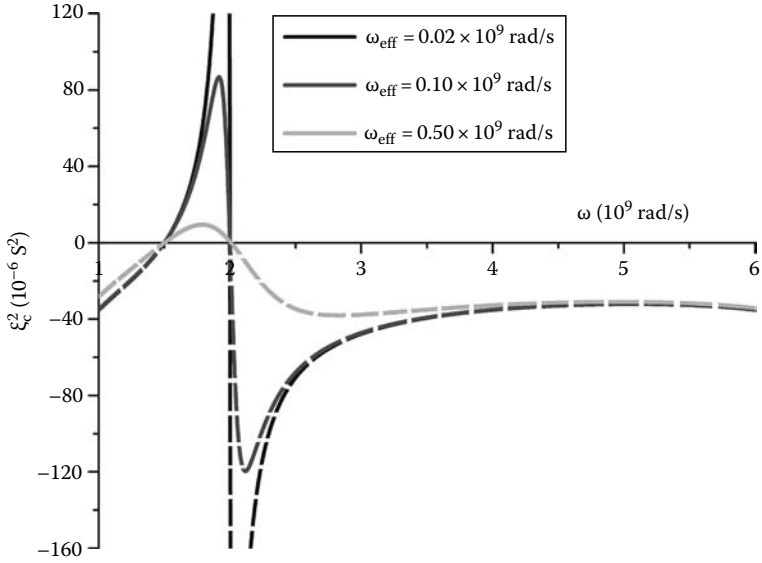

FIGURE 24.16 Chirality control at the scale of ξ_c^2 ($10^{-6} Siemens^2$) to satisfy the n_- condition of gyrotropic nihility for gyrotropic chiral material at different electron collision frequencies: $\omega_p = 8 \times 10^9$ rad/s, $\omega_g = 2 \times 10^9$ rad/s, $\omega_0 = 1.5 \times 10^9$ rad/s, and $\omega_M = 6 \times 10^9$ rad/s.

The off-diagonal elements (i.e., g and l) can be both modified to achieve the nihility condition. By a proper choice of the off-diagonal elements (i.e., g and l), the gyrotropic CN condition of Equation 24.78 can be achieved even for media with a low degree of chirality ξ_c. The frequency under the solid lines in Figure 24.16 is the valid range to meet the gyrotropic CN.

It can be shown from Figure 24.16 that the electron collision frequency ω_{eff} plays an important role in achieving gyrotropic nihility. For high values of ω_{eff}, for instance, for $\omega_{eff} = 0.02 \times 10^9$ rad/s, a much higher chirality is needed to match the requirement of gyrotropic nihility compared with the case when $\omega_{eff} = 0.5 \times 10^9$ rad/s. The smaller the collision frequency is, the higher the chirality needed to satisfy the nihility condition. Therefore, the electron collision in the plasma is found to facilitate the chirality control of gyrotropic nihility. It is due to the fact that self-spin and the collision of electrons may strengthen the degree of magnetoelectric coupling in gyrotropic chiral media, which compensates the nihility requirement for chirality.

Therefore, in order to satisfy the condition of gyrotropic nihility, the frequency should be chosen within a specific range, apart from which gyrotropic CN can never be realized no matter how the chirality is controlled. Once the gyrotropic nihility is satisfied, the refractive indices become

$$n_+^{\text{nih}} = -c_0(\mu + l)\xi_c \tag{24.79a}$$

$$n_-^{\text{nih}} = c_0(l - \mu)\xi_c. \tag{24.79b}$$

It can be found that n_+^{nih} is negative because of $\mu + l > 0$ (Equation 24.45). Of particular interest is the negative refraction for n_-^{nih}, which has resonance in the vicinity of ferromagnetic frequency ω_0. At the frequency range $0 < \omega < \omega_0^- \cup \omega_0 + \omega_M < \omega$, negative refraction occurs in n_-^{nih}.

24.3.4 Bianisotropic Routes

Bianisotropy is conceived as a physical concept describing composites that possess intrinsic mechanisms of magnetoelectric coupling, which includes chiral, bi-isotropic, and gyrotropic chiral media.

The concept of a bianisotropic medium was coined in 1968 by Cheng and Kong [98] defining a medium with the most general linear constitutive relations. It was supposed that such generalized constitutive relations may unify two separate branches of research on electrodynamics and magnetoelectric crystals. In the previous section, gyrotropic chiral materials (chiroplasma and chiroferrite) are very close to the definition of the bianisotropic material in the sense of constitutive relations. Interestingly, new trends of realization of NIMs by using bianisotropic materials will be revisited.

The constitutive relations of a bianisotropic medium are classified as

$$D = \overline{\boldsymbol{\epsilon}} \cdot E + \overline{\boldsymbol{\xi}} \cdot H \tag{24.80a}$$

$$B = \overline{\boldsymbol{\zeta}} \cdot E + \overline{\boldsymbol{\mu}} \cdot H, \tag{24.80b}$$

where

$\overline{\boldsymbol{\epsilon}}$/ $\overline{\boldsymbol{\mu}}$ denotes permittivity/permeability dyadics

$\overline{\boldsymbol{\xi}}$/$\overline{\boldsymbol{\zeta}}$ represents the cross-coupling dyadics. For decades, electromagneticians adopt this postulation of the most general linear magnetoelectric medium. People find that such relations do not violate Maxwell equations, assuming the electric and magnetic dipoles induced in the particles are coupled pairwise. However, in a rigid sense, the constitution should be derived through an averaging process in a microscopic view, which is beyond the scope of the current chapter. In what follows, let us focus on two practical aspects of the bianisotropic role in NIMs.

Bianisotropics is closely correlated with the metamaterial research because small metallic resonant particles may show certain bianisotropic (magnetoelectric) effects. The role of bianisotropy would even result in non-left-handedness in some particular ring resonators [99]. An analytical model thereby was proposed to remove the bianisotropy as well as to reduce the resonant frequency and the electric size, by mirroring the ring at the backside of the substrate with a 180° rotation [21].

Usually, the bianisotropy (magnetoelectric coupling) might be regarded as an undesired property by the majority of researchers in the community of NIMs, hence some symmetrical split-ring structures are proposed [100]. The backward-wave regimes are realized when both the permittivity and permeability have negative real parts in the design of magnetodielectrics.

However, it has been proved that backward waves and negative refraction can exist in bianisotropic materials, for instance, chiral media [72,74,101,102] and gyrotropic chiral media [87,96,103]. It will be shown how the bianisotropy is used to realize NIMs. From the practical point of view, a general bianisotropic medium, a reciprocal uniaxial Ω-medium, can simply be realized by a composite with wire inclusions, defined by the following constitutive relations:

$$D = \epsilon_0 \begin{bmatrix} \epsilon_t & 0 & 0 \\ 0 & \epsilon_t & 0 \\ 0 & 0 & \epsilon_z \end{bmatrix} \cdot E + i\sqrt{\epsilon_0 \mu_0} \begin{bmatrix} 0 & -K & 0 \\ K & 0 & 0 \\ 0 & 0 & 0 \end{bmatrix} \cdot H \tag{24.81a}$$

$$B = \mu_0 \begin{bmatrix} \mu_t & 0 & 0 \\ 0 & \mu_t & 0 \\ 0 & 0 & \mu_z \end{bmatrix} \cdot H + i\sqrt{\epsilon_0 \mu_0} \begin{bmatrix} 0 & -K & 0 \\ K & 0 & 0 \\ 0 & 0 & 0 \end{bmatrix} \cdot E, \tag{24.81b}$$

where K denotes the magnetoelectric coupling.

Since the Ω-medium has been modeled in microwave frequency and checked by experiments [104], this approach is believed to be realistic and reliable, which also provides the possibility of extending current applications from microwaves to the optical wavelength. Traditionally, the creation of a negative permeability in optical wavelength is quite difficult, which restricts the application of metamaterials. Interestingly, the Ω-medium, as proposed in Ref. [105], does not require the permittivity and permeability to have negative real parts. Instead, once the condition of $Re\{\epsilon_t + \mu_t\} < 0$ is satisfied, negative refraction could arise, which is easier to achieve apparently.

This point is especially valuable to the composites with negative permittivity in optics, because the negative real part in permittivity would compensate the contribution of permeability through magnetoelectric coupling. It is due to the fact that the magnitude of resonant magnetoelectric coupling has an order higher than that of resonant magnetic polarizability. By introducing a second ensemble of identical Ω-particles with the stems along x-axis and the loops in $x-z$ plane, this type of structure can futher perform uniform operation for linearly polarized waves of any polarization direction. Backward waves can be generated by the bianisotropy within certain frequency bands, in which the permeability is positive.

24.4 Conclusion

In this chapter, the electromagnetic properties of chiral and bianisotropic (magnetoelectric) composites are intensively investigated, with the particular interest in realization of backward-wave and negative-index regimes. Wide applications in resonator, phase compensator, directive antennas, and quantum devices are also reported. Different medium formalisms of isotropic and gyrotropic magnetoelectric composites are discussed, and it is found that for isotropic magnetoelectric cases the formalisms are all equivalent while for gyrotropic magnetoelectric cases each formalisms have pros and cons in the viewpoints of NIM realization and practical application. The gyrotropy parameters also favor the realization of negative refraction because they will make the wave propagate backward. The eigenmodes at backward-wave regime and their frequency ranges are discussed for dispersive gyrotropic magnetoelectric composites. Based on that, the negative refraction can be achieved by selection of working frequency.

As a more interesting case, the CN, isotropic and gyrotropic, is examined. The energy transport in CN is extensively examined. The effects of magnetoelectric coupling in the energy transport are characterized through numerical studies. A wide range of Brewster angles is discovered and electromagnetic wave through a CN slab is studied. In the following, general nihility routes for magnetoelectric composites to NIMs are proposed for isotropic, nonreciprocal, and gyrotropic chiral composites, where the requirements to meet respective nihility condition such as frequency control and chirality control are also presented. For the isotropic CN, the DBF formalism is proven to be inappropriate due to the lack of physics. A nonreciprocal CN is thus shown, which makes the nihility condition easier to fulfill. Furthermore, the gyrotropic CN, based on the previous study on gyrotropic chiral composites, is investigated and one can find that it provides more degrees of freedom to meet the nihility condition due to the contributions of gyrotropic parameters. Chirality control is presented and it reveals that more of electron collision in plasma could alleviate the chirality requirement for gyrotropic CN. Finally, the bianisotropy is discussed in two separate branches of the metamaterial research. One is to minimize the bianisotropic effects in the design of metal inclusions, which could result in an isotropic negative-index material. On the contrary, the bianisotropic routes to backward-wave regimes are revisited making use of the bianisotropy of certain particular structures (i.e., Ω-medium). In conclusion, magnetoelectric coupling in chiral or generalized bianisotropic media provides the researchers a new avenue to achieve the negative-index materials, with a wide range of exciting potentials in optical region.

References

1. V. G. Veselago, The electrodynamics of substances with simultaneously negative values of ε and μ, *Sov. Phy. Usp.*, 10(4), 509–514, 1968.
2. H. Lamb, On group-velocity, *Proc. London Math. Soc.*, 1, 473–479, 1904.
3. A. Schuster, *An Introduction to the Theory of Optics*, Edward Arnold, London, 1904.

4. H. C. Pocklington, Growth of a wave-group when the group velocity is negative, *Nature*, 71, 607–608, 1905.
5. G. D. Malyuzhinets, A note on the radiation principle, *Sov. Phys. Tech. Physics*, 21, 940–942, 1951.
6. D. V. Sivukhin, The energy of electromagnetic waves in dispersive media, *Opt. Spektrosk.*, 3, 308–312, 1957.
7. R. A. Silin, Possibility of creating plane-parallel lenses, *Opt. Spektrosk.*, 44, 189–191, 1978.
8. J. B. Pendry, A. J. Holden, D. J. Robbins, and W. J. Stewart, Magnetism from conductors and enhanced nonlinear phenomena, *IEEE Trans. Microwave Theory Tech.*, 47(11), 2075–2084, November 1999.
9. J. B. Pendry, A. J. Holden, W. J. Stewart, and I. Youngs, Extremely low frequency plasmons in metallic mesostructures, *Phys. Rev. Lett.*, 76, 4773–4776, 1996.
10. J. B. Pendry, A. J. Holden, D. J. Robbins, and W. J. Stewart, Low frequency plasmons in thin wire structures, *J. Phys.: Cond. Mat.*, 10, 4785–4788, 1998.
11. D. R. Smith, W. J. Padilla, D. C. Vier, S. C. Nemat-Nasser, and S. Schultz, Composite medium with simultaneously negative permeability and permeability, *Phys. Rev. Lett.*, 84, 4184–4187, 2000.
12. D. R. Smith and N. Kroll, Negative refractive index in left-handed materials, *Phys. Rev. Lett.*, 85, 2933–2936, 2000.
13. R. A. Shelby, D. R. Smith, and S. Schultz, Experimental verification of a negative index of refraction, *Science*, 292(5514), 77–79, 2001.
14. R. A. Shelby, D. R. Smith, S. C. Nemat-Nasser, and S. Schultz, Microwave transimission through a two-dimensional, isotropic, left-handed metamaterial, *Appl. Phys. Lett.*, 78, 489–491, 2001.
15. J. B. Pendry, Negative refraction makes a perfect lens, *Phys. Rev. Lett.*, 85, 3966–3969, 2000.
16. G. V. Eleftheriades and K. G. Balmain (Eds.), *Negative-Refraction Metamaterials: Fundamental Principles and Applications*, John Wiley & Sons, IEEE Press, New York, 2005.
17. R. W. Ziolkowski and N. Engheta (Eds.), *Electromagnetic Metamaterials: Physics and Engineering Applications*, John Wiley & Sons, IEEE Press, New York, 2006.
18. A. A. Houck, J. B. Brock, and I. L. Chuang, Experimental observations of a left-handed material that obeys Snell's law, *Phys. Rev. Lett.*, 90, 137401, 2003.
19. J. Brown, Artificial dielectrics, *Prog. Dielectrics*, 2, 195–225, 1960.
20. R. W. Ziolkowski and A. Kipple, Causality and double-negative metamaterials, *Phys. Rev. E*, 68, 026615, 2003.
21. R. Marqués, F. Medina, and R. Rafii-El-Idrissi, Role of bianisotropy in negative permeability and left-handed metamaterials, *Phys. Rev. B*, 65, 144440, 2002.
22. R. Marqués, J. D. Baena, M. Beruete, F. Falcone, T. Lopetegi, M. Sorolla, F. Martin, and J. Gracia, Ab initio analysis of frequency selective surfaces based on conventional and complementary split ring resonators, *J. Opt. A: Pure Appl. Opt.*, 7(2), 38–43, February 2005.
23. Y. J. Hsu, Y. C. Huang, J. S. Lih, and J. L. Chern, Electromagnetic resonance in deformed split ring resonators of left-handed meta-materials, *J. Appl. Phys.*, 96, 1979–1982, 2004.
24. C. R. Simovski and S. He, Frequency range and explicit expressions for negative permittivity and permeability for an isotropic medium formed by a lattice of perfectly conducting ω particles based on the quasi-static lorentz theory, *Phys. Lett. A*, 311, 254–263, 2003.
25. H. Chen, L. Ran, J. Huangfu, X. Zhang, K. Chen, T. M. Grzegorczyk, and J. A. Kong, Left-handed materials composed of only S-shaped resonators, *Phys. Rev. B*, 70, 057605, 2004.
26. H. Chen, L. Ran, J. Huangfu, X. Zhang, K. Chen, T. M. Grzegorczyk, and J. A. Kong, Negative refraction of a combined double S-shaped metamaterial, *Appl. Phys. Lett.*, 86, 151909, 2005.
27. P. Markoš and C. M. Soukoulis, Numerical studies of left-handed materials and arrays of split ring resonators, *Phys. Rev. E*, 65, 036622, 2002.
28. N. Katsarakis, T. Koschny, M. Kafesaki, E. N. Economou, E. Ozbay, and C. M. Soukoulis, Left- and right-handed transmission peaks near the magnetic resonance frequency in composite metamaterials, *Phys. Rev. B*, 70, 201101, 2004.

29. J. F. Woodley, M. S. Wheeler, and M. Mojahedi, Left-handed and right-handed metamaterials composed of split ring resonators and strip wires, *Phys. Rev. E*, 71, 066605, 2005.
30. A. Sihvola, Metamaterials and depolarization factors, *Prog. Electromagn. Res.*, 51, 1–26, 2006.
31. X. D. Chen, B. I. Wu, J. A. Kong, and T. M. Grzegorczyk, Retrieval of the effective constitutive parameters of bianisotropic metamaterials, *Phys. Rev. E*, 71, 046610, 2005.
32. J. B. Pendry and D. R. Smith, Reversing light with negative refraction, *Phys. Today*, 57(6), 37, June 2004.
33. S. O'Brien and J. B. Pendry, Magnetic activity at infrared frequencies in structured metallic photonic crystals, *J. Phys.: Condens. Mat.*, 14, 6383–6394, 2002.
34. S. A. Ramakrishna, Physics of negative refractive index materials, *Rep. Prog. Phys.*, 68, 449–521, 2005.
35. S. O'Brien, D. McPeake, S. A. Ramakrishna, and J. B. Pendry, Near-infrared photonic band gaps and nonlinear effects in negative magnetic metamaterials, *Phys. Rev. B*, 69, 241101, 2004.
36. V. M. Shalaev, W. Cai, U. K. Chettiar, H. K. Yuan, A. K. Sarychev, V. P. Drachev, and A. V. Kildishev, Negative index of refraction in optical metamaterials, *Opt. Lett.*, 30(24), 3356–3358, December 2005.
37. A. Grbic and G. V. Eleftheriades, Sub-wavelength focusing using a negative-refractive-index transmission-line lens, *IEEE Antennas Wireless Propagat. Lett.*, 2, 186–189, 2003.
38. G. V. Eleftheriades, A. K. Iyer, and P. C. Kremer, Planar negative refractive index media using periodically L-C loaded transmission lines, *IEEE Trans. Microwave Theory Tech.*, 50(12), 2702–2712, December 2002.
39. A. K. Iyer, P. C. Kremer, and G. V. Eleftheriades, Experimental and theoretical verification of focusing in a large, periodically loaded transmission line negative refractive index metamaterial, *Opt. Express*, 11(4), 155–157, 2003.
40. O. F. Siddiqui, S. J. Erickson, G. V. Eleftheriades, and M. Mojahedi, Time-domain measurement of negative group delay in negative-refractive-index transmission-line metamaterials, *IEEE Trans. Microwave Theory Tech.*, 52(5), 1449–1454, May 2004.
41. A. Lai, C. Caloz, and T. Itoh, Composite right/left-handed transmission line metamaterials, *IEEE Microwave Mag.*, 5(3), 34–50, September 2004.
42. A. Sanada, C. Caloz, and T. Itoh, Characteristics of the composite right/left-handed transmission lines, *IEEE Microw. Wireless Compon. Lett.*, 14(2), 68–70, February 2004.
43. C. Caloz, A. Sanada, and T. Itoh, A novel composite right-/left-handed coupled-line directional coupler with arbitrary coupling level and broad bandwidth, *IEEE Trans. Microwave Theory Tech.*, 52(3), 980–992, March 2004.
44. C. Caloz and T. Itoh, *Electromangetic Metamaterials*, John Wiley & Sons, New York, 2006.
45. A. Priou and T. Itoh (Eds.), *Electromagnetic Applications of Photonic Band Gap Materials and Structures*, EMW Publishing, Cambridge, MA, 2003.
46. T. Decoopman, G. Tayeb, S. Enoch, D. Maystre, and B. Gralak, Photonic crystal lens: from negative refraction and negative index to negative permittivity and permeability, *Phys. Rev. Lett.*, 97, 073905, 2006.
47. S. Zouhdi, A. V. Dorofeenko, A. M. Merzlikin, and A. P. Vinogradov, Zero width band gap effect in photonic crystals made of metamaterials, *Phys. Rev. B*, 75, 035125, 2007.
48. E. Yablonovitch, An idea for thin subwavelength cavity resonators using metamaterials with negative permittivity and permeability, *Phys. Rev. Lett.*, 58(20), 2059–2062, 1987.
49. P. A. Belov, S. A. Tretyakov, and A. J. Viitanen, Nonreciprocal microwave bandgap structures, *Phys. Rev. E*, 66, 016608, 2002.
50. A. Scherer, T. Doll, E. Yablonovitch, H. O. Everitt, and J. A. Higgins, Mini-special issue on electromagnetic crystal structures, design, synthesis, and applications, *IEEE Trans. Microwave Theory Tech.*, 47(11), 2057–2150, 1999.
51. A. Priou and T. Itoh (Eds.), Special issue on electromagnetic applications of photonic band gap materials and structures, *Prog. Electromagn. Res.*, 41, 61–81, 2003.

52. K. Yasumuto (Ed.), *Electromagnetic Theory and Applications for Photonic Crystals*, CRC Press, Taylor & Francis, Boca Raton, FL, 2006.
53. M. Notomi, Theory of light propagation in strongly modulated photonic crystals: Refractionlike behavior in the vicinity of the photonic band gap, *Phys. Rev. B*, 62, 10696–10705, 2000.
54. C. Luo, S. G. Johnson, and J. D. Joannopoulos, All-angle negative refraction in a three-dimensionally periodic photonic crystal, *Appl. Phys. Lett.*, 81(13), 2352–2354, September 2002.
55. X. Y. Ao and S. L. He, Three-dimensional photonic crystal of negative refraction achieved by interference lithography, *Opt. Lett.*, 29(21), 2542–2554, November 2002.
56. Z. C. Ruan and S. L. He, Coupling between plane waves and bloch waves in photonic crystals with negative refraction, *Phys. Rev. B*, 71, 045111, 2005.
57. Z. C. Ruan and S. L. He, Open cavity formed by a photonic crystal with negative effective index of refraction, *Opt. Lett.*, 30(17), 2308–2310, 2005.
58. J. L. He, J. Yi, and S. L. He, Giant negative Goos-Hanchen shifts for a photonic crystal with a negative effective index, *Opt. Express*, 14(7), 3024–3029, 2006.
59. S. He, Y. Jin, Z. Ruan, and J. Kuang, On subwavelength and open resonators involving metamaterials of negative refraction index, *New J. Phys*., 7, 210, 2005.
60. D. F. Arago, Sur une modification remarquable qu'éprouvent les rayons lumineux dans leur passage á travers certains corps diaphanes, et sur quelques autres nouveaux phénomènes d'optique, *Mem. Inst.*, 1, 93–134, 1811.
61. J. B. Biot, Mémoire sur un nouveau genre d'oscillations que les molécules de la lumière éprouvent, en traversant certains cristaux, *Mem. Inst.*, 1, 1–372, 1812.
62. J. B. Biot, Phénomènes de polarisation successive, observés dans des fluides homogènes, *Bull. Soc. Philomath.*, 190–192, 1815.
63. A. Fresnel, Mémoire sur la double réfraction que les rayons lumineux éprouvent en traversant les aiguilles de cristal de roche suivant des directions parallèles à l'axe, *Oeuvres*, 1, 731–751, 1822.
64. T. M. Lowry, *Optical Rotatory Power*, Dover, New York, 1964.
65. S. Bassiri, C. H. Papas, and N. Engheta, Electromagnetic wave propagation through a dielectric-chiral interface and through a chiral slab, *J. Opt. Soc. Am. A*, 5, 9, 1450–1459, 1988.
66. A. Priou (Ed.), *Bianisotropic and Bi-isotropic Media and Applications, PIER* **9**, EMW Publishing, Cambridge, MA, 1994.
67. J. A. Kong, *Electromagnetic Wave Theory*, 3rd edition, John Wiley, New York, 1990.
68. M. P. Silverman and R. B. Sohn, Effects of circular birefringence on light propagation and reflection, *Am. J. Phys.*, 54, 69–76, 1986.
69. T. G. Kharina, S. A. Tretyakov, A. A. Sochava, C. R. Simovski, and S. Bolioli, Experimental studies of artificial omega med, *Electromagnetics*, 18(4), 423–437, 1998.
70. I. V. Lindell, A. H.Sihvola, S. A Tretyakov, and A. J. Viitanen, *Electromagnetic Waves in Chiral and Bi-Isotropic Media*, Artech House, Boston, London, 1994.
71. A. J. Viitanen and I. V. Lindell, Chiral slab polarization transformer for aperture antennas, *IEEE Trans. Antennas Propagat.*, 39, 75–82, January 1991.
72. J. B. Pendry, A chiral route to negative refraction, *Science*, 306(5700), 1353–1355, 2004.
73. Y. Jin and S. He, Focusing by a slab of chiral medium, *Opt. Express*, 13, 13, 4974–4979, 2005.
74. S. Tretyakov, A. Sihvola, and L. Jylhä, Backward-wave regime and negative refraction in chiral composites, *Photonics and Nanostruct. - Fundamentals Appl.*, 3, 107–115, 2005.
75. A. H. Sihvola and I. V. Lindell, Polarisability and mixing formula for chiral ellipsoids, *Electron. Lett.*, 26(14), 1007–1009, 1990.
76. S. Tretyakov, A. Sihvola I. Nefedov, S. Maslovski, and C. Simovski, Waves and energy in chiral nihility, *J. Electromag. Waves Appl.*, 17(5), 695–706, 2003.
77. C. Zhang and T. J. Cui, Negative reflections of electromagnetic waves in a strong chiral medium, *Appl. Phys. Lett.*, 91, 194101, 2007.

78. A. V. Rogacheva, V. A. Fedotov, A. S. Schwanecke, and N. I. Zheludev, Giant gyrotropy due to electromagnetic-field coupling in a bilayered chiral structure, *Phys. Rev. Lett.*, 97, 177401, 2006.
79. M. Born, On the theory of optical activity. I. General theory of a system of coupled isotropic oscillators. II. Molecules with a binary axis of symmetry, *Proc. Roy. Soc. London Series A, Math. Phys. Sci.*, 150(86), 84–105, 1935.
80. E. U. Condon, Theories of optical rotatory power, *Rev. Mod. Phys.*, 9, 432–457, 1937.
81. A. V. Krasavin, A. S. Schwanecke, M. Reichelt, T. Stroucken, S. W. Koch, E. M. Wright, and N. I. Zheludev, Polarization conversion and focusing of light propagating through a small chiral hole in a metallic screen, *Appl. Phys. Lett.*, 86, 201105, 2005.
82. A. Potts, A. Papakostas, D. M. Bagnall, and N. I. Zheludev, Planar chiral meta-materials for optical applications, *Microelectron. Eng.*, 73–74, 367–371, 2004.
83. V. A. Fedotov, P. L. Mladyonov, S. L. Prosvirnin, A. V. Rogacheva, Y. Chen, and N. I. Zheludev, Asymmetric propagation of electromagnetic waves through a planar chiral structure, *Phys. Rev. Lett.*, 97, 167401, 2006.
84. A. Akyurtlu and D. H. Werner, A novel dispersive FDTD formulation for modeling transient propagation in chiral metamaterials, *IEEE Trans. Antennas Propagat.*, 52(9), 2267–2276, September 2004.
85. A. Semichaevsky and A. Akyurtlu, A new uniaxial perfectly matched layer absorbing boundary condition for chiral metamaterials, *IEEE Antennas Wireless Propagat. Lett.*, 4, 51–54, 2005.
86. C. H. Papas, *Theory of Electromagnetic Wave Propagation*, McGraw-Hill, New York, 1965.
87. C. W. Qiu, H. Y. Yao, L. W. Li, S. Zouhdi, and M. S. Leong, On the constitutive relations of G-chiral media and the possibility to realize negative-index media, *Microw. Opt. Technol. Lett.*, 48, 12, 2534–2538, 2006.
88. L. D. Landau and E. M. Lifshitz, *Electrodynamics of Continuous Media*, 2nd ed, Pergamon Press, Oxford, 1984.
89. V. M. Agranovich, Yu. N. Gartstein, and A. A. Zakhidov, Overcoming the diffraction limit with a planar left-handed transmission-line lens, *Phys. Rev. B*, 73, 045113, 2006.
90. A. Lakhtakia, *Beltrami Fields in Chiral Media*, World Scientific, Singapore, 1994.
91. N. Engheta, An idea for thin subwavelength cavity resonators using metamaterials with negative permittivity and permeability, *IEEE Antennas Wireless Propagat. Lett.*, 1(1), 10–13, 2002.
92. A. Ishimaru, *Electromagnetic Wave Propagation, Radiation, and Scattering*, Prentice Hall, Englewood Cliffs, NJ, 1991.
93. N. Grigorenko, A. K. Geim, H. F. Gleeson, Y. Zhang, A. A. Firsov, I. Y. Khrushchev, and J. Petrovic, Nanofabricated media with negative permeability at visible frequencies, *Nat. Lett.*, 438, 335–338, 2005.
94. A. Lakhtakia, An electromagnetic trinity from "negative permittivity" and "negative permeability", *Intl. J. Infrar. Millim. Waves*, 22, 1734–1741, 2001.
95. M. P. Silverman, Reflection and refraction at the surface of a chiral medium: Comparison of gyrotropic constitutive relations invariant or noninvariant under a duality transformation, *J. Opt. Soc. Am. A*, 3, 830–837, 1986.
96. C. W. Qiu, L. W. Li, H. Y. Yao, and S. Zouhdi, Properties of Faraday chiral media: Green dyadics and negative refraction, *Phys. Rev. B*, 74, 115110, 2006.
97. N. Engheta, D. L. Jaggard, and M. W. Kowarz, Electromagnetic waves in Faraday chiral media, *IEEE Trans. Antennas Propagat.*, 40(4), 367–374, April 1992.
98. D. K. Cheng and J. A. Kong, Time-harmonic fields in source-free bianisotropic media, *J. Appl. Phys.*, 39(12), 5792–5796, 1968.
99. Z. G. Dong, S. Y. Lei, Q. Li, M. X. Xu, H. Liu, T. Li, F. M. Wang, and S. N. Zhu, Non-left-handed transmission and bianisotropic effect in a π-shaped metallic metamaterials, *Phys. Rev. B*, 75, 075117, 2007.

100. T. Koschny, L. Zhang, and C. M. Soukoulis, Isotropic three-dimensional left-handed metamaterials, *Phys. Rev. B*, 71, 121103(R), 2005.
101. C. W. Qiu, H. Y. Yao, S. N. Burokur, S. Zouhdi, and L. W. Li, Electromagnetic scattering properties in a multilayered metamaterial cylinder, *IEICE Trans. Commun.*, E90-B(9), 2423-2429, 2007.
102. C. W. Qiu, S. Zouhdi, and S. Tretyakov, Nonreciprocal and gyrotropic effects of chiral nihility to achieve negative-index materials, *IEEE Trans. Antennas Propagat.*, submitted, 2007.
103. C. W. Qiu and S. Zouhdi, Comment on "negative refractive index in gyrotropically magnetoelectric media", *Phys. Rev. B*, 75, 196101, 2007.
104. A. Serdyukov, I. Semchenko, S. A. Tretyakov, and A. Sihvola, *Electromagnetics of Bi-anisotropic Materials, Theory and Applications*, Gordon and Breech Science Publishers, New York, 2001.
105. S. Tretyakov, C. R. Simovski, and M. Hudlička, Bianisotropic route to realization and matching backward-wave slabs, *Phys. Rev. B*, 75, 153104, 2007.

25

Negative Refraction and Perfect Lenses Using Chiral and Bianisotropic Materials

Sergei A. Tretyakov
Helsinki University of Technology

25.1 Introduction

Bianisotropic media are linear materials characterized by the most general linear relationships between the four field vectors [1], which can be written as

$$\mathbf{D} = \varepsilon_0 \bar{\bar{\varepsilon}} \cdot \mathbf{E} + \bar{\bar{a}} \cdot \mathbf{H}, \tag{25.1}$$

$$\mathbf{B} = \bar{\bar{b}} \cdot \mathbf{E} + \mu_0 \bar{\bar{\mu}} \cdot \mathbf{H}. \tag{25.2}$$

Magnetoelectric coupling, measured by the two dyadic parameters $\bar{\bar{a}}$ and $\bar{\bar{b}}$, appears either due to spatial dispersion in the medium (these terms model spatial dispersion of the first order in terms of the ratio of the inhomogeneity size to the wavelength) or due to nonreciprocity of the material. In reciprocal bianisotropic materials the coupling coefficients satisfy

$$\bar{\bar{b}} = -\bar{\bar{a}}^{\mathrm{T}}, \tag{25.3}$$

where T denotes the transpose operation (in addition, in this case the permittivity and permeability dyadics are symmetric). Thus, the reciprocal magnetoelectric coupling can be described by only one dyadic coupling coefficient, say, $\bar{\bar{a}} = \bar{\bar{\kappa}}$. This dyadic can always be written as

$$\bar{\bar{\kappa}} = \kappa \bar{\bar{I}} + \bar{\bar{N}} + \bar{\bar{J}}, \tag{25.4}$$

where
$\bar{\bar{I}}$ is the unit dyadic
$\bar{\bar{\bar{N}}}$ is a symmetric trace-free dyadic
$\bar{\bar{J}}$ is an antisymmetric dyadic

According to the classification given in Ref. [1], reciprocal bianisotropic media split into classes of chiral media, when $\kappa = \text{trace}\{\bar{\bar{\kappa}}\}$ is nonzero (κ is called the chirality parameter), pseudochiral media when $\kappa = 0$, $\bar{\bar{\bar{N}}} \neq 0$, $\bar{\bar{J}} = 0$, omega media $\kappa = 0$, $\bar{\bar{\bar{N}}} = 0$, $\bar{\bar{J}} \neq 0$, and their combinations.

Nonreciprocal magnetoelectric coupling effects are measured by the nonreciprocity dyadic $\bar{\bar{\chi}} = \bar{\bar{a}} + \bar{\bar{b}}^{\mathrm{T}}$. Similar classification using the representation

$$\bar{\bar{\chi}} = \chi \bar{\bar{I}} + \bar{\bar{\bar{N}}} + \bar{\bar{J}} \tag{25.5}$$

defines Tellegen media with $\chi \neq 0$, pseudo Tellegen media with $\bar{\bar{\bar{N}}} \neq 0$, and moving media with $\bar{\bar{J}} \neq 0$. Note that metamaterials can "emulate" magnetoelectric coupling in moving media although the samples are at rest.

Electromagnetic phenomena in bianisotropic media are very rich, and they have been studied in a large number of publications (see monographs [1,2]). In the following sections, we briefly review some recent results on backward waves and negative refraction phenomena in bianisotropic media.

25.2 Backward Waves in Chiral Media

The constitutive relations for isotropic chiral media read [2]

$$\mathbf{D} = \varepsilon\varepsilon_0\mathbf{E} - j\kappa\sqrt{\varepsilon_0\mu_0}\,\mathbf{H}, \tag{25.6}$$

$$\mathbf{B} = j\kappa\sqrt{\varepsilon_0\mu_0}\,\mathbf{E} + \mu\mu_0\mathbf{H}. \tag{25.7}$$

Here κ is the chirality parameter, measuring the magnetoelectric coupling, which, due to the first-order spatial dispersion effects, allowed for media with mirror-asymmetric microstructure. The eigenwaves in isotropic chiral media are left- and right-circularly polarized plane waves with different propagation constants

$$\beta = (n \pm \kappa)k_0, \tag{25.8}$$

where
$n = \sqrt{\epsilon\mu}$ is the usual refraction index
k_0 is the free-space wave number

From the above formula it is obvious that if the effect of chirality is very strong or the refraction index is very small, one of the propagation constants can have a negative real part. This means that one of the eigenwaves in this case is a backward wave, like in isotropic nonchiral media with negative material parameters.

A possibility for such an effect was noted for the first time probably in Ref. [3], published in 1981. In Ref. [3], a spiral model for a chiral optical molecule and the Lorentz dispersion model for the permittivity were used. A formula for the frequency range of negative refraction was derived. Single-phase chiral substances were considered, and magnetic properties of the medium were neglected. However, for a long time this contribution remained largely forgotten, probably because in naturally occurring chiral materials chirality is a very weak effect, so such exotic regimes were not possible to realize. More recently, with the metamaterial technology emerging, backward waves in chiral materials were

theoretically rediscovered by several authors [4–7]. The existence of backward waves in strongly chiral media with positive permeability and negative permittivity was shown in Ref. [8].

25.2.1 Possible Routes to Realization

There are two known possible approaches to realization of the backward-wave regime in artificial chiral media: the use of a mixture of helixes and resonant dipoles [5] and the use of a composite of only helices [3,4]. In the first approach, the hypothesis [5] is that in the vicinity of the resonant frequency of electric-dipole inclusions the effective permittivity can be very small (the real part can cross zero), whereas the chirality effect (provided by small helical inclusions) remains strong enough, so that the backward-wave condition $\mathrm{Re}\{n\} < \mathrm{Re}\{\kappa\}$ would be satisfied.

Both possibilities were studied in detail and compared in Ref. [9]. In Ref. [9], the methods described in Refs. [1,10] were used to derive mixing equations for the effective material parameters of double-phase chiral mixture, which take into account the coupling between dipoles and helixes. Next, numerical examples were calculated with the use of an introduced general dispersion law for the polarizabilities of helical particles, based on the antenna model of chiral inclusions [11]. This model enables the study of particles with different shapes and electrical sizes.

It has been shown that once the coupling between helices and dipoles is taken into account, there is a stop band in the frequency region where negative refraction is expected to occur following the simple hypothesis of Ref. [5]. However, the negative refraction can still occur in "chiral nihility" materials as has been suggested in Ref. [4]. Backward waves can exist at frequencies higher than the resonant frequency of chiral particles. The role of chirality was seen in widening the backward-wave frequency band and in opening a way to realize new physical effects and possibly create new microwave and optical devices.

25.3 Chiral Materials with the Effective Refraction Index $n = -1$

As follows from analytical models of small-particle polarizabilities (e.g., Ref. [11]), the axial electric and magnetic polarizabilities of small chiral inclusions are proportional to each other, and the proportionality coefficient slowly depends on the frequency [12]. As was noted in Refs. [13,14], this can allow us to create artificial materials with nearly equal permittivity and permeability close to the resonance of the particles. Moreover, there exist "optimal" shapes of helices [15,16] for which all three axial polarizabilities are equal, that is, the normalized electric polarizability, magnetic polarizability, and the magnetoelectric coupling coefficient are all equal.

For the "optimal" shape of helices we have $\epsilon = \mu = 1 \pm \kappa$ (different signs exist for the opposite handedness of the spirals) [16]. At a certain frequency near the fundamental resonance of the helices, the real parts of the permittivities cross zero:

$$\mathrm{Re}\{\epsilon\} = \mathrm{Re}\{\mu\} = 0 \quad \Rightarrow \mathrm{Re}\{\kappa\} = \mp 1. \tag{25.9}$$

The refraction indices of the two modes read

$$n_+ = 1 - j\left(\sqrt{\epsilon''\mu''} - \kappa''\right), \tag{25.10}$$

$$n_- = -1 - j\left(\sqrt{\epsilon''\mu''} + \kappa''\right), \tag{25.11}$$

where $\kappa'' > 0$ for the considered helicity. We see that one of the eigenmodes has the unit refraction index and very low losses, because for the optimal spirals $\epsilon'' \approx \mu'' \approx \kappa''$.

Composite materials formed by such inclusions have many interesting properties. In particular, the effective permittivity is approximately equal to the permeability, allowing matching of composite

slabs to free space (this property is also required for the ideal operation of so-called "invisibility cloak"). Furthermore, in the regime of chiral nihility, one of the two circularly polarized eigenmodes behaves as a wave in free space, with unit effective refraction index and compensated losses. The real part of the refraction index for the other eigenmode equals –1. A linearly polarized wave incident on a slab of such material will split into two circularly polarized components, one of which will propagate as in free space, but the other will refract negatively and suffer enhanced absorption.

25.4 Using Bianisotropic Effects

Bianisotropic materials are characterized by the most general linear relations between the four vectors of electromagnetic fields (e.g., Ref. [1]):

$$\mathbf{D} = \overline{\overline{\epsilon}} \cdot \mathbf{E} + \overline{\overline{a}} \cdot \mathbf{H}, \quad \mathbf{B} = \overline{\overline{\mu}} \cdot \mathbf{H} + \overline{\overline{b}} \cdot \mathbf{E}. \tag{25.12}$$

Here $\overline{\overline{\epsilon}}$ and $\overline{\overline{\mu}}$ are the permittivity and permeability dyadics (in matrix form each of which can be represented in terms of nine complex scalar parameters), and $\overline{\overline{a}}$ and $\overline{\overline{b}}$ are the magnetoelectric coupling dyadics. Magnetoelectric coupling in linear media can result from spatial dispersion and from nonreciprocity of the composite. Bianisotropic media can be classified [1] as chiral and omega media (reciprocal magnetoelectric coupling) and Tellegen and moving media (nonreciprocal coupling).

Among reciprocal bianisotropic materials, omega composites have been found of interest with respect to the realization of backward-wave propagation and negative refraction [17]. Considering in particular the uniaxial omega material (the unit vector along the optical axis is $\mathbf{z}_0$), the constitutive relations can be written as

$$\mathbf{D} = \overline{\overline{\epsilon}} \cdot \mathbf{E} + j\sqrt{\epsilon_0\mu_0}K\overline{\overline{J}} \cdot \mathbf{H}, \quad \mathbf{B} = \overline{\overline{\mu}} \cdot \mathbf{H} + j\sqrt{\epsilon_0\mu_0}K\overline{\overline{J}} \cdot \mathbf{E}, \tag{25.13}$$

where the permittivity and permeability dyadics have the form:

$$\overline{\overline{\epsilon}} = \epsilon_0 \left(\epsilon_t \overline{\overline{I}}_t + \epsilon_z \mathbf{z}_0\mathbf{z}_0\right), \quad \overline{\overline{\mu}} = \mu_0 \left(\mu_t \overline{\overline{I}}_t + \mu_z \mathbf{z}_0\mathbf{z}_0\right). \tag{25.14}$$

$\overline{\overline{I}}_t$ is the two-dimensional unit dyadic defined in the plane orthogonal to $\mathbf{z}_0$: $\overline{\overline{I}}_t = \mathbf{x}_0\mathbf{x}_0 + \mathbf{y}_0\mathbf{y}_0$. The magnetoelectric dyadic is antisymmetric: $\overline{\overline{J}} = \mathbf{z}_0 \times \overline{\overline{I}}_t$. A complex dimensionless parameter K measures the magnetoelectric coupling effect.

Eigenwaves in such media are linearly polarized plane waves, similar to simple magneto dielectrics. For waves propagating along the axis both eigenwaves have the same propagation constant [1]

$$\beta = k_0\sqrt{\epsilon_t\mu_t - K^2}, \tag{25.15}$$

where k_0 is the free-space wave number. The characteristic admittances, however, are different for the waves traveling in the positive and negative directions of the axis z (denoted as Y_+ and Y_-, respectively):

$$Y_\pm = Y_0\sqrt{\frac{\epsilon_t}{\mu_t}}\left(\sqrt{1 - \frac{K^2}{\epsilon_t\mu_t}} \mp j\frac{K}{\sqrt{\epsilon_t\mu_t}}\right). \tag{25.16}$$

Here $Y_0 = \sqrt{\epsilon_0/\mu_0}$ is the free-space wave admittance.

Interesting effects in slabs made of such materials were described in Ref. [18]: it was shown that omega composites can be used to realize absorbing layers, which are matched to free space. Indeed, one can notice that if the material parameters satisfy the condition

$$K = \frac{j}{2}\left(\mu_t - \epsilon_t\right), \tag{25.17}$$

the relationship (Equation 25.16) gives $Y_+ = Y_0$. Then the reflection coefficient from one side of the slab of an arbitrary thickness d equals $R = 0$ and the transmission coefficient reads $T = \exp(-j\beta d)$. Note that the matching condition can be satisfied for arbitrary permittivity and permeability values, provided one can control the coupling coefficient K.

In Ref. [17] it was shown that it is possible to design a bianisotropic material in such a way that it supports linearly polarized backward waves, and a slab made of this material is perfectly matched to free space for the normal direction of propagation. Indeed, if the condition (Equation 25.17) is satisfied, the propagation constant of the eigenwaves in the medium reads (Equation 25.15)

$$\beta = \frac{k_0}{2}\left(\varepsilon_t + \mu_t\right). \tag{25.18}$$

This result shows that the magnetoelectric coupling not only allows one to match the slab to free space but also makes it easier to realize the backward-wave regime. From formula (Equation 25.18) we see that the refractive index in a matched Ω-slab is negative when

$$\mathrm{Re}\{\varepsilon_t + \mu_t\} < 0, \tag{25.19}$$

which is easier to satisfy than the usual conditions

$$\mathrm{Re}\{\varepsilon_t\} < 0, \quad \mathrm{Re}\{\mu_t\} < 0. \tag{25.20}$$

In particular, it is not necessary to realize negative permeability, which can be more difficult at the optical frequencies, than to satisfy Equation 25.19. Composites with negative permittivity and acceptable losses, on the contrary, are available in optics and can be obtained, for example, using dilute arrays of metal nanoparticles embedded in a dielectric matrix. An example of a microwave realization as a composite formed by a lattice of conducting wires and an overlying lattice of Ω-shaped particles was given in Ref. [17].

25.5 Conclusions

Bianistropic media exhibit a number of very interesting and practically useful effects, ranging from optical activity to simulating electromagnetic phenomena in moving media. Many of them have been known for a long time and explored in practical devices, both in optics and in the microwave region. However, not all physically possible magnetoelectric effects exist in natural materials, and, moreover, if they exist, they are often very weak (for instance, chirality in the visible range). Metamaterial technology allows one to realize effects not found in nature, tune the effects for specific applications, and realize strong (resonant) magnetoelectric phenomena in the optical region. The last challenge requires further development of nanotechnologies, as it requires manufacturing of complex-shaped, three-dimensional, nano-sized structures.

References

1. A.N. Serdyukov, I.V. Semchenko, S.A. Tretyakov, and A. Sihvola, *Electromagnetics of Bi-Anisotropic Materials: Theory and Applications,* Amsterdam: Gordon and Breach Science Publishers, 2001.
2. I.V. Lindell, A.H. Sihvola, S.A. Tretyakov, and A.J. Viitanen, *Electromagnetic Waves in Chiral and Bi-Isotropic Media,* Boston and London: Artech House, 1994.
3. B.V. Bokut', V.V. Gvozdev, and A.N. Serdyukov, Special waves in naturally gyrotropic media, *Journal of Applied Spectroscopy,* 34, 701–706, 1981.
4. S. Tretyakov, I. Nefedov, A. Sihvola, S. Maslovski, and C. Simovski, Waves and energy in chiral nihility, *Journal of Electromagnetic Waves and Applications,* 17(5), 695–706, 2003.

5. J. Pendry, A Chiral route to negative refraction, *Science,* 306, 1353–1355, 2004.
6. C. Monzon and D.W. Forester, Negative refraction and focusing of circularly polarized waves in optically active media, *Physical Review Letters*, 95, 123904, 2005.
7. Yi Jin and S. He, Focusing by a slab of chiral medium, *Optics Express,* 13(13), 4979, 2005.
8. H. Dakhcha, O. Ouchetto, and S. Zouhdi, Chirality effects on metamaterial slabs. In *Proc. of Bianisotropics' 2004—10th Conference on Complex Media and Metamaterials,* pp. 132–135, Ghent, Belgium, September 22–24, 2004.
9. S. Tretyakov, A. Sihvola, and L. Jylhä, Backward-wave regime and negative refraction in chiral composites, *Photonics and Nanostructures—Fundamentals and Applications,* 3(2–3), 107–115, 2005.
10. A. Sihvola, *Electromagnetic Mixing Formulas and Applications,* London: IEE Publishing, 1999.
11. S.A. Tretyakov, F. Mariotte, C.R. Simovski, T.G. Kharina, and J.-P. Heliot, Analytical antenna model for chiral scatterers: Comparison with numerical and experimental data, *IEEE Transactions on Antennas and Propagation,* 44(7), 1006–1014, 1996.
12. I.V. Semchenko, S.A. Khakhomov, and A.L. Samofalov, Radiation of circularly polarized electromagnetic waves by the artificial flat lattice with two-turns helical elements. In *Bianisotropics' 2004, 10th International Conference on Complex Media and Metamaterials*, pp. 236–239. Het Pand, Ghent, Belgium, September 22–24, 2004.
13. S.A. Tretyakov, I.S. Nefedov, C.R. Simovski, and S.I. Maslovski, Modelling and microwave properties of artificial materials with negative parameters. In *Advances in Electromagnetics of Complex Media and Metamaterials*, NATO Science Series II, vol. 89, pp. 99–122, Dordrecht: Kluwer Academic Publishers, 2002.
14. S.A. Tretyakov, *Analytical Modeling in Applied Electromagnetics,* Norwood, MA: Artech House, 2003.
15. I.V. Semchenko, S.A. Khakhomov, and E.A. Fedosenko, Effective electron model of the wire helix excitation at microwaves: first step to optimization of pitch angle of helix. In *Advances in Electromagnetics of Complex Media and Metamaterials*, NATO Science Series II, vol. 89, pp. 245–256, Dordrecht: Kluwer Academic Publishers, 2003.
16. I.V. Semchenko, S.A. Khakhomov, and S.A. Tretyakov, Chiral metamaterials with unit negative refraction index. In *Proc. Metamaterials 2007*, Rome, 2007.
17. S.A. Tretyakov, C.R. Simovski, and M. Hudlicka, Bianisotropic route to the realization and matching of backward-wave metamaterial slabs, *Physical Review B,* 75, 153104, 2007.
18. S. Tretyakov and A. Sochava, Proposed composite material for nonreflecting shields and antenna radomes, *Electronics Letters*, 29, 1048, 1993.

26

Bianisotropic Materials and PEMC

Ari Sihvola
Helsinki University of Technology

Ismo V. Lindell
Helsinki University of Technology

26.1 Introduction

Metamaterials are media with unexpected and complicated macroscopic responses. The simplest response in a medium is the plain isotropic dielectric response. There are, however, grounds to claim that all reactions in the material that exceed such behavior could in some sense be termed metamaterial-type effects.

In this chapter the medium response is characterized using bianisotropic material relations. Bianisotropy is defined and various classifications of such media are presented using the concepts of dissipation, reciprocity, isotropy, and magnetoelectric coupling, as well as the mathematical properties of the material parameter dyadics.

In addition, the recently discovered concept of perfect electromagnetic conductor (PEMC) is introduced and analyzed. A PEMC medium possesses remarkable properties and is indeed an excellent example of a metamaterial. The main effect of the PEMC medium as a boundary is to rotate the plane of polarization of the reflected wave, which may find interesting applications in antenna and microwave technologies.

The characterization of bianisotropic materials requires four dyadic parameters. The constitutive relations relate the electric ($\mathbf{E}$) and magnetic ($\mathbf{H}$) field strength quantities to the electric ($\mathbf{D}$) and magnetic ($\mathbf{B}$) flux densities. A general linear material response, which can be anisotropy and contain magnetoelectric coupling at the same time, is called bianisotropic response.

The constitutive relations for bianisotropic materials read

$$\mathbf{D} = \overline{\overline{\epsilon}} \cdot \mathbf{E} + \overline{\overline{\xi}} \cdot \mathbf{H} \tag{26.1}$$

$$\mathbf{B} = \overline{\overline{\zeta}} \cdot \mathbf{E} + \overline{\overline{\mu}} \cdot \mathbf{H}. \tag{26.2}$$

In these relations, the four material parameter dyadics are permittivity $\overline{\overline{\epsilon}}$ and permeability $\overline{\overline{\mu}}$ and two magnetoelectric dyadics $\overline{\overline{\xi}}$ and $\overline{\overline{\zeta}}$, allowing for dependence of the response on the spatial direction of the excitation. The most general bianisotropic material requires 36 parameters for a full constitutive electromagnetic description. However, lacking any preferred direction in the material, the medium

is bi-isotropic and the amount of free parameters decreases to four. In the following sections, let us divide these materials into relevant classes.

26.2 Classes of Bianisotropic Media

The domain spanning the full description of bianisotropic media is indeed large. There are several ways to find order in this space. One important criterion is the amount of spatial symmetry. Let us start with the distinction between isotropic and anisotropic materials. Isotropic media do not possess any special direction in their structure, meaning that the electromagnetic response (and any other response, for that matter) does not depend on how the material is rotated with respect to the field. If this symmetry is broken, the medium is anisotropic. On the level of constitutive parameters, this means that a dyadic description is necessary. For isotropic media, the material parameter dyadics are multiples of the unit dyadic, and scalar multiplications suffice instead of matrix products.

Another important property of certain bianisotropic materials is magnetoelectric coupling, meaning that the parameters $\overline{\overline{\xi}}$ and $\overline{\overline{\zeta}}$ in relations (Equations 26.1 and 26.2) are nonzero. A magnetic field creates electric polarization in the medium, and vice versa, an electric excitation brings forth magnetic response. This motivates us to draw Table 26.1, which shows a four-field division of bianisotropic materials into subclasses when the criteria are isotropy–anisotropy and whether the medium displays magnetoelectric coupling. Note the concept of bi-isotropy, which means that spherical symmetry is connected with magnetoelectric coupling.

The limitation to dyadic material parameters (vector-to-vector relations) means that higher-order multipole effects are not contained in this phenomenological description of matter response. For a more inclusive discussion on the balance between the various electric and magnetic multipole contributions, see Ref. [1].

Another way of making distinctions between various materials is through certain physical restrictions. These set conditions to the material dyadics. If no dissipation is allowed, the medium is lossless. Applied to bianisotropic media and time-harmonic fields, this condition means that the following applies:

$$\overline{\overline{\epsilon}} = \overline{\overline{\epsilon}}^{\dagger}, \quad \overline{\overline{\mu}} = \overline{\overline{\mu}}^{\dagger}, \quad \overline{\overline{\xi}} = \overline{\overline{\zeta}}^{\dagger} \tag{26.3}$$

where the Hermitian operator † denotes a complex conjugate of the transpose.

Another important concept in the electromagnetic material response is reciprocity. Reciprocity means an invariance of a system when the transmitter and receiver are interchanged [2, Section 5.5], [3, Section 15.7]. If the medium is reciprocal, the conditions for the material parameters are [2, Section 5.5] as follows:

$$\overline{\overline{\epsilon}} = \overline{\overline{\epsilon}}^{\mathrm{T}}, \quad \overline{\overline{\mu}} = \overline{\overline{\mu}}^{\mathrm{T}}, \quad \overline{\overline{\xi}} = -\overline{\overline{\zeta}}^{\mathrm{T}} \tag{26.4}$$

where T denotes the transpose of the dyadic. For reciprocal media therefore permittivity and permeability are symmetric dyadics, and the magnetoelectric cross-dyadics each other's negative

TABLE 26.1 Classes of Bianisotropic Materials and the Number of Free Material Parameters in Their Full Characterization

	Direction Independence	Direction Dependence
No magnetoelectric coupling	$\underline{2}(\epsilon, \mu)$ (isotropic)	$\underline{18}(\overline{\overline{\epsilon}}, \overline{\overline{\mu}})$ (anisotropic)
Magnetoelectric coupling	$\underline{4}(\epsilon, \mu, \xi, \zeta)$ (bi-isotropic)	$\underline{36}(\overline{\overline{\epsilon}}, \overline{\overline{\mu}}, \overline{\overline{\xi}}, \overline{\overline{\zeta}})$ (bianisotropic)

transposes. Hence a full characterization of reciprocal bianisotropic materials requires 21 (complex) parameters.

Nonreciprocal effects are contained in two different places in these dyadics: in addition to the antisymmetric parts of $\overline{\overline{\epsilon}}$ and $\overline{\overline{\mu}}$, also both symmetric and antisymmetric parts of the magnetoelectric dyadics can be nonreciprocal. This fact calls for another description of the magnetoelectric dyadics, which separates the reciprocal and nonreciprocal parts:

$$\mathbf{D} = \overline{\overline{\epsilon}} \cdot \mathbf{E} + \left(\overline{\overline{\chi}}^{\mathrm{T}} - \mathrm{j}\overline{\overline{\kappa}}^{\mathrm{T}}\right) \cdot \mathbf{H} \tag{26.5}$$

$$\mathbf{B} = \left(\overline{\overline{\chi}} + \mathrm{j}\overline{\overline{\kappa}}\right) \cdot \mathbf{E} + \overline{\overline{\mu}} \cdot \mathbf{H}. \tag{26.6}$$

The two magnetoelectric dyadics are connected to the previous ones through the following relations:

$$\overline{\overline{\chi}} = \frac{\overline{\overline{\zeta}} + \overline{\overline{\xi}}^{\mathrm{T}}}{2}, \quad \overline{\overline{\kappa}} = \frac{\overline{\overline{\zeta}} - \overline{\overline{\xi}}^{\mathrm{T}}}{2\mathrm{j}}. \tag{26.7}$$

Of these two dyadics, the dyadic $\overline{\overline{\kappa}}$ is termed the chirality dyadic, and it is responsible for the reciprocal magnetoelectric phenomena. $\overline{\overline{\chi}}$ is the nonreciprocal cross-polarization dyadic. Time-harmonic dependence of the fields brings forth complex-valued quantities with the convention $\exp(\mathrm{j}\omega t)$. With the definitions of Equations 26.5 and 26.6, the dyadics $\overline{\overline{\kappa}}$ and $\overline{\overline{\chi}}$ are real for lossless materials.

Materials whose internal structure is handed are examples of materials with $\overline{\overline{\kappa}} \neq 0$. A mixture of handed elements leads to a medium which is also called chiral [4]. Omega medium is a composite of planar Ω-shaped elements that are aligned in uniaxial arrangement [5], and the corresponding chirality dyadic is antisymmetric. On the other hand, a uniformly moving medium is an example of a nonreciprocal magnetoelectric medium [6]. In Table 26.2 bianisotropic materials are classified according to the principles of symmetry and reciprocity.

Figure 26.1 shows some basic mechanisms responsible for the magnetoelectric coupling. If many chiral elements such as the helix of the type in the figure—all of the same handedness—are mixed with random orientations to form a mixture, the macroscopic electromagnetic parameters are equal to scalars, and the chirality parameter κ is not zero [4]. A mirror image of such a medium would leave everything else unchanged except that κ changes sign (the elements switch handedness). Likewise, the nonreciprocity parameter χ is not equal to zero if the microstructure of the material contains coupled permanent electric and magnetic moments, again all with the same type of coupling. The sign of χ is determined whether this coupling is parallel or antiparallel.

Bianisotropic media span a very wide spectrum of material responses sections. In the following sections, let us concentrate on a particular, and still interesting, example of such metamaterials.

TABLE 26.2 Bianisotropic Material Classification According to the Symmetry Properties of the Parameter Dyadics with Material Examples

	$\overline{\overline{\epsilon}}$	$\overline{\overline{\mu}}$	$\overline{\overline{\kappa}}$	$\overline{\overline{\chi}}$
Symmetric part: (6 parameters)	(Reciprocal) Dielectric crystal	(Reciprocal) Magnetic crystal	(Reciprocal) Chiral medium	(Nonreciprocal) Chromium sesquioxide
Antisymmetric part: (3 parameters)	(Nonreciprocal) Magneto-plasma	(Nonreciprocal) Biased ferrite	(Reciprocal) Omega medium	(Nonreciprocal) Moving medium

Source: Sihvola, A. and Lindell, I.V., *Annalen der Physik*, 17(9–10), 787, 2008.

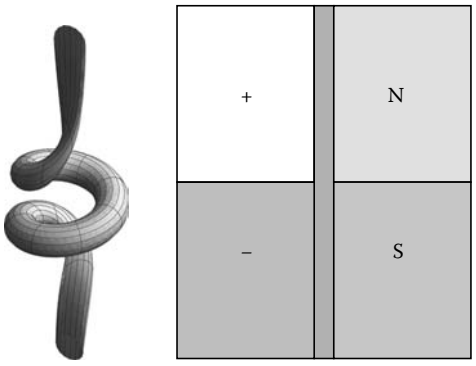

FIGURE 26.1 (a) A chiral (handed) element, which leads to a nonzero chirality parameter κ in the material relations. Changing the handedness of the element changes the sign of κ. (b) Electric and magnetic dipoles glued together form an element that leads to a nonzero magnetoelectric χ parameter in the material relations. This parameter changes sign if the coupling is opposite (the electric and magnetic dipole moments are antiparallel).

26.3 PEMC Medium

The concept of PEMC medium was introduced in 2005 [8]. To gain understanding of the fundamental character of PEMC, it is illuminating to make a slight detour through four-dimensional formalism of electromagnetism. For a full treatment, see Ref. [7].

The three-dimensional (spatial) electric and magnetic one-forms **E**, **H** and two-forms **B**, **D** can be combined as the following two-forms:

$$\mathbf{\Phi} = \mathbf{B} + \mathbf{E} \wedge \mathbf{d}\tau \tag{26.8}$$

$$\mathbf{\Psi} = \mathbf{D} - \mathbf{H} \wedge \mathbf{d}\tau, \tag{26.9}$$

where

$\tau = ct$ as the normalized time variable
$\wedge$ is the wedge (outer) product
$\mathbf{d}\tau$ is the time-like one-form

Then the Maxwell equations can be written compactly as

$$\mathbf{d} \wedge \mathbf{\Psi} = \mathbf{\gamma} \tag{26.10}$$

$$\mathbf{d} \wedge \mathbf{\Phi} = 0. \tag{26.11}$$

To follow the notation in Ref. [9], the electromagnetic two-forms $\mathbf{\Psi}$ and $\mathbf{\Phi}$ are six-dimensional quantities. The source three-form $\mathbf{\gamma}$ combines the spatial electric charge three-form $\boldsymbol{\rho}$ and the spatial electric current two-form **J** into

$$\mathbf{\gamma} = \boldsymbol{\rho} - \mathbf{J} \wedge \mathbf{d}\tau. \tag{26.12}$$

To describe the response of matter in this formalism, we need an additional equation in the form

$$\mathbf{\Psi} = \overline{\overline{M}}|\mathbf{\Phi}. \tag{26.13}$$

Here $\overline{\overline{M}}$ is the medium dyadic. In a given basis it can be represented by a 6×6 matrix. To connect with the discussion in the previous section, we identify $\overline{\overline{M}}$ as an algebraic quantity, which in the general case involves 36 parameters. The bar | denotes the necessary product operation [10].

The relation (Equation 26.13) is quite formal, and the medium dyadic certainly contains complicated relations. However, if this relation is distilled to a single scalar, one could say that we have found the simplest medium:

$$\boldsymbol{\Psi} = M\boldsymbol{\Phi}. \tag{26.14}$$

This is called PEMC. What does it mean? A medium obeying the response of the type in Equation 26.14 is invariant in any affine transformations, including the Lorentz transformation. The consequence is that the medium appears the same for any observer traveling with constant velocity. One could say that this is the only truly isotropic medium, since the medium dyadic is invariant in any linear transformation of the fields.

Let us write the relation (Equation 26.14) between the electric (**E**) and magnetic (**H**) fields and electric (**D**) and magnetic (**B**) displacements. This leaves us with

$$\mathbf{D} = M\mathbf{B} \tag{26.15}$$

$$\mathbf{H} = -M\mathbf{E}. \tag{26.16}$$

The only remaining reference to the medium is M, which is a real scalar admittance-type quantity. The dimension of M corresponds to the units amperes/volt in the SI system. More exactly, the parameter M is a pseudoscalar [11]. As a terminological observation, the identification in the four-dimensional Minkowskian representation of PEMC is axion [12].

Very interesting is the fact that the PEMC medium is a generalization of perfect electric and magnetic conductors (PEC, PMC). The PEC is the idealization of a good conductor [8]

$$1/\epsilon \to 0, \quad \mu \to 0. \tag{26.17}$$

Analogously, the PMC is the dual of PEC:

$$1/\mu \to 0, \quad \epsilon \to 0. \tag{26.18}$$

PEC and PMC make absolute boundaries in the sense that no electromagnetic power can penetrate through them. PEC and PMC are extremely useful concepts in antenna applications. Even if PEC can be approximated fairly well with high-conductivity metals, neither PMC material nor anything resembling it can be found naturally. Several composite structures have been studied and suggested to simulate PMC. These are known as "artificial magnetic conductors" or "high-impedance surfaces" [13].

In light of the special cases of PEC and PMC, the acronym PEMC is a natural choice to describe a medium with conditions (Equations 26.15 and 26.16). In every point within PEMC, a linear combination of fields is zero $(\mathbf{H} + M\mathbf{E} = 0)$ as also a combination of displacements vanishes $(\mathbf{D} - M\mathbf{B} = 0)$, which is obvious from Equation 26.15. The special case $1/M = 0$ leaves us with PEC: $(\mathbf{E} = 0, \mathbf{B} = 0)$ and we arrive at PMC when $M = 0$: $(\mathbf{H} = 0, \mathbf{D} = 0)$.

Equations 26.15 and 26.16 also lead to the conclusion that the Poynting vector flux $\mathbf{E} \times \mathbf{H}$ vanishes inside the PEMC medium. In other words, PEMC does not carry electromagnetic energy momentum [14].

For electrical engineers, the constitutive relations (Equations 26.15 and 26.16) are not the most familiar. A more common way than Equations 26.15 and 26.16 to represent the material relations in engineering literature is the one when the **D** and **B** are response vectors, like in (Equations 26.1 and 26.2)

$$\begin{pmatrix} \mathbf{D} \\ \mathbf{B} \end{pmatrix} = \begin{pmatrix} \epsilon & \xi \\ \zeta & \mu \end{pmatrix} \begin{pmatrix} \mathbf{E} \\ \mathbf{H} \end{pmatrix}, \tag{26.19}$$

where the material matrix C contains the four scalars ϵ, ξ, ζ, and μ, valid for bi-isotropic media. The units of the material parameters are As/(Vm) (ϵ), Vs/(Am) (μ), and s/m (both ξ and ζ).

Equation 26.19 can be written as

$$\begin{pmatrix} \mathbf{D} \\ \mathbf{H} \end{pmatrix} = \frac{1}{\mu} \begin{pmatrix} \epsilon\mu - \xi\zeta & \xi \\ -\zeta & 1 \end{pmatrix} \begin{pmatrix} \mathbf{E} \\ \mathbf{B} \end{pmatrix}, \tag{26.20}$$

with $\xi = \chi - j\kappa$ and $\zeta = \chi + j\kappa$. Therefore, we can write for the bi-isotropic PEMC constitutive relations (compare Equation 26.20 with Equations 26.15 and 26.16)

$$\begin{pmatrix} \epsilon & \chi \\ \chi & \mu \end{pmatrix} = q \begin{pmatrix} M & 1 \\ 1 & 1/M \end{pmatrix}, \quad \text{with} \quad |q| \to \infty. \tag{26.21}$$

Because of the symmetry of the bi-isotropic constitutive relations in the material parameter matrix (Equation 26.21), it follows that PEMC belongs to the class of nonreciprocal bi-isotropic media. This class is also called as Tellegen media [4] since Tellegen in 1948 [15] suggested a corresponding nonreciprocal circuit element, a gyrator.

To further relate PEMC with nonreciprocal bi-isotropic media, it is worth noting that the PEMC medium is an "extreme" form of the Tellegen material. Whereas all bi-isotropic media with any nonzero value for the magnetoelectric pseudoscalar χ are Tellegen media, the character of PEMC requires that its magnitude has to satisfy the relation $\chi^2 = \epsilon\mu$, and hence PEMC is a subclass of Tellegen media. Note also from the symmetry of the matrix (Equation 26.21) that the chirality parameter is zero for PEMC. The connections of the PEMC parameter to the bi-isotropic material parameters are $M = \sqrt{\epsilon}/\sqrt{\mu}$ and $\chi = \sqrt{\mu\epsilon}$, and in addition, ϵ, μ, and χ tend to infinity.

One interesting observation regarding PEMC is that it has a connection to the so-called Post constraint [16, Eq. (6.18)]. In the recent literature this restriction refers to the requirement that the totally antisymmetric part of the four-dimensional constitutive tensor of a general (bianisotropic) linear medium has to vanish. Applied to bi-isotropic media, this is equivalent to the condition $\chi = 0$. Such a condition would not allow the Tellegen parameter. Nonreciprocal bi-isotropic media would be forbidden. The controversy over the Post constraint has been intense in recent years [17–20]. It is perhaps fair to say that the critical study of the nature of the magnetoelectric modulus of antiferromagnetic crystals [11] has conclusively shown that media exist that conflict with the Post constraint.

In conclusion, the characterization of bianisotropic media through the constitutive relations (Equations 26.1 and 26.2) allows much flexibility and certainly encompasses a large variety of metamaterials. The PEMC medium, belonging to the subclass of magnetoelectric and bi-isotropic materials, forms one interesting example of such metamaterials.

Acknowledgment

This work was supported by the Academy of Finland.

References

1. R. E. Raab and O. L. De Lange. *Multipole Theory in Electromagnetism. Classical, Quantum, and Symmetry Aspects, with Applications.* Clarendon Press, Oxford, 2005.
2. J. A. Kong. *Electromagnetic Wave Theory*. EMW Publishing, Cambridge, Massachusetts, 2000.
3. J. G. Van Bladel. *Electromagnetic Fields*. IEEE Press, Wiley, Piscataway, NJ, 2007.
4. I. V. Lindell, A. H. Sihvola, S. A. Tretyakov, and A. J. Viitanen. *Electromagnetic Waves in Chiral and Bi-Isotropic Media*. Artech House, Norwood, MA, 1994.

5. A. A. Sochava, C. R. Simovski, and S. A. Tretyakov. Chiral effects and eigenwaves in bi-anisotropic omega structures. In A. Priou, A. Sihvola, S. Tretyakov, and A. Vinogradov (eds.), *Advances in Complex Electromagnetic Materials*, vol. 28, *NATO ASI Series, 3. High Technology*, pp. 85–102. Kluwer, Dordrecht, 1997.
6. A. H. Sihvola and I. V. Lindell. Material effects in bi-anisotropic electromagnetics. *IEICE Transactions on Electronics*, E78-C(10):1383–1390, October 1995.
7. A. Sihvola and I. V. Lindell. Perfect electromagnetic conductor medium. *Annalen der Physik (Berlin)*, 17(9–10), 787–802, 2008.
8. I. V. Lindell and A. H. Sihvola. Perfect electromagnetic conductor. *Journal of Electromagnetic Waves and Applications*, 19(7):861–869, 2005.
9. I. V. Lindell. *Differential Forms in Electromagnetics*. Wiley and IEEE Press, New York, 2004.
10. I. V. Lindell. Differential forms and electromagnetic materials. In *Theory and Phenomena of Metamaterials*, Chap. 4. Taylor & Francis, Boca Raton, FL, 2009.
11. F. W. Hehl, Yu. N. Obukhov, J-P. Rivera, and H. Schmid. Relativistic nature of a magnetoelectric modulus of Cr_2O_3-crystals: A four-dimensional pseudoscalar and its measurement. *Physical Review A*, 77:022106, 2008.
12. F. W. Hehl and Yu. N. Obukhov. *Foundations of Classical Electrodynamics*. Birkhäuser, Boston, 2003.
13. T. B. A. Senior and J. L. Volakis. *Approximate Boundary Conditions in Electromagnetics*. IEE Publishing, London, 1995.
14. F. W. Hehl and Yu. N. Obukhov. Linear media in classical electrodynamics and the Post constraint. *Physics Letters A*, 334(4):249–259, 2005.
15. B. D. H. Tellegen. The gyrator, a new electric network element. *Philips Research Reports*, 3(2):81–101, 1948.
16. E. J. Post. *Formal Structure of Electromagnetics*. North Holland, Amsterdam, 1962.
17. A. Lakhtakia and W. S. Weiglhofer. Are linear, non-reciprocal, bi-isotropic media forbidden? *IEEE Transactions on Microwave Theory and Techniques*, 42(9):1715–1716, September 1994.
18. A. H. Sihvola. Are non-reciprocal bi-isotropic media forbidden indeed? *IEEE Transactions on Microwave Theory and Techniques*, 43(9):2160–2162, September 1995.
19. A. Lakhtakia and W. S. Weiglhofer. Comment on "Are non-reciprocal bi-isotropic media forbidden indeed?" *IEEE Transactions on Microwave Theory and Techniques*, 43(12):2722–2723, December 1995.
20. A. H. Sihvola. Reply to comment on "Are non-reciprocal bi-isotropic media forbidden indeed?" *IEEE Transactions on Microwave Theory and Techniques*, 43(12):2723–2724, December 1995.

27

Photonic Quasicrystals: Basics and Examples

Alessandro Della Villa
University of Siena

Vincenzo Galdi
University of Sannio

Filippo Capolino
University of California Irvine

Stefan Enoch
Fresnel Institute

Gérard Tayeb
Fresnel Institute

27.1 Introduction and Background

The study of wave interactions with ordered structures represents a classical problem of long-standing interest in electromagnetics (EM) and optical engineering, which has recently received a renewed interest in view of its relevance to the design of metamaterials, photonic crystal (PC) devices, frequency-selective surfaces, artificial impedance surfaces, etc. For the simplest conceivable form of "order," intrinsically associated with the concept of periodicity, the arising wave phenomena are well-understood and accurately predictable via rigorous and powerful modeling tools based on Bloch–Floquet theory.

The EM properties of random geometries, at the opposite extreme of the "order" scale, have also been extensively studied, and stochastic/statistical modeling is typically used in complex (e.g., urban) propagation environments where deterministic approaches and observables would be of little meaning.

Although the above extrema of the "order" scale seem to be well characterized, the "gray zone" in between, which encompasses a broad range of hierarchical order types (from "quasiperiodic" to "quasirandom"), turns out to be still largely unexplored. Although the concept of aperiodicity has traditionally been tied to the concept of amorphousness, the discovery, in 1984, of "quasicrystals" [1,2] has significantly changed this view. Quasicrystals are metallic alloys whose x-ray diffraction spectra exhibit bright spots (typical of crystals), yet display unusual rotational symmetries (e.g., 10-fold) that are known to be incompatible with spatial periodicity. This apparent puzzle and the growing awareness of the important role played by aperiodic order in solid-state physics have

motivated the study of aperiodic structures from a different perspective, in many fields of science and technology.

In this chapter, we review, at an introductory level, some basic aspects pertaining to wave interactions with aperiodically ordered structures, with special emphasis on photonic quasicrystals (PQCs). It should be noted that, in what follows, we use the term "quasicrystal" to describe a rather general deterministic aperiodic arrangement, although the formal definition of the term is still not settled [3]. Starting from a brief description of the geometrical (Section 27.2) and modeling (Section 27.3) aspects, we proceed with a compact review of results and applications from the technical literature (Section 27.4) and illustrate a number of selected prototype two-dimensional (2-D) examples (Sections 27.5 and 27.6).

The reader is referred to Refs. [4,5] for recent reviews on the subject, to Ref. [6] for a comprehensive account of the mathematical background, and to [7] for an up-to-date bibliography database. More specific application-oriented aspects are detailed in a chapter in Vol. II of this handbook [8].

27.2 The Geometry of Aperiodic Order

27.2.1 Generalities

The simplest one-dimensional (1-D) examples of aperiodically ordered structures are provided by aperiodic sequences, such as Fibonacci, Thue-Morse, period-doubling, Rudin-Shapiro, etc. [9,10], which exhibit diverse representative behaviors ranging from quasiperiodic to quasirandom. In what follows, we focus on the more complicated two-dimensional (2-D) case, intrinsically tied with the theory of "aperiodic tilings" [11,12] and directly relevant to the examples illustrated in Sections 27.5 and 27.6. We start, for simplicity, from the periodic case, consisting of an infinite repetition of a given unit cell according to a 2-D lattice

$$\mathbf{r}_{nm} = n\mathbf{p} + m\mathbf{q}, \quad n, m = 0, \pm 1, \pm 2, \ldots, \tag{27.1}$$

with $\mathbf{p}$ and $\mathbf{q}$ denoting two basis vectors of the 2-D vector space $\mathbb{R}^2$. It is well known that the possible rotational symmetries* of such a lattice depend on the unit cell geometry and on the lattice basis vectors $\mathbf{p}$ and $\mathbf{q}$ and cannot be arbitrary. According to the crystallographic restriction theorem [11,12], the only possible rotational symmetries for a 2-D periodic lattice are of the order $K = 2, 3, 4$, or 6. Thus, for instance, square lattices with square unit cells exhibit twofold and fourfold rotational symmetries, but fivefold and eightfold symmetries are not compatible with spatial periodicity [11,12].

27.2.2 Aperiodic Tilings

A 2-D aperiodic tiling consists of an arrangement of polygonal shapes ("tiles") devoid of any translational symmetry and yet capable of covering a plane without overlaps or gaps [11,12]. Most of the 2-D concepts illustrated in this section are generalizations of 1-D concepts related to aperiodic sequences [9,10] and can be in turn generalized to the three-dimensional (3-D) case on replacing polygons by polyhedra. The theory of aperiodic tilings is an inherently multidisciplinary subject, which involves branches of applied physics (crystallography, solid-state physics) and pure and applied mathematics (computational logic, discrete geometry, group theory, and ergodic theory) [6,11,12]. In what follows, we review some qualitative and semiquantitative aspects necessary to understand the basic aperiodic-order-induced wave phenomena.

* By K-fold rotational symmetry we mean the invariance with respect to rotations of angles $2\pi/K$ about a point (and thus, in view of translational invariance, about infinitely many points).

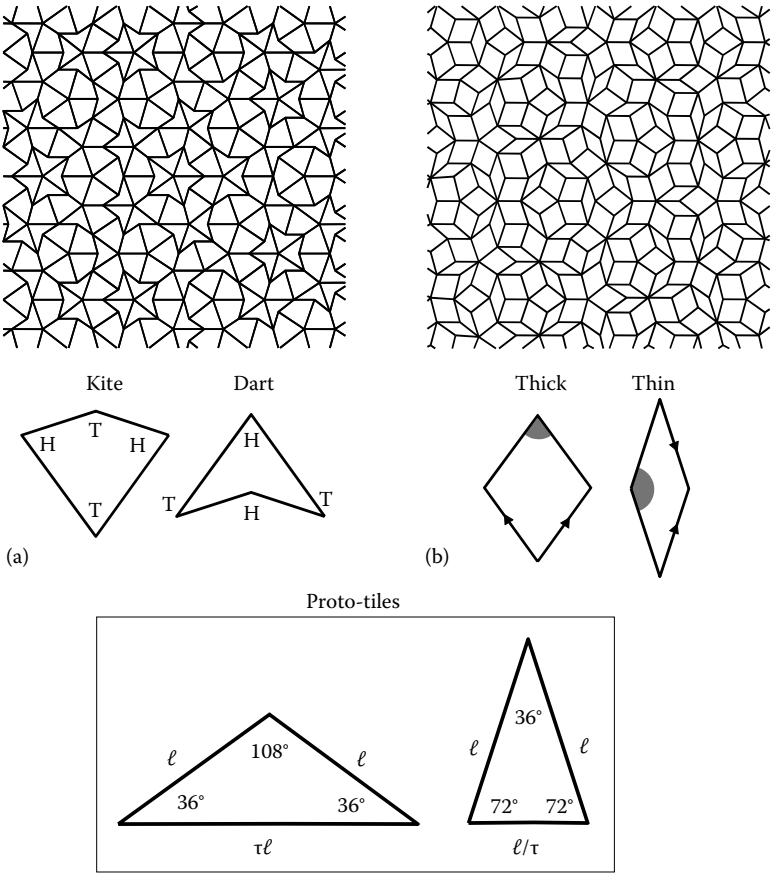

FIGURE 27.1 Penrose tilings in the "kite and dart" (a) and "thick and thin" (b) versions. Both sets of tiles are obtained by proper juxtaposition of two isosceles triangles (see inset) with angles 36°, 36°, 108° and 72°, 72°, 36°, respectively; $\tau = (1 + \sqrt{5})/2$ is the Golden Mean. Two possible labeling schemes are shown for the matching rules that need to be enforced to prevent the creation of periodic (or other uninteresting) patterns. For the kite and dart configuration, vertices marked with the same letters ("H" or "T") must go together. For the thick and thin configuration, two adjacent vertices must both be blank or colored, and two adjacent edges must both be blank or have an arrow pointing in the same direction. (Extracted from Pierro, V., Galdi, V., Castaldi, G., Pinto, I.M., and Felsen, L.B., *IEEE Trans. Antennas Propagat*., 53, 635, 2005. With permission.)

The first examples of aperiodic tilings have been known since the 1960s, within a computational logic context [13,14], and consisted of more than 20,000 tile shapes, thereby constituting no more than mathematical oddities. In 1974, Penrose devised an aperiodic set consisting of two tiles only [15], which constitutes one of the most intriguing and extensively studied paradigms of aperiodic order. In fact, a recent fascinating theory [16] argues that similar patterns were already known and used in medieval Islamic architecture. Figure 27.1 illustrates two examples of a Penrose tiling, with reference to its two most popular versions known as "kite and dart" (Figure 27.1a) and "thick and thin" (Figure 27.1b). Although aperiodic, Penrose tilings display substantial order and symmetry, and their characteristic scale is strictly related to the Golden Mean [12]. Both sets of tiles are derived by proper arrangement of two isosceles-triangle proto-tiles with internal angles 36°, 36°, 108° and 72°, 72°, 36°, respectively. These sets of tiles can cover the plane aperiodically in infinitely many ways, distinguishable only over an infinite plane [12]. In order to prevent the formation of

ordinary periodic (or other uninteresting) patterns, "matching rules" need to be enforced typically by edge-labeling-and-matching schemes (see Figure 27.1).

The reader is referred to Refs. [11,12] for an atlas of known aperiodic tilings which, through various types and degrees of order and symmetry, provides a representative sampling of the realm of "orderly disorder."

27.2.3 Generation Algorithms

Aperiodic tilings can be generated using various algorithms based essentially on four main strategies:

1. Juxtaposition of basic tiles with enforcement of suitable local "matching rules." This apparently obvious algorithmic approach, which consists of starting with a single tile and adding tiles according to local matching rules (like a jigsaw-puzzle), is not the most systematic and straightforward [18].
2. "Cut-and-projection" schemes, where, starting from higher-dimensional periodic lattices), one cuts a certain "slice" out and projects it onto a lower-dimensional domain [12,18]. For instance, the Penrose tilings in Figure 27.1 can be generated via projection of a 5-D periodic lattice onto a planar surface. Figure 27.2 shows the so-called Ammann–Beenker octagonal tiling, another popular example of quasiperiodic tiling that can be generated via cut-and-project schemes.
3. "Dual-grid" schemes, which translate into very simple computer codes [18].
4. Implementation of substitution rules, based on tile decomposition and suitable rescaling (inflation) [12,18], which can be applied to the generation of tilings featuring hierarchical structure. For example, Figure 27.3 illustrates the substitution rules pertaining to the so-called binary tiling [12], whereas Figure 27.4 illustrates the so-called Stampfli inflation rules [19] for the construction of a square-triangle dodecagonal tiling.

The above construction strategies are neither necessarily equivalent nor applicable for all categories of tilings. For instance, while Penrose tilings can be equivalently generated by any one of them, certain

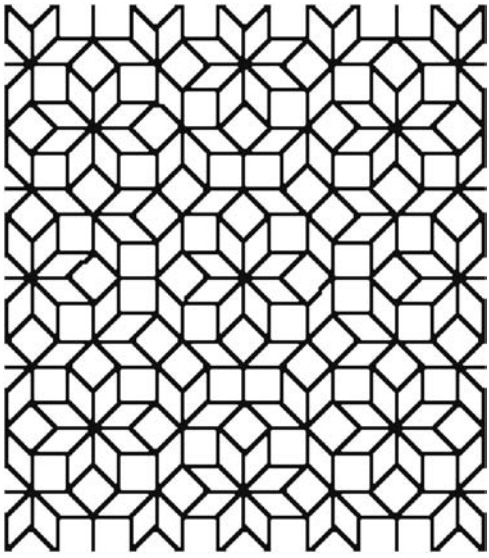

FIGURE 27.2 Example of Ammann–Beenker octagonal tiling generated via a cut-and-projection scheme [12,18].

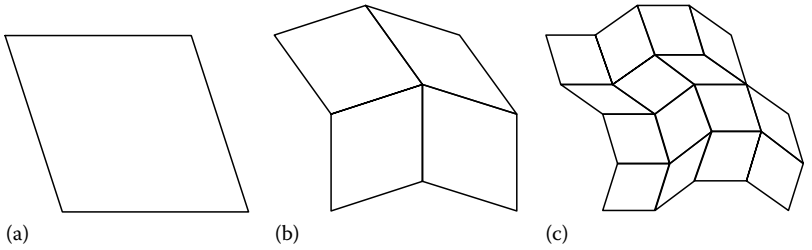

FIGURE 27.3 Initial stage (a) and first two iterations (b, c) of the binary tiling [12].

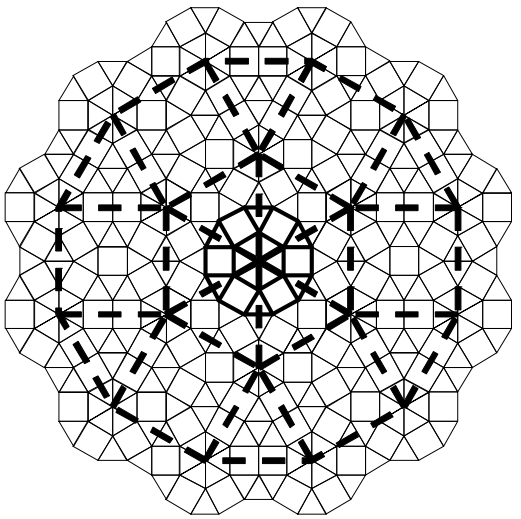

FIGURE 27.4 Illustration of the Stampfli inflation rules for the construction of a square–triangle dodecagonal tiling [19]. The construction, to be iterated up to the desired tiling extension, starts from a dodecagon made of square and equilater-triangle tiles (thick solid line), which is first scaled-up by an inflation factor $\sqrt{3} + 2$ (thick dashed line) and subsequently substituted at each vertex of the inflated version.

tilings can only be generated via matching rules or substitution. The reader is referred to Refs. [11,12, 18] for more theoretical and implementation details as well as computational aspects and tools.

27.2.4 Order vs. Symmetry

In order to understand the key properties of aperiodic tilings, one needs to generalize the traditional concepts of order and symmetry, which are intuitively tied to the concept of periodicity. In aperiodic tilings, order can show up in diverse forms, including the following:

1. Repetitiveness, i.e., occurrence of any bounded region of the whole tiling infinitely often across the tiling [12]. For instance, in Penrose tilings, given any local pattern having a certain diameter, an identical pattern can be found within a distance of two diameters [15].
2. Statistical frequency of occurrence of the individual tiles across the tiling. Again, in Penrose tilings, the fractions of kite and dart (or thick and thin) tiles approach the Golden Mean in the infinite-tiling limit [15].

3. "Forbidden" (noncrystallographic) rotational symmetries in local and/or weak (e.g., statistical) forms. For instance, Penrose tilings display arbitrarily large regions with centers of fivefold rotational symmetry [20]. This local property can be extended globally only in a statistical sense since every finite pattern of tiles can be shown to appear across the tiling in ten (and only ten) different rotational orientations, all with the same statistical frequency [20].
4. Hierarchial structure, i.e., the appearance of certain patterns at different scales, typical of tilings generated via the above-mentioned substitution rules [12,18].

27.3 Theoretical and Computational Tools

As previously mentioned, the study of wave interactions with periodic structures, and of the broad variety of bandgap, waveguiding/confinement, refraction/transmission, filtering, and emission effects attainable, can be addressed using well-established tools and concepts such as Bloch–Floquet theorem, unit cell, Brillouin zone, equifrequency surfaces, and Poisson summation, etc. For instance, the Poisson summation formula [21] provides a very powerful systematic tool for recasting wavefield observables as superpositions of either individual or collective contributions. Typical departures from perfect periodicity in realistic structures, such as truncation (finiteness) and weak perturbations in the spatial period as well as in the excitation (tapering), can be addressed by methods such as those in Refs. [22–25].

By comparison, the study of aperiodically ordered structures entails significant complications, from both theoretical and computational viewpoints. For the simpler case of 1-D structures, capitalizing on a body of theoretical results from discrete geometry and solid-state physics [26–32], analytic parameterization of typical radiation/scattering observables can be addressed in terms of the well-known Floquet–Bragg-type discrete spectral constituents which are typically encountered in the study of strictly or weakly perturbed periodic structures (see, e.g., Refs. [22–25]), plus other (singular continuous and absolutely continuous) spectral constituents that have no counterpart in periodic structures. In this framework, a generalized Poisson-type summation has been applied to several radiation/scattering prototype configurations [33–35]. Concerning the study of the bandgap properties of 1-D PQCs (in the form, e.g., of dielectric multilayers or stub-loaded transmission lines), the trace-map formalism from solid-state physics [36–38] provides a powerful analytic framework.

Generalization of the above tools/results to 2-D nonseparable tiling-based PQC geometries, although possible in principle, is not straightforward. In this connection, approaches to the study of the bandgap properties have been proposed, relying, e.g., on periodic approximants [39–41], on extended-zone schemes in the reciprocal space [42], and on a direct generalization of Bloch–Floquet theory [43]. However, in many applications one is necessarily led to study finite-size structures (e.g., arrays of dielectric rods) via full-wave techniques, such as the scattering-matrix method (based on Fourier–Bessel multipolar field expansions) [44] or the finite-difference-time-domain (FDTD) method [45]. In this framework, bandgap observables based on transmission coefficients are generally ill-defined and not necessarily meaningful, and a physically sound observable can be defined by considering the active power (per unit length) radiated by a line source located inside the structure, in a way that closely resembles the definition of the local density of states (LDOS) [46] in solid-state physics.

27.4 Compact Review of Results and Applications Available in the Literature

During the past decade, several numerical and experimental studies have explored the properties of PQCs. The compact review below, far from being exhaustive, addresses some representative results and applications. The reader is referred to Refs. [4,5,7] for further details and references.

Starting from 1-D structures, Fibonacci-type PQCs (typically in the form of multilayers) have been extensively investigated since the mid 1980s, in connection with their bandgap properties [47,48] as well as the fractal (Cantor) nature of their eigenspectra and the critical localization of their wavefunctions [49,50]. More recent investigations have focused on application-oriented issues, including filtering properties (e.g., see Refs. [51–55]), broad omnidirectional reflection (e.g., see Refs. [56–58]), symmetry-induced perfect transmission [59,60], pulse compression [61], and band-edge resonances [62]. A considerable body of theoretical, numerical, and experimental results are also available for other PQCs based on different types of aperiodic sequences, including the Thue-Morse (e.g., see Refs. [63–69]), period-doubling [70,71], Cantor [72–75], and Rudin-Shapiro [76].

Moving to 2-D structures, most configurations are based on arrays of dielectric or metallic cylindrical rods located at the tile vertices (or centers) of aperiodic tilings. In the first studies, particular interest was devoted to geometries based on the octagonal (e.g., see Refs. [77–80]), Penrose (e.g., see Refs. [80–85]), and dodecagonal (e.g., see Refs. [81,86–88]) tilings, highlighting the possibility of achieving bandgap, waveguiding, and localization effects and investigating the role of various geometrical and constitutive parameters (symmetry order, filling factor, dielectric contrast, and incidence angle, etc.). Further results on the same (or related) geometries are available in Refs. [89–97], and comparative studies have also been carried out (e.g., see Refs. [98,99] and Section 27.5.2). Among the other geometries explored, it is worth mentioning the so-called "circular" PCs (e.g., see Refs. [100,101]), those designed via inverse-Fourier-transform [102], those based on the 2-D version of Fibonacci [103] and Thue-Morse [104] sequences, and those based on Archimedean [40] or other periodic [41,105] approximants.

From the phenomenological viewpoint, several studies have been devoted to the comprehension of the mechanisms underlying the formation of bandgap in PQCs, highlighting the role played by single-rod resonances [106], Bragg-type and multiple scattering, and short-range interactions (e.g., see Ref. [107]). Moreover, attention has also been focused on the study of localization phenomena in defected [84,108,109] and defect-free [110–113] configurations (see also Section 27.5.3) as well as the possible coupling effects (e.g., see Refs. [114,115]).

Among the exceptions to the above rod-based 2-D configurations, there are three examples that are worth mentioning: (a) Planar PQC geometries in Refs. [116,117] (see also Section 27.6), consisting of mushroom-type metallic protrusions laid on a grounded dielectric substrate, which were found to exhibit artificial-magnetic-conductor (AMC) behavior (i.e., in-phase reflection) and strong attenuation of surface waves; (b) arrays of subwavelength holes in metallic screens [118–121], for which enhanced transmission effects were observed; and (c) arrays of metallic nanoparticles [122], which were found to exhibit enhanced localized plasmon modes.

Concerning 3-D structures, only a limited number of results are available, due to the considerable complications in both (theoretical and numerical) modeling and experimental characterization. In particular, PQCs with icosahedral geometry [123] have been fabricated via stereolithography and experimentally characterized at microwave frequencies [124]. Advances in laser-based fabrication technology have recently allowed the construction of silicon PQC structures working at infrared frequencies [125], thereby paving the way to a deeper understanding of the underlying phenomenologies [126].

Fabrication and technological issues are also of great interest, but their treatment falls beyond the scope of this Chapter; the reader is referred to Refs. [5,125,127–137], and the references therein, for a sparse sampling.

Concerning possible applications to EM and optical engineering, aperiodic tilings have recently been proposed as potentially useful geometries in the design of antenna arrays [17,138–140]. Moreover, judicious exploitation of the inherent richness of degrees of freedom, typical of aperiodic geometries, has been proposed within the framework of "bandgap engineering" [141–143]. In this connection, the availability of electrically switchable PQC structures (e.g., see Ref. [144]) opens up interesting perspectives to the design of novel reconfigurable devices and components. Also

worthy of mention are the applications to microcavities and lasers [111,145–148], enhanced stimulated emission [149], add-drop filters for wavelength-division-multiplexing [150,151], negative refraction and "superlensing" [152,153], and directive emission [99]. Finally, the applications to nonlinear optics appear particularly intriguing (e.g., see Refs. [154–158] for a sparse sampling), where one can exploit the inherently superior suitability of PQCs to phase matching for a variety of effects, such as frequency conversion.

As a partial conclusion, from the above results and applications, the most interesting observations can be summarized as follows:

1. Spatial periodicity does not seem to constitute an essential ingredient to obtaining complete bandgaps and other peculiar waveguiding/confinement, refraction/transmission, filtering, and emission effects. Similar properties have been observed in PQC structures.
2. The mechanisms underlying the bandgap formation and other effects in PQCs are very complex and can involve single-element resonances, short- and long-range interactions, as well as multiple scattering phenomena.
3. As compared with their periodic counterparts, PQCs offer potential advantages (e.g., larger bandgaps, lower and/or multiple frequencies of operation, higher isotropy, richer and more wavelength-selective defect states, and easier achievement of phase-matching conditions) via a judicious exploitation of the additional degrees of freedom typically available in aperiodic geometries.

In what follows, we illustrate some representative examples of 2-D PQCs, with focus on two specific configurations: (a) arrays of dielectric rods and (b) planar structures.

27.5 Examples of 2-D PQCs

27.5.1 Geometry

We consider 2-D PQCs composed of parallel infinitely long dielectric circular rods, with identical radius r and relative dielectric permittivity ϵ_r, and excited by a transverse-magnetic EM field (i.e., electric field parallel to the rods) with implied time-harmonic $\exp(j\omega t)$ dependence.

Figure 27.5 displays the prototype PQC (cross-sectional) geometries of interest, generated by placing the cylindrical rods in free space at the tile vertices within a square patch of selected aperiodic tilings, representative of various types and degrees of order and symmetry. Size and scaling are chosen so as to maintain the total size and number of rods identical to that of a reference periodic PC constituted of a square arrangement of 16 × 16 rods, as shown in Figure 27.5a. Besides the already described "thick-and-thin" Penrose tiling in Figure 27.5b (fivefold symmetric) and the octagonal tiling in Figure 27.5e (eightfold symmetric), the binary tiling in Figure 27.5c is also characterized by a fivefold symmetry, while the tilings in Figure 27.5d and f exhibit sevenfold and ninefold symmetry, respectively. With the exception of the binary, all tilings are characterized by a purely discrete, quasiperiodic, spatial spectrum (indicative of long-range order) and are generated by algorithms amenable to cut-and-project schemes (see Section 27.2.3). Conversely, the binary tiling is generated via the substitution scheme in Figure 27.3 and exhibits a spatial spectrum with singular continuous character indicative, of a less-orderly spatial distribution. For all the PQC geometries in Figure 27.5, the same rods radius is chosen, so as to maintain the same filling factor (defined as the ratio between the total area of the rods and the area of the host square).

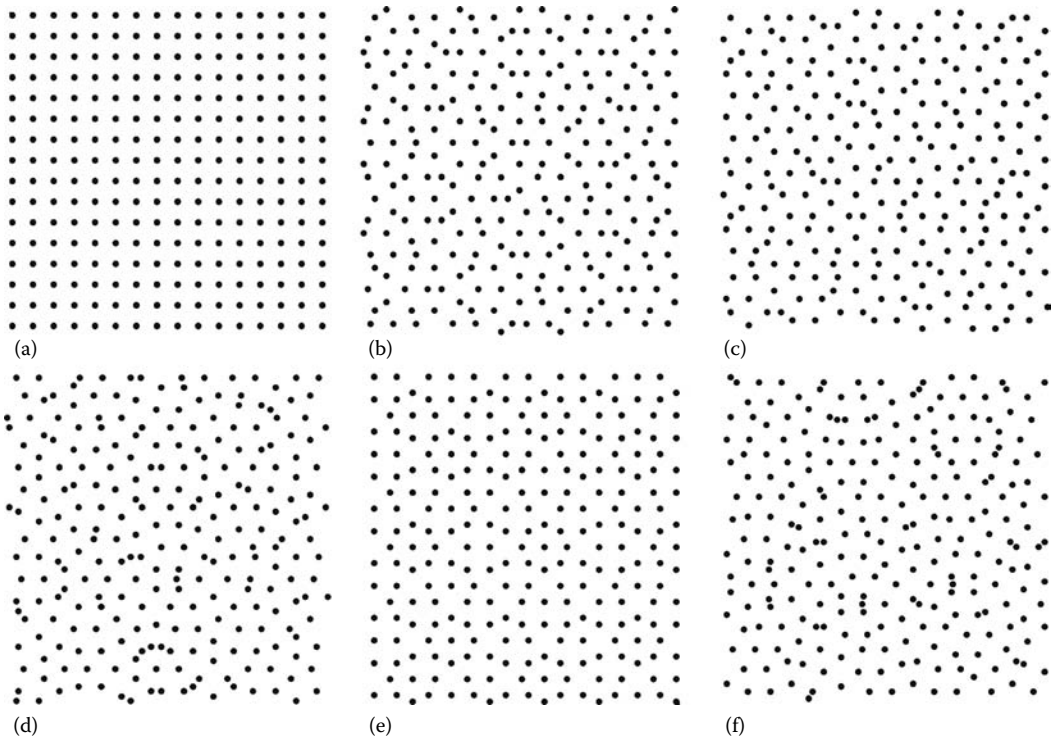

FIGURE 27.5 PC and PQC representative geometries ($N = 256$ dielectric rods): (a) Periodic (period = a); (b) Penrose "thick-and-thin" (fivefold symmetric); (c) Binary (fivefold symmetric); (d) sevenfold symmetric; (e) Octagonal (eightfold symmetric); and (f) ninefold symmetric. (Extracted from Della Villa, A., Galdi, V., Capolino, F., Pierro, V., Enoch, S., and Tayeb, G., *IEEE Antennas Wireless Propagat. Lett*., 5, 331, 2006. With permission.)

27.5.2 Bandgap Properties

As mentioned previously, a physically sound observation to ascertain the bandgap properties of finite-size PC or PQC structures can be defined in a similar way as the LDOS [46] in solid-state physics. Specifically, we consider the active power (per unit length) P_a radiated by a nonphased unit-amplitude electric line-source located inside the structure and identify the bandgaps as those frequency ranges where radiation is strongly inhibited. In the lossless case, for the 2-D scalar case of interest here, we obtain from the Poynting theorem [159, p. 22]

$$P_a(\mathbf{r}_0, \omega) = -\frac{1}{2}\mathrm{Re}\{E(\mathbf{r}_0; \omega)\} = -\frac{\omega\mu_0}{2}\mathrm{Im}\{G(\mathbf{r}_0, \mathbf{r}_0; \omega)\}, \tag{27.2}$$

where $E(\mathbf{r}_0; \omega)$ denotes the electric field (directed along the longitudinal direction of the rods) radiated by the unit-amplitude line-current at $\mathbf{r}_0$, and $G(\mathbf{r}_0, \mathbf{r}_0; \omega)$ denotes the pertinent Green's function evaluated at the source position. For convenience, we define as "radiativity" the normalized radiated power as

$$\rho(\mathbf{r}_0, \omega) = P_a(\mathbf{r}_0, \omega)/P_0(\mathbf{r}_0, \omega), \tag{27.3}$$

where $P_0 = \omega\mu_0/8$ [W/m] is the active power radiated by the unit-amplitude line-source in free space, so that $\rho(\mathbf{r}_0, \omega) = 1$ in the absence of the PQC. In our investigation, the computation of the Green's function in Equation 27.3 is performed via the scattering-matrix method in Ref. [44].

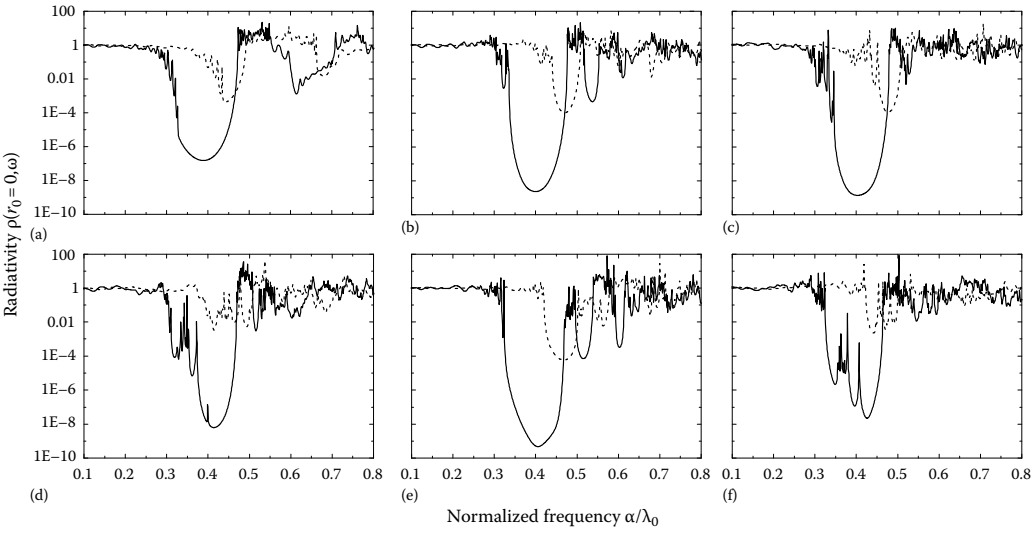

FIGURE 27.6 Radiativity in Equation 27.3 computed at the center of the structure vs. normalized frequency a/λ_0 for the quasicrystal geometries in Figure 27.5 with $r = 0.15a$ (i.e., filling factor=7.07%). Continuous curves: $\epsilon_r = 12$; dashed: $\epsilon_r = 6$. (Extracted from Della Villa, A., Galdi, V., Capolino, F., Pierro, V., Enoch, S., and Tayeb, G., *IEEE Antennas Wireless Propagat. Lett.*, 5, 331, 2006. With permission.)

For the PQC geometries in Figure 27.5, we carried out a comprehensive parametric study of the radiativity response, for several combinations of the rods' permittivity and filling factor values and at various positions $\mathbf{r}_0$, aimed at gaining some insights into the underlying aperiodic-order-induced bandgap phenomena. Some representative results, extracted from Ref. [99], are shown in Figure 27.6, for ~ 7% filling factor and two values of the relative permittivity $\epsilon_r = 6, 12$. In these plots, the radiativity in Equation 27.3 (computed at the center of the structure, $\mathbf{r}_0 = \mathbf{0}$) is displayed as a function of the normalized frequency a/λ_0, with a denoting the period of the reference PC in Figure 27.5a and λ_0 denoting the free-space wavelength. Bandgaps, identified by deep minima of the radiativity, can be observed for both permittivity values, though considerably more pronounced for the higher-contrast case ($\epsilon_r = 12$). As compared with the PC reference case, the PQCs tend to exhibit a generally richer bandgap structure, which typically entails a main bandgap (moderately deeper than the periodic counterpart) plus certain secondary bandgaps at lower and higher frequencies. Moreover, as the symmetry order is increased, several in-band peaks (attributable to localized modes) tend to appear (cf. Figure 27.6d and f).

The wave mechanisms underlying the formation of the various bandgaps are rather complex and generally involve both long- and short-range interactions as well as multiple scattering phenomena. For the Penrose PQC in Figure 27.5b, we carried out a more detailed investigation of the first three bandgaps [107], from which the central and the higher-frequency bandgaps (see Figure 27.6b) turned out to be related to Bragg-type conditions in the Fourier spatial spectrum of the PQC, whereas the lower-frequency bandgap turned out to stem from multiple scattering phenomena (see Ref. [107] for more details). Similar mechanisms, currently under investigation, are expected to take place for the other PQCs.

27.5.3 Localized Modes

As already highlighted (see Section 27.4), another interesting characteristic of PQC structures is the wealth of localization phenomena achievable in both defected [84,108,109] and defect-free [110–113]

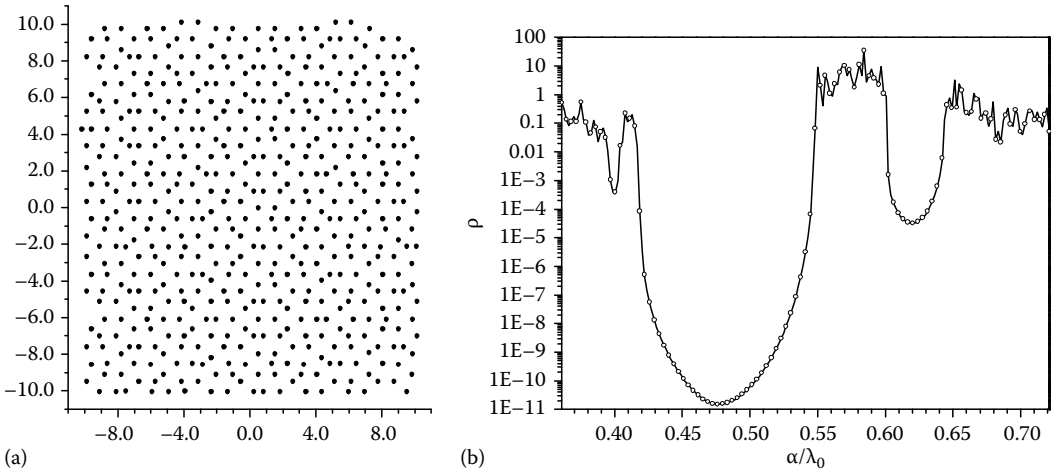

FIGURE 27.7 (a) Penrose PQC made of 530 dielectric rods (of radius $r = 0.116a$ and relative permittivity $\epsilon_r = 12$). (b) Radiativity response computed at $x = y = 0$. (Extracted from Della Villa, A., Enoch, S., Tayeb, G., Capolino, F., Pierro, V., and Galdi, V., *Opt. Expr.*, 14(21), 10021, 2006. With permission.)

configurations. In defected PQC configurations, a richer and more wavelength-selective modal spectrum is typically observed [84,108,109] as compared with their periodic PC counterparts. In Ref. [111], the stimulated emission in a defect-free, Penrose-type, PQC laser was studied, and the modes were found to be localized, at variance to the typical extended modes of the band-edge PC lasers. In Ref. [112], we investigated in detail the nature of these modes, which appear in the transparency bands, and show that they stem essentially from the local arrangement of rods.

Figure 27.7 shows a Penrose PQC made of 530 rods (of radius $r = 0.116a$ and relative permittivity $\epsilon_r = 12$) and the radiativity response (calculated at the central point) as a function of the normalized frequency a/λ_0 normalized frequency, qualitatively similar* to that in Figure 27.6b. Focusing on the behavior of the modes within a transparency band, at certain frequencies one can observe local resonances, which clearly exhibit the fivefold symmetry order of the PQC. Among the several possible examples that were observed, Figure 27.8 shows the radiativity map at the normalized frequency $a/\lambda_0 = 0.726$, above the main bandgap shown in Figure 27.7b.

In order to investigate the process of formation of the localized modes, we modified the structure by removing parts of the PQC outside the resonant region. Figure 27.9 shows some examples of radiativity maps (computed in the same region as in Figure 27.8b) pertaining to increasingly smaller PQCs, obtained by progressively removing certain rods outside the region displayed. Interestingly, while the amplitude of the radiativity associated with the mode slightly changes (~ 20%), the spatial distribution does not. This behavior suggests that the modes have indeed a highly localized nature, as clearly visible from the last example (Figure 27.9c), where, despite the very small structure extent (only 47 rods left), a behavior similar to that of the larger structures is observed. The reduction in the radiativity amplitude can be mainly attributed to a resonance frequency shift rather than a real decrease in the resonance strength.

* Note that here, at variance to Figure 27.6b, the parameter a is defined as the sidelength of the rhombus tiles in the Penrose tiling.

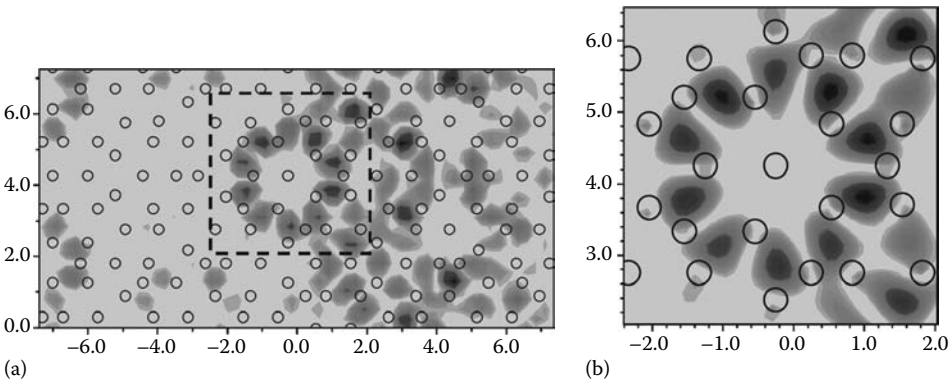

FIGURE 27.8 (a) Radiativity map in gray-scale (dark=high; light=low) pertaining to the upper region of the PQC in Figure 27.7a, at a normalized frequency $a/\lambda_0 = 0.726$. (b) Zoom of a region (dashed square) where a fivefold symmetry is clearly visible. All spatial scales are normalized with respect to a. (Extracted from Della Villa, A., Enoch, S., Tayeb, G., Capolino, F., Pierro, V., and Galdi, V., *Opt. Expr.*, 14(21), 10021, 2006. With permission.)

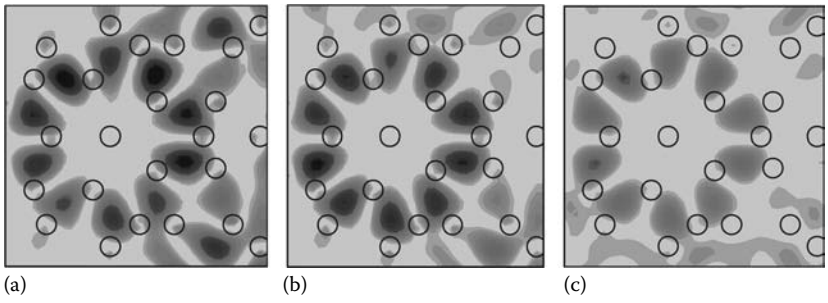

FIGURE 27.9 As in Figure 27.8b but for PQCs of different sizes. (a) 488 rods; (b) 384 rods; and (c) 47 rods. (Extracted from Della Villa, A., Enoch, S., Tayeb, G., Capolino, F., Pierro, V., and Galdi, V., *Opt. Expr.*, 14(21), 10021, 2006. With permission.)

The above results confirm the existence of localized modes observed in previous studies and show that these modes likely originate from interactions among a small number of rods, rather than from undesired fabrication-related defects, and should accordingly be considered as an inherent property of PQC geometries. Indeed, the observed localized modes are only slightly affected by the removal of several rods around (and even relatively close to) the localization region. These conclusions are nontrivial and somehow counterintuitive, as it is well known that band-edge modes in periodic PCs are not localized and that long-range interactions may be involved in the bandgap formation in PQCs (e.g., see Ref. [107]).

Further studies on the nature and properties of modes supported by defect-free PQC slabs are presently under consideration; the reader is referred to Ref. [160] for some preliminary results.

27.6 Examples of Planar PQCs

As a second illustrative example, we consider a planar PQC structure in the form of a textured (mushroom-type) high-impedance surface (HIS). Such structures have recently received considerable attention and are proposed as effective ground planes for improving the electrical and radiative responses of low-profile planar antennas in view of their potential capabilities, within certain frequency ranges, of exhibiting AMC-type behavior (i.e., in-phase reflection), and suppressing the surface-wave (SW) propagation [161].

Nearly all available examples are based on periodic geometries, for which the EM response is well understood (e.g., see Ref. [161]). Recently, a novel geometry was proposed in Ref. [116], based on the quasiperiodic octagonal (Ammann–Beenker) tiling (cf. Figure 27.2). Experimental and numerical studies of this structure revealed a very interesting EM response, in terms of multiple frequencies of operation, highly directive radiation from a small electric dipole laid on it, and broadband suppression of the transverse-electric SW. In Ref. [117], we carried out a comparative study of various HIS configurations based on representative categories of aperiodic tilings, aimed at exploring to what extent the intriguing results observed in Ref. [116] were restricted to that particular (octagonal) geometry or instead whether they were representative of intrinsic properties of rather generic aperiodically ordered configurations. In what follows, we briefly review the results obtained.

We consider three aperiodic geometries based on the Penrose (cf. Figure 27.1), octagonal (cf. Figure 27.2), and dodecagonal (cf. Figure 27.4) tilings. As a reference configuration, we also consider a standard periodic (square) geometry, whose EM response is well known [161]. The structures are obtained by cutting suitably sized regions of the tilings (preserving the local symmetry centers) and placing metallic (copper) tile-shaped patches on top of a metal-backed dielectric substrate with relative permittivity $\epsilon_r = 2.2$ (RT/duroid 5880) and thickness 1.6 mm. The patches, suitably scaled so as to guarantee a constant 0.7 mm gap between them, are finally connected to the ground plane by metallic vias of diameter 0.7 mm. In order to facilitate direct comparison with our results (at least for the octagonal geometry), the patch characteristic sizes are chosen as in Ref. [116], whereas the total structure sizes are set by our current computational resource limitations. All structures feature the same spacing between the metal patches and a comparable number of patches. Figure 27.10a through d shows the top view of the four HIS configurations under analysis; a 3-D view pertaining to the octagonal case is also displayed in Figure 27.10e.

In order to ascertain the possible AMC behavior, we study the radiation characteristics of a small electric dipole, laid parallel to the surface at a very close distance. Recalling basic image theory, the dipole will radiate very poorly when the surface is acting as standard (electric) ground plane and much more efficiently when the surface is acting as an AMC, resulting in a low return loss (RL) [161]. In our simulations, a 16 mm long electric dipole is placed parallel (x-directed) and very close to the surface ($x = y = 0$, $z = 0.7$ mm, i.e., right above its local symmetry center), and the RL ($|S_{11}|$) spectra for the various configurations are computed via a full-wave commercial software package [162]. Figure 27.11 shows the frequency responses within the range 4–12 GHz. For each geometry, one observes some (more or less pronounced) dips in the RL spectrum, corresponding to AMC-type behavior. The results for the octagonal HIS (Figure 27.11a) agree fairly well with those observed in Ref. [116], with three main dips at frequencies ~ 5, 6.5, and 10 GHz. Qualitatively similar behaviors, with less pronounced and frequency-shifted dips, are observed for the dodecagonal (Figure 27.11b) and the Penrose (Figure 27.11c) geometries, whereas the periodic HIS (Figure 27.11d) turns out to exhibit more pronounced, but narrower, dips.

We then studied the radiation characteristics around those frequencies yielding AMC behavior. Periodically textured HIS ground-planes have been proposed for the suppression of the SW propagation, which can yield significant improvements in the radiation pattern quality of planar antennas [161]. Figure 27.12a through d shows some representative radiation patterns observed for the 16 mm long electric dipole laid on the four HIS ground planes, at frequencies (marked as arrows in

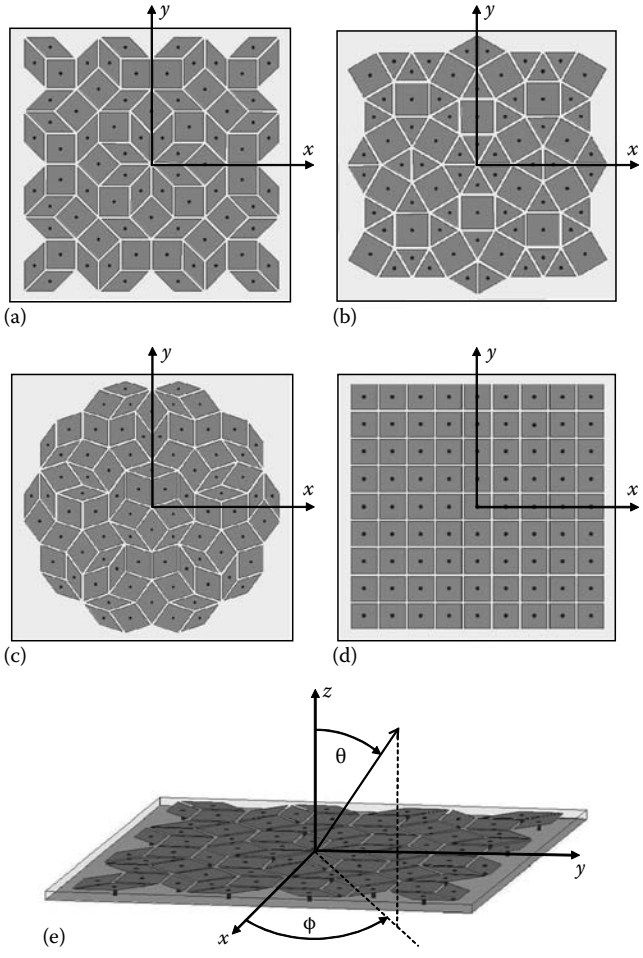

FIGURE 27.10 HIS geometry and parameters: (a)–(d) Top view; (e): Three-dimensional view (octagonal). Metallic (copper) patches of sidelength a_{patch} are laid with a 0.7 mm gap on a metal-backed dielectric substrate of thickness 1.6 mm and relative permittivity $\epsilon_r = 2.2$ and are connected to the ground plane by metallic vias with diameter 0.7 mm. Also shown are the Cartesian and spherical reference coordinate systems, with the origin at the local symmetry center. (a) Octagonal ($a_{\text{square}} = 7.6$ mm, $a_{\text{rhombus}} = 7.3$ mm, total size: 70×70 mm^2); (b) Dodecagonal ($a_{\text{square}} = 7.6$ mm, $a_{\text{triangle}} = 7.1$ mm, total size: 62×62 mm^2); (c) Penrose ($a_{\text{thick}} = 7.6$ mm, $a_{\text{thin}} = 7.2$ mm, total size: 76×76 mm^2); (d) Periodic ($a_{\text{square}} = 7.6$ mm, total size: 76×76 mm^2). (Extracted from Gallina, I., Della Villa, A., Galdi, V., Pierro, V., Capolino, F., Enoch, S., Tayeb, G., and Gerini, G., *IEEE Antennas Wireless Propagat. Lett.*, 7, 54, 2008. With permission.)

Figure 27.11) chosen so as to provide a reasonable tradeoff between high broadside directivity and low RL. As expected, one observes rather clean patterns in the forward direction, with low backward radiation ($\lesssim -15$ dB), thereby qualitatively confirming the results in Ref. [116].

Finally, as in Ref. [116], we consider the SW propagation, for both transverse electric (TE) and magnetic (TM) polarizations. As a meaningful observation, we consider the transmission ($|S_{12}|$) spectra between two small antennas (y-directed 16 mm long electric dipoles for the TE case; z-directed 8 mm long monopoles for the TM case) placed at two opposite ends of the HIS. Results are shown in Figure 27.13 (with the simulation schematics illustrated in the insets) for the four geometries

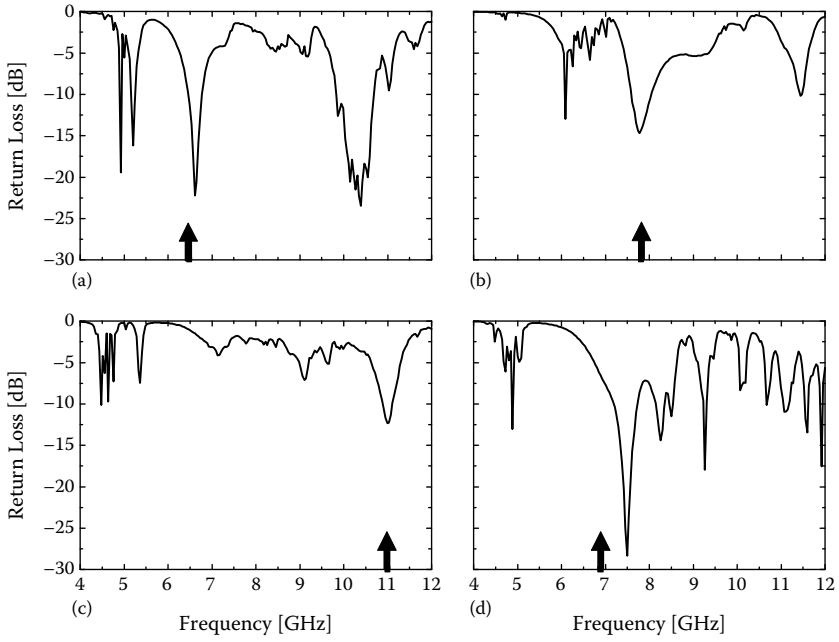

FIGURE 27.11 Geometry and parameters as in Figure 27.10. Return loss ($|S_{11}|$) of an x-directed 16 mm long electric dipole placed at $x = y = 0$, $z = 0.7$ mm (i.e., right above the local symmetry center). (a) Octagonal; (b) dodecagonal; (c) Penrose; and (d) periodic. Arrows mark the frequency values where a reasonable trade-off between RL and broadside directivity (see Figure 27.12) was observed. (Extracted from Gallina, I., Della Villa, A., Galdi, V., Pierro, V., Capolino, F., Enoch, S., Tayeb, G., and Gerini, G., *IEEE Antennas Wireless Propagat. Lett.*, 7, 54, 2008. With permission.)

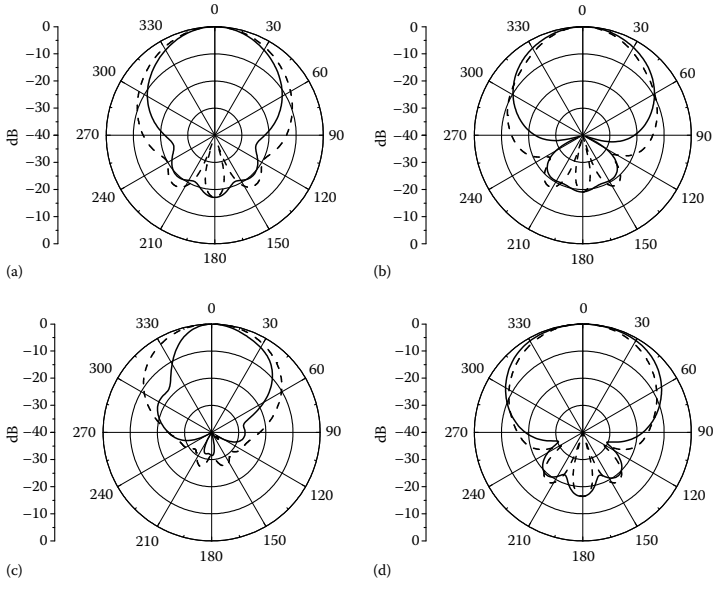

FIGURE 27.12 As in Figure 27.11, but radiation patterns at selected frequency values (marked by arrows in Figure 27.11). (a) Octagonal (6.49 GHz, RL=−11.2 dB); (b) dodecagonal (7.82 GHz, RL=−14.2 dB); (c) Penrose (11 GHz, RL=−12.3 dB); and (d) periodic (6.89 GHz, RL=−6.6 dB). Solid curves: $\phi = 0°$ plane; dashed: $\phi = 90°$ plane. (Extracted from Gallina, I., Della Villa, A., Galdi, V., Pierro, V., Capolino, F., Enoch, S., Tayeb, G., and Gerini, G., *IEEE Antennas Wireless Propagat. Lett.*, 7, 54, 2008. With permission.)

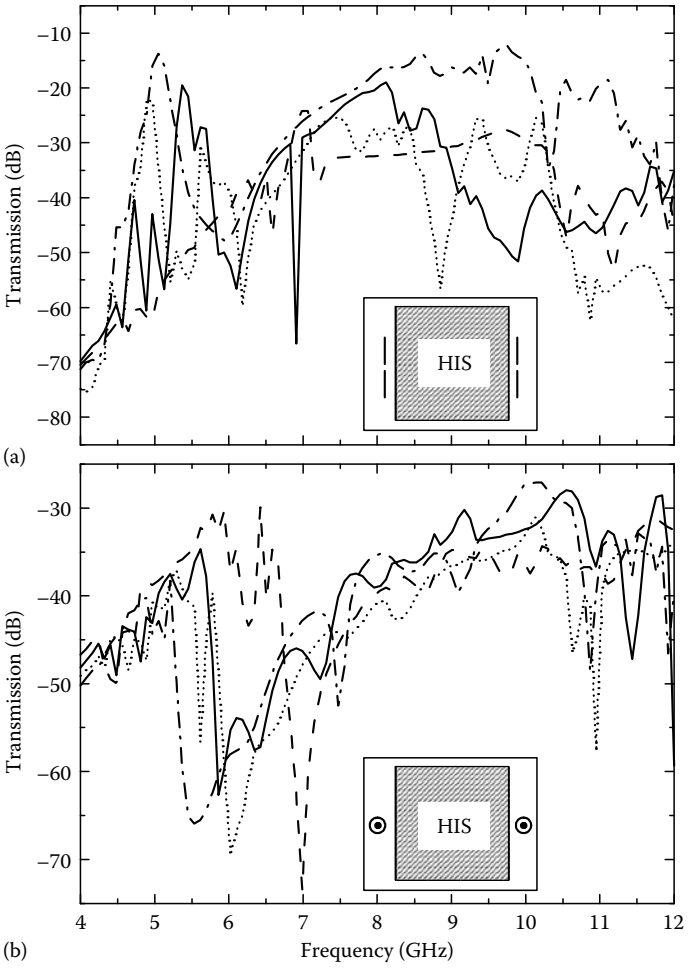

FIGURE 27.13 SW transmission ($|S_{12}|$) spectra for the HIS configurations in Figure 27.10 for TE (a) and TM (b) polarizations (simulation schematics are illustrated in the insets). Solid curves: octagonal (probe separation: 72 mm); dashed: dodecagonal (probe separation: 64 mm); dotted: Penrose (probe separation: 78 mm); dash-dotted: periodic (probe separation: 78 mm). (Extracted from Gallina, I., Della Villa, A., Galdi, V., Pierro, V., Capolino, F., Enoch, S., Tayeb, G., and Gerini, G., *IEEE Antennas Wireless Propagat. Lett.*, 7, 54, 2008. With permission.)

under study. In the TE case (Figure 27.13a), the aperiodic HIS configurations exhibit several bandgaps characterized by strong SW attenuation, whereas the periodic HIS exhibits only one bandgap with significant SW attenuation. In the TM case (Figure 27.13b), several dips and similar attenuation levels are observed for all the geometries.

To sum up, our results confirm those already observed in Ref. [116] (in connection with the octagonal geometry) and reveal the inherent suitability of more general PQC geometries to HIS applications. The availability of further and still largely unexplored degrees of freedom in the lattice geometry could open up new perspectives in the HIS design. Indeed, PQC HIS structures seem potentially capable of yielding multiple AMC bands, strong attenuation of TE and TM SW propagation, and directive broadside radiation.

27.7 Quasi-Conclusions

In this chapter, we have attempted a presentation, at an introductory level, of the basic properties and applications of PQCs, starting from the geometric aspects, proceeding with a compact review of the topical literature, and the illustration of a series of selected prototype examples.

It is worth stressing, once again, that the presentation here is far from exhaustive, and some of the relevant issues involved are as yet unsettled or not completely understood. It is our hope to motivate the reader to further explore this subject, which is not only intriguing but also has potentially interesting applications in EM and optical engineering.

References

1. D. Shechtman, I. Blech, D. Gratias, and J. W. Cahn. Metallic phase with long-range orientational order and no translation symmetry. *Phys. Rev. Lett.*, 53(26):1951–1953, 1984.
2. D. Levine and P. J. Steinhardt. Metallic phase with long-range orientational order and no translation symmetry. *Phys. Rev. Lett.*, 53(26):2477–2480, 1984.
3. R. Lifshitz. Quasicrystals: A matter of definition. *Found. Phys.*, 33(12):1703–1711, 2003.
4. E. Maciá. The role of aperiodic order in science and technology. *Rep. Progr. Phys.*, 69(2):397–441, 2006.
5. W. Steurer and D. Sutter-Widmer. Photonic and phononic quasicrystals. *J. Phys. D.*, 40(13):R229–R247, 2007.
6. M. Baake. A guide to mathematical quasicrystals. In J.-B. Suck, M. Schreiber, and P. Häussler (eds.), *Quasicrystals: An Introduction to Structure, Physical Properties, and Applications*, pp. 17–48. Springer, Berlin, Germany, 2002.
7. http://www.quasi.iastate.edu/bib.html. Database maintained by the Quasicrystal Research Group at Iowa State University, IA.
8. D. S. Chigrin and A. V. Lavrinenko. Photonic quasicrystals in applications. In F. Capolino (ed.), *Handbook of Artificial Materials*, Vol. II. CRC Press, Boca Raton, FL, 2008.
9. M. Queffélec. *Substitution Dynamical Systems – Spectral Analysis*, Vol. 1294 of *Lecture Notes in Mathematics*. Springer, Berlin, Germany, 2002.
10. N. P. Fogg, V. Berthé, S. Ferenczi, C. Mauduit, and A. Siegel (eds.). *Substitutions in Dynamics, Arithmetics, and Combinatorics*, Vol. 1794 of *Lecture Notes in Mathematics*. Springer, Berlin, Germany, 2002.
11. B. Grünbaum and G. C. Shepard. *Tilings and Patterns*. Freeman, New York, 1987.
12. M. Senechal. *Quasicrystals and Geometry*. Cambridge University Press, Cambridge, U.K., 1995.
13. H. Wang. Proving theorems by pattern recognition. *Bell Syst. Tech. J.*, 40:1–41, 1961.
14. R. Berger. The undecidability of the domino problem. *Mem. Am. Math. Soc.*, 66:1–72, 1966.
15. R. Penrose. The rôle of aesthetics in pure and applied mathematical research. *Bull. Inst. Math. Appl.*, 10:266–271, 1974.
16. P. J. Lu and P. J. Steinhardt. Decagonal and quasi-crystalline tilings in medieval Islamic architecture. *Science*, 315(5815):1106–1110, 2007.
17. V. Pierro, V. Galdi, G. Castaldi, I. M. Pinto, and L. B. Felsen. Radiation properties of planar antenna arrays based on certain categories of aperiodic tilings. *IEEE Trans. Antennas Propagat.*, 53(2):635–644, 2005.
18. U. Grimm and M. Schreiber. Aperiodic tilings on the computer. In J.-B. Suck, M. Schreiber, and P. Häussler (eds.), *Quasicrystals: An Introduction to Structure, Physical Properties, and Applications*, pp. 49–66. Springer, Berlin, Germany, 2002.
19. M. Oxborrow and C. L. Henley. Random square-triangle tilings: A model for twelvefold-symmetric quasicrystals. *Phys. Rev. B*, 48(10):6966–6998, 1993.

20. C. Radin. *Miles of Tiles*. American Mathematical Society, Providence, RI, 1999.
21. A. Papoulis. *The Fourier Integral and Its Applications*. McGraw-Hill, New York, 1962.
22. L. Carin and L. B. Felsen. Time-harmonic and transient scattering by finite periodic flat strip arrays: Hybrid (Ray)-(Floquet Mode)-(MOM) algorithm and its GTD interpretation. *IEEE Trans. Antennas Propagat.*, 41(4):412–421, 1993.
23. L. B. Felsen and L. Carin. Diffraction theory and of frequency- and time-domain scattering by weakly aperiodic truncated thin-wire gratings. *J. Opt. Soc. Am. A*, 11(4):1291–1306, 1994.
24. L. B. Felsen and E. Gago-Ribas. Ray theory for scattering by two-dimensional quasiperiodic plane finite arrays. *IEEE Trans. Antennas Propagat.*, 44(3):375–382, 1996.
25. A. Cucini, M. Albani, and S. Maci. Truncated Floquet wave full-wave analysis of large phased arrays of open-ended waveguides with a nonuniform amplitude excitation. *IEEE Trans. Antennas Propagat.*, 51(6):1386–1394, 2003.
26. E. Bombieri and J. E. Taylor. Which distributions of matter diffract? An initial investigation. *J. Physique France*, 47(C3):19–28, 1986.
27. E. Bombieri and J. E. Taylor. Quasicrystals, tilings, and algebraic number theory: Some preliminary connections. *Contemp. Math.*, 64:241–264, 1987.
28. S. Aubry, C. Godrèche, and J. M. Luck. Scaling properties of a structure intermediate between quasiperiodic and random. *J. Stat. Phys.*, 51(5/6):1033–1075, 1988.
29. J. M. Luck. Cantor spectra and scaling of gap widths in deterministic aperiodic systems. *Phys. Rev. B*, 39(9):5834–5849, 1989.
30. C. Godrèche and J. M. Luck. Multifractal analysis in reciprocal space and the nature of the Fourier transform of self-similar structures. *J. Phys. A*, 23(16):3769–3797, 1990.
31. M. Kolář. New class of one-dimensional quasicrystals. *Phys. Rev. B*, 47(9):5489–5492, 1993.
32. M. Kolář, B. Iochum, and L. Raymond. Structure factor of 1D systems (superlattices) based on two-letter substitution rules: I. δ (Bragg) peaks. *J. Phys. A*, 26(24):7343–7366, 1993.
33. V. Galdi, G. Castaldi, V. Pierro, I. M. Pinto, and L. B. Felsen. Parameterizing quasi-periodicity: Generalized Poisson summation and its application to modified-Fibonacci antenna arrays. *IEEE Trans. Antennas Propagat.*, 53(6):2044–2053, 2005.
34. V. Galdi, G. Castaldi, V. Pierro, I. M. Pinto, and L. B. Felsen. Scattering properties of one-dimensional aperiodically ordered strip arrays based on two-symbol substitutional sequences. *IEEE Trans. Antennas Propagat.*, 55(6):1554–1563, 2007.
35. G. Castaldi, V. Galdi, V. Pierro, and I. M. Pinto. Radiation from fibonacci-type quasiperiodic arrays on dielectric substrates. *J. Electromagn. Waves Appl.*, 21(9):1231–1245, 2007.
36. M. Kolář and F. Nori. Trace maps of general substitutional sequences. *Phys. Rev. B*, 42(1):1062–1065, 1990.
37. G. J. Jin, Z. D. Wang, A. Hu, and S. S. Jiang. Quantum waveguide theory of serial stub structures. *J. Appl. Phys.*, 85(3):1597–1608, 1999.
38. X. Wang, U. Grimm, and M. Schreiber. Trace and antitrace maps for aperiodic sequences: Extensions and applications. *Phys. Rev. B*, 62(21):14020–14031, 2000.
39. A. E. Carlsson. Band-gap creation by icosahedral symmetry in nearly-free-electron materials. *Phys. Rev. B*, 47(5):2515–2521, 1993.
40. S. David, A. Chelnokov, and J. M. Lourtioz. Isotropic photonic structures: Archimedean-like tilings and quasi-crystals. *IEEE J. Quantum. Electron.*, 37(11):1427–1434, 2001.
41. Y. Yang and G. P. Wang. Two-dimensional photonic crystals constructed with a portion of photonic quasicrystals. *Opt. Expr.*, 15(10):5991–5996, 2007.
42. M. A. Kaliteevski, S. Brand, R. A. Abram, T. F. Krauss, P. Millar, and R. M. De La Rue. Diffraction and transmission of light in low-refractive index Penrose-tiled photonic quasicrystals. *J. Phys.*, 13(46): 10459–10470, 2001.
43. A. W. Rodriguez, A. P. Mccauley, Y. Avniel, and S. G. Johnson. Computation and visualization of photonic quasicrystal spectra via Bloch's theorem. *Phys. Rev. B*, 77(10):104201, 2008.

44. D. Felbacq, G. Tayeb, and D. Maystre. Scattering by a random set of parallel cylinders. *J. Opt. Soc. Am. A*, 11(9):2526–2538, 1994.
45. A. Taflove and S. C. Hagness. *Computational Electrodynamics: The Finite-Difference Time-Domain Method*, 3rd edn. Artech House, Norwood, MA, 2005.
46. A. A. Asatryan, K. Busch, R. C. McPhedran, L. C. Botten, C. Martijn de Sterke, and N. A. Nicorovici. Two-dimensional Green's function and local density of states in photonic crystals consisting of a finite number of cylinders of infinite length. *Phys. Rev. E*, 63(4):046612, 2001.
47. R. Merlin, K. Bajema, Roy Clarke, F. Y. Juang, and P. K. Bhattacharya. Quasiperiodic GaAs-AlAs heterostructures. *Phys. Rev. Lett.*, 55(17):1768–1770, 1985.
48. S. Tamura and J. P. Wolfe. Acoustic-phonon transmission in quasiperiodic superlattices. *Phys. Rev. B*, 36(6):3491–3494, 1987.
49. M. Kohmoto, B. Sutherland, and K. Iguchi. Localization of optics: Quasiperiodic media. *Phys. Rev. Lett.*, 58(23):2436–2438, 1987.
50. W. Gellermann, M. Kohmoto, B. Sutherland, and P. C. Taylor. Localization of light waves in Fibonacci dielectric multilayers. *Phys. Rev. Lett.*, 72(5):633–636, 1994.
51. E. Maciá. Optical engineering with Fibonacci dielectric multilayers. *Appl. Phys. Lett.*, 73(23):3330–3332, 1998.
52. X. Q. Huang, S. S. Jiang, R. W. Peng, and A. Hu. Perfect transmission and self-similar optical transmission spectra in symmetric Fibonacci-class multilayers. *Phys. Rev. B*, 6324(24):245104, 2001.
53. R. K. Mishra, K. D. Misra, A. P. Misra, and A. K. Tripathi. Design and operating characteristics of a bandpass optical filter with oblique bandgap structures of Fibonacci lattices. *Surf. Rev. Lett.*, 12(1): 47–57, 2005.
54. T. Bo, F. L. Li, and Y. Feng. Transmission properties of quasi-periodic Fibonacci one-dimensional photonic crystal containing negative permittivity/permeability material. *Int. J. Mod. Phys. B*, 21(31): 5221–5229, 2007.
55. S. Golmohammadi, M. K. Moravvej-Farshi, A. Rostami, and A. Zarifkar. Narrowband DWDM filters based on Fibonacci-class quasi-periodic structures. *Opt. Expr.*, 15(17):10520–10532, 2007.
56. D. Lusk, I. Abdulhalim, and F. Placido. Omnidirectional reflection from Fibonacci quasi-periodic one-dimensional photonic crystal. *Opt. Commn.*, 198(4-6):273–279, 2001.
57. J. W. Dong, P. Han, and H. Z. Wang. Broad omnidirectional reflection band forming using the combination of Fibonacci quasi-periodic and periodic one-dimensional photonic crystals. *Chinese Phys. Lett.*, 20(11):1963–1965, 2003.
58. K. B. Abdelaziz, J. Zaghdoudi, M. Kanzari, and B. Rezig. A broad omnidirectional reflection band obtained from deformed Fibonacci quasi-periodic one dimensional photonic crystals. *J. Opt. A*, 7 (10):544–549, 2005.
59. R. W. Peng, X. Q. Huang, F. Qiu, M. Wang, A. Hu, S. S. Jiang, and M. Mazzer. Symmetry-induced perfect transmission of light waves in quasiperiodic dielectric multilayers. *Appl. Phys. Lett.*, 80(17): 3063–3065, 2002.
60. R. W. Peng, Y. M. Liu, X. Q. Huang, F. Qiu, M. Wang, A. Hu, S. S. Jiang, D. Feng, L. Z. Ouyang, and J. Zou. Dimerlike positional correlation and resonant transmission of electromagnetic waves in aperiodic dielectric multilayers. *Phys. Rev. B*, 69(16):165109, 2004.
61. L. N. Makarava, M. M. Nazarov, I. A. Ozheredov, A. P. Shkurinov, A. G. Smirnov, and S. V. Zhukovsky. Fibonacci-like photonic structure for femtosecond pulse compression. *Phys. Rev. E*, 75(3):036609, 2007.
62. L. Dal Negro, C. J. Oton, Z. Gaburro, L. Pavesi, P. Johnson, A. Lagendijk, R. Righini, M. Colocci, and D. S. Wiersma. Light transport through the band-edge states of Fibonacci quasicrystals. *Phys. Rev. Lett.*, 90(5):055501, 2003.
63. R. Riklund and M. Severin. Optical properties of perfect and non-perfect quasi-periodic multilayers: A comparison with periodic and disordered multilayers. *J. Phys. C*, 21(17):3217–3228, 1988.

64. F. Qiu, R. W. Peng, X. Q. Huang, Y. M. Liu, M. Wang, A. Hu, and S. S. Jiang. Resonant transmission and frequency trifurcation of light waves in Thue-Morse dielectric multilayers. *Europhys. Lett.*, 63 (6):853–859, 2003.
65. L. Dal Negro, M. Stolfi, Y. Yi, J. Michel, X. Duan, L. C. Kimerling, J. Leblanc, and J. Haavisto. Photon band gap properties and omnidirectional reflectance in Si/SiO2 Thue-Morse quasicrystals. *Appl. Phys. Lett.*, 84(25):5186–5188, 2004.
66. L. Dal Negro, J. H. Yi, V. Nguyen, Y. Yi, J. Michel, and L. C. Kimerling. Spectrally enhanced light emission from aperiodic photonic structures. *Appl. Phys. Lett.*, 86(26):261905, 2005.
67. X. Y. Jiang, Y. G. Zhang, S. L. Feng, K. C. Huang, Y. H. Yi, and J. D. Joannopoulos. Photonic band gaps and localization in the Thue-Morse structures. *Appl. Phys. Lett.*, 86(20):201110, 2005.
68. L. Moretti, I. Rea, L. Rotiroti, I. Rendina, G. Abbate, A. Marino, and L. De Stefano. Photonic band gaps analysis of Thue-Morse multilayers made of porous silicon. *Opt. Expr.*, 14(13):6264–6272, 2006.
69. H. P. Lei, J. Chen, G. Nouet, S. L. Feng, Q. Gong, and X. Y. Jiang. Photonic band gap structures in the Thue-Morse lattice. *Phys. Rev. B*, 75(20):205109, 2007.
70. E. L. Albuquerque and M. G. Cottam. Theory of elementary excitations in quasiperiodic structures. *Phys. Rep.*, 376(4-5):225–337, 2003.
71. H. Aynaou, E. H. El Boudouti, Y. El Hassouani, A. Akjouj, B. Djafari-Rouhani, J. Vasseur, A. Benomar, and V. R. Velasco. Propagation and localization of electromagnetic waves in quasiperiodic serial loop structures. *Phys. Rev. E*, 72(5):056601, 2005.
72. E. Cojocaru. Forbidden gaps in finite periodic and quasi-periodic cantor-like dielectric multilayers at normal incidence. *Appl. Opt.*, 40(34):6319–6326, 2001.
73. A. V. Lavrinenko, S. V. Zhukovsky, K. S. Sandomirski, and S. V. Gaponenko. Propagation of classical waves in nonperiodic media: Scaling properties of an optical Cantor filter. *Phys. Rev. E*, 65(3):036621, 2002.
74. S. Sengupta, A. Chakrabarti, and S. Chattopadhyay. Electronic transport in a Cantor stub waveguide network. *Phys. Rev. B*, 71(13):134204, 2005.
75. M. Maksimovk and Z. Jaksic. Emittance and absorptance tailoring by negative refractive index metamaterial-based Cantor multilayers. *J. Opt. A*, 8(3):355–362, 2006.
76. M. S. Vasconcelos and E. L. Albuquerque. Transmission fingerprints in quasiperiodic dielectric multilayers. *Phys. Rev. B*, 59(17):11128–11131, 1999.
77. Y. S. Chan, C. T. Chan, and Z. Y. Liu. Photonic band gaps in two dimensional photonic quasicrystals. *Phys. Rev. Lett.*, 80(5):956–959, 1998.
78. S. S. M. Cheng, L. M. Li, C. T. Chan, and Z. Q. Zhang. Defect and transmission properties of two-dimensional quasiperiodic photonic band-gap systems. *Phys. Rev. B*, 59(6):4091–4099, 1999.
79. C. J. Jin, B. Y. Cheng, B. Y. Man, Z. L. Li, D. Z. Zhang, S. Z. Ban, and B. Sun. Band gap and wave guiding effect in a quasiperiodic photonic crystal. *Appl. Phys. Lett.*, 75(13):1848–1850, 1999.
80. M. Hase, H. Miyazaki, M. Egashira, N. Shinya, K. M. Kojima, and S. Uchida. Isotropic photonic band gap and anisotropic structures in transmission spectra of two-dimensional fivefold and eightfold symmetric quasiperiodic photonic crystals. *Phys. Rev. B*, 66(21):214205, 2002.
81. C. J. Jin, B. Y. Cheng, B. Y. Man, Z. L. Li, and D. Z. Zhang. Two-dimensional dodecagonal and decagonal quasiperiodic photonic crystals in the microwave region. *Phys. Rev. B*, 61(16):10762–10767, 2000.
82. M. A. Kaliteevski, S. Brand, R. A. Abram, T. F. Krauss, R. De La Rue, and P. Millar. Two-dimensional Penrose-tiled photonic quasicrystals: From diffraction pattern to band structure. *Nanotechnology*, 11 (4):274–280, 2000.
83. M. A. Kaliteevski, S. Brand, R. A. Abram, T. F. Krauss, R. M. De La Rue, and P. Millar. Two-dimensional Penrose-tiled photonic quasicrystals: Diffraction of light and fractal density of modes. *J. Mod. Opt.*, 47(11):1771–1778, 2000.
84. M. Bayindir, E. Cubukcu, I. Bulu, and E. Ozbay. Photonic band-gap effect, localization, and waveguiding in the two-dimensional Penrose lattice. *Phys. Rev. B*, 63(16):161104, 2001.

85. M. Bayindir, E. Cubukcu, I. Bulu, and E. Ozbay. Photonic band gaps and localization in two-dimensional metallic quasicrystals. *Europhys. Lett.*, 56(1):41–46, 2001.
86. M. E. Zoorob, M. D. B. Charlton, G. J. Parker, J. J. Baumberg, and M. C. Netti. Complete photonic bandgaps in 12-fold symmetric quasicrystals. *Nature*, 404(6779):740–743, 2000.
87. M. E. Zoorob, M. D. B. Charlton, G. J. Parker, J. J. Baumberg, and M. C. Netti. Complete and absolute photonic bandgaps in highly symmetric photonic quasicrystals embedded in low refractive index materials. *Mat. Sci. Eng. B*, 74(1-3):168–174, 2000.
88. X. D. Zhang, Z. Q. Zhang, and C. T. Chan. Absolute photonic band gaps in 12-fold symmetric photonic quasicrystals. *Phys. Rev. B*, 6308(8):081105, 2001.
89. M. A. Kaliteevski, S. Brand, R. A. Abram, T. F. Krauss, R. De La Rue, and P. Millar. The design of two-dimensional photonic quasicrystals by means of a Fourier transform method. *J. Mod. Opt.*, 48 (1):9–14, 2001.
90. M. A. Kaliteevski, S. Brand, R. A. Abram, T. F. Krauss, P. Millar, and R. M. De La Rue. Diffraction and transmission of light in low-refractive index Penrose-tiled photonic quasicrystals. *J. Phys.*, 13(46): 10459–10470, 2001.
91. M. A. Kaliteevski, S. Brand, and R. A. Abram. Directionality of light transmission and reflection in two-dimensional Penrose tiled photonic quasicrystals. *J. Phys.*, 16(8):1269–1278, 2004.
92. B. P. Hiett, D. H. Beckett, S. J. Cox, J. M. Generowicz, M. Molinari, and K. S. Thomas. Photonic band gaps in 12-fold symmetric quasicrystals. *J. Mat. Sci.*, 14(5-7):413–416, 2003.
93. R. C. Gauthier and K. Mnaymneh. Photonic band gap properties of 12-fold quasi-crystal determined through FDTD analysis. *Opt. Expr.*, 13(6):1985–1998, 2005.
94. Y. Lai, Z. Q. Zhang, C. H. Chan, and L. Tsang. Gap structures and wave functions of classical waves in large-sized two-dimensional quasiperiodic structures. *Phys. Rev. B*, 74(5):054305, 2006.
95. D. T. Roper, D. M. Beggs, M. A. Kaliteevski, S. Brand, and R. A. Abram. Properties of two-dimensional photonic crystals with octagonal quasicrystalline unit cells. *J. Mod. Opt.*, 53(3):407–416, 2006.
96. J. L. Yin, X. G. Huang, S. H. Liu, and S. J. Hu. Photonic bandgap properties of 8-fold symmetric photonic quasicrystals. *Opt. Commn.*, 269(2):385–388, 2007.
97. R. C. Gauthier. FDTD analysis of out-of-plane propagation in 12-fold photonic quasi-crystals. *Opt. Commn.*, 269(2):395–410, 2007.
98. Y. Q. Wang, B. Y. Cheng, and D. Z. Zhang. The density of states in quasiperiodic photonic crystals. *J. Phys.*, 15(45):7675–7680, 2003.
99. A. Della Villa, V. Galdi, F. Capolino, V. Pierro, S. Enoch, and G. Tayeb. A comparative study of representative categories of EBG dielectric quasi-crystals. *IEEE Antennas Wireless Propagat. Lett.*, 5: 331–334, 2006.
100. N. Horiuchi, Y. Segawa, T. Nozokido, K. Mizuno, and H. Miyazaki. Isotropic photonic gaps in a circular photonic crystal. *Opt. Lett.*, 29(10):1084–1086, 2004.
101. J. Chaloupka, J. Zarbakhsh, and K. Hingerl. Local density of states and modes of circular photonic crystal cavities. *Phys. Rev. B*, 72(8):085122, 2005.
102. T. D. M. Lee, G. J. Parker, M. E. Zoorob, S. J. Cox, and M. D. B. Charlton. Design and simulation of highly symmetric photonic quasi-crystals. *Nanotechnology*, 16(11):2703–2706, 2005.
103. Z. Ouyang, C. Jin, D. Z. Zhang, B. Y. Cheng, X. D. Meng, G. Z. Yang, and J. Z. Li. Photonic bandgaps in two-dimensional short-range periodic structures. *J. Opt. A*, 4(1):23–28, 2002.
104. L. Moretti and V. Mocella. Two-dimensional photonic aperiodic crystals based on Thue-Morse sequence. *Opt. Expr.*, 15(23):15314–15323, 2007.
105. K. Wang, S. David, A. Chelnokov, and J. M. Lourtioz. Photonic band gaps in quasicrystal-related approximant structures. *J. Mod. Opt.*, 50(13):2095–2105, 2003.
106. C. Rockstuhl, U. Peschel, and F. Lederer. Correlation between single-cylinder properties and bandgap formation in photonic structures. *Opt. Lett.*, 31(11):1741–1743, 2006.

107. A. Della Villa, S. Enoch, G. Tayeb, V. Pierro, V. Galdi, and F. Capolino. Band gap formation and multiple scattering in photonic quasicrystals with a Penrose-type lattice. *Phys. Rev. Lett.*, 94(18):183903, 2005.
108. R. C. Gauthier and K. Mnaymneh. FDTD analysis of 12-fold photonic quasi-crystal central pattern localized states. *Opt. Commn.*, 264(1):78–88, 2006.
109. D. M. Beggs, M. A. Kaliteevski, and R. A. Abram. Properties of microcavities in two-dimensional photonic quasicrystals with octagonal rotational symmetry. *J. Mod. Opt.*, 54(6):881–893, 2007.
110. Y. Q. Wang, X. Y. Hu, X. S. Xu, B. Y. Cheng, and D. Z. Zhang. Localized modes in defect-free dodecagonal quasiperiodic photonic crystals. *Phys. Rev. B*, 68(16):165106, 2003.
111. M. Notomi, H. Suzuki, T. Tamamura, and K. Edagawa. Lasing action due to the two-dimensional quasiperiodicity of photonic quasicrystals with a Penrose lattice. *Phys. Rev. Lett.*, 92(12):123906, 2004.
112. A. Della Villa, S. Enoch, G. Tayeb, F. Capolino, V. Pierro, and V. Galdi. Localized modes in photonic quasicrystals with Penrose-type lattice. *Opt. Expr.*, 14(21):10021–10027, 2006.
113. K. Mnaymneh and R. C. Gauthier. Mode localization and band-gap formation in defect-free photonic quasicrystals. *Opt. Expr.*, 15(8):5089–5099, 2007.
114. Y. Q. Wang, Z. F. Feng, X. S. Xu, B. Y. Cheng, and D. Z. Zhang. Uncoupled defect modes in a two-dimensional quasiperiodic photonic crystal. *Europhys. Lett.*, 64(2):185–189, 2003.
115. Y. Q. Wang, J. Liu, B. Zhang, S. Feng, and Z. Y. Li. Simulations of defect-free coupled-resonator optical waveguides constructed in 12-fold quasiperiodic photonic crystals. *Phys. Rev. B*, 73(15):155107, 2006.
116. H. Q. Li, Z. H. Hang, Y. Q. Qin, Z. Y. Wei, L. Zhou, Y. W. Zhang, H. Chen, and C. T. Chan. Quasiperiodic planar metamaterial substrates. *Appl. Phys. Lett.*, 86(12):121108, 2005.
117. I. Gallina, A. Della Villa, V. Galdi, V. Pierro, F. Capolino, S. Enoch, G. Tayeb, and G. Gerini. Aperiodic-tiling-based mushroom-type high-impedance surfaces. *IEEE Antennas Wireless Propagat. Lett.*, 7: 54–57, 2008.
118. F. Przybilla, C. Genet, and T. W. Ebbesen. Enhanced transmission through Penrose subwavelength hole arrays. *Appl. Phys. Lett.*, 89(12):121115, 2006.
119. T. Matsui, A. Agrawal, A. Nahata, and Z. V. Vardeny. Transmission resonances through aperiodic arrays of subwavelength apertures. *Nature*, 446(7135):517–521, 2007.
120. P. Marthandam and R. Gordon. Polarization-controlled diffraction from a quasicrystal nanohole array in a gold film. *J. Opt. A*, 9(12):1140–1143, 2007.
121. J. Bravo-Abad, A. I. Fernández-Domínguez, F. J. Garcia-Vidal, and L. Martín-Moreno. Theory of extraordinary transmission of light through quasiperiodic arrays of subwavelength holes. *Phys. Rev. Lett.*, 99(20):203905, 2007.
122. R. Dallapiccola, A. Gopinath, F. Stellacci, and L. Dal Negro. Quasi-periodic distribution of plasmon modes in two-dimensional Fibonacci arrays of metal nanoparticles. *Opt. Expr.*, 16(8):5544–5555, 2008.
123. M. Duneau and M. Audier. Quasiperiodic packings of fibres with icosahedral symmetry. *Acta Cryst. A*, 55(4):746–754, 1999.
124. W. N. Man, M. Megens, P. J. Steinhardt, and P. M. Chaikin. Experimental measurement of the photonic properties of icosahedral quasicrystals. *Nature*, 436(7053):993–996, 2005.
125. A. Ledermann, L. Cademartiri, M. Hermatschweiler, C. Toninelli, G. A. Ozin, D. S. Wiersma, M. Wegener, and G. von Freymann. Three-dimensional silicon inverse photonic quasicrystals for infrared wavelengths. *Nat. Mater.*, 5(12):942–945, 2006.
126. C. T. Chan. Bandgap engineering – Quasicrystals enter third dimension. *Nat. Photonics*, 1(2):91–92, 2007.
127. R. C. Gauthier and A. Ivanov. Production of quasi-crystal template patterns using a dual beam multiple exposure technique. *Opt. Expr.*, 12(6):990–1003, 2004.
128. R. C. Gauthier and K. W. Mnaymneh. Design of photonic band gap structures through a dual-beam multiple exposure technique. *Opt. Laser Technol.*, 36(8):625–633, 2004.

129. Y. Roichman and D. G. Grier. Holographic assembly of quasicrystalline photonic heterostructures. *Opt. Expr.*, 13(14):5434–5439, 2005.
130. N. D. Lai, J. H. Lin, Y. Y. Huang, and C. C. Hsu. Fabrication of two- and three-dimensional quasi-periodic structures with 12-fold symmetry by interference technique. *Opt. Expr.*, 14(22):10746–10752, 2006.
131. W. D. Mao, G. Q. Liang, H. Zou, R. Zhang, H. Z. Wang, and Z. H. Zeng. Design and fabrication of two-dimensional holographic photonic quasi crystals with high-order symmetries. *J. Opt. Soc. Am. B*, 23(10):2046–2050, 2006.
132. X. Wang and Y. T. Wing. Quasicrystals fabricated by holographic lithography. *Acta Phys. Sin.*, 55(10): 5398–5402, 2006.
133. W. Y. Tam. Icosahedral quasicrystals by optical interference holography. *Appl. Phys. Lett.*, 89(25): 251111, 2006.
134. Y. Yang and G. P. Wang. Realization of periodic and quasiperiodic microstructures with sub-diffraction-limit feature sizes by far-field holographic lithography. *Appl. Phys. Lett.*, 89(11):111104, 2006.
135. N. D. Lai, J. H. Lin, and C. C. Hsu. Fabrication of highly rotational symmetric quasi-periodic structures by multiexposure of a three-beam interference technique. *Appl. Opt.*, 46(23):5645–5648, 2007.
136. J. Xu, R. Ma, X. Wang, and W. Y. Tam. Icosahedral quasicrystals for visible wavelengths by optical interference holography. *Opt. Expr.*, 15(7):4287–4295, 2007.
137. I. Bita, T. Choi, M. E. Walsh, H. L. Smith, and E. L. Thomas. Large-area 3D nanostructures with octagonal quasicrystalline symmetry via phase-mask lithography. *Adv. Mater.*, 19(10):1403–1507, 2007.
138. V. Galdi, V. Pierro, G. Castaldi, I. M. Pinto, and L. B. Felsen. Radiation properties of one-dimensional random-like antenna arrays based on Rudin-Shapiro sequences. *IEEE Trans. Antennas Propagat.*, 53 (11):3568–3575, 2005.
139. R. J. Mailloux, S. G. Santarelli, and T. M. Roberts. Wideband arrays using irregular (polyomino) shaped subarrays. *Electron. Lett.*, 42(18):1019–1020, 2006.
140. T. G. Spence and D. H. Werner. Design of broadband planar arrays based on the optimization of aperiodic tilings. *IEEE Trans. Antennas Propagat.*, 56(1):76–86, 2008.
141. S. Chakraborty, D. G. Hasko, and R. J. Mears. Aperiodic lattices in a high refractive index contrast. System for photonic bandgap engineering. *Microelectro. Eng.*, 73-74:392–396, 2004.
142. S. Chakraborty, M. C. Parker, and R. J. Mears. A Fourier (k-) space design approach for controllable photonic band and localization states in aperiodic lattices. *Photonics Nanostruct.: Fundam. Appl.*, 3 (2-3):139–147, 2005.
143. Y. Q. Wang, S. S. Jian, S. Z. Han, S. Feng, Z. F. Feng, B. Y. Cheng, and D. Z. Zhang. Photonic band-gap engineering of quasiperiodic photonic crystals. *J. Appl. Phys.*, 97(10):106112, 2005.
144. S. P. Gorkhali, J. Qi, and G. P. Crawford. Switchable quasi-crystal structures with five-, seven-, and ninefold symmetries. *J. Opt. Soc. Am. B*, 23(1):149–158, 2006.
145. K. Nozaki, A. Nakagawa, D. Sano, and T. Baba. Ultralow threshold and single-mode lasing in micro-gear lasers and its fusion with quasi-periodic photonic crystals. *IEEE J. Sel. Top. Quantum Electron.*, 9(5):1355–1360, 2003.
146. K. Nozaki and T. Baba. Quasiperiodic photonic crystal microcavity lasers. *Appl. Phys. Lett.*, 84(24): 4875–4877, 2004.
147. S. K. Kim, J. H. Lee, S. H. Kim, I. K. Hwang, Y. H. Lee, and S. B. Kim. Photonic quasicrystal single-cell cavity mode. *Appl. Phys. Lett.*, 86(3):031101, 2005.
148. P. T. Lee, T. W. Lu, and F. M. Tsai. Octagonal quasi-photonic crystal single-defect microcavity with whispering gallery mode and condensed device size. *IEEE Photonics Technol. Lett.*, 19(9-12):710–712, 2007.
149. X. S. Xu, H. D. Chen, and D. Z. Zhang. Enhancement of stimulated emission in 12-fold symmetric quasi-crystals. *Appl. Phys. B*, 89(1):29–34, 2007.

150. J. Romero-Vivas, D. N. Chigrin, A. V. Lavrinenko, and C. M. Sotomayor-Torres. Photonic quasicrystals for application in WDM systems. *Phys. Status Solidi A*, 202(6):997–1001, 2005.
151. J. Romero-Vivas, D. N. Chigrin, A. V. Lavrinenko, and C. M. Sotomayor-Torres. Resonant add-drop filter based on a photonic quasicrystal. *Opt. Expr.*, 13(3):826–835, 2005.
152. Z. F. Feng, X. D. Zhang, Y. Q. Wang, Z. Y. Li, B. Y. Cheng, and D. Z. Zhang. Negative refraction and imaging using 12-fold-symmetry quasicrystals. *Phys. Rev. Lett.*, 94(24):247402, 2005.
153. E. Di Gennaro, D. Morello, C. Miletto, S. Savo, A. Andreone, G. Castaldi, V. Galdi, and V. Pierro. A parametric study of the lensing properties of dodecagonal photonic quasicrystals. *Photonics Nanostruct.: Fundam. Appl.*, 6(1):60–68, 2008.
154. C. Sibilia, M. Bertolotti, M. Centini, G. D'Aguanno, M. Scalora, M. J. Bloemer, and C. M. Bowden. Linear and nonlinear optical properties of quasi-periodic one-dimensional structures. In *Optical Properties of Nanostructured Random Media*, Vol. 82, pp. 63–91, Springer, Berlin, Germany, 2002.
155. P. Xie, Z. Q. Zhang, and X. D. Zhang. Gap solitons and soliton trains in finite-sized two-dimensional periodic and quasiperiodic photonic crystals. *Phys. Rev. E*, 67(2):026607, 2003.
156. R. Lifshitz, A. Arie, and A. Bahabad. Photonic quasicrystals for nonlinear optical frequency conversion. *Phys. Rev. Lett.*, 95(13):133901, 2005.
157. R. T. Bratfalean, A. C. Peacock, N. G. R. Broderick, K. Gallo, and R. Lewen. Harmonic generation in a two-dimensional nonlinear quasi-crystal. *Opt. Lett.*, 30(4):424–426, 2005.
158. B. Freedman, G. Bartal, M. Segev, R. Lifshitz, D. N. Christodoulides, and J. W. Fleischer. Wave and defect dynamics in nonlinear photonic quasicrystals. *Nature*, 440(7088):1166–1169, 2006.
159. R. F. Harrington. *Time-Harmonic Electromagnetic Fields*. McGraw-Hill, New York, 1961.
160. A. Della Villa, F. Capolino, V. Galdi, S. Enoch, V. Pierro, and G. Tayeb. Analysis of modal propagation in slabs of photonic quasicrystals with Penrose-type lattice. In *Proceedings of First International Congress on Advanced Electromagnetic Materials in Microwaves and Optics (Metamaterials 2007)*, Rome, Italy, Oct. 22–26, 2007.
161. D. Sievenpiper, L. Zhang, R. F. J. Bross, N. G. Alexópolous, and E. Yablonovitch. High-impedance electromagnetic surfaces with a forbidden frequency band. *IEEE Trans. Microwave Theory Tech.*, 47 (11):2059–2074, 1999.
162. Ansoft Corporation. *High Frequency Structure Simulator – User's Guide*. Ansoft Corporation, Pittsburgh, PA, 2003.

V

Transmission-Line-Based Metamaterials

28

Fundamentals of Transmission-Line Metamaterials

Ashwin K. Iyer
University of Toronto

George V. Eleftheriades
University of Toronto

28.1 History

28.1.1 Artificial Dielectrics and Metamaterials

The roughly two decades including and following the Second World War saw a flurry of research into the realization and characterization of "artificial dielectrics," low-loss and lightweight structures designed to mimic the macroscopic electromagnetic response of natural dielectrics. These structures consisted of discrete electromagnetic scatterers (e.g., electrically small metallic inclusions in spherical or wire-like form) arranged into periodic, ordered arrays with lattice constants typically in the millimeter or centimeter range; at RF wavelengths, these dimensions are electrically small enough

that the collective macroscopic response of these scatterers is akin to that of the atoms and molecules in a conventional crystal lattice.

The term "artificial dielectric" was, itself, coined by Winston Kock [1–3], who, in the process of developing them to supplant large and bulky aircraft-mounted lens aerials, formulated a comprehensive and general theory illustrating the direct analogies that artificial dielectrics shared with natural media. For example, at wavelengths on the order of the lattice constant, these structures, like solids, exhibited diffraction effects, and at longer wavelengths, an effective refractive index could be defined (see the works listed in Ref. [4] for an excellent review of the early literature in artificial dielectrics).

The term "metamaterials" denotes artificial materials with properties not available, or not easily obtained, in nature. Thus, rather than aiming to mimic the response of conventional materials, metamaterials seek to transcend the gamut of available material properties by applying established artificial-dielectric techniques. Metamaterial research is a relatively new field, spanning just a few years, but already enjoys a great deal of attention in both the physics and engineering communities, which have slowly but largely come to accept their tremendous potential for application, particularly in the variety with a negative-refractive index (described in the following sections).

28.1.2 The Left-Handed Medium

In the late 1960s, the Russian physicist Victor Veselago published a theoretical paper considering the electrodynamics of hypothetical materials in which permeability and permittivity were simultaneously negative [5]. He showed that such media supported wave propagation, but of a very peculiar type: the electric and magnetic field vectors, along with the wave vector, formed a left-handed (LH) triplet instead of a right-handed (RH) triplet. This led him to designate these materials as "left-handed (LH)" (an unfortunate choice in hindsight, as these materials have no necessary relationship to chiral/optically active materials bearing the same designation; nevertheless, the term is nicely consistent with the phenomenology). An interesting consequence of their "left-handedness" is the fact that these waves exhibit phase and group velocities that are oppositely directed, a phenomenon recognized later on in the electrical engineering community as the well-known backward wave. However, Veselago's most striking and far-reaching conclusion was that simultaneously negative material parameters also implied that the refractive index of an isotropic LH material (LHM) would necessarily be *negative*, leading not only to negative refraction (i.e., a negative angle of refraction predicted by Snell's Law) but also the focusing of the rays emanating from a point source across the *planar* interfaces between an LHM slab and the surrounding air. Thus, such a material was, inherently, also a lens.

It should be noted that the ideas of simultaneously negative material parameters, backward waves, and the implications of a negative refractive index had been briefly and variously considered as early as the turn of the twentieth century (see, for example, Refs. [6–8]); however, it was Veselago's general and comprehensive treatment in the open literature, although it lay obscure for over three decades, that laid the foundation for the present intense research activity in metamaterials.

28.1.3 Negative Refraction

It is easily shown through Snell's Law that the angle of refraction inside a medium with a negative refractive index, when interfaced with a medium with a positive refractive index such as air, must also be negative. Consider the homogeneous and isotropic material interface shown in Figure 28.1. Conventional (positive) refraction ($\theta_r > 0$) is shown by case 1. Negative refraction ($\theta_r < 0$) is shown in case 2, in which the normal component of $\mathbf{k}_2$ is directed toward the interface in accordance with the conservation of its tangential component (phase-matching); nevertheless, the power given by the Poynting vector $\mathbf{S}_2$ continues to flow away from the interface. Thus, this simple depiction of negative refraction, combined with the physical requirement for phase matching (conservation

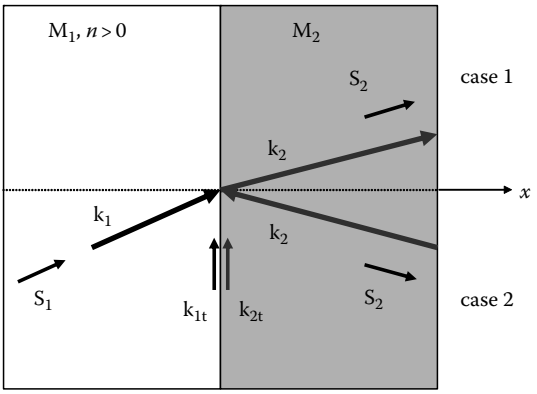

FIGURE 28.1 Phase matching at a two-medium interface. When the medium supports backward waves (case 2), negative refraction takes place. (From Iyer, A.K. and Eleftheriades, G.V., Negative refractive index metamaterials supporting 2D Waves, In *IEEE MTTS International Microwave Symposium Digest*, vol. 2, Seattle, WA, June 2–7, 2002, pp. 1067–1070. With permission.)

of the wave momentum) and power conservation, suggests that wave propagation inside a homogeneous and isotropic medium M_2 exhibiting a negative refractive index necessarily describes a backward wave.

28.1.4 Focusing

By way of the plane-wave expansion of sources, we may consider, as did Veselago, the outcome of placing a point source in front of an LHM slab. As shown in Figure 28.2, the rays emanating from the source are negatively refracted at the lens interfaces and produce foci both inside and outside the slab. It is also clear that the LHM slab is not a lens in the conventional sense, because it does not have a unique optical axis, and as such, cannot focus plane waves impinging on it from infinity.

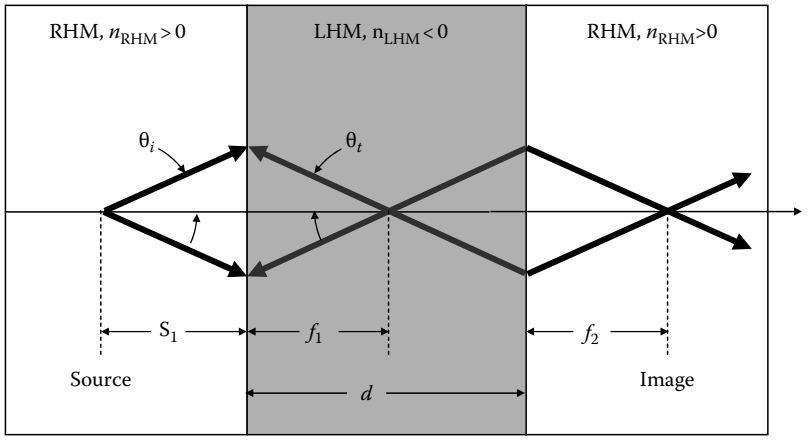

FIGURE 28.2 Rays focused inside and outside an LHM slab embedded in an RH materiel (RHM) by way of negative refraction. (From Iyer, A.K. and Eleftheriades, G.V., Negative-refractive-index transmission line metamaterials, in *Negative Refraction Metamaterials: Fundamental Principles and Applications*, Eleftheriades, G.V. and Balmain, K.G. (Eds.), Wiley-IEEE Press, New York, July 2005, pp. 1–52. With permission.)

However, this can be advantageous for many reasons, including the ability to separately focus two vertically displaced sources. The figure illustrates focusing for a pair of rays incident at a particular angle. Depending on the refractive indices of the LHM slab and the surrounding medium, nonparaxial rays generally experience spherical aberration. However, Veselago showed that an LHM slab embedded in vacuum ($n_{\mathrm{RHM}} = +1$), which possesses a refractive index $n_{\mathrm{LHM}} = -1$, causes all incident and transmitted angles $|\theta_i|$ and $|\theta_t|$ to become equal, and all the constituent rays are focused to the same point. Furthermore, for $n_{\mathrm{LHM}} = -1$, the slab thickness d, source distance s_1, and external focal length f_2 in Figure 28.2 are related through $d = s_1 + f_2$. This means that, as the source is moved toward the first interface, the external focus moves away, and vice versa. It also describes the principle of phase compensation inherent in the LHM slab: the phase lag incurred in the RH material (RHM) regions between the source and external focus is exactly compensated by the phase advance incurred in the LHM slab. In this way, the phase of each propagating spectral component of the source is completely restored at the image plane.

Although its implications are many, the discussion about phase restoration of propagating waves is only half the story of the negative-refractive-index LHM lens. The other half is, of course, the fate of the evanescent spectrum of the source. These spectral components, which contain the finest spatial features of the source, cannot propagate in the medium surrounding the source (vacuum in the present discussion) and instead suffer a rapid decay in their amplitude, evanescing within distances from the source of fractions of a wavelength. In fact, the unavailability of these evanescent components is the reason why no conventional lens, regardless of its transverse size or numerical aperture, can focus the image of a point source to a spot much smaller than a wavelength, a constraint known as the "diffraction limit."

It was not until many decades after Veselago's ideas were published that it was realized that in this respect, too, the LHM flat lens excels. It was shown by John Pendry [12] that the LHM flat lens, when designed to have $\epsilon_{\mathrm{LHM}} = -\epsilon_{\mathrm{RHM}}$ and $\mu_{\mathrm{LHM}} = -\mu_{\mathrm{RHM}}$ (which guarantees that $n_{\mathrm{LHM}} = -n_{\mathrm{RHM}}$ but also that the LHM is impedance-matched the surrounding RHM), is able to restore both the phase of the propagating components of the source and the amplitude of its evanescent components, provided *inter alia* that the lens is placed in the near field of the source. Just as phase compensation implied phase advance in the LHM, amplitude restoration implies the *growth* of the evanescent components inside the LHM, such that their subsequent decay in the RHM restores their amplitude at the focal plane. Thus, an ideal LHM lens designed according to the above (as it turns out, very stringent) constraints, should be able to produce an image of a source down to its finest features. In this sense, the Veselago–Pendry lens is, indeed, a *superlens*. The superlens is especially relevant in this chapter, since it was first realized and experimentally demonstrated using a transmission-line (TL) based metamaterial [13], and a more comprehensive treatment of lenses and superlenses based on TL metamaterials can be found in Chapter 1 of *Applications of Metamaterials*.

28.1.5 Transmission-Line-Based Artificial Dielectric Realizations

The familiar lumped-element model of the transmission line is determined by applying quasi-static field conditions to Maxwell's Equations and obtaining the circuit equations; hence, the analogies between permeability, inductance, permittivity, and capacitance are easily drawn (see Ref. [11] for a concise treatment). That natural media could be represented by distributed L–C circuit networks was recognized in the 1940s by Kron [14], who spatially discretized Maxwell's equations to arrive at Kirchhoff's voltage and current laws for three-dimensional (3D) media, and by Whinnery and Ramo [15], who treated two-dimensional (2D) media. The captivating elegance of the distributed L–C circuit network representation lies in the fact that the capacitive and inductive elements directly determine the constitutive parameters—the desired permittivity and permeability, respectively—of the effective medium.

Of the more exotic (but still conventional) materials examined in the artificial-dielectric community were plasmas. Plasmas are particularly interesting in the present context, because they can possess an isotropic negative permittivity at frequencies below their plasma frequency, ω_p. In 1954, Bracewell proposed that an isotropic plasma could be represented by a TL model in which an inductor was placed in parallel with the shunt capacitance (representing the free-space permittivity), such that their resonant interaction yields a capacitance at high frequencies (representing a positive permittivity) and an inductance at low frequencies (representing a negative permittivity) [16]. Soon afterward, artificial microwave plasmas were realized using arrays of thin metallic wires (see, for example, Ref. [17] and some more recent work in Refs. [18,19]), which can, in the context of Bracewell's work, be seen to inductively load free space.

Attempts at producing magnetic responses using artificial dielectrics were few and far between; first, the main purpose of artificial-dielectrics research was often to design specific refractive indices, of which the simplest property to manipulate was the permittivity; second, the use of simple metallic inclusions could not generate any appreciable magnetic behavior beyond the typical diamagnetic response. However, one very notable suggestion to create unnaturally large artificial permeabilities was offered by Schelkunoff and Friis [20]: it was suggested that a small inductive loop (akin to a magnetic dipole) be loaded in series with a lumped capacitor. The resulting resonant response of the magnetic polarizability results in arbitrarily large positive permeabilities below the series resonance. It would be many years later, however, before the community would reinvent these ideas and see beyond the resonance. An electrodynamic argument for the above results is presented in Section 28.3.

28.1.6 The First LH Metamaterial

In the quest to synthesize a negative-refractive-index LH medium, the problem of realizing an isotropic negative permittivity was not really a problem at all, since there was a well-established electromagnetic precedent in plasmas at frequencies below the plasma frequency. Furthermore, to realize an effectively negative permittivity at microwave frequencies, it was shown that one needed only create a cut off condition by loading free space with thin inductive wires. Realizing an isotropic negative permeability at microwave frequencies, on the other hand, was a much more elusive goal, since such a property does not naturally occur.

In 1999, Pendry independently introduced the split-ring resonator (SRR), a resonant particle amounting, essentially, to Schelkunoff's capacitively-loaded metallic loop [21]. However, the SRR was introduced not only for its strong positive permeability below resonance but also for its strong negative permeability above resonance. The timing of its resurrection was ideal in that the community was searching for an artificial-dielectric "magnetic" microwave plasma that could be assembled with the well-known wire medium to materialize Veselago's vision of the LH medium.

It was not long before the wire and SRR arrays, respectively exhibiting a negative permittivity and negative permeability over a particular range of frequencies, were combined into a composite metamaterial by Shelby, Smith, and Schultz at the University of California in San Diego (UCSD). Needless to say, their landmark experimental work (Ref. [22]) succeeded in verifying the phenomenon of negative refraction and motivated many other important advances in the field of metamaterials. Thus, under the guise of metamaterials, the artificial dielectrics of half a century ago have experienced a remarkable resurgence of interest.

28.2 Transmission-Line Theory of LH Media

Following the seminal and inspiring works of Veselago, Pendry, and the UCSD group, other realizations of the negative-refractive-index LH metamaterial were considered. The development of the wire metamaterial and SRR metamaterial was based on concepts in the physics community, largely

independent of the work in artificial dielectrics carried out in the electrical engineering community many decades earlier. In particular, the very important work done by Kron, Ramo, and Whinnery in the TL modeling of natural dielectric media went unexplored for its potential in describing behaviors not found in nature, in spite of the very hallowed position that TL models occupy in the gamut of electrical engineering techniques. This is mainly because the distributed L–C network representation was meant to be a model for the analysis of natural dielectrics, rather than the synthesis of artificial dielectrics (in fact, it was only four years later that Kock introduced the term "artificial dielectric"). However, distributed L–C networks can be directly synthesized in periodic form using discrete inductors and capacitors; therefore, if TL models of exotic media, like LH media, could be developed, then it is possible that such media could also be realized using TL techniques. The development of such a model is the subject of this section.

28.2.1 Transmission-Line Network Topologies

Let us consider 2D structures for the moment. Kron's work suggests that we may model unbounded wave propagation in conventional dielectrics as TEM propagation in a TL network of the type shown in Figure 28.3a, where the series impedance $Z(\omega)$ and shunt admittance $Y(\omega)$ represent the permeability and permittivity, respectively, through the following relations [11]:

$$\mu(\omega) = \frac{1}{g} \cdot \frac{Z(\omega)/d}{j\omega} \tag{28.1}$$

$$\epsilon(\omega) = g \cdot \frac{Y(\omega)/d}{j\omega}. \tag{28.2}$$

Here, g is a constant that enables the comparison of the characteristic impedance of the TL network Z_0 to the wave impedance of the effective medium η as follows:

$$Z_0 = \sqrt{\frac{Z(\omega)}{Y(\omega)}} = g\sqrt{\frac{\mu(\omega)}{\epsilon(\omega)}} = g\eta. \tag{28.3}$$

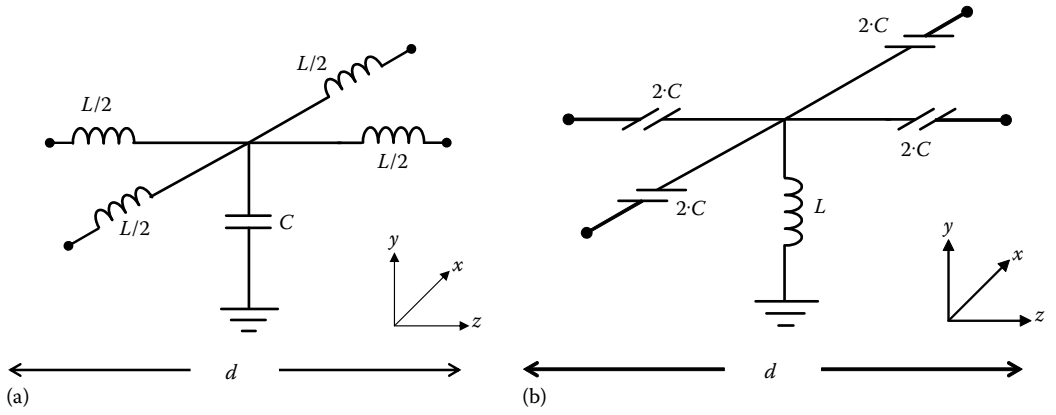

FIGURE 28.3 2D TL unit cells describing media with (a) simultaneously positive, constant parameters and (b) simultaneously negative, dispersive parameters. (From Iyer, A.K. and Eleftheriades, G.V., Negative-refractive-index transmission line metamaterials, in *Negative Refraction Metamaterials: Fundamental Principles and Applications*, Eleftheriades, G.V. and Balmain, K.G. (Eds.), Wiley-IEEE Press, New York, July 2005, pp. 1–52. With permission.)

It is clear that Kron's topology for conventional dielectrics with $Z(\omega) = j\omega L$ and $Y(\omega) = j\omega C$ results in positive, constant material parameters, as predicted. However, this entitlement to specify the permeability and permittivity through the total series inductance and shunt capacitance prompts us to ask whether these parameters can be made negative. Indeed, from the perspective of impedance and admittance, negating $j\omega L$ and $j\omega C$ simply exchanges their reactive and susceptive roles (due to the relationship $-j = 1/j$), so that the series inductor L becomes a frequency-dependent series capacitor $C(\omega)$, and the shunt capacitor C becomes a frequency-dependent shunt inductor $L(\omega)$. The unit cell of the resulting dual structure is shown in Figure 28.3b; its topology is immediately recognized as that of a 2D high-pass filter network, for which the series impedance and shunt admittance are $Z(\omega) = (j\omega C)^{-1}$ and $Y(\omega) = (j\omega L)^{-1}$ respectively.

In the continuous limit (i.e., $d/\lambda \to 0$), the voltage wave equation (V_y between the grid lines and ground) is

$$\frac{\partial^2 V_y}{\partial x^2} + \frac{\partial^2 V_y}{\partial z^2} + \beta^2 V_y = 0, \quad \beta = \pm\sqrt{-Z'Y'}, \tag{28.4}$$

where the propagation constant β is expressed in terms of the total distributed series impedance $Z' = Z(\omega)/d$ and shunt admittance $Y' = Y(\omega)/d$ in each case. The ω–β dispersion curves of Figure 28.4 represent the dispersion relations of the two unit-cell topologies of Figure 28.3 and depict the variation of the propagation constant along a particular axis of propagation in the x–z plane as a function of frequency. The phase velocity at a particular coordinate (ω_0, β_0) can be obtained as the magnitude of the slope of the line from the origin to that point or, equivalently, as the ratio $v_\phi = \omega_0/\beta_0$. The group velocity is defined as the slope of the tangent to the ω–β curve at (ω_0, β_0), taken in the direction of increasing frequency, which is given by $v_g = (\partial\beta/\partial\omega)^{-1}$.

28.2.2 The Conventional (Low-Pass) RH Topology

It is evident from Figure 28.4a that the propagation constant of conventional isotropic RHM, modeled as in Figure 28.3a by a distributed series inductance and shunt capacitance ($L' = L/d$ [H/m]

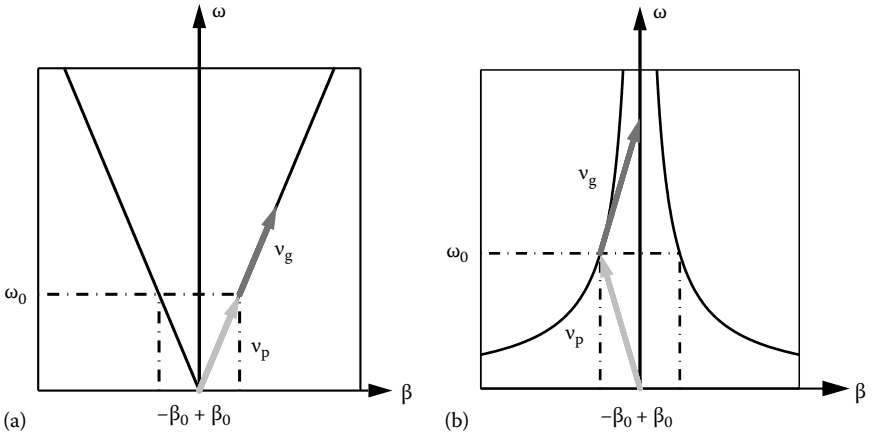

FIGURE 28.4 Dispersion relations for media with (a) simultaneously positive, constant parameters and (b) simultaneously negative, dispersive parameters. (After Iyer, A.K. and Eleftheriades, G.V., Negative-refractive-index transmission-line metamaterials, in *Negative Refraction Metamaterials: Fundamental Principles and Applications*, Eleftheriades, G.V. and Balmain, K.G. (Eds.), Wiley-IEEE Press, New York, July 2005, pp. 1–52.)

and $C' = C/d$ [F/m], respectively), varies proportionally with frequency, which is the characteristic of conventional dielectrics at low frequencies. It is also clear from Figure 28.4a that the resulting phase and group velocities (v_p and v_g, respectively) are parallel and equal (assuming it is also a dispersionless medium) and are given by

$$v_p = \frac{\omega}{\beta} = \frac{1}{\sqrt{L'C'}} = \left(\frac{\partial\beta}{\partial\omega}\right)^{-1} = v_g. \tag{28.5}$$

The choice of the positive root in Equation 28.5 or, equivalently, the positive branch of the ω–β curve, is a convention that establishes the sign of the phase velocity relative to the direction of positive power flow (or group velocity in this case) away from the source. According to this convention, the phase velocity in conventional RH media is positive, and the refractive index, which can be defined as the ratio between the speed of light in vacuum and the phase velocity in the medium, is also positive:

$$n = \frac{c}{v_p} = \frac{\sqrt{L'C'}}{\sqrt{\mu_0\epsilon_0}}. \tag{28.6}$$

The wave impedance of the effective medium is positive and is related to the characteristic impedance of the lossless TL network as follows:

$$\eta_{RH} = \sqrt{\frac{\mu(\omega)}{\epsilon(\omega)}} = \frac{1}{g}\sqrt{\frac{L'}{C'}} = Z_0/g. \tag{28.7}$$

28.2.3 The Dual (High-Pass) LH Topology

Let us now consider the dual network of Figure 28.3b. Applying Equations 28.1 and 28.2 to obtain the effective permittivity and permeability represented by this topology results in

$$\mu(\omega) = \frac{1}{g}\cdot\frac{1/j\omega Cd}{j\omega} = -\frac{1}{g}\cdot\frac{1}{\omega^2 C'} \tag{28.8}$$

$$\epsilon(\omega) = g\cdot\frac{1/j\omega Ld}{j\omega} = -g\cdot\frac{1}{\omega^2 L'}, \tag{28.9}$$

where the distributed parameters $L' = Ld$ and $C' = Cd$ are defined in the peculiar units [H·m] and [F·m], respectively; their meaning is intuitively clear when the parameters are instead represented as $1/L' = (1/L)/d$ and $1/C' = (1/C)/d$.

Thus, in the case of the dual network, the effective material parameters are both negative and functions of frequency. This type of frequency dispersion turns out to be necessary, so as to avoid the violation of causality that would result from negative, time-averaged, stored electric and magnetic energies [4,5].

The propagation constant associated with the dual structure, found through the application of Equations 28.8 and 28.9, boasts an inverse relationship with the frequency that is consistent with its high-pass nature:

$$\beta = -\sqrt{-Z'Y'} = -\frac{1}{\omega\sqrt{L'C'}}. \tag{28.10}$$

Its corresponding ω–β curve in Figure 28.4b illustrates that the dual medium's phase and group velocities are antiparallel:

$$v_p = \frac{\omega}{\beta} = -\omega^2\sqrt{L'C'} = -\left(\frac{\partial\beta}{\partial\omega}\right)^{-1} = -v_g, \tag{28.11}$$

where the choice of the negative root in Equation 28.11 has resulted in a peculiar negative phase velocity, but has, more importantly, ensured a positive group velocity corresponding to the direction of power flow, in accordance with the adopted convention. This implies that the index of refraction must also be negative:

$$n = \frac{c}{v_p} = \frac{-\sqrt{\mu(\omega)\epsilon(\omega)}}{\sqrt{\mu_0\epsilon_0}} = -\frac{1}{\omega^2\sqrt{L'C'\mu_0\epsilon_0}}. \tag{28.12}$$

However, the wave impedance of the effective medium is still positive and, in fact, identical to that corresponding to the conventional network topology:

$$\eta_{LH} = \sqrt{\frac{\mu(\omega)}{\epsilon(\omega)}} = \frac{1}{g}\sqrt{\frac{L'}{C'}} = Z_0/g. \tag{28.13}$$

This suggests that such dual networks may be impedance-matched to their conventional counterparts and brings forward the notion of an interface between the two types of effective media. These interfaces are of interest when arrangements for negative refraction and focusing are considered.

The antiparallel relationship between the phase and group velocities was suggested in the previous discussion on the backward wave in the context of negative refraction and is, moreover, consistent with the well-known fact that periodic high-pass filters support a fundamental backward-wave spatial harmonic [23]. Thus, the simple dual high-pass network provides a simultaneously negative effective permeability and permittivity, the necessary and sufficient conditions for left-handedness and negative refraction, as well as the numerous intriguing applications in lensing and components emerging therefrom.

28.3 Electrodynamics of Negative Material Parameters

The properties of conventional materials are the macroscopic interpretation of field interactions at the atomic or molecular level. The electrodynamics of materials are quite well understood by classical arguments treating electrons in an ac electric field as driven, damped oscillators; although an understanding of the magnetic properties of materials strictly requires a quantum mechanical treatment, classical models of ac magnetic fields causing electrons to orbit their nuclei, thereby yielding a magnetic moment, may apply under certain circumstances, particularly in the analysis of metamaterials, in which magnetic moments are produced directly through current loops.

This section begins with a review of the standard methods of determining permittivity and permeability, followed by a set of analogous arguments that show, intuitively, how negative permittivity and permeability may come about.

28.3.1 Determination of Permittivity

The application of an electric field to a dielectric medium results in the polarization of its constituent positively and negatively charged particles, which can be modeled by an equivalent dipole whose charges $+q$ and $-q$ are displaced by a distance l_{av}, yielding an electric dipole moment $dp = ql_{av}$. When all the dipoles in the medium (volume density of electric dipoles N_e) are aligned, the total dipole moment per unit volume can be expressed as $p = N_e dp = N_e q l_{av}$. This is illustrated in Figure 28.5.

One of the standard methods of determining the macroscopic permittivity of homogeneous dielectrics is to measure the change in capacitance that results when a sample of the dielectric is inserted between the plates of a parallel-plate capacitor. Figure 28.6 illustrates the arrangement,

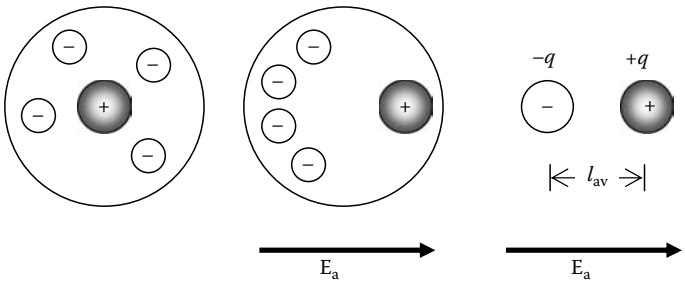

FIGURE 28.5 Polarization due to the application of an electric field $\mathbf{E_a}$, modeled as an equivalent electric dipole consisting of charges $\pm q$ separated by a distance l_{av}.

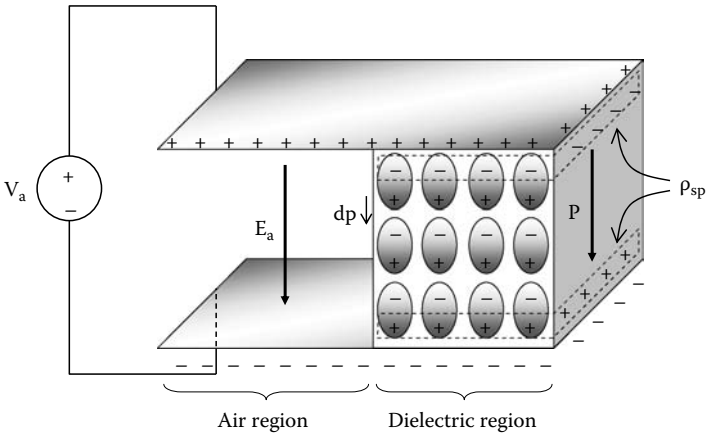

FIGURE 28.6 Determination of the permittivity of a dielectric inserted into a parallel-plate capacitor by measuring the change in capacitance. The source maintains a voltage $\mathbf{V_a}$ across the plates.

which consists of a partially filled parallel-plate capacitor, whose plates are maintained at a potential difference V_a by an external voltage source. The purpose of the vacuum region within the plates is to allow the externally applied field, $\mathbf{E_a}$, to be clearly discerned. This applied field polarizes the bound charges in the dielectric (which we assume can be aligned) so that each dipole has an average dipole moment of dp. However, the adjacent polarized charges oppose each other and so cancel each other in the dielectric region. What remain are the bound charges on the surface of the dielectric, which can be described by a bound surface charge ρ_{sp} [C/m^2]; this is numerically equal to the net electric polarization $\mathbf{P}$, which is directed with the applied field: $\mathbf{D} = \epsilon_0\mathbf{E_a} + \mathbf{P}$. The permittivity of the dielectric ϵ_S [F/m] is defined by the relationship $\mathbf{D} = \epsilon_S\mathbf{E_a}$ and can be obtained by expressing $\mathbf{P}$ in terms of the applied field, $\mathbf{E_a}$, as follows: $\mathbf{P} = \epsilon_0\chi_e\mathbf{E_a}$, where the constant of proportionality χ_e is the electric susceptibility. Thus, $\epsilon_S = \epsilon_0(1 + \chi_e)$.

28.3.2 Determination of Permeability

The atomic model of a magnetic material can be regarded to consist of a negatively charged electron orbiting a positively charged nucleus, which can, in turn, be perceived as a current flowing around a loop of area ds (in the direction opposite to the electron motion since current is defined as the direction of positive-charge flow), as shown in Figure 28.7. This appears as a small magnetic dipole

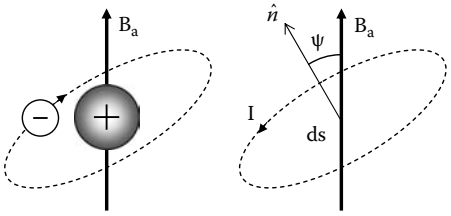

FIGURE 28.7 Magnetization due to the application of a magnetic flux $\mathbf{B_a}$, modeled as an equivalent magnetic dipole consisting of a current I flowing around a loop of area ds.

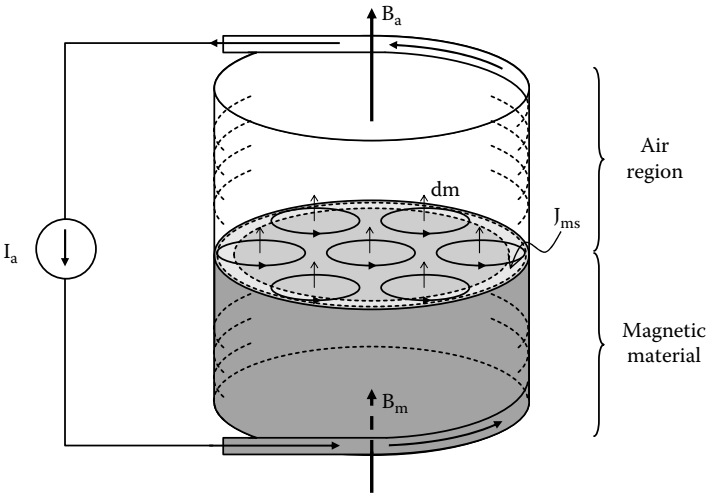

FIGURE 28.8 Determination of the permeability of a magnetic material inserted into a solenoid by measuring the change in inductance. The source maintains a current $\mathbf{I_a}$ in the windings.

with a magnetic dipole moment dm = Ids. The application of a magnetic field, or equivalently, a magnetic flux density $\mathbf{B_a}$, aligns the magnetic dipoles with the fields, such that the total magnetic dipole moment is in the direction of the applied field and given by a net magnetization $\mathbf{M} = N_m\mathbf{dm_{av}} = N_m(I\mathbf{ds})_{\text{av}}$. In analogy to the partially dielectric-filled parallel-plate capacitor of Figure 28.6, consider the solenoid of Figure 28.8 partially filled with a magnetic material whose permeability we would like to measure. The current source maintains a current I_a in the solenoid windings; this current establishes the applied magnetic field $\mathbf{H_a}$, which we associate with total magnetic fluxes $\mathbf{B_a}$ in the vacuum region and $\mathbf{B_m}$ in the magnetic-material region. The applied field induces small current loops (magnetic moments **dm**). However, the adjacent currents between loops travel in opposite directions and so cancel each other out. The remaining currents are confined to the outer edge of the solenoid and can be described by a surface current density $\mathbf{J_{ms}} = \mathbf{M} \times \hat{n}|_{\text{surface}}$ [A/m], which is related to a bound volume current density $\mathbf{J_m} = \nabla \times \mathbf{M}$ [A/m^2]. The total magnetic flux in the magnetic-material region can be expressed as $\mathbf{B_m} = \mu_0(\mathbf{H_a} + \mathbf{M})$, and we can define the permeability of the material μ_S through the relationship $\mathbf{B_m} = \mu_S\mathbf{H_a}$ by expressing the proportionality between the net magnetization $\mathbf{M}$ and the applied magnetic field $\mathbf{H_a}$, $\mathbf{M} = \chi_m\mathbf{H_a}$, where χ_m is the magnetic susceptibility. Thus, $\mu_S = \mu_0(1 + \chi_m)$ [H/m].

28.3.3 Positive Permittivity

Since the polarization vector **P** in polarizable dielectrics in the quasi-static limit is aligned with, and in phase with, the applied field $\mathbf{E_a}$, the surface charges appearing on the upper and lower faces of the dielectric (coming into contact with the plates of the capacitor) neutralize some of the charge on the capacitor plates, which tends to reduce the field in the dielectric region. To maintain a field of $\mathbf{E_a}$, the source V_a must deposit more charge on the plates, which implies that the dielectric permits us to store more energy in the system. The positive permittivity $\epsilon_S = \epsilon_0(1 + \chi_e)$ is guaranteed by the positive electric susceptibility, arising from a positive **P** aligned with, and in phase with, $\mathbf{E_a}$. This is seen by writing Ampère's Law in the dielectric in time-harmonic differential form:

$$\nabla \times \mathbf{H} = j\omega\mathbf{D} = j\omega\epsilon_0\mathbf{E_a} + j\omega\mathbf{P} = j\omega\epsilon_0\mathbf{E_a} + j\omega\epsilon_0\chi_e\mathbf{E_a} = j\omega\epsilon_S\mathbf{E_a}. \tag{28.14}$$

28.3.4 Negative Permittivity

As noted previously, a negative permittivity is not uncommon in nature; plasmas (electrically neutral collections of mobile charged particles) can possess isotropic, naturally negative permittivities below their plasma frequency, ω_P. Common examples of plasmas include the Earth's ionosphere and noble metals at ultraviolet wavelengths.

In an electrical plasma, the free electrons drift according to a drift current density $\mathbf{J_{drift}}$. Assuming the plasma is collisionless, and that only the electrons are mobile,

$$\mathbf{J_{drift}} = N_e(-e)\mathbf{v}, \tag{28.15}$$

where N_e, $-e$, and **v** are the electron density, electron charge, and electron drift velocity, respectively. Now, $\mathbf{F} = \mathrm{m}_e\mathbf{a} = (-e)\mathbf{E_a}$, where m_e is the electron mass, and **a** is the acceleration given by the derivative of **v**, $\mathbf{a} = j\omega\mathbf{v}$. This implies that

$$\mathbf{J_{drift}} = N_e(-e)\frac{\mathbf{a}}{j\omega} = \frac{N_e(-e)}{j\omega}\frac{\mathbf{F}}{\mathrm{m}_e} = \frac{N_e(-e)}{j\omega}\frac{-e\mathbf{E_a}}{\mathrm{m}_e} = \frac{N_e e^2}{j\omega\mathrm{m}_e}\mathbf{E_a}. \tag{28.16}$$

Therefore, whereas the displacement current $\mathbf{J_{disp}} = j\omega\mathbf{D}$ lags $\mathbf{E_a}$ in quadrature, the drift current $\mathbf{J_{drift}}$ evidently leads $\mathbf{E_a}$ in quadrature; thus, the two processes are out of phase with each other. Writing Ampère's Law in the plasma,

$$\nabla \times \mathbf{H} = j\omega\mathbf{D_a} + \mathbf{J_{drift}} = j\omega\epsilon_0\mathbf{E_a} + \frac{N_e e^2}{j\omega\mathrm{m}_e}\mathbf{E_a} = j\omega\left(\epsilon_0 - \frac{N_e e^2}{\omega^2\mathrm{m}_e}\right)\mathbf{E_a}. \tag{28.17}$$

Thus, the effective permittivity inside the plasma is given by

$$\epsilon_S = \epsilon_0\left(1 - \frac{\omega_p^2}{\omega^2}\right), \quad \omega_p = \sqrt{\frac{N_e e^2}{\epsilon_0\mathrm{m}_e}}. \tag{28.18}$$

This permittivity is negative for $\omega < \omega_p$. An intuitive explanation based on Figure 28.6 can also be made [24] and is shown in Figure 28.9. The motion of the negative charges alone in the plasma has been represented more generally in Figure 28.9 as the opposite motion of both negative and positive charges. Keeping in mind that the charges in the plasma are free charges, the 180-degree phase relationship between the $\mathbf{J_{disp}}$ and $\mathbf{J_{drift}}$ terms suggests that the plasma charges drift opposite to the tendency of the applied field to produce a displacement. However, since the charges are not bound, they will naturally deposit themselves on the capacitor plates, which tends to increase the field between the plates. In order to maintain a field of $\mathbf{E_a}$ between the plates, the source $\mathbf{V}_a$ must

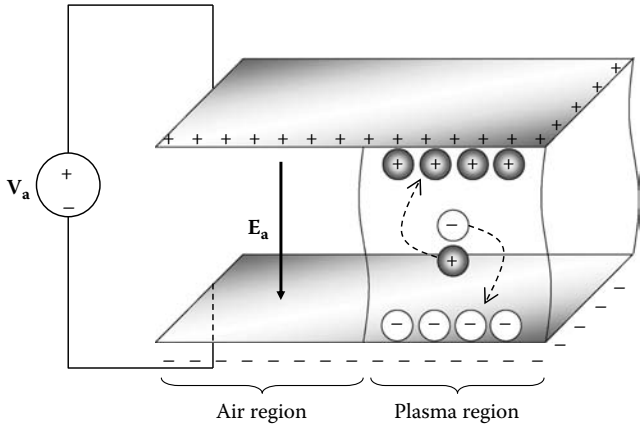

FIGURE 28.9 Free charges in a plasma (motion of mobile negative charges generally represented as opposite motion of both negative and positive charges) drift opposite to the applied field and enhance the field between the plates, requiring the source to absorb charge in order to maintain a voltage $\mathbf{V_a}$.

actually absorb the excess charge. If the drift current deposits a charge on the plates equal to that initially supplied by the source to maintain $\mathbf{E}_a$, then the source must withdraw all of its charge, since this field is now being supported entirely by the plasma. In this case, the source can be removed, and the plasma is in a self-sustained state of oscillation (at its plasma frequency ω_p, where $\epsilon_S = 0$). Below its plasma frequency, the plasma supplies more charge to the plates than does the source, and to maintain the field $\mathbf{E_a}$, the source must actually supply a negative charge. In the last two cases, the medium appears to the source much unlike a capacitor; in fact, it behaves very much akin to an inductor, returning a current to the source under Lenz's Law when excited, a result that is reminiscent of Bracewell's conclusion. This is explicitly seen by considering the effect on the TL model shunt admittance, Y, when a capacitor (with a parallel-plate area-to-height ratio $1/q$) is filled with a plasma whose permittivity is given by Equation 28.18. Therefore,

$$Y = \frac{j\omega\epsilon_S}{q} = \frac{j\omega\epsilon_0}{q}\left(1 - \frac{\omega_p^2}{\omega^2}\right) = j\omega\epsilon_0 q + \frac{\omega_p^2\epsilon_0 q}{j\omega}, \tag{28.19}$$

in which Bracewell's parallel shunt connection of a capacitor $C_p = \epsilon_0 q$ (representing free space) and an inductor $L_p = 1/\epsilon_0\omega_p^2 q$ (representing the plasma) is evident.

28.3.5 Positive Permeability

The sign of the magnetic susceptibility χ_m, hence the sign of the magnetization vector $\mathbf{M}$, decides whether the permeability of a magnetic material is less than or greater than μ_0. Materials in which μ_S is (typically only slightly) greater than μ_0 are either paramagnetic or antiferromagnetic; materials in which μ_S is less than μ_0 are called diamagnetic. For simplicity, let us consider an artificial magnetic medium consisting of electrically very small conducting loops, each as shown in Figure 28.10a, and imagine that such a medium now partially fills the solenoid of Figure 28.8. For generality, the series impedance around each loop (which may include its parasitics and any other lumped loading) has been represented as a single lumped Z_L and indicated in the diagram by a square block. Now, the magnetic dipole moment of a single loop is $\mathbf{dm} = I\mathbf{ds}$. If the loops are assumed circular, then $\mathbf{ds} = \pi r_0^2\hat{\mathbf{n}}$, where r_0 is the radius and $\hat{\mathbf{n}}$ is a unit vector normal to the plane of the loop defined according to

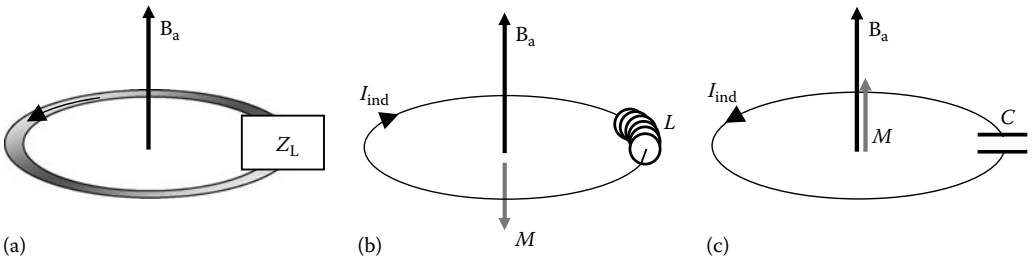

FIGURE 28.10 (a) Generalized magnetic medium whose elemental particle consists of a loop whose total series impedance is lumped into Z_L; (b) Field orientations for $Z_L > 0$ (inductive loop); and (c) Field orientations for $Z_L < 0$ (capacitive loop).

the right-hand rule. Thus, the magnetization produced by a single loop is $\mathbf{dm} = I\pi r_0^2\hat{\mathbf{n}} = \chi_m \mathbf{H_a}/N_m = \chi_m \mathbf{B_a}/\mu_0 N_m$, which can be rewritten as $\mu_0 I\pi r_0^2\hat{\mathbf{n}} = \chi_m \mathbf{B_a}$. Now, Faraday's Law gives

$$\oint \mathbf{E}\cdot\mathbf{dl} = -\frac{d}{dt}\iint \mathbf{B}\cdot\mathbf{ds} = -\frac{d}{dt}(B_a\pi r_0^2) = V_{emf,\,ind}. \tag{28.20}$$

In time-harmonic differential form, $-j\omega B_a\pi r_0^2 = V_{emf,ind} = IZ_L$. However, substituting $B_a = \mu_0 N_m I\pi r_0^2/\chi_m$, we arrive at the following expression for the magnetic susceptibility:

$$Z_L = \frac{-j\omega\mu_0 N_m(\pi r_0^2)^2}{\chi_m} \Rightarrow \chi_m = \frac{-j\omega\mu_0 N_m(\pi r_0^2)^2}{Z_L}. \tag{28.21}$$

This yields a magnetization contribution **dm** given by

$$\mathbf{dm} = \chi_m \mathbf{H_a}/N_m = -j\omega(\pi r_0^2)^2\mu_0 \mathbf{H_a}/Z_L = -j\omega(\pi r_0^2)^2 \mathbf{B_a}/Z_L. \tag{28.22}$$

When considered as a sum over N_m loops, we have a total magnetization

$$\mathbf{M} = -j\omega(\pi r_0^2)^2 \mathbf{B_a} N_m/Z_L. \tag{28.23}$$

This corresponds to an effective permeability given by

$$\mu_S = \mu_0(1 - j\omega\mu_0(\pi r_0^2)^2 N_m/Z_L). \tag{28.24}$$

Here, the negative sign in the second term is indicative of Lenz's Law in action. However, since the sign of $\mathbf{M}\cdot\mathbf{B_a}$ is also dependent on the sign of $X_L = Z_L$, we shall examine the cases of $X_L > 0$ and $X_L = Z_L < 0$ separately.

28.3.5.1 Case 1: Inductive Loop

The condition $X_L > 0$ implies that the loop impedance is inductive. If we let $Z_L = j\omega L$, then

$$dm = \frac{-j\omega(\pi r_0^2)^2 B_a}{j\omega L} = \frac{-B_a}{L}(\pi r_0^2)^2. \tag{28.25}$$

Summing over N_m such loops, we have

$$\mathbf{M} = \frac{-\mathbf{B_a} N_m}{L}(\pi r_0^2)^2 \tag{28.26}$$

and

$$\mu_S = \mu_0 \left(1 - \mu_0 N_m \frac{(\pi r_0^2)^2}{L}\right). \tag{28.27}$$

Equation 28.26 suggests that **M** opposes $\mathbf{B_a}$. In this case, the fields in the vicinity of the loop are as shown in Figure 28.10b. However, $|\mathbf{M}|$ is typically much smaller than $|\mathbf{B_a}|$, and so μ_S is only marginally smaller than μ_0 as a result of **M** being negative. This can be shown by further expanding the loop inductance L in terms of the loop area πr_0^2. This is a typical, and typically weak, diamagnetic response, commonly seen in artificial dielectrics with metallic inclusions. In this case, the magnetic surface current produced due to the magnetization **M** opposes the source current I_a, and the source must deliver more current to maintain the field in the material.

28.3.5.2 Case 2: Capacitive Loop

The condition $X_L < 0$ implies that the loop impedance is capacitive. If we let $Z_L = 1/j\omega C$, then

$$\mathbf{dm} = \frac{-j\omega(\pi r_0^2)^2 \mathbf{B_a}}{1/j\omega C} = \omega^2 \mathbf{B_a} C(\pi r_0^2)^2. \tag{28.28}$$

Summing over N_m such loops, we have

$$\mathbf{M} = \omega^2 \mathbf{B_a} N_m C(\pi r_0^2)^2 \tag{28.29}$$

and

$$\mu_S = \mu_0(1 + \omega^2 \mu_0 N_m C(\pi r_0^2)^2). \tag{28.30}$$

Equation 28.29 suggests that **M** and $\mathbf{B_a}$ are codirected. In this case, the fields are as shown in Figure 28.10c. Again, $|\mathbf{M}|$ is typically much smaller than $|\mathbf{B_a}|$, so μ_S is only slightly larger than μ_0 due to the positive nature of **M**. This is typical of a paramagnetic response, for which the source must absorb the surface current to maintain $\mathbf{B_a}$.

28.3.6 Negative Permeability

It is clear that the permeability typically remains near μ_0 in both of the previous cases. Here, following the suggestion of Schelkunoff and Friis [20], we consider a resonant case.

28.3.6.1 Case 3: Capacitively Loaded Inductive Loop

Let us now consider the loop to possess a total impedance with both inductive and capacitive parts, such that Z_L can be expressed as $Z_L = j\omega L + 1/j\omega C = j\omega L(1 - \omega_0^2/\omega^2)$, where $\omega_0 = 1/\sqrt{LC}$ is the angular loop resonance frequency. Therefore,

$$\mathbf{dm} = \frac{-j\omega(\pi r_0^2)^2 \mathbf{B_a}}{j\omega L(1 - \omega_0^2/\omega^2)} = \frac{-\mathbf{B_a}}{L}(\pi r_0^2)^2 \frac{1}{(1 - \omega_0^2/\omega^2)}. \tag{28.31}$$

Summing over N_m loops,

$$\mathbf{M} = -\frac{\mathbf{B_a} N_m (\pi r_0^2)^2}{L(1 - \omega_0^2/\omega^2)} \tag{28.32}$$

and

$$\mu_S = \mu_0 \left(1 - \frac{\mu_0 N_m (\pi r_0^2)^2}{L(1 - \omega_0^2/\omega^2)}\right). \tag{28.33}$$

Now, the sign of $\mathbf{M} \cdot \mathbf{B_a}$ in Equation 28.32 varies with frequency. For $\omega >> \omega_0$, $\mathbf{M} \cdot \mathbf{B_a}$ is negative, reducing to case 1, and for $\omega << \omega_0$, $\mathbf{M} \cdot \mathbf{B_a}$ is positive, reducing to case 2. However, as $\omega \to \omega_0^-$, $\mu_S \to +\infty$. That is, $\mathbf{M} \cdot \mathbf{B_a}$ is strongly positive, and the source is required to supply a nearly infinite current orbiting in the clockwise direction to maintain the field. As $\omega \to \omega_0^+$, $\mu_S \to -\infty$. In this case, $\mathbf{M}$ is strongly negative, and the source supplies a nearly infinite current orbiting the loop in a clockwise direction. It should be added that the currents are infinite because of the absence of loss in the development, which are easily lumped directly into Z_L.

In the frequency region in which $\mu_S < 0$, $\mathbf{M}$ and $\mathbf{B_a}$ are oppositely directed, but $|\mathbf{M}| > |\mathbf{B_a}|$. This implies that the magnitude of the magnetic surface current due to M is greater than the current being supplied by the source. In order to maintain the field, the source must actually generate a stronger positive current; for example, when the surface current produced by $\mathbf{M}$ becomes equal to the source current, the only way for the source to maintain $\mathbf{B_a}$ is to double its supplied current. In this case, the source appears to "charge" the system. Thus, in the $\mu_S < 0$ region, the system of loaded loops inside the solenoid behaves like a charging capacitor, wherein the source continuously couples energy into the loops.

28.3.7 Equivalent Circuit

In Bracewell's equivalent circuit for a plasma, the inductive component of the shunt branch was revealed by replacing the vacuum inside the distributed capacitance representing free-space propagation with a plasma. In analogy, we now consider the effect of filling the free-space distributed series inductor with a magnetic material possessing the permeability function of Equation 28.33. Representing the TL equivalent lumped series impedance as $Z = j\omega\mu_S d/q$, where $1/q$ is a factor dependent on the geometry of the equivalent TL system and d is the unit-cell length, we have

$$\begin{aligned} Z &= \frac{j\omega\mu_0 d}{q}\left(1 - \frac{\mu_0 N_m(\pi r_0^2)^2}{L(1-\omega_0^2/\omega^2)}\right) \\ &= \frac{j\omega\mu_0 d}{q} + \frac{\omega^2 N_m(\mu_0\pi r_0^2)^2 d/q}{j\omega L + 1/j\omega C} \\ &= j\omega L_s - \frac{(j\omega L_M)^2}{Z_L}. \end{aligned} \tag{28.34}$$

The new symbols introduced in the last line of Equation 28.34 reveal that Z is, in fact, the image impedance of the free-space lumped series inductance $L_s = \mu_0 d/q$ coupled to the ring impedance $Z_L = j\omega L + 1/j\omega C$ via a mutual inductance $L_M = \mu_0\pi r_0^2\sqrt{N_m d/q}$. Thus, when this system of loaded rings is placed in free space (with a permittivity represented by the shunt capacitance C_s and neglecting the electrical response, if any, of the rings), the TL equivalent circuit representing propagation through the system is as shown in Figure 28.11.

28.4 Transmission-Line Metamaterials and the Split-Ring Resonator Connection

28.4.1 The Recipe for Broadband, Low-Loss Left-Handedness

Figure 28.11 is a variant of the TL model of the wire/SRR medium presented in [25,26], in which the shunt branch additionally contains an inductive contribution, serving to negate the permittivity. In the last reference, it was shown that the frequency region in which the effective permeability function of Equation 28.34 assumed negative values corresponds the frequency region in which the series branch of Figure 28.11 is capacitive, as dictated by the TL model of NRI metamaterials. However,

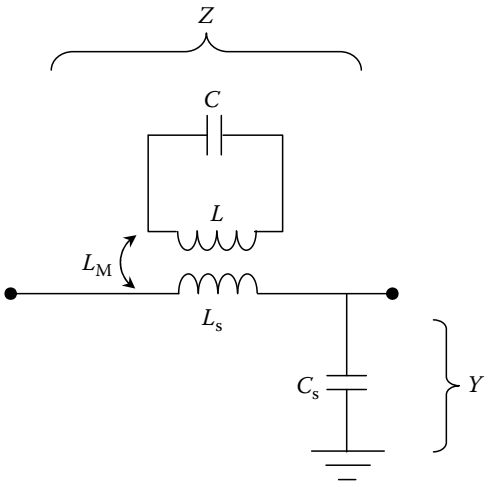

FIGURE 28.11 TL equivalent circuit representing a medium achieving a negative permeability through an L–C resonance mechanism.

this necessary series capacitance is obtained between two (often closely spaced) resonances, which implies that the mechanism by which this is achieved is inherently narrowband and lossy unless steps are taken to maximize the available bandwidth. This is very much unlike the TL metamaterial, which exhibits inherently broadband and low-loss negative material parameters, in spite of its L–C topology, and so it should be interesting to consider how or whether the two can be related.

The TL model of conventional dielectrics possesses a "low-pass" topology, and the dual LH model possess a "high-pass" topology. However, it is clear that neither ideal transmission line possesses any cutoff frequency; in fact, in this "continuous" limit, they are infinitely broadband, as shown in Section 28.2. This attribute is a result of the fact that the individual L–C resonators (unit cells) comprising the lines are so tightly coupled by virtue of electrical connection to their adjacent counterparts that their local resonance property is converted into a propagation phenomenon. To illustrate, consider the one-dimensional (1D) periodic array of loops (period d) shown in Figure 28.12a. As before, the loops possess a self-inductance L and are loaded by a lumped capacitance C described by a total loop impedance Z_L, and they can, without too great a loss of generality, be regarded as circular loops of radius r_0. As discrete resonators, the loops provide a negative effective permeability within a well-defined (typically narrow) bandwidth. However, consider the limit in which $d \to 2r_0$; in this limit, the loops can no longer be regarded as discrete resonators since their mutual coupling becomes significant. Indeed, as shown in Figure 28.12b, it can be appreciated intuitively that the isolated loops become conjoined and form what appears to be an LH transmission line, where the capacitive loading C_0 appears in series and the inductance of the loops $L_0 = L/2$ appears in shunt. Thus, it appears that it may be possible to produce left-handedness from capacitively loaded loops alone, provided that the loops are tightly coupled to each other. This conclusion, as well as portions of the following analysis, can be found in Ref. [27].

As an approximation to the full mutual coupling problem implicating all loops in the infinite 1D array, we apply here a nearest-neighbor approximation that describes the magnetic moment of the nth loop, m_n, in terms of the (quasi-static) z-directed magnetizing fields produced by the $(n-1)$th and $(n+1)$th loops alone. That is,

$$\mathrm{m}_n = \chi_\mathrm{m}\{H^z_{n,n-1} + H^z_{n,n-1}\}, \tag{28.35}$$

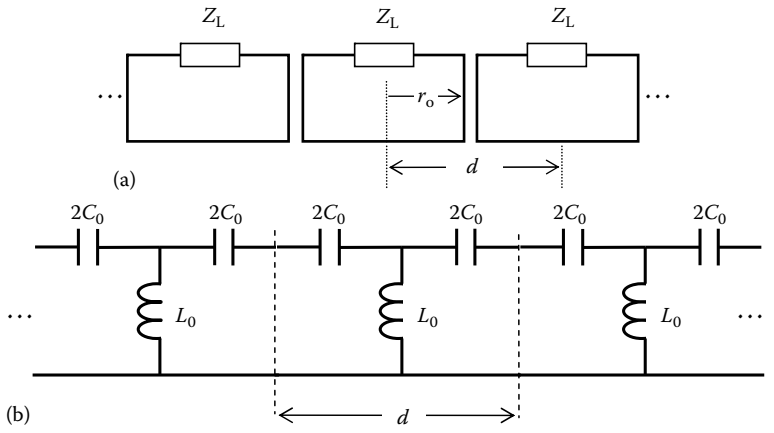

FIGURE 28.12 (a) 1D array of mutually coupled capacitively loaded inductive loops and (b) unit cell for a continuous LH transmission line, formed by connection of loops in (a).

where χ_m is the magnetic susceptibility of an isolated loop. Assuming the loops are small, the in-plane static fields produced by the $(n \pm 1)$th loop a radial distance r away is given by

$$H^z_{n,n\pm1} = -\frac{m_{n\pm1}}{4\pi\mu_0|r|^3}. \tag{28.36}$$

We may also insist that m_n is a periodic function such that

$$m_{n\mp1} = m_n e^{\pm j\beta d}, \tag{28.37}$$

which suggests the desired traveling-wave solutions with propagation constant β. Substituting Equations 28.37 and 28.36 into Equation 28.35 and using the expression for χ_m given previously in Equation 28.22, the dispersion equation is determined to be

$$\cos(\beta d) = -\frac{L}{2M_c}\left(1 - \frac{\omega_0^2}{\omega^2}\right), \quad M_c = -\mu_0\frac{(\pi r_0^2)^2}{2\pi d^3}, \tag{28.38}$$

where M_c can be regarded as the mutual inductance linking adjacent loops and the factor $p = -L/2M_c$ can be called the normalized coupling coefficient. This type of dispersion bears interesting similarities to two others described in the literature: the first is the dispersion of the magnetoinductive surface wave [28] supported by a chain of coplanar loops, and the second is the dispersion of the continuous 1D dual transmission line, which we have described as the limiting case of connected coplanar loops, from which p is absent. Both types of dispersion describe LH wave propagation. In fact, it can be seen that the dispersion of the continuous 1D dual transmission line is akin to that of the magnetoinductive wave when $p = 1$, which suggests a "perfect" coupling between loops by virtue of their connection. Figure 28.13 shows the dispersion diagram as a function of p. Indeed, the structure possesses a broad LH bandwidth that increases with p; i.e., as the discrete-resonance property of the rings gives way to their mutual coupling. A measure of the bandwidth of the LH region is given by the following expression:

$$BW_p = 2\omega_0^2 p/(p^2 - 1), \tag{28.39}$$

from which it can be seen that as the normalized coupling coefficient $p \to 1$, the left-handed bandwidth $BW_p \to \infty$. Conversely, when the loops are completely decoupled ($p \to \infty$), the left-handed bandwidth is diminished to zero.

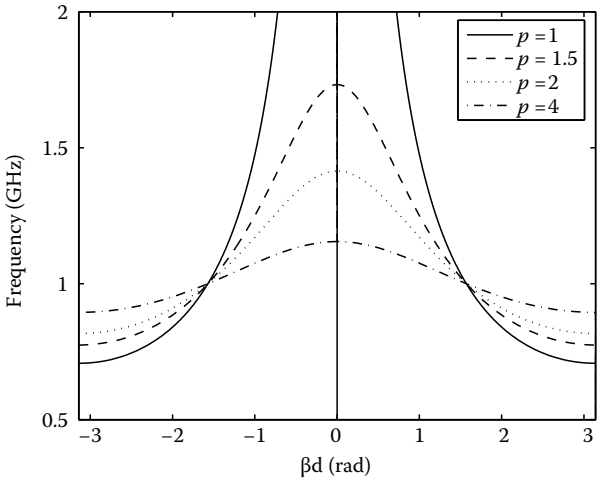

FIGURE 28.13 Dispersion diagram illustrating bandwidth enhancement as the mutual coupling coefficient $p = -L/2M_c \to 1$. (From Eleftheriades, G.V., *IEEE Microw. Wireless Comp. Lett.*, 17, 412, 2007. With permission.)

Losses may be introduced by representing the resonance frequency as complex, i.e., $\omega_0 \to \omega_0(1 + j/2Q)$, where Q is the quality factor describing the resonance. In the low-loss regime, the resulting decay component, αd, of the now complex propagation constant can be expressed as follows:

$$\alpha d \cong \frac{(p/Q)(\omega_0/\omega)^2}{\sqrt{1 - p^2[1 - (\omega_0/\omega)^2]}}. \tag{28.40}$$

Figure 28.14 illustrates the loss as a function of frequency for various values of p. It is clear that the loss associated with a particular Q is minimized as $p \to 1$, the same condition that yielded a maximum bandwidth. Thus, it is not the absence of resonators that makes TL metamaterials simultaneously

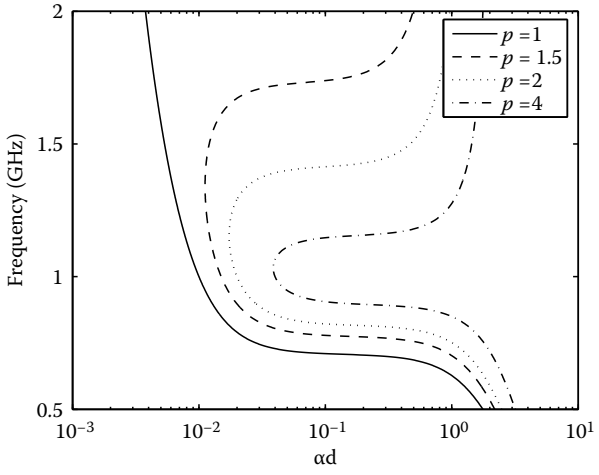

FIGURE 28.14 Dispersion of attenuation factor illustrating that minimum loss is achieved as the mutual coupling coefficient $p = -L/2M_c \to 1$. (From Eleftheriades, G.V., *IEEE Microw. Wireless Comp. Lett.*, 17, 412, 2007. With permission.)

broadband and low loss; rather, it is the tight coupling between their constituent lumped resonant sections.

For completeness, the previous analysis may be repeated taking into account retardation effects that appear in practical, periodic implementations of the dual TL metamaterial, employing a host (RH) TL medium. These effects can be shown to impose further constraints on bandwidth and loss, which may be mitigated by minimizing their electrical length (the interested reader is referred to Ref. [27] for further details). The effect of the requisite host medium on the dispersion properties of the dual TL is discussed in Section 28.5.

28.4.2 Free-Space Coupling to a Transmission-Line-Based Metamaterial

The structure shown in Figure 28.12 describes magnetoinductive surface wave-like propagation along a tightly coupled array of loops, resembling a 1D TL metamaterial, which inherently supports LH propagation. However, this is limited to 1D and so does not offer any insight into coupling into such a metamaterial from free space. On the other hand, Figure 28.11 describes coupling between free space and isolated loaded loops resulting in a frequency region of negative permeability, but requires a negation of the permittivity (e.g., using wires) to produce LH propagation. It should be interesting to consider the propagation characteristics of a bulk mode coupling from free space into a tightly coupled array of loaded loops, specifically to determine whether such a system could also produce large LH bandwidths and low losses, and whether additional wires would be needed. For this purpose, consider the unit cell shown in Figure 28.15. The mutual impedance coupling the host free-space transmission line (represented as a π-model with impedance Z_h and admittance Y_h) to the array of loaded loops is Z_{Mh}, and the mutual impedance coupling each loop to its neighbors is Z_{ML}. Invoking the Floquet–Bloch boundary conditions shown in Equation 28.41 yields the dispersion of the complex propagation constant γ shown in Equation 28.42:

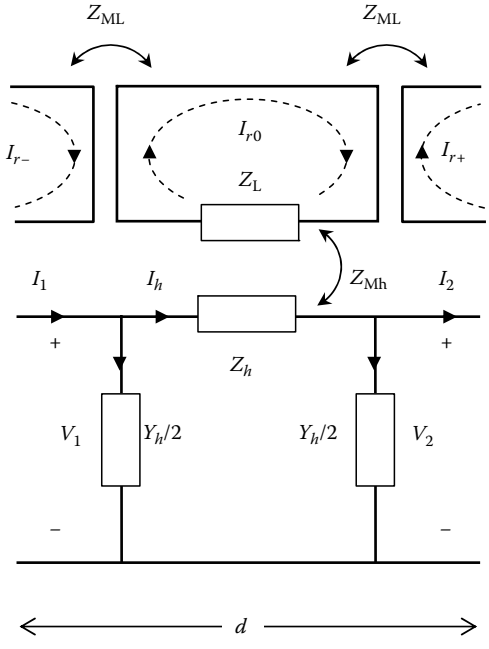

FIGURE 28.15 Unit cell modeling coupling from free space (represented as a π-network with impedance Z_h and admittance Y_h) to a TL metamaterial represented as an array of tightly coupled rings.

$$V_2 = V_1 e^{-\gamma d}$$
$$I_2 = I_1 e^{-\gamma d}$$
$$I_{r-} = I_{r0} e^{+\gamma d}$$
$$I_{r+} = I_{r0} e^{-\gamma d} \tag{28.41}$$

$$\left[\cosh \gamma d - \left(1 + \frac{Y_h Z_h}{2}\right)\right]\left[\cosh \gamma d - \frac{Z_L}{2Z_{ML}}\right] = \frac{Y_h Z_{Mh}^2}{4Z_{ML}}. \tag{28.42}$$

The host transmission line and the loop array may be regarded to be decoupled when $Z_{Mh} = 0$, which renders the right-hand side of Equation 28.42 null. In this case, the dispersion equation is satisfied by the existence of two decoupled modes:

$$\cosh \gamma d = 1 + \frac{Y_h Z_h}{2} = \cosh \gamma_h d \tag{28.43}$$

$$\cosh \gamma d = \frac{Z_L}{2Z_{ML}} = \cosh \gamma_L d. \tag{28.44}$$

To properly interpret these results, let us consider the typical case in which the mutual impedances Z_{Mh} and Z_{ML} are inductive. In this case, Equation 28.43 describes propagation through free space, unloaded by the loop array, where the free-space inductance and capacitance embedded in Z_h and Y_h, respectively, are positive; Equation 28.44 is identical to Equation 28.38 in the lossless case for $\gamma = j\beta$ and describes LH propagation in the coupled loops, where Z_{ML}^{-1} can be interpreted as the shunt inductance required to produce a negative permittivity, and where the series capacitance required for a negative permeability is obtained directly from the ring capacitance C embedded in Z_L. Hence, we can rewrite (28.42) in a simpler form:

$$[\cosh \gamma d - \cosh \gamma_h d][\cosh \gamma d - \cosh \gamma_L d] = \frac{Y_h Z_{Mh}^2}{4Z_{ML}}, \tag{28.45}$$

which illustrates that this is a system of coupled modes in which the free-space bulk mode is forward (RH) and the coupled-loop mode is backward (LH). The right-hand side of Equation 28.45 can be regarded as the coupling constant, and the frequency at which the coupling is strongest is obtained from the condition $\cosh \gamma_L d = \cosh \gamma_h d$.

To test these ideas, let us denote that Z_{Mh} and Z_{ML} correspond to inductances L_{Mh} and L_{ML}. Furthermore, we insist that $C = 1$pF and $L = 25.33$nH, so that the loop resonance frequency $\omega_0 = 1$GHz and that the per-unit-length inductance and capacitance of the host transmission line L_h and C_h are equal to the free-space permeability and permittivity, respectively (i.e., $Z_0 = \eta_0$ in this case). We shall also assign the periodic structure a period of $d = 20$mm, which is one-fifteenth of the free-space wavelength at the loop resonance frequency. The discussion that follows examines various combinations of the mutual coupling factors L_{Mh} and L_{ML}.

28.4.2.1 Case 1: Decoupled System

It was shown that the host transmission line and loop array may be decoupled by setting $Z_{Mh} = 0$. In this case, we expect to see a forward-wave (RH) dispersion curve representing free-space propagation and a backward-wave (LH) dispersion curve whose bandwidth depends on the mutual inductance L_{ML} between adjacent loops. Accordingly, setting $L_{Mh} = 0$ and choosing L_{ML} from the case $-L/2L_{ML} = p = 1.5$ examined previously in Figure 28.13 for the isolated coupled-loop array, we obtain the dispersion curves shown in Figure 28.16 (dark curves, propagation constant; light curves, decay constant). Indeed, the backward-wave curve corresponds to that in Figure 28.13 for $p = 1.5$ and does not interact with the forward-wave dispersion of the host transmission line.

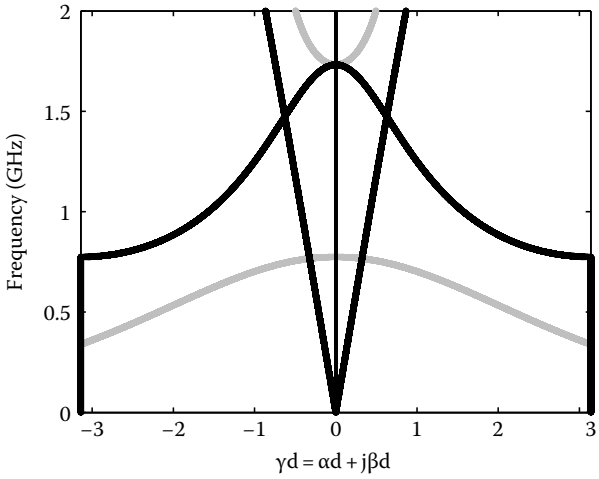

FIGURE 28.16 Dispersion diagram showing the solutions to Equation 28.45 when the host transmission line and coupled-loop array are decoupled ($L_{Mh} = 0$), but the loops are coupled to their nearest neighbors, for $-L/2L_{ML} = p = 1.5$ (dark curves, propagation constant; light curves, decay constant).

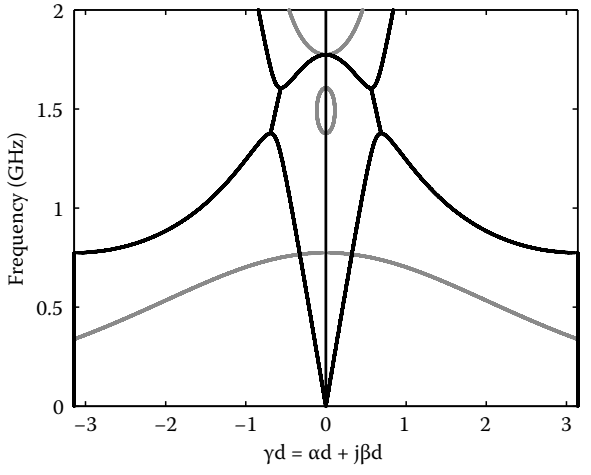

FIGURE 28.17 Dispersion diagram showing the coupled dispersion curves of the host transmission line and coupled-loop array when $L_{Mh} = 0.125L_h$, for $-L/2L_{ML} = p = 1.5$ (dark curves, propagation constant; light curves, decay constant).

28.4.2.2 Case 2: General Coupled System

We now examine a more general case in which the host transmission line and coupled-loop array are coupled by a mutual inductance (chosen to be $L_{Mh} = 0.125L_h$), and once again we consider only the case $-L/2L_{ML} = p = 1.5$. The resulting dispersion curves are shown in Figure 28.17 and possess a number of very interesting features. First, the forward wave and backward wave interact most strongly where their dispersion curves intersect (i.e., where the modes are phase-matched); away from the point of intersection, the two coupled dispersions approach their isolated values, and at any given frequency they can be described as either propagating ($\gamma = j\beta$) or evanescent ($\gamma = \alpha$).

However, inside the region of interaction, both modal solutions are complex, in that they possess both propagating and evanescent features. Such complex solutions are observed whenever there is coupling between backward and forward waves, as in conventional leaky-wave antennas operating on negative (backward-wave) spatial harmonics [29] and their TL metamaterial counterparts operating on a fundamental negative spatial harmonic [30,31], the dispersions of the shielded Sievenpiper high-impedance surface [32], and in the operation of high-directivity TL metamaterial coupled-line couplers [33]. Indeed, the model of Figure 28.15 can be used to represent any of these systems in the quasi-static limit (a more detailed and accurate treatment could be achieved using multiconductor TL analysis, which would account for both inductive and capacitive coupling between the lines as well as their electrical length—for example, see Ref. [34]).

28.4.2.3 Case 3: Isolated *L–C* Resonator Limit

The other interesting case to consider is that in which Z_{Mh} remains finite, but $Z_{ML} \to 0$, suggesting that, although there is coupling between the host transmission line and individual loops, the loops in the array do not couple to their adjacent neighbors and so appear as isolated L–C resonators. From Equation 28.44, we see that this results in $\cosh \gamma_L d \to \infty$, and it can be shown that the only propagating solution for γd is as follows:

$$\cosh \gamma d = 1 + \frac{1}{2} Y_h \left(Z_h - \frac{Z_{Mh}^2}{2Z_L} \right). \tag{28.46}$$

Expectedly, this is the dispersion relation corresponding to the unit cell of Figure 28.11, and the factor $Z_i = Z_h - Z_{Mh}^2/2Z_L$ is the image impedance of the isolated loop seen via the mutual impedance Z_{Mh}. We know that $Z_i < 0$ corresponds to a negative effective permeability. Setting $L_{Mh} = 0.5L_h$ and $L_{ML} = 0$ ($p \to \infty$) in Equation 28.45, we produce the dispersion curves shown in Figure 28.18. Here, the solutions in all frequency regions are either propagating or attenuating (as in Figure 28.16), and the inherent backward-wave bandwidth observed when the loops were tightly coupled has diminished to zero. Instead, the dispersion flattens out at the loop-resonance frequency, ω_0, leading to a stopband (containing evanescent solutions only), which, according to Equation 28.33, represents a frequency

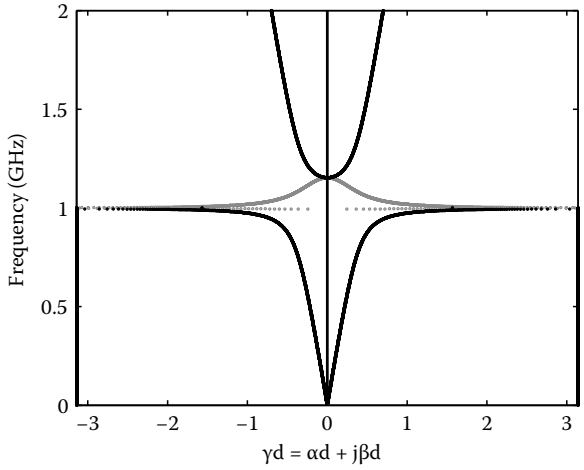

FIGURE 28.18 Dispersion diagram showing the coupled dispersion curves of the host transmission line and loop array ($L_{Mh} = 0.5L_h$) when the loop-to-loop mutual inductance $L_{ML} = 0$ (darkly shaded curves, propagation constant; lightly shaded curves, decay constant).

region of negative effective permeability. Propagation is restored at a frequency $\omega_P > \omega_0$ at which the free-space series inductance L_h dominates and the effective permeability is once again positive.

The solution to the condition $\cosh \gamma_L d = \cosh \gamma_h d$ represents the frequency of intersection of the forward-wave and backward-wave dispersions, and it is straightforward to show that, as $L_{ML} \to 0$, the intersection frequency approaches ω_0. Thus, although the coupling phenomena shown in Figures 28.17 and 28.18 appear to be different, the above development proves that they are fundamentally one and the same; indeed, the stopband present in both cases is the result of the coupling between the host transmission line and loop array, and this stopband generally contains complex solutions for any degree of loop-to-loop coupling, which may, at times, contain evanescent-only solutions. The differences lie in their dispersion characteristics outside the stopband; when the loops are tightly coupled to one another, the propagation characteristics are dominated by the coupled-loop array, which is akin to a dual LH transmission line possessing a simultaneous negative permittivity and permeability; accordingly, a broadband and low-loss region of left-handedness is produced, but it is interrupted in the vicinity of the stopband. However, it is clear that weakening the coupling between loops in the array gives way to a dispersion akin to that of an isolated SRR, which is described by a negative permeability alone, and for which external wires are additionally required to restore left-handedness. Thus, it may be concluded from this analysis that, for a given L_{Mh} describing the loading of free space by the loop array, the property of left-handedness built inherently into the system of tightly coupled loops supporting an LH TL mode is necessarily compromised by the requirement of coupling to such a mode from free space. That is, in general, the dispersion properties of the coupled system are a hybrid between those described by the unit cells in Figures 28.12 and 28.11, the former of which requires external wires to restore an uninterrupted, broadband LH passband, and the latter of which requires external wires to produce LH at all. The requirement for external wires is strengthened in the application of broadband metamaterials to free-space lensing or superlensing, where the frequency of operation is identically equal to the frequency of intersection between the backward-wave and forward-wave dispersions, the latter of which follows the light line.

28.5 Periodically Loaded Transmission-Line Metamaterials

The unique properties of the dual LH topology described in Section 28.2 were obtained in the continuous limit ($d/\lambda \to 0$), in which the topology represents what may be described as a "purely" LH material. However, any practical realization of such a structure, as in the case of the SRR/wire metamaterial, is a periodic one, and as such, must contain some RH component to its dispersion. In the case of the SRR/wire metamaterial, this RH contribution is provided by the air or dielectric separating the wires and resonant inclusions. Similarly, in an L–C-based periodic implementation, the periodicity is provided by a host TL medium, which may be appropriately loaded using lumped inductors and capacitors. This model, known as the negative-refractive-index transmission-line (NRI-TL), is a hybrid model that rigorously accounts for the distributed effects of the host medium and the lumped nature of the series-capacitive and shunt-inductive loading. As a result, its validity is not limited to the continuous, or homogeneous, limit, although this is often the regime of greatest interest and accordingly, much of this section will be devoted to it. It will be shown that the NRI-TL model is a most general and complete description of the RH- and LH components of LH dispersion, and it can be applied to any periodic electromagnetic structure, including SRR-based metamaterials (as exemplified by the model of Figure 28.11) as well as optical/plasmonic implementations [35,36].

The NRI-TL metamaterial can be implemented as a 1D structure, modeling TEM propagation in a transmission line filled with an NRI material (or equivalently, plane-wave propagation for a single direction in an unbounded NRI material); in 2D form it is a planar structure akin to a parallel-plate waveguide filled with an NRI material; finally, as a 3D structure, the NRI-TL metamaterial resembles a bulk NRI material. Each implementation has its own rigorous formulations for extracting its dispersion and impedance properties; however, on-axis TEM-mode propagation in any of these structures

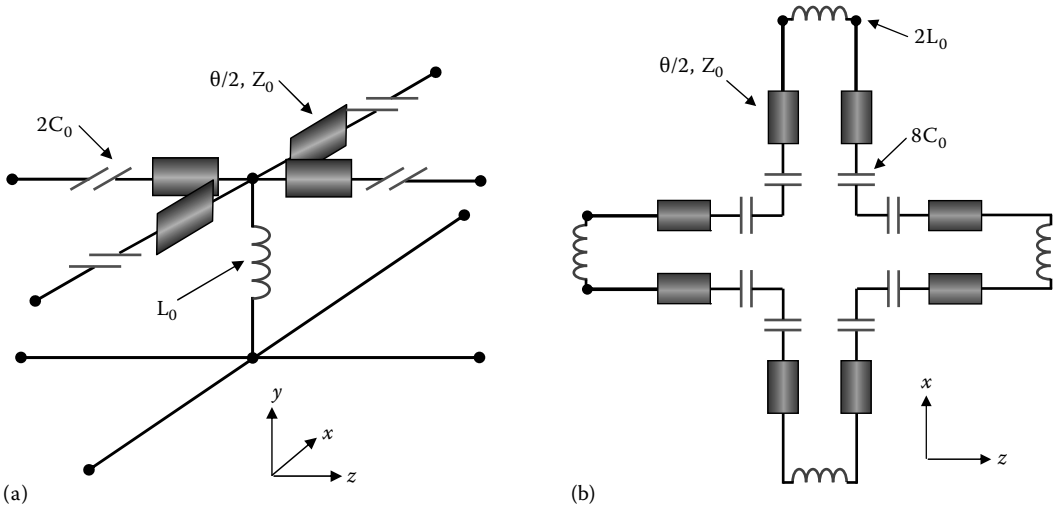

FIGURE 28.19 Symmetric NRI-TL unit cells in the (a) shunt, and (b) series NRI-TL topology.

often reduces to a 1D unit cell. Accordingly, the following analysis will concentrate on the 2D structure, which represents a desirable compromise between mathematical complexity and intuition, in that it intuitively supports the notions of refraction and focusing; moreover, the discussion shall be limited to propagation on-axis, for which a 1D unit cell can be obtained and a great deal of intuition gained. An analysis of the 2D NRI-TL structure is also justified by the fact that the first realizations of NRI-TL metamaterials involved planar structures supporting 2D waves [9,10]. There exist two 2D NRI-TL metamaterial topologies, shown in Figures 28.19a and 28.19b, which are known respectively as the shunt node and the series node; the terminology, which is borrowed from the TL matrix (TLM) method of time-domain modeling, is appropriate, since these unit cells are constructed, respectively, by the shunt and series interconnection of 1D NRI-TLs. As a result, the topology of Figure 28.19a is excited by quasi-TM fields (predominantly y-directed electric fields), whereas that of Figure 28.19b responds to quasi-TE fields (predominantly y-directed magnetic fields). The reader will note that the series capacitors (shunt inductors) of the shunt node (series node) have been represented as $2C_0$ ($2L_0$) to render the unit cell symmetric. We shall restrict the following analysis to the shunt node; the analysis for the series node proceeds in a similar manner and can be found in Ref. [37]. The constituent 1D NRI-TLs consist of a cascade of lumped series capacitors and shunt inductors arranged in a dual topology distributed as shown over the (finite) length of a host TL medium. The TL segments (characteristic impedance $Z_0 = Y_0^{-1}$) each have a length $d/2$ and can be represented by a phase shift, $\theta/2 = kd/2$, where k is the propagation constant in the medium filling the segments. The microstrip transmission line is a most appropriate host RH medium for the planar NRI-TL implementation discussed here, and we shall assume it to possess positive material parameters ϵ_P and μ_P, such that $k = \omega\sqrt{\epsilon_P \mu_P}$ and $Z_0 = g\sqrt{\mu_P/\epsilon_P}$, where g is a constant related to the geometry of the microstrip (including its height h, width w, and relative permittivity ϵ_r) determined from a quasi-static mapping of the fields. Figure 28.21 depicts examples of microstrip-based NRI-TL metamaterials employing discrete lumped loading (e.g., with chip inductors and capacitors [10]) and printed lumped elements (e.g., vias and interdigitated capacitors [38,39]).

The 4×4 transmission ($ABCD$) matrix of the unit cell of Figure 28.19a is obtained by cascading the 2×2 transmission matrices of the constituent elements. The periodic structure is then constructed by cascading an infinite number of such unit cells. A periodic analysis of the NRI-TL structure links the terminal field quantities (voltages and currents) by applying the Floquet–Bloch boundary conditions along the two axes, which yield traveling wave solutions with an effective NRI-TL propagation

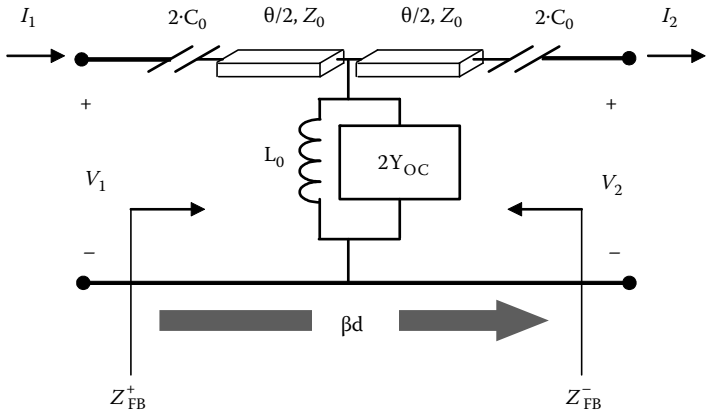

FIGURE 28.20 Equivalent circuit for axial propagation along a 2D periodically loaded NRI-TL metamaterial. (From Iyer, A.K. and Eleftheriades, G.V., Negative-refractive-index transmission line metamaterials, in *Negative Refraction Metamaterials: Fundamental Principles and Applications*, Eleftheriades, G.V. and Balmain, K.G. (Eds.), Wiley-IEEE Press, New York, July 2005, pp. 1–52. With permission.)

constant (or Floquet–Bloch wave vector), β, that see an effective NRI-TL characteristic impedance (or Floquet–Bloch impedance), Z_{FB}. The full 2D periodic analysis can be found in Ref. [40]. In this section we treat the simpler, but highly intuitive, case of on-axis propagation in which the 2D structure can be reduced to the unit cell depicted in Figure 28.20, where the additional shunt admittance Y_{oc} is produced by open-circuit conditions in the transverse direction [10]. The resulting dispersion equation from which β is determined is shown in Equation 28.47, and the Floquet–Bloch impedance is given in Equation 28.48:

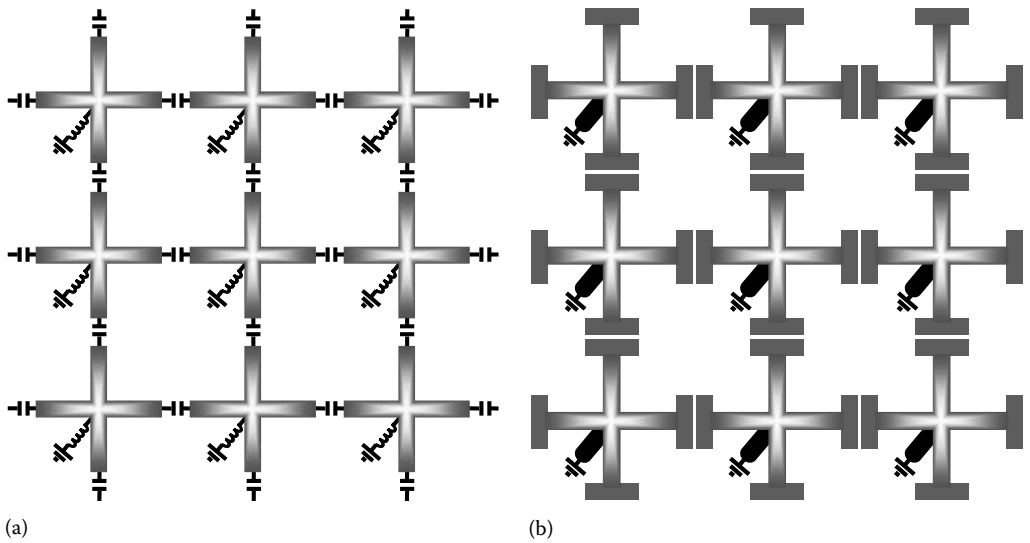

FIGURE 28.21 NRI-TL medium employing a microstrip host medium loaded using (a) discrete inductors and capacitors and (b) vias and printed gaps. (From Iyer, A.K. and Eleftheriades, G.V., Negative-refractive-index transmission line metamaterials, in *Negative Refraction Metamaterials: Fundamental Principles and Applications*, Eleftheriades, G.V. and Balmain, K.G. (Eds.), Wiley-IEEE Press, New York, July 2005, pp. 1–52. With permission.)

$$\cos\beta d = \left\{\cos\theta - \frac{1}{2\omega^2 L_0 C_0}\cos^2\frac{\theta}{2} + \frac{1}{2\omega}\left(\frac{1}{C_0 Z_0} + \frac{1}{L_0 Y_0}\right)\sin\theta\right\} - \sin\frac{\theta}{2}\left(2\sin\frac{\theta}{2} - \frac{1}{\omega C_0 Z_0}\cos\frac{\theta}{2}\right) \tag{28.47}$$

$$Z_{\mathrm{FB}}^{\pm} = \pm\frac{Z_0\tan\dfrac{\theta}{2} - \dfrac{1}{2\omega C_0}}{\tan\dfrac{\beta d}{2}}. \tag{28.48}$$

28.5.1 Dispersion Characteristics

The dispersion of the continuous LH transmission line depicted in Figure 28.4b illustrated that its LH bandwidth was infinite. A similar result can also be obtained from Equation 28.47 as the electrical length of the interconnecting TL segments $\theta \to 0$ (the continuous limit), adjusted for the 2D nature of the medium. However, these electrical lengths contribute the necessary retardation component that permits a practical, periodic realization of NRI-TL metamaterials. Thus, it is of great interest to know the effect of the TL segments on the dispersion relation when their electrical length is not negligible, for this is unavoidable in practice.

Figure 28.22 depicts the frequency response of the propagation constant determined from Equation 28.47 for the representative loading values $L_0 = 5.6$ nH and $C_0 = 1.0$ pF, and period $d = 5$ mm; θ and Z_0 are computed from the microstrip and substrate parameters $\epsilon_r = 2.94$, $h = 1.524$ mm,

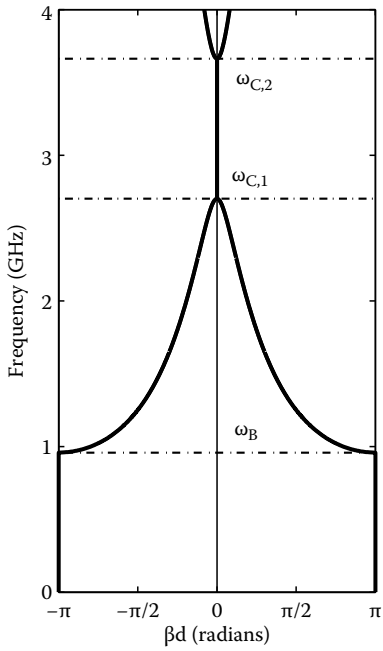

FIGURE 28.22 Dispersion relation for a representative NRI-TL medium obtained through periodic analysis. The lowest left-handed (LH) passband is enclosed by frequencies ω_B and $\omega_{C,1}$. (From Iyer, A.K. and Eleftheriades, G.V., Negative-refractive-index transmission line metamaterials, in *Negative Refraction Metamaterials: Fundamental Principles and Applications*, Eleftheriades, G.V. and Balmain, K.G. (Eds.), Wiley-IEEE Press, New York, July 2005, pp. 1–52. With permission.)

and $w = 0.4$ mm, using standard formulas [41]. It is evident that the inclusion of the TL segments has significantly enriched the dispersion features; specifically, while the insistence on periodicity has retained the LH nature of the lowest passband, its bandwidth has been rendered finite by a lower bound, ω_B, and an upper bound $\omega_{C,1}$ due to the onset of a stopband inside which β is complex. The stopband forbids propagation between frequencies $\omega_{C,1}$ and $\omega_{C,2}$, and RH propagation is restored beyond $\omega_{C,2}$. In fact, the pattern of successive alternating LH and RH passbands separated by stopbands repeats *ad infinitum* and is due to the periodic phase properties of the interconnecting TL segments. Each set of bands represents higher-order spatial harmonics (Floquet–Bloch modes) associated with the period chosen; nevertheless, the most important feature of Figure 28.22 is the fact that the fundamental spatial harmonic is LH. This is in stark contrast to conventional RH materials as well as photonic crystal- or electromagnetic bandgap-type metamaterials, in which any backward-wave-type behavior is limited to higher-order negative spatial harmonics.

Here, the lower bound ω_B corresponds to the Bragg reflection condition $\beta d = \pi$ (i.e., one-half wavelength per period). It can be shown that ω_B is predominantly affected by the loading elements L_0 and C_0, since the interconnecting transmission lines are electrically very small at such low frequencies, and consequently the NRI-TL cascade behaves like a simple high-pass filter at resonance. The reader will recall that, in conventional RH materials, the large phase shifts and small guided wavelengths leading to Bragg conditions are achieved at high frequencies due to the direct proportionality of β and ω; conversely, in NRI-TL metamaterials, these large phase shifts and small guided wavelengths are achieved at low frequencies due to the inverse relationship between β and ω. Phrased another way, the effective wavelength in the NRI-TL metamaterial $\lambda_{eff} = 2\pi/\beta$ varies directly, rather than inversely, with frequency. Furthermore, λ_{eff} and the wavelength in the (RH) host TL medium λ_0 vary inversely. These fundamental properties of NRI-TL metamaterials suggest a wide range of possibilities in the miniaturization of distributed structures.

28.5.2 The Effective Medium Limit: Determining the Effective Permittivity and Permeability

When $\beta d = 0$, we have encountered the edge of the stopband, $\omega_{C,1}$. However, in the frequency region of propagation approaching $\omega_{C,1}$, it is possible that both θ and βd are electrically very small, and the effective wavelengths λ_{eff} and λ_0 are comparably much larger than the period d. Indeed, this limit is known as the effective medium limit, in which the periodic structure appears homogeneous to waves propagating inside it, and it is in this regime that we may attribute to the structure effective properties such as permittivity, permeability, refractive index, and wave impedance. At such low frequencies, θ is sufficiently small that we may apply a Taylor expansion on the terms $\sin\theta$ and $\cos\theta$ that retains only the first two terms. The resulting approximation of Equation 28.47 is as follows:

$$\cos\beta d = 1 - \frac{\theta^2}{2} - \frac{1}{2\omega^2 L_0 C_0} + \frac{1}{2\omega}\left(\frac{1}{C_0 Z_0} + \frac{1}{L_0 Y_0}\right)\theta - \frac{\theta}{2}\left(\theta - \frac{1}{\omega C_0 Z_0}\right). \tag{28.49}$$

Finally, if we restrict ourselves to the region in which $\beta d \to 0$, we may apply a similar expansion to the term $\cos\beta d$, which directly produces βd:

$$\begin{aligned}(\beta d)^2 &\approx \left\{\left(\theta - \frac{1}{\omega C_0 Z_0}\right)\left(\theta - \frac{1}{\omega L_0 Y_0}\right)\right\} + \theta\left(\theta - \frac{1}{\omega C_0 Z_0}\right) \\ &= \left(\theta - \frac{1}{\omega C_0 Z_0}\right)\left(2\theta - \frac{1}{\omega L_0 Y_0}\right).\end{aligned} \tag{28.50}$$

By expressing θ and Z_0 in terms of the host TL permittivity ϵ_P, permeability μ_P, and geometry-dependent constant g, the axial propagation constant in the effective medium limit is given to be

$$\beta = \pm\omega\sqrt{\left(2\epsilon_P - \frac{g}{\omega^2 L_0 d}\right)\left(\mu_P - \frac{1/g}{\omega^2 C_0 d}\right)} = \pm\omega\sqrt{\epsilon_N(\omega)\mu_N(\omega)}, \tag{28.51}$$

which has also been represented in terms of $\epsilon_N(\omega)$ and $\mu_N(\omega)$, the effective material parameters that we seek. Of course, an expression for β alone cannot produce isolated equations for these parameters, and so we must apply our assumptions to the Floquet–Bloch impedance Z_{FB} as well:

$$Z_B = \frac{\omega\mu_P g - \frac{1}{\omega C_0 d}}{\beta} = g\sqrt{\frac{\mu_P - \frac{1/g}{\omega^2 C_0 d}}{2\epsilon_P - \frac{g}{\omega^2 L_0 d}}} = g\sqrt{\frac{\mu_N(\omega)}{\epsilon_N(\omega)}}. \tag{28.52}$$

Using these two expressions, the effective constitutive parameters of the NRI-TL metamaterial in the effective medium limit are determined to be

$$\mu_N(\omega) = \mu_P - \frac{1/g}{\omega^2 C_0 d} \tag{28.53}$$

$$\epsilon_N(\omega) = 2\epsilon_P - \frac{g}{\omega^2 L_0 d}. \tag{28.54}$$

Whereas the effective material parameters in the continuous case were negative over all frequencies, the imposed periodicity causes each of $\epsilon_N(\omega)$ and $\mu_N(\omega)$ to contain both a positive contribution due to the host transmission line and a negative, dispersive contribution due to the periodic loading (corresponding to a negative effective susceptibility). Consequently, the material parameters are only negative where the loading elements C_0 and L_0 dominate the frequency response. It can be shown that the factor of 2 before the relative permittivity ϵ_P of the host medium is a direct consequence of the transverse (capacitive) loading of the axial propagation characteristics due to the 2D nature of the medium [10,11]. Accordingly, as in an unloaded 2D microstrip grid, the characteristic impedance seen by a wave propagating axially through the 2D NRI-TL structure is less than that seen in a 1D transmission line by a factor of $\sqrt{2}$.

It is clear from the form of Equations 28.53 and 28.54 that the NRI-TL effective material parameters are strongly negative at low frequencies and positive at high frequencies. The LH passband of NRI-TL metamaterials represents the frequency region in which $\epsilon_N(\omega)$ and $\mu_N(\omega)$ are simultaneously negative, and the RH passband at higher frequencies is formed where both material parameters are positive. In the intervening stopband, one of the two parameters is negative, whereas the other remains positive. The zeros of Equations 28.53 and 28.54 represent the frequencies at which the transition from negative to positive values is made and correspond to the edges of the stopband. These may also be regarded as the "plasma frequencies" of the effective medium and possess the following form:

$$\omega_{C,1} = \sqrt{\frac{1}{C_0 g \mu_{Pd}}}, \quad \mu_N(\omega_{C,1}) = 0 \tag{28.55}$$

$$\omega_{C,2} = \sqrt{\frac{1}{L_0 \frac{2\epsilon_{Pd}}{g}}}, \quad \epsilon_N(\omega_{C,2}) = 0. \tag{28.56}$$

Since the plasma frequencies depend inversely on the period d of the metamaterial, the stopband cutoffs are pushed to infinity as the period d is reduced, arbitrarily widening the bandwidth of the LH passband and essentially restoring the continuous case [10,25]. This observation represents a very important feature of NRI-TL metamaterials–that the close packing of the periodic inclusions produces large LH bandwidths–and is reminiscent of the developments in Section 28.4 leading to the

same conclusion. Moreover, it suggests that the dispersion characteristics of the NRI-TL metamaterial are inherently controllable.

One subtle point in the above development is that the geometrical factor g was factored in Z_{FB} as it was factored in the characteristic impedance Z_0 of the host transmission line; thus, Equations 28.51 and 28.52 essentially suggest that the propagation characteristics of the periodically loaded NRI-TL metamaterial in the homogeneous limit are equivalent to those obtained by replacing the material filling the original transmission line (ϵ_P, μ_P) with the NRI-TL effective constitutive parameters $\epsilon_N(\omega)$ and $\mu_N(\omega)$, which assumes that the original field mapping (hence g) is maintained.

28.5.3 Closure of the Stopband

In conventional periodic structures, stopbands are frequency regions in which propagation is forbidden as a result of the interaction between two spatial harmonics carrying power in opposite directions, and the degree of coupling between these harmonics (which determines the size of the stopband) is largely determined by the strength of the periodic perturbation. Thus, the only way to eliminate a stopband in a conventional periodic structure is to remove all perturbation; of course, this obviates any notion of periodicity, and so is not an option for all practical intents and purposes.

Now, consider Equations 28.55 and 28.56, describing the edges of the first stopband. It appears that the size of the stopband can be diminished to zero simply by setting $\omega_{C,1} = \omega_{C,2}$. This is satisfied by the following condition:

$$\sqrt{\frac{1}{C_0 g \mu_P d}} = \sqrt{\frac{1}{L_0 \frac{2\epsilon_P d}{g}}} \Rightarrow \sqrt{\frac{L_0}{C_0}} = g\sqrt{\frac{\mu_P}{2\epsilon_P}} = \sqrt{\frac{L'}{C'}} = Z_0, \tag{28.57}$$

which is an impedance-matched condition described by a host-medium characteristic impedance equal to that of the underlying purely LH distributed medium consisting of the loading elements alone. Furthermore, the impedance-matched condition is independent of both frequency and the period d, provided that we are within the effective medium regime. The condition of closing the stopband in a TL-based NRI metamaterial (Equation 28.57) was originally reported in Equation 29 of Ref. [10] and subsequently adopted by Sanada et al. [42], who have referred to it as a "balanced" condition.

Thus, we can guarantee closure of the stopband by selecting the loading element values L_0 and C_0 according to Equation 28.57. Beginning with the dispersion relation of Figure 28.22 and choosing $L_0 = 10$ nH to comply with Equation 28.57, the resulting dispersion relation is presented in Figure 28.23 (of course, Equation 28.57 could have also been satisfied by decreasing the loading capacitance C_0). The absence of a stopband also suggests that the impedance-matched condition permits, at least in theory, the restoration of a nonzero group velocity at the point $\beta = 0$. In fact, it has been shown in Ref. [11] that the closure of the first stopband through Equation 28.57 guarantees that all stopbands at each one of the infinitely many $\beta = 0$ points are also closed.

Another way to express Equation 28.57 is as follows:

$$\sqrt{\frac{\mu_P - \frac{1/g}{\omega^2 C_0 d}}{2\epsilon_P - \frac{g}{\omega^2 L_0 d}}} = \sqrt{\frac{\mu_P}{2\epsilon_P}} \Rightarrow \eta_{NRI-TL} = \eta_{TL}. \tag{28.58}$$

Phrased this way, it appears that the impedance-matched condition also guarantees that the wave impedance of the periodically loaded 2D NRI-TL metamaterial matched to the effective wave impedance of an unloaded 2D TL grid. This is an important result, because it provides a prescription for the design of interfaces between positive-refractive-index (PRI) effective media and NRI-TL metamaterials, which are essential to the demonstration of negative refraction, focusing, and perfect lensing. Equation 28.58 tells us that a 2D NRI-TL metamaterial is ideally interfaced with a

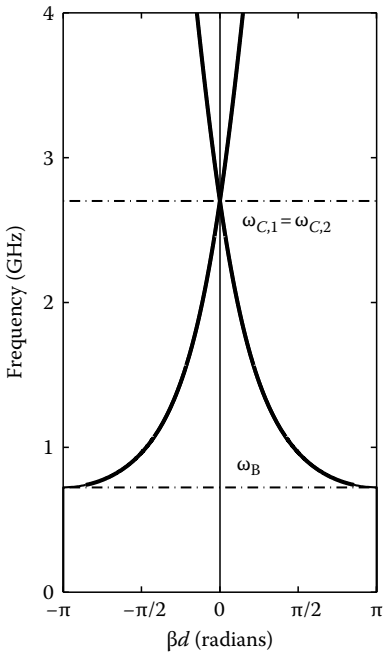

FIGURE 28.23 Dispersion relation describing an NRI-TL medium with a closed stopband, as obtained through periodic analysis. Closure of the stopband is achieved through the application of Equation 28.57. (From Iyer, A.K. and Eleftheriades, G.V., Negative-refractive-index transmission line metamaterials, in *Negative Refraction Metamaterials: Fundamental Principles and Applications*, Eleftheriades, G.V. and Balmain, K.G. (Eds.), Wiley-IEEE Press, New York, July 2005, pp. 1–52. With permission.)

2D unloaded TL host grid, and owing to its frequency insensitivity, their impedance match can be maintained everywhere within the effective medium regime.

28.5.4 Equivalent Unit Cell in the Effective Medium Limit

Just as it was possible to extract an effective permeability and permittivity from the series impedance and shunt admittance of the continuous LH TL unit cell, respectively, it is also possible to produce an equivalent lumped-element unit cell from the effective material parameters describing the periodic NRI-TL structure in the effective-medium limit. The series impedance Z and shunt admittance Y of this equivalent unit cell, which correspond to the effective parameters of Equations 28.53 and 28.54, respectively, are obtained as follows:

$$Z = j\omega g \mu_N(\omega) d = j\omega L' d + \frac{1}{j\omega C_0} \tag{28.59}$$

$$Y = j\omega \frac{1}{g} \epsilon_N(\omega) d = j\omega 2C' d + \frac{1}{j\omega L_0}, \tag{28.60}$$

where the quantities $L' = \mu_{P_g}/d$ and $C' = \epsilon_{P/g} d$, describing only the host medium, can be recognized as the 1D TL distributed inductance and capacitance, respectively, related to the host medium parameters by the geometric constant g. Thus, as depicted in Figure 28.24, the series branch of the equivalent unit cell consists of an inductor, contributed by L' over the length d in series with a capacitor provided by the loading, and the shunt branch consists of a capacitor, contributed by $2C'$ over the length d of the unit cell, in parallel with an inductor provided by the loading. This topology also reveals from

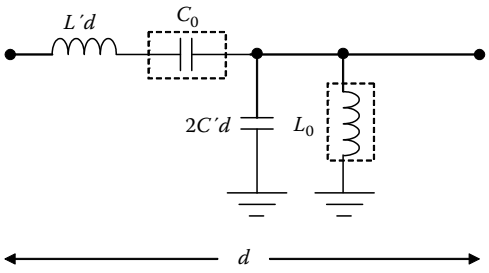

FIGURE 28.24 Unit cell for the practical NRI-TL network describing axial propagation in the homogeneous limit. (From Iyer, A.K. and Eleftheriades, G.V., Negative-refractive-index transmission line metamaterials, in *Negative Refraction Metamaterials: Fundamental Principles and Applications*, Eleftheriades, G.V. and Balmain, K.G. (Eds.), Wiley-IEEE Press, New York, July 2005, pp. 1–52. With permission.)

another perspective that the host medium contributes positively to the material parameters, whereas the loading contributes negatively [10]. In the absence of loading, the material parameters degenerate to those of the host medium, modeled in Figure 28.24 by an inductor and capacitor arranged in a low-pass topology. When the loading is dominant, the material parameters become negative, and the equivalent unit cell is restored to the dual topology. Thus, it is seen that the equivalent unit cell of Figure 28.24, along with the dispersion relation from which it was derived, includes the complete RH and LH responses of the periodically loaded NRI-TL metamaterial [10]. Thus, the NRI-TL model is a general model that can be reduced to the unit cell of Figure 28.24 in the homogeneous limit, in which it has also been referred to as a composite right-/left-handed (CRLH) metamaterial. This topology also accounts for the magnetic and electric plasma frequencies (Equations 28.55 and 28.56), which are, respectively, equal to the series and shunt resonance conditions in Figure 28.24. This perspective also reveals that the closure of this stopband by way of the impedance-matched condition of Equation 28.57, in fact, causes the series and shunt branches of Figure 28.24 to resonate at the same frequency, at which the equivalent circuit represents a direct connection from input to output (see also Ref. [43]). Thus, in this regime, the periodicity of the NRI-TL unit cell is effectively removed, and the metamaterial appears perfectly homogeneous.

28.6 Conclusion

Distributed L–C network topologies have long been used to describe the electromagnetic properties of homogeneous media, particularly in the lumped-element modeling of transmission lines. In conventional materials, a series inductor and a shunt capacitor, respectively, describe positive permeability and permittivity. In this chapter, it has been shown that, by reversing the positions of these two elements, their impedance and admittance are effectively negated; in the effective-medium regime in which the wavelength is much longer than the period of the structure, this is tantamount to negating the effective parameters of the medium represented by the network. With simultaneously negative permittivity and permeability, such a "dual" medium possesses the property of "left-handedness," indicated by its support of backward waves and, in 2D and 3D, a negative index of refraction. Electrodynamic arguments based on the motion of charges in an electrical plasma and on the effective-medium properties of capacitively loaded resonant loops were also presented and support an intuitive understanding of the "dual" TL topology.

Although other metamaterials, particularly those based on split-ring resonators (SRRs), have successfully demonstrated left-handedness by way of resonant behaviors, the transmission-line (TL) based metamaterial has distinguished itself by large left-handed bandwidths and low losses. In this

chapter, it was shown that it is not the absence of resonators in TL metamaterials but the tight coupling between individual resonators that leads to their broadband and low-loss properties. A study of coupling between a TL metamaterial and free space was also presented and reveals that the broadband dual TL behavior and resonant SRR behavior are two ends of a continuous spectrum in which a stopband (containing generally complex solutions to the propagation constant) is formed in the region of coupling. In both the dual TL and SRR cases, external wires may be required to restore left-handed propagation in this region. These results may be of importance in the design of broadband, low-loss volumetric and 3D metamaterials for free-space excitation, which are further discussed in Chapter 1 of *Applications of Metamaterials*.

Finally, the problem of realization of the continuous dual TL is addressed by the negative-refractive-index transmission-line metamaterial, which is based on the idea that such a material can be synthesized by periodically loading a host transmission-line medium with lumped inductors and capacitors in the dual configuration. The essential dispersion features of the practical NRI-TL metamaterial reveal that it shares the broadband and low-loss properties of its continuous counterpart.

Acknowledgment

The work described in this chapter was supported by the Natural Sciences and Engineering Research Council (NSERC) of Canada.

References

1. W. E. Kock, Radio lenses, *Bell Lab. Rec.*, 24, 177–216, May 1946.
2. W. E. Kock, Metallic delay lenses, *Bell Syst. Tech. J.*, 27, 58–82, January 1948.
3. W. E. Kock, Metal lens antennas, In *Proc. IRE and Waves and Electrons*, pp. 828–836, November 1946.
4. R. E. Collin, *Field Theory of Guided Waves*, 2nd edn., Wiley-IEEE Press, Toronto, 1990.
5. V. G. Veselago, The electrodynamics of substances with simultaneously negative values of ϵ and μ, *Sov. Phys. Usp*, 10(4), 509–514, January–February 1968 (translation based on the original Russian document, dated 1967.)
6. H. Lamb, On Group-Velocity, *Proc. London Math. Soc.*, 1, 473–479, 1904.
7. A. Schuster, *An Introduction to the Theory of Optics*, Edward Arnold, London, 1904, pp. 313–318.
8. L. I. Mandel'shtam, Group velocity in a crystal lattice, Trans. by E. F. Kuester (available at http://ece-www.colorado.edu/ kuester/mandelshtam1945.pdf) of original document appearing in *Zh. Eksp. Teor. Fiz.*, 15, 475–478, 1945. Also available is a relevant lecture of Prof. Mandel'shtam discussing the concept of negative refraction a year earlier in 1944: http://ece-www.colorado.edu/ kuester/mandelshtam1944.pdf.
9. A. K. Iyer and G. V. Eleftheriades, Negative refractive index metamaterials supporting 2-D waves, in *IEEE MTT-S International Microwave Symposium Digest*, vol. 2, June 2–7, 2002, Seattle, WA, pp. 1067–1070.
10. G. V. Eleftheriades, A. K. Iyer, and P. C. Kremer, Planar negative refractive index media using periodically L–C loaded transmission lines, *IEEE Trans. Microw. Theory Tech.*, 50(12), 2702–2712, December 2002.
11. A. K. Iyer and G. V. Eleftheriades, Negative-refractive-index transmission-line metamaterials, in *Negative-Refraction Metamaterials: Fundamental Principles and Applications*, G. V. Eleftheriades and K. G. Balmain (eds.), Wiley-IEEE Press, New York, July 2005, pp. 1–52.
12. J. B. Pendry, Negative refraction makes a perfect lens, *Phys. Rev. Lett.*, 85(18), 3966–3969, October 2000.

13. A. Grbic and G. V. Eleftheriades, Overcoming the diffraction limit with a planar left-handed transmission-line lens, *Phys. Rev. Lett.*, 92, 117403, March 2004.
14. G. Kron, Equivalent circuit of the field equations of Maxwell, *Proc. IRE*, 32(5), 289-299, May 1944.
15. J. R. Whinnery and S. Ramo, A new approach to the solution of high-frequency field problems, *Proc. IRE*, 32(5), 284-288, May 1944.
16. R. N. Bracewell, Analogues of an ionized medium: Applications to the ionosphere, *Wireless Eng.*, 31, 320–326, December 1954.
17. W. Rotman, Plasma simulation by artificial dielectrics and parallel-plate media, *IRE Trans. Antennas Propag.*, AP-10(1), 82–85, January 1962.
18. J. B. Pendry, A. J. Holden, W. J. Stewart, and I. Youngs, Extremely low frequency plasmons in metallic mesostructures, *Phys. Rev. Lett.*, 76(25), 4773–4776, June 1996.
19. D. F. Sievenpiper, M. E. Sickmiller, and E. Yablonovitch, 3D wire mesh photonic crystals, *Phys. Rev. Lett.*, 76(14), 2480–2483, April 1996.
20. S. A. Schelkunoff and H. T. Friis, *Antennas: Theory and Practice*, John Wiley & Sons, Inc., New York, 1952, pp. 584–585.
21. J. B. Pendry, A. J. Holden, D. J. Robbins, and W. J. Stewart, Magnetism from conductors and enhanced nonlinear phenomena, *IEEE Trans. Microw. Theory Tech.*, 47(11), 2075–2084, November 1999.
22. R. A. Shelby, D. R. Smith, and S. Schultz, Experimental verification of a negative index of refraction, *Science*, 292, 77–79, April 6, 2001.
23. S. Ramo, J. R. Whinnery, and T. Van Duzer, *Fields and Waves in Communication Electronics*, 3rd edn., John Wiley & Sons, Toronto, Canada, 1994.
24. H. G. Booker, *Cold Plasma Waves*, Martinus Nijhoff Publishers, Boston, MA, 1984, pp. 26–27.
25. G. V. Eleftheriades, O. Siddiqui, and A. K. Iyer, Transmission line models for negative refractive index media and associated implementations without excess resonators, *IEEE Microw. Wireless Components Lett.*, 13(2), 51–53, February 2003.
26. J. D. Baena, J. Bonache, F. Martin, R. Marqués Sillero, F. Falcone, T. Lopetegi, M. A. G. Laso, et al. Equivalent-circuit models for split-ring resonators and complementary split-ring resonators coupled to planar transmission lines, *IEEE Trans. Microw. Theory Tech.*, 53(4), 1451–1461, December 2002.
27. G. V. Eleftheriades, Analysis of bandwidth and loss in negative-refractive-index transmission-line (NRI-TL) media using coupled resonators, *IEEE Microw. Wireless Compon. Lett.*, 17(6), 412–414, 2007.
28. E. Shamonina, V. Kalinin, K. H. Ringhofer, and L. Solymar, Magnetoinductive waves in one, two, and three dimensions, *J. Appl. Phys.*, 92(10), 6252–6261, November 2002.
29. A. Hessel, General characteristics of traveling-wave antennas, in *Antenna Theory*, vol. 1, R. E. Collin and F. J. Zucker (eds.), McGraw-Hill, New York, 1969, pp. 151–258.
30. A. Grbic and G. V. Eleftheriades, Experimental verification of backward-wave radiation from a negative refractive index metamaterial, *J. Appl. Phys.*, 92(10), 5930–5935, 2002.
31. A. K. Iyer and G. V. Eleftheriades, Leaky-wave radiation from a two-dimensional negative-refractive-index transmission-line metamaterial, in *Proc. of 2004 URSI EMTS International Symposium on Electromagnetic Theory*, May 26, 2004, Pisa, Italy, pp. 891–893.
32. F. Elek and G. V. Eleftheriades, Dispersion analysis of the shielded Sievenpiper structure using multiconductor transmission-line theory, *IEEE Microw. Wireless Comp. Lett.*, 14(9), 434–436, September 2004.
33. R. Islam, F. Elek, and G. V. Eleftheriades, Coupled-line metamaterial coupler having co-directional phase but contra-directional power flow, *Electron. Lett.*, 40(5), 315–317, 2004.
34. F. Elek and G. V. Eleftheriades, Simple analytical dispersion equations for the shielded Sievenpiper structure, in *IEEE MTT-S International Microwave Symposium Digest*, June 11–16, 2006, San Francisco, CA, pp. 1651–1654.
35. N. Engheta, A. Salandrino, and A. Alù, Circuit elements at optical frequencies: nanoinductors, nanocapacitors, and nanoresistors, *Phys. Rev. Lett.*, 95, 095504, Aug. 2005.

36. A. K. Sarychev and V. M. Shalaev, Plasmonic nanowire materials, in *Negative-Refraction Metamaterials: Fundamental Principles and Applications*, G. V. Eleftheriades and K. G. Balmain (eds.), Wiley-IEEE Press, New York, July 2005, pp. 313–338.
37. A. K. Iyer and G. V. Eleftheriades, Volumetric layered transmission-line metamaterial exhibiting a negative refractive index, *J. Opt. Soc. Am. B. (JOSA-B)*, Focus Issue on Metamaterials, 23, 553–570, Mar. 2006.
38. A. Grbic and G. V. Eleftheriades, Dispersion analysis of a microstrip-based negative refractive index periodic structure, *IEEE Microw. Wireless Comp. Lett.*, 3(4), 155–157, April 2003.
39. G. V. Eleftheriades, Planar negative refractive index metamaterials based on periodically L–C loaded transmission lines, in *Workshop on Quantum Optics*, Kavli Institute for Theoretical Physics, University of Santa Barbara, July 11, 2002, http://online.kitp.ucsb.edu/online/qo02/eleftheriades/
40. A. Grbic and G. V. Eleftheriades, Periodic analysis of a 2-D negative refractive index transmission line structure, *IEEE Trans. Antennas Propag.*, Special Issue on Metamaterials, 51(10), 2604–2611, October 2003.
41. D. M. Pozar, *Microwave Engineering*, 2nd edn., John Wiley & Sons, Toronto, 1998.
42. A. Sanada, C. Caloz, and T. Itoh, Characteristics of the composite right/left-handed transmission lines, *IEEE Microw. Wireless Comp. Lett.*, 14(2), 68–70, February 2004.
43. A. Alù and N. Engheta, Pairing an epsilon-negative slab with a mu-negative slab: Resonance, tunneling, and transparency, *IEEE Trans. Antennas Propag.*, Special Issue on Metamaterials, 51(10), 2558–2571, October 2003.

29

Corrugated Rectangular Waveguides: Composite Right-/Left-Handed Metaguides

Islam A. Eshrah
Cairo University

Ahmed A. Kishk
The University of Mississippi

Alexander B. Yakovlev
The University of Mississippi

Allen W. Glisson
The University of Mississippi

29.1 Introduction

Metamaterial transmission lines were recently introduced [1–4] as structures supporting left-hand (LH) propagation [5–12] in addition to the conventional right-hand (RH) propagation. Realizations and applications for composite right-/left-handed transmission lines were surveyed in Ref. [4], where some devices of improved response or more compact design were proposed. Among all guided-wave structures, waveguides are characterized by their low losses, high power handling capability, and absence of leakage and other extraneous phenomena due to their closed geometries. Examining the LH propagation phenomena in these structures is thus in order. Recently, periodically loaded rectangular waveguides were shown to exhibit backward-wave propagation [12–14]. In particular, in Ref. [12] it has been shown that periodically loaded split-ring resonators (SRR) in hollow waveguide create a LH propagation even if the transverse dimensions of the waveguide are much smaller than the free-space wavelength. SRR and complementary SRR (CSRR) have been proposed in Refs. [15,16] in the design of compact waveguide filters based on the subwavelength self-resonance properties of SRR and CSRR. In Ref. [13], an equivalence between waveguide propagation below cutoff and

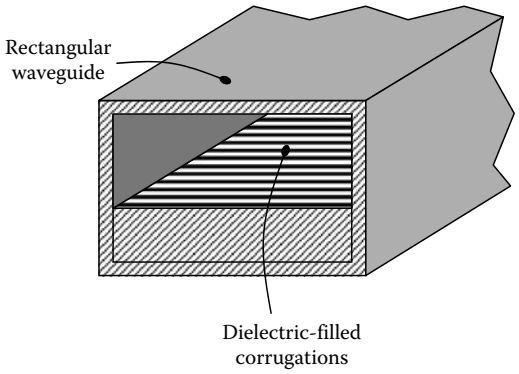

FIGURE 29.1 Infinite rectangular waveguide with dielectric-filled corrugations.

effective parameters of "electric and magnetic plasma" has been studied theoretically and experimentally. Waveguide miniaturization with the use of periodically loaded SRR has been discussed in Ref. [14] with the experimental verification of backward-wave propagation below the cutoff.

In this chapter, the modal and dispersion characteristics of rectangular waveguides with dielectric-filled corrugations depicted in Figure 29.1 are studied to investigate the possibility of their supporting backward waves, i.e., waves that exhibit phase advance in the direction of propagation. The proposed structure is analyzed using a number of approaches: equivalent circuit modeling, spectral analysis, and analysis using asymptotic boundary conditions. Results are compared with those obtained using several commercial software packages.

29.1.1 Corrugated Waveguides

Conventionally, corrugated waveguides have been used in horn antenna applications [17], where the corrugated surface serves as a high-impedance surface required to support hybrid modes that improve the radiation characteristics. A new function for the corrugated surface may, however, be sought to support backward waves in the waveguide, viz. a capacitive immittance surface. For LH waves to propagate, the guiding structure should provide series capacitance and shunt inductance within some frequency range. Since evanescent transverse electric (TE) modes of traditional waveguides are known to have inductive nature and the corrugations can introduce series capacitance with the proper choice of the corrugations parameters, then it is expected that LH propagation can be allowed to occur below the cutoff of the TE dominant mode of the noncorrugated waveguide. Among the parameters that can be varied for the corrugations are the length, width, depth, dielectric material, and period as well as the position on the broad wall as the corrugations are not necessarily of wall-to-wall extent.

29.1.2 Equivalent Circuit Model for TE and TM Modes in Rectangular Waveguides

Expressing the transverse electric and magnetic fields for a rectangular waveguide mode using the vector modal functions and the modal voltage and current [18], circuit models shown in Figure 29.2a, c, and d can be constructed for propagating TE and transverse magnetic (TM) modes, evanescent TE mode, and evanescent TM mode, respectively. The circuit model in Figure 29.2b corresponds to LH propagation, which does not normally occur in conventional waveguides.

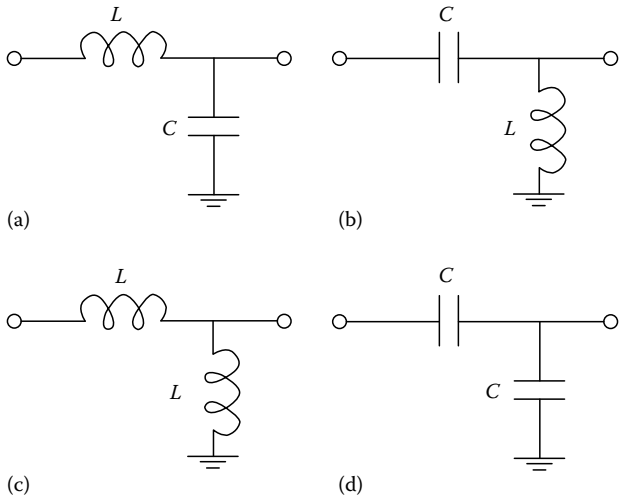

FIGURE 29.2 Equivalent circuit model for a differential transmission line section: (a) RH propagation, (b) LH propagation, (c) evanescent TE mode, and (d) evanescent TM mode.

29.1.3 Why Corrugated Waveguides as Left-Handed Guided-Wave Structures?

To accommodate LH propagating waves, the equivalent circuit model of the waveguide should be of the form depicted in Figure 29.2b. Since evanescent TE modes have inherent shunt inductance, then to create a medium with an effective negative refractive index, only a series capacitance is required to overcome the effect of the line series inductance.

For rectangular waveguides, transverse slots are known to be series discontinuities. For the slot to have an overall capacitive immittance, it can be loaded by a short-circuited waveguide stub with depth greater than a quarter guided wavelength and less than half a guided wavelength. However, for this to be true, the slot waveguide must have a real characteristic impedance, i.e., it should operate above cutoff. This can be guaranteed if it is filled with a dielectric to bring down the cutoff frequency of the stub waveguide. The periodic slots with the dielectric-filled stubs can be simply viewed as dielectric-filled corrugations. It is important to emphasize that these corrugations do not serve as a high-impedance surface (soft surface) as they are commonly used, but rather as capacitive immittance surface.

29.2 Analysis Techniques

29.2.1 Equivalent Circuit Model

The equivalent circuit model for a period p in the waveguide with dielectric-filled corrugations is depicted in Figure 29.3. The waveguide is assumed to have a characteristic impedance Z_g for the dominant mode, the corrugation aperture (the slot) is modeled as a resonant LC circuit, and the corrugation (the waveguide stub) is assumed to have a characteristic impedance Z_s and depth d.

For sufficiently narrow slots and a sufficiently small period of the corrugations, the effective per-unit-length inductance and capacitance of the transmission line (TL) model of the corrugated waveguide may be found using

$$C'_{\text{eff}} = C', \quad L'_{\text{eff}} = L' - \frac{j}{\omega p Y_{\text{corr}}}. \tag{29.1}$$

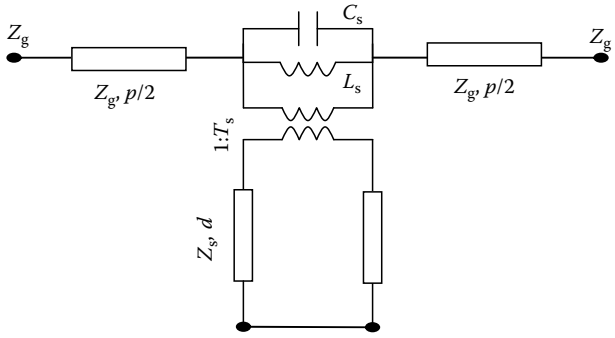

FIGURE 29.3 Equivalent circuit model for a period in a waveguide with dielectric-filled corrugations.

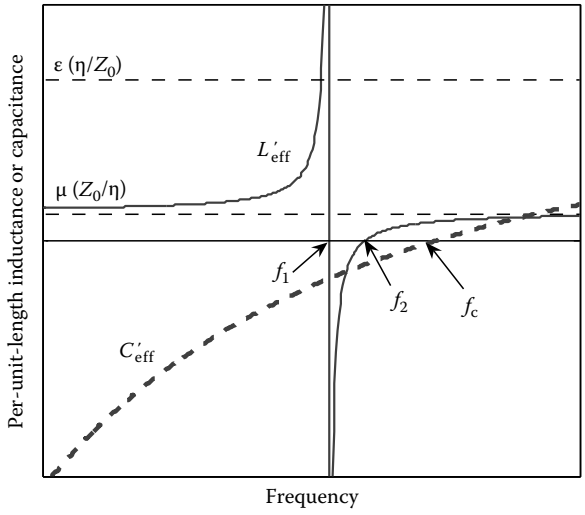

FIGURE 29.4 Typical curves for the effective per-unit-length inductance and capacitance of the transmission line model. The scale of the inductance and capacitance is not the same.

where

$$L' = 2\mu\frac{b}{a}, \quad C' = \varepsilon\frac{a}{2b}\left(1-(f_c/f)^2\right),$$
$$Y_{corr} = j\omega C_s + \frac{1}{j\omega L_s} + \frac{\cot(\beta_s d)}{jT_s^2 Z_s}. \tag{29.2}$$

Within some frequency range higher than the stub cutoff and lower than the main waveguide cutoff, and with the proper choice of the corrugation depth and period, C'_{eff} and L'_{eff} are negative corresponding to a shunt inductance and a series capacitance, respectively. The typical behavior of the per-unit-length effective parameters is depicted in Figure 29.4. It is clear that below the cutoff frequency f_c of the dominant mode of the corresponding smooth-walled waveguide, C'_{eff} is negative yielding a shunt inductance. Within the frequency range $f_1 < f < f_2$ where the contribution of the capacitance provided by the corrugation exceeds that of the waveguide inductance, a series capacitance is achieved, and thus LH propagation can be supported. Whereas Figure 29.4 shows the case

where $f_1 < f_2 < f_c$, and different dimensions may result in $f_1 < f_c < f_2$. The propagation constant β may thus be computed in the different frequency ranges using

$$\beta = \begin{cases} \omega\sqrt{L'_{\text{eff}}C'_{\text{eff}}}, & f > f_{\text{RH}} \\ -\omega\sqrt{L'_{\text{eff}}C'_{\text{eff}}}, & f_1 < f < f_{\text{LH}} \\ -j\omega\sqrt{|L'_{\text{eff}}C'_{\text{eff}}|}, & \text{elsewhere} \end{cases}, \tag{29.3}$$

where

$f_{\text{RH}} = \max\{f_c, f_2\}$
$f_{\text{LH}} = \min\{f_c, f_2\}$

In Equation 29.3 the first and second branches correspond to RH and LH propagation, respectively, and the third branch corresponds to evanescence occurring when the per-unit-length parameters have opposite signs. Alternatively, the propagation constant may be obtained using the Bloch–Floquet theorem as

$$\beta = \frac{1}{p}\cos^{-1}\left(1 - \frac{\omega^2 p^2 L'_{\text{eff}}C'_{\text{eff}}}{2}\right). \tag{29.4}$$

It is important to notice that for relatively electrically long slots that have wall-to-wall extent, the effect of the slot admittance is dominated by the stub waveguide admittance. Moreover, the transformer turns ratio is unity. This facilitates the analysis of the structure even more, alleviates the need for determining the slot circuit parameters, and hence helps speed up the design procedure using the circuit model.

29.2.2 Spectral Analysis

A more rigorous analysis technique may be sought by solving the source-free problem of propagation in the corrugated waveguide. This may be done by invoking Floquet's theorem to reduce the problem to the analysis of one period. A typical procedure is followed [19] to obtain the dispersion relation and the modal field distribution. As expected, the dispersion relation turns out to be the result of matching two admittances on both sides of the corrugated interface with some averaging factor related to the corrugation width-to-period ratio. This is very similar to the transverse resonance method [20].

29.2.3 Asymptotic Boundary Conditions

Another approach that is less sophisticated than the spectral or modal analysis is the use of the asymptotic corrugation boundary conditions (ACBCs) [21]. Application of the ACBCs in the analysis of planar and cylindrical surfaces was studied in Refs. [21–23]. The ACBCs were also used in the analysis of cylinders with arbitrary cross-section in the frequency domain and time domain as well as the analysis of longitudinally corrugated bodies of revolution [24]. Though approximate, the use of the ACBCs tremendously simplifies the solution procedure of corrugated surfaces. For a sufficiently electrically small period, the ACBCs provide solutions with good accuracy while taking into account the effect of the corrugation width-to-period ratio.

Simply put, the ACBCs require that the electric field component along the corrugations vanish whereas the tangential components orthogonal to the corrugations on both sides of the corrugated surface be related by the width-to-period ratio.

If only one wall of the waveguide is corrugated, enforcing the ACBCs yields a dispersion relation that can be viewed again as a transverse resonance phenomenon. This can be neatly modeled as shown in Figure 29.5.

The power and simplicity of using the ACBCs is manifested in the more complicated problem of a waveguide with corrugated opposite walls. Though more involved than the one-walled case, the

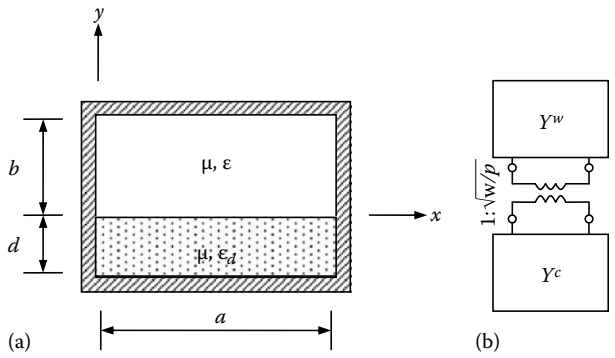

FIGURE 29.5 Rectangular waveguide with one dielectric-filled corrugated wall: (a) transverse cross-section and (b) equivalent network model. (From Eshrah, I.A. and Kishk, A.A., *IET Proc. Microw. Antennas Propag.*, 153, 221, 2006. With permission.)

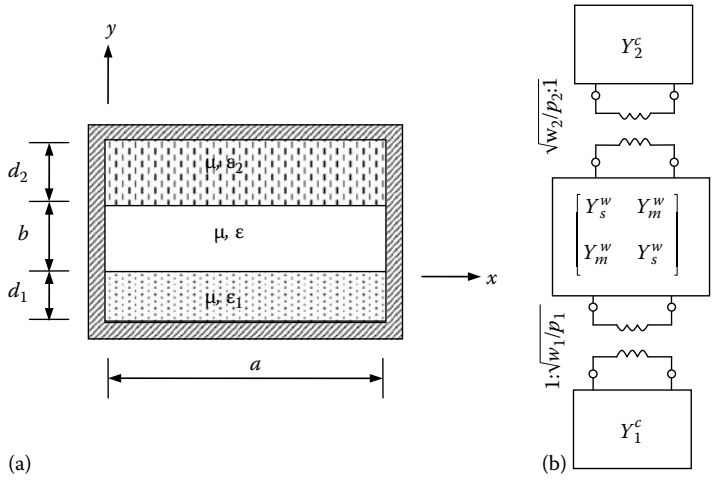

FIGURE 29.6 Rectangular waveguide with two dielectric-filled corrugated walls: (a) transverse cross-section and (b) equivalent multiport network model. (From Eshrah, I.A. and Kishk, A.A., *IET Proc. Microw. Antennas Propag.*, 153, 221, 2006. With permission.)

ACBCs yield the dispersion relation and the field expressions in the waveguide and corrugations in a straightforward manner. The dispersion relation in this case can be modeled as shown in Figure 29.6.

29.2.4 Green's Function Approach

If the source is present in the solution domain as shown in Figure 29.7, the previous techniques will not be able to determine the behavior of the excited structure. Although commercial software packages may be used to obtain a solution for such problem, the simulation time and memory might be prohibitively large due to the minute details in the problem, viz., the narrow corrugations. The Green's function method is a powerful tool used in the analysis of a variety of canonical problems. Invoking

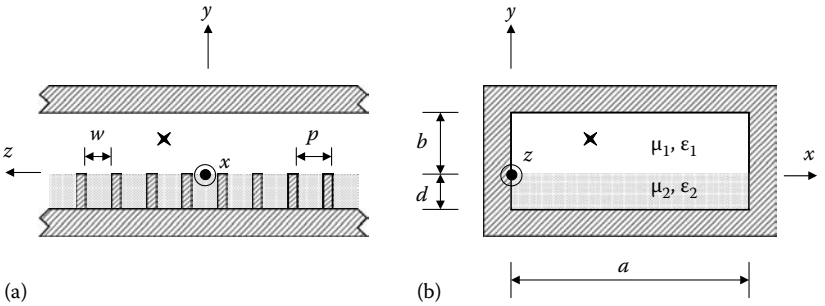

FIGURE 29.7 Cross-section in the rectangular waveguide with dielectric-filled transverse corrugation: (a) longitudinal view and (b) transverse view. The cross indicates that the source is in region 1 (the waveguide). (From Eshrah, I.A. and Kishk, A.A., *IEEE Trans. Microwave Theory Tech.*, 55, 355, 2007. With permission.)

the surface equivalence principle [20] to solve problems of radiation and/or scattering in regions with known Green's functions reduces the problem to that of discretizing the surface of the object in the background medium. The solution procedure using the surface integral equation for such problems is usually much faster in terms of computational time and more manageable in terms of memory storage requirements compared with other full-wave techniques that require the discretization of the whole region.

For closed-boundary (waveguide) problems Green's functions can be obtained in the form of the eigenfunction expansion as the solution of corresponding dyadic wave equations subject to appropriate boundary conditions on a waveguide surface. A framework of dyadic Green's functions for multilayered rectangular waveguides has been developed in Refs. [26–29] for the analysis of microstrip structures and spatial power combining applications. In Ref. [30], a procedure for developing dyadic Green's functions based on the eigenfunction expansion method has been described for various waveguide problems.

The eigenfunction expansion method can be used to obtain the Green's function for the rectangular waveguide with dielectric-filled corrugations. The goal of deriving the Green's function for this structure is to be able to speed up the analysis procedure for finite sections of the corrugated waveguide, design transitions and matching sections to and from conventional waveguides, and most importantly analyze the scattering properties of obstacles in this metaguide and the coupling to external loads or radiators, such as dielectric resonator antennas excited by waveguide probes as studied in Ref. [31] for conventional waveguides.

The following approach is used in the derivation: The spectral domain representation of the Green's function is adopted to reduce the problem to a one-dimensional problem in the transverse direction perpendicular to the corrugated surface. Then the inverse Fourier transform (IFT) is used to obtain the spatial domain expressions on determining the poles in the spectral parameter complex plane. To simplify the derivation, the ACBCs are used to characterize the corrugated interface.

29.2.4.1 Development of Green's Functions

The ACBCs are first mapped from the electric and magnetic fields to the electric scalar and magnetic vector potentials to determine the boundary conditions imposed on the potentials as well as the nonzero components of the Green's dyadics. For sufficiently narrow corrugations, the electric scalar potential vanishes inside the corrugations and on the corrugation interface. Thus, the potential within the waveguide will be subject to homogeneous Dirichlet boundary conditions on the PEC

walls as well as the corrugated wall. Using the eigenfunction expansion method [30], the electric scalar potential Green's function can be obtained [32,33].

For the magnetic vector potential, the ACBCs are enforced and mapped to the potential, and then the Fourier transform is invoked to obtain the spectral representation of the corrugation Green's function. Applying the boundary conditions in the spectral domain determines the solution of the spectral domain Green's function.

The transformation from the spectral to the spatial domain is then carried out using an IFT procedure, which requires the determination of the poles of the spectral Green's function in the complex wave number plane. The expressions readily exhibit the occurrence of two sets of poles. The first set of poles represents the contribution of the conventional (smooth-walled) waveguide modes. The second set of poles corresponds to the resonances of the admittances on both sides of the corrugated interface.

On determining the poles of the spectral domain representation, the IFT is applied to obtain the spatial domain expressions [32]. It is worth mentioning that the residue integrals involve removable singularities but no branch cuts. This corresponds to propagation in an equivalently closed structure with no direct radiation. The Green's functions for a semiinfinite waveguide or a cavity can be obtained using similar modifications to those in Ref. [33].

29.2.4.2 Applications

29.2.4.2.1 Probe Excitation

The derived Green's function can be used to analyze problems where an impressed or equivalent electric source exists in the waveguide region. A simple problem that can be used to verify the derived expressions is the probe excitation problem depicted in Figure 29.8. The method of moments (MoM) is employed to solve for the unknown probe current and determine the input impedance seen by a delta-gap source at the probe end. Following the same procedure as that described in Ref. [31] for a probe in a smooth-walled waveguide yields the required expressions for the MoM matrix and excitation vector. Subsequently, the input impedance is computed on inverting the MoM matrix (Figure 29.8).

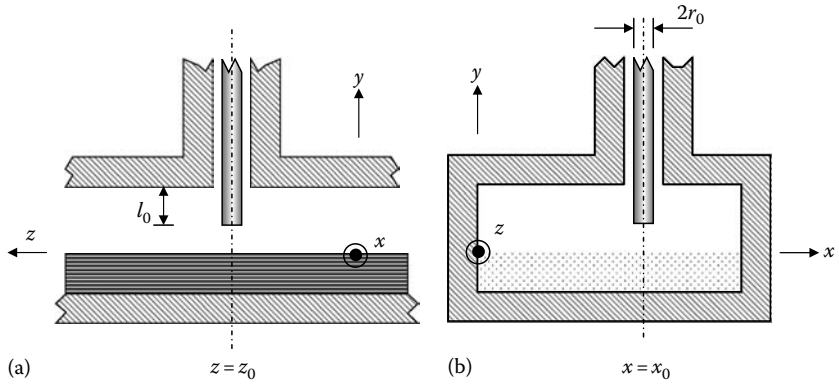

FIGURE 29.8 Probe excitation of the corrugated waveguide. (From Eshrah, I.A. and Kishk, A.A., *IEEE Trans. Antennas Propagat.*, 55, 1124, 2007. With permission.)

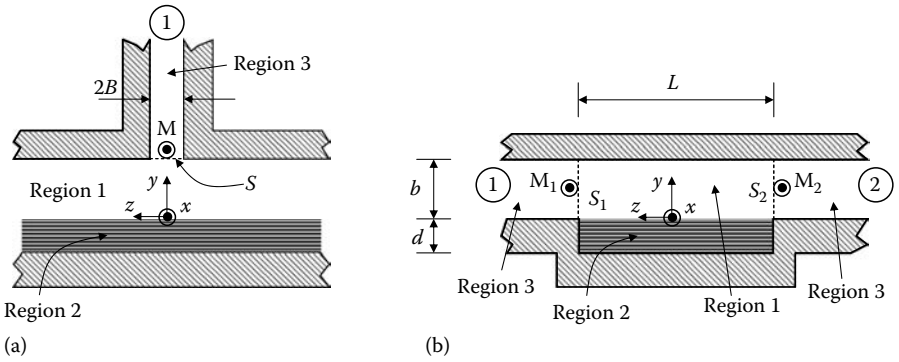

FIGURE 29.9 Geometry of the problems used to verify the derived Green's functions: (a) T-junction and (b) waveguide transition. The metaguide is infinite (matched) in the T-junction problem. (From Eshrah, I.A. and Kishk, A.A., *IEEE Trans. Microwave Theory Tech*., 55, 1124, 2007. With permission.)

29.2.4.2.2 Series T-Junction

To verify the derived Green's functions, the simple example of a series or E-plane T-junction is considered. In the geometry depicted in Figure 29.9a, the dominant mode of the narrow feed waveguide (denoted as region 3) is incident at port 1. Invoking the surface equivalence principle [20], the problem may be solved by considering the equivalent problem where the aperture is shorted out, and unknown magnetic currents are introduced on both sides of the surface *S*.

29.2.4.2.3 Waveguide Transition

The transition from a conventional waveguide to the corrugated waveguide is another interesting example that can be solved using the derived Green's functions. For the geometry shown in Figure 29.9b, both waveguides, the corrugated and noncorrugated, have equal cross-sectional dimensions. The corrugated section has a length of *L*. The noncorrugated waveguides are filled with a dielectric. In view of the equivalence principle, the cavity and the short-circuit waveguide Green's functions are used to analyze the corrugated section and the noncorrugated waveguide ports, respectively. The modifications to the derived Green's functions to obtain its cavity counterpart can be found in Ref. [33].

29.3 Results, Observations, and Phenomena

29.3.1 Experimental Verification

To verify the wave propagation below the cutoff, a prototype of the corrugated waveguide was realized as shown in Figure 29.10. The corrugations were built by stacking rectangular pieces milled off a Rogers high-frequency laminate (RO3010) with a dielectric constant of 10.2 and thickness of 1.27 mm. The rectangles have dimensions of 17 and 3.7 mm. An artificial wall was inserted in a standard X-band waveguide section of length 8.8 mm to reduce the width to 17 mm and raise the cutoff frequency to 8.82 GHz. Figure 29.11 shows the measured insertion loss with and without the corrugations. Experimental results are compared with those obtained using QW3D [34]. The waveguide is excited using standard X-band adapters connected to an HP8510 Network Analyzer.

The discrepancies between the experimental and simulation results are attributed to the imperfections in the hand-assembly manufacturing process of this simple prototype, namely, the air gap

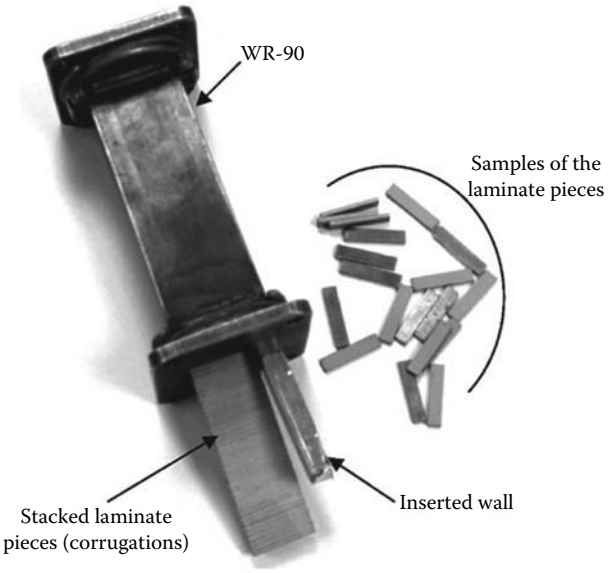

FIGURE 29.10 Manufactured corrugated waveguide prototype showing the artificial conducting wall, the corrugations inserted in the waveguide, and some pieces of the laminate before stacking them to form the corrugations. (From Eshrah, I.A., Kishk, A.A., Yakovlev, A.B., and Glisson, A.W., *IEEE Trans. Microwave Theory Tech.*, 53, 3298, 2005. With permission.)

between the laminate pieces and the bottom wall of the waveguide, which is very crucial in the operation of the structure since it is based on the fact that the corrugations are short circuited. The effect of the air gap on the transmission coefficient is also shown in Figure 29.11, where the simulation results with and without an air gap of 0.1 mm are depicted. Other sources of discrepancy include the possible nonuniform air gap between the corrugations and the artificial wall inserted in the waveguide and the air gaps between the corrugations themselves.

It is worth mentioning that the effect of the dielectric and conductor losses was taken into consideration in the finite-difference time-domain (FDTD) simulation. That is why the transmission in the LH band experiences some attenuation, which is dominated by the dielectric losses (a loss tangent of 0.0023 at 10 GHz). For a lossless dielectric, the total transmission is observed in the LH band. The ripples in the transmission bands are due to the mismatch between the waveguide ports and the corrugated waveguide section, which results in standing waves that vary the response of the system with frequency.

To verify the phase advance phenomenon within the LH propagation band, the method suggested in Ref. [14] is employed, where the phase of the transmission coefficient S_{21} for a reference waveguide section is compared with that obtained for slightly longer sections that have 4 and 8 more cells. The phase advance over a portion of the LH band is plotted in Figure 29.12 as obtained from the simulation. Notice the linear increase in phase with the increase in the number of cells at every frequency point.

29.3.2 Dispersion Characteristics for Dominant Mode

To act as a capacitive immittance surface, the corrugations should be from a quarter guided-wavelength to a half guided-wavelength deep. In the following results, the corrugation depth is chosen

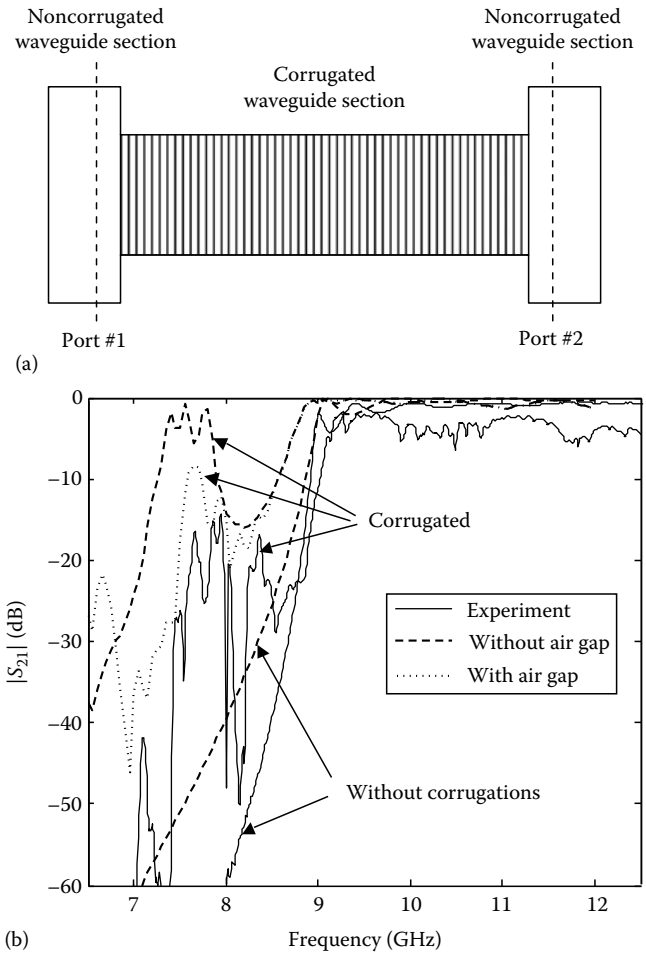

FIGURE 29.11 The insertion loss for a rectangular waveguide with and without the corrugations. The simulation results are plotted for the cases with and without an air gap between the corrugation and the bottom wall. (From Eshrah, I.A., Kishk, A.A., Yakovlev, A.B., and Glisson, A.W., *IEEE Trans. Microwave Theory Tech.*, 53, 3298, 2005. With permission.)

to satisfy this condition within a frequency range below the cutoff frequency of the main waveguide. Figure 29.13 depicts the dispersion diagram for a reference case where the corrugated waveguide has the following parameters: cross-section 17 mm × 6.46 mm, wall-to-wall corrugations of width, depth, and period of 1.27, 3.7, and 1.5 mm. The waveguide is air-filled, whereas the corrugations, dielectric constant is 10.2. Four bands are distinguished in the figure: an RH pass band above the cutoff frequency f_c of the TE^z_{10} mode of the noncorrugated waveguide ($\Re[k_{z0}] > 0$ and $\Im[k_{z0}] = 0$), an LH pass band in the frequency range $f_1 < f < f_2$ ($\Re[k_{z0}] < 0$ and $\Im[k_{z0}] = 0$), two stop bands in the ranges $f_2 < f < f_c$ and $f < f_1$ where the waves are evanescent ($\Re[k_{z0}] = 0$ and $\Im[k_{z0}] < 0$). The curve in Figure 29.13 was obtained by solving the dispersion relation. The comparison with a high-frequency structure simulator (HFSS) [36] exhibits an excellent agreement.

The waveguide characteristic impedance of the dominant mode is real and positive in the LH and RH propagation bands and assumes positive imaginary values (inductive) elsewhere, as shown in Figure 29.14.

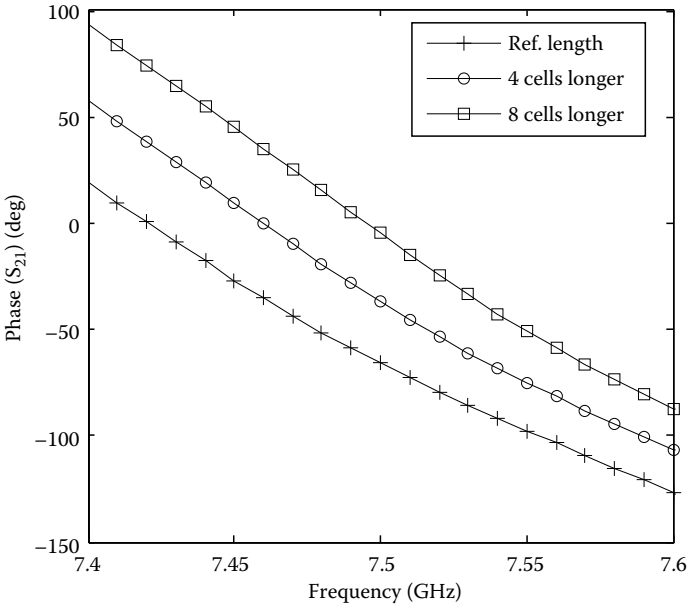

FIGURE 29.12 Comparison between the phase of the transmission coefficient S_{21} of a reference waveguide section and a longer section. (From Eshrah, I.A., Kishk, A.A., Yakovlev, A.B., and Glisson, A.W., *IEEE Trans. Microwave Theory Tech*., 53, 3298, 2005. With permission.)

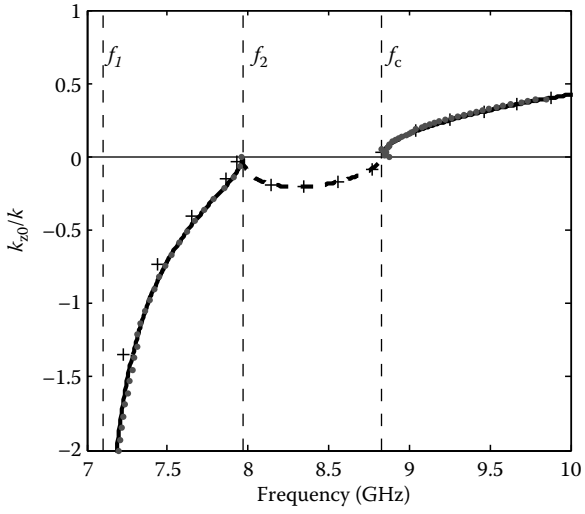

FIGURE 29.13 Dispersion characteristics of the dominant TE^x_{01} mode. Lines: present theory (solid: real part and dashed: imaginary part), dots: HFSS, and pluses: circuit model (L = 6.788 nH, C = 47.711 fF, and T = 1.0). (From Eshrah, I.A., Kishk, A.A., Yakovlev, A.B., and Glisson, A.W., *IEEE Trans. Antennas Propagat*., 53, 3673, Nov. 2005. With permission.)

The effective per-unit-length capacitance and inductance of the equivalent transmission line model of the waveguide assume negative values in the LH pass-band range, where the former is negative due to the evanescence condition and the latter is dominated by the capacitance offered by the

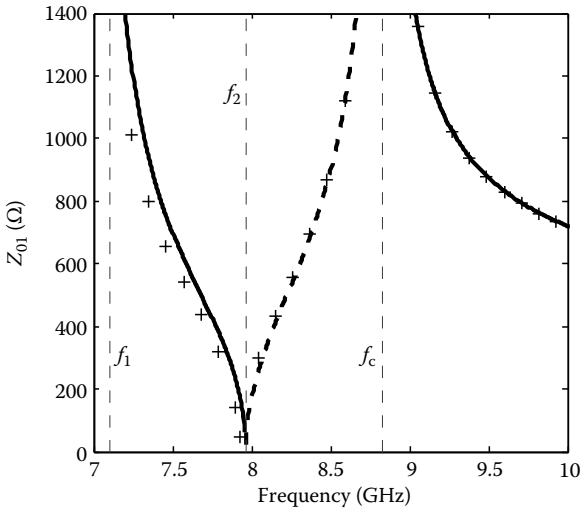

FIGURE 29.14 Characteristic impedance of the dominant TE_{01}^{x} mode (solid: real part and dashed: imaginary part), symbols: circuit model (L = 6.788 nH, C = 47.711 fF, and T = 1.0). (From Eshrah, I.A., Kishk, A.A., Yakovlev, A.B., and Glisson, A.W., *IEEE Trans. Antennas Propagat.*, 53, 3673, Nov. 2005. With permission.)

corrugations. Figures 29.13 and 29.14 also compare the values of the propagation constant and characteristic impedance estimated using the equivalent circuit model to those obtained using the present theory. It can be seen that the circuit analysis succeeds in predicting the dispersion behavior of the structure with very good accuracy, except in the range where k_{z0} assumes relatively high values. This is expected since the validity of the circuit model was based on the assumption that the period is much less than the guided wavelength; a condition that is violated for high values of k_{z0}.

29.3.3 Parametric Studies and Bandwidth Control

Since the evanescence region extends below the cutoff frequency f_c, it can be inferred that the bandwidth of the LH propagation is controlled by the corrugations, viz., the frequency range where the series capacitance of the corrugations overcomes the series inductance of the waveguide. Thus a study of the effect of the corrugation parameters is important to assess their impact on the LH propagation bandwidth.

First, the effect of reducing the waveguide width a is investigated. For wall-to-wall corrugations, i.e., l/a = 1, Figure 29.15 shows the variation of the propagation constant k_{z0} with the waveguide width a. The results show that the LH propagation can be supported while reducing the waveguide width as long as the corrugations support propagating waves below the cutoff of the main waveguide. Since the corrugations are filled with a dielectric that has $\varepsilon_{rd} > 1$, then the width can be arbitrarily reduced with this condition satisfied. Reducing the other dimension, i.e., the waveguide height b, has a significant effect on the propagation constant as depicted in Figure 29.16. As the waveguide height decreases, the upper frequency f_2 increases, whereas the lower frequency f_1 remains almost unchanged, thus yielding an overall increase in the LH propagation bandwidth. Indeed, at a certain value of b (in this case $b = 2.75$ mm), f_2 is equal to f_c. Below this value of b, f_2 becomes greater than f_c, and the RH propagation occurs for $f > f_2$ as observed in the case with b = 2.46 mm in Figure 29.16. In general, the RH propagation starts at $f > f_{RH}$ and the LH propagation occurs in the range $f_1 < f < f_{LH}$, where $f_{RH} = \max\{f_c, f_2\}$ and $f_{LH} = \min\{f_c, f_2\}$. The same result was reached and understood in terms of the equivalent circuit model.

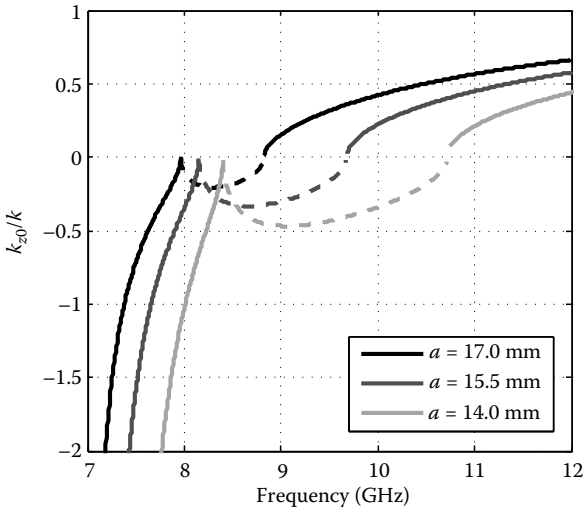

FIGURE 29.15 The effect of reducing the waveguide width a on the propagation constant k_{z0}. (From Eshrah, I.A., Kishk, A.A., Yakovlev, A.B., and Glisson, A.W., *IEEE Trans. Antennas Propagat.*, 53, 3673, Nov. 2005. With permission.)

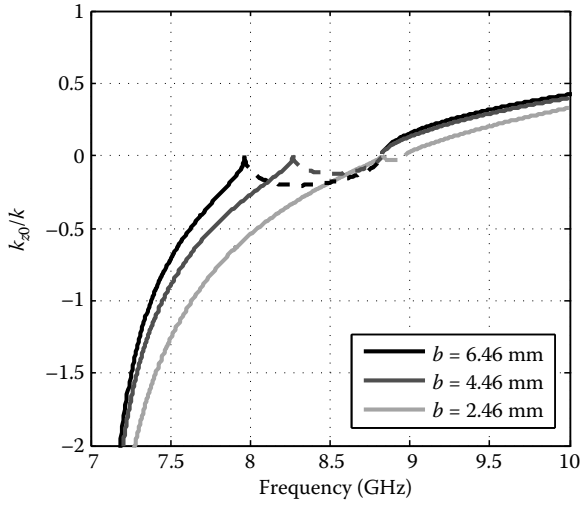

FIGURE 29.16 The effect of reducing the waveguide height b on the propagation constant k_{z0} (a = 17 mm). (From Eshrah, I.A., Kishk, A.A., Yakovlev, A.B., and Glisson, A.W., *IEEE Trans. Antennas Propagat.*, 53, 3673, Nov. 2005. With permission.)

Next, The effect of the corrugation length l on the dispersion characteristics is studied. Fixing a at 17 mm, the curves in Figure 29.17 are generated for values of l from 17 mm to 11 mm. As the corrugation length decreases, the cutoff of the corrugation waveguide increases yielding a longer corrugation wavelength and thus an electrically shorter corrugation. This results in a positive shift in the LH propagation band where the corrugations regain the electrical depth necessary for the capacitive surface behavior. It is interesting to notice that the balanced condition for the composite RH/LH waveguide,

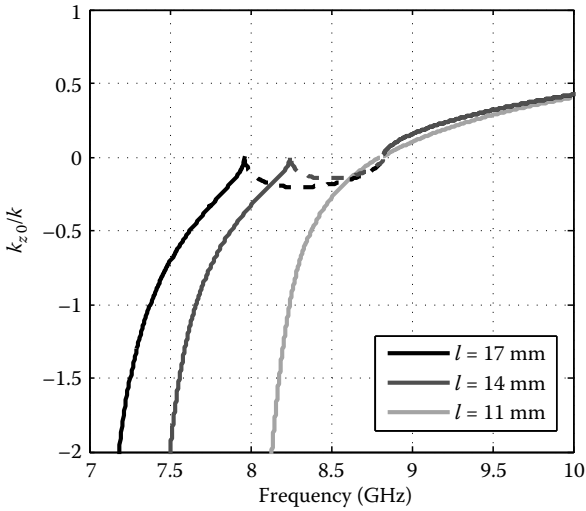

FIGURE 29.17 The effect of the corrugation length to the waveguide width ratio l/a on the propagation constant k_{z0} (a = 17 mm). (From Eshrah, I.A., Kishk, A.A., Yakovlev, A.B., and Glisson, A.W., *IEEE Trans. Antennas Propagat.*, 53, 3673, Nov. 2005. With permission.)

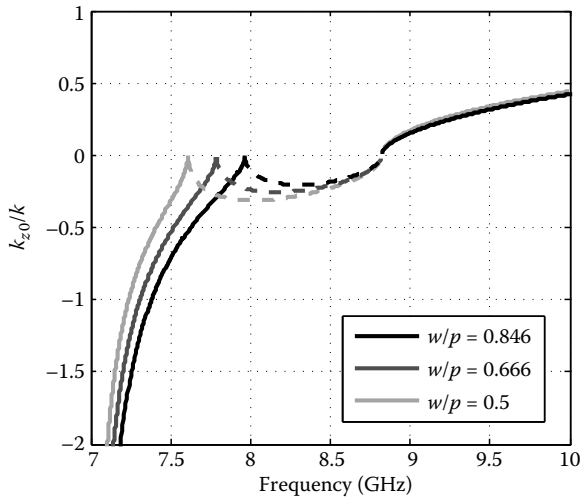

FIGURE 29.18 The effect of the corrugation width-to-period ratio w/p on the propagation constant k_{z0} (w = 1.27 mm). (From Eshrah, I.A., Kishk, A.A., Yakovlev, A.B., and Glisson, A.W., *IEEE Trans. Antennas Propagat.*, 53, 3673, Nov. 2005. With permission.)

viz., $f_2 = f_c$, can be achieved with the proper choice of the corrugation dimensions as observed in Figures 29.16 and 29.17.

Another important design parameter is the corrugation width-to-period ratio. As predicted by the equivalent circuit model, the higher the value of w/p, the wider the LH propagation bandwidth, due to the increase in the average capacitance offered. This is illustrated by the curves depicted in Figure 29.18. For a fixed w/p ratio, however, variations in the corrugation period have virtually no effect on the dispersion characteristics.

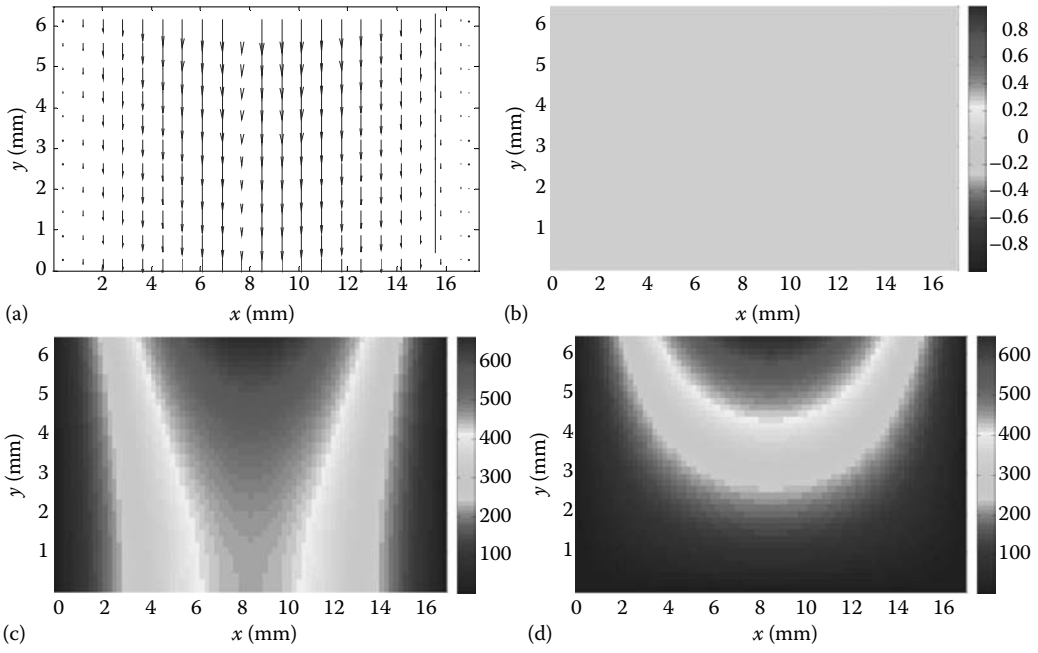

FIGURE 29.19 Electric field distribution in the *XY* plane ($z = 0$) of the TE_{01}^{x} mode in the LH band: (a) vector field plot, (b) $|E_x^w|$, (c) $|E_y^w|$, and (d) $|E_z^w|$. (From Eshrah, I.A., Kishk, A.A., Yakovlev, A.B., and Glisson, A.W., *IEEE Trans. Antennas Propagat.*, 53, 3673, Nov. 2005. With permission.)

29.3.4 Modal Field Distribution for Dominant Mode

Field plots for the dominant mode in the LH pass band are depicted in Figures 29.19 and 29.20 for the electric and magnetic fields, respectively, in the cross-sectional plane in the main waveguide. In comparison to the modal distribution of the TE_{10}^{z} mode of the conventional waveguide, this mode is characterized by the longitudinal component of the electric field, which peaks in the vicinity of the corrugation interface (the capacitive surface).

29.3.5 Asymptotic Boundary Conditions

Figure 29.21 compares between the dispersion characteristics obtained using the ACBC and those obtained using the modal solution for the same width-to-period ratio but different physical values of the period p. Whereas excellent agreement is noticed for w/p approaching unity and small values of p, discrepancies start to appear between both solutions for small w/p and increases as p increases. Still the maximum relative frequency shift in the case of $w/p = 0.5$ is less than 0.3%. The results depicted in the figure focus on the range where the propagation constant is negative, i.e., the LH pass band. The RH propagation characteristics in the RH pass bands are almost identical to the conventional smooth-walled waveguide and are thus not shown here.

Using the same dimensions for the two-walled corrugated waveguide, Figure 29.22 depicts the dispersion characteristics for identical corrugations showing the even and odd modes for $w/p = 0.95$. The increase in bandwidth for the odd mode is due to the effective reduction in the waveguide height to half the physical value as pointed out before. The RH even mode is beyond the frequency range under consideration and is thus not shown in the figure. Notice that there is a gap between the LH and RH pass bands in this case, which is usually referred to as an unbalanced condition [4]. This

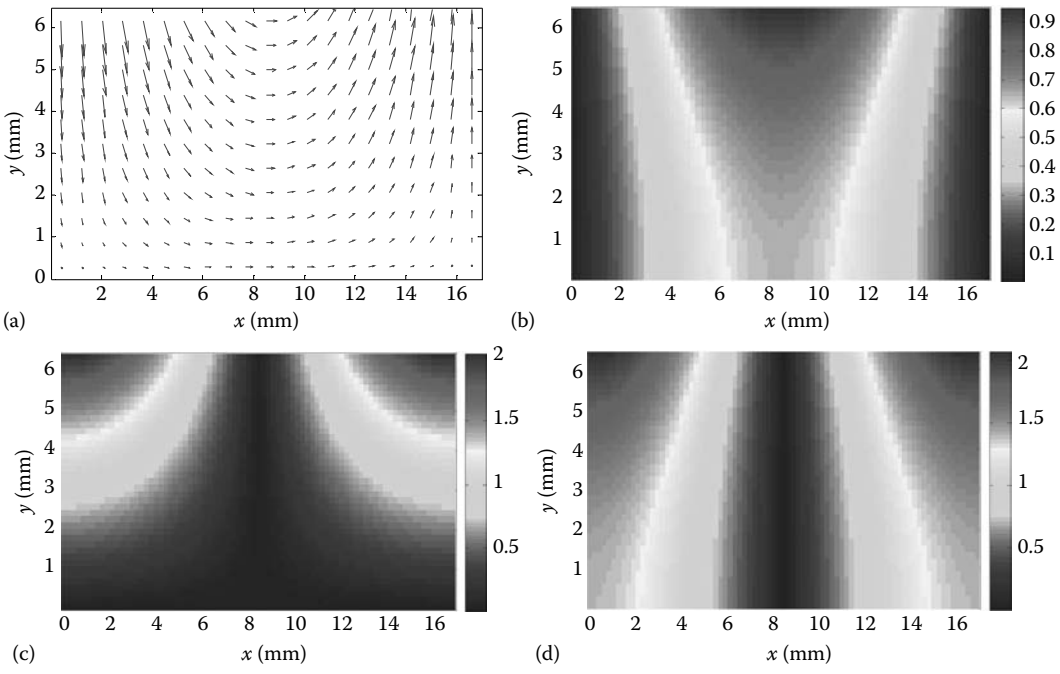

FIGURE 29.20 Magnetic field distribution in the XY plane ($z = 0$) of the TE^x_{01} mode in the LH band: (a) vector field plot, (b) $|H^w_x|$, (c) $|H^w_y|$, and (d) $|H^w_z|$. (From Eshrah, I.A., Kishk, A.A., Yakovlev, A.B., and Glisson, A.W., *IEEE Trans. Antennas Propagat.*, 53, 3673, Nov. 2005. With permission.)

gap (or stop band) results in the frequency range where the corrugations are not capacitive and the frequency is below the cutoff of the corresponding smooth-walled waveguide; these two conditions do not allow the waveguide to support LH or RH propagation. A balanced condition may be achieved as shown in Figure 29.23, where the LH and RH cutoff frequencies coincide, when corrugations of different depths are used. Thus, an improved bandwidth may be achieved with the proper tuning of the corrugation parameters as predicted by the equivalent circuit model in Ref. [35].

29.3.6 Complete Dispersion Diagram for Transverse Wave Number

Solving the dispersion relation for the metaguide modes results in the values for the transverse wave number κ_{ml} and subsequently the propagation constant β_{ml}. The curves in the dispersion diagram pertain to a specific mode if the transverse field distribution has the same features as the frequency varies. According to this criterion, Figure 29.24 defines what values of κ_m correspond to which mode. The dominant mode ($m = 1$ and $l = 0$) has the real values of κ_m always bounded by 0 and $\pi/2$ whereas the imaginary values range from 0 to ∞. By examining the behavior of the fields in the y-direction, one can readily see that for this range of real values of κ_m or for any value of the imaginary values of κ_m, the cosine (sine) distributed field components have no nulls (maxima) in the range $0 < y < b$. The next high-order mode ($m = 1$ and $l = 1$), for which κ_m is always real and bounded by $\pi/2$ and $3\pi/2$, has one null (maximum) for the cosine (sine) distributed field components. Thus, the index l has the same meaning as in conventional waveguides, viz., the number of nulls (maxima) of the field components along the y-direction. It is interesting to observe the deviation of the normalized transverse wave number $\kappa_{ml}b$ relative to its PEC waveguide counterpart $k_{yn}b$, which assumes integer

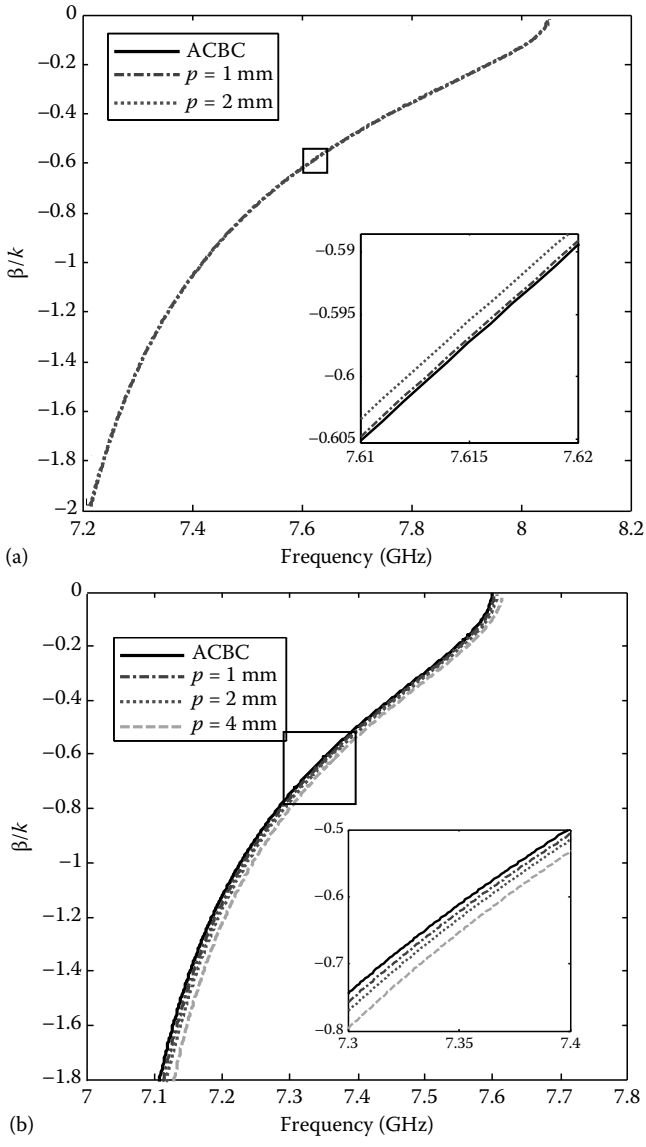

FIGURE 29.21 Dispersion characteristics of a one-walled corrugated waveguide obtained using the ACBC and the full-wave modal solution in Ref. [19] for a fixed width-to-period ratio and different physical values of the period: (a) $w/p = 0.95$ and (b) $w/p = 0.5$. (From Eshrah, I.A. and Kishk, A.A., *IET Proc. Microw. Antennas Propag.*, 153, 221, 2006. With permission.)

values of π. At the frequencies where the corrugated surface acts as a high-impedance surface (PMC surface), the curve for $\kappa_{11}b$ splits into two branches that start from odd multiples of $\pi/2$.

The corresponding curves for the normalized propagation constant β_{ml}/k_1 are shown in Figure 29.25. Notice that only the positive solutions of the real and imaginary parts are shown. In the range between 0.8π and π for $k_1 a$, the 10 mode exhibits LH propagation as was shown in Ref. [35] since both the effective per-unit-length inductance and capacitance are negative. The other ranges where β_{10}/k_1 is real or imaginary correspond to RH propagation or evanescence, respectively. The

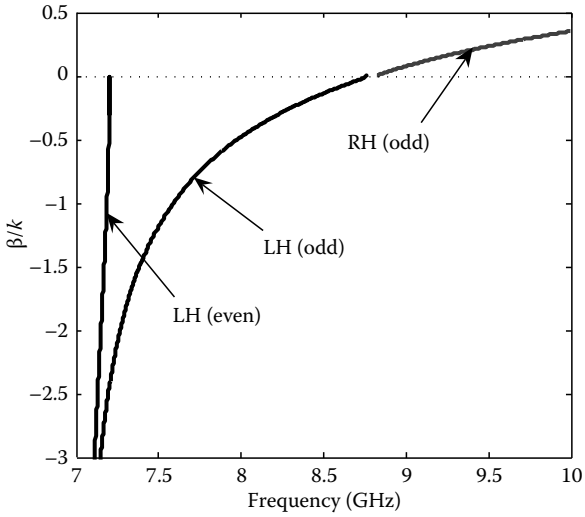

FIGURE 29.22 Dispersion characteristics of a two-walled corrugated waveguide with identical corrugations. (From Eshrah, I.A. and Kishk, A.A., *IET Proc. Microw. Antennas Propag.*, 153, 221, 2006. With permission.)

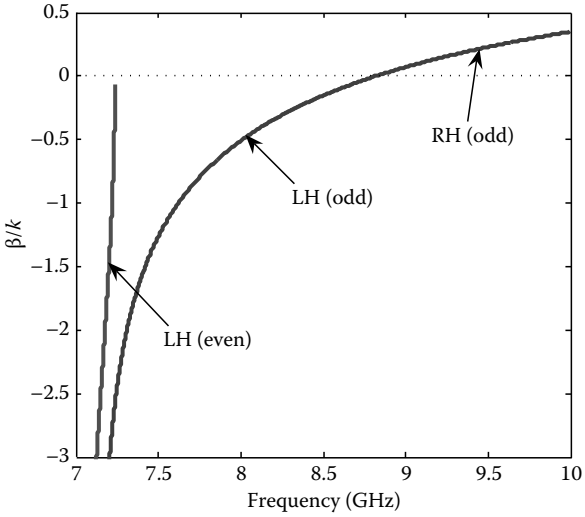

FIGURE 29.23 Dispersion characteristics of a two-walled corrugated waveguide with different corrugations: d_1 = 3.7 mm and d_2 = 3.65 mm. (From Eshrah, I.A. and Kishk, A.A., *IET Proc. Microw. Antennas Propag.*, 153, 221, 2006. With permission.)

asymptotic behavior of the 10 mode characteristics occur at the frequencies where the corrugated surface acts as a high-impedance surface. Notice that the normalized cutoff wave number of the 10 and 11 modes of the PEC waveguide are π and 2.815π, respectively. The shown dispersion curves are obtained for a = 17 mm, b = 6.46 mm, d = 3.7 mm, $w/p = 0.84$, $\varepsilon_1 = \varepsilon_0$, $\varepsilon_2 = 10.2\varepsilon_0$, and $\mu_1 = \mu_2 = \mu_0$.

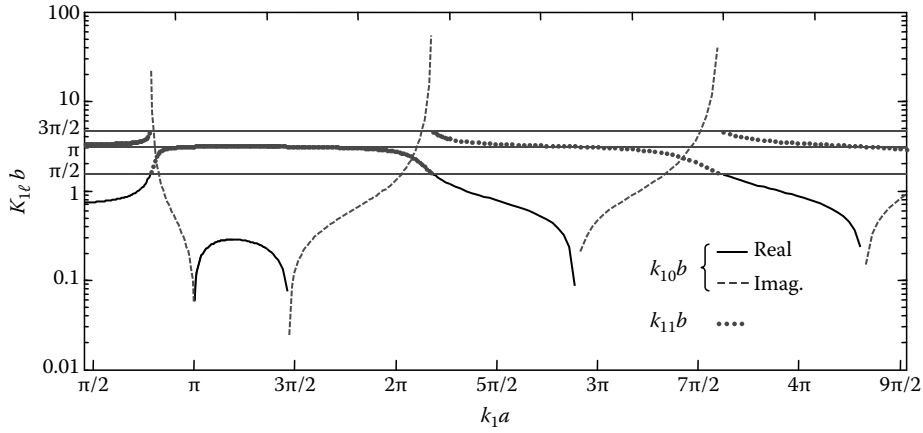

FIGURE 29.24 The normalized wave number $\kappa_{ml}\,b$ vs. the normalized frequency k_1a for the $m = 1, l = 0, 1$ modes. (From Eshrah, I.A. and Kishk, A.A., *IEEE Trans. Antennas Propagat.*, 55, 355, 2007. With permission.)

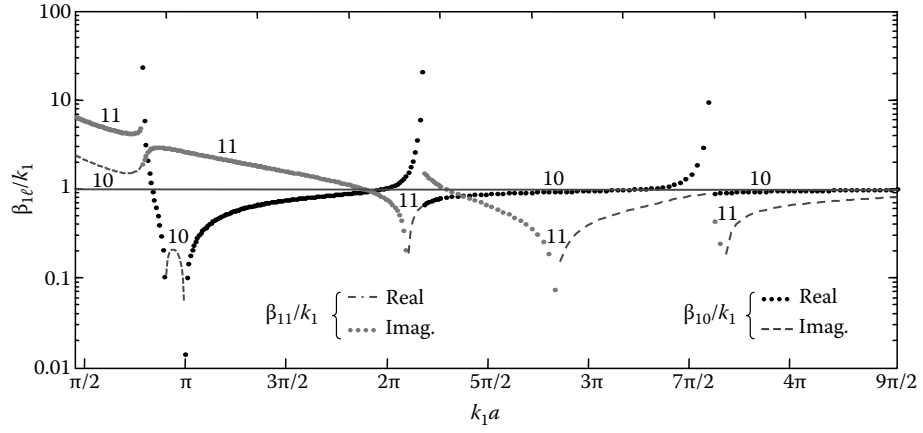

FIGURE 29.25 The normalized propagation constant β_{ml}/k_1 vs. the normalized frequency k_1a for the $m = 1, l = 0, 1$ modes. Only the positive solutions are shown. (From Eshrah, I.A. and Kishk, A.A., *IEEE Trans. Antennas Propagat.*, 55, 355, 2007. With permission.)

29.3.7 Input Impedance of a Probe Exciting the Metaguide

The input impedance of a probe extending from a coaxial line into the waveguide through the noncorrugated broad wall is computed as outlined in Section 29.2.4. The results obtained using the MoM incorporating the present theory are compared with those obtained from an FDTD simulator QuickWave-3D [34], where the actual physical structure (not the asymptotic one) was modeled. Therein, the following parameters were used: $w = 0.84$ mm, $p = 1$ mm, $d = 3.7$ mm, $l_0 = 3$ mm, and $r_0 = 0.25$ mm. For a probe centered with respect to the broad wall, i.e., $x_0 = a/2$, the input resistance and reactance are plotted in Figure 29.26. The input resistance decreases as the probe is offset from the center as shown in Figure 29.27 for a probe at $x_0 = a/4$. In Figures 29.26 and 29.27, the input impedance exhibits a nonzero real part between 7 and 8 GHz ($k_1a = 0.8\pi$ and 0.9π, respectively) and a peak at the cutoff of the RH propagation at 8.8 GHz ($k_1a = \pi$).

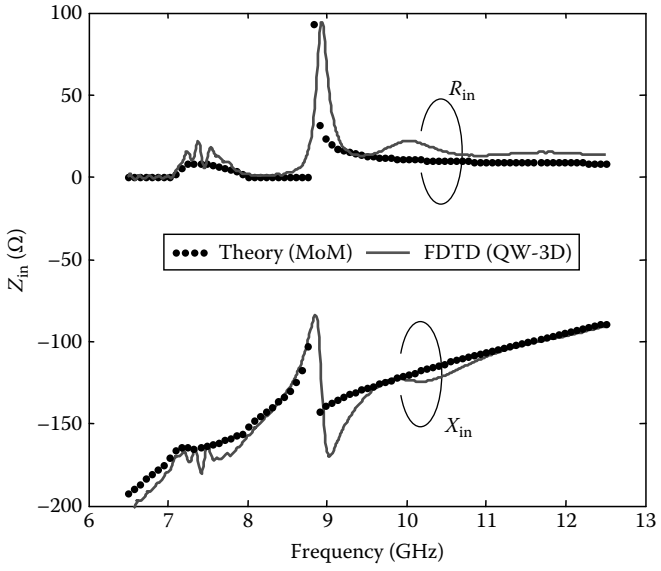

FIGURE 29.26 The input impedance at the base of a centered probe. (From Eshrah, I.A. and Kishk, A.A., *IEEE Trans. Antennas Propagat.*, 55, 355, 2007. With permission.)

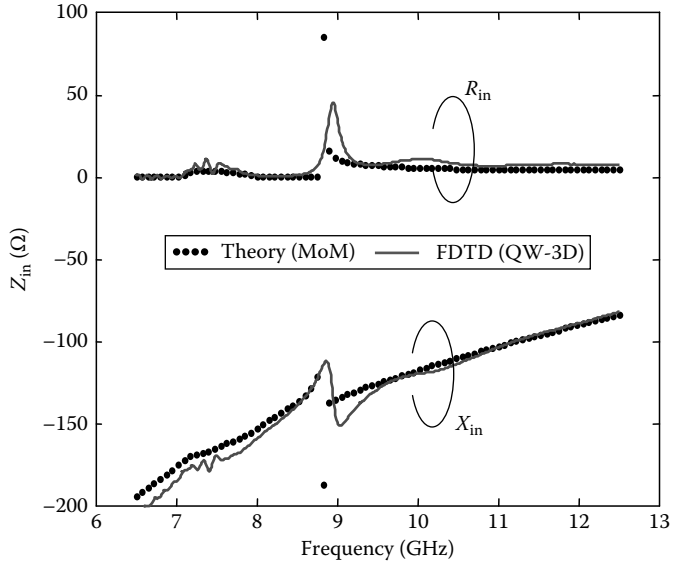

FIGURE 29.27 The input impedance at the base of a probe at $x_0 = a/4$. (From Eshrah, I.A. and Kishk, A.A., *IEEE Trans. Antennas Propagat.*, 55, 355, 2007. With permission.)

The oscillation in the FDTD results is due to the incomplete absorption of the waves at the waveguide ports by the Mur or the PML absorbing boundaries. The highly oscillatory nature of the structure as well as the fine mesh used in FDTD make the comparison in terms of the computational time and memory requirements in favor of the MoM solution. This can be easily understood

since only the probe is discretized in the MoM solution, and the zeroes of the dispersion relation are computed and stored before the matrix filling and inversion starts.

29.3.8 Waveguide Discontinuities and Transitions

Another comparison of the present theory with FDTD simulations using QuickWave-3D [34] is conducted for the waveguide discontinuities and transitions. Figure 29.28 depicts the reflection coefficient for the T-junction problem of Figure 29.9a. The oscillations in the results of the FDTD simulator are due to the imperfect absorption of the absorbing boundaries at the ends of the corrugated waveguide [32].

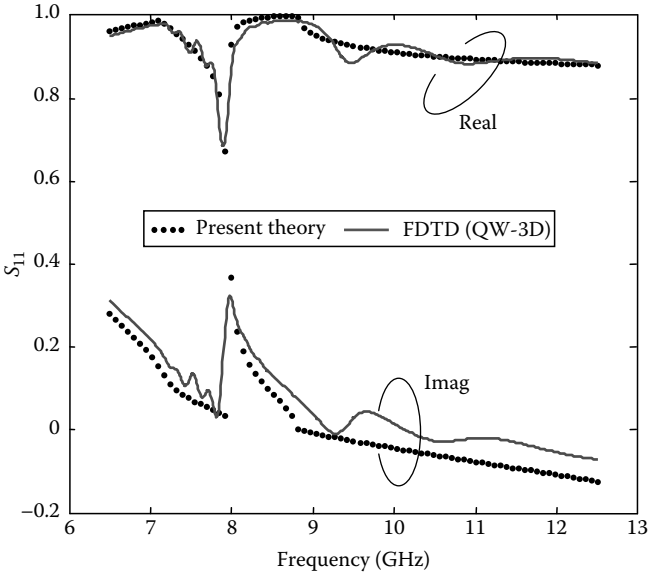

FIGURE 29.28 Reflection coefficient for the T-junction of Figure 29.9a. (From Eshrah, I.A. and Kishk, A.A., *IEEE Trans. Microwave Theory Tech.*, 55, 1124, 2007. With permission.)

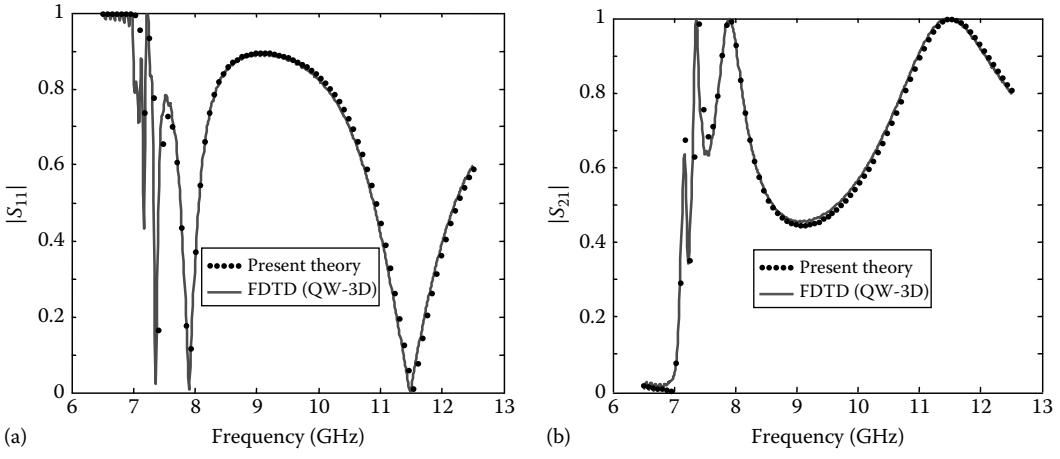

FIGURE 29.29 Scattering parameters of the waveguide transition of Figure 29.9b: (a) $|S_{11}|$ and (b) $|S_{21}|$. (From Eshrah, I.A. and Kishk, A.A., *IEEE Trans. Microwave Theory Tech.*, 55, 1124, 2007. With permission.)

The scattering parameters for the waveguide transition of Figure 29.9b are given in Figure 29.29. The results were obtained using a one-term approximation for the magnetic currents, which suggests that the interaction with the high-order modes is not significant in this case. The absence of the absorbing boundary conditions (waveguide ports are used) in this case yields excellent agreement between both results [32].

References

1. G. V. Eleftheriades, A. K. Iyer, and P. Kremer, Planar negative refractive index media using periodically L-C loaded transmission lines, *IEEE Trans. Microwave Theory Tech.*, 50, 2702–2712, Dec. 2002.
2. G. V. Eleftheriades, O. Siddiqui, and A. K. Iyer, Transmission line models for negative refractive index media and associated implementations without excess resonators, *IEEE Microw. Wireless Compon. Lett.*, 13, 51–53, Feb. 2003.
3. T. Decoopman, O. Vanbésien, and D. Lippens, Demonstration of a backward wave in a single split ring resonator and wire loaded finline, *IEEE Microw. Wireless Compon. Lett.*, 14, 507–509, Nov. 2004.
4. A. Lai, C. Caloz, and T. Itoh, Composite right/left-handed transmission line metamaterials, *IEEE Microwave Mag.*, 5, 34–50, Sept. 2004.
5. V. G. Veselago, The electrodynamics of substances with simultaneously negative values of ε and μ, *Sov. Phys. Usp.*, 10(4), 509–514, 1968.
6. J. B. Pendry, A. J. Holden, D. J. Robbins, and W. J. Stewart, Magnetism from conductors and enhanced nonlinear phenomena, *IEEE Trans. Microw. Theory Tech.*, 47, 2075–2081, 1999.
7. J. B. Pendry, Negative refraction makes a perfect lense, *Phys. Rev. Lett.*, 85(18), 3966–3969, 2000.
8. D. R. Smith, W. J. Padilla, D. C. Vier, S. C. Nemat-Nasser, and S. Shultz, Composite medium with simultaneously negative permeability and permittivity, *Phys. Rev. Lett.*, 84(18), 4184–4187, 2000.
9. R. A. Shelby, D. R. Smith, and S. Shultz, Experimental verification of a negtive index of refraction, *Science*, 292(5514), 77–79, 2001.
10. N. Engheta, An idea for thin subwavelength cavity resonators using metamaterials with negative permittivity and permeability, *IEEE Antennas Wireless Propag. Lett.*, 1(1), 10–13, 2002.
11. A. Alù and N. Engheta, Pairing an epsilon-negative slab with a mu-negative slab: resonance, tunneling and transparency, *IEEE Trans. Antennas Propag.*, 51, 2558–2571, Oct. 2003.
12. R. Marqués, J. Martel, F. Mesa, and F. Medina, Left-handed-media simulation and transmission of em waves in subwavelength split-ring-resonator-loaded metallic waveguides, *Phys. Rev. Lett.*, 183901–183904, Oct. 2002.
13. J. Esteban, C. Camacho-Penalosa, J. E. Page, T. M. Martin-Guerrero, and E. Marquez-Segura, Simulation of negative permittivity and negative permeability by means of evanescent waveguide modes theory and experiment, *IEEE Trans. Microw. Theory Tech.*, 53, 1506–1514, April 2005.
14. S. Hrabar, J. Bartolic, and Z. Šipůs, Waveguide miniaturization using uniaxial negative permeability metamaterial, *IEEE Trans. Antennas Propag.*, 53, 110–119, Jan. 2005.
15. F. Martín, F. Falcone, J. Bonache, R. Marqués, and M. Sorolla, A new split ring resonator based left handed coplanar waveguide, *Appl. Phys. Lett.*, 83, 4652–4654, Dec. 2003.
16. N. Ortiz, J. D. Baena, M. Beruete, F. Falcone, M. A. G. Laso, T. Lopetegi, R. Marqués, F. Martín, J. García-García, and M. Sorolla, Complementary split-ring resonator for compact waveguide filter design, *Microw. Opt. Technol. Lett.*, 46, 88–92, July 2005.
17. P. J. B. Clarricoats and A. D. Olver, *Corrugated Horns for Microwave Antennas*. London, UK: Peter Peregrinus Ltd, 1984.
18. N. Marcuvitz, *Waveguide Handbook*. London, UK: Peter Peregrinus Ltd, 1986.
19. I. A. Eshrah, A. A. Kishk, A. B. Yakovlev, and A. W. Glisson, Spectral analysis of left-handed rectangular waveguides with dielectric-filled corrugations, *IEEE Trans. Antennas Propag.*, 53, 3673–3683, Nov. 2005.

20. C. A. Balanis, *Advanced Engineering Electromagnetics*. New York: John Wiley & Sons, 1989.
21. P.-S. Kildal, A. A. Kishk, and Z. Šipůs, Asymptotic boundary conditions for strip-loaded and corrugated surfaces, *Microwave Opt. Technol. Lett.*, 14, 99–101, Feb. 1997.
22. Z. Šipůs, H. Merkel, and P.-S. Kildal, Green's functions for planar soft and hard surfaces derived by asymptotic boundary conditions, *IEE Proc. – Part H*, 144, 321–328, Oct. 1997.
23. A. A. Kishk, P.-S. Kildal, A. Monorchio, and G. Manara, An asymptotic boundary conditions for corrugated surfaces and its application to calculate scattering from circular cylinders with dielectric filled corrugations, *IEE Proc. – Part H*, 145, 116–122, Feb. 1998.
24. A. A. Kishk, Electromagnetic scattering from transversely corrugated cylindrical structures using the asymptotic boundary conditions, *IEEE Trans. Antennas Propagat.*, 52, 3104–3108, Nov. 2004.
25. I. A. Eshrah and A. A. Kishk, Analysis of left-handed rectangular waveguide with dielectric-filled corrugations using the asymptotic corrugation boundary condition, *IET Proc. – Microw. Antennas Propag.*, 153, 221–225, June 2006.
26. A. B. Yakovlev, A. Khalil, C. W. Hicks, A. Mortazawi, and M. B. Steer, The generalized scattering matrix of closely spaced strip and slot layers in waveguide, *IEEE Trans. Microw. Theory Tech.*, 48, 126–137, Jan. 2000.
27. A. B. Yakovlev, S. Ortiz, M. Ozkar, A. Mortazawi, and M. B. Steer, Electric dyadic green's functions for modeling resonance and coupling effects in waveguide-based aperture-coupled patch arrays, *ACES Journal*, 17, 123–133, July 2002.
28. M. V. Lukic and A. B. Yakovlev, Magnetic potential green's dyadics of multilayered waveguide for spatial power combining applications, *J. Electromagn. Waves Appl.*, 17(4), 597–598, 2003.
29. A. B. Gnilenko and A. B. Yakovlev, Electric dyadic green's functions for applications to shielded multilayered transmission line problems, *IEE Proc. – Microw. Antennas Propag.*, 146, 111–118, April 1999.
30. G. W. Hanson and A. B. Yakovlev, *Operator Theory for Electromagnetics: An Introduction*. New York: Springer-Verlag, 2001.
31. I. A. Eshrah, A. A. Kishk, A. B. Yakovlev, and A. W. Glisson, Excitation of dielectric resonator antennas by a waveguide probe: Modeling technique and wideband design, *IEEE Trans. Antennas Propag.*, 53, 1028–1037, March 2005.
32. I. A. Eshrah and A. A. Kishk, Magnetic-type dyadic green's functions for a corrugated rectangular metaguide based on asymptotic boundary conditions, *IEEE Trans. Microw. Theory Tech.*, 55, 1124–1131, June 2007.
33. I. A. Eshrah and A. A. Kishk, Electric-type dyadic green's functions for a corrugated rectangular metaguide based on asymptotic boundary conditions, *IEEE Trans. Antennas Propag.*, 55, 355–363, Feb. 2007.
34. QWED, *QuickWave3D: A General-Purpose Electromagnetic Simulator Based on Conformal Finite-Difference Time-Domain Method*. Available at: http://www.qwed.com.pl/
35. I. A. Eshrah, A. A. Kishk, A. B. Yakovlev, and A. W. Glisson, Rectangular waveguide with dielectric-filled corrugations supporting backward waves, *IEEE Trans. Microw. Theory Tech.*, 53, 3298–3304, Nov. 2005.
36. Ansoft corporation, *HFSS: High Frequency Structure Simulator*. Available at: http://www.ansoft.com/

VI

Artificial Surfaces

30

Frequency-Selective Surface and Electromagnetic Bandgap Theory Basics

J. (Yiannis) C. Vardaxoglou
Loughborough University

Richard Lee
Loughborough University

Alford Chauraya
Loughborough University

30.1 Introduction to Frequency Selective Surface and Electromagnetic Bandgap Structures

Since the suggestion that creating a periodicity in dielectric materials could prevent the propagation of electromagnetic waves at certain frequencies in 1987 [1], there has been much work, both theoretical and experimental, in the field of photonic crystals to create a so called photonic bandgap (PBG) material, generally termed as electromagnetic bandgap (EBG)

A photonic crystal is a structure with a periodic arrangement of high dielectric constant cavities embedded within a low dielectric region; these will introduce "gaps" into the energy band structure for the photon states at Bragg planes and provoke a range of forbidden energies for the photons [2,3].

This range of forbidden frequencies is called the photonic bandgap in which propagation is forbidden in certain directions. For cases at certain frequencies, the photonic crystal will prohibit propagation of an electromagnetic wave at any incident angle, direction, and polarization; this is termed as the absolute photonic bandgap.

Photonic crystals of two and three dimensions are being investigated intensively [4]. 3-D photonic crystals will have lattice periodicity in three dimensions and at frequencies in the absolute photonic bandgap region, thereby prohibiting propagation in any direction. Figure 30.1a shows an example of a 3-D square lattice photonic crystal surrounded by air. In some cases, it can also be surrounded by a low dielectric material. Fabrication of such a photonic crystal lattice is still a challenge at present.

A 2-D photonic crystal is easier to fabricate; it possesses periodicity only in the x–y plane and is finite in the z-direction. Figure 30.2 shows an example of a 2-D square lattice photonic crystal surrounded by air. Frequencies in its absolute photonic bandgap region will be prohibited for any in-plane propagation (perpendicular to the x–y plane) for any polarization and any direction along the x–y plane. Propagation in the z-direction will not see any bandgap since there is no dielectric variation in the z-direction [5–10].

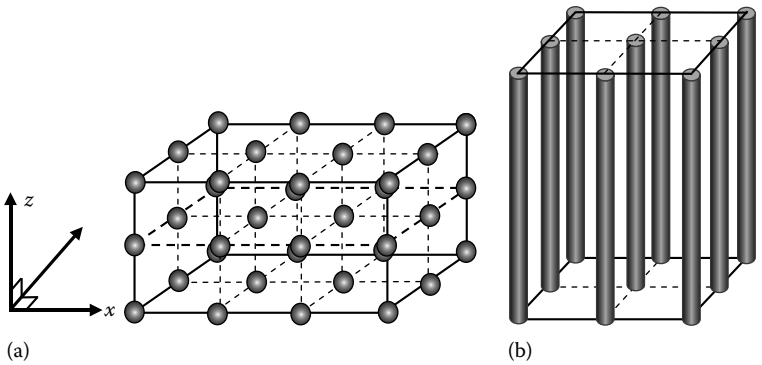

FIGURE 30.1 (a) Part of a 3-D square lattice photonic crystal. (b) Part of a 2-D square lattice photonic crystal surround by air.

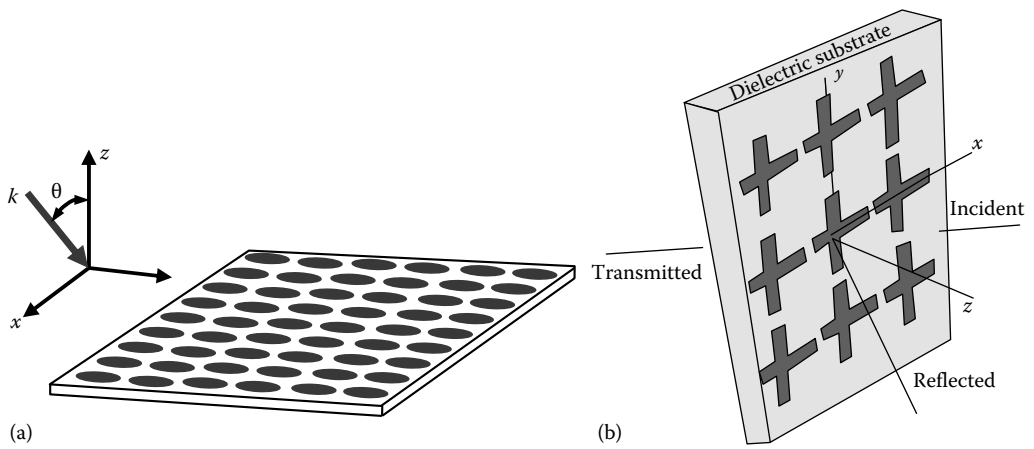

FIGURE 30.2 (a) Part of an FSS array as a 2-D planar metallodielectric PBG crystal. (b) Perspective of a crossed dipole periodic array.

Recent years have also seen potential applications for photonic crystals, which have been investigated primarily in the microwave frequency region. One of the applications is an optimized dipole antenna on a photonic bandgap crystal. By fabricating the antenna on the EBG material with the driving frequency in the stopband, no power would be allowed to transmit into the EBG material, thus most of the power would be radiated in the desired direction [11–13]. Another application utilizes the PBG as a band reject filter within a waveguide [14].

EBG materials have also been investigated for microstrip circuit applications and have exhibited very high suppression in the stopband [15,16]. It has also been shown that EBG structures can suppress surface waves from microstrip antennas and also improve their directivity [17,18].

30.2 Two-Dimensional Planar Metallodielectric Arrays and Frequency-Selective Surface

Original EBG research was done in the optical region [1], but EBG properties are scaleable and applicable to a wide range of frequencies. In recent years, there has been an increasing interest in the microwave and millimeter-wave applications of EBG structures. However, contributors working in the field of PBG structures in the microwave and millimeter-wave regions still retain the "photonic band gap" terminology. This terminology has caused some controversy in the microwave community. A recent paper by Oliner [19] has tried to clarify that the terminology is inappropriate and such structures should be classified under "microwave periodic structure." However, the "photonic bandgap" terminology is adapted at the beginning of this chapter and subsequently used throughout.

Currently, research has also extended to metallodielectric EBG, which is replacing the periodic high dielectric constant cavities of the photonic crystal with periodic metallic elements. In microwave and millimeter-wave regions, such structures exhibit a much larger electromagnetic stopband than the PBG [20,21]. The 2-D planar version of metallodielectric photonic crystal is in effect a type of frequency-selective surface (FSS).

FSSs are 2D periodic arrays of metallic elements or apertures that exhibit stopband and passband characteristics when excited by an electromagnetic wave at an angle arbitrary to the plane of the array (Figure 30.3). For example, a periodic array of conductors will reflect polarized incident waves at some frequencies (stopband) and remain transparent to these waves at other frequencies.

If the incident angle θ is increased to 90° from the normal, the incidence will be along the plane of the FSS array. When exploring the propagation mode along the plane of the FSS array, this structure

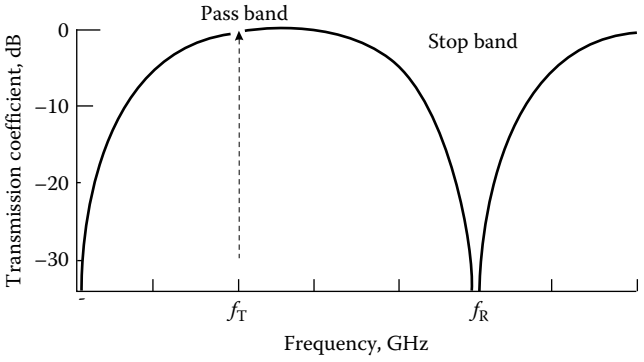

FIGURE 30.3 Typical frequency response of an FSS.

can be regarded as a planar version of a 2-D metallodielectric EBG structure, and it will exhibit bandgap properties in the plane of the array. If the bandgap extends throughout the irreducible Brillouin zone (Section 30.9), an absolute photonic bandgap is achieved.

The unique properties and practical uses of FSSs realized over many years have produced an extensive body of work in both academic and industrial sectors [22]. Historically, the essential behavior of these surfaces stems from mesh and strip grating concepts exploited in the optical region. At microwave frequencies, the applications of FSSs are predominantly for antenna systems in fixed as well as mobile services; see [23–27]. Published reports of basic properties of simple structures in the cm-wave region go back as far as 1946 [28,29], albeit the name FSS was not used until much later on. Accuracy in the modeling of their electromagnetic properties began to take shape during the late 1960s [30,31] when a lot of experience was gained from the phased array work of that era [32]. With the advent of digital computers, efficient analyses, and broadband measurement techniques, the understanding and sophistication in the FSS design and fabrication has steadily grown [33–37]. Notwithstanding the fact spacecraft missions and satellite antennas have successfully utilized FSS technology.

FSSs are essentially array structures that consist of a plurality of thin conducting elements, often printed on a dielectric substrate for support. Figure 30.2b shows part of an array of conducting dipoles in a cross-arrangement, otherwise known as the crossed dipole element. Frequently, these arrays take the form of periodic apertures in a conducting plane, Babinet's complement of the former. They behave as passive electromagnetic filters. Figure 30.3 shows a typical transmission coefficient response of an array of conductors, whereby polarized incident waves are reflected by the surface at some frequencies (reflection band or stopband), while the surface is transparent to these waves at other frequencies (transmission band or passband). f_R is the resonant frequency and the center of the stopband, and f_T is the beginning of the passband. The bandwidths are normally defined by the −10 dB level in reflection and −0.5 dB level in transmission. For the conducting array case, the resonance is due to high element currents induced, which are small near the passband. The surface is acting as a metallic sheet at resonance. If an array of apertures were to be used, the plot in Figure 30.3 would be its reflection coefficient response. This perforated screen is mostly reflective and exhibits a passband at resonance which results from strong fields in the apertures. The elements are periodically arranged on a certain lattice geometry. This may be a simple square or off-axis triangular lattice with unequal sides.

This chapter concentrates on the analysis of doubly periodic metallic arrays (on dielectric sheets) to obtain a bandgap from such a structure. The control of the bandgap is governed by array parameters such as the type of element, physical dimension, lattice parameters, and dielectric constants of the substrates. It lays out the theory and techniques used in the analysis of FSS. The analysis of propagation along the surface is achieved by evaluating the propagation constant within the irreducible Brillouin zone to predict the propagation modes. Section 30.9 also explores the properties and effects of the reciprocal lattice and its irreducible Brillioun zone from its respective direct lattice and array element.

Section 30.10 discusses the use of a dipole array with the aim of achieving a bandgap in a certain direction of illumination. It incorporates the study of propagation and bandgap properties of surface waves present on such structures with arrays printed on them.

30.3 Array Analysis

In this section, the modal analysis of an infinite planar array of a single-layer FSS in a multiple-dielectric substrate is presented. The approach here is based on the total fields from an array structure of a periodic nature where the tangential field transverse electric (TE) and transverse magnetic (TM) components can be expanded in terms of Floquet modes [32].

This modal analysis method was applied originally by Chen [30] for induced current on the conducting plates of a 2-D array in free space. Montgomery [33] included a dielectric substrate on which a periodic array of thin conductors was printed.

This section describes the theory of Floquet's theorem using the periodicity of the FSS. In fact, Floquet's theorem is an adaptation of the Fourier series theorem for periodic functions. It enables a modal description for the field in terms of a complete, orthogonal set of modes (Floquet modes) in the vicinity of each element of the array, which is excited uniformly in amplitude but with a linearly varying phase [32].

The array element is assumed to be infinitely thin and perfectly conducting. This array is sandwiched in between the first two dielectric layers, followed by four dielectric layers behind the array. The fields near the surface in each layer are expanded in terms of Floquet modes for different dielectric media. Using the standard electromagnetic boundary conditions, the fields are matched at the boundaries to derive an integral equation in terms of the unknown induced current on the conducting elements [38]. Using the method of moments (MOMs) [39,40], the integral equation is reduced into a linear system of simultaneous equations. These equations are solved for the induced current, and then, the reflected and transmitted field amplitudes can be determined. With the reflected and transmitted fields, the reflection and transmission coefficients can be derived.

For the modal analysis of FSS, presented first, the polarized incident plane wave is at an arbitrary direction with the angle θ to the z-axis and the FSS array in the x–y plane (Figure 30.4).

To determine the stopband or photonic bandgap characteristic of the FSS array, the propagation of the incident wave should be in the x–y plane ($\theta = 90°$) at any arbitrary direction with angle ϕ, with respect to the x-axis (Figure 30.4). The array with periodicity in two dimensions will exhibit a stopband in the plane of the double periodicity. The method used here to explore the possible bandgap for such an array is similar to the modal analysis of FSS. So in the first part of this chapter, the modal analysis used for FSS is presented in detail in Sections 30.4 through 30.7. The difference in the analysis of bandgap for the array in the x–y plane is presented in Section 30.8.

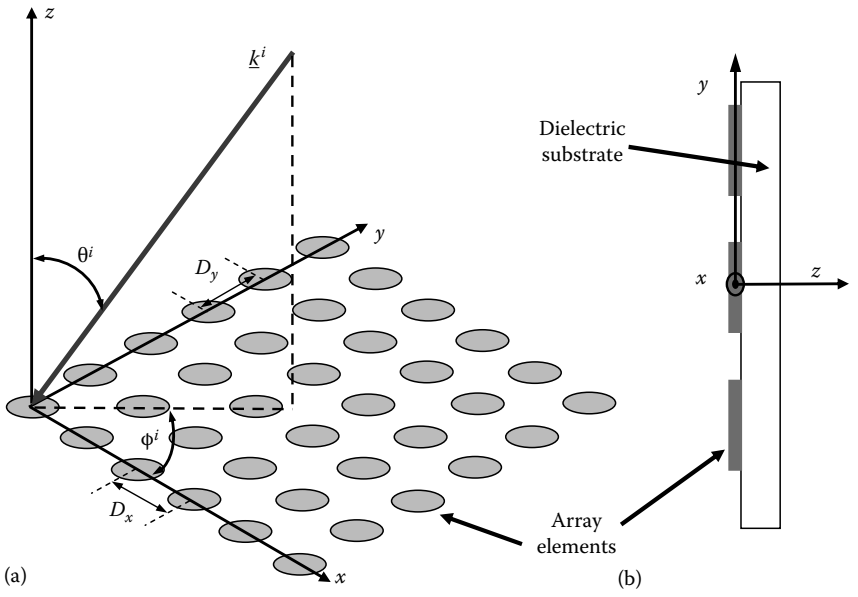

FIGURE 30.4 (a) Geometry of a square lattice array. (b) Side view of the FSS array.

To determine the completed bandgap for a structure, it is necessary to evaluate the propagation modes in all directions within the 2-D plane. This is achieved by exploring the propagation mode within the irreducible first Brillouin zone (Section 30.9).

In Section 30.9, the reciprocal lattice and its respective Brillouin zone are presented [41–45]. It has been discovered that the symmetrical relationship of the first Brillouin zone and the array elements do play a part in determining the irreducible first Brillouin zone.

30.4 Modal Analysis of Planar FSS

In this section, the modal analysis of a single FSS array in a multiple-dielectric substrate is presented. With the periodic placement of the elements of the array, the modal analysis of Floquet's theorem is used to describe the fields which are expanded in terms of Floquet modes [22,38].

When the array is illuminated by an incident plane wave, currents will be induced on the conducting elements. By matching the fields at the different boundaries, an integral equation for the unknown currents is obtained. Using the MOMs [39,40], the integral equation can be reduced to a linear system of simultaneous equations. The unknown current is expressed as a series of basis functions. With a numerical algorithm group (NAG) routine [46] which utilizes Crout's factorization, the unknown coefficients of the basis functions are obtained. The current coefficients allow one to obtain the reflected and transmitted field amplitudes. Thus, from the total reflected and transmitted field, the reflection and transmission coefficients are calculated.

The FSS array is assumed to be infinite and each element is located in a unit cell, which is distributed in a periodic configuration. The conducting elements are printed on a dielectric substrate, and the conductors are assumed to be infinitely thin and perfectly conducting.

The array on the dielectric substrate is considered to lie in the x–y plane, and it is excited by a linearly polarized plane wave incident in an arbitrary direction with angle θ to the z-axis and ϕ to the x-axis (Figure 30.4). The lattice vectors D_x and D_y specify the two periodicity axes on which the conducting elements are arranged.

For an arbitrary lattice (Figure 30.5), the element is placed along arbitrary axes $\hat{u}$ and $\hat{v}$ vectors. The arbitrary lattice vectors $\underline{D}_u$ and $\underline{D}_v$ with α as the angle between $\underline{D}_u$ and $\underline{D}_v$ and α_1 as the angle between $\underline{D}_u$ and the x-axis

$$\begin{aligned} \underline{D}_u &= D_u(\cos\alpha_1\hat{x} + \sin\alpha_1\hat{y}) \\ \underline{D}_v &= D_v(\cos\alpha_2\hat{x} + \sin\alpha_2\hat{y}) \end{aligned} \tag{30.1}$$

where

$\alpha_2 = \alpha + \alpha_1$

$D_u = |\underline{D}_u|$, $D_v = |\underline{D}_v|$

30.4.1 Modal Field Representation

The modal representation of the field of the array in scalar Floquet modes [1] is given as

$$\Xi_{pq}(x, y, z) = \Psi_{pq}(x, y)\, e^{\pm j\beta_{pq}Z} \tag{30.2}$$

where the Floquet indices are $p, q = 0, \pm1, \pm2, \pm3, \ldots$

The negative j term denotes propagation in the positive direction, and the positive j term denotes propagation in the negative direction

where

$$\Psi_{pq}(x, y) = e^{-j\underline{k}_{tpq}\cdot\underline{r}} \tag{30.3}$$

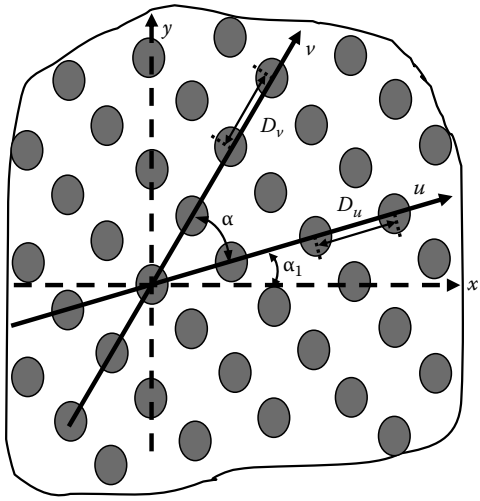

FIGURE 30.5 An FSS array on an arbitrary lattice.

Thus, from Equations 30.2 and 30.3

$$\theta_{pq}(\underline{r}, z) = \psi e^{-j\underline{k}_{tpq}\cdot\underline{r}} e^{\pm j\beta_{pq}Z} \tag{30.4}$$

where $\underline{r} = x\hat{x} + y\hat{y}$
and

$$\begin{aligned}\underline{k}_{tpq} &= k_{tx}\hat{x} + k_{ty}\hat{y}\\ \underline{k}_{tpq} &= \underline{k}_{t00} + p\underline{k}_1 + q\underline{k}_2\\ &= (k_{0x} + pk_{1x} + qk_{2x})\hat{x} + (k_{0y} + pk_{1y} + qk_{2y})\hat{y}\end{aligned} \tag{30.5}$$

and

$$\begin{aligned}\underline{k}_{t00} &= \underline{k}_{00x} + \underline{k}_{00y}\\ &= k_0 \sin\theta\cos\phi\hat{x} + k_0 \sin\theta\sin\phi\hat{y}\end{aligned}$$

where

$$k_0 = \frac{2\pi}{\lambda}$$

$$\underline{k}_1 = -\frac{2\pi}{A}\hat{z}\times\underline{D}_v \quad \underline{k}_2 = -\frac{2\pi}{A}\hat{z}\times\underline{D}_u \quad A = |\underline{D}_u \times \underline{D}_v|$$

where A is periodic unit cell area.

Using the relationship given, $\underline{k}_1$ and $\underline{k}_2$ can be shown to be

$$\underline{k}_1 = \underline{k}_{1x} + \underline{k}_{1y} \quad \underline{k}_2 = \underline{k}_{2x} + \underline{k}_{2y} \quad A = D_u D_v \sin\alpha$$

$$\underline{k}_{1x} = \frac{2\pi}{D_u}\frac{\sin\alpha_2}{\sin\alpha} \quad \underline{k}_{2x} = -\frac{2\pi}{D_v}\frac{\sin\alpha_1}{\sin\alpha}$$

$$\underline{k}_{1y} = -\frac{2\pi}{D_u}\frac{\cos\alpha_2}{\sin\alpha} \quad \underline{k}_{2y} = \frac{2\pi}{D_v}\frac{\cos\alpha_1}{\sin\alpha}$$

The propagation constant is given as

$$\beta_{pq} = \sqrt{k^2 - \underline{k}_{tpq} \cdot \underline{k}_{tpq}} \tag{30.6}$$

where $k = k_o\sqrt{\varepsilon_r}$.

For the propagating wave, $k^2 > \underline{k}_{tpq} \cdot \underline{k}_{tpq}$ and

$$\beta_{pq} = \sqrt{k^2 - \underline{k}_{tpq} \cdot \underline{k}_{tpq}}$$

where β_{pq} is real and positive.

For the evanescent wave, $k^2 < \underline{k}_{tpq} \cdot \underline{k}_{tpq}$ and

$$\beta_{pq} = -j\sqrt{\underline{k}_{tpq} \cdot \underline{k}_{tpq} - k^2}$$

where β_{pq} is imaginary and negative.

The tangential electromagnetic field in the plane of the array can be expressed in terms of both TM and TE vector Floquet modes.

The subscript m that has the values 1 and 2 denoting TM and TE modes, respectively.

The TM vector has its magnetic component parallel to the plane of the array ($H_{zpq} = 0$).

The transverse component of the TM modes are

$$\underline{E}_{tpq} = \frac{\underline{k}_{tpq}}{\left|\underline{k}_{tpq}\right|}\Psi_{pq} = \underline{\kappa}_{1pq}\Psi_{pq} \tag{30.7}$$

$$\underline{H}_{tpq} = \eta_{1pq}\hat{z} \times \underline{\kappa}_{1pq}\Psi_{pq} \tag{30.8}$$

The TE vector has its electric component parallel to the plane of the array ($E_{zpq} = 0$).

The transverse component of the TE modes are

$$\underline{E}_{tpq} = \underline{\kappa}_{2pq}\Psi_{pq} \tag{30.9}$$

$$\underline{H}_{tpq} = \eta_{2pq}\hat{z} \times \underline{\kappa}_{2pq}\Psi_{pq} \tag{30.10}$$

where η_{1pq} and η_{2pq} are the modal admittance of TM and TE modes, respectively.

$$\text{TM}: \eta_{1pq} = \frac{k\eta}{\beta_{pq}} \tag{30.11}$$

$$\text{TE}: \eta_{2pq} = \frac{\beta_{pq}\eta}{k} \tag{30.12}$$

where $\eta = \sqrt{\varepsilon/\mu}$, and ε and μ are the permittivity and permeability of the medium, respectively.

$$\begin{aligned}\underline{E}(\underline{r}, z) &= \sum_{pq}\left(a_{1pq}\underline{E}_{1pq}(\underline{r}, z) + a_{2pq}\underline{E}_{2pq}(\underline{r}, z)\right) \\ &= \sum_{pq}\left(a_{1pq}\Psi_{pq}(\underline{r})\,\underline{\kappa}_{1pq}e^{\pm j\beta_{pq}z} + a_{2pq}\Psi_{pq}(\underline{r})\,\underline{\kappa}_{2pq}e^{\pm j\beta_{pq}z}\right)\end{aligned}$$

Thus, the tangential field can be expressed as a combination of the vector TM and TE Floquet modes. For example, the electric field can be written as

$$\underline{E}(\underline{r}, z) = \sum_{mpq} a_{mpq}\Psi_{pq}(\underline{r})\,\underline{\kappa}_{mpq}e^{\pm j\beta_{pq}z} \tag{30.13}$$

where a_{1pq} and a_{2pq} are the amplitude of the TM and TE modes.

And similarly, the magnetic field

$$\underline{H}(\underline{r},z) = \pm \sum_{mpq} \eta_{mpq} a_{mpq} \Psi_{pq}(\underline{r})\, e^{\pm j\beta_{pq} z}\, \hat{z} \times \underline{\kappa}_{mpq} \tag{30.14}$$

30.5 Formulation of Scattering from an FSS with Multiple Dielectrics

30.5.1 Fields at Different Interfaces

Figure 30.6 shows the cross-sectional view of an FSS array embedded in five layers of dielectric substrates surrounded by air. The different dielectric substrates will modify the admittance seen by the wave when traveling through it. The superscript presented here in the equation denotes the different dielectric layer substrates, with S_n as the thickness, η^n as the modal admittance, and T^n, with negative z dependence, as the field amplitude of the forward traveling waves. Likewise R^n with positive z dependence would be the field amplitude of the backward traveling waves.

For this example, the FSS array is assumed to be sandwiched between the first and second layer [38]. With the incident field $\underline{E}^{\text{inc}}$, the modal tangential electromagnetic field for each region is as follows.

For $Z \le Z_0$

$$\underline{E}^{-}(\underline{r},z) = \underline{E}^{\text{inc}} + \sum_{mpq} R^{-}_{mpq} e^{+j\beta^0_{pq} z} \Psi_{pq}(\underline{r})\, \underline{\kappa}_{mpq} \tag{30.15}$$

$$\underline{H}^{-}(\underline{r},z) = \underline{H}^{\text{inc}} - \sum_{mpq} \eta^a_{mpq} R^{-}_{mpq} e^{+j\beta^0_{pq} z} \Psi_{pq}(\underline{r})\, \hat{z} \times \underline{\kappa}_{mpq}$$

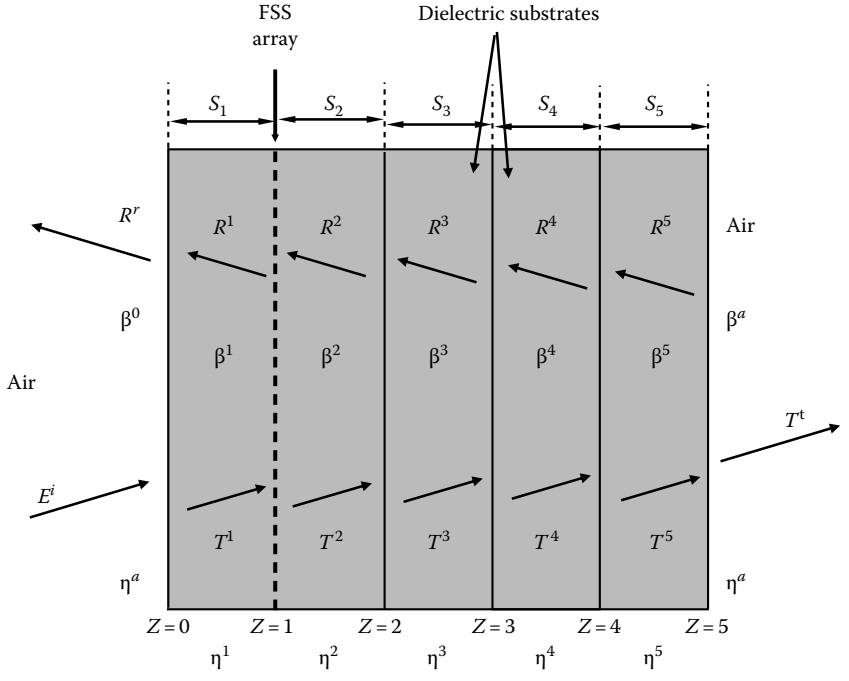

FIGURE 30.6 A single FSS array embedded in between the first two dielectric layers.

For $Z_n \le Z \le Z_{n+1}$ (for layer $n = 1, 2, 3, 4$)

$$\underline{E}^n(\underline{r}, z) = \sum_{mpq} \left(T^n_{mpq} e^{-j\beta^n_{pq} z^n} + R^n_{mpq} e^{+j\beta^n_{pq} z^n} \right) \Psi_{pq}(\underline{r})\, \underline{\kappa}_{mpq}$$
$$\underline{H}^n(\underline{r}, z) = \sum_{mpq} \eta^n_{mpq} \left(T^n_{mpq} e^{-j\beta^n_{pq} z^n} - R^n_{mpq} e^{+j\beta^n_{pq} z^n} \right) \Psi_{pq}(\underline{r})\, \hat{z} \times \underline{\kappa}_{mpq} \tag{30.16}$$

For $Z \ge Z_5$

$$\underline{E}^+(\underline{r}, z) = \sum_{mpq} T^+_{mpq} e^{-j\beta_{pq} z} \Psi_{pq}(\underline{r})\, \underline{\kappa}_{mpq}$$
$$\underline{H}^+(\underline{r}, z) = \sum_{mpq} \eta^a_{mpq} T^+_{mpq} e^{-j\beta_{pq} z} \Psi_{pq}(\underline{r})\, \hat{z} \times \underline{\kappa}_{mpq} \tag{30.17}$$

For a single FSS structure, the incident field is given in terms of the zeroth order Floquet mode $(p, q = 0)$ as

$$\underline{E}^{\text{inc}}(\underline{r}, z) = \sum_{m=1}^{2} T^{\text{inc}}_{m00} e^{-j\beta_{00} z} \Psi_{00}(\underline{r})\, \underline{\kappa}_{m00}$$
$$\underline{H}^{\text{inc}}(\underline{r}, z) = \sum_{m=1}^{2} \eta^a_{m00} T^{\text{inc}}_{m00} e^{-j\beta_{00} z} \Psi_{00}(\underline{r})\, \hat{z} \times \underline{\kappa}_{m00} \tag{30.18}$$

However, the prediction program for propagation constants (β_x, β_y) along the x–y plane does not have any incidence fields; the incidence fields and scattered fields are combined as the total fields (see Section 30.9).

With the modal tangential electromagnetic fields for each dielectric layer defined in Equations 30.15 through 30.17, boundary conditions are applied by matching or equating the fields between two layers at their common boundary. Working backward from the last layer toward the first boundary, an expression of the reflected amplitude, R^-_{mpq}, in terms of the surface current density, $\underline{J}$, can be derived.

The field amplitudes can be formed using the mode orthogonality in Equations 30.16 and 30.17 and matching at boundary $Z = Z_5$.

Magnetic field:

$$\eta^5 \left(T^5 e^{-j\beta^5_{pq} z_5} - R^5 e^{+j\beta^5_{pq} z_5} \right) = \eta^a T^+ e^{-j\beta^a_{pq} z_5} \tag{30.19}$$

Electric field:

$$T^5 e^{-j\beta^5_{pq} z_5} + R^5 e^{+j\beta^5_{pq} z_5} = T^+ e^{-j\beta^a_{pq} z_5} \tag{30.20}$$

Placing the magnetic field Equation 30.19 over the electric field Equation 30.20 at boundary Z_5, an expression can be obtained that relate the reflective field to that of the transmitted field for that boundary.

Magnetic field/electric field:

$$\frac{\eta^5 \left(T^5 e^{-j\beta^5_{pq} z_5} - R^5 e^{+j\beta^5_{pq} z_5} \right)}{\left(T^5 e^{-j\beta^5_{pq} z_5} + R^5 e^{+j\beta^5_{pq} z_5} \right)} = \frac{\eta^a_{mpq} T^n_{mpq} e^{-j\beta_{pq} z}}{T^n_{mpq} e^{-j\beta_{pq} z}}$$
$$R^5 = \left(\frac{\eta^5 - \eta^a}{\eta^5 + \eta^a} \right) e^{+j2\beta^5_{pq} z_5} T^5$$
$$R^5 = \rho^5_{mpq} T^5 \tag{30.21}$$

Likewise at boundary $Z = Z_4$,matching the fields and equating the magnetic field over the electric field using Equation 30.21 gives

$$\frac{\eta^4\left(T^4e^{-j\beta^4_{pq}z_4} - R^4e^{+j\beta^4_{pq}z_4}\right)}{\left(T^4e^{-j\beta^4_{pq}z_4}R^4e^{+j\beta^4_{pq}z_4}\right)} = \frac{\eta^5T^5\left(e^{-j\beta^5_{pq}z_4}\rho^5e^{+j\beta^5_{pq}z_4}\right)}{T^5\left(e^{-j\beta^5_{pq}z_4} + \rho^5e^{+j\beta^5_{pq}z_4}\right)}$$

$$\frac{\eta^4\left(T^4e^{-j\beta^4_{pq}z_4} - R^4e^{+j\beta^4_{pq}z_4}\right)}{\left(T^4e^{-j\beta^4_{pq}z_4} + R^4e^{+j\beta^4_{pq}z_4}\right)} = \eta^5\omega^5_4$$

$$R^4 = \rho^4_{mpq}T^4 \tag{30.22}$$

For all boundaries,

$$\rho^n_{mpq} = \left(\frac{\eta^n_{mpq} - \omega^{n+1}_n\eta^{n+1}_{mpq}}{\eta^n_{mpq} + \omega^{n+1}_n\eta^{n+1}_{mpq}}\right)e^{+j2\beta^n_{pq}z_n} \tag{30.23}$$

where $\omega\omega^{n+1}_{nmpq}$ is denoted as $\omega\omega^{n+1}_n$
and

$$\omega^{n+1}_n = \frac{e^{-j\beta^n_{pq}z_{n-1}} - \rho^n_{mpq}e^{+j\beta^n_{pq}z_{n-1}}}{e^{-j\beta^n_{pq}z_{n-1}} + \rho^n_{mpq}e^{+j\beta^n_{pq}z_{n-1}}} \tag{30.24}$$

At the last medium $(Z \geq Z_5)$, $\omega\omega^a_5 = 1$.

Working toward $Z = Z_1$, where the FSS array is located, the electric field is continuous.

$(\underline{E}_1 = \underline{E}_2)$: The magnetic field is continuous except on the conductors where it is discontinuous; $\underline{H}_1 - \underline{H}_2 = \hat{z} \times \underline{J}$ where $\underline{J}$ is the unknown surface current density.

At $Z = Z_1$ (magnetic field)

$$\underline{H}_1(\underline{r}, z_1) - \underline{H}_2(\underline{r}, z_2) = \frac{\underline{J}_{mpq}}{A}$$

$$\eta^1\left(T^1e^{-j\beta^1_{pq}z_1} - R^1e^{+j\beta^1_{pq}z_1}\right) - \eta^2\left(T^2e^{-j\beta^2_{pq}z_2} - \rho^2e^{+j\beta^2_{pq}z_2}\right) = \frac{\underline{J}_{mpq}}{A}$$

Electric field:

$$T^1e^{-j\beta^1_{pq}z_1} + R^1e^{+j\beta^1_{pq}z_1} = T^2\left(e^{-j\beta^2_{pq}z_2} - \rho^2e^{+j\beta^2_{pq}z_2}\right)$$

Likewise working with the magnetic and electric fields at $Z = Z_1$,

$$R^1_{mpq} = \rho^1_{mpq}T^1_{mpq} - \frac{e^{-j\beta^1_{pq}z_1}}{\left(\eta^1_{mpq} + \omega^2_1\eta^2_{mpq}\right)}\frac{\tilde{J}_{mpq}}{A} \tag{30.25a}$$

where

$$\alpha = \frac{e^{-j\beta^1_{pq}z_1}}{\left(\eta^1_{mpq} + \omega^2_1\eta^2_{mpq}\right)}$$

$$\tilde{J}_{mpq} = \left\langle \underline{J}(\underline{r}) \cdot \underline{\kappa}_{mpq}, \Psi_{pq}(\underline{r}) \right\rangle_{A'} = \underline{\tilde{J}}_{pq} \cdot \underline{\kappa}_{mpq}$$

With some algebraic manipulation,

$$R^1_{mpq} = \rho^1_{mpq}T^1_{mpq} - \left(e^{-j\beta^1_{pq}z_0} + \rho^1_{mpq}e^{+j\beta^1_{pq}z_0}\right)\tau^1_{mpq}\frac{\tilde{J}_{mpq}}{2\eta^1_{mpq}A} \tag{30.25b}$$

where $n > 0$

$$\tau^n_{mpq} = \frac{e^{-j\beta^n_{pq}z_n} + \rho^n_{mpq}e^{+j\beta^n_{pq}z_n}}{e^{-j\beta^n_{pq}z_{n-1}} + \rho^n_{mpq}e^{+j\beta^n_{pq}z_{n-1}}} \tag{30.26a}$$

$$\tau^0_{mpq} = \frac{e^{-j\beta^0_{pq}z_0} + \rho^0_{mpq}e^{+j\beta^0_{pq}z_0}}{2\eta^0_{mpq}} \tag{30.26b}$$

Similarly working at Z_0, the reflected field amplitude, R^-_{mpq}, can be arrived at

$$R^-_{mpq} = \delta_{p0}\delta_{q0}\rho^0_{m00}T^{\text{inc}}_{m00} - \tau^0_{mpq}\tau^1_{mpq}\frac{\tilde{J}_{mpq}}{A} \tag{30.27}$$

Having attained the reflected field amplitude for the transmitted field amplitude, work at $Z = Z_1$ with R^1_{mpq} from Equation 30.25a

$$T^1e^{-j\beta^1_{pq}z_1} + R^1e^{+j\beta^1_{pq}z_1} = T^1\left(e^{-j\beta^2_{pq}z_2} - \rho^1e^{+j\beta^2_{pq}z_2}\right) - \alpha\frac{\tilde{J}_{mpq}}{A}e^{-j\beta^2_{pq}z_2} \tag{30.28}$$

Working toward $Z = Z_5$ with some algebraic manipulation, the transmitted field amplitude [4] can be arrived at

$$T^+_{mpq}e^{-j\beta_{pq}z_5} = \tau^5_4\tau^4_3\tau^3_2\tau^2_1\tau^1_0\left(\delta_{p0}\delta_{q0}e^{j\beta_{pq}z_0}\left(1+\rho^0_{m00}\right)T^{inc}_{m00} - \omega_{mpq}\frac{\tilde{J}_{mpq}}{A}\right) \tag{30.29}$$

where

$$\omega_{mpq} = \tau^0_{mpq}\tau^1_{mpq}e^{j\beta_{pq}z_0} + \frac{e^{j\beta^1_{pq}S_1} - e^{-j\beta^1_{pq}S_1}}{2\eta^1_{mpq}} \tag{30.30}$$

30.5.2 Electric Field Integral Equation

With the boundary condition, that is, the electric field will vanish over the perfect conductor at $Z = Z_1$:

$$\begin{aligned}&\underline{E}^1(\underline{r}, z_1) = 0 \quad \underline{r} \in A'\\ &\sum_{mpq}\left(T^1_{mpq}e^{-j\beta^1_{pq}z^1} + R^1_{mpq}e^{+j\beta^1_{pq}z^1}\right)\Psi_{pq}(\underline{r})\,\underline{\kappa}_{mpq} = 0\end{aligned} \tag{30.31}$$

Working with Equation 30.28, substitute T^1_{mpq} into T^-_{mpq} and express it in terms of R^-_{mpq} using Equation 30.27:

$$T^1_{mpq}e^{-j\beta^1_{pq}z^1} + R^1_{mpq}e^{+j\beta^1_{pq}z^1} = \tau^0_{mpq}\left(\delta_{p0}\delta_{q0}e^{j\beta_{pq}z_0}\left(1+\rho^0_{m00}\right)T^{\text{inc}}_{m00} - \omega\frac{\tilde{J}_{mpq}}{A}\right)$$

Substituting in Equation 30.31

$$\sum_{mpq}\left[\tau^0_{mpq}\left(\delta_{p0}\delta_{q0}e^{j\beta_{pq}z_0}\left(1+\rho^0_{m00}\right)T^{\text{inc}}_{m00} - \omega\frac{\tilde{J}_{mpq}}{A}\right)\right]\Psi_{pq}(\underline{r})\,\underline{\kappa}_{mpq} = 0$$

Therefore, the electric field integral equation (EFIE) is

$$\sum_{mpq}C^{\text{scat}}_{mpq}\tilde{J}_{mpq}\Psi_{pq}(\underline{r})\,\underline{k}_{mpq} = \sum_{m=1}^{2}C^{nsc}_{m00}T^{\text{inc}}_m\Psi_{00}(\underline{r})\,\underline{\kappa}_{m00} \tag{30.32}$$

where

$$C_{mpq}^{\text{scat}} = \frac{\tau_{mpq}^{1}\omega_{mpq}}{A} \tag{30.33a}$$

$$C_{m00}^{\text{nsc}} = e^{j\beta_{00}z_0}\tau_{m00}^{1}\left(1+\rho_{m00}^{0}\right) \tag{30.33b}$$

30.6 Method of Moments

The MOM used here is to solve the integral equation by reducing it to a linear system of simultaneous equations [39,40].

The purpose is to approximate the unknown current induced on the conductors within the unit cell in terms of an infinite series of $\boldsymbol{N}$ orthogonal basis functions. But, the solution converges as $\boldsymbol{N} \to \infty$. Therefore, for computational efficiency, a certain $\boldsymbol{N}$ is chosen when the results converge. Although the approximation of the induced current will be better if $\boldsymbol{N}$ is increased, this is at the expense of computation time and resources. To save computation time and resources, a finite $\boldsymbol{N}$ is chosen such that when N is increased the result will only differ by a very small amount.

With N series of basis functions, the induced current can be expressed as

$$\underline{J}(\underline{r}) = \sum_{n=1}^{N} c_n \underline{h}_n\left(\underline{r}_n\right) \quad \underline{r}_n \in A' \tag{30.34}$$

where

A' is the conducting area of the unit cell
$\underline{h}_n(\underline{r}_n)$ are the current bases functions
c_n are the complex amplitude of the currents

The computation of the bases function depends on the type of conductor (dipole, tripole). The calculation of bases function for each type of conductor will be dealt with in Section 30.10.

By substituting Equation 30.34 into the EFIE Equation 30.32 and taking the inner product with the weighting functions, h_i, according to Galerkin's method, the result is a set of equations that can be written in matrix form as

$$\begin{bmatrix} Z_{11} & Z_{12} & \cdot & \cdot & Z_{1N} \\ Z_{21} & Z_{22} & \cdot & \cdot & Z_{2N} \\ \cdot & \cdot & Z_{in} & \cdot & \cdot \\ \cdot & \cdot & \cdot & \cdot & \cdot \\ Z_{M1} & Z_{M2} & \cdot & \cdot & Z_{MN} \end{bmatrix} \begin{bmatrix} c_1 \\ c_2 \\ \cdot \\ \cdot \\ c_n \end{bmatrix} = \begin{bmatrix} \tilde{E}_1^{nsc} \\ \tilde{E}_2^{nsc} \\ \cdot \\ \cdot \\ \tilde{E}_M^{nsc} \end{bmatrix} \tag{30.35}$$

where

$\tilde{E}_i^{nsc}$ is the excitation vector (Equation 30.36)
Z_{MN} is a matrix $M \times N$ and is independent of the excitation (Equation 30.37)
c_n is the unknown coefficient of the bases function

and

$$\tilde{E}_i^{nsc} = \sum_{m=1}^{2} C_{m00}^{nsc}\, T_{m00}^{\text{inc}}\, \tilde{h}^*\left(\underline{k}_{tpq}\right) \tag{30.36}$$

$$Z_{in} = \sum_{mpq} C_{mpq}^{\text{scat}}\, \tilde{h}_i^*\left(\underline{k}_{tpq}\right) \tilde{h}_n\left(\underline{k}_{tpq}\right) \tag{30.37}$$

Here, the weighting functions are the same as the basis functions, calculated using a method known as the Ritz–Galerkin method.

Therefore, to obtain the unknown coefficients c_n in Equation 30.35, a matrix inversion of $[Z_{MN}]$ is performed that utilizes Crout's factorization in a NAG routine [46] from the NAG Library.

$$[c_n] = [Z_{MN}]^{-1} \left[\tilde{E}_i^{nsc} \right] \tag{30.38}$$

With c_n coefficients computed, the unknown induced current can be determined (Equation 30.34). Substituting the induced current Equations 30.27 and 30.29, the reflected and the transmitted field amplitudes can be determined. In Section 30.7, using the reflected and the transmitted fields, the reflection and transmission coefficients are derived.

30.7 Reflection and Transmission Coefficients

Substituting the reflected field amplitude Equation 30.27 in the electric field Equation 30.15 and taking only the total reflected field at $Z = Z_0$

$$\underline{E}_{\mathrm{t}}^{\mathrm{r}}(\underline{r}, z_0) = \sum_{mpq} R_{mpq}^{-} e^{+j\beta_{pq} z_0} \Psi_{pq}(\underline{r})\, \underline{\kappa}_{mpq} \tag{30.39}$$

With the zero-order mode being the dominant mode and always propagating, the total reflected electric field is

$$\underline{E}_{\mathrm{t}}^{\mathrm{r}}(\underline{r}, z_0) = \sum_{m} \delta_{p0}\delta_{q0}\rho_{m00}^{0} T_{m00}^{\mathrm{inc}} \Psi_{00}(\underline{r})\, \underline{k}_{m00} - \sum_{mpq} \tau_{mpq}^{0}\tau_{mpq}^{1} \frac{\tilde{J}_{mpq}}{A} \Psi_{pq}(\underline{r})\, \underline{\kappa}_{mpq} \tag{30.40}$$

and the total tangential transmitted electric field at $Z = Z_5$ is

$$\underline{E}_{\mathrm{T}}^{\mathrm{t}}(\underline{r}, z_5) = \sum_{mpq} T_{mpq}^{+} e^{-j\beta_{pq} z_5} \Psi_{pq}(\underline{r})\, \underline{\kappa}_{mpq} \tag{30.41}$$

Likewise, substituting the transmitted field amplitude Equation 30.29 into the total tangential transmitted electric field Equation 30.41

$$\underline{E}_{\mathrm{T}}^{\mathrm{t}}(\underline{r}, z_5) = \tau_{mpq}^{\alpha} \sum_{mpq} \delta_{p0}\delta_{q0} e^{j\beta_{pq} z_0} \left(1 + \rho_{m00}^{0}\right) T_{m00}^{\mathrm{inc}} \Psi_{00}(\underline{r})\, \underline{\kappa}_{m00} - \sum_{mpq} \omega_{mpq} \frac{\tilde{J}_{mpq}}{A} \Psi_{pq}(\underline{r})\, \underline{\kappa}_{mpq} \tag{30.42}$$

where $\tau_{mpq}^{\alpha} = \tau_{mpq}^{5}\tau_{mpq}^{4}\tau_{mpq}^{3}\tau_{mpq}^{2}\tau_{mpq}^{1}$.

The total reflected electric field at $Z = Z_0$ and total transmitted electric field at $Z = \mathbf{Z}_5$ can also be expressed in terms of

$$\underline{E}^{\mathrm{rT}}(\underline{r}, z_0) = \left(R_x^{\mathrm{r}}\hat{x} + R_y^{\mathrm{r}}\hat{y} + R_z^{\mathrm{r}}\hat{z}\right) e^{j\beta_{pq} z_0} \Psi_{pq}(\underline{r}) \tag{30.43}$$

where

$$R_x^{\mathrm{r}} = R_{mpq}^{-} \kappa_{m00x} \tag{30.43a}$$

$$R_y^{\mathrm{r}} = R_{mpq}^{-} \kappa_{m00y} \tag{30.43b}$$

$$R_z^{\mathrm{r}} = -\frac{\left(R_x^{\mathrm{r}} \sin\theta\cos\phi + R_y^{\mathrm{r}} \sin\theta \sin\phi\right)}{\cos\theta} \tag{30.43c}$$

The total transmitted electric field at $Z = Z_5$

$$\underline{E}^{\mathrm{tT}}(\underline{r}, z_5) = \left(T_x^{\mathrm{t}}\hat{x} + T_y^{\mathrm{t}}\hat{y} + T_z^{\mathrm{t}}\hat{z}\right) e^{-j\beta_{pq}z_5}\Psi_{pq}(\underline{r}) \tag{30.44}$$

where

$$T_x^{\mathrm{t}} = T_{mpq}^{+}\kappa_{m00x} \tag{30.44a}$$

$$T_y^{\mathrm{t}} = T_{mpq}^{+}\kappa_{m00y} \tag{30.44b}$$

$$T_z^{\mathrm{t}} = -\frac{\left(T_x^{\mathrm{t}}\sin\theta\cos\phi + T_y^{\mathrm{t}}\sin\theta\sin\phi\right)}{\cos\theta} \tag{30.44c}$$

The copolar components of the total reflected and transmitted field are obtained by projecting them onto the total incident field direction $\underline{B}^{i}$

$$\underline{E}^{\mathrm{rc}}(\underline{r}, z_0) = E^{\mathrm{rc}}(\underline{r}, z_0)\,\underline{B}^{\mathrm{inc}} \tag{30.45}$$

where $E^{\mathrm{rc}}(\underline{r}, z_0) = \underline{E}^{\mathrm{rT}}(\underline{r}, z_0) \cdot \underline{B}^{\mathrm{inc}}$ and for the copolar component of the transmitted electric field

$$\underline{E}^{\mathrm{tc}}(\underline{r}, z_5) = E^{\mathrm{tc}}(\underline{r}, z_5)\,\underline{B}^{\mathrm{inc}}$$

where

$$E^{\mathrm{tc}}(\underline{r}, z_5) = \underline{E}^{\mathrm{tT}}(\underline{r}, z_5) \cdot \underline{B}^{\mathrm{inc}} \tag{30.46}$$

For a given FSS with a plane wave incident at an arbitrary direction with the angle θ to the z-axis; the reflection and transmission coefficients in the copolar direction are given as

$$R_{\mathrm{coeff}}^{\mathrm{cpo}} = \frac{E^{\mathrm{rc}}(\underline{r}, z_0)}{E^{\mathrm{Tinc}}(\underline{r}, z_0)} = R_x^{\mathrm{r}}B_x^{\mathrm{inc}} + R_y^{\mathrm{r}}B_y^{\mathrm{inc}} + R_z^{\mathrm{r}}B_z^{\mathrm{inc}} \tag{30.47}$$

$$T_{\mathrm{coeff}}^{\mathrm{cpo}} = \frac{E^{\mathrm{tc}}(\underline{r}, z_5)}{E^{\mathrm{Tinc}}(\underline{r}, z_5)} = T_x^{\mathrm{t}}B_x^{\mathrm{inc}} + T_y^{\mathrm{t}}B_y^{\mathrm{inc}} + T_z^{\mathrm{t}}B_z^{\mathrm{inc}} \tag{30.48}$$

30.8 Propagation along the Surface (*x*–*y* Plane)

The purpose of this research is to determine if there exists any bandgap (stopband) that appeared in the 2D plane of periodicity. Thus, it is essential to explore all possible propagation modes that exist along the 2D of the array. For the analysis of propagation along the x–y plane, the angle θ from Equation 30.4 is set to 90° giving

$$\underline{k}_{tpq} = \underline{k}_{t00} + p\underline{k}_1 + q\underline{k}_2 \tag{30.49a}$$

where

$$\begin{aligned}\underline{k}_{t00} &= \underline{k}_{00x} + \underline{k}_{00y} \\ &= k_0\cos\phi\,\hat{x} + k_0\sin\phi\,\hat{y}\end{aligned} \tag{30.49b}$$

For a lossless case, $k_{00x} = \beta_x$, $k_{00y} = \beta_y$.

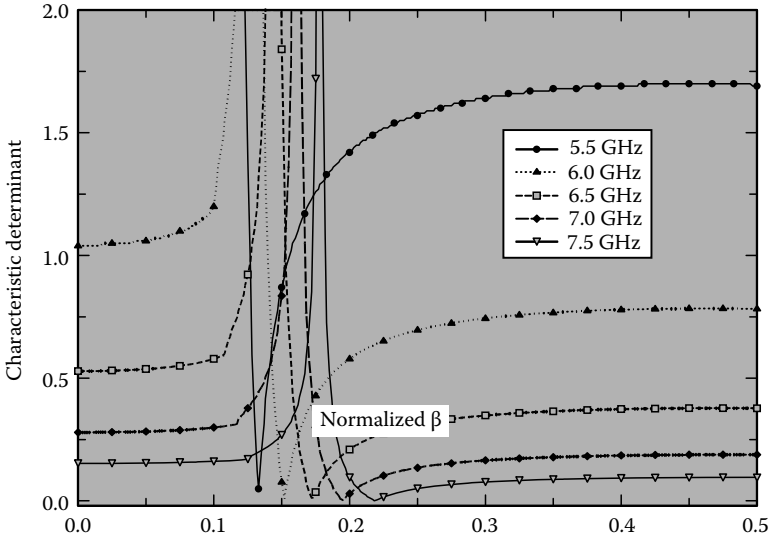

FIGURE 30.7 Propagation mode determined from a plot of characteristic determinant.

The analysis is similar to that of the derivation in the planar FSS problem until the methods of moment in Equation 30.35. The incident field is not specified and Equation 30.37 becomes

$$\begin{bmatrix} Z_{11} & Z_{12} & \cdot & \cdot & Z_{1N} \\ Z_{21} & Z_{22} & \cdot & \cdot & Z_{2N} \\ \cdot & \cdot & Z_{in} & \cdot & \cdot \\ \cdot & \cdot & \cdot & \cdot & \cdot \\ Z_{M1} & Z_{M2} & \cdot & \cdot & Z_{MN} \end{bmatrix} \begin{bmatrix} c_1 \\ c_2 \\ \cdot \\ \cdot \\ c_n \end{bmatrix} = \begin{bmatrix} 0 \\ 0 \\ \cdot \\ \cdot \\ 0 \end{bmatrix} \tag{30.50}$$

which is

$$[Z_{MN}][7c_n] = [0] \tag{30.51}$$

For this set of homogeneous linear equations to have nontrivial solutions [8], the determinant of the matrix $[Z]$ must be zero. This is known as the characteristic determinant of $[Z]$. The elements of matrix [Z] are shown in Equation 30.37. By varying β from 0 to the boundary of the irreducible Brillouin zone (see explanation in Section 30.9), all the corresponding characteristic determinants of $[Z]$ are plotted out for each β. From the characteristic determinant plot, all the true set minima obtained correspond to each individual propagation mode.

In Figure 30.7, a graph of computed characteristic determinants is shown. In this case, β is varying from 0 to π/a (boundary of the irreducible Brillouin zone). The graph shows that there is a propagation mode for β normalized values 0.133, 0.152, 0.173, 0.193, and 0.22 at frequencies 5, 5.5, 6, 6.5, 7, and 7.5 GHz, respectively.

By exploring the whole 2-D irreducible Brillouin zone, all the possible modes that exist on the x–y plane could be found. The range of frequencies where there is an absence of any propagation mode is considered a bandgap (stopband).

30.9 Direct and Reciprocal Lattices in Two Dimensions

A direct lattice describes the way the physical elements are arranged [13]. Usually, it is a periodic array in which the identical elements are spaced at equal distances from one another along two lines

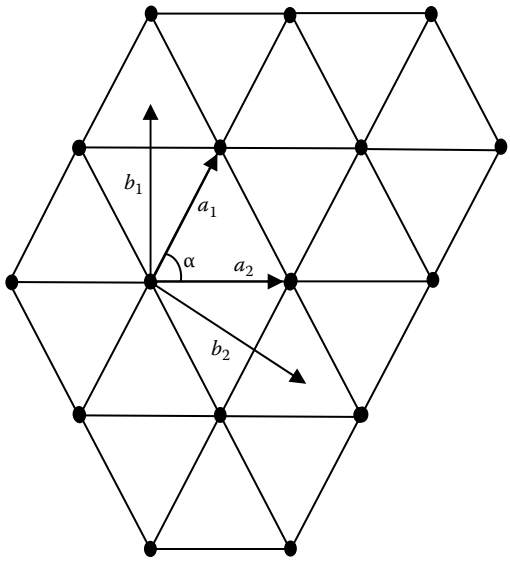

FIGURE 30.8 Direct triangle lattice.

intersecting at an arbitrary angle α. This type of lattice is also called a Bravais lattice. In other words, it is an array with an arrangement and orientation that appears exactly as the normalised β from whichever point the array is viewed. From the triangular lattice shown in Figure 30.8, taking a_1 and a_2 as basis vectors drawn from the element chosen as the origin of the lattice, the vector coordinate of any element in the lattice is then given by

$$R_{n_1 n_2} = n_1 a_1 + n_2 a_2 \tag{30.52}$$

where n_1 and n_2 are integers.

From the direct lattice, the vectors $\underline{a}_1$ and $\underline{a}_2$ are written in their matrix Cartesian coordinates as row vectors:

$$A = \begin{bmatrix} a_{1X} & a_{1Y} \\ a_{2X} & a_{2Y} \end{bmatrix} \tag{30.53}$$

The concept of reciprocal lattice is found in many solid-state physics textbooks. From the example above, the reciprocal lattice which is transposed from the matrix A will arrange its vectors $\underline{b}_1$ and $\underline{b}_2$ as column vectors:

$$B = \begin{bmatrix} b_{1X} & b_{2X} \\ b_{1Y} & b_{2Y} \end{bmatrix} \tag{30.54}$$

For the given direct lattice with vectors $\underline{a}_1$ and $\underline{a}_2$, a reciprocal lattice can be defined with its own basis vectors $\underline{b}_1$ and $\underline{b}_2$ given by the Equation 30.54.

$$(a_i . b_k) = \delta_{ik} \tag{30.55}$$

where

$i = 1, 2$ $k = 1, 2$,

δ_{ik} is the Kronecker δ symbol, defined by

$$\begin{aligned} \delta_{ik} &= 1 \quad i = k \\ &= 0 \quad i \neq k \end{aligned} \tag{30.56}$$

Therefore, the matrix product of the direct lattice and the reciprocal lattice are

$$\begin{aligned} A \cdot B &= \begin{bmatrix} a_{1X} & a_{1Y} \\ a_{2X} & a_{2Y} \end{bmatrix} \begin{bmatrix} b_{1X} & b_{2Y} \\ b_{1Y} & b_{2Y} \end{bmatrix} \\ &= \begin{bmatrix} a_{1X}b_{1X} + a_{1Y}b_{1Y} & a_{1X}b_{2X} + a_{1Y}b_{2Y} \\ a_{2X}b_{1X} + a_{2Y}b_{1Y} & a_{2X}b_{2X} + a_{2Y}b_{2Y} \end{bmatrix} \\ &= \begin{bmatrix} (a_1 \cdot b_1) & (a_1 \cdot b_2) \\ (b_2 \cdot a_1) & (a_2 \cdot b_2) \end{bmatrix} \end{aligned} \tag{30.57}$$

From Equation 30.56,

$$A \cdot B = \begin{bmatrix} 1 & 0 \\ 0 & 1 \end{bmatrix} = \delta \tag{30.58}$$

where δ is the unit matrix. From this it follows that

$$\begin{aligned} B &= A^{-1} \\ B &= \frac{1}{|A|} * C^T \end{aligned} \tag{30.59}$$

where C^{T} is the adjoint of matrix A and matrix C consists of cofactors of the elements in A.

One can conclude from the above equation that $\underline{a}_1$ is perpendicular to $\underline{b}_2$ and $\underline{a}_2$ is perpendicular to $\underline{b}_1$ (see Figure 30.8). The components of the reciprocal lattice can be obtained from the direct lattice by the relationship given by Equation 30.59 [42]:

$$\begin{aligned} b_{1X} &= \frac{a_{2Y}}{a_{1X}a_{2Y} - a_{1Y}a_{2X}} \quad & b_{2X} &= \frac{-a_{1Y}}{a_{1X}a_{2Y} - a_{1Y}a_{2X}} \\ b_{1Y} &= \frac{-a_{2X}}{a_{1X}a_{2Y} - a_{1Y}a_{2X}} \quad & b_{2Y} &= \frac{a_{1X}}{a_{1X}a_{2Y} - a_{1Y}a_{2X}} \end{aligned} \tag{30.60}$$

With the hexagonal direct lattice based on the vectors $\underline{a}_1$ and $\underline{a}_2$ with an angle α, which is π/3 between them, the respective reciprocal lattice is another hexagonal lattice, turned thought an angle π/6 with vectors $\underline{b}_1$ and $\underline{b}_2$.

The parallelogram formed by $\underline{b}_1$ and $\underline{b}_2$ defines the unit cell of the 2D reciprocal lattice Figure 30.9. The reciprocal lattice is also a periodic array with its elements are spaced at equal distance from one another along two lines $\underline{b}_1$ and $\underline{b}_2$ intersecting at a arbitrary angle which in this case is also equal to α.

However, it is more convenient to build a unit cell of the same area but is symmetric with respect to the elements of the reciprocal lattice Figure 30.10 [45]. This is defined as the 2D first Brillouin zone. The first Brillouin zone, also known as the Wigner–Seitz cell [47] of the reciprocal lattice, states that the region of space in the reciprocal lattice that is closer to the lattice element than any other is known the first Brillouin zone.

For each element, there exists higher-order zones and each of these zones covers an area equal to that of the first zone.

Any individual zone can be reduced to the first zone by taking its sections and giving them a translation parallel and equal to one of the vectors of the reciprocal lattice. This is obvious for the second zone in Figure 30.10. For the third zone, by a mosaic arrangement, the different sections can be exactly put together to cover the first one given the necessary translation.

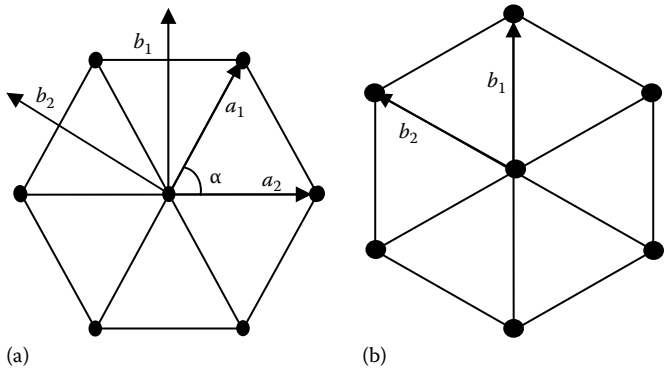

FIGURE 30.9 (a) The direct lattice and (b) its respective reciprocal lattice.

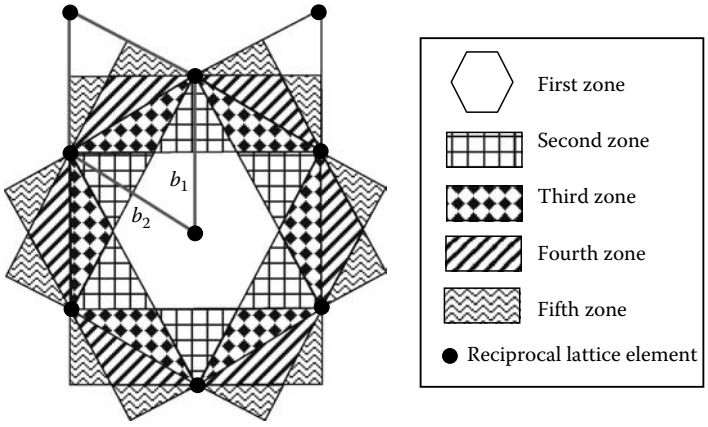

FIGURE 30.10 The reciprocal lattice of Figure 30.8 and its zone distribution.

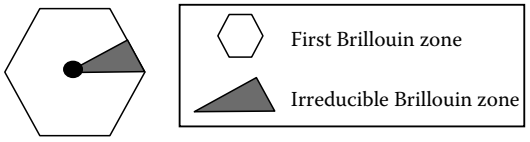

FIGURE 30.11 The irreducible first Brillouin zone.

Due to symmetric and periodic properties within the first Brillouin zone, the smallest region (the shaded portion in Figure 30.11) of the first Brillouin zone is irreducible. Thus, it will be sufficient to just consider only the irreducible zone as the rest are just mirror reflections of it.

Another example for a 2D square direct lattice, the corresponding reciprocal lattice, is also a square lattice with its vector $\underline{b}$ as shown in Figure 30.12b.

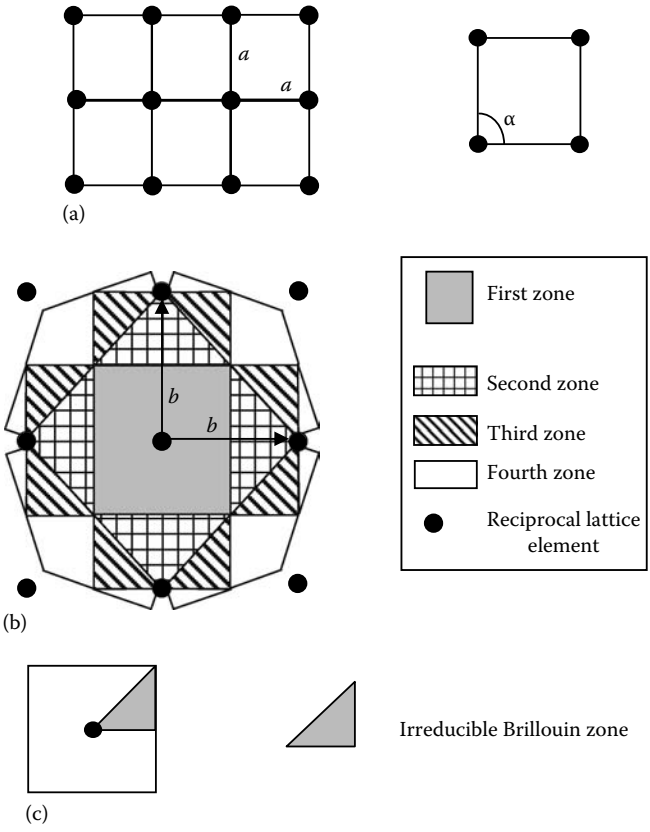

FIGURE 30.12 (a) Square direct lattice, (b) the respective reciprocal lattice, and (c) its irreducible first Brillouin zone.

30.9.1 Irreducible Brillouin Zone and the Array Element

It has been discovered in the course of this research that the irreducible Brillouin zone also depends on the circular symmetric nature of the array element. The angles between lines of symmetry for the array element and the first Brillouin zone must be taken into consideration.

The larger angle of the two is chosen for the irreducible Brillouin zone provided that the smaller angle is a factor of it. If not, a next larger angle is chosen as the irreducible Brillouin zone, which is a factor of the two angles.

As in Figure 30.11, if the array element is assumed to have circular symmetric properties like a dot or a circle, the irreducible Brillouin zone will be determined by the angle between the lines of symmetry of its first Brillouin zone. In Figure 30.13a, for triangular lattice, the angle between the lines of symmetry of its first Brillouin zone is 30°. For the square lattice in Figure 30.13b, the angle will be 45°.

In the case of a dipole as the array element, it has only two lines of symmetry (Figure 30.14a), thus the dipole is only quarterly symmetric (90°), whereas the angle of symmetry for the first Brillouin zone of a square and triangular lattice is 45° and 30° (Figure 30.14), respectively. Therefore, the irreducible Brillouin zone must cover at least 90° of the first Brilliouin zone.

For the tripole array element, the response depends on the contribution of the current in each of the three legs of the tripole. The response would be the same in the direction A and A', B and B', and

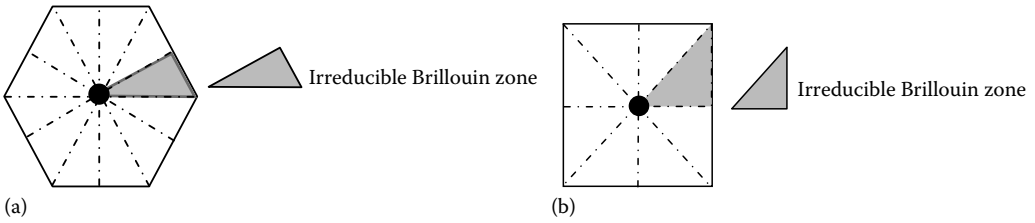

FIGURE 30.13 (a) Line of symmetry in the first Brillouin zone of a triangular lattice. (b) Line of symmetry in the first Brillouin zone of a square lattice.

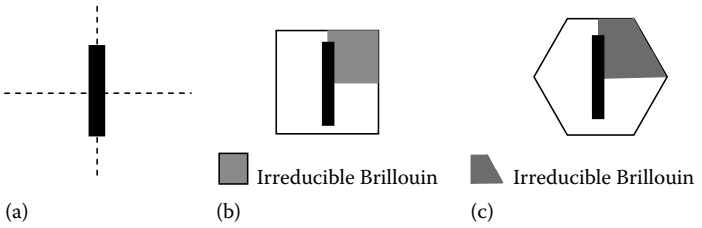

FIGURE 30.14 (a) Line of symmetry of the dipole. (b) Irreducible first Brillouin zone of a dipole in a square reciprocal lattice. (c) Irreducible first Brillouin zone of a dipole in a hexagonal reciprocal lattice.

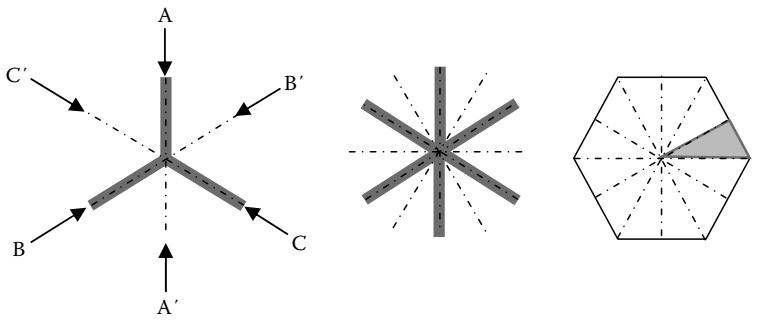

FIGURE 30.15 Lines of symmetry for a tripole and the first Brillouin zone of a triangular lattice.

C and C'. Thus, the angle of symmetry for the tripole array is 30°; coincidentally the first Brillouin zone of the triangular lattice is also 30° (Figure 30.15). So the irreducible Brillouin zone will be 30°.

For a tripole in a square lattice, the angle of symmetry for its first brillouin zone is 45° and the angle of symmetry for the tripole array is 30°. The angle 45° cannot be chosen as the irreducible Brillouin zone because 30° is not a factor, thus, the next higher angle is chosen. In this case, it is 90° in which both angles are its factor (Figure 30.16).

30.10 Planar 2D EBG Using a Dipole Conducting Array

From Section 30.6, the complex coefficient of the basis functions, which represented the current distribution on the dipole conductor, is needed for the calculation of Z_{mn} (Equation 30.37), assuming the width of the dipole element is small compared to the length and does not contribute

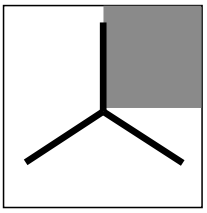

FIGURE 30.16 The irreducible Brillouin zone of a tripole in a square lattice.

to the computing of the basis functions. Thus, the current induced in the dipole elements will be predominantly along its length. The bases functions are sinusoidal and are in an arbitrary direction $\hat{v}$ [38].

$$h_n^c = \frac{1}{\sqrt{\mathrm{NR}}} \cos \frac{n\pi v}{L} \tag{30.61a}$$

$$h_n^c = \frac{1}{\sqrt{\mathrm{NR}}} \sin \frac{n\pi v}{L} \tag{30.61b}$$

where n is the number of the basis function

NR = $WL/2$ is the normalization factor due to the orthogonality of these bases.

For example, assuming five basis functions across the conductors ($n = 5$), which would consist of cosine terms $n = 1,\ 3,\ 5$ and sine terms $n = 2,\ 4$. In Figure 30.16, the conductor is aligned along the y-axis($\hat{y} = \hat{v}$).

Assuming the width of the dipole to be small, the contribution to the bases functions will come from the length of the dipole (which is position along the y-axis). The Floquet transform of Equation 30.61a and b are

$$\underline{\tilde{h}}_n^c = \tilde{h}_{ny}^c \hat{y} \tag{30.62a}$$

$$\underline{\tilde{h}}_n^s = \tilde{h}_{ny}^s \hat{y} \tag{30.62b}$$

and

$$\tilde{h}_{ny}^c = \tilde{m}_x \left(\tilde{p}_{ny} + \tilde{q}_{ny} \right) \tag{30.63a}$$

$$\tilde{h}_{ny}^s = j\tilde{m}_x \left(-\tilde{p}_{ny} + \tilde{q}_{ny} \right) \tag{30.63b}$$

where

$$\tilde{p}_{ny} = \frac{\sin\left[\left(\frac{n\pi}{L} + k_y\right)\frac{L}{2}\right]}{\left(\frac{n\pi}{L} + k_y\right)\frac{L}{2}} \qquad \tilde{q}_{ny} = \frac{\sin\left[\left(\frac{n\pi}{L} - k_y\right)\frac{L}{2}\right]}{\left(\frac{n\pi}{L} - k_y\right)\frac{L}{2}}$$

and

$$\tilde{m}_x = \sqrt{\mathrm{NR}} \frac{\sin\left(k_x \frac{W}{2}\right)}{k_x \frac{W}{2}}$$

For the cross-dipole, eight basis functions are applied; four basis functions will represent the vertical conductor element as in the dipole element case (Figure 30.17) and another four basis functions will represent the horizontal element (Figure 30.18). The Floquet transform of the basis functions for the

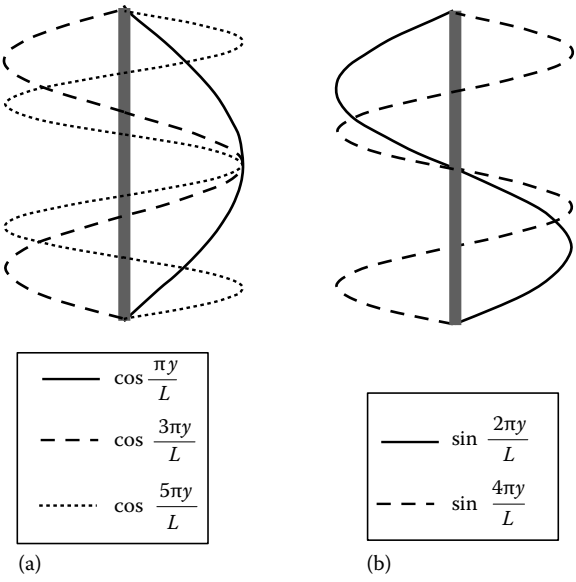

FIGURE 30.17 Dipole with five bases functions along the y-axis: (a) cosine terms and (b) sine terms.

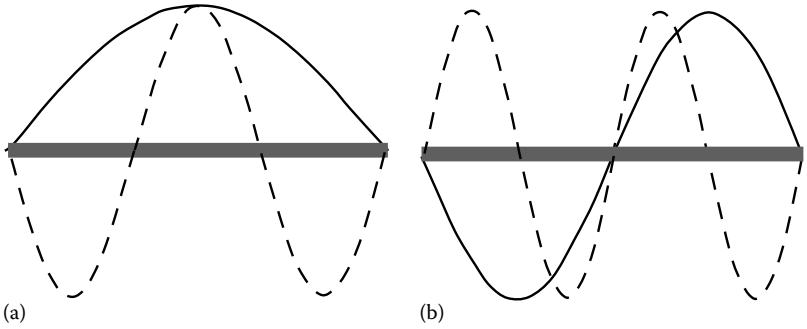

FIGURE 30.18 Cross-dipole with another four bases functions representing the horizontal element: (a) cosine terms and (b) sine terms.

horizontal element can be readily obtained from Equations 30.62 and 30.63 with changes made for the contribution from the x-axis.

30.11 Dipole Array Results and Discussion

The process of modeling is to scan the phase constants (β) for each frequency and obtain the respective characteristic determinant of the matrix $[Z]$ in Equation 30.37. The whole range of the characteristic determinants for each frequency is plotted out. From the plot, all minima are recorded and this is repeated for the whole range of frequencies. Finally, the corresponding phase constants (β) for all the true minima are plotted out against frequency to determine the location of the bandgap.

The process of determining the minima of the characteristic determinant Equation 30.37 while scanning the irreducible Brillioun zone is a tedious and time-consuming task. The condition for selection is that the minima should be of a sharp and deep nature. But, due to the effect of the conductor, sometimes the minima might not be obvious. A few selection criteria have to be taken into consideration to determine a true set of minima that represent a propagation mode. First, the minima would preferably be of a sharp and deep nature. Second, true minima will shift as the frequency increases. Third, the set of true minima will continue when the Brillouin zone scan change directions. Fourth, when the Brillouin zone scan ends in a closed loop, the set of minima must meet at the same frequency that the scan began.

Finally, caution has to be taken to discard the minima that correspond to the transverse electromagnetic mode which will also appear as a true set of minima in the simulation result.

The step size used for the frequency and phase constants (β) have to be tested to ensure if all the propagating modes are recorded. This is a case of accuracy at the expense of computational time and resources. The usual step size used is 0.2 GHz (frequency) and 0.00167 (propagation constant, β) but in cases of ambiguity that arise, finer step sizes are taken to extract the solution.

The dipole arrays are modeled with different lattice and element dimension. The array discussed in this section has its 2-D lattice of periodicity $D = 10$ and 8 mm, the dipole length $L = 7.5$ and 6 mm, and width $W = 0.6$ mm.

30.12 Dipole Dimension $D = 10$ mm, $L = 7.5$ mm

The square lattice has its element spaced out periodically on two axes separated by an angle $\alpha = 90°$. The two arrays modeled have a dielectric constant (ε_r) 2.2 and thickness (s) 1.125 mm. Due to the symmetric and periodic properties of the first Brillouin zone and the dipole element (Section 30.9.1), the shaded region is determined as the irreducible Brillouin zone (Figure 30.12b). Propagation in this region is the same as the other three quadrants and this has been verified from the modeling. The maximum phase constant (β_x and β_y) in the direction of x- and y-axes within the irreducible Brillouin zone is π/a.

For the graph in Figure 30.19, the horizontal axis represents the phase constant of the propagation mode in various directions, and the vertical axes are both normalized and nonnormalized frequency.

For the dipole array in Figure 30.19, with $\varepsilon_r = 2.2$, thickness $s = 1.125$ mm, the first mode, that is, the surface wave, starts at zero frequency. In the direction (Γ–X) in which the plane of propagation is parallel to the dipole, the surface wave ceases at 11.6 GHz. This is the beginning of the band gap along the x-direction which starts at 11.6 GHz and ends at 30.5 GHz. As the propagation direction moves from x-axis toward the y-axis, the stopband narrows until it meets at 14.7 GHz, and in the y-direction, it ceases to have a stopband. Thus, from the modeling, it shows that there is no absolute bandgap for this dipole array.

Figure 30.20 shows a measurement carried out in three different directions with respect to the dipole element array. At 0°, which is propagation in the x-axis, the beginning of the bandgap is measured to be 11.7 GHz. As the propagation direction changes to 75° the bandgap closes up to 1 GHz from 14.5 to 15.5 GHz. Finally, at 90°, which is the y-direction, there is full propagation.

It is observed that there is a gain of 5 dB before the stopband in the x-direction; this is because the dipole array behaves as guiding elements for the transmitting Vivaldi antenna. In the passband frequencies, it concentrates the fields on the dielectric slab in the direction of the receiving antenna. Naturally, in the y-direction where the dipole is aligned along the propagation direction, the gain diminishes.

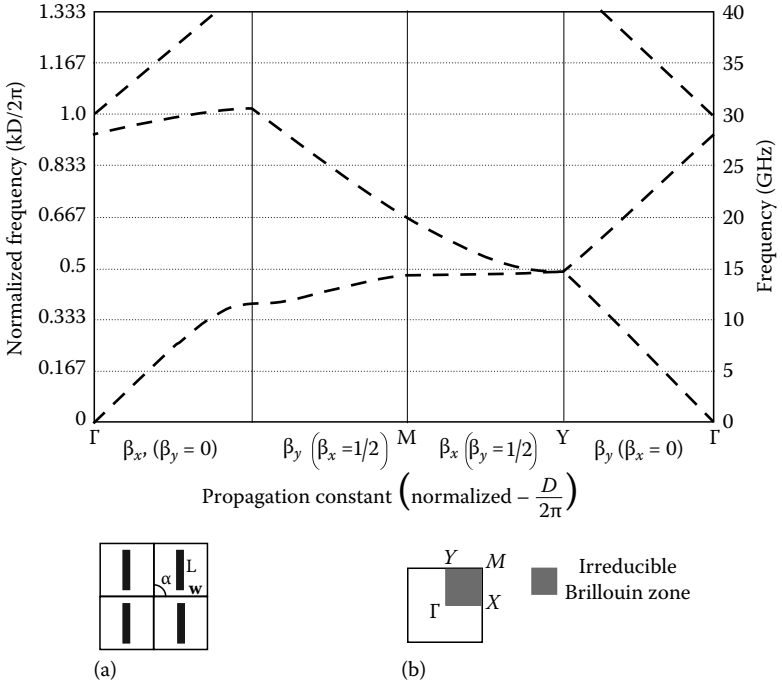

FIGURE 30.19 Band structure for the first few TE modes of the vertical dipole array: (a) direct lattice and (b) reciprocal lattice and its first Brillouin zone, $L = 7.5$ mm, $W = 0.6$ mm, $D = 10$ mm, $\varepsilon_r = 2.2$, thickness $s = 1.125$ mm, and $\alpha = 90°$.

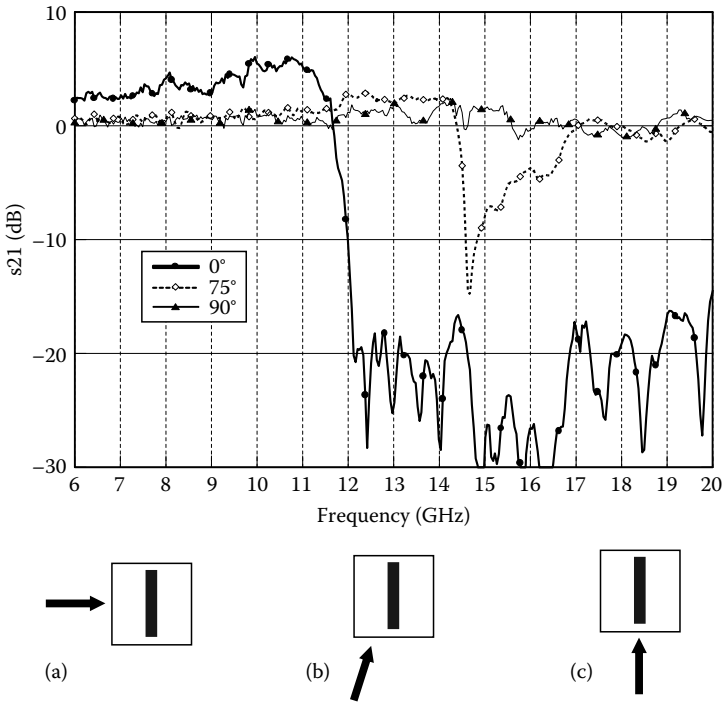

FIGURE 30.20 Measurement results of the dipole array from Figure 30.19 (a) 0° (x-direction), (b) 75°, and (c) 90° (y-direction).

From the measurements, it agrees well with the modeling prediction that there is no bandgap in the y-direction. The predicted bandgap of this array for all the planar directions from the modeling also coincides well with the measurements.

30.13 Dipole Dimension $D = 8$ mm, $L = 6$ mm

The second dipole array (Figure 30.21) has a square lattice of 8 mm and a dipole length of 6 mm with the same dielectric constant and thickness as described in Section 30.10. The bandgap starts at 14.2 GHz in the x-direction for this array. Likewise the bandgap narrows as the propagation direction changes toward the y-axis. Finally, when the propagation direction is along the length of the dipole, there is full propagation. The reason that the dipole does not have an absolute bandgap is because the width of the dipole is small, thus the contribution will come from the length of the dipole. With respect to the length of the dipole along the y-axis, the propagation in the x-axis will evidently achieve the largest bandgap.

It is observed that as the lattice and dipole dimensions get smaller, the bandgap frequency shifts up. The beginning of the stopband for x-direction shifts up from 11.6 to 14.2 GHz between these two dipole arrays. In the y-direction, the bandgap narrows to end at 14.7 and 17.9 GHz for the two dipole arrays. From these examples, different arrays can be designed to control the desired frequency stopband for a dielectric slab.

Measurements for this dipole array are also presented in three directions with respect to the dipole element (Figure 30.22). At 0° where propagation is in the x-direction, the beginning of the bandgap

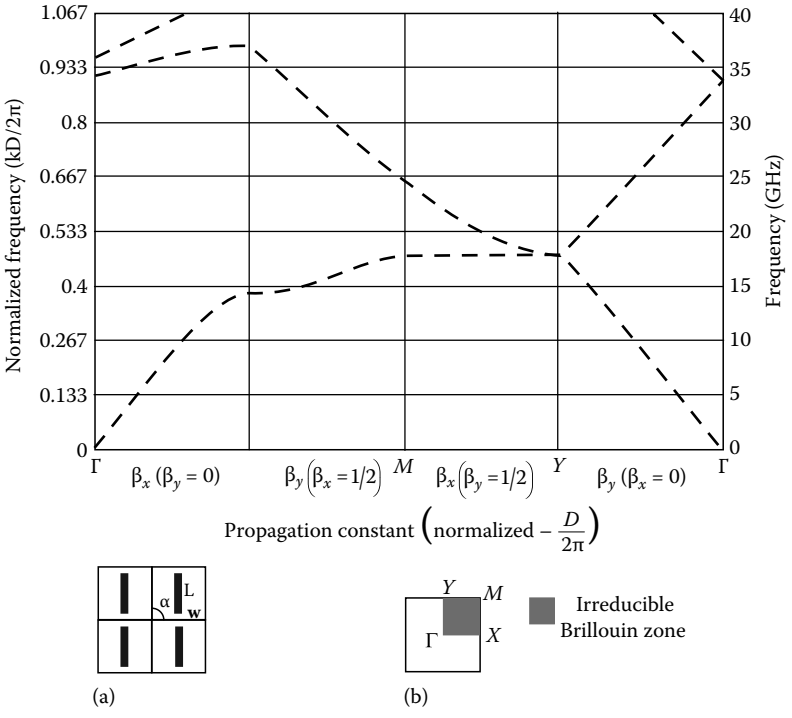

FIGURE 30.21 Band structure for the first few modes of the vertical dipole array: (a) direct lattice and (b) reciprocal lattice and its first Brillouin zone, $L = 6$ mm, $W = 0.6$ mm, $D = 8$ mm, $\varepsilon_r = 2$, thickness $T = 1.125$ mm, and $\alpha = 90°$.

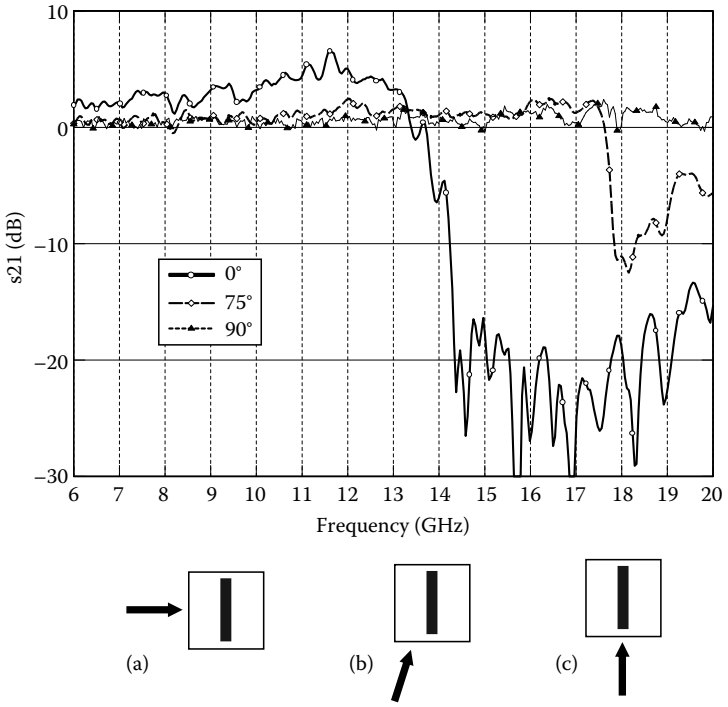

FIGURE 30.22 Measurement results of the dipole array from Figure 30.21 (a) 0° (x-direction), (b) 75°, and (c) 90° (y-direction).

is measured to be 14.3 GHz. At 75° the bandgap starts to narrow at 17.5 GHz and ends at 19.1 GHz before surface wave propagation at 90° (y-direction).

The measurements agree well with the modeling of the bandgap frequency for this array in all the planar directions.

30.14 Conclusion

This chapter has described the theory of FSS and planar EBGs. It discussed the propagation of electromagnetic fields in all planar directions within the bandgap frequencies.

The analysis has been modeled to enable calculation of propagation modes in the plane of the array. By means of an example, the bandgap for dipole arrays were investigated and the effects of lattice configuration, dielectric constant, and element parameters on the bandgap width and location have also been demonstrated. Selection criteria are established to enable the analysis of propagation modes along the plane of the array.

References

1. Yablonovitch, E., Inhibited spontaneous emission in solid-state physics and electronics, *Physical Review Letters*, 58(20), May 1987, 2059–2062.
2. Russell, P.S.J., Photonic band gaps, *Physics World*, 5, August 1992, 37–42.
3. Yablonovitch, E., Photonic crystals, *Journal of Modern Optics*, 41(2), 1994, 173–194.
4. Joannopoulos, J.D., Meade, R.D., and Winn, J.N., *Photonic Crystals—Molding the Flow of Light*, Princeton University Press, Princeton, NJ, 1995.

5. Meade, R.D., Brommer, K.D., Rappe, A.M., and Joannopoulos, J.D., Existence of a photonic band gap in two dimensions, *Applied Physics Letters*, 61(41), July 1992, 495–497.
6. Robertson, W.M., Arjavalingam, G., Meade, R.D., Brommer, K.D., Rappe, A.M., and Joannopoulos, J.D., Measurement of photonic band structure in a two-dimensional periodic dielectric array, *Physical Review Letters*, 68(13), March 1992, 2023–2026.
7. Lin, S.Y., Arjavalingam, G., and Robertson, W.M., Investigation of absolute photonic band gaps in two-dimensional dielectric structures, *Journal of Modern Optics*, 44(2), 1994, 385–393.
8. Villeneuve, P.R. and Piche, M., Photonic band gaps in two-dimensional square lattices: Square and circular rods, *Physics Review B*, 46(8), August 1992, 4973–4975.
9. Villeneuve, P.R. and Piche, M., Photonic band gaps in two-dimensional square and hexagonal lattices, *Physics Review B*, 46(8), August 1992, 4969–4972.
10. Yang, H.Y.D., Finite difference analysis of 2-D photonic crystal, *IEEE Transactions on Microwave Theory and Techniques*, 44(12), December 1996, 2688–2695.
11. Brown, E.R. and Mcmahon, O.B., High zenithal directivity from a dipole antenna on a photonic crystal, *Applied Physics Letters*, 68(9), February 1996, 1300–1302.
12. Cheng, S.D., Biswas, R., Ozbay, E., Mccalmont, S., Tuttle, G., and Ho, K.M., Optimized dipole antennas on photonic band gap crystals, *Applied Physics Letters*, 67(23), December 1994, 3399–3401.
13. Sigalas, M.M., Biswas, R., and Ho, K.M., Theoretical study of dipole antennas on photonic band-gap materials, *Microwave and Optical Technology Letters*, 13(4), November 1996, 205–209.
14. Caloz, C., Zurcher, J.-F., and Skrivervik, A.K., Measurement of a 2-D photonic crystal in a waveguide, *Proceedings of the 10th IEEE Nice-International Symposium on Antennas*, JINA 98, Nice, France, 1998, 627–630.
15. Radisic, V., Qian, Y., and Itoh, T., FDTD simulation and measurement of new photonic band-gap structure for microstrip circuits, *International Symposium on Electromagnetic Theory*, Thessaloniki, Greece, May 1998, 843–845.
16. Rumsey, I., Piket-May, M., and Kelly, R.K., Photonic bandgap structures used as filters in microstrip circuits, *IEEE Microwave and Guided Wave Letters*, 8(10), October 1998, 336–338.
17. Contopanagos, H., Zhang, L., and Alexopoulos, N.G., Thin frequency-selective lattices integrated in novel compact MIC, MMIC and PCA architectures, *IEEE Transactions on Microwave Theory and Techniques*, 46(11), November 1998, 1936–1948.
18. Qian, Y., Coccioli, R., Sievenpiper, D., Radisic, V., Yablonovitch, E., and Itoh, T., A microstrip patch antenna using novel photonic band-gap structures, *Microwave Journal*, 42, January 1999, 66–76.
19. Oliner, A.A., Periodic structures and photonic-band-gap terminology: Historical perspectives, *29th European Microwave Conference*, Munich, Germany, October 1999, 295–298.
20. Mcintosh, K.A., Mcmahon, O.B., and Verghese, S. Three-dimension metalodielectric photonic crystals incorporating flat metal elements, *Microwave and Optical Technology Letters*, 17(3), February 1998, 153–156.
21. Brown, E.R. and Mcmahon, O.B., Large electromagnetic stop bands in metallodielectric photonic crystals, *Applied Physics Letters*, 67, October 1995, 2138.
22. Vardaxoglou, J.C., *Frequency Selective Surface—Analysis and Design*, Research Studies Press, Taunton, England, 1997.
23. Schennum, G.H., Frequency-selective surfaces for multiple frequency antennas, *Microwave Journal*, 16, 1973, 55–57.
24. Arnaud, J.A., and Pelow, F.A., Resonant grid quasi-optical diplexers, *American Telephone & Telegraph Co., The Bell System Technical Journal*, 54(2), 1975, 263–283.
25. Agrawal, V.D. and Imbriale, W.A., Design of a dischroic Casegrain subreflector, *IEEE Transactions on Antennas and Propagation*, AP-27(4), July 1979, 466–473.
26. Ando, M., Ueno, K., Kumazawa, H., and Lagoshima, K., AK/C/S bands satellite antenna with frequency selective surface, *Electronics and Communications in Japan*, 66-B, 1983, 1665–1680.

27. Comtesse, L.E., Langley, R.J., Parker, E.A., and Vardaxoglou, J.C., Frequency selective surfaces for dual and triple band offset reflector antennas, *Proceedings of the 17th Microwave European Conference*, Rome, September 1987, 208–211.
28. Macfarlane, G.G., Quasi-stationary field theory and its application to diaphragms and junctions in transmission lines and waveguides, *Journal of the Institute of Electrical Engineers*, 93, Pt. III-A, 1946, 703–719.
29. Booker, H.G., Slot aerials and their relation to complementary wire aerials (Babinet's principle), *Journal of the Institute of Electrical Engineers*, 93, Pt. III-A, 1946, 620–626.
30. Chen, C.C., Scattering by a two-dimensional periodic array of conducting plates, *IEEE Transactions on Antennas and Propagation*, AP-18(5), 1970, 660–665.
31. Chen, C.C., Transmission through a conducting screen perforated periodically with apertures, *IEEE Transactions on Microwave Theory and Techniques*, MTT-18, 1970, 627–632.
32. Amitay, N., Galindo, V., and Wu, C.P., *Theory and Analysis of Phased Array Antennas*, Interscience, New York, 1972.
33. Montgomery, J.P., Scattering by an infinite periodic array of thin conductors on a dielectric sheet, *IEEE Transactions on Antennas and Propagation*, AP-23(1), 1975, 70–75.
34. Luebbers, R.J. and Munk, B.A., Mode matching analysis of biplanar slot arrays, *IEEE Transactions on Antennas and Propagation*, AP-27, 1979, 441–443.
35. Parker, E.A., Langley, R.J., Cahill, R., and Vardaxoglou, J.C., Frequency selective surfaces, *Proceedings of International Conference on Atomic Physics*, 83(1), 1983, 454–463.
36. Mittra, R., Chan, C.H., and Cwick, T., Techniques for analysing frequency selective surfaces—A review, *IEEE Proceedings*, 76(12), 1988, 1953–1615.
37. Orta, R., Savi, P., and Tsacone, R., Recent developments in frequency selective surfaces, *JINA'92*, Nice, France, 1992, 223–232.
38. Vardaxoglou, J.C., *Frequency Selective Surface—Analysis and Design*, Research Studies Press, Taunton, England, 1997, Chapter 2.
39. Harrington, R.F., Matrix methods for field problems, *Proceedings of the IEEE*, 55(2), February 1967, 136–149.
40. Harrington, R.F., *Field Computation by Moment Methods*, MacMillian, New York, 1968.
41. Stroud, K.A., *Further Engineering Mathematics*, English Language Book Society/Macmillan, 1990.
42. Joannopoulos, J.D. Meade, R.D., and Winn, J.N., *Photonic Crystals—Molding the Flow of Light*, Princeton University Press, Princeton, NJ, 1995.
43. Brillouin, L., *Wave Propagation in Periodic Structures*, Dover Publications, New York, 1953, Chapter 6.
44. Desjonqueres, M.C. and Spanjaard, D., *Concepts in Surface Physics*, Springer-Verlag, Berlin, 1993, Chapter 3.
45. Ashcroft, N.W. and Mermin, N.D., *Solid State Physics*, Saunders College, Philadelphia, PA, 1976, Chapters 4–5.
46. 'Subroutine F04ADF and F03ADF', Numerical Algorithm Group (NAG) MK. 13.
47. Kittel, C., *Introduction to Solid State Physics*, John Wiley, New York, 1996, Chapters 1–2.

31

High-Impedance Surfaces

George Goussetis
Heriot-Watt University

Alexandros P. Feresidis
Loughborough University

Alexander B. Yakovlev
The University of Mississippi

Constantin R. Simovski
Helsinki University of Technology

31.1 Introduction

The concept of impedance was initially introduced by Heaviside (1886) in the context of currents and voltages, in order to describe the constant ratio V/I in AC circuits. In the 1930s, the notion of impedance was generalized by Schelkunoff, who recognized that the impedance concept could be used to describe the ratio of the transverse electric field over transverse magnetic field, since this depends solely on the host medium of propagation for each electromagnetic mode [1]. The concept of surface impedance follows as a model to describe the interaction of electromagnetic waves with interfaces between materials or thin sheets (e.g., [1–7]). In the context of complex surfaces, that typically consist of periodic (or quasiperiodic) arrangements with low profile compared to the wavelength, the use of the term impedance implies homogenization; the complex surface is modeled by an equivalent uniform surface, which is characterized by an effective impedance value. The reader is referred to [4,5] for further references on these techniques.

The term high-impedance surface (HIS) was introduced in [6] in order to describe complex 2.5D surfaces (i.e., planar surface that includes via connectors to the ground). The term HIS in this context reflects the following two properties:

1. In-phase full reflection of incident plane waves
2. Suppression of all propagating surface waves

It is straightforward to see that an ideal surface with very high surface impedance ($Z_s \to \infty$) will fully reflect incident waves in phase for all angles of incidence and will not support any surface waves. In practice, the equivalent surface impedance is a function of both the frequency and the transverse wavenumber (and hence the incidence angle). Therefore the two general properties of HIS mentioned above in general do not coincide in the frequency domain and for all angles of incidence [7,8]. The surface that exhibits the former is also referred to as artificial magnetic conductor (AMC), reflecting the duality of this property to that of the perfect electric conductors (PEC) [6–10]. Surfaces that suppress all propagating surface waves are also termed as Electromagnetic Band Gap (EBG) structures, in accordance with the term photonic bandgap (PBG) introduced by [11,12] to describe periodically modulated structures that do not support real solutions to Maxwell equations.

Since the introduction of HIS in [6], several authors have investigated complex structures that produce either or both of the above mentioned HIS properties. The term HIS has been employed to describe a variety of geometries. Often, these consist of a doubly periodic aperture [13] or metallic [14] array printed on a grounded dielectric slab. In order to simplify the fabrication, several authors have omitted the grounding vias [7–16]. The structures resemble frequency selective surfaces (FSS) [17] printed on grounded dielectric substrates and planar reflect arrays [18]. Other realizations include the volumetric topologies that do not require metallic ground plane [19,20], multilayer arrays [21], as well as convoluted and other complex geometries [22,23] for miniaturized designs.

The topic of HIS has attracted significant attention [24]. Among the first applications proposed for these surfaces were as ground planes for low-profile dipole-type antennas [6]. The zero reflection phase guarantees a 3 dB gain enhancement for a horizontal source located in close proximity to the HIS surface, rather than distractive interference predicted by the image theory for perfect electric conductors. Several other practical applications were suggested, including the suppression of surface modes in reflector backed patch arrays [15], transverse electromagnetic (TEM) waveguides [25,26], profile reduction of resonant cavity antennas [16], design for mobile phones [27], and others (see Part II of this book).

In this chapter, we review recent works on HIS. Commencing from the definitions and the experimental evidence of the effects associated with HIS, we proceed to review proposed variations of HIS, analysis techniques, performance characteristics, synthesis considerations and an overview of proposed applications of HIS.

31.2 Definitions and HIS Topologies

In this section, we provide the definitions of the phenomena associated with HIS. The term EBG is introduced in relation to the surface waves traveling along interfaces. The term AMC is introduced in the context of reflection from metamaterial surfaces. The necessary background required by the nonexpert to follow is outlined. Subsequently, some common HIS are reviewed, with emphasis on the first HIS that was proposed.

31.2.1 Electromagnetic Bandgap Surfaces

Interfaces between dielectric and/or metallic elements typically support waves, with fields that are to a greater or lesser extend confined to the interface. This type of waves is often referred to as "surface waves," as they are typically bound to interfaces (these are an analogy to the optical surface plasmons [30]). In the limit case of a PEC in free space, the fields extend an infinite distance into space, and therefore surface waves do not exist in the limit of infinite conductivity. Practical metallic surfaces (free-standing or insulated by a thin dielectric slab) conduct finite AC currents and support surface waves [1]. Similarly, interfaces between dielectrics with a contrast in the permittivity can be shown to

support surface waves [2]. For a more detailed treatment on surface waves and their properties, the reader is referred to [2].

In the context of HIS, the properties of the surface waves can be found by assigning an equivalent surface impedance [4]. Consider a surface characterized by an isotropic equivalent surface impedance Z_s and associated with unit vector **n**. For surface waves, according to the broad definition of the surface impedance the following boundary condition is satisfied [4]:

$$\mathbf{E}_t = Z_s \mathbf{n} \times \mathbf{H} \tag{31.1}$$

where

$\mathbf{E}_t$ is the tangential electric field

H is the magnetic field on the surface

The solution of Maxwell equations is typically obtained as two independent sets of solutions, namely, transverse electric (TE) and transverse magnetic (TM) waves [1]. In the usual terminology, TE waves have zero electric field in the direction of propagation, while TM waves have zero magnetic field in the direction of propagation. For the sets of TE and TM waves, the surface impedance definition above suggests that [4]:

$$\text{TM waves}: \ \mathrm{E}_x = Z_s \mathrm{H}_y$$
$$\text{TE waves}: \ \mathrm{E}_y = -Z_s \mathrm{H}_z$$

High value of the surface impedance ($Z_s \to \infty$) therefore implies that surface waves cannot propagate along the surface, since the surface is approximated by an open circuit. Although smooth interfaces between real materials typically support surface waves [2], it is possible to suppress those within a frequency band by introducing a periodic patterning and exploiting the EBG.

EBG materials represent a class of artificial periodic metamaterials that prohibit propagation of electromagnetic waves within a particular frequency band. They have emerged as a direct microwave analogue to PBG materials (photonic crystals) used in the optical regime [11,12], and were investigated extensively in recent years with regard to applications in RF, microwave and millimeter-wave frequencies (see also other chapters of this book). Like photonic crystals, EBG materials are in general periodic arrangements. The larger scale of the wavelength and the reduced losses of metals allows for more flexibility in the realization of microwave EBG structures, which often include metallic and resonant elements in the unit cell (e.g., [31,32]). In the context of HIS, the EBG property refers to two-dimensional (2D) low profile periodic arrangements. EBG surfaces composed of periodic metallic elements on dielectric substrates were studied [33–36] as an alternative to 2D photonic crystals formed by inhomogeneities in a dielectric host medium. Extending the techniques used in the analysis of FSS arrays, dispersion curves of the propagation constant along the substrate's surface can be obtained, and hence the properties of the HIS can be examined for specific array geometries.

31.2.1.1 Leaky and Surface Waves

Traditionally, the term surface waves was used to describe waves bounded at the interface [1,2], with field strength that decays exponentially away from it. These waves are characterized by tangential wavenumbers larger than that of free-space plane waves and are therefore termed as slow waves, since their phase velocity is less than the speed of light. However, it is also possible to excite "fast" waves at an interface; those have wavenumbers less than that of free-space plane waves. In unshielded environments, fast waves match the free-space plane wavenumber at a certain angle and hence they radiate. Due to their property of "leaking" energy to free-space as they propagate along the surface, these waves are also termed as leaky waves [37,38].

When discussing the surface waves along an interface and the EBG, a broad definition includes bandgap for all TE and TM slow and fast waves. For several applications, such as component isolation

(see Chapter 21 of *Applications of Metamaterials*), it can be justified to include suppression of leaky waves as a requirement of a HIS, as these can indeed contribute toward unwanted coupling. However, since leaky waves decay exponentially due to radiation, various authors refer to surface wave EBG with a more strict definition of slow waves [6].

31.2.1.2 Dispersion Diagrams

Dispersion diagrams associated with guiding structures are graphical representations of the wavenumber variation with frequency. For free space, the dispersion is represented by a straight line that obeys

$$k_0 = \frac{2\pi f}{c} \tag{31.2}$$

where f is the frequency and $c = 3 \times 10^8$ m/s. This line, often referred to as "light line," is known to separate the (k_0, f) plane into two semi-infinite planes of slow and fast waves. For guiding structures, dispersion diagrams contain useful information regarding the properties of propagation.

According to the above, a HIS exhibits an EBG, i.e., a frequency range where no real solution satisfies Maxwell equations. EBGs are conveniently represented in dispersion diagrams [39]. Most of the common HIS realizations involve 2D periodic arrays. For such structures, the Irreducible Brillouin Zone (IBZ) (i.e., the range of wavenumbers that correspond to physically distinct waves—see also discussion below) defines the unit cell in the reciprocal (wavenumber) space. A full characterization of the surface waves along an infinite periodic structure involves mapping each point of the IBZ to its corresponding frequency. Such a mapping is known as dispersion diagram. Bandgaps are identified as those frequency bands that do not correspond to any real wavenumber solution (in the lossless case). Although a complete dispersion characterization requires the mapping of all wavenumbers in the IBZ, for HIS it is common to show the dispersion around the contour of the IBZ. In Section 31.2.1.2.1, the terms BZ and the IBZ are discussed in some more detail.

31.2.1.2.1 Brillouin Zone and Irreducible Brillouin Zone

As mentioned above, for infinite periodic structures, all possible wavenumbers can be reduced to values within the IBZ. Although a rigorous description of reciprocal lattices and definitions of the BZ and IBZ are out of the scope (the reader is referred to e.g., [12]), in this section we provide an illustration for the one-dimensional (1D) case and some practical examples for the 2D case.

By definition, any periodic structure consists of an infinite arrangement of a minimum unit cell. The fact that the arrangement is infinite and that all unit cells are identical, suggests that they are also indistinguishable. This gives rise to the fact that electromagnetic fields are repeated at unit cell edges apart from a phase shift. The electric field of a propagating wave in a lossless 1D structure, periodic along z and with D_z being the length of the unit cell (periodicity), can therefore be written as

$$\mathbf{E}(x, y, z + D_z) = e^{-j\beta D_z} \cdot \mathbf{E}(x, y, z) \tag{31.3}$$

In Equation 31.3, β is the wavenumber characteristic to the propagation within the periodic structure. Note that for periodic structures the usual wave propagation term $e^{j\beta z}$ is meaningful only at discrete points along z, at equal distances D_z. As a consequence of Equation 31.3, the electric field in an infinite periodic structure can be described by a solution of the form:

$$\mathbf{E}(x, y, z) = e^{-j\beta z} \cdot \mathbf{E}_{\mathrm{p}}(x, y, z) \tag{31.4}$$

where $\mathbf{E}_{\mathrm{p}}$ is a periodic function of z with period D_z:

$$\mathbf{E}_{\mathrm{p}}(x, y, z + nD_z) = \mathbf{E}_{\mathrm{p}}(x, y, z) \tag{31.5}$$

for n integer. Mathematically this is known as the Floquet theorem [39].

According to this description, the value of the phase difference between the fields at the two edges of a unit cell is obtained by βD_z. This can always be reduced within the range $[-\pi, \pi]$. This limits the possible values of the wavenumber to values in the range $[-\pi/D_z, \pi/D_z]$. For the 1D case employed here as an example, this range represents the BZ corresponding to the periodicity D_z, which yields all possible mathematically different values of the wavenumber corresponding to the periodic structure. Hence all other wavenumber values relevant to the propagation within a periodic structure can be reduced to values within the BZ. In other words, the BZ contains all physically distinct wavenumbers for an infinite periodic structure.

The symmetry of the structure under consideration with respect to the $\pm z$-axis suggests a further reduction of the BZ while still maintaining all physically useful information; waves propagating in the positive or negative z-direction (with wavenumbers $\pm\beta$), apart from the different direction, share identical characteristics. Hence all physical information included in the BZ $[-\pi/D_z, \pi/D_z]$ can be summarized in the range $\beta \in [0, \pi/D_z]$. The IBZ is defined as the BZ reduced by all possible symmetries.

The above can be generalized for the 2D periodic case. In the following, three practical examples of a rectangular, a square, and a hexagonal lattice of the direct lattice are given. For each case, the direct lattice, the reciprocal lattice, the BZ and IBZ as well as the light line around the contour of the IBZ are presented (Figures 31.1 through 31.3).

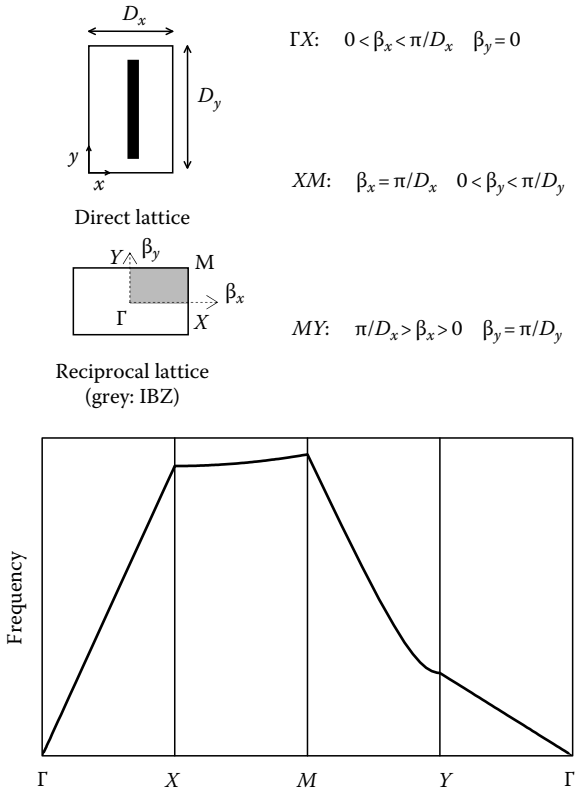

FIGURE 31.1 Unit cell in the direct and reciprocal space and light line for a 2D periodic arrangement of linear dipoles in a rectangular lattice.

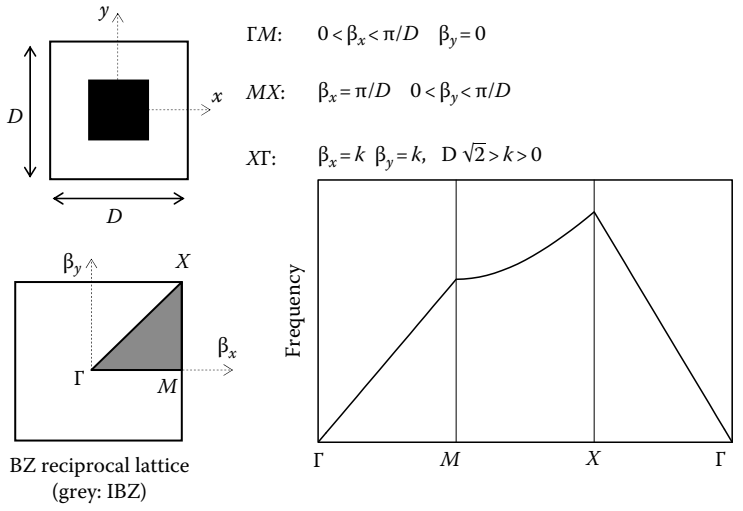

FIGURE 31.2 Unit cell in the direct and reciprocal space and light line for a 2D periodic arrangement of linear dipoles in a square lattice with square symmetry.

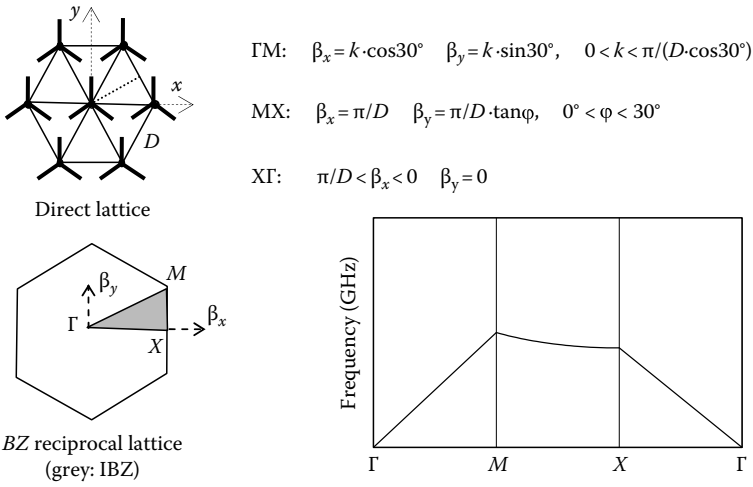

FIGURE 31.3 Unit cell in the direct and reciprocal space and light line for a 2D periodic arrangement in a hexagonal lattice.

31.2.1.3 Experimental Testing of EBG

Several arrangements were reported in the literature for the experimental testing of 2D EBG structures. The target is to launch surface waves at one end of a (finite) surface and detect the relative field strength at the other end. The levels of the signal strength at the receiving end vs. frequency typically reveals the EBG frequency range. A complete characterization of surface waves typically requires two different configurations, for TE and TM modes, respectively, as these two sets of surface waves modes are typically orthogonal.

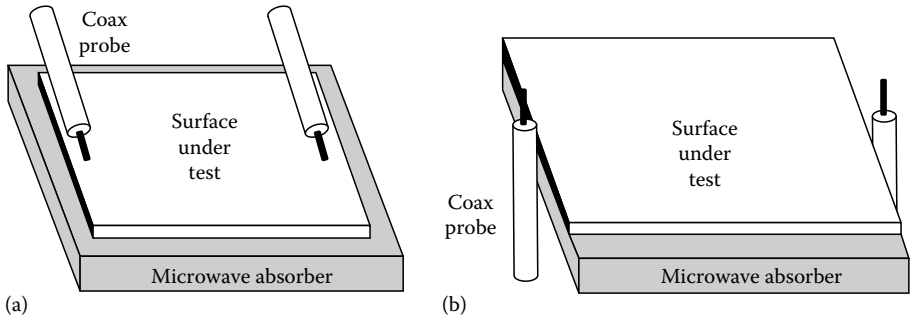

FIGURE 31.4 Schematic representation for the excitation of (a) TE and (b) TM surface waves in order to identify the associated EBGs. (From Sievenpiper, D., Lijun, Z., Broas, R.F., Alexopoulos, N.G., and Yablonovitch, E., *IEEE Trans. Microw. Theory Tech.*, 47(11), 2059, Nov. 1999. With permission.)

FIGURE 31.5 Photograph of an experimental setup employed to identify EBG of HIS using a pair of horn antennas and a tunnel formed by absorbers.

A setup suggested in [6] is schematically represented in Figure 31.4. A pair of short monopoles is positioned at the two ends of the surface under test (SUT). Depending on the orientation of the monopoles, TM and TE modes can selectively be excited and detected. TE modes require monopoles parallel to the SUT, while for TM modes the monopole is normal to the surface.

Another configuration is based on introducing the SUT in a "tunnel" formed between absorbers (Figure 31.5). The tunnel is then illuminated by a horn antenna and another horn antenna in line with the launching employed as detector. TE/TM bandgaps can be detected by rotating the antennas so that the polarization is parallel/normal to the surface.

31.2.2 Artificial Magnetic Conductor

Surfaces that fully reflect incident waves with a 0° reflection phase are referred to as a perfect magnetic conductors (PMC), due to this property being complementary to perfect electric conductor (PEC). Since free magnetic charges are not known to exist in nature, there is not any material that produces scattering properties that resemble those of a PMC. A complex layered structure that upon illumination from an incident wave performing as an equivalent AMC was initially reported in [6]. Apart from any thermal losses, this structure fully reflects incident waves with a 0° reflection phase. In practice, the reflection phase of AMCs cross zero at just one frequency. It is a custom to define the useful bandwidth of an AMC as the frequency range where incident waves are reflected with a phase that varies between +90° and −90°, since these phase values would not cause destructive interference between direct and reflected waves [6].

The obvious assumption that HIS has a low profile compared to the wavelength is clearly important for AMCs. In practice, AMC is often realized as metallic periodic arrays printed on a grounded dielectric substrate, with or without vias that connect the metallic elements to the ground plane [7,8,13–16]. For these structures, the above assumption suggests that the thickness of the dielectric slab is in principle small compared to the wavelength. Moreover, it is interesting to note that the AMC effect typically refers to reflection properties in the far field.

31.2.2.1 Reflection from an HIS

The reflection coefficient experienced when a guiding medium of characteristic impedance Z_0 is terminated at an impedance Z_L is given by [1]

$$R = \frac{Z_L - Z_0}{Z_L + Z_0} \tag{31.6}$$

For high termination impedance ($Z_L \to \infty$), the reflection coefficient is +1, i.e., the reflection phase introduced by a very high impedance termination is identically zero for all frequencies. A more realistic model of a practical HIS suggests a dispersive (i.e., varying with frequency) impedance [6,7,16]. Simple first-order approximation lumped element models for HIS [6,16] suggest that for frequencies in the vicinity of the AMC operation the dispersion of the surface can be modeled by *LC* resonators. A more accurate (semianalytical) approximation for the surface impedance of HIS consisting of periodic metallic arrays in close proximity of a ground plane [7] employs Foster's theorem, which suggests that for practical scenarios impedance zeros alternate with impedance poles. In both cases, it appears that away from the frequency where a plane wave incident on a practical HIS experiences a high impedance value, the surface exhibits low surface impedance for plane waves with the same properties (polarization and incidence angle).

A typical reflection response by a practical HIS is given in Figure 31.6. As shown in Figure 31.6, the AMC operation occurs exactly at a single frequency point. Note that in the ideal lossless case, the reflection magnitude is identically equal to unity. In practical scenarios that include losses, some energy is dissipated as ohmic and dielectric (thermal) losses and therefore the reflection coefficient is less than 1. As will also be discussed in Section 31.3, the resonant nature of the AMC effects suggests the excitation of strong currents on the metallic elements and strong fields in the dielectrics. As a result the reflection magnitude exhibits a local minimum at the AMC frequency. Similar to FSS [17], the reflection characteristics from a periodic metallic (or metallodielectric) array also vary with the angle of incidence as well as the polarization. This is true also for practical AMC surfaces. In terms of homogenized impedance, this suggests a variation of the impedance with the angle of incidence as well as with the incidence polarization [4,5,40]. In general, although the reflection phase curve from the same HIS surface will always resemble that of Figure 31.6, the center frequency and the bandwidth will vary for different polarizations and/or angles of incidence.

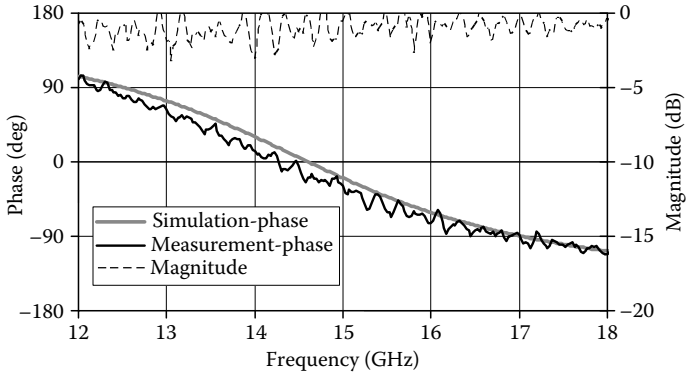

FIGURE 31.6 Typical reflection characteristics of a HIS. (From Feresidis, A.P., Goussetis, G., Wang, S., and Vardaxoglou, J.C., *IEEE Trans. Antennas Propag.*, 53(1), 209, Jan. 2005. With permission.)

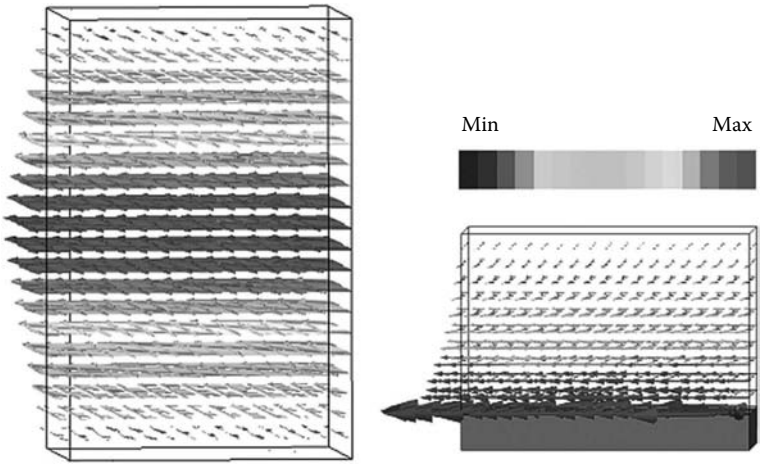

FIGURE 31.7 Simulated distribution of the E-field tangential to the side walls for the first-order resonance of a cavity formed between two metal surfaces (left) a metal surface and a practical AMC surface (right).

A practical illustration of the effect of an AMC is shown in Figure 31.7 depicting the distribution of the electric field tangential to the parallel plates of a 1D resonant cavity for the first-order resonant mode. For a resonator formed between two infinite metallic parallel plates, the tangential electric field is zero at the metallic surfaces (assuming no ohmic losses) and maximum in the center following a sinusoidal distribution. This is shown in the left of Figure 31.7. Basic electromagnetic theory predicts that a magnetic conductor along the symmetry plane, where the tangential electric field is maximum, would not affect the resonant characteristics, i.e., the field distribution or the resonant frequency. Figure 31.7 on the right shows full-wave results [28] of the field distribution for a cavity with half the profile, where one of the two metal side walls was substituted by a practical AMC surface that consists of square patch array [29]. The latter is designed to reflect with zero phase at the resonant frequency. The reduced profile of the cavity (for the same resonant frequency) as well as the field distribution shown in Figure 31.7 illustrate in practice the performance of AMCs.

31.2.2.1.1 Grating Lobes

The interaction of electromagnetic waves with periodic arrangements is conveniently modeled, expanding the fields in a finite truncation of the complete set of Floquet space harmonics [39,42]. The free-space TEM wave corresponds to the fundamental zeroth-order Floquet space harmonic. Higher-order harmonics have larger wavenumber components tangential to the periodic surface, and therefore have reduced phase velocity along the surface. For far-field incidence, only a free-space TEM wave with phase velocity equal to the speed of light needs to be considered and therefore typically the incidence can be expressed as the fundamental zeroth-order harmonic. However, rigorous modeling requires that in the vicinity of the array higher-order harmonics are considered. For lower frequencies, all the associated higher-order harmonics are slow waves. In this regime, they are surface waves confined to the surface and decay exponentially away from it. This is translated into imaginary values of the propagation constant normal to the surface and imaginary reflection angles. In this case, while a rigorous full-wave treatment requires consideration of higher-order harmonics in the vicinity of the array, in the far field they are typically ignored.

With increasing frequency, it is possible that some higher-order space harmonics become fast waves along the plane of the array (although still "slower" than the zeroth-order), i.e., their tangential wavenumber is less than the TEM wavenumber in free space (although still larger than the tangential wavenumber of the zeroth-order). These harmonics, could then "match" a free-space wave and they become propagating away from the surface. Simple wavenumber matching [6] suggests that in this case they will appear in the far field at an angle different from the zeroth-order harmonic, i.e., at an angle different from the reflection of the incidence. As a result, the magnitude of the reflection coefficient at the angle of incidence will be less than unity even in the lossless case, since some energy is directed at different angles. In the FSS literature, the reflection lobes produced by radiating higher-order Floquet harmonics are known as "grating lobes." It is out of the scope of this chapter to expand further on this topic, which is well covered in the literature of FSS [17] and phased arrays antennas [42]. Attention of the reader is drawn to the fact that for increasing frequency, most HIS (which involve 2D periodic structures) will produce grating lobes. Grating lobes are often unwanted in this context, and avoiding those is then another design consideration.

31.2.2.1.2 TE and TM Polarization

In referring to the polarization of the wave incident to the HIS, a common terminology involves the use of two orthogonal sets, the TE and TM polarizations. These abbreviations for transverse electric and transverse magnetic refer to the polarization of the wave with respect to the surface. Hence, the TE wave incidence has zero electric field component normal to the surface, while the TM incidence has a zero magnetic field components normal to the surface. Any plane wave incident to a surface can be decomposed into a TE and a TM component. A graphical example of the TE and TM incidence on dipole HIS is shown in Figure 31.8.

31.2.2.2 Experimental Testing of AMC

The experimental validation of the AMC property involves measuring the reflection phase of incident waves from the surface. According to the previous discussion, the reflection phase from practical HIS varies with the angle as well as the polarization of the incident wave. This implies that the measurement of the AMC property is made in the far-field (ensuring plane-wave incidence) and for well-defined polarization as well as angle of incidence.

Another implied fact when considering reflection from an HIS is related to the reference plane where reflection is considered to take place. While physical interfaces between materials can indeed be assumed planar, HIS are complex surfaces with a finite profile. The surface approximation of practical HIS suggests that the profile is typically low compared to the wavelength. Nevertheless, the wave experiences a phase shift as it propagates through the finite height of the HIS and therefore

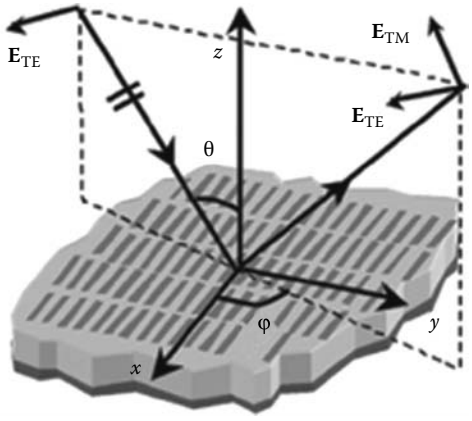

FIGURE 31.8 Example of TE and TM incidence on an HIS consisting of a periodic dipole array. (From Maci, S., Caiazzo, M., Cucini, A., and Casaletti, M., *IEEE Trans. Antennas Propag.*, 53(1), 70, Jan. 2005. With permission.)

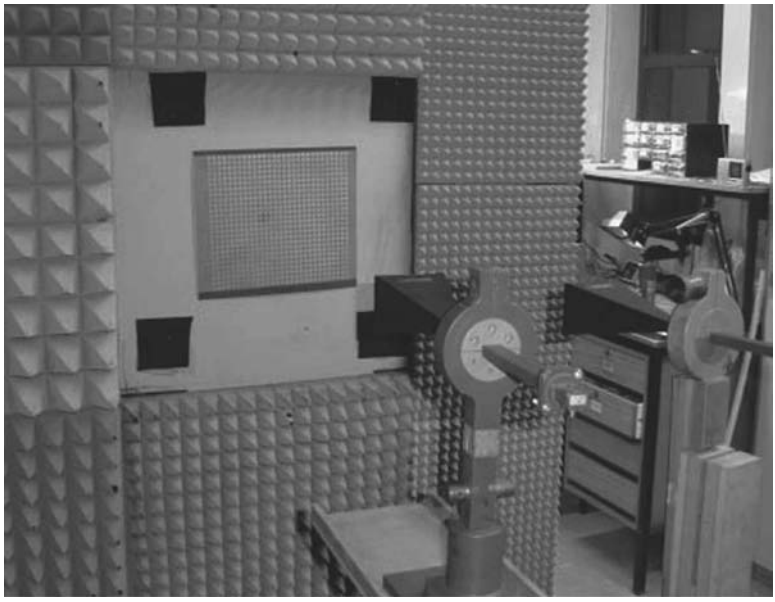

FIGURE 31.9 Experimental setup for testing the AMC performance.

the reflection phase in the far field depends on the reflection reference plane; the dependence is stronger for HIS involving thicker dielectric substrates.

The most generic technique for experimentally assessing the AMC operation of HIS involves a setup graphically depicted in Figure 31.9. Two antennas point at the SUT at an equal angle either side from the normal. The experimental measurement is set up within an anechoic environment in order to avoid unwanted noise. One antenna acts as a transmitter, while the other as a receiver. The antennas are located at sufficient distance from the SUT, so that the latter interacts only with the far field. Horn antennas are often preferred since they are simple solutions offering directive beams as well as polarization purity. The antennas are connected to the two-ports of a vector network

analyzer. The experiment is based on measuring the complex S12 between the two ports, which is an indication of the reflection from the SUT. In order to normalize for the phase shift undergone along the path from the antennas to the SUT and back, an identical measurement is taken where the SUT is substituted by a flat metal surface. The reflection phase and magnitude from the SUT can then be obtained by normalizing the two measurements, assuming that the reflection from the solid metal plane is −1.

An alternative method for measuring the reflection from a HIS that involves a waveguide terminated at the SUT was reported [43]. The procedure is essentially the same: the other end of the waveguide is connected to a VNA port and the reflection (as obtained from an *S*11 measurement) is normalized with a reference involving an identical measurement with a metal plane termination. While this method ensures an anechoic environment and is accurate, it is somehow limited in the range of polarizations and incident angles of the incoming plane wave. For the case of the usual rectangular waveguides operating in the fundamental mode, this technique yields the reflection for TE waves at angles that are specified by the frequency and the wavenumber [1].

31.2.3 Sievenpiper (Mushroom) Structure

HIS were first introduced by D. Sievenpiper et al. in 1999 in UCLA [6], where a so-called "mushroom" type structure was proposed. The impetus behind this work was to realize an artificial metallic surface that, unlike normal conductors, would reflect incident waves with zero phase shift and, at the same time, it would stop propagation of surface waves within a forbidden frequency band. Thus, the surface would behave as an effective magnetic conductor, with vanishing tangential magnetic field and very large impedance values according to Equation 31.1.

The cross section of the mushroom structure is shown in Figure 31.10. Metallic patches are printed on a dielectric substrate backed by a metallic ground. The patches are connected to the ground with vertical metallic posts or so-called vias in PCB technology. Figure 31.10 shows a perspective view of the "mushroom-type" HIS with square shaped metallic patches. Similar implementations were also presented using hexagonal metallic patches on a triangular lattice [6].

31.2.3.1 Reflection Properties

Upon plane-wave incidence, the mushroom-type HIS exhibits an AMC response. It is interesting to note that, assuming normal plane-wave incidence, the vertical vias do not affect the reflection phase response. A simple analytical model that was used initially as a rough approximation describes the structure as an effective parallel *LC*-circuit and is shown in Figure 31.11. In this model, the inductance *L* is associated with the current flowing between two successive mushrooms, while the capacitance *C* is associated with the fields polarized between two successive patches.

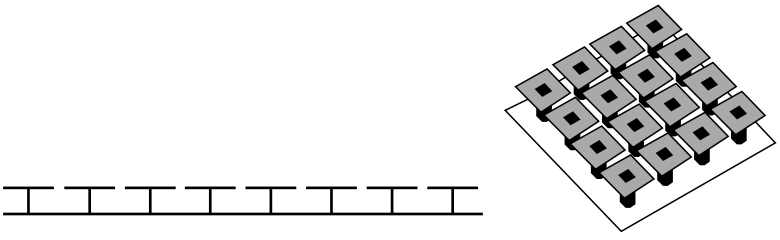

FIGURE 31.10 Cross-section and bird's eye view of the first HIS proposed by Sievenpiper et al. (Sievenpiper, D., Lijun, Z., Broas, R.F., Alexopoulos, N.G., and Yablonovitch, E., *IEEE Trans. Microw. Theory Tech.*, 47(11), 2059, Nov. 1999. With permission.)

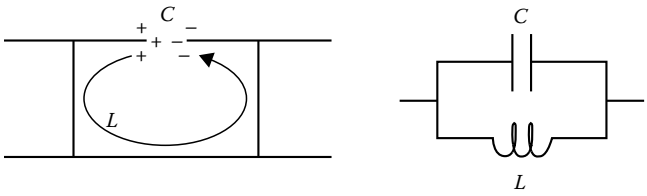

FIGURE 31.11 Schematic representation of the current induced in the mushroom HIS and equivalent circuit. (Sievenpiper, D., Lijun, Z., Broas, R.F., Alexopoulos, N.G., and Yablonovitch, E., *IEEE Trans. Microw. Theory Tech.*, 47(11), 2059, Nov. 2000. With permission.)

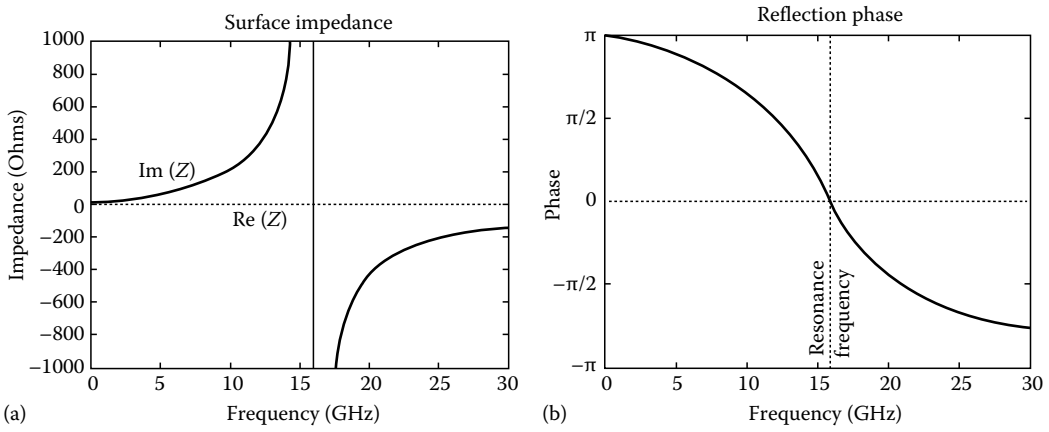

FIGURE 31.12 Equivalent surface impedance and reflection phase for the HIS of Figure 31.10 calculated by the equivalent circuit of Figure 31.11. (From Sievenpiper, D., Lijun, Z., Broas, R.F., Alexopoulos, N.G., and Yablonovitch, E., *IEEE Trans. Microw. Theory Tech.*, 47(11), 2059, Nov. 2000. With permission.)

According to this model, the impedance of the surface can be approximated by the impedance of the parallel *LC*-circuit, consisting of the sheet capacitance (C) and sheet inductance (L):

$$Z = \frac{j\omega L}{1 - \omega^2 LC} \tag{31.7}$$

L and C can be calculated using quasistatic approximations and well-known analytical formulas, depending on the geometries and dimensions of the structure [44]. The surface impedance varies as shown in Figure 31.12a, with a resonance frequency of $\omega_o = 1/\sqrt{LC}$. At resonance the impedance becomes infinite, thus approximating the infinite impedance of a HIS, which in turn corresponds to a 0° reflection coefficient (Figure 31.12b). At lower frequencies the impedance is inductive and at higher frequencies it is capacitive.

31.2.3.2 Band Structure

The dispersion diagram for the mushroom structure demonstrated in [6] is reproduced in Figure 31.13a. Full-wave finite element method was used to obtain the dispersion diagram. The 2D EBG for bounded surface waves is marked with grey. Note that this is an absolute bandgap, i.e., for all polarizations (TE and TM) and all directions of propagation (leaky wave modes are excluded). In particular, the highlighted EBG region lies below the first-order TE surface mode and above the

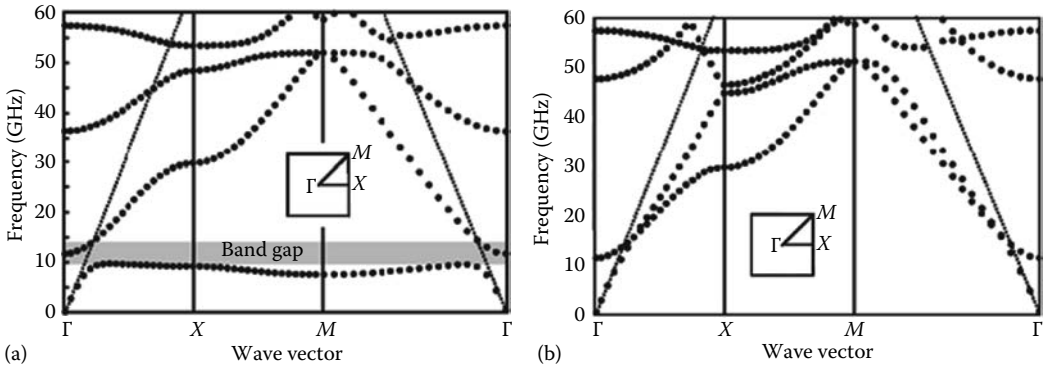

FIGURE 31.13 (a) Dispersion diagram of the mushroom structure proposed by [6] (From Sievenpiper, D., Lijun, Z., Broas, R.F., Alexopoulos, N.G., and Yablonovitch, E., *IEEE Trans. Microw. Theory Tech.*, 47(11), 2059, Nov. 2002. With permission.). (b) Dispersion diagram for the same structure in the absence of vias. (From Sievenpiper, D., High-impedance electromagnetic surfaces, PhD thesis, UCLA, Los Angeles, CA, 1999 (available online at http://www.ee.ucla.edu/ labs/photon/thesis/ThesisDan.pdf).)

first-order TM mode (the identification of the modes is not evident from this figure but can be done either by observing the fields in a full-wave simulator or experimentally as discussed above). It is interesting to note that although the printed square patch array is responsible for the EBG of the TE modes, the TM bandgap occurs as a result of the vertical vias. This is evident in Figure 31.13b, showing the dispersion diagram of the same structure in the absence of vias. As shown the low frequency TM bandgap disappears in the absence of the vias.

The above can be illustrated using the equivalent circuit of Figure 31.11. At low frequencies, the surface impedance is inductive and therefore a fundamental TM mode is supported with zero cut-off frequency and follows the light line [4]. When the periodic HIS structure starts resonating, an additional TM backward wave is supported. As the frequency increases, the two TM modes (forward and backward) intersect and coupling of fields with opposite directions occurs resulting in a stop band, which is referred to here as a bandgap [45].

The lowest TE mode has a cut-off (it is not supported at lower frequencies where the surface impedance is inductive [4]), which corresponds to the resonant frequency of the structure (see previous section). At this point, TE standing waves are excited, oscillating across the surface at the *LC* resonant frequency. Increasing the frequency, the TE mode behaves as a leaky wave with increasing phase constant and finally crosses the light line at which point it becomes a bounded surface wave. Since the E-field has no vertical component for TE modes, this mode remains largely unaffected by the presence of the vertical vias. Therefore, the fundamental TE mode is essentially the TE mode supported by the proposed structure without the vertical conducting posts, as it is shown in Figure 31.13b.

31.2.3.3 Measured Performance

The measured performance of a HIS consisting of a triangular array of hexagonal patches connected to the ground plane with vertical vias was obtained using the measurement set-up described in Section 31.2.1.3. The HIS has a periodicity of 2.54 mm and a gap of 0.15 mm between the patches. The thickness of the board is 1.55 mm, and the dielectric constant is 2.2 [6]. The bandgap is evident in the two measurements of Figure 31.14, showing both TM and TE surface wave transmission responses. The bandgap is measured between the TM band edge at approximately 11 GHz and the TE band edge at approximately 17 GHz. The reflection phase for normal plane wave incidence (Figure 31.15) crosses

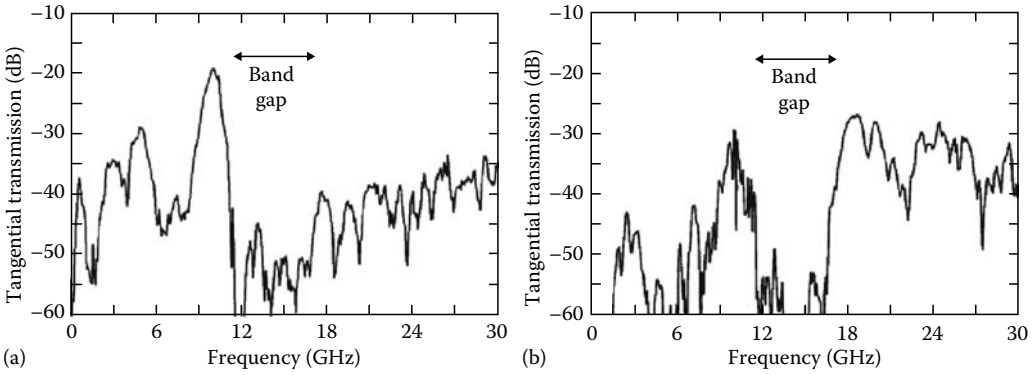

FIGURE 31.14 Measured surface wave transmission along a two-layer HIS (a) TM, (b) TE. (From Sievenpiper, D., Lijun, Z., Broas, R.F., Alexopoulos, N.G., and Yablonovitch, E., *IEEE Trans. Microw. Theory Tech.*, 47(11), 2059, Nov. 2003. With permission.)

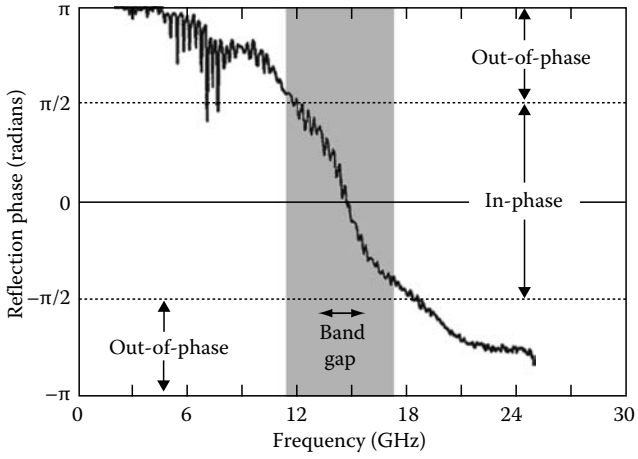

FIGURE 31.15 Measured reflection coefficient. (From Sievenpiper, D., Lijun, Z., Broas, R.F., Alexopoulos, N.G., and Yablonovitch, E., *IEEE Trans. Microw. Theory Tech.*, 47(11), 2059, Nov. 2004. With permission.)

zero at the resonant frequency of the structure. Within the range of phase values $\pi/2$ and $-\pi/2$, plane waves are reflected in-phase rather than out-of-phase. This range coincides with the measured TM/TE surface-wave bandgap, with the TM and TE band edges falling approximately at the points where the phase crosses through $\pi/2$ and $-\pi/2$, respectively.

31.2.4 Uniplanar HIS

Grounding vias complicate the fabrication of AMC surfaces, particularly at upper microwave and millimeter-wave frequencies. In order to simplify the fabrication, several research groups have worked on implementing AMC surfaces without vias in a completely planar (also mentioned as "uniplanar") configuration [7,8,13,15,16]. These structures are essentially periodic FSS [17], printed on grounded dielectric slabs. The first uniplanar HIS was reported in [13]. The authors termed this surface as uniplanar compact photonic bandgap (UCPBG). A schematic layout of the UCPBG structure

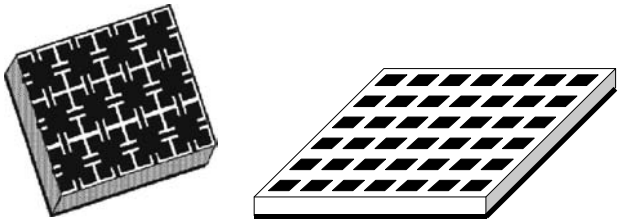

FIGURE 31.16 (a) Schematic representation of the uniplanar compact photonic band gap (UCPBG) proposed by Fei-Ran et al. [13] (From Fei-Ran, Y., Kuang-Ping, M., Yongxi, Q., and Itoh, T., *IEEE Trans. Microw. Theory Tech.*, 47(8), 1509, Aug. 1999. With permission) (b) Schematic representation a uniplanar HIS involving an array of conducting elements. (From Goussetis, G., Feresidis, A.P., and Vardaxoglou, J.C., *IEEE Trans. Antennas Propag.*, 54(1), 82, Jan. 2006. With permission.)

is shown in Figure 31.16a. Essentially, this is a periodic array of apertures shaped in Jerusalem crosses on a conducting metal sheet [17], printed on a grounded dielectric slab. The reflection phase properties as well as the dispersion diagram of the UCPBG are reported in [25] and [46], respectively. Other authors [7,8,15] have suggested periodic arrays of conducing elements, such as the square patch array shown in Figure 31.16b.

It is important to note that the presence of vias in this mushroom-type structure imposes an electromagnetic bandgap at the same frequency range as the AMC property. In other words, the mushroom structure exhibits high surface impedance for both normally incident and surface waves at the same frequency band. Hence, it reflects a normally incident plane wave with zero phase shift, therefore behaving as an AMC, and at the same frequency does not support surface waves, therefore behaving as an EBG. In studies reported in [7,8], it was demonstrated that in the absence of vias, the EBG does not normally coincide with the AMC frequency band. This can deteriorate the benefits of AMC surfaces in certain applications, where surface wave suppression is advantageous.

31.3 HIS: Operating Principles and Physical Insight

In this section the physical phenomena and the mechanisms underlying HIS operation are discussed. The discussion is limited for HIS without vias (uniplanar). For the case of HIS with vias, the reader is referred to the discussion in the previous section as well as to [44]. Initially a resonant cavity model based on ray optics is presented [16], which gives insight into the AMC operation of HIS. Subsequently, the resonant phenomena occurring in uniplanar HIS are studied in detail [8] using full-wave simulations and the AMC and EBG operation are discussed.

31.3.1 Doubly Periodic Metallic Arrays (FSS)

Although a rigorous treatment of doubly periodic arrays of either conducting electrically isolated elements or perforated apertures in a conducing sheet is out of the scope of this chapter, those features required in the following discussions are presented for completeness. Such structures were extensively studied in the context of FSS and the reader is referred to the relevant literature for an in-depth analysis (e.g., [17,53]).

The transmission and reflection response (in the far-field) of doubly periodic planar arrays of electrically isolated conducting elements excited by incident plane waves in general resemble the one depicted in Figure 31.17a. This is a generic response; in practice, the transmission and reflection

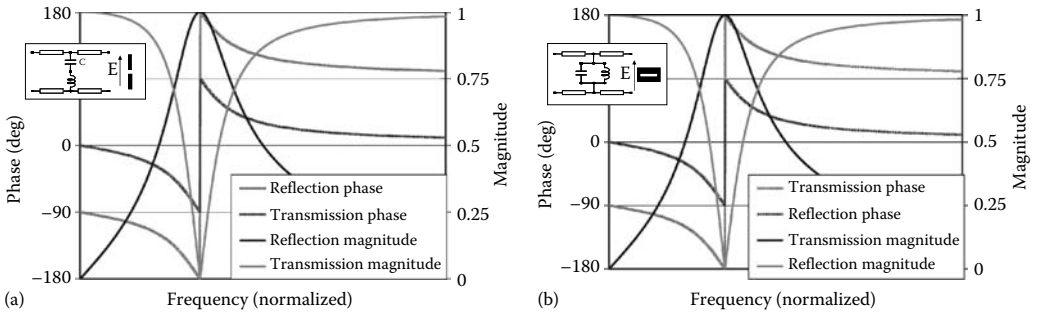

FIGURE 31.17 Generalized transmission and reflection response for (a) capacitive array of conducting elements and (b) inductive array of perforated apertures. The insets show simple *LC* circuits that produce a similar response as well as examples of unit cells for linear polarization (also shown).

are dependent on the geometry, angle of incidence, polarization and as mentioned above will also produce grating lobes. However the general features are evident. Doubly periodic arrays of conducting elements in general are characterized by a resonant frequency, at which they perform as conducting sheets. In the vicinity of the resonance, they perform as partially reflective screens (PRS), with associated transmission and reflection magnitude and phase characteristics. This response is similar to that of a series *LC* resonator in shunt, as shown in the inset of Figure 31.17a. For frequencies below the resonance, they have predominantly capacitive characteristics, and therefore this type of arrays are also referred to as capacitive screens. An example of a capacitive screen is a dipole array, with two unit cells shown in the inset of Figure 31.17a together with the required polarization of the incident field.

The dual structure of the dipole array is that of dipole slots perforated in an all-metal sheet. The unit cell is shown in the inset of Figure 31.17b together with the required polarization of the incident field. Duality suggests that this structure will share similar characteristics but, instead of a bandstop response, will produce a bandpass response. At resonance, doubly periodic arrays of perforated slots in all-metal surfaces are transparent to incident plane waves. Their far-field response shares the characteristics of a shunt *LC* resonator in shunt topology as shown in Figure 31.17b. As before, this is just a generic response. The response of practical arrays will vary with incidence angle, polarization, element geometry, and lattice and will also produce grating lobes above a certain frequency.

31.3.2 Resonant Cavity Model for AMC Operation

In order to get physical insight into the mechanisms underlying the AMC operation, a simple ray optic model can be employed. This model assumes an AMC consisting of a 2D periodic array printed on a grounded dielectric slab. Consider the case where a radiating source is placed in free space and adjacent to the periodic array (Figure 31.18). The periodic array in the absence of the ground plane is essentially a FSS [17]. Incident plane waves on the array are partially reflected and partially transmitted with an associated phase shift [16]. In this context, the periodic array is termed as PRS. Following the paths of the direct and the reflected waves and taking into account the various phase shifts introduced to them, the resonance condition of the cavity formed between the periodic array and the ground plane can be easily derived. The PEC introduces a phase shift of π. The PRS introduces a phase shift equal to the phase of its transmission coefficient, φ_T. If $\varphi_2 - \varphi_1$ is the phase difference between direct and reflected waves, the resonance condition is written as follows:

$$\phi_2 - \phi_1 = 2\phi_T - \frac{2\pi}{\lambda} 2S - \pi = 2N\pi, \quad N = 0, 1, 2 \ldots \tag{31.8}$$

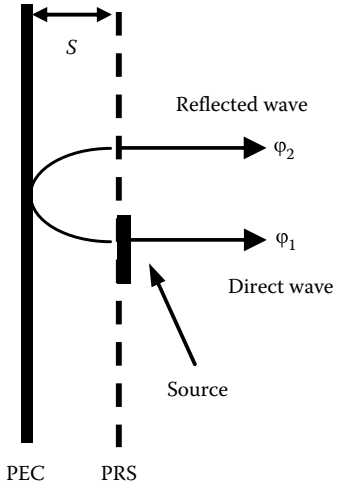

FIGURE 31.18 Resonant cavity model for AMC operation: schematic representation of the cross section of an HIS consisting of a periodic array in proximity to an all-metal ground plane. (From Feresidis, A.P., Goussetis, G., Wang, S., and Vardaxoglou, J.C., *IEEE Trans. Antennas Propag.*, 53(1), 209, Jan. 2005. With permission.)

where S is the distance between the PRS and the PEC ground plane. This resonant cavity behaves as a PMC (at normal incidence) since it reflects normal incident waves with zero phase shift. Consequently, placing a simple point source in close proximity to the PRS would result in constructive interference between direct and reflected waves at the cavity resonance. According to this ray model, a cavity formed by a PEC and a PRS and having external excitation, performs as an AMC when the resonance condition (Equation 31.8) is met. Hence, considering Equation 31.8 as the condition for AMC operation (assuming normal incidence), a relationship between the transmission phase of the PRS, the substrate thickness, and the center (or PMC) operating frequency is obtained.

The relation between the PRS characteristics and the functioning of the AMC cavity is demonstrated by means of an example which shows that two different periodic arrays having same reflection and transmission characteristics at frequency f_0 are interchangeable in an AMC cavity that operates at f_0. Figure 31.18a shows the reflection coefficient (magnitude and phase) of two periodic arrays of square patches. The geometries of the two arrays are $L = 4.15\,\text{mm}$, $D = 4.50\,\text{mm}$ for the first screen named PRS1 and $L = 6.00\,\text{mm}$, $D = 10.00\,\text{mm}$ for the second screen named PRS2, where L and D is the length of the square patch element and the square unit cell, respectively. PRS1 resonates (i.e., is fully reflective) at 60.5 GHz and PRS2 at 26.0 GHz. The reflectivity and transmission phase at 21.7 GHz is identical for the two screens. Figure 31.18b shows the full-wave simulation results for two AMC cavities of the same thickness S employing PRS1 and PRS2, respectively. The thickness S was determined from Equation 31.8 so that the AMC cavities operate at 21.7 GHz. In order to have good agreement between the ray model and the full-wave results, we are working at the second ($N = 1$) rather than the first ($N = 0$) resonant mode of the cavity (see Equation 31.8). As predicted by the ray model, the full-wave AMC responses are centered at the same frequency 21.7 GHz, where the transmission phase values are common. For different cavity thickness, each PRS results in different AMC center frequency.

It is worth noting that according to Equation 31.8, the second resonant mode of the AMC cavity lies at a frequency approximately three times that of the first resonant mode. Thus, the resonant cavity model provides a new explanation for the large separation between the first and second AMC frequencies of grounded square patch arrays that was also studied in [15]. Moreover, the low reflection

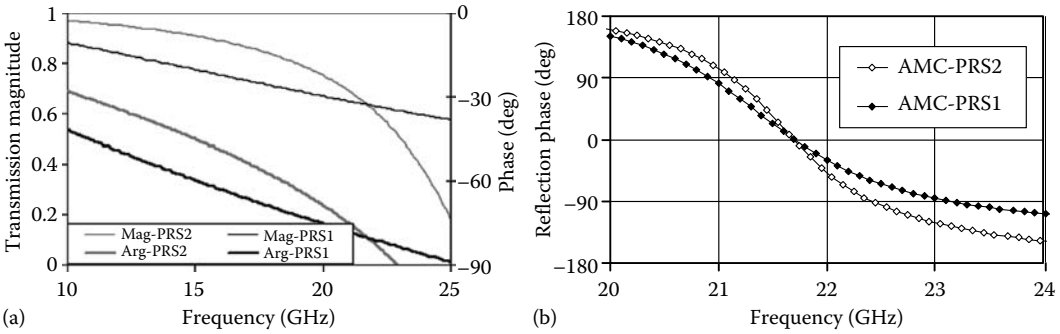

FIGURE 31.19 (a) Simulated transmission magnitude and phase for two different free-standing periodic arrays PRS1 and PRS2 (b) AMC reflection responses for same cavity with PRS1 and PRS2, respectively. (From Feresidis, A.P., Goussetis, G., Wang, S., and Vardaxoglou, J.C., *IEEE Trans. Antennas Propag.*, 53(1), 209, Jan. 2005. With permission.)

magnitude observed at the second AMC frequency can be explained by the fact that for increasing N the side lobes of the resonant cavity radiation pattern increase, as described in [47,48].

31.3.3 Resonance Phenomena in Uniplanar HIS

In this section, we investigate the resonant phenomena occurring in uniplanar HIS, and in particular, in a surface comprising of a doubly periodic array of metallic elements in proximity to a ground plane [8]. The investigation is largely based on studying the currents excited on the metallic elements of the array. The discussion commences with the resonant phenomena of a free-standing periodic array (i.e., in the absence of ground plane) upon illumination with a normally incident plane wave. Capacitive arrays (i.e., arrays of electrically isolated conducting elements) of course require a dielectric substrate to support them. However in the following discussion and in order to maintain simplicity, the array is considered free-standing in vacuum, illuminated by a normally incident plane wave while no ohmic losses are assumed. Having obtained insight from the free-standing case, we proceed to study the physics in a similar scenario but when the array is in proximity to a ground plane. The outcome of this study is in good agreement with the resonant cavity model presented above. Finally the AMC and EBG effects of uniplanar HIS are discussed in relation to the resonant phenomena observed.

31.3.3.1 Free-Standing Doubly Periodic Array of Metallic Elements

Free-standing doubly periodic arrays of metallic elements were studied for many years in the context of FSS and their behavior is well understood [15]. The incident polarization is assumed to be suitable to excite the metallic elements—i.e., in the case of linear dipole elements the electric field to have a component parallel to the direction of the dipoles. It is well known that for incidence at the resonant frequency of the array, the latter performs as a fully metalized screen; incident waves are fully reflected with a phase reversal [17]. Moreover, at resonance the current is in phase with the incident field, i.e., the impedance seen by the incident wave is purely ohmic (real), since the capacitive and inductive parts cancel out. In addition, a maximum current magnitude is excited on the elements.

The above are briefly demonstrated here by means of an example based on a free-standing square patch (of length 6.1 mm) array arranged in a square lattice (periodicity 9.9 mm). Full wave simulation results are obtained using a Floquet modal analysis of the unit cell, which leads to the formulation of an integral equation (IE) and its solution using Galerkin method of moments (MoM) [53]. The method was extensively described in the literature and is known to be a fast and accurate technique for the characterization of such structures. Figure 31.20a shows the transmission and reflection response

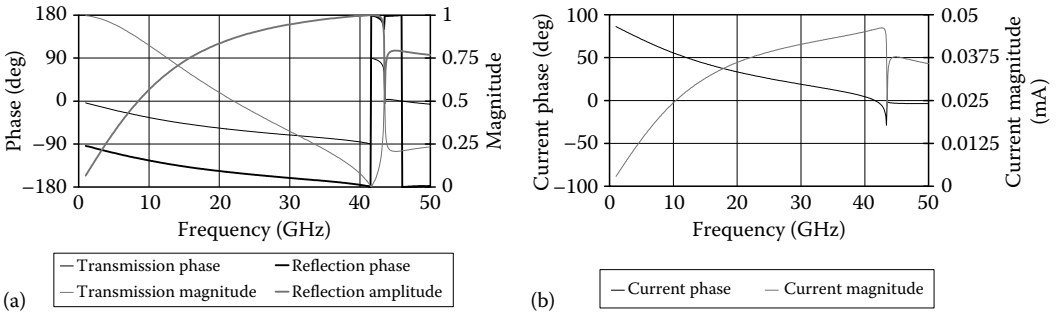

FIGURE 31.20 Plane wave normally incident on free-standing square patch (of edge length 6.1 mm) array with periodicity 6.9 mm: (a) transmission and reflection response and (b) currents excited on the elements. (From Goussetis, G., Feresidis, A.P., and Vardaxoglou, J.C., *IEEE Trans. Antennas Propag.*, 54(1), 82, Jan. 2006. With permission.)

of the capacitive FSS illuminated with a normally incident plane wave. Figure 31.20b shows the magnitude and phase of the currents excited on the elements, assuming incident field of magnitude 1 V/m. The array resonance occurs at 41.5 GHz, where the current phase is 0°.

31.3.3.2 FSS in Proximity to a Ground Plane

For periodic arrays in close proximity to a ground plane some subtle differences emerge. Due to the ground plane, incident waves are fully reflected at all frequencies. However in this type of structure, careful investigation reveals that two distinct resonant phenomena occur for a normally incident wave. In the following, we assume a free-standing array in proximity to an all-metal ground plane illuminated as above by a normally incident wave.

As above, we can identify the array resonance at the frequency where the currents excited on the array are in phase with the incident wave (i.e., zero current phase). At this frequency, the incident wave is reflected from the periodic array with a phase reverse, as in the case of the free-standing array resonance. However, it can be found that there also occurs a Fabry–Perot type of resonance at the cavity formed between the ground plane and the array [16,48,54]. The Fabry–Perot resonance occurs at frequencies different from the array resonance. This strong cavity-type resonance excites maximum currents on the elements (which in general are out of phase with the incident wave) and the incident wave is reflected with a zero phase shift.

These resonance phenomena are demonstrated by means of an example. The periodic array of Figure 31.20 is considered at distance 1.13 mm from an infinite ground plane. The structure is initially illuminated with a normally incident plane wave of amplitude 1 V/m. Figure 31.21 shows the reflection phase of the normally incident plane wave and the excited current (magnitude and phase) on the elements. As in the free-standing case, the array resonance is identified by the zero current phase. This resonance shares the same characteristics with the resonance of the free-standing case. It occurs at the same frequency and the currents excited are of equal magnitude and phase to the current excited in the free-standing case (Figure 31.20b). However at around 15.9 GHz the Fabry–Perot resonance occurs, indicated by the nearly maximum current magnitude excited on the elements. The current phase however is not zero but around 90°, i.e., a capacitive phase of the periodic array is observed [55] indicating that the array itself is not at resonance. The normally incident wave "sees" a high surface impedance (open circuit) and is reflected with zero reflection phase.

As the angle of the TE incident plane wave moves from normal to grazing incidence, the frequency characteristics of the two resonances (Fabry–Perot and array resonance) vary. Figure 31.22a shows the reflection phase response of the structure of Figure 31.21 as the incident angle varies from 10°

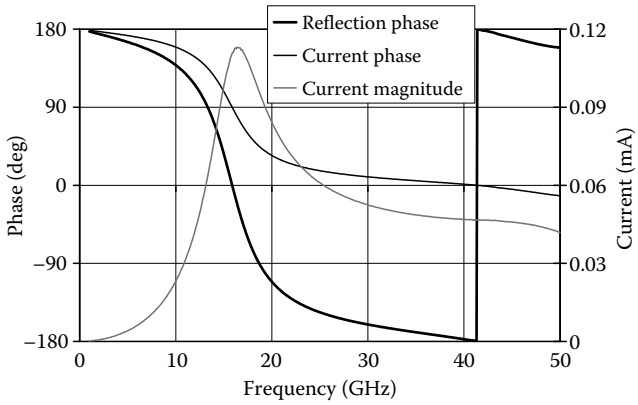

FIGURE 31.21 Plane wave normally incident on square patch (of edge length 6.1 mm) array with periodicity 6.9 mm at distance 1:13 mm from a ground plane: reflection phase for incident plane wave and currents excited on the elements. (From Goussetis, G., Feresidis, A.P., and Vardaxoglou, J.C., *IEEE Trans. Antennas Propag.*, 54(1), 82, Jan. 2006. With permission.)

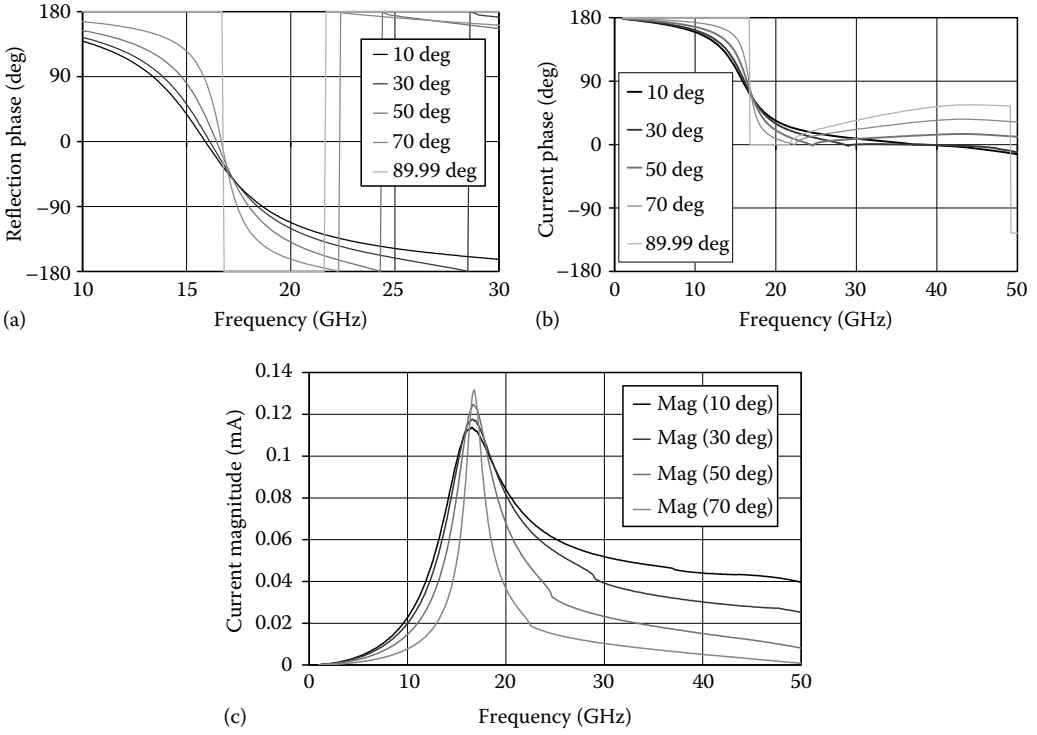

FIGURE 31.22 (a) Reflection phase response, (b) current phase, and (c) magnitude for the array of Figure 31.21 and for varying incident angles. (From Goussetis, G., Feresidis, A.P., and Vardaxoglou, J.C., *IEEE Trans. Antennas Propag.*, 54(1), 82, Jan. 2006. With permission.)

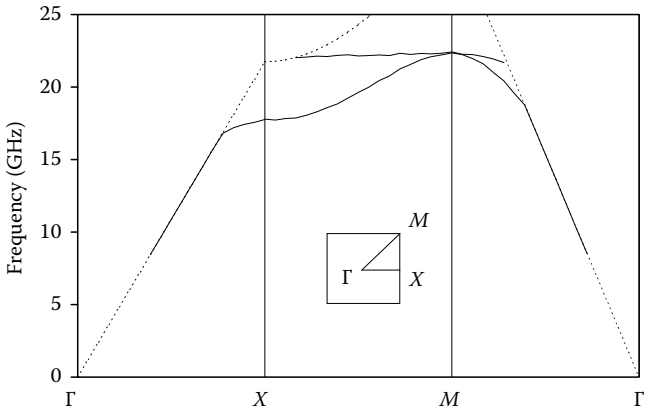

FIGURE 31.23 Dispersion relation for the array of Figure 31.21. (From Goussetis, G., Feresidis, A.P., and Vardaxoglou, J.C., *IEEE Trans. Antennas Propag.*, 54(1), 82, Jan. 2006. With permission.)

(close to normal incidence) to 89.99° (almost surface wave). The current phase and magnitude are shown in Figure 31.22b and c, respectively. Note that while the Fabry–Perot resonant frequency (and the AMC operation) remains nearly constant due to the periodicity being small compare to the wavelength (see Section 31.3.3.3 and [55]), the array resonance shifts to significantly lower frequencies. At 90° incidence, the plane wave response is not a valid description any more. Instead the structure is characterized by the dispersion relation of surface waves along the contour of the BZ, shown in Figure 31.23. The MoM formulation for the derivation of the dispersion diagrams is similar as for normal incidence, only now the excitation is set to zero, the tangential wavenumbers are set to correspond to a particular point on the x-axis of the dispersion diagram and the eigen frequencies are specified so that the homogenous problem accepts real solutions [57]. A TE bandgap emerges along the ΓX direction at about 17.5 GHz. This frequency corresponds with a very good accuracy to the frequency where the array resonates for 89.99° incidence (zero current phase in Figure 31.22b). This is a good indication that the array resonance is the underlying physical mechanism of the EBG.

Further validation for the resonant cavity model for AMC operation comes by considering the effect of increasing the substrate thickness. Indeed the resonant cavity model predicts that thicker substrates (i.e., larger distance between the PRS and the all-metal ground plane) produce larger cavities that resonate at lower frequencies. This is indeed validated by numerical results [16]. These are presented in Section 31.5.2.2 and Figure 31.42.

31.3.3.3 AMC and EBG Operation

Based on the above study, we can now relate each of the AMC and EBG properties with one of the two distinct resonant phenomena observed. The AMC operation emerges by virtue of the resonance of the cavity formed between the periodic array and the ground plane. To a ray optics approximation, the cavity resonance critically depends on the thickness of the cavity and the value of the transmission phase ϕ_T provided by the periodic array, according to the following resonance condition:

$$\phi_T = k_z \cdot S - (2N+1) \cdot \frac{\pi}{2}, \quad N = 0, 1, 2 \ldots \tag{31.9}$$

where k_z is the propagation constant along the normal to the surfaces. Equation 31.9 is derived from ray optics, and hence is more accurate for the higher values of N ($N \geq 1$) but the basic physics is the same for a thin AMC ($N = 0$).

The EBG emerges as a result of the array resonance and the array periodicity. The surface waves in a periodic structure below the bandgap are a superposition of traveling and standing waves [2]. At the lower EBG cutoff frequency, the half-guided wavelength becomes equal to the periodicity and a standing wave is formed. Successive elements are, in this case, out of phase and a bandgap emerges. At the higher cutoff of the bandgap, there is a similar standing wave, only now the spatial locations of energy maximums and nulls are interchanged. The upper cutoff frequency is typically defined by the periodicity of the lattice. The EBG bandwidth occurs due to the variation of the spatial location of energy concentration in these two limit cases.

31.4 Analysis Techniques

The analysis of HIS refers to ways of modeling the interaction of electromagnetic properties of those structures. Analytical techniques were reported in order to produce the equivalent impedance of a periodic surface (e.g., [4,5,40,41,44]). Alternatively, semianalytical methods were reported, which are based on extraction, interpolation, and analytical extrapolation of the impedance (admittance) of doubly periodic surfaces [7]. The technique is based on approximation of the impedance (admittance) function as a rational function, whereby the problem reduces to the estimation of its poles and zeros. The most rigorous (and usually computationally intensive) family of techniques are rigorous full-wave techniques. Following a simple ray-optics model for the AMC operation proposed in [16], this section presents an overview of these methods.

31.4.1 Analytical Methods

Here we present a summary of analytical expressions describing the interaction of a plane wave with dense doubly periodic arrays printed on a thin grounded dielectric slab. The interaction with an incident plane wave (that produces an effective AMC) and the propagation of surface waves (that yields an EBG) is treated separately in the following.

31.4.1.1 Analytical Models: Incident Plane Wave (AMC)

Analytical techniques can be applied to model the reflection of incident plane waves from a variety of printed HIS structures. The technique is based on extracting an equivalent surface for the HIS, which allows transforming the rigorous electromagnetic problem into a circuit problem. The model is based on the full-wave solution of a scattering problem in the quasistatic limit, and enables one to accurately capture the physics of plane-wave interaction with HIS structures by modeling a single unit cell of a periodic grid with a single Floquet mode. It is based on the homogenization of grid impedance in terms of effective inductance and capacitance obtained from the averaged impedance boundary condition.

Specific examples for an array of printed patches and Jerusalem crosses will be considered to demonstrate a methodology for analytical modeling. The geometry of an HIS structure realized by an array of 2D periodic printed patches on a grounded dielectric slab with an obliquely incident uniform plane wave is shown in Figure 31.24a. The parameters of the grid (Figure 31.24b) are such that the grid period is much smaller than the effective wavelength (described below) and strip width is much smaller than the grid period. These constraints are critical in the design of dense HIS structures with desired characteristics (wideband response of the reflection phase and stable resonance properties for oblique incidence) and at the same time enable to homogenize the grid surface impedance in terms of effective circuit parameters with the application of transmission line network schematically shown in Figure 31.25.

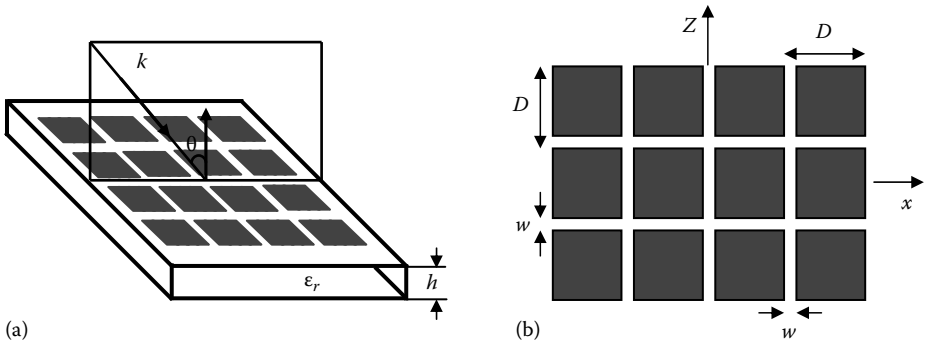

FIGURE 31.24 (a) Geometry of HIS structure realized by an array of 2D periodic patches printed on a grounded dielectric slab with an obliquely incident uniform plane wave. A plane of incidence is shown, where **k** is the wave vector in the propagating direction and θ is the angle of incidence; (b) FSS grid of printed patches. All dimensions are in mm: $D = 2$, $w = 0.2$, and $h = 1$. Permittivity of substrate is 10.2.

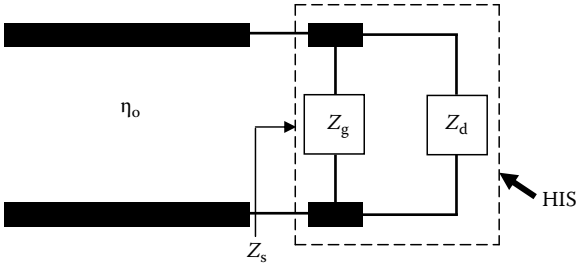

FIGURE 31.25 Transmission line network analysis of HIS structure characterized by surface impedance Z_s obtained as a parallel connection of grid impedance Z_g and grounded dielectric slab impedance Z_d. Here, η_0 is the characteristic impedance of free space.

Following the formalism presented in [4,40], the HIS surface impedance Z_s is obtained as a parallel connection of grid impedance Z_g and grounded dielectric slab impedance Z_d,

$$Z_s = \frac{Z_g Z_d}{Z_g + Z_d} \tag{31.10}$$

resulting in the parallel resonance condition, $Z_d + Z_g = 0$. In the lossless case, this condition suggests a capacitive nature of the grid in order to compensate an inductive impedance of the grounded dielectric slab leading to a high surface impedanceZ_s.

For obliquely incident TE-polarized plane wave, the impedance of the grounded dielectric slab Z_d is obtained as [4],

$$Z_d^{TE}(\omega, \theta) = \frac{j\eta_0}{\sqrt{\varepsilon_r - \sin^2\theta}} \tan(k_{nd} h) \tag{31.11}$$

and for an obliquely incident TM-polarized plane wave,

$$Z_d^{TM}(\omega, \theta) = \frac{j\eta_0}{\sqrt{\varepsilon_r - \sin^2\theta}} \tan(k_{nd} h) \left(1 - \frac{\sin^2\theta}{\varepsilon_r}\right) \tag{31.12}$$

where $k_{nd} = \omega\sqrt{\varepsilon_0\mu_0}\sqrt{\varepsilon_r - \sin^2\theta}$ is the wavenumber in the dielectric slab in the normal direction. The reflection coefficients of the TE and TM-polarized obliquely incident plane waves are obtained from an equivalent transmission line model (Figure 31.25), as follows [4]:

$$\Gamma^{TE} = \frac{Z_s^{TE}\cos\theta - \eta_0}{Z_s^{TE}\cos\theta + \eta_0}, \quad \Gamma^{TM} = \frac{Z_s^{TM} - \eta_0\cos\theta}{Z_s^{TM} + \eta_0\cos\theta}.$$

Below we present a summary of expressions for grid impedance Z_g of an array of printed patches and Jerusalem crosses, which are obtained in the quasistatic limit of full-wave scattering problems via the averaged impedance boundary condition and expressed in terms of effective circuit parameters (inductance and capacitance) as homogenized surface grid impedance.

31.4.1.1.1 Array of Printed Patches

The expressions of homogenized grid impedance of the patch array on the air–dielectric interface are obtained by first considering the strip mesh with square holes and then applying the approximate Babinet principle [4], resulting in the capacitive grid impedance of the complementary structure (i.e., array of patches) [40],

$$Z_g^{TM} = -j\frac{\eta_{eff}}{2\alpha} \qquad Z_g^{TE} = -j\frac{\eta_{eff}}{2\alpha\left(1 - \frac{1}{2}\left(\frac{k_z}{k_{eff}}\right)^2\right)} \tag{31.13}$$

where $\eta_{eff} = \eta_0/\sqrt{\varepsilon_{eff}}$, $\varepsilon_{eff} = (\varepsilon_r + 1)/2$, $k_{eff} = k_0\sqrt{\varepsilon_{eff}}$, $k_z = k_0\sin(\theta)$, and α is the grid parameter of an electrically dense array of ideally conducting strips (with the period much smaller than the effective wavelength)

$$\alpha = \frac{k_{eff}D}{\pi}\ln\left(\csc\left(\frac{\pi w}{2D}\right)\right) \tag{31.14}$$

Here, D is the period of patch array and w is the gap width, such that $w << D$ [4].

The self-resonant grid model agrees very well with the full-wave analysis for normal and oblique incidence for both the TE and TM polarizations of plane waves. The results for the reflection phase of printed patch HIS structure (with geometry and dimensions shown in Figure 31.24) with the TE and TM-polarized oblique plane-wave excitation are shown in Figures 31.26 and 31.27, respectively, and compared with those generated by the full-wave commercial software program (EMPiCASSO [59]) showing a good agreement in a wide frequency band (in [40] the behavior of reflection phase with respect to the angle of incidence is also compared with Ansoft HFSS [28], Fourier modal method, and the MoM showing a good agreement).

31.4.1.1.2 Array of Printed Jerusalem Crosses

The geometry of an HIS structure realized by the 2D periodic printed Jerusalem cross FSS is shown in Figure 31.28. The grid impedance of the series resonance grid is obtained in terms of an effective inductance L_g and effective capacitance C_g, and for TM and TE-polarized oblique plane-wave excitation is given by

$$Z_g^{TM} = j\omega L_g\left(1 - \left(\frac{k_z}{k_{eff}}\right)^2\right) + \frac{1}{j\omega C_g} \qquad Z_g^{TE} = j\omega L_g + \frac{1}{j\omega C_g} \tag{31.15}$$

where the inductance is that of the strip grid of period D and strip width w ($w << D$) [4],

$$L_g = \frac{\eta_{eff}\alpha}{2\omega} \tag{31.16}$$

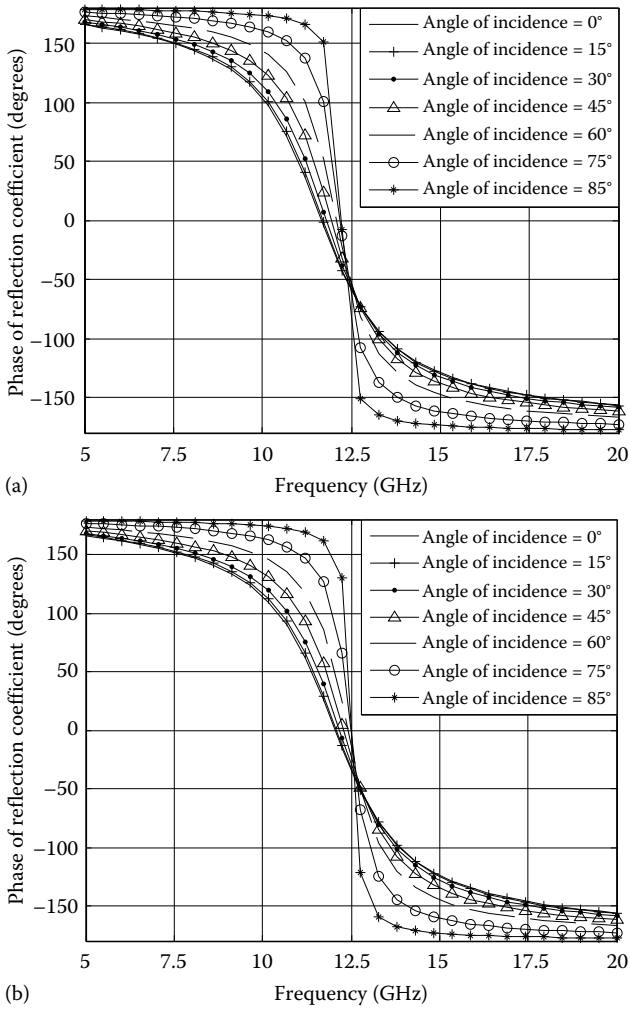

FIGURE 31.26 Comparison between the analytical and full-wave results for the reflection phase of printed patch HIS structure with the TE-polarized oblique plane wave excitation: (a) analytical results and (b) simulation results (EMPiCASSO [59]).

Here, α is the grid parameter given by Equation 31.14, and η_{eff}, ε_{eff}, k_{eff} are the parameters of the effective medium described above.

The effective capacitance between Jerusalem crosses was derived in [58] in the solution of scattering from a thin capacitive diaphragm in rectangular waveguide,

$$C_g = \frac{\varepsilon_0 \varepsilon_r d}{\pi}\left(\ln \operatorname{cosec}\left(\frac{\pi g}{2D}\right) + F\right) \tag{31.17}$$

where $F = Qu^2/\left(1 + Q\left(1-u\right)^2\right) + \left(du\left(3u-2\right)/4\lambda\right)^2$, $Q = \sqrt{1-\left(d/\lambda\right)^2}$, $u = \cos^2\left(\pi g/2d\right)$, $\lambda = 2\pi/k$

Figures 31.29 and 31.30 demonstrate the analytical and full-wave results for the reflection phase of Jerusalem cross HIS structure (with geometry and dimensions shown in Figure 31.28) with the TE and TM-polarized oblique plane-wave excitation. It can be seen that analytical results agree well with

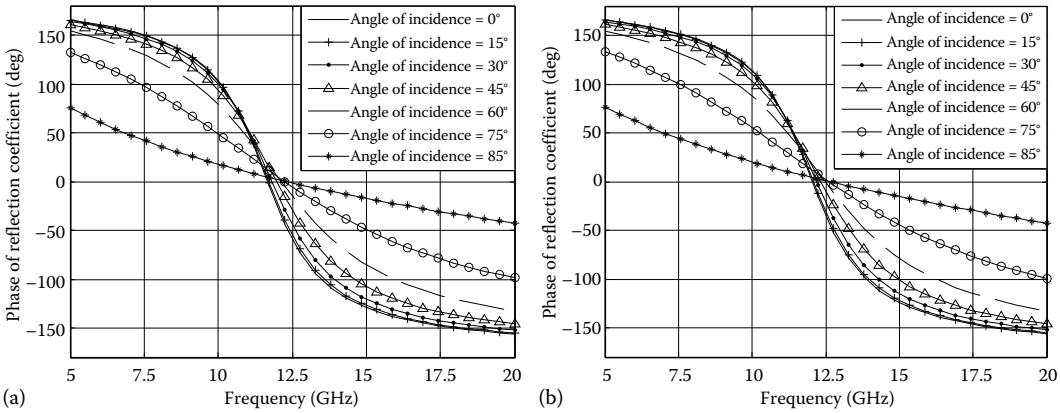

FIGURE 31.27 Comparison between the analytical and full-wave results for the reflection phase of printed patch HIS structure with the TM-polarized oblique plane wave excitation: (a) analytical results and (b) simulation results (EMPiCASSO [59]).

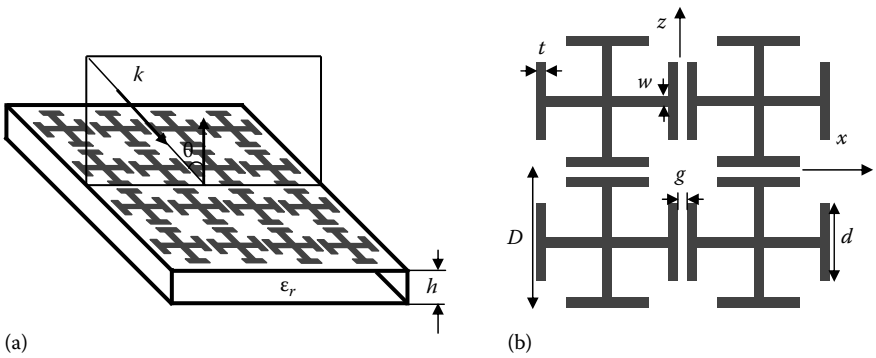

FIGURE 31.28 (a) Geometry of 2D periodic Jerusalem cross HIS structure printed on a grounded dielectric slab; (b) FSS grid of printed Jerusalem crosses. All dimensions are in mm: $g = 0.1$, $d = 2.8$, $t = w = 0.2$, $D = 4$, and $h = 6$. Permittivity of substrate is 2.7.

the full-wave results obtained by commercial software EMPiCASSO [59] for a wide range of variation of incidence angle within the frequency band of interest.

It should be noted that the frequency bandwidth of the printed patch and Jerusalem cross HIS structures (wherein the reflection phase changes between +90° and −90°) significantly varies with respect to the incidence angle. For the TE-polarized plane wave excitation the bandwidth decreases as the incidence angle increases (see Figures 31.26 and 31.29), and for the TM-polarized excitation the bandwidth increases with increase of the incidence angle (see Figures 31.27 and 31.30). Later in this chapter, we will discuss HIS configurations with a more complicated FSS pattern (based on complementary patch/slot unit cell) in order to achieve a wideband AMC performance and stable resonance properties with respect to the angle of incidence.

31.4.1.2 Analytical Models: Surface waves (EBG)

At a grazing angle of incidence ($\theta = 90°$) the solution of the plane-wave problems considered above is no longer valid, and the analysis turns into the characterization of surface modes in the 2D periodic

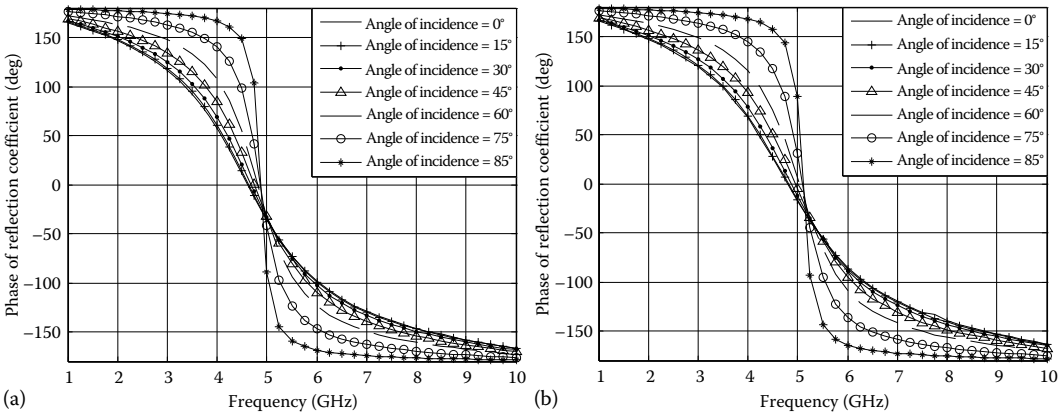

FIGURE 31.29 Comparison between the analytical and full-wave results for the reflection phase of Jerusalem cross HIS structure with the TE-polarized oblique plane wave excitation: (a) analytical results and (b) simulation results (EMPiCASSO [59]).

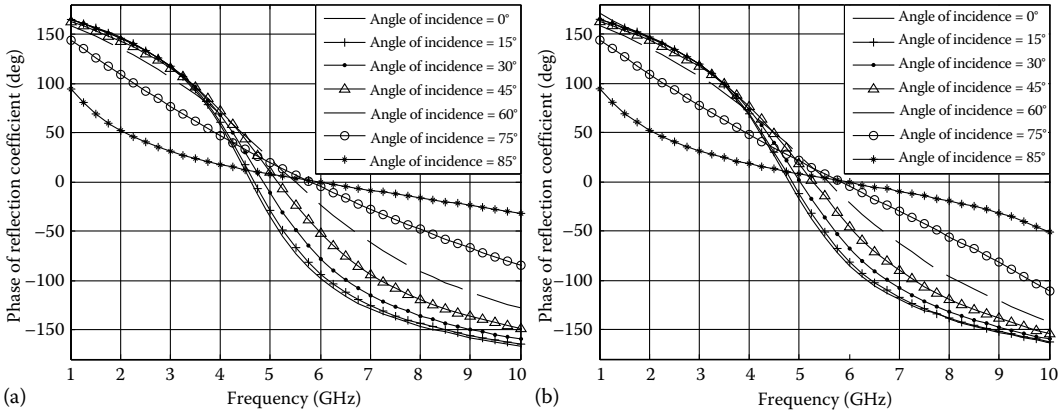

FIGURE 31.30 Comparison between the analytical and full-wave results for the reflection phase of Jerusalem cross HIS structure with the TM-polarized oblique plane wave excitation: (a) analytical results and (b) simulation results (EMPiCASSO [59]).

FSS grid printed on a grounded dielectric slab. In this section, two analytical models for the analysis of natural modes of HIS structures are discussed [41]. In the first model, the surface waves are studied for propagation along the impedance surface obtained as a parallel connection of grid impedance and impedance of the grounded dielectric slab. The second model is based on the implementation of a two-sided impedance boundary condition in the boundary-value problem for a grounded dielectric slab. It should be noted that both models result in the same dispersion equations for surface waves.

31.4.1.2.1 Model I

A transmission line network of an HIS structure is shown in Figure 31.25, wherein the surface impedance Z_s is obtained as a parallel connection of grid impedance Z_g and grounded dielectric slab impedance Z_d, enables one to formulate the problem for natural modes of impedance surface as

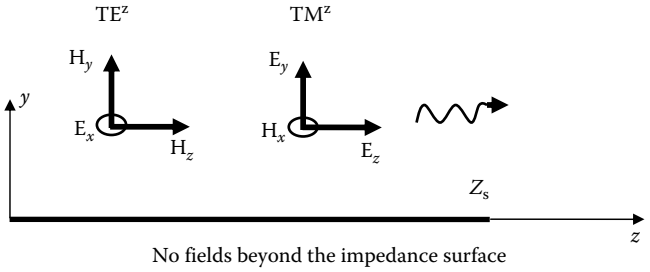

FIGURE 31.31 Surface waves propagating along the impedance surface characterized by the surface impedance Z_s.

demonstrated in Figure 31.31 [4]. The impedance surface characterized by Z_s supports TM^z and TE^z surface waves.

The solution of Helmholtz's equations for H_x (TM^z-modes) and E_x (TE^z-modes) components subject to the impedance boundary condition,

$$\mathbf{E} = Z_s \hat{y} \times \mathbf{H} \quad \text{at } y = 0 \tag{31.18}$$

where for TM^z-even surface-wave modes,

$$E_z = -Z_s^{TM} H_x \quad \text{at } y = 0 \tag{31.19}$$

and for TE^z-odd surface-wave modes,

$$E_x = Z_s^{TE} H_z \quad \text{at } y = 0 \tag{31.20}$$

results in the following dispersion equations for the propagation constant k_z of TM^z and TE^z modes, respectively,

$$k_z^{TM} = k_0 \sqrt{1 - \left(\frac{Z_s^{TM}}{\eta_0}\right)^2} \tag{31.21}$$

$$k_z^{TE} = k_0 \sqrt{1 - \left(\frac{\eta_0}{Z_s^{TE}}\right)^2} \tag{31.22}$$

where η_0 and k_0 are the characteristic impedance and wavenumber of free space, respectively. It should be noted that the expressions for the surface impedance of HIS structures Z_s derived in the solution of plane-wave problems are functions of the propagation constant k_z.

31.4.1.2.2 Model II

Consider geometry of a grounded dielectric slab with a periodic planar grid structure positioned at the air–dielectric interface and characterized by the surface impedance Z_g (Figure 31.32).

By solving Helmholtz's equations in the air and dielectric regions for H_x (TM^z-modes) and E_x (TE^z-modes) components subject to appropriate boundary conditions on the ground plane (at $y = 0$) and infinity, and by implementing a two-sided impedance boundary condition for the grid at the air–dielectric interface,

$$\mathbf{E}_1 = \mathbf{E}_2 = Z_g \hat{y} \times (\mathbf{H}_1 - \mathbf{H}_2) \quad \text{at } y = h \tag{31.23}$$

where for TM^z-even surface-wave modes,

$$E_{z1} = E_{z2} = -Z_g^{TM} (H_{x1} - H_{x2}) \quad \text{at } y = h \tag{31.24}$$

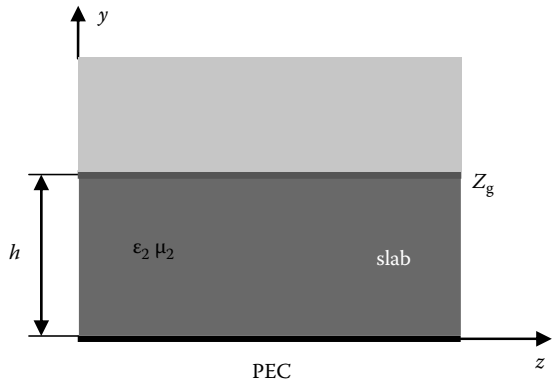

FIGURE 31.32 Geometry of a grounded dielectric slab with FSS grid on the air–dielectric interface.

and for TE^z-odd surface-wave modes,

$$\mathrm{E}_{x1} = \mathrm{E}_{x2} = Z_{\mathrm{g}}^{\mathrm{TE}} \left(\mathrm{H}_{z1} - \mathrm{H}_{z2}\right) \quad \text{at } y = h \tag{31.25}$$

the dispersion equations for TM^z-even and TE^z-odd modes of the structure depicted in Figure 31.32 are obtained,

$$k_{y2} \tanh\left(k_{y2}h\right) = -Z_{\mathrm{g}}^{\mathrm{TM}} \frac{j\omega\varepsilon_2 k_{y1}}{j\omega\varepsilon_1 Z_{\mathrm{g}}^{\mathrm{TM}} + k_{y1}} \tag{31.26}$$

$$\frac{\mu_2}{\mu_1} k_{y1} + k_{y2} \coth\left(k_{y2}h\right) = -\frac{j\omega\mu_2}{Z_{\mathrm{g}}^{\mathrm{TE}}} \tag{31.27}$$

Here, $k_{yi} = \sqrt{k_z^2 - k_i^2}$, $k_i = \omega\sqrt{\varepsilon_i\mu_i}$, $i = 1, 2$. For HIS structures with the grid positioned on the air–dielectric interface, $\varepsilon_1 = \varepsilon_0$, $\varepsilon_2 = \varepsilon_r\varepsilon_0$, and $\mu_1 = \mu_2 = \mu_0$. The wavenumber k_{y1} induces branch points in the complex k_z-plane at $k_z = \pm k_1$. Proper modes (above cutoff) reside on the proper Riemann sheet where $\mathrm{Re}\left(k_{y1}\right) > 0$ (wave dependence is of the form $e^{-k_{y1}y}$), and improper modes (below cutoff) reside on the improper Riemann sheet where $\mathrm{Re}\left(k_{y1}\right) < 0$. Branch cuts which separate proper and improper Riemann sheets are defined by $\mathrm{Re}\left(k_{y1}\right) = 0$, leading to the hyperbolic branch cuts,

$$\mathrm{Im}\left(k_z\right) = \frac{\mathrm{Im}\left(k_1\right)\mathrm{Re}\left(k_1\right)}{\mathrm{Re}\left(k_z\right)}, \quad \left|\mathrm{Re}\left(k_z\right)\right| < \left|\mathrm{Re}\left(k_1\right)\right| \tag{31.28}$$

It should be noted that the dispersion equations of Model II can be derived from the dispersion equations of Model I, by substituting the expressions of dielectric impedance obtained in the solution of the plane-wave problem. These models utilize the expressions of surface grid impedance obtained in the quasistatic limit of the full-wave scattering problem via the averaged impedance boundary condition in terms of effective circuit parameters. It appears that the Model I is a more general one since it enables to integrate more complex substrates in the dispersion equations, such as wire medium and dielectric slab with spherical inclusions (in the assumption that these metamaterials are properly homogenized). However, Model II gives a better physical insight for proper and improper surface-wave solutions and can be used for the calculation of fields in the slab region.

31.4.1.2.3 Surface Waves in Square Patch and Jerusalem Cross Arrays

The analysis of surface waves was performed for arrays of patches and Jerusalem crosses printed on a grounded dielectric slab. In the first example of HIS composed of a patch array on a grounded slab

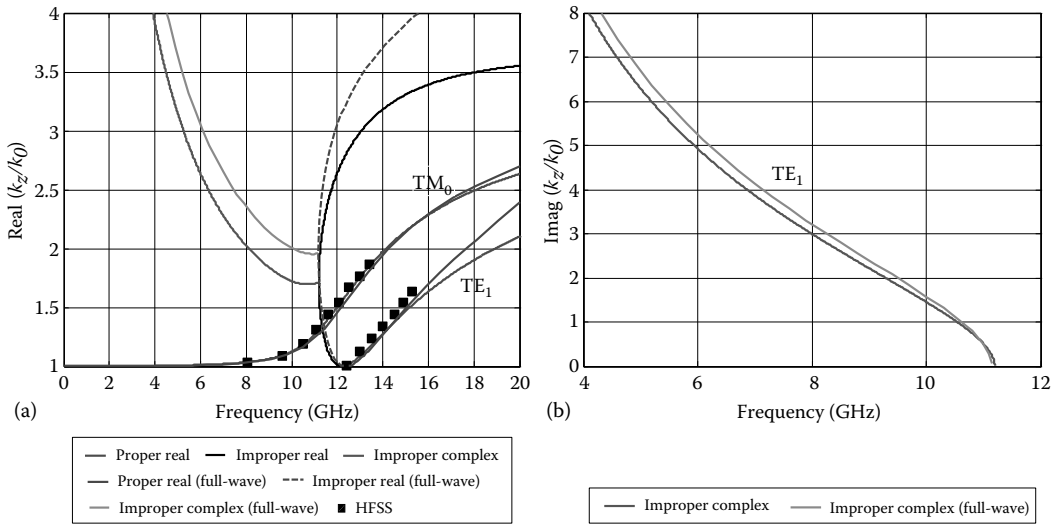

FIGURE 31.33 Dispersion behavior of proper real (bound) and improper real and complex solutions of patch HIS structure (Figure 31.24); (a) real part of normalized propagation constant and (b) imaginary part of normalized propagation constant. The analytical results are compared with the full-wave results of P. Baccarelli et al. [60].

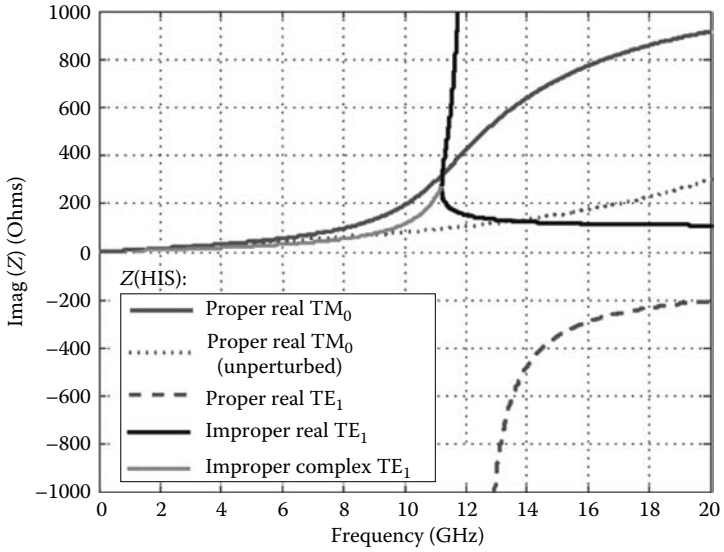

FIGURE 31.34 Surface impedance Z_s of the patch HIS (Figure 31.24) "seen" by the surface-wave modes.

(with geometry and dimensions shown in Figure 31.24), the dispersion behavior of TM_0 and TE_1 surface-wave modes, including proper real and improper real and complex solutions, is shown in Figure 31.33, and compared with the full-wave solution obtained both by the IE method as in [60] and by HFSS [28]. A good agreement between the analytical and full-wave results is observed at low frequencies within the limits of homogenization of HIS structure. Some disagreement is noticed for improper (real and complex) solutions and for proper solutions at higher frequencies. Figure 31.34 demonstrates the dispersion behavior of surface impedance of the HIS structure Z_s "seen" by the

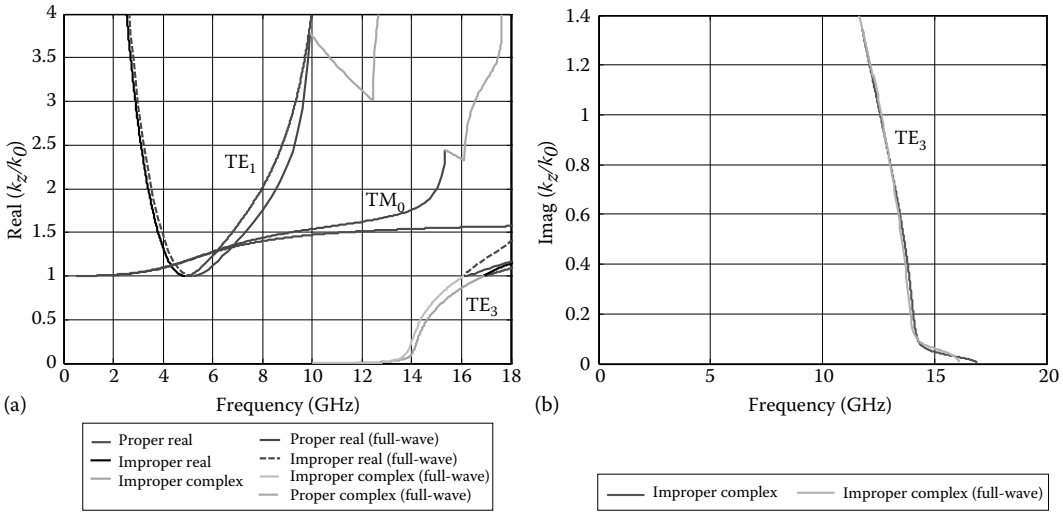

FIGURE 31.35 Dispersion behavior of proper real (bound) and improper real and complex solutions of Jerusalem cross HIS structure (Figure 31.28); (a) real part of normalized propagation constant and (b) imaginary part of normalized propagation constant. The analytical results are compared with the full-wave results of P. Baccarelli et al. [60].

surface-wave modes in Figure 31.33. An interesting observation is that in the HIS structure composed of printed patches (with grid period much smaller than effective wavelength) no stopband occurs between TM and TE surface-wave modes at low frequencies, wherein the structure experiences AMC properties.

In the second example of the HIS structure realized by the array of Jerusalem crosses printed on a grounded dielectric slab (with the geometry and dimensions shown in Figure 31.28), the results of analytical modeling are demonstrated in Figure 31.35 for the dispersion behavior of TM_0, TE_1, and TE_3 surface-wave modes (proper and improper real and complex solutions), showing good agreement with the full-wave results of [60].

It can be seen that the physics of surface-wave behavior of proper and improper solutions is captured by the analytical model. However, the analytical model does not predict correctly the bandstop behavior at higher frequencies associated with Bragg's diffraction in the first BZ (stopbands of TM_0 and TE_1 modes, indicated as proper complex solutions in Figure 31.35a, [60]).

Figure 31.36 demonstrates the dispersion behavior of surface impedance of the Jerusalem cross HIS structure "seen" by the surface-wave modes in Figure 31.35.

31.4.2 Semianalytical Methods

Although analytical techniques can be very efficient for the modeling of HIS geometries such as those considered here, the equivalent surface impedance is limited to a family of array geometries. Some geometrical characteristics can be parameterized (e.g., square patch width or periodicity), but different element geometries would require new analytical expressions that are not always available. One technique based on full-wave modeling to obtain a general expression for the equivalent impedance of doubly periodic arrays was proposed in [7] and termed as "pole-zero" method. This technique uses a small number of full-wave simulations of the reflection from the HIS under consideration to produce a general expression of the impedance (admittance) of the array. The latter can be

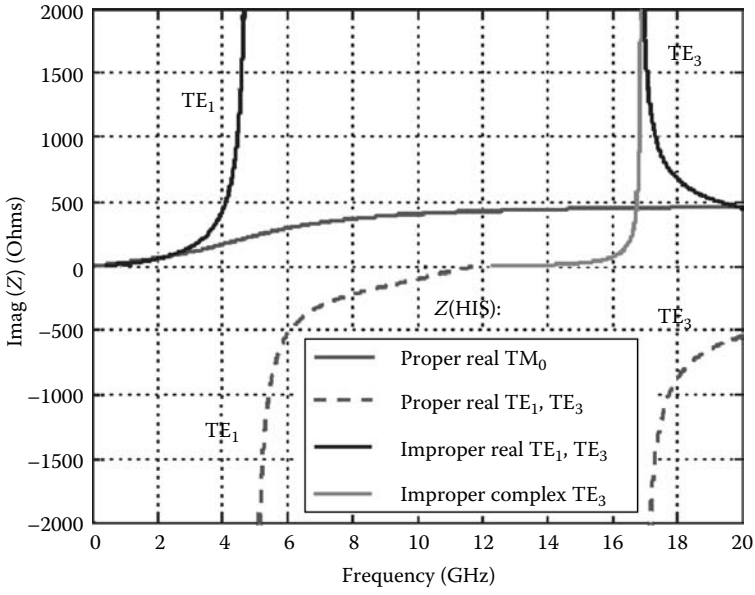

FIGURE 31.36 Surface impedance Z_s of the Jerusalem cross HIS "seen" by the surface-wave modes.

used to produce general reflection characteristics (e.g., at different angles of incidence) and also the dispersion characterization of the surface waves.

The equivalent surface impedance concept implies the homogenization assumption as above. As in the previous section, the impedance model is valid for one propagating Floquet space harmonic at any angle. Moreover, the impedance description is not valid in the vicinity of the surface, where higher-order (evanescent) Floquet space harmonics have not decayed to a negligible level. However it is important to note that the "pole and zero" method does not necessarily require small unit cells compared to the wavelength and is indeed valid for arrays with periodicity comparable to the wavelength [7]. In the following it will be outlined for the case of a capacitive array.

The technique commences with the observation that in the absence of losses, the equivalent array admittance, which in general is a function of both frequency and the tangential wavenumber, is purely reactive. Moreover, it can be demonstrated that the reactance respects the Foster's theorem for every real tangential wavenumber [7]. As a result of Foster's reactance theorem, the reactance function possesses the same pole-zero analytical properties as a passive "driving point" *LC*-function of frequency. These properties imply that the frequency function can be well approximated by a rational function with poles and zeros located along the real axis. An array of electrically isolated conductors (capacitive array), in the quasistatic limit behaves like a shunt capacitance in the transmission line, and therefore the admittance exhibits a zero at the origin. On the basis of the above, the equivalent admittance for a capacitive array is approximated as a ratio of polynomials for the TE and TM case [7].

The task of extracting the expressions for the admittance now reduces in extracting the poles and zeros, which in general are wavenumber dependent. Central aspect of the method is the identification of poles and zeros in the ω-plane starting from full-wave data. A full-wave simulator is employed to model the reflection characteristics of the uniplanar HIS under consideration. Subsequently the reflection phase is compared with that of the substrate in the absence of the array. The points where the two curves cross each other correspond to the array being transparent to the incident wave. According to Figure 31.25, this suggests an open circuit for the array impedance, i.e., an admittance null. Similarly, the admittance poles are the points where the reflection phase from the HIS is 180°.

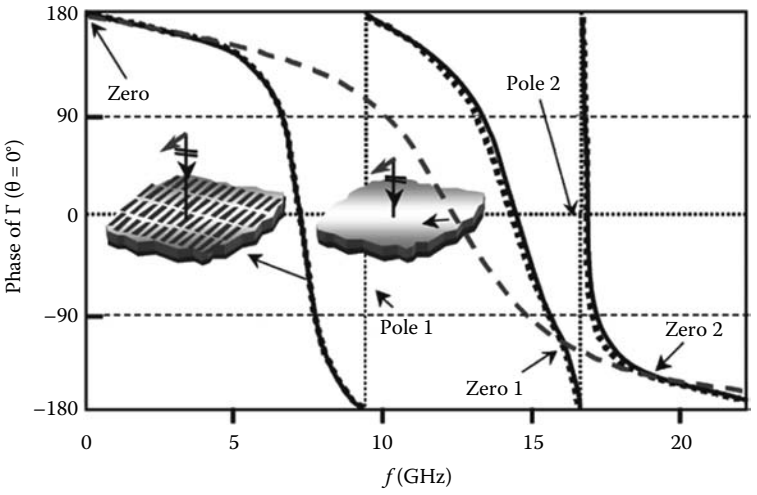

FIGURE 31.37 Phase of the reflection coefficient for normal incidence. Full-wave results for printed slab (continuous line), and for unprinted grounded slab (dashed line) are compared. Zeros of the equivalent FSS admittance are located at the frequency were the two curves intersect; zeros are located at the jump of phase. The results from the network synthesis (dotted line) are obtained by matching two pole-zero pairs. (From Maci, S., Caiazzo, M., Cucini, A., and Casaletti, M., *IEEE Trans. Antennas Propag.*, 53(1), 70, Jan. 2005. With permission.)

At these points the reflection occurs as a result of the resonance of the periodic array, which performs as an open circuit. This is graphically illustrated by means of an example in Figure 31.37.

The key aspect of this technique is that although the admittance of the array is very dispersive, the poles and zeros vary smoothly with the wavenumber. This allows for interpolation and extrapolation (in the case of slow waves) of the poles with low-order polynomials [7]. This only requires a few full-wave simulations for the reflection phase for different angles of incidence, to provide poles and zeros for few different wavenumbers. The admittance value obtained can then be utilized for other angles of incidence or for dispersion characterization [7].

31.4.3 Numerical Methods

There is a variety of full-wave techniques that were employed for the rigorous modeling of HIS. Both frequency-domain and time-domain techniques were reported to accurately predict the reflection phase from HIS. In all cases, in order to obtain the AMC characteristics, the HIS structure is illuminated with a plane wave and the phase of the reflected wave is extracted. For dispersion characterization in spectral domain methods, the eigenvalue problem is formed by setting the excitation to zero and solving a homogeneous problem. In time-domain methods, a wideband excitation is set within the unit cell and the resonances of the structure (obtained after inverse Fourier transforming to the frequency domain) are identified as the supported modes [67,68]. Rigorous description of the full-wave techniques can be found in the literature (e.g., [17,62–68] and references within) and is out of the scope of this chapter.

31.5 Performance Characteristics

In this section, we discuss performance characteristics of HIS. In particular, we commence by reporting studies on simultaneous AMC and EBG characteristics for uniplanar HIS (without vias).

Subsequently we proceed to discuss techniques to improve AMC features, such as bandwidth and angular stability. This section concludes with reports of miniaturized HIS.

31.5.1 Simultaneous AMC and EBG Characteristics for Uniplanar HIS

In this section we study the AMC and EBG characteristics of uniplanar periodic metallic arrays printed on grounded dielectric substrate and we present a method to control the spectral position of these two properties. In particular, we investigate the effect of the array parameters on both the EBG and AMC frequency bands and we show that we can tailor the spectral position of the two properties almost independently by altering the periodicity of a square patch array. From a practical point of view, this allows the flexibility to design uniplanar arrays with either one or both of these properties, depending on the requirements of the application. Based on this study, it is revealed that with varying array periodicity, the AMC band moves opposite to the FSS resonance in frequency. On the contrary, it is shown that the EBG frequency follows the trend of the FSS resonance. Finally numerical and experimental results for a uniplanar surface with both EBG and AMC operations are presented.

31.5.1.1 Tailoring the EBG and AMC Using Array Periodicity

In this section, we study the AMC and EBG properties of a practical structure consisting of a capacitive array over a grounded dielectric substrate (Figure 31.16b). It is demonstrated that in the absence of vias, the AMC and EBG bands do not in general coincide in the frequency domain. We have considered an array of square patches of size $L = 6.1$ mm, and square unit cell with periodicity D. The dielectric substrate permittivity is $\varepsilon_r = 2.2$ and the thickness 1.13 mm. Four different arrays are studied with periodicities (D) 6.9, 7.9, 8.9, and 9.9 mm, respectively. In all the four cases, the grating lobe region lies well above the resonance of the array.

31.5.1.1.1 AMC Characteristics

Figure 31.38 shows the reflection phase of a normally incident plane wave of strength 1 V/m for the four structures under consideration. The magnitude and phase of the currents excited on the elements are also shown. The smallest periodicity, 6.9 mm, yields an AMC frequency of 12.1 GHz, which increases to 14.1 GHz for the largest periodicity, 9.9 mm. This trend is in contrast with the array resonance, which is indicated by the zero current phase in Figure 31.38 and reduces as the periodicity of the array increases. Therefore the spectral separation between the AMC frequency and the array resonance reduces as the periodicity of the metallic array increases (Figure 31.38). This observation is important for our discussion later on.

As in Figure 31.21, the current levels at the Fabry–Perot resonance are nearly three times higher than those in the array resonance. The current magnitude levels are lower for more closely packed elements. According to Lenz's law in a quasistatic approach, this is due to the increasingly opposing mutual inductance between neighbor colinear elements with cophase currents.

31.5.1.1.2 Electromagnetic Bandgap Characteristics

Figure 31.39 shows the dispersion curves for the four structures under consideration. Only bounded surface-wave modes are presented. Due to the presence of the dielectric, TM modes have a stronger horizontal electric field component and a TM bandgap also emerges in the ΓX direction. As shown, the common TE/TM surface-wave bandgap cutoff drops from around 15 GHz for array periodicity 6.9 mm to around 13.8 GHz for periodicity 9.9 mm. Investigation of the fields in the full-wave simulation revealed that for the smaller periodicity (6.9 mm) the TM mode has a cutoff at higher frequency than the TE. However, in the case of the array with large periodicity (9.9 mm) the cutoff of the TE mode occurs at higher frequencies than the TM. The common TE/TM bandgap in the ΓX direction extends from 15 to 19 GHz for the array with periodicity 6.9 mm and from to 13.8 to 14.9 GHz for the

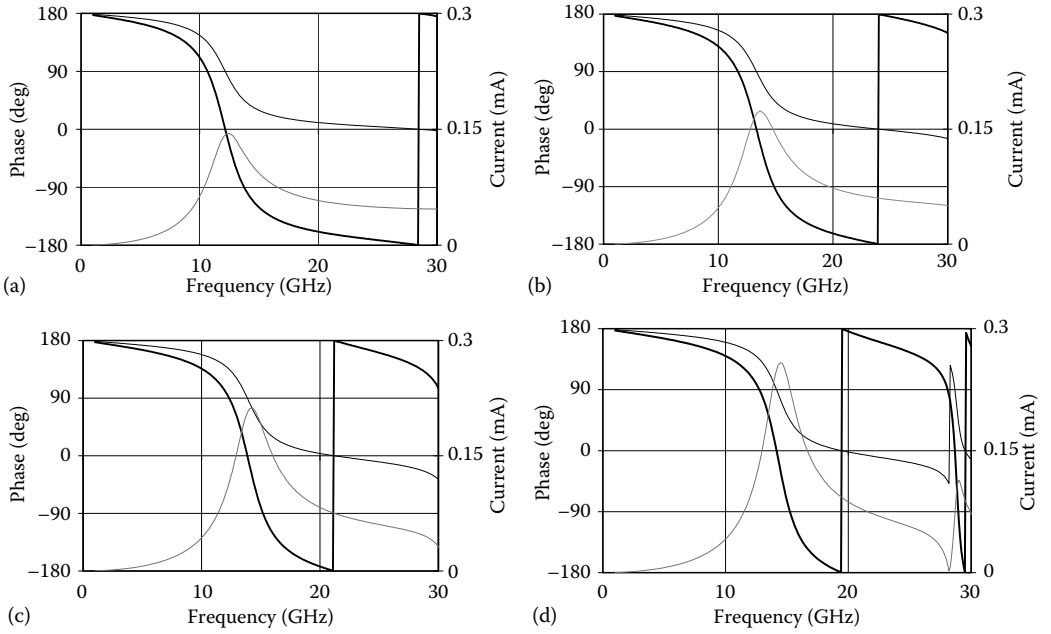

FIGURE 31.38 Plane wave normally incident on square patch (element size L = 6.1 mm) array with periodicity (a) D = 6.9 mm, (b) D = 7.9 mm, (c) D = 8.9 mm, (d) D = 9.9 mm and printed on grounded dielectric of thickness S = 1.13 mm and permittivity ε_r = 2.2: reflection phase for normally incident plane wave (thick black line) and current excited on the elements; thin black line: phase, thin grey line: magnitude. (From Goussetis, G., Feresidis, A.P., and Vardaxoglou, J.C., *IEEE Trans. Antennas Propag.*, 54(1), 82, Jan. 2006. With permission.)

array with periodicity 9.9 mm. The bandgap becomes slightly narrower along the XM path of the Brillouin contour.

The analysis of this subsection suggests that the lowest cutoff frequency of the bandgap drops for larger periodicity of the array. This trend follows the reduction of the resonant frequency of the array over the grounded dielectric (i.e., zero current phase) shown in Figure 31.38.

31.5.1.1.3 Emerging Trends

Following the investigation on the AMC and EBG characteristics of a metallic periodic array on grounded dielectric substrate, the emerging trend is that as the array periodicity is increased the AMC frequency goes up, while the EBG frequency drops. These trends are illustrated and quantified in the diagram of Figure 31.40, where the AMC and EBG bandwidth for the four arrays under investigation are presented. Here the AMC bandwidth is defined as the frequency range where the fields are reflected with a phase between −90° and 90°. Figure 31.40 shows the upper and lower frequency for AMC operation and the EBG in the ΓX direction for varying array periodicity, as obtained with full-wave MoM method.

As the periodicity of the array increases, the EBG frequency drops. In particular, it is evident that the upper cutoff drops with the periodicity linearly. The lower cutoff also drops almost linearly, but for higher periodicities, the TE mode surpasses the TM mode, resulting in narrower common TE/TM bandgap. Although the array resonance decreases, the AMC operation goes up in frequency for larger unit cells. Assuming a fixed thickness for the dielectric substrate, the transmission phase value ϕ_T that satisfies Equation 31.8 goes up in frequency for larger array periodicity. This explains the AMC trend.

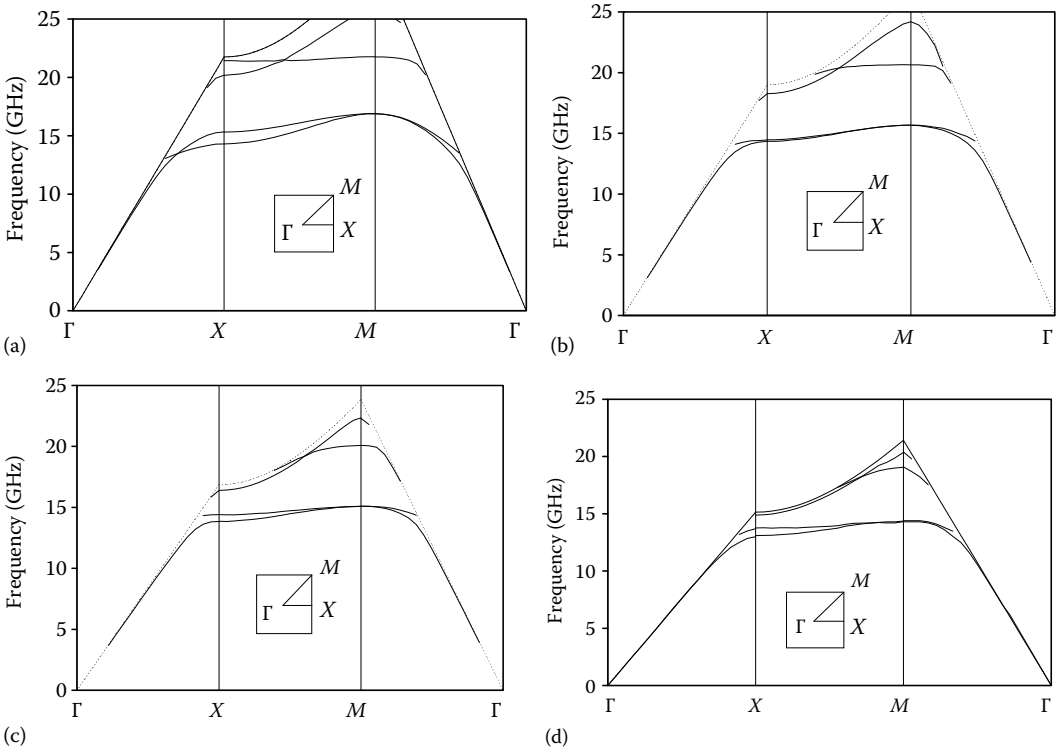

FIGURE 31.39 Dispersion relation of square patch (element size $L = 6.1$ mm) array with periodicity (a) $D = 6.9$ mm, (b) $D = 7.9$ mm, (c) $D = 8.9$ mm, and (d) $D = 9.9$ mm and printed on grounded dielectric of thickness $S = 1.13$ mm and permittivity $\varepsilon_r = 2.2$. (From Goussetis, G., Feresidis, A.P., and Vardaxoglou, J.C., *IEEE Trans. Antennas Propag.*, 54(1), 82, Jan. 2006. With permission.)

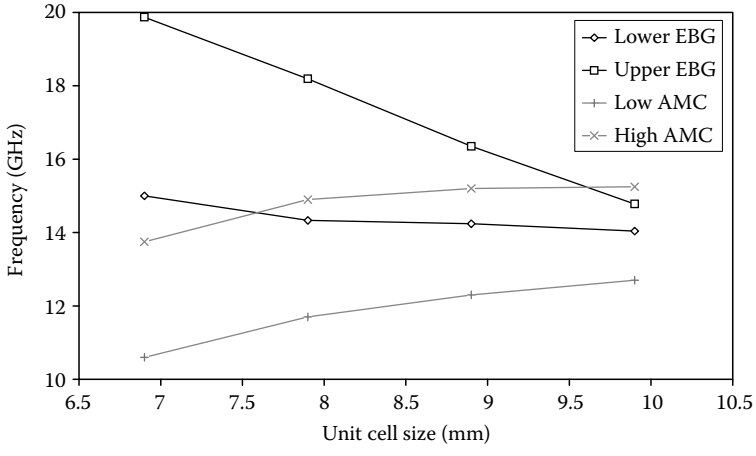

FIGURE 31.40 Lower and upper frequency for EBG and AMC for square patch array ($L = 6.1$ mm) with varying unit cell summarizing the results of Figures 31.38 and 31.39. (From Goussetis, G., Feresidis, A.P., and Vardaxoglou, J.C., *IEEE Trans. Antennas Propag.*, 54(1), 82, Jan. 2006. With permission.)

As shown in Figure 31.40, there is a range of periodicities of the array where the two pairs of curves overlap. This area corresponds to simultaneous AMC and EBG operations in the frequency domain.

31.5.1.1.4 Experimental Results

To validate our conclusions and demonstrate an AMC surface without vias exhibiting surface wave EBG, the array with unit cell 9.9 mm was etched on a dielectric substrate of thickness 1.13 mm and $\varepsilon_r = 2.2$. The overall array consisted of 26 × 29 elements. The AMC and EBG properties of the fabricated prototype were measured. For the EBG measurement, the structure was positioned between absorbing materials. Two horn antennas are used as the transmitter and receiver on either side of the surface, as shown in Figure 31.5. The measured EBG responses are shown in Figure 31.41a. The TM mode has a cutoff at 13.1 GHz and the TE mode at 13.8 GHz. A common TE and TM bandgap is found between 13.8 and 14.9 GHz in the ΓX direction and is highlighted in Figure 31.41. The absolute bandgap is somewhat narrower, 14.4–14.9 GHz as shown in the dispersion diagram (Figure 31.39d). Very good agreement between measurement and simulation is observed.

The reflection characteristics of the same structure were also measured for normal incidence. The periodicity is small enough for the grating lobe region to be well above 20 GHz. The reflection phase of the AMC is taken in the far field using horn antennas and is then normalized with respect to an identical measurement in the absence of the array. The simulated and measured AMC responses of this structure are shown in Figure 31.41b. Note that there are two pairs of curves for the AMC measurement and simulation. This is due to the finite thickness of the AMC structure and hence the two different possible definitions of the reflection reference plane. This can be either the plane of the array or the ground. Thus, one result is taken assuming reflection at the array plane (REF: ARRAY) and another assuming reflection at the ground plane (REF: GROUND). In both cases, very good agreement between simulated and experimental results is observed. The AMC band (−90° to 90°) lies between 13.3–16.45 and 12.55–15.2 GHz, respectively. The measured bandgap region is highlighted in the graph. Simultaneous AMC and EBG (ΓX) operation of 1.1 GHz (~7.5%) bandwidth was achieved.

31.5.2 AMC Bandwidth

Both Foster's theorem for the admittance of periodic arrays [7] and the resonant cavity model for AMC operation [16] suggest that AMC bands are separated by frequency points of reflection

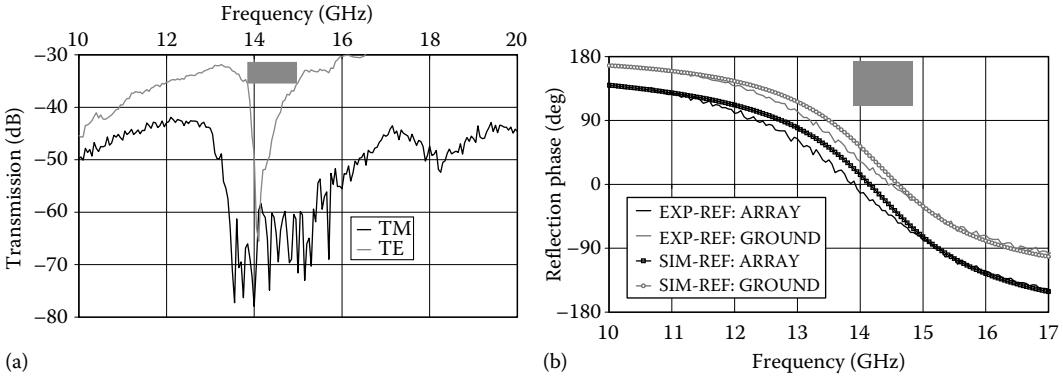

FIGURE 31.41 (a) Measured EBG performance for square patch array. In mm: patch 6.1, unit cell 9.9, dielectric thickness 1.15 ($\varepsilon_r = 2.2$). Shaded is the Bandgap region (ΓX). (b) Measured AMC response for square patch array. In mm: patch 6.1, unit cell 9.9, dielectric thickness 1.15 ($\varepsilon_r = 2.2$). Shaded is the Bandgap region (ΓX). (From Goussetis, G., Feresidis, A.P., and Vardaxoglou, J.C., *IEEE Trans. Antennas Propag.*, 54(1), 82, Jan. 2006. With permission.)

with phase reversal. This imposes fundamental limits in the AMC bandwidth of HIS. One suggestion to overcome this limit is to produce multiple AMC bands closely located in the frequency and then introduce thermal losses on the surface as means to introduce degeneracy between these modes [21]. This was indeed demonstrated to increase the AMC bandwidth, at the cost of power loss [21]. In the following, we investigate further the bandwidth of AMC operation for the lossless case based on the resonant cavity model of Section 31.3.2.

31.5.2.1 Effect of Transmission Response of the PRS

According to Equation 31.9 and for a wideband AMC, an optimum periodic array would require its transmission coefficient phase to linearly increase with frequency with a gradient of $2\pi S/c$, where S is the thickness of the HIS and c the speed of light in the dielectric medium [16,48]. This would result in a wideband cavity that would satisfy the resonance condition (Equation 31.9) for all frequencies. While increasing transmission phase with frequency is not feasible for a capacitive screen, this conclusion suggests that among two screens with equal reflectivity, greater AMC bandwidth will be observed for the one with slower varying transmission phase. This is demonstrated using full-wave results in the example mentioned in Section 31.3.2 (Figure 31.19). PRS1 has slower transmission phase variation with frequency compared to PRS2 (Figure 31.19a). The AMC bandwidth for PRS1 is 30% wider than that of PRS2, for the same substrate thickness (Figure 31.19b).

For simple element geometries, such as dipoles, tripoles or square patches [17], a slower transmission phase variation with frequency is produced by more closely packed arrays. As a general conclusion according to the above we can say that more closely packed arrays produced larger AMC bandwidths compared to more sparsely packed arrays of the same element.

31.5.2.2 Effect of Substrate Thickness

The resonant cavity AMC model predicts that for a fixed periodic array with an approximately frequency independent phase, the AMC frequency decreases as the dielectric thickness increases (see Equation 31.8). Furthermore, from Figure 31.17 it is evident that away from the array resonance, the PRS phase variation with frequency is slower, which in turn corresponds to broader AMC bandwidth. Therefore, in general, with increasing substrate thickness the AMC frequency decreases and the bandwidth is improved. This is also consistent with the analysis of reflect array antennas [18].

The effect of substrate thickness is demonstrated here in Figure 31.42, using full-wave analysis. A parametric study of the AMC response for a fixed square patch PRS with lattice periodicity 10 mm and element of 6 mm is presented. The dielectric constant of the substrate is 2.2. The reflection phase for AMCs printed on substrates of thickness (noted here as t) equal to 0.8, 1.13, and 2.0 mm is shown in Figure 31.42. Thicker substrates produce AMC response at lower frequencies in agreement with the resonant cavity model for AMC operation (see Section 31.3). Moreover, as the AMC operation shifts to lower frequencies, the variation of the transmission phase through the capacitive array becomes less rapid. This can be seen from the generic response of a capacitive array shown in Figure 31.17a. Hence the AMC bandwidth becomes larger, as predicted by Equation 31.8 and is shown in Figure 31.42. We can generalize this conclusion to the claim that thicker substrates typically produce AMC with larger bandwidths.

31.5.3 AMC Angular Stability

In this section, we present two designs of HIS configurations based on the use of complementary (patch/slot) array elements in the unit cell in order to achieve a wideband AMC performance and stable resonance properties with respect to the incidence angle [61]. A study on the angular stability of single layer AMCs is presented in [55,56].

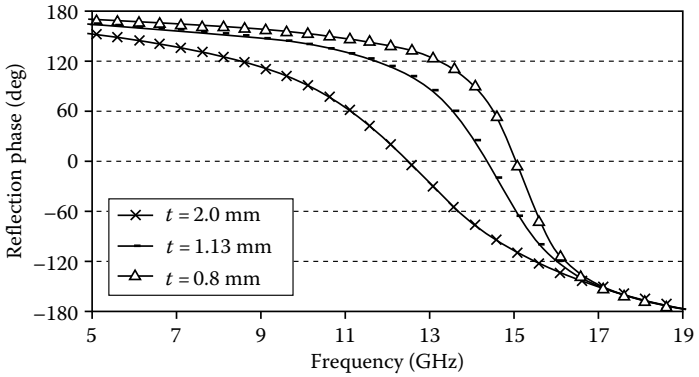

FIGURE 31.42 Parametric study of AMC performance with thickness (noted *t*) of dielectric slab. (From Feresidis, A.P., Goussetis, G., Wang, S., and Vardaxoglou, J.C., *IEEE Trans. Antennas Propag.*, 53(1), 209, Jan. 2005. With permission.)

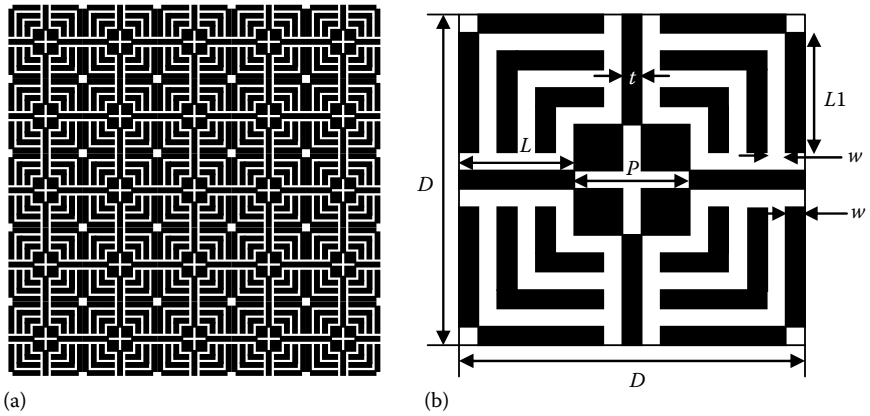

FIGURE 31.43 HIS structure composed of complementary patch/slot in conjunction with *L*-shaped split rings: (a) FSS grid, (b) unit cell. All dimensions are in mm: $D = 4.75$, $L = 1.5$, $L1 = P = 1.75$, $t = w = 0.25$. Substrate thickness is 2.54 mm and substrate permittivity is 6.15.

Design I

In the proposed HIS design (with geometry and dimensions shown in Figure 31.43), the unit FSS cell is composed of square patch with a cross slot in conjunction with the *L*-shaped split rings. Also, split cross FSS elements are used in the design (as it can be seen in Figure 31.43a). The proposed complex HIS structure consists of 2D symmetric grid as a combination of complementary FSS elements, which simultaneously interact with the TE and TM-polarized electromagnetic fields and control the resonance properties of HIS structure. At normal incidence, the proposed HIS structure exhibits a wide AMC frequency band ranging from 7.94 to 12.5 GHz.

In the case of oblique incidence with the angle of plane wave excitation varying from 0° to 60°, the HIS structure exhibits stable resonance characteristics for both the TE and TM polarizations, resulting in a deviation of 4.48% (shift in the resonance frequency from 10.04 to 10.49 GHz) for TE polarization and 6.27% of deviation in the case of TM polarization (shift in the resonance frequency from 10.04 to 10.67 GHz) as shown in Figure 31.44.

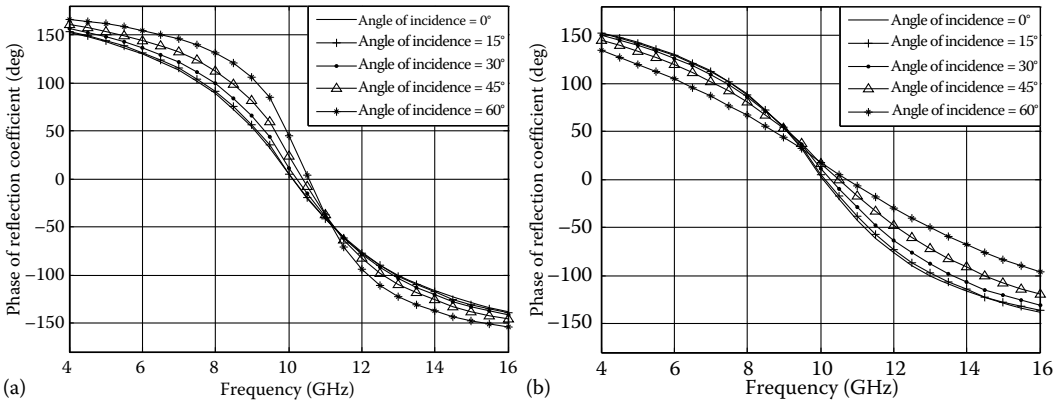

FIGURE 31.44 Stability of resonance frequency and wideband characteristics of the HIS structure in Figure 31.43 with respect to the angle of plane wave incidence: (a) TE polarization, (b) TM polarization.

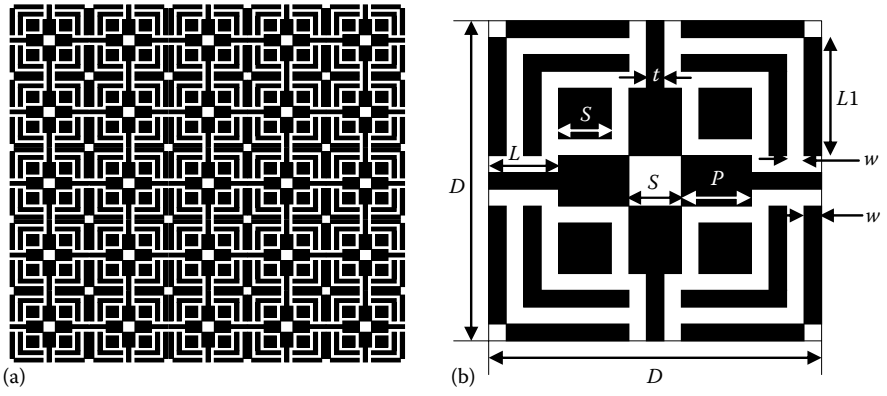

FIGURE 31.45 HIS structure composed of split cross FSS elements in conjunction with patches and L-shaped split rings: (a) FSS grid, (b) unit cell. All dimensions are in mm: $D = 4.75$, $L = 1$, $P = 1$, $L1 = 1.75$, $S = 0.75$, $t = w = 0.25$. Substrate thickness is 2.54 mm and substrate permittivity is 6.15.

Design II

In the second example, the HIS structure (with geometry and dimensions shown in Figure 31.45) is realized by split cross FSS elements in conjunction with patches and *L*-shaped split rings. At normal incidence, the proposed HIS structure resonates (no phase reversal in the reflection phase) at 9.74 GHz and results in the AMC bandwidth of 45.48% ranging from 7.71 to 12.41 GHz.

In the case of oblique incidence with the angle of plane-wave excitation varying from 0° to 60°, the HIS structure exhibits stable resonance characteristics for both the TE and TM polarizations, resulting in a deviation of 4.52% (shift in the resonance frequency from 9.74 to 10.18 GHz) for TE-polarized excitation and 6.46% of deviation in the case of TM polarization (shift in the resonance frequency from 9.74 to 10.37 GHz) as shown in Figure 31.46.

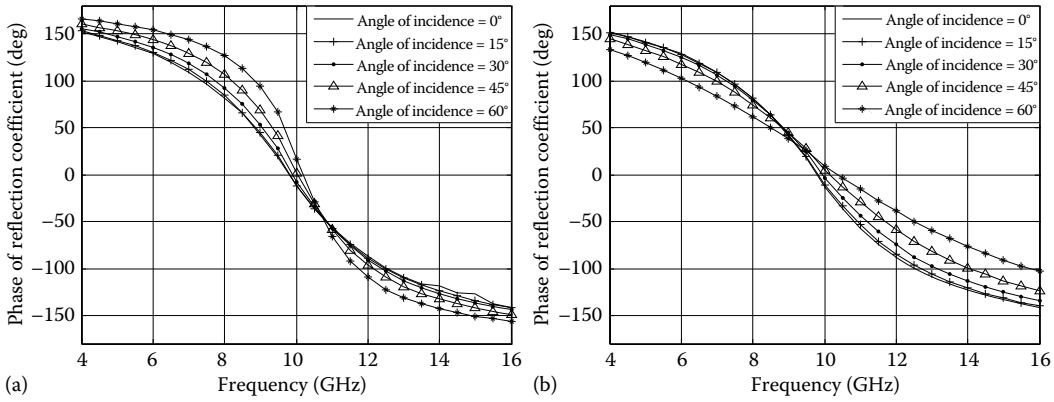

FIGURE 31.46 Stability of resonance frequency and wideband characteristics of the HIS structure (Design II) with respect to the angle of plane wave incidence: (a) TE polarization, (b) TM polarization.

31.5.4 Miniaturization

Miniaturization of microwave components and antennas has become increasingly important in recent years. Modern wireless communication terminals require small microwave elements which are pertinent to high level of integration into compact light-weight systems. In this context, miniaturization of EBG structures is an important consideration for the microwave engineer. Miniaturization of a resonant element can be achieved by reducing the resonant frequency maintaining its maximum physical dimension, i.e., by fitting a longer effective electrical length in a fixed physical space. These techniques were applied in the past in small antennas and compact microwave circuits [49]. In the context of Metallodielectric Electromagnetic Band Gap (MEBG) structures, the length of a dipole or dipole-type element can be reduced in a similar fashion using reentrant or convoluted geometries leading to miniaturized array elements [50]. Multilayer topologies were also reported, whereby a significant reduction of the resonant frequency of MEBG arrays is achieved [51].

In the following, the miniaturization of EBG surfaces using closely coupled array topologies is initially presented by means of dispersion diagrams as well as measurements for linear dipole elements and tripole elements. In addition, complex geometries such as convoluted and periodically loaded tripoles are investigated for printed elements on a single dielectric substrate. A combination of the two techniques is implemented and experimental results are presented for closely coupled complex element arrays resulting in further size reduction of the unit cell. The proposed techniques are subsequently applied to the miniaturization of AMC structures using the same family of elements. Finally, by means of an example, the application of miniaturized MEBG surfaces in the performance enhancement of a mobile handset antenna is presented.

31.5.4.1 Miniaturized MEBG Structures

Two techniques for the miniaturization of MEBGs are discussed. The first method is based on two arrays positioned in close proximity with appropriate shifts relative to each other, in order to achieve maximum element coupling and increase the miniaturization factor. This technique is presented in Section 31.5.4.1.1 by means of full-wave dispersion diagrams validated by experimental characterization. The second technique is based on the principle that complex element geometries can increase the resonant current path, packing more electrical length in a fixed physical space. The concept is presented in Section 31.5.4.1.2 by means of examples based on tripole type arrays. The two methods are combined to achieve further miniaturization. A large part of this work is based on characterizing

the EBG of periodic arrays on ungrounded dielectric slabs. According to the definition of HIS given at the beginning of this chapter, these are not HIS, as they do not fully reflect incident waves at all frequencies and all angles. However the miniaturization techniques discussed here mainly refer to EBG features, which are shared between grounded and ungrounded arrays. Moreover, similar techniques can be applied for the case of grounded arrays. This is shown in Section 31.5.4.1.3, which presents the miniaturization techniques for AMC surfaces consisting of printed metallic arrays on grounded dielectric substrates are described.

31.5.4.1.1 Close Coupling

Dipole element arrays printed on a single dielectric substrate are employed here as an example (Figure 31.47). The IBZ is also shown in Figure 31.47 for the dipoles arranged on a rectangular lattice. Assuming small width w, the dipoles only impose a boundary condition on electric field components along y-axis. Among the surface-wave modes supported by the dielectric slab, only those with an electric field component parallel to the y-axis can excite currents on the dipoles. The effect of the periodic dipole array is hence evident only on those modes and at the vicinity of the resonance. In general, those are TE modes for propagation along the x-axis (ΓX part of the IBZ), TM modes for propagation along the y-axis ($Y\Gamma$ part of the IBZ), and hybrid TE/TM modes for oblique direction of propagation ($X \rightarrow M \rightarrow Y$ in the IBZ). For typical values of permittivity and thickness of the dielectric substrates, TM modes have very weak longitudinal electric field component. Hence conducting arrays printed on typical substrates exhibit slow wave region and EBGs for TE modes only.

Figure 31.48a shows the dispersion diagram for a single layer dipole MEBG printed on grounded dielectric substrate of thickness $S_{\text{sub}} = 1.15$ mm and permittivity $\varepsilon_r = 2.2$. Floquet modal analysis and Galerkin MoM were used for the formulation of the homogeneous problem for deriving the dispersion curves. The EBG in the ΓX direction emerges in the TE mode at 7.34 GHz. At this frequency, the half free-space wavelength is 20.43 mm. This suggests a $\lambda/2$ resonance for the single layer dipole array, with some variation attributed to the permittivity of the substrate, the mutual impedances between the dipole elements and the fringing capacitances at the edges of each dipole. The TM mode simply

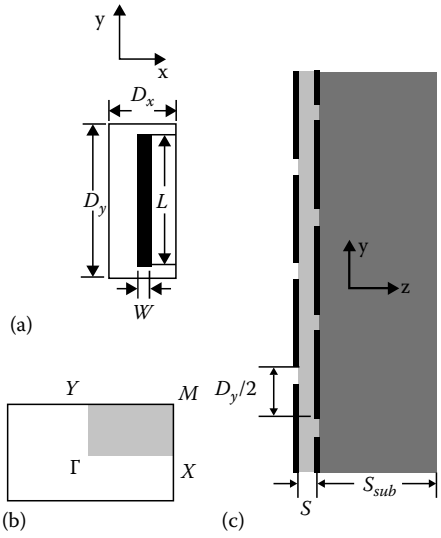

FIGURE 31.47 Layout of closely coupled dipole array in a rectangular lattice: (a) unit cell, (b) reciprocal lattice and (c) cross-section. (From Feresidis, A.P., Apostolopoulos, G., Serfas, N., and Vardaxoglou, J.C., *IEEE Trans. Antennas Propag.*, 52(5), 1149, 2004. With permission.)

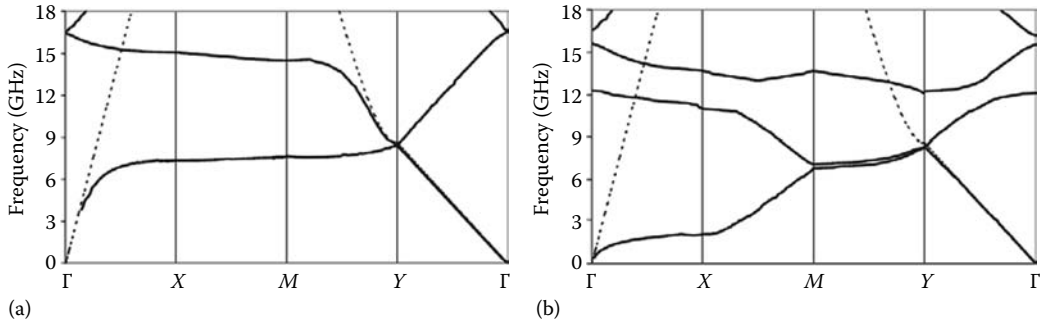

FIGURE 31.48 Dispersion diagram of (a) single layer dipole MEBG with D_y = 17.5 mm, D_x = 5 mm, L = 15.5 mm and W = 0.5 mm printed on substrate with S_{sub} = 1.15 mm and ε_r = 2.2 (b) double layer CCMEBG with separation distance S = 100 μm and ε_r = 3.2. (From Vardaxoglou, J.C., Goussetis, G., and Feresidis, A.P., *IEE Proc. Microw. Antenna and Propag.*,1(1), 234, 2007 (special issue on Metamaterials). With permission.)

follows the light line and is not shown here. In the XM and MY parts of the dispersion diagram, the resonant mode that excites the dipoles and produces the bandgap is a hybrid TE/TM mode. In YΓ, the dispersion is very similar to the unperturbed case (without the array), with the fundamental TM mode following the light line.

In an equivalent circuit approach, the bandgap emerges by virtue of the resonance of an equivalent *LC*-circuit [6,23]. The inductance emerges from the currents induced on the dipole elements and the capacitance is formed in the inter-element space. Therefore, reduced frequency can be achieved by increasing the capacitance value. This in turn can be achieved by careful coupling of two arrays, leading to closely coupled arrays. For the dipole geometry, miniaturization arising from the close coupling of the two arrays is maximized by shifting the second layer with respect to the first by $D_y/2$ [51]. Here the two arrays are assumed on either side of a dielectric surface of thickness 100 μm and permittivity ε_r = 3, and the two-layer structure lies on the same substrate as above (Figure 31.1c). The dispersion diagram for the closely coupled MEBG (CCMEBG) structure is shown in Figure 31.48b. The EBG for the TE modes emerges at 2.1 GHz, suggesting a miniaturization of 3.5:1. Due to the asymmetrical geometry of the unit cell, the cutoff frequency increases rapidly as the wave vector along the y-axis is introduced. However, the effect of close coupling is now also evident in the first harmonic of the TM mode in YΓ.

In order to validate the accuracy of the above dispersion diagrams, the arrays were fabricated and the bandgap was experimentally assessed. Two antipodal Vivaldi antennas printed on a common substrate (S_{sub} = 1.15 mm, ε_r = 2.2) were used as receiver and transmitter [51]. The measured transmission normalized with respect to the transmission in the absence of the array is shown in Figure 31.49. The -10 dB cutoff for the single layer array is at 7.33 GHz, which is in very good agreement with the dispersion diagram. For the double layer case, the cutoff is measured at 1.8 GHz, still in good agreement with the prediction from the dispersion diagram. The variation of less than 15% in this case is attributed to the inaccuracy of the thin dielectric parameters, and particularly its thickness. The apparent positive transmission below the bandgap is due to the fact that the shown result is normalized to an identical measurement in the absence of the array, and indicates an antenna gain increase in the slow wave region of the array.

Due to their geometry, dipole arrays are highly polarization dependent. In order to achieve a TE bandgap throughout the IBZ, tripole elements are employed. Figure 31.50 shows the measured surface wave transmission response for a closely coupled tripole array [51]. Here the dimensions are L = 7.0 mm, W = 5.0 mm, periodicity D = 14.0 mm and the thickness of the dielectric between the two arrays is 50 μm. Owing to the small separation of the layers and the increased width of the tripoles,

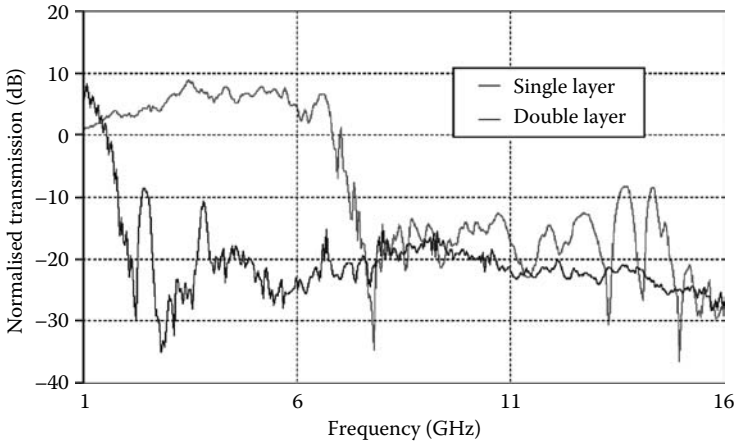

FIGURE 31.49 Measured transmission of surface waves for the two EBG arrays of Figure 31.48. (From Vardaxoglou, J.C., Goussetis, G., and Feresidis, A.P., *IEE Proc. Microw. Antenna and Propag.*, 1(1), 234, 2007 (special issue on Metamaterials). With permission.)

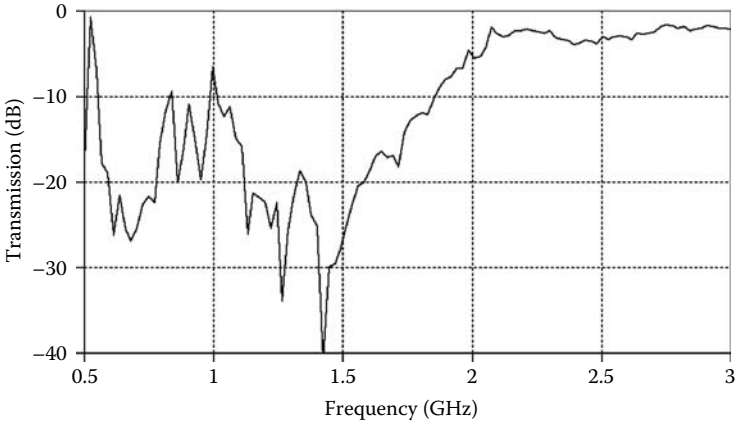

FIGURE 31.50 Experimental measurement of the transmission of surface wave through a closely coupled tripole array (layout as in Figure 31.3), with D = 14 mm. (From Vardaxoglou, J.C., Goussetis, G., and Feresidis, A.P., *IEE Proc. Microw. Antenna and Propag.*, 1(1), 234, 2007 (special issue on Metamaterials). With permission.)

the associated capacitance increases resulting in the cutoff dropping below 600 MHz. The electrical size of the unit cell is in the order of $\lambda/35$.

31.5.4.1.2 Complex Elements

An alternative technique for reducing the physical dimension of MEBG structures is based on the use of complex elements geometries within the unit cell. In this section, the miniaturization achieved from complex element geometries is presented by means of comparative examples. The cutoff frequencies of arrays with fixed lattices (fixed unit cell) are compared for simple element geometries and more complex (loaded) variations.

The EBG properties of periodically loaded, interdigital and convoluted tripole element arrays are presented. The unit cell is hexagonal with D = 3.2 mm (see Figure 31.3). Figure 31.51 shows the

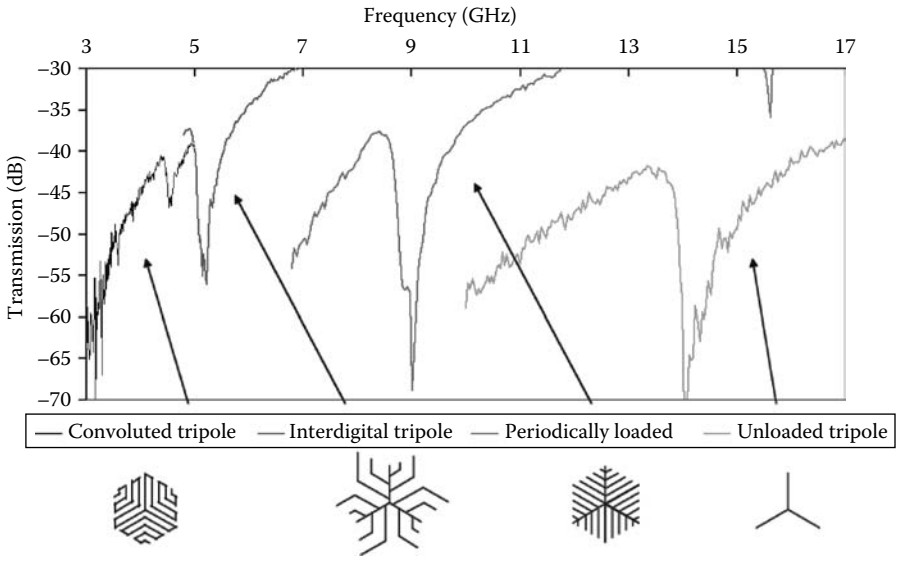

FIGURE 31.51 Measured transmission response for TE surface wave incidence for unloaded, periodically loaded, interdigital and convoluted tripole arrays (layout as in Figure 31.3) with D = 3.2 mm on a dielectric substrate of thickness 1.15 mm and ε_r = 2.2. (From Vardaxoglou, J.C., Goussetis, G., and Feresidis, A.P., *IEE Proc. Microw. Antenna and Propag.*, 1(1), 234, 2007 (special issue on Metamaterials). With permission.)

measured TE surface wave bandgaps for the arrays with unit elements shown as insets. Two horn antennas were used as transmitter and receiver, positioned on either side of a tunnel formed by absorbers, where the MEBG array lies. By rotating the horns appropriately, TE surface wave polarization is obtained. The EBG response of the unloaded tripole array on the same lattice is shown for comparison. The convoluted tripoles are more compact with a miniaturization factor of 3:1, whereas the interdigital tripoles have a better bandwidth (~20% fractional bandwidth). Periodically loaded tripoles were also implemented using fractal loadings yielding similar performance with the uniformly loaded tripoles. Other fractal elements reported in the literature include Peano curves and interwoven element [14,22,52], such as those shown in Figure 31.52, achieving similar levels of miniaturization.

The two techniques studied thus far can be combined. Figure 31.53 shows the measured response of a CCMEBG that comprises a layer of interdigital tripole elements and a second layer with simple tripoles, with relative shift and rotation as shown in Figure 31.4. For comparison, the measured response of the single layer interdigital tripole array is also shown.

31.5.4.1.3 AMC Responses

When printed on a grounded dielectric substrate, MEBG arrays fully reflect incident plane waves. Furthermore, within a frequency range, on the grounded MEBG the reflection occurs with zero or near-zero degrees phase. This behavior is the dual of an electric conductor, hence the term AMC surface. The miniaturization concepts presented above for the dispersion characteristics of surface waves can also be applied for the miniaturization of AMC surfaces.

Closely coupled arrays were demonstrated to reduce the FSS resonant frequency of periodic arrays [51]. According to the resonant cavity model, this would lead to miniaturized AMC response. This is demonstrated here by means of numerical simulations. Figure 31.54, shows the reflection phase of normally incident plane waves to single and closely coupled dipole arrays printed on the same substrate with the addition of a ground plane backing. The dimensions of the unit cell, as shown in

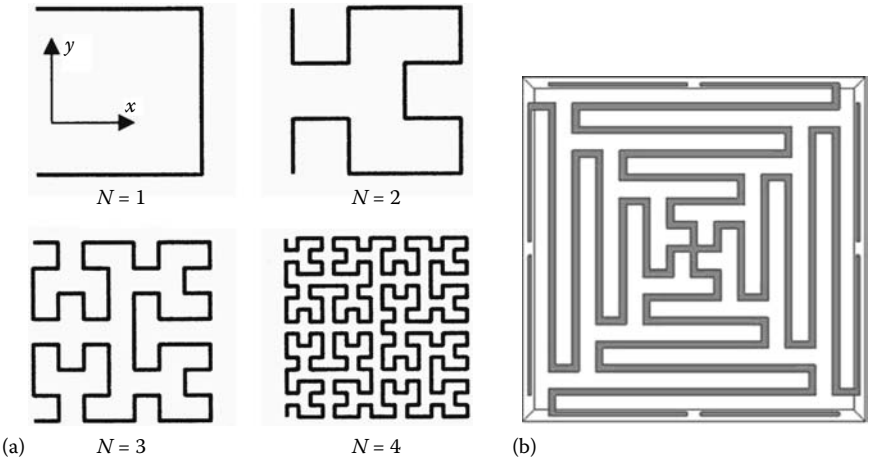

FIGURE 31.52 (a) Peano curves for miniaturized elements of HIS reported in [14] (From McVay, J., Engheta, N., and Hoorfar, A., *IEEE Microw. Wireless Compon. Lett.*, 14(3), 130, 2004. With permission.) and (b) interwoven elements reported in [22,52] (From Huang, F., Batchelor, J.C., and Parker, E.A., *Electron. Lett.*, 42(14), 788, 2006. With permission.)

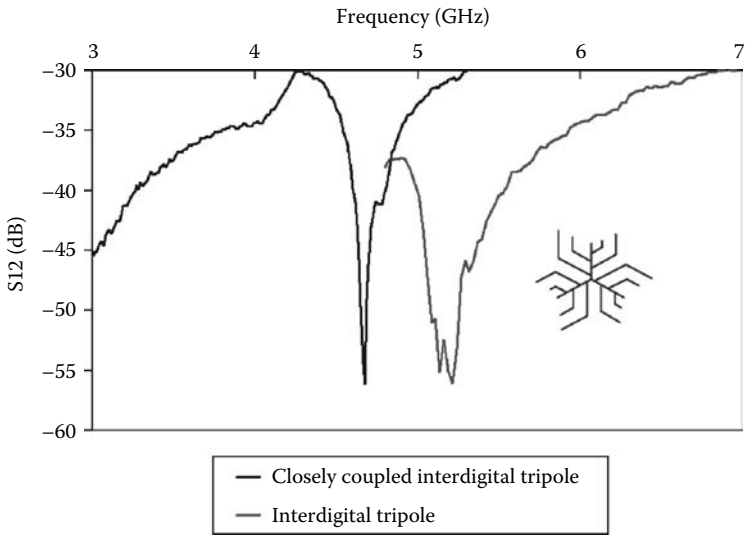

FIGURE 31.53 Measurement of the single layer and closely coupled interdigital tripole MEBG of Figure 31.51. For CCMEBG separation distance $S = 0.05\,\text{mm}$, $\varepsilon_r = 3.0$. (From Vardaxoglou, J.C., Goussetis, G., and Feresidis, A.P., *IEE Proc. Microw. Antenna and Propag.*, 1(1), 234, 2007 (special issue on Metamaterials). With permission.)

Figure 31.47 are $D_y = 6.1\,\text{mm}$, $D_x = 2\,\text{mm}$, $L = 5.5\,\text{mm}$ and $W = 0.5\,\text{mm}$. Floquet modal analysis and the MoM were used for the simulation [53]. As shown the AMC frequency drops from 15GHz to 5.5GHz, corresponding to a miniaturization factor of about 3:1.

Defining the AMC bandwidth as the frequency range with reflection phase −90° to +90°, the single layer array performs as an AMC between 13.1 and 16.8 GHz, corresponding to 24.5% fractional bandwidth, while the CCMEBG array between 5.1 and 5.8 GHz, corresponding to a fractional

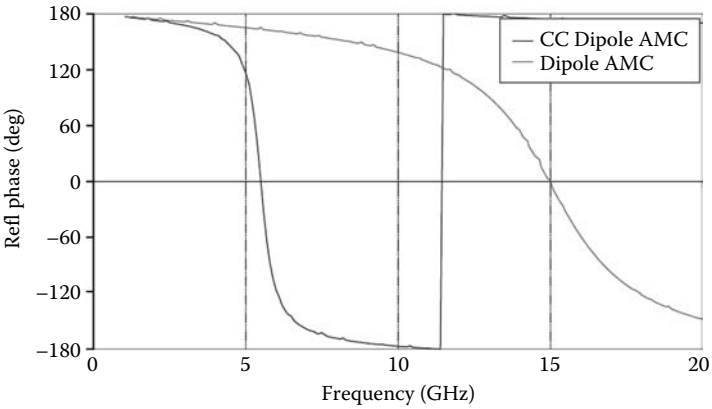

FIGURE 31.54 Reflection phase response for single and closely coupled dipole (length 5.5 mm width 0.5 mm) AMCs with unit cell 6.1 × 2 mm on substrate of thickness 1.13 mm and $\varepsilon_r = 2.20$ (From Vardaxoglou, J.C., Goussetis, G., and Feresidis, A.P., *IEE Proc. Microw. Antenna and Propag.*, 1(1), 234, 2007 (special issue on Metamaterials). With permission.)

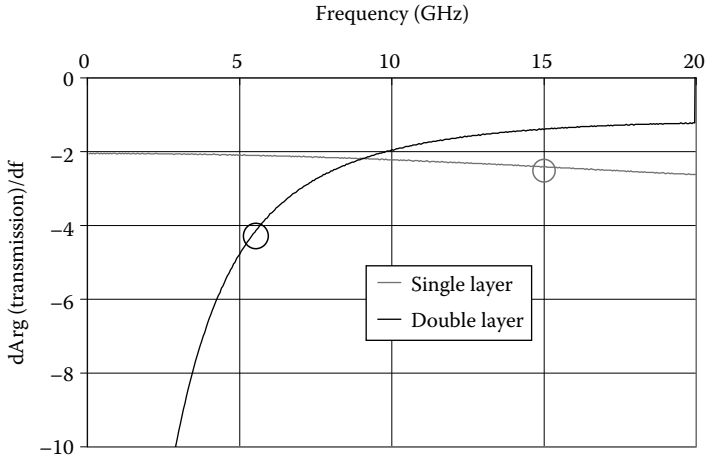

FIGURE 31.55 Calculated derivative of the transmission phase against frequency for the two free-standing FSSs of Figure 31.54—circles denote the AMC operating frequency. (From Vardaxoglou, J.C., Goussetis, G., and Feresidis, A.P., *IEE Proc. Microw. Antenna and Propag.*, 1(1), 234, 2007 (special issue on Metamaterials). With permission.)

bandwidth1 of 3%. The relative reduction in the AMC bandwidth occurs due to the rapid phase variation of the array in the vicinity of the AMC response, in accordance with the resonant cavity model. To quantify this, Figure 31.55 shows the derivative of the transmission phase with respect to the frequency for the single and double layer arrays without the dielectric support. The zero reflection phase frequencies of the corresponding AMCs are noted with circles on this curve. As shown, in the vicinity of the AMC frequency the array's phase variation is almost twice as fast for the closely coupled array case as compared with the single layer case. Taking into account the resonant cavity model, this explains why the fractional bandwidth of the closely coupled array is nearly half of that in the single layer case.

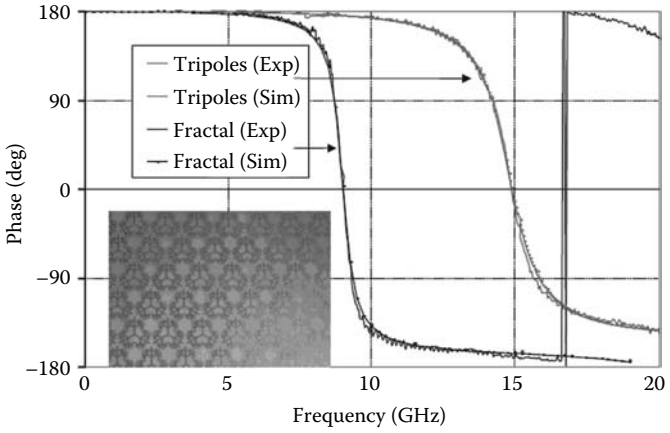

FIGURE 31.56 Measurement of the AMC response produced by the single layer unloaded tripole and fractal arrays of Figure 31.51 on substrate of thickness 1.13 mm and $\varepsilon_r = 2.2$. (From Vardaxoglou, J.C., Goussetis, G., and Feresidis, A.P., *IEE Proc. Microw. Antenna and Propag.*, 1(1), 234, 2007 (special issue on Metamaterials). With permission.)

A miniaturized AMC surface can also be produced using arrays of complex element geometries. Figure 31.56 shows the simulated and measured response for the fractal-type of tripole arrays (shown as inset). For comparison, the measured and simulated AMC response of the unloaded tripole array is shown in grey. The AMC frequency drops from about 15 GHz to 9 GHz, corresponding to a miniaturization factor of 1.66:1. As in the CCMEBG case, the fractional bandwidth also reduces from 11.3% to 6% (Figure 31.56).

References

1. D. Pozar, *Microwave Engineering*, Addison-Wesley, Reading, MA, 1993.
2. R.E. Collin, *Field Theory of Guided Waves*, IEEE Press, New York, 1991.
3. J.D. Jackson, *Classical Electrodynamics*, John Wiley & Sons, New York, 1999.
4. S. Tretyakov, *Analytical Modeling in Applied Electromagnetics*, Artech House, Norwood, MA, 2003.
5. E.F. Kuester, M.A. Mohamed, M. Piket-May, and C.L. Holloway, Averaged transition conditions for electromagnetic fields at a metafilm, *IEEE Trans. Antennas Propag.*, 51(10), 2641–2651, Oct. 2003.
6. D. Sievenpiper, Z. Lijun, R.F. Broas, N.G. Alexopoulos, and E. Yablonovitch, High-impedance electromagnetic surfaces with a forbidden frequency band, *IEEE Trans. Microw. Theory Tech.*, 47(11), 2059–2074, Nov. 1999.
7. S. Maci, M. Caiazzo, A. Cucini, and M. Casaletti, A pole-zero matching method for EBG surfaces composed of a dipole FSS printed on a grounded dielectric slab, *IEEE Trans. Antennas Propag.*, 53(1), 70–81, Jan. 2005.
8. G. Goussetis, A.P. Feresidis, and J.C. Vardaxoglou, Tailoring the AMC and EBG characteristics of periodic metallic arrays printed on grounded on grounded dielectric substrate, *IEEE Trans. Antennas Propag.*, 54(1), 82–89, Jan. 2006.
9. S.A. Tretyakov and C.R. Simovski, Dynamic model of artificial impedance surfaces, *JEMWA*, 17(2), 131–145, 2003.
10. M. Hiranandani, A.B. Yakovlev, and A.A. Kishk, Artificial magnetic conductors realized by frequency selective surfaces on a grounded dielectric slab for antenna applications, *IEE Proc. Microw. Antennas Propag.* (Part H), 153(5), 487–493, 2006.

11. E. Yablonovitch, Inhibited spontaneous emission in solid-state physics and electronics, *Phys. Rev. Lett.*, 58, 2059–2062, 1987.
12. J.D. Joannopoulos, R.D. Meade, and J.N. Winn, *Photonic Crystals: Molding the Flow of Light*, Princeton University Press, Princeton, NJ, 1995.
13. Y. Fei-Ran, M. Kuang-Ping, Q. Yongxi, and T. Itoh, A uniplanar compact photonic-bandgap (UC-PBG) structure and its applications for microwave circuit, *IEEE Trans. Microw. Theory Tech.*, 47(8), 1509–1514, Aug. 1999.
14. J. McVay, N. Engheta, and A. Hoorfar, High impedance metamaterial surfaces using Hilbert-curve inclusions, *IEEE Microw. Wireless Compon. Lett.*, 14(3), 130–132, Mar. 2004.
15. Y. Zhang, J. von Hagen, M. Younis, C. Fischer, and W. Wiesbeck, Planar artificial magnetic conductors and patch antennas, *IEEE Trans. Antennas Propag.*, 53(1), Jan. 2005, 209-215.
16. A.P. Feresidis, G. Goussetis, S. Wang, and J.C. Vardaxoglou, Artificial magnetic conductor surfaces and their application to low profile high-gain planar antennas, *IEEE Trans. Antennas Propag.*, 53(1), 209–215, Jan. 2005.
17. B. Munk, *Frequency Selective Surfaces: Theory and Design*, John Wiley & Sons, New York, 2000.
18. D.M. Pozar, S.D. Targonski, and H.D., Syrigos, Design of millimeter wave microstrip reflectarrays, *IEEE Trans. Antennas Propag.*, 45(2), 287–296, Feb. 1997.
19. A. Erentok, P.L. Luljak, and R.W. Ziolkowski, Characterization of a volumetric metamaterial realization of an artificial magnetic conductor for antenna applications, *IEEE Trans. Antennas Propag.*, 53(1), Part 1, 160–172, Jan. 2005.
20. I. Ederra, B.M. Pascual, A.B. Labajos, J. Teniente, R. Gonzalo, and P. de Maagt, Experimental verification of the reduction of coupling between dipole antennas by using a woodpile substrate, *IEEE Trans. Antennas Propag.*, 54(7), 2105–2112, July 2006.
21. Y.E. Erdemli, K. Sertel, R.A. Gilbert, D.E. Wright, and J.L. Volakis, Frequency-selective surfaces to enhance performance of broad-band reconfigurable arrays, *IEEE Trans. Antennas Propag.*, 50(12), 1716–1724, Dec. 2002.
22. S. Tse, B.S. Izquierdo, J.C. Batchelor, and R.J. Langley, Reduced sized cells for electromagnetic bandgap structures, *Electron. Lett.*, 39(24), 1699–1701, Nov. 2003.
23. J.C. Vardaxoglou, G. Goussetis, and A.P. Feresidis, Miniaturisation schemes for MEBG structures, *IEE Proc. Microw. Antennas and Propag.*, 1(1), 234–239, Jan. 2007 (special issue on Metamaterials).
24. Special issue on artificial magnetic conductors, soft/hard surfaces, and other complex surfaces, *IEEE Trans. Antennas Propag.*, 53(1), Jan. 2005.
25. F-R. Yang, K-P. Ma, Y. Qian, and T. Itoh,A novel TEM waveguide using uniplanar compact photonic-bandgap (UC-PBG) Structure, *IEEE Trans. Microw. Theory Tech.*, 47(11), 2092–2098, Nov. 1999.
26. M. Caiazzo, S. Maci, and N. Engheta, A metamaterial surface for compact cavity resonators, *IEEE Antennas Wireless Propag. Lett.*, 3, 261–264, 2004.
27. R.F.J. Broas, D.F. Sievenpiper, and E. Yablonovitch, A high-impedance ground plane applied to a cellphone handset geometry, *IEEE Trans. Microw. Theory Tech.*, 49(7), 1262–1265, July 2001.
28. HFSS: High Frequency Structure Simulator based on the Finite Element Method, v. 9.2.1, Ansoft Corporation, 2004. Available at: http://www.ansoft.com/
29. G. Goussetis, A.P. Feresidis, and R. Cheung, Quality factor assessment of subwavelength cavities at FIR frequencies, *J. Opt. A*, 9, s355–s360, Aug. 2007.
30. S.A. Maier, *Plasmonics Fundamentals and Applications*, Springer, New York, 2007.
31. R. Abhari and G.V. Eleftheriades, Metallo-dielectric electromagnetic bandgap structures for suppression and isolation of the parallel-plate noise in high-speed circuits, *IEEE Trans. Microw. Theory Tech.*, 51(6), 1629–1639, June 2003.
32. W.M. Merrill, C.A. Kyriazidou, H.F. Contopanagos, and N.G. Alexopoulos, Electromagnetic scattering from a PBG material excited by an electric line source, *IEEE Trans. Microwave Theory Tech.*, 47, 2105–2114, Nov. 1999.
33. K.A. McIntosh, O.B. McMahon, and S. Verghese, Three-dimension metalodielectric photonic crystals incorporating flat metal elements, *Microw. Opt. Technol. Lett.*, 17(3), 153–156, 1998.

34. M. Bozzi, S. Germani, L. Minelli, L. Perregrini, and P. de Maagt, Efficient calculation of the dispersion diagram of planar electromagnetic band-gap structures by the MoM/BI-RME method, *IEEE Trans. Antennas Propag.*, 53(1), 29–35, 2005.
35. P. Baccarelli, S. Paulotto, and C. Di Nallo, Full-wave analysis of bound and leaky modes propagating along 2D periodic printed structures with arbitrary metallisation in the unit cell, *IET Microw. Antennas Propag.*, 1(1), 217–225, 2007.
36. A.S. Barlevy and Y. Rahmat-Samii, Characterization of electromagnetic band-gaps composed of multiple periodic tripods with interconnecting vias: Concept, analysis, and design, *IEEE Trans. Antennas Propag.*, 49, 343–353, Mar. 2001.
37. C.A. Balanis, *Antenna Theory*, Wiley, New York, 1982.
38. A.A. Oliner and R.C. Johnson (eds.), Leaky-wave antennas, in: *Antenna Engineering Handbook*, 3rd edn., McGraw-Hill, New York, 1993, Chap. 10.
39. R.E. Collin, *Foundations for Microwave Engineering*, McGraw-Hill, New York 1992.
40. O. Luukkonen, C. Simovski, G. Granet, G. Goussetis, D. Lioubtchenko, A.V. Raisanen, and S.A. Tretyakov, Simple and accurate analytical model of planar grids and high-impedance surfaces comprising metal strips or patches, *IEEE Trans. Antenna Propag.*, 56(6), 1624–1632, June 2008.
41. A.B. Yakovlev, C.R. Simovski, S.A. Tretyakov, O. Luukkonen, G.W. Hanson, S. Paulotto, and P. Baccarelli, Analytical modeling of surface waves on high impedance surfaces, NATO Advanced Research Workshop: Metamaterials for secure information and communication technologies, Marrakesh, Morocco, May 7–10, 2008, pp. 184–193.
42. N. Amitay, Y. Galindo, and C.P. Wu, *Theory and Analysis of. Phased Array Antennas*. Wiley-Interscience, New York, 1972.
43. C. Mias, and J.H. Yap, A varactor-tunable high impedance surface with a resistive-lumped-element biasing grid, *IEEE Trans. Antennas Propag.*, 55(7), 1955–1962, July 2007.
44. D. Sievenpiper, High-impedance electromagnetic surfaces, PhD thesis, UCLA, Los Angeles, CA, 1999 (available online at http://www.ee.ucla.edu/labs/photon/thesis/ThesisDan.pdf).
45. F. Elek and G.V. Eleftheriades, Dispersion analysis of the shielded Sievenpiper structure using multiconductor transmission-line theory, *IEEE Microw. Wireless Compon. Lett.*, 14(9), 434–436, Sept. 2004.
46. R. Coccioli, Y. Fei-Ran, M. Kuang-Ping, and T. Itoh, Aperture-coupled patch antenna on UC-PBG substrate, *IEEE Trans. Microw. Theory Tech.*, 47(11), 2123–2130, Nov. 1999.
47. G.V. Trentini, Partially reflecting sheet arrays, *IRE Trans. Antennas Propag.*, AP-4, 666–671, 1956.
48. A.P. Feresidis and J.C. Vardaxoglou, High gain planar antenna using optimised partially reflective surfaces, *IEE Proc. Microw. Antennas Propag.*, 148(6), 345–350, Dec. 2001.
49. K. Fujimoto, A. Henderson, K. Hirasawa, and J.R. James, *Small Antennas*, Research Studies Press, John Wiley & Sons, New York, 1987.
50. G. Goussetis, A.P. Feresidis, and J.C. Vardaxoglou, Periodically loaded 1 metallodielectric EBG structures, *IEE Proc. Microw. Antennas Propag.*, 151(6), 481–485, Dec. 2004.
51. A.P. Feresidis, G. Apostolopoulos, N. Serfas, and J.C. Vardaxoglou, Closely coupled metallodielectric electromagnetic band gap (CCMEBG) structures formed by double layer dipole and tripole arrays, *IEEE Trans. Antennas Propag.*, 52(5), 1149–1158, May 2004.
52. F. Huang, J.C. Batchelor, and E.A. Parker, Interwoven convoluted element frequency selective surfaces with wide bandwidths, *Electron. Lett.*, 42(14), 788–790, July 2006.
53. R. Mittra, C.H. Chan, and T. Cwik, Techniques for analyzing frequency selective surfaces-a review, *Proc. of the IEEE*, 76(12), 1593–1615, Dec. 1988.
54. A.C. Lima and E.A. Parker, Microwaves, Fabry–Perot approach to the design of double layer FSS, *IEE Proc. Microw. Antennas Propag.*, 143(2), 157–162.
55. C.R. Simovski, P. de Maagt, S.A. Tretyakov, M. Paquay, and A.A. Sochava, Angular stabilization of resonant frequency of artificial magnetic conductors for TE-incidence, *Electron. Lett.*, 40(2), 92–93, 2004.

56. C.R. Simovski, P. de Maagt, I.V. Melchakova, High-impedance surfaces having stable resonance with respect to polarization and incidence angle, *IEEE Trans. Antennas Propag.*, 53(3), 908–914, Mar. 2005.
57. Y. Guo, G. Goussetis, A.P. Feresidis, and J.C. Vardaxoglou, Efficient modeling of novel uniplanar left-handed metamaterials, *IEEE Trans. Microw. Theory Tech.*, 53(4), 1462–1468, Apr. 2005.
58. N. Marcuvitz, *Waveguide Handbook*, Peter Peregrinus Ltd., London, U.K., 1986.
59. EMPiCASSO, EMAG Technologies Inc. Available at: http://www.empicasso.com
60. P. Baccarelli, S. Paulotto, and C. Di Nallo, Full-wave analysis of bound and leaky modes propagating along 2D periodic printed structures with arbitrary metallisation in the unit cell, *IET Microw. Antennas Propagat.*, 1(1), 217–225, 2007.
61. G. Gampala and A.B. Yakovlev, Artificial magnetic conductors for wideband antenna applications, in *Proceedings of ACES Conference*, Verona, Italy, Mar. 2007, pp. 242–247.
62. T.K. Wu, *Frequency Selective Surface and Grid Array*, John Wiley & Sons, New York, 1995.
63. C.C. Chen, Transmission of Microwave through perforated flat plates of finite thickness, *IEEE Trans. Microw. Theory Tech.*, MMT-21(1), 1–6, 1973.
64. R. Orta, R. Tascone, and R. Zich, A unified formulation for the analysis of general frequency selective surfaces, *Electromagnetics*, 5(4), 307–324, 1985.
65. R. Orta, R. Tascone, and R. Zich, Multiple dielectric loaded perforated screen as frequency selective surfaces, in *IEE Proc. H. Microwaves Opt. Antennas*, 135(2), 75–82, Apr. 1988.
66. W. Changhua and J.A. Encinar, Efficient computation of generalized scattering matrix for analyzing multilayered periodic structures, *IEEE Trans. Antennas Propag.*, 43(11), 1233–1242, Nov. 1995.
67. P. Kosmas, A.P. Feresidis and G. Goussetis, Periodic FDTD analysis of a 2-D leaky-wave planar antenna based on dipole frequency selective surfaces, *IEEE Trans. Antennas Propag.*, 55(7), 2006–2012, July 2007.
68. T. Kokkinos, C.D. Sarris, and G.V. Eleftheriades, Periodic FDTD analysis of leaky-wave structures and applications to the analysis of negative-refractive-index leaky-wave antennas, *IEEE Trans. Microw. Theory Tech.*, 54(4), Part 1, 1619–1630, June 2006.

VII

Tunable and Nonlinear Metamaterials

32

Tunable Surfaces: Modeling and Realizations

Chinthana Panagamuwa
Loughborough University

J. (Yiannis) C. Vardaxoglou
Loughborough University

This chapter takes a detailed look at research carried out in the area of tunable surfaces. The reader will be introduced to a number of different tuning techniques that were developed over the years.

32.1 Introduction

32.1.1 Why Have Tunable Surfaces?

Traditional electromagnetic bandgap (EBG) materials were always bound to a fixed frequency response. Conducting elements normally etched on substrates maintain fixed geometric patterns, and these types of surfaces were limited in their frequency performance. It would be advantageous for devices that function at a fixed frequency to have the ability to adapt, making it possible to operate at a number of different frequencies without replacing the hardware. This is especially true in deep-space applications or where the cost of regularly accessing the equipment is prohibitively high. In such cases, there are obvious advantages in having the ability to remotely reconfigure the operating characteristics.

With advances in electronics and the continuous creation of new applications, tunable surfaces have become a reality. At first, tunable frequency-selective surfaces (FSS) provided a method for dynamically controlling the transmission and reflection characteristics of an incident wave. It became possible to reduce the size of the unit cell, improve the bandwidth, and shift the operating frequency in real-time.

As the number of surface designs grew, more and more applications emerged where the tunable surface was one part of a complex structure. Today, tunable surfaces can play a key role in multi-banding reflector antennas, tunable filters, and phased arrays. Designs that show frequency tunability while also maintaining good frequency stability for increasingly larger angles of incidence for both horizontal and vertical polarizations are emerging. Applications were found in low profile antennas

and beam steering antennas. When tunable surface is used in combination with reconfigurable antenna, the ability to tune the surface makes it possible for the operating frequency of the antenna to be tracked by the supporting surface. This allows dynamic control of surface waves at different frequencies. This also allows a low-profile antenna to maintain zero degree phase shift at the high impedance surface (HIS) for different frequencies. Such novel designs illustrate the versatility of tunable surface designs, and this will no doubt lead to improvements in current applications and the development of many more in the future.

32.1.2 Basics of How to Achieve Tuning

Tunable surfaces mainly rely on the principle of changing the surface impedance of a periodic array through novel control methods. Over the past few decades, research groups around the world have developed new techniques, each with their own unique features, advantages and disadvantages, for changing the characteristics of tunable surfaces. In the case of EBGs, the tuning may involve the addition/removal of a bandpass/stop response at a particular frequency or even the shifting of the bandpass/stop from one frequency to another. For HISs, the phase of the reflected wave could be controlled or the frequency at which the reflected wave has zero phase could be tuned.

Control of tunable surfaces can be achieved through a number of stimuli. Changing the dielectric properties of the substrate through ferroelectric control [1–6] and varying the positions and dimensions of the cell elements through physical manipulation [8–11] were some of the earliest methods of tuning. Active devices such as PIN diodes [12–20], Varactor diodes [21–26], and microelectromechanical systems (MEMs) [27–31] were more recently incorporated onto surfaces. Novel techniques using photoconductivity were also demonstrated [32–37]. Other interesting techniques include using a changeable liquid as the substrate [38], generating the elements in an array using a controllable plasma [39], and using liquid crystals as a substrate [40]. Section 32.2 examines these different techniques in more detail.

32.2 EBG Tuning Techniques

32.2.1 Ferrite and Ferroelectric Substrates

The permeability of a ferrite substrate can be changed by biasing the material with a magnetic field. If an EBG is printed on a ferrite substrate, the ability to change the permeability of the substrate makes it possible to tune the operating frequency of the EBG. Some of the earliest techniques developed for tuning FSS were based on biasing ferrite substrates with a DC magnetic fields [1–5].

Substituting a ferroelectric material instead of a ferrite-based material as the substrate allows the permittivity to be tuned using a biasing electric field [6,7]. Tuning the permittivity of the substrate also gives control over the resonance frequency of the periodic structure. The use of ferroelectric material is covered in more detail in this chapter.

32.2.2 Mechanical Tuning

In many ways, mechanical tuning can be seen as a very simple method for tuning frequency characteristics of surfaces. As there is no need for biasing lines and electrical motors needed to physically move, various surfaces can be placed at a safe distance and electromagnetic interference and unwanted coupling can be minimized.

A mechanically tunable HIS is presented in [8]. The HIS made from patches in a mushroom configuration has a second layer of patches placed on top with a DC insulating dielectric between the two layers. Mechanically generated lateral movements of the top layer with respect to the fixed bottom layer adjust the overlap area between the plates and thus change the capacitance between neighboring

cells. This tunes the resonance frequency of the surface and also tunes the reflection phase for a fixed frequency.

In [9], Lockyer et al. presented a mechanically reconfigurable FSS made of two closely coupled adjacent dipole arrays. Small lateral displacement of one array compared to the other perturbs the strong fields in their separation region and so provides a method of controlling the FSS resonant frequency. The prototype in Figure 32.1a shows a computer-controlled micropositioning test-bed with two dipole arrays, each printed on a thin dielectric substrate, initially positioned parallel and in close proximity to each other. While their separation distance (S) is held constant, the stepper actuator moves the second array (FSS2) such that the overlap (DS) is changed.

When FSS2 is lined up with FSS1, i.e., DS = 0, the incident plane wave would effectively see a single FSS because FSS2 would be mostly masked by FSS1. Increasing the displacement DS laterally shifts FSS2 with respect to FSS1, so that the apertures in the surface are gradually covered up. An incident plane wave sees an actual increase in the dipole elements' lengths, along with a change in the coupling between the arrays. This control of the elements' lengths allows the frequency response of the surface to be tuned. When FSS2 is fully displaced, the apertures are closed and the surface becomes an array of strips. Detailed analysis of the coupling between elements on two layers is given in [10].

The dipoles in each surface were arranged on a square lattice, D = 6 mm and were printed on a 0.037 mm thick dielectric substrate of dielectric constant 3. The dipole lengths were L_1 = 3.25 mm and L_2 = 4.5 mm for FSS1 and FSS2, respectively.

Figure 32.1b shows the effect of changing DS on the frequency response of a normal incidence plane wave. The separation distance S was set to 50 μm in the predictions. Varying DS between 0 and 3 mm, the resonance frequency of the FSS layers can be tuned by 15 GHz from 29 to 14 GHz.

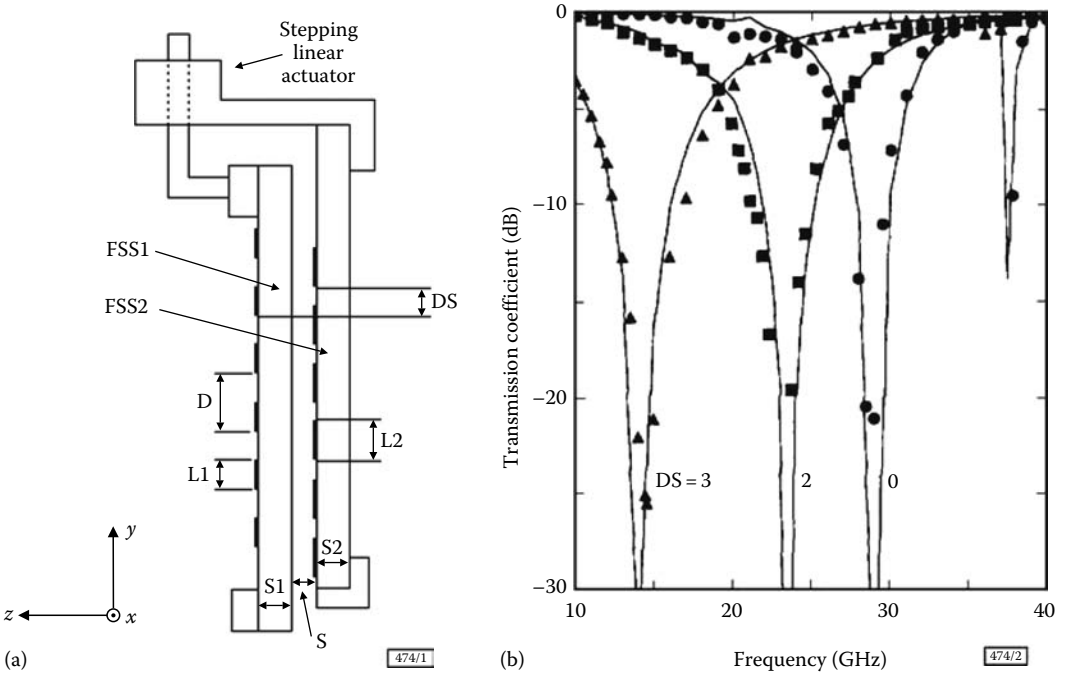

FIGURE 32.1 (a) Cross-sectional view of reconfigurable FSS jig using dipole arrays. (b) Effect of different DS values on plane wave response. Key: –, predicted; ●, DS = 0 mm; ■, DS = 2 mm; and ▲, DS = 3 mm. (From Lockyer, D., Moore, C., Seager, R., Simpkin, R., and Vardaxoglou, J.C., *Electron. Lett*., 30(1), 1258, 1994. With permission.)

A mechanically tunable FSS is presented in [11] with good frequency stability for oblique angles using a double-layer FSS with square-loop slot elements. It uses a similar technique to the previous designs whereby one FSS layer is laterally displaced with respect to the other. The actual tunable range covers 1.90–3.20 GHz.

32.2.3 PIN Diodes

PIN diodes have found considerable use in RF circuits and devices due to their ability to act as fast switches. In contrast to the standard PN diode, a PIN diode has a wide near intrinsic layer sandwiched between the n-type and p-type layers. When reverse biased, the diode has a very high resistance in parallel with a capacitance. When forward biased, the diode has a very low resistance.

In [12], Chang et al. use pin diodes to switch transmission through an active FSS on and off at 2.3 GHz. The construction of the unit cell and its equivalent circuit is shown in Figure 32.2a through c. A unit cell has a square metallized island loading a square aperture and a PIN diode connecting the square island to the top part of the aperture.

Figure 32.2e and f shows the equivalent circuits for a PIN diode when reverse and forward biased, respectively. L_2 accounts for the lead inductance of the diode package and is constant in both modes of operation. Equations for the FSS surface impedance with the PIN diodes in both on and off states were derived as follows [12]:

$$Z_{\mathrm{OFF}} = \frac{2j\omega L_1}{4 - \omega^2 L_1 C_1} \tag{32.1}$$

$$Z_{\mathrm{ON}} = \frac{-j\omega^3 L_1 L_2 C_1 - 2j\omega^3 L_1 L_2 C_2 + j\omega L_1}{2\omega^4 L_1 L_2 C_1 C_2 - \omega^2 L_1 C_1 - 2\omega^2 L_2 C_1 - 4\omega^2 L_2 C_2 + 2} \tag{32.2}$$

Chang use lumped elements in an EM simulation software to model the on and off states of the diodes. The presented results show good agreement among modeled, calculated, and measured results. At 2.3 GHz, switching the diodes on achieves an insertion loss greater than 25 dB, while with the diodes switched off, the FSS has almost near perfect transmission at this frequency.

Following a similar theme of loaded apertures, in [13] Kiani et al. use circular aperture elements with four PIN diodes per element to achieve FSS stopband control for oblique as well as normal TE incidence at 2.45 GHz. The front and back of the unit cells is shown in Figure 32.3. The PIN diodes are modeled as lumped RLC elements in an EM simulation software package. Transmission and reflection results show good frequency stability for incident angles of 0°–45°.

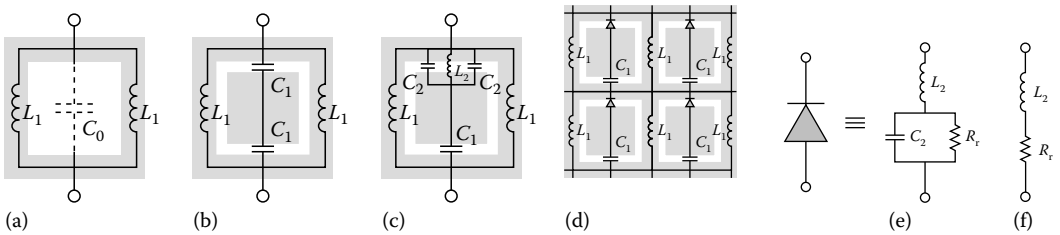

FIGURE 32.2 Simple model of FSS unit cell (a) with squared aperture, (b) with squared loop with island loading, and (c) with squared loop connected to metal plates. Equivalent circuit model of (d) active FSS unit cell with PIN diode, (e) the reverse bias equivalent circuit, and (f) the forward equivalent circuit. (From Chang, K., Kwak, S.-I., and Yoon, Y.J., Equivalent Circuit Modeling of Active Frequency Selective Surfaces, *IEEE Radio and Wireless Symposium*, 2008, pp. 663–666. With permission.)

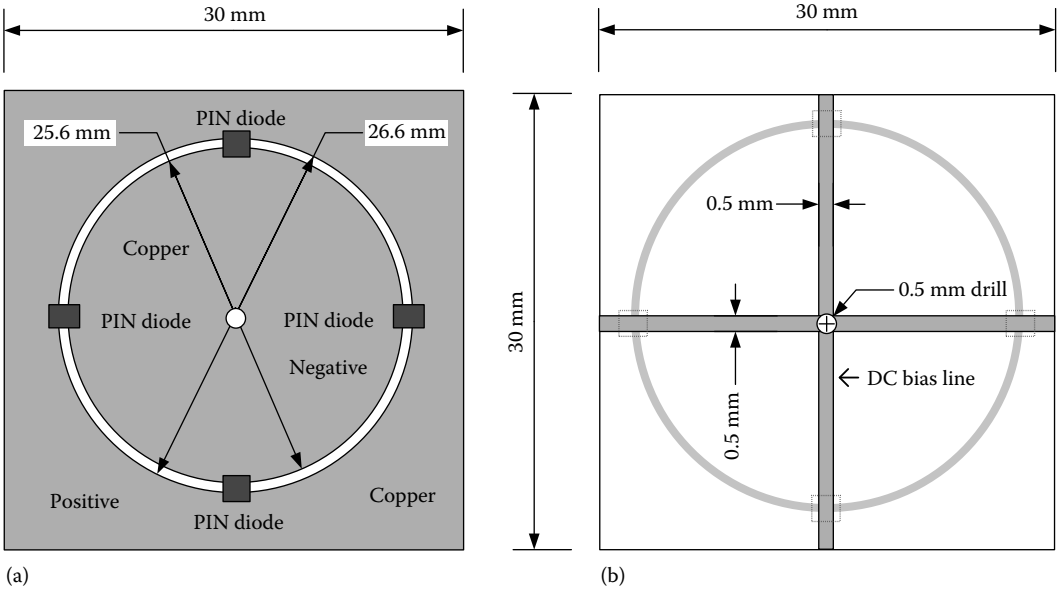

FIGURE 32.3 The layout of a unit cell. (a) Front side and (b) reverse side. (From Kiani, G.I., Esselle, K.P., Weily, A.R., and Ford, K.L., Active Frequency Selective Surface Using PIN Diodes, *IEEE Antennas and Propagation International Symposium*, 2007, pp. 4525–4528. With permission.)

Kiani et al. [14] has also extended the design to a square aperture loops with four PIN diodes per unit cell, compared to Chang's one PIN diode in Figure 32.2. Biasing feed lines are printed on the reverse side in a diagonal fashion so that both horizontally and vertically polarized wave couple equally. This design shows good frequency stability for both parallel and perpendicular polarizations for incidence angles up to 60°.

Martynyuk et al. [15] use the loading of ring slot resonators with PIN diodes to achieve frequency control of a FSS. Two diodes, one at the top of the ring slot and the other at the bottom, connect the metallic island to the surrounding sheet. When the diodes are reverse biased (−30 V), the FSS is nearly transparent to the incident wave near resonant frequency of 10.7 GHz. Conversely, when forward biased with 50 mA, the FSS behaves more like a metallic sheet and most of the energy is reflected, giving a transmission coefficient of about −25 dB. The "on" diode was modeled as a 1.5Ω resistor, whereas the "off" diode was modeled as a 4 kΩ resistor and a 0.053 pF capacitor in parallel.

In [16], Chang et al. present a tunable FSS constructed from segmented half-square loops. As shown in Figure 32.4, two PIN diodes are inserted in each unit cell to connect the upper and lower segments together.

When the diodes are forward biased (on), a low resistive path connects the square segments and the surface looks like an infinite periodic array of square loops. When the diodes are reverse biased (off), they act predominantly as an extra capacitive load between the half squares and the array resonates at a higher frequency, but at the original frequency, the surface is transparent to the incident waves. Hence, it can be made either reflecting or transmitting, according to the applied bias.

The equivalent circuit for the square loop is a series LC circuit. C_d and R_d are PIN diode capacitance and resistance, respectively. When the diode is forward biased, C_d is short circuited. Measured and calculated results show that when the PIN diodes are forward biased with 1 V, there is a stop band at 12.6 GHz. When the biasing is removed, the stop band moves to 36 GHz leaving full transmission for the array at 12.6 GHz.

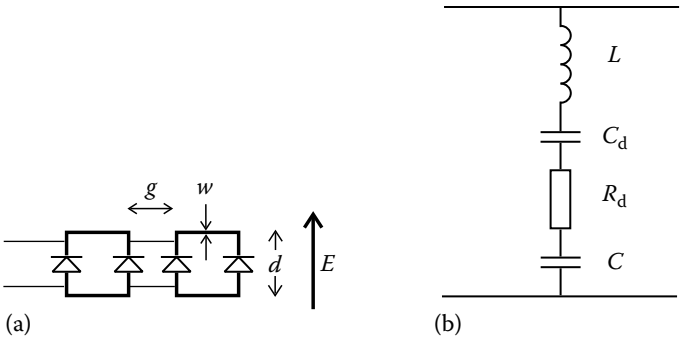

FIGURE 32.4 (a) Active square loop array geometry including bias lines. (b) Equivalent circuit for active array. (From Chang, T.K., Langley, R.J., and Parker, E.A., *IEEE Microw. Guided Wave Lett.*, 3(10), 387, 1993. With permission.)

Tennant and Chambers [17] have used PIN diodes and an FSS to design a novel single-layer active microwave absorber with a controllable frequency response between 9 and 13 GHz. Having based their topology on a conventional Salisbury Screen [18], the traditional resistive layer was replaced by a periodic grid of bow-tie dipole elements controlled by PIN diodes. The overall thickness of the active absorber was less than 5 mm including the back-plane, 4 mm thick Rhocell 51 foam ($\varepsilon_r = 1.05,\ \tan\delta = 0.0017$), and the "face-down" active FSS circuit board. With only 0.08 mA forward bias current of the PIN diodes, a reflectivity level less than −20 dB is achieved between 9.5 and 12.5 GHz.

Further examples of the use of PIN diodes in active FSS to control transmission are demonstrated in [19,20]. As in the previous examples, the transmission through the FSS is blocked by forward biasing the diodes. This ability to remove the bandpass is the most common control achieved through PIN diodes on FSS.

32.2.4 Varactor Diodes

Varactor diodes have found many uses in RF applications, especially in tunable devices. Varying levels of reverse bias voltage across the varactor diode gives varying amounts of capacitance. In applications where control of the surface impedance is important, this ability to change the surface reactance was utilized in many novel designs.

The equivalent circuit of the varactor diode is shown in Figure 32.5 [21]. The diode is assumed to have a junction capacitance C_v, a series resistance r_v, a package capacitance C_p, and a parasitic inductance L_p. Varactor diodes are normally employed in regions where variable capacitance would have a large impact on the surface impedance and thus change the operating frequency of the surface.

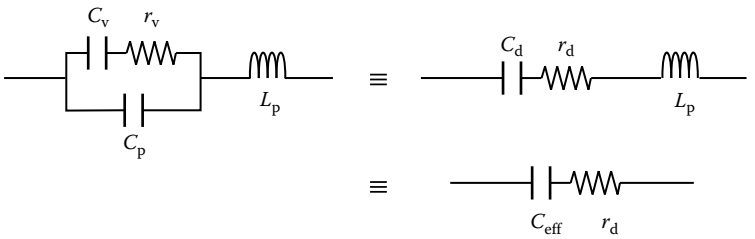

FIGURE 32.5 Equivalent circuit of the varactor diode. (From Mias, C. and Haur Yap, J., *IEEE Trans. Antennas Propag.*, 55(7), 1955, 2007. With permission.)

A number of novel designs were proposed that use varactor diodes to achieve frequency control and some of these will be examined next.

Sievenpiper et al. [22] introduced varactor diodes between square metal plates of a HIS to tune the capacitance between the mushroom-shaped conducting elements. The resonance frequency and the reflection phase of a HIS can be controlled by tuning the capacitance and/or the inductance. The sheet inductance is related to the magnetic permeability and the thickness of the substrate. Other than by magnetically tuning of a ferrite substrate or mechanically tuning the thickness of the substrate, it is difficult to change the inductance. The capacitance, on the other hand, is easier to control. This can be achieved by changing the geometry and arrangement of the metal plates [8] or by adding tunable lumped capacitors as shown in Figure 32.6. There are two 1.6 mm thick RD5880 substrates sandwiched between three layers of metallization. The top layer contains the square patches, the middle layer the ground plane, and the bottom layer has the biasing network for the varactor diodes.

By changing the voltage applied to the varactor diodes between 0 and 20 V, the resonance frequency can be tuned over a range of about 2.5–4.5 GHz. Reflection magnitude results for the tunable surface are shown in Figure 32.7. Higher resonance frequencies can be achieved by alternating between two voltages on every other row. This effectively doubles the lattice period and extents the top frequency to nearly 5 GHz.

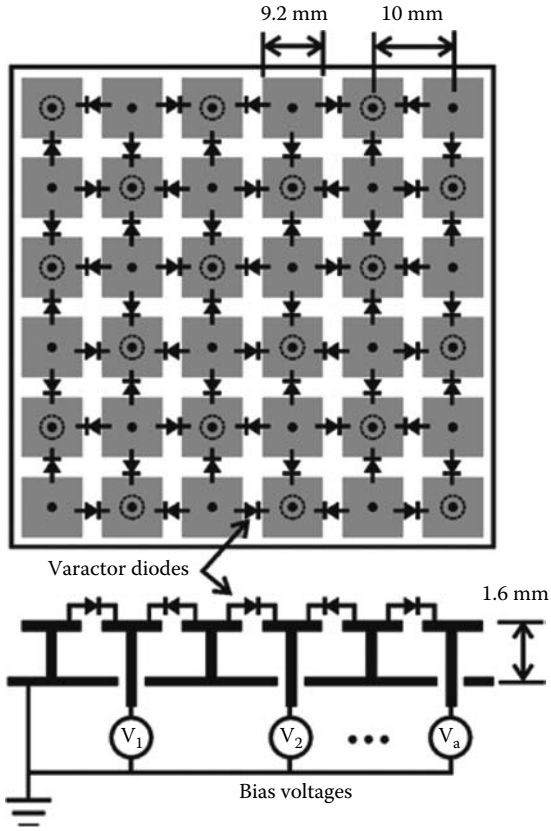

FIGURE 32.6 Electrically tunable impedance surface, with varactor diodes between neighbouring pairs of plates. Half of the plates are grounded, and the other half are attached to control wires on the back of the surface. The diodes are oriented in opposite directions in each alternate row. (From Sievenpiper, D.F., Schaffner, J.H., Song, H.J., Loo, R.Y., and Tangonan, G., *IEEE Trans. Antennas Propag.*, 51(10), 2713, 2003. With permission.)

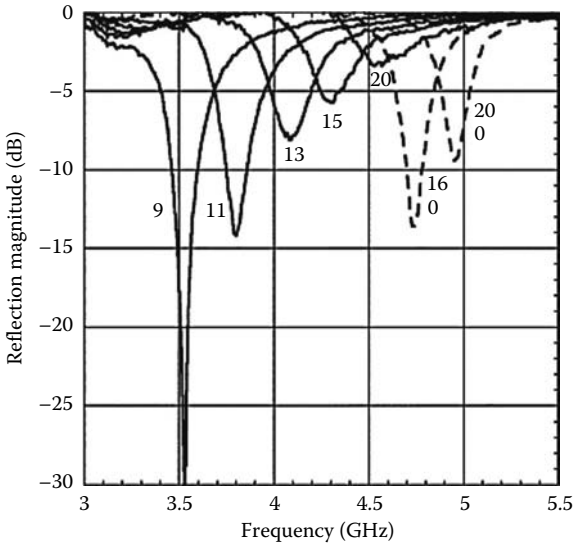

FIGURE 32.7 Reflection magnitude for various voltages. The solid lines correspond to a uniform voltage ranging from 9 to 20 V, which provide a tuning range of 3.5–4.5 GHz. For the dashed lines, two different voltages were applied to alternate rows, which double the effective period, splitting the resonance in two, and pushing the upper resonance to nearly 5 GHz. (From Sievenpiper, D.F., Schaffner, J.H., Song, H.J., Loo, R.Y., and Tangonan, G., *IEEE Trans. Antennas Propag.*, 51(10), 2713, 2003. With permission.)

Mias [23] used varactor diodes in a tunable FSS structure consisting of vertical and horizontal convoluted dipole elements. A FR4 substrate is used (thickness = 1.6 mm, $\varepsilon_r = 4.6$) with one half of the convoluted dipole printed on each side. The structure is designed with a novel resistive lumped-element biasing grid. The specially designed highly resistive biasing grid suppresses unwanted resonances and improves the surface's frequency response. The top and bottom surfaces of the FSS are shown in Figure 32.8. This particular design is able to block both vertically and horizontally polarized waves with the stop band tunable from 2.37 to 2.55 GHz. The FSS transmission responses for different varactor biasing voltages are shown in Figure 32.9.

Other surface tuning techniques using varactor diodes are given in [15,24–26].

32.2.5 Microelectromechanical Systems

As a relative newcomer to the filed of reconfigurable devices, RF MEMS have quickly found favor in many research laboratories world wide. As mechanical contact switches, MEMS provide high isolation when open and low insertion loss when closed. MEMS are actuated using static voltages that draw very little current. They are also used in configurations that provide a variable capacitance rather than a simple on–off switch.

In [27], Schoenlinner et al. demonstrated a switchable FSS operating around 30 GHz using RF MEMS bridges on a 500 μm thick glass substrate. To ensure polarization independence, 90° rotational symmetry is achieved using four-legged loaded elements as unit cells. Figure 32.10a and b shows the unit cell of the FSS with (a) showing the locations of the MEMS bridges and (b) showing the biasing bridges connecting the tips of neighboring unit cells. Four RF MEMS per unit cell are arranged symmetrically around the center of the cross dipole as this is where the electric field is strongest and the variable capacitance offered by the MEMS bridges can be most effectively applied. The complete FSS is composed of 909 unit cells and 3636 MEMS bridges.

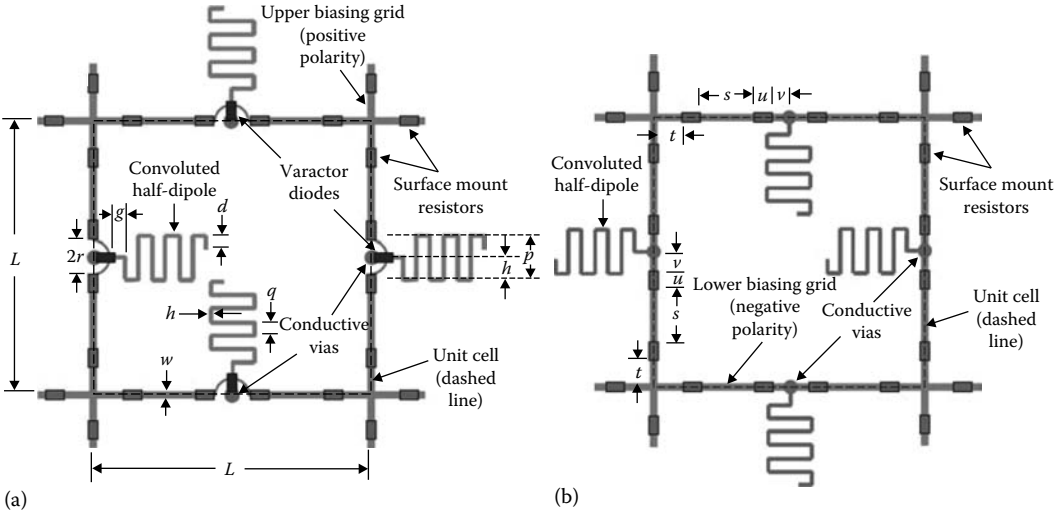

FIGURE 32.8 (a) Upper metallization layer of the FSS and (b) lower metallization layer of the FSS. $L = 32\,\text{mm}$, $G = 2\,\text{mm}$, $q = 1.5\,\text{mm}$, $w = 1\,\text{mm}$, $d = 1\,\text{mm}$, $h = 2\,\text{mm}$, $p = 4\,\text{mm}$, $r = 2\,\text{mm}$, $v = 2\,\text{mm}$, $u = 2\,\text{mm}$, $s = 6\,\text{mm}$, $t = 4\,\text{mm}$. The dashed-line square indicates the periodic unit cell of the FSS. (From Mias, C. and Haur Yap, J., *IEEE Trans. Antennas Propag.*, 55(7), 1955, 2007. With permission.)

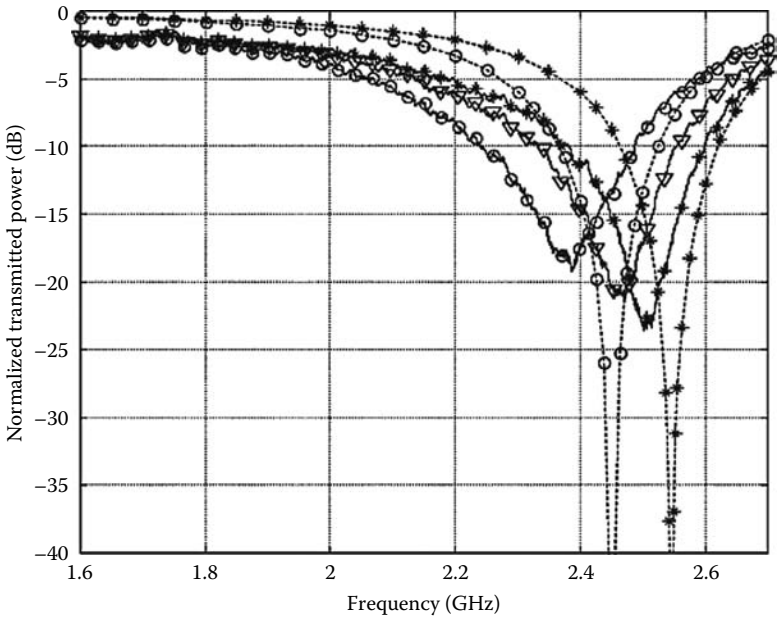

FIGURE 32.9 Experimental values (solid lines) of the normalized transmitted power for various varactor reverse bias voltages: (o), 0 V ($C_T = 2\,\text{pF}$ approx.); (∇), 15 V; (*), 30 V ($C_T = 2\,\text{pF}$ approx.). Numerical results are also shown (dashed lines): (o), $C_T = 2\,\text{pF}$ (approx.); (*): $C_T = 20\,\text{pF}$ (approx.). (From Mias, C. and Haur Yap, J., *IEEE Trans. Antennas Propag.*, 55(7), 1955, 2007. With permission.)

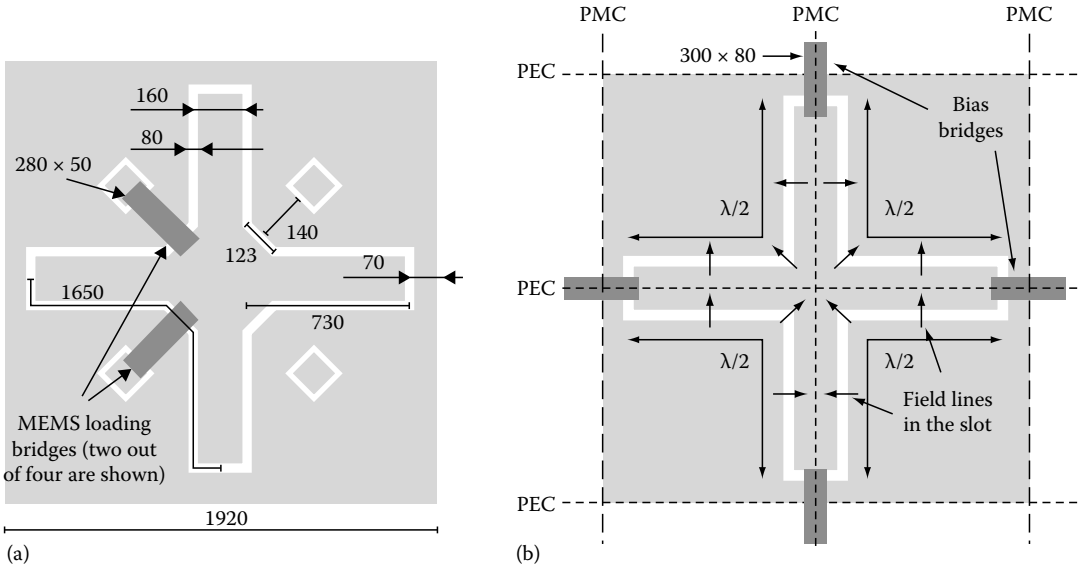

FIGURE 32.10 (a) Unit cell of the switchable FSS with bridges for capacitive loading of the slot, and dimensions in micrometers. (b) Unit cell with four bias bridges (loading bridges not shown). (From Schoenlinner, B., Abbaspour-Tamijani, A., Kempel, L.C., and Rebeiz, G.M., *IEEE Trans. Microw. Theory Tech.*, 52(11), 2474, 2004. With permission.)

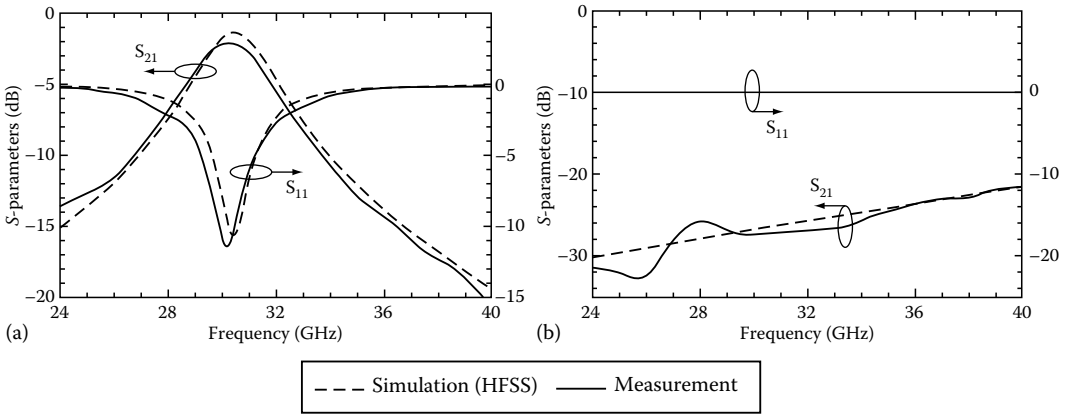

FIGURE 32.11 Measured transmission and reflection coefficients of the FSS versus frequency in comparison with the HFSS simulation: (a) with MEMS bridges in the up- and (b) downstate positions (V = 17 V). (From Schoenlinner, B., Abbaspour-Tamijani, A., Kempel, L.C., and Rebeiz, G.M., *IEEE Trans. Microw. Theory Tech.*, 52(11), 2474, 2004. With permission.)

Figure 32.11a and b shows the transmission and reflection coefficients of the FSS with the MEMS bridges in the up- and downstates, respectively. In the upstate, the FSS resonates at 30.2 GHz and has a low insertion loss of 2 dB in its bandpass region. With the application of 17 V to the MEMS, the bridges are forced down and the capacitive loading of the cross-dipoles are effectively changed. The change in surface impedance removes the bandpass at 30.2 GHz. In the downstate, the FSS has a transmission less than −27.5 dB.

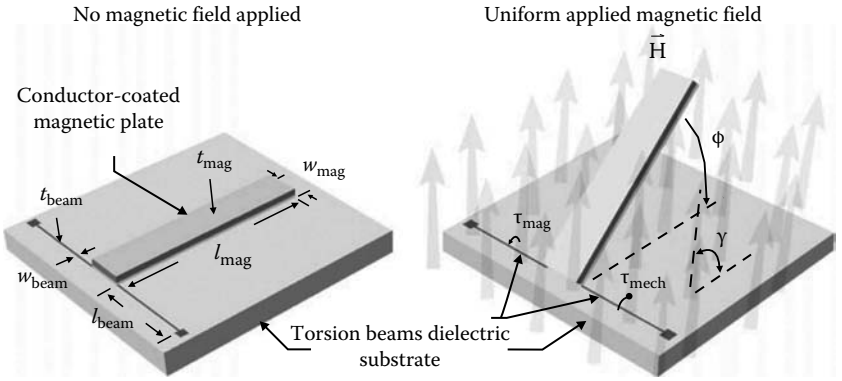

FIGURE 32.12 Ferromagnetic microactuators with stabilizing torsional flexures, driven by off-chip magnetic fields. (From Zendejas, J.M., Gianvittorio, J.P., Rahmat-Samii, Y., and Judy, J.W., *J. Microelectromech. Syst.*, 15(3), 613, 2006. With permission.)

In [28], Zendejas et al. applied a magnetic field to control ferromagnetic microactuators acting as dipole elements in a FSS array. As shown in Figure 32.12, the magnetic field causes the dipole elements to be tilted away from the supporting substrate surface so that an incident RF plane wave is presented with an effectively shortened dipole element. As the tilt angle effectively controls the visible length of the dipoles, the operating frequency of the FSS can be adjusted by changing the magnetic field strength.

The measured results for different dipole element tilt angles are shown in Figure 32.13. Transmission coefficients better than −14 dB can be achieved for tilt angles up to 30°. The operating frequency of the FSS can be usefully tuned between 85 and 87 GHz.

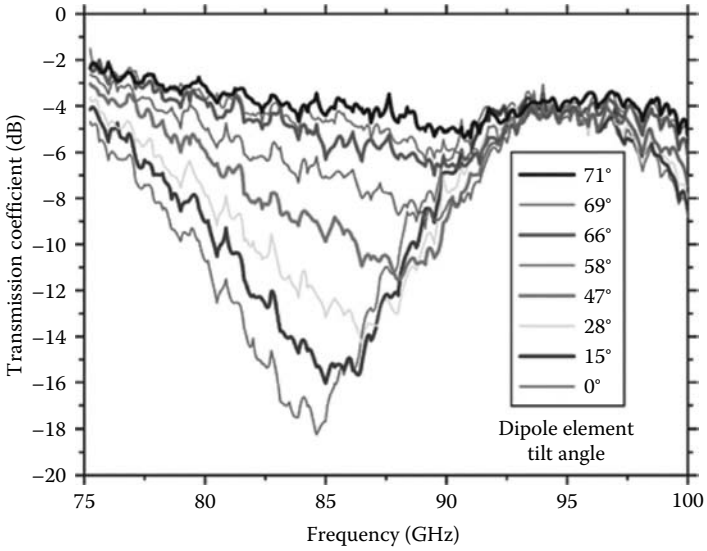

FIGURE 32.13 A family of measured frequency responses for a reconfigurable MEMS FSS illuminated by a normally incidence source. (From Zendejas, J.M., Gianvittorio, J.P., Rahmat-Samii, Y., and Judy, J.W., *J. Microelectromech. Syst.*, 15(3), 613, 2006. With permission.)

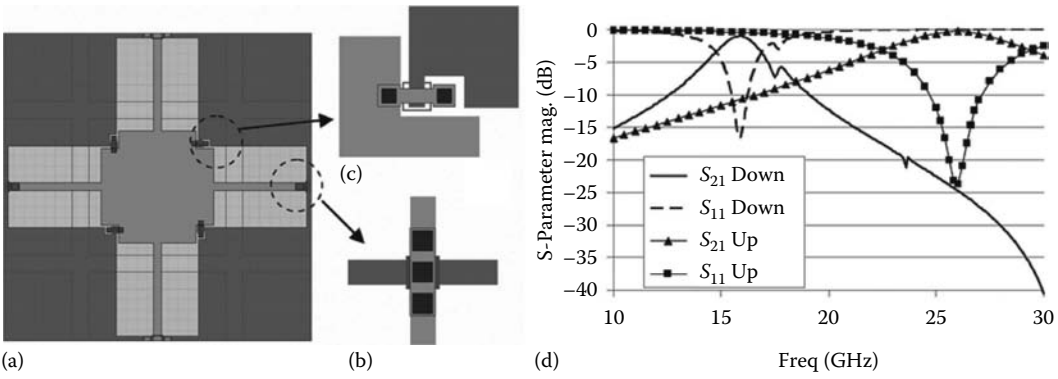

FIGURE 32.14 (a) Single FSS unit cell with MEMS structures. (b) Crossover bridge which provides DC isolation between the overlapping grids. (c) Two-state MEMS switched capacitor. (d) Simulated *S*-parameters for MEMS switches up and down. (From Coutts, G.M., Mansour, R.R., and Chaudhuri, S.K., A MEMS-Tunable Frequency-Selective Surface Monolithically Integrated on a Flexible Substrate, *IEEE/MTT-S International Microwave Symposium*, 2007, pp. 497–500. With permission.)

In [29], Coutts et al. presented a MEMS-tunable FSS integrated onto a flexible substrate. As shown in Figure 32.14a, the FSS consists of two overlapping grids of patches, with the patches in one grid larger than the patches in the other. Each patch on both grids has its own interconnecting tracks that connect the patch to its four neighboring patches in the same grid. DC isolation between the two grids is maintained by using crossover bridges where the interconnecting tracks cross. These bridges are shown in Figure 32.14b. Capacitive coupling between patches on both grids are strongest at the corners due to their close proximity to each other. MEMS capacitors are integrated into the corners of all patches (see Figure 32.14c) so that the capacitance between the patches can be tuned.

Simulated results for the tunable FSS are given in Figure 32.14d. They show that when the MEMS switch capacitors are in the upstate, the FSS resonates at 25.9 GHz with an insertion loss of 0.33 dB. When the capacitors are in the downstate, the resonance frequency shifts to 15.9 GHz with an insertion loss of 0.99 dB. Preliminary measured results show good correlation with simulations.

MEMS switchers are used to provide a variable capacitance for a tunable HIS in [30]. The supply voltage to the MEMS changes the separation gap between two layers of DC isolated patches and so tunes the capacitance of the HIS. Changing the impedance of the surface allows the phase of the reflected waves to be tuned. Further use of MEMS in a tunable metamaterial is presented in [31]. Since their introduction, MEMS have improved their reliability, and as they consume very little power the number of switches that can be used on a tunable surface designs is no longer a constraining factor.

32.2.6 Photonic Control of FSS

Optical control of a metamaterial unit cell consisting of a split ring resonator (SRR) was demonstrated theoretically and experimentally in [32] by Degiron et al. Their design incorporates a small lightly doped silicon dice fixed in the gap of a 3 × 4 mm SRR. The dice is illuminated with an 815 nm laser diode through a multimode optical fiber which increases the conductivity of the silicon by generating electron–hole pairs. This changes the properties of the unit cell from that of a SRR to a square loop. The design of the SRR is shown in Figure 32.15. A simplified model is used to describe the effects of illumination.

As the electron–hole plasma is generated mainly at the surface of the silicon, the dice is treated as a bilayer structure whose first 10 μm under the surface are uniformly illuminated. Equations that

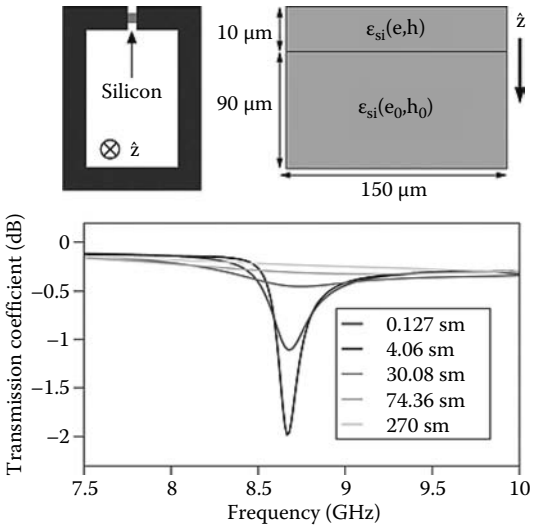

FIGURE 32.15 (a) Geometry of the controllable SRR (length 3 mm, height 4 mm, and thickness 0.017 mm) and cross-sectional view of the simulated piece of silicon. (b) Simulated transmission coefficient (S21 parameter) as a function of frequency for increasing levels of photodoping. The data are normalized against the transmission of the unloaded waveguide. (From Degiron, A., Mock, J.J., and Smith, D.R., Optical Control of Metamaterial Unit Cells at Microwave Frequencies, *International Symposium on Signals, Systems and Electronics*, 2007, pp. 209–212. With permission.)

link the permittivity to the carrier density are used to characterize the top layer. The bottom layer is treated as dark silicon.

Figure 32.15b shows the change in the transmission coefficient with increasing silicon conductivity. The SRR has a resonance at about 8.7 GHz which is completely destroyed by the conducting silicon bridging the gap.

A photoinduced inductive grid array generated in a silicon wafer was suggested by Lockyer et al. [33]. A silicon wafer is totally illuminated with near infrared light through an optical mask having the desired dimensions of the grid as shown in Figure 32.16. The mask ensures that only the desired sections of the silicon wafer are exposed to the light. Although silicon in the dark state acts as a dielectric, the generation of a plasma of electron–hole pairs due to photon absorption in the exposed areas reduces its dielectric permittivity and increases its conductivity. When the illumination is removed, the electron–hole pair density is reduced because of recombination and silicon wafer returns to its original dielectric state. So, the device can be seen as a temporal grid of pseudometallic elements.

Microwave transmission properties of the device can be controlled by varying the intensity of the incident light source and the exposure time. Numerical simulation of the plasma generated through optical excitation of silicon can be done through a system of equations presented in [34]. The equations include photon absorption, carrier recombination, and diffusion and also take account of temperature increase in the wafer. This allows the plasma density to be calculated as a function of time and depth. In Figure 32.17, the simulated effect of an incident 20 ns light pulse on the reflection coefficient of the FSS surface is shown at a number of time intervals.

Following the same principle of illuminating the entire silicon wafer, Lockyer et al. have also shown bandpass control using an array of printed [35] and doped [36] aperture dipoles. Aluminium was deposited on the silicon wafer creating a FSS of printed dipoles with a bandpass at 24 GHz. A similar effect was achieved by highly doping the wafer with a dipole array pattern and a FSS bandpass was

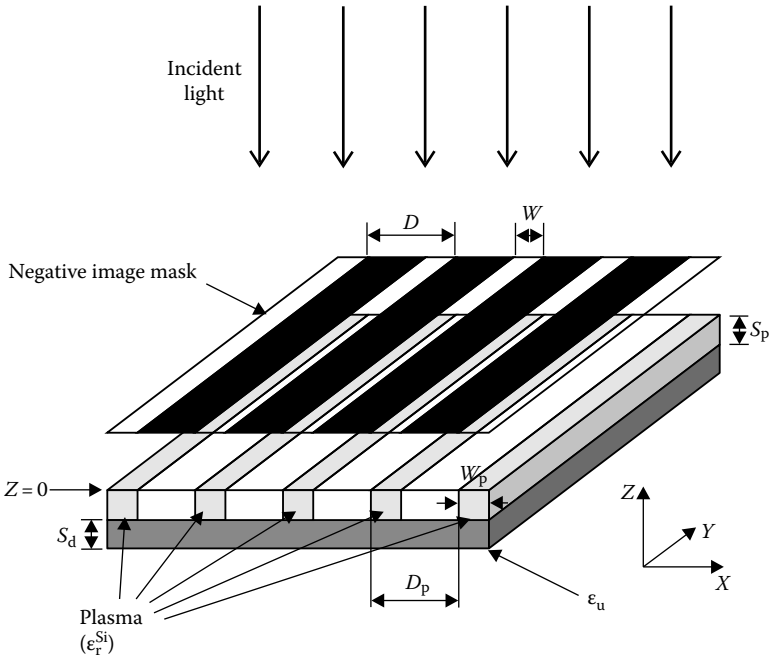

FIGURE 32.16 Array generation using an optical mask. (From Lockyer, D.S., Vardaxoglou, J.C., and Kearney, M.J., *IEEE Trans. Microw. Theory Tech.*, 47(7), 1391, 1999. With permission.)

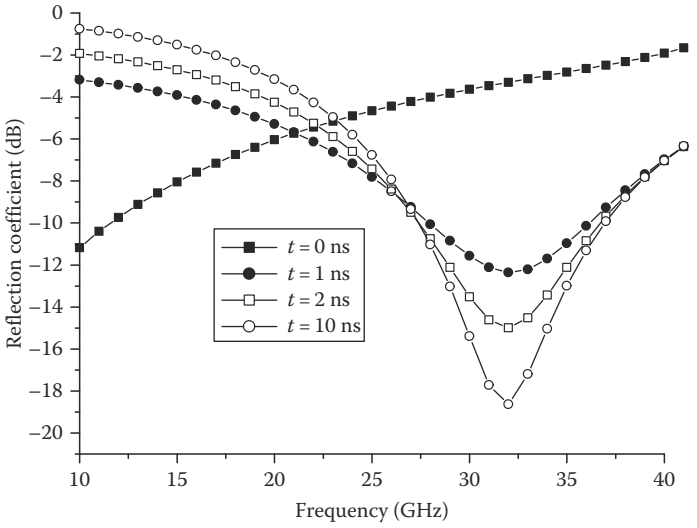

FIGURE 32.17 Reflection coefficient of the photogenerated grid illuminated by a single exciting pulse with pulse width 20 ns, wavelength 1064 nm, and intensity 10^5 W/cm^2 as a function of time (grid dimensions are D = 4 mm and W = 1 mm).

achieved at 36 GHz. When illuminated with near infrared light, the silicon surfaces were flooded with an electron–hole plasma creating a near metallic state. In this configuration, the bandpass regions were blocked and most of the incident RF energy was reflected.

A theoretical study in [37] suggests the use of optically controlled photoconducting silicon switches in a FSS made of an array of dipole and cross-dipole elements. Each of the unit cells are connected to their neighboring cells using these silicon switches. Using a genetic algorithm, certain activation patterns have been shown to tune the bandpass of the FSS. Such a system would require individual control of all the switches.

32.3 Conclusion

This chapter has introduced the reader to a number of popular surface-tuning techniques. Tunable surfaces have already found use in a number of applications including beam steering antennas, tunable phase shifters, and filters. Tuning allows for the unit cell size to be reduced and can provide improvements in the bandwidth. In most cases, frequency and/or phase characteristics are tuned over a fixed range by gaining control over the capacitance between conducting elements in the periodic structure. In some designs, the resonant structures are transformed into near complete metallic walls by shorting out the unit cells and thus blocking the transmission of incident waves. Active devices such as PIN diodes, varactor diodes, and MEMS have been used in many novel designs. Equivalent circuits have been derived for PIN and varactor diodes, and often, lumped elements are used in EM simulation software to model these devices in tunable surfaces. Other techniques have also included control of the substrate characteristics using magnetic and electric fields, mechanical movement of one periodic structure with respect to another, and the use of photoconductivity to generate grids on silicon wafers.

References

1. Chang, T. K., R. J. Langley, and E. A. Parker. 1994. Frequency selective surfaces on biased ferrite substrates. *Electronics Letters* 30 (75):1193–1194.
2. Li, G. Y., Y. C. Chan, T. S. Mok, and J. C. Vardaxoglou. 1995. Analysis of frequency selective surfaces on biased ferrite substrate. *IEEE Antennas and Propagation Society International Symposium* 3:1636–1639.
3. Chan, Y. C., G. Y. Li, T. S. Mok, and J. C. Vardaxoglou. 1996. Analysis of a Tunable Frequency-Selective Surface on an in-plane biased ferrite substrate. *Microwave and Optical Technology Letters* 13 (2):59–63.
4. Liu, Y., C. G. Christodoulou, and N. E. Buris. 1997. A full wave analysis method for frequency selective surfaces on ferrite substrates. *Journal of Electromagnetic Waves and Applications* 11:593–607.
5. Liu, Y., C. G. Christodoulou, P. F. Wahid, and N. E. Buris. 1995. Analysis of frequency selective surfaces with ferrite substrates. *IEEE Antennas and Propagation Society International Symposium* 3:1640–1643.
6. Parker, E. A. and S. B. Savia. 2001. Active frequency selective surfaces with ferroelectric substrates. *IEE Proceedings—Microwave Antennas & Propagation* 148(2):103–108.
7. Oyhenart, L. and V. Vigneras. 2006. Tunable photonic crystals using ferroelectric materials. *13th IEEE International Conference on Electronics, Circuits and Systems*, 407–410.
8. Sievenpiper, D., J. Schaffner, J. J. Lee, and S. Livingston. 2002. A steerable leaky-wave antenna using a tunable impedance ground plane. *IEEE Antennas and Wireless Propagation Letters* 1:179–182.
9. Lockyer, D., C. Moore, R. Seager, R. Simpkin, and J.C. Vardaxoglou. 1994. Coupled dipole arrays as reconfigurable frequency selective surfaces. *Electronics Letters* 30(1):1258–1259.
10. Lockyer, D., R. Seager, and J. C. Vardaxoglou. 1996. Reconfigurable FSS using multilayer conducting and slotted array structures. *IEE Colloquium on Advances in Electromagnetic Screens, Radomes and Materials*, 1–6.

11. Ma, D. and W. X. Zhang. 2007. Mechanically tunable frequency selective surface with square-loop-slot elements. *Journal of Electromagnetic Waves and Applications* 21(15):2267–2276.
12. Chang, K., S.-I. Kwak, and Y. J. Yoon. 2008. Equivalent circuit modeling of active frequency selective surfaces. *2008 IEEE Radio and Wireless Symposium*, 663–666.
13. Kiani, G. I., K. P. Esselle, A. R. Weily, and K. L. Ford. 2007. Active frequency selective surface using PIN diodes. *2007 IEEE Antennas and Propagation International Symposium*, 4525–4528.
14. Kiani, G. I., K. L. Ford, K. P. Esselle, and A. R. Weily. 2007. Oblique incidence performance of an active square loop frequency selective surface. *Second European Conference on Antennas and Propagation*, 11–16.
15. Martynyuk, A. E., J. I. Martinez Lopez, and N. A. Martynyuk. 2005. Active frequency-selective surfaces based on loaded ring slot resonators. *Electronics Letters* 41(1):2–4.
16. Chang, T. K., R. J. Langley, and E. A. Parker. 1993. An active square loop frequency selective surface. *IEEE Microwave and Guided Wave Letters* 3(10):387–388.
17. Tennant, A. and B. Chambers. 2004. A single-layer tunable microwave absorber using an active FSS. *IEEE Microwave and Wireless Components Letters* 14(1):46–47.
18. Salisbury, W. W. 1952. Absorbent body for electromagnetic waves. U.S. Patent 2,599,944.
19. Chang, T. K., R. J. Langley, and E. A. Parker. 1996. Active frequency-selective surfaces. *IEE Proceedings—Microwave Antennas Propagation* 143(1):62–66.
20. Cahill, B. M. and E. A. Parker. 2001. Field switching in an enclosure with active FSS screen. *Electronics Letters* 37(4):244–245.
21. Mias, C. and J. Haur Yap. 2007. A varactor-tunable high impedance surface with a resistive-lumped-element biasing grid. *IEEE Transactions on Antennas and Propagation* 55(7):1955–1962.
22. Sievenpiper, D. F., J. H. Schaffner, H. J. Song, R. Y. Loo, and G. Tangonan. 2003. Two-dimensional beam steering using an electrically tunable impedance surface. *IEEE Transactions on Antennas and Propagation* 51(10):2713–2722.
23. Mias, C. 2005. Varactor-tunable frequency selective surface with resistive-lumped-element biasing grids. *IEEE Microwave and Wireless Components Letters* 15(9):570–572.
24. Reyneta, O. and O. Acherb. 2004. Voltage controlled metamaterials. *Applied Physics Letters* 84(7):1198–1200.
25. Hum, S. V., M. Okoniewski, and R. J. Davies. 2005. Realizing an electronically tunable reflectarray using varactor diode-tuned elements. *IEEE Microwave and Wireless Components Letters* 15(6):422–424.
26. Lee, H.-J., R. J. Langley, and K. L. Ford. 2007. Tunable active EBG. *Second European Conference on Antennas and Propagation*, Edinburgh, pp. 11–16.
27. Schoenlinner, B., A. Abbaspour-Tamijani, L. C. Kempel, and G. M. Rebeiz. 2004. Switchable low-loss RF MEMS Ka-band frequency-selective surface. *IEEE Transactions on Microwave Theory and Techniques* 52(11):2474–2481.
28. Zendejas, J. M., J. P. Gianvittorio, Y. Rahmat-Samii, and J. W. Judy. 2006. Magnetic MEMS reconfigurable frequency-selective surfaces. *Journal of Microelectromechanical Systems* 15(3):613–622.
29. Coutts, G. M., R. R. Mansour, and S. K. Chaudhuri. 2007. A MEMS-tunable frequency-selective surface monolithically integrated on a flexible substrate. *IEEE/MTT-S International Microwave Symposium*, 497–500.
30. Chicherin, D., S. Dudorov, D. Lioubtchenko, V. Ovchinnikov, S. Tretyakov, and A. V. Räisänen. 2006. MEMS-based high-impedance surfaces for millimeter and submillimeter wave applications. *Microwave and Optical Technology Letters* 48(12):2570–2573.
31. Hand, T. and S. Cummer. 2007. Characterization of tunable metamaterial elements using MEMS switches. *IEEE Antennas and Wireless Propagation Letters* 6:401–404.
32. Degiron, A., J. J. Mock, and D. R. Smith. 2007. Optical control of metamaterial unit cells at microwave frequencies. *International Symposium on Signals, Systems and Electronics*, 209–212.

33. Lockyer, D. S., J. C. Vardaxoglou, and M. J. Kearney. 1999. Transmission through optically generated inductive grid arrays. *IEEE Transactions on Microwave Theory Techniques* 47(7):1391–1397.
34. Doumanis, E. T., A. A. Kontogeorgos, D. P. Korfiatis, K. -A. Th. Thoma, and J. C. Vardaxoglou. 2006. Plasma concentration and its effect on inductive grid arrays. *European Conference on Antennas & Propagation*.
35. Lockyer, D. S., J. C. Vardaxoglou, and M. J. Kearney. 1999. Plane wave transmission response of selectively doped and micromachined silicon wafers under optical illumination. *International Topical Meeting on Microwave Photonics*, 169–172.
36. Lockyer, D. S., J. C. Vardaxoglou, and G. J. Ensell. 2000. A study of doped patch and dipole antenna arrays with photonic interactions. *International Topical Meeting on Microwave Photonics*, 152–155.
37. Liang, X., D. H. Werner, and B. Weiner. 2007. A novel concept for reconfigurable frequency selective surfaces based on silicon switches. 2007. *Microwave and Optical Technology Letters* 49(1):109–114.
38. Hu, W., R. Dickie, R. Cahill, H. Gamble, Y. Ismail, V. Fusco, D. Linton, N. Grant, and S. Rea. 2007. Liquid crystal tunable mm wave frequency selective surface. *IEEE Microwave and Wireless Components Letters* 17(9):667–669.
39. Anderson, T., I. Alexeff, J. Raynolds, E. Farshi, S. Parameswaran, E. P. Pradeep, and Jyothi Hulloli. 2007. Plasma frequency selective surfaces. *IEEE Transactions on Plasma Science* 35(2):407–415.
40. De C. Lima, A. C., E. A. Parker, and R. J. Langley. 1994. Tunable frequency selective surface using liquid substrates. *Electronics Letters* 30(4):281–282.

33

Ferroelectrics as Constituents of Tunable Metamaterials

Orest G. Vendik
St. Petersburg Electrotechnical University

Svetlana P. Zubko
St. Petersburg Electrotechnical University

33.1 Introduction

At the present time, ferroelectric materials are under interest for practical applications at microwave technique. The characteristic features of the ferroelectric materials are high value of the dielectric constant and dependence of the dielectric constant on applied biasing field. The ferroelectric inclusions are used as tunable components in multifunctional metamaterials. The traditional devices such as phase shifters for steerable antenna arrays, tunable resonators and tunable filters for telecommunication, and radar systems form the area of practical applications of the ferroelectric materials. Being compared with ferrites and semiconductor, the devices based on ferroelectrics might be advantageously distinguished by more simple fabrication technology, smaller controlling circuit energy consumption, and good compatibility with high temperature superconductors (HTS).

The first attempts of practical applications of ferroelectrics were connected with experimental realization of harmonic generator [1], phase shifter [2], and microwave parametric amplifies [3,4]. Careful

investigations of the microwave dielectric properties of ferroelectric bulk samples were fulfilled by K. Bethe at Philips Research Laboratory [5]. The rectangular waveguide partially filled with a ferroelectric slab was considered as a possible version of a waveguide phase shifter. Realizations of waveguide structures with bulk ferroelectric slabs led to difficulties in matching because of a large value of the bulk dielectric constant.

The essential progress was achieved when thin ferroelectric films on dielectric substrate had been used as a part of ferroelectric microwave devices [6–12]. A set of planar structures were realized and investigated: planar capacitor, coplanar- and slot-line waveguides, and rectangular waveguide loaded with a thin ferroelectric film covered by conducting strips for delivering the biasing voltage. The first real success in microwave applications of the ferroelectric materials was realization and examining of a low noise parametric amplifier based on a thin-film $SrTiO_3$ planar capacitor. A widespread of ferroelectric microwave devices was predicted [11,12]. One can remember that at the same time new semiconductor microwave devices had been developed: low noise parametric amplifier, low noise transistor amplifier, *p–i–n* diode phase shifter. Those devices were based on a well-mastered semiconductor fabrication technology. At that period, ferroelectrics failed the competition with semiconductors because ferroelectric devices needed developing a new technology and could not provide considerably better characteristics than semiconductor devices. Concurrently, it emerged that the insertion loss of the ferroelectric films at microwave frequencies was much higher than the loss of a good quality single crystal of the same composition. The films deposited on a dielectric substrate have a defected structure. The quality of the film deposition technique had to be improved.

In 1986, HTSs have been discovered. Great efforts have been applied to develop the HTS film technology. Fortunately, the chemical nature and the crystallographic structure of HTS and ferroelectric materials are similar, and a success in HTS technology was used for a progress in the ferroelectric film technology. The epitaxial compatibility of HTS and ferroelectric films provides a possibility to realize some favorable designs based on low loss HTS transmission lines and tunable ferroelectric components. The interest in HTS applications at microwaves led to practical developing of the microwave cryoelectronics at liquid nitrogen temperature. The microwave dielectric losses of ferroelectrics like $SrTiO_3$ and $KTaO_3$ at liquid nitrogen temperature are smaller than the losses of other ferroelectric materials suitable for applications at room temperature. Thus, developing the HTS technology spurred up the new interest in ferroelectrics at microwaves [13–18].

The progress in the ferroelectric film technology and industrial demands for microwave tunable subsystems like phased array antennas and electronically tunable filters support the effort to develop room temperature ferroelectric components with relatively small microwave insertion loss. Some experts wrote that there was no reason to assert that such components will not be developed in the immediate future [19,20].

In recent publication, one can find descriptions of some prototypes of microwave components based on ferroelectric film structures. Going from laboratory prototypes to commercial production of such components is a challenge to microwave engineers who are required now to master the principles of applications of ferroelectric components at microwaves. One should pay attention to possibility to design and manufacture ferroelectric phase shifters as monolithic microwave integrated circuits [21,22], which are promising for a realization of phased-array antennas based on the ferroelectric phase shifters as low cost mass production.

During some years, the devices based on transmission lines with anomalous dispersion are under great interest [23–25]. The conventional transmission line with the positive phase velocity can be referred to as the right-handed transmission line (RHTL). One can consider such a transmission line as a network formed by a combination of series inductors and shunt capacitors. If the capacitors and inductors are interchanged (the dual transmission line), the phase velocity becomes negative and such line is referred to as the left-handed transmission line (LHTL). The combination of RHTL and LHTL is referred to as the composite right/left-handed transmission line (CRLH TL). The tuneable

capacitors can be used as the components of such lines. The ferroelectric phase shifters based on combination of transmission line sections with negative and positive dispersion can be used for designing miniature microwave devices operating in a wide frequency range, and may be considered as a novel version of the microwave devices.

The goal of this chapter is to deliver the physical foundations of ferroelectricity and to describe main properties of the ferroelectrics at microwave frequencies. Designing some microwave components based on ferroelectrics films are discussed. Phenomenological models [26–34] of a dielectric response and microwave losses [19,20,28,35] of the ferroelectric samples were used for deriving correct and simple formulas, which can be used for a design of the ferroelectric microwave components [31–34]. The formulas are used for developing CAD of ferroelectric microwave devices and subsystems.

33.2 Main Items of Ferroelectricity Physics

The goal of this section is to give the definition of ferroelectricity and to describe dielectric properties of the ferroelectric materials: appearance of spontaneous polarization, large value of dielectric constant, and dependence of the dielectric constant on temperature and applied voltage.

Dielectric response and the loss factor of a ferroelectrics will be considered for a bulk sample and for a thin-film sample.

Displacive type of ferroelectrics will be considered. The typical representatives of this type of ferroelectrics are $SrTiO_3$, $BaTiO_3$, and their solid solutions. Just these materials are used in the microwave technology. Two groups of the displacive type of ferroelectrics should be distinguished: conventional ferroelectrics and incipient ferroelectrics. The conventional ferroelectrics exhibit ferroelectric phase transition, which is characterized by the spontaneous polarization at the temperature below the temperature of the phase transition. Incipient ferroelectrics have no spontaneous polarization; however, they exhibit the strong temperature dependence of dielectric permittivity and remarkable dielectric nonlinearity.

33.2.1 Spontaneous Polarization

In Figure 33.1, the typical hysteresis loop of a ferroelectric sample is presented. Two characteristic parameters of the hysteresis loop should be distinguished: the residual spontaneous polarization P_s and the coercive force E_C. An observation of the hysteresis loop can be realized with a simple circuit including an oscilloscope (Figure 33.2). The voltage across the ferroelectric sample containing an electric charge $Q(t)$ is applied to the horizontal plates of the oscilloscope. The voltage across the linear capacitor $U_C(t)$ is proportional to the polarization of the ferroelectric sample and is applied to the vertical plates. Such a scheme was presented by Sawyer and Tower in Ref. [36]. See also Kittel's *Introduction to Solid State Physics* [37].

The spontaneous polarization is a function of thermodynamic temperature T and is zero, if $T > T_C$ (Figure 33.3). Appearance of the spontaneous polarization at $T < T_C$ is an effect of the phase transition, which separates two states of the material with the different symmetry: ferroelectric state ($T < T_C$) and paraelectric state ($T > T_C$). The temperature T_C is called the Curie temperature of the ferroelectric phase transition.

Distinguishing features of ferroelectrics are (1) spontaneous polarization, (2) very high value of dielectric permittivity, (3) dependence of dielectric permittivity on temperature, and (4) dependence of dielectric permittivity on biasing voltage.

In order to discuss the appearance of the spontaneous polarization and the dielectric nonlinearity of a ferroelectric, one should consider the phenomena in the crystal lattice of the material. The crystal

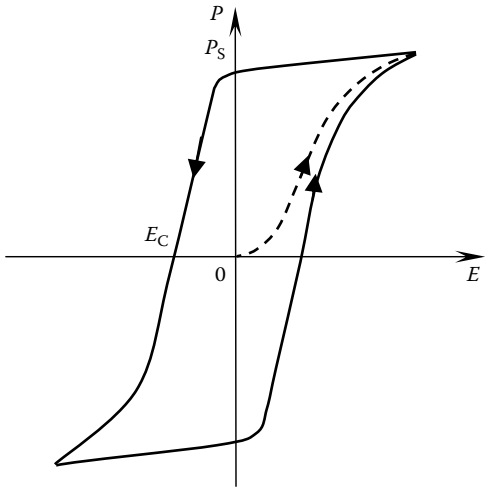

FIGURE 33.1 Ferroelectric hysteresis loop.

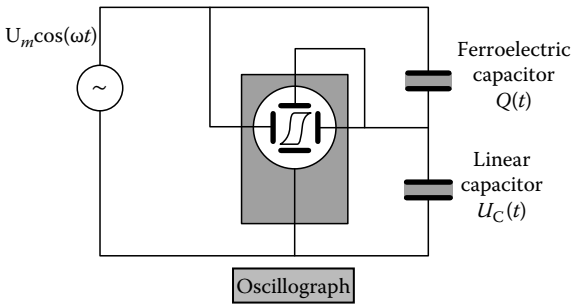

FIGURE 33.2 Diagram of measurement procedure of the ferroelectric hysteresis loop.

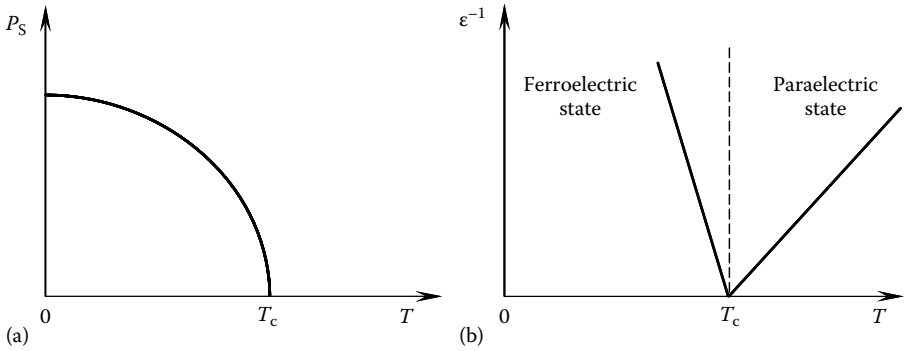

FIGURE 33.3 Temperature dependence of spontaneous polarization (a) and inverse dielectric permittivity of ferroelectrics demonstrating the second-order phase transition (b).

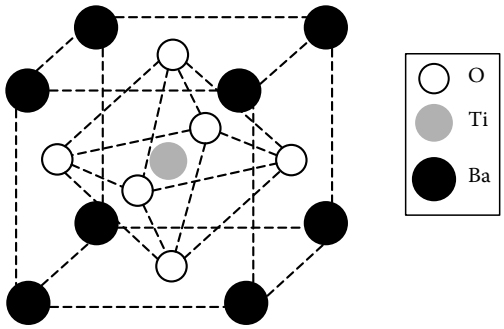

FIGURE 33.4 Crystal lattice cell of $BaTiO_3$.

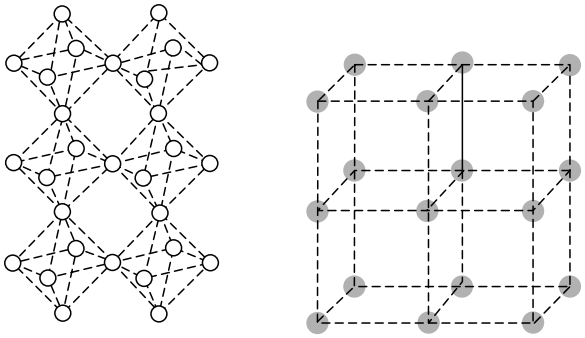

FIGURE 33.5 Oxygen sublattice (a) and titanium sublattice (b).

lattice cell of a typical ferroelectric, barium titanate ($BaTiO_3$) is shown in Figure 33.4. The crystal structure of barium titanate is called the perovskite crystal structure. The perovskite is a mineral $CaTiO_3$, which has the same structure as $BaTiO_3$, but is not a ferroelectric. Polarization of the barium titanate is a result of displacement of Ti and O sublattices. That is why $BaTiO_3$ is called the displacement type ferroelectric. The structure of Ti and O sublattices is shown in Figure 33.5.

Mutual displacement of Ti and O sublattices is followed by a formation of an electric dipole (Figure 33.6) and polarization of the crystal. The polarization is defined as

$$P = q\,x/V_c, \tag{33.1}$$

where
q is the charge
x is the displacement
V_c is the volume of the crystal cell

In order to give rise to the mutual displacement of Ti and O sublattices, the energy should be applied. The potential energy as a function of the mutual displacement of Ti and O sublattices x is illustrated in Figure 33.7, where three different forms of the potential energy diagram are presented:

(a) Ferroelectric state: $T < T_C$
(b) Nonlinear paraelectric state: $T \cong T_C$
(c) Linear dielectric state: $T > T_C$

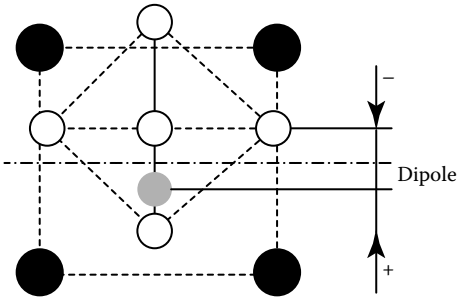

FIGURE 33.6 Mutual displacement of Ti and O sublattices.

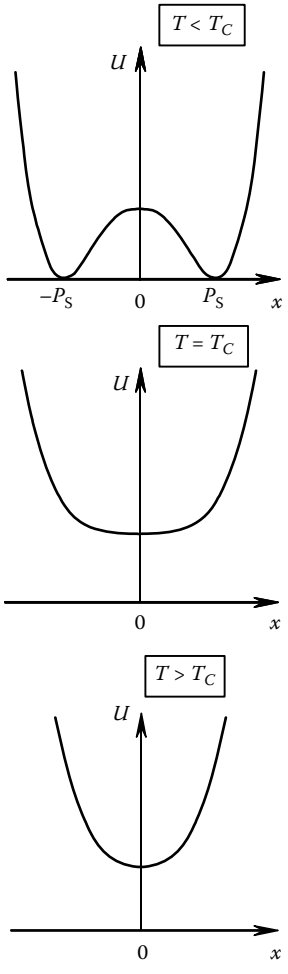

FIGURE 33.7 Coordinate dependence of Ti ion potential energy.

In the case (a), the potential energy diagram has two minima and consequently two equilibrium states of the crystal lattice, which correspond to the different signs of the spontaneous polarization.

In the case (c), the potential energy diagram fits the Hook's law:

$$U(x) = kx^2. \tag{33.2}$$

In this case, the force between sublattices is proportional to the displacement (deformation):

$$F(x) = 2kx. \tag{33.3}$$

That means that the polarization is proportional to the applied electric field, that the dielectric response of the material is linear.

In the case (b), the potential energy diagram does not obey Hook's law and the dielectric response of the material is nonlinear.

33.2.2 Second-Order Phase Transition

For authentic description of appearance of the spontaneous polarization in a ferroelectric sample, the Landau theory of the second-order phase transition should be used. The main concepts of the theory are as follows:

1. Order parameter is introduced as a main feature of the phase transition.
2. Order parameter of a ferroelectric is the spontaneous polarization.
3. Free energy density of a sample is taken as a power series with respect to the polarization:

$$F(P, T) = \frac{1}{2}a(T)\,P^2 + \frac{1}{4}b(T)\,P^4, \tag{33.4}$$

where $a(T)$ and $b(T)$ are the expansion coefficients.

Equation 33.4 for free energy density, as a function of a ferroelectric polarization, is known as the Ginzburg–Devonshire equation.

The system is in equilibrium, if

$$\partial F(P, T)/\partial P = 0.$$

That is followed by the equation:

$$P[a(T) + b(T)P^2] = 0.$$

The solution to the equation is

$$P(T) = \begin{cases} 0 & \text{for } \frac{a(T)}{b(T)} > 0 \\ \pm\sqrt{-\frac{a(T)}{b(T)}} & \text{for } \frac{a(T)}{b(T)} < 0. \end{cases} \tag{33.5}$$

The dependence of the polarization on temperature described by Equation 33.5 corresponds to the graph presented in Figure 33.3a. Appearance of the polarization in the point $T = T_C$ is an exhibition of the second-order phase transition.

The dielectric permittivity of a ferroelectric sample can be found in the following way. The electric field strength and the inverse dielectric susceptibility are presented as follows:

$$E(P, T) = \frac{\partial F(P, T)}{\partial P}; \quad \chi^{-1} = \frac{\partial E(P, T)}{\partial P}.$$

For a ferroelectric sample with a high permittivity, the inverse dielectric susceptibility is practically equal to the inverse permittivity. Thus, the permittivity can be found as

$$\varepsilon(T) = \left[\frac{\partial^2 F(P,T)}{\partial P^2}\right]^{-1}. \tag{33.6}$$

Taking after Landau, we suppose that

$$a(T) = \alpha_T(T - T_C), \quad \alpha_T = 1/C_C, \tag{33.7}$$

where C_C is the Curie constant.

And next:

$$b(T) = \beta = \text{const}. \tag{33.8}$$

On substituting Equation 33.4 into Equation 33.6 and using the solution (Equation 33.5), we find:

$$\varepsilon(T)^{-1} = \begin{cases} \frac{1}{C_C}(T - T_C) & \text{for } T > T_C \\ \\ -\frac{2}{C_C}(T - T_C) & \text{for } T > T_C \end{cases}. \tag{33.9}$$

This is so-called Curie–Weiss law. The dependence of the dielectric constant on temperature in form (Equation 33.9) is adequate to the perfect defectless ferroelectric crystal. Such dependence is shown in Figure 33.8a for the case of a high-quality ceramics sample of solid solution $Ba_xSr_{1-x}TiO_3$ (BSTO).

33.2.3 Incipient Ferroelectrics

As distinct from $BaTiO_3$, the crystals of $SrTiO_3$ and $KTaO_3$ do not manifest the spontaneous polarization at any temperature although they demonstrate a very high dielectric permittivity and a strong nonlinear dielectric response. The crystals of $SrTiO_3$ and $KTaO_3$ are called the incipient ferroelectrics.

Behavior of the incipient ferroelectrics at low temperature is determined by the quantum oscillations of the crystal lattice [38]. The quantum consideration was used by Barrett, who derived the following formula for the temperature dependence of the dielectric constant:

$$\varepsilon(T) = \frac{C_C}{T_C \eta(T)}; \quad \eta(T) = \frac{1}{2}\frac{T_1}{T_C}\frac{1}{\tanh(T_1/2T)} - 1, \tag{33.10}$$

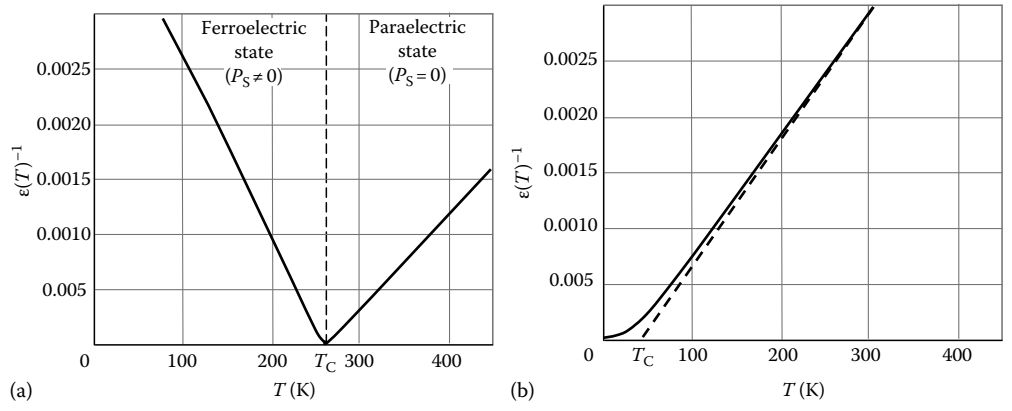

FIGURE 33.8 Temperature dependence of inverse dielectric permittivity of (a) typical ferroelectrics (BSTO) and (b) incipient ferroelectrics ($SrTiO_3$).

where T_1 is a characteristic temperature, which selects out the low temperature region where the quantum effects are important and the Curie–Weiss law is not fulfilled.

Later, the equation for $\eta(T)$ was derived in the form of Debye integral [26,39,40]:

$$\eta(T) = \left(\frac{\theta_F}{T_c}\right) \Psi\left(\frac{T}{\theta_F}\right) - 1, \tag{33.11}$$

where

$$\Psi(z) = \frac{1}{4} + z^2 \int_0^{1/z} x/[\exp(x) - 1]\mathrm{d}x, \quad z = \frac{T}{\theta_F}. \tag{33.12}$$

$\theta_F = h\nu_F/k_B$ is an analog of the Debye temperature for the sublattice oscillations, which are responsible for the ferroelectric polarization, ν_F is the cut-off frequency for the Debye spectrum of the crystal sublattice mentioned.

Using reasonable approximation, Equation 33.12 can be rewritten in the more simple form [26,41]:

$$\eta(T) = \frac{\theta_F}{T_c}\sqrt{\frac{1}{16} + \left(\frac{T}{\theta_F}\right)^2} - 1. \tag{33.13}$$

In the temperature region $0 \leq (T/\theta_F) \leq 2$, approximation error in comparison with the Debye integral is less than 0.1%.

The dependence of inverse dielectric permittivity on temperature for single crystal of $SrTiO_3$ is illustrated in Figure 33.8b.

In the case of room temperature ferroelectric ($T \gg \theta_F$), Equations 33.11 through 33.13 are transformed into the following simple formula:

$$\eta(T) = \frac{T}{T_C} - 1 \quad \text{for } T > T_C. \tag{33.14}$$

The Curie constant of the sample of solid solution BSTO is a function of the composition factor x (relative concentration of Ba). Figure 33.9 shows T_C of BSTO as a function of x. The data presented were obtained by many groups of investigators [5,42–44]. Alongside with the high-quality single crystals, samples of ceramics of the same compound are frequently used. Experimental data obtained for different samples of BSTO ceramics show that T_C of ceramics is a little bit higher than T_C of the BSTO high-quality single crystals (Figure 33.9). Ceramics are characterized by the fluctuations of composition. Grains of a ceramic sample can have different stoichiometry, which means that the distribution of Ba and Sr ions along the sample is inhomogeneous. This is followed by the presence of pores and cavities and by some extension of grains. The extension of the grains in the ceramic sample is followed by increasing the Curie temperature of the material. The same can be said about partially defected crystals. It is remarkable that Curie temperatures of a higher quality single crystal and partially defected crystal or ceramic samples coincide at $x = 0$ and $x = 1$, but diverge at $x = 0.5$.

33.2.4 Dielectric Response of a Ferroelectric Sample

Figure 33.10 shows a sandwich capacitor formed as a planar layer of a ferroelectric with normal metal or superconducting electrodes. The thickness of the electrodes as well as fringing fields is not taken into account. Ordinary experimental technique consists of applying to the capacitor small "ac" and large "dc" voltages simultaneously. The ac voltage is used for measurement of the dielectric characteristics under the dc bias. Let us take into account that in the case of zero volume charge density the displacement $D(x)$ does not depend on the coordinates. Thus:

$$D = D_{dc} + D_{ac}, \tag{33.15}$$

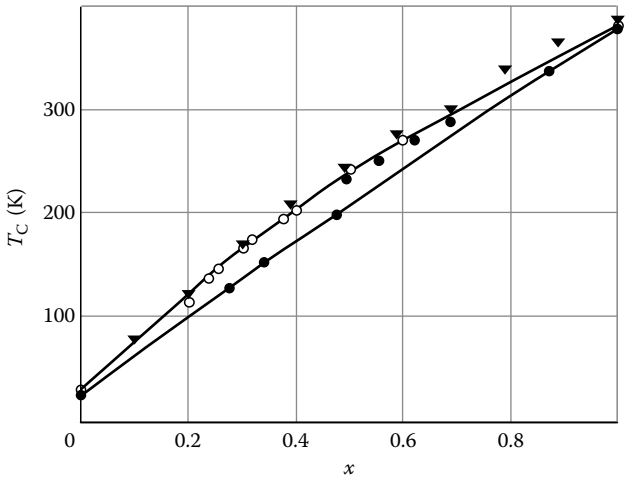

FIGURE 33.9 Dependence of Curie temperature of BSTO on barium concentration. The following references were used: filled circles [5] (single crystals); triangle [43]; open circles [44] (ceramics).

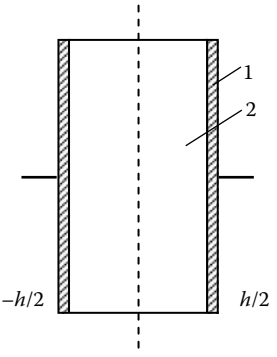

FIGURE 33.10 Parallel-plate capacitor as a simplified general structure, 1, electrodes; 2, ferroelectric layer.

where the terms D_{dc} and D_{ac} are connected with the components of the charge Q_{dc} and Q_{ac} on the capacitor electrodes constant and alternating in time respectively:

$$D_{dc} = \frac{Q_{dc}}{S}, \quad D_{ac} = \frac{Q_{ac}}{S}, \tag{33.16}$$

where S is the area of the capacitor electrodes.

For the ac components of the polarization, one has

$$P_{ac}(x) = \frac{Q_{ac}}{S} - \varepsilon_0 E_{ac}(x). \tag{33.17}$$

Let us find Q_{dc} as a function of the dc voltage U_B applied to the electrodes of the capacitor. In order to do so, the Ginzburg–Devonshire Equation 33.4 should be used. Taking derivative with respect to P, one obtains

$$Q + \frac{Q^3 \varepsilon(T)}{(D_N S)^2} = \varepsilon_0 \varepsilon(T) \frac{SU}{h}, \tag{33.18}$$

where D_N is the normalizing displacement; Equation 33.16 is taken into account.

It is well-known that the free energy minima correspond to the roots of the cubic equation with respect to the ferroelectric polarization. For dimensionless variables, Equation 33.18 can be written as follows:

$$y^3 + 3\eta(T)y - 2\xi(E) = 0, \tag{33.19}$$

where

$$y = \frac{Q_{dc}}{D_N S}\sqrt{3\varepsilon_{00}}, \tag{33.20}$$

$$\xi(E) = \sqrt{\left(\frac{E}{E_N}\right)^2 + \xi_S^2}, \tag{33.21}$$

$$E_N = \frac{2D_N}{\varepsilon_0(3\varepsilon_{00})^{3/2}}. \tag{33.22}$$

Here, y is the reduced polarization, which is a function of the temperature T and the biasing field E. Parameter $\eta(T)$ is introduced with Equation 33.13 or 33.14. The additional model parameters are used: ε_{00} is the analog of the Curie constant; E_N is the normalizing biasing field; ξ_S is the statistical dispersion of the biasing field.

A short comment about the parameter ξ_S is given in Ref. [26]. Real (defected) crystals and ceramic samples are characterized by the presence of built-in electric field and mechanical strains, which are generated by defects, nonhomogeneities, and structure damages. The effects caused by the defects can be quantitatively described by the parameter ξ_S, which may be considered as a characteristic of the material quality. For single crystals $\xi_S = 0.01, \ldots, 0.05$, and for ceramic samples $\xi_S = 0.5, \ldots, 1.5$.

33.2.4.1 Dielectric Response in Ferroelectric and Paraelectric States

If the following inequality is fulfilled

$$\xi(E)^2 + \eta(T)^3 \geq 0. \tag{33.23}$$

Equation 33.19 has one real root, which gives a simple relation between y and ξ under the given η. From the physical point of view, the single root to Equation 33.19 corresponds to the absence of the spontaneous polarization and the presence of the polarization induced by the biasing field. In other words, the inequality (Equation 33.23) determines the conditions under which the sample is in the paraelectric state.

Under the condition:

$$\xi(E)^2 + \eta(T)^3 < 0. \tag{33.24}$$

Equation 33.19 has three real roots. One of the roots is connected with an unstable state and therefore has no physical sense.

For $\xi = 0$, the roots corresponding to the stable ferroelectric and paraelectric states of the sample are

$$\begin{aligned} y_{1,2} &= \pm\sqrt{-3\eta(T)}. \\ y_3 &= 0. \end{aligned} \tag{33.25}$$

The roots $y_{1,2}$ correspond to the spontaneous polarization. Existence of the spontaneous polarization determines the ferroelectric state of the sample.

Let us take the normalized polarization as a root of Equation 33.19 for the paraelectric state. The square of the normalized polarization is read as

$$y(E,T)^2 = [(\xi(E)^2 + \eta(T)^3)^{1/2} + \xi(E)]^{2/3} + [(\xi(E)^2 + \eta(T)^3)^{1/2} - \xi(E)]^{2/3} - 2\eta(T). \tag{33.26}$$

Differentiating Equation 33.18 with respect to U, one obtains the capacitance of the bulk capacitor with respect to the small alternating voltage:

$$C(U) = (\varepsilon_0 S/h)\left[(\varepsilon(T))^{-1} + \frac{3{Q_{dc}}^2}{(D_N S)^2}\right]^{-1}. \tag{33.27}$$

Using the notations (Equation 33.20 and 33.22), one can rewrite Equation 33.27 as follows:

$$C(U) = \left(\frac{\varepsilon_0 \varepsilon_{00} S}{h}\right)\left[\eta(T) + y^2\right]^{-1}, \tag{33.28}$$

or taking into account Equation 33.26, one obtains C in the form:

$$C(E,T) = \frac{\varepsilon_0\ \varepsilon_{00} S/h}{\left[(\xi(E)^2 + \eta(T)^3)^{1/2} + \xi(E)\right]^{2/3} + \left[(\xi(E)^2 + \eta(T)^3)^{1/2} - \xi(E)\right]^{2/3} - \eta(T)}. \tag{33.29}$$

Thus, the effective dielectric constant of the ferroelectric in the paraelectric state is read as a follows:

$$\varepsilon(E,T) = \frac{\varepsilon_{00}}{G(E,T)}, \tag{33.30}$$

where

$$G(E,T) = [(\xi(E)^2 + \eta(T)^3)^{1/2} + \xi(E)]^{2/3} + [(\xi(E)^2 + \eta(T)^3)^{1/2} - \xi(E)]^{2/3} - \eta(T), \tag{33.31}$$

when the condition (Equation 33.23) is fulfilled.

The solution to Equation 33.19 was found under the condition (Equation 33.23) by using Cardano's formula for one real root of the cubic equation. For the sample in the ferroelectric state under the condition (Equation 33.24), there is no such simple analytical equation for the solution to Equation 33.19. The numerical solution to Equation 33.19 was approximated by the following formula:

$$G(E,T) = \xi(E)^{2/3} + \frac{1}{4}[\xi(E)^2 + \eta(T)^3]\xi(E)^{1/3} - 2\eta(T), \tag{33.32}$$

when the condition (Equation 33.24) is fulfilled.

Figure 33.11 illustrates the dependence of the dielectric permittivity of a ferroelectric sample BSTO for $x = 0.5$ and $\xi_S = 1$ as a function of temperature and biasing field simulated with Equations 33.30 through 33.32. The typical values of the model parameters for BSTO samples are presented in Table 33.1.

33.2.4.2 Stationary (dc) Ferroelectric Polarization

In the frame of the model considered, the stationary ferroelectric polarization is presented as

$$P(E,T) = \frac{3}{2}\varepsilon_0 \varepsilon_{00}(x) E_N(x) y(E,T), \tag{33.33}$$

where $y(E,T)$ is a normalized value of the ferroelectric polarization.

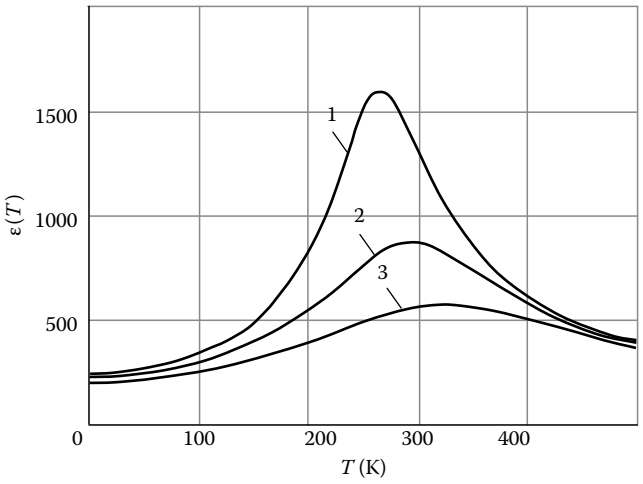

FIGURE 33.11 Temperature dependence of dielectric permittivity for biasing field $E = 0$ (1), 100 kV/cm (2), and 200 kV/cm (3).

TABLE 33.1 Model Parameters for BSTO Samples

x	T_C (K)	θ_F (K)	D_N (C/m^2)	E_N (kV/cm)	ε_{00}	ξ_S
0	42	175	4.2	19	2080	0.018
0.5	245	175	4.2	226	400	1.0

In accordance with Equations 33.31 through 33.33, the normalized value of the ferroelectric polarization is given by the following equation:

1. For the case $a(E, T) \geq 0$

$$y(E, T) = \left(a(E, T)^{1/2} + \xi(E)\right)^{1/3} - \left(a(E, T)^{1/2} - \xi(E)\right)^{1/3}. \tag{33.34}$$

2. For the case $a(E, T) < 0$

$$y(E, T) = \frac{1}{4}a(E, T)\xi(E)^{1/3} + \xi(E)^{2/3} - 3\eta(T). \tag{33.35}$$

One can see from Equations 33.33 and 33.34 that for $\xi > 0$, the averaged polarization is not equal to zero at any temperature even under zero-biasing field. That kind of polarization should be considered as the residual ferroelectric polarization in the ferroelectric sample in a paraelectric state [28,41]. Dependence of the averaged stationary ferroelectric polarization of the solid solution BSTO on temperature for different values of composition parameters x is shown in Figure 33.12. The residual polarization of a sample in the paraelectric state shown in Figure 33.12a is caused by the charged defects. In Figure 33.12b, simulation of the polarization in ferroelectric state of the $BaTiO_3$ ($x = 1$) as a function of temperature is shown in comparison with the experimentally obtained data [45]. Fracture of the experimental curve corresponds to the phase transitions between the different crystallographic structures of $BaTiO_3$. In the case of the solid solution BSTO for $x < 0.8$, the polarization curve becomes smooth and near to the form of the simulated curve.

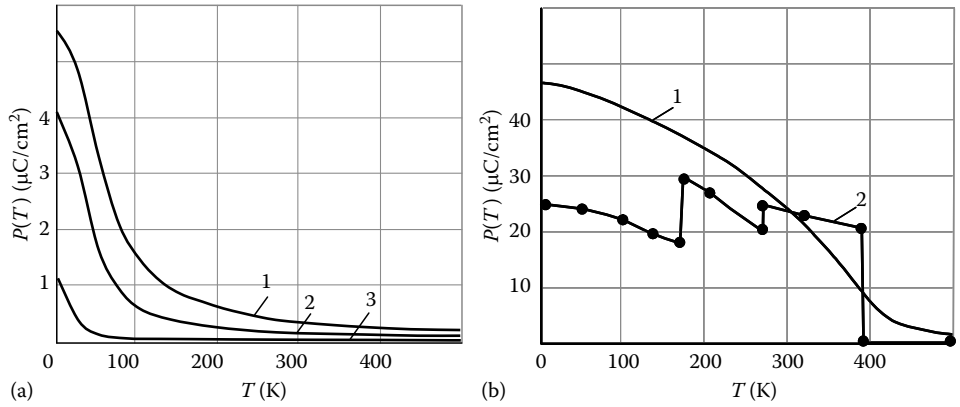

FIGURE 33.12 Temperature dependence of residual polarization for $SrTiO_3$ (a): curves 1, 2, and 3 correspond to $\xi_S = 0.7, 0.3, 0.02$; and spontaneous polarization for BaTiO3 (b): simulation (curve 1) and experimental data (curve 2).

33.2.5 Curie Temperature and the Maximum Dielectric Permittivity Temperature

Three temperature points are important for characterization of the properties of a ferroelectric sample: (1) the Curie temperature, (2) temperature of the maximum dielectric permittivity, and (3) ferroelectric phase transition temperature.

The point at the temperature scale, in which the spontaneous polarization turns into zero, is the point of the phase transition. This point determines the Curie temperature of the sample of the perfect crystal structure. For a real (slightly defected) crystal or ceramics, all three mentioned above temperatures are different.

33.2.5.1 Curie Temperature

For a bulk ferroelectric sample (defected crystals, ceramics, incipient ferroelectrics) of different quality, for the case $T \gg T_C, \theta_F$, one may write the following equation:

$$\varepsilon^{-1}(T) = \varepsilon_{00}^{-1}\left(\frac{T}{T_C} - 1\right). \tag{33.36}$$

Equation 33.36 describes the tangential to the curve $\varepsilon^{-1}(T)$ depicted in the region $T \gg T_C, \theta_F$. The point of crossing the tangential and the temperature axis determines the Curie temperature. The described procedure is a standard way of the experimental determination of the Curie temperature. However, in order to obtain an acceptable accuracy, one should measure $\varepsilon^{-1}(T)$ up to a considerably higher temperature.

33.2.5.2 Temperature of the Maximum Dielectric Permittivity

The maximum dielectric permittivity temperature T_m of a defected crystal or ceramics can be found from the solution to equation $d\varepsilon(T)/dT = 0$:

$$T_m = T_C\sqrt{\left[\left(\frac{1}{2}\xi(E)\right)^{2/3} + 1\right]^2 - \left(\frac{\theta_F}{4T_C}\right)^2}. \tag{33.37}$$

In the case of $x > 0.5$, one has $T_C > \theta_F$ and (Equation 33.37) can be rewritten in the form:

$$T_m = T_C\left[1 + \left(\frac{1}{2}\xi(E)\right)^{2/3}\right]. \tag{33.38}$$

The external biasing field, as well as the built-in electric field and the mechanical strains, displaces the temperature maximum of the dielectric permittivity. Maximum of the dielectric permittivity of BSTO samples takes place at the temperature higher than the Curie temperature of the material ($T_m \geq T_C$). The equality ($T_m = T_C$) can take place only in the case of a perfect crystal. For a high-quality incipient ferroelectric crystal ($x = 0$), one can observe $T_m = 0$.

33.2.5.3 Ferroelectric Phase Transition Temperature

It can be shown that for the case $\xi \neq 0$ spontaneous polarization appears as a jump. The application of an external field transforms the second-order phase transition into the first-order phase transition. The temperature of the phase transition as a function of the external or built-in biasing field can be found under the condition $\xi(E)^2 + \eta(T)^3 = 0$, which gives

$$T_C' = T_C\sqrt{(1 - \xi^{2/3})^2 - \left(\frac{\theta_F}{4T_C}\right)^2}. \tag{33.39}$$

For $x > 0.5$:

$$T_C' = T_C(1 - \xi^{2/3}). \tag{33.40}$$

Summarizing the results exhibited in Equations 33.36 through 33.40, one can write the following line of inequalities:

$$T_C' < T_C < T_m, \tag{33.41}$$

where
- T_C' is the temperature of the phase transition in a real slightly defected sample
- T_C is the Curie temperature of a perfect crystal
- T_m is the temperature of the maximum of the dielectric permittivity

The line of inequalities (Equation 33.41) is illustrated by Figure 33.13.

33.2.6 Nonlinearity of the Dielectric Response

Ferroelectric materials are under great interest due to its dielectric nonlinearity. Both typical ferroelectrics and incipient ferroelectrics demonstrate strong nonlinear dependence of the dielectric permittivity on the applied electric field (see Figure 33.14). Under the applied field, the dielectric permittivity decreases and the maximum of permittivity is shifted to higher temperatures. Nonlinearity of ferroelectrics allows building electrically tunable microwave devices.

33.3 Dielectric Response of Thin Films (Size Effect)

33.3.1 Size Effect

When the characteristic size of a sample of some material (the thickness of the film or the size of polycrystalline film grains) turns out to be smaller than some critical value, the properties of material

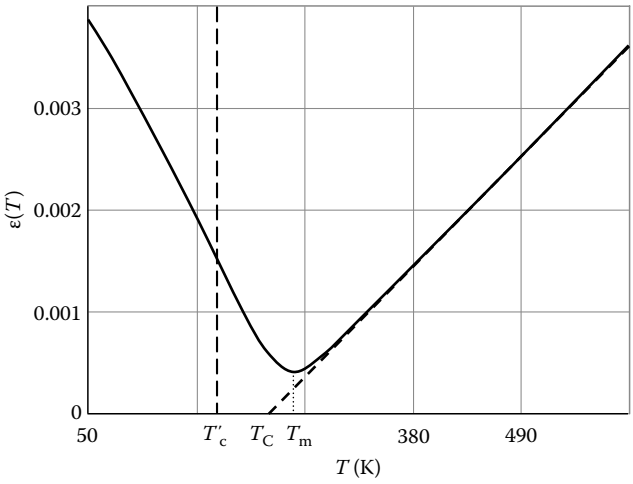

FIGURE 33.13 Temperature dependence of inverse dielectric permittivity of a real ferroelectric sample.

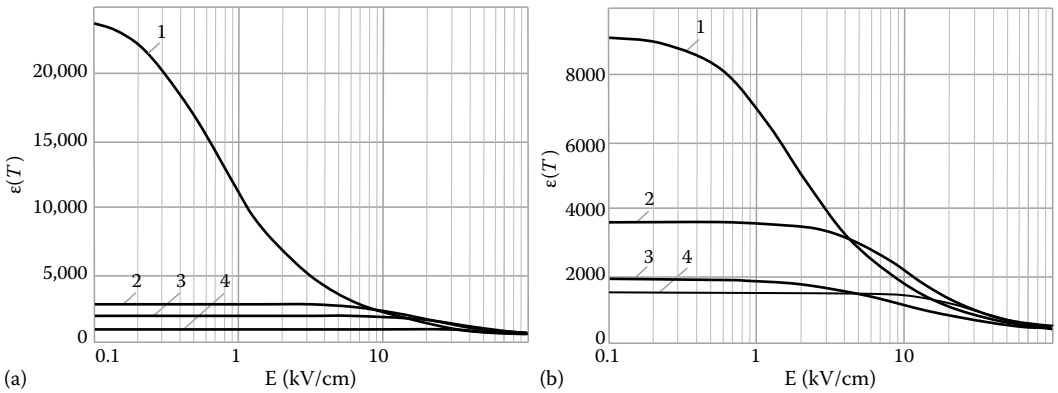

FIGURE 33.14 Dielectric permittivity of $SrTiO_3$ as a function of dc biasing field at different temperatures: T = 4.2 K(1), T = 60 K(2), T = 78 K(3), T = 140 K(4) for ξ_S = 0.02(a) and dielectric permittivity of $Ba_{0.65}$ $Sr_{0.35}$ TiO_3 as a function of dc biasing field at different temperatures: T = 230 K(1), T = 260 K(2), T = 290 K(3), T = 340 K(4) for ξ_S = 1 (b).

change significantly [46]. This phenomenon is called size effect. In the case of ferroelectric materials, the dependence of dielectric permittivity of the sample on its size (especially the thickness of a ferroelectric film) is of primary interest (Figure 33.15). The simplest explanation of the size effect is based on a supposition about existence of strongly defected or chemically alien region between principal ferroelectric layer and electrode.

In this section, the interface between ferroelectric and electrode material will be taken into account as a pure separation between two different crystal lattices without specific inclusions or chemical impurities. In the frame work of the pure interface between the ferroelectric and electrode material in parallel-plate capacitor, various reasons were suggested to explain the size effect phenomenon: (1) the correlation of the ferroelectric polarization and freezing of the dynamic polarization on the electrode surface [27,48,49], (2) the formation of a thin subelectrode layer of a nonferroelectric polarization (so-called "dead" layer model) [50], (3) the contribution of the semiconductor Schottky barrier near the electrode to the field distribution. In agreement with some previous considerations [50], no

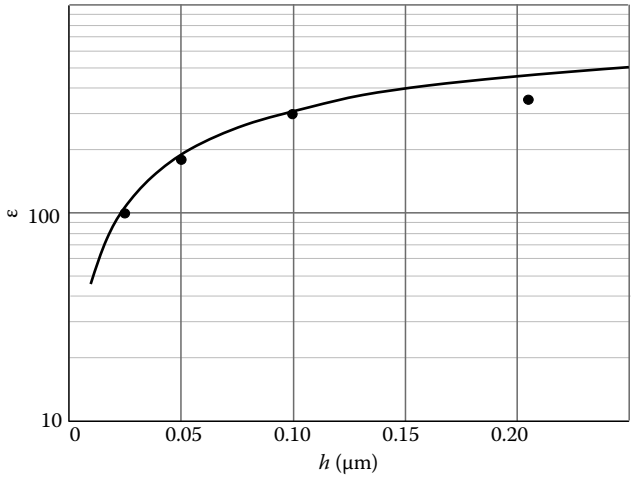

FIGURE 33.15 Effective dielectric constant of a thin film $Ba_{0.5}Sr_{0.5}TiO_3$ at room temperature as a function of the film thickness. The curve is simulated by formula (Equation 33.30); the points are taken from Ref. [47].

charge transfer through the interface between the ferroelectric and electrode material in parallel-plate capacitor will be taken into account.

33.3.1.1 Correlation of the Ferroelectric Polarization

The correlation model is based on the concept of the spatial correlation of the dynamic polarization inside a ferroelectric sample, which is followed by a nonlocal connection between the electric field and the ferroelectric polarization. The parameter responsible for the manifestation of the size effect is the correlation radius, which is generally found from the dispersion relation for the ferroelectric mode determined by neutron inelastic scattering. The experimental dependencies (points) of the frequencies of the longitudinal and transverse optical modes on the wave number at $T = 296\,\mathrm{K}$ are shown in Figure 33.16 [51].

As follows from the equation of motion of the ion-polarization vector, the spatial dispersion of the longitudinal and transverse modes in a medium of arbitrary symmetry is determined by the correlation tensor of rank 4 [52].

The dispersion equation for the optical modes in a cubic medium has the form [52,53]:

$$\begin{aligned}&\left\{\left[\omega_{\mathrm{OT}}^2(0,T)-\omega^2+s_{\mathrm{t}}\right]\left(a_{\mathrm{t}}k^2-\omega^2\right)-k^4v_{\mathrm{t}}^2\right\}^2\\&\times\left\{\left[\omega_{\mathrm{OL}}^2(0,T)-\omega^2+s_{\mathrm{L}}\right]\left(a_{\mathrm{L}}k^2-\omega^2\right)-k^4v_{\mathrm{L}}^2\right\}=0\end{aligned},\tag{33.42}$$

where

$$\begin{aligned}&s_{\mathrm{t}}=\frac{1}{A(T)}\lambda_3\omega_{\mathrm{OT}}^2(0,T),\quad s_{\mathrm{L}}=\frac{3\varepsilon_\infty(\varepsilon(T)-\varepsilon_\infty)}{\varepsilon(T)(\varepsilon_\infty+2)}\lambda_1\omega_{\mathrm{OL}}^2(0,T),\\&v_{\mathrm{t}}^2=\frac{1}{A(T)}\cdot\frac{\varepsilon_0}{\rho_{\mathrm{r}}}\omega_{\mathrm{OT}}^2(0,T)\theta_3^2,\quad v_{\mathrm{L}}^2=\frac{3\varepsilon_\infty(\varepsilon(T)-\varepsilon_\infty)}{\varepsilon(T)(\varepsilon_\infty+2)}\cdot\frac{\varepsilon_0}{\rho_{\mathrm{r}}}\omega_{\mathrm{OL}}^2(0,T)\theta_1^2.\end{aligned}\tag{33.43}$$

$$a_{\mathrm{t}}=\frac{c_3}{\rho_{\mathrm{r}}};\quad a_{\mathrm{L}}=\frac{c_1}{\rho_{\mathrm{r}}};\quad A(T)=\frac{(\varepsilon_\infty+2)}{3(\varepsilon(T)-\varepsilon_\infty)}.\tag{33.44}$$

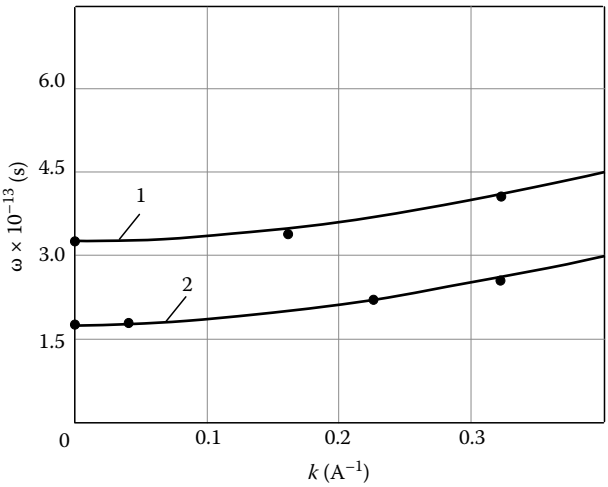

FIGURE 33.16 Dependence of the frequency of the longitudinal (curve 1) and transverse (curve 2) optical modes on the wave number k[100] at $T = 296$ K for $SrTiO_3$.

Here, T is temperature; $\varepsilon(T)$ (see Equations 33.30 through 33.32) and ε_∞ are the values of permittivity corresponding to the frequencies $\omega \ll \omega_i$, $\omega \gg \omega_i$, respectively (ω_i is the eigenfrequency of the ionic component of polarization); ε_0 is permittivity of free space; ρ_r is the density of material; θ_1 and θ_3 are the tensor components responsible for the relationship between nonuniform mechanical displacement and polarization; c_1 and c_3 are the elasticity–tensor components.

The components λ_1, λ_2, and λ_3 are referred to as the correlation parameters of a material. They are the nonzero components of the correlation tensor for a medium with a cubic structure (to which a ferroelectric crystal in a paraelectric phase belongs). The connection of λ_1, λ_2, and λ_3 with components of the fourth-order correlation tensor for the medium is as follows:

$$\lambda_1 = \lambda_{xxxx} = \lambda_{yyyy} = \lambda_{zzzz}, \lambda_2 = \lambda_{xxzz} = \lambda_{yyxx} = \lambda_{zzyy} = \lambda_{zzxx} = \lambda_{xxyy} = \lambda_{yyzz}, \lambda_3 = \lambda_{xyxy} = \lambda_{yzyz} = \lambda_{zxzx}.$$

Excluding from Equations 33.42 through 33.44, the connection between the acoustic and optical branches ($\nu_t \to 0$, $\nu_L \to 0$) [52,53], we obtain the dispersion equations for the transverse (ω_{OT}) and longitudinal (ω_{OL}) optical modes for the crystallographic direction [100] of the vector k:

$$\begin{aligned} \omega_{OT}(k, T) &= \sqrt{\omega_{OT}^2(0, T) + \omega_{OT}^2(0, T) A^{-1}(T) \lambda_3 k^2} \\ \omega_{OL}(k, T) &= \sqrt{\omega_{OL}^2(0, T) + \omega_{OL}^2(0, T) A^{-1}(T) \varepsilon_\infty \varepsilon(T)^{-1} \lambda_1 k^2} \end{aligned}. \tag{33.45}$$

The curves in Figure 33.16 are plotted by using Equation 33.45. The values of the correlation parameters for the longitudinal (λ_1) and transverse (λ_3) waves used in the calculation were determined by processing the experimental data on the dependence of the transverse mode frequency on the wave vector (circles) and the temperature dependence of the permittivity of $SrTiO_3$ [52–54]. The value of ε_∞ was determined from the refractive index n. At optical frequencies, $n \cong 3.5$ and $\varepsilon_\infty = n^2 \cong 12$. The values of correlation parameters for ferroelectric materials are presented in Table 33.2.

The spatial distribution of the polarization in a ferroelectric layer is described by a second-order differential equation derived from the expansion of the free energy in the order parameter (polarization in the case under consideration). In accordance with Landau theory of phase transitions, the

TABLE 33.2 Correlation Parameters of Ferroelectrics

Material	λ_1 (Å^2)	λ_3(Å^2)
$SrTiO_3$ [52]	3.5	0.17
$KTaO_3$ [55]	53.7	0.47

free energy density of a ferroelectric can be written in the following form [56]:

$$F(P,T) = \frac{1}{2}a\,P^2 + \frac{1}{4}b\,P^4 + \delta\,|\mathrm{grad}\,P|^2\,. \tag{33.46}$$

The spontaneous polarization is determined in Equation 33.46 as a function of coordinates. Being a function of coordinates, the polarization must obey boundary conditions.

For one-dimensional (1D) approach, Equation 33.46 without the term responsible for the nonlinearity of the material can be transformed as follows [48,54]:

$$-2\lambda_1\frac{d^2P(x)}{dx^2} + \frac{P(x)}{\varepsilon(T)} = \varepsilon_0 E(x), \tag{33.47}$$

where

P is the polarization
$\varepsilon(T) = \varepsilon_{00}/\eta(T)$ is the permittivity of a bulk material in the case of uniform polarization
$\eta(T)$ is given by Equation 33.13
E is the biasing field

A solution to Equation 33.47 for a medium infinite in the direction x, i.e., with the boundary conditions

$$\frac{dP(x)}{dx}\Big|_{x\to\infty} = 0\,; \quad \frac{dP\,(x)}{dx}\Big|_{x\to-\infty} = 0 \tag{33.48}$$

can be written in the integral form:

$$P(x) = \int_{-\infty}^{\infty} K\,(x-x')E\,(x')dx' \tag{33.49}$$

with the kernel

$$K\,(x-x) = K\exp\left(-\frac{|x-x'|}{\rho(T)}\right), \tag{33.50}$$

where $K = \varepsilon_0\varepsilon(T)/2\rho(T)$ and $\rho(T)$ is the correlation radius:

$$\rho(T) = \sqrt{\varepsilon(T)\lambda}. \tag{33.51}$$

Figure 33.17 shows the mutual shift of the titanium and oxygen sublattices, which is responsible for the ferroelectric polarization in displacement type ferroelectrics such as BSTO. The relative shift of the sublattices is associated with the formation of a soft mode. The mode is soft, because the elasticity of the structure formed due to the relative shift of the sublattices is small. The rigidity of the sublattices themselves is much higher than the rigidity counteracting their mutual shift. The rigidity of the sublattices determines the spatial correlation of the polarization and, accordingly, the correlation radius. The correlation radius for the transverse wave $\rho_{(T)}\ T = \sqrt{\varepsilon(T)\lambda_3}$ is significantly smaller than that for the longitudinal wave $\rho_L(T) = \sqrt{\varepsilon(T)\lambda_1}$. Apparently, the reason is that the rigidity of the titanium and strontium sublattices with respect to the compression and extension (Figure 33.17a) is much higher than their rigidity with respect to shear strains (Figure 33.17b).

Equation 33.49 describes the nonlocal connection between the polarization $P(x)$ and the electric field $E(x)$. The nonlocal connection is illustrated in Figure 33.17.

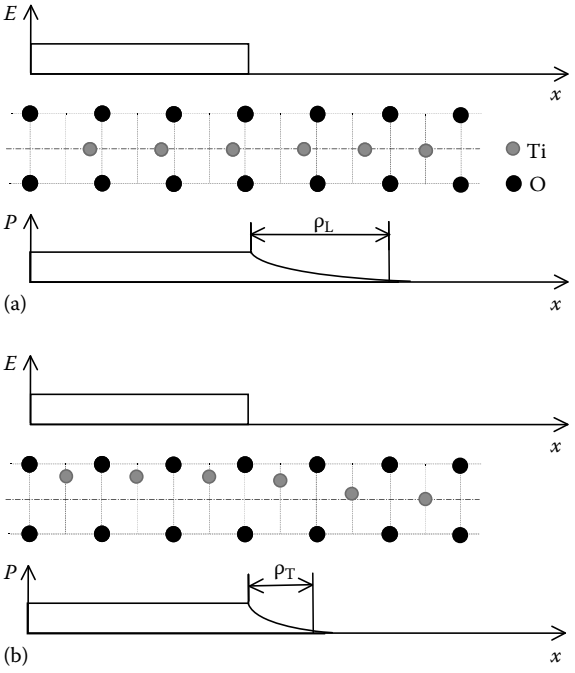

FIGURE 33.17 Spatial distribution of biasing field and polarization: (a) longitudinal mode; (b) transverse mode.

33.3.1.2 Boundary Conditions for Dynamic Polarization on the Interface between Ferroelectric Layer and Electrodes

The principal role belongs to the boundary conditions for the dynamic ferroelectric polarization. Firstly, we consider the specific boundary conditions on the interface between the ferroelectric layer and the electrode, which are defined as a blocking of the dynamic ferroelectric polarization. The blocking of the ferroelectric polarization was experimentally observed by electron diffraction experiment as a consequence of the distortion of the periodicity of the ferroelectric crystal [57]. This experimental result was in agreement with a numerical simulation, which revealed the existence of a strong electric field appearing as a result of the distortion of the lattice near the crystal surface. This field takes place in a thin layer with the thickness of a few lattice constants [58,59]. The blocking of the dynamic ferroelectric polarization was called "zero" boundary conditions [48]. If the periodicity of the crystal lattice is not distorted on the boundary of the ferroelectric crystal, the blocking of the ferroelectric polarization does not exist and the size effect is suppressed. This situation is referred to as the "free" boundary conditions. Such a situation can be realized, for example, in a parallel-plate ferroelectric capacitor with conducting electrodes made from material with the crystal structure being close to the perovskite structure [48]. As a suitable material for the electrode, the HTS $YBa_2\,Cu_3\,O_{7-x}$ or stontium rutinate $SrRuO_3$ (SRO) can be selected. The suppression of the size effect was experimentally demonstrated in SRO/$SrTiO_3$/SRO parallel-plate capacitor [27,60]. This experimental result is in agreement with the spatial correlation model with free boundary conditions for the dynamic ferroelectric polarization. Suppression of the blocking of the ferroelectric polarization in $BaTiO_3$ in the case of the free boundary conditions was theoretically approved by first-principles investigation of ultrathin $BaTiO_3$ films with SRO electrodes [61].

Let us take into account that

$$D = P(x) + \varepsilon_0 E(x),$$

then the solution to Equation 33.47 for the case div$D = 0$ and the "zero" boundary conditions for $P(x)$ gives the distinctive polarization distribution across the ferroelectric layer inside the parallel-plate capacitor [27,41,48,49]:

$$P_{ac}(x)\big|_{x=\pm h/2} = 0, \tag{33.52}$$

$$P_{ac}(x) = P_{max} \times \left(1 - \frac{\cosh(\alpha x)}{\cosh(\alpha h/2)}\right), \tag{33.53}$$

$$P_{max} = \frac{Q_{ac}}{S}\left[1 - \frac{1}{\varepsilon(T)}\right], \tag{33.54}$$

$$\alpha = 1\Big/\sqrt{2\lambda_1}. \tag{33.55}$$

where

Q_{ac} is the charge on the capacitor electrodes

S is the electrode area

Example of this polarization distribution is shown in Figure 33.18a.

Blocking of the polarization is followed by the appearance of the depolarizing electric field near the capacitor electrodes (Figure 33.18b). As it was shown above (see Equation 33.49 and Figure 33.17), the polarization is nonlocally connected with the electric field inside the ferroelectric layer. Integration of the field gives the voltage drop across the capacitor. Using surface charge density on the electrodes ($Q_{Sur} = D$) and the voltage drop one can find effective permittivity of the film, which now is a function of the film thickness (size effect). The effective dielectric constant of the film with zero boundary conditions is described as

$$\frac{1}{\varepsilon_{eff}} = \frac{1}{\varepsilon_f(T)} + \frac{2}{\alpha h}, \tag{33.56}$$

where h is the thickness of the film. For $SrTiO_3$ $\alpha = 2.1 \times 10^9$ 1/m.

For BSTO correlation parameter depends on the composition factor x. In general case, the size-effect parameter α of the displacive ferroelectric BSTO can be found from dielectric measurements or from inelastic neutron scattering on the ferroelectric lattice oscillations [49]. Figure 33.19 shows the dependence of α on Ba concentration [41,54].

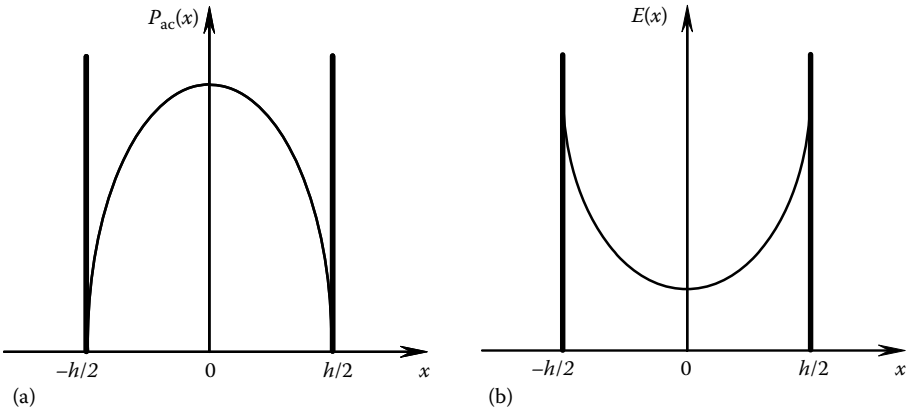

FIGURE 33.18 Distribution of the polarization (a) and electric field (b) inside parallel-plate capacitor.

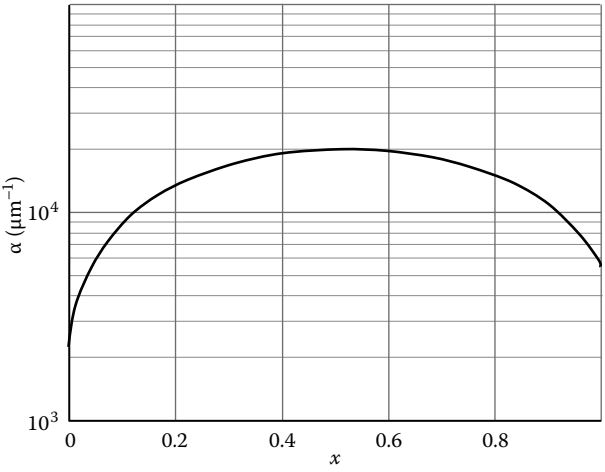

FIGURE 33.19 Dependence of the parameter α on the concentration of Ba in the compound BSTO.

33.3.1.3 Effective Dielectric Constant of a Thin-Film Sample

The effective dielectric constant of a thin-film sample can be simulated with formula (Equation 33.56), if the size-effect parameter α, the film thickness, and the bulk permittivity of the material are known.

The size effect manifests itself differently at different orientations of the ferroelectric-polarization vector with respect to the boundaries of the ferroelectric layer [41,54]. Figure 33.20 shows the ferroelectric structures with different orientations of an external field. In the structures shown in Figure 33.20a and b, the dynamic polarization can be conditionally considered as a standing longitudinal wave and a transverse wave, respectively. To calculate the size effect in a parallel-plate (sandwich) capacitor (Figure 33.20a), the correlation parameter for a "longitudinal wave" λ_1 should be used. To calculate the size effect in a planar capacitor (Figure 33.20b), the correlation parameter for a "transverse wave" λ_3 should be used.

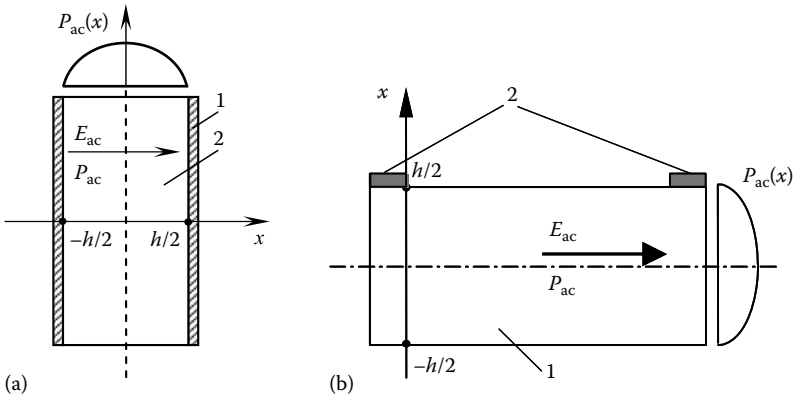

FIGURE 33.20 Ferroelectric structures with different orientations of an external field: (a) structure with a standing longitudinal wave, (b) structure with a standing transverse wave. 1, electrodes; 2, ferroelectric layer.

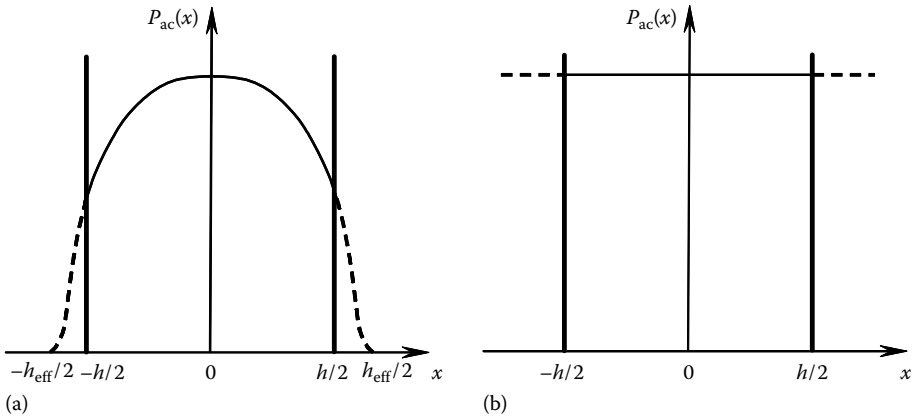

FIGURE 33.21 Distribution of polarization inside parallel-plate capacitor in the case of intermediate (a) and free (b) boundary conditions.

33.3.1.4 Suppression of the Size Effect

Boundary conditions (Equation 33.52) are not always satisfied: for example, in the structure in which a ferroelectric is adjacent to a high temperature superconductor $YBa_2Cu_3O_{7-\delta}$ (YBCO), polarization can partially penetrate the electrode (Figure 33.21a). The penetration depth of the polarization in the YBCO electrode is determined by the YBCO permittivity and the correlation parameter. For example, for a longitudinal wave, the penetration depth of the polarization in the electrode is about 20 nm [26,41]. This case corresponds to the so-called intermediate boundary conditions.

In this case, the effective thickness of the ferroelectric layer h_{eff} may be introduced. When a ferroelectric contacts a material with the same crystal structure, for example, $SrRuO_3$ (SRO) [27,60,62], free boundary conditions (Equation 33.48) should be implemented. That is followed by a uniform distribution of the polarization in the film, independent of its thickness (Figure 33.21b).

Obviously, the relationship between the effective (h_{eff}) and geometric (h) thickness of the ferroelectric layer depends on the boundary conditions. Zero, free, and intermediate boundary conditions correspond to $h_{eff} = h$, $h_{eff} \to \infty$, and $h < h_{eff} < \infty$, respectively.

33.3.2 Nature of So-Called "Dead Layer" in a Parallel-Plate Capacitor

The dead layer model is based on the supposition of existence of layer with nonferroelectric polarization near the electrodes of the parallel-plate capacitor. The dielectric film is supposed to be consisting of three layers: principal layer with the dielectric constant ε_f and the thickness h, separated from the electrodes on each side by nonferroelectric "dead layers" with the dielectric constant ε_d and the thickness h_d. The dead layer model was first mentioned in 1959 [63,64] and described using some different procedures but up to now the origin of dead layer is not well understood [65,66].

33.3.2.1 Primary Model of the "Dead Layer"

In the case of a parallel-plate capacitor with the dead layer (see Figure 33.22), the effective dielectric constant is described as follows [63]:

$$\frac{1}{\varepsilon_{eff}(T)} = \frac{1}{\varepsilon_f(T)} + \frac{2h_d}{\varepsilon_d h}, \tag{33.57}$$

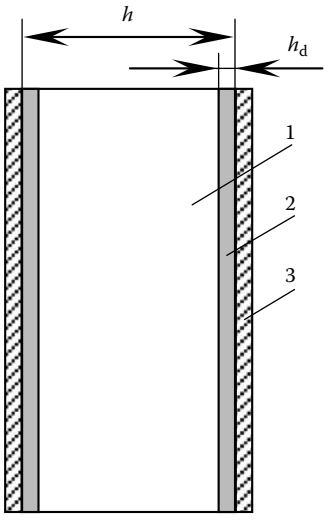

FIGURE 33.22 Model of the dead layer: 1, ferroelectric layer; 2, dead layer; 3, electrode.

where

$\varepsilon_{eff}(T)$ is the effective dielectric constant of the film

$\varepsilon_f(T)$ is the dielectric permittivity of ferroelectric as a function of temperature

For the "dead layer" model, the dependence of dynamic ferroelectric polarization in the sample on coordinates can be described as follows:

$$P(x) = \begin{cases} P_{max} & \text{for } |x| \le \left(\frac{h}{2} - h_d\right) \\ 0 & \text{for } \left(\frac{h}{2} - h_d\right) < |x| \le \frac{h}{2} \end{cases}. \tag{33.58}$$

The dynamic ferroelectric polarization is supposed to be equal to zero in the dead layer, at the same time the nonferroelectric polarization exists in the dead layers. The layer with the nonferroelectric polarization is characterized by the dielectric constant ε_d, which is not yet defined and will be later discussed. The nature of disappearance of the ferroelectric polarization in the "dead layer" will be explained later as well.

Figure 33.23 illustrates run of the dielectric polarization in a parallel-plate capacitor for two models considered: curves 1 and 2 correspond to Equations 33.53 and 33.58 accordingly.

Comparison of Equations 33.56 and 33.57 is followed by the conclusion that the thickness of the dead layer is

$$h_d = \frac{\varepsilon_d}{\alpha}. \tag{33.59}$$

The numerical value of ε_d was found as a result of extension of the experimental curve: $\varepsilon_{exp} = f(1/T)$ for perovskite type crystals for the limit $T \to \infty$ [37]: $\varepsilon_{exp} \to \varepsilon_d \cong 40$. As it was mentioned above, ε_d is the dielectric permittivity of the nonferroelectric modes of the crystal lattice oscillations.

On substituting $\varepsilon_d \cong 40$ and the correlation parameter $\alpha \cong 2 \times 10^{10}$ 1/m ($x = 0.5$, Figure 33.19) into Equation 33.59 one obtains for BSTO parallel-plate capacitor the following parameters of the dead layer $h_d \cong 2$ nm. Thus:

$$\varepsilon_d \cong 40, \quad h_d \cong 2\,\text{nm}. \tag{33.60}$$

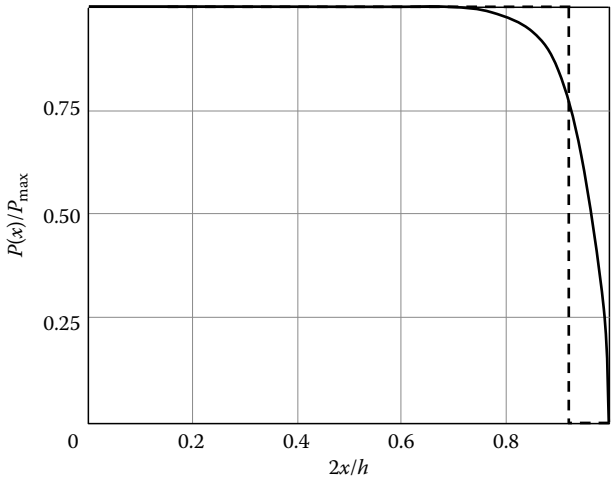

FIGURE 33.23 Normalized polarization in the correlation model (solid line) and in the model of dead layer (dashed line).

These values are confirmed by the experimental data [67], obtained for a thin-film $Ba_{0.7}\,Sr_{0.3}\,TiO_3$ parallel-plate capacitor. In this work the h_d/ε_d ratio and the product $h_d \times \varepsilon_d$ were obtained through the measurements of the capacitance–voltage and the current–voltage characteristics. Combining these data, the dead layer thickness and dead layer dielectric constant were experimentally estimated as

$$\varepsilon_d = 42.6, \quad h_d = 2.8\,\text{nm}. \tag{33.61}$$

These values are in a good agreement with the result obtained above (see Equation 33.60) on the known value of the parameter α.

33.3.2.2 Real (Nondefected) Nature of the "Dead Layer"

The values ε_d and α are fundamental parameters of the material, which are determined by the properties of nonferroelectric and ferroelectric phonon modes of the crystal and are unrelated with defect or chemical structure of the interface region. The thickness of the dead layer is a secondary parameter, which can be considered as a coherence length of formation of the order parameter of the ferroelectric phase transition, characterized by the soft mode oscillation. The eigenfrequency of the ferroelectric and the soft mode space dispersion are strongly connected with the temperature of the ferroelectric phase transition T_c. The conformity of h_d with T_c is illustrated by Table 33.3.

One may compare the ferroelectric phase transition with the superconducting one. Table 33.4 illustrates the conformity of the coherence length of the superconducting state ξ with the superconducting phase transition temperature T_c [68].

TABLE 33.3 Curie Temperature and Dead Layer Thickness of Ferroelectrics

Material	T_c(K)	h_d(nm)
$SrTiO_3$	40	20
$Ba_{0.5}\,Sr_{0.5}\,TiO_3$	220	2

TABLE 33.4 Characteristics of Superconducting Materials

Material	T_c (K)	ξ (nm)
Ta	4.4	90
Nb	9.2	40
Nb_3Sn	18	3
$YBa_2 Cu_3 O_{7-x}$	90	2

Confrontation of the data from Tables 33.3 and 33.4 confirms affinity of the nature of two phase transitions considered.

The above mentioned first-principles investigation of ultrathin $BaTiO_3$ films with SRO electrodes [61] in confrontation with the discussed model of the correlation of the ferroelectric polarization may be considered as confrontation of the Bardeen, Cooper, and Schrieffer theory of the superconductivity and the Ginzburg–Landau phenomenological theory of superconductivity. In order to support this confrontation, the scheme of the Abrikosov vortex and the scheme of the dead layers near the electrodes are shown in Figure 33.24. In the both examples, the solution to the Ginzburg–Landau equation (superconducting phase transition) and Ginzburg–Devonshire equation (ferroelectric phase transition) for the order parameters of the phase transitions (see captions to the figures) are followed by the formation of the models, in which the coherence length plays the decisive role.

One should take into account that the description of the size effect is based on the correlation of the ferroelectric polarization in conjunction with the zero boundary conditions. It should be reminded

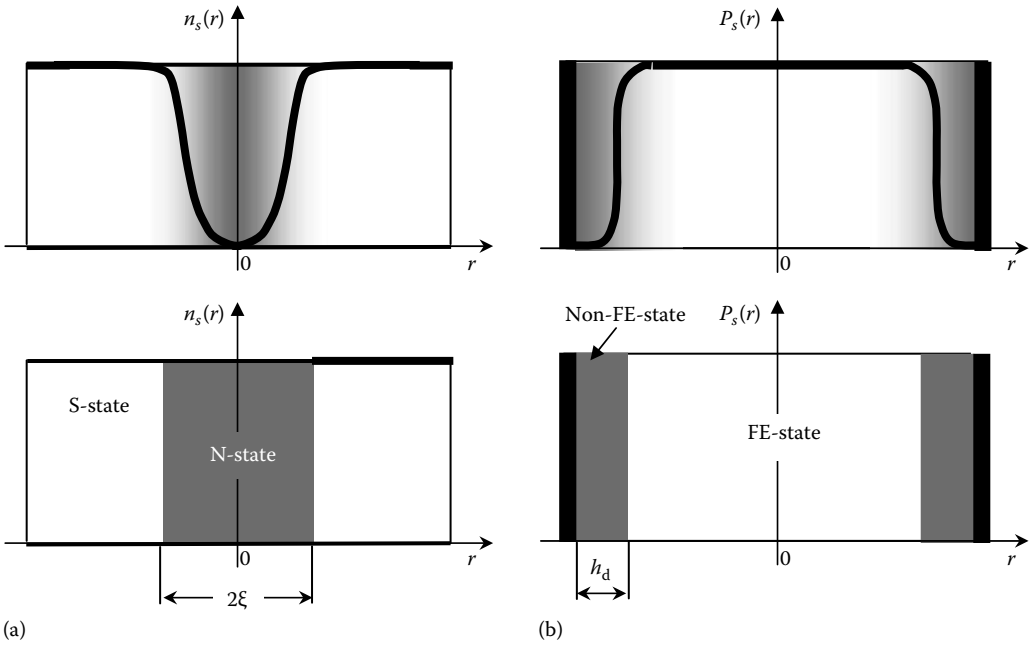

FIGURE 33.24 Spatial distribution of order parameter: (a) in a super conducting film (density of "super electrons"); (b) in a ferroelectric capacitor (spontaneous polarization). The solid lines on the top pictures present the solutions to the Ginzburg–Landau equation (a) and the Ginzburg–Devonshire equation (b). The filled area on the bottom pictures corresponds to the N-core of the Abrikosov vortex (a) and the "dead layers" in the parallel-plate ferroelectric capacitor (b).

that under the relevant boundary conditions the "dead layers" in a ferroelectric parallel-plate capacitor do not exist and the size effect is suppressed [27,48,62].

The dead layer model could be useful as a basis of the simulations for practical use.

33.4 Microwave Properties of Ferroelectrics

In this section, the main physical phenomena responsible for dissipation of the microwave energy in the ferroelectric material will be described. Some simple formulas will be presented which can be used for a simulation of the loss-factor of ferroelectric material at microwave frequency as a function of temperature and the biasing field.

33.4.1 Dielectric Response of STO and BSTO as a Function of Temperature, Biasing Filed, and Frequency

Response function of a ferroelectric can be written in the form of dielectric susceptibility [45,69]:

$$\chi(\omega) = \frac{\chi(0)\omega_c^2}{\omega_c^2 - \omega^2 - i\omega\gamma + \frac{\delta^2}{1+i\omega\tau}}, \tag{33.62}$$

where

ω is the frequency
ω_c is the eigenfrequency of the ferroelectric mode
γ is the intrinsic dissipation factor of the ferroelectric mode
τ is the relaxation time of an additional relaxation mechanism responsible for the dissipation of the ferroelectric mode oscillation energy
δ is the coupling coefficient of the relaxation mechanism and the ferroelectric mode

33.4.1.1 Eigenfrequency of the Ferroelectric Mode of Crystal Lattice Oscillation

When temperature of the ferroelectric crystal is near to the Curie temperature, elasticity of the sublattice displacement becomes softer. That leads to increase in the dielectric permittivity $\varepsilon_f(T)$ and decrease in value of the eigenfrequency of the ferroelectric mode of crystal lattice oscillation $\omega_c(T)$. The well-known Lidden–Sakse–Teller relation [37] claims that

$$\omega_c^2(T)\varepsilon_f(T) = \text{const.} \tag{33.63}$$

The smaller ω_c, the higher is permittivity and tunability of the ferroelectric material. Because of a small value of elasticity of the sublattice displacement responsible for the value of the eigenfrequency, the ferroelectric mode is called the soft mode. Figure 33.25 illustrates the temperature dependence of $\omega_c^2(T)$ of $SrTiO_3$.

In the case, when there are many relaxation mechanisms, the behavior of the dielectric response in the frequency region near to the eigenfrequency of the ferroelectric mode $\omega \cong \omega_c$ becomes complicated [53]. Fortunately the goal of this section is investigation of the loss factor in the microwave frequency region $f \leq 100$ GHz. That allows to exclude the frequency region $f > 100$ GHz and simplify the problem. One may assume that in Equation 33.62 $\omega^2 = 0$. Some years ago the assumption was applied [70] that contributions into loss factor given by all loss mechanisms in general are proportional to the frequency. Now, we may say that detailed consideration of a few relaxation processes leads to the specific dependence of the loss factor on the frequency in the microwave frequency range.

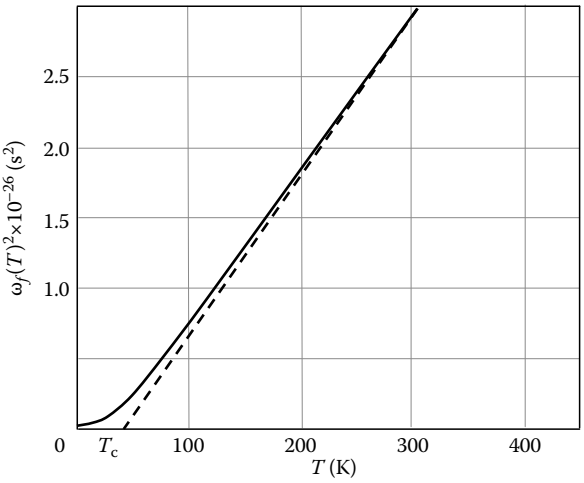

FIGURE 33.25 Temperature dependence of soft mode eigenfrequency of $SrTiO_3$.

33.4.1.2 Complex Dielectric Permittivity of a Ferroelectric Material

Let us generalize Equation 33.62 for the case $\omega \ll \omega_c$. Take into account that for the high dielectric permittivity of a ferroelectric material, the permittivity may be supposed to be equal to susceptibility. Thus we have

$$\varepsilon(E, T, \omega) = \frac{\varepsilon_{00}}{G(E, T) + \sum_{q=1}^{4} \Gamma_q(E, T, \omega)}, \tag{33.64}$$

where $G(E, T)$ is the real part of the Green function for a dielectric response of the ferroelectrics. For a description of the real part of the Green function, a simple and correct model is used. The model was described in Section 33.2.1: Equations 33.30 through 33.32. In Equation 33.64, the notation presented by Equations 33.13, 33.21, and 33.22 was used.

In accordance with the above-formulated conditions, $\omega \ll \omega_c$, $G(E, T)$ does not depend on the frequency. Γ_q present the loss contribution of qth loss mechanisms and are the complex functions of the frequency.

The loss factor is defined as follows:

$$\tan\delta(E, T, \omega) = \frac{\mathrm{Im}[\varepsilon(E, T, \omega)]}{\mathrm{Re}[\varepsilon(E, T, \omega)]}. \tag{33.65}$$

In the frame of the model considered, the stationary ferroelectric polarization $P(E, T)$ is used. The stationary ferroelectric polarization is presented by Equation 33.33, where $y(E, T)$ is a normalized value of the ferroelectric polarization.

We consider BSTO with arbitrary value of composition factor x (relative concentration of barium). The agreement of the model presentation with respect to the experimental dependence of the dielectric permittivity on temperature and biasing field was demonstrated earlier [26,41].

In the frequency range $\omega < 100$ GHz, the typical displacement type of ferroelectrics STO and BSTO has small frequency dispersion of dielectric permittivity. The frequency dependence of the dielectric permittivity of BSTO is illustrated in Figure 33.26 for the case $T = 290$ K, $x = 0.5$, $\xi_S = 0.7$, and two values of the biasing field $E = 0$ and $E = 300$ kV/cm.

Now, we will concentrate on the frequency dependence of the imaginary part of the dielectric permittivity or of the loss factor of the material.

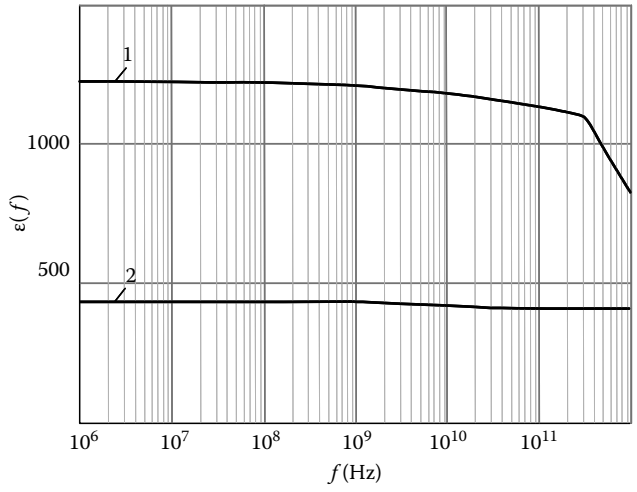

FIGURE 33.26 Frequency dependence of the dielectric permittivity of $Ba_{0.5}\,Sr_{0.5}\,TiO_3$ at $T = 290$ K, $E = 0$ (curve 1), and $E = 300\,\text{kV/cm}$.

33.4.2 Fundamental Loss Mechanisms in a Perfect Ferroelectric Crystal

We consider a perfect ferroelectric crystal without mechanical strain and built-in electric field generated by charge defects. The dissipation of the soft mode oscillation energy is caused by the scattering of the mode on the thermal oscillation of the crystal lattice without the biasing field or under the influence of a homogeneous external biasing field.

33.4.2.1 Multiphonon Scattering of the Ferroelectric Soft Mode

The fundamental channel of the soft mode energy dissipation is a nonlinear interaction between soft mode oscillations and thermal oscillations of the crystal lattice. It is so-called multi-phonon interaction, which was considered by many authors [32,71–73]. The nonlinear interactions of the optical phonons are responsible for the ferroelectric phase transition and for revealing a high value of dielectric constant of the ferroelectrics. It means that the interactions between the soft mode oscillations and thermal oscillations of the crystal lattice, which are responsible for the dissipation, determine at the same time the ferroelectric nature of the material. That is why this loss mechanism is called the fundamental one. The numerical characteristics of the fundamental loss are described by the same qualitative parameters, which are responsible for the ferroelectric properties of the crystal.

In accordance with the Lidden–Sakse–Teller relation, the eigenfrequency of the soft mode is

$$\omega_C\,(E,T) = \omega_{00}\sqrt{G(E,T)}. \tag{33.66}$$

Moreover, the maximum frequency in the spectrum of optical phonons in the crystal ω_M should be involved. For that, one may use the frequency corresponding to the Debye temperature responsible for the formation of the ferroelectric response of the incipient ferroelectrics:

$$\hbar\omega_M = k_B\theta_F. \tag{33.67}$$

For further consideration, the formula for dissipation of the soft mode in the incipient ferroelectrics from Refs. [53,72,73] is used. That gives

$$\Gamma_1(E,T,\omega) = -i\frac{\pi}{8}\frac{\omega_{00}}{\omega_M^2}\left(\frac{T}{T_c}\right)^2 G^{-1/2}(E,T)\omega. \tag{33.68}$$

The coefficient $\omega_{00}(x)$, ω_M can be found from inelastic neutron scattering: $\omega_{00}(x) = 0.67(1 + 6x) \times 10^{13}$/s; $\omega_M = 2.6 \times 10^{13}$/s, where x is Ba concentration.

33.4.2.2 Contribution of the Quasi-Debye Scattering

The origin of the quasi-Debye mechanism of loss is the relaxation of the crystal phonon distribution [35,73]. The application of "dc" field to a centrosymmetric crystal causes the time modulation of the phonon distribution function by the "ac" field. The change of the phonon distribution function leads to change of the dielectric response of the crystal. The dielectric response is inevitably delayed for a certain time interval, which is called the relaxation time. The relaxation of the phonon distribution function gives rise to the dielectric loss in a similar way as the relaxation of the gas of dipoles gives rise to the loss in the Debye theory. It is why the loss mechanism considered is called the quasi-Debye one.

The contribution of the quasi-Debye mechanism into the dielectric response of the sample was found [35] in form:

$$\Gamma_2(E, T, \omega) = \frac{A_2}{(1 + i\omega/2\pi f_2)} \frac{y^2(E, T)}{[1 + \xi^2(E)]}, \tag{33.69}$$

where

$f_2 = 30$ GHz [32] is the inverse relaxation time of change of the phonon distribution function
$A_2(x) = 0.8(1 + 20x)^{-1}$ is a coefficient characterizing the rate of the contribution of the mechanism considered.

33.4.3 Losses in a Real Ferroelectric Crystal

The properties of real ferroelectric samples differ from an ideal single crystal sample dramatically. The presence of charged defects results in additional losses in material. Using the ferroelectrics in a planar capacitor as a thin film leads to excitation of loss mechanism associated with transformation of energy into high frequency acoustic waves.

33.4.3.1 Contribution of Charged Defects

In many cases, the ferroelectric crystal comprises some charged defects. The electrostriction under the static electric field produced by the charged defects leads to an induced piezoelectric effect and is followed by the excitation of acoustic vibrations in the sample. The frequency dependence of the energy dissipation has a character of the relaxation process. The relaxation time is determined by the characteristic size of the defect configuration, which depends on the growing process of the sample. The contribution of the charged defects into losses in ferroelectrics was investigated in Ref. [74]. The result of the investigation can be presented as follows:

$$\Gamma_3(E, T, \omega) = \frac{A_3 \xi_S^2}{1 + i\,(\omega/2\pi f)}. \tag{33.70}$$

Integrating the wide experimental information, we may suppose the most reasonable value of the inverse relaxation time is $f_3 \cong 10$ GHz. The contribution rate of the mechanism considered is proportional to the density of the charged defects. In Equation 33.70, ξ_S was substituted instead of the defect density reasoning that parameter ξ_S as a characteristic of the crystal quality is connected with the defect density. On the basis of comparison results obtained with the formulas developed and the numerical estimations given in Refs. [11,74], one may suppose that $A_3 \cong 0.05$.

It is reasonable to stress the difference between the quasi-Debye and charge defect mechanisms of losses. In the case of the quasi-Debye loss, the energy of the microwave field is immediately

transformed into the heat of the crystal lattice. The higher is polarization, being spontaneous or induced by applied voltage, the higher is the energy dissipation through the quasi-Debye mechanism. In the case of the charge defect mechanism, the microwave field is transformed first into the high frequency acoustic waves. And then the acoustic waves are dissipated by the crystal lattice. The intensity of the induced piezoelectric transformation does not depend on the applied voltage or polarization. The applied voltage suppresses the inverse dielectric permittivity and as a result of that, the higher the applied voltage, the smaller is the contribution of charge defect mechanism to losses.

33.4.3.2 Contribution of an Acoustic Wave Emission in Thin-Film Planar Structure

Emission of high frequency acoustic waves from the gap of a planar structure due to electrostriction transformation [75,76] can be observed in a planar ferroelectric capacitor:

$$G(E,T) = \frac{\varepsilon(E,T)}{\varepsilon_{00}}. \tag{33.71}$$

Experimental data on the microwave losses of a thin-film ferroelectric planar structure in this case were presented in Ref. [77].

33.4.3.3 Low-Frequency Relaxation

Experimental investigations of BSTO samples [11] have shown the diffused maximum of loss tangent around the frequency $f = 10$ MHz. The nature of that was not properly explained. Phenomenologically, it can be attributed to a relaxation process and described by the following formula:

$$\Gamma_4(\omega) = \frac{A_4}{1 + i\omega/(2\pi f_4)}, \tag{33.72}$$

where

ω is the frequency at which the dielectric characteristics of the material are measured
A_4 and f_4 are the parameters of the model: $A_4 = 0.005$, $f_4 = 10$ MHz.

33.4.4 Total Microwave Losses in a Perfect and Real (Defected) Ferroelectric Crystal as a Function of Frequency, Temperature, and Biasing Field

In this section, the features of loss-factor of a perfect and real (defected) ferroelectric crystal as a function of frequency, temperature, and biasing field are considered.

In Figure 33.27, the result of simulation for a high-quality single crystal ($\xi_S = 0.018$) of $SrTiO_3$ ($x = 0$) at $T = 78$ K is presented.

In Figure 33.28, the result of simulation of loss-factor for a moderate quality film or ceramic layer of BSTO ($x = 0.5$, $\xi_S = 0.7$) is presented. All simulated curves are in a good agreement with experimental data.

33.5 Ferroelectrics in Tuneable Metamaterials

As it was written above (Chapter 1), electromagnetic metamaterials are defined as artificial structures with specific properties, which cannot be observed in natural materials. Properties of such artificial structures depend on dielectric and/or magnetic characteristics of components, which are used for formation of the structure. If ferroelectric components are used as ingredients of the structure, the characteristics of the structure can be changed due to change of the dielectric permittivity of the ferroelectric component as a result of applying the biasing voltage to the component.

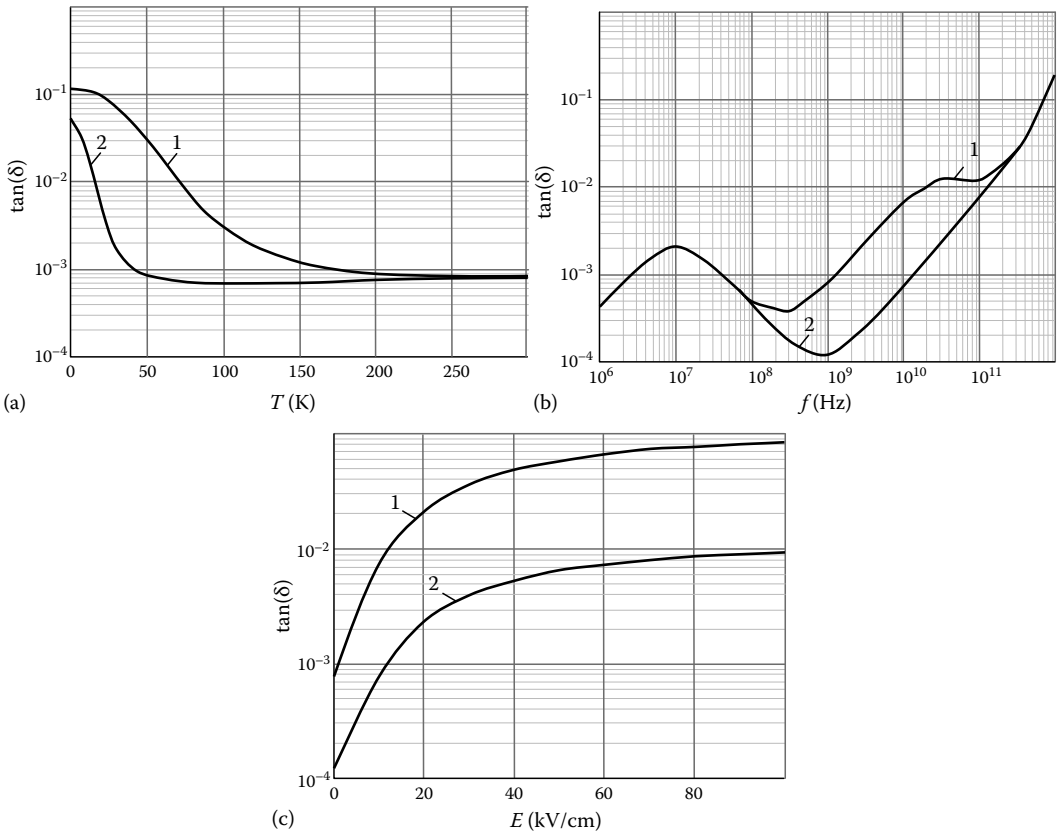

FIGURE 33.27 Loss-factor of a single crystal of $SrTiO_3$ ($\xi_S = 0.018$) as a function of (a) temperature for $f = 10$ GHz, $E = 0$ (curve 2), and $E = 10$ kV/cm (curve 1); (b) frequency for $T = 80$ K, $E = 0$ (curve 2), and $E = 10$ kV/cm (curve 1), (c) biasing field for $f = 1$ GHz (curve 2) and $f = 10$ GHz (curve 1).

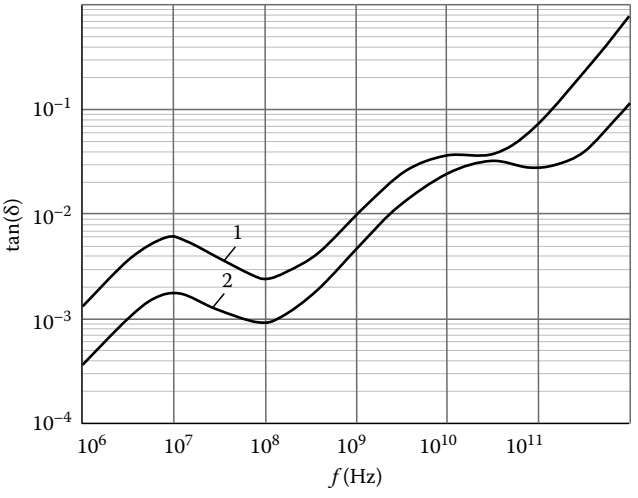

FIGURE 33.28 Loss-factor of a layer of BSTO ($x = 0.5$, $\xi_S = 0.7$) for $T = 290$ K, $f = 10$ GHz, and $E = 0$ (curve 1), and $E = 400$ kV/cm (curve 2).

Thus, the metamaterial structure becomes a tuneable one. The tunability of metamaterial structures or metamaterial devices is very promising for expansion of practical application of such structures or devices.

In the most general case, the metamaterial structure is required to be three-dimensional (3D) and isotropic. As we know, there is no suggestion about a possible way to design a 3D tuneable metamaterial structure. In this section, we consider a version of a 2D tuneable metamaterial structure. The 2D tuneable metamaterial is referred to as a tuneable metasurface. The metasurface was suggested and investigated by Sievenpiper et al. [78]. Sievenpiper described a tuneable metasurface based on application of tuneable semiconductor varactors. We will consider a version of a tuneable metasurface based on application of ferroelectric tuneable capacitors.

A wide interest is called forth by a combination of transmission lines with forward electromagnetic waves and backward electromagnetic waves. In the transmission lines with the forward electromagnetic waves, the electric field, the magnetic field, and the propagation vector form the right-handed triad. Therefore, the transmission lines with the forward electromagnetic waves are called the "RHTL." The lines with the backward electromagnetic waves are characterized by the left-handed triad and consequently are called the " LHTL." The majority of transmission lines (microstrip line, coplanar line, etc.) have properties of the RHTL. In order to realize the LHTL, one needs to use a special combination of reactive components, which can be considered as the metamaterial structure. Thus, LHTL is the 1D metamaterial. Both RHTL and LHTL can be designed as specific tuneable 1D metamaterial structure.

33.5.1 Tuneable Metasurface Based on Ferroelectric Tuneable Capacitors

Scheme of a tuneable metasurface is presented in Figure 33.29. The characteristic feature of a metasurface is its surface impedance. In order to find the surface impedance of the metasurface, the reflection coefficient of the electromagnetic wave normally incident on the surface should be found. The space,

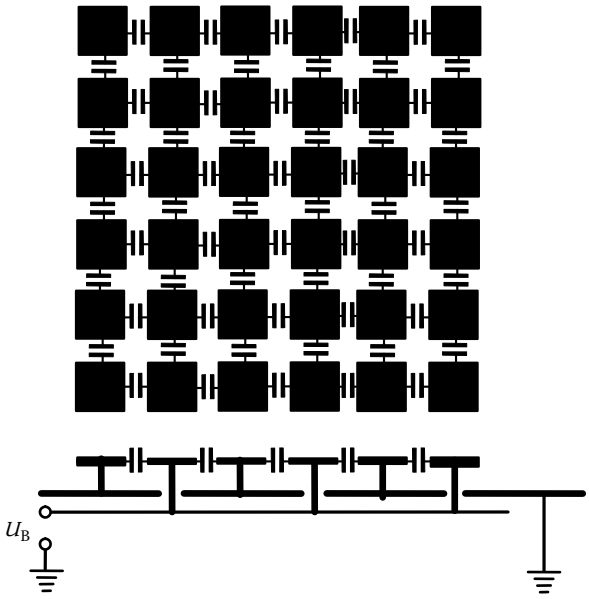

FIGURE 33.29 Scheme of a tuneable metasurface.

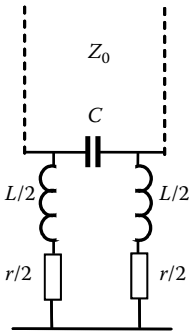

FIGURE 33.30 Scheme of the resonant cell connected with the elementary waveguide.

in which the incident wave propagates in the direction to the metasurface, can be divided into elementary waveguides. Each elementary waveguide is loaded by the resonant cell that consists of a capacitor and a short-circuited transmission line section. This transmission line section can be considered as an elementary inductance. The scheme of the resonant cell connected with the elementary waveguide is shown in Figure 33.30. The characteristic impedance of the waveguide is denoted as Z_0. Impedance of the resonant cell is determined by the following equation:

$$Z_{\text{cell}}(f) = \left[(iX_0 f/f_0 + r)^{-1} + (-iX_0 f_0/f)^{-1}\right]^{-1}, \tag{33.73}$$

where

f is the operational frequency
f_0 is the resonant frequency
X_0 is the characteristic impedance of the resonant circuit
r is the real part of the resonant circuit impedance, which is determined by the quality factor Q: $r = X_0/Q$.

Reflection coefficient is read as follows:

$$\Gamma(f) = \frac{Z_{\text{cell}}(f) - Z_0}{Z_{\text{cell}}(f) + Z_0}. \tag{33.74}$$

The phase shift (in degrees) and the attenuation (in dB) of the reflected wave with respect to the incident wave are read as follows:

$$\varphi(f) = \arg(\Gamma(f))\frac{180}{\pi}, \quad L(f) = 20\log(|\Gamma(f)|). \tag{33.75}$$

It is reasonable to suppose: $Z_0 = 377$ Ohm (the characteristic impedance of free space) and to consider the characteristic impedance of the resonant circuit to be determined by a sheet capacitance C_0, with units of [F/square], and a sheet inductance L_0, with units of [H/square]: $X_0 = (L_0/C_0)^{1/2}$.

Let us consider the case when $f_0 = 10$ GHz, $X_0 = 100$ Ohm ($C_0 = 0.17$ pF/square), $Q = 50$. Figure 33.31 illustrates the simulation of the phase shift (in degrees) and the attenuation (in dB) in accordance with Equation 33.75. Three curves on the graph correspond to three capacitances of the tunable capacitors 1 – 0.24, 2 – 0.17, and 3 – 0.12 pF.

The most interesting point on the graph in Figure 33.31a is the resonant point, in which the phase shift of the reflected wave is equal to zero. At this point, the incident wave is reflected from the metasurface as from "magnetic wall." Along the "magnetic wall," the tangential component of the magnetic

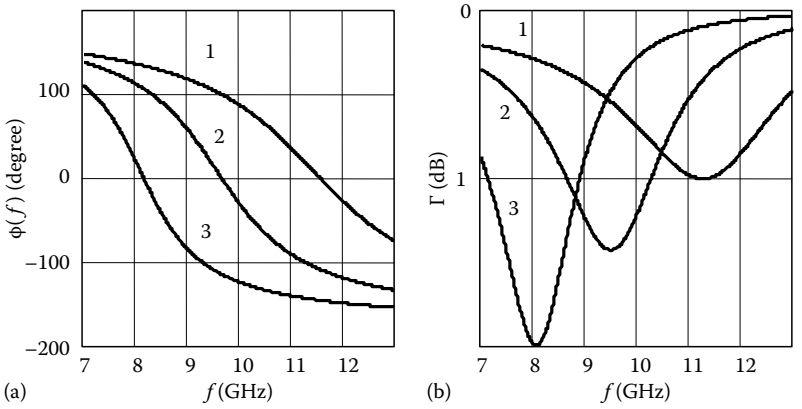

FIGURE 33.31 Frequency dependence of phase shift (a) and the attenuation (b) of the wave reflected from resonant cell.

field is equal to zero. The "magnetic wall" forms the complementary boundary condition for the boundary condition of the conventional "electric wall." Such complementary boundary conditions make it possible to successfully solve a set of problems in engineering electrodynamics. Unfortunately, the "magnetic wall" retains its favorable properties in a restrained frequency band near the resonant frequency of the cell. From the graph of Figure 33.31a, one may find that the deviation of the phase shift of the reflected wave is not more than ±10° from zero in the frequency band, which is not more than 0.25 GHz. In a much higher frequency band, the metasurface can be used, if the resonant frequency of the metasurface cell can be changed due to tunability of the capacitors. The graphs in Figure 33.31a show that in the case of the capacitor tunability $n = 2$ ($n = C_{\max}/C_{\min}$), the operational frequency band of a metasurface used as a good "magnetic wall" comes up to 4 GHz. Thus application of ferroelectric tunable capacitors as constituents of a metasurface sufficiently expands the area of the practical use of the metasurfaces in the microwave engineering.

33.5.2 Composite Right/Left-Handed Transmission Line

The typical CRLH TL section is shown in Figure 33.32. The section is formed by parallel and series resonant circuits.

The impedance of the series circuit reads as

$$Z_1(f, C_1) = i\omega L_1(1 - iQ^{-1}) + \left[i\omega C_1(1 - i\tan\delta)\right]^{-1}. \tag{33.76}$$

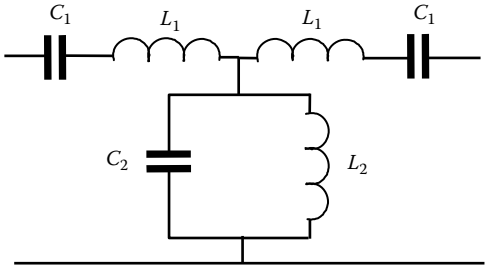

FIGURE 33.32 Section of CRLH TL.

The impedance of the parallel circuit reads as

$$Z_2(f, C_2) = \left[i\omega C_2(1 - i\tan\delta) + \left[i\omega L_2(1 - iQ^{-1}) \right]^{-1} \right]^{-1}. \tag{33.77}$$

The energy dissipation in the section is described by the loss factor of the capacitors tan δ and quality factor of the inductors Q. In the next section, the capacitors C_1 and C_2 will be presented as tuneable ferroelectric varactors.

For a description of the scattering parameters of the section, the ABCD matrix can be used. The ABCD matrix is convenient for investigation of cascade connection of the sections. The ABCD matrix of the section showed in Figure 33.32 is

$$A(f, C_1, C_2) = \begin{bmatrix} 1 + \frac{Z_1(f,C_1)}{Z_2(f,C_2)} & \frac{Z_1(f,C_1)\cdot[Z_1(f,C_1)+2Z_2(f,C_2)]}{Z_2(f,C_2)} \\ \frac{1}{Z_2(f,C_2)} & 1 + \frac{Z_1(f,C_1)}{Z_2(f,C_2)} \end{bmatrix}. \tag{33.78}$$

The ABCD matrix (Equation 33.78) can be converted into S-matrix and the scattering parameters of the section can be obtained. Now, for an example, we use the following selection of the filter component: $L_1 = 1.5$ nH, $L_2 = 3.0$ nH, $Q = 100$, $C_1 = 1.0$ pF, $C_2 = 0.5$ pF, $\tan\delta = 0.01$. All resonators being a part of the section have the same resonant frequency $f_0 = 4.9$ GHz, and different characteristic impedance:

$$\sqrt{\frac{L_1}{C_1}} = 38.75\,\text{Ohm}, \quad \sqrt{\frac{L_2}{C_2}} = 77.5\,\text{Ohm}. \tag{33.79}$$

The scattering parameters of the T-section are shown in Figure 33.33. One can see that the section is a typical third-order band pass filter. The phase response is zero at the frequency corresponding

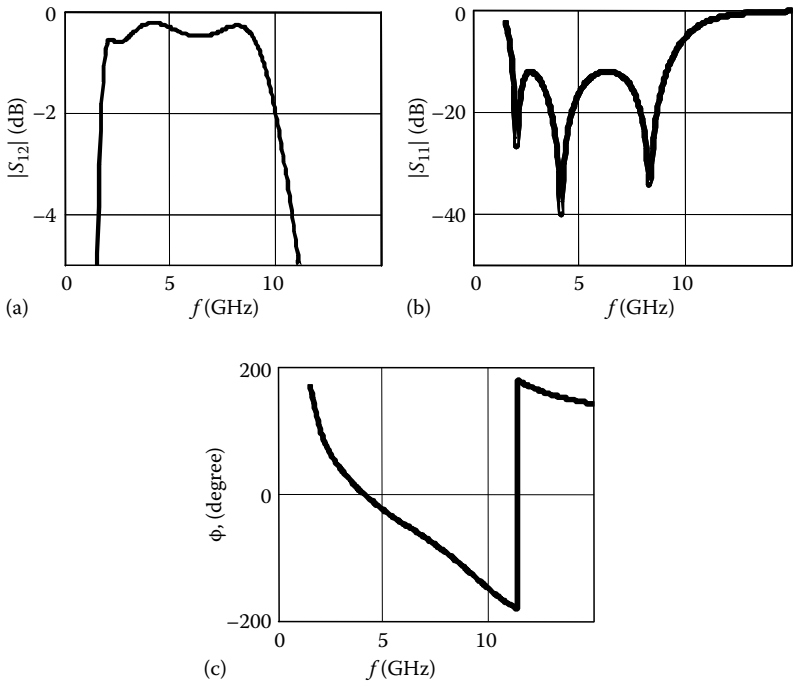

FIGURE 33.33 Frequency dependence of scattering parameters of the section shown in Figure 33.32.

to the central peak of the transmission and reflection characteristics of the filter (f_0 = 4.9GHz). At the frequency below f_0, the section is an LHTL and at the frequency above f_0 the section is an RHTL.

33.5.3 Tuneable Zero-Order Resonator on CRLH TL

Let us consider the section shown in Figure 33.32 with the following filter component: $L_1 = 21$ nH, $L_2 = 42$ nH, $Q = 250$, $C_1 = 0.075$ pF, $C_2 = 0.0375$ pF, $\tan\delta = 0.01$. All resonators being a part of the section have the same resonant frequency $f_0 = 4.01$ GHz and the following characteristic impedance:

$$\sqrt{\frac{L_1}{C_1}} = 1058\ \text{Ohm}, \quad \sqrt{\frac{L_2}{C_2}} = 529\ \text{Ohm}. \tag{33.80}$$

The scattering parameters of the T-section simulated for $Z_0 = 50$ Ohm are shown in Figure 33.34. As in the previous example, the phase response is zero at the frequency corresponding to the central peak of the transmission characteristic of the filter. One may number the peaks of the transmission characteristic shown in Figure 33.34a in the following way −1, 0, +1. The central peak corresponds to the zero phase response. This peak is usually named as the peak of zero-order resonance [23,24]. The zero-order resonant frequency can be tuned by changing the capacitance of the capacitors C_1 and C_2. Let us take for the example $C_1 = 2C$, $C_2 = C$, and the capacitance C is changed under the biasing voltage in the range 0.025–0.05 pF. Figure 33.35 illustrates the position of the zero-order resonance peaks for three values of the capacitance C: 0.025, 0.0375, and 0.05 pF.

One may conclude that, if CRLH TL section is equipped with ferroelectric tuneable capacitors, it can be used for designing different kinds of tuneable filters.

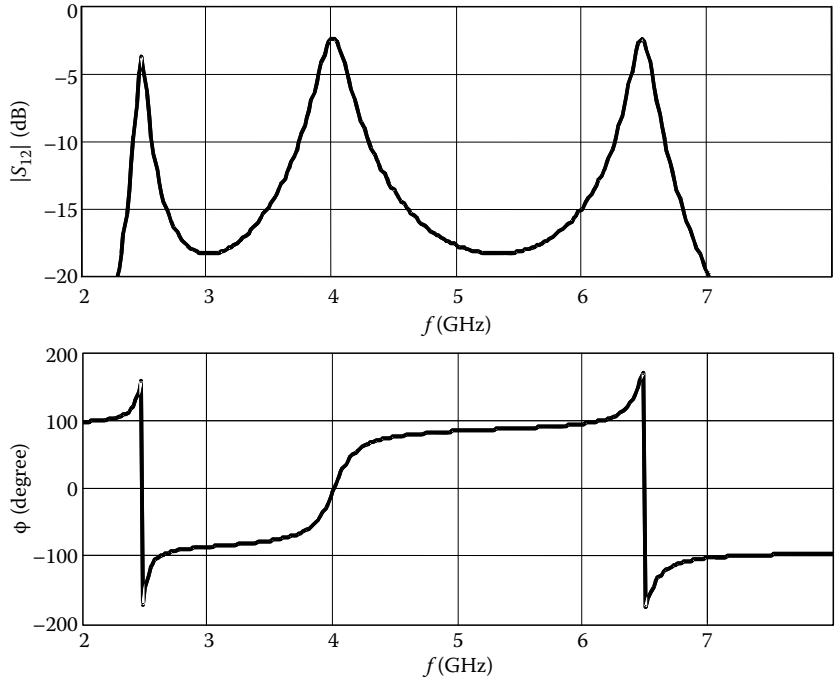

FIGURE 33.34 Frequency dependence of scattering parameters of the T-section simulated for $Z_0 = 50$ Ohm.

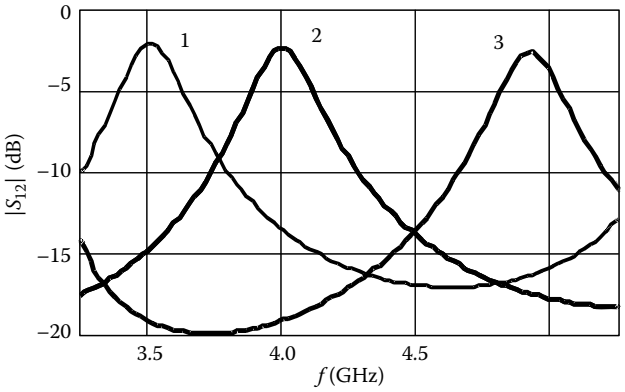

FIGURE 33.35 Frequency dependence of scattering parameter for different values of capacitance.

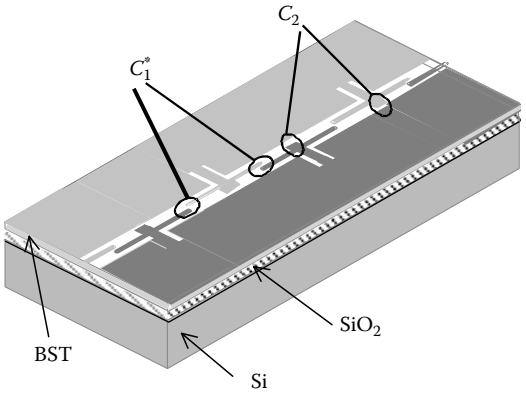

FIGURE 33.36 Layout of coplanar line phase shifter.

33.5.4 Phase Shifter on CRLH TL

Let us consider a CRLH TL structure as cascaded sections schematically shown in Figure 33.32. Figure 33.36 illustrates the phase shifter comprising four such sections [25]. The scattering parameters of the phase shifter can be formed through ABCD matrix of cascaded sections. On the involution matrix presented by Equation 33.78, one obtains

$$A_{\text{ph-sh}}(f, C) = [A(f, C_1, C_2)]^m, \tag{33.81}$$

where m is number of sections.

In Equation 33.78, the following equality was used

$$C_1 = 2C, \quad C_2 = C. \tag{33.82}$$

The series capacitors shown in Figure 33.36 have capacitance in half of C_1. Thus

$$C_1^* = C. \tag{33.83}$$

The capacitance of all capacitors C is tuneable and can be changed in the range 0.7–1.4 pF. The coplanar line was designed as a layered structure on silicon substrate containing ferroelectric film

TABLE 33.5 Layers of the Structure and Their Characteristics

Layer	Thickness (μm)	Dielectric Constant
Pt/Au	0.5	—
$Ba_{0.25}$ $Sr_{0.75}$ TiO_3 (BSTO)	0.3	150
Pt/Au	0.5	—
SiO_2	0.43	4
Si	380	11.7

(BSTO) [25]. The layer parameters are presented in Table 33.5 [25]. The series capacitors C_1^* and the shunt capacitors C_2 are formed as parallel-plate structures using the ferroelectric layer. The inductors are implemented as coplanar line sections. The size of the phase shifter is $3.5 \times 1.5 \times 0.38\,\text{mm}^3$. The tunability of the ferroelectric film is $n = 2$ for 25 V of biasing voltage.

The phase shifter provides the tuneable phase shift in frequency range 18–24.5 GHz. Figure 33.37 illustrates the scattering parameters and the phase shift simulated as function of the biasing voltage

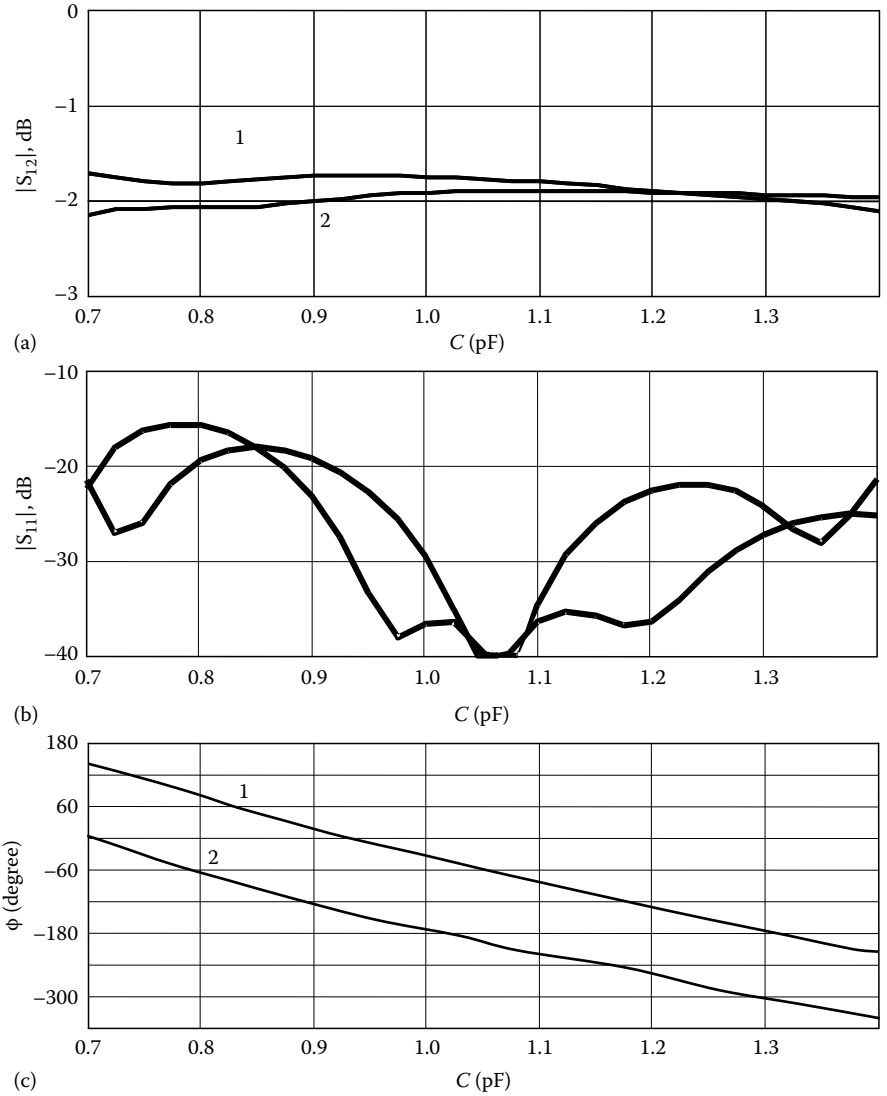

FIGURE 33.37 Scattering parameters and the phase shift of coplanar phase shifter.

at different frequencies for the phase shift comprising six T-sections. The insertion loss shown in Figure 33.37a was simulated for loss factor of the ferroelectric film $\tan\delta = 0.01$ at zero-biasing voltage.

A monolithic CRLH TL phase shifter based on ferroelectric varactors using the four T-sections described above was demonstrated by group of Gevorgian [80]. It was shown that CRLH TLs may be used for a realization of phase shifters providing a differential phase shift with flat frequency dependence around the center frequency. The prototype presented was really the first example exhibiting the metamaterial structure in combination with ferroelectric varactors as a basis of planar integrated phase shifter. Unfortunately, the measured parameters of the four section phase shifter (the phase shift $\Delta\varphi = 60°$ and the insertion loss 4–5 dB) may not be considered as a final solution of the problem. The significant improvement of the phase shifter parameters can be reached by moving up in two directions: (1) increasing of the commutation quality factor of the varactor [81], (2) improvement of the conducting quality of the copper film used in the device [82].

References

1. M. Di Domenico, D.A. Johnson, and R.H. Pantell, Ferroelectric garmonic generator and the large-signal microwave characteristics of ferroelectric ceramics, *J. Appl. Phys*., 33(5), 1697–1706 (1962).
2. Y.M. Poplavko, Electrically controllable microwave devices based on ferroelectric ceramics, *RTE* (Moscow, in Russian), 7(8), 1458–1464 (1962).
3. S.N. Das, Quality of a ferroelectric material, *IEEE Trans. MTT*, 12(7), 440–445 (1964).
4. S.N. Das and K.W.H. Foulds, Application of barium titanate to microwave parametric amplification, *IEEE Trans. MTT*, 13(2), 245–250 (1965).
5. K. Bethe, Über das mikrowellen verhalten nichlineare dielectrika (in German), *Philips Res. Rep.*, (Suppl. 2), 1–110, (1970).
6. O.G. Vendik, I.G. Mironenko, and L.T. Ter-Martirosyan, Some properties and applications of ferroelectrics at microwaves, *J. Phys. Paris,* Colloque C2, 33(Suppl. 4), C2.277–C2.280 (1972).
7. O.G. Vendik, G.D. Loos, and L.T. Ter-Martirosyan, Planar ferroelectric capacitors for the microwave devices, *RTE* (Moscow, in Russian), 17(10), 2241–2244 (1972).
8. O.G. Vendik, L.T. Ter-Martirosyan et al., Cooled parametric amplifier on strontium titanate, *Radiotekhnika i Elektronika* (Moscow, in Russian), 17(9), 1981–1984 (1972).
9. O.G. Vendik, Dielectric nonlinearity of the displacive ferroelectrics at UHF, *Ferroelectrics*, 12, 85–90 (1976).
10. O.G. Vendik, L.T. Ter-Martirosyan et al., Low noise ferroelectric microwave parametric amplifier, *RTE* (Moscow, in Russian), 23(1), 175–179 (1978).
11. L.T. Ter-Martirosyan et al., *Ferroelectrics at Microwaves* (In Russian), Moscow, Publishing House Sovietskoye Radio, 1979.
12. O.G. Wendik, Technologie und Anwendungen ferroelektrischer Schichten in der Mikroelektronik (in German), *Nachrichtentechnik-Elektronik*, 30(12), 504–512 (1980).
13. D. Galt, C. Price, J.A. Beall, and R.H. Ono, Characterization of tunable thin film microwave $YBa_2\,Cu_3\,O_{7-x}/SrTiO_3$ coplanar capacitor, *Appl. Phys. Lett.*, 63(22), 3076–3080 (1993).
14. O.G. Vendik, L.T. Ter-Martirosyan, A.I. Dedyk, S.F. Karmanenko, and R.A. Chakalov, High-T_c superconductivity: New applications of ferroelectrics at microwave frequencies. *Ferroelectrics*, 144(1–4), 33–43 (1993).
15. O.G. Vendik, I.G. Mironenko, and L.T. Ter-Martirosyan, Superconductors spur application of ferroelectric films, *Microw RF*, 33(7), 67–70 (1994).
16. S.S. Gevorgian, D.I. Kaparkov, and O.G. Vendik, Electrically controlled HTSC/ferroelectric coplanar waveguide, *IEE Proc. Microw. Antennas Propag*., 141(6), 501–503 (1994).

17. A.T. Findikoglu, Q.X. Jia, I.H. Campbell, X.D. Wu, D. Reagor, C.B. Mobourquette, and D. McMurry, Electrically tunably coplanar transmission line resonator using $YBa_2\ Cu_3\ O_{7-x}$/$SrTiO_3$ bilayers, *Appl. Phys. Lett*., 66(26), 3674–3676 (1995).
18. O.G. Vendik, E.F. Carlsson, P.K. Petrov et al., HTS/ferroelectric CPW structures for voltage tunable phase shifters, *Proceedings of the 27th EuMC*, Vol. 1, pp. 196–202, 1997, London.
19. M.J. Lancaster, J. Powel, and A. Porch, Thin film ferroelectric microwave devices, *Supercond. Sci. Technol.,* 11, 1323–1334 (1998).
20. O.G. Vendik, E.K. Hollmann, A.B. Kozyrev, and A.M. Prudan, Ferroelectric tuning of planar and bulk microwave devices, *J. Supercond.*, 12(2), 325–338 (1999).
21. V. Sherman, K. Astafiev, A. Tagantsev, N. Setter, I. Vendik, and O. Vendik, Design and investigation of ferroelectric digital phase shifter, *Proceedings of the 31st EuMC*, Vol. 3, pp. 185–188, September 2001, London.
22. V. Sherman, K. Astafiev, N. Setter, A. Tagantsev, O. Vendik, I. Vendik, S. Hoffmann-Eifert, and R. Waser, Digital reflection-type phase shifter based on a ferroelectric planar capacitor, *IEEE Microw. Wirel. Compon. Lett.*, 11(10), 407–409 (2001).
23. A. Lai, C. Caloz, and T. Itoh, Composite right/left-handed transmission line metamaterials, *IEEE Microw. Mag.*, 5(3), 34–50 (2004).
24. C. Caloz and T. Itoh, *Electromagnetic Metamaterials: Transmission Line Theory and Microwave Applications*, Wiley Interscience, Hoboken, NJ, 2006.
25. O.G. Vendik, I.B. Vendik, D.V. Kholodnyak, S.P. Zubko, and E.V. Serebryakova, Electronically controlled phase shifters based on composite right/left-handed transmission line, *Proceedings of the EuMC35*, pp. 909–912, October 2005, Paris.
26. O.G. Vendik and S.P. Zubko, Modeling the dielectric response of incipient ferroelectrics, *J. Appl. Phys.*, 82(9), 4475–4483 (1997).
27. O.G. Vendik, S.P. Zubko, and L.T. Ter-Martirosyan, Experimental evidence of the size effect in thin ferroelectric films, *Appl. Phys. Lett.*, 73(1), 37–39 (1998).
28. O.G. Vendik, L.T. Ter-Martirosyan, and S.P. Zubko, Microwave losses in incipient ferroelectrics as function of the temperature and the biasing field, *J. Appl. Phys.*, 84(29), 993–998 (1998).
29. O.G. Vendik, S.P. Zubko, and M.A. Nikol'skiĭ, Modeling and calculation of the capacitance of a planar capacitor containing a ferroelectric thin film, *Techn. Phys.*, 44(4), 349–353, 1999 [*Zh. Tekh. Fiz*., 69(4), 1–7 (1999)].
30. O.G. Vendik and L.T. Ter-Martirosyan, Influence of charged defects on the dielectric response of incipient ferroelectrics, *J. Appl. Phys.*, 87(3), 1435–1439 (2000).
31. O.G. Vendik and M.A. Nikol'skiĭ, Simulation of a multilayer planar capacitor, *Tech. Phys.*, 46(1), 112–116 (2001) [*Zh. Tekh. Fiz*., 71(1), 117–121 (2001)].
32. O.G. Vendik and S.P. Zubko, Modeling microwave dielectric characteristics of thin ferroelectric films for tunable planar structures, *Integr. Ferroelectr.*, 34(1–4 Pt. 5), 215–226 (2001).
33. I. Vendik, O. Vendik, V. Pleskachev, A. Svishchev, and R. Woerdenweber, Design of tunable ferroelectric filters with a constant fractional bandwidth, *IMS Dig.*, 3, 1461–1464 (2001).
34. P. Yudin, M. Nikol'ski, O. Vendik, S. Zubko, and I. Vendik, Extracting the model parameters of ferroelectric thin film from the experimental characteristics of the capacitance of a planar capacitor, *Proceedings of the 31st EuMC*, 1, 415–418, 2001, St. Petersburg.
35. A. Tagantsev, dc-electric-field-induced microwave loss in ferroelectrics and intrinsic limitation for the quality factor of a tunable component, *Appl. Phys. Lett.*, 76(9), 1182–1184 (2000).
36. C.B. Sawyer and C.H. Tower, Rochelle salt as a dielectric, *Phys. Rev*., 35, 269 (1930).
37. Ch. Kittel, *Introduction to Solid State Physics*, John Wiley & Sons, New York, 1971.
38. J.H. Barrett, Dielectric constant in perovskite type crystals, *Phys. Rev.,* 86, 118–120 (1952).
39. O.G. Vendik, Soft mode in a ferrolelectric crystal, *Fiz. Tverd. Tela (Leningrad),* 14, 989 (1972) [*Sov. Phys. Solid State,* 14, 849 (1972)].

40. S. Nishi, H. Kawamura, and K. Murase, Study of lattice instability by mm-wave magnetoplasma reflection in PbTe–SnTe compound semiconductors, *Phys. Status Solidi B*, 97, 581–590 (1980).
41. O.G. Vendik and S.P. Zubko, Ferroelectric phase transition and maximum dielectric permittivity of displacement type ferroelectrics ($Ba_x\ Sr_{1-x}\ TiO_3$), *J. Appl. Phys.*, 88(9), 5343–5350 (2000).
42. K. Bethe and F. Welz, Preparation and properties of (Ba,Sr)TiO_3 single-crystals, *Mater. Res. Bull.*, 6(4), 209 (1971).
43. Smolenskii G.A. and Rozgachev K.F., Segnetoelektricheskie svoistva tverdykh rastvorov v sisteme titanat bariya titanat stronsiya, *Zh. Tekh. Fiz*., 24(10), 1751–1760 (1954).
44. L. Benguigui, Disodered ferroelectrics: $Ba_x\ Sr_{1-x}\ TiO_3$ single crystals, *Phys. St. Solidi (a)*, 46(1), 337–342 (1978).
45. G.A. Smolenskii, *Ferroelectrics and Related Materials*, Gordon and Breach, New York, 1985.
46. J.C. Burfoot and J.R. Slack, *J. Phys. Soc. Jpn.,* 28(Suppl. P) 417, 1970.
47. P. Padmini, T.R. Taylor, M.J. Lefevre, A.S. Nagra, R.A. York, and J.S. Speck, Realization of high tunability barium strontium titanate thin films by rf magnetron sputtering, *Appl. Phys. Lett.*, 75(20), 3186–3188 (1999).
48. C. Zhou and D.M. Newns, Intrinsic dead layer effect and the performance of ferroelectric thin film capacitors, *J. Appl. Phys*., 82, 3081–3088, 1997.
49. S.P. Zubko, Modeling dielectric response and losses of ferroelectrics at microwave frequencies, *Integr. Ferroelectr.*, 43(1), 71–80 (2002).
50. O.G. Vendik and L.T. Ter-Martirosyan, Size effect in layered structures: Ferroelectric/normal metal and ferroelectric/high-Tc superconductor, *Phys. Solid State*, 36(11), 1778–1781 (1994).
51. R.A. Cowley, Lattice dynamics and phase transitions in strontium titanate, *Phys. Rev.*, 134(4A), A981–A997 (1964).
52. O.G. Vendik and I.G. Mironenko continuos model of the ferroelectric mode, *Sov. Phys. Solid State,* 16(11), 2230–2234 (1974) [*Fiz. Tverd. Tela (Leningrad)*, 16(11), 3445–3451 (1974)].
53. V.G. Vaks, *Introduction into Microscopic Theory of Ferroelectrics*, Nauka, Moscow, 1973 (in Russian).
54. O.G. Vendik and S.P. Zubko, Size effect in displacive ferroelectrics, *Crystallogr. Rep.,* 49(6), 2004, 1046–1052. [Translated from *Kristallografiya* (in Russian), 49(6), 1144–1150 (2004).]
55. S.P. Zubko, Influence of the size effect on the permittivity of potassium tantalate forming part of a film capacitor, *Tech. Phys. Lett.*, 24(11), 839–841 (1998) [*Pisma ZhTF*, 24(21), 23–29 (1998)].
56. A.F. Devonshir, Theory of barium titanate—Part I, *Philos. Mag.*, 40, 1040–1063 (1949)—Part II, *Philos. Mag.*, 42, 1065–1079 (1951).
57. M. Anliker, H.R. Brugger, and W. Känzig, Das Verhalten von kolloidalen Seignetteelektrika III, Bariumtitanat $BaTiO_3$, *Heiv. Phys. Acta*, 27, 99–123 (1954).
58. O.G. Vendik, Potential of the point crystal lattice of a bounded crystal, *Phys. Stat. Sol*., 28, 789–796 (1968).
59. O.G. Vendik and L.A. Rosenberg, The microscopic theory of surface phenomena in ferroelectric crystals, *J. Phys. Soc. Jpn.*, 28(Suppl.), 413–415 (1970).
60. M. Izuha, K. Abe, and N. Fukushima, Electrical properties of all-perovskite oxide ($SrRuO_3$/$Ba_x\ Sr_{1-x}\ TiO_3$/$SrRuO_3$), *Jpn. J. Appl. Phys.,* Part 1 36(9B), 5866–5869 (1997).
61. G. Gerra, A.K. Tagantsev, N. Setter, and K. Parlinski, Ionic polarizability of conductive metal oxides and critical thickness for ferroelectricity in $BaTiO_3$, *Phys. Rev. Lett.*, 96, 107603–107605 (2006).
62. S.B. Deshu and O.G. Vendik, Suppression of size effects in ferroelectric films, *Integr. Ferroelectr.,* 28(1–4), 175–192 (2000).
63. M.E. Drougard and R. Laundauer, On the dependence of the switching time of barium titanate crystals on their thickness, *J. Appl. Phys*., 30(11), 1663–1668 (1959).
64. R. Kretschmer and K. Binder, Surface effects on phase transitions in ferroelectrics and dipolar magnets, *Phys. Rev. B*, 20(3), 1065–1076 (1979).
65. A.K. Tagantsev, V.O. Sherman, K.F. Astafiev, J. Venkatesh, and N. Setter, Ferroelectric materials for microwave tunable applications, *J. Electroceram.*, 11, 5–66 (2003).

66. M. Stengel and N.A. Spaldin, Origin of the dielectric dead layer in nanoscale capacitors, *Nature* 443, 679–682 (2006).
67. B. Chen, H. Yang, L. Zhao et al. Thickness and dielectric constant of dead layer in $Pt/(Ba_{0.7}\,Sr_{0.3})/YBa_2\,Cu_3\,O_{7-x}$ capacitor, *Appl. Phys. Lett.,* 84(4), 583–585 (2004).
68. Ch. P. Poole Jr., H.A. Farach, and R.J. Creswick, *Superconductivity*, AP Inc., London, 1995.
69. R. Blinc and B. Zheksh, *Soft Modes in Ferroelectrics and Antiferroelectrics*, Elsevier, New York, 1974 (Mir, Moscow, 1975—in Russian).
70. B.D. Silverman, Microwave absorption in cubic strontium titanate, *Phys. Rev.* 125A, 1921 (1962).
71. B.Y. Balagurov, V.G. Vaks, and B.I. Shklovsky, *Fiz. Tverd. Tela (Leningrad)*, 12(1), 89–99 (1970). [*Sov. Phys. Solid State*, 12(1), 70–77 (1970)].
72. O.G. Vendik, Attenuation of ferroelectric mode in SrTiO sub 3-type crystals, *Fiz. Tverd. Tela (Leningrad)*, 17(6), 1683–1690 (1975) [*Sov. Phys. Solid State*, 17(6), 1096–2003 (1975)].
73. A.K. Tagantsev, Dielectric losses in displacive ferroelectrics, *Zh. Eksp. Theor. Fiz.*, 86(6), 2215–2228 (1984) [*JETP* 59(6), 1290–1300 (1984)].
74. O.G. Vendik and L.M. Platonova, Losses in ferroelectric materials influenced by charged defects, *Fiz. Tverd. Tela (Leningrad)*, 13(6), 1617–1625 (1971) [*Sov. Phys. Solid State*, 13(6), 1353–1359 (1971)].
75. O.G. Vendik and L.T. Ter-Martirosyan, Electrostriction microwave loss mechanism in planar capacitor based on strontium titanate film,*Tech. Phys.*, 44, 954 (1999).
76. O.G. Vendik and A.N. Rogatchev, Electrostriction microwave loss mechanism in ferroelectric film and experimental confirmation, *Tech. Phys. Lett.,* 25, 702 (1999).
77. J.M. Pond, S.W. Kirchoffer, W. Chang, J.S. Horwitz, and D.B. Chrisey, Microwave properties of ferroelectric thin films, *Integr. Ferroelectr.*, 22(1–4), 317–328 (1998).
78. D.F. Sievenpiper, J.H. Schaffner, H.J. Song, R.Y. Loo, and G. Tangonan, Two-dimensional beam steering using an electrically tunable impedance surface, *IEEE Trans. Antennas Propag.*, 51(10), 2713–2722 (2003).
79. V.V. Pleskachev and I.B. Vendik, The commutation quality factor of electrically controlled microwave device components, *Tech. Phys. Lett.*, 29(12), 1018–1020 (2003).
80. A. Vorobiev, P. Rundqvist, K. Khamchane, and S. Gevorgian, Silicon substrate integrated high *Q*-factor parallel-plate ferroelectric varactors for microwave/millimeter wave applications, *Appl. Phys. Lett.*, 83(15), 3144–3146 (2003).
81. D. Kuylenstierna, A. Vorobiev, P. Linnér, and S. Gevorgian, Composite right/left handed transmission line phase shifter using ferroelectric varactors, *IEEE Microw. Wirel. Comp. Lett.*, 16(4), 167–169 (2006).
82. I.B. Vendik, O.G. Vendik, and E.L. Kollberg, Commutation quality factor of two-state switching devices, *IEEE Trans. MTT*, 48(5), 802–808 (2000).

34

Spin Waves in Multilayered and Patterned Magnetic Structures

Natalia Grigorieva
St. Petersburg Electrotechnical University

Boris Kalinikos
St. Petersburg Electrotechnical University

Mikhail Kostylev
University of Western Australia

Andrei Stashkevich
University of Paris

34.1 Introduction

In recent years, the idea of artificial composite materials (metamaterials) has received significant attention in both physics and engineering. Metamaterials are designed to demonstrate the physical properties, which are not usually found in nature. The first "magnetic metamaterials" were fabricated by combining lattices of metallic split-ring resonators placed on dielectric substrates. The lattices of resonant elements are capable of producing strong magnetic response at radio, microwave, and optical frequencies. Due to this capability, such composites are commonly called magnetic metamaterials (see, e.g., [1–4]).

To separate this notion from the case of magnetic metamaterials, which are considered in this chapter, we use the name "magnonic crystals" by analogy with man-made photonic crystals [5–9]. This novel class of metamaterials is composed from the constituent elements that are magnetic (ferromagnetic, ferrimagnetic, antiferromagnetic) by themselves. Such artificial crystals represent magnetic media in which the magnetic properties are varied periodically. The simplest type of one-dimensional (1D) magnonic crystals is a multilayered periodic structure composed of magnetic

layers with different magnetization or an array of thin ferromagnetic films separated by nonmagnetic spacers. Years ago, before the term "metamaterials" became universal, such periodic magnetic-thin-film layered structures were called magnetic superlattices [10–15]. Their properties have been extensively studied in connection with possible applications in optics and microwaves (see, e.g., [10,11]).

Until now, several different layered structures of magnetic and nonmagnetic materials have been fabricated. Examples of these include multilayers constructed by alternating layers of ferromagnets with nonmagnets (Ni/Mo, Fe/Si, Gd/Y, Co/Ru, Co/Cu), ferromagnets with ferromagnets (ferromagnetic interfacial coupling—Fe/Ni and antiferromagnetic interfacial coupling—Fe/Gd, Co/Gd), ferromagnets with helimagnets (Gd/Dy), and ferromagnets with antiferromagnets (Fe/Cr). There are also structures with alternated helical or conical magnets with nonmagnets (Dy/Y, Ho/Y, Er/Y) and antiferromagnets with antiferromagnets (FeF_2/CoF_2, Fe_2O_4/NiO). For more details see references in [16]. The variety of magnetic materials used as building blocks in multilayers has led to an enormous range of the resulting magnetic behavior. Moreover, some exotic spin configurations found in multilayered systems can lead to anomalous field and temperature behavior (i.e., phase transitions) [16].

A survey of the literature shows that it is still too complicated to fabricate multilayered structures with rigorous periodicity. Due to this and due to the simplicity in the fabrication technology, 1D- and two-dimensional (2D)-patterned structures (e.g., arrays of stripes [17–19], wires [20–22], dots [23–27], and holes [28]) based on ferromagnetic films became more preferential.

Another type of the magnetic periodic structures, which should be mentioned here, is made from a continuous magnetic film with periodically varied properties. Such structures could be created by varying any parameter that influences the dispersion characteristics of spin waves. Similar systems were extensively studied in literature [29–36].

Magnetic multilayered, patterned and other magnetic periodic structures have attracted significant attention because of a wide range of fascinating properties. The properties of such composite systems can be significantly different from those of any of its initial components. Spin-wave propagation through such structures is prohibited within some restricted bands. Such magnonic crystals operating at the microwave frequency range should compliment the photonic crystals operating at the light frequency band.

It is to be emphasized that contrary to the photonic crystals the response parameters of magnonic crystals can be easily tuned by changing the bias static magnetic field. In other words, magnetic metamaterials are electrically tunable [37,38]. Moreover, a rich variety of new effects appear in magnonic crystals, which do not exist in the photonic crystals. This is related to the specific properties of the eigen excitations (spin waves) in the magnonic crystals. Due to the possible nonreciprocality of the dispersion relations, strong surface and bulk anisotropy and the presence of exchange boundary conditions at all interfaces of the system such as magnetic structures suppose unique propagation characteristics of spin waves. In addition, the inhomogeneity of the internal static magnetic field inside each element of the metamaterial leads to the existence of new quantum states.

One of the most interesting effects, which have already found a practical application, is giant magnetoresistance (GMR). The appearance of GMR in multilayered structures is due to the changes in the conduction electron scattering mechanism. For example, in Fe/Cr multilayered system, the resistivity of the metallic structure can be changed by over 60% at room temperature under the influence of a magnetic field.

Another novel behavior was observed in Co/Pt- and Co/Pd-multilayered structures, where the perpendicular uniaxial anisotropy energy is significantly enhanced with the decrease of the Co layer thickness [39]. Using this multilayered structure enables one to prepare a macroscopic bulk sample with properties determined by the large surface anisotropy energy at the Co/Pt interfaces.

In multilayered and patterned structures, collective effects can play a significant role [17,18,40]. Even in layered magnetic–non magnetic systems, one may have a new collective excitation because

the magnetic films interact via long-range dipolar fields. Of course, in the magnetic/magnetic structures, spins interact via both the short-range exchange interaction and the long-range dipolar fields. A combination of these interactions leads to new dispersion properties of the system [41]. Thus, the periodicity introduces band gaps in the dispersion relations for the fundamental excitations in the structure. Besides, new dynamic modes and new static configurations appear in the periodic structures.

Multilayered and patterned structures have very wide applications. They could be used to design various microelectronic devices such as electronically tuned bandstop and bandpass microwave filters, microwave switches, and microwave signal processing devices [8,9,37,39,42]. Magnetic periodic structures are already used in magnetoresistive heads and magnetic and for magneto-optical recording [16]. The structures that exhibit GMR are promising as the new generation of spin valve sensors. A special configuration of altered magnetic layers could also be used to fabricate a nonreciprocal magnonic crystal with one-directional transparency or to obtain the structures with anisotropic conversion of SWMs (magneto-photonic crystals) [8,9,37,43].

For several decades, when the magnetic metamaterials have attracted special attention, various theoretical approaches have been elaborated and used to consider the problem of multilayered and patterned structures. The first calculations were restricted to the dipolar limit [44–46]. Next, volume anisotropy contributions were included [47]. This early work neglected exchange contributions as well as the possible influence of magnetic interface anisotropies on the spin-wave modes (SWMs). At the same time, pure exchange modes in multilayers have been considered by several authors [13,15,39, 48–53]. The first attempts to include all interactions and apply various exchange boundary conditions were presented in the papers [41,54,55].

It should be noted that a rigorous theory of the magnonic crystals is very cumbersome due to ferromagnetic resonance (FMR) and spin-wave phenomena. Existence of spin waves significantly modifies the metamaterial response as compared to the nonmagnetic media. Even a rigorous spin-wave theory for a single magnetic thin film is rather complicated [42,56–59]. Now, it is clear that the theories, which consider pure dipole or exchange modes, cannot adequately describe most of the processes in such complicated systems. Only the dipole-exchange theoretical technique, which includes surface and bulk anisotropy, is suitable in this case. This common approach will be presented here in the chapter as well as a brief review of several other techniques will be given.

During the last decade, the problem of spin-wave propagation in ferromagnetic film-structures with periodically and weakly varied parameters draw new attention due to the fabrication technology and the appearance of novel materials. This problem was analyzed in various limiting cases and for different structures (see [5,6,8,14,16,19,60–64] and references therein). Even some exotic periodic structures were considered by several authors [20,21,23,24,28,40,65–70].

On the other hand, magnetic periodic structures have been extensively investigated experimentally. Various experimental techniques, for example, the Brillouin light scattering (BLS) spectroscopy [18,71,72], magneto-optic Kerr microscopy [73], ferromagnetic resonance spectroscopy [74], polarized neutron reflectometry [75,76], and others have been elaborated and used for these investigations. A good many of the investigations have been performed by means of the BLS spectroscopy because it provides the possibility to retrieve information on the distribution of dynamic magnetization on each element of the periodic array [64,77–79] and on spin-wave dispersion of the periodic structure as a whole [69,80,81]. Otherwise, similar data can be obtained by means of the Kerr microscopy [82,83] or by the micro-BLS technique [84,85], which simultaneously ensures a submicron spatial resolution and a high resolution in temporal frequencies. An exhaustive review of the experimental work on magnetic periodic structures can be found in Refs. [39,63,64].

This chapter provides a review of the basic theoretical work concerned with the magnetic periodic structures (magnonic crystals). The general role of magnetic tunable metamaterials is discussed. A brief report of existing theoretical approaches used in this area is presented. A detailed description of SWM approach is given for multilayered and patterned magnetic structures. This theoretical

approach includes dipole–dipole and exchange interactions as well as electrodynamics and exchange boundary conditions. The energy of bulk and interface anisotropies is taken into account. The theory is based on the tensorial Green's function method and spin-wave normal mode expansion technique previously elaborated for a single ferromagnetic film. Exact and approximate dispersion relations for some particular cases of fundamental and technological interest are derived, analyzed, and discussed. Special attention is paid to the fundamental role of the periodicity in such structures. Band theory is constructed for multilayered structures. Peculiarities of dipole-exchange spin waves in the multilayered nano-structures are considered. A role of the additional structuring in the dynamic magnetic properties of metamaterials is discussed. Basic pattern geometries such as arrays of micro- and nano-patterned stripes and planar arrays of nano-dots are considered. Formation of collective modes on arrays of nano-objects is discussed. A physical picture of the formation and transformation of spin-wave spectrum for the multilayered and patterned structures is given for two types of structures, namely, magnetic/nonmagnetic and magnetic/magnetic multilayers.

34.2 Dipole-Exchange Spin Waves in Multilayered Structures

After pioneer works of Damon and Eshbach [86] and Herring and Kittel [87] in the early 1950s, a lot of articles were published where the experimental data concerning the spin waves in ferromagnetic films were objectionably described by either dipole or exchange interaction taken into account separately. Later, a considerable discrepancy between the theory and experiment forced a new wave of theoretical investigations in this field, and since then many and more articles appeared where different analytical and numerical methods were suggested for solving the problems. These articles were taking into account both dipole–dipole and exchange interactions. In this chapter, we will consider the general case of the dipole-exchange spin waves. Since our main treatment concerns multilayered structures, another type of interaction called interlayer interaction has to be taken into account. This interaction can also have the dipolar and exchange nature. We will include these types optionally. So, one should accurately distinguish between intra- and interlayer interactions.

In this section, we give a closed picture of the problem under consideration and emphasize possible difficulties in solving it. A brief review of present situation in theoretical investigations in this field is done. We will concentrate our attention on the method suggested by Kalinikos et al. [42,54,57–59,88] because of the clarity of the physical description and the relative simplicity of analytical solutions that can be obtained by this method.

34.2.1 Formulation of the Problem

To make our consideration more general, let us consider an infinite stack of layers with arbitrary spatial and magnetic properties. Ferromagnetic layers are assumed to be magnetized to saturation by a static bias magnetic field $\mathbf{H}_0$ of an arbitrary direction, which is determined by angles θ_0 and ϕ_0 (see Figure 34.1). Saturation magnetization of ferromagnetic films $\mathbf{M}_{0i}$ has arbitrary values, but always directed along z_i-axis in each layer. The type and strength of anisotropy in ferromagnetic layers can also differ. Index i, here and below, numbers the layer in the stack. Sometimes without loosing the generality, we drop this index to expel unnecessary complexity of the equations.

The Landau–Lifshitz equation of motion for magnetization $\mathbf{M}_i$ in i-layer in most common form can be written as [89,90]:

$$\frac{\partial \mathbf{M}_i(\mathbf{r},t)}{\partial t} = -|g|\,\mu_0\left[\mathbf{M}_i(\mathbf{r},t)\times\mathbf{H}_i^{\text{eff}}(\mathbf{r},t)\right] - \lambda_i\mathbf{M}\times(\mathbf{M}\times\mathbf{H}) \tag{34.1}$$

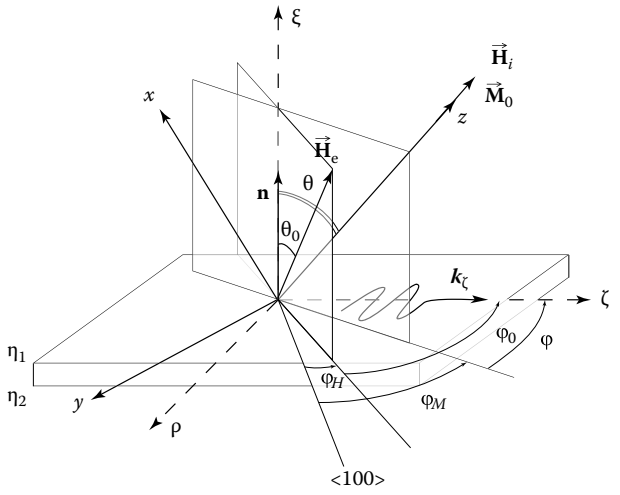

FIGURE 34.1 Geometry of the problem and orientation of coordinate axes.

where

$\mathbf{H}_i^{\text{eff}}$ is a total effective magnetic field inside each ferromagnetic layer
$|g|$ is the modulus of the gyromagnetic ratio for electron spin
μ_0 is the permeability of vacuum

The term containing the relaxation frequency λ_i is taken in the form suggested by Gilbert [91]. As far as we are not interested in the effects related with relaxation, in further calculations the last term will be omitted.

We introduce usual linearization in terms of the deviation $\mathbf{m}(\mathbf{r}, t)$ from equilibrium magnetization $\mathbf{M}_0$. We assume that fluctuations in $\mathbf{M}$ and $\mathbf{H}$ associated with the spin waves are small compared to the static values. This condition is almost always fulfilled for thermally driven spin waves at temperatures considerably less than T_c. We split $\mathbf{M}$ and $\mathbf{H}$ into frequency-independent static parts $\mathbf{M}_0$ and $\mathbf{H}_0$ and dynamic parts $\mathbf{h}$ and $\mathbf{m}$:

$$\begin{aligned} \mathbf{M}_i(\mathbf{r}, t) &= \mathbf{M}_{0i} + \mathbf{m}_i(\mathbf{r}, t), \quad |\mathbf{m}| \ll |\mathbf{M}_0| \\ \mathbf{H}_i(\mathbf{r}, t) &= \mathbf{H}_{0i} + \mathbf{h}_i(\mathbf{r}, t), \quad |\mathbf{h}| \ll |\mathbf{H}_0| \end{aligned} \tag{34.2}$$

Then, the effective magnetic field is assumed to be a sum of the internal static magnetic field, the variable dipole and exchange fields, and a variable field of magnetocrystalline anisotropy:

$$\mathbf{H}_i^{\text{eff}}(\mathbf{r}, t) = \mathbf{H}_i^s + \mathbf{h}_i^{\text{ex}}(\mathbf{r}, t) + \mathbf{h}_i^d(\mathbf{r}, t) + \mathbf{h}_i^a(\mathbf{r}, t) \tag{34.3}$$

The internal static magnetic field in the presence of anisotropy can be found as

$$\mathbf{H}_i^s = \mathbf{H}_{0i} + \mathbf{H}_i^d + \mathbf{H}_i^a \tag{34.4}$$

where

$\mathbf{H}_0$ is an external bias magnetic field
$\mathbf{H}^d$ is the macroscopic constant demagnetization field
$\mathbf{H}^a$ is the constant field of magnetocrystalline anisotropy

The direction of the resulting internal magnetic field $\mathbf{H}^s$ coincides with the direction of the constant magnetization $\mathbf{M}_0$. The demagnetization field $\mathbf{H}^d$ is due to the shape anisotropy and

usually can be found through effective demagnetization factors of the corresponding sample shape. Demagnetization factors for ellipsoidal and nonellipsoidal samples were calculated by Osborn [92] and Joseph and Schlomann [93], respectively.

The variable exchange field in its most general form within a continuum approach is found from Gibbs free energy functional as

$$\mathbf{h}_i^{\mathrm{ex}}(\mathbf{r},t) = \int d^3\mathbf{r}' J(|\mathbf{r}-\mathbf{r}'|)\cdot \mathbf{M}_i(\mathbf{r}',t) \tag{34.5}$$

where $J(|\mathbf{r}-\mathbf{r}'|)$is the exchange integral of the magnetic material. This general form of exchange term is needed for the case of strong exchange interaction between layers in the stack, when the exchange interaction appears to be necessarily nonlocal in the main equation of motion as well as in the exchange boundary conditions (Hoffmann's boundary conditions). Such situation appears when different magnetic layers are in contact or if the nonmagnetic spacer is very thin ($d < 30\,\mathring{\mathrm{A}}$) (e.g., see [41,50]). Variable exchange field measures the exchange torque density due to any nonuniformity in the orientation of M and in the case of local direct exchange interaction it can be found as

$$\mathbf{h}_i^{\mathrm{ex}}(\mathbf{r},t) = \frac{2A_i}{\mu_0 M_{0i}^2}\nabla^2\mathbf{m}_i(\mathbf{r},t) \tag{34.6}$$

where A is the exchange stiffness constant. In most of the particular cases under consideration, this rough expression is quite enough for calculations.

The next term in Equation 34.3 is the time- and position-dependent dipole field $\mathbf{h}^d$, resulting from traveling spin waves. The variable dipolar field has an important effect on the spin-wave spectrum, since it gives rise to a coupling of SWMs in different layers of a multilayer across the nonmagnetic spacer. This effect becomes small only if the in-plane spin-wave propagation wave vector tends to zero, i.e., for nearly standing spin waves, or if the in-plane propagation wave vector becomes very large so as the stray dipolar field is confined to the magnetic layers.

The dipole field is a result of the nonlocal electromagnetic interaction between all spins in the magnetic film thus Maxwell's equations should be involved in the consideration to find the dipole field in explicit form. In the absence of electric and magnetic charges and currents, Maxwell's equations can be written as [94]

$$\begin{aligned} \nabla\times\mathbf{H} &= \frac{\partial\mathbf{D}}{\partial t}, \quad \nabla\cdot(\mathbf{H}+\mathbf{M}) = 0 \\ \nabla\times\mathrm{E} &= -\mu_0\frac{\partial(\mathbf{H}+\mathbf{M})}{\partial t}, \quad \nabla\cdot\mathbf{D} = 0 \end{aligned} \tag{34.7}$$

Their solutions must satisfy usual electrodynamic boundary conditions:

$$\begin{aligned} &\mathbf{n}\times(\mathbf{H}_1-\mathbf{H}_2)\big|_s = 0 && \mathbf{n}\times(\mathbf{E}_1-\mathbf{E}_2)\big|_s = 0 \\ &\mathbf{n}\cdot((\mathbf{H}_1+\mathbf{M}_1)-(\mathbf{H}_2+\mathbf{M}_2))\big|_s = 0 && \mathbf{n}\cdot(\mathbf{D}_1-\mathbf{D}_2)\big|_s = 0 \end{aligned} \tag{34.8}$$

In microwave calculations, we usually utilize the solution of this problem in the magnetostatic approximation. But in some special cases, for example, when the electromagnetic wavelength is of the order of sample size (in the limit of small $\mathbf{k}$) or if we study magneto-optic effects, the magnetostatic approximation does not work any longer, hence we should solve the full set of Maxwell's equations. As a result of solving Maxwell's equations, a connection between the variable magnetization and the dipole field should be found. In the frame of the Green's function formalism considered here, this relation can be obtained in integral form (see below).

The last term in Equation 34.3 is the effective field of magnetocrystalline anisotropy $\mathbf{h}^a(\mathbf{r}, t)$. It can be calculated if the expressions for the density of anisotropy energy are known:

$$\mathbf{h}_i^a(\mathbf{r}, t) = -\nabla_M U^{\text{ani}} \tag{34.9}$$

where U^{ani} is the usually defined magnetic volume anisotropy energy density.

For the linear problem, when the condition $\mathbf{m}(\mathbf{r}, t) \ll \mathbf{M}_0$ is fulfilled, we can calculate the effective magnetic field associated with magnetocrystalline anisotropy using the method of effective demagnetization factors of anisotropy. In the framework of this method, the effective magnetic field of anisotropy $\mathbf{H}^a(\mathbf{r}, t)$ is represented as

$$\mathbf{H}_i^a(\mathbf{r}, t) = \mathbf{H}_i^a + \mathbf{h}_i^a(\mathbf{r}, t) = -\underline{\mathbf{N}}_i^a \mathbf{M}_{0i} - \underline{\mathbf{N}}_i^a \mathbf{m}_i(\mathbf{r}, t) \tag{34.10}$$

where $\underline{\mathbf{N}}_i^a$ is the tensor of effective demagnetization factors of magnetocrystalline anisotropy for ith layer. The components of this tensor can be demagnetization factors of any type of anisotropy or the sum of demagnetization factors of different types of anisotropy taken into account simultaneously. For example, the calculation of the components of $\underline{\mathbf{N}}_i^a$ for the case of a ferromagnetic ellipsoid having cubic and uniaxial anisotropy and the arbitrary direction of the crystallographic axes with respect to its geometrical axes is presented in papers [59,95–97].

The last question, which should be cleared up is the determination of the equilibrium orientation of the saturation magnetization $\mathbf{M}_{0i}$ in the anisotropic film. The equilibrium orientation of $\mathbf{M}_{0i}$ is characterized by angles $\varphi = \varphi_i$ and $\theta = \theta_i$ (see Figure 34.1). They are usually determined from the condition of minimization of the magnetic energy density in each ferromagnetic film separately [59,90].

In principle, we have to find the static equilibrium orientations of the magnetizations for the layered system before calculating the spin-wave frequencies. Due to interface anisotropies and exchange coupling effects, the static equilibrium magnetization direction might differ from the bulk one. It should be noted that in general case the direction of the magnetization is a function of the position in each magnetic layer of multilayered structure. In the absence of anisotropy, the external magnetic field $\mathbf{H}_0$ and the saturation magnetization $\mathbf{M}_0$ always have the same value of angle φ ($\varphi_0 = \varphi$) and thus lie in one vertical plane, but with different θ_0 and θ (see Figure 34.1). In the presence of anisotropy, in addition to different θ, we have also different φ_0 and φ, i.e., now $\mathbf{H}_0$ and $\mathbf{M}_0$ lie in different vertical planes. But in any case, the direction of the internal static magnetic field $\mathbf{H}^s$ always coincides with the direction of the constant magnetization $\mathbf{M}_0$. We also stress here that in general case $\mathbf{H}_i$, θ_i, and φ_i are different for all ferromagnetic films formed the structure.

Now making use of linearization procedure, we apply relation (Equation 34.2) to the equation of motion (Equation 34.1) with (Equation 34.3). Since $\mathbf{m}(\mathbf{r}, t)$ and $\mathbf{h}(\mathbf{r}, t)$ are both assumed to be small in magnitude compared with the static field components, in the linearized equation, we neglect the quantities of a second order and for variable magnetization we arrive to the following equation of motion:

$$\begin{aligned}&\frac{\partial \mathbf{m}(\mathbf{r}, t)}{\partial t} + |g|\,\mu_0\left[\mathbf{m}(\mathbf{r}, t) \times \mathbf{H}^s(\mathbf{r}, t)\right] + |g|\,\mu_0\left[\mathbf{M}_0 \times (\mathbf{h}^{\text{ex}}(\mathbf{r}, t) + \mathbf{h}^a(\mathbf{r}, t))\right] \\ &\quad = -|g|\,\mu_0\left[\mathbf{M}_0 \times \mathbf{h}^d(\mathbf{r}, t)\right]\end{aligned} \tag{34.11}$$

Substituting Equations 34.6 through 34.10 and $\mathbf{h}^d$ from the system (Equation 34.7), we obtain the Landau–Lifshitz equation of motion for the dynamic magnetization in the form of integro-differential equation:

$$\begin{aligned}&\frac{\partial \mathbf{m}_i(\mathbf{r}, t)}{\partial t} + |g|\,\mu_0 \mathbf{m}_i(\mathbf{r}, t) \times \left(\mathbf{H}_{0i} - \underline{\mathbf{N}}_i^d \mathbf{M}_{0i} - \underline{\mathbf{N}}_i^a \mathbf{M}_{0i}\right) + |g|\,\mu_0 \mathbf{M}_{0i} \\ &\quad \times \left(\frac{2A_i}{\mu_0 M_{0i}^2}\nabla^2 \mathbf{m}_i(\mathbf{r}, t) - \underline{\mathbf{N}}_i^a \mathbf{m}_i(\mathbf{r}, t)\right) = -|g|\,\mu_0 \mathbf{M}_{0i} \times \mathbf{h}_i^d(\mathbf{r}, t)\end{aligned} \tag{34.12}$$

This equation while written for all components of vector $\mathbf{m}(\mathbf{r}, t)$ and for all layers in the structure gives us the coupled system of $3N$ integro-differential equations [54]. This system includes variable dipole and exchange fields in each layer, as well as static demagnetization field and Zeeman energy, with the constant and variable field of magnetocrystalline anisotropy also taken into account. As a result of introducing of the Green's function formalism, this system already includes the interlayer long-range dipole coupling between all layers in the structure through the nondiagonal terms of $\mathbf{h}_i^d(\xi, k_\zeta)$.

As follows from Equation 34.12, the exact solution of the linearized integro-differential equation of motion for the variable magnetization cannot be obtained without imposing additional "boundary" condition due to the exchange energy term $\nabla^2\mathbf{M}$. Thus, the electromagnetic field in a magnetic material must satisfy not only the usual boundary conditions of the Maxwell theory, but also the "exchange boundary condition" which arises from the Landau–Lifshitz equation of motion. Physically the introduction of the exchange boundary condition is caused by the difference of surface and bulk forces affected on the atomic magnetic moments. We can take this difference into account by applying an additional "boundary" condition, instead of implementing the complex mechanism of an exact account of the influence of surface on the bulk variable magnetization.

From the variation of Landau–Lifshitz equation of motion with respect to $\mathbf{M}(\mathbf{r}, t)$, we obtain the condition that the sum of all surface torques must be zero at each interface. So the indirect exchange boundary condition in the most common form reads:

$$\frac{2A}{M_S^2}\mathbf{M}(\mathbf{r}, t) \times (\mathbf{n} \cdot \nabla)\mathbf{M}(\mathbf{r}, t) - \frac{\delta^2}{M_S M_S'(g\mu_B)^2} \iint \mathrm{d}x'\mathrm{d}y' J_{\mathrm{eff}}(|\mathbf{r} - \mathbf{r}'|)\mathbf{M}(\mathbf{r}, t) \times \mathbf{M}(\mathbf{r}', t) + \frac{1}{M_S}\mathbf{M}(\mathbf{r}, t) \times \nabla_M U_{\mathrm{Surf}} = 0 \tag{34.13}$$

with $\mathbf{n} = \pm\mathbf{u}_\xi$ being the surface normal of the films, $\mathbf{r}$ refers to the surface of one magnetic layer, $\mathbf{r}'$ is the surface of the neighboring magnetic layer, so that $|\xi - \xi'| = d$.

In the exchange boundary condition (Equation 34.13), the first term gives the contribution from the anisotropy of the exchange interaction on the surface of the film, the second term determines the nonlocal exchange interaction between two adjacent layers, and the last one gives the contribution from the surface anisotropy energy U_{Surf}. In this form, the coupling of the two layers is interpreted as a torque exerted by the magnetization at the surface of one layer on the moments at the surface of the other one across the nonmagnetic medium. Obviously, for finite interlayer thickness, one has to take into account a nonlocal character of the exchange coupling across the nonmagnetic spacer.

Opposite to the single-film case, it should be noted that the exchange boundary conditions for multilayered structures have to include an additional torque resulting from the exchange interaction between the magnetic films in addition to the usual surface anisotropy term. The necessity of this term was first demonstrated by Hoffman et al. [97,98].

Considering the case of uniaxial surface anisotropy and taking into account only the first anisotropy constant, we arrive to the surface anisotropy energy density in following form:

$$U_{\mathrm{Surf}} = -\frac{K_1}{M_S^2}(\mathbf{M} \cdot \mathbf{n})^2 \quad \text{and} \quad H_{\mathrm{Surf}} = \nabla_M U_{\mathrm{Surf}} = \frac{2K_1}{M_S^2}(\mathbf{M} \cdot \mathbf{n})\mathbf{n} \tag{34.14}$$

where $\mathbf{n}$ is a unit vector normal to the surface, directed out of the surface.

When the two adjacent layers are in close contact or if the spacer thickness is negligibly small, one can use the local type of exchange coupling between layers and we arrive to so-called Hoffmann boundary conditions with the interface anisotropy included [41]:

$$\left[\frac{2K_s}{M_n^2}\mathbf{M}_n(\mathbf{r},t)\times(\mathbf{n}_n\cdot\mathbf{M}_n(\mathbf{r},t))\mathbf{n}_n+\frac{2A}{M_n^2}\mathbf{M}_n(\mathbf{r},t)\times\frac{\partial\mathbf{M}_n(\mathbf{r},t)}{\partial n}\right]\Bigg|_{\xi=L_n}$$
$$-\frac{2A_{12}}{M_nM_{n'}}\mathbf{M}_n(\mathbf{r},t)\times\mathbf{M}_{n'}(\mathbf{r},t)\Big|_{\xi=L_{n'-1}}=0$$
$$\left[\frac{2K_s}{M_{n'}^2}\mathbf{M}_{n'}(\mathbf{r},t)\times(\mathbf{n}_{n'}\cdot\mathbf{M}_{n'}(\mathbf{r},t))\mathbf{n}_{n'}-\frac{2A}{M_{n'}^2}\mathbf{M}_{n'}(\mathbf{r},t)\times\frac{\partial\mathbf{M}_{n'}(\mathbf{r},t)}{\partial n'}\right]\Bigg|_{\xi=L_{n'-1}}$$
$$-\frac{2A_{12}}{M_nM_{n'}}\mathbf{M}_{n'}(\mathbf{r},t)\times\mathbf{M}_n(\mathbf{r},t)\Big|_{\xi=L_n}=0 \tag{34.15}$$

Here $\partial/\partial\mathbf{n}$ is a partial derivative with respect to the surface normal unit vector. The latter points from the interface out of the magnetic layer. Symbol L_n refers to the upper surface of the lower of two adjacent layers with number n, while $L_{n'-1}$ indicates the lower surface of the upper layer n'. ($n' = n+1$). In Equation 34.15, A is usual ferromagnetic exchange constant and A_{12} is a constant describing the exchange coupling between the magnetic layers across the interlayer. Here, we consider the case of ferromagnetic exchange coupling, i.e., $A_{12} > 0$. Obviously, the value of both exchange constants must depend on the direction of the surface plane relative to the crystallographic axes of ferromagnet.

Recently, the Hoffmann exchange boundary conditions have been reexamined and small corrections have been shown to be necessary [49,99]. Additional terms are included to resolve difficulties with these boundary conditions in some limiting cases (for example, in the case of all equivalent layers when $d \to 0$). Mills co-workers [49,99] give both the microscopic and macroscopic evidences of the additional terms in the Hoffman boundary conditions.

In the case of the magnetic/nonmagnetic layered structure for $d > 60\,\mathring{\mathrm{A}}$, the exchange coupling between neighboring layers can be neglected and so-called Rado–Weertman boundary condition has to be fulfilled [89].

If we perform all our calculations for variable magnetization in the linear limit, we must also linearize the exchange boundary conditions. In the frame of our consideration in the long-wavelength limit, the linearized version of the Rado–Weertman boundary condition reads

$$\mathbf{M}_0\times\frac{\partial\mathbf{m}}{\partial n}+\frac{K_s}{A}\left[(\mathbf{n}\cdot\mathbf{m})\mathbf{n}\times\mathbf{M}_0+(\mathbf{n}\cdot\mathbf{M}_0)\mathbf{n}\times\mathbf{m}\right]=0 \tag{34.16}$$

Let us introduce here so-called spin pinning parameter $\eta = K_s/A\,[\mathrm{cm}^{-1}]$ characterizing the ratio of surface anisotropy energy and nonuniform exchange energy. η may be positive or negative depending on the sign of K_s, i.e., depending on whether the easy plane of the magnetic crystal is parallel or perpendicular to the surface.

For real materials, any possible combination of parameters A, K_s, and A_{12} can be realized. Moreover, in multilayered systems, all these parameters can vary from layer to layer in the stack and even A_{12} and η can be different for different surfaces of the same film.

In practical calculations, several limiting cases are usually utilized. For instance, it is well known that for permalloy (Py) films the case of free surface spins is often experimentally found. Thus, in this case the so-called Ament–Rado exchange boundary conditions can be used as a good approximation [100]:

$$\frac{\partial\mathbf{m}}{\partial n}\Big|_{\xi=\pm\frac{d}{2}}=0\qquad(K_S=0) \tag{34.17}$$

Due to the present growth technique, the spin pinning parameter now can be controlled almost in all materials by the ion implantation technology. So for special purposes, the films with totally pinned

surface spins can be easily obtained. In this case, Kittel's exchange boundary conditions can be used for regular calculations [101]:

$$\mathbf{m}\big|_{\xi=\pm\frac{d}{2}} = 0 \qquad (K_S = \infty) \tag{34.18}$$

We emphasize that the applicability of all these limiting cases should be estimated in each particular case not only by the value of the material parameter η, but also by the velocity of variation of the dynamic magnetization in the direction normal to the surface.

The most complicated case in calculations of spin-wave spectrum of the magnetic multilayer appears when the interlayer nonmagnetic spacer is very thin ($d < 30$ Å) or tends to zero (if we consider the multilayer stack of alternating ferromagnetic and/or antiferromagnetic layers with different magnetic properties). Both of these cases need to account all of the interactions including the exchange coupling between the magnetic layers. Thus, the full Hoffmann boundary conditions should be applied for each interface and the system of exchange boundary conditions for all layers become coupled. The solution of this system of $2N$ equations determines the normal modes and corresponding transverse wave numbers k_n of SWMs. The allowed values of wave numbers k_n should be obtained from the condition of vanishing determinant of $2N$ three-diagonal matrix of the coupled exchange boundary conditions.

34.2.2 Analytical Approaches

An understanding of the full spin-wave spectrum of magnetic structures is the key to solving many fundamental and applied problems in this field. A lot of theories and approaches were developed for solving this problem in numerous particular cases. This part of our chapter is not intended to be a full review of such a vast subject, but we will give a brief introduction to the present situation in this field.

The description of spin-wave processes in multilayered and patterned structures is based, in general, on the consideration of two aspects: interactions in the spin-system of each element formed the structure, and the coupling between elements. Each of these contributions is formed by the long-range dipole–dipole interaction, short-range exchange interaction, and surface and bulk anisotropy.

Various theoretical and computer techniques were elaborated: plain (or partial) waves approach [15,41,44,53,56,102], transfer matrix technique [13–16,52,60,74], spin wave modes (SWM) approach [42,54,55,57–59,88,96], variational method [56], effective medium approach [5,6,12], magnon scattering [103], a dynamical matrix approach [104] (dots), conformal mapping approach using the extinction theorem [105] (wires), spin-wave operator technique, and the Hamiltonian formalism [49,51,65,98,99,101,106,107], micromagnetic simulations, etc.

All these methods were developed for one purpose alone—to calculate the spin-wave spectrum in different magnetic structures. The authors used "a macroscopic continuum theory" as well as "the microscopic technique." First is based on the simultaneous solution of Maxwell's equations (usually without retardation, in magnetostatic limit) with the linearized Landau–Lifshitz equation of motion for magnetization, together with appropriate exchange (or the surface spin pinning) and electrodynamics boundary conditions. The last one utilizes the microscopic Hamiltonian of the magnetic system [49,51,98,99,101,106,107].

From the early days, macroscopic and microscopic approaches to the theory of magnetic structures were elaborated in parallel. In some cases concerned with the effect of exchange interaction, we cannot do without microscopic theory. For instance, the nonlocal exchange interaction in thin films, Hoffmann exchange boundary conditions, the effects of RKKY oscillations and GMR cannot be explained in the frame of macroscopic theory alone. But as soon as we are not dealt with the microscopic theory here, so we will present the review of the various theories elaborated in the frames of the macroscopic approach only.

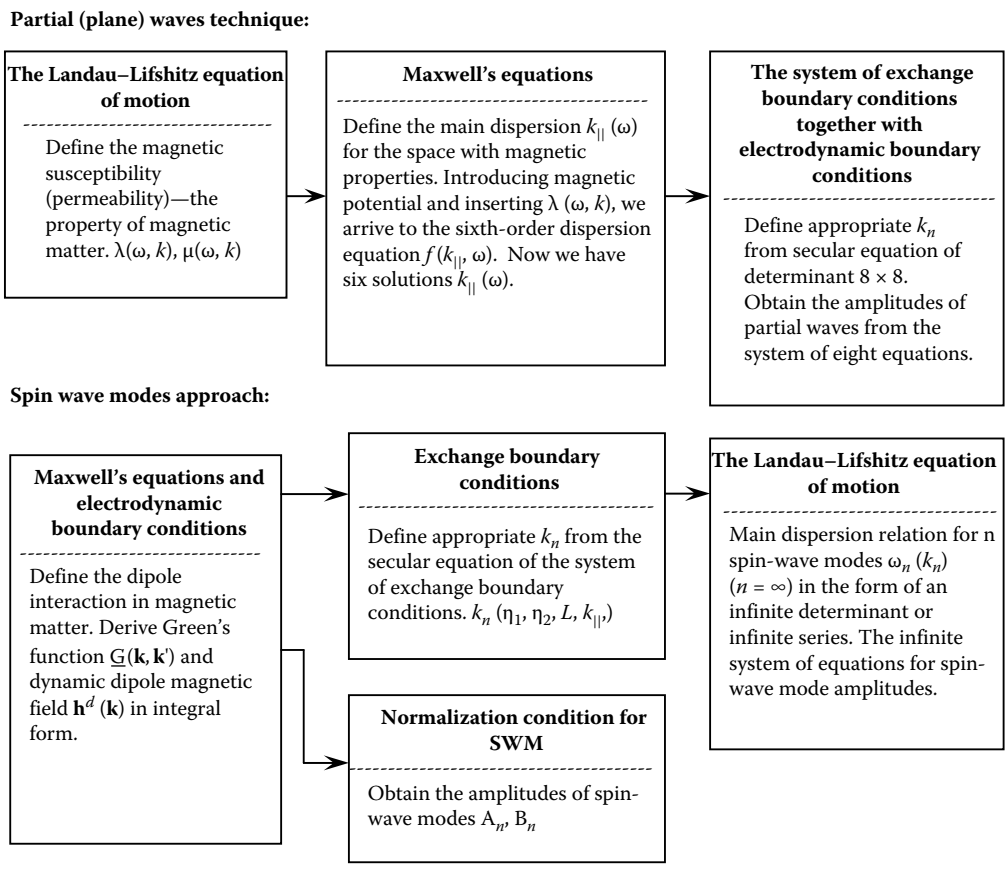

FIGURE 34.2 Schematic illustration of two main approaches.

Two main approaches for solving macroscopic eigenvalue boundary problem may be distinguished in the phenomenological dipole-exchange theory: the plane (or partial) wave (PW) technique and the SWM approach. Both of them are dealt with solving the Landau–Lifshitz equation of motion for magnetization simultaneously with Maxwell's equations with appropriate exchange and electrodynamic boundary conditions and both of them finally give the same result, which was shown in Ref. [57]. But, the fundamental difference between them lies in the sequence of calculation. Figure 34.2 shows the principal way of calculations in PW and SWM approaches.

34.2.2.1 Plane Wave Approach

The most popular among the macroscopic theories albeit not the best is the "plane (or partial) wave approach." The calculation procedure according to this approach is as follows [16,41,44,53,89,100, 102,105,108]. Solving the magnetostatic Maxwell equations together with the Landau–Lifshitz torque equation of motion (sometimes by introducing of the scalar magnetic potential for describing the dipole magnetic field and then expanding this potential in the series of plane waves), we arrive to a secular equation, which, for given k_{11}, is a dispersion relation between the spin-wave frequency ω and $k_\perp$-in-plane component of wave vector. The six solutions of this sixth-order dispersion equation give the coefficients for the system of boundary conditions, formed from Maxwell's boundary conditions and exchange boundary conditions (Hoffman or Rado–Weertman upon your taste). In order to fulfill the boundary conditions simultaneously for all interfaces in the multilayered system, the determinant of the system of $2 + 6N + 2(N - 1)$ linear equations must be equal to zero (here N is the number of

magnetic layers in the structure). So one should solve numerically the dispersion relation together with the bicubic characteristic equation. But for given k_{11}, ω, and evaluated from the sixth-order secular equation $k_\perp$, the value of the boundary condition determinant can differ from zero. So in a root finding routine ω is varied and the boundary condition determinant is calculated until the value of the boundary condition determinant fulfills a convergence criterion.

Thus, the investigation of the nature of the roots of the sixth-order characteristic equation and their dependences on the structure parameters and the external magnetic field is the main aspect of the PW approach. Actually, it is well-known Holstein–Primakoff and Herring–Kittel problem, which cannot be solved in an explicit form. Moreover, these partial waves each taken separately cannot be observed. Only appropriate combination of these waves, which give the distributions $\mathbf{h}^d(z)$ and $\mathbf{m}(z)$ could be observed and have a physical meaning in this sense [57].

Indeed, the dispersion equation together with the characteristic equation, represents exact solutions of the corresponding boundary problem. But, the dispersion properties of dipole-exchange spin waves in this case are hidden in the transcendental dispersion relations. Thus, the final result according to this approach can be obtained only by direct numerical calculations except several very simple limiting cases.

It is worth noting that recently the PW approach was adopted for calculations of the spin-wave spectra of multilayer systems, see Refs. [14,15,41,60].

34.2.2.2 Transfer Matrix Technique

The transfer matrix formalism is one of the simplest ways to extend the single layer theory on multilayer case [8,13–16,43,52,60,74]. The equation, which appears in this approach, is an ordinary matrix equation, which occurs often in linear circuit analysis. The ratio of the electric to magnetic fields gives the surface impedance of the sample and the real part of the surface impedance can be related to the sample ferromagnetic resonance (FMR) absorption.

Various modifications of the transfer matrix formalism have been widely used for the analysis of electromagnetic properties of stratified media in acoustic and optics [109,110], and later they were applied to the magnetic structures [8,9,13,15,32,33]. Ordinary transfer matrix $\underline{\mathbf{T}}$ relates the amplitudes of internal electric and magnetic fields at all interfaces (include first and last surfaces of the stack). It is derived from usual electrodynamics boundary conditions for the tangential components of the microwave **E** and **H** fields, taken simultaneously with the spin boundary conditions for magnetization, which follows from Landau–Lifshtz equation of motion. The relation between variable magnetization and internal magnetic fields is given through Maxwell's equation. The detailed discussion of this method applying to the magnetic superlattices can be found in numerous works [14–16,60,111]. Here, we only point out several important features of this method.

The main advantage of the transfer matrix approach lies in the fact that based on the set of the transfer matrices $\underline{\mathbf{T}}_m$ obtained for individual constitutive layers, one can immediately obtain the spectrum of an arbitrary complex stack. Since we successively eliminate variables using the boundary conditions at each interface, we never have to work with a system with more than six linear equations. The additional layers do not increase the number of final equations. Moreover, using this method, one can easily calculate the response of the semi-infinite and finite superlattices where new surface modes appear [14].

Unfortunately, this method is successively used only in the cases of "pure" exchange [111] or "pure" dipolar modes [15], and usually it gives only FMR spectrum. In more complicated cases, the applicability of this approach is mostly ambiguous and the calculation results are quite difficult for physical interpretation. While applying this method to different cases, one should clearly understand at any stage of calculations how to select correct physical solutions, what additional conditions (for example, the energy conservation for reciprocal case) should be required to exclude nonphysical

stray solutions. In some cases such complexity may lead to a confused result. Here, instead of the complexity of calculations, we meet with the complexity of the result interpretation.

Moreover, usually the transfer matrix approach includes only the ground state of the ferromagnetic system. The ground state in this consideration is a spatially uniform magnetization in each layer with no spin reconstruction at the interfaces. But in real systems, the local magnetization at the interfaces may differ from corresponding bulk one and this can lead to spin reconstructions at the interfaces. But these effects are not considered by transfer matrix theory. However, this method gives a unique opportunity for simple inclusion of the defects in infinite structures and to consider periodic systems with constitutive elementary unit (two to three different layers in elementary unit) [14].

The first real attempt to combine transfer matrix approach with SWM technique was done by Rojdestvenski et al. in Ref. [74] for the interpretation of BLS experiments. The authors used a traditional transfer matrix formalism to derive the spectrum of dipole-exchange spin waves in infinite and semi-infinite magnetic multilayers consisting of identical magnetic layers separated by nonmagnetic spacers.

34.2.2.3 Effective Medium Approximation

The effective medium approximation is a relatively simple approach, which correctly gives the frequencies of the surface and $k_\parallel T = 0$ bulk modes (here T is a period of the structure). In this case, the superlattice is described as a single effective medium. Authors of Ref. [12] applied this method to the superlattices in Voigt geometry, and in Ref. [16] the effective medium approximation was adapted for the description of canted multilayers.

The essence of this method is as follows. The dynamic response of each magnetic layer is written in terms of the dipolar fields in each layer via the Landau–Lifshitz equation of motion. Next, an average fluctuating magnetization **m** is defined as the sum of the fluctuating magnetizations created by the two sets of spins of adjacent films. The boundary conditions on normal fields introduce "filling factors" into the poles of the susceptibilities, which shift the resonance frequencies according to the relative thickness of the magnetic and nonmagnetic films. Primarily this method of field continuity arguments was used by Agranovich and Kravtsov [112]. Spatial averaging gives mean values of the field components B_x, H_y, and H_z and the effective-medium permeability $\underline{\boldsymbol{\mu}}^e$ is the tensor that relates these three to the other three continuous components H_x, B_y, and B_z:

$$\underline{\boldsymbol{\mu}}^e = \begin{pmatrix} \mu^e_{xx} & i\mu^e_{xy} & 0 \\ -i\mu^e_{yx} & \mu^e_{yy} & 0 \\ 0 & 0 & \mu^e_{zz} \end{pmatrix} \tag{34.19}$$

where $\mu^e_{xx} = \left((f_1/\mu) + f_2\right)^{-1}$, $\mu^e_{xy} = \mu^e_{yx} = (f_1\mu_\perp)/(f_1 + f_2\mu)$, $\mu^e_{yy} = f_1\mu + f_2 - (f_1 f_2 \mu_\perp^2)/(f_1 + f_2\mu)$, $\mu^e_{zz} = 1$. (this case also includes uniaxial antiferromagnets). Here μ and $\mu_\perp$ are the two independent components of the permeability tensor μ of the starting magnetic material, f_1 and f_2 are the volume fractions (or filling factors) of the magnetic and spacer material, respectively. $f_1 = d_1/T$ and $f_2 = d_2/T$. Then, the derivation of the dispersion equation for the Damon–Eshbach (DE) mode proceeds in a standard way with this effective-medium permeability μ^e.

This approximation works when $QT \ll 1$(T is the period of superlattice, Q is the Bloch wavevector) is satisfied, so that the wavelength is much larger than the period T, the observed modes are near the center of the mini zone (Brillouin zone) so that the stop-band reflections do not occur. The second condition requires that the modulation depth be larger compared with the penetration depth of DE mode in the superlattice.

Since the superlattice can be described as a single effective medium, then the calculation of the DE mode properties becomes an exact problem. It should be noted that in general case the effective medium calculation of the surface-mode frequency gives the same result as an expansion to first order in $k_\parallel T$ of the dispersion relation obtained using the transfer matrix method.

Another way to treat the periodic structure as an inhomogeneous medium with periodic properties (e.g., the array of cylinders) was suggested by Puszkarski and Krawczyk and others [5,6]. This approach can be used not only for magnetic/nonmagnetic structures, but also for magnetic/magnetic structures with different parameters.

A theoretical model includes the following quantities: spontaneous magnetization M_{s1} and M_{s2}, and exchange constants A_1 and A_2 homogeneous in one or two directions but varying with the position in the directions of periodicity. The introduction of variables $M_{s1}(\mathbf{r})$ and $A(\mathbf{r})$ leads to the other form of the exchange magnetic field:

$$\mathbf{h}^{ex}(\mathbf{r}) = \nabla \frac{A}{\mu_0 M_s^2} \nabla \mathbf{M}(\mathbf{r}) \tag{34.20}$$

instead of Equation 34.6.

M_s and A are the functions of $\mathbf{r}$, they can be expanded in the Fourier series by the $\mathbf{Q}$ reciprocal lattice vector, and then using Bloch's theorem for $\mathbf{m}(\mathbf{r})$ we arrive at the infinite set of linear equations for the Fourier expansion coefficients m_1 and m_2. Then the system should be solved numerically.

The advantage of this method is that the composite structure is considered as an infinite medium with periodic parameters, so there is no need in any boundary condition neither electromagnetic nor exchange. Obviously, the number of reciprocal lattice vectors should not be very huge especially in the expansions of M_s and A, because the number of the terms in Fourier expansion determines the sharpness of the interface between two materials, more terms give more sharpness. But, in fact, due to the diffusion, the real interface never has been an ideal plane so some blur is quite useful here. Thus, this "approximation" seems to be more accurate and close to reality than the exact theory.

34.2.2.4 Method of Tensorial Green's Functions

The Green's function method concerns only the representation of the dynamic dipole field in the integral form. It can be considered as a first stage of the SWM approach (see Figure 34.2), when one should solve Maxwell's Equation 34.7 to obtain the relation between the dynamic dipole field and variable magnetization in integral form. However, the final integro-differential equation of the whole problem can be solved by any other analytical or numerical method. This form of representation of the dynamic dipole field is very comfortable for further derivings and calculations.

In particular case of the linear problem, the solution of Maxwell's Equation 34.7 in each separate layer of the stack (see Figure 34.1) can be written in the form of plane waves:

$$\mathbf{m}_i(\mathbf{r}, t) = \mathbf{m}_i(\xi, k_\zeta) e^{-jk_\zeta \zeta + j\omega t}, \quad \mathbf{h}_i^d(\mathbf{r}, t) = \mathbf{h}_i^d(\xi, k_\zeta) e^{-jk_\zeta \zeta + j\omega t} \tag{34.21}$$

Here and below, we assume that the in-plane wave vector k_ζ is always positive. $\mathbf{m}_i(\xi, k_\zeta), \mathbf{h}_i^d(\xi, k_\zeta)$ are Fourier-amplitudes of variable magnetization and variable dipole field, correspondingly.

Since we consider the multilayered structure, we must include the nonlocal effects of the dipole fields of all ferromagnetic layers formed the structure. Due to the linearity of the problem (Equation 34.2), the Fourier amplitude of the resulting dipole field can be represented as the superposition of the Fourier amplitudes of the dipolar fields of all ferromagnetic layers:

$$\mathbf{h}^d(\xi, k_\zeta) = \sum_{j=1}^{N} \mathbf{h}_j^d(\xi, k_\zeta) \tag{34.22}$$

This is one of the central ideas of this approach. Physically, it reflects the dipole–dipole interaction in a spin-system of a film as well as coupling between ferromagnetic films through their "individual" dipole fields.

In each film, the relation between the Fourier amplitudes of variable dipole field $\mathbf{h}_i^d(\xi, k_\zeta)$ and variable magnetization can be defined in integral form through generalized tensorial Green function $\underline{\mathbf{G}}_{\xi\rho\zeta}(\xi, \xi'; k_\zeta)$ of a single layer problem (see, e.g., [58,88]):

$$\mathbf{h}_j^d(\xi, k_\zeta) = \int \underline{\mathbf{G}}_{\xi\rho\zeta}(\xi, \xi'; k_\zeta)\mathbf{m}_j(\xi', k_\zeta)\mathrm{d}\xi' \tag{34.23}$$

The tensorial Green function has the same form for all layers made of one material. We should note that the generalized tensorial Green function (opposite to the classic Green function of the equation) depends on the chosen coordinate system and particular sample geometry (through the boundary conditions). However, for many cases, it can be found in closed form.

For example, a single-film tensorial Green function of Maxwell's equations in magnetostatic limit (i.e., without retardation) in the Cartesian coordinate system $\xi\eta\zeta$ has the following form [58]:

$$\underline{\mathbf{G}}_{\xi\rho\zeta}(\xi, \xi', k_\zeta) = \begin{pmatrix} G^P - \delta(\xi - \xi') & 0 & -jG^Q \\ 0 & 0 & 0 \\ -jG^Q & 0 & -G^P \end{pmatrix} \tag{34.24}$$

where the components of matrix elements are

$$G^P = \frac{k_\zeta}{2} e^{-k_\zeta|\xi-\xi'|}, \quad G^Q = G^P \mathrm{sign}(\xi - \xi')$$

Here $\mathrm{sign}(\xi - \xi') = \begin{cases} 1, & \text{when } \xi - \xi' \geq 0 \\ -1, & \text{when } \xi - \xi' < 0 \end{cases}$

We should note that the tensorial Green function depends strongly on the symmetry of the initial Maxwell's equations. For the simplicity of further calculations, one should use a proper coordinate system (spherical, cylindrical, or other instead of Cartesian). For example, in the problem of infinite cylindrical wire, the tensorial Green function in cylindrical coordinate system has all nine elements, but only four of them are independent.

Thus, the tensorial Green function can be quite different for different cases and is strongly distinguished from the single-film one. Moreover, for multilayered systems you cannot use the tensorial Green function of bulk material and in some cases even single-film Green function does not match. The form of the components of the tensorial Green function depends not only on the properties of the ferromagnetic material, but also on the interface geometry and the properties of the surrounding media. This influence always presents at electrodynamics boundary conditions and finally determines the behavior of the tensorial Green function. For instance, if we consider the problem of the infinite stack of three-layered structures—metal–ferromagnetic–dielectric—we should utilize the generalized Green function of such three-layered sandwich system. Some information about the tensorial Green function for the plane sandwiched structures can be found in Refs. [42,72,113,114]. We stress that in each specific case one should solve first the appropriate electrodynamics problem and get the proper form of the integral relation between variable dipole field and variable magnetization.

While searching the tensorial Green function, we assume ζ-axis of the coordinate system $\xi\rho\zeta$ to be oriented along the direction of propagation of spin waves in the structure (see Figure 34.1). For the convenience of further analysis, we now introduce for each ferromagnetic film a new coordinate system $x_i y_i z_i$ in which the axis z_i is parallel to the direction of saturation magnetization $\mathbf{M}_{0i}$ of the film. The transition from the coordinate system $\xi\rho\zeta$ to the coordinate system $x_i y_i z_i$ can be done by means of orthogonal transformations of rotation through angles φ_i and $\left(\theta_i - \pi/2\right)$. The matrices of these transformations are of the form:

$$\underline{\mathbf{T}}_\varphi = \begin{pmatrix} 1 & 0 & 0 \\ 0 & \cos\varphi_i & -\sin\varphi_i \\ 0 & \sin\varphi_i & \cos\varphi_i \end{pmatrix}, \quad \underline{\mathbf{T}}_{\theta-\pi/2} = \begin{pmatrix} \sin\theta_i & 0 & -\cos\theta_i \\ 0 & 1 & 0 \\ \cos\theta_i & 0 & \sin\theta_i \end{pmatrix} \tag{34.25}$$

More information about orthogonal coordinate transformations can be found in Ref. [90].

The application of coordinate transformations (Equation 34.25) to the tensorial Green function (Equation 34.24) in following way:

$$\underline{\mathbf{G}}^{i}_{xyz}(\xi,\xi',k_\zeta) = \underline{\mathbf{T}}_{\theta_i-\pi/2}\underline{\mathbf{T}}_{\varphi_i}\underline{\mathbf{G}}^{i}_{\xi\rho\zeta}(\xi,\xi',k_\zeta)\left(\underline{\mathbf{T}}_{\varphi_i}\underline{\mathbf{T}}_{\theta_i-\pi/2}\right)^{T} \tag{34.26}$$

results in the equation for tensorial Green's function $\underline{\mathbf{G}}^{i}_{xyz}(\xi,\xi',k_\zeta)$ in each layer of the stack in new coordinate system $x_i y_i z_i$.

34.2.2.5 SWM Approach

All above-mentioned macroscopic theories cannot be called pure analytical, since at a particular stage all of them include numerical calculations. But numerical modeling usually gives the results only for several specific cases and cannot give the whole picture. Truly, analytical among all methods can be called only the SWM technique. Hence, from here and below we devote our discussion to the detailed description of this analytical approach.

The SWM approach with reference to the multilayer problem is based on the solution of the integro-differential equation for variable magnetization in each layer of the system, which follows from the initial system of equations consisting of linearized equation of motion for the magnetization, Maxwell's equations, and the electrodynamics and exchange boundary conditions (Figure 34.2). In these integro-differential equations, the exchange and magnetostatic dipole–dipole interactions as well as the surface and bulk anisotropies are taken into account. In general case, the calculations are performed for arbitrary magnetized multilayers. By means of a tensorial Green function for the solution of Maxwell's equations, dispersion laws for the collective SWM frequencies can be derived in a form suitable for physical interpretation and for comparison with experiments. To solve these integro-differential equations, an expansion of the variable magnetization in the infinite series of SWMs is used. SWMs form a complete set of vector functions satisfying the exchange boundary conditions.

This method allows one to derive the exact dipole-exchange spin-wave dispersion relation, in terms of a vanishing infinite determinant or an infinite convergent series. One of the useful features of SWM approach is the possibility of deriving an approximate dispersion relation within a perturbational approach for a wide range of particular cases in simple explicit form. This allows one to give a clear physical picture of the dipole-exchange spin-wave spectrum for complicated systems and its dependence on each structure parameter.

For the treatment of an infinite stack of periodic multilayers, Bloch's theorem can be easily incorporated into this approach for the description of the band structure of the spin-wave energies and in the frames of perturbational approach then may be applied a tight binding approximation. Spin waves in such multilayers are coupled via their long-range magnetostatic dipole fields and nonlocal interlayer exchange interaction, thus they form a characteristic new mode and the new structure of energy spectrum appear.

Since our consideration will be closely connected with the implementation of this method for different applications, we presume to present here in Figure 34.3 the general scheme of calculations in the frames of this approach. According to this scheme, we find that a few separated problems arise in the process of calculations such as the determination of the components of the tensorial Green function, obtaining the effective demagnetization factors, the eigenvalue problem for the differential operator with appropriate exchange boundary conditions, and the determination of the approximate dispersion relation by means of perturbation theory. Some of them were already discussed above and other will be considered below in this chapter.

All these separate problems can be solved independently and by means of any mathematical methods you prefer. But at the end, we always get one system of linear algebraic equations where all

General scheme of obtaining the solution in the framework of spin-wave mode approach.

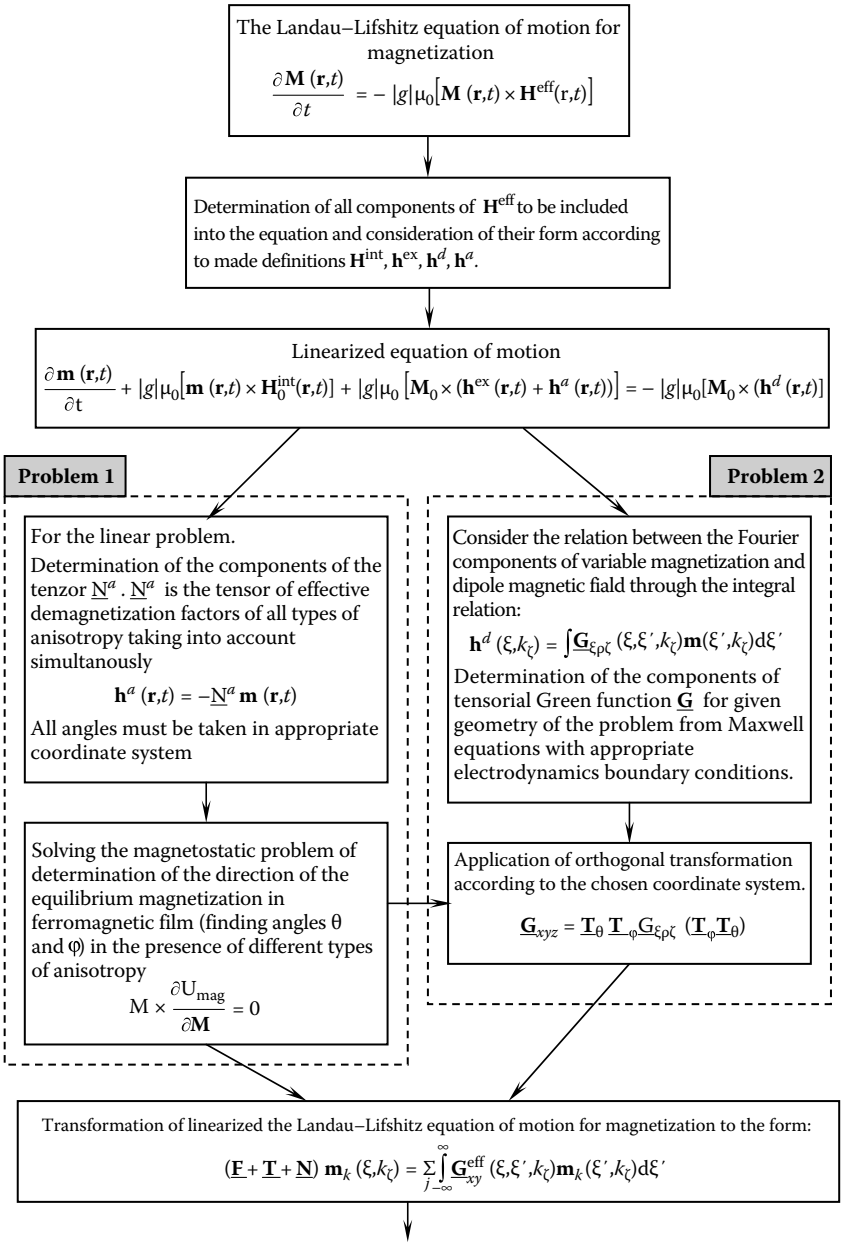

FIGURE 34.3 The main steps in solving boundary value problem through SWM approach.

(*continued*)

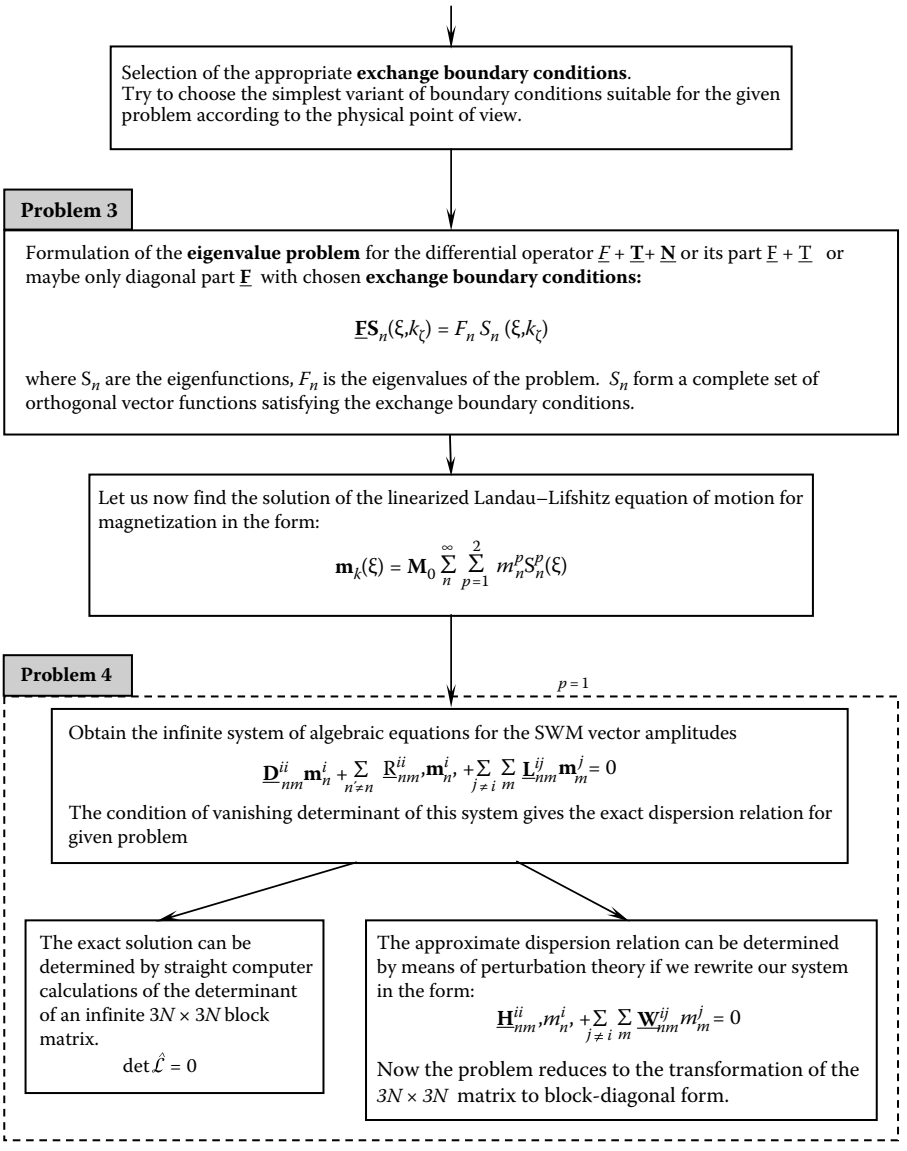

FIGURE 34.3 (continued) The main steps in solving boundary value problem through SWM approach.

interactions and physical effect are already taken into account. Moreover, the results of solving these separate problems can be used then for calculations in other cases with similar conditions.

Thus, the main feature of SWM approach is that in spite of the fact that for each special case we choose different accuracy of calculations and use different approximations for solving intermediate problems, but finally we always obtain a physically perfect and clear solution. The illustration of the successful implementation of this method in numerous cases as well as the comparison with experimental data can be found in Refs. [42,54,55,57–59,62,63,88,96] and references therein.

34.2.3 Spin-Wave Normal Mode Expansion Technique

Let us now, following the scheme Figure 34.3, obtain the spin-wave spectrum in the frames of SWM approach. One of the central problems of SWM approach is the selection of proper functions as the normal modes for SWM expansion technique. It should be noted that the problem of the selection of a set of appropriate functions for expansion is closely related with the problem of the optimal choice of exchange boundary conditions. In most cases, we are forced to take as normal modes the eigenfunctions of pure exchange operator due to the complexity of the exchange boundary conditions, since the selected functions should satisfy the appropriate micromagnetic boundary conditions.

In this chapter, we will give the most common approach to a wide class of problems thus on the first stage we will not use Bloch's theorem, but instead calculate the SWMs for finite number of layers, since this approach bears more relevance to most experimental investigations. Bloch's theorem will be applied in the next sections.

As it was mentioned above, the SWM approach can be applied to a large variety of magnetic structures, but here we restrict to the case of multilayered structure consisting of an arbitrary number of ferromagnetic layers separated by a nonmagnetic spacer (Figure 34.4), all parameters of the ferromagnetic films can differ. Note that the model includes both dipole and exchange interaction as well as electrodynamic and exchange boundary conditions with the interlayer exchange coupling and anisotropy of the ferromagnetic media also can be taken into account if it is needed. Various ways could be suggested for the selection of trial functions for solving the system of integro-differential Equation 34.12 with appropriate exchange boundary. However, we can outline several options how to do this better. Some of probable functions are already suggested in Ref. [42,54,57–59].

Owing to the linearity of the problem, the solution of the system consisting of N equations of motion for magnetization followed from Equation 34.12 can be written in the form of plane waves (Equation 34.21), where axis ζ is assumed to be parallel to the direction of propagation of spin wave. These expansions account for the fact that the translation invariance holds in the $\zeta-\rho$-plane where the films are assumed to be unbounded, but not along the ξ-direction. Here k_ζ is the in-plane component of the full wavevector of the spin waves. For the convenience of future analysis, we will write the equation of motion for each layer in new coordinate system $x_i y_i z_i$, in which axis z_i is parallel to the

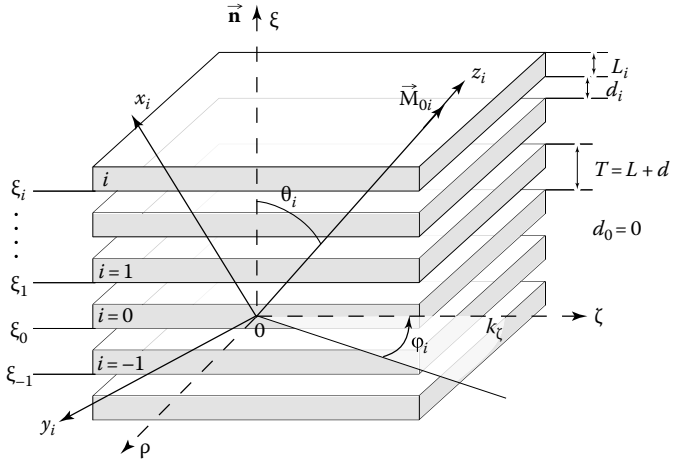

FIGURE 34.4 Geometry of magnetic multilayered structure and orientation of the coordinate axes.

direction of the saturation magnetization M_{0i}. Due to the above-introduced transformations, vector of variable magnetization becomes 2D:

$$\mathbf{m}_i(\xi, k_\zeta) = \mathbf{u}_{xi} m_i^x(\xi, k_\zeta) + \mathbf{u}_{yi} m_i^y(\xi, k_\zeta) = \begin{pmatrix} m_i^x \\ m_i^y \end{pmatrix} \tag{34.27}$$

where $\mathbf{u}_{xi}$ and $\mathbf{u}_{yi}$ are unit vectors. We use index i to indicate parameters of the ith layer, but when appropriate this index is omitted for an improved clarity of the equations.

These calculations lead to a system of N coupled homogeneous integro-differential equations for the Fourier amplitudes of variable magnetization:

$$\begin{aligned} &\underline{\mathbf{F}}_i \mathbf{m}_i(\xi - \xi_i, k_\zeta) + \underline{\mathbf{T}}_i \mathbf{m}_i(\xi - \xi_i, k_\zeta) \\ &\quad = -\underline{\mathbf{N}}_i \mathbf{m}_i(\xi - \xi_i, k_\zeta) + \sum_{j=-\infty}^{\infty} \int_0^{L_j} \underline{\mathbf{G}}_{xy}^{ij}(\xi - \xi_i, \xi' - \xi_j, k_\zeta) \mathbf{m}_j(\xi' - \xi_j, k_\zeta) \mathrm{d}\xi' \end{aligned} \tag{34.28}$$

here ξ_i is an absolute coordinate of i-layer:

$$\xi_i = -\mathrm{sign}(i)\frac{L_0}{2} - \frac{\mathrm{sign}(i)+1}{2} L_{-1} + \sum_{l=0}^{i} \left[\mathrm{sign}(i) d_l + \frac{\mathrm{sign}(i)+1}{2} L_{l-1} + \frac{\mathrm{sign}(i)-1}{2} L_l \right] \tag{34.29}$$

and $\mathbf{m}_i(\xi, k_\zeta)$ is the vector Fourier amplitude of the plane spin wave. Here $d_0 \equiv 0$, and $\mathrm{sign}(i) = \begin{cases} 1, & \text{when } i \geq 0 \\ -1, & \text{when } i < 0 \end{cases}$

$\underline{\mathbf{F}}_i$ is the linear matrix-differential operator:

$$\underline{\mathbf{F}}_i = \frac{\omega_{\mathbf{H}i}}{\omega_{\mathbf{M}i}} - \frac{2A_i}{\mu_0 M_{0i}^2} \left(\nabla_\xi^2 - k_\zeta^2 \right) \begin{pmatrix} 1 & 0 \\ 0 & 1 \end{pmatrix} \tag{34.30}$$

$\underline{\mathbf{T}}_i$ includes nondiagonal terms:

$$\underline{\mathbf{T}}_i = i \frac{\omega}{\omega_{\mathbf{M}i}} \begin{pmatrix} 0 & -1 \\ 1 & 0 \end{pmatrix} \tag{34.31}$$

and $\underline{\mathbf{N}}_i$ represents bulk anisotropy:

$$\underline{\mathbf{N}}_i = \begin{pmatrix} \mathrm{N}_i^{xx} & \mathrm{N}_i^{xy} \\ \mathrm{N}_i^{yx} & \mathrm{N}_i^{yy} \end{pmatrix} \tag{34.32}$$

here $\omega_{\mathbf{H}i} = |g| \mu_0 \mathbf{H}_i$, $\omega_{\mathbf{M}i} = |g| \mu_0 \mathbf{M}_{0i}$.

The solution of this integro-differential equation, satisfying the appropriate exchange boundary conditions, gives the full spectrum of dipole-exchange spin waves in a ferromagnetic film.

To solve the set of integro-differential Equation 34.28, we apply the expansion of the Fourier amplitudes of the spatially varying magnetization $\mathbf{m}_i(\xi, k_\zeta)$ in an infinite series of complete orthogonal vector functions $\mathbf{S}_{ni}^p(\xi)$, the so-called SWMs, in each layer separately:

$$\mathbf{m}_i(\xi, k_\zeta) = \mathbf{M}_{0i} \sum_n^{\infty} \sum_{p=1}^{2} m_{in}^p \mathbf{S}_{in}^p(\xi) \tag{34.33}$$

where m_{in}^p are the SWM amplitudes, and the normal modes $\mathbf{S}_{ni}^p(\xi)$ are found as the eigenvectors of the differential-matrix operator with appropriate exchange boundary conditions.

The problem of determination of the eigen-functions of linear differential operator with corresponding boundary conditions is a particular case of general Sturm–Liouville problem and may be formulated as follows:

$$\begin{aligned} &\underline{\mathbf{F}}_i \mathbf{S}_i(\xi) = F_i \mathbf{S}_i(\xi) \\ &\underline{\mathbf{B}}_{1i} \mathbf{S}_i(\xi) = 0, \quad \text{when} \quad \xi = \xi_i + L_i \\ &\underline{\mathbf{B}}_{2i} \mathbf{S}_i(\xi) = 0, \quad \text{when} \quad \xi = \xi_i \end{aligned} \tag{34.34}$$

Since the SWM $\mathbf{S}_{ni}^{p}(\xi)$ are the eigenfunctions of the Sturm–Liouville problem, they should form a complete set of the orthogonal functions, which must satisfy the condition of the orthonormality over the interval of their existence Ω:

$$\int_{\Omega} d\xi \, \mathbf{S}_{ni}^{p}(\xi) \mathbf{S}_{n'i'}^{p'*}(\xi) = L \delta_{nn'} \delta_{pp'} \delta_{ii'} \tag{34.35}$$

where δ is the Kronecker delta.

Vector functions $\mathbf{S}_{ni}^{p}(\xi)$ can be expressed as a product of eigen-vector of the linear differential matrix operator and eigenfunctions $\Phi_{ni}^{p}(\xi)$, which should satisfy appropriate micromagnetic boundary conditions. The eigenfunctions $\Phi_{ni}^{p}(\xi)$ give the spin-wave magnetization distribution across the film in the standing spin-wave regime ($k_\zeta = 0$) for corresponding problem, with n the number of half wavelength of a standing wave within one film thickness.

It should be noted that in different situations vector functions $\mathbf{S}_{ni}^{p}(\xi)$ and eigenfunctions $\Phi_{ni}^{p}(\xi)$ can be quite different. This fact depends mostly on the form of spin-pinning conditions, rather than the form of differential-matrix operator. If we omit the interlayer exchange interaction, the Rado–Weertman (Equation 34.16), Kittel's (Equation 34.18), or Ament–Rado (Equation 34.17) exchange boundary conditions can be applied. Such model is applicable when the distances between ferromagnetic films in magnetic/nonmagnetic structure are large compared with the length of effective exchange coupling. This situation usually occurs in such structures.

In the case of Rado–Weertman exchange boundary conditions, the solutions become rather complex. Due to this complexity, the normal modes should be found as the eigen-functions of pure exchange operator (or sometimes as the eigen-functions of the whole diagonal part of the full operator $\underline{\mathbf{F}}_i + \underline{\mathbf{T}}_i + \underline{\mathbf{N}}_i$). In this case, operators of boundary conditions in Equation 34.34 according to Equation 34.16 in considered coordinate system have the following form [58]:

$$\begin{aligned} \underline{\mathbf{B}}_{1i} &= \begin{bmatrix} \dfrac{\partial}{\partial \xi} + \eta_{1i} \cos 2\theta_i & 0 \\ 0 & \dfrac{\partial}{\partial \xi} + \eta_{1i} \cos^2 \theta_i \end{bmatrix} \\ \underline{\mathbf{B}}_{2i} &= \begin{bmatrix} -\dfrac{\partial}{\partial \xi} + \eta_{2i} \cos 2\theta_i & 0 \\ 0 & -\dfrac{\partial}{\partial \xi} + \eta_{2i} \cos^2 \theta_i \end{bmatrix} \end{aligned} \tag{34.36}$$

where η_{1i} and η_{2i} are the pinning parameters on the upper and lower surfaces of the film with number i. η_{1i} and η_{2i} are related with the phenomenological constant of surface anisotropy. ($\eta = K_{\text{surf}}/A$). Here, we also take into account the direction of surface normals.

We should emphasize that this form of mixed exchange boundary conditions was derived for the case of uniaxial surface anisotropy [115]. Deriving the solution of eigenvalue problem for the diagonal operator of Equation 34.28, we obtain vector eigenfunctions $\mathbf{S}_{ni}^{p}(\xi)$ in following form:

$$\mathbf{S}_{ni}^{1}(\xi) = \begin{pmatrix} \Phi_{ni}^{x}(\xi) \\ 0 \end{pmatrix}, \quad \mathbf{S}_{ni}^{2}(\xi) = \begin{pmatrix} 0 \\ \Phi_{ni}^{y}(\xi) \end{pmatrix} \tag{34.37}$$

the functions $\Phi_{ni}^{p}(\xi)$ which satisfy the exchange boundary conditions 34.36 can be found as

$$\Phi_{ni}^{p}(\xi) = A_{ni}^{p}\left[\cos\left(k_{ni}^{p}(\xi-\xi_i)\right) + \frac{\eta_{2i}^{p}}{k_{ni}^{p}}\sin\left(k_{ni}^{p}(\xi-\xi_i)\right)\right] \tag{34.38}$$

Quantities k_{ni}^{p} as in previous case may be interpreted as SWM transverse wave numbers, but they are determined by the equations:

$$\left[\left(k_{ni}^{p}\right)^2 - \eta_{1i}^{p}\eta_{2i}^{p}\right]\tan\left(k_{ni}^{p}L_i\right) = k_{ni}^{p}\left(\eta_{1i}^{p} + \eta_{2i}^{p}\right) \tag{34.39}$$

where $\eta_{1,2}^{x} = \eta_{1,2}\cos 2\theta$, $\eta_{1,2}^{y} = \eta_{1,2}\cos^2\theta$, $\eta_{1,2}$ are the pinning parameters on upper and lower surfaces of the film (without loss the generality we omit here the layer indices i).

Constants A_{ni}^{p} for this case of exchange boundary conditions may be obtained from the normalization condition (Equation 34.35) for the SWM. For more detailed discussion and exact form of constants A_{ni}^{p} see Ref. [58].

The eigenvalues F_{ni}^{p} of the considered boundary problem are given by

$$F_{ni}^{p} = \frac{\omega_{Hi}}{\omega_{Mi}} + \frac{2A_i}{\mu_0 M_{0i}^2}k_\zeta^2 + \frac{2A_i}{\mu_0 M_{0i}^2}\left(k_{ni}^{p}\right)^2 \tag{34.40}$$

in the case without including anisotropy term, and

$$F_{ni}^{p} = \frac{\omega_{Hi}}{\omega_{Mi}} + \frac{2A_i}{\mu_0 M_{0i}^2}k_\zeta^2 + \frac{2A_i}{\mu_0 M_{0i}^2}\left(k_{ni}^{p}\right)^2 + N_i^{pp} \tag{34.41}$$

with the bulk anisotropy taken into account.

The solutions of the transcendental Equation 34.39 have been extensively discussed in literature, especially in the connection with the phenomenon of spin-wave resonance (SWR), because physically the solutions (Equation 34.38) describe the distributions of magnetization of standing spin waves ($k_\zeta = 0$) across the film thickness. This equation has the infinite number of real solutions for arbitrary values of pinning parameters. These solutions correspond to the bulk modes of SWR. Besides, this equation may have one or two imaginary solutions corresponding to hyperbolic or surface SWR modes. The areas of different number of imaginary solutions with the appropriate conditions on η_1^p, η_2^p are presented in Ref. [58].

The SWMs for the simple cases of Kittel's and Ament–Rado exchange boundary conditions and their applicability are discussed in numerous works (see, e.g., [54,57,58] and references therein). It was shown that such solutions give excellent results for more particular cases of interest and coincide with experimental data quite well.

More complicated case occurs when we try to include the interlayer exchange interaction in the magnetic structure. The application of the Hoffmann exchange boundary conditions is undoubtedly necessary in the case of magnetic/magnetic multilayers. In this situation, we have no choice but to take the eigenfunctions of pure exchange operator as a set of normal SWMs and for defining allowed values k_{ni}^{p} we should solve the system of $2N$ (N is the number of layers in the multilayered system) coupled Hoffmann exchange boundary conditions.

A full set of SWMs represents the orthogonal basis in which the integro-differential Equation 34.28 has a block-diagonal form. Following SWM approach, any combination of eigen functions of differential operator can be taken as a set of normal modes. But in some special cases, we can outline the rules for selection of the most convenient functions.

For example, in the papers [57–59] distributions of the variable magnetization corresponding to the spin-wave resonance frequencies were utilized. They were found as eigenfunctions of the differential operator in the SWR regime ($k_\zeta = 0$). A similar choice of normal modes for the expansion of

$m_i(\xi, k_\zeta)$ may be convenient for a specific geometry (specific direction of the bias magnetization) since we utilize the exact solution of Equation 34.28 in the important regime of standing spin waves $k_\zeta = 0$. However, in the case of an arbitrary direction of bias magnetization when we want to find the dispersion equation describing the angular dependence of the spin-wave spectrum, it is convenient to use as the normal modes the eigenfunctions of the pure exchange operator.

Fortunately, a large number of ferromagnetic resonance experiments in thin films can be explained in terms of a single cosinusoidal or single decaying exponential function. However, this is not the case in general, especially where intensities are concerned, and it is important to distinguish between "pinned modes" and modes with "pinned intensities." The former have $m = 0$ at the surfaces, and the latter have intensities corresponding to single cosinusoidal functions with $m = 0$ at the surface [56].

34.2.4 General Dispersion Relation

Now, we come to the determination of the dispersion characteristics for spin waves in the layered magnetic/nonmagnetic structure. We proceed to consider the structure consisting of N anisotropic ferromagnetic films separated by nonmagnetic layers. The thickness of the ferromagnetic films along ξ-direction is $L_i\,(i = 1, 2, \ldots, N)$ and for separating layers it denotes d_i. The films are magnetized to saturation by a uniform external magnetic field of an arbitrary direction. The saturation magnetizations $\mathbf{M}_{0i}$ have arbitrary values in each film and, in general case, the anisotropy of all ferromagnetic layers can also be different. Thus, following the scheme in Figure 34.3, we arrive to the "Problem 4." According to SWM approach for the case of an infinite layered system (Figure 34.4) with mixed exchange boundary conditions (Equation 34.36), that could be different at all interfaces, we obtain the infinite system of algebraic equations for vector Fourier amplitudes of a variable magnetization (Equation 34.28).

Substituting expansion (Equation 34.33) for the $\mathbf{m}_i(\xi)$ into Equation 34.28 and using the orthogonality condition for SWM, we obtain the infinite system of $(2 \cdot N \cdot \infty)$ coupled linear algebraic equations for SWM amplitudes m_{in}^{p} and after some simple transformations it can be rewritten in most general matrix form:

$$\underline{\mathbf{D}}_{nn}^{ii}\mathbf{m}_n^i + \sum_{n' \neq n} \underline{\mathbf{R}}_{nn'}^{ii}\mathbf{m}_{n'}^i + \sum_{j \neq i}\sum_m \underline{\mathbf{L}}_{nm}^{ij}\mathbf{m}_m^j = 0 \tag{34.42}$$

The indices i, n, p correspond to the layer i and indices j, m, r numbered the same functions in the layer j.

Here $\underline{D}_{nn}^{ii}$ and $\underline{R}_{nn'}^{ii}$ are the square matrices, which describe the dipole and exchange interactions inside layer i and also take into account the influence of anisotropy:

$$\underline{\mathrm{D}}_{nn}^{ii} = \begin{bmatrix} F_{ni}^{x} + \sin^2\theta_i + \mathrm{A}_i(P_{nn}^{xx})^{ii} + (N_{xx}^{a})^i & \mathrm{C}_i(P_{nn}^{xy})^{ii} + (N_{xy}^{a})^i(T_{nn}^{xy})^{ii} \\ & -j\left(\frac{\omega}{\omega_{Mi}}(T_{nn}^{xy})^{ii} - \mathrm{D}_i(Q_{nn}^{xy})^{ii}\right) \\ \mathrm{C}_i(P_{nn}^{yx})^{ii} + (N_{yx}^{a})^i(T_{nn}^{yx})^{ii} & F_{ni}^{y} + \mathrm{E}(P_{nn}^{yy})^{ii} + (N_{yy}^{a})^i \\ +j\left(\frac{\omega}{\omega_{Mi}}(T_{nn}^{yx})^{ii} + \mathrm{D}_i(Q_{nn}^{yx})^{ii}\right) & \end{bmatrix}$$

$$\underline{\mathrm{R}}_{nn'}^{ii} = \begin{bmatrix} \mathrm{A}_i(P_{nn'}^{xx})^{ii} + j\mathrm{B}_i(Q_{nn'}^{xx})^{ii} & \mathrm{C}_i(P_{nn'}^{xy})^{ii} + (N_{xy}^{a})^i(T_{nn'}^{xy})^{ii} \\ & -j\left(\frac{\omega}{\omega_{Mi}}(T_{nn'}^{xy})^{ii} - \mathrm{D}_i(Q_{nn'}^{xy})^{ii}\right) \\ \mathrm{C}_i(P_{nn'}^{yx})^{ii} + (N_{yx}^{a})^i(T_{nn'}^{yx})^{ii} & \mathrm{E}_i(P_{nn'}^{yy})^{ii} \\ +j\left(\frac{\omega}{\omega_{Mi}}(P_{nn'}^{yx})^{ii} + \mathrm{D}_i(Q_{nn'}^{yx})^{ii}\right) & \end{bmatrix} \tag{34.43}$$

Here, the angle functions are

$$A_i = \cos^2\varphi_i - \sin^2\theta_i\left(1+\cos^2\varphi_i\right); \qquad B_i = -\cos\varphi_i \sin 2\theta_i;$$
$$C_i = \tfrac{1}{2}\cos\theta_i \sin 2\varphi_i; \qquad D_i = -\sin\varphi_i \sin\theta_i; \qquad E_i = \sin^2\varphi_i$$

and F_{ni}^{p} are the eigenvalues of the boundary problem (Equations 34.34 and 34.36) for differential operator $\underline{\mathbf{F}}_i$ and are given by Equation 34.40; k_{ni}^{p} is the transverse component of the full spin-wave wavevector, which is determined by Equation 34.39; $n, n' = 1, 2, 3, \ldots, N$; $p, p' = 1, 2$; $i, j = -\infty, \ldots, -2, -1, 0, 1, 2, \ldots, \infty$. The expressions for the effective demagnetization factors of anisotropy $N_i^{pp'}$ in several cases of interest are presented in Refs. [58,59,95,96] and references therein.

The matrices $\underline{L}_{nm}^{ij}$ in Equation 34.42 include the influence of the dipole fields from all other layers of the system on the considered layer i, and in general case $\underline{L}_{nm}^{ij}$ have the following form:

$$\underline{L}_{nm}^{ij} = \frac{\omega_{Mj}}{\omega_{Mi}}\begin{bmatrix} a_j(P_{nm}^{x_ix_j})^{ij} + jb_j(Q_{nm}^{x_ix_j})^{ij} & u_j(P_{nm}^{x_iy_j})^{ij} + js_j(Q_{nm}^{x_iy_j})^{ij} \\ c_j(P_{nm}^{y_ix_j})^{ij} + jd_j(Q_{nm}^{y_ix_j})^{ij} & h_j(P_{nm}^{y_iy_j})^{ij} + jt_j(Q_{nm}^{y_iy_j})^{ij} \end{bmatrix} \tag{34.44}$$

where

$a_j = A_j f_2(\theta) + C_j f_1(\varphi) f_1(\theta) + F_j f_2(\varphi) f_1(\theta)$; $b_j = B_j f_2(\theta) + D_j f_1(\varphi) f_1(\theta) + G_j f_2(\varphi) f_1(\theta)$
$u_j = C_j f_2(\theta) + E_j f_1(\varphi) f_1(\theta) + H_j f_2(\varphi) f_1(\theta)$; $s_j = D_j f_2(\theta) + I_j f_2(\varphi) f_1(\theta)$
$c_j = C_j f_2(\varphi) - F_j f_1(\varphi)$; $d_j = D_j f_2(\varphi) - G_j f_1(\varphi)$
$h_j = E_j f_2(\varphi) - H_j f_1(\varphi)$; $t_j = -I_j f_1(\varphi)$

Here $f_1(x) = \sin\left(x_i - x_j\right)$; $f_2(x) = \cos\left(x_i - x_j\right)$—the angle functions, which arise due to the transformations from coordinate system of j-layer to the coordinate system of i-layer, and

$$F_j = \frac{1}{2}\sin 2\theta_j\left(1+\cos^2\varphi_j\right); \quad G_j = \cos\varphi_j \cos 2\theta_j; \quad H_i = -\frac{1}{2}\sin\theta_j \sin 2\varphi_j; \quad I_j = -\sin\varphi_j \cos\theta_j$$

If we consider all layers with one type and same orientation of anisotropy, we should put $\theta_i = \theta_j$ and $\varphi_i = \varphi_j$.

Matrix elements $(P_{nn'}^{pp'})^{ij}$ and $(Q_{nn'}^{pp'})^{ij}$ in Equations 34.43 and 34.44 represent dipole–dipole interaction between SWM in each layer and between all layers in system; therefore, we will call them dipole matrix elements. They are given by

$$\left(P_{nm}^{pr}(k_\zeta)\right)^{ij} = \left(P_{mn}^{rp}(k_\zeta)\right)^{ji} = \frac{1}{L_i}\int_0^{L_i}\Phi_{ni}^{p}(\xi-\xi_i)\int_0^{L_j}G_j^{P}(\xi-\xi_i,\xi'-\xi_j,k_\zeta)\Phi_{mj}^{r}(\xi'-\xi_j)\mathrm{d}\xi\mathrm{d}\xi'$$

$$\left(Q_{nm}^{pr}(k_\zeta)\right)^{ij} = -\left(Q_{mn}^{rp}(k_\zeta)\right)^{ji} = \frac{1}{L_i}\int_0^{L_i}\Phi_{ni}^{p}(\xi-\xi_i)\int_0^{L_j}G_j^{Q}(\xi-\xi_i,\xi'-\xi_j,k_\zeta)\Phi_{mj}^{r}(\xi'-\xi_j)\mathrm{d}\xi\mathrm{d}\xi'$$

$$\left(T_{nn'}^{pp'}\right)^{ii} = \left(T_{n'n}^{p'p}\right)^{ii} = \frac{1}{L_i}\int_0^{L_i}\Phi_{ni}^{p}(\xi-\xi_i)\Phi_{n'i}^{p'}(\xi-\xi_i)\mathrm{d}\xi \tag{34.45}$$

The physical meaning of the matrix elements $\left(P_{nm}^{pr}(k_\zeta)\right)^{ij}$ and $\left(Q_{nm}^{pr}(k_\zeta)\right)^{ij}$ is as follows. When the exchange boundary conditions are symmetrical on two surfaces of the films formed structure, the elements $\left(P_{nm}^{pr}(k_\zeta)\right)^{ij}$ describe dipole interaction of the SWM having one and the same type of symmetry, and the elements $\left(Q_{nm}^{pr}(k_\zeta)\right)^{ij}$ describe dipole interaction of the SWM having opposite types

of symmetry. But if we take the asymmetrical type of the exchange boundary conditions or include the anisotropy, the broken symmetry of the whole problem leads to the dipole interaction of all SWMs in the structure. One useful property of the dipole matrix element $\left(Q_{nm}^{pr}(k_\zeta)\right)^{ij}$ follows from this statement—$\left(Q_{nn}^{pp}(k_\zeta)\right)^{ii} \equiv 0$ always for equal indices in the same layer. For the matrix element $\left(T_{nn'}^{pp'}\right)^{ii}$, we have $\left(T_{nm}^{pr}\right)^{ij} \equiv 0$ for all indices corresponding to the different layers. Matrix element $\left(P_{nm}^{pr}(k_\zeta)\right)^{ij}$ as a function of dimensionless longitudinal wave number $k_\zeta L_i$ always varies in the range $0 < P_{nm_i}^{pr} < 1$ when $0 < k_\zeta L_i < \infty$.

It should be noted that when the films formed the structure are moved apart, the matrix elements $\left(P_{nm}^{pr}(k_\zeta)\right)^{ij}$ and $\left(Q_{nm}^{pr}(k_\zeta)\right)^{ij}$ tend to zero for $i \neq j$ and the system of Equation 34.42 splits into N uncoupled infinite systems of equations describing the wave processes in separate films. In the long-wave limit ($k_\zeta L_i \ll 1$), a very simple expression for $\left(P_{nm}^{pr}(k_\zeta)\right)^{ij}$ and $\left(Q_{nm}^{pr}(k_\zeta)\right)^{ij}$ can be obtained (see Ref. [58]).

At first glance, the system of equations for the SWM amplitudes, Equation34.42 looks complicated and fairly difficult to grasp. But owing to the symmetry properties in particular cases (for example, in perpendicularly or tangentially magnetized films with totally pinned or totally unpinned surface spins), the appropriate solutions, both exact and approximate, could be found in a comparatively simple form.

In general case, the infinite system (Equation 34.42) gives the exact dispersion of the linear spin-wave processes in anisotropic magnetic/nonmagnetic multilayered structures and enables us to obtain the expressions for the spin-wave spectrum and the distribution of the variable magnetization of eigenwaves across the film thickness.

The infinite system of homogeneous algebraic Equation 34.42 has a simple physical interpretation. The condition of vanishing the determinant of this system yields the exact dispersion relation for the dipole-exchange spin waves, propagating in anisotropic ferromagnetic structure with an arbitrary value of k_ζ:

$$\det \left| \underline{\mathbf{D}}_{nn}^{ii} + \sum_{n' \neq n} \underline{\mathbf{R}}_{nn'}^{ii} + \sum_{j \neq i} \sum_{m} \underline{\mathbf{L}}_{nm}^{ij} \right| = 0 \tag{34.46}$$

The zeroes of this determinant give the eigenfrequencies of the multilayered structure under consideration. It is worth noting that due to Equations 34.43 and 34.44 the infinite matrix system (Equation 34.42) is always Hermitian. Therefore, the dispersion equation for dipole-exchange spin waves obtained from Equation 34.46 always gives real values for the spin-wave eigen-frequencies. In other words, the problem of determination of the exact dispersion law $\omega(k_\zeta)$ for spin waves in anisotropic layered structure is reduced to the problem of calculating the eigenvalues of the block matrix of the infinite system (Equation 34.42). The eigenvalue problem can be solved by different methods. One of these, which allow us to obtain the approximate analytical solution, is the perturbation theory approach.

Without presenting here the results obtained in Refs. [42,54,57–59], we point out that the infinite system of the homogeneous Equation 34.42 can be solved exactly in many cases. In doing so, the amplitudes of all the SWMs as well as the spin-wave spectrum can be found. Presented theory describes spin-wave branches of the dispersion spectrum for any value of $n > 1$ (not only for $n = 0$), as well as it covers the whole region of the wave vectors k_ζ (not only the regions of $k_\zeta = 0$ and $k_\zeta > 10^6$ cm^{-1}, as usual). Moreover, the competing effects of the exchange and dipolar interactions are interpreted correctly in the frames of this method.

It should be emphasized that the system of homogeneous equations for the SWM amplitudes (Equation 34.42) was derived with simultaneous regard for both dipole and exchange interactions, as well as electromagnetic and exchange boundary conditions. This system rigorously describes the

wave process in the magnetically biased magnetic/nonmagnetic multilayers and it may be used for the precise analysis of the dipole-exchange spin-wave spectrum as well as the spectrum of purely dipolar spin waves (in the limit $A = 0$). Besides, the exact dispersion relation obtained in the frames of SWM approach may be written in different forms, namely, in the form of an infinite series and in the form of the infinite determinant. The dispersion relation in the form of the infinite series is most convenient in the direct numerical calculations especially in some particular cases, while the form of an infinite determinant is very useful for the deriving the approximate solution in the frames of the perturbation theory [54,57,59,96].

As was mentioned above, the main feature of the SWM approach is the universality of the obtained results. We can consider any type of ferromagnetic structure with any number of layers (finite or infinite) and using Equation 34.46 we immediately arrive to the exact solution of the considered problem, which is convenient for further numerical calculations.

It is worth noting that the dispersion relation in the form of infinite determinant (Equation 34.46) suits almost for any possible case because the form of eigen-functions $\Phi^{p}_{ni}(\xi)$ is not determined here. Thus according to the particular boundary conditions, the appropriate functions $\Phi^{p}_{ni}(\xi)$ can be substituted in the dipole matrix elements $\left(P^{pr}_{nm}(k_\zeta)\right)^{ij}$ and $\left(Q^{pr}_{nm}(k_\zeta)\right)^{ij}$, and the particular dispersion relation will be obtained from this general form (Equation 34.46). Moreover, very small changes are needed to transform this equation to the case of another geometry of the problem. For example, in the case of an infinite array of cylindrical wires, only the components of the tensorial Green function should be replaced by the corresponding ones from the solution of Maxwell equations for a single ferromagnetic wire and the expansion of variable magnetization should be taken by the Bessel functions rather than cosines functions.

Finally, we note that the general results of the present part can be used as the starting point in more sophisticated analyses.

34.2.5 Approximate Dispersion Relation

To obtain the approximate solution in explicit form, let us slightly reorganize matrix Equation 34.42 and bring it to the proper form for applying perturbation theory method. We consider the diagonal part of the infinite determinant as an unperturbed operator and the non diagonal part as an operator of perturbation. After simple transformations, we arrive to the system (Equation 34.42) in matrix form:

$$\underline{\mathbf{H}}^{ii}_{nn} m^{i}_{n} + \sum_{n' \neq n} \underline{\mathbf{W}}^{ii}_{nn'} m_{n'} + \sum_{j \neq i} \sum_{m} \underline{\mathbf{Y}}^{ij}_{nm} m^{j}_{m} = 0 \tag{34.47}$$

where

$$\underline{\mathbf{H}}^{ii}_{nn} = \underline{\mathbf{I}} \det \underline{D}^{ii}_{nn}, \quad \underline{\mathbf{W}}^{ii}_{nn'} = \left(\underline{D}^{ii}_{nn}\right)^{-1} \underline{R}^{ii}_{nn'} \det \underline{D}^{ii}_{nn}, \quad \underline{\mathbf{Y}}^{ij}_{nm} = \left(\underline{D}^{ii}_{nn}\right)^{-1} \underline{\mathrm{L}}^{ij}_{nm} \det \underline{D}^{ii}_{nn} \tag{34.48}$$

and $\left(\underline{D}^{ii}_{nn}\right)^{-1}$ is defined through the relation $\left(\underline{D}^{ii}_{nn}\right)^{-1} \underline{D}^{ii}_{nn} = \underline{\mathbf{I}}$, $\underline{\mathbf{I}}$ is a unit matrix. The physical interpretation of the operators $\underline{\mathbf{W}}^{ii}_{nn'}$ and $\underline{\mathbf{Y}}^{ij}_{nm}$ is as follows. Operator $\underline{\mathbf{W}}^{ii}_{nn'}$ describes the interaction between SWMs of different types ($n \neq n'$) inside one layer i, and is caused by the nondiagonal part of the magnetic dipole–dipole interaction $\left(R^{pp}_{nn'}\right)^{ii}$, while $\underline{\mathbf{Y}}^{ij}_{nm}$ includes the long-range dipole interaction between SWMs taken in different films of multilayered structure, which is due to the influence of variable magnetic field from all ferromagnetic layers in stack with $i \neq j$ and is determined by matrix

elements $\left(L_{nm}^{pr}\right)^{ij}$. We emphasize that the exchange interaction, the diagonal part of the dipole–dipole interaction, and the diagonal part of volume anisotropy are described by the unperturbed diagonal operator $\underline{\mathbf{H}}_{nn}^{ii}$.

Now, we may represent the infinite system 34.47 in the form of the matrix equation:

$$\underline{\mathcal{L}}\mathbf{m} = 0 \tag{34.49}$$

where

operator L is an infinite block-matrix whose elements are square matrices (Equation 34.48)
m is an infinite column vector consisting of SWM vector amplitudes of all layers.

The dispersion equation for dipole-exchange SW eigen-waves in this notation may be expressed as

$$\det \underline{\mathcal{L}} = 0 \tag{34.50}$$

In general case of an arbitrary surface anisotropy and arbitrary direction of magnetization, the problem of evaluation of the dispersion relation may be reduced to the problem of diagonalization of the block matrix $\underline{\mathcal{L}}$ and may be solved approximately using classical perturbation theory [116].

We represent the block matrix $\underline{\mathcal{L}}$ as a sum of two matrices consisted of its diagonal $\underline{\mathbf{H}}_{nn}^{ii}$ and non diagonal $\underline{\mathbf{W}}_{nn'}^{ii}$, $\underline{\mathbf{Y}}_{nm}^{ij}$ parts. In the zero-order approximation, the dispersion relation of the entire multilayered system consists of the independent sets of the dispersion curves typical for separate (uncoupled) layers of the system. Thus, no interaction (i.e., no repulsion) between the dispersion branches is taken into account here. As it was shown in Ref. [57], the matrix equation for variable magnetization (Equation 34.47) in zero-order approximation gives following dispersion equation:

$$\left(\frac{\omega_{ni}(k_\varsigma)}{\omega_M}\left(T_{nn}^{yx}\right)^{ii} + D_i\left(Q_{nn}^{yx}\right)^{ii}\right)^2 = \left(F_{ni}^x + \sin^2\theta_i + A_i\left(P_{nn}^{xx}\right)^{ii} + \left(N_{xx}^a\right)^i\right)$$
$$\left(F_{ni}^y + E_i\left(P_{nn}^{yy}\right)^{ii} + \left(N_{yy}^a\right)^i\right) - \left(C_i\left(P_{nn}^{yx}\right)^{ii} + \left(N_{yx}^a\right)^i\left(T_{nn}^{yx}\right)^{ii}\right)^2 \tag{34.51}$$

This dispersion relation for each layer i describes the propagating spin wave with number n in the assumption that there is no crossing points between any modes from any two or more films. Since this condition is fulfilled, the dispersion relation (Equation 34.51) remains true in the first-order approximation too.

In the case when both components of the magnetization vector **m** (m_x and m_y) are pinned uniformly $\eta_{1,2}^x = \eta_{1,2}^y = \eta_{1,2}$, but still differently on different sides of the films ($\eta_1^p \neq \eta_2^p$), the dispersion Equation 34.51 can be rewritten in the form of a well-known dispersion equation for the spin wave in the unlimited ferromagnetic media (see Ref. [87]):

$$\omega_{ni}^2(k_\varsigma) = \omega_{M_{0i}}F_{ni}\left[\omega_{M_{0i}}F_{ni} + \omega_{M_{0i}}\left(\left(\mathbf{F}_{nn}\right)_i + \left(\mathbf{F}_{nn}^a\right)_i\right)\right] \tag{34.52}$$

where

$$\left(\mathbf{F}_{nn}\right)_i = \sin^2\theta_i - \left(P_{nn}\right)^{ii}\sin^2\theta_i\cos^2\varphi_i + \left(P_{nn}\right)^{ii}\left[\cos^2\theta_i + \frac{\omega_{M_{0i}}}{F_{ni}}\left(1 - \left(P_{nn}\right)^{ii}\right)\sin^2\varphi_i\sin^2\theta_i\right] \tag{34.53}$$

$$\left(\mathbf{F}_{nn}^a\right)_i = \left(N_{xx}^a\right)^i + \left(N_{yy}^a\right)^i + \frac{\omega_{M_{0i}}}{F_{ni}}\left[\left(N_{xx}^a\right)^i\left(N_{yy}^a\right)^i + \left(N_{yy}^a\right)^i\sin^2\theta_i - \left(\left(N_{xy}^a\right)^i\right)^2\right]$$
$$+ \frac{\omega_{M_{0i}}\left(P_{nn}\right)^{ii}}{F_{ni}}\left\{\left(N_{yy}^a\right)^i\left[\cos^2\varphi_i - \sin^2\theta_i\left(1 + \cos^2\varphi_i\right)\right]\right.$$
$$\left. + \left(N_{xx}^a\right)^i\sin^2\varphi_i - \left(N_{xy}^a\right)^i\cos\theta_i\sin 2\varphi_i\right\} \tag{34.54}$$

In the isotropic limit $\mathbf{F}^{a}_{nn} = 0$, Equation 34.52 reduces to the approximate dispersion equation for spin waves in isotropic ferromagnetic film.

This equation can be easily used for practical calculations of dispersion characteristics of either dipole-exchange spin waves or magnetostatic waves ($A_i = 0$) in ferromagnetic films. In particular, numerical calculations show that in the long-wave part of the spectrum ($k_\zeta L \ll 1$) in the case of unpinned surface spins and without anisotropy, Equation 34.52 gives the results which coincide very accurately with the results obtained from the non-exchange dispersion equations (see Ref. [86]).

In practice, it is interesting to have the approximate dispersion equations in the explicit form for the particular cases of definite orientations of crystallographic axes and bias magnetic field in the anisotropic films. Several useful cases were derived in Ref. [59]. More detailed discussion and approximate dispersion relations for other particular cases can be found in Refs. [54,57,58].

As it was mentioned above, in the zero-order approximation, we take into account the whole diagonal part of the dipole-exchange operator, and thus in the first-order approximation the obtained relation remains in force. But, the analysis shows that the dispersion curves corresponding to the different numbers $n \neq m$ and different layers $i \neq j$ of the system may cross each other, i.e., there may be frequency degeneracy in some points of the spin-wave spectrum ($\det \underline{\mathbf{D}}^{ii}_{nn} = \det \underline{\mathbf{D}}^{jj}_{mm}$). If such crossing points arise, then the situation yields a secular dispersion equation, which will lift this degeneracy by taking into account the dipole–dipole hybridization of the "interacting" dispersion branches.

In multilayered structure, there are two types of the dipole–dipole "interaction": the hybridization between SWMs inside one ferromagnetic film and the interlayer dipole interaction, i.e., hybridization between the SWMs from different films. Thus, we have two possible cases, which are illustrated qualitatively in Figure 34.5. First, when the dispersion branches inside one ferromagnetic film cross each other (Figure 34.5a). Second, when the dispersion branches of different films have the common energies (Figure 34.5b). In these cases, we should use different secular equations to lift the degeneracy. The question, what case should be chosen in the problem under consideration, should be cleared up in each particular case by the zero-order approximation dispersion. For the first case (Figure 34.5a), the secular equation is

$$\det \begin{bmatrix} \underline{\mathbf{D}}^{ii}_{nn} & \underline{\mathbf{R}}^{ii}_{nn'} \\ \underline{\mathbf{R}}^{ii}_{n'n} & \underline{\mathbf{D}}^{ii}_{n'n'} \end{bmatrix} = 0 \tag{34.55}$$

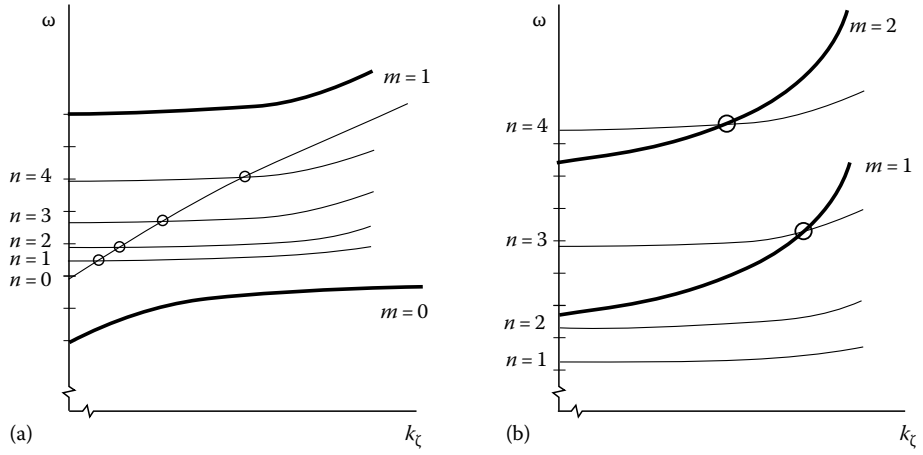

FIGURE 34.5 Two possibilities of dipole–dipole interaction between the dispersion branches of two ferromagnetic films: (a) hybridization of SWMs for one and the same film and (b) hybridization between SWMs for different films.

And the form of the secular equation for the second case (Figure 34.5b) has the form:

$$\det\begin{bmatrix} \underline{\mathbf{D}}_{nn}^{ii} & \underline{\mathbf{L}}_{nm}^{ij} \\ \underline{\mathbf{L}}_{mn}^{ji} & \underline{\mathbf{D}}_{mm}^{jj} \end{bmatrix} = 0 \tag{34.56}$$

Obviously, the difference between these two cases lies in the form of the nondiagonal matrix elements, which should be used to account for the corresponding dipole–dipole interaction. Hybridization of the crossing dispersion branches leads to the formation of dipole "gaps" in the dipole-exchange spin-wave spectrum. The decrease of the spin-wave group velocity in the spectral regions of hybridization causes an increase in the spatial attenuation of propagating spin waves in these regions. In experiments, this effect manifests itself in the form of oscillations in the propagation loss characteristic and can be observed in perpendicularly as well as tangentially magnetized structures [117–119].

For the particular cases of perpendicularly and tangentially magnetized ferromagnetic films with pinned and unpinned surface spins and for mixed exchange boundary conditions, the explicit form of the zero-order dispersion relations and the form of secular equations can be found in Refs. [54, 57–59].

Since the dispersion Equations 34.51 through 34.54 remain in force in the first-order approximation of the perturbation theory, the first nontrivial correction to the dispersion law in non-generate case appears only in the second-order approximation of the perturbation theory.

The detailed discussion of the frames of applicability of the first-order approximation and the higher-order terms of the dispersion relation can be found in Ref. [58].

34.3 Periodic Structures as Metamaterials: Band Theory of Infinite Film Stack

In previous sections, we consider the multilayered structure with arbitrary parameters, and derive exact and approximate dispersion relation by means of SWM technique and perturbation theory approach. Let us now apply the same methods to the array of identical ferromagnetic films separated by equal nonmagnetic layers. Such periodic multilayered systems can be called metamaterials, because of their especial behavior, different from multilayered structures with arbitrary parameters. As we know from quantum theory of solid state, the periodic structure shows the unique propagation behavior for waves and excitations in it.

Rapid progress in such techniques as molecular beam epitaxy or metal-organic chemical vapor deposition enables to grow the systems with predetermined film thicknesses and with sharp interfaces. Such systems seem to provide a new type of material, which does not exist naturally. Accordingly, it is now possible to investigate the properties of very accurately defined stacks of alternating magnetic and nonmagnetic thin films. Spin waves of magnetic multilayers have been the first genuinely collective effect studied in these new materials [50]. Ferromagnetic films in such structures are always coupled via their long-range magnetostatic dipolar fields, thus forming characteristic new modes of the stack—collective SWMs. These modes arise in a range of wavevectors experimentally accessible by BLS techniques.

As in any periodic structure, the collective modes in such magnetic metamaterials are characterized by a periodic dispersion curve comprised of Brillouin zones, in case the spin waves propagate *in the direction of periodicity* (perpendicular to the film surfaces). Stop and allowed bands appear in the spectra of spin waves propagating in the direction of periodicity due to the reflection near boundaries of the Brillouin zone. In the case when the excitations propagate in the film plane (i.e., in the direction *perpendicular to the direction of periodicity*), the effect of the formation of the collective modes manifests itself through splitting of the initial discrete dispersion spectra into the set of bands. Both of these situations can be described in the frames of SWM approach.

Let us build a band theory of the magnetic metamaterial by analogy with electron band structure in solid states. For the treatment of an infinite stack of periodic multilayers, we introduce Bloch's theorem to describe the resulting band structure of the spin-wave energies. A well-known example of excitations in a periodic system is the allowed energy states of a 1D Kronig–Penney model. The resulting collective excitations are Bloch wave eigen states and are the excitations in the individual wells modulated by a function that has the periodicity of the lattice. The Bloch wave vector is proportional to the inverse of a wavelength that specifies the relative phase between the standing-wave functions in neighboring potential wells. The case of an infinite periodic structure of identical ferromagnetic layers separated by nonmagnetic spacer will then correspond to the analogue case of the approximate electronic band theory named tight binding model [16].

The SWM formalism can be easily extended on the spin-wave band theory of an infinite multilayered structure. As it was mentioned above, the same formalism can be applied to the cases of parallel and perpendicular propagation of the resulting excitations (spin waves) relative to the direction of periodicity in such structure. We consider here the case of the in-plane propagation of the resulting excitations in the infinite stack of identical ferromagnetic films of thickness L separated by nonmagnetic layers of thickness d Figure 34.4. To describe the variable magnetization in ξ-direction the Bloch theorem should be applied [120]. In general form variable magnetization of the whole structure is given by a Bloch-type function:

$$\mathbf{m}_{stack}(\mathbf{r}, t) = \mu(\mathbf{r}, t)e^{jQ\xi} \tag{34.57}$$

where the Bloch wave vector $-\pi/T \le Q < \pi/T$ and $\mu(\mathbf{r}, t)$ necessarily should be a periodic function:

$$\mu(\xi, \rho, \zeta, t) = \mu(\xi + nT, \rho, \zeta, t) \tag{34.58}$$

Evidently, $\mu(\mathbf{r}, t) = 0$ in all nonmagnetic regions of the stack.

Here we shall consider the case where the magnetostatic coupling between different layers is weak compared to the dipolar interactions within each layer. In a perturbational approach we then may apply a *tight binding approximation* (in analogy with the tight binding approximation in electron-band theory or in the theory of Frenkel exitons). Expanding the periodic function $\mu(\mathbf{r}, t)$ in the series by the initial single-film eigenmodes and inserting the whole solution $\mathbf{m}_{stack}(\mathbf{r}, t)$ into Equation 34.34 we can obtain the expanding coefficients:

$$\mu(\xi, \rho, \zeta, t) = \sum_{j=-\infty}^{+\infty} e^{-jQ(\xi-\xi_j)}\mathbf{m}(\xi - \xi_j, \rho, \zeta, t) \tag{34.59}$$

It should be noted that the periodic part in Equation 34.57 $\mu(\mathbf{r}, t)$ in itself is not a solution of the eigenmode problem (Equation 34.34) but the whole function $\mathbf{m}_{\text{stack}}(\mathbf{r}, t))$ with $\mu(\mathbf{r}, t)$ in the form of Equation 34.59 already satisfies the boundary problem (Equation 34.34).

It is clear that now $\mathbf{m}_{\text{stack}}(\mathbf{r}, t)$ will have the following form:

$$\mathbf{m}_{\text{stack}}(\mathbf{r}, t) = \sum_{j=-\infty}^{+\infty} e^{jQ\xi_j}\mathbf{m}(\xi - \xi_j, \rho, \zeta, t) \tag{34.60}$$

Thus, the resulting collective modes $\mathbf{m}_{\text{stack}}(\mathbf{r},t)$ are the modes of the single films modulated by a function that has the periodicity of multilayered structure.

The single layer magnetization $\mathbf{m}(\mathbf{r}, t)$ now corresponds to the lattice periodic part $\mu(\mathbf{r}, t)$ of the Bloch function. Therefore $\mathbf{m}(k_\zeta, \xi - \xi_j)$ is identical for all layers j. The coefficients m_{in}^p of the expansion in terms of SWMs do not depend on the layer number j, in contrast to the above case of a finite multilayer treated by Equation 34.33.

In the case of the electron band theory the condition of applicability of the tight binding approximation (i.e., when we take only one term in the sum over all states for each single atom) includes the condition of small overlapping of the electron wave functions from different atoms (quantum wells). In the case under consideration functions $\mathbf{m}(\mathbf{r}, t)$ represent the eigen modes of dynamic magnetization in different layers of the structure. Thus here the tight binding approximation is fairy good, because the dynamic magnetizations $\mathbf{m}(\mathbf{r}, t)$ from different layers cannot directly overlap each other, they can interact only through the dynamic dipole fields. Thus the condition of applicability of tight binding approximation always works. Moreover for the highest modes this condition is satisfying better, since for these modes the magnetic fields are confined inside the ferromagnetic layers, thus the SWMs from different layers cannot interact even through the stray fields.

Moreover, the other condition of applicability of the tight binding approximation is that the allowed zones should be much less than the energy interval between two neighboring spectral lines. This condition in the case of thin films is satisfied for all modes, but better for higher modes due to the exchange interaction, since the spectral lines at higher frequencies are rare and the splitting for higher modes is much less (due to less interaction between modes at higher frequencies).

In a manner analogous to the above cases we now obtain the algebraic equations for spin-wave amplitudes m_{in}^{p} by setting the number i of the arbitrary chosen reference layer to zero:

$$\left[\underline{\mathbf{D}}_{nn}^{ii}\mathbf{m}_{n}^{i} + \sum_{\substack{j\neq i \\ n=m}} \underline{\mathbf{L}}_{nm}^{ij}\mathbf{m}_{m}^{j}\right] + \sum_{\substack{n'\neq n \\ n'=m'}} \left[\underline{\mathbf{R}}_{nn'}^{ii}\mathbf{m}_{n'}^{i} + \sum_{j\neq i} \underline{\mathbf{L}}_{nm'}^{ij}\mathbf{m}_{m'}^{j}\right] = 0 \tag{34.61}$$

The exact solution of the infinite system (Equation 34.61) can be obtained following the same lines as for multilayered structures before.

Obviously due to the periodicity of the structure the dispersion in each block of the block diagonal matrix $\underline{\mathcal{L}}$ will have the same form. Thus in our approximation we can take one block to describe the dispersive characteristics of the whole system. Applying the condition of vanishing determinant of this system we arrive to the exact dispersion equation for an infinite stack of identical ferromagnetic films.

As we see in the case of an infinite layers stack, the magnetic field inside the film with number j is created by a series of $N = \infty$ ferromagnetic layers arranged with the period $T = L + d$. In this case the contribution from variable magnetic fields of all layers of the system can be taken into account via summation over corresponding SWMs taken with the corresponding phase shift $e^{jQ(jT)}$ in corresponding layers of the system. According to the perturbation theory method in the diagonal approximation the dispersion equation one can easily obtain the dispersion relation of an infinite stack in explicit form.

For a simple case of a perpendicularly magnetized periodic multilayered structure with totally unpinned surface spins on the surface of ferromagnetic films (Ament–Rado exchange boundary condition Equation 34.17) in the zero-order approximation the dispersion equation have the following form [55]:

$$\omega_n^2(k_\zeta) = \Omega_{nk}\left(\Omega_{nk} + \omega_{\mathbf{M}}P_{nn}^{ii}\right) - \Omega_{nk}\omega_{\mathbf{M}}\frac{4}{1+\delta_{0n}}\frac{k_\zeta^4 \cdot e^{-k_\zeta T}}{\left(k_\zeta^2 + (k_{ni})^2\right)^2}\frac{1-(-1)^n ch(k_\zeta L)}{k_\zeta L}$$
$$\times \frac{\left(\cos(QT) - e^{-k_\zeta T}\right)}{1 - 2e^{-k_\zeta T}\cos(QT) + e^{-2k_\zeta T}} \tag{34.62}$$

where $\Omega_{nk} = \omega_{\mathbf{M}}F_{ni}^{p}$ and F_{ni}^{p} is the eigen value of the considered boundary problem (Equations 34.40 and 34.41).

This form of dispersion equation is very suitable for a discussion of the physically relevant effects. It consists of two terms. The first represents the well-known approximate dispersion relation for one ferromagnetic film [57]. This term includes the contribution of the exchange interaction and of Zeeman gap due to the applied magnetic field, the contribution of the magnetostatic fields to the spin-wave energies in a bulk ferromagnetic medium, and also it describes the interaction of different SWMs via the dipole fields surrounding each film and takes into account the finite thickness L of the film. The second term represents the dipole coupling between spin waves in the different films of the stack.

Since we consider the system of all identical ferromagnetic layers with equal spacers between them, then the new collective modes arises and the dispersion curves of spin-wave spectrum split into bands, i.e., allowed zones appear for each eigen mode. Substituting $Q = 0$ and $Q = \pi/T$ one can calculate for each SWM the top and the bottom of the corresponding allowed zone of the spectrum $\omega_n(k_\varsigma)$.

For a multilayer consisting of N ferromagnetic films, each branch n of the corresponding single-film spectrum splits into N branches due to the formation of the coupled modes of the stack. In the infinite periodic structure the spectrum represents the series of allowed zones. The splitting of the branches, i.e., the band width, decreases with increase of the total wave vector $K^2 = k_\zeta^2 + k_n^2$ because for short wave-length of the spin wave the nonlocal nature of the dipolar interaction has an averaging effect, thus reducing the influence of the magnetostatic contribution, and the exchange interaction within each layer becomes dominant. Moreover, the frequency width of the allowed zone results in the splitting of the dispersion modes of an individual film due to dipolar coupling, and it decreases with increasing nonmagnetic spacers because of a corresponding decrease in the interlayer coupling. This evolution is qualitatively illustrated in Figure 34.6. Here the transition from a single film to a double layer and to an infinite stack is shown.

The above discussion in this chapter concerns the case when the direction of the periodicity of the structure and the direction of the spin-wave propagation are perpendicular to each other. In order to eliminate misunderstanding it is worth mentioning that in this special case, although applying Bloch's theorem, we never obtain any Brillouin zones in the dispersion spectrum of spin waves and no

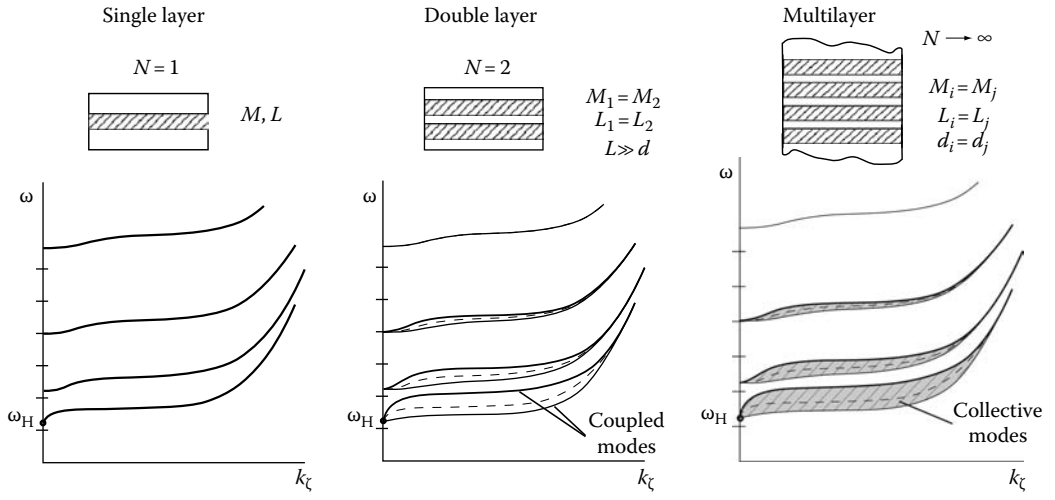

FIGURE 34.6 Qualitative illustration of the formation of the dipole-exchange spectrum starting from single-film spectrum through double-layer coupled modes to the band structure of the collective modes in the infinite multilayer in the presence of the interlayer dipole–dipole interaction.

effects like full reflection can appear in such configuration. Here the periodicity of the structure can produce only the simplest spectrum transformations, such as splitting of initial spin-wave branches into continuous bands of a finite width. There are no propagating spin waves in the direction of periodicity thus the formalism of Brillouin diagrams and the conception of forbidden and allowed zones is meaningless in this case. We should underline that in the problem under consideration only standing spin waves can arise in the direction of the periodicity.

The opposite situation occurs if we consider the propagation of the spin waves in the direction of the structure periodicity. Now applying Bloch's theorem and deriving the dispersion relation we obtain fundamentally new spin-wave spectrum, where each initial mode consists of a series of allowed and forbidden bands which are comprised in a first Brillouin zone. These SWMs of coupled multilayers cannot be explained in terms of modified single film properties, because these are new states—collective modes. But, this is a separate complicated problem, which is out of present consideration. However, we can point out some articles and books dealing with this question.

The detailed discussion of a vast amount of periodic structures and the wave propagation in them can be found in a review paper by Elachi [121]. Author gives a detailed analysis of a general solution for the wave equation in a symmetry periodic medium in both the Floquet and the coupled waves approach.

Another work [8] is concerned with the periodic multilayered magnetic structure, consisting of altering ferromagnetic layers of same thickness but different magnetization. The main feature of the dispersion plots in this work is the presence of the stop band caused by the periodicity of the structure and reflection of the SWs at the boundaries. It is to be emphasized that unlike the photonic crystal bands the magnonic bands can be tuned by an external magnetic field.

Finally, it should be noted that the case of periodic multilayered structures is mostly exotic and technologically difficult for implementation. But, using this simple example, we can demonstrate the main features of the whole variety of periodic structures and develop a common approach to a theoretical investigation of such structures. From the aspect of applicability, the periodic planar and volume structures seemed to be more interesting, because propagating spin waves are easily excited in such structures and their band structure can be investigated experimentally.

Recently, several papers reported about highly ordered 1D, 2D, three-dimensional (3D) magnetic periodic structures. Let us mentioned here some of the traditional periodic configurations. Among planar 1D structures, we select the array of rectangular stripes. A lot of work was devoted to such patterned structures made of different magnetic materials [18,19,73,122–124]. Moreover, arrays of double-layer [125,126] and tri-layered wires [127] were investigated both experimentally and theoretically. Two dimensional-patterned structures are represented by the arrays of square [26,128,129] and circular dots [9,24,25,27], as well as by the nets of holes (antidot arrays) [28], arrays of elliptical permalloy dots [130], NiFe/Cu/NiFe tri-layered circular dots [131], permalloy square ring arrays [132], array of $Ni_{81}Fe_{19}$ rectangular prisms [68], etc. The theory of band structure in such systems was elaborated in Refs. [24,128].

Among the 2D periodic composites, we should note the arrays of magnetic cylindrical nanowires (rods) embedded in magnetic or nonmagnetic substrate. The theory of the collective spin waves in such structures [5,6,40,133] and several experimental papers [20–22,38,134–136] were published in the past 10 years. The possibility to develop 3D periodic magnetic structures (magnonic crystals) was discussed in Refs. [5,7].

It is appropriate to mention here some interesting, even exotic, samples of periodicity which are represented in literature. For example, authors [65] consider the magnetic multilayer system in which thin ferromagnetic films are separated by nonmagnetic spacers following a Fibonacci sequence. The obtained results show the splitting of the frequency bands in the dipole-exchange spin-wave spectrum and the fractal aspect of the spectrum induced by the non-periodic aspect of the structure. Thus, we see that different periodic structures attract a great interest in various fields of application.

34.4 Dispersion Properties of Spin Waves in Thin Films and Multilayered Structures

The discussion is now given for several general principles of the spin-wave spectrum formation in different magnetic metamaterials. Generally, a large variety of magnetic (periodic) structures can be now fabricated due to the considerable progress in the growth technology. Here, we suggest some simple classification of various types of magnetic periodic structures:

1. Bulk structures
   a. Multilayers
      i. Infinite
      ii. Semi-infinite
      iii. Finite
   b. 2D arrays of magnetic nanowires
      i. Circular cross section
      ii. Rectangular cross section
      iii. Other geometry
   c. 3D arrays of magnetic elements (superlattices)
2. Planar patterned structures
   a. Arrays of identical magnetic stripes
   b. 1D, 2D arrays of planar magnetic elements
      i. Circular dots (elliptical)
      ii. Rectangular dots
      iii. Other geometry
   c. Magnetic quantum nets or 1D, 2D arrays of antidotes (holes)

Another classification can be given according to the peculiarities of the spectrum formation. We can divide all magnetic periodic structures into two groups. "The first group" in this classification includes the structures made of one magnetic material with nonmagnetic spacer between elements. These structures may have different geometry, for example, multilayers, arrays of wires or dots, 2D and 3D-arrays of different elements. Their common feature is that the magnetic elements are surrounded by nonmagnetic media. The properties of such structures can be varied through altering the geometry of the structure as well as the direction and value of the bias magnetic field. "The second group" consists of two or more magnetic materials periodically alternated in space. Again, the form of alternating elements can be quite different and sometimes exotic. The properties of such compositions may be considerably different from those of initial bulk materials formed the structure.

The proposed classification is conditional because even the nonmagnetic spacer in the structures of the first type can govern the magnetic properties of metamaterial (as in Gd/Y superlattices the antiferromagnetic coupling exist between ferromagnetic films due to the presence of Y as nonmagnetic spacer) or can improve the interlayer interaction (as in the case of metallic spacer: the exchange interaction would be much stronger and Hoffmann exchange boundary conditions should be used even when spacer is relatively thick). On the other hand, in the magnetic/magnetic structures, some spacer between magnetic layers always exists due to the technology of fabrication or due to the crystallographic and physical properties of the surfaces in contact. Moreover, some structures may contain as a spacer different passive and active materials: ferroelectrics, semiconductors, nonlinear, and nonreciprocal media. But such special cases are beyond the scope of this chapter.

One more interesting class of the artificial materials, which can be called the second group, is the magnetic quantum nets. One of the examples of such type of metamaterial is the magnetic film with circular (or other) holes arranged in 2D array (array of antidots) [28]. In some cases, such net materials can contain the wires or bubbles of nonmagnetic material incorporated into the bulk magnetic (3D nets). Obviously, if the inclusions are made of another magnetic material, we arrive to the particular case of the second group in our classification. But even when the holes are filled by the nonmagnetic material, we cannot treat such systems by the theoretical approach of the first group. It should be noted that such systems are very similar to sonic crystals [137] or photonic crystals [138], with spin waves instead of sound or electromagnetic (light) waves. Here, the spin waves propagate in periodically inhomogeneous (or perturbed) medium.

So our classification is based mostly on the difference of interface conditions and dominated interactions in each type of the structure. For example, when we consider the structures of the first group (magnetic/nonmagnetic structures) in most cases of interest, the interlayer exchange interaction can be neglected due to the relatively large distances between magnetic elements (i.e., $d \gg R_{\text{exchange}}$). Thus, the Rado–Weertman exchange boundary conditions can be applied at the interfaces of the structure. Vice versa, in the case of magnetic/magnetic structures, the interlayer exchange interaction dominates and one should use the full Hoffmann exchange boundary conditions for calculation of the dispersion spectrum in such systems.

Fortunately, the same separation we find in the classification of areas of application for such artificial magnetic materials. Magnetic/nonmagnetic structures are mainly applied in signal processing (for both optic and microwave frequencies), while magnetic/magnetic structures are used in data storage and read/write magnetic devices (due to the effect of GMR).

In further analysis, we will concentrate our attention on the multilayered and later 1D-patterned structures (arrays of magnetic stripes). The spectrum of the magnetic excitations in such artificial structures presents many unique features, which are absent in bulk and single-film systems. But to describe them, one should first discuss the basic features of the SWMs in a single magnetic film. Thus, it will be helpful to recall briefly some certain principles of the formation of single-film spin-wave spectrum and then to draw an analogy between similar cases for the compound systems.

34.4.1 Single-Film Spectrum

In Figure 34.7, the most important features of single-film spectrum formation are illustrated [58,139]. It should be noted that it is impossible to draw a general system of dispersion curves for dipole-exchange spin waves in anisotropic ferromagnetic film of arbitrary thickness and for arbitrary direction of external magnetic field (as it can be done in non-exchange case Figure 34.7a), but we can point out some basic tendencies of the dispersion modifications, which allow us to predict the evolution of the whole spectrum in most special cases.

34.4.1.1 Perpendicular Magnetization

Let us start from the simplest case of perpendicularly magnetized ferromagnetic film (Figure 34.7). For small k_ζ, the dependence $\omega(k_\zeta)$ is principally due to dipole effects; for big k_ζ the exchange energy dominates the dipole energy. For rather large k_ζ, a quadratic k_ζ dependence (usual for exchange SW) in dispersion law takes over. The main branch has the biggest initial slope, i.e., the main SWM has the biggest group velocity. In the non-exchange limit ($A = 0$), the spectrum consists of the dispersion branches beginning at $\omega = \omega_H$ (Figure 34.7a). When the exchange interaction is incorporated, it shifts up the higher branches with $n > 0$. The value of the frequency shift increases with increasing eigen-wave number and with decreasing film thickness L. This frequency shift may cause the crossing of the dispersion curves corresponding to the higher spin waves with the dispersion curve of the main spin wave (Figure 34.7b [1 and 2]). In the crossing points of the dispersion branches, the

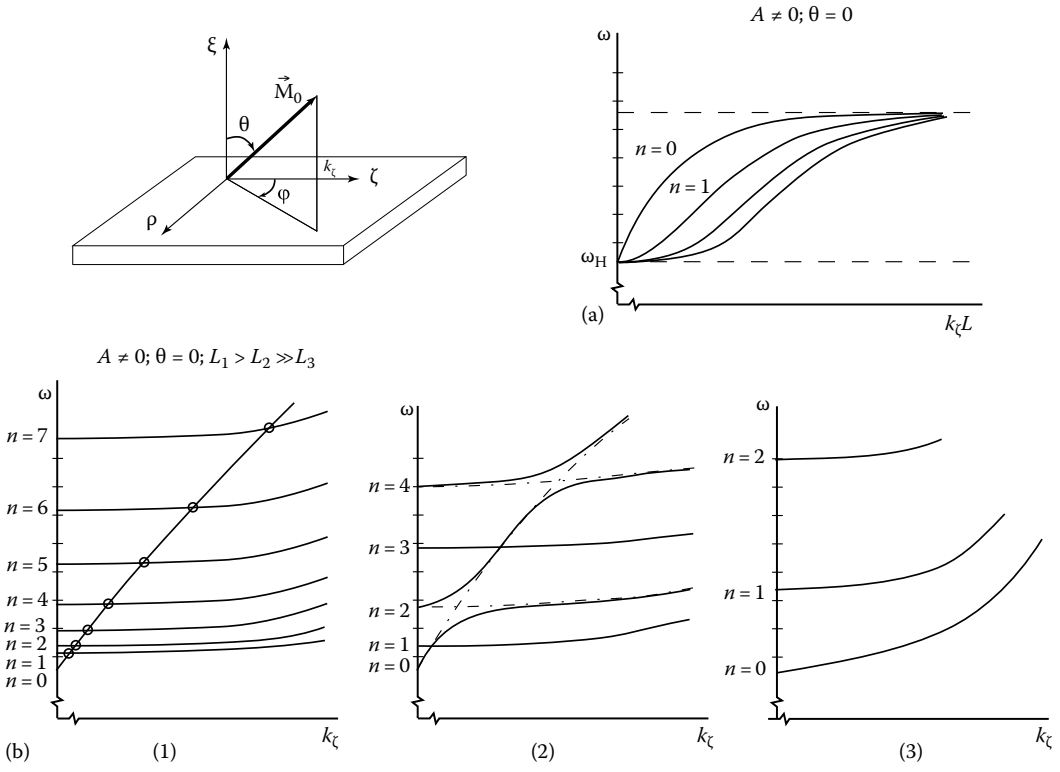

FIGURE 34.7 Qualitative illustration of single film spectra: (a) spin-wave spectrum in non-exchange limit and (b) formation of the dipole-exchange spin-wave spectrum for three different film thickness $L_1 > L_2 \gg L_3$.

dipole–dipole brunch repulsion takes place and dipole "gaps" in the spin-wave spectrum are formed (Figure 34.7b2).

The dipole–dipole repulsion causes the decrease of the spin-wave group velocity in the regions of hybridization, which leads to an increase in the spatial attenuation of propagating spin wave in these regions. In experiments, this effect manifests itself in the form of oscillations in the propagation loss characteristic of the experimental device (delay line) [119], and can be observed in perpendicularly as well as tangentially magnetized ferromagnetic film.

Analysis shows that the values of the dipole gaps depend heavily on the film thickness and surface spin pinning conditions (surface anisotropy). This phenomenon was exhaustively investigated in Ref. [57].

The decreasing of the film thickness L leads to the increasing of the frequency distances between the dispersion branches:

$$\left((\omega_{n+1} - \omega_n) \sim \frac{2A}{\mu_0 M_s^2}(2n+1)\left(\frac{\pi}{L}\right)^2\right)$$

and at the same time to the decreasing of the slopes of the dispersion curves. So, at some L even the lowest brunch has such a low slope that it does not give any crossings in the dipole-exchange area of the spectrum (Figure 34.7b3). This case is usually realized in multilayered structures.

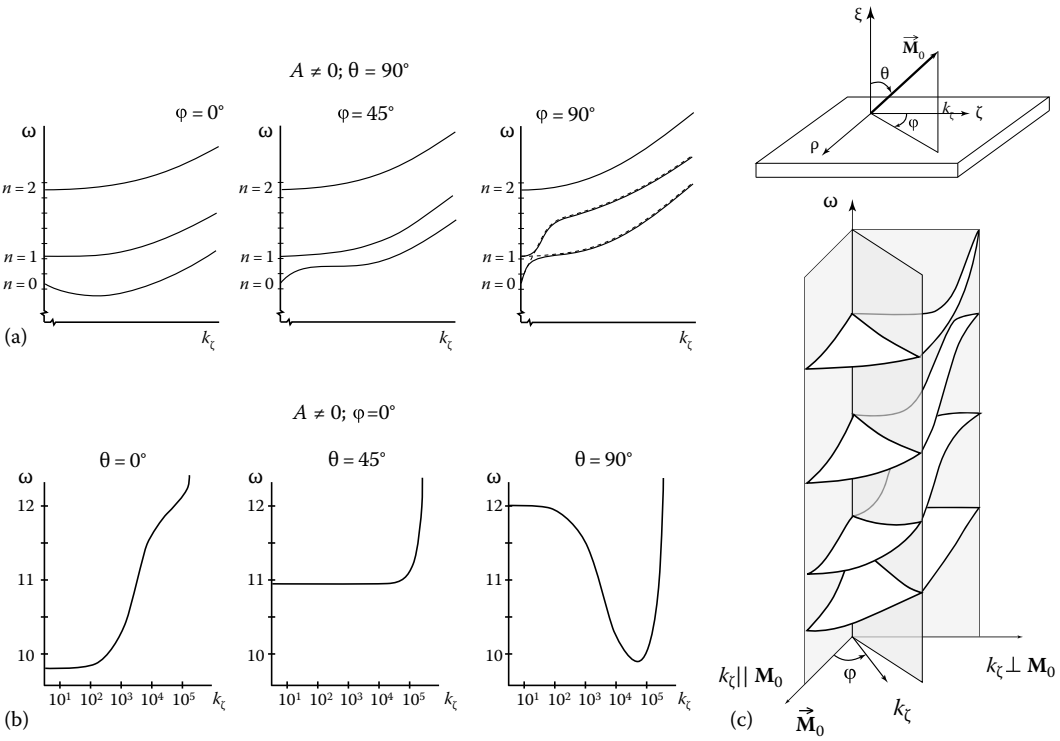

FIGURE 34.8 Transformation of the dipole-exchange spin-wave spectrum for different directions of static magnetization: (a) transformation of spectrum for tangentially magnetized ferromagnetic film with pinned surface spins for various azimuth angles; (b) dispersion curves for the lowest SWM ($n = 0$) propagating in the film with totally unpinned surface spins for various polar angles; and (c) sketch of the dipole-exchange dispersion surfaces for a tangentially magnetized film.

34.4.1.2 In-Plane Magnetization

For the case of the in-plane magnetization, calculations show that the form of the SWMs symmetry is distorted when the direction of spin-wave propagation deviates from the direction of the static field, so we can speak only about quasi-symmetric and quasi-antisymmetric spin waves (opposite to the previous case of the perpendicular magnetization). The most pronounced distortion from the "pure" type of symmetry is exhibited by transverse spin waves, the lowest type of which has a surface-like character of $m_k(\xi)$ (see Figure 34.8a). This "mixed" symmetry is a distinguishing characteristic of spin waves in a tangentially magnetized film. All the waves with mixed form of symmetry demonstrate field-displacement nonreciprocity, i.e., their distributions $m_k(\xi)$ are reversed from one film surface to another with the change of the bias field direction to the opposite one.

Longitudinal spin waves. The dipole-exchange spectrum of longitudinal spin waves ($\theta = 90°$, $\phi = 0°$) is always described by noncrossing dispersion branches. A distinctive feature of the dipole-exchange spectrum is the presence of two zones corresponding to spin waves with negative and positive dispersion. With decreasing film thickness L the minimum value of the spin-wave eigen-frequency at the sag point increases and at some L can completely disappear.

Transverse spin waves. In the Voigt configuration, i.e., when M_0 perpendicular to k_ζ ($\theta = 90°$, $\varphi = 90°$), the dispersion branches in the dipole-exchange spectrum also may cross each other. The brunch repulsions now take place between all modes because of their mixed type of the symmetry. But in thin films, due to the large frequency shift, the repulsions again may not exist at all.

When φ increases the uniform mode transforms for some range of propagation directions into DE surface mode, the amplitude of which varies exponentially across the film. This is accompanied by an increasing in the mode frequency. Thus, DE-modes at some angles φ begins to cross the bulk-type modes (Figure 34.8a) and hybridized with them.

It should be stressed that in general case the behavior of the dispersion branches due to the change of external magnetic field direction is rather complicated and depends strongly on the particular choice of film parameters. So, we shall mention here only some features. If we consider the rotation of the system when $\theta = 90°$, φ is any (Figure 34.8c), the in-plane rotation of the external field causes the transformation of spin-wave spectrum with the negative slope to the positive one.

Another effect is produced by the rotation in vertical plane (θ_0 is changed and φ = constant)—the origins of the dispersion branches move along the frequency axis owing to the variation of the demagnetization factors (see Figure 34.8b). So, now as we consider the rotation in two planes separately, it is possible to imagine qualitatively the reconstruction of the spectrum due to the arbitrary variation of bias field. But these considerations are too general and it is necessary to provide direct calculations to detect all details of the spectrum in each separate case.

34.4.1.3 Influence of the Magnetocrystalline Anisotropy

The experiments [119] showed that the form of dipole-exchange spin-wave spectrum and particularly the width of dipole "gaps" depends significantly on the orientation of the crystallographic axis of the film with respect to the orientation of the bias magnetic field. Later, the theoretical treatments [57,59] revealed that the inclusion of the magnetic anisotropy does not change the number of modes in the dipole-exchange spin-wave spectrum but leads to the uniform frequency shift of the dispersion branches and to the modification of the group velocity of the dipole-exchange spin waves, especially of the lowest branches. Spin waves with negative group velocity arise in the presence of the uniaxial anisotropy, for example. It was shown in Ref. [59] that the sign of the effect (negative or positive slope of dispersion curves) for the volume SWMs in a tangentially magnetized ferromagnetic film is determined by following conditions:

$$N^a_{xx} - N^a_{yy} \neq 0; \quad N^a_{xy} \neq 0 \tag{34.63}$$

In the case when the first condition is fulfilled and the second is not, the sign of the group velocity of these volume waves coincides with the sign of the difference $N^a_{xx} - N^a_{yy}$. When both conditions are fulfilled, the anisotropy leads to the occurrence of two new families of dispersion branches corresponding to positive and negative dispersion.

Moreover, the anisotropy even in a perpendicularly magnetized film can lead to the dependence of the spin-wave eigenfrequency on the angle φ (i.e., on the direction of wave propagation in the film plane) when the ellipticity of polarization of propagating spin waves is broken in the presence of anisotropy. In Ref. [59], one can find the result of numerical calculations of the description spectrum for two types of magnetocrystalline anisotropy (uniaxial and cubic) and the detailed analysis is done there for several particular cases of orientation of the external magnetic field and crystallographic axis relative to the surface plane. In further discussion, we will omit the influence of bulk anisotropy, but it can be easily taken it into account in the framework of the above-declared theory.

34.4.1.4 Surface Anisotropies

Another factor, which can considerably change the spin-wave spectrum, is the presence of surface anisotropies. Surface anisotropies strongly influence the spin-wave frequencies especially for small film thickness and for nonzero wave vectors different surface anisotropies on each side of the film imply changes in the spin-wave frequencies upon the inversion of propagation direction.

The surface anisotropies K_s (or in other words spin-pinning parameters η_1, η_2) influence mostly on the symmetry of SWMs. Different pinning parameters on the two surfaces of the film break the pure

symmetry of modes even in the case of perpendicularly magnetized film thus leading to a repulsion of all crossing branches in the dipole-exchange spin-wave spectrum (opposite to the case when $\eta_1 = \eta_2$ and crossing branches with different symmetry do not interact). The difference of pinning parameters on two sides of the ferromagnetic film can lead to the additional nonreciprocity of spectrum in Voigt configuration.

It should be noted that surface anisotropies may be uniaxial as well as unilateral (nonreciprocal). More complex case when the easy plane is a conical surface with the axis parallel to interface normal is also available.

As one can see, the single-film dipole-exchange spectrum can be rather complex and quite different. Rich variety of the dispersion spectrum arises due to the difference in geometric and magnetic properties of the films under consideration. Since the single-film problem is not a subject of this book for more detailed information, we refer the reader to the classical works of following authors: Kalinokos et al. [42,57–59], Hillebrands [41], Vayhinger and Kronmuller [50,55], and Sparks [56,108], where the peculiarities of a single-film dipole, exchange and dipole-exchange spectrum in ferromagnetic films and single-film structures are described and numerous examples are presented. Also, vast amount of works can be suggested on close themes [51,56,103,108], as well as many excellent reviews [63,140–142].

34.4.2 Magnetic/Nonmagnetic Multilayered Structures

For simplicity and clarity of further narration, we will consider the multilayers composed of very thin magnetic films, in other words the initial layers must be thin enough to form a non-crossing dipole-exchange spectrum (see Figure 34.7b(3)). This assumption is done because the excessive complexity of the initial spectrum will hide the substantial features of interlayer interaction under our consideration. So, we will take the simplest case, which can be easily extended on more complex cases of initial spectrum.

It has to be noted that generally the formation of the dipole-exchange spectrum in any type of the magnetic system goes under the competition between the dipole–dipole interaction, the inhomogeneous exchange interaction, and the influence of magnetocrystalline and surface anisotropy. To elucidate the role of these forces, we consider them acting independently on the initial spectrum and show this process gradually.

The sketches in Figure 34.9 qualitatively illustrate the successive transformation of the spin-wave spectrum of an isolated ferromagnetic film (Figure 34.9a) through the double-layer system (Figure 34.9b through d) to an infinite multilayered structure (Figure 34.9c through e). All the spectra are given for the case of out-of-plane magnetization and without including the influence of magnetocrystalline anisotropy. (As it was mentioned above, we take the spectrum with non-crossing modes, so there is no dipole repulsion of initial branches.)

Figure 34.9a through c show the influence of the interlayer dipole–dipole interaction on the formation of the band of the collective modes, while Figure 34.9a, d, and e series represents the effect of the interlayer exchange interaction (here we consider ferromagnetically coupled magnetic layers $A_{12} > 0$). The influence of these two forces can be shown independently in the assumption that one of them is much greater than the other, and such situations are frequently occur in practice. Let us discuss this phenomenon in detail first considering the multilayered "magnetic/nonmagnetic structure" (according to our classification), since in most experimentally investigated structures the ferromagnetic films are separated by some nonmagnetic spacer.

34.4.2.1 Influence of the Dipole Interlayer Interaction

The basic features of the dipole-exchange modes in superlattices and multilayers are similar to those of SWMs in bilayers, as it was thoroughly analyzed in Refs. [39,41,42,50,54,55]. Thus, let us first consider interaction of two identical ferromagnetic films with the multimode spectrum.

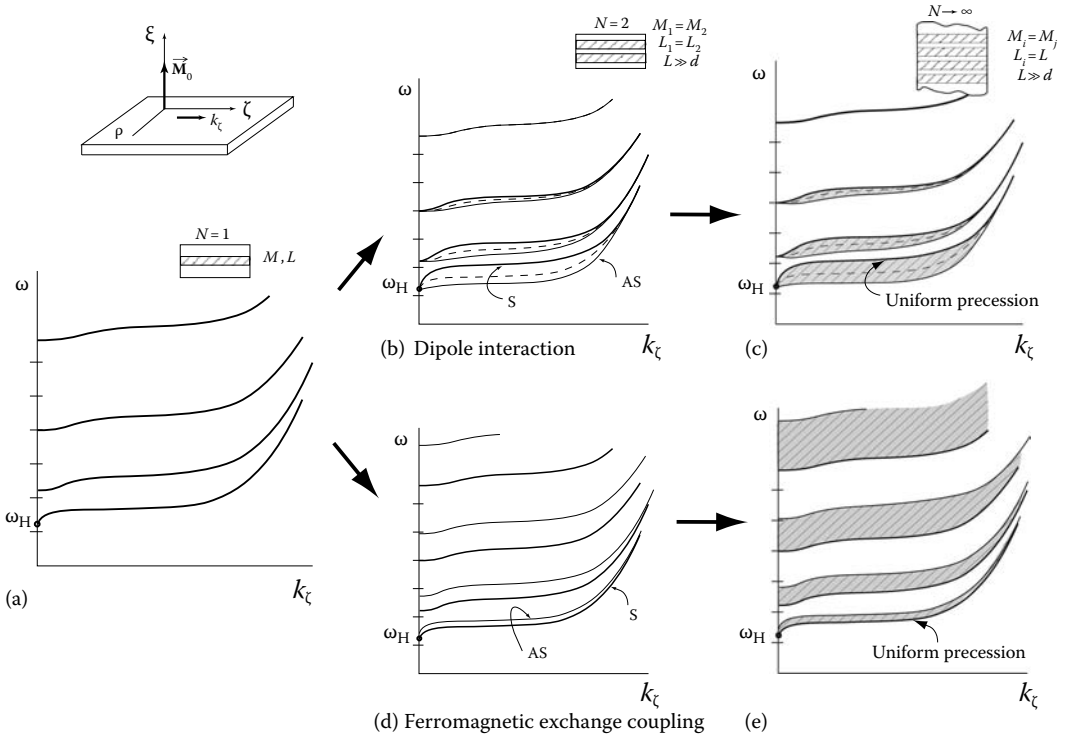

FIGURE 34.9 Qualitative picture for the dipole-exchange spin-wave spectrum formation in multilayered structures starting from single-film spectrum (a) through double-layer coupled modes to the band structure of the collective modes: (b), (c) in the presence of the dipole–dipole interlayer interaction and (d), (e) exchange interlayer interaction only.

The process of the formation of the spin-wave spectrum for the structure of two identical ferromagnetic films separated by a nonmagnetic spacer but coupled via their long-range magnetostatic dipole fields (Figure 34.9b) can be qualitatively described as follows. The precessing magnetic dipoles generate a macroscopic magnetic field with the frequency and wavevector of the spin wave. If there is another film at a distance d, it will couple to the field generated by the propagating mode. The coupling modifies the spectrum of excitations, which now are collective states of both films. This magnetostatic coupling produces two effects: a redistribution of the dynamic magnetization on each element and a corresponding frequency shift of the dispersion curves.

If the structure has very thick spacer, we have a doubly degenerate single film spectrum (Figure 34.9a). While bringing films together the strong dipole interaction arises and, as a result, the degeneracy of initial branches of identical films is lifted (Figure 34.9b). Due to the nature of the dipole interaction, the branch lowest in energy is always that for which the transverse moment at the surface of the adjacent layers is 180° out of phase. Thus, two new characteristic modes appear for each branch of spectrum—"antisymmetric mode (AS)," which has a lower frequency than initial branches and "symmetric mode (S)" with the dispersion branch at higher frequency than that for a single film. This statement remains true for multilayer systems also (Figure 34.9c). Here, we use terms "symmetric" and "antisymmetric" not in the sense of the symmetry of SWMs in separate films (in general case of exchange boundary conditions and in the presence of anisotropy, there are no pure symmetric and antisymmetric single-film solutions), but to outline the symmetry of the final coupled modes,

which can be really symmetric or antisymmetric due to the symmetry of the three-layer sandwich (two identical ferromagnetic layers and nonmagnetic spacer between them, if have a luck).

As the number of magnetic films in the stack increases, the spin-wave spectrum becomes more complicated and in general case one finds as many branches filled in between the symmetric and antisymmetric modes as many ferromagnetic films are contained in the structure. Obviously, due to the interlayer interaction, the dispersion relation in magnetic multilayer systems is significantly modified from that of a single layer one. Finally, for the infinite superlattice, separate modes form a band of bulk modes, which are collective states of the whole stack (Figure 34.9c). The highest branch (the top of the band) corresponds to the symmetric distribution of the variable magnetization in adjacent layers of the structure—"uniform precession" and the lowest one (the bottom of the band) corresponds to the antisymmetric distribution of $\mathbf{m}(\xi)$ in the neighboring layers.

In an infinite stack, the modes for each n form a band governed by the Bloch wave vector $Q = 0 \ldots \pi/T$. The density of states for each band diverges at the band edges and shows the asymmetric energy dependence over the bandwidth. For small k_ζ, the density of states is greatest near the bottom of the band. For larger k_ζ, the density of states becomes more uniform across the band [44].

It should be noted that in the infinite multilayer structures, consisting of equal ultrathin ferromagnetic films separated by equal nonmagnetic spacers, the lowest manifold of energy levels, which develops from the single-film uniform modes, can be described by ignoring higher levels only for relatively weak interlayer coupling. For strong interlayer coupling and/or for film thicknesses at which the level separation is not great enough, one has to include the internal dynamics of the films, i.e., the influence of higher modes should be accounted [41,42,52–54,60].

The strength of the frequency splitting of the initially degenerated modes depends on the distance between films, on the mode number (n) and on the spin-wave wavelength (k_ζ). This dependence becomes clear from the character of the dipolar interaction across the nonmagnetic layer.

The dynamic magnetization induces the stray dipole field outside the magnetic, through which films can interact. The main feature of this field is that it vanishes when k_ζ tends to zero and becomes very weak for large k_ζ ($k_\zeta \geq 10^6$ cm^{-1}). It means that for $k_\zeta = 0$ the degeneracy holds on and the origins of spin-wave dispersion branches of the layered film structure are SWR frequencies of the separate films formed structure. (This is true only if we neglect the interlayer exchange interaction, i.e., $A_{12} = 0$.) Thus, the dipolar collective modes exhibit their unique properties only for small but nonzero wave vectors ($k_\zeta L_i \sim 0.5$). For the case of large k_ζ, the dipole (stray) field is localized near the film surface and, therefore, has small effect on the neighboring films. Moreover, the dynamic dipole field for the higher modes ($n > 1$) is also confined in the ferromagnetic film and the stray field outside it again is very small (see Refs. [54,57,86]). Although the dipole interaction shows the maximum repulsion for the lowest (dipole) modes and becomes negligible for exchange modes with large number n, the exchange-dominated spin-wave branches are also affected by magnetostatic interlayer coupling. This fact is demonstrated in Figure 34.9b. The frequency splitting of all dipole-exchange modes decreases with increasing nonmagnetic spacer d because of a corresponding decrease in the interlayer coupling.

In the case of transverse ($k_\zeta \perp \mathbf{H}_i$), in-plane wave propagation fundamental modes of initial film have quasi-surface nature. So, it is clear that in this case the nonreciprocity of spin-wave dispersion characteristics with the change of the direction of the bias magnetic field will occur. Since the strength of coupling of the initial SWMs depends on the amplitude of the field in the nonmagnetic layers, thus the strongest coupling due to dipolar interactions occurs between the surface waves of individual magnetic films. In the infinite multilayer systems, the surface modes can form a collective "bulk" wave, in which the envelope function over the whole stack is periodic with a significant phase and/or amplitude shift of the magnetic moments from one layer to the other (see Figure 34.10a). The excitations in each magnetic film are surface modes and are localized to one surface of the film. But, the collective modes are oscillatory and therefore form the bulk

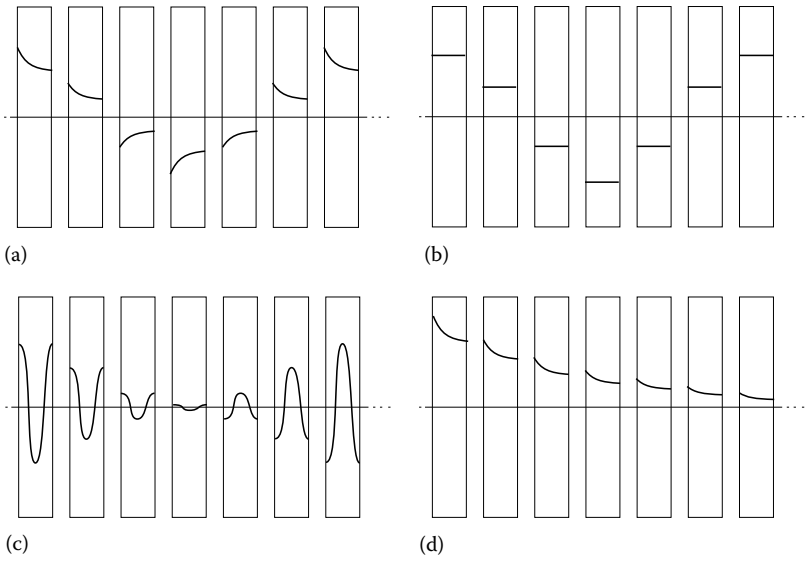

FIGURE 34.10 Transverse distribution of variable magnetization across the structure thickness. (a) Bulk collective modes formed by single-film surface modes; (b) bulk collective modes formed by single-film uniform modes; (c) bulk collective modes formed by single-film exchange-type modes; and (d) surface collective modes formed by single-film surface modes.

modes of a multilayer [44,60]. The collective modes can exist also on semi-infinite superlattices and finite multilayers and can be localized to the outermost layers of a structure as "surface" modes (Figure 34.10d).

For thick magnetic films with $L > 100$ nm, more complex initial spectrum with crossing dispersion curves can occur. In a crossover regime, the dipolar-type modes and exchange-type modes mix their character and the dipole interaction between them leads to a repulsion of initial branches, thus dipole "gaps" are formed. When several films with such complex initial spectrum are brought in contact in the crossover region, a dipole repulsion occurs between different branches of the spectrum. Due to the combined influence of dipolar and exchange energies, splitted dipolar-type modes, which are now intersected and hybridized with exchange-type modes of higher values of n, show a characteristic mode repulsions in crossing points, which lead to a pronounced frequency gap. The calculations of such complex dipole-exchange spectrum for multilayered structures were presented in Refs. [50,54,55].

As it was mentioned above, the value of the dipole gaps depends heavily on the film thickness and interface anisotropy. Although in the thick-layer regime the energetic contribution of the interface anisotropies is very small, the gap width is determined primarily by K_s. For negative values of K_s, the gap width shrinks virtually to zero and then increases for even small values of K_s. For very small magnetic layer thickness ($d < 50$ Å), the interface anisotropy contributions become dominant and the dipolar-type modes exhibit a characteristic increase in frequency, also they become bulk mode-like in each layer, with minor stray fields in the spacer layer, thus their coupling reduces and the spectrum become degenerate. For the exchange-type modes, a weak but significant dependence of their frequencies on the interface anisotropy constants was established [41].

A detailed discussion of the influence of different parameters on the formation of the dipole-exchange spin-wave spectrum for double-layered and multilayered structures plotted for several types of initial single film spectrum can be found in Refs. [41,54,55].

34.4.2.2 Influence of the Exchange Interaction

An important issue is the possible role of interlayer exchange coupling in "magnetic/nonmagnetic" multilayers. The influence of the exchange interaction on the processes in multilayers was extensively studied last decade by means of neutron reflectometry [75,76]. But due to the complex nature of nonlocal exchange interaction, it is difficult to make a direct theoretical calculation of the spectrum of infinite multilayered system. We will try here to predict some evident modifications in the dipole-exchange spectrum, which are caused by the exchange interaction between the adjacent layers, based on some calculations made for the double-layered systems in Refs. [41,50]. In other words, we will simply interpolate these results on the infinite number of layers to build a qualitative picture of the effect under consideration.

Exchange coupling between the films, contrary to dipolar coupling, is very sensitive to the thickness of the spacer, which is almost insensitive in the discussed range of thicknesses (30–60 Å). The nature of the interlayer exchange interaction can be roughly described as follows. The spins at the surface of one ferromagnetic layer, assumed to act as well-localized magnetic moments, produce a magnetic polarization of the conduction electrons of the adjacent nonmagnetic metal. Because of the high degree of delocalization of the conduction electrons, this polarization will propagate with some decay over the thickness of the nonmagnetic layer and will finally interact with the spins at the surface of neighboring ferromagnetic film. The result is an effective coupling between the spins at the surface of two magnetic layers, which, of course, is nonlocal.

For simplicity, we will consider that indirect exchange coupling can be either ferromagnetic or antiferromagnetic and we neglect possible RKKY-oscillations. The exchange coupling constant A_{12} is assumed to be proportional to $\exp(-d/d_0)$ where d is the thickness of the nonmagnetic spacer and d_0 is the characteristic decay length ($d_0 = 10$ Å), i.e., the Ornstein–Zernicke form of the exchange integral is taken here [41,50]. Thus for $d > 60$ Å, the interlayer exchange will be negligible.

In Figure 34.9d, we sketch the dispersion curves for the double-layer structure, in which the exchange interlayer interactions prevail over the dipole interaction between films. One can see that due to the exchange interaction, the initial degeneracy is lifted for all modes. But, now the mode with lower energy corresponds to the magnetization vectors resonating in-phase in different films. (We suppose here the interlayer exchange interaction of ferromagnetic type.) This dispersion branch is the same as the uniform mode of a single layer system. This is due to the fact that the exchange energy does not produce any dynamic contribution to the resonance condition. For the higher mode, now resonating out-of phase, the exchange energy introduces an extra field to the dispersion relation. Here, as everywhere before the interlayer exchange coupling constant $A_{12} > 0$ for ferromagnetic coupling between the adjacent layers and $A_{12} < 0$ for antiferromagnetic coupling. So, if the two ferromagnetic layers are parallel coupled, the exchange energy increases as the magnetization vectors deviate from the parallel orientation and therefore the antisymmetric mode is observed at the higher frequency than the symmetric one. But if antiferromagnetic coupling arises, the antisymmetric mode shifts to the lower frequency region and the uniform mode again stay unchanged.

Also, we assume here that the magnetization $\mathbf{M}_0$ in both layers is still aligned parallel by strong external field $\mathbf{H}^{\text{ext}}$ and in any case out-of-phase coupling yields a modification in frequency while the in-phase coupling does not.

It is interesting to follow the transformations of the form of the transverse dynamic magnetization profiles, with increasing of the interlayer exchange coupling. In Figure 34.11, we present the smooth transition from double-layer system to the film of double thickness (for $k_\zeta = 0$ and in the case of unpinned). These qualitative sketches illustrate the transformation of the transverse magnetization profiles under the influence of growing interlayer exchange constant A_{12} (which is equivalent to the reducing of interlayer spacer, as we assume the exponential dependence of A_{12} from d). Thus, reducing the interlayer spacer, we increase the value of A_{12} till it becomes equal to the bulk exchange constant A—this is the condition of the full contact of coupling films. For the infinite layered system

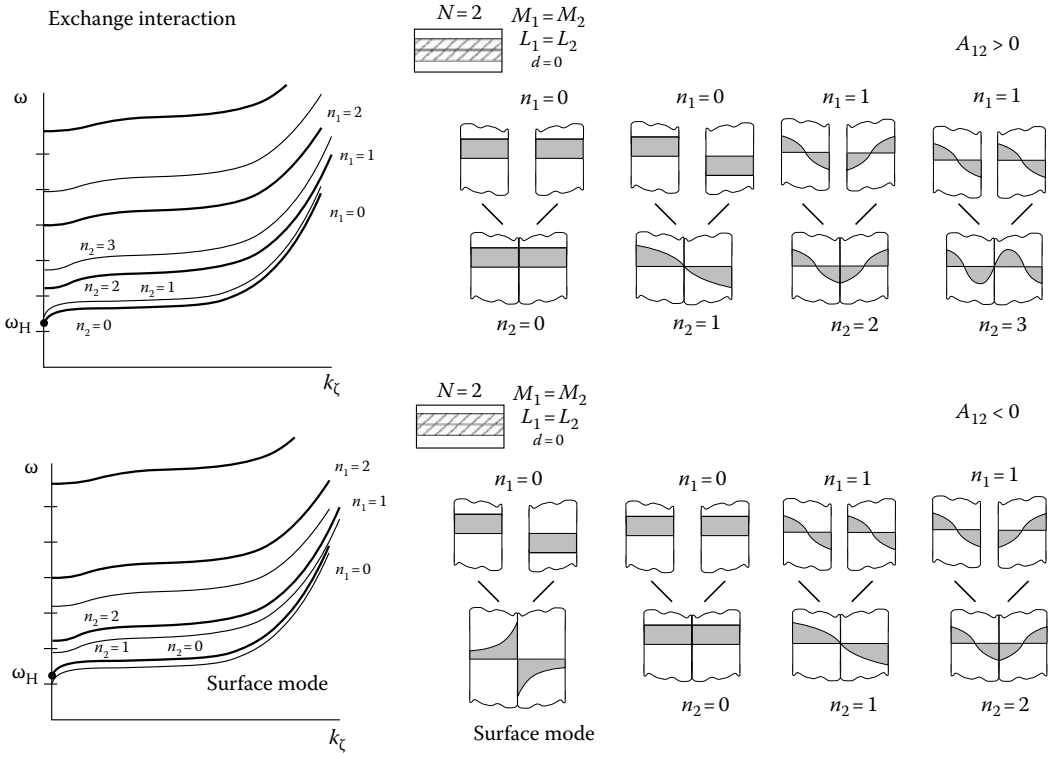

FIGURE 34.11 Dispersion of the low-lying modes of double-layer system for two types of the interlayer exchange interaction: ferromagnetic $A_{12} > 0$ and antiferromagnetic $A_{12} < 0$.

in the limit $A_{12} = A$ (and $d = 0$), the stack becomes simply equivalent to an infinite homogeneous system. The gaps between the bands vanish and we arrive to the spectrum of a continuous ferromagnetic material.

As we see from Figure 34.11 for double-layer system, when $k_\zeta = 0$, there are the symmetric-like solutions which are almost eigenvalues for standing spin waves in a single film of thickness L and in addition there appear the antisymmetric-like modes, which are energetically higher because the ferromagnetic exchange coupling favors a parallel alignment of the spins at the two inner surfaces of the magnetic layers relative to each other. Therefore, the spin-wave magnetization $|\mathbf{m}(\mathbf{k}, \xi)|$ is reduced toward these surfaces, causing an increase in bulk exchange energy. We use here the names "symmetric-like" and "antisymmetric-like" since the symmetry is slightly broken by the presence of the dipolar interaction. Going from infinite separation ($d \to \infty$) to vanishing distance ($d \to 0$) between the magnetic films (which is equivalent to the increase of A_{12}), we find a smooth transition from the standing spin wave of a single film of thickness L to that of combined film of thickness $2L$. Such smooth transition can be achieved only if the interlayer exchange interaction is taken into account. In the case when we take only the dipole–dipole interlayer interaction and neglect the exchange interaction (i.e., we use Rado–Weertman boundary conditions instead of Hoffman ones), a transition from single-film solutions to the double-thick ones is impossible.

Simultaneously, as A_{12} increases (with decreasing d), the degeneracy of initially uncoupled modes is lifted and the antisymmetric-like modes shift up on the energy scale and finally converge to the frequencies of the odd exchange modes of the layer of double thickness. Thus, in the full coupling limit, i.e., when the interlayer coupling A_{12} becomes equal to that inside the films A, the bilayer becomes

equivalent to a single homogeneous film with doubled thickness. The symmetric-like modes, on the other hand, are insensitive to the interlayer coupling. This behavior is the consequence of the fact that symmetric-like modes in such bilayer are continuous at the interface and the antisymmetric-like modes have discontinuous profiles at the interface and thus are strongly affected by the interlayer coupling. We mention here that in the absence of interlayer exchange coupling the discontinuity of the transverse magnetization at the interface is much larger for exchange modes than for the dipolar mode, thus the splitting of the higher modes is much larger (Figure 34.9d).

It should be noted that the nonlocal exchange interaction integrates over the region of order of penetration depth, and if the spin-wave wavelength in the film plane is much smaller than this region the averaging will have an annihilating effect so for large k_ζ the effect of exchange coupling became much smaller and reduces to the effect, which is equivalent to a strong surface spin pinning.

The splitting of the spin-wave branches depends on the indirect exchange coupling constant and the penetration depth. Both of these parameters depend on the choice of the nonmagnetic metal and on the quality of the interfaces between the magnetic and nonmagnetic layers. Generally, the dependence of the value of splitting on both parameters shows saturation behavior. Obviously, in the wavevector region $k_\zeta > 0$, the dipolar fields will also have a strong influence on the final spectrum. But the exchange interaction still plays the crucial role in the limit of $d \to 0$.

Due to the interlayer exchange coupling, the dispersion relation in magnetic multilayer systems is significantly modified from that of a single layer system. Besides the uniform mode observed (or the acoustic mode) in a single layer system, there also exist a number of exchange coupled bulk modes in multilayer structures each of which corresponds to a nearly uniform precession within each magnetic layer but a significant phase and/or amplitude shift of the magnetic moment from one layer to the other (see Figure 34.10b).

For weakly coupled systems, the first-order bulk mode ($n = 1$) is the dominant mode, while for strongly coupled systems, the surface mode normally has the larger intensity in the FMR spectra (in perpendicularly magnetized structures). In the infinite multilayered systems, the initially degenerate single-film modes split into bands due to the interlayer exchange interaction. The bottom of the band has the same frequency as the degenerate mode and the top shifts to the even numbered modes of the film of sum thickness of all layers (Figure 34.9e) for the case of ferromagnetic coupling.

For the case of "antiferromagnetic coupling" ($A_{12} < 0$), the antiparallel alignment of the magnetic moments at the inner surfaces of the two adjacent layers is favored. If we assume that the magnetization M_0 in layers is still aligned parallel by a strong external field, the symmetric modes are still unchanged, but now the antisymmetric SWMs are lowered in energy (see Figure 34.11). In the case of Voigt configuration, the lowest branches have a surface character, different from all other modes. They form damped waves in ξ direction with complex wave vector. The lowest (surface) branch appears only for filling factor $f > 0.8$.

In the structures of alternating ferromagnetic/nonmagnetic layers with antiparallel alignment of the films magnetization, the most interesting feature in the Voigt configuration is the nonreciprocity of the spin-wave spectrum. For the symmetrical bilayers with parallel (ferromagnetic) coupling, the wave spectrum is reciprocal, but for similar bilayers with antiparallel alignment of the film magnetizations, the corresponding spin-wave spectrum is nonreciprocal. In Figure 34.12, the two lowest modes of an exchange-coupled bilayer are shown versus the interlayer exchange constant for two opposite wave vectors k_ζ. The discontinuity of the wave spectrum at $A_{12} = 0$ results from the change of the ground state configuration from parallel at $A_{12} > 0$ to antiparallel at $A_{12} < 0$.

This effect can be observed for DE-modes in the symmetric multilayered structures with antiferromagnetic exchange coupling, as well as for all modes in the structures with asymmetric unit cell. The nonreciprocity is a simple consequence of some asymmetry in the wave propagation. The modes of given wavevector are localized, say, at the internal surfaces, whereas the modes with opposite wavevectors propagate on external surfaces of the bilayer. Because of the lack of rotational symmetry, the appropriate spin-wave spectrum is nonreciprocal even if the structure is symmetric but displays

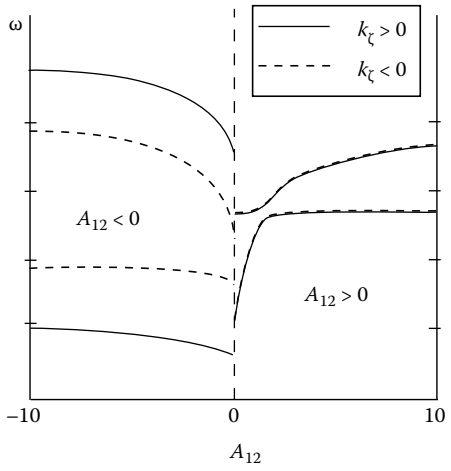

FIGURE 34.12 Two lowest modes of an exchange-coupled bilayer vs. the interlayer exchange constant for $k_\zeta > 0$ (full lines) and for $k_\zeta < 0$ (dash lines).

antiferromagnetic interlayer exchange coupling. In this case, the nonreciprocity also occurs for all multilayers containing a finite number of complete elementary bilayers. For a structure with the last unit incomplete, rotational symmetry is restored and the spectrum becomes reciprocal.

One can find a lot of interesting effects in multilayered structures simply changing the parameters of this periodic spacer, for example, in quasiperiodic layered structures. Quasiperiodic systems, like Fibonacci sequences, are intermediate between completely periodic and completely random systems. They have a particularly interesting excitation spectrum in the form of a Cantor set [65,143,144].

34.4.3 Magnetic/Magnetic Multilayered Structures

In the case of magnetic/magnetic structures, all above-mentioned interlayer coupling mechanisms act in the same way but due to the difference of the initial single film spectrum there are some pecularities.

It is useful to consider first the structure consisting of two ferromagnetic films with different parameters. Here, two principal situations are possible. First, the initial dispersion branches of ferromagnetic films-formed layered structure do not cross each other. For such non-symmetrical double-layer, there is no degeneracy of initial dispersion branches (except an accidental one) and consequently no level splitting occurs. In this case, the dipole and exchange interaction between ferromagnetic films causes only the variation of the shape of dispersion branches. Second, the initial spectra of ferromagnetic films-formed layered structure cross each other. In this case, the dipole interaction in crosspoints causes the repulsion of spin-wave dispersion branches and the exchange interaction leads to the additional increase in frequency for repulsing branches. This repulsion leads to the appearance of dipole "gaps" in spin-wave spectrum, similarly, as it was discussed in the single-film case. The width of these gaps depends on the parameters of the structure and the symmetry of interacting SWMs [54]. In both cases, the arisen modes are neither even nor odd. Consequently, all modes depend on the interlayer coupling, contrary to the symmetrical bilayer when the even modes are insensitive to the interlayer coupling.

Let us consider now "magnetic/magnetic multilayered system" consisting of the unit cells composed of two magnetic films with different magnetic properties. The infinite number of such unit cells form the periodic structure with a period $T = L_1 + L_2$. Different magnetic parameters can be

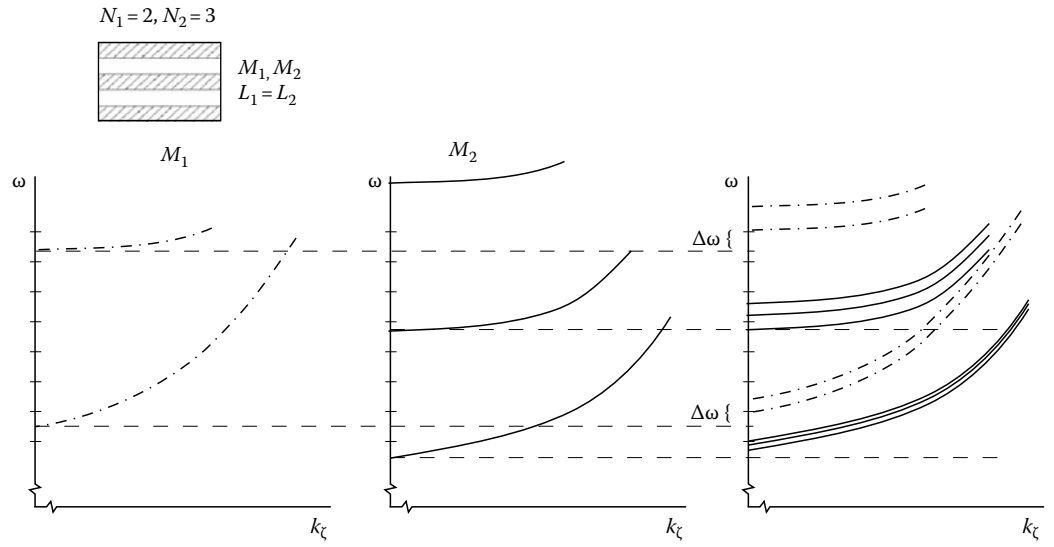

FIGURE 34.13 Qualitative illustration of the formation of coupled modes in five-layered structure under the influence of the interlayer exchange interaction.

altered in such structures: saturation magnetization, *g* factor, interface anisotropies, etc. The SWMs of each magnetic layer in this structure are coupled to those of adjacent layers both by the dipolar coupling mechanism as well by interlayer exchange. The strong coupling between the different magnetic layers via an indirect exchange mechanism leads to the splitting of the initially degenerate modes (even at $k_\zeta = 0$). In the limit of an infinite number of layers, the multilayered structure gains new properties as a metamaterial, and the eigen states form a band of the collective SWMs. The frequency splitting of dipole-exchange modes again strongly depends on the interlayer exchange constant A_{12}, but now with increasing interlayer exchange the modes of one magnetic material show strong mode repulsion from the other material's modes. This increases the frequencies of the first material much more than the frequency splitting due to the lift of degeneracy does (see Figure 34.13). For the lowest modes, we have the same situation as in previous case. There are two initially degenerate dipolar-type modes corresponding to different magnetic materials, which are splits to a band for $A_{12} \neq 0$. But for semi-infinite structure in Voigt configuration, we will have also one dipolar stack surface mode, which is insensitive to exchange.

The main peculiarities of spectrum formation of two-magnetic structure can be easily observed in Figure 34.13. Here, we present the qualitative picture of the spectrum formation in a five-layer stack. Two layers of ferromagnetic material M_1 and three layers made of material with M_2. Two groups of dispersion curves can be related with sublattices M_1 and M_2. It is well seen that except splitting of initial modes the dispersion curves of the material M_1 are shifted up from the initial state due to the interlayer exchange interaction (if the interlayer exchange interaction assumed to be ferromagnetic-type).

It should be noted that when the structure is rotated relative to the direction of the external magnetic field, the origins of the dispersion branches are moving along the frequency axis owing to the variation of the demagnetization factors. If we consider the rotation when $\varphi = 90°$ and θ_0 is any, the origins of the dispersion branches of different films moved to each other due to the different demagnetization fields of the films. So, there are such values of θ_0 when the origins of the different modes coincide. These values θ_0 depend on the structure parameters and on the number of dispersion branches.

34.4.4 Formation of Band Structure in Multilayers

In the periodic structures (or in superlattice), the additional translational symmetry in the direction of periodicity causes the significant changes in the dispersion characteristics [145]. New periodicity induces the formation of Brillouin zones in energy spectrum of the magnetic structure [16], stop and allowed bands appear (see below Figure 34.18a).

From the critical value of filling factor f_c, any periodic structure transforms to a new type of the material (metamaterial or artificial material), i.e., the composed structures exhibit new features and form a new band structure different from that of single components. This is the common feature for all periodic structures and superlattices [14], photonic [146–152], phononic [153], sonic [137], magnonic crystals [5,6,9,20], etc.

Such new hand structure usually is built applying the Bloch function formalism. However, the spectrum band structure comprised of Brillouin zones appears usually for media, where the direction of periodicity coincides with the direction of eigen excitations progagation. In multilayers, such new band structures exist in the direction perpendicular to the usual in-plane wave propagation; therefore, the new behavior of the system should be investigated mostly through the modifications in general dipole-exchange spin-wave spectrum, although thermal spin waves can be excited in any direction. Here, we note that even in 1D-structures (like multilayers), the new band structure undoubtedly exists in the direction of periodicity and we can calculate it using the common Bloch function approach. The opposite situation appears in patterned structures where the direction of the spin-wave propagation and the direction of periodicity coincide and below we consider the spectrum formation in such structures.

The above given qualitative illustration of some features of the formation of the spin-wave spectrum elucidates the general role of interlayer exchange and dipole interactions, but it only briefly outlines the main problems in this field. Obviously, more sophisticated analysis required in each special case.

34.5 Planar Patterned Metamaterials

The physics of nano-patterned magnetic structures has driven extensive research in recent years, both static and dynamic behavior having been investigated. The applied aspect of these studies should not be underestimated, either. A rapid increase of processor speeds in modern computers has led to the necessity of writing gigabits of information in a fraction of a second. The latter means that the magnetic system is excited at gigahertz rates and the inevitable generation of spin waves will strongly influence the response of magnetic recording media. With this respect, it is necessary to prevent the mutual influence of adjacent magnetic elements through inevitable coupling via dynamic dipolar magnetic fields of individual elements. The key parameter governing such coupling is the spatial separation of elements. To minimize the overall size of the structure, it must be kept as small as possible. On the other hand, if the elements are brought too close together, spurious "collective" magnetostatic modes will be excited through this increased coupling. In the case of nanodots, where the fundamental magnetic state corresponds to a vortex configuration, this leads to a considerable mutual influence between the dots during the magnetization reversal [154], as well as to a magnetostatic coupling [155] between the dynamic modes of individual vortices [156]. Similarly, in the case of nanowires of cylindrical cross section, both in theory [40] and in experiment [134], collective modes, due to the interplay between individual wires, were reported.

On the other hand, the coupling between individual magnetic elements can be used to advantage in magnonic structures on the basis of patterned YIG films [8,9]. In this case, it plays a positive role and is instrumental in the formation of collective purely magnetostatic modes in such low-loss structures. By appropriately choosing the patterning geometry, one can realize tailor-made dispersion characteristics, which are extremely important for the applications in microwave signal processing.

To investigate the main properties of the confined objects, two different cases are discussed here in details. We consider a multilayered stripe (vertical architecture) to clear up the role of interlayer dipole and exchange interaction in the confined systems and their role in the formation of the coupled standing-wave modes. Then, in order to study the basic properties of the collective SWMs on a periodic nanostructure, we have restricted our analysis to an ideal model object: a 1D array of ferromagnetic stripes (horizontal architecture). Thus, simple and efficient numerical procedures can be developed, backed by analytical expressions providing for more physical insight. Special attention will be paid to a transition from individual modes localized on separate stripes to collective modes existing on arrays of stripes coupled by the long-range dipole interaction. The latter are described by Bloch type solutions and demonstrate the features characteristic of wave processes in periodic media, such as formation of stop bands and Brillouin zones.

34.5.1 Direct Space Green's Function

The long-range dipole interaction is instrumental in the formation of collective modes on arrays of ferromagnetic objects. Besides, its role is of primary importance in the description of the behavior of the modes existing within each individual stripe, especially in the most interesting case of the fundamental mode. Since the translational symmetry is no longer observed in a patterned film along the patterning direction, the Fourier space Green's function proposed in previous sections is to be redefined in the direct space, as it has been proposed by Guslienko et al. [62].

To construct the Green's function in the confined system, we start with the simplest geometry of a monolayer film confined in one direction (Figure 34.14). We again assume the Green's function as a relation between dipole magnetic field and the dynamic magnetization:

$$\mathbf{h}(k,x,z) = \int_0^L \mathrm{d}z' \int_0^w \mathrm{d}x' \underline{\mathbf{G}}(k,x,x',z,z')\mathbf{m}(x',z') \tag{34.64}$$

But to distinguish $\mathfrak{g}$ this one from those introduced in previous sections, we will call Green's function (Equation 34.64) "direct space" Green's function. Here, we use the fact that the element is infinite in y-direction and that the distribution of the magnetization along y can be represented in the form of a propagating plane wave. In other words, from Maxwell's equations in magnetostatic limit, we now seek a "mixed" Green's function, which is direct-space along x and of Fourier type in the y direction.

In practical calculations, we use the fact that the "aspect ratio" of the element is small $p = L/w \ll 1$, which makes the dependence of the dipole field and the dynamic magnetization on z irrelevant, i.e., the element thickness L is small enough in order to push the first exchange mode out of the range of existence of the lowest, the so-called "magnetostatic," mode. The latter allows one to reduce the initial 2D problem to a 1D problem by averaging Equation 34.64 across the film thickness L, since we assume

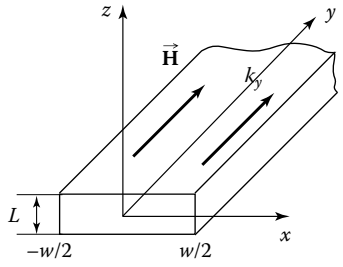

FIGURE 34.14 Single-stripe geometry.

that the spins on the upper ($z = L$) and lower ($z = 0$) surfaces of the element are unpinned, which is well confirmed by the BLS measurements of spin-wave spectra in patterned metallic magnetic films [157]. Such an approach for the patterned structure was first suggested in Ref. [62].

If we take now $k = 0$, then we arrive to the Green's function first obtained by Guslienko et al. in order to describe transverse spin-wave resonances in thin metallic magnetic stripes [62]:

$$G_{0_{\alpha,\beta}}(\mathbf{r},\mathbf{r}') = -\frac{1}{4\pi}\frac{\partial}{\partial\alpha}\frac{\partial}{\partial\beta'}\frac{1}{|\mathbf{r}-\mathbf{r}'|} \tag{34.65}$$

where $\alpha, \beta = x, y, z$.

Applying Equation 34.64 to Equation 34.65, one arrives at a 1D tensorial Green's function described by a 3×3 matrix with the following nonzero elements:

$$\begin{aligned}
G_{zzk}(x-x') &= -\int_0^\infty \left(\frac{1}{a}-\frac{1}{b}\right)\frac{\cos(ky)}{\pi L}\mathrm{d}y,\\
G_{xxk}(x-x') &= -\int_0^\infty \frac{1}{b^4}\left[y^2(a-b)-\frac{p^2(x-x')^2}{a}\right]\frac{\cos(ky)}{\pi L}\mathrm{d}y-\delta(x-x')\\
G_{yyk}(x-x') &= -\delta(x-x')-G_{xxk}(x-x')-G_{zzk}(x-x')\\
G_{yxk}(x-x') &= -G_{xyk}(x-x') = -\int_0^\infty \frac{2j}{b^2}\left[b-a-\frac{L^2}{a}\right]y(x-x')\frac{\sin(ky)}{\pi L}\mathrm{d}y
\end{aligned} \tag{34.66}$$

where $b = \sqrt{(x-x')^2+y^2}$, $a = \sqrt{b^2+L^2}$, and $\delta(x-x')$ is the Dirac delta function. All other components of Green's function vanish. Physically, the expressions (Equation 34.66) describe an average dipole field of a stripe, placed at the point x'. The stripe is infinitesimally thin in the direction x, infinitely long in the direction y, and has a width L in the direction z. The average dipole field strength is "measured" at the point x at any z between 0 and L. In particular, for $w = \infty$ and m independent from x, Equation 34.64, averaged across the film thickness L, reduces to the dipole element P_{00} used in the previous chapters.

34.5.2 Coupled Standing-Wave Modes on a Multilayer Stripe

Exchange coupled multilayers, characterized by the effect of giant magneto-resistance, are of particular interest, both for fundamental science and technology. That is why they are extensively investigated, theoretically and experimentally, due to their numerous important applications to information storage and processing.

To study the basic properties of coupled standing-wave modes in multilayered stripe, let us consider the geometry given in Figure 34.15, where N ferromagnetic layers of different thickness L_i are placed parallel at a distance d_i from each other. The external magnetic field assumed to be directed along y-axis. In this case, coupled modes of the structure should be described by a system of N linearized Landau–Lifshitz equations, where long-range dipole interaction between all the layers is taken into account:

$$\sum_\beta A^{(i)}_{\alpha\beta}(\omega)m^{(i)}_\beta(x) = \sum_\beta\sum_{j=1}^{N} G^{(ij)}_{\alpha\beta}(x,x')\otimes m^{(j)}_\beta(x') \tag{34.67}$$

In this equations, $\otimes$ sign denotes convolution in the sense of Equation 34.64 but already averaged over z, $\omega_H = |g|\mu_0 H$ and $\omega_M = |g|\,\mu_0 M_s$, as in previous sections, and

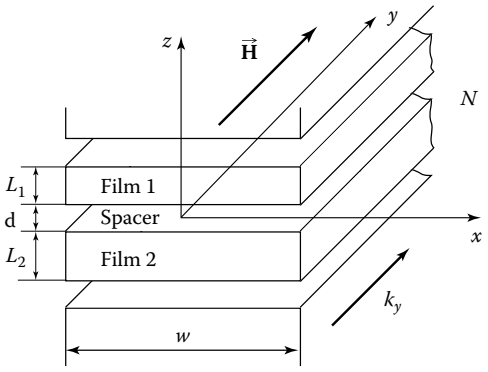

FIGURE 34.15 Multilayered magnetic stripe geometry.

$$A^{(i)}_{\alpha\beta}(\omega) = \begin{vmatrix} \dfrac{\omega_H}{\omega^{(i)}_M} & j\dfrac{\omega}{\omega^{(i)}_M} \\ -j\dfrac{\omega}{\omega^{(i)}_M} & \dfrac{\omega_H}{\omega^{(i)}_M} \end{vmatrix}$$

Greek characters here correspond to two coordinates, i.e., $\alpha = x, z$ and $\beta = x, z$. The summing over j implies taking into account the dipole contribution of all N ferromagnetic layers to the field in layer "i." Green's functions $G^{(ij)}_{\alpha\beta}(x, x')$ includes the diagonal elements, describing the intralayer dipole fields for $i = j$, as well as the interlayer dipole interaction when $i \neq j$.

If we restrict our analysis to a simple case of a ferromagnetic bilayer which consists of two layers with thicknesses L_1 and L_2, which are placed at a distance d in the direction z, the tensorial Green's functions for intralayer dipole fields can be taken in form (Equation 34.66) and the components of Green's function describing the dipole coupling between layers, which are first derived in Ref. [158], have the following form:

$$\begin{aligned} L_1 G^{(12)}_{xx}(x-x') &= L_2 G^{(21)}_{xx}(x-x') = -L_1 G^{(12)}_{zz} = -L_2 G^{(21)}_{zz}(x-x') \\ &= -\ln \frac{[(d+L_1)^2 + (x-x')^2][(d+L_2)^2 + (x-x')^2]}{[d^2 + (x-x')^2][(d+L_1+L_2)^2 + (x-x')^2]} \end{aligned}$$

$$\begin{aligned} L_1 G^{(12)}_{xz}(x-x') &= -L_1 G^{(12)}_{zx}(x-x') = -L_2 G^{(21)}_{xz}(x-x') = L_2 G^{(21)}_{zx}(x-x') \\ &= 2\left(\operatorname{atan}\frac{d+L_1+L_2}{x-x'} - \operatorname{atan}\frac{d+L_1}{x-x'} - \operatorname{atan}\frac{d+L_2}{x-x'} + \operatorname{atan}\frac{d}{x-x'}\right) \end{aligned} \tag{34.68}$$

Here, $G^{(ij)}_{\alpha\beta}$ describes the α-component of the dipole field in the ith layer, which is induced by the β-component of the magnetization profile in the jth layer. The dipole field is averaged across the thickness of ith layer and the dynamic magnetization in both layers is assumed to be homogeneous along z and y, thus $k = 0$.

It should be noted that all nonvanishing components of Green's function (Equation 34.66) for $k = 0$ are symmetric with respect to $x - x'$. This results in a set of eigenmodes which consists of purely symmetric $\mathbf{m}(x) = \mathbf{m}(-x)$ and purely antisymmetric $\mathbf{m}(x) = -\mathbf{m}(-x)$ resonances [62]. As one sees from Equation 34.68, the diagonal components $G^{(ij)}_{xx}$ and $G^{(ij)}_{zz}$ $(i, j = 1, 2; i \neq j)$ are also symmetric. Thus, they should preserve the symmetry of the eigenmodes, when two monolayer stripes become coupled by the magnetostatic interaction. However, the anti-diagonal component $G^{(ij)}_{xz}(s)$ is

antisymmetric in $x - x'$. This should result, in the general case, in a break of symmetry; an admixture of an antisymmetric contribution to previously symmetric eigenmodes and vice versa, when two monolayer stripes become coupled.

Hopefully, the calculation shows that the symmetry maintaining contribution of the components of Green's function (Equation 34.68) prevails mix-symmetry ones for the whole range of mode numbers n. To estimate these contributions to the overall magnetostatic field penetrating from one stripe into another, we involve matrix elements:

$$P_{\alpha\alpha}^{ij}(n) = \frac{1}{w}\int_{-w/2}^{w/2} \sin\left(\frac{2\pi x}{w}\right) dx \int_{-w/2}^{w/2} G_{\alpha\alpha}^{(ij)}(x-x') \sin\left(\frac{2\pi x'}{w}\right) dx'$$

$$Q_{\alpha\beta}^{ij}(n) = \frac{1}{w}\int_{-w/2}^{w/2} \cos\left(\frac{2\pi x}{w}\right) dx \int_{-w/2}^{w/2} G_{\alpha\beta}^{(ij)}(x-x') \sin\left(\frac{2\pi x'}{w}\right) dx' \tag{34.69}$$

$P_{\alpha\alpha}^{ij}(n)$ gives the contribution of the diagonal components to the magnetostatic energy of antisymmetric modes of the initially uncoupled stripes due to coupling. $Q_{\alpha\beta}^{ij}(n)$ gives the contribution to the energy due to admixture of symmetric states to the previously antisymmetric resonances. This fact allows us to neglect the anti-diagonal components of Green's function (Equation 34.68) in the equations for the magnetization dynamics and to obtain simple equations describing resonances in symmetric structures.

Neglecting the anti-diagonal components of the Green's function, we arrive to purely symmetric and purely antisymmetric solutions. This allows one to reduce the number of equations. Assuming the solutions $m_{xs}(x) = \varepsilon_s m_{zs}(x)$, $m_{xa}(x) = \varepsilon_a m_{za}(x)$, one obtains from the Landau–Lifshitz equation of motion two identical algebraic equations for the frequencies of the symmetric and asymmetric modes:

$$\left(\frac{\omega_{ns(a)}}{\omega_M}\right)^2 = \left(\frac{\omega_H}{\omega_M} + 1 + \lambda_{ns(a)}\right)\left(\frac{\omega_H}{\omega_M} - \lambda_{ns(a)}\right) \tag{34.70}$$

where $\lambda_{ns(a)}$ is the n th solution of the eigenvalue problem:

$$\lambda_{s(a)} m(x) = \int_{w/2}^{w/2} G_{zz}^{s(a)}(x-x') m(x') dx' \tag{34.71}$$

And the coefficients ε_s and ε_a represent the ellipticity of magnetization precession in the symmetric and antisymmetric modes, respectively.

Figure 34.16 shows the results of a numerical solution of Equation 34.70 with Equation 34.71 for a symmetric bilayer stripe with the thickness $L_1 = L_2 = L = 20$ nm and width $w = 1500$ nm, and the distance between magnetic layers $d = 3$ nm. Their saturation magnetization for each stripe ($4\pi M_s$) is 17 kg. The magnetic field applied along the stripe is 1000 Oe. One clearly sees that the frequencies of antisymmetric resonances are smaller than those of symmetric ones. The physical reason for such behavior is as follows. Let us consider the in-plane component of the dynamic magnetization m_x in a symmetric bilayer stripe $L_1 = L_2$. We see that for small thicknesses of the nonmagnetic spacer, the dipole field of the symmetric (acoustic) mode on a bilayer stripe is close to that of a monolayer stripe of double thickness $2L_1$. A larger thickness means a larger aspect ratio p and a larger effective magnetic charge at the lateral stripe edges $x = \pm w/2$. Furthermore, the magnetostatic field of the first layer penetrating the second layer (see Equation 34.68) is contra-directed with respect to the dynamic magnetization in it. Therefore, the magnetostatic energy of the symmetric mode and thus its frequency should be larger than those of the mode with the same number on a monolayer stripe with thickness L_1.

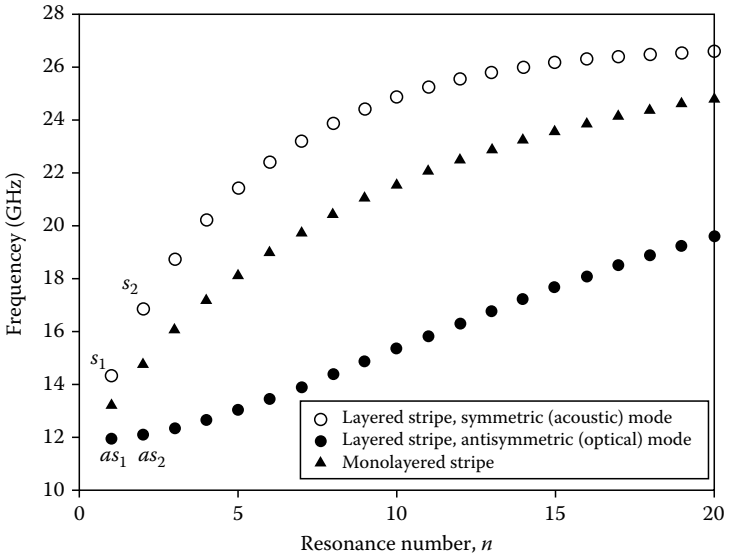

FIGURE 34.16 Spectrum of resonances on a symmetric tri-layered structure, calculated numerically. The open circles show the symmetric (acoustical) resonances (curve 1) and the filled ones show antisymmetric (optical) ones (curve 2). For comparison, the spectrum of a monolayer stripe of the same thickness is also shown in the figure.

Now let us consider an antisymmetric mode. The m_x component is of opposite direction in the layers in this case. It creates effective charges of opposite sign at the edges of layers. The dipole field of a layer penetrating another layer of the structure is now of the same direction with the dynamic magnetization in this layer which decreases the overall magnetostatic energy compared to the case of noninteracting layers. Therefore, the frequency of the antisymmetric (optical) mode on the bilayer stripe should be smaller than that of the monolayer stripe with the thickness L_1. Thus, our considerations show that the frequency of the symmetric mode should be higher than that of the antisymmetric mode, as one sees from Figure 34.16.

Obviously, Figure 34.16 can be regarded as a dispersion curve, ω as a function of a wave number k_x, whose values are quantized $n\Delta k_x$ $(0 < n < \infty)$ due to the finite width of the stripe. In the limit case of an infinite film $p = 0$, when w tends to infinity, the wave number step Δk_x becomes infinitesimal thus transforming the dependence $\omega\,(n\Delta k_x)$, otherwise discrete into a continuous curve. Note that the "curvature" of this dispersion curve varies with the aspect ratio p, since the ratio of the cross-section area of the edge zones (of order L^2), where the effective magnetic charges deform the originally sinusoidal wave profile, to the overall layer cross-section area $L \cdot w$ varies with p.

In Refs. [125,127], the theory outlined above was verified by experiments on BLS of light by thermal magnons. The experimental results are in a good agreement with the theory.

34.5.3 Role of the Interlayer Exchange Interaction

It can be showed that the main effect of the interlayer exchange interaction between the layers of a metallic magnetic bilayer film is a substantial inhomogeneity of the profile of the dynamic magnetization along the z direction. The inhomogeneity results in a noticeable contribution of intra-layer exchange stiffness to the effective magnetic field of layers. The main manifestation of this is a shift of spin-wave dispersion branches, as a whole, to higher or lower frequencies depending on the sign of the constant of the interlayer exchange interaction. For weakly exchange-coupled layers, the

inhomogeneity of the z -profile of dynamic magnetization is strong enough to produce a noticeable exchange frequency shift, but still small to introduce a significant variation of the structure of the dynamic dipole field within the interacting layers. If so, any in-plane inhomogeneous spin-wave oscillation will have the same exchange frequency shift as the in-plane homogeneous precession. Then, the frequency shift due to the interlayer exchange coupling may be introduced directly into final expressions for spin-wave dynamics using the substitution $H \to H + \alpha M_s k_z^2$, where k_z is obtained from solution of the boundary-value problem for the exchange-field operator with Hoffmann interlayer exchange boundary conditions [53]. In this expression, H is the internal static magnetic field, M_s is the saturation magnetization, and α is the exchange constant of layers (assumed to be the same in all layers).

This simplified approach proved to be efficient for the description of real in plane confined multilayer structures [126].

34.5.4 Formation of Collective Modes and Brillouin Zones

In this part, we analyze the "horizontal geometry": formation of collective Bloch modes on an infinite array of monolayers. The latter is rich in interesting physical phenomena, such as creation of stop-bands and Brillouin zones, typical of periodic magnonic structures.

Let us consider an infinite array extending in the direction x consisting of parallel dipole-coupled magnetic stripes (Figure 34.17). The dipole field in each particular stripe is a sum of the fields induced by dynamic magnetizations in all other stripes:

$$\mathbf{h}(k,x) = \sum_{n=-\infty}^{\infty} \int_{-\infty}^{\infty} \mathrm{d}x' \underline{\mathbf{G}}(k, x - x') \mathbf{m}_n(k, x') \tag{34.72}$$

The magnetization motion in this case represents a collective wave. That is why k is the same in all stripes.

As far as the structure is periodic along the x-axis, therefore the dynamic dipole field and the dynamic magnetization can be described in the frames of Bloch's waves formalism. In the similar form, as it was done earlier (see Equations 34.57 through 34.59), we represent dynamic dipole magnetic field as a product of the Bloch wave and a periodic part $\tilde{\boldsymbol{h}}(x, k_x, k_y)$ and in the reduced zone scheme we have:

$$\tilde{\mathbf{h}}(k_x, k_y, x) = \int_0^w \mathrm{d}x' \tilde{\mathbf{G}}(k_x, k_y, x - x') \tilde{\mathbf{m}}(k_x, k_y, x') \tag{34.73}$$

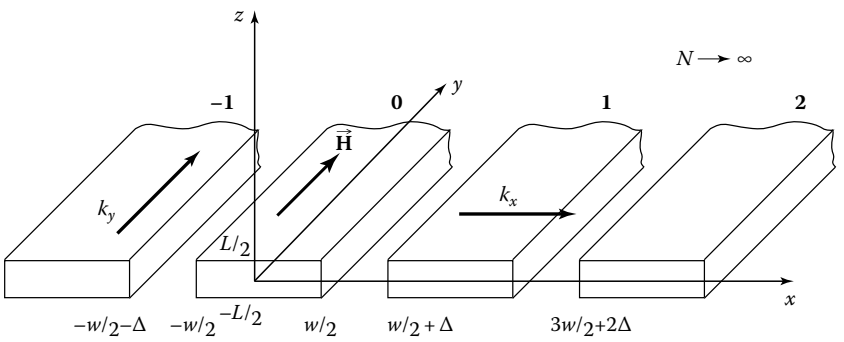

FIGURE 34.17 Infinite array of dipole-coupled magnetic stripes.

Green's function of a periodic structure in the reduced zone scheme reads:

$$\tilde{\mathbf{G}}(k_y, k_x, x - x') = \sum_{n=-\infty}^{\infty} \underline{\mathbf{G}}(k_y, x - x' + nT) \exp\left(ik_x(nT - (x - x'))\right) \tag{34.74}$$

where $\underline{\mathbf{G}}(k_y, x - x')$ is given by Equation 34.66.

Since $\varphi = \arctan(k_y/k_x)$ is the propagation angle of the collective mode, Equations 34.73 and 34.74 together with the linearized Landau–Lifschitz equation allow one to describe dynamics of spin-wave eigen-excitations propagating in an arbitrary direction on a periodical array of parallel magnetic stripes. In this expression, k_y can take any real value, whereas k_x can be limited to the first Brillouin zone $-(\pi/T) < k_x \leq (\pi/T)$.

If we consider now a particular case of a collective mode propagating along the x-axis, i.e., $k_y = 0$. In this case, Green's function (Equation 34.74) has the same form as Green's function of a single stripe [62]. Therefore, the same algebraic Equation 34.70 remains valid. The corresponding eigenvalue–eigenfunction problem is now for the integral operator, as follows:

$$\lambda(k_x)\,\tilde{m}_z(k_x, x) = \int_0^w dx' \tilde{G}_{zz}(k_x, x - x')\tilde{m}_z(k_x x') \tag{34.75}$$

where $\tilde{G}_{zz}(k_x, x - x')$ is a corresponding component of $\underline{\mathbf{G}}(k_y, x - x')$.

The integral operator (Equation 34.75) has an infinite set of discrete eigenvalues λ_n which continuously depend on k_x. The transition from a continuous film to a structured one is characterized by creation of stop-bands and Brillouin zones, typical of periodic photonic, phononic, and magnonic structures. The periodicity of the dispersion $\omega_n(k_x)$, known as Brillouin's zone structure, is another important feature of Bloch's type modes on a periodic structure. The width of each Brillouin's zone is equal to $2\pi/T$. In the middle of the first Brillouin's zone $k_x = 0$ and the expression (Equation 34.75) reduces to

$$\tilde{G}_{\uparrow\uparrow}(s) = \sum_{n=-\infty}^{\infty} G_{zz}(s + nT) \tag{34.76}$$

This expression reveals the trivial fact that for $k_x = 0$ the magnetization vector in all stripes precesses in phase. Similarly, at the edge of the first Brillouin zone $k_x = \pm(\pi/T)$, one has

$$\tilde{G}_{\uparrow\downarrow}(s) = \sum_{n=-\infty}^{\infty} (-1)^n G_{zz}(s + nT) \tag{34.77}$$

which shows that the neighboring stripes are now in anti-phase.

The most practically interesting case is the lowest-frequency collective mode. Obviously, it is formed by coupling of lowest resonances across independent stripes. Therefore, the profile of the dynamic magnetization across stripes in this mode should be quasi-homogeneous. Keeping in mind that in the limiting case $\Delta = 0$, one should retrieve a homogeneous precession of the magnetization in an unstructured film, the profile of dynamic magnetization across the stripes on an array of coupled stripes should be more homogeneous than for an independent stripe. This is why the dipole field of each stripe penetrates its neighboring stripes making the spatial variation of the field along x smaller. The profile of dynamic magnetization follows the profile of the dipole field, mathematically described by Equation 34.75, which makes $\mathbf{m}(x)$ smoother than in independent stripes. The magnetostatic field penetrating the neighboring stripes appears to be codirected with the dynamic magnetization in them; therefore, the coupling decreases the overall magnetostatic energy. As a result, the frequency decreases compared to the case of individual stripes. At the edge of the first Brillouin zone, the dynamic magnetization in neighboring stripes points in opposite directions (see Equation 34.77).

In this case, the dipole field induced by the magnetization in each stripe is contra-directed to both the dynamic magnetization in the stripe itself and the dynamic magnetization in neighboring stripes. Thus, the overall magnetostatic energy is in this case larger than for uncoupled stripes. Therefore, at the edge of the Brillouin zone, one has the largest frequency for the lowest mode.

For the second mode and all other even modes, the situation is opposite. For $k_x = 0$, the dynamic magnetization in neighboring stripes points in opposite directions at the edges of the gap. This results in the highest frequency for these modes. At the edge of the first Brillouin zone, the magnetization at the both edges of the same gap is of the same direction; therefore, the frequency at $k_x = (\pi/T)$ is minimum and the dispersion of even modes between $k_x = 0$ and $k_x = (\pi/T)$ is negative.

Formation of Brillouin zones is illustrated in Figure 34.18a. The eigenvalues can be easily calculated numerically. In Figure 34.18b are given the results of such numerical estimations for a periodic 1D array of permalloy stripes with thickness of 20 nm and width $w = 175$ nm. The spacing was equal to $\Delta = 35$ nm which corresponds to a period of $T = 210$ nm and, consequently, the

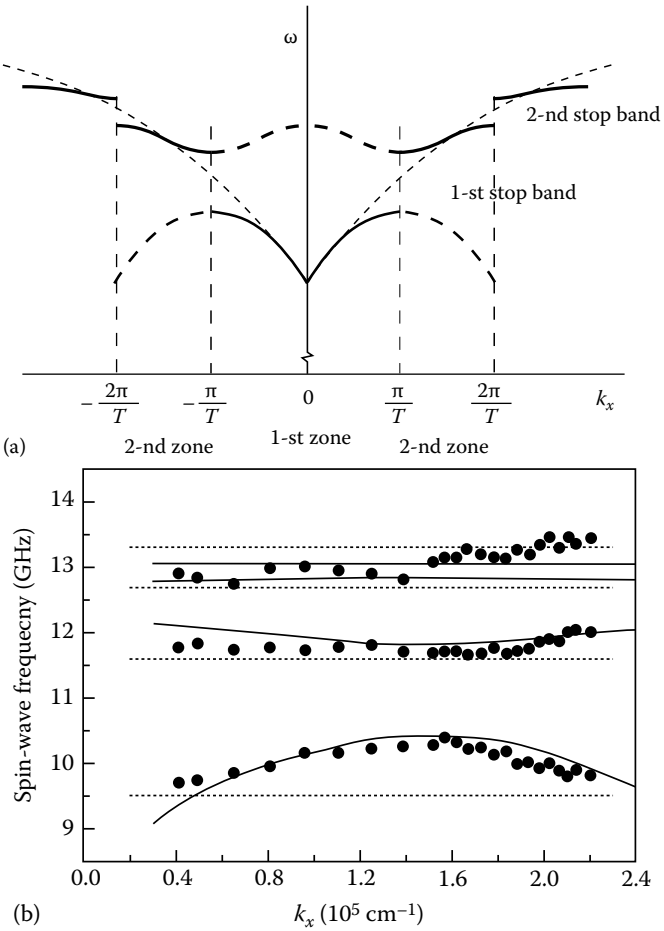

FIGURE 34.18 Formation of band structure in the infinite array of magnetic stripes: (a) qualitative theoretical spectrum, (b) experimental and calculated dispersion of the spin-wave frequency modes for an infinite array of permalloy wires. The continuous curves were calculated using the theoretical model described in the text. Dotted lines are the calculated frequencies for the resonant spin modes for an isolated wire.

upper limit of the first Brillouin zone is equal to $k_x = 1.5 \times 10^5$ cm^{-1}. The continuous curves were calculated using the theoretical model described in the text. Dotted horizontal lines are the calculated frequencies for the resonant spin modes for an isolated wire. Experimental results in the range $0 < k_x < 2.2 \times 10^5$ cm^{-1} obtained using the BLS technique are given with filled circles [73]. They extend well beyond the upper limit of the first Brillouin zone. One sees that the spectrum represents a set of modes separated from one another in frequency by stop-bands, manifesting the above-described features.

Since the dipole field outside the stripes decreases with n, coupling of stripes decreases with an increase in mode number. As a result, the modes become less dispersive with an increase in n. As one sees from Figure 34.18, the higher-order modes are practically dispersionless.

34.5.5 Microwave Properties of Planar Patterned Metamaterials

Let us now discuss peculiarities of microwave properties of the planar metamaterials in the form of coupled metallic magnetic stripes. As one sees from Figure 34.18, the periodic medium with the geometry of Figure 34.17 possesses a number of frequency stop bands. Since the array is periodic only in one direction, the stop bands exist only for the wave propagation directions for which k_x component of the full in-plane vector $k = \sqrt{k_x^2 + k_y^2}$ does not vanish. Elsewhere, it will be shown that for $k = k_y$ the gaps collapse.

The width of stop bands depends on the stripe dipole coupling. The latter in the first place depends on the stripe separation Δ/w and the mode number. The smaller the stripe coupling, the larger the stop bands.

An important property of such metamaterial is that the central frequencies of pass bands can be tuned by varying the applied static magnetic field. For $\Delta/w \ll 1$, the lowest frequency of the lowest collective mode $\omega_{n=1}(k_x = 0)$ is close to the lower frequency boundary of the spin-wave band in an unstructured monolayer film $\omega_\perp = \sqrt{\omega_H(\omega_H + \omega_M)}$. Therefore, with an increase in the static field, the lowest pass band shifts in frequency with the slope which decreases with H_i: $\partial\omega/\partial H_i = 2|g|\mu_0\sqrt{\omega_M/\omega_H}$.

Obviously, the increase in the stop-band width with the increase of the stripe separation Δ is due to a decrease in the slope $v_{gn}(k) = \partial\omega_n(k)/\partial k$ of dispersion branches. The smaller is v_{gn}, the smaller is the frequency range of existence of the mode $\Delta\omega_n \approx v_{gn}(k_x = 0)\,\pi/T$. On the other hand, the slope v_{gn} represents the collective mode group velocity. The calculation shows that the dependence $v_{gn}(k_x)$ is almost linear for small k_x values. Thus, the group velocity can be controlled by adjusting Δ, which allows one to design a microwave delay line with a necessary delay time.

In this section, we have considered in detail the basic geometry of patterned planar metamaterials: an array of 1D stripes with the external magnetic field applied along the axis of the stripes. In this case, the distribution of the static magnetization inside the stripes is homogeneous. This assumption has made it possible to arrive at important results by means of purely analytical calculations, which provide deeper physical insight.

However, if the magnetic field is applied in any other direction, the interior static magnetization can become highly inhomogeneous. The latter gives rise to strongly localized dipole-exchange modes, existing in so-called spin-wave wells, first discovered experimentally and explained qualitatively in Ref. [81]. Detailed quantitative description, relying on numerical simulations and analytical calculations, has been provided, correspondingly, in Refs. [159] and [17,160]. It should be noted that in the case of less straightforward configurations application of numerical approaches becomes more and more justified. For example, the numerical technique based on the finite element method [79] has proved efficient for NiFe/Cu/NiFe tri-layered stripes [161] and permalloy stripes coupled to a permalloy continuous film [162], subjected to a perpendicular magnetic field. In the latter case, numerical simulations have been backed up with analytical calculations.

Alternative numerical techniques for simulations of spin-wave behavior on patterned metamaterials include an ad hoc code elaborated on the basis of the finite difference approach [163] and straightforward application of the object-oriented micromagnetic framework (OOMMF) [164]. In the latter case, the spin configuration resulting from purely static calculations is used as an initial state for the dynamic calculation. To obtain the dynamic response, the system is excited by a short pulse (see, e.g., [27]). Though being extremely powerful, numerical methods are very time consuming. For this reason, they lack in efficiency compared to analytical approaches for theoretical description of collective modes that are not localized on a single stripe.

34.6 Conclusion

In conclusion, we note that the delivered method of tensorial Green function and SWM approach can be used not only for ferromagnetic–dielectric structures, but also for any structures containing metal screens, semiconductor layers, and for pure ferromagnetic structures. The SWM approach has been successfully used in the theory of response functions for dipole-exchange spin waves in ferromagnetic layered structures, in the theory of impedance of spin-wave transducers, in the theory of parametric instability of spin waves, and in the theory of spin-waves envelope solitons. Thus, the SWM approach could be successfully used for solving various problems on the linear and nonlinear dynamics of spin-wave and multiwave processes in magnetic metamaterials.

Due to the numerous variations in the composition of magnetic structures and different magnetic field orientations, the amount of work that has been done over the past several years is enormous. It is, therefore, quite difficult to give a comprehensive overview of the whole work associated with magnetic multilayered and patterned media.

The problems discussed in this section are not merely those we face while considering excitations in artificial magnetic structures. Our discussion was restricted mostly to periodically layered and patterned structures, though this is not the only possibility. With the growing fabrication technology, one can now produce layered systems with arbitrary designed parameters, strictly controlled during the fabrication process. Some important classes of layered systems (quasiperiodic and randomly layered structures) were mentioned above very shortly.

Also, it is worth mentioning that the stepwise character of the magnetic properties at the interface between films is not only one opportunity for such structures. More realistic cases are sinusoidal-like or trapezoid-like variation of the appropriate properties and parameters. It should be emphasized that there are several other problems, which are not discussed here due to limited space, and undoubtedly the additional ones will arise as new structures appear.

References

1. Smith, D. R., Pendry, J. B., and Wiltshire, M. C. K. 2004. Metamaterials and negative refractive index. *Science* 305: 788–792.
2. Yen, T. J., Padilla, W. J., Fang, N., et al. 2004. Terahertz magnetic response from artificial materials. *Science* 303(5663): 1494–1496.
3. Smith, D. R., Padilla, W. J., Vier, D. C., et al. 2000. Composite medium with simultaneously negative permeability and permittivity. *Phys. Rev. Lett.* 84: 4184–4187.
4. Smith, D. R. and Pendry, J. B. 2004. Reversing light with negative refraction. *Phys. Today* 57: 37–43.
5. Puszkarski, H. and Krawczyk, M. 2003. Magnonic crystals—the magnetic counterpart of photonic crystals. *Solid State Phenom.* 94: 125–134.
6. Vasseur, J. O., Dobrzynski, L., Djafari-Rouhani, B., et al. 1996. Magnon band structure of periodic composites. *Phys. Rev. B* 54(2): 1043–1049.

7. Krawczyk, M. and Puszkarski, H. 2005. Theory of spin-wave frequency gaps in 3D magnonic crystals. Application to manganites. *Condens. Mat.*, no.1 (April): 1–14. cond-mat/0504073.
8. Nikitov, S. A., Tailhades, Ph., and Tsai, C. S. 2001. Spin waves in periodic magnetic structures—magnonic crystals. *J. Magn. Magn. Mater*. 236: 320–330.
9. Vysotski, S. L., Nikitov, S. A., and Filimonov, Yu. A. 2005. Magnetostatic spin waves in two-dimensional periodic structures (magnetophoton crystals). *JETP* 101(3): 547–553.
10. Cottam, M. G. 1994. *Linear and Nonlinear Spin Waves in Magnetic Films and Superlattices*, Singapore: World Scientific Publishing Company.
11. Cottam, M. G. and Lockwood, D. J. 1986. *Light Scattering in Magnetic Solids*. New York: John Wiley & Sons.
12. Wang, X.-Z. and Tilley, D. R. 1994. Magnetostatic surface and guided modes on lateral-magnetic-superlattice films. *Phys. Rev. B* 50(18): 13472–13479.
13. Albuquerque, E. L., Fulko, P., Sarmento, E. F., and Tilley, D. R. 1986. Spin-waves in a magnetic superlattice. *Solid State Commun*. 58(1): 41–44.
14. Barnas, J. 1992. Exchange modes in ferromagnetic superlattices. *Phys. Rev. B* 45(18): 10427–10437.
15. Barnas, J. 1988. Spin waves in superlattices. II. Magnetostatic modes in the Voigt configuration. *J. Phys. C: Solid State Phys.* 21: 4097–4112.
16. Camley, R. E. and Stamps, R. L. 1993. Magnetic multilayers: Spin configurations, excitations and giant magnetoresistance. *J. Phys.: Condens. Mat.* 5: 3727–3786.
17. Kostylev, M. P. and Sergeeva, N. A. 2006. Collective and individual modes on one-dimensional bi-layered magnetic structures. In *Magnetic Properties of Laterally Confined Nanometric Structures*. (ed.) G. Gubiotti, pp. 183–207. Kerala, India: Transworld Research Network.
18. Kostylev, M. P., Stashkevich, A. A., and Sergeeva, N. A. 2004. Collective magnetostatic modes on a one-dimensional array of ferromagnetic stripes. *Phys. Rev.* B 69: 064408-1–064408-7.
19. Guslienko, K. Yu., Pishko, V., Novosad, V., et al. 2005. Quantized spin excitation modes in patterned ferromagnetic stripe arrays. *J. Appl. Phys.* 97: 10A709-1-3.
20. Saib, A., Vanhoenacker-Janvier, D., Huynen, I., et al. 2003. Magnetic photonic band-gap material at microwave frequencies based on ferromagnetic nanowires. *Appl. Phys. Lett.* 83(12): 2378–2380.
21. Encinas-Oropesa, A., Demand, M., Piraux, L., et al. 2001. Effect of dipolar interactions on the ferromagnetic resonance properties in arrays of magnetic nanowires. *J. Appl. Phys.* 89(11): 6704–6706.
22. Goglio, G., Pignard, S., Radulescu, A., et al. 1999. Microwave properties of metallic nanowires. *Appl. Phys. Lett.* 75(12): 1769–1771.
23. Zivieri, R. and Stamps, R. L. 2006. Theory of spin wave modes in tangentially magnetized thin cylindrical dots: A variational approach. *Phys. Rev. B* 73: 144422-1-17.
24. Guslienko, K. Yu. and Slavin, A. N. 2000. Spin-waves in cylindrical magnetic dot arrays with in-plane magnetization. *J. Appl. Phys*. 87(9): 6337–6339.
25. Kakazei, G. N., Wigen, P. E., Guslienko, K. Yu., et al. 2004. Spin-wave spectra of perpendicularly magnetized circular submicron dot arrays. *Appl. Phys. Lett.* 85(3): 443–445.
26. Gubbiotti, G., Conti, M, Carlotti, G, et al. 2004. Magnetic field dependence of quantized and localized spin wave modes in thin rectangular magnetic dots. *J. Phys.: Condens. Mat.* 16: 1–13.
27. Gubbiotti, G., Madami, M., Tacchi, et al. 2006. Normal mode splitting in interacting arrays of cylindrical permalloy dots. *J. Appl. Phys.* 99: 08C701-1-3.
28. Vavassori, P., Gubbiotti, G., Zangari, G. et al. 2002. Lattice symmetry and magnetization reversal in micron-size antidot arrays in permalloy film. *J. Appl. Phys.* 91(10): 7992–7994.
29. Tsutsumi, M., Sakaguchi, Y., and Kumagai, N. 1977. Behavior of the magnetostatic wave in a periodically corrugated YIG slab. *IEEE Trans. Microw. Theory Technol.* MTT-25: 224–228.
30. Parekh, J. P. and Tuan, H. S. 1977. Reflection of magnetostatic surface wave at a shallow groove on a YIG film. *Appl. Phys. Lett.* 31(10): 709–712.
31. Seshadri, S. R. 1979. Magnetic wave interactions in a periodically corrugated YIG film. *IEEE Trans. Microw. Theory Technol.* MTT-27(2): 199–204.

32. Owens, J. M., Smith, C. V., Lee, S. N., et al. 1978. Magnetostatic wave propagation through periodic metallic gratings. *IEEE Trans. Magn*. MAG-14(5):820–825.
33. Carter, R. L., Owens, J. M., Smith, C. V., et al. 1982. Ion-implanted magnetostatic wave reflective array filters. *J. Appl. Phys.* 53(3): 2655–2657.
34. Chang, N. S. and Matsuo, Y. 1979. Magnetostatic surface wave propagation on a periodic YIG film layer. *Appl. Phys. Lett.* 35(4): 352–354.
35. Niu-Nui Chen, Slavin, A. N., and Cottam, M. G. 1993. Gap solitons in periodic structures: Modulated magnetic thin films. *Phys. Rev. B* 47(14): 8667–8671.
36. Kolodin, P. A. and Hillebrands, B. Spin-wave propagation across periodically corrugated thin metallic ferromagnetic films. *J. Magn. Magn. Mater*. 161: 199–202.
37. Tsai, C. S., Qiu, G., Gao, H., et al. 2005. Tunable wideband microwave band-stop and band-pass filters using YIG/GGG-GaAs layer structures. *IEEE Trans. Magn.* 41(10): 3568–3570.
38. Encinas, A., Demand, M., Vila, L., et al. 2002. Tunable remanent state resonance frequency in arrays of magnetic nanowires. *Appl. Phys. Lett.* 81(11): 2032–2034.
39. Zhang, Z. and Wigen, P. E. 1995. Magnetic resonance in exchange coupled multilayer systems. In *High Frequency Processes in Magnetic Materials*. (eds.), G. Srinivasan, and A.N. Slavin, pp. 164–199. Singapore: World Scientific Publishing Company.
40. Arias, R. and Mills, D. L. 2003. Theory of collective spin waves and microwave response of ferromagnetic nanowire arrays. *Phys. Rev. B* 67: 094423-1-15.
41. Hillebrands, B. 1990. Spin-wave calculations for multilayered structures. *Phys. Rev. B* 41(1): 530–540.
42. Kalinikos, B. A. and Kolodin, P. A. 1992. Excitation of propagating dipole-exchange spin waves in ferromagnetic double-film structure. *IEEE Trans. Magn.* 28(5): 3204–3206.
43. Figotin, A. and Vitebsky, I. 2001. Nonreciprocal magnetic photonic crystals. *Phys. Rev. E* 63:066609-1-17.
44. Camley, R. E., Rahman, T. S., and Mills, D. L. 1983. Magnetic excitations in layered media spin waves and the light-scattering spectrum. *Phys. Rev. B* 27(1):261–277.
45. Grüberg, P. and Mika, K. 1983. Magnetostatic spin-wave modes of a ferromagnetic multilayer. *Phys. Rev. B* 27: 2955–2963.
46. Emtage, P. R. and Daniel, M. R. 1984. Magnetostatic waves and spin waves in layered ferrite structures. *Phys. Rev. B* 29: 212–220.
47. Rupp, G., Wettling, W., and Jantz, W. 1987. Surface spin waves in anisotropic magnetic multilayers. *Appl. Phys. A: Mater. Sci. Process*. 42: 45–55.
48. Van Stapele, R. P., Greidanus, F. J. A. M., and Smits, J. W. 1985. The spin-wave spectrum of layered magnetic thin films. *J. Appl. Phys.* 57(4): 1282–1290.
49. Mills, D. L. 1992. Spin-waves in ultra thin exchange coupled ferromagnetic multilayers: The boundary condition at the interface. *Phys. Rev. B* 45(22): 13100–13104.
50. Vayhinger, K. and Kronmuller, H. 1988. Spin wave theory of exchange coupled ferromagnetic multilayers. *J. Magn. Magn. Mater.* 72: 307–314.
51. Milton Pereira, J., Jr. and Cottam, M. G. 2000. Exchange-dominated surface spin waves in ferromagnetic and antiferromagnetic films. *J. Appl. Phys.* 87(9): 5941–5943.
52. Vittoria, C. 1988. Ferromagnetic resonance of exchange-coupled magnetic layers. *Phys. Rev. B* 37(4): 2387–2390.
53. Vohl, M., Barnas, J., and Grunberg, P. 1989. Effect of interlayer exchange coupling on spin-wave spectra in magnetic double layers: Theory and experiment. *Phys. Rev. B* 39(16): 12003–12012.
54. Kalinikos, B. A. and Kolodin, P. A. 1995. Spectrum of microwave spin waves in magnetic multilayers. In *High Frequency Processes in Magnetic Materials*. (eds.), G. Srinivasan and A. N. Slavin, pp. 137–163. Singapore: World Scientific Publishing Company.
55. Vayhinger, K. and Kronmuller, H. 1986. Propagating spin waves in ferromagnetic multilayers. *J. Magn. Magn. Mater.* 62: 159–168.

56. Sparks, M. 1970. Ferromagnetic resonance in thin films. I. Theory of normal-mode frequencies. *Phys. Rev. B* 1(9): 3831–3856.
57. Kalinikos, B. A. 1994. Dipole-exchange spin-wave spectrum of magnetic films. In *Linear and Nonlinear Spin Waves in Magnetic Films and Superlattices*. (ed.), M. G. Cottam, pp. 89–156. Singapore: World Scientific Publishing Company.
58. Kalinikos, B. A. and Slavin, A. N. 1986. Theory of dipole-exchange spin wave spectrum for ferromagnetic films with mixed exchange boundary conditions, *J. Phys. C: Solid State Phys.* 19: 7013–7033.
59. Kalinikos, B. A., Kostylev, M. P., Kozhus, N.V., et al. 1990. The dipole-exchange spin wave spectrum for anisotropic ferromagnetic films with mixed exchange boundary conditions. *J. Phys.: Condens. Mat.* 2: 9861–9877.
60. Barnas, J. 1994. Spin waves in multilayers. In *Linear and Nonlinear Spin Waves in Magnetic Films and Superlattices*, (ed.), M. G. Cottam, pp. 157–206. Singapore: World Scientific Publishing Company.
61. Kruglyak, V. V., Hicken, R. J., Kuchko, A. N., et al. 2005. Spin waves in a periodically layered magnetic nanowire. *J. Appl. Phys.* 98: 014304-1-4.
62. Guslienko, K. Yu., Demokritov, S. O., Hillebrands, B., et al. 2002. Effective dipolar boundary conditions for dynamic magnetization in thin magnetic stripes. *Phys. Rev. B* 66(13): 132402-1-4.
63. Demokritov, S. O., Hillebrands, B., and Slavin, A. N. 2001. Brillouin light scattering studies of confined spin waves: Linear and nonlinear confinement. *Phys. Rep.* 348: 441–489.
64. Gubiotti, G. 2006. *Magnetic Properties of Laterally Confined Nanometric Structures*, Italy: Transworld Research Network.
65. Milton Pereira Jr., J. and Costa Filho, R. N. 2005. Dipole-exchange spin waves in Fibonacci magnetic multilayers. *Phys. Lett. A.* 344: 71–76.
66. Al-Wahsh, H. 2004. Stop bands and defect modes in a magnonic chain of cells showing single-cell spectral gaps. *Phys. Rev. B* 69: 012405-1-4.
67. Arias, R. and Mills, D. L. 2004. Theory of of collective spin-wave modes of interacting ferromagnetic spheres. *Phys. Rev. B* 70: 104425.
68. Gubbiotti, G., Candeloro, P., Businaro, L., et al. 2003. Spin-wave frequency discretization in submicron rectangular prisms. *J. Appl. Phys.* 93(10): 7595–7597.
69. Chui, S. T., and Hu, Liangbin. 2002. Theoretical investigation on the possibility of preparing left-handed materials in metallic magnetic granular composites. *Phys. Rev. B* 65: 144407-1-6.
70. Bromwich, T. J., Kohn, A., Petford-Long, A. K., et al. 2005. Remanent magnetization states and interactions in square arrays of 100- nm cobalt dots measured using transmission electron microscopy. *J. Appl. Phys.* 98: 053909-1-8.
71. Albini, L., Carlotti, G., Gubbiotti, G., et al. 2001. In situ investigation of ultrathin Fe/Cu(110) films by Brillouin light scattering. *J. Appl. Phys.* 89(11): 7383–7385.
72. Gubbiotti, G., Carlotti, G., Albertini, F., et al. 2003. Dependence of the perpendicular anisotropy in Co/Au multilayers on the number of repetitions. *J. Appl. Phys.* 93(10): 7050–7052.
73. Gubbiotti, G., Tacchi, S., Carlotti, G., et al. 2005. Magnetostatic interaction in arrays of nanometric permalloy wires: A magneto-optic Kerr effect and a Brillouin light scattering study. *Phys. Rev. B* 72: 224413-1-7.
74. Rojdestvenski, I. V., Cottam, M. G., and Slavin, A. N. 1996. Dipole-exchange spin wave spectra of exchange-coupled magnetic multilayers calculated by transfer matrix formalism. *J. Appl. Phys* 79(8): 5724–5726.
75. Adenwalla, S., Felcher, G. P., Fullerton, E. E., et al. 2006. Polarized-neutron-reflectivity confirmation of 90° magnetic structure in Fe/Cr(001) superlattices. *Phys. Rev. B* 53(5): 2474–2480.
76. Van de Kruijs, R. W. E., Rekveldt, M. Th., Fredrikze, H., et al. 2002. Magnetic interlayer exchange coupling in epitaxial Fe/Si/Fe(001) studied by polarized neutron reflectometry. *Phys. Rev. B* 65: 104440-1-7.
77. Jorzick, J., Demokritov, S. O., Mathieu, C., et al. 1999. Brillouin light scattering from quantized spin waves in micron-size magnetic wires. *Phys. Rev. B* 60: 15194–15200.

78. Chérif, S. M., Roussigné, Y., and Moch, P. 1999. Effect of anisotropy on Brillouin spectra of stripe-structured cobalt layers. *Phys. Rev. B* 59: 9482–9490.
79. Roussigné, Y., Chérif, S. M., Dugautier, C., et al. 2001. Experimental and theoretical study of quantized spin-wave modes in micrometer-size permalloy wires. *Phys. Rev. B* 63: 134429–134436.
80. Grimsditch, M., Guedes, I., Vavassori, P., et al. 2001. Brillouin scattering and diffracted magneto-optical Kerr effect from arrays of dots and antidots (invited). *J. Appl. Phys.* 89: 7096–7100.
81. Jorzick, J., Demokritov, S. O., Hillebrands, B., et al. 2002. Spin wave wells in nonellipsoidal micrometer size magnetic elements. *Phys. Rev. Lett.* 88: 047204–047207.
82. Park, J. P., Eames, P., Engebretson, D. M., et al. 2002. Spatially resolved dynamics of localized spin-wave modes in ferromagnetic wires. *Phys. Rev. Lett.* 89: 277201–277204.
83. Tamaru, S., Bain, J. A., van de Veerdonk, R. J. M., et al. 2004. Measurement of magnetostatic mode excitation and relaxation in permalloy films using scanning Kerr imaging. *Phys. Rev B.* 70: 104416-1-9.
84. Perzlmaier, K., Buess, M., Back, C. H., et al. 2005. Spin-wave eigenmodes of permalloy squares with a closure domain structure. *Phys. Rev. Lett.* 94: 057202–057205.
85. Demidov, V. E., Demokritov, S. O., Hillebrands, B., et al. 2004. Radiation of spin waves by a single micrometer-sized magnetic element. *Appl. Phys. Lett.* 85: 2866–2868.
86. Damon, R. W. and Eshbach, J. R. 1961. Magnetostatic modes of a ferromagnet slab. *J. Phys. Chem. Solids* 19(3/4): 308–320.
87. Herring, C. and Kittel, C. 1951. On the theory of spin waves in ferromagnetic media. *Phys. Rev.* 81: 869–880.
88. Vendik, O. G., Kalinikos, B. A., and Chartoryzhskii, D. N. 1977. Instability of spin waves in tangentially magnetized thin ferromagnetic films. *Sov. Phys.-Solid State*. 19: 222–227; Chartoryzhskii, D. N., Kalinikos, B. A., and Vendik, O. G. 1976. Parallel pump spin wave instability in thin ferromagnetic films. *Solid State Comm.* 20: 985–989.
89. Rado, G. T. and Weertman, J. R. 1959. Spin-wave resonance in a ferromagnetic metal. *J. Phys. Chem. Solids.* 11:315–333.
90. Stancil, D. D. 1992. *Theory of Magnetostatic Waves*. New York: Springer-Verlag.
91. Gilbert, T. A. 1955. Equation of motion of magnetization. *Armor Research Foundation* Rep. No 11, Chicago, IL.
92. Osborn, J. A. 1945. Demagnetizing factors of the general ellipsoid. *Phys. Rev.* 67(11–12): 351–357.
93. Joseph, R. I. and Schlomann, E. 1965. Demagnetizing field in nonellipsoidal bodies. *J. Appl. Phys.* 36(5): 1579–1593.
94. Felsen, L. B. and Marcuvitz, N. 1973. *Radiation and Scattering of Waves*. New Jersey: Prentice-Hall.
95. Belyakov, S. V. 1984. Ferromagnetic resonance in ferrite ellipsoid with cubic crystallographic anisotropy. *Electron. Tech. Ser. 1 Electronica SVCH.* 6(366): 35–42.
96. Belyakov, S. V., Kalinikos, B. A., and Kozhus, N. V. 1989. Dipole-exchange spin-wave dispersion in monocrystalline anisotropic magnetic films. Part 1. Dipole-exchange spectrum of spin waves. *Electron. Tech. Ser. 1 Electronica SVCH.* 1(415): 22–28.
97. Hoffmann, F. 1970. Dynamic pinning induced by nickel layers on permalloy films. *Phys. Status Solidi.* 41(2): 807–813.
98. Hoffmann, F., Stankoff, A., and Pascard, H. 1970. Evidence for an exchange coupling at the interface between two ferromagnetic films. *J. Appl. Phys.* 41: 1022–1013.
99. Pashaev, Kh.M. and Mills, D. L. 1991. Ferromagnetic-resonance spectrum of exchange-coupled ferromagnetic bilayers. *Phys. Rev. B* 43: 1187–1189.
100. Ament, W. S. and Rado, G. T. 1955. Electromagnetic effects of spin wave resonance in ferromagnetic metals. *Phys. Rev.* 97(6): 1558–1566.
101. Kittel, C. 1958. Exitation of spin waves in a ferromagnet by a uniform field. *Phys. Rev.* 110(6): 1295–1297.
102. Gann, V. V. 1967. Nonuniform resonance in a ferromagnetic plate. *Sov. Phys.-Solid State*. 8(11): 2537–2540.

103. Arias, R. and Mills, D. L. 1999. Extrinsic contributions to the ferromagnetic resonance response of ultrathin films. *Phys. Rev. B* 60(10): 7395–7409.
104. Grimsditch, M., Giovannini, L., Montoncello, F., et al. 2004. Magnetic normal modes in ferromagnetic nanoparticles: A dynamical matrix approach. *Phys. Rev. B* 70: 054409-1-7.
105. Arias, R. and Mills D. L. 2004. Magnetostatic modes in ferromagnetic nanowires. *Phys. Rev. B* 70: 094414-1-11.
106. Costa Filho, R. N., Cottam, M. G., and Farias, G. A. 1998. Spin-wave interactions in ultrathin ferromagnetic films: The dipole-exchange regime. *Solid State Commun.* 108(7): 439–443.
107. Ruderman, M. A. and Kittel, C. 1954. Indirect exchange coupling of nuclear magnetic moments by conduction electrons. *Phys. Rev.* 96(1): 99–102.
108. Sparks, M. 1970. Effect of exchange on magnetostatic modes. *Phys. Rev. Lett.* 24(21): 1178–1180.
109. Soukoulis, C. M. 1996. (ed.) *Photonic Band Gap Materials*. Dordrecht, the Netherlands: Kluwer Academic.
110. Yariv, A. and Yeh, Pochi. 1984. *Optical Waves in Crystals*. New-York: Wiley-Interscience.
111. Barnas, J. 1992. Spin waves in superlattices. IV. The exchange-dominated region. *J. Phys.: Condens. Mat.* 4: 4849–4855.
112. Agranovich, V. M. and Kravtsov, V. E. 1985. Notes on crystal optics of superlattices. *Solid State Commun.* 55: 85–90.
113. Zivieri, R., Giovannini, L., Nizzoli, F., et al. 2001. Brillouin scattering cross section in Fe(110)/Cu(111)/Fe(110) asymmetric bilayers. *J. Appl. Phys.* 89(11): 7077–7079.
114. Gubbiotti, G., Carlotti, G., Montecchiari, A., et al. 2000. Brillouin light scattering study of ferromagnetically coupled Cu/Fe(110)/Cu/Fe(110)/Cu/Si(111) heterostructures: Bilinear exchange magnetic coupling. *Phys. Rev. B* 62(23): 16109–16115.
115. Soohoo, R. F. 1965. *Magnetic Thin Films*. New York: Harper and Row.
116. Landau, L .D. and Lifshitz, F. M. 1965. *Quantum Mechanics Non-Relativistic Theory*. 2nd edn. London: Pergamon.
117. Adam, J. D., O'Keeffe, T. W., and Patterson, R. W. 1979. Magnetostatic wave to exchange resonance coupling. *J. Appl. Phys.* 50: 2446–2448.
118. Kalinikos, B. A., Kovshikov, N. G., and Slavin, A. N. 1983. Observation of spin-wave solitons in ferromagnetic films. *Sov. Phys-JETP Lett.*, 38: 413–417.
119. Andreev, A. S., Gulyaev, Yu. V., Zil'berman, P. E. et al. 1984. Propagation of magnetostatic waves in iron-yttrium-garnets of sub-micron thickness. *Sov. Phys-JETP.* 86(3): 1005–1015.
120. Bloch, F. 1931. On the theory of magnetisation of ferromagnetic single crystals. *Phys. Z.* 32: 290–290.
121. Elachi, C. 1976. Waves in active and passive periodic structures: A review. *Proc. IEEE* 64(12): 1666–1698.
122. Matsuyama, K., Komatsu, S., and Nozaki, Y. 2000. Magnetic properties of nanostructured wires deposited on the side edge of patterned thin film. *J. Appl. Phys.* 87(9): 4724–4726.
123. Pietzsch, O., Kubetzka, A., Bode, M., et al. 2000. Real-Space observation of dipolar antiferromagnetism in magnetic nanowires by spin-polarized scanning tunneling Spectroscopy. *Phys. Rev. Lett.* 84(22): 5212–5215.
124. Adeyeye, A. O., Husain, M. K., and Ng, V. 2002. Magnetic properties of lithographically defined lateral $Co/Ni_{80}Fe_{20}$ wires. *J. Magn. Magn. Mater*. 248: 355–359.
125. Sergeeva, N. A., Cherif, S. M., Stachkevitch, A. A., et al. 2004. Spin-waves in ferromagnetic double layers: effect of a lateral patterning. *Phys. Stat. Sol. (c)* 1(7): 1587–1590.
126. Sergeeva, N. A., Cherif, S. M., Stachkevitch, A. A., et al. 2005. Spin waves quantization in patterned exchange-coupled double layers. *J. Magn. Magn. Mater*. 288: 250–258.
127. Gubbiotti, G., Kostylev, M., Sergeeva, N., et al. 2004. Brillouin light scattering investigation of magnetostatic modes in symmetric and asymmetric NiFe/Cu/NiFe trilayered wires. *Phys. Rev. B* 70: 224422.

128. Bayer, C., Jorzick, J., Hillebrands, B., et al. 2005. Spin-wave excitations in finite rectangular elements of $Ni_{80}Fe_{20}$. *Phys. Rev. B* 72: 064427-1-12.
129. Gubbiotti, G., Albini, L., Carlotti, G., et al. 2000. Finite size effects in patterned magnetic permalloy films. *J. Appl. Phys.* 87(9): 5633–5635.
130. Gubbiotti, G., Carlotti, G., Okuno, T., et al. 2005. Spin dynamics in thin nanometric elliptical permalloy dots: A Brillouin light scattering investigation as a function of dot eccentricity. *Phys. Rev. B* 72: 184419-1-8.
131. Gubbiotti, G., Madami, M., Tacchi, S., et al. 2006. Field dependence of spin excitations in NiFe/Cu/NiFe trilayered circular dots. *Phys. Rev. B* 73: 144430-1-6.
132. Goncharov, A. V., Zhukov, A. A., Metlushko, V. V., et al. 2006. In-plane anisotropy of coercive field in permalloy square ring arrays. *J. Appl. Phys.* 99: 08Q508-1-3.
133. Liu, H. Y., Wang, Z. K., Lim, H. S., et al. 2005. Magnetic-field dependence of spin waves in ordered permalloy nanowire arrays in two dimensions. *J. Appl. Phys.* 98: 046103-1-3.
134. Wang, Z. K., Kuok, M. H., Ng, S. C., et al. 2002. Spin-wave quantization in ferromagnetic nickel nanowires. *Phys. Rev. Lett.* 89(2): 027201-1-3.
135. Peng, Y., Shen, T. -H., and Ashworth, B. 2003. Magnetic nanowire arrays: A study of magneto-optical properties. *J. Appl. Phys.* 93(10): 7050–7052.
136. Hyun Min, J., Ung Cho, J., Kim, Y. K. et al. 2006. Substrate effects on microstructure and magnetic properties of electrodeposited Co nanowire arrays. *J. Appl. Phys.* 99: 08Q510-1-2.
137. Miyashita, T. 2005. Sonic crystals and sonic wave-guides. *Meas. Sci. Technol.* 16: R47–R63.
138. Joannopoulos, J. D., Villeneuve, P. R., and Fan, S. 1997. Photonic crystals: putting a new twist on light. *Nature* 386: 143–149.
139. Gurevich, A. G. and Melkov, G. A., 1994. *Magnetic Oscillation and Waves*. Moscow: Nauka.
140. Wolfram, T. and De Wames, R. E. 1972. Surface dynamics of magnetic materials. *Prog. Surf. Sci.* 2: 233 (ed.) S. G. Davison, Oxford: Pergamon.
141. Puszkarski, H. 1979. Theory of surface states in spin wave resonance. *Prog. Surf. Sci.* 9: 191–247.
142. Patton, C. E. 1984. Magnetic excitations in solids. *Phys. Rep.* 103(5): 251–315.
143. Xiong, S. 1987. Spin waves in quasi-periodic layered structures. *J. Phys. C: Solid State Phys.* 20(10): L167–L174.
144. Kolar, M. and Ali, M. K., 1989. Magnetic excitations in some generalised Fibonacci layered structures. *J. Phys.: Condens. Mat.* 1: 823–828.
145. Brillouin, L. and Parodi, M. 1956. *Propagation des Ondes dans les Milieux Periodiques*. Paris: Malson Dunod.
146. Yariv, A. and Yeh, P. 1984. *Optical Waves in Crystals*. New York: A Wiley-Interscience Publication.
147. Laso, M. A., Erro, M. J., Benito, D., et al. 1999. Analysis and design of 1-D photonic bandgap microstrip structures using a fiber grating model. *Microw. Opt. Technol. Lett.* 22: 223–226.
148. Xinhua Hu, Chan, C. T., Jian Zi, et al. 2006. Diamagnetic response of metallic photonic crystals at infrared and visible frequencies. *Phys. Rev. Lett.* 96: 223901-1-4.
149. Weber, M. and Mills, D. L. 1983. Interaction of electromagnetic wave with periodic gratings: Enhanced fields and the reflectivity. *Phys. Rev. B.* 27(5): 2698–2709.
150. Mingaleev, S. F. and Kivshar, Y. S. 2002. Effective equations for photonic-crystal waveguides and circuits. *Opt. Lett.* 27(4): 231–233.
151. Plihal, M. and Maradudin, A. A. 1991. Photonic band structure of two-dimentional systems: The triangular lattice. *Phys. Rev. B* 44(16): 8565–8571.
152. Sainidou, R., Djafari-Rouhani, B., Pennec, Y., et al. 2006. Locally resonant phononic crystals made of hollow spheres or cylinders. *Phys. Rev. B* 73: 024302-1-7.
153. Kushwaha, M. S., Halevi, P., Martinez, G., et al. 1994. Theory of acoustic band structure of periodic elastic composites. *Phys. Rev. B* 49(4): 2313–2322.
154. Shibata, J., Shigeto, K., and Otani, Y. 2003. Dynamics of magnetostatically coupled vortices in magnetic nanodisks. *Phys. Rev. B.* 67: 224404-1-5.

155. Novosad, V., Grimsditch, M., Guslienko, K. Yu. et al. 2002. Spin excitations of magnetic vortices in ferromagnetic nanodots. *Phys. Rev. B* 66: 052407-1-4.
156. Novosad, V., Guslienko, K. Yu., Shima, H., et al. 2002. Effect of interdot magnetostatic interaction on magnetization reversal in circular dot arrays. *Phys. Rev. B* 65: 060402(R)-1-4.
157. Jorzick, J., Demokritov, S. O., Mathieu, C. et al. 1999. Brillouin light scattering from quantized spin waves in micron-size magnetic wires. *Phys. Rev. B* 60(22): 15194–15200.
158. Kostylev, M. P., Stashkevich, A. A., Sergeeva, et al. 2004. Spin wave modes localised on a nano stripe with two dipole coupled layers. *J. Magn. Magn. Mater.* 278: 397–406.
159. Roussigné, Y., Chérif, S. -M., and Moch, P. 2004. Spin waves in a magnetic stripe submitted to a perpendicular magnetic field. *J. Magn. Magn. Mater.* 268(1–2): 89–94.
160. Kostylev, M. P., Gubbiotti, G., Hu, J. -G., et al. 2007. Dipole-exchange propagating spin-wave modes in metallic ferromagnetic stripes. *Phys. Rev. B* 76: 054422-1-8.
161. Gubbiotti, G., Carlotti, G., Ono, T., et al. 2006. High frequency magnetic excitations in patterned NiFe/Cu/NiFe trilayered stripes subjected to a transverse magnetic field. *J. Appl. Phys.* 100: 023906-1-4.
162. Gubbiotti, G., Tacchi, S., Carlotti, G., Ono, T., et al. 2007. Discrete modes of a ferromagnetic stripe dipolarly coupled to a ferromagnetic film: a Brillouin light scattering study. *J. Phys.: Condens. Mat.* 19: 246221-1-14.
163. Vukadinovic, N. and Boust, F. 2007. Three-dimensional micromagnetic simulations of magnetic excitations in cylindrical nanodots with perpendicular anisotropy. *Phys. Rev. B* 75: 014420-1-8.
164. Donahue, M. J. and D. G. Porter. 2004. *OOMMF User's Guide. Version 1.1b2*. Gaithersburg, MD: National Institute of Standards and Technology. http://math.nist.gov/oommf.

35

Nonlinear Metamaterials

Mikhail Lapine
Universitat Osnabruck

Maxim Gorkunov
Institute of Crystallography

35.1 Introduction

With the rapid progress in the field of metamaterials over the course of last years, it is not surprising that we came across the idea of nonlinear metamaterials as soon as the basics for macroscopic description have been developed and close analogy to optical crystals revealed. Pioneering publications [1,2] on the new subarea date back to 2003, reporting two approaches to proceed with nonlinear effects in metamaterials. As we shall see below, the two approaches are the same in essence, yet different analysis methodologies were developed, each proving advantageous depending on the problem under consideration.

It is clear that nonlinear optics, on the one hand, and microwave engineering with nonlinear components on the other, proved fruitful over more than half a century; metamaterials allowed then for an efficient synthesis of knowledge gained in both research areas.

Later on, the subject attracted attention of many research groups [3–12], and we will next address in detail some of particular research achievements in these and numerous further publications.

35.2 Providing Nonlinearity

The wide variety of methods providing metamaterials with nonlinear response can be divided, conceptually, into three approaches, which are schematically introduced in Figure 35.1.

The first one is, structurally, a most straightforward one, following directly from the analogy to optical crystals. In crystals, various intrinsic nonlinearities (mostly on the atomic level) naturally provide nonlinear response starting from moderate intensities. In metamaterials, with the structural

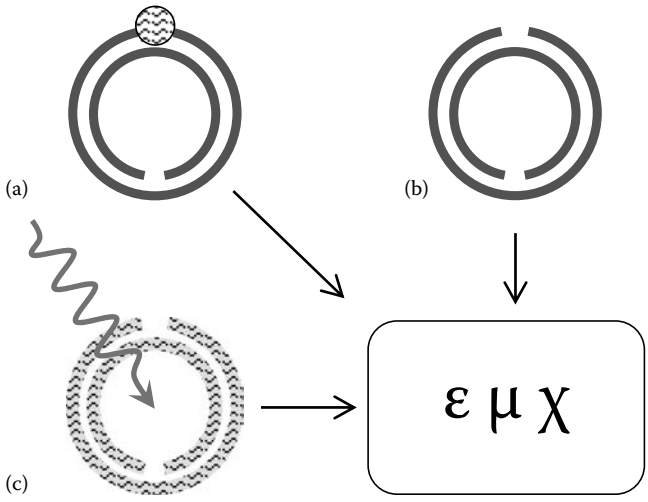

FIGURE 35.1 Providing nonlinearity to metamaterials (conceptual illustration): (a) insertion, (b) immersion, and (c) extreme intensity; theoretical description in terms of metamacroscopic parameters.

units being artificially assembled, the response (up to very high amplitudes of the fields and currents) is essentially linear as long as the effective contour comprises linear components (basically, inductance, capacitance, and resistance). A very natural way to achieve nonlinearity is, therefore, to add a nonlinear component (such as a diode) to the linear contour, that is, to insert it into the structural element, and that was suggested in 2003 giving birth to the whole subject [1]. Now we call this an *insertion* method (Figure 35.1a).

General logic underlying the first approach, however, was not really new. A long time before metamaterials came into play, in 1991, Kalinin and Shtykov considered [13] an amorphous medium built with randomly oriented dipoles each being loaded with a diode. The goal there was to achieve phase conjugation at microwave frequencies in wave-only scheme. The authors found, however, that the emerging third-order nonlinear susceptibility is suppressed by dissipation so that the efficiency of that particular design remained doubtful at that time.

The second approach is quite natural as well, aiming to complement linear response of metamaterial elements with nonlinear properties of the host medium, in which the fields, resonantly enhanced within metamaterial elements, become nonlinearly coupled. We now call that an *immersion* method (Figure 35.1b). This alternative suggestion followed shortly in 2003 [2] and stimulated rapid development of this research direction.

The grounding idea of this approach dates back to 1999 [14] and in essence it suggests to exploit advantageous properties of metamaterials: individual elements can be specifically designed and it is, in particular, possible to achieve highly inhomogeneous electromagnetic fields distribution with the structural unit, so that the fields become enhanced remarkably. So placing an external nonlinear medium within the areas of enhanced field eventually leads to overall nonlinear response.

However different the two approaches might appear, there is, in fact, much in common between them. Indeed, as it was just mentioned, when metamaterial element is immersed into nonlinear host, the nonlinear response of the latter occurs at most within certain areas where fields are enhanced. For instance, for a ring resonator, electric field is by many orders of magnitude stronger within the gap so the nonlinearity is, in essence, the same as if it was provided by a nonlinear device placed there in the contour. This similarity holds as long as the wavelength is much larger than the element size, so, as long as metamaterial concept is valid. Therefore, basic phenomenological description can be

the same for both the methods, while further details must be taken into account for more specific analysis of particular implementations for various nonlinear phenomena.

The difference between the insertion and immersion roads lies rather in the area of implementation. Insertion allows for a very detailed design with any available device being placed at any point in the structure unit, depending on specific needs, so it is somewhat more precise. However, this way becomes increasingly difficult as the intended frequency grows and elements must become smaller. For small elements, it is more feasible to use any variety of immersion, e.g., by printing nanostructures on a nonlinear substrate. Roughly speaking, insertion is therefore more appropriate for microwave range while immersion may prove efficient for infrared and optics.

We should say a few words also on the third approach (Figure 35.1c), which is however much less developed in theory as a rigorous description here is hindered by severe complications that numerous effects of different scale and origin come into play. The logic here is that with the amplitudes and frequencies of incident waves being high enough, intrinsic nonlinearity of metal surface, scattering phenomena on edges, and even quantum effects may add to the mechanisms described above. At the same time, the importance of any specific design in the sense outlined above, becomes diminished. In practice, this situation also often implies that the element size is not much smaller than the wavelength (as it is currently in optical range). Consequently, it is hardly feasible to provide a transparent theory—at least, not a generally applicable one—for such cases, and research attempts rather follow an empirical method, trying and failing. This direction is so far predominantly experimental; it can be traced back to 2006 [15] in metamaterial context. At the same time, earlier works on related subjects [16] may help to provide more theoretical insight into underlying phenomena.

From the theoretical point of view, all the approaches finally aim to provide a universal description of possible nonlinear processes in terms of effective medium parameters (linear ϵ and μ) including nonlinear susceptibilities of required order (Figure 35.1). Therefore, theoretical work splits into two directions, one pursuing rigorous analytical derivation of nonlinear properties starting from very detail of metamaterial internal structure (being thus a *metamacroscopic* theory), while the other concentrating on the description of particular phenomena departing from phenomenological effective parameters as predefined ones. Although the latter saves effort required for analyzing particular structure, it should be exercised with more care than in optics, as there are much more peculiarities in metamaterials which might be crucial for the description.

A close way to practical implementation is to employ nonlinear devices within transmission-line realizations of metamaterials [17,18]. This approach is addressed in more detail in Part VI of this handbook.

35.3 Metamacroscopic Theory for Low Nonlinearity

As we mentioned above, the theoretical basics for description of both the insertion and immersion approaches—apart from specific features added by any particular configuration—must be essentially the same. Taking into account the importance of these general basics, in this section we will describe in detail how metamaterials featuring nonlinearity can be analyzed for a case of low amplitudes: when nonlinear contribution is small with respect to linear response. For the ease of explanations, however, we assume by default that the nonlinearity is provided using insertion approach.

Below, we show how the macroscopic properties of metamaterial can be controlled by the parameters of the structure elements, their arrangement, and the characteristics of nonlinear insertions.

35.3.1 Macroscopic Description of Metamaterials: Basic Principles

It is important to note that, properties of metamaterials with respect to electromagnetic waves can be described in terms of macroscopic permittivity and permeability, if the wavelength inside the medium is much larger than both the element size and the distances between neighboring elements.

For magnetic metamaterials, considered in this section, we shall focus on the magnetic properties, described with (linear) permeability and nonlinear magnetic susceptibilities.

In agreement with the macroscopic theory [19–21], the resonance frequency of the permeability is not determined solely by structure element characteristics, but depends markedly on the lattice parameters as well.

In most cases, when the dimensions of the element are much smaller than the wavelength, it can be described in terms of an effective electric contour, characterized with effective resistance R, inductance L, and capacitance C. To this end, we assume that the current, magnetically induced in the contour, is the same along the contour line.

The simplest example of such an element is a split conductive ring, for which contour parameters can be easily estimated theoretically. Various complex elements, like split ring resonators [14,22], also can be represented by effective contours, provided that the current cross-section is small enough compared to the element size [23,24,45]. Should the effective contour parameters escape from analytical treatment, they can be easily determined experimentally by studying resonant properties of a single element [26]. Accordingly, below we consider resonant elements in general, turning to particular examples where necessary.

We suppose such flat elements to be arranged so that their planes are parallel (normal to the z-axis) and the elements form a kind of regular lattice. As in the local response theory [19,20], we postulate that the response is formed at distances much smaller than the wavelength, i.e., we can neglect retardation while considering interactions of the individual elements. This quasistatic limit allows us to separate magnetic effects from electric ones so that only the magnetic field affects the magnetization of the medium, defining the permeability. In a quasistatic approximation, the problem can be reduced to the behavior of metastructure in an external homogeneous oscillating magnetic field.

35.3.2 Split Ring with In-Series Nonlinear Insertion

Considering nonlinear coupling in metamaterials, we are interested in the relationship between the magnetization of metamaterial and the macroscopic magnetic fields inside it, at all the frequencies involved. We have seen that magnetization is determined by the currents, induced in individual elements by the fields of propagating waves. Should the response of an element be nonlinear, a coupling between these currents arises. Obviously, mutual interaction of elements remains linear and is not relevant at this stage. Consequently, in the metamaterial of split rings with nonlinear insertions, wave coupling is provided on the level of structure elements. Thus we are first looking for the relationship between currents and voltages, induced at all the interacting frequencies, analyzing a single element, subjected to oscillating magnetic field.

Supposing the time dependence of fields and currents to have the oscillating form $e^{-i\omega t}$, one can write the electromotive force $\mathcal{E}_n$ in the nth element, induced by the external field $\mathcal{H}$, as

$$\mathcal{E}_n = i\omega\mu_0 S\mathcal{H}, \tag{35.1}$$

where S is an effective area of the contour, which determines the magnetic flux via element.

The linear properties of each element are defined by the same self-impedance so that we can write

$$Z = -i\omega L + \frac{i}{\omega C} + R, \tag{35.2}$$

where we treat the self-inductance L, the capacitance C, and the resistance R, as predefined.

The DC current–voltage characteristic of an insertion at low voltages can be approximated by

$$I = \frac{1}{\mathcal{R}_0}(U + \gamma U^2), \tag{35.3}$$

where
I is the current through the insertion to which the voltage U is applied
$\mathcal{R}_0$ is the ohmic resistance of insertion
γ is a parameter standing for the nonlinearity

Here the voltage should be much smaller than $\tilde{U} \sim 1/\gamma$.

In the AC case, it is necessary to account for frequency dispersion, which is easier to do if one deals with Fourier components. Accordingly, we substitute all the time dependencies by sums of monochromatic components, so that, e.g., the time dependence of the current is $I(t) = \sum_\vartheta I(\omega_\vartheta)e^{-i\omega_\vartheta t}$, $\vartheta = \pm 1, \pm 2, \ldots$, where we use the notation with $\omega_{-\vartheta} \equiv -\omega_\vartheta$, $I(\omega_{-\vartheta}) \equiv I^*(\omega_\vartheta)$, which includes automatically the complex conjugates.

Due to the nonlinear term in Equation 35.3, Fourier components at combinational frequencies will be coupled. Keeping up to bilinear in I terms, we can represent the voltage–current characteristic as the following:

$$U(\omega_\vartheta) = \mathcal{Z}(\omega_\vartheta)I(\omega_\vartheta) + \frac{1}{2}\sum_\eta \gamma(\omega_\vartheta; \omega_\eta, \omega_\vartheta - \omega_\eta) \times \mathcal{Z}(\omega_\vartheta - \omega_\eta)\mathcal{Z}(\omega_\eta)I(\omega_\vartheta - \omega_\eta)I(\omega_\eta), \tag{35.4}$$

where
$\gamma(\omega_\vartheta; \omega_\eta, \omega_\vartheta - \omega_\eta)$ is generally complex
$\mathcal{Z}(\omega)$ is the linear impedance of the insertion, i.e., $\mathcal{Z} \to \mathcal{R}_0$ at $\omega \to 0$

Clearly, the response of the whole element depends on the particular position and connections of the insertion, implemented into the split ring. However, for a reasonable arrangement, the element with insertion can be still described by effective contour. If the nonlinearity is low, the current in the element with insertion under the action of external e.m.f. is determined by

$$\big(Z(\omega) + \mathcal{Z}(\omega)\big)I(\omega) + U^{(2)}(\omega) = \mathcal{E}(\omega), \quad \text{with} \tag{35.5}$$

$$U^{(2)}(\omega) = \frac{1}{2}\sum_\eta \zeta(\omega_\vartheta; \omega_\eta, \omega_\vartheta - \omega_\eta)I(\omega_\vartheta - \omega_\eta)I(\omega_\eta), \tag{35.6}$$

where $U^{(2)}$ is the nonlinear part of the response. Here the nonlinear properties of insertion are described with the parameter ζ, which generally depends on the insertion characteristics (γ and $\mathcal{Z}$) as well as on the way of inserting. For example, if the insertion is implemented in-series into a split conductive ring:

$$\zeta(\omega_\vartheta; \omega_\eta, \omega_\upsilon) = \gamma(\omega_\vartheta; \omega_\eta, \omega_\upsilon)\mathcal{Z}(\omega_\upsilon)\mathcal{Z}(\omega_\eta). \tag{35.7}$$

Now we are ready with the response of a single element.

35.3.3 Quadratic Magnetic Susceptibility

Turning to analysis of the whole metamaterial, we follow the macroscopic approach, developed for magnetic metamaterials [27].

Let the centers of the metamaterial elements be located at the points $\mathbf{r}_n$. These points are assumed to form a regular spatial lattice so that each element has the same surrounding. We suppose the material of the structure elements to be nonmagnetic so that the magnetization is only due to the currents induced in the contours. Though in general one should consider the full tensor of the permeability, from the chosen geometry it is obvious that the magnetization has only z-component,

i.e., only μ_{zz} differs from unity. Therefore, only the z-component of the magnetic field is important, and the problem becomes scalar. Further we omit all appearing z and zz indices for the ease of notation.

In linear case, using the multi-impedance matrix allows to write

$$\mathcal{E}_n = ZI_n + \sum_{n' \neq n} Z_{nn'} I_{n'}, \tag{35.8}$$

where

I_n is the current induced in the nth element
Z is the self-impedance
$Z_{nn'}$ is the mutual impedance between the elements n and n'

In order to take the insertions into account, we extend the impedance equation (Equation 35.8) in accordance with Equation 35.5, arriving at system

$$\big(Z(\omega) + \mathcal{Z}(\omega)\big) I_n(\omega) + \sum_{n' \neq n} Z_{nn'}(\omega) I_{n'}(\omega) + U_n^{(2)}(\omega) = \mathcal{E}_n(\omega), \tag{35.9}$$

where $\mathcal{E}_n(\omega)$, the same for all the elements, is given by Equation 35.1;

$$\mathcal{E}(\omega) = i\mu_0 S\omega \mathcal{H}(\omega). \tag{35.10}$$

We remind that in the homogeneous metamaterial all the currents, induced by e.m.f. (Equation 35.10), are equal, and so the system (Equation 35.9) is reduced to the equation

$$\Big[Z(\omega) + \mathcal{Z}(\omega) + \sum_{n' \neq n} Z_{nn'}(\omega)\Big] I(\omega) + U^{(2)}(\omega) = \mathcal{E}(\omega). \tag{35.11}$$

For the ease of notation, we combine all the impedances involved, into

$$Z_\Sigma(\omega) = Z(\omega) + \mathcal{Z}(\omega) + \sum_{n' \neq n} Z_{nn'}(\omega). \tag{35.12}$$

Rewriting Equation 35.11 for multiple frequencies, with the help of Equation 35.6 we obtain a system:

$$Z_\Sigma(\omega_\vartheta) I(\omega_\vartheta) = \mathcal{E}(\omega_\vartheta) + \frac{1}{2} \sum_\eta \zeta(\omega_\vartheta; \omega_\eta, \omega_\vartheta - \omega_\eta) I(\omega_\vartheta - \omega_\eta) I(\omega_\eta). \tag{35.13}$$

The system (Equation 35.13) shows that the current component at each frequency is determined not only by the e.m.f. at that frequency, but also by the current components induced at two other frequencies, so that a three-wave interaction occurs. Accordingly, we consider below ω_1, ω_2, and ω_3, such that $\omega_1 + \omega_2 = \omega_3$. Then from Equation 35.13 we get for the current induced at ω_3:

$$Z_\Sigma(\omega_3) I(\omega_3) = \mathcal{E}(\omega_3) + \zeta(\omega_3; \omega_1, \omega_2) I(\omega_1) I(\omega_2). \tag{35.14}$$

For the linear in ζ approximation we can substitute $I(\omega_2)$ and $I(\omega_1)$ in the right-hand side of Equation 35.14 for the expressions, obtained from Equation 35.13 written for ω_1, ω_2, neglecting the terms with ζ. Then we can express $I(\omega_3)$ via $\mathcal{E}(\omega_1)$, $\mathcal{E}(\omega_2)$, and $\mathcal{E}(\omega_3)$.

The averaged media magnetization, defined as the magnetic moment density, is given by

$$M = \aleph SI, \tag{35.15}$$

where the volume concentration ℵ is introduced. Thus, for the magnetization at ω_3 we get

$$M(\omega_3) = \frac{i\aleph\mu_0 S^2\omega_3}{Z_\Sigma(\omega_3)}\mathcal{H}(\omega_3) - \frac{\zeta(\omega_3;\omega_1,\omega_2)\aleph\mu_0^2 S^3\omega_1\omega_2}{Z_\Sigma(\omega_3)Z_\Sigma(\omega_2)Z_\Sigma(\omega_1)}\mathcal{H}(\omega_1)\mathcal{H}(\omega_2), \tag{35.16}$$

where we used relations (Equations 35.10 and 35.15).

The total microscopic magnetic field (in the sense of being microscopic with respect to metamaterial properties) at the point $\mathbf{r}$ is given by the sum of the external field and the contribution of the separate elements:

$$H_{\text{mic}}(\mathbf{r}) = \mathcal{H} + \sum_n H_l(\mathbf{r} - \mathbf{r}_n), \tag{35.17}$$

where the function $H_l(\mathbf{r}')$ is defined as the value of the z-component of the magnetic field induced by the element, located at the coordinate origin, at the point $\mathbf{r}'$. According to the Biot-Savart's law $H_l(\mathbf{r}')$ can be presented as an integral along the contour:

$$H_l(\mathbf{r}') = \frac{I}{4\pi}\int \frac{[\mathrm{d}\mathbf{l}\times(\mathbf{r}'-\mathbf{s})]_z}{|\mathbf{r}'-\mathbf{s}|^3}, \tag{35.18}$$

where the vector $\mathbf{s}$ is the radius vector of that point of the contour, where $\mathrm{d}\mathbf{l}$ is taken.

Since all the unit cells are identical, the field distribution is the same in all the cells. Therefore, the macroscopic averaging can be performed over the volume $V_m = \aleph^{-1}$ of one unit cell with any number m. The averaged value of the microscopic magnetic field (Equation 35.17) yields the macroscopic induction:

$$B = \mu_0\langle H_{\text{mic}}\rangle = \mu_0\mathcal{H} + \frac{\mu_0}{V_m}\sum_n \int_{V_m} \mathrm{d}\mathbf{r}\, H_l(\mathbf{r} - \mathbf{r}_n). \tag{35.19}$$

The radius vector $(\mathbf{r} - \mathbf{r}_n)$ passes all the cells with centers at $(\mathbf{r}_m - \mathbf{r}_n)$, where m takes all possible values. The summation over all n in Equation 35.19 provides the result which is independent of the particular number m so that we can write

$$B = \mu_0\mathcal{H} + \aleph\mu_0\sum_{n'}\int_{V_{n'}} \mathrm{d}\mathbf{r}H_l(\mathbf{r}) = \mu_0\mathcal{H} + \aleph\mu_0\int_V \mathrm{d}\mathbf{r}H_l(\mathbf{r}). \tag{35.20}$$

The integration in the last term is to be performed over the large macroscopic volume V of the whole medium. We take the latter as the limit of a large sphere O, centered at the coordinate origin, with the radius r_s tending to infinity. Using the relation

$$\lim_{r_s\to\infty}\int_O \mathrm{d}\mathbf{r}\frac{\mathbf{r}'-\mathbf{s}}{|\mathbf{r}'-\mathbf{s}|^3} = -\frac{4\pi}{3}\mathbf{s}, \tag{35.21}$$

it is easy to obtain

$$\int_O \mathrm{d}\mathbf{r}H_l(\mathbf{r}) = \frac{2}{3}SI = \frac{2}{3}\frac{M}{\aleph}, \tag{35.22}$$

which enables us to conclude that generally

$$B = \mu_0\left(\mathcal{H} + \frac{2}{3}M\right), \tag{35.23}$$

notwithstanding the structure element's peculiarities.

With the general definition $B = \mu_0(H + M)$, we can express

$$\mathcal{H} = H + \frac{1}{3}M. \tag{35.24}$$

Using this relation, we can solve Equation 35.16 for $M(\omega_3)$. In the linear approximation we obtain $M(\omega_3) = \chi_M(\omega_3)H(\omega_3)$, where the factor

$$\chi_M(\omega) = \frac{\mu_0 \aleph S^2 \omega}{-\frac{1}{3}\mu_0 \aleph S^2 \omega - iZ_\Sigma(\omega)}. \tag{35.25}$$

stands for the linear part of the magnetic susceptibility.

The sum of the matrix elements is determined by the mutual inductance between elements. For example, in the limit of thin wires it is given by the double integral along the contours:

$$Z_{nn'} = i\omega \frac{\mu_0}{4\pi} \iint \frac{(d\,\mathbf{l}_n \cdot d\,\mathbf{l}_{n'})}{|\mathbf{s}_n - \mathbf{s}_{n'}|}. \tag{35.26}$$

Thus, the sum can be represented as

$$\sum_{n' \neq n} Z_{nn'}(\omega) = -i\omega\mu_0 r\Sigma, \tag{35.27}$$

where

r is some characteristic dimension of the element

Σ is a dimensionless parameter which depends only on geometry (lattice metastructure) and can be calculated numerically (see [27] for some examples)

One can see that the relation (Equation 35.25) is affected by the lattice order via the sum Σ only. This summation is performed over all the elements, i.e., over the macroscopic volume. This volume should be the same as for the averaging procedure, and we use the same spherical limit. Actually, it is necessary to perform the summation only over a finite and relatively small number of elements that are located in the volume near the nth one. Further increase in the radius r_s does not influence the summation result. For a good numerical accuracy of a few percent it is sufficient to set r_s to be only six times larger than the lattice constant. This satisfactory value of the distance r_s can be considered as a characteristic length of the local response L_{resp}. Although for different lattice types and various lattice constants L_{resp} differs in magnitude, it is, as a rule, of the order of several interelement distances. The length L_{resp} is the parameter the wavelengths and sample dimensions should be compared with to make the macroscopic effective response approach valid.

Note that, the corresponding permeability $\mu(\omega) = 1 + \chi_M(\omega)$, upon algebraic conversion, can be rewritten in the general resonance form:

$$\mu(\omega) = 1 - \frac{A\omega^2}{\omega^2 - \omega_r^2 + i\Gamma\omega}, \tag{35.28}$$

with the resonance amplitude and width

$$A = \mu_0 S^2 \aleph L^{-1} \frac{\omega_r^2}{\omega_0^2}, \quad \Gamma = RL^{-1} \frac{\omega_r^2}{\omega_0^2}, \tag{35.29}$$

and the resonance frequency of the medium

$$\omega_r = \omega_0 \left(1 + \mu_0 r\Sigma L^{-1} + \frac{1}{3}\mu_0 S^2 \aleph L^{-1}\right)^{-1/2} = \omega_0 \left(\frac{L_\Sigma}{L} + \frac{1}{3}\frac{\mu_0 \aleph S^2}{L}\right)^{-1/2}, \tag{35.30}$$

where we introduced a combined mutual and self-inductance $L_\Sigma = L + \mu_0 r\Sigma$, using relation (Equation 35.27).

Consequently, $\chi_M(\omega)$ shows resonance behavior with the resonance frequency (Equation 35.30).

Returning to the first order nonlinear consideration and keeping the terms linear in ζ, we express finally $M(\omega_3)$ in a form which is analogous to the polarization of a medium with quadratic dielectric nonlinearity:

$$M(\omega_3) = \chi_M(\omega_3)H(\omega_3) + \chi_M^{(2)}(\omega_3;\omega_1,\omega_2)H(\omega_1)H(\omega_2) \tag{35.31}$$

with the quadratic nonlinear susceptibility

$$\chi_M^{(2)}(\omega_3;\omega_1,\omega_2) = \frac{\zeta(\omega_3;\omega_1,\omega_2)}{i\mu_0 S^3\omega_3}\,\aleph^{-2}\chi_M(\omega_1)\chi_M(\omega_2)\chi_M(\omega_3). \tag{35.32}$$

Analyzing the structure of Equation 35.32, it is easy to notice that the first factor is completely determined by the single element properties. Its multiplication with the linear susceptibilities taken at the frequencies of interacting waves performs a kind of renormalization and can be treated as the result of the influence of the surroundings. This kind of renormalization appears, for instance, in the derivation of nonlinear dielectric susceptibility in optical materials [28,29]. Like the optical nonlinearity, the nonlinearity of the magnetic metamaterial increases resonantly as one of the frequencies involved approaches the resonance of the linear susceptibility.

35.3.4 Practical Estimates for Low Nonlinearity

To estimate the macroscopic characteristics of the nonlinear metamaterial of the presented type, we consider an example of metastructure based on split rings with radius $r_0 = 2\,\text{mm}$ and wire diameter $r_w = 0.1\,\text{mm}$, arranged with the density $\aleph \sim r_0^{-3}$. Among numerous diode types, backward diodes were reported to possess the best sensitivity and the highest nonlinearity [30,31]. Such a diode insertion, having a cross-section, similar to the wire, is characterized [31] by $\gamma \approx 30\,\text{V}^{-1}$ and $\mathcal{Z} \approx \mathcal{R}_0 \approx 10\,\Omega$. Although diodes might allow for higher nonlinearity, Equation 35.4 is valid only under the assumption that the nonlinear contribution is much smaller than the linear one. They become comparable when the current reaches characteristic value $\tilde{I}(\omega)\sim\left(|\gamma\mathcal{Z}(\omega)|\right)^{-1}$, which corresponds to the magnetization $\tilde{M}(\omega) = nS\tilde{I}(\omega)$. Accordingly, the magnetic field in the metamaterial must be much lower than $\tilde{H}(\omega) = \tilde{M}(\omega)/\chi_M(\omega)$. Assuming that the pump frequency is ω_1, and $H(\omega_1) \sim 0.1\tilde{H}(\omega_1)$, using Equation 35.7, we can estimate the maximal amplitude of the nonlinear modulation of the magnetic susceptibility as

$$\chi_M^{(2)}(\omega_2;\omega_0,\omega_1)H(\omega_1) \sim 0.1\frac{\mathcal{Z}(\omega_2)}{\mu_0\aleph S^2\omega_3}\chi_M(\omega_1)\chi_M(\omega_2). \tag{35.33}$$

For frequencies not close to the resonance, we can assume $\chi_M(\omega_1)\chi_M(\omega_2) \sim 1$, which provides a noticeable nonlinear contribution of the order of 0.001 with the pump field limited by about 0.1 A/m.

The nonlinearity can be further enhanced by either decreasing the diode cross-section (that raises $\mathcal{Z}$), or choosing the frequencies closer to the resonance. However, both of these ways are accompanied by the increase of dissipation losses in the media. For practical purposes one has to ensure that the losses do not exceed the nonlinear contribution. To remain in the transparency region $\text{Re}[\chi_M(\omega)] \gg \text{Im}[\chi_M(\omega)]$ the condition $\left|1-\omega_r^2/\omega^2\right| \gg \mathcal{R}_0/\omega L$ must be fulfilled (the overall ohmic resistance R of the whole element is build mostly by the diode resistance $\mathcal{R}_0$). Then the figure of merit for this metastructure takes a simple form:

$$\frac{\chi_M^{(2)}(\omega_2;\omega_0,\omega_1)H(\omega_1)}{\text{Im}[\chi_M(\omega_2)]} \sim \frac{|\mathcal{Z}(\omega_2)|}{\mathcal{R}_0}\,\frac{1-\omega_r^2/\omega_3^2}{1-\omega_r^2/\omega_2^2}, \tag{35.34}$$

and its larger values are favorable. This relation shows that choosing one of the frequencies closer to the resonance one can win in the parameters at one frequency, but inevitably loose at the other. The ratio (Equation 35.34) appears to be independent of the diode cross-section. Nonlinearity and losses grow equally as the diode gets smaller. Therefore, the only way to improve (Equation 35.34) is to increase the ratio $|\mathcal{Z}(\omega)|/\mathcal{R}_0$. As in backward diodes the linear impedance is mostly concerned with the ohmic losses, $|\mathcal{Z}(\omega)| \sim \mathcal{R}_0$, their usage can be limited by significant damping.

The above estimates show that in the limit of low nonlinearity a remarkable modulation of the susceptibility is accompanied by substantial dissipation. Certainly, applying higher pump fields will provide higher nonlinear contribution. However, high nonlinearity would make the susceptibility expansion in the form (Equation 35.31) inapplicable, and the corresponding analysis requires an extended approach, described in the next section.

The theory outlined above provides general phenomenology which is applicable for any type of nonlinear insertion or surrounding host medium, so that effective magnetization is determined by magnetic fields expanded in a power series (see Equation 35.31), and nonlinear susceptibilities of required order can be found, given any particular element characteristics.

Expression (Equation 35.31) shows a clear analogy to the relationship between electric polarization and electric fields, well-known in nonlinear optics [19,20,28]. Therefore, in spite of the completely different physical background, one can deal with the nonlinear interaction of electromagnetic waves in the proposed metamaterial using the well-developed apparatus of the nonlinear optics. The general symmetry of Maxwell equations with respect to the magnetic field–electric field transposition allows to expect that the whole variety of known nonlinear optical processes can have corresponding analogy in metamaterials.

35.4 Nonlinear Phenomena and Processes

Below we will briefly overview the current progress in analyzing various nonlinear phenomena and peculiarities of nonlinear processes available in metamaterials.

35.4.1 Frequency Conversion

It has been clearly shown that for the interaction of waves being relatively weak, nonlinear frequency conversion is described with the apparatus fully analogous to nonlinear optics [1,3]. Moreover, it is a specific advantage of metamaterials that the unusual linear properties of metamaterials, e.g., negative refraction, may result in interesting peculiarities of wave interaction.

For example, when the pump wave propagates in backward regime inside nonlinear metamaterial, it is possible to achieve second harmonic (SH) generation in the direction of reflected wave [32]. In a case that a SH wave is a backward wave, dispersion relations ensure that the material is opaque with regards to the pump, and thus generation commences in a thin surface layer. This provides a possibility to realize subwavelength imaging at a doubled frequency [33]. Furthermore, one can combine two or more different structural elements within metamaterial, with the resonant frequencies so chosen that all the interacting waves would match the vicinity of medium resonances. This way, a resonant enhancement of nonlinear interaction can be achieved so that in thin samples, the intensity of SH wave can be enhanced by more than one order in magnitude [34].

Recently, peculiar features associated with phase-locked harmonic generation, and interesting spatio temporal pulse propagation effects were reported [35].

For example, for a pump incident onto nonlinear metamaterial with negative parameters, if the interaction occurs outside of phase-matching conditions, the pump generates a reflected SH signal, part of which is able to immediately leave the medium, while part of it is generated just inside the medium, but is not able to escape as it becomes trapped by the pump.

Figure 35.2 shows a few snapshots of the SH generation in a negative-index metamaterial (NIM) slab divided into linear and nonlinear regions. It can be seen that the first pulse is generated backward, while two pulses are seen to depart from the entry surface, one downward, which refracts according to material dispersion and Snells law, one upward, phase-locked and trapped by the pump pulse. The authors show that although the index of refraction at the SH frequency is positive, nevertheless, the signal refracts negatively, following the pump pulse. Once the pulse reached the interface that separates a linear from a nonlinear NIM, the SH pulse is freed from the pulse, and is retro reflected in the direction whence it came [35].

Specific features of nonlinear metamaterials become clearly evident as the intensity of the interacting waves grow. For a strong pump wave $H(\omega_1)$, nonlinear magnetization can be expressed in a generalized form:

$$M(\omega_3) = \chi_M(\omega_3)H(\omega_3) + Y\big(\omega_3; H(\omega_1); \omega_1, \omega_2\big)H(\omega_2), \tag{35.35}$$

where the nonlinear modulation Y depends on $H(\omega_1)$ in a complicated way determined by the characteristics of nonlinear insertions [36]. Varying these characteristics, one can obtain a peaking

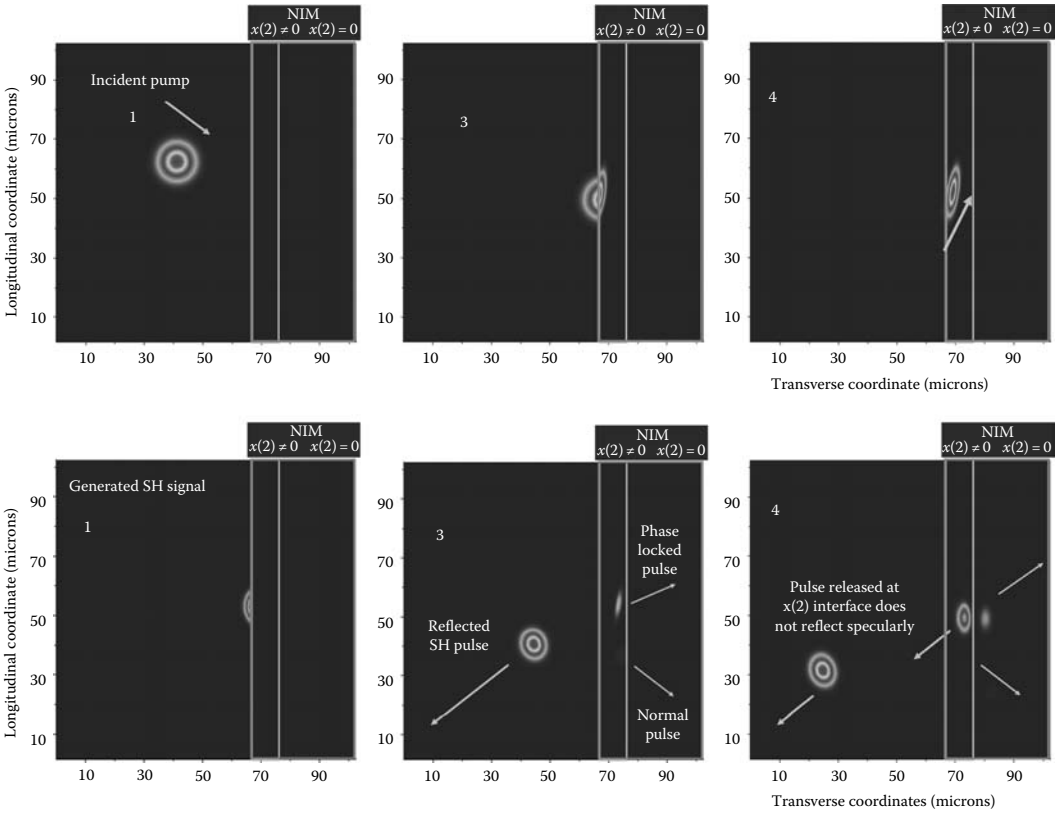

FIGURE 35.2 SH generation (oblique incidence of the pump; undepleted regime) on a negative-index metamaterial (NIM) which is divided into linear and nonlinear portions. Upper series: snapshots of the pump propagation. Lower series: corresponding snapshots of the generated pulses. In snapshot "3" three SH components are visible: reflected pulse; normal pulse (which refracts downward); and phase-locked pulse that follows the same trajectory as the pump. (Reproduced from Roppo, V., Centini, M., de Ceglia, D., Vicenti, M.A., Haus, J.W., Akozbek, N., Bloemer, M.J., and Scalora, M., *Metamaterials*, 2(2–3), 135, 2008. With permission.)

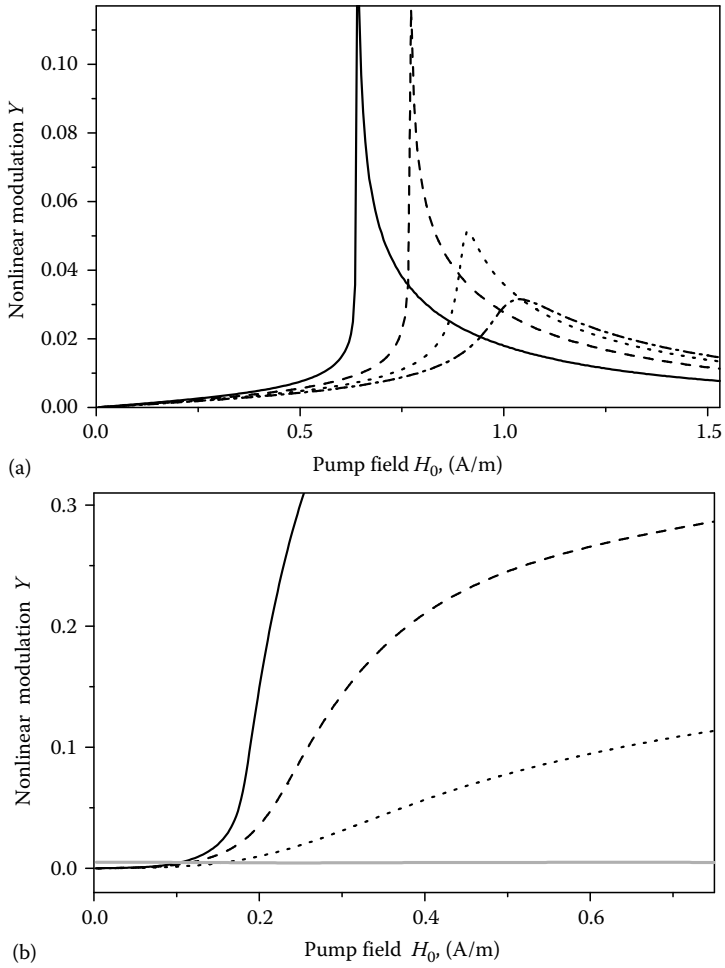

FIGURE 35.3 Nonlinear modulation of magnetization depending on pump wave amplitude, insertion-type nonlinearity. (a) Peaking pattern is typical for backward diodes; various patterns owe to different voltage–current characteristics. (b) Threshold growth pattern is observed with varactors or ferroelectric films; specific curve pattern is determined by particular varactor characteristics [36].

(Figure 35.3a) or an abruptly growing (Figure 35.3b) patterns of nonlinear modulation dependence over the pump intensity, so that the wave interaction is dramatically enhanced, respectively, in a certain narrow range of field amplitude, or above certain threshold value. This provides an important practical advantage, allowing for efficient control over nonlinear coupling through subtle pump amplitude alterations.

Further detailed aspects and particular designs for achieving parametric amplification and SH generation are discussed in many other groups [37,38].

It is pleasant to note that the early idea of microwave phase conjugation which we already mentioned [13] was eventually revisited with a promising design based on periodic lattice of varactor-loaded dipoles [39].

35.4.2 Nonlinear Wave Propagation, Multistability, and Solitons

When phase-matching conditions for various frequency-converging processes are not fulfilled, wave propagation in nonlinear metamaterials occurs in a monochromatic regime. In certain frequency range however, conditions of propagation depend crucially on the signal amplitude. For example, bistability of wave propagation is predicted for the frequencies being close to zero-points or to the resonances of magnetic permeability [2,4]. Switching between the propagation regimes occurs with a hysteresis-type pattern, showing some analogy to the critical phenomena in nonlinear optics and to the phase transition thermodynamics.

Alike most nonlinear media, metamaterials can support solitons, resulting in the propagation of stable signals with an essentially inhomogeneous intensity distribution. For the time being, an impressive variety of soliton types and propagation regimes is described [7,40–42]. More specific effects are expected in the vicinity of permeability resonance. It was shown that, for a signal with amplitude high enough, no stationary wave propagations takes place. Under these conditions, observed when the signal frequency is close to the resonant one, reflected signal intensity fluctuates with time, while the wave inside metamaterial is transformed into periodic solitary set (Figure 35.4) [40,43].

It is well-known that nonlinearity may drastically affect the spectrum and propagation of surface waves, moreover, may even cause the surface states to cease [44]. Similar phenomena were analyzed when studying surface wave propagation along the boundary of nonlinear metamaterials, showing qualitative analogy to the effects known in solid-state physics [9]. At the same time, certain novel phenomena were described, in particular, arising from the counterpropagating energy flows at the two sides of the boundary, caused by negative refractive index inside metamaterial [45]. Figure 35.5 shows that the energy flow associated with surface wave, may occur along the wave

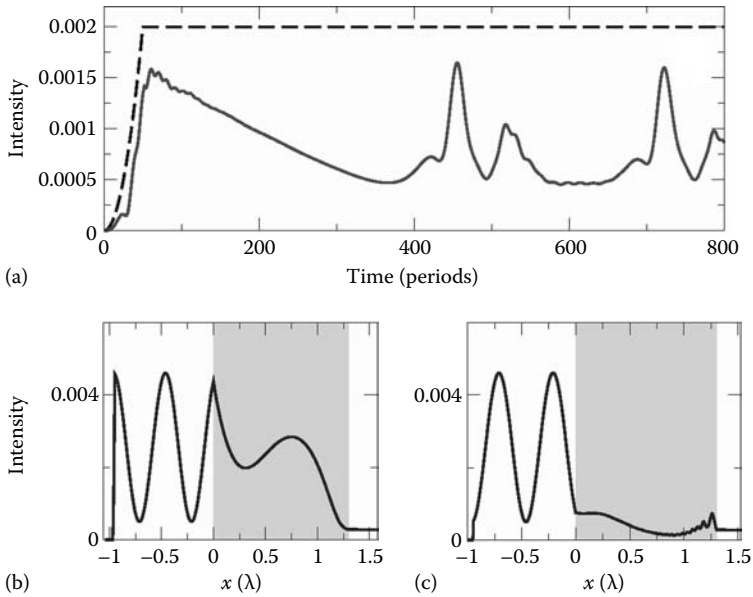

FIGURE 35.4 Instabilities observed in metamaterial (immersion-type nonlinearity): intensities of the incident (dash line) and reflected (solid line) wave (a) varying with time (measured in wave oscillation periods); spacial distribution of the magnetic (b) and electric (c) field amplitudes. Thin metamaterial layer is shown as a grey area. (Reproduced from Zharova, N.A., Shadrivov, I.V., Zharov, A.A., and Kivshar, Y.S., *Opt. Express*, 13, 1291, 2005. With permission.)

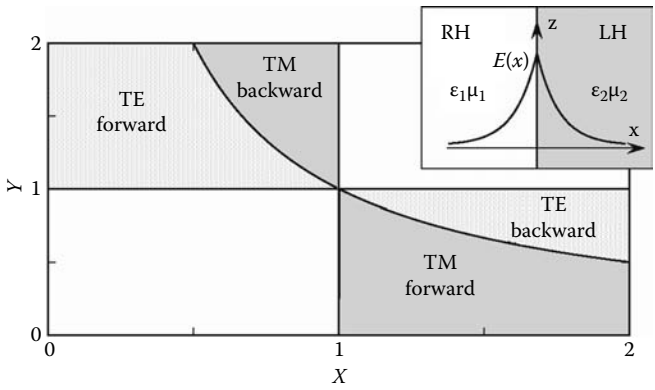

FIGURE 35.5 Permitted ranges of transverse electric (TE) and transverse magnetic (TM) polarizations for forward and backward surface waves on the boundary between media with positive (ϵ_1, μ_1) and negative (ϵ_2, μ_2). Axes show the absolute values of the parameter ratios ($x = |\epsilon_2|/\epsilon_1$, $y = |\mu_2|/\mu_1$). Inset shows the problem geometry and field distributions in the surface wave. (Reproduced from Shadrivov, I.V., Sukhorukov, A.A., Kivshar, Y.S., Zharov, A.A., Boardman, A.D., and Egan, P., *Phys. Rev. E*, 69, 016617, 2004. With permission.)

vector as well as in the opposite direction. Subtle variations of the wave intensity affect the field distribution of the surface mode and therefore allow for efficient switching of the energy transfer direction. Analogous switching opportunities were also predicted for nonlinear metamaterial waveguides [46].

Quite recently, interesting forms of dispersion- and diffraction-management and their impact upon soliton behavior have been considered, for metamaterials having negative phase behavior and at the same time being both active and stable [42,47]. With the nonlinear diffraction suggested, it should be possible to reduce the distance otherwise wasted just to create a stable usable beam (Figure 35.6). This can be achieved in a regular structure, or by introducing an exotic kind of inhomogeneity into the metamaterial. Diffraction-management can be evaluated as an average effect over the whole structure. In such systems, accumulation of phase can be made to vary in sign, and it is possible, in principle, that diffraction could be made extremely small. This could lead to very narrow solitons

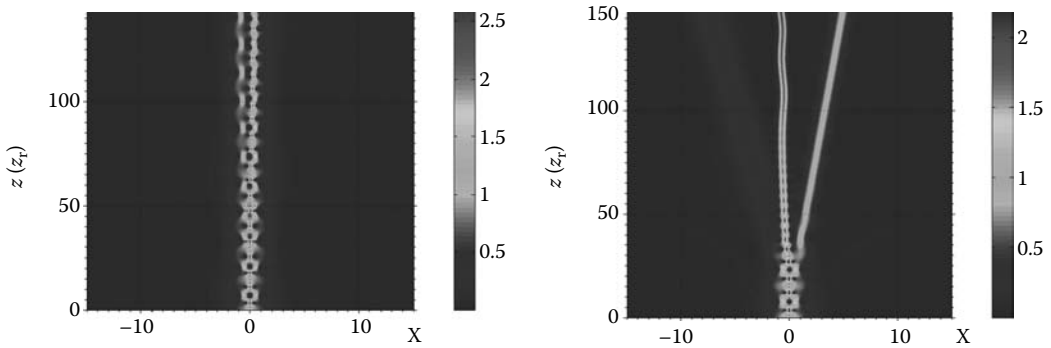

FIGURE 35.6 Diffraction-managed soliton. Evolution of the intensity distributions for an initial input, that has a random signal imposed upon it, modulating its amplitude by 5%: (left) with no correction for nonlinear diffraction, (right) with nonlinear diffraction at 10% level. (Reproduced from Boardman, A.D., King, N., Mitchell-Thomas, R.C., Malnev, V.N., and Rapoport, Y.G., *Metamaterials*, 2(2–3), 145, 2008. With permission.)

that will then be controlled by nonlinear diffraction—so narrow that it can be used to increase data capacity and enhance magneto-optical storage possibilities [42].

35.4.3 Nonlinear Effects with Magnetoinductive Waves

Nonlinear effects in metamaterials in connection with magnetoinductive waves are discussed in Chapter 36 of this handbook, and here we shall only provide a few general remarks and key references.

Generally, involvement of the quasistationary modes in nonlinear processes appears to be quite fruitful owing to low velocities of magnetoinductive waves, leading to the short range of nonlinear interaction. On the other hand, phase matching for the waves of different frequencies proves to be hardly possible as the magnetoinductive spectrum is rather narrow [48]. A class of processes available for a uniform metamaterial this way, refers to parametric interaction of magnetoinductive waves of the same frequency with the "light" modes having wavelengths many orders of magnitude larger. Similar phenomena are long known in ferrites with excited magnons [49]. In metamaterials, an emerging parametric instability of the "light" modes may also occur at certain frequencies and/or amplitudes.

Phase-matching problem, however, can be efficiently solved with multiresonant metamaterials, which offer several branches of dispersion curves [50]. This way, one can easily adjust the necessary parameters so as to satisfy phase-matching conditions for nonlinear interaction of magnetoinductive waves related to different dispersion branches.

In experiment, significant progress is achieved with parametric amplification using rotational resonance of magnetoinductive waves [51].

35.4.4 Tuning and Switching

Apart from various explicitly nonlinear phenomena outlined so far, nonlinear metamaterials open a way to tune the linear properties, allowing for wave propagation control with external fields of waves. As it was shown experimentally [52], biasing a varactor included into metamaterial element, it is possible to change the resonant characteristics remarkably. Detailed theoretical analysis suggests that nonlinear metamaterials can be efficiently tuned [53].

In particular, it is possible to tune metamaterial permeability using an additional wave propagating inside nonlinear metamaterial (or, alternatively, using external varying magnetic field). Such wave causes homogeneous variation of the refractive index, which can be controlled by adjusting the wave amplitude and/or frequency.

On the metamicroscopic level, tuning wave affects resonant frequency and quality factor of individual elements, which in turn affect the resonant frequency and resonance width of the metamaterial permeability. The latter determines the band gap and controls the propagation of weak signal waves through the medium. Consequently, metamaterial can be switched between transmitting, reflecting, and absorbing states.

Particular tuning capabilities depend strongly on the type of nonlinearity. For instance, use of insertions with variable resistance enables tuning of the material transparency (switching between transmitting and absorbing states), in a wide frequency range. Variable capacitance insertions offer control over position of the metamaterial resonance. Shifting the resonance one can switch the whole medium between all the three states with respect to a signal wave at a given frequency.

It was shown that in this way, relatively thin slab (of the order of one wavelength thickness) provides very efficient tuning (Figure 35.7).

Experimental work in this direction [54–56] is well in progress (Figure 35.8).

A related promising research direction is concerned with compensating dissipation with nonlinear [57] or even active metamaterials [47].

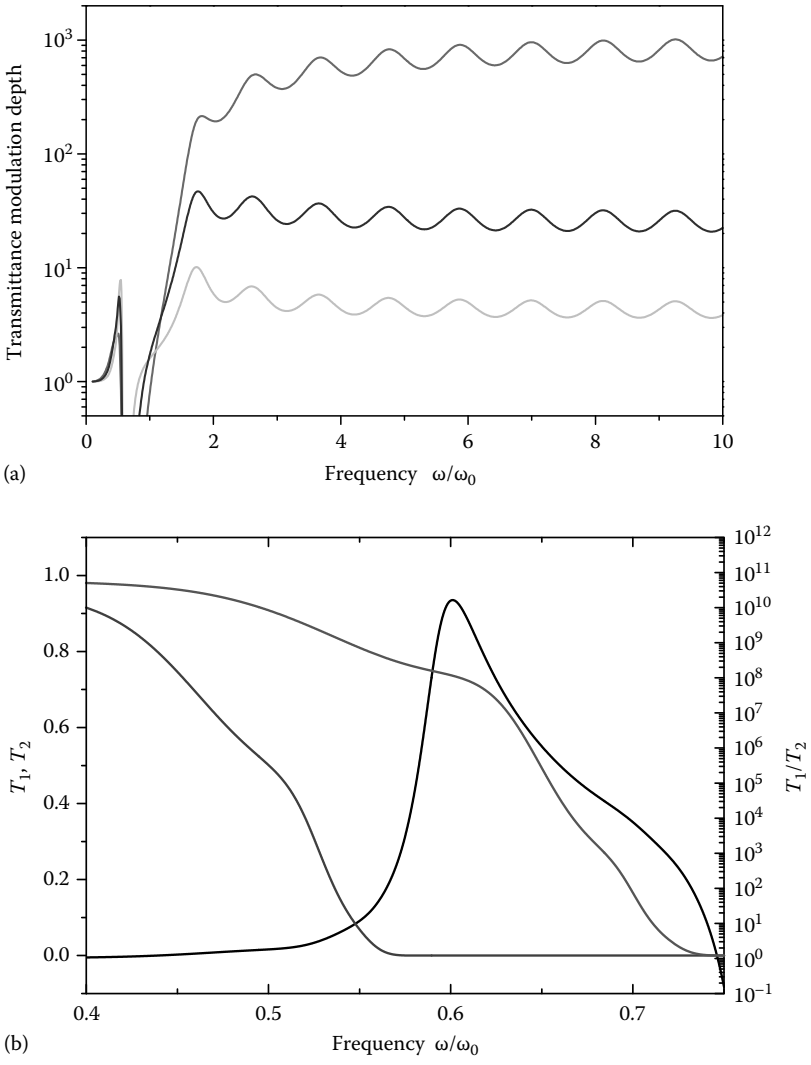

FIGURE 35.7 Tuning efficiency for a thin slab of nonlinear metamaterial. (a) Relative change of slab transmittance for the 5-fold (lower line), 10-fold (middle line), and 20-fold (upper line) decrease of the quality factor induced by tuning wave. (b) Tuning of the slab transmittance with a 30% shift of the band gap induced by tuning wave. Transmittances of the nontuned slab (lower grey line), of the slab with shifted resonance (upper grey line), and resulting transmission modulation (black line) are shown [53].

There are several chapters within this handbook (see Part VI), tackling other approaches to tunable and active metamaterials.

35.5 Concluding Remarks

It is important to note that, the majority of publications on nonlinear metamaterials tend to treat macroscopic characteristics as predefined ones, merely using the resulting parameters for the description of nonlinear phenomena. Such an approach does no take into account specific influence

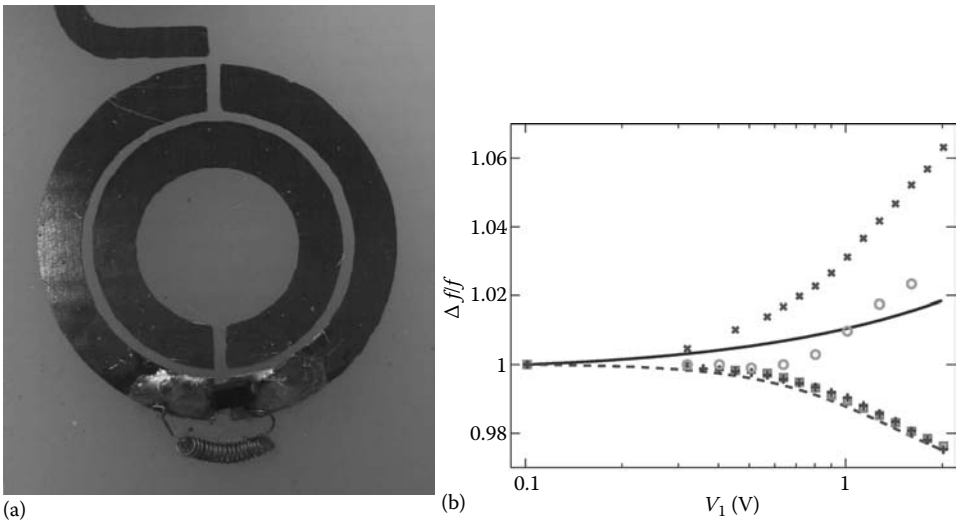

FIGURE 35.8 Experimental observations on tuning a single metamaterial element. (a) Split-ring resonator with inserted varactor (optionally) shunted with an inductive coil to prevent zero-harmonic "memory" effect (courtesy of the authors of Ref. [54]). (b) Shift of the resonant frequency of such split-ring resonator *vs.* diode biasing voltage, (i) predicted analytically without (solid line) and with (dash line) coil, (ii) calculated numerically without (○) and with (+) coil, and (iii) measured without (×) and with (□) coil. (Reproduced from Powell, D.A., Shadrivov, I.V., Kivshar, Y.S., and Gorkunov, M.V., *Appl. Phys. Lett.*, 91, 144107, 2007. With permission.)

of the internal (microscopic) structure of metamaterials, which cannot be always neglected. This imposes evident limitations on the validity of the obtained results. For example, it is clear that the effects of the transition layer forming the boundary of metamaterials, are crucially essential for the surface waves; that strong spatial dispersion must be taken into account for the analysis of solitons; that magnetostatic excitons are important for the nonlinear processes around resonance frequencies, that the effects of microscopic disorder prove to be rather remarkable [58], and so on.

Obviously, correct interpretation of the future experiments, as well as further development, require consistent accounting for the peculiarities of the microscopic metamaterial structure in the spirit outlined in the first sections.

References

1. M. Lapine, M. Gorkunov, and K. H. Ringhofer. Nonlinearity of a metamaterial arising from diode insertions into resonant conductive elements. *Phys. Rev. E*, 67:065601(R), 2003.
2. A. A. Zharov, I. V. Shadrivov, and Y. S. Kivshar. Nonlinear properties of left-handed metamaterials. *Phys. Rev. Lett.*, 91:037401, 2003.
3. V. M. Agranovich, Y. R. Shen, R. H. Baughman, and A. A. Zakhidov. Linear and nonlinear wave propagation in negative refraction metamaterials. *Phys. Rev. B*, 69:165112, 2004.
4. S. O'Brien, D. McPeake, S. A. Ramakrishna, and J. B. Pendry. Near-infrared photonic band gaps and nonlinear effects in negative magnetic metamaterials. *Phys. Rev. B*, 69:241101(R), 2004.
5. M. Scalora, M. S. Syrchin, N. Akozbek, E. Y. Poliakov, G. D. Aguanno, N. Mattiucci, M. J. Bloemer, and A. M. Zheltikov. Generalized nonlinear Schrödinger equation for dispersive susceptibility and permeability: Application to negative index materials. *Phys. Rev. Lett.*, 95:013902, 2005.
6. N. Lazarides and G. P. Tsironis. Coupled nonlinear Schrödinger field equations for electromagnetic wave propagation in nonlinear left-handed materials. *Phys. Rev. E*, 71:036614, 2005.

7. M. Marklund, P. K. Shukla, L. Stenflo, and G. Brodin. Solitons and decoherence in left-handed metamaterials. *Phys. Lett. A*, 341:231–234, 2005.
8. R. S. Hegde and H. G. Winful. Optical bistability in periodic nonlinear structures containing left handed materials. *Microw. Opt. Technol. Lett.*, 46(6):528–530, 2005.
9. S. A. Darmanyan, M. Neviere, and A. A. Zakhidov. Nonlinear surface waves at the interfaces of left-handed electromagnetic media. *Phys. Rev. E*, 72(3):036615, 2005.
10. A. D. Boardman and K. Marinov. Radiation enhancement and radiation suppression by a left-handed metamaterial. *Microw. Opt. Technol. Lett.*, 48(12):2512–2516, 2006.
11. I. R. Gabitov, R. A. Indik, N. M. Litchinitser, A. I. Maimistov, V. M. Shalaev, and J. E. Soneson. Double-resonant optical materials with embedded metal nanostructures. *J. Opt. Soc. Am. B*, 23(3):535–542, 2006.
12. P. Kockaert, P. Tassin, G. van der Sande, I. Veretennicoff, and M. Tlidi. Negative diffraction pattern dynamics in nonlinear cavities with left-handed materials. *Phys. Rev. A*, 74(3):033822, 2006.
13. V. A. Kalinin and V. V. Shtykov. On the possibility of reversing the front of radio waves in an artificial nonlinear medium. *J. Commun. Technol. Electron.*, 36:96–102, 1991. (Originally in: *Radiotekhnika i Elektronika*, 11:2275–2281, 1990).
14. J. B. Pendry, A. J. Holden, D. J. Robbins, and W. J. Stewart. Magnetism from conductors and enhanced nonlinear phenomena. *IEEE Trans. Microw. Theory Tech.*, 47:2075–2084, 1999.
15. M. W. Klein, C. Enkrich, M. Wegener, C. M. Soukoulis, and S. Linden. Single-slit split-ring resonators at optical frequencies: Limits of size scaling. *Opt. Lett.*, 31:1259–1261, 2006.
16. N. I. Zheludev and V. I. Emel'yanov. Phase matched second harmonic generation from nanostructured metallic surfaces. *J. Opt. A: Pure Appl. Opt.*, 6(1):26–28, 2004.
17. C. Caloz, I. Lin, and T. Itoh. Characteristics and potential applications of nonlinear left-handed transmission lines. *Microw. Opt. Technol. Lett.*, 40(6):471–473, 2004.
18. A. B. Kozyrev, H. Kim, A. Karbassi, and D. W. van der Weide. Wave propagation in nonlinear left-handed transmission line media. *Appl. Phys. Lett.*, 87:121109, 2005.
19. L. D. Landau and E. M. Lifschitz. *Electrodynamics of Continuous Media*. Pergamon Press, Oxford, 1984.
20. M. I. Ryazanov. *Condensed Matter Electrodynamics*. Nauka, Moscow, 1984.
21. V. M. Agranovich and V. L. Ginzburg. *Spatial Dispersion in Crystal Optics and the Theory of Excitons*. Wiley, New York, 1967.
22. R. A. Shelby, D. R. Smith, S. C. Nemat-Nasser, and S. Schultz. Microwave transmission through a two-dimensional, isotropic, left-handed metamaterial. *Appl. Phys. Lett.*, 78:489–491, 2001.
23. E. Shamonina, M. Lapine, K. H. Ringhofer, and L. Solymar. In *Proceedings of the Progress in Electromagnetics Research Symposium*, Cambridge, MA, USA, p. 249, 2002.
24. R. Marqués, F. Medina, and R. Rafii-El-Idrissi. Role of bianisotropy in negative permeability and left-handed metamaterials. *Phys. Rev. B*, 65:144440, 2002.
25. M. Shamonin, E. Shamonina, V. Kalinin, and L. Solymar. Resonant frequencies of a split-ring resonator: analytical solutions and numerical simulations. *MOTL*, 44(2):133–136, 2005.
26. P. Gay-Balmaz and O. J. F. Martin. Electromagnetic resonances in individual and coupled split-ring resonators. *J. Appl. Phys.*, 92(5):2929–2936, 2002.
27. M. Gorkunov, M. Lapine, E. Shamonina, and K. H. Ringhofer. Effective magnetic properties of a composite material with circular conductive elements. *Eur. Phys. J. B*, 28:263–269, 2002.
28. N. Bloembergen. *Nonlinear Optics*. Benjamin, New York, 1965.
29. M. Schubert and B. Wilhelmi. *Einführung in die nichtlineare Optik*. Teubner, Leipzig, 1971.
30. S. M. Sze. *Physics of Semiconductor Devices*. Wiley, New York, 1981.
31. J. N. Schulman, D. H. Chow, and D. M. Jang. InGaAs zero bias backward diodes for millimeter wave direct detection. *IEEE Electron. Dev. Lett.*, 22:200, 2001.
32. I. V. Shadrivov, A. A. Zharov, and Y. S. Kivshar. Second-harmonic generation in nonlinear left-handed metamaterials. *J. Opt. Soc. Am. B*, 23(3):529–534, 2006.

33. A. A. Zharov, N. A. Zharova, I. V. Shadrivov, and Y. S. Kivshar. Subwavelength imaging with opaque nonlinear left-handed lenses. *Appl. Phys. Lett.*, 87:091104, 2005.
34. M. Gorkunov, I. V. Shadrivov, and Y. S. Kivshar. Enhanced parametric processes in binary metamaterials. *Appl. Phys. Lett.*, 88:071912, 2006.
35. V. Roppo, M. Centini, D. de Ceglia, M. A. Vicenti, J. W. Haus, N. Akozbek, M. J. Bloemer, and M. Scalora. Anomalous momentum states, non-specular reflections, and negative refraction of phase-locked, second harmonic pulses. *Metamaterials*, 2(2–3):135–144, 2008.
36. M. Lapine and M. Gorkunov. Three-wave coupling of microwaves in metamaterial with nonlinear resonant conductive elements. *Phys. Rev. E*, 70:066601, 2004.
37. A. K. Popov and V. M. Shalaev. Negative-index metamaterials: Second-harmonic generation, Manley-Rowe relations and parametric amplification. *Appl. Phys. B*, 84(1–2):131–137, 2006.
38. A. B. Kozyrev, H. Kim, and D. W. van der Weide. Parametric amplification in left-handed transmission line media. *Appl. Phys. Lett.*, 88:264101, 2006.
39. O. Malyuskin, V. Fusco, and A. G. Schuchinsky. Microwave phase conjugation using nonlinearly loaded wire arrays. *IEEE Trans. Antenn. Propag.*, 54(1):192–203, 2006.
40. N. A. Zharova, I. V. Shadrivov, A. A. Zharov, and Y. S. Kivshar. Nonlinear transmission and spatiotemporal solitons in metamaterials with negative refraction. *Opt. Express*, 13(4):1291–1298, 2005.
41. I. V. Shadrivov and Y. S. Kivshar. *J. Opt. A: Pure Appl. Opt.*, 7:S68–S72, 2005.
42. A. D. Boardman, N. King, R. C. Mitchell-Thomas, V. N. Malnev, and Y. G. Rapoport. Gain control and diffraction-managed solitons in metamaterials. *Metamaterials*, 2(2–3):145–154, 2008.
43. I. V. Shadrivov, A. A. Zharov, N. A. Zharova, and Y. S. Kivshar. Nonlinear left-handed metamaterials. *Radio Sci.*, 40:RS3S90, 2005.
44. A. G. Litvak and V. A. Mironov. *Izv. VUZov: Radiofizika*, 11:1911, 1968 (in Russian).
45. I. V. Shadrivov, A. A. Sukhorukov, Y. S. Kivshar, A. A. Zharov, A. D. Boardman, and P. Egan. Nonlinear surface waves in left-handed materials. *Phys. Rev. E*, 69:016617, 2004.
46. Boardman A. D., Egan P., and Velasco L. Control of planar nonlinear guided waves and spatial solitons with a left-handed medium. *J. Opt. A: Pure Appl. Opt.*, 7(2):S57–S67, 2005.
47. A. D. Boardman, Y. G. Rapoport, N. King, and V. N. Malnev. Creating stable gain in active metamaterials. *J. Opt. Soc. Am. B*, 24(10):A53–A61, 2007.
48. E. Shamonina, V. A. Kalinin, K. H. Ringhofer, and L. Solymar. Magnetoinductive waves in one, two, and three dimensions. *J. Appl. Phys.*, 92:6252–6261, 2002.
49. F. R. Morgenthaler. Longitudinal parametric excitation of magnons in a two-sublattice ferrimagnetic crystal. *Phys. Rev. Lett.*, 11:69, 1963.
50. O. Sydoruk, O. Zhuromskyy, E. Shamonina, and L. Solymar. Phonon-like dispersion curves of magnetoinductive waves. *Appl. Phys. Lett.*, 87:072501, 2005.
51. R. R. A. Syms, L. Solymar, and I. R. Young. Three-frequency parametric amplification in magnetoinductive ring resonators. *Metamaterials*, 2(2–3):122–134, 2008.
52. O. Reynet and O. Acher. Voltage controlled metamaterial. *Appl. Phys. Lett.*, 84:1198–1200, 2004.
53. M. Gorkunov and M. Lapine. Tuning of a nonlinear metamaterial band gap by an external magnetic field. *Phys. Rev. B*, 70:235109, 2004.
54. I. V. Shadrivov, S. K. Morrison, and Y. S. Kivshar. Tunable split-ring resonators for nonlinear negative-index metamaterials. *Opt. Express*, 14(20):9344–9349, 2006.
55. D. A. Powell, I. V. Shadrivov, Y. S. Kivshar, and M. V. Gorkunov. Self-tuning mechanisms of nonlinear split-ring resonators. *Appl. Phys. Lett.*, 91:144107, 2007.
56. I. V. Shadrivov, A. B. Kozyrev, D. W. ran der Weide, Y. S. Kivshar. Tunable transmission and harmonic generation in nonlinear metamaterials. *Appl. Phys. Lett.*, 93: 161903, 2008.
57. A. K. Popov and V. M. Shalaev. Compensating losses in negative-index metamaterials by optical parametric amplification. *Opt. Lett.*, 31(14):2169–2171, 2006.
58. M. Gorkunov, S. A. Gredeskul, I. V. Shadrivov, and Y. S. Kivshar. Effect of microscopic disorder on magnetic properties of metamaterials. *Phys. Rev. E*, 73:056605, 2006.

36

Magnetoinductive Waves I: Theory

O. Sydoruk
University of Erlangen-Nuremberg

O. Zhuromskyy
University of Erlangen-Nuremberg

A. Radkovskaya
Lomonosov Moscow State University

E. Shamonina
University of Erlangen-Nuremberg

L. Solymar
Imperial College

36.1 Introduction

It has been known for quite a long time that chains of magnetically coupled resonators can support waves. Their properties were studied, for example, for applications in filters, slow wave structures, and proton accelerators [1,3,6]. In 2002, Shamonina et al. [7] pointed out that the same magnetoinductive (MI) waves propagate on chains of resonant elements constituting magnetic metamaterials. Experimental verification [17] and generalization for two and three dimensions [8] followed shortly afterward.

In this chapter, we present the basic theory of MI waves. We start in Section 36.2 with the magnetic coupling between two elements. We proceed with infinite lattices in Section 36.3 and finite arrays in Section 36.4.

We aimed here at covering a wide range of topics concerned with MI waves, introducing concepts possibly briefly. Those looking for details are encouraged to resort to original publications whose list is given at the end of the chapter. This chapter is followed by Chapter 14 of the book "*Applications of Metamaterials*" where we discuss potential applications of MI waves for signal guiding and processing, subwavelength imaging and focusing, detection, and amplification of weak signals in magnetic resonance imaging.

36.2 Magnetic Coupling between Resonant Elements

Although in general quite complicated, the properties of metamaterial elements can be in many cases described by only three parameters: self-inductance, L; self-capacitance, C; and self-resistance, R. The inductance and capacitance determine the resonant frequency:

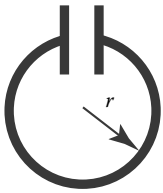

FIGURE 36.1 Capacitively loaded loop.

$$\omega_0 = \frac{1}{\sqrt{LC}} \tag{36.1}$$

and the resistance characterizes losses, which are also often described by the quality factor:

$$Q = \frac{1}{R}\sqrt{\frac{L}{C}}\,. \tag{36.2}$$

We assume that the elements are circular loops made up of metallic wires, and that currents along the elements are uniformly distributed.* Capacitively loaded loop, shown schematically in Figure 36.1, is the simplest practical realization. The radius of the loop and the cross-section of the metallic wire determine the inductance. The resonant frequency can be varied then by changing the value of the load capacitance.

A current-carrying loop produces a magnetic field. If two such loops are put close to each other then the magnetic field of the first loop can create a nonzero flux through the surface of the second one. This is the mechanism of magnetic coupling between the elements. Its quantitative measure is the mutual inductance, M, defined as [4,9]

$$M = \frac{\Phi_{12}}{I_2} = \frac{\Phi_{21}}{I_1}\,, \tag{36.3}$$

where

Φ_{12} is the magnetic flux from the first element through the surface of the second one
Φ_{21} is the magnetic flux from the second element through the surface of the first one
I_1 and I_2 are the currents in the first and second element, respectively

If the wavelength is small enough to neglect retardation effects, M is purely real. For identical elements we shall often use a normalized quantity, the coupling constant, defined as

$$\kappa = \frac{2M}{L}\,. \tag{36.4}$$

The sign and the absolute value of the mutual inductance depend on the form, relative position, and orientation of the elements. The expressions for the mutual inductance for circular loops available in literature [4,9] can be easily generalized for the case of arbitrary radiuses and orientations. Let us consider several configurations that we will use later. The elements chosen are two identical loops of radius $r = 10$ mm made of metallic wires of circular cross section of radius 1 mm. Their self-inductance is then found as $L = 33$ nH.

In our first example, the elements are in the axial configuration: their centers lie on an axis that is perpendicular to the planes of both elements as shown in the inset to Figure 36.2a. The value of

* It is true if the circumference of the loops is much smaller than the electromagnetic wavelength.

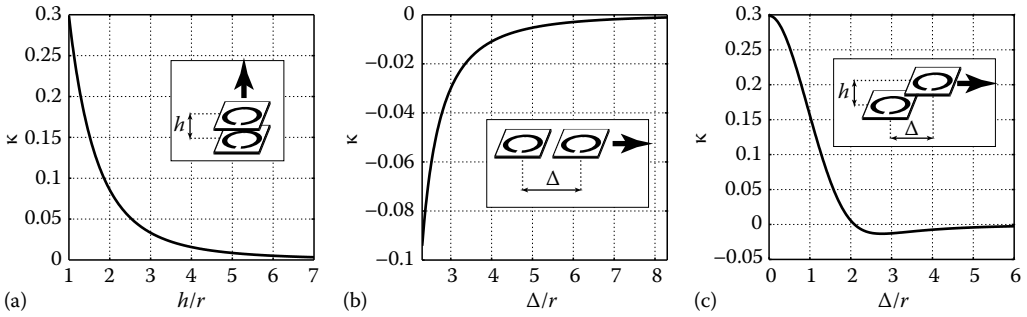

FIGURE 36.2 Coupling constant between a pair of circular loops for different configurations: axial (a), planar (b), and mixed (c).

the coupling constant, κ, as a function of the distance between the elements' centers, h, is shown in Figure 36.2a. It can be seen that the coupling constant is positive and it decreases with h.

In the second example, the elements are in the planar configuration: they lie in the same plane as shown in the inset to Figure 36.2b. The value of the coupling constant as a function of the distance between the elements' centers, Δ, is shown in Figure 36.2b. Now κ is negative; its absolute value is larger for smaller separation between the loops.

In the third example, the elements are in a mixed configuration: they lie in two parallel planes with the separations h and Δ between the centers as shown in Figure 36.2c. The distance h is fixed at the value $h = r$. The value of the coupling constant as a function of Δ is shown in Figure 36.2c. Its behavior is now more complicated: the coupling constant is positive for $\Delta < 2r$ and negative for $\Delta > 2r$.

36.3 Infinite Lattices

Infinite lattices of interacting elements may support waves. A prominent example, known from most undergraduate courses in solid-state physics, is a chain of particles connected by mechanical springs. This is the simplest model leading to propagation of acoustic waves and to the dispersion of phonons in solid. Analogously, the coupling between magnetic metamaterial elements leads to propagation of MI waves. We shall start the discussion of their properties with one-dimensional arrays for which interaction between only nearest neighbors is present. Then we generalize the treatment, first, by including higher-order interactions and, second, by considering two- and three-dimensional arrays.

36.3.1 Dispersion for One-Dimensional Arrays

Schematic presentations of an axial and a planar one-dimensional array of metamaterial elements are shown in Figure 36.3a and b. As shown in Section 36.2, the value of the mutual inductance between two elements declines fast as the distance between them increases. One can, therefore, account only for coupling between the nearest-neighbors in an array. The corresponding equivalent circuit is shown in Figure 36.3c. For harmonic variation of signals with the frequency ω we can write Kirchhoff's equation for the voltage drop in the nth element as

$$\left(j\omega L + \frac{1}{j\omega C} + R\right) I_n + j\omega M\left(I_{n+1} + I_{n-1}\right) = 0\,, \tag{36.5}$$

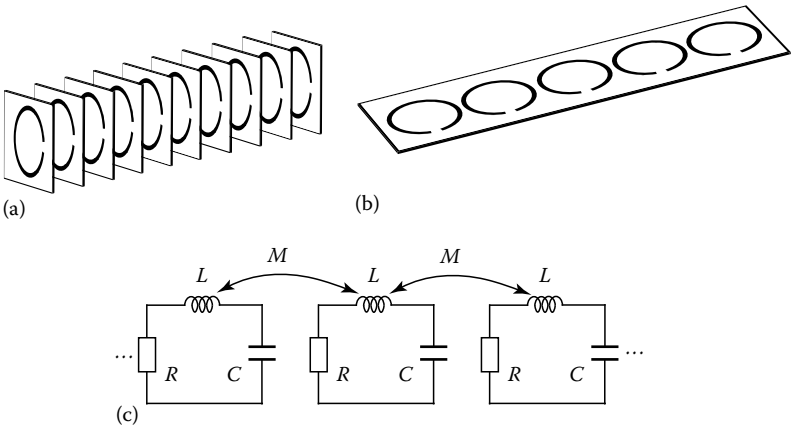

FIGURE 36.3 Schematic presentation of an axial (a) and planar (b) one-dimensional arrays supporting MI waves and their equivalent circuit (c).

where

I_n, I_{n+1}, and I_{n-1} are the currents in the nth, $(n+1)$th, and $(n-1)$th elements, respectively
j is complex unity

The solutions are in the form of a traveling wave

$$I = I_0 \exp(-jka)\,, \tag{36.6}$$

where

k is the wave number
a is the period of the array

Substituting Equation 36.6 into Equation 36.5 the dispersion relation for MI waves is obtained in the form

$$j\omega L + \frac{1}{j\omega C} + R + 2j\omega M \cos ka = 0\,. \tag{36.7}$$

In the presence of losses, k is complex and can be written in the form $k = \beta - j\alpha$ with the propagation, β, and the attenuation, α, coefficients. For low losses

$$\omega = \frac{\omega_0}{\sqrt{1 + \kappa \cos \beta a}}, \tag{36.8}$$

and

$$\alpha a = \frac{1}{Q\kappa \sin \beta a}\,. \tag{36.9}$$

As follows from Equation 36.8, MI waves can propagate in the frequency region:

$$\frac{1}{\sqrt{1+|\kappa|}} < \frac{\omega}{\omega_0} < \frac{1}{\sqrt{1-|\kappa|}}\,. \tag{36.10}$$

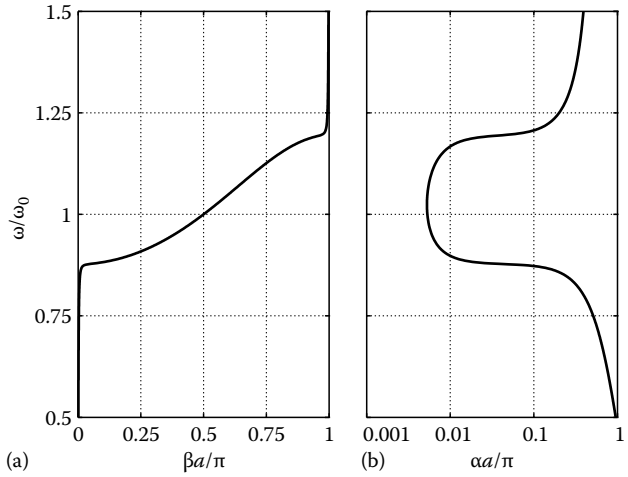

FIGURE 36.4 Dispersion of MI waves for an axial array: propagation coefficient (a) and attenuation coefficient (b).

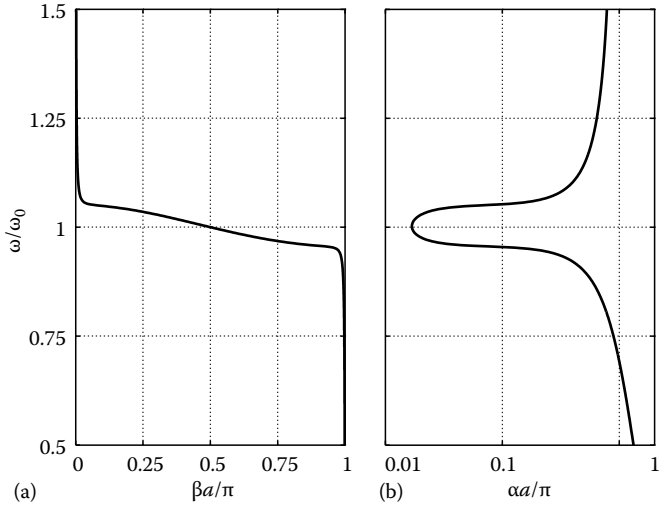

FIGURE 36.5 Dispersion of MI waves for a planar array: propagation coefficient (a) and attenuation coefficient (b).

Figure 36.4 shows the dispersion for an axial array. For the elements we have taken loops described in the previous section with self-inductance $L = 33$ nH. The period of the array is $a = 11$ mm, yielding $\kappa = 0.3$. The resonant frequency $\omega_0/(2\pi) = 63.87$ MHz is obtained by taking $C = 188$ pF. The quality factor is 200. In axial arrays, MI waves are forward waves.

Figure 36.5 shows the dispersion curves for a planar array. The inductance, capacitance, and quality factor are the same as in the previous example. For the period of the array, which cannot be now smaller than the diameter of the loop, we take $a = 23$ mm yielding $\kappa = -0.1$. MI waves are now backward waves. Since the absolute value of the coupling constant is here smaller than in the previous example, the pass band for MI waves is narrower (compare Figures 36.4 and 36.5).

36.3.2 Dispersion in the Case of Higher-Order Interactions

For small separation between the elements, higher-order interactions may also play a role. Interaction between the element m and the element n in an array is characterized by the coupling constant of pth order, κ_p with $p = |m - n|$. Note that nearest-neighbor coupling constant is the first-order one in this notation. The generalization of the dispersion equation is straightforward [8]. Its simplest form is

$$\omega = \frac{\omega_0}{\sqrt{1 + \sum_{p=1}^{\infty} \kappa_p \cos p\beta a}}. \tag{36.11}$$

This equation is more difficult to analyze than Equation 36.8 for nearest neighbors only, and therefore, it is recommended to fabricate arrays with negligible higher-order couplings. A possible solution is to use elongated elements, as suggested in Ref. [16]. A detailed experimental and theoretical study of the higher-order interactions can be found in Ref. [15].

36.3.3 Dispersion for Two- and Three-Dimensional Lattices: Negative Refraction

A two-dimensional configuration is shown schematically in Figure 36.6a. The elements are arranged into a square lattice with the period a. Along the y-axis the elements are in the axial configuration with the positive coupling constant between the nearest neighbors, κ_y. Along the x-axis they are in the planar configuration with the negative coupling constant, κ_x. For simplicity, we shall neglect higher-order mutual inductances and assume lossless elements. The dispersion equation then takes the form

$$\omega = \frac{\omega_0}{\sqrt{1 + \kappa_x \cos \beta_x a + \kappa_y \cos \beta_y a}}. \tag{36.12}$$

The first Brillouin zone, reflecting the symmetry of the system, has a square shape. The corresponding dispersion diagram is shown in Figure 36.6b by isofrequency curves ($a = 23$ mm, $\kappa_x = -0.1$, $\kappa_y = 0.06$, and the remaining parameters taken from the previous examples).

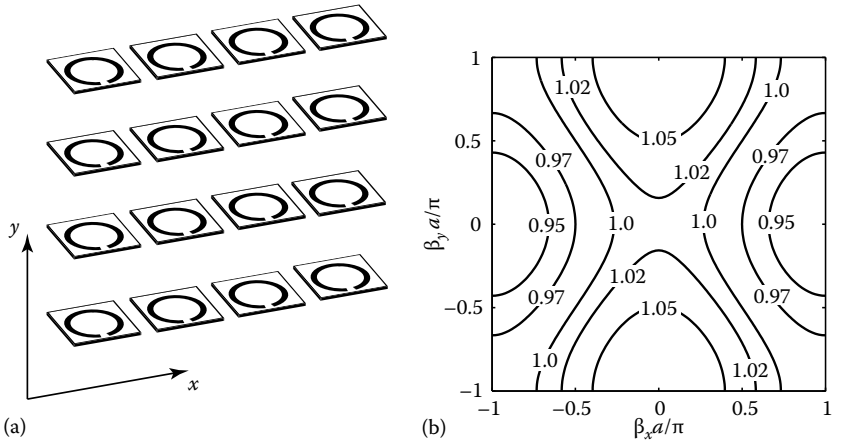

FIGURE 36.6 Schematic presentation of a two-dimensional array (a) and the corresponding dispersion of MI waves (b). The numbers on the isofrequency curves are the ratio ω/ω_0.

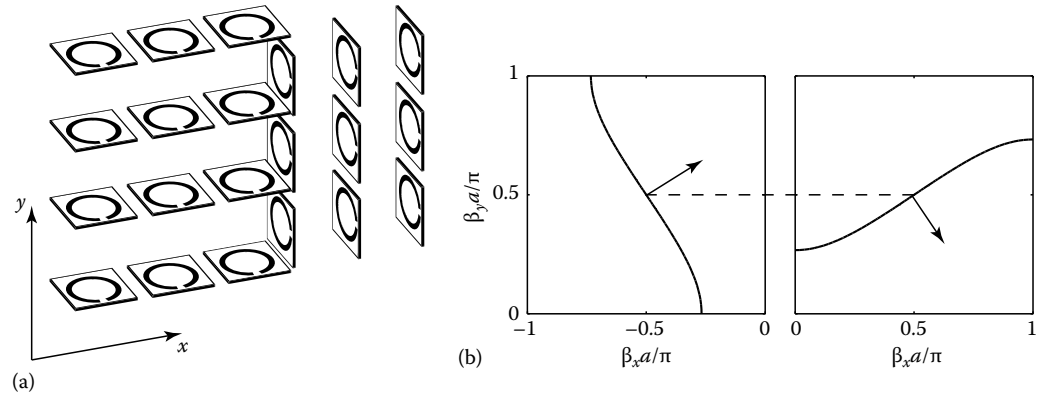

FIGURE 36.7 Negative refraction of MI waves at the boundary of two-dimensional arrays. Schematic presentation of a configuration (a) and the direction of the group velocity in the right-hand side and left-hand side arrays for $\omega = \omega_0$ and $\beta_{\text{left}} a/\pi = (-0.5, 0.5)$.

A boundary between two two-dimensional arrays is shown in Figure 36.7a. Structurally both arrays are identical but the array on the right-hand side is rotated by 90°. A MI wave incident on the boundary (say, from the left-hand side) will refract; the refracted wave should satisfy the boundary condition $\beta_{y\,\text{left}} = \beta_{y\,\text{right}}$. The relation between $\beta_{x\,\text{left}}$ and $\beta_{x\,\text{right}}$ is then determined by the dispersion equation. Let us take a wave at the frequency ω_0 that in the array on the left-hand side has the propagation constant $\beta_{\text{left}} a/\pi = (-0.5, 0.5)$. The group velocity is perpendicular to the corresponding isofrequency curve; its direction is shown by the arrow on the left-hand side diagram in Figure 36.7b. To satisfy the boundary conditions the refracted wave in the array on the right-hand side should have the propagation constant $\beta_{\text{right}} a/\pi = (0.5, 0.5)$. The angle between the group velocities determines the angle of refraction, and it is negative in Figure 36.7b. A more detailed study of positive and negative refraction of MI waves can be found in Ref. [14].

36.3.4 Coupled Arrays

In the discussion above, we have everywhere assumed identical elements. A unit cell, however, can contain an arbitrary number of elements [2]. The simplest, but nevertheless important, example is arrays with two resonant elements per unit cell. Suggested from the analogy between MI waves and acoustic waves in solids, they got the name "diatomic arrays" [11].

General "diatomic" configurations can be formed by two coupled arrays. A schematic presentation of two coupled arrays is shown in Figure 36.8a. A unit cell consists of two elements, one exactly above the other. The mutual inductance between the elements in a unit cell, M, is, therefore, positive. Both the upper and lower elements are coupled to the elements from the neighboring unit cells. In the simplest case, it is sufficient to take into account a single mutual inductance, M_1, between nearest neighbors in the top and bottom lines. Since the elements of the top and of the bottom lines are in the planar configuration, M_1 is negative.

The corresponding MI wave dispersion relation can be written as [10]:

$$\left(j\omega L + \frac{1}{j\omega C_1} + R_1 + 2j\omega M_1 \cos ka\right)\left(j\omega L + \frac{1}{j\omega C_2} + R_2 + 2j\omega M_1 \cos ka\right) = -\omega^2 M\,. \qquad (36.13)$$

The elements have the same form and, hence, equal self-inductances, but note that the capacitances of the elements in the top, C_1, and bottom, C_2, lines can be different, yielding two different

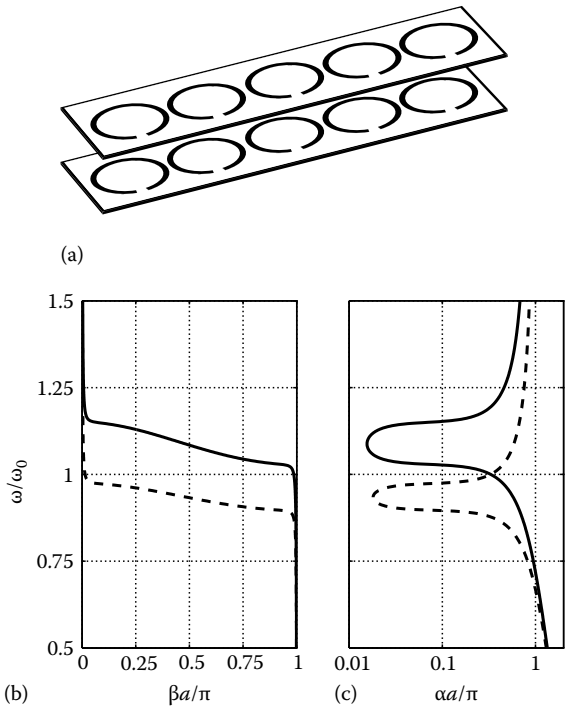

FIGURE 36.8 Schematic presentation of two coupled arrays (a): propagation (b) and attenuation (c) coefficients for MI waves.

resonant frequencies. The resistances of the elements from the top and bottom lines are denoted by R_1 and R_2, respectively. Equation 36.13 is in the form of coupled wave equations with the coupling coefficient $-\omega^2 M$. If $M = 0$ then the expressions in the brackets on the left-hand side are independently equal to zero giving the dispersion relations for MI waves in uncoupled arrays.

The dispersion curves of the coupled arrays of Figure 36.8a are shown. The parameters of the elements are, as in previous examples, $L = 33$ nH, $C_1 = C_2 = 188$ pF, $Q_1 = Q_2 = 200$. The vertical separation between the lines is 10 mm giving $\kappa = 2M/L = 0.3$, and the period of the array is 23 mm giving $\kappa_1 = 2M_1/L = -0.1$. The dispersion has now two branches that originate from two identical uncoupled dispersion curves (see Figure 36.5) shifting upwards and downwards from their initial position.

Changing the resonant frequency of the elements and the coupling between them it is possible to tailor the dispersion of MI waves in coupled arrays. In particular, conditions for phase matching between a signal and pump MI waves, required for parametric amplification, can be satisfied. We shall return to this problem in Chapter 14 of *Applications of Metamaterials*.

Note also that the coupling coefficient in Equation 36.13 is constant. In the general case, it can depend on the value of ka leading to more complicated dispersion (for more detail, see Ref. [10]).

36.3.5 Experimental Verification

Theoretically predicted dispersion relations were verified in a number of experimental studies. In 2003, Wiltshire et al. [17] investigated one-dimensional planar and axial arrays made up by capacitively loaded loops. In 2004, they studied experimentally the propagation of MI waves in arrays made up of Swiss rolls [18]. In another experimental study concerned with higher-order interactions [15], a dispersion curve has been successfully obtained from measurements on a 30-element array.

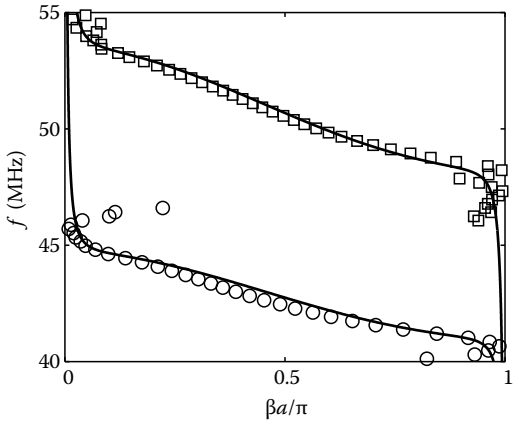

FIGURE 36.9 Experimentally determined (circles and squares) and theoretically predicted (solid lines) dispersion relation for a diatomic array.

Propagation of MI waves in coupled arrays was studied experimentally in Refs. [5,10] for a number of configurations. Experimental and theoretical dispersion curves for the configuration of Figure 36.8a are shown in Figure 36.9. The elements were split pipes loaded by bulk capacitors. The resonant frequency of the elements was $\omega/(2\pi) = 46.2 \pm 0.2$ MHz, and the quality factor $Q = 105 \pm 5$. The period of the array was $a = 24$ mm, and the distance between the top and bottom lines was $h = 10$ mm, yielding the mutual inductances in Equation 36.13 as $M_1 = -0.045L$ and $M = 0.15L$. The experimental dispersion was determined from the values of currents in six neighboring elements in order to take reflections into account.

36.4 Finite Arrays

As we have seen above, the properties of MI waves in infinite arrays can be exhaustively described by a dispersion relation. Practical realizations are, of course, finite giving rise to the boundary and excitation problems. In principle, any excitation (e.g., in form of an external voltage source) can be imposed on arbitrary elements of an array. Consequently, there are no traveling waves in the general case, and the dispersion relation cannot be used to determine the currents.

36.4.1 Impedance Matrix

The currents in finite arrays can be determined by resorting to an impedance matrix which is constructed as follows [4]. For all elements of an array, it is possible to write Kirchhoff's equations similar to Equation 36.5 taking the external voltages into account. They all can be written in a compact matrix form:

$$\mathbf{ZI} = \mathbf{V}, \tag{36.14}$$

where

I is a vector of currents in the elements
V is the vector of the corresponding voltages
Z is the impedance matrix

Its main diagonal contains the self-impedances of the elements and the off-diagonal elements contains the mutual impedances:

$$\mathbf{Z} = \begin{pmatrix} Z_{\text{self }1} & Z_{\text{mut }1,2} & \cdots & Z_{\text{mut }1,m} & \cdots & Z_{\text{mut }1,N} \\ Z_{\text{mut }1,2} & Z_{\text{self }2} & Z_{\text{mut }2,3} & \cdots & Z_{\text{mut }2,n} & \vdots \\ Z_{\text{mut }1,3} & Z_{\text{mut }2,3} & Z_{\text{self }3} & Z_{\text{mut }3,4} & \cdots & \vdots \\ \vdots & \ddots & \ddots & \ddots & \ddots & \vdots \\ \vdots & \cdots & \cdots & \ddots & \ddots & Z_{\text{mut }(N-1),N} \\ Z_{\text{mut }1,N} & \cdots & Z_{\text{mut }m,N} & \cdots & Z_{\text{mut }(N-1),N} & Z_{\text{self }N} \end{pmatrix}, \tag{36.15}$$

where

$Z_{\text{self }n} = j\omega L_n + 1/(j\omega C_n) + R_n$ and $Z_{\text{mut }m,n} = Z_{\text{mut }n,m} = j\omega M_{mn}$ $(m, n = 1 \ldots N)$

N is the total number of elements

This form of the impedance matrix can be applied for one-, two-, and three-dimensional arrays; it takes coupling between all the elements into account. For a given excitation, the currents are found by inverting Equation 36.14:

$$\mathbf{I} = \mathbf{Z}^{-1}\mathbf{V}\,. \tag{36.16}$$

36.4.2 Boundary Conditions: Terminal Impedances

In one-dimensional waveguides, the power is transferred from the first to the last element. It will be totally absorbed in the last element if there is no reflection from the end, or in other words, if there is a traveling MI wave of the form $I_n = I_0 \exp(-jka)$. If only nearest neighbors are taken into account then the last element should be loaded by a matching impedance, Z_T, whose value can be found as [8]

$$Z_T = j\omega M \exp(-jka)\,. \tag{36.17}$$

The value of the matching impedance is generally complex (it is purely resistive only at the resonant frequency, for which $\beta a = \pm \pi/2$) and frequency dependent. The current distributions for the properly matched axial and planar arrays consisting each of 25 elements with the parameters from Section 36.3.1 are shown in Figure 36.10a and b. The value of the propagation constant chosen

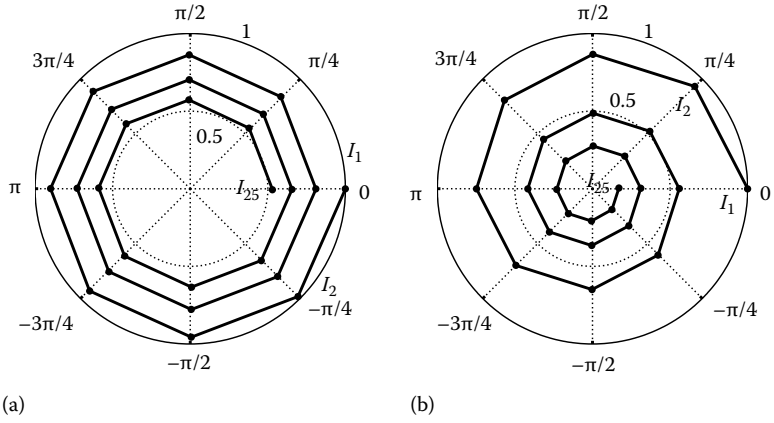

FIGURE 36.10 Current distributions in the axial (a) and planar (b) arrays of 25 elements.

is $|\beta|a = \pi/4$. It can be seen that the current distributions are spirals corresponding to lossy traveling waves. The losses for the planar array are larger than for the axial one, in accordance with Figures 36.4 and 36.5.

For significant higher-order interactions a single matching impedance cannot satisfy conditions for traveling wave propagation; for interactions up to pth order, matching impedances should be inserted in the last p elements of the array. Since it is not easily realizable in practice, reflections from the end should be taken into account [13].

36.5 Interaction with Electromagnetic Waves

We have so far considered MI waves independently of electromagnetic waves. The excitation was in the form of voltage sources put in one or several elements of an array. What happens if an electromagnetic wave is incident upon a magnetic metamaterial supporting MI waves?

Interaction of electromagnetic waves with magnetic metamaterials was considered in a number of recent studies. The customary approach is based on an effective medium theory, where the interaction is described in terms of an effective magnetic permeability. The magnetic permeability is usually frequency dependent and may reach both positive and negative values. We shall, however, resort here to a different approach based on transmission line theory [12] and look at the simplest, one-dimensional, case. A schematic presentation of an electromagnetic wave incident upon a planar metamaterial array is shown in Figure 36.11a. The magnetic field is perpendicular to the plane of the loops allowing for

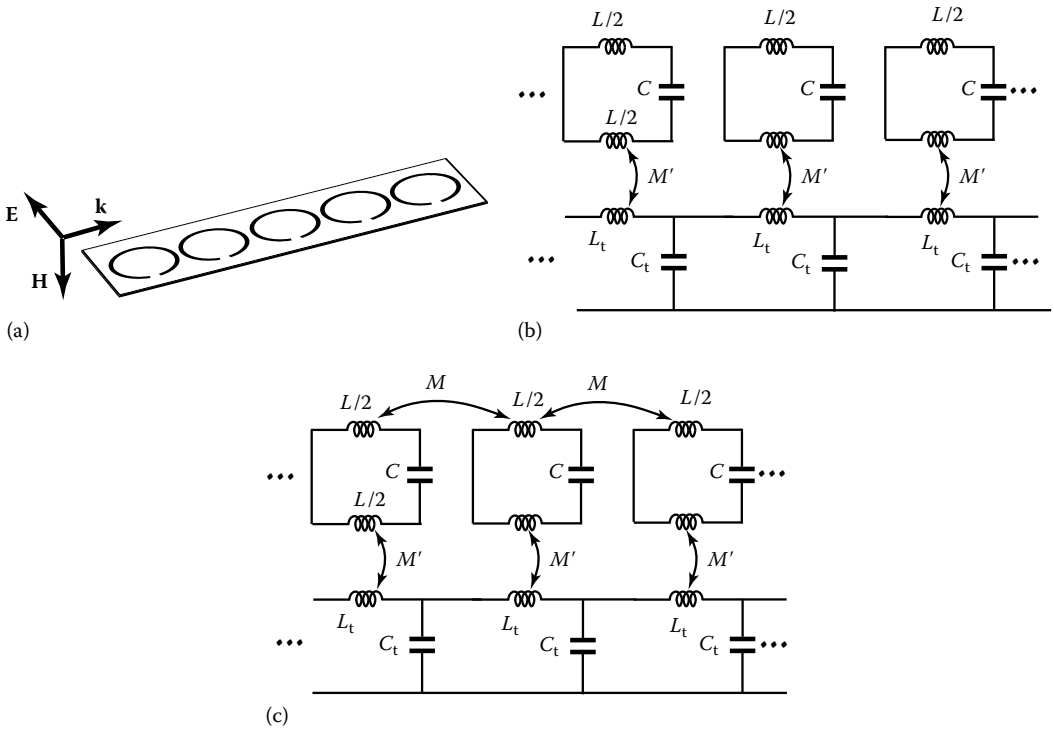

FIGURE 36.11 (a) Schematic presentation of an electromagnetic wave propagating along a planar array of metamaterial elements; equivalent circuit of a transmission line loaded by metamaterial elements without (b) and with (c) interaction between the resonant elements.

the excitation of current; the wave vector is directed along the array. The electromagnetic wave is presented by an *LC* transmission line in Figure 36.11b and c. The values of the inductance, L_t, and capacitance, C_t per unit length are

$$L_t = \mu_0 a \quad \text{and} \quad C_t = \varepsilon_0 a\,, \tag{36.18}$$

where

μ_0 and ε_0 are the permeability and permittivity of free space
a is the period of the array

The metamaterial elements are presented by resonant *LC* circuits in Figure 36.11b and c (the losses are neglected). The coupling between the electromagnetic wave and the elements is presented by the mutual inductance M':

$$M' = \frac{\pi r_0^2 \mu_0}{a}\,, \tag{36.19}$$

where r_0 is the radius of an element.

We shall consider here two cases. In the first one, shown in Figure 36.11b, the individual elements are uncoupled, and, consequently, MI waves are not supported by the array. The dispersion equation has in this case the form [12]

$$\left[\omega^2 - \omega_0^2\right]\left[\omega^2 - 4\omega_t^2 \sin^2 \frac{ka}{2}\right] = q^2\omega^4\,, \tag{36.20}$$

where ω_0 is the resonant frequency of the metamaterial elements:

$$\omega_t = \frac{1}{\sqrt{L_t C_t}}\,,$$

and

$$q = \frac{M'}{\sqrt{L_t L}}\,.$$

In the second case, shown in Figure 36.11c, the metamaterial elements are coupled to each other via the mutual inductance, M. The dispersion equation then takes the form

$$\left[\omega^2(1 + \kappa\cos(ka)) - \omega_0^2\right]\left[\omega^2 - 4\omega_t^2 \sin^2 \frac{ka}{2}\right] = q^2\omega^4. \tag{36.21}$$

The difference between Equations 36.20 and 36.21 is the term "$1 + \kappa\cos(ka)$" in the left-hand side bracket of Equation 36.21. It is responsible for the magnetic interaction between the elements. If $q = 0$ then Equation 36.21 yields two waves propagating independently of each other: one is the pure electromagnetic wave and the other is the MI wave.

We shall now plot the dispersion relations given by Equations 36.20 and 36.21 using the numerical parameters from Section 36.3.1 (see Figure 36.5) yielding $q = 0.56$ and $\omega_t/\omega_0 = 32.5$. The dispersion curves are shown in Figure 36.12. Figure 36.12a shows the Brillouin zone up to $ka/\pi = 0.1$. It can be seen that coupling of the electromagnetic wave to the resonant elements leads to stop bands in both, coupled and uncoupled, cases. The stop band for the coupled case (solid lines) moves up in frequency compared to the uncoupled case (dotted lines). Another difference can be seen from Figure 36.12b, where the full Brillouin zone is shown. For high values of ka, the dispersion curve for the uncoupled case degenerates into a line $\omega = \omega_0$, whereas the dispersion curve for the coupled case follows the trend of a backward MI wave. There is a point around $ka = 0.1\pi$, where the group velocity is zero for the coupled case. It also should be noted that the dispersion relations (Equations 36.20 and 36.21) have been obtained in the quasistatic approximation neglecting retardation effects.

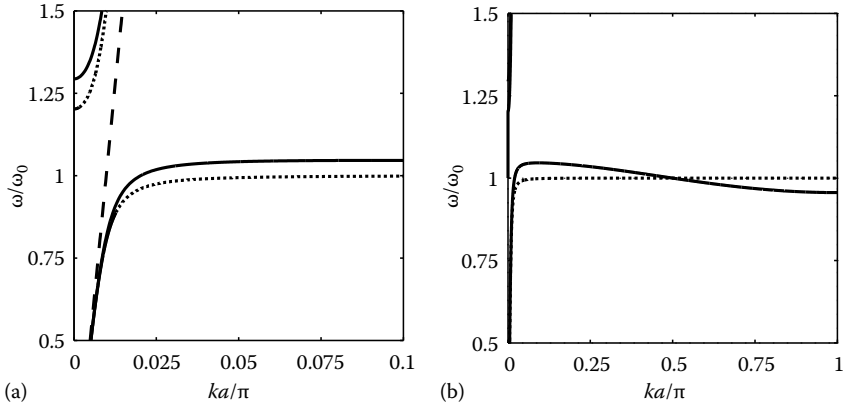

FIGURE 36.12 Dispersion diagrams predicted by Equation 36.20 (dotted lines) and Equation 36.21 (solid lines): (a) the first Brillouin zone up to $ka/\pi = 0.1$, (b) the full first Brillouin zone. Also shown is the light line (dashed line).

References

1. G. I. Atabekov. *Linear Network Theory*. Pergamon Press, Oxford, 1965.
2. L. Brillouin. *Wave Propagation in Periodic Structures*. Dover, New York, 1953.
3. B. C. Knapp, E. A. Knapp, G. J. Lucas, and J. M. Potter. Resonantly coupled accelerating structures for high-current proton Linacs. *IEEE Trans. Nucl. Sci.*, 12:159–165, 1965.
4. L. D. Landau and E. M. Lifschitz. *Electrodynamics of Continuous Media*. Pergamon Press, Oxford, 1984.
5. A. Radkovskaya, O. Sydoruk, M. Shamonin, E. Shamonina, C. J. Stevens, G. Faulkner, D. J. Edwards, and L. Solymar. Experimental study of a bi-periodic magnetoinductive waveguide: Comparison with theory. *IET Microw. Antennas Propag.*, 1:80–83, 2007.
6. R. A. Silin and V. P. Sazonov. *Slow Wave Structures*. National Lending Library for Science and Technology, Boston SPA, U.K., 1971.
7. E. Shamonina, V. A. Kalinin, K. H. Ringhofer, and L. Solymar. Magneto-inductive waveguide. *Electron. Lett.*, 38:371–373, 2002.
8. E. Shamonina, V. A. Kalinin, K. H. Ringhofer, and L. Solymar. Magnetoinductive waves in one, two, and three dimensions. *J. Appl. Phys.*, 92:6252–6261, 2002.
9. L. Solymar. *Lectures on Electromagnetic Theory*. Oxford University Press, Oxford, 1976.
10. O. Sydoruk, A. Radkovskaya, O. Zhuromskyy, E. Shamonina, M. Shamonin, C. J. Stevens, G. Faulkner, D. J. Edwards, and L. Solymar. Tailoring the near-field guiding properties of magnetic metamaterials with two resonant elements per unit cell. *Phys. Rev. B.*, 73:224406-1–224406-12, 2006.
11. O. Sydoruk, O. Zhuromskyy, E. Shamonina, and L. Solymar. Phonon-like dispersion curves for magnetoinductive waves. *Appl. Phys. Lett.*, 87:072501-1–072501-3, 2005.
12. R. R. A. Syms, E. Shamonina, V. Kalinin, and L. Solymar. A theory of metamaterials based on periodically loaded transmission lines: Interaction between magnetoinductive and electromagnetic waves. *J. Appl. Phys.*, 97:064909-1–064909-6, 2005.
13. R. R. A. Syms, E. Shamonina, and L. Solymar. Absorbing terminations for magneto-inductive waveguides. *IEE Proc. Microw. Antennas Propag.*, 152:77–82, 2005.
14. R. R. A. Syms, E. Shamonina, and L. Solymar. Positive and negative refraction of magnetoinductive waves in two dimensions. *Eur. Phys. J. B*, 46:301–308, 2005.
15. R. R. A. Syms, O. Sydoruk, E. Shamonina, and L. Solymar. Higher order interactions in magneto-inductive waveguides. *Metamaterials*, 1:44–51, 2007.

16. R. R. A. Syms, I. R. Young, and L. Solymar. Low-loss magneto-inductive waveguides. *J. Phys. D: Appl. Phys.*, 39:3945–3951, 2006.
17. M. C. K. Wiltshire, E. Shamonina, I. R. Young, and L. Solymar. Dispersion characteristics of magneto-inductive waves: Comparison between theory and experiment. *Electron. Lett.*, 39:215–217, 2003.
18. M. C. K. Wiltshire, E. Shamonina, I. R. Young, and L. Solymar. Experimental and theoretical study of magneto-inductive waves supported by one-dimensional arrays of "Swiss Rolls." *J. Appl. Phys.*, 95:4488–4493, 2004.